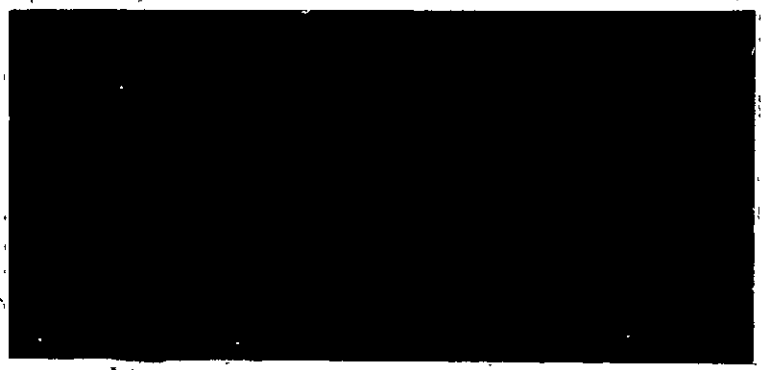


E76-10076  
CR-144537

"Made available under NASA sponsorship  
in the interest of early and wide dis-  
semination of Earth Resources Survey  
Program information and without liability  
for any use made thereof."

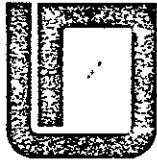


(E76-10076) DESIGN DATA COLLECTION WITH SKYLAB MICROWAVE RADIOMETER-SCATTEROMETER S-193, VOLUME 1 Final Report (Kansas Univ. Center for Research, Inc.) 682 p HC \$16.25 N76-14559  
CSCI 08B G3/43 00076 Unclas



THE UNIVERSITY OF KANSAS CENTER FOR RESEARCH, INC.  
2385 Irving Hill Rd.—Campus West • Lawrence, Kansas 66044





THE UNIVERSITY OF KANSAS SPACE TECHNOLOGY CENTER  
Raymond Nichols Hall

2291 Irving Hill Drive—Campus West Lawrence, Kansas 66045

Telephone:

Remote Sensing Laboratory  
RSL Technical Report 243-12

DESIGN DATA COLLECTION WITH SKYLAB  
MICROWAVE RADIOMETER-SCATTEROMETER S-193

Final Report

NASA Contract NAS 9-13331

Volume 1

Prepared for:

Principal Investigations Management Office  
Technical Monitor: Mr. Larry B. York  
NASA Lyndon B. Johnson Space Center  
Houston, Texas 77058

Prepared by:

Richard K. Moore, Principal Investigator  
Fawwaz T. Ulaby, Co-Principal Investigator  
Arun Sobti, Project Engineer  
Saad T. Ulaby, Research Technician  
Evan C. Davison, Research Technician  
Samut Siriburi, Research Assistant  
University of Kansas Center for Research, Inc.  
Remote Sensing Laboratory  
Lawrence, Kansas 66045

**ORIGINAL CONTAINS  
COLOR ILLUSTRATIONS**

Original photography may be purchased from  
EROS Data Center  
10th and Dakota Avenue  
Sioux Falls, SD 57198



THE UNIVERSITY OF KANSAS SPACE TECHNOLOGY CENTER  
Raymond Nichols Hall

2291 Irving Hill Drive—Campus West Lawrence, Kansas 66045

Telephone:

Title of Investigation: Design Data Collection with Skylab/EREP Microwave  
Instrument S-193

Title of Report: Design Data Collection with Skylab Microwave Radiometer-  
Scatterometer S-193 -- Final Report

RSL Technical Report 243-12

September, 1975

NASA Contract NAS 9-13331

EREP Investigation: 549 M

Prepared for:

Principal Investigations Management Office  
Technical Monitor: Mr. Larry B. York  
NASA Lyndon B. Johnson Space Center  
Houston, Texas 77058

Prepared by:

Richard K. Moore, Principal Investigator  
Fawwaz T. Ulaby, Co-Investigator  
Arun Sobti, Project Engineer  
Saad T. Ulaby, Research Technician  
Evan C. Davison, Research Technician  
Samut Siriburi, Research Assistant  
University of Kansas Center for Research, Inc.  
Remote Sensing Laboratory  
Lawrence, Kansas 66045

Type of Report: Final Report

## TABLE OF CONTENTS

	<u>Page</u>
1. Introduction	1
2. Contractual Summary	3
3. Pre-mission Activities	4
3.1 Summary	4
3.2 Analysis of Sensor	5
3.3 Study of Atmospheric Effect upon S-193 Radscat Signals	5
3.4 Summary of Previous Microwave Measurements	6
4. Activities During Mission	7
5. Post-mission Activities	7
5.1 Data Description and Analysis	7
5.2 Summary of Principal Results	7
5.2.1 Summary of Ensemble Statistics	13
5.2.2 Design Data for Radar Systems	18
5.3 Other Statistical Analyses of S-193 Data	20
5.4 Special Site Studies	20
5.5 Comparison of S-193 Radscat Data with Simple Theoretical Models	22
5.6 Image-like Display of S-193 Radscat Data	23
6. Conclusions Relevant to Future Missions and Sensors	23
7. Publications and Presentations Under This Contract	26

## APPENDICES

- A. Terrain Response to an Orbiting Microwave Radiometer/Scatterometer (703 pp.)
- B. Cluster Analysis of Skylab Radiometer and Scatterometer Data (26 pp.)
- C. Backscatter Response at 13.9 GHz For Major Terrain Types As Seen From Orbit (21 pp.)
- D. Satellite Microwave Observations of the Utah Great Salt Lake Desert (34 pp.)
- E. Preliminary Results from SL-4 (Winter) Measurements with the Skylab S-193 Radiometer/Scatterometer (9 pp.)
- F. Microwave Scattering Measurements Over Brazil at 13.9 GHz (12 pp.)

## LIST OF FIGURES

<u>Figure No.</u>	<u>Title</u>	<u>Page</u>
1	Cross-track contiguous data takes over U.S.A. during SL2 and SL3 missions considered in designing data catalog.	9
2	In-track contiguous data segments over U.S.A. during SL2 and SL3 missions considered in design of data catalog.	10
3	In-track non-contiguous data segments over U.S.A. during SL2 and SL3 missions considered in design of data catalog.	11
4	Data flow diagram for Stage II of processing.	12
5	Summary of angular scatterometric response for VV polarization from S-193 scatterometer operations during SL2 and SL3.	14
6	Summary of angular scatterometric response over ocean surfaces for VV and HV polarizations from S-193 scatterometer operations during SL2 and SL3.	15
7	Summary of angular radiometric response for VV polarization from S-193 radiometer operations during SL2 and SL3.	16
8	Summary of angular radiometric response over ocean surfaces from S-193 radiometer, non-contiguous mode operations during SL2 and SL3.	17

## LIST OF TABLES

<u>Table No.</u>	<u>Title</u>	<u>Page</u>
1	Summary of optimal regression equations describing the angular backscatter from North America and from the ocean.	19

## ABSTRACT.

The Skylab S-193 13.9 GHz radiometer-scatterometer was the first combined active-passive, and indeed the first active microwave instrument to examine the earth from space. In this study, primarily of land responses but including some statistics of ocean responses, numerous conclusions of value for future spacecraft system design were reached. Specifically,

- (1) The mean response of the land areas to the scatterometer was found to be well represented by

$$\begin{aligned}\sigma^{\circ} &= 1.667 \exp(-\theta/5.595^{\circ}) \quad 0 < \theta < 11^{\circ} \\ &= 0.3635 \exp(-\theta/29.55^{\circ}) \quad 11^{\circ} < \theta < 45^{\circ}\end{aligned}$$

with quite small variation about these values because of the averaging over the large resolution cell of the S-193.

- (2) The radiometer response over land was found to be largely independent of angle of incidence, with the values of effective temperature nearly all lying between 200 and 300° C. Over the ocean the response was similar in angular behavior but higher than the theoretical, flat-ocean values.
- (3) The correlation between radar and radiometer responses of the same ground elements is small, but that between scatterometer polarizations and between signals from angles between 15 and 45° is large.
- (4) Systems with this coarse resolution cannot effectively identify major land-use categories, although vegetation and soil moisture categorizations are likely to be more successful.
- (5) Good correlation exists between both radiometer and scatterometer signals and soil moisture, with the radiometer correlation higher.
- (6) The methods used for analyzing radar response from unknown planets have been applied to the Earth response with interesting results.

The report also contains extensive background information on microwave response of the earth, on the effect of the atmosphere on microwave responses with the S-193 type of instrument, and on the calibration and potential errors in the S-193 measurement.

DESIGN DATA COLLECTION WITH SKYLAB MICROWAVE  
RADIOMETER-SCATTEROMETER S-193  
— FINAL REPORT —

1. Introduction

The flight of the S-193 provided the first opportunity to view Earth with radar from space as well as the first opportunity for simultaneous radar and passive-microwave viewing of Earth from space (passive systems alone have been used to observe Earth from space before). Consequently numerous significant results of this experiment were to be expected, and they have indeed been observed. The coarse resolution of the S-193 scatterometer of course precluded the fine-resolution views of Earth from space that will be possible when synthetic-aperture imaging radars fly in space, but the very coarseness of the resolution provided a radar view that is not only the first from space but also the first from any platform for which signals from such large areas have been averaged.

Some of the specific significant results obtained are tabulated below:

(1) Design curves have been produced for future space radar systems that will use large initial resolutions; these will be useful in designing imaging radars with much finer resolutions because of the nature of the synthetic-aperture image production process. Over land the mean scattering coefficient at 13.9 GHz is found to be well-represented by

$$\begin{aligned}\sigma^{\circ} &= 1.667 \exp(-\theta/5.595^{\circ}) \quad 0 < \theta < 11^{\circ} \\ &= 0.3635 \exp(-\theta/29.55^{\circ}) \quad 11^{\circ} < \theta < 45^{\circ}\end{aligned}\tag{1}$$

The mean is somewhat higher at larger incidence angles than that expected on the basis of previous measurements, but the most significant result is that the variability over land is only a few dB about the mean. As a result, the design power levels for future systems can be made much smaller than previously thought possible. Details are given in Section 8.2 of Appendix A. Over oceans the situation is more complicated (see Section 8.1.4, Appendix A).

(2) Design data for future radiometers have been compiled. Because of the smaller dynamic range of radiometers and because radiometers have been flown in space at frequencies higher and lower than 13.9 GHz, these data are of less significance than those for the radar. One interesting result here, however, is the finding that over the approximately 50° range of incidence angles of the S-193

the radiometer response of terrain, in the average, is independent of angle of incidence. Details are given in Sections 8.1 and 8.9 of Appendix A.

(3) The correlation observed between radar and radiometer response of the same terrain elements is found to be small. Consequently, the use of a combined radar-radiometer instrument for future measurements will provide significantly more information than either alone. Details are in Section 8.3 of Appendix A.

(4) The correlation observed between responses with different polarizations is sufficiently high that use of multiply-polarized coarse-resolution sensors over land is of questionable merit. This result is different from that observed with fine-resolution imaging radars, where multiple polarizations have been shown useful. Details are in Section 8.3 of Appendix A.

(5) High correlation is observed between the responses at angles of incidence beyond  $15^{\circ}$ . Thus, in the ranges of incidence appropriate to most imaging applications, the actual angle used is not critical—at least with this coarse resolution. Details are in Section 8.3, Appendix A.

(6) With this coarse resolution responses are difficult to separate from different standard land-use categories. The size and type of vegetation, and the moisture content of the soil, appear to be the most important factors in differentiating the microwave responses; but land-use categories such as "agriculture" contain too wide a variety of such quantities to have distinctive responses. In the undeveloped areas of Brazil, where large homogeneous areas contain almost the same vegetation, such separation is possible. Thus, in areas of more fragmented land use finer-resolution sensors seem necessary to identify land uses with microwaves, but in areas with extensive regions of homogeneity the coarse-resolution sensor has promise. For details see Sections 8.4, 8.5, 8.6, and 8.10 of Appendix A along with Appendices B and C.

(7) The response of both microwave coarse-resolution sensors to soil moisture has been demonstrated. Most measurements used in these analyses were at about  $30^{\circ}$  incidence angle, and at this angle the radiometer response correlates better with soil moisture than does the scatterometer response. Recent ground-based measurements (Ulaby, Cihlar, and Moore, 1975)\* indicate the scatterometer response would be better at incidence angles around  $10^{\circ}$ , but the data sets available for the S-193 experiment did not permit adequate analysis of its response at these angles. For details see Section 8.7 of Appendix A and Appendix D.

---

\* See references in Appendix A.

(8) Since the S-193 provided the first radar look at Earth from space, the techniques used by radar astronomers to analyze unknown planets could be applied to Earth and thereby tested. Dielectric constants obtained by these analyses are of the expected size, but the  $4.5^{\circ}$  to  $5^{\circ}$  mean slopes obtained are somewhat hard to interpret in terms of our knowledge of the surface of our planet. See Section 8.9 of Appendix A for details.

The remainder of the body of this report deals with a summary of the activities in Skylab EREP investigation 549-M, and a somewhat more detailed summary of results. Most of the technical details are presented in the appendices. The majority of the technical work is documented in Appendix A.

Because of the late arrival of usable microwave data from the SL4 mission, only a brief description is given in Appendix E of these analyses. A subsequent report will be issued with a more detailed analysis of SL4 findings.

## 2. Contractual Summary

The University of Kansas Center for Research, Incorporated, hereby reports the work done under NASA contract NAS-91331 (EREP Task 549-M). This final report covers the period from 3-26-72 to 9-30-75. During the period of the contract the significant results were conveyed to NASA through the Principal Investigations Management Office and through numerous publications and presentations.

The initial contract from NASA, dated 3-26-72, was to have terminated on 7-1-73. It was extended several times, with the termination for SL2 and SL3 data finally at 9-30-75 and for SL4 data at 12-31-75. Significant preliminary results were reported during the period of the contract.

The initial statement of work was broken down into three phases: pre-mission, during-mission and post-mission. The extensions were for the post-mission analysis phase. During the pre-mission phase of the contract, the University of Kansas prepared for the receipt and analysis of Skylab S-193 data. Also during this phase, past measurements on scattering and emission were collated for later comparison with Skylab data. The University of Kansas assisted NASA in the planning of the EREP missions to fulfill requirements of this study. This activity became more prominent during the mission phase of the contract. A near-real-time feedback was expected during the mission phase for the purpose of planning and evaluating the EREP mission.

The post-mission activity constituted the bulk of the analysis. From the data obtained from the S-193 radiometer/scatterometer, the following tasks were to be performed.

### 1. Design of Near-Vertical Scattering Catalog.

Using the S-193 scatterometer data from modes that provided backscattering coefficient near nadir incidence, a catalog of responses was to be prepared. This was to have been augmented by data from the S-193 altimeter.

### 2. Design of General Scattering Catalog.

From the S-193 data, augmented where possible by the S-193 altimeter data, a catalogue of backscattering response for various terrain types was to be prepared. These data were to be compared to data from prior measurements.

### 3. Comparison of Backscattering Coefficient Obtained from S-193 Scatterometer and S-193 altimeter.

Data obtained from the backscatter mode experiment of the S-193 altimeter were to be compared to those obtained by the S-193 scatterometer over the same terrain.

### 4. Effects of Clouds on Radiometer/Scatterometer Signals.

It was expected that the S-193 radiometer could be used to detect regions of clouds and thereby be used to correct the signal levels for the S-193 scatterometer. The capability of the S-193 radiometer as a cloud and rain sensor was to be gauged.

With a growing familiarity with the S-193 data, the initial scope of the contract was altered with the consent of NASA. In particular, proposed use of S-193 altimeter data for the design of the scattering data catalogue was eliminated and no comparison between S-193 scatterometer and S-193 altimeter data was made. This modification was proposed upon careful examination of the S-193 altimeter operating modes and the difficulty of making meaningful comparisons.

In essence, all of the tasks of the statement of work (as modified later) were completed. The pre-mission and the during-mission phase of the contract will be covered in a very brief summary; work done during these phases has already been reported to NASA. The emphasis of this report is to present the significant findings from the work performed under this contract by the University of Kansas.

## 3. Pre-Mission Activities

### 3.1 Summary

The pre-mission phase of the activity consisted of generating a state of preparedness for receipt of S-193 radiometer/scatterometer data. In particular, an exhaustive literature survey was conducted for obtaining documentation on scattering and emission measurement programs. The backscatter measurement programs were reviewed and possible schemes for comparing data from different investigations were suggested. This was neces-

sitated by the great difference in absolute magnitude noted between the reported measurement by various programs over supposedly similar terrain types. The detail of this comprehensive catalogue of pre-Skylab scatterometer measurements was documented and sent to NASA as CRES Technical Report 243-2 by King and Moore. A similar one for the radiometric emission was also planned, but after substantial effort it was found that no meaningful comparisons could be made between radiometer measurement programs because of lack of data regarding the operating systems or the atmosphere and/or the lack of calibration.

A necessary part of the preparation of Skylab data was to locate sites as candidates for observation with the S-193 sensor where a comparison with theory appeared promising. This was done by breaking up all terrain scenes into nine major categories and requesting that sufficient data for all were obtained.

Various computer programs were written to obtain statistics and to translate the data from the format of NASA generated tapes to those compatible for processing at our processing facility.

Topographic maps, weather reporting summaries and other auxiliary data as required for interpretation of S-193 data were acquired.

### 3.2 Analysis of Sensor -- S-193 radiometer/scatterometer.

Before one can describe the data produced from the S-193 radiometer/scatterometer one must know the operational capabilities of the sensors. To this end statistical analyses were undertaken to establish the precision for the radiometer and the scatterometer. Expressions describing the variances of the measurements were derived for both sensors. The resolution of the scatterometer as specified at .0707 for the normalized standard deviation in the ITNC mode with a -30dB backscattering coefficient, with 90% confidence was met during system testing. The precision of the radiometer was estimated to be less than  $1.16^{\circ}\text{K}$  for all temperatures above  $100^{\circ}\text{K}$ . Other sources of error in the measurements were explored and details are provided in chapter six of Appendix A.

### 3.3 Study of Atmospheric Effects upon S-193 Radiometer/Scatterometer Signals.

Before the first EREP mission work had already started on studying the effects of the intervening atmosphere on microwave signals to the S-193 radiometer/scatterometer. Models of the atmosphere were constructed based upon theoretical and earlier empirical evidence and estimating the absorption/emission due to various constituents of the atmosphere under various meteorological conditions. A complete simulation of the atmospheric effects upon an active and a passive sensor operating at 13.9 GHz with dual polarization was

conducted. Verification of the simulation model was found by computing corrections due to the atmospheric effects and observing that certain correlations between ground observables and Skylab measurements were increased as expected.

Due to unavailability of the upward-looking radiometer contemplated in the experiment design, the ability of the S-193 radiometer as a cloud and rain sensor was not quantitatively measured. It was, however, shown through the empirical models and simulations that the clouds and rain would have a significant effect upon the S-193 radiometer signals. Unfortunately, over regions of precipitation, variations in the soil moisture also occur, and it has been observed that the radiometer is highly sensitive to soil moisture variations (see chapter eight in Appendix A).

Results from the study of atmospheric effects are provided in chapter five of Appendix A.

#### 3.4 Summary of Previous Microwave Measurements

An extensive study was made of microwave measurements reported in the literature prior to the Skylab mission. The results for the scattering coefficient study were reported in detail in Technical Report 243-2 by King and Moore. Results of the radiometer study were to have been in another technical report, but observations reported by the different investigators were so incompatible that the report was never completed.

The basic conclusion reached in the scattering study is that absolute calibrations used by the different investigators are so inconsistent that comparisons are extremely difficult; this problem was compounded by the variety of usually inexact descriptions of the terrain. Ultimately it was found necessary to use the range of measurements of agricultural terrain at  $50^\circ$  incidence angle as a standard of comparison, since most investigators did report agricultural measurements at this angle. Thus, the extensive coverage of the S-193 experiment provided the first opportunity to report a truly wide range of terrain backscatter measurements over an extensive series of areas described uniformly, if imperfectly.

Since this report was issued, measurements made at the University of Kansas in another program have been reported in detail by Ulaby and his coworkers; since the bibliography on this topic is so lengthy for the past two years, it is not presented here. The measurements now cover the frequency range 1-18 GHz with incidence angles from nadir to  $70^\circ$  and multiple polarizations. All measurements, however, have been of agricultural terrain either without vegetation or with field crops found in the Lawrence, Kansas, and College Station, Texas, areas.

#### 4. Activities During Mission

The University of Kansas actively assisted NASA/JSC in mission planning. Of special significance was a study conducted after it was learned that due to a malfunction in the deployment of some solar panels, EREP would have to be substantially curtailed. This, it was pointed out, was due to the excessive power drains encountered during ZLV orientation of the spacecraft. A study, documented as CRES Technical Report 243-3 by Pintar and Sobti, specified conditions under which the S-193 could operate credibly for purposes of collecting scattering and emission data.

The University of Kansas assisted and made recommendations towards any decisions concerning the operation of the S-193 Radscat system for purposes of designing a data catalog. A specific example of such assistance was the attendance at a conference at NASA/JSC to determine at what angle to pin the antenna during SL4.

The search and acquisition of supporting data was an on-going activity. Weather information at time of overpass and for a few days prior to overpass was collected from four passes. Land-use maps of target sites had the spatial location and extent of target cells plotted on them. A computer-compatible tape containing the weather report of 535 weather reporting stations for four specific times was obtained from the National Severe Weather Forecasting Station in Kansas City.

#### 5. Post-Mission Activities

##### 5.1 Data Description and Analysis

Most of the work was in the post-mission phase of the contract. The extensions to the contract periods were necessitated by the schedule of the data dissemination. Due to problems in the processing of the Skylab S-193 radiometer/scatterometer data, the University of Kansas did not receive data until August, 1973 for the SL2 mission (first occupancy). These data were later found to be of dubious quality and reprocessed data were received in September, 1974. The data from the second occupancy (SL3) were obtained between 6-27-74 and 9-26-74. The data for the third occupancy (SL4) had problems due to a hardware malfunction during the SL4 mission. These data were received at the University around March, 1975, in "raw" form and were processed under another contract. They first became available for analysis in June, 1975. Apart from the S-193 radiometer/scatterometer data received from NASA, color negatives from the S-190A and S-190B cameras from selected sites were also received. These were used as supporting evidence in the compilation of the catalog on microwave scattering and emission. The S-193 data were received on tape and in the form of tabulations and plots. Most of the

analyses were performed using the magnetic tapes, although occasionally the tabulations and plots were also consulted.

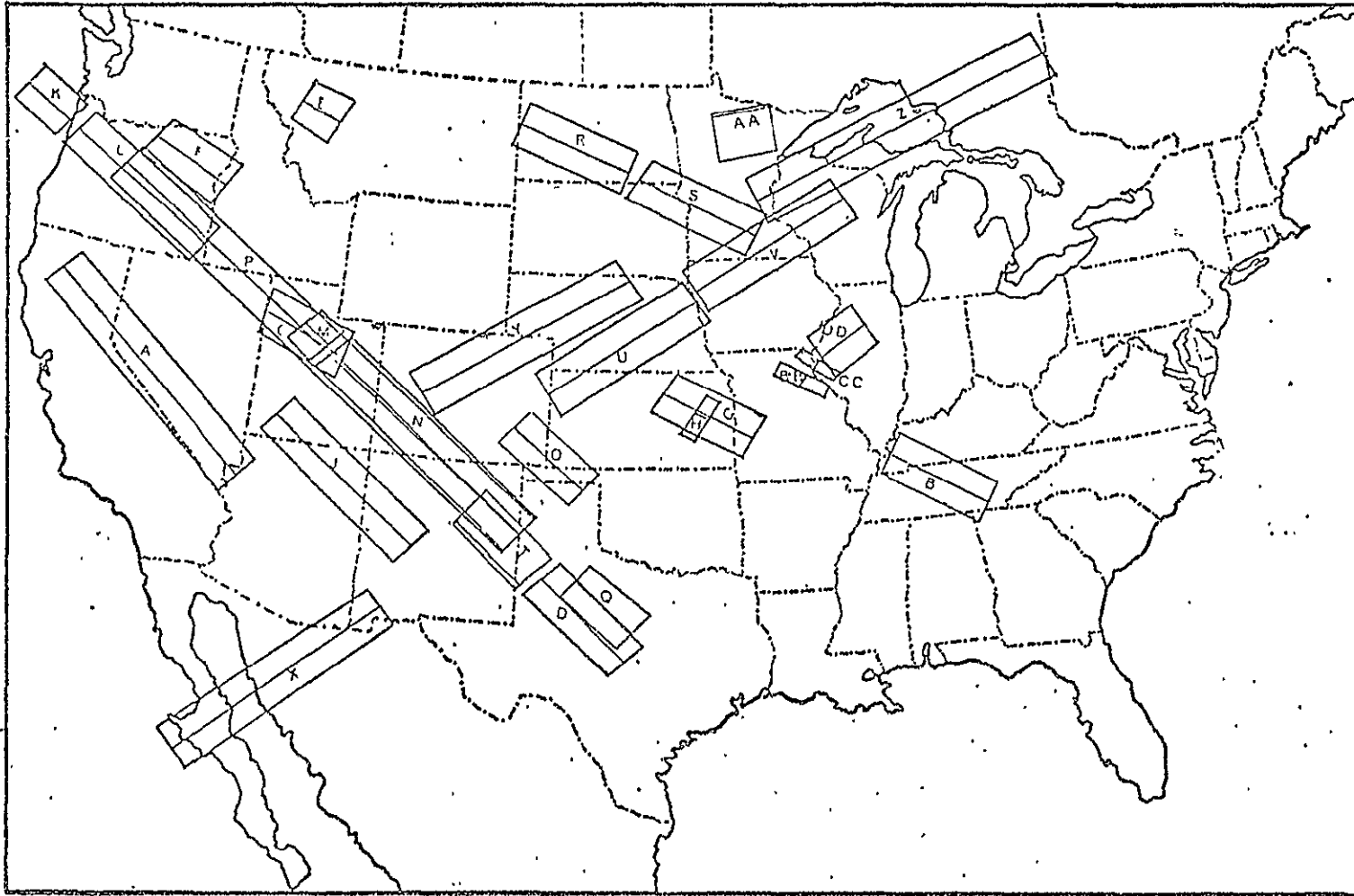
As further ancillary data to aid the investigation of the S-193 data, topographic maps with a scale of 1:250,000 were obtained for all regions in the United States. Land-use maps and potential natural vegetation maps (Kuchler) were also collected for the U.S. Weather reporting station summaries were used to get temperature and rainfall values for 5 days prior to and for the day of each pass for many stations lying close to the pass. These data along with some ERTS mosaics provided further ancillary data used for interpretation of S-193 data.

The first occupancy of Skylab lasted from 30 May, 1973, to 14 June, 1973. During this occupancy, 12 EREP missions were flown apart from a calibration experiment pointing to deep space and the lunar background and one special mission over Hurricane Ava in the Pacific. The number of EREP missions was limited because each mission required the Skylab vehicle to be in a Z-Local-Vertical orientation rather than in the Solar Pointing orientation. Failure of one of the power panels caused a drain on the electrical power production of the Skylab vehicle so that a displacement from Solar Pointing (which is optimal for solar power production) was minimized.

The second occupancy of Skylab lasted from 3 August, 1973, to 21 September, 1973. During this occupancy a total of 28 EREP missions and 2 lunar calibration passes were conducted. The targets viewed included ocean surfaces and land surfaces over many parts of the world. Special emphasis during the data takes was, however, given to targets within the continental United States. The inclination of the Skylab orbit was  $50^\circ$ , so that only regions lying with  $\pm 50^\circ$  latitude could be viewed. The orbital radius ranged from 6802 to 6810 kilometers with a very slight eccentricity.

The S-193 radiometer/scatterometer data used to compile the data catalogue are described in chapter seven of Appendix A. Figures 1, 2 and 3 show the data segments over the continental U.S.A. using the cross-track contiguous (CTC), In-track-Contiguous (ITC) and In-track Non Contiguous (ITNC) modes of operation. The total number of observations including all polarizations, angles and modes was over 40,000. The CTC mode provided the greatest amount of data. Data with the CTC pitch- $29^\circ$  mode over South America (mainly Brazil) were used to compare responses over that region with the responses over North America.

CROSS-TRACK CONTIGUOUS



REPRODUCIBILITY OF THE ORIGINAL PAGE IS POOR.

Figure 1. Cross-track contiguous data takes over U.S.A. during SL2 and SL3 missions considered in designing data catalogue.

IN-TRACK CONTIGUCUS

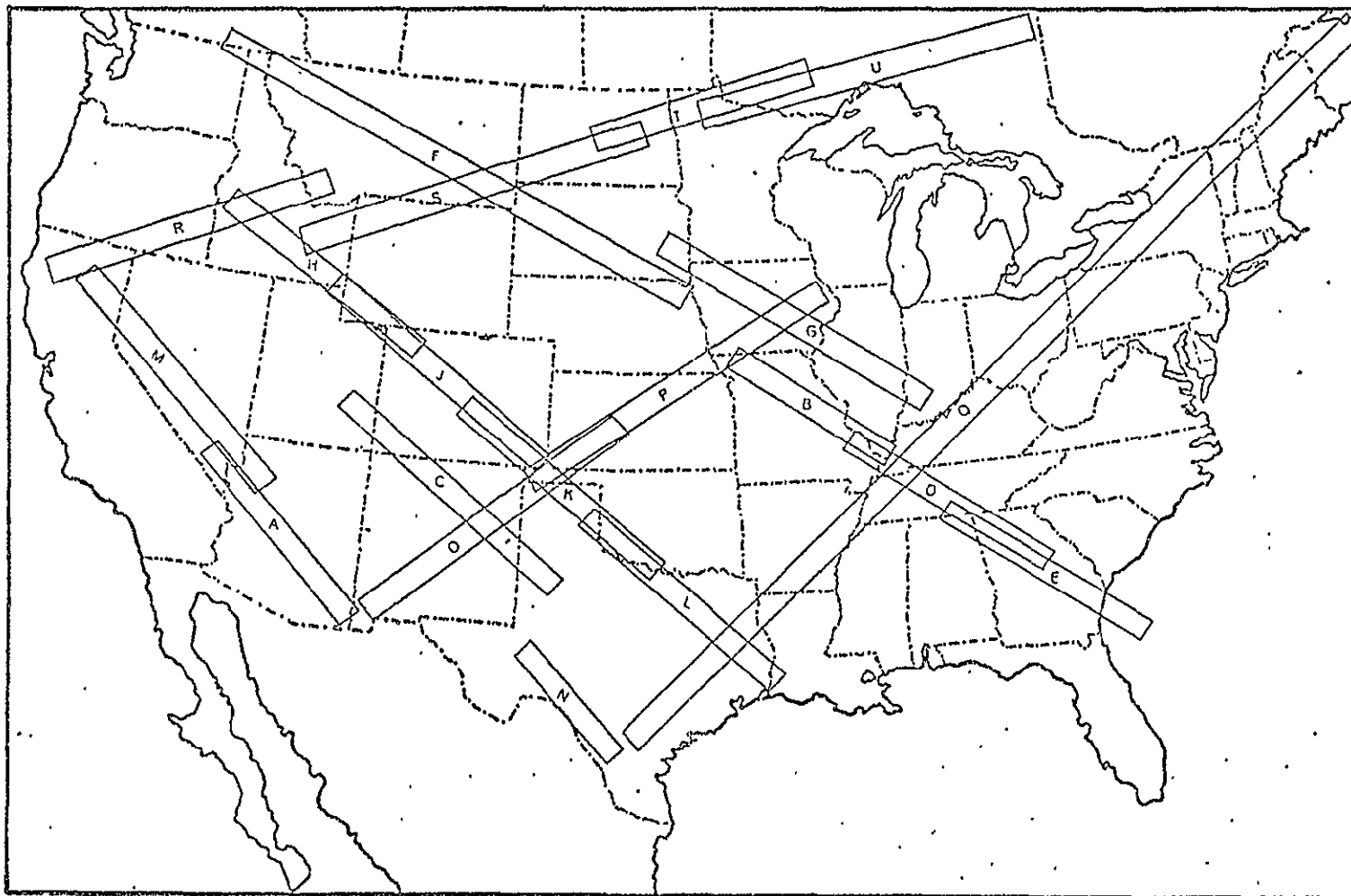
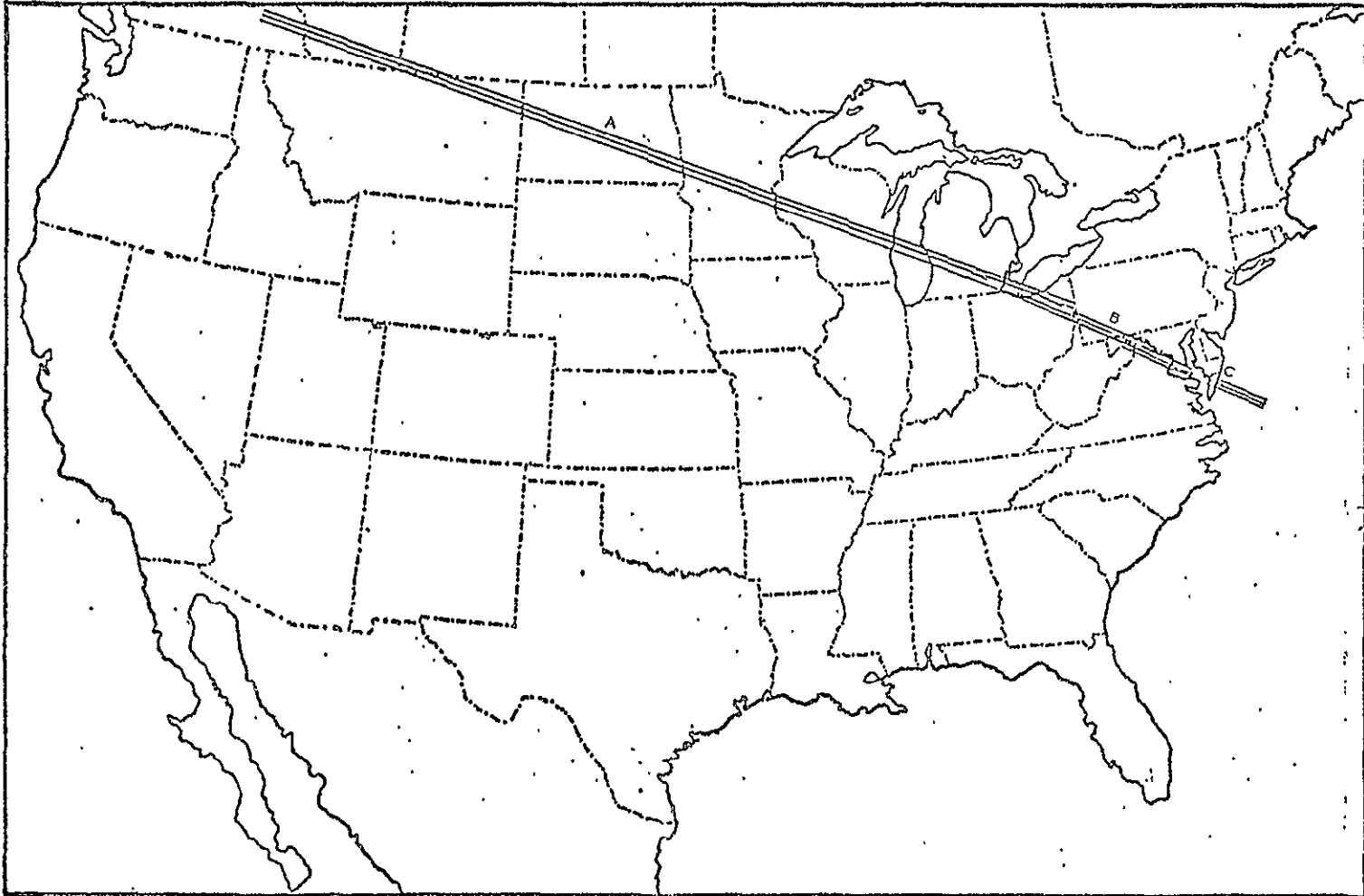


Figure 2. In-track contiguous data segments over U.S.A. during SL2 and SL3 missions considered in design of data catalogue.

IN-TRACK NON-CONTIGUOUS



REPRODUCIBILITY OF THE  
ORIGINAL PAGE IS POOR

Figure 3. In-track non-contiguous data segments over U.S.A. during SL2 and SL3 missions considered in design of data catalogue.

ORIGINAL PAGE IS  
OF POOR QUALITY

12

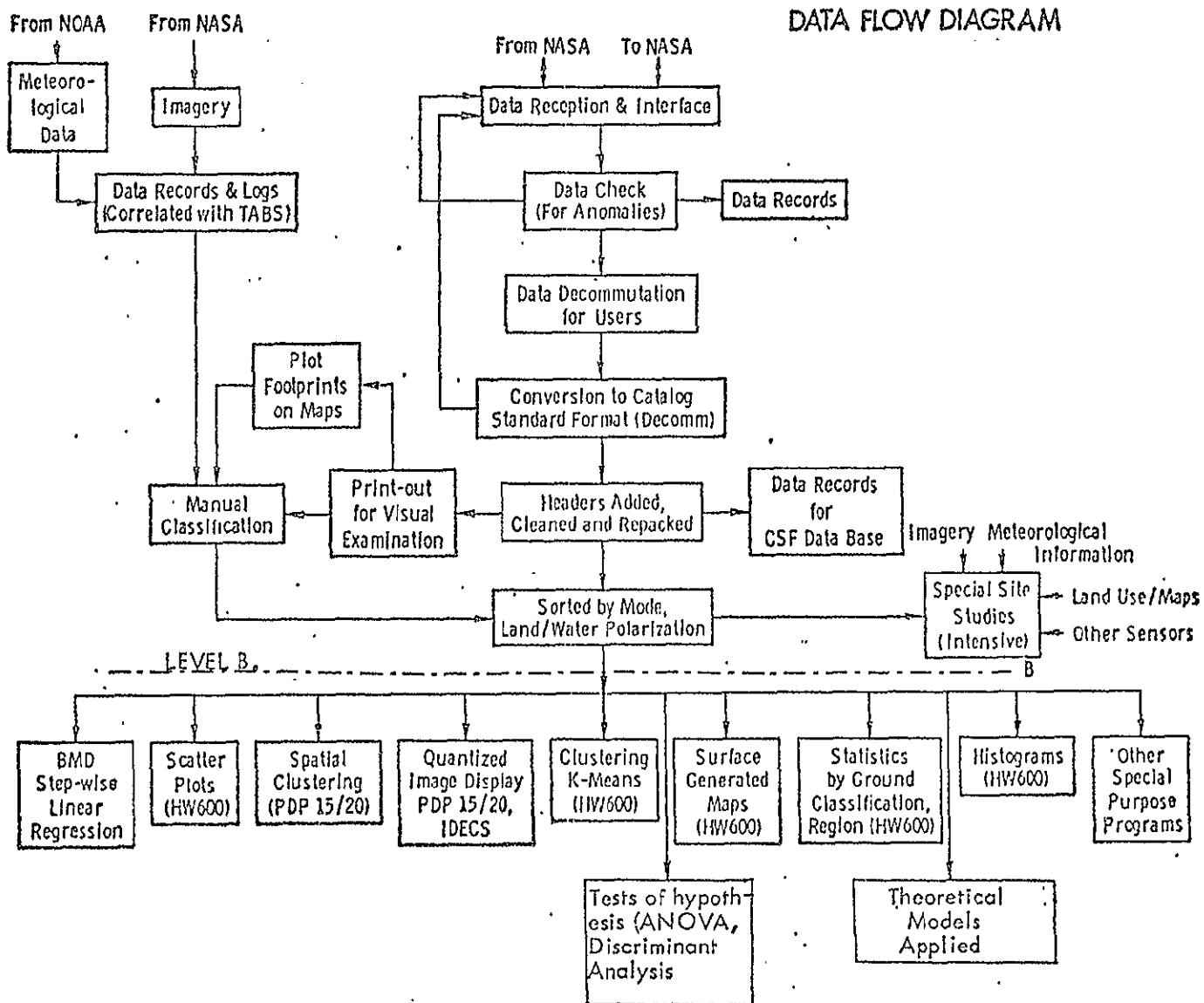


Figure 4. DATA FLOW DIAGRAM FOR STAGE II OF PROCESSING

Chapter seven of Appendix A describes the evolution and flow of the data to prepare the catalog. Figure 4 shows the data flow chart for the effort conducted at the University of Kansas.

## 5.2 Summary of Principal Results

### 5.2.1. Summary of Ensemble Statistics

No consistent trend of angular variation was observed for the brightness temperature over North America. A distinct angular trend was observed for ocean surfaces. The backscatter measurements over both land and ocean show extremely consistent trends. It was found that due to the large spatial extent of the target footprint and the associated averaging effect, the dynamic ranges of the backscatter response at all angles were less than those measured by finer-resolution sensors. Details of these results are provided in chapter eight of Appendix A. As an example, the backscattering coefficient with vertical polarization for an ensemble of targets in North America versus incidence angle is shown in figure 5. At each angle the mean, upper and lower deciles of the response and the number of samples is shown. Polynomials and exponentials describing the angular decay have also been computed and are reported in chapter eight of Appendix A. As a further example of the results obtained, figure 6 shows the angular decay of the backscattering coefficient with vertical polarization over ocean surfaces. The decay is much steeper than for land targets and the spacing between upper and lower deciles is larger than for land targets. The cross-polarized backscatter over the ocean has a very small range between upper and lower decile and this range increases with angle. Figure 7 shows the angular response of the radiometric brightness temperature over North America and the lack of an angular trend is clearly illustrated. These data have not been compensated for physical temperature or atmospheric effects so the bounds between deciles are a little larger than they would be with these corrections. The response with horizontal polarization over land for both the scatterometer and for the radiometer is similar to the vertical. The scattering response with horizontal polarization over the ocean is also similar to that with vertical polarization. Figure 8 shows the radiometric response as a function of incidence angle for ocean surfaces; notice that the angular variations are quite consistent with those reported by aircraft- and tower-mounted measurements.

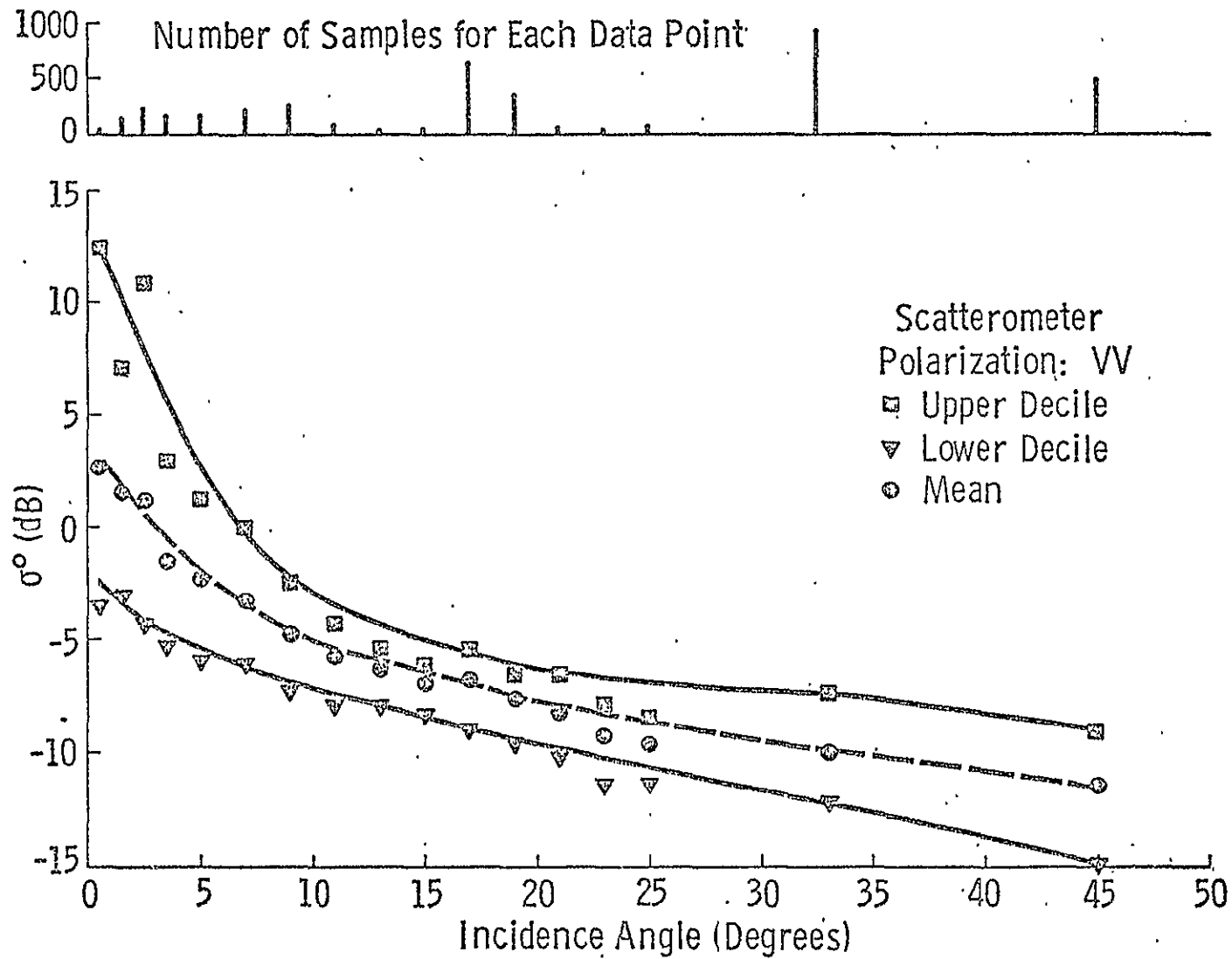


Figure 5. Summary of angular scatterometric response for VV polarization from S-193 scatterometer operations during SL2-SL3.

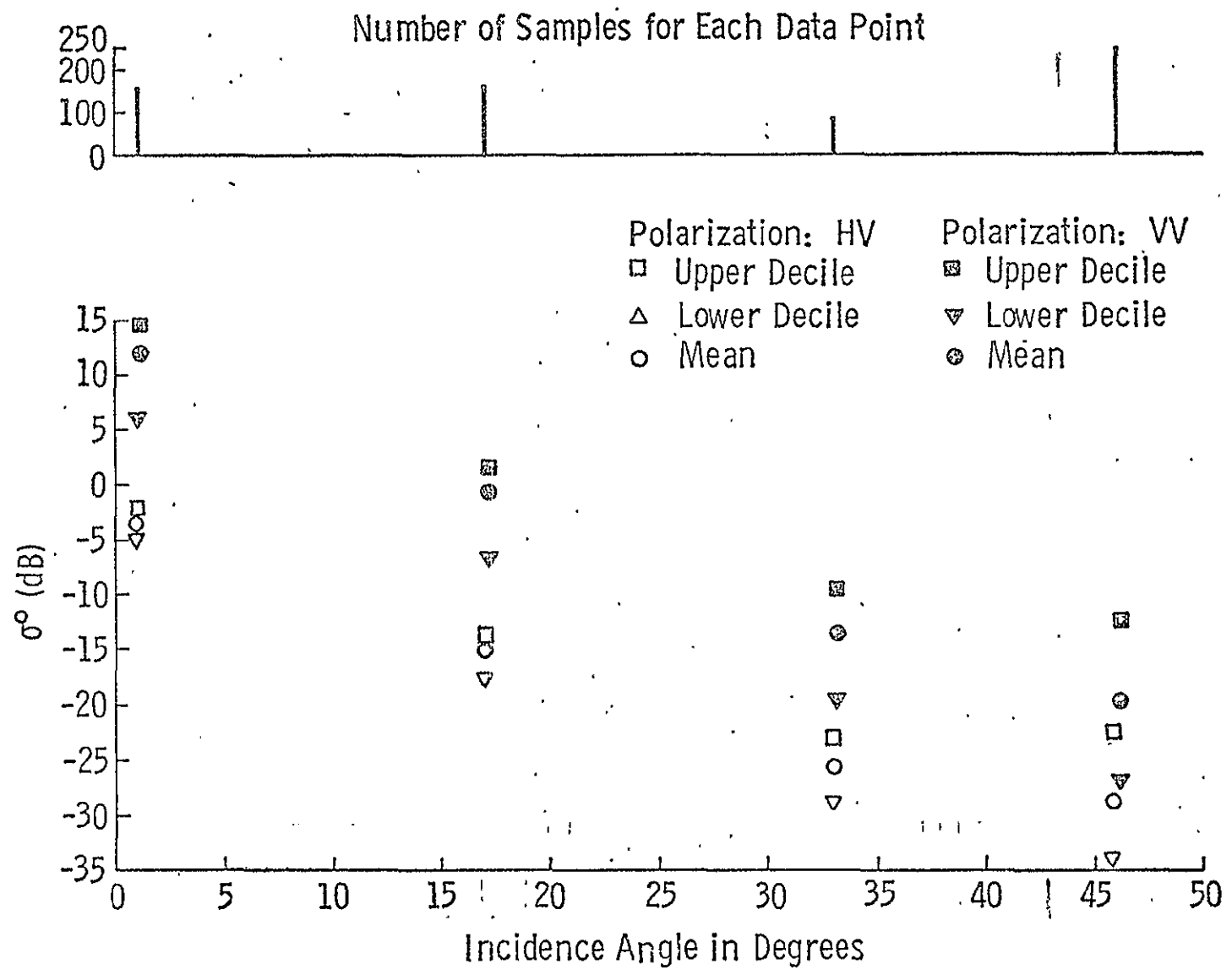


Figure-6. Summary of angular scatterometric response over ocean surfaces for VV and HV polarizations from S-193 scatterometer operations during SL2-SL3.

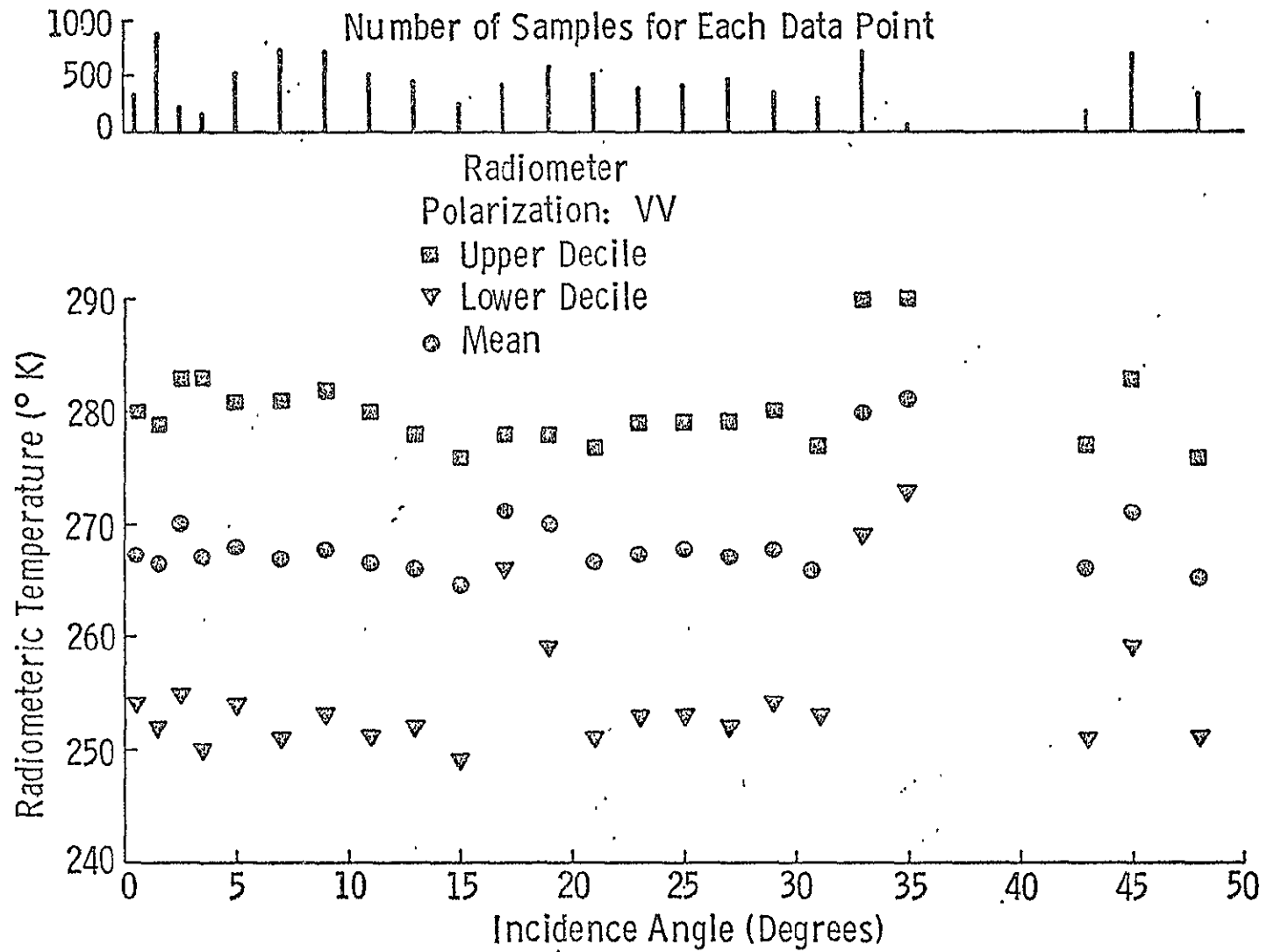


Figure 7. Summary of angular radiometric response for VV polarization from S-193 radiometer operations during SL2-SL3.

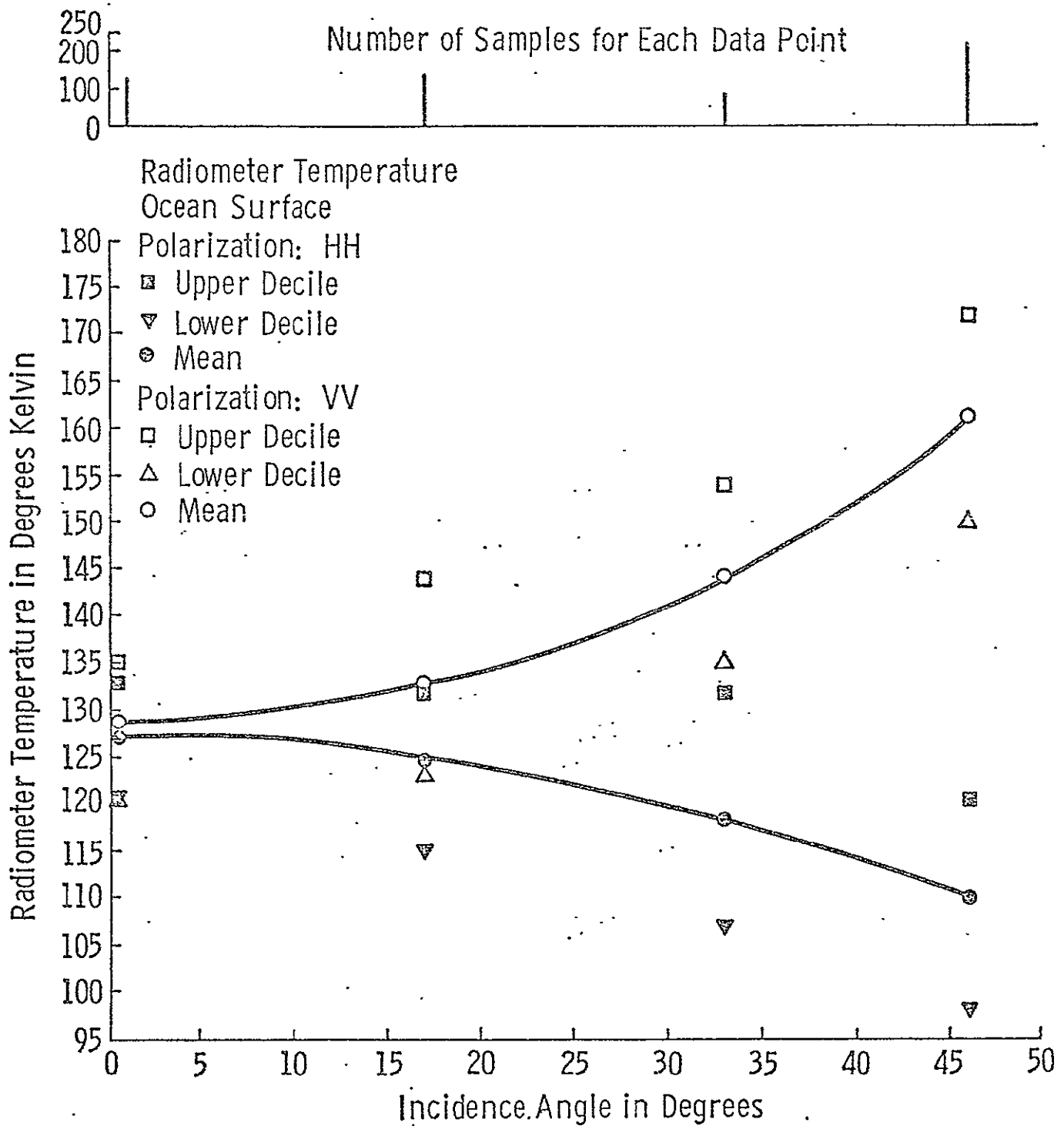


Figure 8. Summary of angular radiometric response over ocean surfaces from S-193 radiometer, non-contiguous mode operations during SL2-SL3.

### 5.2.2. Design Data for Radar Systems

The purpose of a data catalog of the microwave response of various terrain was to aid in the design of future radar and radiometer sensors.

From the ensemble statistics prepared for the North American targets and for the ocean surface, some equations have been computed which describe the mean angular behaviour of the backscattering coefficient. These equations may be helpful, along with the summary curves showing means and upper and lower deciles of backscatter vs. angle, in the design of future radar systems.

The North American targets seemed to be best described by either a fourth order polynomial in incidence angle  $\theta$  up to  $50^\circ$ , or by an exponential of the form

$$\sigma^\circ = k_1 e^{-\theta/k_2} \quad (2)$$

for the range of incidence angles  $0^\circ - 11^\circ$  and another such exponential from  $11^\circ - 49^\circ$ . A summary table of the best fits as obtained from a stepwise linear regression analysis for the North American region and for ocean surfaces is provided in Table 1. The polynomials do not describe the  $\sigma^\circ$  vs.  $\theta$  decay beyond  $50^\circ$ . A fourth order polynomial was obtained as a best fit for some cases where the variables to be entered for regression were chosen by the procedure considered. The variables were chosen in the order of the uncertainty they removed in the behaviour of the dependent variable, namely  $\sigma^\circ$ . The exponentials and polynomials were also computed for two separate sections of the  $\sigma^\circ$  vs.  $\theta$  response because a qualitative curve appears to be composed of two quite distinct regions. The correlation coefficient for each of the fits is also shown in the summary table. The fits seem to be excellent for some instances and all show a correlation better than 0.93. All except one are better than 0.97. In interpreting the relationships, please note that the polynomials are fit to  $\sigma^\circ$  expressed in dB and the exponentials are fits to  $\sigma^\circ$  expressed in numerics.

It is interesting to note that backscatter from land follows two types of decay curves: one from near nadir to approximately  $11^\circ$ , and another from  $11^\circ$  out to  $47^\circ$ . Actually, the data at incidence angles between  $11^\circ$  and  $17^\circ$  is very scarce so that the incidence angle where the cross-over occurs may not be  $11^\circ$ , but instead higher. The ocean seems to follow an exponential decay and is fit very well with a third-order polynomial. There is no noticeable distinction between the decay in backscatter for the  $0^\circ - 11^\circ$  and  $11^\circ - 47^\circ$  angle groups for the ocean as there is in the case for land.

TABLE 1.

SUMMARY OF OPTIMAL REGRESSION EQUATIONS DESCRIBING  
THE ANGULAR BACKSCATTER FROM NORTH AMERICA AND FROM THE OCEAN

Target	Polarization	Type Of Fit	Region of Fit	Function of Theta	Correlation Coefficient
N. America	VV	Polynomial	0° - 45°	$1.656 + 0.0196\theta^2 - .84266\theta^3 - .000004\theta^4$	0.9988
N. America	VV	Polynomial	0° - 11°	$3.09145 - 1.1939\theta + 0.03506\theta^2$	0.9971
N. America	VV	Polynomial	11° - 45°	$-6.81362 - 0.002\theta^2$	0.9989
N. America	VV	Exponential	0° - 11°	$1.667 \exp(-\theta/5.595)$	0.9713
N. America	VV	Exponential	11° - 45°	$.3635 \exp(-\theta/29.551)$	0.9296
Ocean	VV	Polynomial	0° - 49°	$13.11133 - 0.57\theta - 0.01874\theta^2 + .00033\theta^3$	0.9992
Ocean	HH	Polynomial	0° - 49°	$14.004 - .59865\theta - 0.05642\theta^2 + 0.00032\theta^3$	0.9998
Ocean	HV	Polynomial	0° - 49°	$-3.1064 - .61619\theta - 0.01487\theta^2 + 0.00031\theta^3$	0.9981
Ocean	VV	Exponential	0° - 49°	$15.60763 \exp(-\theta/6.13)$	0.9882
Ocean	HH	Exponential	0° - 49°	$21.91891 \exp(-\theta/5.348)$	0.9946
Ocean	HV	Exponential	0° - 49°	$0.317157 \exp(-\theta/6.99)$	0.9777

NOTE: Polynomials are for  $\sigma^\circ$  in dB; Exponentials are for  $\sigma^\circ$  in numeric.

In summary, it appears that the land backscatter may be a two-process phenomenon; one predominating in near nadir region ( $0^{\circ}$  -  $11^{\circ}$ ) and the other in the region from  $11^{\circ}$  -  $47^{\circ}$ . The ocean backscatter, on the other hand, appears to be a single-process phenomenon, although theory suggests it, too, is a dual phenomenon.

### 5.3 Other Statistical Analyses of S-193 data.

A number of statistical exercises were conducted on the S-193 radiometer/scatterometer data to determine various aspects of its characteristics. In particular a correlation analysis, an analysis of variance (one-way layout), a linear discriminant analysis and two clustering analyses were conducted. The results from these analyses may be found in chapter eight of Appendix A. The results of the clustering analysis are further elaborated in Appendix B.

In general it was found that there is a very low correlation between the radiometer and the scatterometer signals. This reinforces the arguments that each is relatively more sensitive to different factors in the terrain scene and hence that the use of the two sensors in consort should provide more information than available through the operation of either singly.

The correlations between the various sensor configurations of the S-193 have been computed and are provided in chapter eight of Appendix A. In particular it was found that the backscattering responses for vertical and horizontal polarization show a significant correlation. This implies that, at least at this gross resolution, the use of the two polarizations appears redundant. It was also found that the backscatter over land was correlated for incidence angles between  $15^{\circ}$  and  $40^{\circ}$  off nadir. This means that side-looking radars operating at these incidence angles could easily account for the far range effect.

The results from the analysis of variance, clustering analyses and the linear discriminant analysis showed that with such gross resolution both in the S-193 sensor and in the assigning of categories by examination of topographic maps and imagery, the major land-use categories do not have unique microwave responses. This was the crux of the results obtained through the exhaustive analysis using these techniques.

Details of the results from these analyses may be found in chapter eight of Appendix A.

### 5.4 Special Site Studies

Due to shortage of time and resources, only a few sites could be exhaustively studied. These sites were picked because of a readily apparent correlation or influence

of some ground parameter, or, because a pass was sufficiently long that the targets covered under the same sensor configuration were hopefully distinct in their microwave response. Different sites were given varying measures of considerations. Many sites were analysed by first performing a manual classification on each target footprint and then subjecting the manually classified data to a computer statistical analysis. From some sites, only samples were taken which were manually classified and again subjected to a computer analysis. All the manually classified sites were then pooled to compute the response of various terrain types. Details of the response of major terrain types as seen by the Skylab scatterometer are provided in Appendix C. These responses are compared to the responses reported by other investigators using aircraft-based and ground-based sensors.

Three sites were given much more consideration than all the other sites: Texas Site, Utah Site and Brazil. Details of the results from the Texas site study can be found in chapter eight of Appendix A. Details of the results from the Utah Site can be found in Appendix D. Details of results from the Brazilian site can be found in Appendix F. The Texas and Utah sites were found to be of significant interest because of the wide dynamic range in the response that could not be readily explained by vegetation or topography. The Brazilian region provided large areas of homogeneous terrain.

From the Texas site study a correlation of  $-0.77$  between emissivity and an estimate of soil moisture called the Antecedent Precipitation Index (API) was obtained. The correlation of API with the backscattering coefficient was  $0.62$ . The API was computed according to

$$API = \sum_{i=0}^5 (0.85)^i R_i$$

$R_i$  = precipitation in inches on day  $i$ .

Analyses of the S-193 data over the Utah Site showed that the backscatter and emission were strongly influenced by contributions from subsurface layers of sediment saturated with brine. This phenomenon was also observed by the S-194 radiometer operating at 1.4 GHz and by the Nimbus 5 ESMR (Electrically Scanning Microwave Radiometer) operating at 19.35 GHz.

Certain correlations were observed between the backscatter response at approximately  $33^\circ$  and the configuration of ground targets in Brazil as discerned from coarse-

scale maps, Boundaries of major biomes as identified from image-like displays of Brazil seemed to agree with those from the maps.

### 5.5 Comparison of S-193 Radiometer/Scatterometer Data with Simple Theoretical Models

This is the first time that a radar with such coarse resolution has viewed the earth from afar. This provided an opportunity for us to compare the results obtained from earth with those obtained from other planets. The analyses and interpretations, conducted similar to those used by radar astronomers, showed that the ocean and land in North America are comparably rough, with the ocean having a slightly smaller mean slope. Both the oceans and land appear smoother than either the moon or Venus. Selected targets in the midwest region of the U.S.A. showed that, as expected, the forest was roughest and that farmland was the smoothest. The Fresnel reflection coefficient for the ocean was much larger than that for land (as expected) but considerably less than that measured by prior programs. Details are provided in chapter eight of Appendix A.

It has often been suggested that a Gaussian autocorrelation function of the surface height was more descriptive of an ocean surface near nadir and that an exponential autocorrelation function was more descriptive for land. Our results show that the mean slope and the reflection coefficient computed by assuming either of these two autocorrelation functions over land and ocean are remarkably similar. The reflection coefficient computations are sensitive to the absolute level of the backscattering coefficient. The dielectric constants for various targets computed from the Fresnel reflection coefficient were considerably lower than any measured heretofore and appear suspect.

A plane surface model was used to describe the ocean surface and based upon dielectric constant data, an emissivity was computed for various physical temperatures. Details are provided in chapter eight of Appendix A. Assuming a simple model for the atmospheric effects and a standard atmosphere as described in chapter five of Appendix A, the S-193 radiometer data were reduced to surface brightness temperatures. As expected it was found that the emissivities computed from S-193 data were higher than those predicted for a plane surface. There was a sizable difference at nadir between the emissivity from S-193 measurements and for the planar surface prediction. Prior measurements have indicated that the sensitivity of emissivity to roughness is small at nadir. It has also been reported by measurements that this sensitivity is greater for horizontal polarization, and further, that it increases with incidence angle till about  $55^\circ$ . This is also predicted by the geometric optics model. It was observed that the deviation of the mean S-193 response from that of a planar surface was considerably larger for horizontal polarization than for vertical polarization at  $46^\circ$  incidence.

Based upon the above mentioned and other simplistic assumptions, it was determined that the sensitivity of the radiometric response with horizontal polarization at  $46^\circ$  incidence was approximately  $0.94^\circ\text{K}/\text{m}/\text{sec}$ . Based upon this figure, the mean wind speed of the oceans in the summer months was computed as 16.3 knots.

It is interesting to observe that even though the radiometer is sensitive to atmospheric effects and that no account was taken in the atmospheric corrections for variations in atmospheric effects from the mean profile considered, the mean wind speed computed is reasonably close to the value predicted by the radar which is comparatively impervious to atmospheric effects. The mean wind speed as computed by the radar was found to be approximately 13 knots.

#### 5.6 Image-like Display of S-193 Radiometer/Scatterometer Data

Even though the S-193 scatterometer was not an imaging system, image-like presentations can be prepared from some data obtained from some of its modes (particularly the cross-track contiguous mode). These images show clearly the variation of the microwave response over an area and are very helpful in interpreting the response. It was shown that microwave response variations due to soil moisture variations can be easily discerned as can boundaries of major biomes.

Details of the analyses and the consequent results are provided in chapter eight of Appendix A. The two regions chosen as candidates for producing these image-like displays were the Texas soil-moisture site and the Brazilian forest region. The Texas site showed great variations in both backscatter and radiometer response and these could be readily correlated with soil moisture variations. The Brazilian forest region was a candidate due to its large areas of homogeneity which were commensurate with imaging with such a coarse-resolution sensor as the S-193. Color and black and white images are provided in chapter eight of Appendix A and in Appendix F.

#### 6. Conclusions Relevant to Future Missions and Sensors

The observations with S-193 have provided radar design information for systems to be flown on spacecraft (in the future), but only at 13.9 GHz and for land areas (only) over the United States and Brazil (in our analysis) plus a few other areas of the world for which this kind of analysis has not been made. (Furthermore, the) observations only extended out to about  $50^\circ$  angle of incidence. Thus, both extension to other environments and extension to other frequencies and angles of incidence would be useful in future missions.

The value of a sensor with such a gross resolution for most overland resource and status monitoring systems seems marginal, with the possible exception of mon-

itoring soil moisture and major vegetation variations. / Conceivably this resolution might be adequate for some ice and snow monitoring and for observing the movement of the freeze-thaw line; but the orbit of Skylab precluded its testing for sea ice monitoring, the resolution is inadequate for monitoring snow in the mountains, and the results of the freeze-thaw line study are being reported under a different Skylab experiment (540-A2). It seems clear both from the results of this study and the related University of Kansas Skylab soil moisture study and from recent ground-based measurements over a wide frequency range by Ulaby, Cihlar, and Moore (1975) that a system for soil moisture measurement should operate at steep angles of incidence and at a lower frequency than 13.9 GHz.

The complementary nature of the scatterometer and radiometer systems has been demonstrated by the correlation analysis. Although radiometers must have spatial resolutions dictated by antenna size, radars can use synthetic-aperture techniques to achieve much finer resolutions. / Since the finer resolutions seem necessary for most resource monitoring tasks, the results of this study suggest that future systems might include radars and radiometers using the same larger antenna to achieve moderately improved spatial resolution for the radiometer while the synthetic aperture technique is used with the radar to embed a fine-resolution radar image in the footprint of the radiometer. Thus, in the areas where the resolution achieved by the radiometer is adequate the advantages of the multiple-look radar-radiometer capability can be achieved, while in other areas that are more finely dissected the radar can be used alone; furthermore, the radar image can be used to determine the degree of dissection in any particular radiometer cell and thereby establish whether or not the radiometer response from that cell can be expected to be useful.

The multiplicity of modes in the S-193 sensor complicated both the system development and its employment. / Future systems can certainly get by with a less complicated mode set. Another problem that arose in employment of the S-193 was that even with the many modes available the exact combinations needed sometimes could not be achieved. For example, some experiments would have been possible and desirable if it had been possible to point the antenna in a given direction and make a continuous series of measurements to produce a line of data all with the same parameters, yet this was not possible. This suggests that a future system that is intended for experimental purposes should have a software-controllable mode set rather than a hard-wired one.

An attempt was made in the design of the S-193 to arrange optimum integration times for each angle and type of measurement. This unnecessarily complicated the design of the instrument, since the gains in precision achieved in this way were marginal. Either a software-controllable integration time or a set of only two or three integration times would have been better. Many times during the flight of S-193 it would have been desirable to be able to look at the signals from each individual pulse transmitted by the scatterometer, with integration performed on the ground. Future systems should have this capability. Of course use of software-controlled integration times would permit this, but the capability should be provided even if fixed integration times are used for normal operation.

## 7. Publications and Presentations Under This Contract

### Technical Reports

- 243-1 Ulaby, F.T., "Clear Sky Atmospheric Absorption and Emission at 13.9 GHz," June, 1973.
- 243-2 King, C. and R. K. Moore, "A Survey of Terrain Radar Backscatter Coefficient Measurement Programs," December, 1973.
- 243-3 Pintar, J. and A. Sobti, "Analysis of Conditions for Operating the S-193 Rad/Scat in Solar Pointing Mode," July, 1973.
- 243-4 Sobti, A., R. K. Moore and S. Ulaby, "Backscatter Response at 13.9 GHz for Major Terrain Types as Seen from Orbit," September, 1975.
- 243-5 Sobti, A., S. Siriburi and R. K. Moore, "Cluster Analysis of Skylab Radiometer and Scatterometer Data," August, 1975.
- 243-6 Ulaby, F.T., L.F. Dellwig and T. Schmutge, "Satellite Microwave Observations of the Utah Great Salt Lake Desert," August, 1975.
- 243-7 Moore, R. K., "Design Data for Radars Based on 13.9 GHz Skylab  $\sigma^0$  Measurements," November, 1974.
- 243-8 Moore, R. K., F.T. Ulaby, A. Sobti and T. Bush, "Statistics of K-Band Microwave Response of the United States with a Satellite-Borne Radiometer/Scatterometer," October, 1974.
- 243-9 Ulaby, F.T., J. Barr, A. Sobti and R.K. Moore, "Soil Moisture Detection by Skylab's Microwave Sensors," November, 1974.
- 243-10 Sobti, A., "Terrain Response to an Orbiting Microwave Radiometer/Scatterometer," August, 1975.
- 243-11 Sobti, A. and E.C. Davison, "Microwave Scattering Measurements Over Brazil at 13.9 GHz," September, 1975.
- 243-12 Moore, R.K., F.T. Ulaby, A. Sobti, S. Ulaby, S. Siriburi, E. Davison, "Design Data Collection with Skylab Microwave Radiometer/Scatterometer S-193, Final Report," September, 1975.

### Technical Memorandum

- 243-1 King, C., "A Survey of Terrain Radar Backscatter Coefficient Measurement Program," July, 1973.

## Papers and Presentations

- Moore, R.K., et al., "Simultaneous Active and Passive Microwave Response of Earth-Skylab Radsat Experiment," presented at the 9th International Symposium on Remote Sensing, Ann Arbor, Michigan, April, 1974.
- Moore, R.K., "Skylab Microwave Sensing Preliminary Results," Statement to Subcommittee on Manned Space Flight of the Committee on Science and Astronautics, U.S. House of Representatives, February 20, 1974.
- Sobti, A., R.K. Moore, and S.T. Ulaby, "The Influence of Soil Moisture on the Microwave Response from Terrain as Seen from Orbit," to be presented at the 10th International Symposium on Remote Sensing, Ann Arbor, Michigan, October, 1975.
- Sobti, A., and R. K. Moore, "Correlations Between Microwave Scattering and Emission from Land and Sea at 13.9 GHz for Various Incidence Angles and Polarizations," to be presented at The 1975 USNC/URSI - IEEE Meeting, Boulder, Colorado, October, 1975.
- Itbos, A. and Eroom, K.R., "New Radar Astronomical Observations of Planet Earth at 13.9 GHz," to be presented at The 1975 USNC/URSI - IEEE Meeting, Boulder, Colorado, October, 1975.
- Sobti, A., R.K. Moore, and S.T. Ulaby, "Comparison of Skylab Active and Passive Microwave Measurements With Simple Theoretical Models," to be presented at The 1975 USNC/URSI - IEEE Meeting, Boulder, Colorado, October, 1975.
- Ulaby, F.T., A. Sobti, J. Barr and R.K. Moore, "Can Microwave Sensors Measure Soil Moisture from Space?" The 1974 USNC/URSI - IEEE Meeting, Boulder, Colorado, October, 1974.
- Moore, R.K., "Remote Sensing of the Earth With Microwaves - Progress and Problems," 18th General Assembly of URSI, Lima, Peru, August, 1975.

-APPENDIX A

TERRAIN RESPONSE TO AN

ORBITTING MICROWAVE RADIOMETER/SCATTEROMETER



**THE UNIVERSITY OF KANSAS SPACE TECHNOLOGY CENTER**  
**Raymond Nichols Hall**

2291 Irving Hill Drive—Campus West Lawrence, Kansas 66045

Telephone:

TERRAIN RESPONSE TO AN ORBITING MICROWAVE  
RADIOMETER/SCATTEROMETER

Remote Sensing Laboratory  
RSL Technical Report 243-10

Arun Sobti

August, 1975

Supported by:

NATIONAL AERONAUTICS AND SPACE ADMINISTRATION  
Johnson Spacecraft Center  
Houston, Texas 77058

Contract NAS 9-13331

Organization Full Name: The University of Kansas Center for Research, Inc.  
2291 Irving Hill Drive - Campus West  
Lawrence, Kansas 66045

Title of Investigation: Design Data Collection with SKYLAB/EREP Microwave Instrument S-193

Title of Report: Terrain Response to an Orbiting Microwave Radiometer/Scatterometer

Period Covered: 3-26-73 through 12-31-75

NASA Contract: NAS 9-13331

EREP Investigation: 549 M

Principal Investigator: Professor Richard K. Moore

Date Written: August 1, 1975

Monitor and Address: Mr. Larry York  
Earth Observations Division  
Science and Applications Directorate  
NASA Manned Spacecraft Center  
Code TF 3  
Houston, Texas 77058

Type of Report: Advanced Report of Significant Results

## VITAE

Arun Sobti was born in [REDACTED] in [REDACTED]. His family moved to New Delhi, India in 1947, and he is a citizen of India. He received his schooling at Lawrence School Sanawar, a boarding school in the Himalayas. He graduated from high school in 1962. After a year of Pre-Engineering in Government College Chandigarh he was admitted to Panjab Engineering College, Chandigarh. He graduated with a B.S.E.E. from there in 1967 and was admitted to the masters program at the University of Kansas in electrical engineering. He graduated with a master's degree in 1968 and went to work for Western Union. At Western Union he was involved in the design and development of PCM terminals using TDM techniques for multiplexing slow speed data. He returned to the University of Kansas in 1969 to pursue the Ph.D. degree. During his stay at the university, he was first employed as a teaching assistant to teach a digital logic design laboratory. He joined the Remote Sensing Laboratory, University of Kansas in 1970 and was initially involved in the design and development of hardware and software techniques for image interpretation and analysis. He was transferred in 1972 to a project to monitor the design and development of the Skylab radiometer/scatterometer built by General Electric.

He worked with NASA in the planning and operation of the S-193 radiometer/scatterometer experiment. He was then involved in the subsequent processing of data from these sensors. He is a member of Eta Kappa Nu and an associate member of Sigma Xi.

## ACKNOWLEDGEMENTS

To say that this work would not have been possible without the patient guidance of my advisor, Dr. Richard K. Moore, would be a gross understatement. He not only suggested the topic, guided me through the necessary research, but also served as an inspiration in all my work at the Remote Sensing Laboratory. To him I am eternally grateful. I am also much obliged to Dr. F.T. Ulaby for his patience and guidance. He gave of himself and his time more than most candidates for such a degree would receive from their major advisors. To the other members of my committee, I extend my gratitude for their counsel and constructive criticism.

A study as extensive as this could not possibly have been accomplished by one person alone. I wish to acknowledge the kind assistance of my fellow students on the "catalog project". I would especially like to thank Howard Reeves for his help in programing; Evan Davison, Samut Siributi and Saad Ulaby for their help in the manual interpretation and drafting; John Barr for his help on the soil moisture study and Saad again for his help in putting this volume together. To the other students and staff of the Remote Sensing Laboratory who contributed to this study I am truly thankful.

I wish to thank Nancy Ivey, Becky Hansen and Sally Salb for typing the manuscript and Janet Shambaugh and Vera Sehon for help with the drafting. To Sarah Fulkerson for helping with the bibliography and proof reading much of the manuscript, I am very grateful.

Without the support of NASA contract NAS 9-13331 none of this would have been possible. I am indebted to NASA for providing the financial support and data for conducting this research.

Finally, to my family who did not give up hope even after these many years, I am truly grateful.

# TERRAIN RESPONSE TO AN ORBITING MICROWAVE RADIOMETER/SCATTEROMETER

Arun Sobti, Ph.D.  
University of Kansas, 1975

The Skylab manned space vehicle carried on board a composite microwave radiometer/scatterometer (designated along with an altimeter as S-193), operating at 13.9 GHz, as part of the Earth Resources Experiment Package. Data from the radiometer and scatterometer are analyzed to satisfy two objectives: to provide design information for future fine resolution sensors, and, to explore the capabilities and limitations of geoscientific investigation with such gross resolution microwave sensors. For the first objective a catalogue of the microwave response over various terrain was to be prepared.

Histograms of the distribution of backscatter and radiometric brightness temperature are generated for various angles and polarizations for an ensemble of targets in North America, South America and the ocean. Due to the large spatial averaging involved, the dynamic range of backscatter responses at any angle are smaller than those for fine resolution sensors. These dynamic ranges which are a function of incidence angle are larger for the ocean than for land.

The mean backscattering coefficient versus incidence angle is described by polynomial and exponential expressions for both ocean and land. Scattering from land appears as a two-process phenomenon (one governing  $0^\circ - 11^\circ$  and the other  $11^\circ - 47^\circ$ ) whereas ocean appears as only one.

As expected, land appears like a rough surface at 2.16 cms to the radiometer. The ocean surface does, however, exhibit the expected angular characteristic in its radiometric response.

Correlations between the response of a target to various sensor configurations are calculated. The correlation between the radiometric response and the back-scattering coefficient is very small.

Exercises in clustering and linear discriminant analysis show that terrain categories as identified by maps and imagery are not necessarily separable in their microwave response. The sensitivity of both the radiometer and scatterometer to soil moisture are established by examination of an area in Texas.

Applying the geometric optics model and the physical optics model with exponential autocorrelation function to the radar scatterometer data and interpreting the results in radar astronomer's parlance, we find that the earth is smoother than both the moon and Venus. The ocean is only slightly smoother than land. The radiometric data over the ocean is compared to the predictions from a plane surface model.

Image-like presentations produced from backscatter and radiometric temperature data over Texas and Brazil clearly illustrate variations in the response due to soil moisture variations and identify boundaries of major biomes.

A detailed sensor analysis is conducted for the scatterometer; the expected variance of the measurement is computed for both a Gaussian and a uniform signal spectrum. The minimum number of independent samples is 27. An expression is derived for the radiometer bias error. The precision of the radiometer is computed with and without AGC effects included. Various other analyses are described to illustrate the limitations of the sensor and to efficiently compute the illumination integral in the radar equation.

An analysis of the atmospheric effects upon microwave signals shows that for clear sky conditions the scatterometer is almost impervious to the atmosphere. The radiometer is sensitive to the atmosphere but the effect can be adequately compensated by considering a standard atmospheric profile with existing surface conditions. Scatterometer signals will suffer significant attenuation from heavy clouds. The radiometer is very sensitive to clouds and the effects are a function of the water content and temperature of the cloud and the radiometric temperature of the target. Moderate to heavy rain renders data useless even from the scatterometer.

Two simulation packages, one for atmospheric effects and the other for simulating the radiometer/scatterometer on Skylab are described. Some sample results from these simulations are provided.

## TABLE OF CONTENTS

	<u>Page</u>
ACKNOWLEDGEMENT	
ABSTRACT	
CHAPTER 1	
1.0 Introduction	1
CHAPTER 2 THEORETICAL ASPECTS OF SCATTERING	11
2.1 The Terrain Backscatter Experiment	12
2.2 Theoretical Models for Scattering	14
2.2.1 Simple Models	14
2.2.2 Statistical Models	
2.2.2.1 Spetner and Katz Random- Scatterer Model	15
2.2.2.2 Spetner and Katz Specular Point Model	16
2.2.3 Katzin's Model	21
2.2.4 Complete Models	25
2.2.4.1 Physical Optics Approach	27
2.2.4.2 Ray Optics Technique	30
2.2.4.3 Geometric Optics Approach	31
2.2.4.4 Method of Small Perturbation	33
2.2.4.5 Composite Rough Surfaces	37
2.2.4.5.1 Non-Coherent Approach	38
2.2.4.5.2 Coherent Approach	39
2.2.4.6 Surface Roughness of Assumed Slopes	43
CHAPTER 3 RADIOMETRIC EMISSION FROM TERRAIN	45
3.0 Introduction	45
3.1 Microwave Properties of a Surface	46
3.2 The Radiometric Brightness Temperature Experiment	52
3.3 Apparent Brightness Temperature Concept	54
3.4 Equation of Radiative Transfer	56
3.5 Emissivity and Bistatic Scattering Coefficients	60
3.6 Surface Models	64
3.6.1 Very Rough Surface — Lambert Law Model	64
3.6.2 Planar Surface Model	66
3.6.3 Geometric Optics Model	66
3.6.4 Physical Optics Model	67
3.6.5 Composite Model	68
3.6.6 Empirical Model	68



	<u>Page</u>
CHAPTER 6 DESCRIPTION AND ANALYSIS OF S-193 RADIOMETER/ SCATTEROMETER	233
6.1 General Description	233
6.2 Experiment Design	233
6.3 Modes of Operation of S-193 Radiometer/Scatterometer	235
6.3.1 In-Track Non-Contiguous	235
6.3.2 Cross-Track Non-Contiguous	239
6.3.3 In-Track Contiguous	239
6.3.4 Cross-Track Contiguous	241
6.4 Characteristics of Operation of S-193 Scatterometer	247
6.5 Scatterometer Sensor Analysis	248
6.5.1 Sensor Measurement Analysis	248
6.5.2 Sensor Measurement Analysis Considering a Gaussian Signal Spectrum	259
6.5.3 Number of Independent Samples	267
6.5.4 Precision of Power Received Measurement	270
6.5.5 Specification, Verification and Expectation of Normalized Standard Deviation for Power Received Measurements	272
6.6 Radiometer Operating Characteristics	290
6.7 Radiometer Precision and Bias Errors	292
6.8 Antenna Pattern Analysis	305
6.9 Illumination Integral Analysis	313
6.10 Polarization Performance of S-193 Antenna	318
6.11 System Transfer Functions	325
CHAPTER 7 DATA PROCESSING	327
7.0 Introduction	327
7.1 Evolution of S-193 Radiometer/Scatterometer Data for Design of Data Catalogue	337
7.2 Purpose of Analysis	344
7.2.1 Ensemble Statistics of Microwave Response	344
7.2.2 Microwave Response Statistics of Manually Classified Categories	345
7.2.3 Terrain Features from Microwave Response	346
7.2.3.1 Non-Supervised Spatial Clustering Procedure	346
7.2.3.2 K-Means Clustering Procedure	348
7.2.4 Regression Analysis	349
7.2.5 Correlation Analysis	349
7.2.6 General Linear Hypothesis	350
7.2.7 Discriminant Analysis	351
7.2.7.1 General	351
7.2.7.2 Step-Wise Discriminant Analysis Procedure	351
7.2.8 Comparison of Microwave Backscatter Response with Theoretical Scattering Models	352
7.3 Display of Microwave and Supportive Data	355
7.4 Processing Philosophy and Data Management	356
7.5 Special Analyses of S-193 Microwave Data	358
7.5.1 General	358
7.5.2 Review of Radiometer Transfer Function	358

	<u>Page</u>
CHAPTER 8 RESULTS	365
8.0 Introduction	365
8.1 Ensemble Statistics	366
8.1.1 General	366
8.1.2 Statistics of Response from North America	368
8.1.3 Backscatter Response from South America	398
8.1.4 Statistics of Response from Ocean Surfaces	401
8.1.5 Summary of Ensemble Statistics	431
8.2 Design Data for Radar Systems	443
8.3 Correlation Study Results	446
8.4 Analysis of Variance Results	457
8.5 Linear Discriminant Analysis Results	463
8.6 Clustering Results	468
8.7 Special Site Studies	475
8.8 Scan Performance	500
8.9 Comparison of S-193 Data with Theoretical Models	503
8.9.1 Comparison of S-193 Backscatter Data with Theoretical Models	503
8.9.2 Comparison of S-193 Radiometer Data with Theoretical Models	512
8.10 Display of S-193 Data	518
CHAPTER 9 CONCLUSIONS	525
9.0 Summary and Conclusions	525
9.1 Concluding Remarks	531
APPENDIX ONE Description of Selected Hardware Subassemblies of the S-193 Sensor	549
APPENDIX TWO Some Notes on Regression Analysis	557
APPENDIX THREE Selected Results from Simulation Study	564
APPENDIX FOUR Description of Simulation Program Package	578
APPENDIX FIVE Listing of Computer Programs	607

## LIST OF FIGURES

	Page
Figure 2.1	13
2.1	13
2.2	17
2.3	17
2.4	18
2.5	28
2.6	41
2.7	42
3.1	51
3.2	52
3.3	59
3.4	65
4.1a	75
4.1b	76
4.1c	77
4.1d	78
4.2	80
4.3	82
4.4	83
4.5a	84

	<u>Page</u>
Figure 4.5b $\sigma^{\circ}$ as a function of wind velocity, $\lambda = 3.2$ cm. After Grant and Yaplee, 1957.	84
4.6 Backscattering coefficient vs. incidence angle. X-band, horizontal polarization. After Reitz et., 1959.	86
4.7 Goodyear adjusted data (+11.5 dB) HH polarization. Compared with NRL (Ament et al.) data (+6.1 dB) reference of 0 dB for $\sigma^{\circ}$ for heavy vegetation at $43^{\circ}$ . From King and Moore, 1974.	87
4.8 Backscatter coefficient of road surfaces Ku-band. After Cosgriff et al., 1960.	88
4.9a Ohio State farmland data, Ku-band, polarization vv. After Cosgriff et al., 1960.	89
4.9b Backscatter coefficient for farmland, Ohio State, Ku-band, polarization V. After Peake and Oliver, 1969.	90
4.10 Effects of snow cover on grass at X-, Ku- and Ka-bands. After Cosgriff et al., 1960.	91
4.11a Effect of rain on asphalt road. After Cosgriff et al., 1960.	93
4.11b Effect of spraying water on asphalt road. After Cosgriff et al., 1960.	93
4.11c Effects of light rain on 3' alfalfa and grass. After Cosgriff et al., 1960.	93
4.11d Effect of light rain on 3' alfalfa and grass. After Cosgriff et al., 1960.	93
4.12 Backscatter coefficient of various volcanic soils. After Shultz et al., 1969.	94
4.13 Backscatter of limestone quarry surfaces. After Shultz et al., 1969.	95
4.14 Radar cross-section of Pisgah Crater. After Mesenthin, 1967.	96
4.15 Scattering coefficient for sea ice off Point Barrow, Alaska. After Parashar, 1974.	98
4.16a Distribution of mean scattering coefficient of agricultural fields. Polarization: HH; $\theta$ : $10^{\circ}$ incidence. From King and Moore, 1974.	99
4.16b Distribution of mean scattering coefficient of agricultural fields. Polarization: VV; $\theta$ : $20^{\circ}$ incidence. From King and Moore, 1974.	100
4.16c Distribution of mean scattering coefficient of agricultural fields. Polarization: VV; $\theta$ : $30^{\circ}$ incidence. From King and Moore, 1974.	101
4.16d Distribution of mean scattering coefficient of agricultural fields. Polarization: VV; $\theta$ : $40^{\circ}$ incidence. From King and Moore, 1974.	102

	<u>Page</u>
Figure 4.16e	Distribution of mean scattering coefficient of agricultural fields. Polarization: VV; $\theta$ : $50^\circ$ incidence. From King and Moore, 1974. 103
4.16f	Distribution of mean scattering coefficient of agricultural fields. Polarization: VV; $\theta$ : $60^\circ$ incidence. From King and Moore, 1974. 104
4.17	Normalized spectral response curves. From Waite, 1970. 106
4.18	Broad band spectral data at $30^\circ$ look angle. From Ulaby et al., 1972. 107-108
4.19	Scattering coefficient as a function of look angle. Soil type: Pawnee clay loam, rms surface height = 2.5 cm. (a) 4.7 GHz, 4.3 percent moisture. (b) 7.1 GHz, 4.3 percent moisture. (c) 4.7 GHz, 30.2 percent moisture. (d) 7.1 GHz, 30.2 percent moisture. Ulaby, 1974. 109
4.20	(a) Scattering coefficient as a function of moisture content in the top 5 cm. Frequency is 4.7 GHz. (b) Scattering coefficient as a function of moisture content in the top 5 cm. Frequency is 5.9 GHz. (c) Scattering coefficient as a function of moisture content in the top 5 cm. Frequency is 7.1 GHz. From Ulaby et al., 1974. 110-112
4.21	Relative plots of $\sigma^0$ vs. $\theta$ for various terrain types. After Janza et al., 1959. 113
4.22	$16^\circ$ incidence, original data. From King and Moore, 1974. 117
4.23	$16^\circ$ incidence, relative $\sigma^0$ . (Normalized to one incidence angle.) After King and Moore, 1974. 118
4.24	$16^\circ$ incidence, relative $\sigma^0$ . Normalized to farmland data at $52^\circ$ HH polarization. From King and Moore, 1974. 119
4.25a	Upwind radar scatterometer ocean data, Mission 156. After Bradley, 1970. 121
4.25b	Normalized upwind radar scatterometer ocean data, Mission 156. After Bradley, 1970. 121
4.26a	Brightness temperature compared to volume soil moisture, bare ground, clear sky. After Edgerton, 1971. 124
4.26b	Brightness temperature compared to volume soil moisture, bare ground, clear sky. After Edgerton, 1971. 125
4.27	Comparison of radiometric temperatures, 37.0 GHz, vertical polar- ization. After Edgerton and Trexler, 1972. 127

	<u>Page</u>
Figure 4.28 13.4 GHz radiometric temperatures of Playa sediments with variable moisture. After Edgerton, 1971.	128
4.29 Measured dry snow brightness temperatures. After Meier and Edgerton, 1971.	129
4.30 Calculated and measured emissivities for asphalt and concrete at 16.5 GHz. After Porter, 1966.	130
4.31 Observed brightness temperatures vs. nadir angle at 1.55 cms over smooth and rough portions of the Salton Sea. Each point is an average of 6 consecutive points at that angle. From Nordberg et al., 1970.	131
4.32 Plot of 21.1 cm brightness temperatures vs. soil moisture from Phoenix, Arizona. From Schmugge et al., 1972.	133
4.33 Individual measurements at 8.36 and 19.34 GHz of the vertical and horizontal components of brightness temperature and the percentage polarization of the sea at 55° incidence angle are plotted vs. wind speed. The solid lines are linear least-squares solutions to the data. From Hollinger, 1970.	134
5.1 Radiosonde sample northeast of warm front.	147
5.2 Radiosonde sample warm sector of cyclone.	148
5.3 Radiosonde sample Azores in sub-tropical night.	149
5.4 Radiosonde sample Swan Island (tropical).	150
5.5 Pressure vs. temperature; Topeka radiosonde profile and corresponding model profile, June 21, 1972, at 12.00 hrs. (GMT), 10% cloudy.	151
5.6 Pressure vs. temperature for Topeka radiosonde and corresponding model profile June 22, 1972, at 0.00 hrs. (GMT), overcast sky.	152
5.7 Attenuation due to oxygen (vs. temperature) $P_o = 1013.25$ mb	159
5.8 Attenuation due to water vapor vs. surface temperature $P_o = 1013.25$ mb; $P = 5.0$ gms/m <sup>3</sup> .	160
5.9 Attenuation due to water vapor vs. surface temperature $P_o = 1013.25$ mb $P = 8.0$ gms/m <sup>3</sup> .	161
5.10 Attenuation due to water vapor vs. surface temperature $P_o = 1013.25$ mb; $P = 11.0$ gms/m <sup>3</sup> .	162
5.11 Attenuation due to water vapor vs. surface temperature $P_o = 1013.25$ mb; $P = 14.0$ gms/m <sup>3</sup> .	163
5.12 Attenuation due to water vapor vs. surface temperature $P_o = 1013.25$ mb; $P = 17.0$ gms/m <sup>3</sup> .	164

	<u>Page</u>
Figure 5.13 Attenuation due to water vapor vs. surface temperature $P_0 = 1013.25$ mb; $P = 20.0$ gms/m <sup>3</sup> .	165
5.14 Emission and transmittance vs. water vapor content.	166
5.15 Emission and transmittance vs. water vapor content.	167
5.16 Emission and transmittance vs. water vapor content.	168
5.17 Emission and transmittance vs. water vapor content.	169
5.18 Emission and transmittance vs. surface temperature $RHO = 8$ gms/m <sup>3</sup> .	170
5.19 Total transmittance computed for actual radiosonde profile and model profile (warm sector).	172
5.20 Total transmittance computed for actual radiosonde and model profile (warm sector).	173
5.21 Total transmittance computed for actual radiosonde profile and modelled profile (for Bermuda high).	174
5.22 Total transmittance computed for actual radiosonde profile and model profile (Swan Island).	175
5.23 Total transmittance for model profile and radiosonde profile of Topeka radiosonde data June 21, 1972, at 12.00 hrs (GMT).	176
5.24 Total transmittance for radiosonde and modelled profile or atmosphere June 22, 1972 0.00 hrs. Topeka radiosonde.	177
5.25 Difference in transmittance between warm wave front and Boer model (midlatitude models).	178
5.26 Difference in transmittance between Boer model and Bermuda high (midlatitude model).	179
5.27 $T_{atm}$ for warm wave front and U.S. standard model.	180
5.28 $T_{atm}$ for warm sector of cyclone and U.S. standard model.	181
5.29 $T_{atm}$ for Azores in sub-tropical heights and U.S. standard model.	182
5.30 $T_{atm}$ for Swan Island profile and U.S. standard model.	183
5.31 $T_{atm}$ for a radiosonde profile and model profile Topeka, June 21, 1972 at 12.0 hrs. (GMT).	184
5.32 $T_{atm}$ for radiosonde and model profile. Topeka, June 22, 1972, at 0.00 hrs. (GMT).	185
5.33 Difference between $T_{atm}$ computed on the basis of actual profile and modelled profiles	186
5.34 Attenuation coefficient for clouds. From Benoit, 1968.	191
5.35 Attenuation due to clouds (Kreiss's Classification).	193
5.36 Attenuation by clouds (Porter's Classification).	194

	<u>Page</u>
Figure 5.37 Atmospheric attenuation and transmittance with clouds present-- a sample case.	195
5.38a Distribution of precipitation rate with altitude for Case I.	198
5.38b Concentration of precipitation rate in $\text{g m}^{-3}$ with height, for Case I.	198
5.39 Concentration of precipitation in $\text{g m}^{-3}$ , with height, for Case II.	198
5.40 Concentration of precipitation in $\text{g m}^{-3}$ , with height, for Case III.	198
5.41 Vertical temperature distribution for situations of widespread precipi- tation.	199
5.42 Steady-state water content of clouds for a situation similar to Case I and for surface intensities of 2, 5, 10, and 20 $\text{mm h}^{-1}$ (derived from Wexler and Atlas, 1958).	200
5.43 Steady-state water content of clouds for a situation similar to case II, for surface rain intensities of 2, 5, and 20 $\text{mm h}^{-1}$ (derived from Wexler and Atlas, 1958).	200
5.44 Attenuation (dB/km) due to rain. After Benoit, 1968.	203
5.45 Emissivity of calm ocean vs. angle of incidence used in simulation.	206
5.46 Emissivity of sandy soil vs. incidence angle for various soil moisture conditions. From F. T. Ulaby, 1975.	207
5.47 Emissivity vs. incidence angle for sandy soil with 3 different soil moisture conditions. From F. T. Ulaby, 1975.	208
5.48 Simulated results for northeast of warm front sample; polarization HH, ocean surface.	211
5.49 Simulated results for warm sector of cyclone sample; polarization HH, ocean surface.	212
5.50 Simulated results for Azores in subtropical high sample; polarization HH, ocean surface.	213
5.51 Simulated results for Swan Island tropical sample; polarization HH, ocean surface.	214
5.52 Simulated results for northeast of warm front sample; polarization VV, ocean surface.	216
5.53 Simulated results for warm sector of cyclone sample; polarization VV, ocean surface.	217
5.54 Simulated results for Azores in sub-tropical high sample; polarization VV, ocean surface.	218

		<u>Page</u>
Figure 5.55	Simulated Results for Swan Island tropical sample; polarization VV, ocean surface.	219
5.56	Simulated results for northeast of warm front sample; polarization HH, sand surface.	220
5.57	Simulated results for Swan Island tropical sample; polarization HH, sand surface.	221
5.58	Simulated results for northeast of warm front sample; polarization VV, loam surface.	223
5.59	Simulated results for Swan Island tropical sample; polarization VV, loam surface.	224
5.60	Simulated results for Topeka sample with surface temperature at 283° K; polarization HH, sand surface.	226
5.61	Simulated results for Topeka sample with surface temperature at 283° K; polarization VV, sand surface.	227
5.62	Simulated results for Topeka sample with surface temperature at 283° K; polarization VV, loam surface.	228
5.63	Simulated results for cloudy and not cloudy conditions over a sand surface for two surface temperatures, polarization VV.	229
5.64	Simulated results for cloudy and not cloudy conditions over a sand surface for two surface temperatures.	230
6.1	Block diagram of S-193 system.	236
6.2	Pictorial view of the In-Track Non-Contiguous Mode.	237
6.3	Cross-Track Non-Contiguous Mode.	240
6.4	In-Track Contiguous Mode.	242
6.5	Cross-Track Contiguous Mode.	242
6.6	Block diagram of signal path through S-193 scatterometer.	248
6.7	Transmitted power spectrum.	249
6.8a	Normalized standard deviation vs. ratio of noise density to signal density.	276
6.8b	Normalized standard deviation vs. integration time of signal to noise.	277
6.9	Region of acceptance for testing normalized standard deviation specifications.	278

		<u>Page</u>
Figure 6.10	"Radiometer Processor Block Diagram" from GE Calibration Data Report.	291
6.11	Ratio of the temperature resolution of a two-reference temperature radiometer (with AGC) to the resolution of a conventional balanced-Dicke radiometer.	304
6.12	S-193 Radiometer/Scatterometer antenna pattern, horizontal polarization.	307
6.13	S-193 Radiometer/Scatterometer antenna pattern, vertical polarization.	307
6.14	Beam Efficiency for S-193 Antenna.	311
6.15	Beam Efficiency for S-193 Antenna.	312
6.16	Geometry of illumination for S-193 measurements.	314
6.17	Incremental (relative) energy contribution to illumination integral in beam angle from antenna boresight.	319
6.18	Cumulative energy contribution to illumination integral in beam angle from antenna boresight.	320
6.19	Geometry for a pitch and roll excursion measurement.	321
7.1	Cross-Track Contiguous data takes over U.S.A. during SL2, SL3 missions considered in Design of Data Catalogue.	334
7.2	In-Track Contiguous data segments over U.S.A. during SL2, SL3 missions considered in Design of Data Catalogue.	335
7.3	In-Track Non-Contiguous data segments over U.S.A. during SL2, SL3 missions considered in Design of Data Catalogue.	336
7.4	S-193 Radiometer/Scatterometer Data Processing Flow.	338
7.5	Data flow diagram for Stage II of processing.	341
7.6	The non-supervised spatial processing approach.	347
8.1	Histogram of the scatterometer backscatter coefficient, between $1.0^\circ$ and $2.0^\circ$ , V Polarization, North America.	371
8.2	Histogram of the scatterometer backscatter coefficient between $2.0^\circ$ and $3.0^\circ$ , H Polarization, North America.	372
8.3	Histogram of the scatterometer backscatter coefficient, between $2.0^\circ$ and $3.0^\circ$ , V Polarization, North America.	373
8.4	Histogram of the scatterometer backscatter coefficient, between $8.0^\circ$ and $10.0^\circ$ , V Polarization, North America.	374

		<u>Page</u>
Figure 8.5	Histogram of the scatterometer backscatter coefficient, between 16.0° and 18.0°, V Polarization, North America.	376
8.6	Histogram of the scatterometer backscatter coefficient, between 32° and 36°, V Polarization, North America.	377
8.7	Histogram of the scatterometer backscatter coefficient, between 32° and 36°, H Polarization, North America.	378
8.8	Histogram of the scatterometer backscatter coefficient, between 42.0° and 50.0°, VV Polarization, North America.	379
8.9	Histogram of the scatterometer backscatter coefficient, between 42.0° and 50.0°, HH Polarization, North America.	380
8.10	Histogram of the Radiometer Brightness Temperature, between 1.0° and 2.0°, V Polarization, North America.	381
8.11	Histogram of the Radiometer Brightness Temperature, between 1.0° and 2.0°, H Polarization, North America.	383
8.12	Histogram of the Radiometer Brightness Temperature, between 2.0° and 3.0°, V Polarization, North America.	384
8.13	Histogram of the Radiometer Brightness Temperature, between 2.0° and 3.0°, H Polarization, North America.	385
8.14	Histogram of the Radiometer Brightness Temperature, between 8.0° and 10.0°, V Polarization, North America.	387
8.15	Histogram of the Radiometer Brightness Temperature, between 8.0° and 10.0°, H Polarization, North America.	388
8.16	Histogram of the Radiometer Brightness Temperature, between 16.0° and 18.0°, V Polarization, North America.	389
8.17	Histogram of the Radiometer Brightness Temperature, between 16.0° and 18.0°, H Polarization, North America.	390
8.18	Histogram of the Radiometer Brightness Temperature, between 18.0° and 20.0°, V Polarization, North America.	391
8.19	Histogram of the Radiometer Brightness Temperature, between 18.0° and 20.0°, H Polarization, North America.	392
8.20	Histogram of the Radiometer Brightness Temperature, between 32.0° and 36.0°, V Polarization, North America.	394
8.21	Histogram of the Radiometer Brightness Temperature, between 32.0° and 36.0°, H Polarization, North America.	395

		<u>Page</u>
Figure	8.22 Histogram of the Radiometer Brightness Temperature, between $42.0^{\circ}$ and $50.0^{\circ}$ , V Polarization, North America.	396
	8.23 Histogram of the Radiometer Brightness Temperature, between $42.0^{\circ}$ and $50.0^{\circ}$ , H Polarization, North America.	397
	8.24 Generalized vegetation patterns in Barzil in Relation to S-193 Passes.	399
	8.25 Histogram of the Scatterometer Backscatter Coefficient, between $32.0^{\circ}$ and $34.0^{\circ}$ , V Polarization, South America.	400
	8.26 Histogram of the Scatterometer Backscatter Coefficient, between $32.0^{\circ}$ and $34.0^{\circ}$ , H Polarization, South America.	402
	8.27 Histogram of the Scatterometer Backscatter Coefficient, between $0^{\circ}$ and $2^{\circ}$ , VV Polarization, Ocean.	403
	8.28 Histogram of the Scatterometer Backscatter Coefficient, between $0^{\circ}$ and $2^{\circ}$ , HH Polarization, Ocean.	405
	8.29 Histogram of the Scatterometer Backscatter Coefficient, between $0^{\circ}$ and $2^{\circ}$ , VH Polarization, Ocean.	406
	8.30 Histogram of the Scatterometer Backscatter Coefficient, between $0^{\circ}$ and $2^{\circ}$ , HV Polarization, Ocean.	407
	8.31 Histogram of the Scatterometer Backscatter Coefficient, between $16^{\circ}$ and $18^{\circ}$ , VV Polarization, Ocean.	408
	8.32 Histogram of the Scatterometer Backscatter Coefficient, between $16^{\circ}$ and $18^{\circ}$ , HH Polarization, Ocean.	409
	8.33 Histogram of the Scatterometer Backscatter Coefficient, between $16^{\circ}$ and $18^{\circ}$ , VH Polarization, Ocean.	411
	8.34 Histogram of the Scatterometer Backscatter Coefficient, between $16^{\circ}$ and $18^{\circ}$ , HV Polarization, Ocean.	412
	8.35 Histogram of the Scatterometer Backscatter Coefficient, between $32^{\circ}$ and $34^{\circ}$ , VV Polarization, Ocean.	413
	8.36 Histogram of the Scatterometer Backscatter Coefficient, between $32^{\circ}$ and $34^{\circ}$ , HH Polarization, Ocean.	414

		<u>Page</u>
Figure	8.37 Histogram of the Scatterometer Backscatter Coefficient, between 32° and 34°, VH Polarization, Ocean.	415
	8.38 Histogram of the Scatterometer Backscatter Coefficient, between 32° and 34°, HV Polarization, Ocean.	416
	8.39 Histogram of the Scatterometer Backscatter Coefficient, between 42° and 50°, VV Polarization, Ocean.	417
	8.40 Histogram of the Scatterometer Backscatter Coefficient, between 42° and 50°, HH Polarization, Ocean.	418
	8.41 Histogram of the Scatterometer Backscatter Coefficient, between 42° and 50°, VH Polarization, Ocean.	419
	8.42 Histogram of the Scatterometer Backscatter Coefficient, between 42° and 50°, HV Polarization, Ocean.	420
	8.43 Histogram of the Radiometer Brightness Temperature, between 0.0° and 2.0°, V Polarization, Ocean.	423
	8.44 Histogram of the Radiometer Brightness Temperature, between 0.0° and 2.0°, H Polarization, Ocean.	424
	8.45 Histogram of the Radiometer Brightness Temperature, between 16.0° and 18.0°, V Polarization, Ocean.	425
	8.46 Histogram of the Radiometer Brightness Temperature, between 16.0° and 18.0°, H Polarization, Ocean.	426
	8.47 Histogram of the Radiometer Brightness Temperature, between 32.0° and 34.0°, V Polarization, Ocean.	427
	8.48 Histogram of the Radiometer Brightness Temperature, between 32.0° and 34.0°, H Polarization, Ocean.	428
	8.49 Histogram of the Radiometer Brightness Temperature, between 42.0° and 50.0°, V Polarization, Ocean.	429
	8.50 Histogram of the Radiometer Brightness Temperature, between 42.0° and 50.0°, H Polarization, Ocean.	430
	8.51 Summary of angular scatterometer response for VV Polarization from S-193 Scatterometer operations during SL2-SL3.	432
	8.52 Summary of angular scatterometer response for HH Polarization from S-193 Scatterometer operations during SL2-SL3.	433

<u>Figure</u>		<u>Page</u>
8.53	Standard deviations of backscatter measurement versus angle of incidence for VV and HH Polarization over North America.	434
8.54	Summary of angular radiometric response for VV polarization from S-193 radiometer operations during SL2-SL3.	435
8.55	Summary of angular radiometric response for HH polarization from S-193 radiometer operations during SL2-SL3.	436
8.56	Standard deviations of S-193 Radiometer measurement (VV and HH polarizations) versus angle of incidence for North America targets from SL2-SL3 operations.	437
8.57	Summary of angular scatterometric response over ocean surfaces for VV and HV polarizations from S-193 scatterometer operations during SL2-SL3.	438
8.58	Summary of angular scatterometric responses over ocean surfaces for HH polarizations from SL2-SL3 data.	439
8.59	Summary of angular scatterometric response over ocean surfaces for HV polarizations from SL2-SL3 data.	440
8.60	Summary of angular scatterometric response over ocean surfaces for VH polarization from SL2-SL3 data.	441
8.61	Summary of angular radiometric response over ocean surfaces from S-193 radiometer, non-contiguous mode operations during SL2-SL3.	442
8.62	Texas site (6-5-73) Soil Site Map.	477
8.63	June 1 Rainfall Extrapolated to a 46 x 59 Grid Over Texas Site.	480
8.64	June 2 Rainfall Extrapolated to a 46 x 59 Grid Over Texas Site.	481
8.65	June 3 Rainfall Extrapolated to a 46 x 59 Grid Over Texas Site.	482
8.66	June 4 Rainfall Extrapolated to a 46 x 59 Grid Over Texas Site.	483
8.67	June 5 Rainfall Extrapolated to a 46 x 59 Grid Over Texas Site.	484

		<u>Page</u>
Figure 8.68	Composite Rainfall History (API) for June 1-5 Extrapolated to a 46 x 59 Grid Over Texas Site.	485
8.69	Radiometer Temperatures Extrapolated to a 46 x 59 Grid Over Texas Site.	486
8.70	June 5 Daily Maximum Temperatures Extrapolated to a 46 x 59 Grid Over Texas Site.	487
8.71	Backscattering Coefficient Extrapolated to a 46 x 59 Grid Over Texas Site.	488
8.72	Scatter Plot of Radiometric Temperature and API Over Texas Site.	490
8.73	Scatter Plot of Backscatter in dB and $API_b$ Over Texas Site.	491
8.74	Scatter Plot of Emissivity and $API_b$ Over Texas Site.	492
8.75	Scatter Plot of Emissivity and API Over Texas Site.	493
8.76	Scatter Plot of Backscatter in dB and API Over Texas Site.	494
8.77	Scatter Plot of Backscatter and API Over Texas Site.	495
8.78	Scatter Plot of Emissivity and Normalized API Over Texas Site.	497
8.79	Scatter Plot of Backscatter and Normalized API Over Texas Site.	498
8.80	Instantaneous Field of View Five Angle Footprint (Scatterometer) For In-Track Non-Contiguous Mode.	501
8.81	Instantaneous Field of View for Five Angle Footprint (Scatterometer) For In-Track Contiguous Mode.	502
8.82	Five sample Backscatter Responses for computation of Mean Slope and Reflection Coefficient by Lunar Theories.	507
8.83	Comparison of emissivities computed from S-193 radiometer measurements over ocean and some predicted values based upon a plane surface model.	516
8.84	Pseudo-Images Produced from Backscatter Response with Cross-Track Contiguous, Pitch 29° Mode of S-193 Operation on Day 162, Pass 8 SL-2 Over Brazil.	520
8.85	Pseudo-Images Produced from Backscatter Response with Cross-Track Contiguous, Pitch 29° Mode of S-193 Operation on Day 161, Pass 7, SL-2 over Brazil.	521
8.86	Pseudo-Images Produced from Backscatter Response with Cross-Track Contiguous, Pitch 29° Mode of S-193 Operation. Pass 5, Day 156.	522



	<u>Page</u>
Figure C-11 Spatial orientation of targets viewed with CTC pitch $29.4^\circ$ , roll $0^\circ$ mode scatterometer operation. Footprints for first and last pulse at each measurement period are shown. Equatorial latitude, orbit height 435 kms. From Sobti, 1974.	575
C-12 Spatial orientation of targets viewed with CTC pitch $40.1^\circ$ , roll $0^\circ$ mode scatterometer operation. Footprints for first and last pulse at each measurement period are shown. Equatorial latitude, orbit height 435 kms. From Sobti, 1974.	576
C-13 True incidence angle vs. pitch or roll angle for an orbit height of 435 kms. From Sobti, 1974.	577
D-1 Macro flow chart for simulation program.	582
D-2 Block diagram for simulation program controls.	587

## LIST OF TABLES

	<u>Page</u>
Table 2.1 Summary table of backscattering coefficient for various wave-length regions. From Katz and Spetner, 1960.	18
3.1 Average dielectric properties of rocks from Campbell and Ulrich, 1969.	50
4.1 Terrain scattering response catalog from open literature. From King and Moore, 1974.	72
4.2 Emissivity for some targets at 1.6 and 3.2 cms. From Melenteyev and Rabinovich, 1972.	137
5.1 Rotational states for oxygen absorption. After Meeks and Lilley, 1963.	156
6.1a S-193 Non-Contiguous Mode dwell sequence.	244
6.1b In-Track Contiguous Mode dwell sequence.	243
6.1c Cross-Track Contiguous measurement sequence per scan.	245
6.2 Minimum and maximum expected signal to noise density ratios during S-193 R/S operation.	272
6.3 Integration times for scatterometer measurements.	273
6.4 Doppler and IF Filter Bandwidths for S-193 scatterometer operation.	274
6.5 Expected precision--In-Track contiguous (system noise temperature--1200°K).	281
6.6 Expected precision--Cross-Track contiguous (system noise temperature--1200°K).	282
6.7 Expected precision--Cross-Track contiguous (system noise temperature--1200°K).	283
6.8 Expected precision--In-track contiguous (system noise temperature--1200°K).	284
6.9 Expected precision--Cross-track contiguous (system noise temperature--1200°K).	285
6.10 Link calculations ITNC and CTNC modes.	287
6.11 Link calculation--ITC mode.	288
6.12 Link calculations--CTC (scat only) mode.	289
6.13 Resolution of S-193 Radiometer, assuming no gain changes during measurement (Dicke radiometer operation).	299
6.14 Resolution of S-193 Radiometer with AGC effects included.	305

		<u>Page</u>
Table 6.15	Results of antenna pattern measurements.	306
6.16	S-193 antenna one-way beam efficiencies.	310
6.17	S-193 antenna two-way beam efficiencies	310
6.18	Effective beamwidths for the S-193 antenna (in degrees).	313
7.1	Data segments of CTC mode used in Design of Data Catalogue.	329
7.2	Data segments of ITC mode of operation used in Design of Data Catalogue.	331
7.3	Data segments of ITNC mode of operation used in Design of Data Catalogue.	333
7.4	Mode-dependent gain adjustment factors for the radiometer.	363
8.1	Summary of optimal regression equations describing the angular backscatter from North America and from the ocean	444
8.2	Correlation Matrix for 15 of the 30 sensor configurations of ITNC mode operation. Responses considered are $\sigma_{VV}^o$ , $T_{BV}$ , and $T_{BH}$ at five angles of incidence.	448
8.3	Correlation Matrix for 10 sensor configurations of ITNC mode. Responses considered are $\sigma_{VV}^o$ and $\sigma_{HH}^o$ at five angles of incidence.	450
8.4	Correlation Matrix for 10 sensor configurations of ITNC mode. Responses considered are $\sigma_{VH}^o$ and $\sigma_{HH}^o$ at five angles of incidence.	452
8.5	Correlation Matrix for 10 sensor configurations of ITNC mode. Responses considered are $\sigma_{VH}^o$ and $T_{BV}$ for five angles of incidence.	453
8.6	Correlation Matrix of $\sigma_{VV}^o$ at five angles of incidence from ITC data.	455
8.7	Correlation Matrix $\sigma_{VV}^o$ at five angles of incidence considering data from ITC pass on Day 253.	456
8.8	Analysis of variance, one-way lay-out for backscatter response of terrain categories at $33^\circ$ .	459
8.9	Classification summary and classification functions.	465
8.10	Classification summary using ITC (VV) backscatter data at $42^\circ$ , $33^\circ$ , $17^\circ$ from North America targets.	466

		<u>Page</u>
Table 8.11	Classification summary using ITC (VV) backscatter response at 42°, 33°, 17° for pass from Texas to Maine. The underlying distributions were created by considering only homogeneous areas.	466
8.12	Proportions of land use and Physiographic categories in clusters produced by considering backscatter Coefficients at 42°, 33°, 17° from ITC (VV) data. Only U.S. and some ocean targets are considered.	470
8.13	Results of clustering analysis considering radiometer and scatterometer responses from CTC Pitch 29° operation.	472
8.14	Results of cluster analysis considering scatterometer responses from CTC Pitch 29° operation.	472
8.15a	Results of cluster analysis using 42°, 33°, 17° from ITC (VV) data for Texas to Maine. Pass on Day 253.	474
8.15b	Comparable results by using spatial clustering rather than K-means clustering. (Gradient Threshold = 1)	474
8.16	Summary table showing linear fits and correlations between various soil moisture estimates and the S-193 microwave response for the Texas site (Day 156)	499
8.17	Summary of results showing the computed R.M.S. Slope and Reflection coefficient by considering a Gaussian and an Exponential autocorrelation function.	508
8.18	Comparisons of Mean Slope As computed by various Suggestions in the Literature (expressed in degrees)	509
8.19	Dielectric Constants Computed From Reflection Coefficients for the Exponential Autocorrelation Function.	511
8.20	Summary of results showing emissivities computed from a place surface model using dielectric constant data and using S-193 Data	515

## CHAPTER ONE:

### 1.0 INTRODUCTION

The response of terrain to a radiometer and scatterometer on an orbital platform is documented in this study. The scatterometer part of the S 193 radiometer/scatterometer experiment conducted as part of the Earth Resources Experiment Package on Skylab provides the first opportunity of studying the response of terrain from orbital heights. The radiometer part of the experiment had the best resolution of any radiometer that has ever operated in space. Data from these sensors were analyzed to describe the differential backscattering coefficient and the radiometric brightness temperature of terrain.

A major motivation for the analysis of these data was to add to the limited information available on the backscatter response and the radiometric emission of terrain. For example, Moore [Skolnik, 1970] writes "Although many programs have measured the scattering coefficient of the ground, the lack of coordinated research over the necessary long period of time make available data from carefully controlled measurements rare indeed." A similar situation exists for radiometric brightness temperature.

Although ground-based measurement programs are exhaustive in coverage of their targets, there is no expedient method by which the fine grain data can be extrapolated to a grosser resolution context. Without denying these measurement programs credit for aiding in the solution of the general problem of scattering by non-uniform surfaces, it must be pointed out that they are of limited value in aiding the identification/recognition of terrain surfaces from a remote platform with coarse resolution. Aircraft based measurement programs have been numerous, but for many of these, the primary objective was to determine optimum design parameters for specialized radars. Regardless of their precision and coordination with supporting ground truth, the measurement programs have, to date, viewed only a small fraction of the natural terrain surfaces. The operation of the radiometer and scatterometer on board Skylab provided data over more regions than the entire set of aircraft and ground based sensors. The resolution of the S 193 sensors was, however, very much larger than those for any aircraft based sensor, and consequently the identification/discrimination criterion was based upon much more gross classifications of ground truth. The results of this study will, however, influence the design of future fine resolution sensors.

A major unsolved problem of electromagnetic theory is interaction of electromagnetic waves with non-uniform surfaces. The scattering theoreticians have ardently tackled this problem for surfaces that can be modelled mathematically. Chapter Two describes some of the theoretical models proposed. These models range from the simple rough surface model proposed by Clapp [1946] for certain surfaces, to the composite model [Chan and Fung 1973], where the tangent plane approximation is used to solve for the large scale structures and the small perturbation theory is used for the small scale structures and the two are coherently summed. These models get more complicated as they approach the real-life distribution of most surfaces. This composite model has been used to predict the backscattering over the ocean; its capability for land targets is severely limited by the inability to determine the necessary descriptors (rms roughness, spectrum probability density functions of slope) or to satisfy some of the assumptions needed for the land.

With the understanding that only a very small fraction of all terrain scenes can be considered mathematically tractable, scattering theory can only be considered an aid to the interpretation of terrain by its microwave response. An empirical scheme is obviously required. The first step of preparing such a scheme, if there exists one, is to collect and catalogue the responses measured from terrain. This first step provides another source motivation for this study.

The concept of brightness temperature has been known for a long time. Measurements of the brightness temperature were conducted by astronomers long before radiometers were used for earth observations. Chapter Three provides a brief background of the concept of brightness temperature and then describes the relationship between the bistatic scattering coefficients and the emissivity of a target as suggested by Peake [1959]. The theoretical models to describe the emissivity of a target have depended on models to describe the bistatic scattering coefficients. These, again, range from the simple rough surface model suggested by Peake [1960] to the composite model used by Wu [1972] to describe the radiometric temperature from an ocean surface. As in the case of scattering models, empirical evidence has also been used to dictate models Peake, [1962]. The bibliography contains numerous references where a more exhaustive review may be found.

A data catalogue of the microwave response of terrain from orbital heights must be added to, and compared and contrasted with measurements conducted to date. To actually present the data from measurement programs for scattering and emission would

be prohibitively copious. A flavor of the types of measurements performed and some examples of the results are, however, provided in Chapter four. Six major scatterometer measurement programs (including aircraft and ground based) and seven major radiometer measurement programs are reviewed. Some others are also listed. Examples of some comparisons of the backscatter response from various measurement programs as described by King and Moore [1974] are provided. No such comparisons could be made for the radiometer measurements because of uncertainties in the physical temperature, atmospheric effects and antenna parameters associated with the various programs.

The operational results from a sensor in space when looking down on the earth can sometimes be degraded by the atmosphere. For sensors operating in the optical region, the presence of clouds eliminates any information from the ground reaching the sensor on an orbiting satellite. To determine the effects of the atmosphere upon the S193 radiometer/scatterometer a detailed study was conducted. The details are provided in Chapter Five. A Simulation package was designed so that various parameters including the apparent (or antenna) brightness temperature, excess temperature, transmittance and many more, could be predicted for various combinations of targets and atmospheric conditions. It was found that at the wavelength of the S-193 radiometer/scatterometer the attenuation due to oxygen can be ignored because the variations caused by oxygen attenuation are only 0.076 dB. The attenuation varies linearly with uncondensed water vapor content and variations due to temperature or pressure for a fixed water vapor concentration are small. It is shown that a modelled atmospheric profile as described in Chapter five, using surface values for temperature, pressure and humidity predicts the total effects of the atmosphere as well as the actual radiosonde. There seems to be a problem in applying the standard model profile for atmospheric conditions where a temperature and/or humidity inversion occurs. The effect of clouds is a function not only of the water content but also of the temperature of the clouds. Various cloud models are examined. The effect of clouds is more severe for some models (some of Kreiss's [1968] classification) than for others (Porter [1970]). The effects of rain are examined. From the simulation package it was found that the higher the physical temperature or emissivity of the target, the less the error due to the atmosphere. In the absence of rain or clouds and for temperate region characterized by lower water vapor

concentration, the effects of the atmosphere upon the scatterometer signal can be compensated by a fixed transmission loss to a first approximation. For radiometer measurements the effect of the atmosphere are much more severe and no such approximation is valid.

A problem with the documentation of results from most measurement programs is that the sensors are not adequately described. A proper interpretation of the results cited by an investigation must consider the instrumentation employed. A brief description of the operating modes of the S-193 instrument is provided in Chapter six. Descriptions of some of the major subassemblies of the S-193 radiometer/scatterometer are included in the appendix. A sensor analysis for both the radiometer and the scatterometer is provided in Chapter six. It was found that, based upon statistical models for noise and signal, the number of independent samples will always be greater than 27. Two types of input signal spectrum (Gaussian and rectangular) are considered and the resulting precision and number of independent samples, are compared. It was found that the Gaussian spectrum case has more independent samples for high signal-to-noise ratio than a rectangular spectrum. Both have the same number of independent samples for very low signal-to-noise ratios. Expressions describing the signal measurement variance for both cases are derived.

Expressions describing the precision of the radiometer are derived for two cases: considering no gain fluctuations during the radiometer measurement and considering gain changes due to AGC action. It was found that the computed precision is much better when the gain changes are not considered. In fact, as the limit of the ratio of AGC time constant to the signal time constant approaches infinity the two cases become alike. The bias errors of the radiometer measurement are derived. The precision of the S-193 radiometer was found to lie within  $0.37^{\circ}$  to  $1.4^{\circ}\text{K}$  over the dynamic range of measurements.

The antenna pattern of a radiometer is critical to the retrieval of brightness temperature from a voltage recording. The S-193 antenna is examined in terms of computing efficiencies and establishing the distribution of energy across  $4\pi$  steradians. It was found that the beam efficiency is approximately 84% for the two principal polarizations. It is shown that the poor isolation of the S-193 antenna will cause a substantial error in the cross-polarized measurements (as much as 3 dB).

The illumination integral defined as the quantity in square brackets in the equation

$$\sigma^{\circ}(\psi) = \frac{(4\pi)^3}{\lambda^2} \left(\frac{P_r}{P_t}\right) \cdot L_1 L_2 \left[ \iint_{\Omega} \frac{G_o^2 f(\theta, \phi, \psi)}{R^4(\theta, \phi, \psi)} d\theta d\phi \right]^{-1}$$

needs to be known for each incidence angle and orbital height of the sensor. Computing this integral repeatedly is very costly and time-consuming. An approximate value (good to within 0.2% for nominal orbital heights) can, however, be found expediently. Details of the derivation may be found in chapter six. The poor isolation of the S-193 antenna can cause problems in defining the polarizations for a target that exhibits polarization selectivity. A simple analysis describes this effect when both pitch and roll excursions of the antenna are commanded.

To examine the characteristics of the microwave response of terrain as seen by the S-193 sensors, many individual and distinct studies are required. This is the first time that a radar has operated in space to measure the backscatter from terrain surfaces. The results of the examination of the data obtained from these sensors will no doubt be helpful for the design of future sensors. Some of the questions addressed in the requirements of the design are answered by the analyses contained in this work. We have tried to compute many of the helpful parameters. Since there were so many distinct and sometimes isolated analyses which were conducted, a whole chapter was devoted to the description of the data processing involved.

Chapter seven describes the evolution and nature of the data and in capsule form describes the various analyses conducted. Some of the descriptions included in Chapter seven are intended for the reader to have a better appreciation of the results presented in Chapter eight. Others are included to show the various efforts involved in compiling the results presented in Chapter eight.

Due to the spatial averaging involved, the range between deciles of the backscatter response from North American targets is much smaller than that observed by fine resolution sensors. The range between deciles is maximum at around  $1.5^{\circ}$  ( $10$  dB) and a minimum around  $17^{\circ}$  ( $4.6$  dB). The backscatter response does show a distinct angular decay from a mean at  $1.5^{\circ}$  of  $1.6$  dB to a mean of  $-11.66$  dB at  $45^{\circ}$ . The response for vertical and horizontal polarization is similar, but the mean is higher at  $45^{\circ}$  for horizontal polarization ( $-10.8$  dB). No angular characteristics of the radiometer temperature over land targets in North America was observed to exist. The response for both vertical and horizontal polarization are similar, suggesting that

the land surfaces appear like rough surfaces at this wavelength. The scatter in the data is quite large (range between deciles of approximately  $30^{\circ}\text{K}$ ) and this may be substantially reduced if one corrects for physical temperatures of targets and for atmospheric affects.

The backscatter response from South America at  $33^{\circ}$  was much higher than that over North America. In fact the lower decile of the response from South America was higher than the mean over North America. The range between deciles of the response from South America is less than one half that over North America. These results are expected because the South American region is composed mainly of forests.

The backscatter response from ocean surfaces also shows an expected angular characteristic with the decay being sharper than for land surfaces. The mean at  $1.5^{\circ}$  is approximately 10 dB higher than land (at 12.3 dB) and lower at  $45^{\circ}$  by approximately 8 dB (at -19.1 dB). The range between deciles is larger than that for land. The response for horizontal polarization is similar to that for vertical polarization except at the further angle of incidence where the backscatter from vertical polarization is higher. The cross polarized backscatter is lower than the dominant polarized backscatter by about 16 dB (at -3.7 dB) at  $1.5^{\circ}$  and only by 6 dB at  $45^{\circ}$ . The range between deciles for the cross polarized backscatter is only 2.5 dB at  $1.5^{\circ}$  and this increases with incidence angle till at  $45^{\circ}$  it is approximately 12 dB. An interesting statistic obtained from this analysis was that the lower decile from land targets at  $1.5^{\circ}$  was only -3.0 dB. This is much higher than the value obtained by finer resolution sensors. This implies that the design of altimeters for orbital platforms need consider a value much higher than they presently do for the minimum signal level. Since the range between deciles is so small for the backscatter response one must increase the precision requirements of radars to obtain a larger number of distinguishable levels. However, this also means that preprocessing dynamic range for a synthetic-aperture radar need only be quite small.

Based upon the ensemble statistics generated some empirical equations to describe the angular decay of backscatter are provided. These equations should be used in the design of future radar systems. It appears as though land backscatter is a two-process phenomenon with the decay rate being one type from  $0^{\circ} - 11^{\circ}$  and another from  $11^{\circ} - 47^{\circ}$ . Ocean backscatter on the other hand, appears to be a single phenomenon. The backscatter data are fitted by polynomials and exponentials.

It has been suggested by Moore and Ulaby (1969) that a combination of

a scatterometer and a radiometer can provide more information than is available by operating each instrument singly. If, however, the correlation coefficient between the response of the radiometer and the scatterometer over diverse target and atmospheric conditions is very high, then the use of the two sensors operated jointly is redundant. On the other hand, if the correlation between the response of the two is not high, then it can be assumed that the sensitivity of each sensor to target and atmospheric differences is not similar, and, indeed, information obtained from one sensor could augment that from the other. A similar argument exists for operation of the scatterometer and radiometer with various polarization configurations and for operation at various angles of incidence. It was found that the correlation of the radiometric response with the backscatter response was less than 0.33 for the ocean at  $33^\circ$  incidence and less than 0.1<sup>o</sup> over land at  $33^\circ$ . The correlations between radiometric response and scatterometric response at all angles of observation of the S-193 system were always less than 0.40. There was a high correlation between the radiometric response with vertical and horizontal polarization at the same incidence angle. The correlations in the backscatter response over ocean for vertical and horizontal polarizations were smaller at larger angles of incidence than at the smaller ones, but the correlations were all above 0.865 when considering the same incidence angle. The correlations between the backscatter response over ocean for the same polarization for two incidence angles were greater when the two angles were adjacent. The correlation between the cross polarized backscatter and dominant polarized backscatter was maximum near nadir (0.97) and remained fairly high for all angles in the in-track modes. The correlation between the cross polarized backscatter and the radiometric temperature was very small. Over land, the correlation was high between the backscatter at  $17^\circ$ ,  $30^\circ$  and  $41^\circ$ . Over South America, which appeared to be a much rougher surface judging from the high backscatter at  $33^\circ$ , the correlations between the response with vertical and horizontal polarization was 0.96. These results should be helpful in the design of future multiple sensor, multiple incidence angle or multiple polarization sensors.

A major purpose in the installation of a sensor in space to monitor earth resources is to monitor phenomenon in near real time. Since this is the first opportunity to study data from a combined radiometer/scatterometer operating in space, the features that can be recognized or the phenomenon to which the sensors are sensitive were not known. It was suspected that soil moisture variations could be monitored. Examination of

radiometer/scatterometer data over a site in Texas showed that there was a correlation of  $-0.81$  between the emissivity (at  $33^\circ$ ) and the soil moisture. The correlation of soil moisture with the scatterometer response was  $0.61$ . Details of this study may be found in chapter eight.

To ascertain if, with the gross resolution of the S-193 sensors, the terrain categories appeared differentiable a number of exercises were conducted. An analysis of variance, one-way lay-out design was tested using the backscatter response at  $33^\circ$  for various categories. The results showed that according to the microwave response, the same terrain categories from different geographic regions appeared to belong to different populations. This was also true sometimes for the same category in the same geographic location but at different epoch times. A possible explanation could be soil moisture variations or vegetation biomass variations. Some categories like the evergreen forest formations in Brazil, however, appear different from all other categories. Details are provided in chapter eight for many cases.

A stepwise linear discriminant analysis and a couple of clustering procedures were applied using groups of microwave response as the variables. The results showed that the sets of microwave response considered could not discriminate or recognize the terrain categories. The variations in soil moisture, vegetation density and manual assignment could be potential sources for the failure. In other words, the coarse-resolution radar seems to see different categories than those readily identified by geographers.

Being the first time that a radar with coarse resolution has viewed the earth from afar, we felt that the conditions were analogous to those of radar observations of the planets. Consequently analyses similar to those used in radar astronomy provide a chance for interesting comparisons. The surface descriptors as defined by radar astronomers were found for the earth. There are basically two types of surface models used in their formulations: a surface with a Gaussian height autocorrelation and a surface with exponential height autocorrelation function. These models were used to compute the reflection coefficient and mean slope of various regions of the earth. It was found that the ocean surfaces have a roughness (mean slope) which is comparable to that of land, although it is slightly smaller. Farmland in the Midwest U.S.A. was "smoother" than the ocean. The earth was found to be "smoother" than the moon or the planet Venus.

The reflection coefficients for the ocean appeared lower than those measured by aircraft based programs. Receiver saturation is probably the cause for some of these results. The dielectric constants computed from the reflection coefficients were much lower than those anticipated and a possible explanation could again be the saturation of the receiver.

The land surfaces appear in their radiometric response to be like Lambertian surfaces. The ocean surface was modelled as a plane surface. Theoretical estimates of the emissivity for an ocean surface based upon dielectric constant data obtained from Wu (1973) were computed for various physical temperatures of the ocean. These values were compared to the emissivities obtained by computing the surface brightness temperature from S-193 radiometer measurements. The atmospheric effects were computed for a standard profile with surface values considered typical of a temperate climate on a clear day over the ocean. It was found that the emissivities computed from the S-193 data were higher than those predicted by the plane surface model. The difference between the emissivity computed from S-193 data and for the plane surface model were larger for horizontal polarization than for vertical polarization at  $46^\circ$  incidence. This suggests that horizontal polarization is more sensitive to roughness, and, indeed this result is in accordance with prior measurements and with theoretical predictions based upon the geometric optics model.

By applying some very simple assumptions and calibrating our results for a case where wind speed on an ocean surface were known, an empirical estimate of the radiometric sensitivity (horizontal polarizations) to wind speed was found to be  $0.94^\circ\text{K/m/sec}$  at  $46^\circ$ . The mean wind speed over the ocean surfaces was computed as 16.3 knots. This compares to a mean wind speed of 13 knots computed from radar measurements which are relatively impervious to the atmosphere.

A problem with microwave data from a non-imaging sensor is that its display becomes very difficult. It is not possible for an interpreter of these data to view curves or sets of numbers and mentally collate them with their spatial location. The S-193 cross track contiguous mode was effectively a mapping mode. The data (both for the radiometer and scatterometer) obtained from the pitch offset  $29^\circ$  submode were used to prepare image-like representations of the response. The interpolations were performed on a digital computer and the digitized image displayed on a video monitor through a density-to-hue converter. Both gray tone and color images were produced. Examples are provided in Chapter eight. These images illustrated pictorially the variations in the microwave response over Texas due to soil moisture variations. Major vegetation types can be distinguished as is shown by images over Brazilian forests.

Chapter nine offers a summary of the results and provides a critique of the experiment. In essence the critique suggests that not enough effort was spent in the ultimate analysis or interpretation of the data from the experiment relative to that expended

on the hardware design. The instrument was far too complex and could have provided adequate results with many less modes or submodes and polarization states. Other hardware critique is minor and some recommendations for the design of future sensors are provided.

There are five appendices. Appendix one provides a brief description of some of the rf hardware assemblies. Appendix two contains some notes on regression analysis as germane to our analyses. Appendix three contains some sample figures showing the spatial distribution of the targets for the various modes of S-193 operation and some curves showing variations of parameters required in the radar equation with incidence angle. Appendix four contains a brief description of a simulation package for the operation of the S-193 on its orbital platform. Appendix five contains a listing of two major programs employed in this study. Both are simulation packages: one for the S-193 operation in orbit and the other for the atmospheric effects on the microwave signals.

## CHAPTER TWO

### THEORETICAL ASPECTS OF SCATTERING

#### 2.0 INTRODUCTION

Successful radars have been designed for many years for the purpose of detection and range-finding. It is relatively recent that the design of these sensors has reached a sophistication that makes them attractive for identifying, mapping, or discriminating various terrain targets.

To interpret the experimental data, to predict the return from inaccessible terrain or to carry out a complete analysis of radar system operation it is essential to have theoretical models from which the return can be calculated. Serious attempts to analyze the scattering of electromagnetic waves by rough surfaces and interfaces did not begin until about 1950. To date, a definite theoretical model that can adequately predict the interaction of electromagnetic waves with all non-uniform surfaces has not been achieved. To predict the return, numerous models have been proposed. These models depend upon the surface characteristics (geometry, roughness, dielectric constant) and sensor characteristics (polarization, wavelength, incidence angle, area of target illumination). The difficulties in modelling the interaction are: (1) solution of the electromagnetic scattering problem once the surface has been characterized properly and (2) classifying the actual terrain into categories for which a suitable theoretical model exists, or available experimental data is consistent. The solution of electromagnetic scattering can be found exactly for certain target types (unfortunately these targets are not found in natural terrain) and approximately for some others. An exact description of target characteristics in general is not possible for terrain. An alternate approach has been to solve the electromagnetic scattering problem for certain models of target characteristics. Classifying an actual terrain target into one of the categories amenable to solution can be based upon appearance (photographic or visual), through experience, based upon an experimental determination of the characteristics of the terrain return signal; or theoretically on the basis of the type of model used to represent the terrain.

It must be realized that surface descriptions used in the mathematical models are greatly simplified for computational facility. Natural terrain surfaces are therefore only approximated by these surface descriptions. Since it is not possible to approximate each individual surface, a statistical description of a class of surfaces is used in most models. These statistical descriptions are also oversimplified.

Most theories assume isotropic statistics. One can clearly see that the ability of a model to predict the return from a certain target depends upon how well the target characteristics fit the assumed statistical description and fulfill the other necessary assumptions necessary for a solution.

## 2.1 The Terrain Backscatter Experiment

The basic terrain backscatter experiment consists of illuminating a sector of terrain of area  $A$ , located at a distance  $R$  by a high gain antenna and measuring the energy scattered back towards the source. The average received power is given by the radar equation (Kerr, 1951)

$$P_r = \frac{P_t G_t G_r \sigma \lambda^2 F_t^2 F_r^2}{(4\pi)^3 R^4} \quad (1)$$

where

$P_r$  = received signal power (at antenna terminals)

$P_t$  = transmitted signal power (at antenna terminals)

$G_t$  = transmitting antenna gain

$G_r$  = receiving antenna gain

$\sigma$  = radar target cross section

$\lambda$  = wavelength

$F_t$  = pattern propagation factor for transmitting antenna to target path

$F_r$  = pattern propagation factor for target to receiving antenna path

$R$  = radar to target range

The parameter  $\sigma$ , the average radar cross-section of the terrain, is for a random homogeneous terrain, proportional to the area contributing to the return at any instant. To eliminate the effects of the radar parameters (pulse width, beamwidth, etc.) which dictate the area viewed, a parameter that is descriptive only of the ground is more convenient. Such a parameter,  $\sigma^0$ , the differential backscattering coefficient (scattering coefficient per unit area) is used to describe the terrain return.

It is only meaningful to ascribe such a parameter to terrain if the area illuminated can be considered as many individual scattering elements that scatter with random phase such that superposition of power is allowed on the average. If such a condition is satisfied then, for  $n$  scatterers, the return power is given by

$$P_r = \sum_{i=1}^n \frac{P_{t_i} G_{t_i} G_{r_i} \sigma_i \lambda^2 (F_{t_i}^2 F_{r_i}^2)}{(4\pi)^3 R_i^4} \quad (2)$$

$$= \sum_{i=1}^n \frac{P_{t_i} G_{t_i} G_{r_i} \lambda^2 (\sigma_i / \Delta A_i) \Delta A_i (F_{t_i}^2 F_{r_i}^2)}{(4\pi)^3 R_i^4}$$

This concept is, however, only valid on the average power (random phase assumption) so that average power is given by

$$\bar{P}_r = \sum_{i=1}^n \frac{P_{t_i} G_{t_i} G_{r_i} \sigma^0 \Delta A_i (F_{t_i}^2 F_{r_i}^2)}{(4\pi)^3 R_i^4} \quad (3)$$

where  $\sigma^0 = \frac{1}{n} \sum_{i=1}^n \frac{\sigma_i}{\Delta A_i}$

In the limit this summation may be replaced by an integral given by

$$\bar{P}_r = \frac{1}{(4\pi)^3} \int_{\text{illuminated area}} \frac{P_t G_t G_r \sigma^0 F_t^2 F_r^2}{R^4} dA \quad (4)$$

Some authors chose to describe the terrain return in terms of the scattering cross-section per unit projected area [Cosgriff et al, 1960], called  $\gamma$ . This parameter is related to  $\sigma^0$  as (see fig. 2.1)

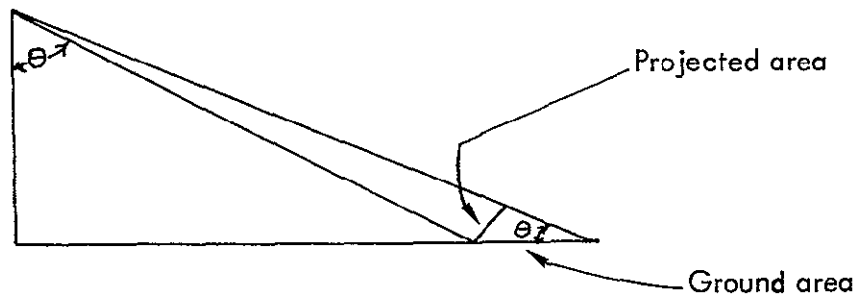


FIGURE 2.1  
Geometry for defining backscattering coefficient.

As can be seen a solution for  $\sigma^o$  from equation (4) requires inverting an integral. It should be pointed out that  $\sigma^o$  as it appears in equation (4) is a function of incidence angle and ground location

$$\sigma^o = \sigma^o(\theta, \phi, \text{location})$$

Where  $\theta, \phi$  are the nadir and azimuth angles respectively.

Certain simplifying assumptions, valid for narrow beam and short pulses, make the inversion of the integral relatively easy.

## 2.2 Theoretical Models for Scattering

### 2.2.1 Simple Models

The earlier radar terrain return models, prompted by radar design parameter requirements only, considered the return to be independent of surface parameters. As in optics, the terrain return was described by a Lambert-law variation of intensity [Clapp, 1946]. The backscattering coefficient was then given by

$$\sigma^o = k \cos^2 \theta \quad (5)$$

where

$k$  = some undetermined constant

$\theta$  = angle of incidence

This model can be applicable for certain very rough surfaces in the range of incidence angles from  $10^\circ$  off nadir to about  $50^\circ$  or even further. Clapp [1946] proposed a second model consisting of a single layer of spheres,  $N$  per unit area, each with a scattering coefficient  $\alpha_k$  giving

$$\sigma^o = N \alpha_k \quad (6)$$

This model may be applicable to certain types of vegetation such as a field of oats in head where the heads represent a single layer of scatterers. A third model proposed by Clapp consisted of many layers of spheres each of which absorbed a fraction  $(1-\delta)$  of the energy falling on it, and reradiated the remainder isotropically. Then

$$\sigma^o = \delta \cos \theta \quad (7)$$

This model was in good agreement with Clapp's measurements and with some subsequent measurements [Campbell, 1958].

Katz and Spetner proposed two models, one that considers the rough-surface type approach mentioned above and the other which also takes into account the specular reflection characteristics.

### 2.2.2.1 Spetner and Katz Random-Scatterer Model

Taking a statistical approach to radar backscattering, Spetner and Katz [1960] assumed that radar return from the earth's surface is composed of a summation of returns from a large number of incoherent independent scatterers. For independent scatterers, the normalized radar cross-section is the product of the density of scatterers per unit area,  $\rho_s$ , and the average radar cross-section of a single scatterer  $\sigma_1$ , i.e.

$$\sigma^o = \rho_s \sigma_1 \quad (8)$$

To make  $\sigma^o$  dependent upon the wavelength  $\lambda$ , they consider that a sufficiently short wavelength the average density of scatterers on the surface is independent of wavelength. As the wavelength gets longer, neighboring scatterers became more coherent with each other and hence must be grouped as a single scatterer. If  $\rho_o$  is the number of actual scatterers per unit area of the surface, then the density of "effective" scatterers is given by

$$\rho_s = \begin{cases} \rho_o & \lambda < (C_1/\rho_o)^{1/2} \\ C_1/\lambda^2 & \lambda > (C_1/\rho_o)^{1/2} \end{cases} \quad (9)$$

Where  $C_1$  is some constant of the order of unity. To compute the average scatterer cross section,  $\sigma_1$  two cases are considered. For wavelengths small as compared to the scatterer, the scattered power can be written as

$$\sigma_1 = A_s \rho \frac{4\pi A_s}{\lambda^2} \quad , \quad \lambda \text{ small} \quad (10)$$

where  $A_s$  is the effective area of the scatterer,  $\rho$  is its power reflection coefficient and the remaining term describes the 'gain' of the scatterer.

For wavelengths which are large as compared to the scatterer, a Rayleigh-type scattering can be considered to give

$$\sigma_1 = C_2 v^2 / \lambda^4 \quad \lambda \text{ large, } C_2 \gg 1 \quad (11)$$

where  $v$  is the volume of the scatterer. The isotropic-type scatterers considered in this model have no dependence on  $\theta$ . To consider the transition between the applicability of equation (10) and equation (11), one can rewrite these equations as

$$\sigma_1 = \begin{cases} A_s \rho \frac{4\pi A_s}{\lambda^2} & \lambda < \lambda_0 \\ C_2 v^2 / \lambda^4 & \lambda > \lambda_0 \end{cases} \quad (12)$$

Combining equations (9) and (12) gives the final expressions for  $\sigma^0$ . Table 2.1 gives the results for  $\sigma^0$  for the various wavelength regions. Figure 2.2 shows the graphic form of the wavelength dependence of  $\sigma^0$ .

#### 2.2.2.2 Spetner and Katz Specular Point Model

As a further refinement to the random scatterer model, Spetner and Katz [1960] proposed another model. They assumed that the surface was reflecting, was of irregular shape but continuous, and had continuous derivatives. They claimed that the contribution to the radar return came from two sources: the energy reflected from the large facets of the surface which are oriented perpendicular to the line of sight, and the energy which is scattered isotropically by the small scatterers. Thus,

$$\sigma^0 = p_{ss} \sigma_{1s} + p_{sL} \sigma_{1L} \quad (13)$$

Where  $p_{ss}$ ,  $p_{sL}$  are the scatterer densities of small and large scatterers and  $\sigma_{1s}$  and  $\sigma_{1L}$  are the radar cross-sections of the two scatterer cases respectively. The first term on the right hand side is the case of the random scatterer model and has been described above. To compute  $p_{sL}$ , the authors compute the probability of finding a specular point per unit area.

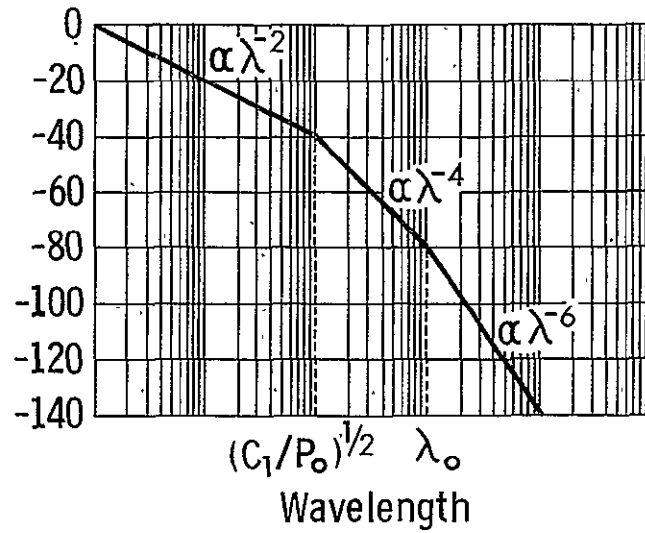


Figure 2.2. Wavelength dependence of normalized radar cross section (random scatterer model). From Spetner and Katz, 1960.

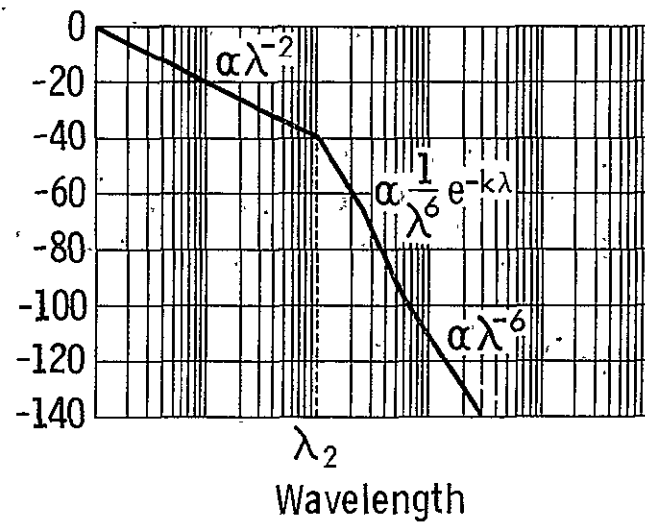


Figure 2.3. Wavelength dependence of normalized radar cross section (specular point model). From Spetner and Katz, 1960.

TABLE 2.1

	$\lambda < \lambda_0$	$\lambda > \lambda_0$
$\lambda < (C_1/p_0)^{1/2}$	$\sigma^o = \frac{4\pi p_0 \rho A^2 s}{\lambda^2}$	$\sigma^o = \frac{C_2 p_0 v^2}{\lambda^4}$
$\lambda > (C_1/p_0)^{1/2}$	$\sigma^o = \frac{4\pi C_1 \rho A^2 s}{\lambda^4}$	$\sigma^o = \frac{C_1 C_2 v^2}{\lambda^6}$

Table 2.1. Summary table of backscattering coefficient for various wavelength regions. (From Katz and Spetner, 1960.)

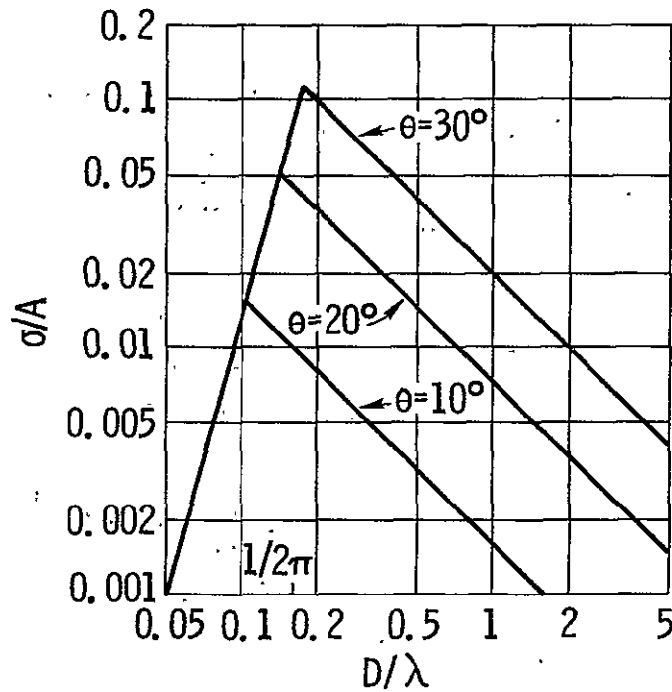


Figure 2.4  $\sigma/A$  for inclined circular disks. From Katzin, 1957.

If the probability density of the surface slopes is given by

$$q_f(z_x, z_y) dz_x dz_y \quad (14)$$

where  $z$  represents the height of the surface above some datum plane and

$$z_x = \frac{dz}{dx} \quad \text{and} \quad z_y = \frac{dz}{dy} \quad (15)$$

Assuming that the second derivatives

$$z_{xx} = \frac{\partial^2 z}{\partial x^2}, \quad z_{xy} = \frac{\partial^2 z}{\partial x \partial y}, \quad z_{yy} = \frac{\partial^2 z}{\partial y^2} \quad (16)$$

are statistically independent,  $p_{sL}$  becomes

$$p_{sL} = \langle |z_{xx} z_{yy} - z_{xy}^2| \rangle q_f(\alpha, \beta) \quad (17)$$

Transforming to cylindrical coordinates, we can write  $\alpha$  and  $\beta$  in terms of the incidence angle

$$\alpha = z_x = \tan\theta$$

$$\beta = z_y = 0$$

If  $z_x$  and  $z_y$  are jointly Gaussian with zero means and with equal variances,  $s^2$ , and if they are statistically independent, then

$$p_{sL} = \frac{\langle |z_{xx} z_{yy} - z_{xy}^2| \rangle}{2\pi s^2} \exp(-\tan^2\theta/2s^2) \quad (18)$$

To introduce the effect of wavelength, the authors define  $s_0^2$  as the variance of the slope measured at the surface and  $s^2$  as the "effective" slope variance which depends upon wavelength. The effective slope is obtained by smoothing the actual slope with a smoothing length of  $\lambda$ . For a slope spectrum, defined as  $(\text{slope})^2/\text{wave number}$  versus wave number, which is rectangular and has a cut-off at  $(\lambda_2)^{-1}$ , the mean squared slope is given by

$$s^2 = \begin{cases} s_0^2 & \lambda < \lambda_2 \\ s_0^2 \lambda/\lambda_2 & \lambda > \lambda_2 \end{cases} \quad (19)$$

Thus we can say

$$P_{SL}(90^\circ) = \begin{cases} C_3 / \lambda^2 & \lambda < \lambda_2 \\ C_3 / \lambda^2 & \lambda > \lambda_2 \end{cases} \quad (20)$$

Once again considering the radar cross-section of a scatterer large as compared to a wavelength as that of a flat plate (as in the random scatterer model) and that of a scatterer small as compared to a wavelength like an isotropic scatterer, we can define a region of transition as

$$\sigma_i = \begin{cases} 4\pi A_s \rho / \lambda^2 & \lambda < \lambda_2 \\ C_4 \rho / \lambda^4 & \lambda > \lambda_2 \end{cases} \quad (21)$$

Therefore, the final expressions for the normalized radar cross-section of an irregular reflecting surface having a Gaussian slope distribution and a flat slope spectrum which is sharply cut off at a frequency  $= \lambda_2^{-1}$ .

$$\sigma^0 = \begin{cases} 4\pi A_s C_3 \rho \frac{1}{\lambda^2} \exp(-\tan^2 \theta / 2s_\theta^2) & (22) \\ \frac{C_3 C_4}{\lambda^6} \exp(-\tan^2 \theta) \lambda / 2s_\theta^2 \lambda_2 + \frac{C_5}{\lambda^6} \end{cases}$$

Figure (2.3) shows the variation of  $\sigma^0$  with wavelength. Unfortunately the assumptions required of this particular slope spectrum are very seldom, if ever met in actual terrain. The concept of a composite scattering model, however, was elaborated upon by other models which are described below. The applicability of this model was tested by the authors using airborne radar data.

### 2.2.3 Katzin's Model

Katzin [1957] proposed a model to explain the backscattering from the sea surface at angles close to grazing. He later adapted his model for small incidence angles and felt that his models adequately described the backscatter from the sea surface. His efforts were motivated by observations over the sea surface which could not be explained by earlier investigations [Goldstein, 1946]. Among these was the "critical angle" effect; there was a critical grazing angle below which  $\sigma^{\circ}$  decreased very rapidly with decreasing angle and above which it rose much more slowly or remained constant. This critical angle decreased with increasing frequency. Some of the other unexplained characteristics of  $\sigma^{\circ}$  observed over the sea were a pronounced dependence of  $\sigma^{\circ}$  on polarization state, a frequency dependence around  $\lambda^{-4}$  for calm seas and  $\lambda^{\circ}$  for rough seas, a "spikiness" appearance of  $\sigma^{\circ}$  on an A-scope presentation for radar with very short pulse-widths. Katzin tried to explain these effects through the use of the reflection interference phenomenon. From this reflection phenomenon and the observed frequency response, Katzin postulated that the return was due to small facets which overlie the main large-scale wave pattern or swell. To explain the scattering process from small facets he took into account the fact that at grazing angles the magnitude of  $\sigma^{\circ}$  was in the neighborhood of  $10^{-4}$  which implied a highly directive type mechanism. Since the most directive elements were flat plates he considered the facets to be discs or rectangular plates. He invoked certain assumptions in creating his model.

1. The surface of the sea is the superposition of facets of various sizes, with orientations distributed about the mean sea surface.
2. The facets are assumed to move randomly, so that their phases are independent.
3. Shadowing and diffraction effects from edges of the facet are ignored.

Two types of plates are treated: (1) whose area  $A$  is large as compared to the wavelength; (2) whose area is small as compared to a wavelength. For a flat plate whose dimensions are large relative to the wavelength, the maximum backscatter occurs when the plate is parallel to the incident wave front and is proportional to  $A/\lambda^2$ . For inclined plates, the maximum backscattered power varies as  $\cos^2\theta$  (where  $\theta$  is incidence angle).

These results applied to the sea surface suggest that for plates large relative to the important backscattering at high incidence angles (low grazing angles) will come from the heads of the wave crests where the slopes are steepest and face the observer. For circular plates (or for an average of an ensemble of rectangular plates distributed over a range of azimuth angles), the backscatter is

$$\frac{\sigma}{A} \propto \left(\frac{\lambda^2}{A}\right)^{1/2} \quad (23)$$

For plates whose dimensions are small relative to  $\lambda$ , the scattering is not strongly dependent on angle and is

$$\frac{\sigma}{A} \propto \left(\frac{A}{\lambda^2}\right)^2 \quad (24)$$

The intermediate size facets, however, cannot be easily treated so Katzin suggests an extrapolation from both ends to find a region of demarcation. For circular disks, the resulting behavior as a function facet diameter (in terms of wavelength) for various facet tilts is shown in Figure 2.5. From the figure it can be seen that the backscatter is greatest from discs with a diameter  $D_1$  of about  $\lambda/2\pi$  or a circumference of about a half wavelength. Clearly, the return is a function of size distribution. An assumption invoked for achieving a workable result was that the slope distribution and size distribution of the facets were independent of each other. To predict a return of  $\sigma^0$  proportional to  $\lambda^{-n}$ , Katzin assumed that the number of facets per unit area is

$$N = N_0 A^{-(n+4)/2} \quad (25)$$

where  $N_0$  is a constant.

If  $\rho(s)$  is the probability density of facet slope, and  $\bar{\sigma}$  as the effective radar area, then

$$\sigma^0 = \iint N(A) \rho(s) \bar{\sigma}(s, A) dA ds \quad (26)$$

We have already established, however, that  $\bar{\sigma}$  is computed separately for small plates and for large plates.

Integrating over area, for the smallest facet  $A_0$ , through the breakpoint  $A_1$  to the largest facet size  $A_2$  can be replaced by integrating from  $A_0 = 0$  to  $A_2 = \infty$  if  $N(A)$  decreases very rapidly for the region less than  $A_0$  and greater than  $A_2$ . This is assumed to be the case so

$$\sigma^\circ = \int N(A) \bar{\sigma} dA = N_0 F(\theta_d) \lambda^{-n} \quad (27)$$

and 
$$F(\theta_d) = \left[ \frac{2.5}{(n+1)(4-n)} \right] f_1^{(4-n)/5} f_2^{(n+1)/5} \quad (28)$$

where 
$$f_1(\theta_d) = (4\pi^{3/2})^{-1} \tan^2 \theta_d \sec \theta_d$$

$$f_2(\theta_d) = \left( \frac{4^5}{9} \right) (1 + \cos^2(\theta_d/2))^2$$

where  $\theta_d$  is the angle that the disc makes with the normal  $f_1$  and  $f_2$  are computed for scattering from large and small circular discs.

For low-angle scattering,  $f_2$  is not great so that the average value of the factor  $(1 + \cos^2(\theta_d/2))$  may be taken to be 2

Then 
$$f_2 = 2^{11}/9 = k_1 \quad (29)$$

and 
$$\sigma^\circ = N_0 \lambda^{-n} G(s) \quad (30)$$

where 
$$G(s) = \int P(s) F(s) ds$$

Values of  $\rho(Z_x, Z_y)$  from Cox and Munk [1954] data were used in the model to get the theoretical estimate versus measured data. The model predicted an upwind to downwind  $\sigma^\circ$  ratio as

$$\frac{\sigma_u^\circ}{\sigma_d^\circ} = \frac{1 + 2 \cdot 10^{-3} W}{1 - 2 \cdot 10^{-3} W} \quad (31)$$

where  $\sigma_u^0$  = upwind backscatter  
 $\sigma_d^0$  = downwind backscatter  
 $W$  = wind speed in knots

For a wind speed of 20 knots this gives a ratio of 0.34 dB. Experimentally a ratio of up to 5 dB is observed. This is explained by Katzin as due to a lack of consideration for shadowing and multiple reflection.

Extrapolation of his model, originally conceived to explain effects at small grazing angles shows, however, that at near-vertical incidence some of the facets are viewed broadside and reflect exactly like flat plates— giving a significant backscatter. For near-vertical incidence, Katzin reasons that the back-scattered power will be proportional to the fraction of the surface which can be considered a large facet. The small facet will mainly scatter isotropically and back-scattered power intercepted will be consequently less.

Although this model has been bypassed by many investigators in their quest for a better model to explain scattering, it is the opinion of this author that if certain discrepancies in this model are compensated, this model could prove very valuable in the understanding of the terrain return problem. Katzin's treatment of facets that are not too small or too large as compared to a wavelength is rather crude. This intermediate size facet may strongly influence the shape of the  $\sigma^0$  vs  $\theta$  curve between low incidence angles to low grazing angles. His treatment does not consider diffraction effects from edges of disks and he considers no shadowing. The total random movement of the facets may be an applicable assumption for certain exploring wavelengths over the ocean surface but can quite often be an erroneous one — especially for low enough frequencies. The terrain problem could perhaps be better solved by not assuming a reflection coefficient close to unity as in the case of the large facet ocean surface. The basic characteristics of the  $\sigma^0$  predicted for terrain by this model were compared to Grant and Yaplee's [1957] data and showed encouraging similarities. The ocean surface predictions were compared to Macdonald's [1956] data and showed characteristics similar to the observed data. Khamsi [1974] has recently extended Katzin's effort to explain the scattering for intermediate angles of incidence and for intermediate sized facets. Khamsi has tried to explain the scatter from terrain employing this approach.

#### 2.2.4 Complete Models

The models for terrain backscatter which hold more promise of adequately describing the electromagnetic scattering from non-uniform rough surfaces over the entire range of incidence angles are referred to here as complete models. There are varied approaches to the formulation and solution of the problem. Each model, or theory makes some assumptions to obtain a solution; and many of them are applicable to only a very restricted class of terrain.

There are basically two types of models: a statistical model or a geometric model. These terms will be elucidated in the course of this brief treatise on scattering models. The problem of electromagnetic scattering can be handled mathematically for only two extreme cases of surface roughness (a descriptor of the surface) — slightly rough surfaces and very rough surfaces. The intermediate range of roughness is handled by extrapolation for these cases, or, by assuming a surface to consist of both types of surface — the very rough superimposed on a slightly rough surface. Numerous articles describing the postulates, the surface descriptors and the solution techniques have been published. The state of the theory is making advances to understand all the known phenomena which affect scattering. Each new model proposed, of necessity, gets more complicated, and with the onset of greater computational facilities gets more mathematically involved and numerically tedious to solve. A review of the complete models may be found in Fung [1966], Barrick et al [1967], Cosgriff, Peake and Taylor [1960]. Some of the later composite models have recently appeared in the literature [Chan and Fung, 1973]. The bibliography contains an extensive list of references. Rather than detail the mathematical derivations, which may be found elsewhere, the effort here will concentrate upon describing the formulation of the problem, the assumptions involved, the range of applicability of each model. The models for terrain scattering may be roughly classified into four types based upon their approach and their applicability to terrain surfaces.

1. Wavelength small as compared to surface roughness
2. Wavelength large as compared to surface roughness
3. Composite surfaces
4. Surface roughness of geometric shapes

For the first three types of surfaces, statistical models of the surface are invoked, where the roughness height itself is treated as a random variable. One must choose or specify the surface probability density function or correlation coefficient. For the fourth case, termed a geometric model, the surface is considered to be made up of given geometric shapes but arranged or distributed in a random fashion. This model is not unlike the Katz and Spetner model formulation, but the scattering phenomenon is treated more rigorously, and from other shapes than an isotropic or flat-plate surface. The statistical models [cases 1,2,3] seem more reasonable since nature rarely composes a surface of given geometric shapes.

#### 1. Wavelength Small as Compared to Surface Roughness — Very Rough Surface

Stated simply, a very rough surface is one for which the rms roughness height,  $h$ , is many times larger than a wavelength. All the scattered power from such a surface is then considered incoherent (i.e. the phase angle of the scattered field becomes uniformly distributed between 0 and  $2\pi$  and hence the average value of the scattered field is zero; only the average scattered power is non-zero). Three different optics approaches have been proposed to solve for the scattered power: Physical optics, Ray optics and Geometrical optics. All three of these approaches apply to a class of rough surfaces which satisfy the following restrictions.

1. The local surface radii of curvature at nearly every point on the surface are significantly larger than the wavelength.
2. To neglect shadowing and multiple reflection, the surface slopes are relatively small ( $< 1$ ).
3. The roughness is isotropic in all directions. (Not always assumed)
4. The surface area illuminated is much larger than the correlation length.
5. The mean squared roughness height,  $h^2$ , is greater than or equal to wavelength squared.
6. The surface height correlation coefficient is parabolic at the origin.

Multiple scattering has not yet been accounted for but Beckmann [1965] has proposed a "shadowing function" to correct for shadowing.

### 2.2.4.1 Physical Optics Approach

The main theme in the development of this approach is the estimation of the scattered field in the far-zone. The starting point for this estimation is the solution of the vector form of Helmholtz integral equations called the Stratton-Chu integral equations [Stratton, 1941]. These are

$$\bar{E}(\rho) = -\frac{1}{4\pi} \int_S \left[ j\omega\mu (\hat{n} \times \bar{H}) \phi - (\hat{n} \times \bar{E}) \times \nabla\phi + (\hat{n} \cdot \bar{E}) \nabla\phi \right] da \quad (32)$$

$$\bar{H}(\rho) = \frac{1}{4\pi} \int_S \left[ j\omega\epsilon (\hat{n} \times \bar{E}) \phi - (\hat{n} \times \bar{H}) \times \nabla\phi - (\hat{n} \cdot \bar{H}) \nabla\phi \right] da \quad (33)$$

These integral equations represent the fields at the observations point. In general these fields cannot be computed. Applying the tangent plane, or Kirchoff approximation, however, the total fields can be computed. The first such analysis (in the western literature) was that of Davies [1955]. The tangent plane approximation states that the field at each point on the surface may be represented as the sum of the incident wave and a wave reflected from the plane tangent to the surface at the given point. The criterion for the validity of this approximation is

$$4\pi P \cos \theta \gg \lambda \quad (34)$$

where  $P$  is the smaller of the two principal radii of curvature at the point. Another criterion exists if the point considered is a point of inflection. These conditions restrict the method to work for locally flat surfaces composed of irregularities of small curvatures. It is not valid for angles near grazing. Many investigators have since extended the results by Davies, among them are Hagfors [1964], Beckmann [1963], Hughes [1962], Fung [1964], Hayre [1961]. Fung extended the results to show that the first and second derivatives of the surface distribution are important for angles of incidence greater than  $20^\circ$ . His formulation agreed with experimental data over a wider range of incidence angles than the other theories historically earlier than his.

The problem was however, restricted to a perfectly conducting plane and his surface correlation function was chosen specifically to match experimental data. Although Semenov [1965] has also used the basic physical optics formulation, his approach has been to solve for both a rough surface and a specular part of the return. This model, however, is classified here as a composite model and described later in the section. The solution of the Stratton-Chu integral equations is generally obtained for two cases: a perfectly conducting surface and a homogeneous rough surface. Beckmann and Spizzichino, solve the scalar form of Helmholtz's equations to give the backscattered field as (see Figure (2.5))

$$E_s = \frac{j k e^{j k R_0}}{4 \pi R_0} \int_{-x}^x \int_{-y}^y (2 R (z_x \cos \theta + z_y \sin \theta) e^{-z j \vec{k} \cdot \vec{r}}) dx dy \quad (35)$$

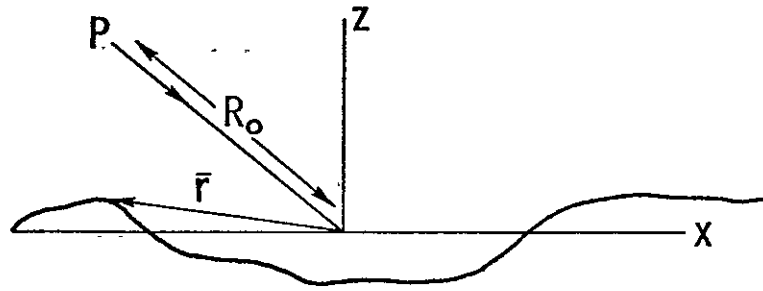


Figure 2.5. Scattering geometry.

where

$$k = \frac{2\pi}{\lambda}$$

$R_0$  = distance from point p (observation point for backscatter case) to origin

$\hat{k}$  = unit vector along scattered field direction

$\hat{r}$  = radius vector to origin from point on rough surface

$x, y$  = dimensions of rough surface

$R$  = reflection coefficient

$Z_x, Z_y$  = partial derivatives  $\frac{\partial z}{\partial x}$ ,  $\frac{\partial z}{\partial y}$  (slopes in x and y direction)

To compute a similar scattered field with the vector notation, but ignoring second derivatives of the slopes, we arrive at a similar result.

The tangent plane approximation, ignoring the second derivative terms, therefore does not contain any cross-polarized component. To compute the average back-scattered power, the stationary phase approximation is invoked and the average power

$$P = \langle \bar{E}_s \cdot \bar{E}_s^* \rangle$$

$$P = \iiint \iiint e^{-2jk \sin \theta (y-y')} \langle e^{2jk \cos \theta (z(x,y) - z(x',y'))} \rangle dx dx' dy dy' \quad (36)$$

where  $\langle e^{2jk \cos \theta (z(x,y) - z(x',y'))} \rangle = \iint e^{2jk \cos \theta (z(x,y) + z(x',y'))} p(z, z') dz dz'$

If  $v_1 = 2k \cos \theta$

$v_2 = -2k \cos \theta$

and  $v_1$  and  $v_2$  are distributed as jointly Gaussian variables, we have

$$P(\theta) = \iiint \iiint e^{-2jk \sin \theta (y-y')} \cdot \frac{-(2k \sigma \cos \theta)^2}{[1 - \rho(x, y; x', y')]} dx dx' dy dy' \quad (37)$$

where

$\rho(x, y)$  = correlation coefficient between  $v_1$  and  $v_2$

$\sigma$  = standard deviation of  $v_1$  and  $v_2$  (assumed equal)

Making the assumption that the process is stationary and isotropic (independent of azimuth) let  $\xi = y - y'$

$w = x - x'$

Then

$$P(\theta) = 4D^2 \int_0^\infty J_0(2k \sin \theta) e^{-[k_0(1 - \rho(\xi))] \xi} d\xi \quad (38)$$

where  $D$  is the dimension (length and breadth of the surface)

$J_0(x)$  = zero-order Bessel function

$$\frac{|u|}{2D} \ll 1 \quad \text{and} \quad \frac{|v|}{2D} \ll 1 \quad \text{as the integrand vanishes}$$

The frequency dependence of equation (38) is determined by the argument of the zero-order Bessel function and the constant  $K_0$ . The contribution of the Bessel function decreases with an increase in its argument, i.e. it decreases with either an increase in frequency or incidence angle. The factor  $K_0$  dictates the dependence of the integral upon the relative roughness of the surface in terms of wavelength. The description of the surface is introduced through the surface autocorrelation function (of height). The most commonly used autocorrelation functions are either exponential, gaussian or some combination of the two. Many correlation functions have been suggested [Davies, 1954, Hayre and Moore, 1961; Fung and Moore, 1966], but the autocorrelation function that best fits a particular set of data clearly cannot be generally acceptable. Since this formulation is only an aid to the insight of the scattering phenomenon, these autocorrelation functions serve a useful purpose only in this regard.

#### 2.2.4.2 Ray Optics Technique

Muhleman [1964] proposed another theory to estimate the power scattered by a very rough surface. In his formulation he considers that the rough surface is initially approximated by a grid of small flat planes, all of which are connected to form the rough surface. This is in some ways like Katzin and one of Katz and Spetner's models. This model, another facet model, then considers each element to reflect power specularly and the direction of reflection is determined by the direction of its normal. The amount of power reflected in any direction is then equal to the power reflected by each element in that direction times the number of facets reflecting in that direction. The summation does not include any phasor effects. The number of facets oriented to provide reflection in a given direction is the probability density function for surface slopes. The reflection from each facet is computed based upon Fresnel reflection coefficients. Hagfors [1966] showed that the probability density function for surface slopes appearing in Muhleman's result for scattered power can be easily related to the surface (height density if the surface is Gaussian).

In doing so, he showed that one must divide Muhleman's result by the cosine of the angle between the local surface normal and the mean plane normal.

The ray optics approach, although it sheds much needed insight into the scattering process from a rough surface, is lacking in rigorous mathematical derivation. This approach considers only scattered energy or power and not the fields themselves; hence phase relationships between fields from different regions are totally ignored. Diffraction effects and patterns, due to phase interferences and divergence of rays due to curved phase wavefronts are ignored. The model is, however, only as good as one can describe the probability density function of the surface slopes, and this is perhaps its greatest shortcoming.

#### 2.2.4.3 Geometric Optics Approach

This approach is the application of the stationary phase principle to the Kirchoff Integral for the complex scattered field. The result shows that scattering from a portion of a quadric curving surface does indeed radiate specularly. The scattering cross section of such a curved surface is

$$\sigma = \pi |R_1 R_2| \quad (39)$$

where  $|R_1 R_2|$  is product of the two principal radii at the specular point. A very rough surface consists of many such specular points. This approach explicitly derives the average number of specular points on a rough surface and their average Gaussian curvature,  $R_1 R_2$ . Like the Ray Optics approach, the power returned is almost completely described by the surface descriptor. Kodis [1966] formulated the rough surface problem rigorously and showed by stationary phase that the scattering cross section for a rough surface can be expressed as

$$\sigma = \left\langle \pi \sum_{i,j=1}^N (|R_{1i} R_{2i}| \cdot |R_{1j} R_{2j}|)^{1/2} e^{j(\phi_i - \phi_j)} \right\rangle \quad (40)$$

where

$N$  = total number of specular points

$R_{1i}, R_{2i}$  = Gaussian curvature at  $i$ -th point

$\phi_i, \phi_j$  = phase at  $i$ -th,  $j$ -th points respectively

This result is analogous to, but of a different form from that computed by Mitzner [1964] who considered the problem by calculating the coherency matrix of the reflected wave. By employing the restriction  $p, h > \lambda$ , one can derive the fact that  $\phi_i$  and  $\phi_j$  are uniformly distributed. Hence the average scattering cross-section becomes

$$\langle \sigma \rangle = \pi \left\langle \sum_{i=1}^N |R_{1i} R_{2i}| \right\rangle \quad (41)$$

Assigning an average Gaussian curvature to the specular points, the average scattering cross-section per unit area for incident and scattered polarization states  $i$  and  $j$  is

$$\sigma_{uv}^o = \pi n \langle |R_i R_j| \rangle |R_{ij}|^2 \quad (42)$$

where  $n = \frac{\langle N \rangle}{A}$

$A$  = area of scattering surface

$R_{uv}$  = Fresnel reflection coefficient at specular point for polarization states  $i, j$  (= vertical or horizontal)

The results obtained from this approach are identical to the results obtained from the previous two approaches for a Gaussian surface. So, although the approach is quite different from the other two the scattering properties are again described by adequately modelling the surface.

## 2. Wavelength Large as Compared to Surface Roughness -- A Slightly Rough Surface

A slightly rough surface is one which has a small scale of roughness as compared to the exploring wavelength, i.e. whose r.m.s. roughness height is much smaller than a wavelength. The incoherent component of the scattering is computed using a small perturbation technique. There are basically two approaches to solve for the (incoherent) power; both rely on the small perturbation approach in their solution, but the formulation of the problem is distinct.

The restrictions to both of these techniques are

1.  $\frac{\partial z}{\partial x}, \frac{\partial z}{\partial y} < 1.0$  , surface slopes are relatively small
2.  $\frac{2\pi}{\lambda} z(x,y) < 1.0$  , roughness height is small compared to a wavelength.
3.  $\langle \frac{\partial^2 z}{\partial x^2} \rangle = \langle \frac{\partial^2 z}{\partial y^2} \rangle$  , the surface is isotropic.  $\langle \rangle$  indicates an average over an ensemble of surfaces.

#### 2.2.4.4.1 Method of Small Perturbation

The treatment considered here [Bass and Bocharov, 1958] , applicable to any surface where an appropriate orthogonal curvilinear coordinate system can be used [Mitzner, 1964] . The basic concept is to replace the effect of the surface roughness by an equivalent source distribution of the mean surface, i.e. if a surface can be described by  $z(x,y) = z_0(r_0)$  where  $r_0$  is a point on the unperturbed plane surface, then the perturbed electric field can be written as

$$\hat{E}(\bar{r}) = \hat{E}^0(\bar{r}) + \delta \hat{E}(\bar{r}) + \delta^2 \hat{E}(\bar{r}) + \dots \dots \dots (43)$$

where  $E^0$  is the total (incident plus reflected unperturbed field and  $\delta E(r)$  is the perturbation field of order  $n$ . Expanding the right hand side by a Taylor series, satisfying boundary conditions and using Kirchoff's formula the field everywhere can be found. The solution is actually applicable to a perturbed plane surface and can be made to work for statistically rough surfaces as shown by Mitzner [1964].

#### 2.2.4.4.2 Small Perturbation Technique--Rayleigh-Rice Approach

A model originally formulated by Rice [1951] and developed by Peake [1959] , utilizing the small perturbation approach has perhaps been most satisfactory in solving the incoherent scattered field from a statistically slightly rough surface. Since the tangent plane approximation is not employed, all of the accompanying approximations such as neglect of multiple scattering and shadowing are avoided. It further exhibits a polarization dependence and it is valid in the lower frequency limit. The main idea involved in solving the problem is to assume a representation in a series of plane waves for each component of the scattered field with random coefficients.

Let the height correlation function be  $\overline{z^2} \rho(\xi, \eta)$  then

$$\overline{z^2} \rho(\xi, \eta) = \langle f(x+\xi, y+\eta) f(x, y) \rangle \quad (46)$$

where  $\overline{z^2} = \langle f^2(x, y) \rangle$  with  $\langle f(x, y) \rangle = 0$  i.e.  $\rho(0, 0) = 1$

The quantities  $W(p, q)$  and  $\overline{z^2} \rho(\xi, \eta)$  are seen to be a Fourier transform pair. Considering the case of a perfectly conducting surface the total fields can be written as

$$\begin{aligned} E_x &= \sum A_{mn} E(m, n, z) \\ E_y &= z_j \sin(k \cos \theta z) e^{-jk \sin \theta x} + \sum B_{mn} E(m, n, z) \\ E_z &= \sum C_{mn} E(m, n, z) \end{aligned} \quad (47)$$

The first term in  $E_y$  is just the sum of the incident and specularly reflected waves from a perfectly flat surface, and the terms  $E(m, n, z)$  are propagating or scattered plane waves.

$$\begin{aligned} E(m, n, z) &= \exp[-ja(mx+ny) - jb(m, n, z)] \\ b(m, n, z) &= \begin{cases} (k^2 - a^2 m^2 - a^2 n^2)^{1/2}, & m^2 + n^2 < k^2/a^2 \\ (a^2 m^2 + a^2 n^2 - k^2)^{1/2}, & m^2 + n^2 > k^2/a^2 \end{cases} \quad (48) \end{aligned}$$

To determine the horizontal and vertical components of the plane wave scattered field in a given direction  $\theta_s, \phi_s$  it is first necessary to relate the wave numbers  $a_m$  and  $a_n$  to the propagation constant of the plane wave in spherical coordinates. Making a transformation we find

$$\begin{aligned} a_m &= k \sin \theta_s \cos \phi_s \\ a_n &= k \sin \theta_s \sin \phi_s \end{aligned} \quad (49)$$

Physically this means representing these fields as a superposition of plane waves in all directions. These coefficients are then determined approximately using boundary conditions and the divergence relations in space. A very brief description of the mathematical treatment is presented here; for a detailed analysis, the reader is referred to Peake [1959], Barrick and Peake [1967], or Rice [1951]. The former two references are, however, more appropriate for understanding the physical concepts involved. Valenzuela [1967] has extended the same technique described here to obtain expressions for the second order perturbation correction terms for backscatter from a dielectric or perfectly conducting surface. The notation used here will be that of Peake [1959]. The rough surface described by its height  $z = f(x, y)$  at every point  $x, y$ , may be expanded in a Fourier series

$$z = f(x, y) = \sum_{-\infty}^{\infty} \sum_{-\infty}^{\infty} P(m, n) e^{-ja [mx + ny]} \quad (44)$$

$$a = 2\pi/L$$

m, n integers

where  $L$  = dimensions of square block of surface. Since  $Z$  is real  $P(m, n) = p^*(-m, -n)$ . Rice considers a surface random if an average over an infinite set of such elements leads to  $\langle P(m, n) \rangle = 0$ , which implies the randomness of individual coefficients. Then

$$\langle (P(m, n) P^*(m, n)) \rangle = \left(\frac{\pi}{L}\right)^2 W(p, q) \quad (45)$$

where  $p = \frac{2\pi m}{L}$ ,  $q = \frac{2\pi n}{L}$

This implies that the average exists and defines the spectral density function  $W(p, q)$ . Also it can be shown that

$$\langle P(m, n) P(u, v) \rangle = 0$$

c-2

Then the horizontal and vertical components of the scattered field in the direction corresponding to  $m, n$  are

$$E_h^s(m, n) = (-A_{mn} \sin \phi_s + B_{mn} \cos \phi_s) e^{ja(mx+ny)} \cdot e^{jb(m, n, z)} \quad (50)$$

$$E_v^s(m, n) = (A_{mn} \cos \theta_s \cos \phi_s + B_{mn} \cos \theta_s \sin \phi_s - C_{mn} \sin \theta_s) e^{ja(mx+ny)} \cdot e^{jb(m, n, z)} \quad (51)$$

Now noting that a small solid angle  $d\Omega$  in spherical coordinates is given by

$$d\Omega = \sin \theta_s d\theta_s d\phi_s = \left(\frac{a}{k}\right)^2 \frac{1}{\cos \theta_s} dm dn \quad (52)$$

Thus the incremental intensity flowing per unit solid angle is given by (for horizontal pol)

$$\Delta = \frac{\langle |E_h^s(\theta_s, \phi_s)|^2 \rangle}{\Delta\Omega} = \frac{4k^2\pi^2}{L^2} \cos^2 \theta_s \cos^2 \phi_s \cdot \frac{\Delta m \Delta n}{\Delta\Omega} \quad (53)$$

$$W \left[ k(\sin \theta_s \cos \phi_s - \sin \theta), k \sin \theta_s \sin \phi_s \right]$$

$\frac{\Delta m \Delta n}{\Delta\Omega}$  from equation (51) is

$$\frac{\Delta m \Delta n}{\Delta\Omega} = \frac{k^2 L^2 \cos \theta}{4\pi^2} \quad (54)$$

Therefore the average intensity at the receiver is

$$\langle |E_h^s|^2 \rangle = \Delta \frac{\langle |E_h^s(\theta_s, \phi_s)|^2 \rangle}{\Delta\Omega_s} = \frac{k^2 L^2 \cos \theta_s}{4\pi^2} \quad (55)$$

Therefore, the average scattering coefficient per unit surface area at the observation point is given by

$$\sigma_{hh}^{\circ}(\theta_s, \phi_s) = 4\pi k^4 \cos^2 \theta \cos^2 \theta_s \cos \phi \cos^2 \phi_s W \left[ \frac{k(\sin \theta_s \cos \phi_s - \cos \theta)}{k \sin \theta_s \sin \phi_s} \right]$$

For backscattering  $\theta = \theta_s$  and  $\phi_s = \pi$  so that, assuming an isotropic surface, the terrain return parameter  $\sigma^{\circ}$  becomes

$$\sigma_h^{\circ}(\theta) = \frac{8k^4}{4} \frac{\cos^2 \theta}{\sin \theta} \frac{1}{z^2} \int_0^{\infty} J_0(2kr \sin \theta) \rho(r) dr \quad (56)$$

where the spectral density function has been replaced by the height autocorrelation function.

A similar procedure can be used to compute the scattering coefficients for other polarization states. The problem of surfaces which are not perfectly conducting has been tackled by Barrick and Peake [1967], and Rice [1951]. Barrick and Peake treat the case for a rough surface with permeability and permittivity  $\mu_r$  and  $\epsilon_r$  by describing a set of four matrix elements which take into account these parameters. It can be seen from the result that the average intensity of the scattered field in a given direction varies in direct proportion to the surface roughness spectral strength at surface roughness frequency. The integral can be evaluated by considering a surface autocorrelation function. The choice of these is usually limited to an exponential or a Gaussian.

#### 2.2.4.5 Composite Rough Surfaces

The two-scale composite rough surface model is one which comprises a surface of large undulations with irregularities superimposed. This model can be divided into sub classes: 1) the large undulations are larger than the area illuminated; and 2) there are many large undulations within the area illuminated. Case (1) becomes a special case of the small perturbation approach except that the plane is tilted. Making an adjustment for the incidence angles, this case can be treated by the methods discussed above. The second case becomes more complicated. There have been two approaches to solve for this scattering model (1) to treat the small scale scattering incoherent with the large scale undulations and simply sum the scattered power as computed for the two cases (this approach has been documented by Semenov [1966], Wright [1968], Valenzuela [1967]); and (2) to estimate the total scattered fields for the two cases and to assume that phasor relationships are maintained in the summation. This approach has been documented

by Chan and Fung [1969, 1973]. For the incoherent assumption, the contribution from the small irregularities may be computed by summing powers from the large facets constituting the large undulations. This computation of energy from the small irregularities is then equivalent to solving the problem by a small perturbation type approach. Chan and Fung proposed two approaches to solve the problem with no non-coherent assumption. The first one [1969] treats the problem by computing fields on a composite surface defined by

$$Z(x,y) = Z(x,y) + S(x,y) \quad (57)$$

where  $Z(x,y)$  represents the large undulations and  $S(x,y)$  represents the small scale irregularities. The problem is then solved by the small perturbation approach. The second approach [1973] with no non-coherent assumption, was one which used a modified Kirchoff's method employing the equivalent surface field. This is like the method described in section (2) where an equivalent field is introduced to account for irregularities. The large scale surface field on  $Z(x,y)$  estimated by the tangent plane approximation is modified to include the effect of  $S(x,y)$ .

#### 2.2.4.5.1 Non-Coherent Approach

The non-coherent approximation as described above has been used by Semenov [1965], Wright [1968] and Valenzuela [1967]. The concept of all of them is similar; their motivations, applications of results and notations, however, would tend to make one look on them as dissimilar. The basic concept is to consider the scattering cross-section to be the sum of the scattering cross-section due to the large undulating surface computed by the tangent plane approximation and the ensemble average of the small irregularities over each of the tilted planes, i.e.

$$\gamma_j(\theta; \theta_s, \phi_s) = \gamma_j^t(\theta; \theta_s, \phi_s) + \langle \gamma_j^s(\theta; \theta_s, \phi_s) \rangle \quad (58)$$

Semenov [1966] arrived at the following result in his solution to the scattered field from such a surface after the tangent plane approximation

$$\overline{E^s} = \frac{jk e^{jkR}}{4\pi R} \int_{-1/2}^{1/2} \int_{-1/2}^{1/2} \overline{F}(z_x, z_y) e^{jk[\hat{k}_i - \hat{k}_s] \cdot \vec{r}} dx dy \quad (59)$$

where all the terms used have been described in the physical optics approach except the term  $\bar{F}(z_x, z_y)$ . This factor is a function of the local normal to the surface and the local Fresnel reflection coefficients at each surface point. This factor is pulled out of the integrand because of the stationary phase approximation and is evaluated from surface slopes. The only regions that contribute are those which have a surface normal which will allow specular reflection. The remaining integral is not solved this way but instead the scattered field is squared to get scattered intensity and then averaged. The averaging technique is based upon multiplying the integral by the joint probability density functions of the surface heights at two different surface points and then integrating over these two random variables. Relating this directly to scattering cross-sections, the procedure is then described by

$$\langle r^t(\theta; \theta_s, \phi_s) \rangle = \iint_{-\infty}^{\infty} r_j^t(\theta', \phi', \theta_s', \phi_s') P(z_x, z_y) (1 + z_x + z_y)^{1/2} dx dy. \quad (60)$$

where  $\theta', \phi'$  are the local incidence angles

$\theta_s', \phi_s'$  are the local scattering angles

$P(z_x, z_y)$  is the joint probability density function of the surface slopes.

The local incidence and scattering angles can be transformed into a set of reference angles for all surfaces. Then by assuming a joint probability density function of the surface heights, the average can be computed. The probability density functions employed are usually Gaussian. The parameters (e.g. rms slope) are usually assigned according to empirical data. Wright's model [1968] is essentially the same.

#### 2.2.4.5.2 Coherent Approach

This approach has been labelled a coherent approach, simply because the non-coherent assumption is not made. The problem has been tackled by the same two investigators in two ways. Since their second approach is simpler to interpret and reduces to known results more easily, it will be described here. Fung and Chan [1973] apply Bass and Bocharov's [1958] equivalent field concept to Valenzuela's [1967] results to obtain the first order fields.

Then using a linear approximation to the Fresnel reflection coefficients they arrive at a result which is decomposed into two parts. For a detailed description of the mathematical analysis, the reader is referred to their work. The general form of their results for scattering cross-section are given in the form

$$\sigma_{pp} = \sigma_{1pp} + \sigma_{2pp} \quad (61)$$

$\sigma_{1pp}$  is the result obtained by using Kirchoff's method for a single scattering surface. The value of  $\sigma_{2pp}$  for a case where the large scale undulations are absent reduces to the result obtained by the small perturbation method (for the illumination region stretching to infinity). For isotropically rough surfaces and for regions where the dimensions of the surface is many times larger than the individual inclined surfaces; their result (in their notation) is

$$\begin{aligned} \sigma_{2pp} = & \pi k^2 \sigma_s^2 \int_0^{2L} \int_{-\infty}^{\infty} \left\{ |T_{pp} + G(TD_{pp} + R'C_{pp})|^2 W \right. \\ & + V_z \frac{\partial W}{\partial q} \operatorname{Re} (TGC_{pp} [TC_{pp} (TC_{pp} + G(TD_{pp} + R'C_{pp}))^*] \\ & \left. + |TGC_{pp}|^2 V_z^2 \frac{\partial^2 W}{\partial q^2} / 4 \right\} + J_0 (\xi \sqrt{(u+k\sin\theta)^2 + v^2}) \\ & e^{-\kappa(1-\rho)} \Big] du dv d\xi d\xi \end{aligned} \quad (62)$$

The individual terms are defined in their work. The term  $T$ , is a function of the reflection coefficient,  $G$ ,  $D_{pp}$ ,  $C_{pp}$  are functions of the angle of incidence,  $W$  is the roughness spectrum,  $\rho$  is the correlation function,  $\sigma$  is the variance of the slope height;  $u, v$  are variables that can be interpreted as frequency components of the small scale irregular surface. A careful examination of this equation reveals that instead of a specific pair of  $u, v$  used in the small perturbation result, in this result all values of  $u, v$  are required. Physically this means that the large undulations are responsible for making all components of  $s(x, y)$  effective in the scattering process. They also define the weighting function on the contributions of the different frequency components of  $s(x, y)$ . In other words, this expression is seen to define the interaction between the large and the small scatterers.

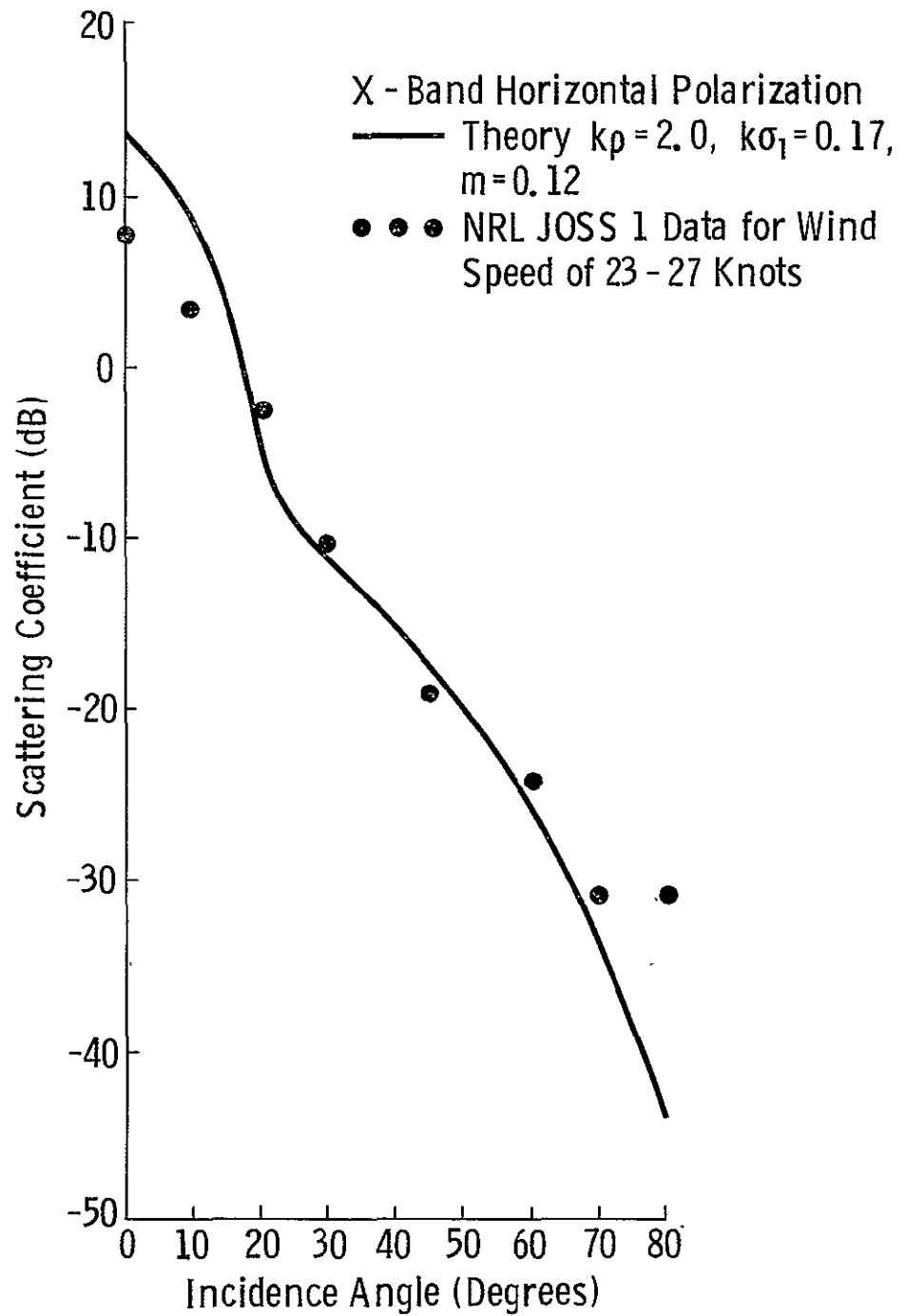


Figure 2.6. Comparison of computed and measured backscatter characteristics. From Chan and Fung, 1973.

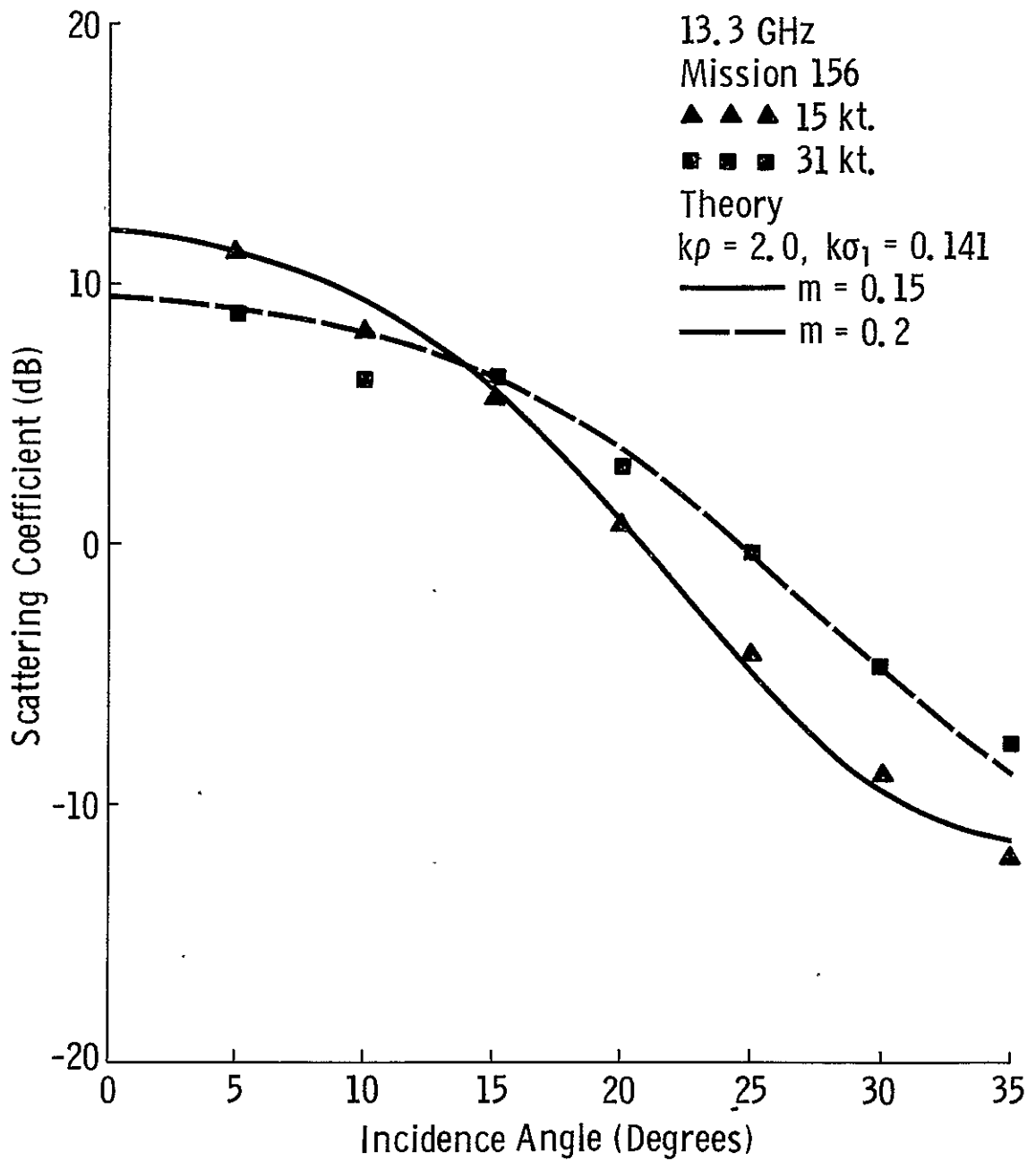


Figure 2.7. Comparison of computed and measured backscatter characteristics. From Chan and Fung, 1973.

### 2.2.4.6 Surface Roughness of Assumed Shapes

Often the problem of scattering from a given surface is approached by considering a distribution of specific shapes of targets. Twersky [1956] documented a method of determining the reflection coefficient and the differential scattering cross section per unit area of a random distribution of arbitrary bosses on a ground plane. The method is based upon computing the scattering from a single boss and then averaging over the ensemble taking into account multiple coherent scattering. Explicit expressions are derived from hemispheres and circular semi-cylinders. For a detailed description the reader is referred to Twersky's work [1957].

Peake [1959] computed the scattering from long, thin lossy cylinders. For surfaces covered with certain types of vegetation, such as grass, flags, etc. he considered thin, long, lossy cylinders a representative model. The probability density function of the cylindrical axis is used in the calculation of the returned power. The assumptions involved in his formulation are:

1. Diameter of cylinders be much less than a wavelength.
2. The length of the cylinders is large.
3. They are lossy enough so that incident radiation is considerably attenuated in passing through them.

With these approximations, the scattering cross-section becomes in Peake's notation

$$\gamma_h = \left( \frac{NA^2 k^2}{4\pi \sin \theta} \right) \frac{\left[ \frac{(\epsilon_1 - 1)^2 + \epsilon_2^2}{35} \right] \left[ 3 + \frac{16}{1 + \epsilon_1} + \frac{96}{(1 + \epsilon_1)^2} \right]}{\left[ \left( \frac{3}{5} \right) (\alpha_h/k)^2 + \left( \frac{4}{5} \right) (1 + 2 \sin^2 \theta) \right]} \quad (63)$$

$$\gamma_v = \left( \frac{NA^2 k^2}{4\pi \sin \theta} \right) \frac{\left[ \frac{(\epsilon_1 - 1)^2 + \epsilon_2^2}{35} \right] \left[ 3 + \frac{16}{(1 + \epsilon_1)} + \frac{96}{(1 + \epsilon_1)^2} + \cos^2 \theta - \frac{(12 + \frac{8}{(1 + \epsilon_1)} - \frac{64}{(1 + \epsilon_1)^2})}{(1 + \epsilon_1)^2} \right]}{\left[ \left( \frac{3}{5} \right) (\alpha_v/k)^2 + \left( \frac{4}{5} \right) (1 + 2 \sin^2 \theta) \right]}$$

where  $A$  = cross-sectional area of cylinders

$N$  = Number of cylinders per unit area of surface

$\epsilon_1 + j\epsilon_2$  = Complex dielectric constant of cylinder material

$1/\alpha$  = Depth at which the incident wave has been reduced to  $1/e$  of its original field strength

$$\alpha_h = 3/8 (AN\epsilon_2) \operatorname{cosec} \theta \left[ 1 + \frac{12}{(\epsilon_1 + 1)^2} \right]$$

$$\alpha_v = 3/8 (AN\epsilon_2) \operatorname{cosec} \theta \left[ 1 + \frac{12}{(1 + \epsilon_1)^2} + \cos^2 \theta \left( 1 - \frac{4}{(1 + \epsilon_1)^2} \right) \right]$$

This result is for a probability density function of the cylinder axes proportional to  $\cos^2(s)$  of being in an element of solid angle making an angle  $s$  with the vertical. Peake admits that this slight preference for vertical polarization may not be necessarily characteristic of the terrain. Peake has tried to validate this result by using data collected at Ohio State [Cosgriff, Peake and Taylor 1960]. The problem in comparison, as is always the case, boils down to not being able to describe the surface exactly.

## CHAPTER THREE

### RADIOMETRIC EMISSION FROM TERRAIN

#### 3.0 INTRODUCTION

Passive detection for measuring thermal radiation has been used since 1931. The original emphasis was in the avenue of astronomy. The use of microwave radiometers for astronomy did not really get popular until Dicke [1946] proposed a technique to lessen errors in measurements. As the sophistication of hardware increased to where the measurement precision was tolerable for terrain sensing, radiometers grew in popularity for measuring the emission from terrain. While terrain emission measurements were being performed with microwave radiometers, another group of scientists used them to look upward at the atmosphere. These scientists were attempting to find the distribution of atmospheric constituents through a study of their emission spectra. Scientists working in the infrared band of the spectrum had related the emission to the reflectivity of a material. It was much later that Peake [1959] related the concept of emissivity to the bistatic scattering coefficient for the microwave part of the spectrum. Although the nomenclature employed in relating the reflectivity (scattering) and emission for the IR case and the microwave case are different the concepts are similar. An extension of Kirchoff's laws in the broadest sense were used to relate the bistatic scattering coefficients to emissivity. The concept of emissivity can also be related to absorptivity through the laws of thermodynamic equilibrium. The absorptivity and hence the emissivity is a function of the complex dielectric constant of a surface. Each medium acts upon the intensity of radiation passing through it. In cases of terrain emission measurements, the models postulated assume that no energy passes through the target. This assumption is not made for atmospheric sensing.

The measurement of thermal radiation is recorded by using a radiometer with a directional antenna. Unlike the radar backscatter experiments, no illuminating energy is transmitted by the radiometer and all regions in  $4\pi$  space are potential sources for thermal radiation to the receiver. The weighting of the incoming thermal radiation is, however, dictated by the antenna pattern of the radiometer. Since a measurement corresponds to a weighted average of radiation arriving from all angles, in general, an exact estimate of the radiation emitted from any particular source is not possible. Approximation to the antenna pattern and multiple looks at targets can, however, help in estimating a solution.

Radiometry must also contend with the deleterious effects of the atmosphere upon the radiation traveling through it. These considerations have been studied and are reported in Chapter Five.

Emissivity can be calculated from bistatically measured omnidirectional scattering observations. Since these are difficult and time consuming measurements, the usual procedure is to describe the surface by some statistical descriptor of its roughness shape, and apply theory (usually geometric optics, physical optics or small perturbation) to compute the bistatic coefficients.

In what follows, a necessary background is provided to appreciate the theoretical efforts to estimate the emission from terrain. For those who have a clear understanding of the basic definitions, section 3.5 describes the relationship between the emissivity and the bistatic scattering coefficients. The models for the bistatic scattering coefficients have been described in chapter 2. Therefore, it is seen that the combination of an active and passive microwave sensor has potential for verifying various existing models.

### 3.1 Microwave Properties of a Surface

To understand the interaction of electromagnetic energy with terrain, we must describe the terrain surface in terms of some properties which govern such an interaction. We have already seen that surface roughness and Fresnel reflection coefficients appeared in all of the models for scattering. Surface roughness has already been explained in chapter 2. In what follows, a brief explanation is presented of the dielectric properties of matter that govern the reflection coefficient.

Consider as a starting point Maxwell's equations

$$\nabla \cdot \vec{E} = 0 \quad (1)$$

$$\nabla \cdot \vec{H} = 0 \quad (2)$$

$$\nabla \times \vec{E} = -\mu_0 \frac{\partial \vec{H}}{\partial t} \quad (3)$$

$$\nabla \times \vec{H} = \partial \vec{E} + \epsilon' \epsilon_0 \frac{\partial \vec{E}}{\partial t} \quad (4)$$

where  $\vec{E}$  = Electric field vector

$\vec{H}$  = magnetic field vector

$\mu_0$  = permeability of medium  
(assumed to be that of vacuum).

$\epsilon'$  = relative permittivity of medium

$\epsilon_0$  = permittivity of vacuum

$\sigma$  = effective conductivity of  
medium

$\mu_0 = 4\pi \times 10^{-7}$   
henrys per meter

$\epsilon_0 = 10^{-9}/36\pi$  farads per meter

These equations are for a medium devoid of any pockets of static charge.

The term  $\sigma$  includes all dissipative effects, assigning a loss factor  $\epsilon''$  to the medium then

$$\sigma = \omega \epsilon_0 \epsilon'' \quad (5)$$

Now if the components of  $\vec{E}$  and  $\vec{H}$  are sinusoidal, Maxwell's fourth equation becomes

$$\begin{aligned} \nabla \times \vec{H} &= (\omega \epsilon_0 \epsilon'' + j\omega \epsilon' \epsilon_0) \vec{E} \\ &= j\omega \epsilon_0 (\epsilon' - j\epsilon'') \vec{E} \\ &= \epsilon_0 (\epsilon' - j\epsilon'') \frac{\partial \vec{E}}{\partial t} \end{aligned} \quad (6)$$

The quantity in parenthesis is called the complex relative dielectric constant of the medium. One way to look at the components is to associate  $\epsilon'$  with the ability to store electric energy and  $\epsilon''$  with the losses that occur in the medium. The total complex relative dielectric constant,  $\epsilon_r = \epsilon' - j\epsilon''$  is often listed in tables giving either both the real and imaginary parts, or a real part and the ratio ( $\epsilon''/\epsilon'$ ), called the "loss-tangent."

Consider now the wave equations of the electromagnetic field. Consider further that the waves are traveling in the x-direction (of a coordinate system) and the travelling wave is a plane wave.

Then, (see for example Ramo et al [1967, pp. 246])

$$\begin{aligned}\frac{\partial^2 \vec{E}}{\partial x^2} &= \mu \epsilon \frac{\partial^2 \vec{E}}{\partial t^2} \\ &= \mu_0 \epsilon_0 (\epsilon' - j\epsilon'') \frac{\partial^2 \vec{E}}{\partial t^2}\end{aligned}\quad (7)$$

and

$$\frac{\partial^2 \vec{H}}{\partial x^2} = \mu_0 \epsilon_0 (\epsilon' - j\epsilon'') \frac{\partial^2 \vec{H}}{\partial t^2}\quad (8)$$

respectively.

A set of solutions for equations (7) and (8) are [Ramo et al 1967],

$$\vec{E} = \vec{E}_0 e^{-\alpha x} e^{-j\beta x}\quad (9)$$

$$\vec{H} = \vec{H}_0 e^{-\alpha x} e^{-j\beta x}\quad (10)$$

where  $\vec{E}_0, \vec{H}_0$  are the initial values of  $\vec{E}$  and  $\vec{H}$ , where

$$\begin{aligned}\alpha &= \text{Im}(\omega \sqrt{\mu \epsilon_r}) \\ &= \omega \sqrt{\frac{(\mu_0 \epsilon_0 \epsilon')}{2} [(1 + (\epsilon''/\epsilon')^2)^{1/2} - 1]}\end{aligned}\quad (11)$$

$$\begin{aligned}\beta &= \text{Re}(\omega \sqrt{\mu \epsilon_r}) \\ &= \omega \sqrt{\frac{(\mu_0 \epsilon_0 \epsilon')}{2} [(1 + (\epsilon''/\epsilon')^2)^{1/2} + 1]}\end{aligned}\quad (12)$$

$\alpha, \beta$  are called the attenuation factor and phase factor respectively. The attenuation factor will be used in Chapter Five to compute the effect of the atmosphere upon the microwave signals. Extensive measurements have been made of the permittivity of water at various frequencies, temperatures, salinities; empirical expressions have been documented to compute these constants when required. Dielectric properties of soils, rocks, kinds of vegetation, and many man-made materials have also been measured.

At microwave frequencies, most earth surfaces in the absence of any water content have  $\epsilon'$  between 1.7 and 6 and a  $\epsilon''/\epsilon'$  ratio  $10^{-3}$  to  $-1$  (Ulaby, 1974). Table (3.1) gives the average dielectric properties of rocks at 450 MHz and 35 GHz, from Campbell and Ulrichs [1969]. These quantities are almost temperature independent. Since the dielectric properties of surface are very much dependent upon water content, the dielectric properties of water have been studied extensively. The complex dielectric constant of pure water exhibits Debye relaxation (Debye, 1929). Saxton and Lane [1952] extended Debye's expressions for water containing salt as follows

$$\epsilon'_{\omega} = \epsilon_{\infty} + \frac{\epsilon_s - \epsilon_{\infty}}{1 + (\omega^2 \tau^2)} \quad (13)$$

$$\epsilon''_{\omega} = (\omega \tau) \frac{\epsilon_s - \epsilon_{\infty}}{1 + \omega^2 \tau^2} + \frac{\sigma_i}{2\pi f \epsilon_0} \quad (14)$$

where  $\tau$  is the relaxation time

$\epsilon_{\infty}$  is the relative permittivity at high frequencies

$\epsilon_s$  is the static relative permittivity

$\sigma_i$  is the ionic conductivity

$\epsilon_s, \tau, \sigma_i$  are functions of temperature and salinity only. Paris [1969] provides a thorough review of the electrical properties of water.

The dielectric constant of soils varies as the soil moisture content. An example of the effect of soil moisture on some soils is provided in Fig. (3.1) [Cihlar and Ulaby, 1974]. The measurement of the dielectric constants of soils have been conducted in laboratories, but a very limited bank of information on the values for various soil moisture condition over a range of frequencies is available.

The dielectric constant of vegetation has been related to the "water by volume" contained in the vegetation. Approximations to estimate the dielectric constants of certain types of vegetation are provided by Carlson [1967] based upon his empirical results.

Rock	Source	450 MHz		35 GHz	
		tan		tan	
andesite, hornblende	Mt. Shasta, Calif.	5.1	0.004	5.0	0.014
anorthosite	Essex County, N.Y.	6.8	0.008	6	0.016
basalt	Lintz, Rhenish-Prussia, Germany	8.9	0.018	9.2	0.09
basalt	Somerset County, N.J.	8.0	0.03	8.6	0.07
basalt, amygdaloidal	Keweenaw County, Mich.	7.2	0.014	7.6	0.023
basalt, hornblende	Chaffee County, Colo.	6.7	0.013	6.5	0.04
basalt, leucite-nepheline tephrite	Laacher See, Germany	5.6	0.0103	5.3	0.023
basalt, olivine	Jefferson County, Colo.	8.1	0.017	8.0	0.09
basalt, porphyry, olivine	Boulder County, Colo.	8.2	0.016	8.1	0.06
basalt, tholeiitic	Columbia River, N.E. of Madras, Ore.	9.6	0.09	8.0	0.112
basalt, vesicular	Chaffee County, Colo.	7	0.017	5.3	0.04
gabbro, bytownite	Duluth, Minn.	7	0.02	7	0.018
granite, alkali	Quincy, Mass.	5.2	0.023	5.3	0.023
granite, aplite	Boulder County, Colo.	5.2	0.019	4.9	0.009
granite, biotite	Westerly, R.I.	6	0.02	5.7	0.05
granite, biotite	Llano, Texas	5.4	0.007	5.5	0.015
granite, graphic	Auburn, Maine	5.0	0.004	5.0	0.008
granite, hornblende	Rockport, Mass.	6	0.010	5.2	0.01
granite, porphyritic biotite	St. Cloud, Minn.	5.5	0.011	5.6	0.02
obsidian	Lake County, Ore.	6.8	0.13	5.6	0.05
obsidian	Newberry Caldera, Ore.	5.5	0.0134	5.4	0.0381
peridotite, mica	Tompkins County, N.Y.	6.0	0.034	5.3	0.034
peridotite, Olivine (dunite)	Jackson County, N.C.	6.2	0.01	6.1	0.02
peridotite, changing to serpentine	Lowell, Vt.	7.5	0.008	7.6	0.011
phonolite	Beacon Hill, near Cripple Creek, Colo.	6.5	0.03	6.3	0.020
pumice	Millard County, Utah	2.5	0.007	2.4	0.02
rhyolite	Castle Rock, Colo	3.38	0.015	3.41	0.007
serpentine	Cardiff, Md.	6.4	0.011	6.4	0.04
serpentine	Rogue River, N.W. of Grant's Pass, Ore.	7	0.019	6.4	0.06
syenite, augite (larvikite)	Larvik, Norway	8	0.05	6.7	0.2
trachyte	Mineral Hill, near Cripple Creek, Colo.	5	0.026	5.43	0.025
tuff, grey	near Cripple Creek, Colo.	6.1	0.06	5.4	0.07
tuff, rhyolitic	Ennis, Mont.	3.6	0.006	3.4	0.02
tuff, semi-welded	Bend Quarry, Ore.	2.6	0.011	2.6	0.03
volcanic ash	Chaffee County, Colo.	3.4	0.07	2.84	0.014
volcanic ash shale	near Florissant, Colo.	2.7	0.03	2.6	0.015

Table 3.1

Average Dielectric Properties of Rocks from Campbell and Ulrich [1969]

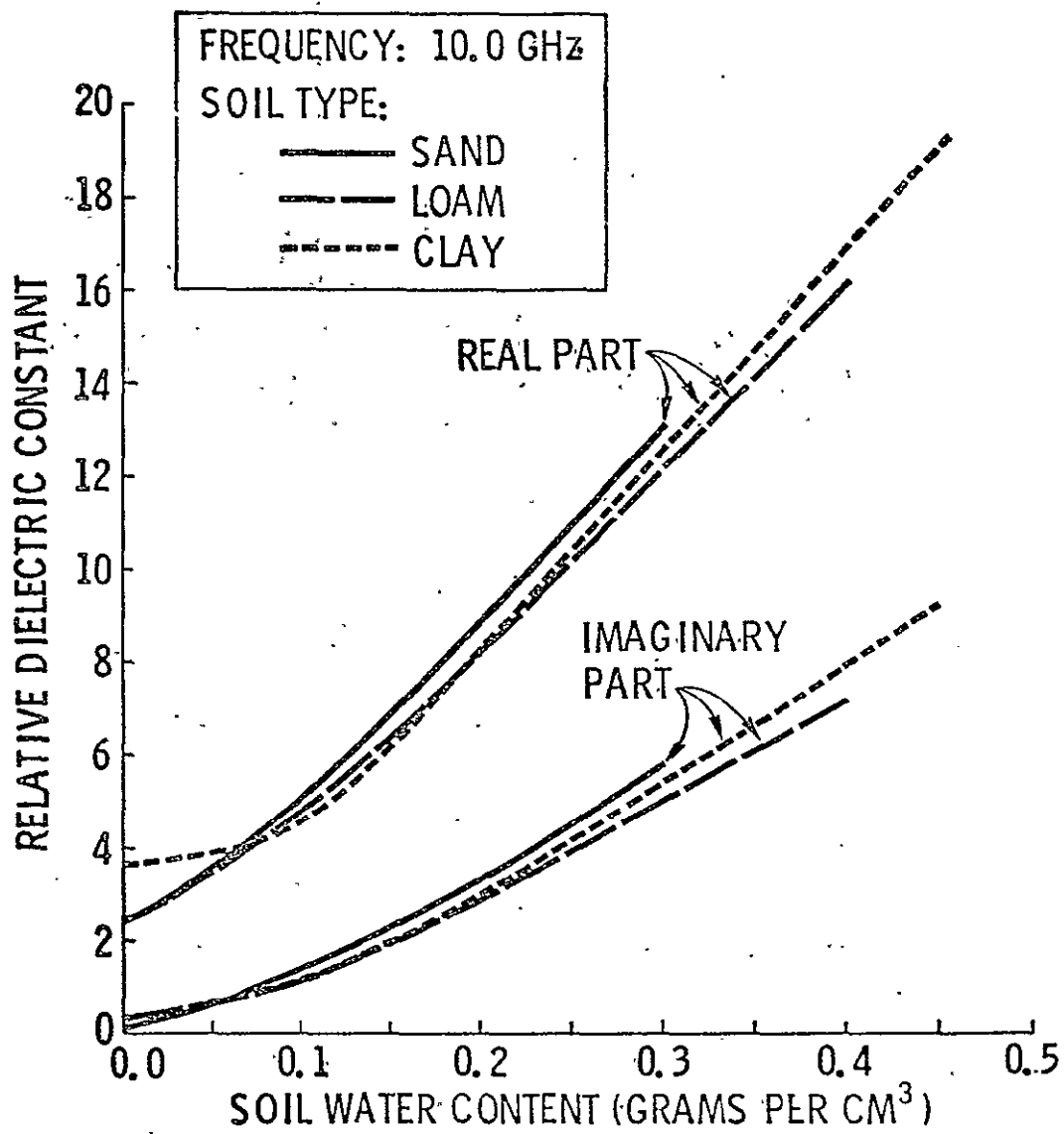


Figure 3.1. Effect of soil moisture on dielectric constant for sand, loam, and clay soils at 10 GHz. After Cihlar and Ulaby, 1974.

### 3.2 The Radiometric Brightness Temperature Experiment

Before going into the theoretical aspects of radiative transfer and the models for radiometric emissivity, let us examine the basic experiment which measures the brightness temperature, or emissivity. A high-gain directional antenna coupled to a receiver (usually with its own calibration source) views a solid area dictated by the antenna pattern. The thermal radiation actually arrives from all points in  $4\pi$  space in which the antenna is immersed; the weighting function of this incident radiation is the antenna power pattern, i.e.

$$T_{aP} = \frac{1}{G_{max}} \iint_{4\pi} T_b(\theta, \phi) G_p(\theta, \phi) d\theta d\phi \quad (15)$$

$$G_{max} = \iint_{4\pi} G_p(\theta, \phi) d\theta d\phi$$

where  $T_a$  = total radiation at antenna interface

$T_b(\theta, \phi)$  = incident radiation from angles  $\theta, \phi$

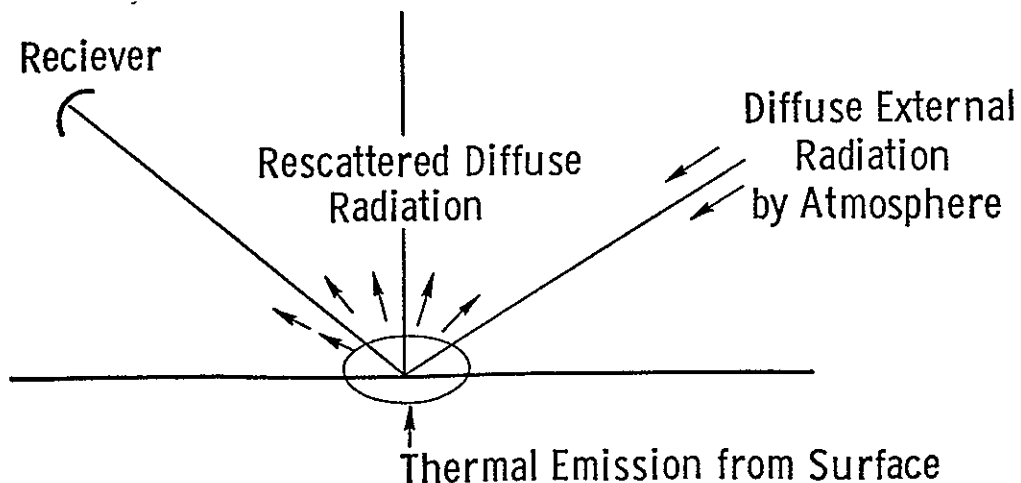
$G(\theta, \phi)$  = antenna power pattern

$\theta, \phi$  = nadir and azimuth angles

P = v or h polarization

One can see that the measurement recorded (voltage corresponding to  $T_a$ ) is a weighted average of all contributions from  $4\pi$  space. To retrieve the actual contributions would seem a formidable task. To compound the difficulties, let us consider a practical situation for a radiometer looking down on a terrain surface. (see Fig. 3.2)

Figure 3.2 Sources of Thermal Emission



There are three sources of thermal radiation arriving at the antenna. They are

1. The natural thermal radiation of the terrain surface radiated in the direction of the radiometer, attenuated by the intervening medium (atmosphere).
2. The direct diffuse radiation emitted by the atmosphere in the direction of the radiometer.
3. The radiation from the atmosphere which upon rescattering (or reflection) by the terrain surface is radiated in the direction of the radiometer. This is subject to the same attenuation by the atmosphere in the path as the terrain radiation.

The radiation incident at the antenna from an angle  $\theta$  (assuming symmetry about  $\theta$ ) is therefore

$$T_a(\theta) = L(\theta) [T_b(\theta) + T_{sc}(\theta)] + T_{atm}(\theta) \quad (16)$$

where  $L$  = Transmissivity (opacity) of atmosphere

$T_b$  = Terrain surface emission

$T_{sc}$  = Rescattered emission

$T_{atm}$  = Direct diffuse emission

A radiometric measurement therefore corresponds to

$$T_{a_p}(\theta) = \frac{1}{G_{max}} \int_0^{\pi} \left\{ [L(\theta, \theta')] [T_{b_p}(\theta, \theta') + T_{sc}(\theta, \theta')] + T_{atm}(\theta, \theta') \right\} G(\theta, \theta') d\theta' \quad (17)$$

where  $\theta$  is the incidence angle that the line of sight vector from the radiometer makes with the surface normal. In general  $T_{atm}$  is not considered a function of  $\theta$  or polarization.  $T_{sc}$  is considered a function of polarization inasmuch as the scattering properties of the surface are polarization dependent. As we describe the equations of radiative transfer, the forms of  $L(\theta)$  and  $T_{sc}$  will become clear.

There are many approximations made to solve for  $T_b$ . Not all of them are justified, but the literature abounds with measurements reporting  $T_a$  and inferring from these measurements as though they had obtained  $T_b$ . A simple approximation made for cases where the antenna is highly directional and has a high main beam efficiency (ratio of main beam energy to total pattern energy) is to consider

$$\hat{T}_a(\theta) = K_{M_b} T_{M_b}(\theta) + (1 - K_{M_b}) T_{SL}(\theta) \quad (18)$$

where

- $K_{mb}$  = main beam efficiency
- $T_{bm}$  = radiometric temperature of prime target (or main beam target)
- $T_{sL}$  = average temperature of side lobe targets

Those investigators who use  $T_b$  for inferences (in their own data sets only) are actually assuming that all terrain surfaces are at the same physical temperature; for it is not the apparent brightness temperature that is indicative of terrain type, but emissivity. For aircraft and land-based radiometers, this assumption is often reasonable; for spacecraft sensors, this assumption is seldom, if ever, valid. There are investigators who feel that  $T_a$  is a good enough descriptor of the apparent brightness temperature and they are assuming that either  $K_{mb}$  is very nearly one and that the second term can be ignored. It becomes very difficult to compare such data from various investigators because each data set is a non-calibrated (biased by atmospheric contribution, antenna losses, antenna efficiency, etc.) measure of brightness temperature. It is even harder to compare emissivities because the physical temperature of targets is not always provided.

### 3.3 Apparent Brightness Temperature Concept

The intensity of radiant electromagnetic energy is defined as the amount of radiant energy falling per unit of frequency ( $\nu$ ), of time ( $t$ ), of solid angle ( $\Omega$ ), and of surface area normal to the direction of radiation ( $a$ ), i.e.

$$I(\nu, \omega, t) = \frac{dE_\nu}{da d\Omega dt d\nu} \quad (19)$$

Consider the intensity field in an enclosure of constant temperature. A constant temperature implies thermodynamic equilibrium. Let the intensity of radiation emitted by an elemental area  $dA$  be  $I(\nu, T)$ , then

$$dE_\nu = I(\nu, T) dA d\nu dt d\Omega \quad (20)$$

The form of  $I(\nu, T)$  was found by Plank (1906) to be

$$I(\nu, T) = \frac{2h\nu^3}{c^2} (e^{h\nu/kT} - 1) \quad (21)$$

where

$T$  is temperature in degrees Kelvin

$h$  is Planck's constant ( $6.623 \times 10^{-34}$  joules/second)

$c$  is the speed of light

$k$  is Boltzmann's constant ( $1.38 \times 10^{-23}$  joules/ $^{\circ}$ K)

For frequencies in the microwave regions and temperatures over  $200^{\circ}$ K,  $(h\nu/kt)$  is much less than one and an expansion by Maclaurin series is reasonable.

$$\exp(h\nu/kt) = h\nu/kt + h^2\nu^2/2k^2T^2 + \dots \quad (22)$$

Therefore, 
$$I(\nu, T) = \frac{2k\nu^2}{c^2} T \quad (23)$$

This approximation is called Rayleigh-Jeans radiation law. A perfect radiator is called a blackbody; this implies that it absorbs completely all radiation incident upon it. The emission from a blackbody is completely random, so if one were to assign two orthogonal polarization states, then the polarized intensity of emission would be

$$I_p = \frac{k\nu^2}{c^2} T \quad (24)$$

A natural body is seldom, if ever, a perfect blackbody, but is assumed that the form of emission is like that of a blackbody, so that the polarized intensity is given by

$$J_p = \epsilon_p I_p \quad (25)$$

It is clear that  $\epsilon_p$  has a range from 0 to 1; it is called the polarized emissivity. Most investigators have followed this seemingly logical assumption that all natural bodies emit randomly and, therefore, should have no preference to arbitrary polarizations. Paris [1969] argues that this is not true because most surfaces favor either the vertical or horizontal polarization states and, therefore, a definition of brightness temperature should include polarized radiant intensities. From eqs. (23) and (25), one can define a polarized brightness temperature as

$$T_p = \left( c^2 / k^2 \nu^2 \right) J_p \quad (26)$$

and then from (26) and (25) one has

$$T_p = \epsilon_p T \quad (27)$$

where  $T$  is the physical or thermometric temperature of the surface.

### 3.4 Equation of Radiative Transfer

We have shown that the concept of intensity of radiation and that of brightness temperature are related through a term that for fixed frequencies is constant. We shall only be considering a fixed frequency case. Assume that the medium in which radiation is transported has ability both to absorb and emit radiation. If the medium absorbs radiation in traveling a path  $dz$ , let us say it absorbs proportional to  $\alpha dz$ , where  $\alpha$  is the absorption coefficient. If the medium also emits radiation, let us say that a volume  $dV$  emits proportional to  $j_\nu$ . Then considering the intensity of radiation, we have

$$\text{absorbed energy} = \alpha dz da d\Omega dt d\nu I_\nu \quad (28)$$

$$\text{emitted energy} = j_\nu dV da d\Omega dt d\nu \quad (29)$$

We find now that the radiation field changes along the path. Consider a cylinder (one dimensional case), the energy entering the cylinder is  $I_\nu$  equal to

$$\text{Energy in} = I_\nu da d\Omega d\nu dt \quad (30)$$

Let the energy leaving the cylinder be  $I_\nu + dI_\nu$ , then this is equal to

$$\text{Energy out} = (I_\nu + dI_\nu) da d\Omega d\nu dt \quad (31)$$

Substituting equation (30) and (31) into equations (28) and (29) we have

$$\begin{aligned} (I_\nu + dI_\nu) da d\Omega d\nu dt &= I_\nu da d\Omega d\nu dt \\ &\quad - I_\nu \alpha_\nu dz da d\Omega d\nu dt \\ &\quad + j_\nu da dz d\Omega d\nu dt \end{aligned} \quad (32)$$

where we have used  $dV = da dz$ .

Then after some necessary abbreviation, we find

$$\frac{dI_{\nu}}{ds} = -\alpha_{\nu} I_{\nu} + \epsilon_{\nu} \quad (33)$$

This then is the equation which determines the change in intensity of radiation transmitted through an absorbing and emitting medium. It is called the equation of radiative transfer. A solution of this equation yields the intensity of radiation at a distance  $z$  as [Chandrasekhar, 1960]

$$I_{\nu}(z) = I_{\nu}(0) e^{-\int_0^z \alpha_{\nu}(z') dz'} + \int_0^z j_{\nu}(z') e^{-\int_{z'}^z \alpha_{\nu}(z'') dz''} dz' \quad (34)$$

This is the equation of radiative transfer in integral form.

Now, let us apply this to the case of a radiometer looking vertically down at a terrain surface. We have already established that the polarized intensity is related to the brightness temperature through a constant (at a particular frequency) so we shall replace the intensity in equation (34) by a temperature. Let the absorption coefficient of the atmosphere (at a fixed frequency) be  $\alpha$ . Let us further only consider the radiation field traveling upwards from the surface to the radiometer through the intervening atmosphere. Then  $I_{\nu}(0)$  is the total upwelling radiation from the surface entering the atmosphere. This is composed of the direct radiation from the surface and the reflected radiation from the atmosphere. Denoting this sum by  $T_t$ , we find the temperature at height  $z$  to be

$$T_a(z) = T_t e^{-\int_0^z \alpha(z') dz'} + \int_0^z T_M(z') \alpha(z') e^{-\int_{z'}^z \alpha(z'') dz''} dz' \quad (35)$$

Assume that the emissivity of the surface is  $\epsilon$  then,  $T_t$  can be written as

$$T_t = \epsilon T_g + (1 - \epsilon) \int_z^0 T_M(z') \alpha(z') e^{-\int_{z'}^0 \alpha(z'') dz''} dz' \quad (36)$$

Where

$T_g$  = terrain surface temperature  
 and  $(1-\epsilon)$  = reflectivity of terrain surface

Then from equation (35) and equation (36), we have

$$T_a(z) = e^{-\int_0^z \alpha(z') dz'} \left[ \epsilon T_g + (1-\epsilon) \int_z^0 T_m(z') \alpha(z') e^{-\int_{z'}^z \alpha(z'') dz''} dz' \right] + \int_0^z T_m(z') \alpha(z') e^{-\int_{z'}^z \alpha(z'') dz''} dz' \quad (37)$$

Comparing this equation with equation (16) we find

$$L(0) = e^{-\int_0^z \alpha(z') dz'}$$

$$T_{sc}(0) = [1 - \epsilon(0)] \left[ \int_0^z \alpha(z') T_m(z') e^{-\int_{z'}^z \alpha(z'') dz''} dz' \right]$$

$$T_{atm}(0) = \left[ \int_0^z T_m(z') \alpha(z') e^{-\int_{z'}^z \alpha(z'') dz''} dz' \right]$$

$$T_b(0) = \epsilon T_g$$

For any oblique incidence, the path length of the radiation field through the atmosphere is larger than at vertical incidence. Further, the emissivity of the surface is a function of angle. If we consider an angle of incident  $\theta$ , the path length through the atmosphere (assuming a flat earth) is

$$R = h \sec \theta$$

Since the atmosphere has been considered plane-stratified, the absorption coefficient for a vertical distance  $h$  will translate to an absorption coefficient  $\alpha \sec \theta$  for an oblique distance  $R$ .

Hence, the antenna temperature at an angle  $\theta$ , at height  $z$  is given by

$$T_a(\theta, z) = e^{-\sec \theta \int_0^z \alpha(z') dz'} \left[ \epsilon(\theta) T_g + (1 - \epsilon(\theta)) \int_z^{\infty} T_m(z') \alpha(z') e^{-\sec \theta \int_{z'}^0 \alpha(z'') dz''} dz' \right] + \int_0^z T_m(z') \alpha(z') e^{-\sec \theta \int_{z'}^z \alpha(z'') dz''} dz'$$

(38)

Here we have considered a case for an arbitrary polarization. The polarization dependent term on the right hand side is the emissivity of the surface. This form of the equation of radiative transfer (polarized) will be invoked in chapter 5 dealing with atmospheric effects.

### 3.5 Emissivity and Bistatic Scattering Coefficients

As mentioned above the apparent temperature measured is a weighted average of contributions arriving from  $4\pi$  space. Emission from a particular solid-angle (cone) cannot be found exactly. To estimate such emission however, Peake [1959] in a classic paper related the emissivity to the bistatic differential scattering coefficients of a surface. The required relationships cannot be better described than by Peake, and so his form and notation will be used. Consider the surface to be an infinite plane (with irregularities superimposed) (see Figure 3.3).

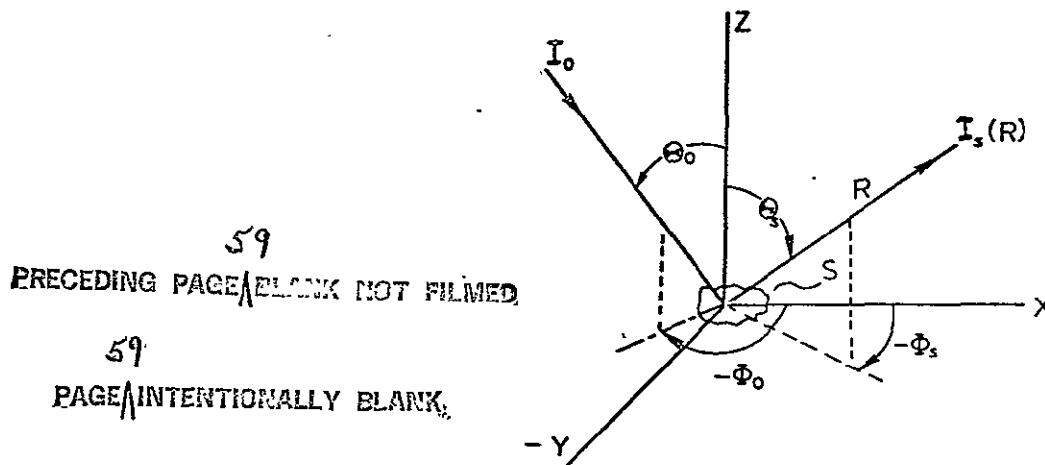


Figure 3.3. Geometry of the Scattering Problem.

If radiation of intensity  $I_0$  (watts per meter<sup>2</sup>) falls at an angle of incidence  $\theta_0$  and azimuth  $\phi_0$  on a given element of surface area  $S$ , and if a receiver at an angle  $\theta_s, \phi_s$  at a distance  $R$  from this surface receives an intensity  $I_s$ , the differential scattering coefficient  $\gamma(\theta_0, \phi_0; \theta_s, \phi_s)$  is defined by

$$\gamma(\theta_0, \phi_0; \theta_s, \phi_s) = \frac{4\pi R^2}{S \cos \theta_0} \cdot \frac{I_s}{I_0} \quad (39)$$

For any general surface, the scattered radiation  $I_s$ , and thus  $\gamma$  consists of two parts, a specular or coherent part. This is computed by assuming a plane tangent to the entire surface and computing the reflected power and a diffuse or incoherent part. This is treated by physical optics or by the small perturbation theory approach. For the specular part  $\gamma$  is a  $\delta$  function, for the diffuse part  $\gamma$  is a function of  $S$ , the surface area, and the distance  $R$ . The area  $S$  must be greater than any significant structural feature contained in it. Abbreviating the angles  $\theta_0, \phi_0$  as  $\alpha$  (as in Peake [1959]) and  $\theta_s, \phi_s$  as  $s$ , we can write the relationship between the scattering coefficients due to reciprocity as

$$\cos \theta_0 \gamma_{ij}(\alpha, s) = \cos \theta_s \gamma_{ji}(s, \alpha) \quad i, j \text{ either vertical or horizontal polarization} \quad (40)$$

Before applying Kirchoff's law, let us define the albedo of a surface. Albedo of a surface is defined as the fraction of power incident from an angle  $\theta_0, \phi_0$  that is rescattered, i. e.

$$A(\theta_0, \phi_0) = \int \frac{I_s R^2}{S I_0 \cos \theta_0} d\Omega_s \quad (41)$$

The integration is over the upper hemisphere. From equations (39) and (41) and by applying the polarization properties of the surface

$$A_i(\theta_0, \phi_0) = \frac{1}{4\pi} \int [\gamma_{ii}(\alpha, s) + \gamma_{ij}(\alpha, s)] d\Omega_s \quad \begin{matrix} i = h \text{ or } v \\ j = v \text{ or } h \end{matrix} \quad (42)$$

The absorption coefficient is defined as the fraction of power that is absorbed by the surface from an incident direction  $\theta_o, \phi_o$ . The types of surfaces considered here are presumed to be infinite in depth, so that the absorption coefficient  $\alpha$  is related to the albedo as

$$\alpha_i(\theta_o, \phi_o) = 1 - A_i(\theta_o, \phi_o) \quad i = h \text{ or } v \quad (43)$$

The power  $dP_i$  incident with horizontal polarization on an element of surface of area  $S$  from a range of solid angles  $d\Omega_o$  in direction  $(\theta_o, \phi_o)$  is

$$dP_i = I_v d\Omega_o S \cos \theta_o \quad (44)$$

The power leaving the surface (due to thermal emission from the surface) is

$$dP_s = \epsilon_h(\theta_o, \phi_o) I_v d\Omega_o S \cos \theta_o \quad (45)$$

The power reflected by the surface into  $d\Omega_o$  with horizontal polarization is

$$dP_r = \frac{I_v d\Omega_o S}{4\pi} \int [\gamma_{hh}(s, o) + \gamma_{vh}(s, o)] \cos \theta_s d\Omega_s \quad (46)$$

Now assume that the incident power is equal to the sum of the emitted and reflected power of the same polarization,

$$dP_i = dP_s + dP_r$$

Therefore

$$1 = \epsilon_h(\theta_o, \phi_o) + (4\pi)^{-1} \int \frac{\cos \theta_s}{\cos \theta_o} [\gamma_{hh}(s, o) + \gamma_{vh}(s, o)] d\Omega_s \quad (47)$$

By the reciprocity relations this becomes

$$1 = \epsilon_h(\theta_o, \phi_o) + \frac{1}{4\pi} \int [\gamma_{hh}(o, s) + \gamma_{hv}(o, s)] d\Omega_s$$

$$\text{or } 1 = \epsilon_h(\theta_o, \phi_o) + \alpha_h(\theta_o, \phi_o) \quad (48)$$

A similar equation can be derived for vertical polarization

$$1 = \epsilon_v(\theta_o, \phi_o) + \alpha_v(\theta_o, \phi_o) \quad (49)$$

Equation (48) and (49) constitute the generalized form of Kirchoff's law. From this result and the notion of apparent temperature as in Equation (24)

$$T_{s_h}(\theta_o, \phi_o) = \frac{1}{4\pi} \int [T_h(\theta_s, \phi_s) \gamma_{hh}(s, o) + T_v(\theta_s, \phi_s) \gamma_{vh}(s, o)] \frac{\cos \theta_s}{\cos \theta_o} d\Omega_s \quad (50)$$

which from the reciprocity relations becomes

$$T_{s_h}(\theta_o, \phi_o) = \frac{1}{4\pi} \int [T_h(s) \gamma_{hh}(o, s) + T_v(s) \gamma_{hv}(o, s)] d\Omega_s \quad (51)$$

and similarly

$$T_{s_v}(\theta_o, \phi_o) = \frac{1}{4\pi} \int [T_v(s) \gamma_{vv}(o, s) + T_h(s) \gamma_{vh}(o, s)] d\Omega_s \quad (52)$$

So, we have presented the relationship between the apparent temperature of a target and its scattering coefficients. The advantage of this formulation is: whereas the radiometric temperature measured by a radiometer is a sum of many temperature sources making individual contributions from a specific source almost impossible to estimate precisely, the scattering coefficients can be measured. Once numerous measurements of scattering coefficient of a particular surface type have been made, mathematical models to describe these surfaces can be made and checked. As in the case of scattering the models constructed are applicable to certain types of terrain only. This does not imply that measurements made with a radiometer are not needed. Measurements of radiometric emission with highly directional antennas narrows the precision to a small value. In most cases of radiometry application these precision values are tolerable.

### 3.6 Surface Models

The surface models, used in scatter theory often consist of two types — a very rough surface model and a very smooth surface mode. The notions of rough and smooth have the same interpretation as in Chapter Two (i.e. roughness in terms of exploring wavelengths). The general aim here is to calculate an expression for  $(\gamma_{ij} + \gamma_{ji})$ , integrate this over the upper hemisphere, and multiply by the physical temperature to get an estimate for the brightness temperature of a target. If we concentrate our attention now only on computing the emissivity, with the understanding that a multiplication by the temperature will provide the brightness temperature we start with equation (47). The surface models invoked merely estimate  $\gamma_{ii} + \gamma_{ij}$ .

#### 3.6.1 Very Rough Surface — Lambert Law Model

The simplest model that is appropriate here is the Lambert-law model [Peake, 1966]. A Lambert law surface (Chapter Two) has a  $\gamma(\theta_i, \theta_s)$  that is proportional to  $\cos \theta_i \cos \theta_s$  i.e.

$$\sigma_{ij}(i, s) + \sigma_{ji}(i, s) = \gamma_0 \cos \theta_i \cos \theta_s \quad (53)$$

with  $\gamma_0$  as some constant related to the dielectric constant of the surface. This model implies that the emissivity of the surface is independent of viewing angle, i.e.

$$\epsilon_j = 1 - \frac{\gamma_0}{4} \quad (54)$$

This, of course, would be the limiting case of a very rough surface. There is no explicit wavelength dependence (although  $\gamma_0$  can be wavelength dependent. Peake has used this model to estimate the brightness temperature from large blocks of pumice, where the surface exhibits no specular return and the scattered power is due mainly to diffused scattering. He has compared results from such a model against measurements taken at the Mono Craters, California and found that indeed the radiometric emission is almost independent of the incidence angle as shown in fig. 3.4.

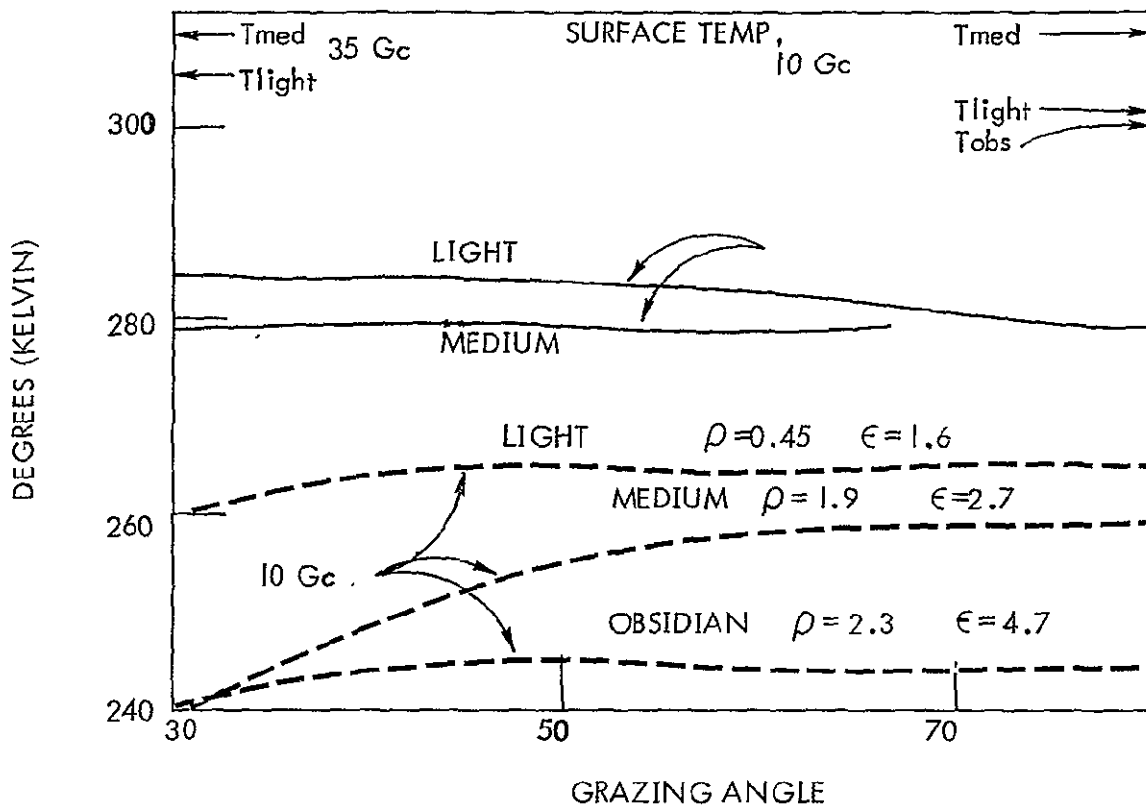


FIGURE 3.4 APPARENT TEMPERATURE OF THREE PUMICES (MONO, CALIFORNIA). FROM PEAKE ET AL [1966].

### 3.6.2 Planar Surface Model

A very smooth surface can be approximated by a plane and the scattering can be considered to be specular or coherent. For such a model the emissivity is given by

$$\epsilon_j(\theta_o) = 1 - |R_j(\theta_o)|^2 \quad j = v \text{ or } h$$

where  $R_j(\theta_o)$  is the  $j$ -polarized complex reflection coefficient given by

$$R_h(\theta_o) = \frac{\cos \theta_o - \sqrt{\mu_r \epsilon_r - \sin^2 \theta_o}}{\cos \theta_o + \sqrt{\mu_r \epsilon_r - \sin^2 \theta_o}}$$
$$R_v(\theta) = \frac{\mu_r \epsilon_r \cos \theta_o - \sqrt{\mu_r \epsilon_r - \sin^2 \theta_o}}{\mu_r \epsilon_r \cos \theta_o + \sqrt{\mu_r \epsilon_r - \sin^2 \theta_o}}$$

This is an idealized model and surely not a reasonable descriptor of natural terrain, but as a first-step approximation it is worth considering.

### 3.6.3 Geometric Optics Model

A model was propounded by Stogryn [1967] to explain the microwave emission of the sea surface. This model utilizes the Kirchoff or tangent plane approximation and rather than consider an infinitely conducting surface which many authors choose to solve for, the reflection is modified to include the finite complex dielectric constant of the ocean surface. He considers a Gaussian surface in two dimensions with local radii of curvature much much larger than a wavelength. The scattering coefficients are then given by

$$\gamma_{ij}(\theta_o, \theta_s) = f_{ij} \exp \left[ -\frac{1}{2B^2} \left\{ \frac{\alpha^2}{g_x^2} + \frac{\beta^2}{g_y^2} \right\} \right] / 2 \cos \theta_o B^2 g_x g_y$$

The coordinate axes  $x$  and  $y$  are taken to lie along the principal directions of the surface (coordinates for which the cross-products in the two-dimensional Gaussian distribution function vanish).  $g_x$  and  $g_y$  are the rms slopes along the  $x$  and  $y$  axes respectively. The quantities  $\alpha$ ,  $\beta$  and  $B$  depend only on the direction of incidence and scatter considered. The function  $f_{ij}$  takes into account the complex reflection coefficients of the surface. Using estimates of mean sea slope from Cox and Munk's data, Stogryn compared his results against measured sea brightness temperatures. His model does well for smooth seas but disagrees with observed measurements for rough seas.

### 3.6.4 Physical Optics Model\*

This approach again starts with the Kirchoff approximation but instead the resulting Kirchoff integral for isotropic scattering

$$\langle E_s \cdot E_s^* \rangle = 2\pi S |k|^2 |f|^2 \int \left\{ J_0 \left( \sqrt{2k^2 \sin^2 \theta_s \cos^2 \theta_s + k^2 \sin^2 \theta_s} \xi \right) \exp \left[ -k (\cos \theta_o + \cos \theta_s) \sigma^\circ (1 - \rho(\xi)) \right] \cdot \xi \right\} d\xi$$

is not evaluated by assuming a Gaussian autocorrelation function as many authors do. It is possible to evaluate this integral approximately without assuming a specific form of  $\rho(\xi)$  provided it is differentiable and parabolic at the origin. Thus by expanding  $\rho(\xi)$  and  $\xi_o$  where the factor reaches a maximum,  $\langle E \cdot E^* \rangle$  can be approximated by the first two terms in the expansion. From this then  $\gamma_{ij} + \gamma_{jj}$  can be found as. [Ulaby and Fung, 1970]

$$\gamma_{ij} + \gamma_{jj} = (|f_{ij}|^2 B^2 C_o) / \left\{ 2 \cos \theta_o [B^4 + C_o (\alpha^2 + \beta^2)^{3/2}] \right\}$$

where  $f_{ij}$  contains the fresnel reflection terms,  $C_o$  is a parameter related to the microwave wavelength and the standard deviation and correlation function of the surface heights.  $B$  is a function of the incidence angles. For a sufficiently smooth surface, the first derivative of  $\rho(\xi)$  at  $\xi$  becomes small compared with its second derivative and under these conditions the results from this model have been shown to reduce to Stogryn's geometric optics model.

\* The name physical optics model is reserved for models which set up the problem according to the Kirchoff integral. The model discussed here therefore falls in this category.

The physical optics model predicts a dependence of emissivity on surface roughness even at normal incidence and the curves tend to flatten out as the scale of roughness is increased.

### 3.6.5 Composite Model

Recently Wu [1973] developed another scattering theory to better estimate the microwave emission from the sea. Extending the two scale theory propounded by Semeynov, Wu considered the effect of the small irregularities upon the large scale undulations. This is done in two ways; (1) by modifying the Fresnel reflection coefficients of the large undulations due to the small irregularities, and (2) accounting for the effect of the large undulations upon the small irregularities by averaging scattering cross-sections of the small irregularities over the surface normals of the large undulations. The results seem to fit the experimental data better over the entire range of incidence angles. It shows that the sea-surface is better modelled by a two-surface than a single surface model.

### 3.6.6 Empirical Model

All of the statistical models have attempted to predict the emission from a relatively homogeneous surface as the ocean. The only models invoked to predict the emission from land have been due to Peake [1966]. Apart from the Lambert law model, Peake proposed other empirical models. As an example, for tall grass and weeds where the scattering is predominantly due to diffuse scatter, Peake suggested that

$$\gamma_{ii}(\theta_0, S) + \gamma_{ij}(\theta_0, S) = \frac{\gamma_{oi}}{2} (\cos \theta_0 + \cos \theta_s) \sec \theta_0$$

where  $\gamma_{oi}$  is a constant for polarization  $i$ . Therefore

$$\epsilon_i(\theta_0) = 1 - \gamma_{oi}/4 \left( 1 + \frac{1}{2} \sec \theta_0 \right)$$

This is a modification to the Lambert law model.

## CHAPTER FOUR

### REVIEW OF RADIOMETER/SCATTEROMETER MEASUREMENTS

#### 4.0 Introduction

Passive detection at optical or near-optical wavelengths had been, for the most part, the major tool for remote sensing. The microwave region had been exploited by radio astronomers for a long time before radiometers were used for terrestrial observations. Active sensors in the microwave region were used mainly for detection, range-finding, navigation, or weather sensing. Microwave radiometer measurements to measure the apparent brightness temperature of land surfaces have been made since the 1950's. Radar backscatter measurements have been made since the 1940's. The only measurements programs that employed active and passive sensors in the microwave region simultaneously were the Skylab and AAFE\* programs. Data from these programs shall not be discussed here, but rather, measurement programs in the pre-Skylab era will be enumerated. Since the measurement programs for the radiometer and the scatterometer are distinct, they will be discussed separately.

#### 4.1 Backscatter Measurement Programs

Measurements of the radar-backscatter have been made in numerous measurement programs. They have been made from bridges and truck booms, from low and high altitude aircraft, and once from a rocket. Unfortunately, various factors involved in the measurement schemes make comparisons between data from various programs difficult. The most notable of these factors is the lack of absolute calibration of the measuring instruments; other factors compounding the difficulty are the tremendous difference in target resolution cell size and the lack of detailed knowledge of the target scene. The lack of absolute calibration can perhaps be compensated for by some normalizing scheme, so that relative, rather than absolute values of  $\sigma^0$ , the backscatter coefficient, can be meaningfully compared. The difference in resolution cell sizes makes comparison valid under the assumption that the larger resolution cell contains only the target type encountered in the smaller resolution cell. This can be a ludicrous assumption in comparing data from a truck mounted scatterometer, with a target resolution of  $.22 \text{ m}^2$ , [Cosgriff et al, 1960] to data from a sensor such as the S-193 scatterometer, on-board Skylab, which has a minimum size resolution cell of a 100 sq kms! The lack of detailed knowledge about the target scene for which backscatter measurements are recorded not only makes comparisons difficult, but often renders the data meaningless. Some measurement

---

\*AAFE--Advanced Applications Flight Experiments.

programs conducted have detailed information about the targets including, in some cases, photographs; others only have a general description of the categories as observed by the pilot of a test aircraft. One, for example, has designated the target an "English Countryside" and documented the radar-backscatter. [Macfarland and Davies: 1958]

Experiments conducted include measurements at various microwave frequencies, various transmit-receive polarizations and span a range of incidence angles from nadir to grazing. The S-193 scatterometer operates at 13.9 GHz and has a range of incidence angles from nadir to  $52^\circ$  off nadir. An excellent comprehensive review of backscatter measurement programs has been documented by King and Moore [1974], with emphasis on frequencies and incidence angles near those of the S-193 scatterometer. Unfortunately, the only continuous frequency spectral measurements available were at 4-18 GHz, Ulaby [1974], and the highest frequency at which a complete set of near-vertical measurements were found at 3.8 GHz. [Edison et al, 1959].

Comparisons between data of various measurement programs should be made with caution because the backscatter is a function not only of the surface properties (dielectric properties, surface roughness and inhomogeneities in the subsurface) but also of the sensor properties--wavelength, incidence angle, polarization. Very few terrain categories have been observed by different measurement programs using the same sensor characteristics. Since the resolution of the S-193 scatterometer is so gross only broad categories can possibly be recognized. With this in mind, King and Moore [1974] selected the following categories in reporting on the measurements programs.

1. Grassland
2. Farmland (Cropland)
3. Forest
4. Desert
5. Residential-Commercial area
6. Swamps
7. Pavements
8. Volcanic areas
9. Snow-covered terrain

These classifications were made for two reasons: 1) the categories are visually separable (i.e., they can be recognized in photographs) and 2) the set chosen encompasses nearly all the measurements made. Selection of these classifications is certainly not electromagnetically unique. Use of pavements as an individual category may seem ludicrous in terms of its contributions to the return from an S-193 footprint but it is

included because it was extensively studied by Ohio State University and is significant for fine-resolution radars.

For a brief but comprehensive review of the measurement programs, the reader is referred to King and Moore [1974]. Many figures included in this brief treatise have been taken from their work. To provide a basis for comparison between data from the different programs, King and Moore [1974] have applied two normalizing schemes to the data. In one the data from each category in each program are normalized to a single look angle, in the other the data are normalized to one category--farmland at one look angle-- $50^\circ$ . Examples are provided after a description of some of the major measurement programs.

#### 4.2 Major Measurement Programs

Six institutions have conducted long-term comprehensive measurement programs for backscatter: U.S. Naval Research Laboratory airborne [Ament et al, 1959], and bridge-mounted [Grant and Yaplee, 1957], radars; Goodyear Aerospace Corporation airborne radars [Reitz et al, 1959], [Newbry, 1961]; Ohio State University truck-mounted systems [Cosgriff et al, 1960], [Oliver et al, 1969], [Shultz et al, 1969], [Peake and Cost, 1968]; NASA/MSC airborne scatterometer [Masenthin, 1967], [Lundien, 1967], [Rouse, 1969], [Parashar, 1973], [Cullen and Bradley, 1969], [Dickey et al, 1974], [King, 1973]; and the University of Kansas [Ulaby, 1974], [Ulaby et al, 1974]; Sandia Corporation airborne (near vertical) [Edison et al, 1959], [Janza et al, 1959]. Other institutions have also conducted backscatter measurements and a brief account of their efforts as found in the open literature appear below.

The measurement programs conducted for each of the categories listed above, the first author, affiliation, sensor platform, frequency bands and sensor viewing angle as compiled from open literature by King and Moore appears as table 4.1.

##### 4.2.1 Naval Research Laboratory Measurements

The Naval Research Laboratory has been one of the leading institutions in cataloging radar terrain return. Two programs have been documented, one which employed an aircraft based scatterometer and the other which used a bridge-mounted scatterometer. In both of these programs a significant amount of data is over water, for the aircraft measurement program this body of water includes ocean surfaces. Since these programs are distinct they will be discussed in turn.

NRL (Ament et al, 1959) has operated for several years a four-frequency radar system mounted in a WV-2 aircraft. This system operates at 428 MHz (P-band),

TABLE 4.1  
TERRAIN CATALOG FROM OPEN LITERATURE  
From King and Moore, 1974.

Category	1st Author	Year	Affiliation	Platform	Frequency Bands	Sensor Viewing Angles (Incidence)
SEA ICE	Parashar	1973	KU	Aircraft	P, Ku	5° - 60°
	Rouse	1969	KU	Aircraft	Ku	5° - 60°
FARMLAND	Ulaby	1973	KU	Truck	C	0° - 70°
	King	1972	KU	Aircraft	P, Ku	5° - 60°
	de Loor	1972	Netherlands	Tower	X, Ka	80° - 89°
	Oliver	1969	Ohio State	Truck	L, X, Ku, Ka	10° - 80°
	Cullen	1969	KU	Aircraft	Ku	5° - 60°
	Eklund	1969	Sweden	Aircraft, Tower	X	60°, 85°, 89°
	Peake	1968	Ohio State	Truck	X	10° - 80°
	Simonett	1967	KU	Aircraft	Ka	45°
	Ericson	1966	Sweden	Aircraft	X	60°, 85°, 89°
	Linell	1966	Sweden	Tower	X	
	Cosgriff	1960	Ohio State	Truck	X, Ku, Ka	10° - 80°
	Reitz	1959	Goodyear	Aircraft	X	30° - 80°
	Edison	1959	Sandia Corp/UNM	Aircraft	P, S	0° - 30°
	Janza	1959	Sandia Corp/UNM	Aircraft	P, S	0° - 30°
FOREST	King	1970	Aerospace Corp.	Tower	mm	0° - 45°
	Eklund	1969	Sweden	Aircraft	X	60°, 85°, 89°
	Ericson	1966	Sweden	Aircraft	X	60°, 85°, 89°
	Newbry	1961	Goodyear	Aircraft	X	30° - 80°
	Edison	1959	Sandia Corp/UNM	Aircraft	P, S	0° - 30°
	Janza	1959	Sandia Corp/UNM	Aircraft	P, S	0° - 30°
	Reitz	1959	Goodyear	Aircraft	X	30° - 80°
	Ament	1958	NRL	Aircraft	P, L, S, X	10° - 90°
	Grant	1957	NRL	Bridge	X, K, Ka	0° - 80°
GRASSLAND	King	1970	Aerospace Corp.	Tower	mm	0° - 45°
	Reitz	1959	Goodyear	Aircraft	X	30° - 80°
	Grant	1957	NRL	Bridge	X, K, Ka	0° - 80°

TABLE 4.1  
(Continued)

Category	1st Author	Year	Affiliation	Platform	Frequency Bands	Sensor Viewing Angle (Incidence)
SWAMPS	Ericson	1966	Sweden	Aircraft	X	60° , 85° , 89° 30° - 80° 0° - 80°
	Reitz	1959	Goodyear	Aircraft	X	
	Grant	1957	NRL	Bridge	X, K, Ka	
DESERT	Brown	1968	JPL-CIT	Rocket	L	(Rocket)
	Newbry	1961	Goodyear	Aircraft	X	30° - 80°
	Edison	1959	Sandia Corp/UNM	Aircraft	P, S	0° - 30°
	Janza	1959	Sandia Corp/UNM	Aircraft	P, S	0° - 30°
	Reitz	1959	Goodyear	Aircraft	X	30° - 89°
	Ament	1958	NRL	Aircraft	P, L, S, X	10° - 90°
VOLCANIC	Shultz	1969	Ohio State	Truck	L, X, Ku, Ka	10° - 80°
	Lundien	1967	KU	Aircraft	Ku	5° - 60°
	Masenthin	1967	KU	Aircraft	Ku	5° - 60°
RESIDENTIAL COMMERCIAL	Barnum	1971	Stanford	Moving Probe	K	65° - 85° 60° , 85° , 89° 30° - 80° 0° - 30° 0° - 30° 10° - 70°
	Ericson	1966	Sweden	Aircraft	X	
	Newbry	1961	Goodyear	Aircraft	X	
	Edison	1959	Sandia Corp/UNM	Aircraft	P, S	
	Janza	1959	Sandia Corp/UNM	Aircraft	P, S	
	Ament	1958	NRL	Aircraft	P, L, S, X	
SNOW COVER	Venier	1972	CRC, Canada	Window & Bridge	K	Vertical
	Cosgriff	1960	Ohio State	Truck	X, Ku, Ka	10° - 80°
	Edison	1959	Sandia Corp/UNM	Aircraft	P, S	0° - 30°
	Janza	1959	Sandia Corp/UNM	Aircraft	P, S	0° - 30°
HIGHWAY PAVEMENT	Lundien	1971	Waterways Exp. Sta.	Truck	Sweep Frequency 0.2-7 GHz	Vertical
	King	1970	Aerospace	Tower	mm	0° - 45°
	Cosgriff	1960	Ohio State	Truck	X, Ku, Ka	10° - 80°

1225 MHz (L-band), 4455 MHz (C-band) and 8910 (X-band). The antennas used were fixed narrow conical beams (as opposed to a scanning antenna at each frequency; all four transmit-receive polarization pairs could be recorded. The variation of backscatter over incidence angle was recorded by tilting the antenna in pitch to a selected angle, and flying repeatedly for different angles over "similar" terrain. While this is quite acceptable over an ocean surface (which was their primary target) which can be considered homogeneous over large stretches, it causes the land targets to be grossly defined. The identification of target areas was by pilot comment.

The four major categories of land areas investigated were New Mexico desert land with low sparse vegetation, New Jersey woods (pine trees with heavy undergrowth and occasional snow patches), the city of Chicago, and a portion of Lake Michigan immediately adjacent to the city of Chicago. Figures 4.1a-d show the angular backscatter response for VV, HH, HV and VH polarizations at X-band (8.9 GHz) for the four terrain categories.

NRL also conducted many experiments to measure the backscatter from ocean surfaces. To obtain a more exact specification of the variation of the backscatter from the sea with increasing sea roughness, and to determine a worst-case condition for sea clutter, NRL (Daley et al, 1970) conducted a set of measurements in the North Atlantic (near Ireland). Data recorded off the coast of San Juan, Puerto Rico, in July 1965 are documented by Daley et al [1968] over an angular range of nadir to  $86^\circ$  and from calm sea conditions to moderately rough sea conditions characterized by 5 to 7 foot wave heights and 10 to 20 knot winds. Another set of measurements was made by NRL personnel [Daley et al, 1971] with the same sensor in the vicinity of Bermuda. More recently another measurement programs conducted by these same personnel [Daley et al, 1973] at NRL documented radar backscatter off the eastern coast of the United States. The data collected by NRL in all these and many earlier missions provides the largest bank of over-ocean data. There have been varied contentions as to the dependence of the backscatter response to surface roughness and hence to wind speed and wave height. To even enter into discussion regarding the theorized angular behavior of the radar backscatter with sea roughness would be too voluminous to report in this brief treatise. Extensive investigations of the NRL data by researchers at the University of Kansas [Claassen and Fung, 1973] show, however, that the conclusions reached by examination of NASA/MSC measurement data do indeed apply to the NRL data for the 1969 Northern Ireland (North Atlantic) mission and the 1970 Bermuda

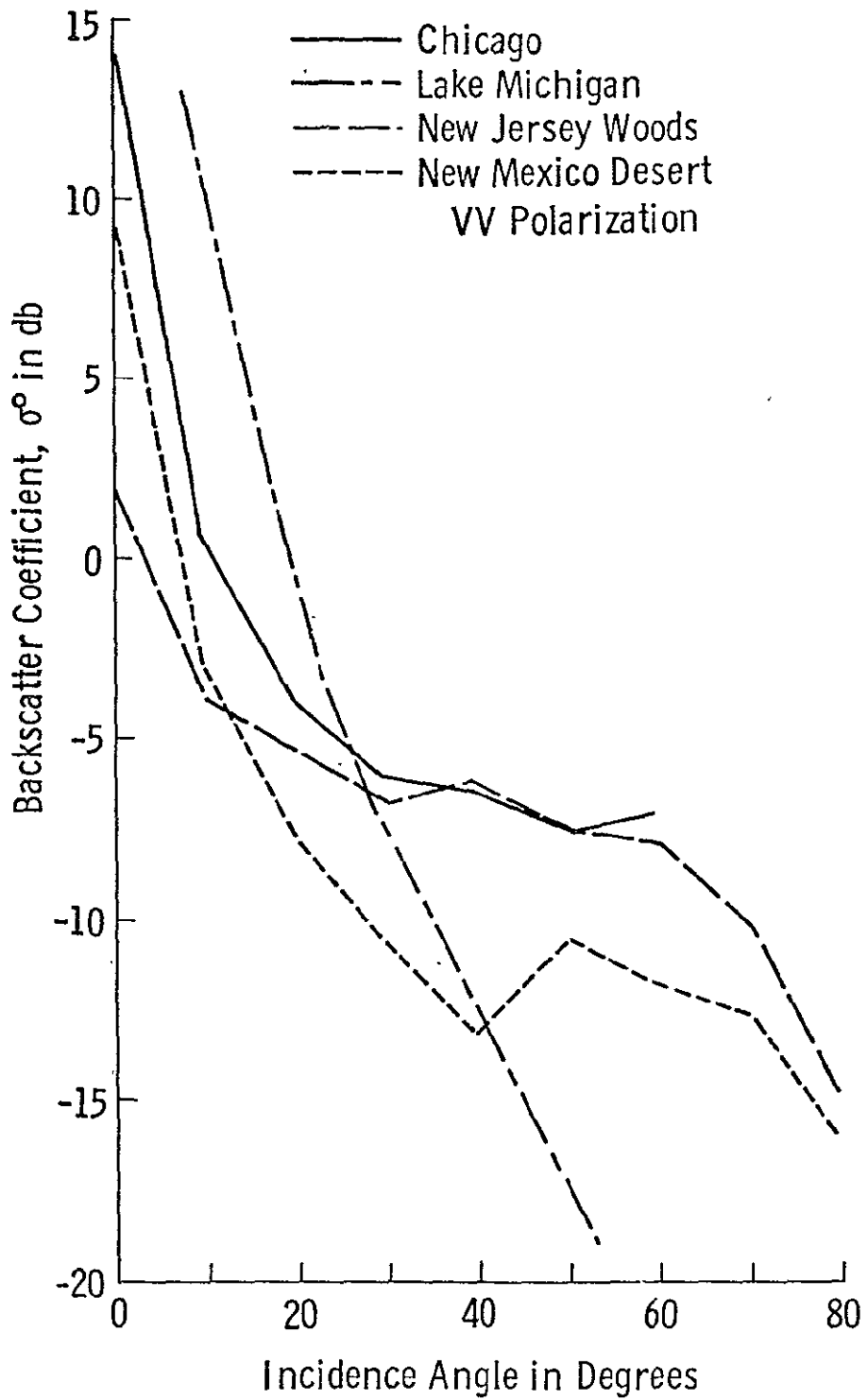


Figure 4.1a. Backscatter coefficient at X-band for four terrain targets. (After Ament, et al.)

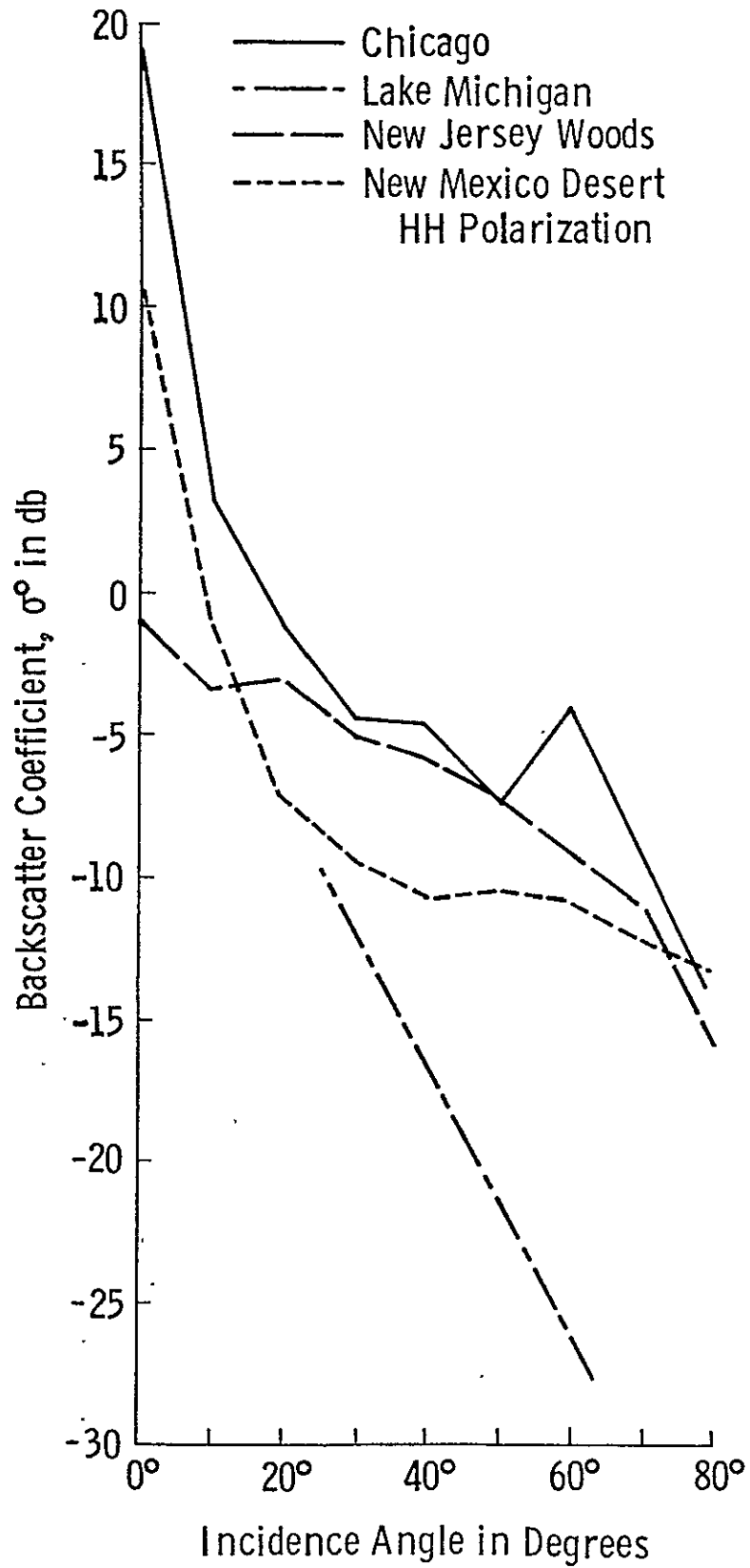


Figure 4.1b. Backscatter coefficient at X-Band for four terrain targets. (After Ament, et al.)

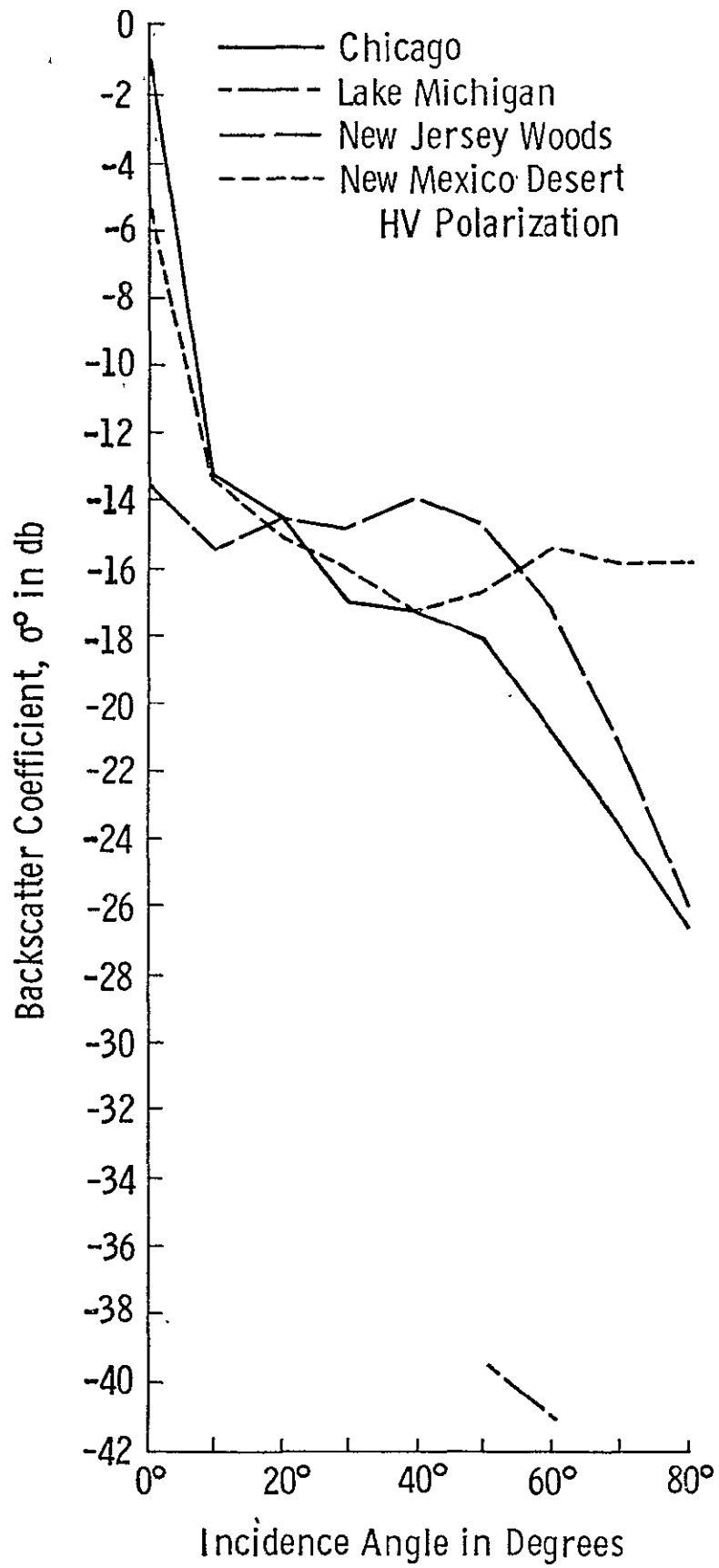


Figure 4.1c. Backscatter coefficient at X-band for four terrain targets. (After Ament, et al.)

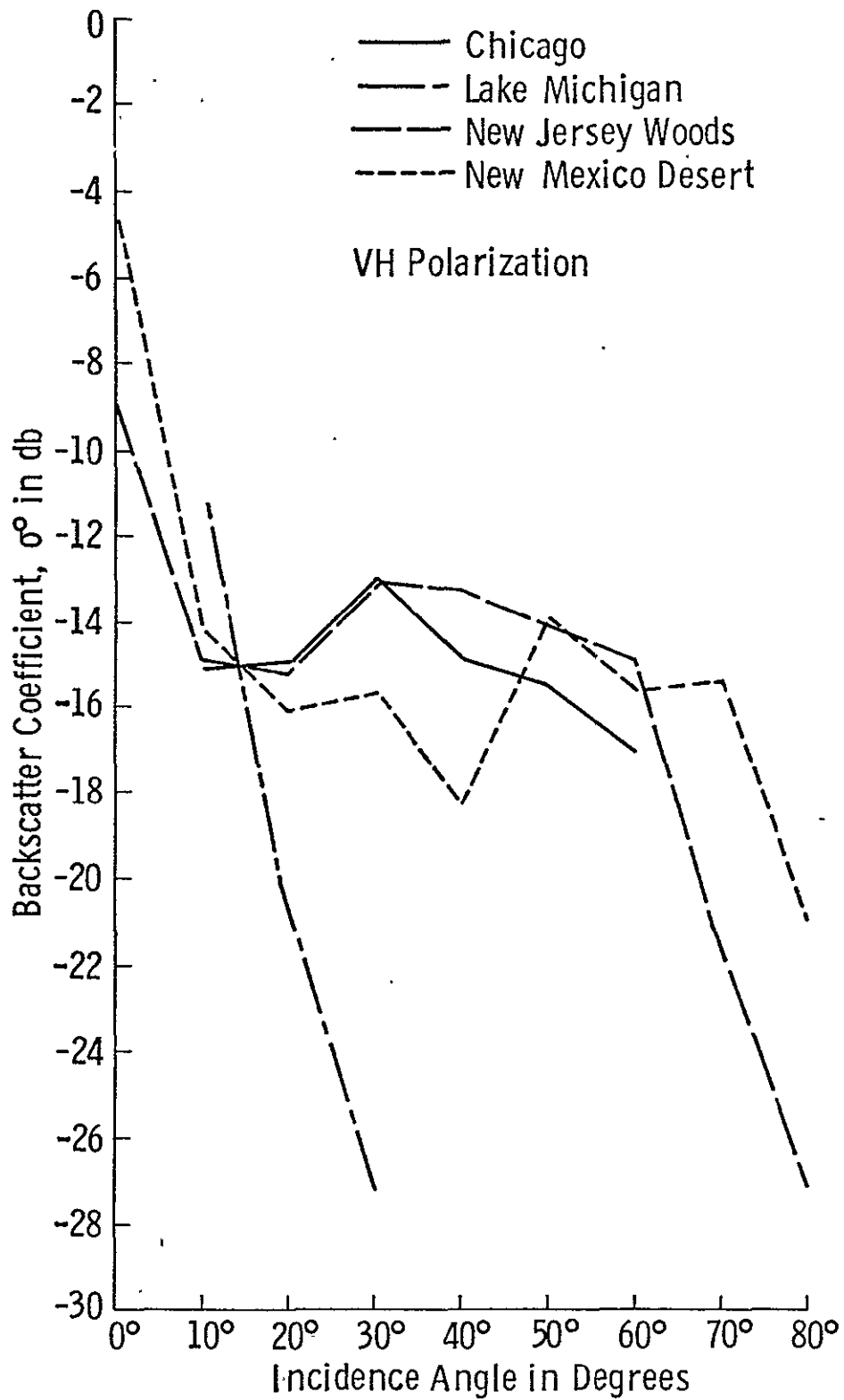


Figure 4.1d. Backscatter coefficient at X-band for four terrain targets. (After Ament, et al.)

(JOSSI) mission. This is in contrast to the conclusions reached by NRL personnel who did not discount a bias error between missions. An example of the NRL measurement for oceanic backscatter is provided in Figure 4.2 a-d. The wind response as analyzed by Claassen and Fung (using NRL data) is provided in Figures 4.3 a-b. They have shown the separation due to bias between the two missions (Northern Ireland and Bermuda) and found a regression equation relating  $\sigma^{\circ}$  to log of the wind speed.

Another NRL measurement program was reported by Grant and Yaplee [1957]. Three radars operating at 3.2 cms [X-band], 1.25 cms [K-band], and 8.6 mms [Ka-band] were used to obtain backscatter coefficient information from ocean and land targets. The radars were mounted on bridges that were at least 30 meters away from land targets and 45 meters away from water surfaces. Figures 4.4a-e show some examples of Grant and Yaplee's data. Figure 4.4a shows  $\sigma^{\circ}$  vs  $\theta$  (incidence angle) for a tree-covered terrain in full foliage in New Orleans. Figures 4.4b and 4.4c shows the contribution of moisture to a terrain in Port Arthur, Texas, with tall weeds and flags. Figure 4.4d and 4.4e show the  $\sigma^{\circ}$  vs  $\theta$  response for a non-homogeneous target made up of a variety of terrain types. Figure 4.5a and b show the  $\sigma^{\circ}$  vs  $\theta$  response for 1.25 cms and 3.2 cm wavelengths respectively for various wind speeds.

The NRL measurement programs, both aircraft and bridge-mounted suffer from a lack of adequate information regarding the land targets: The corresponding description of ocean surface data is much better.

#### 4.2.2 Goodyear Aerospace Corporation

The Goodyear Aerospace Corporation used an imaging radar operating at 9.375 GHz (X-band) to obtain scattering coefficient data over a variety of land targets. The backscatter responses reported by Reitz et al [1959] were computed by recording pulse-by-pulse the return used to produce the imagery. The ground descriptions were more complete than the NRL measurements with aerial photographs being used to supplement the radar images for terrain description. The antenna was designed to provide a uniform illumination over a wide range of incidence angles from  $20^{\circ}$  to  $80^{\circ}$  off nadir in the cross-track direction. The areas included in this study were widely different terrain types in five states in the United States. The imaged areas included irrigated farmland in Arizona, forest and meadows in Minnesota, trees and marsh along the New Jersey coast, mangrove islands and swamps in Florida, dry pine forest and grassland in Arizona, desert region in both Arizona and California and Bristol dry lake bed in California.

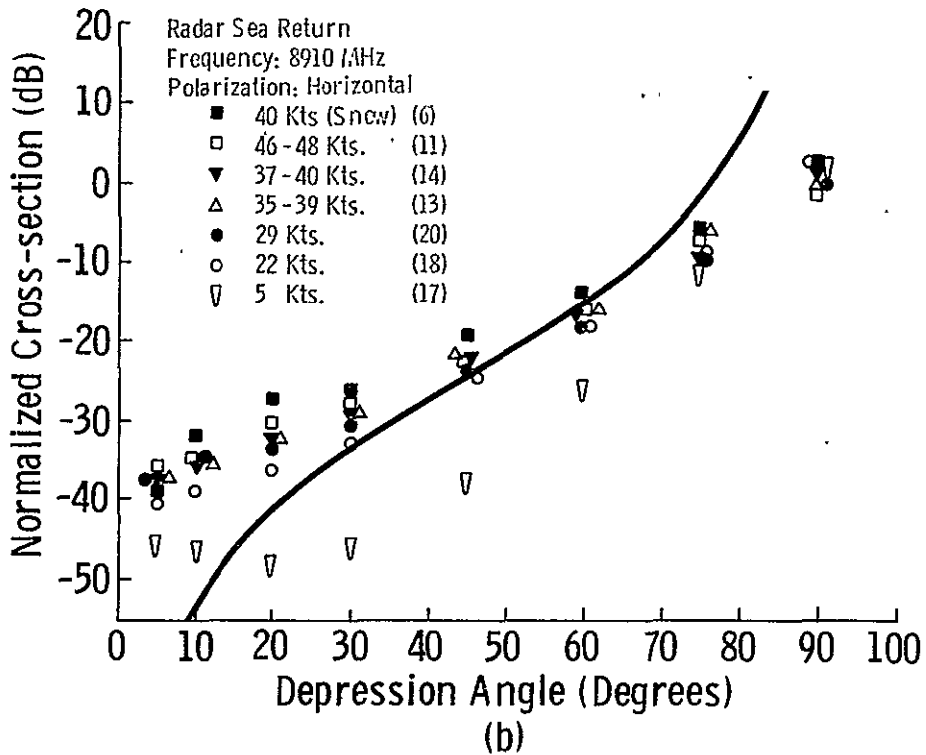
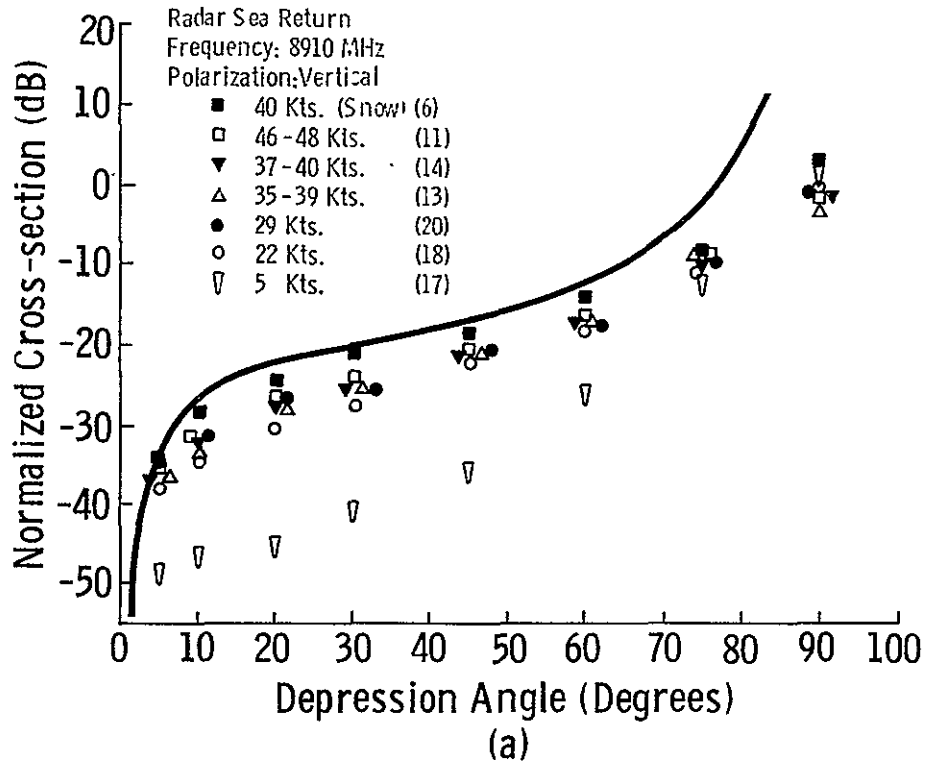


Figure 4.2. Normalized radar cross-section  $\sigma^0$  of the ocean vs. depression angle for (a) direct, vertically polarized, and (b) direct, horizontally polarized radar signals at X-band frequency (8910 MHz). All data are for upwind conditions. After Dailey, et al., 1970. Data from North Atlantic.

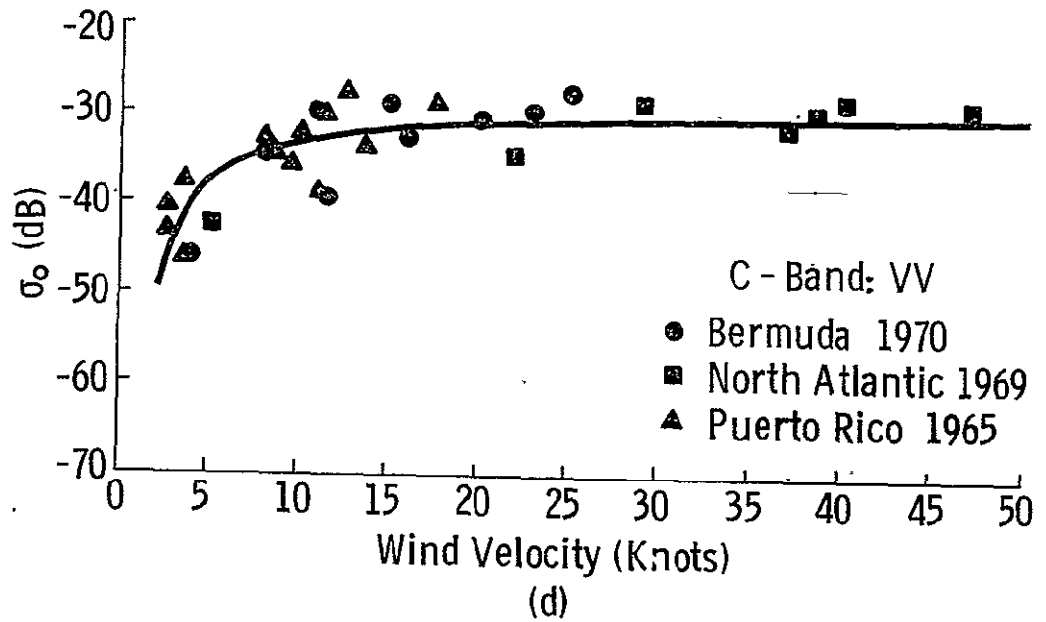
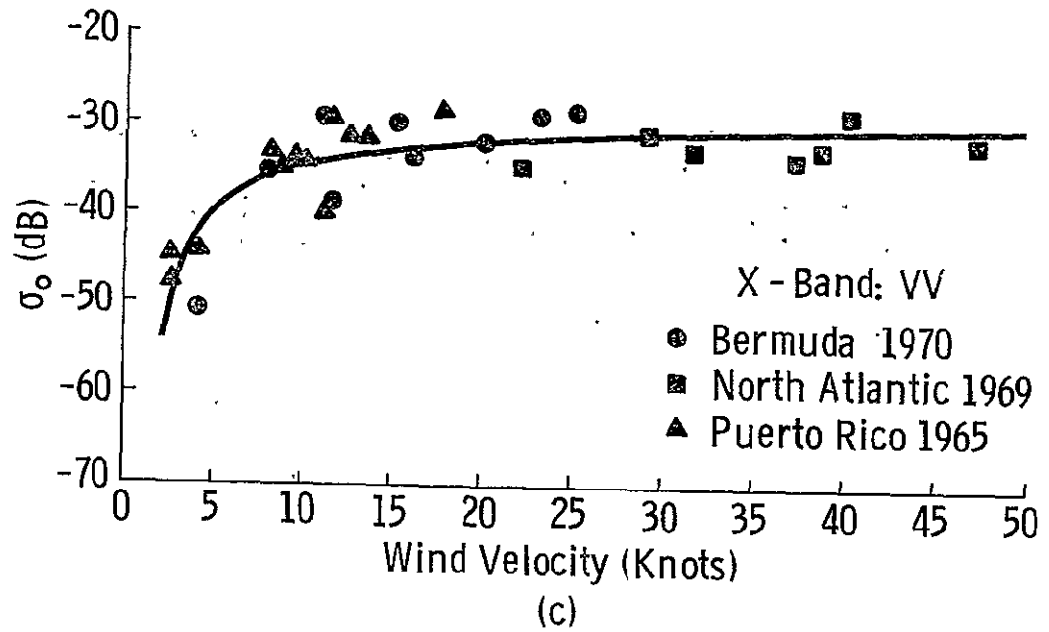
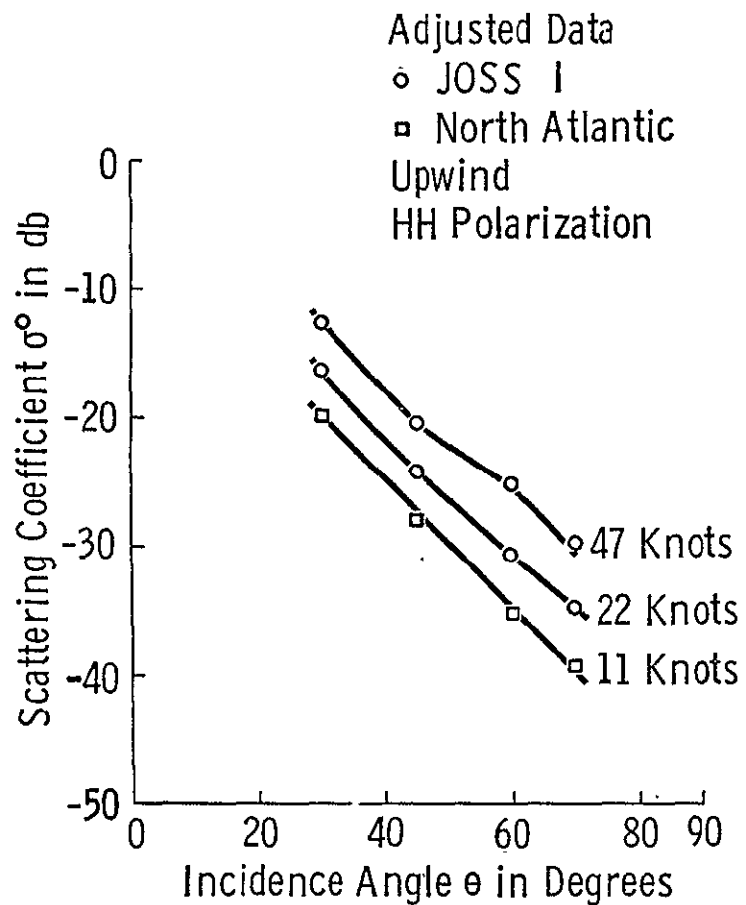
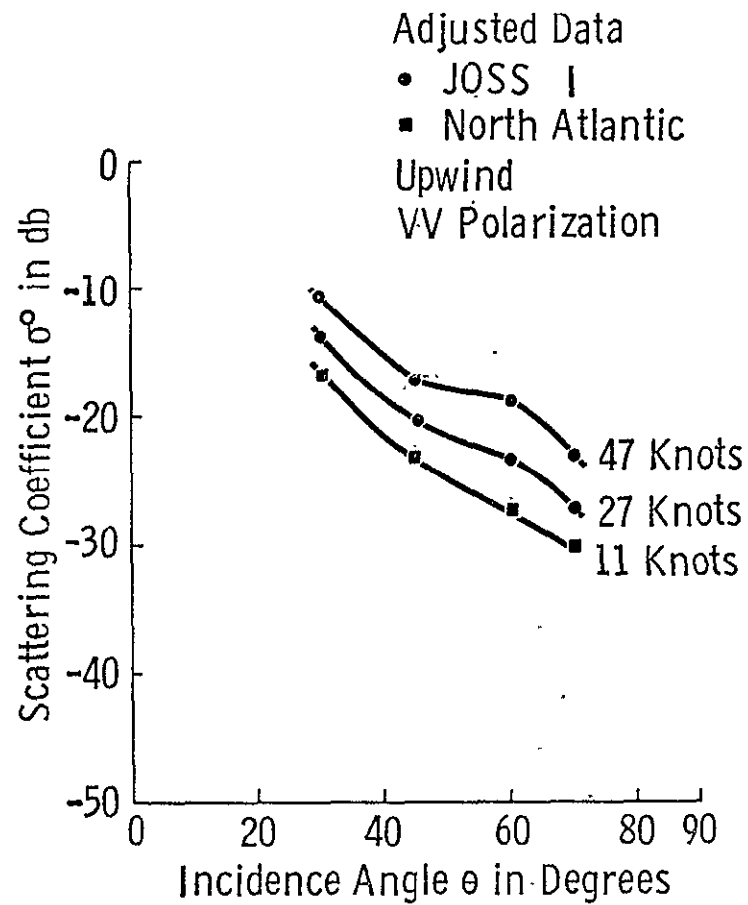


Figure 4.2. Median NRCS of the sea vs. wind velocity; X- and C-bands upwind,  $10^\circ$  depression angle. After Dailey, et al., 1971. Data from JOSS-1 mission.



(A) X-Band, Upwind, HH Polarization



(B) X-Band, Upwind, VV Polarization

Figure 4.3.  $\sigma^0$  vs.  $\theta$  plots of adjusted NRL ocean data for X-band upwind cases. (Courtesy of J. P. Classen and H. S. Fung).

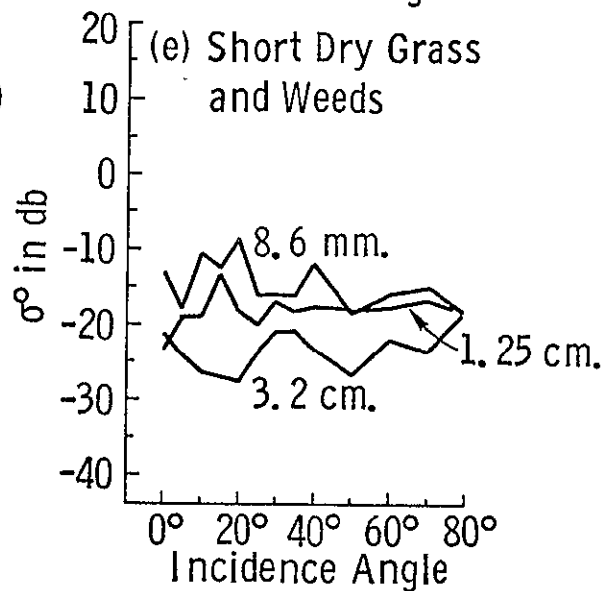
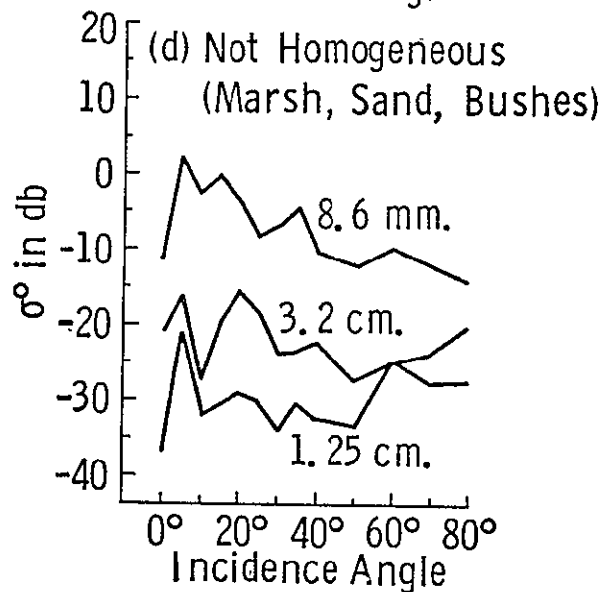
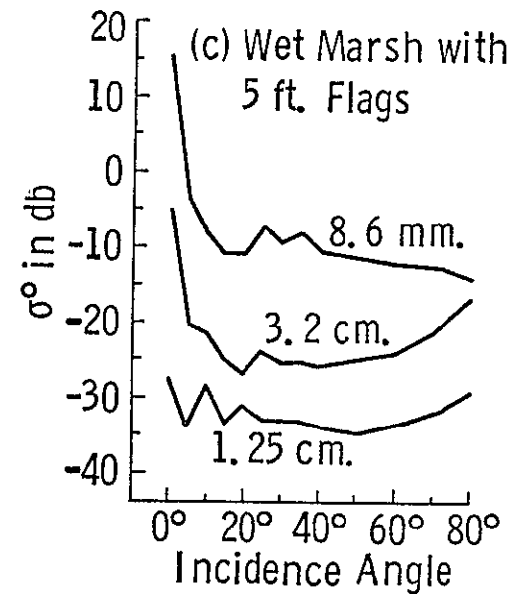
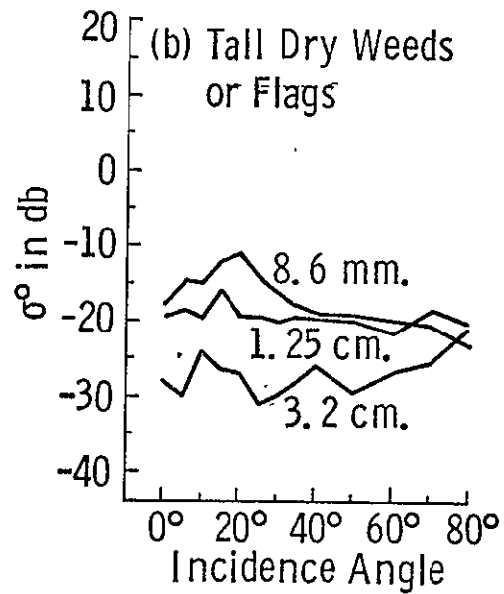
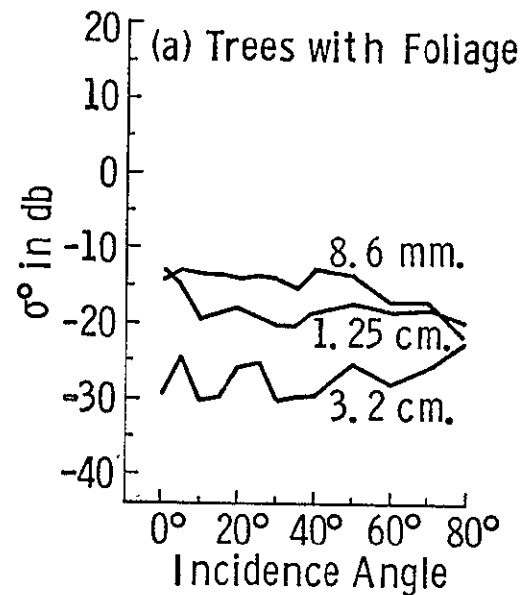


Figure 4.4.  $\sigma^0$  Values for different types of terrain. After Grant and Yaplee.

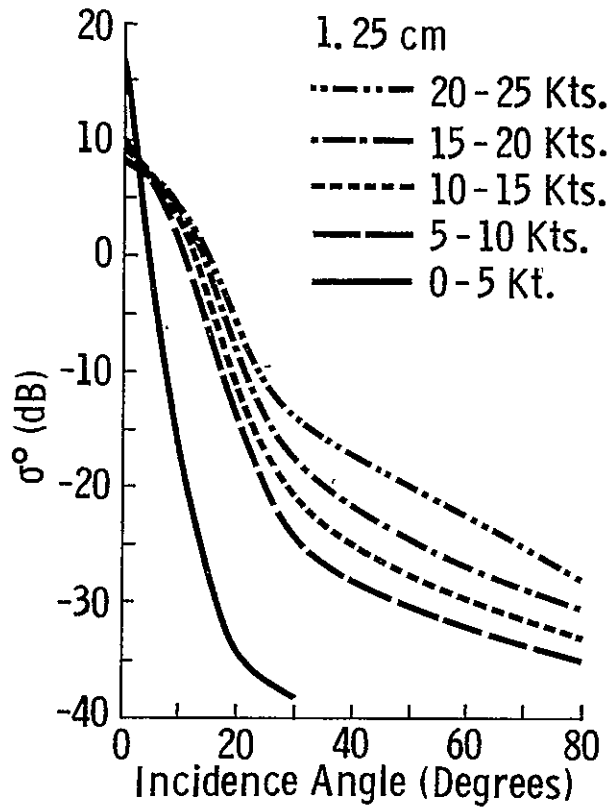


Figure 4.5a.  $\sigma^0$  as a function of wind velocity,  $\lambda=1.25$  cm. After Grant and Yaplee, 1957. (Water)

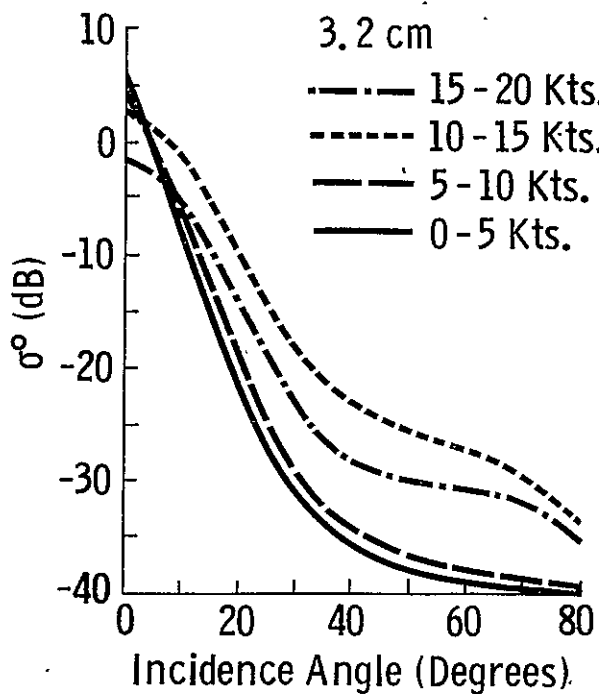


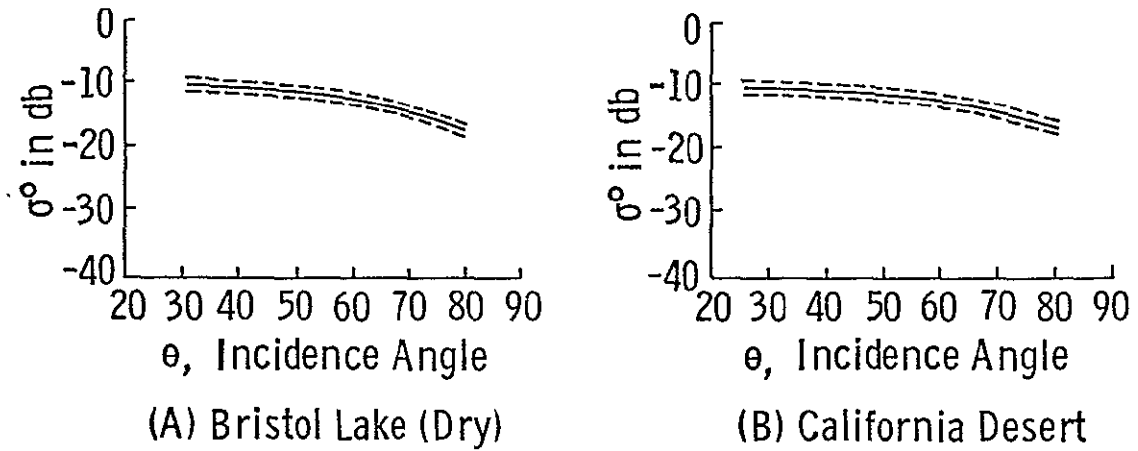
Figure 4.5b.  $\sigma^0$  as a function of wind velocity,  $\lambda=3.2$  cm. After Grant and Yaplee, 1957.

Figures 4.6 a-d show some of the results obtained, the solid lines are average backscatter values and the dashed line indicates bounds for approximately 70% of the data. Newbry [1961] in reporting these data showed that the backscatter grouped into bands that can be associated with gross terrain characteristics. Grant and Yaplee's [1959] data over the ocean is shown for comparison. A comparison of the NRL data to that of Goodyear after some adjustment (vegetation data at  $48^\circ$  is arbitrarily set to 0 dB for both sets) is shown in Figure 4.7 [King and Moore, 1974]. The NRL data showed the same rank order in terrain return as the Goodyear data, but did not fall within the bands set by the latter.

#### 4.2.3 Ohio State University Measurements

The Ohio State University ElectroScience Laboratory has, since the 1950's, been conducting terrain radar return measurements. They have conducted both monostatic and bistatic scattering coefficient measurements. The system used has been a set of CW doppler radars operating at 10 GHz (X-band), 15.5 GHz (Ku-band), mounted on a hydraulic boom of a truck. The Doppler signal was generated by driving the truck along the terrain surface to be measured. Measurements have been reported by Cosgriff, Peake and Taylor [1960], Oliver and Peake [1969], Shultz et al [1969], and for the bistatic case by Peake and Cost [1968]. A comprehensive record of scattering measurements and associated scattering theories is provided in a two-volume book entitled Radar Terrain Handbook, published by the Ohio State University. The scattering measurements performed by the Ohio State University are limited to targets with a resolution cell size of .002 sq.ms to  $5.32 \times 10^{-4}$  sq. ms. The measurements as reported by Cosgriff et al [1960] are basically of three terrain categories: road surfaces, agricultural terrains and moisture or precipitation-affected terrain. A variety of target types with these categories were studied. Figure 4.8 shows the backscatter for VV polarization from the different road pavements examined at Ku-band; notice that the data could be grouped into three distinct bands. No definite bands can, however, be ascribed to farmland data as can be seen in Figure 4.9a [Cosgriff et al] and Figure 4.9b [Oliver and Peake, 1969].

The dynamic range of farmland is around 13 dB, greatly exceeding the 5 dB band prescribed by Goodyear. The seasonal changes and the maturation of crops, coupled with the soil moisture conditions can cause a large change in the  $\sigma^\circ$  vs  $\theta$  response. The effects of precipitation on terrain surfaces is complex, Figure 4.10 shows that at X-band and Ka-band, snow increased the backscatter from grass but the reverse is observed at Ku-band. The effects of rain on backscatter are shown in



— Averaged Data  
 - - - - Data Spread Approx. 70% of Data

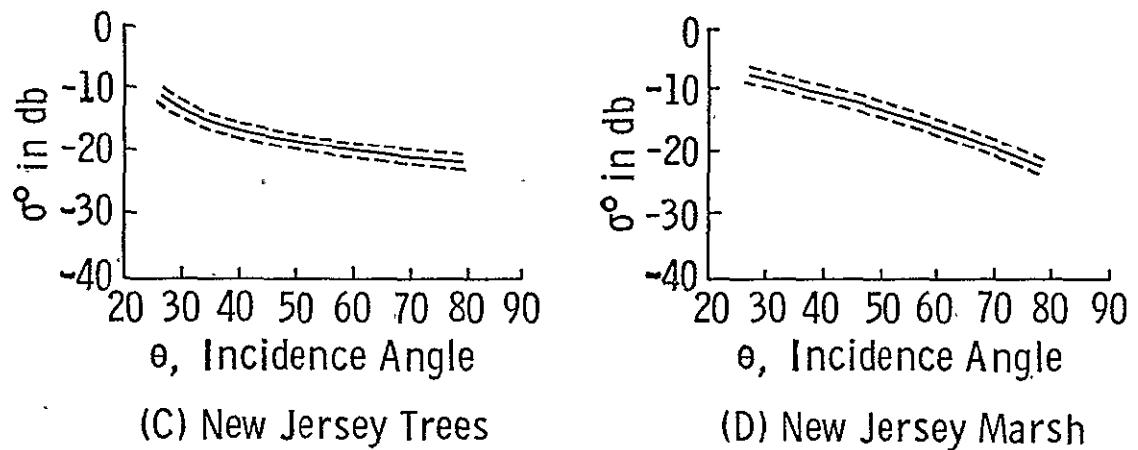


Figure 4.6. Backscattering coefficient vs. incidence angle. X-band, horizontal polarization. After Reitz, et al., 1959.

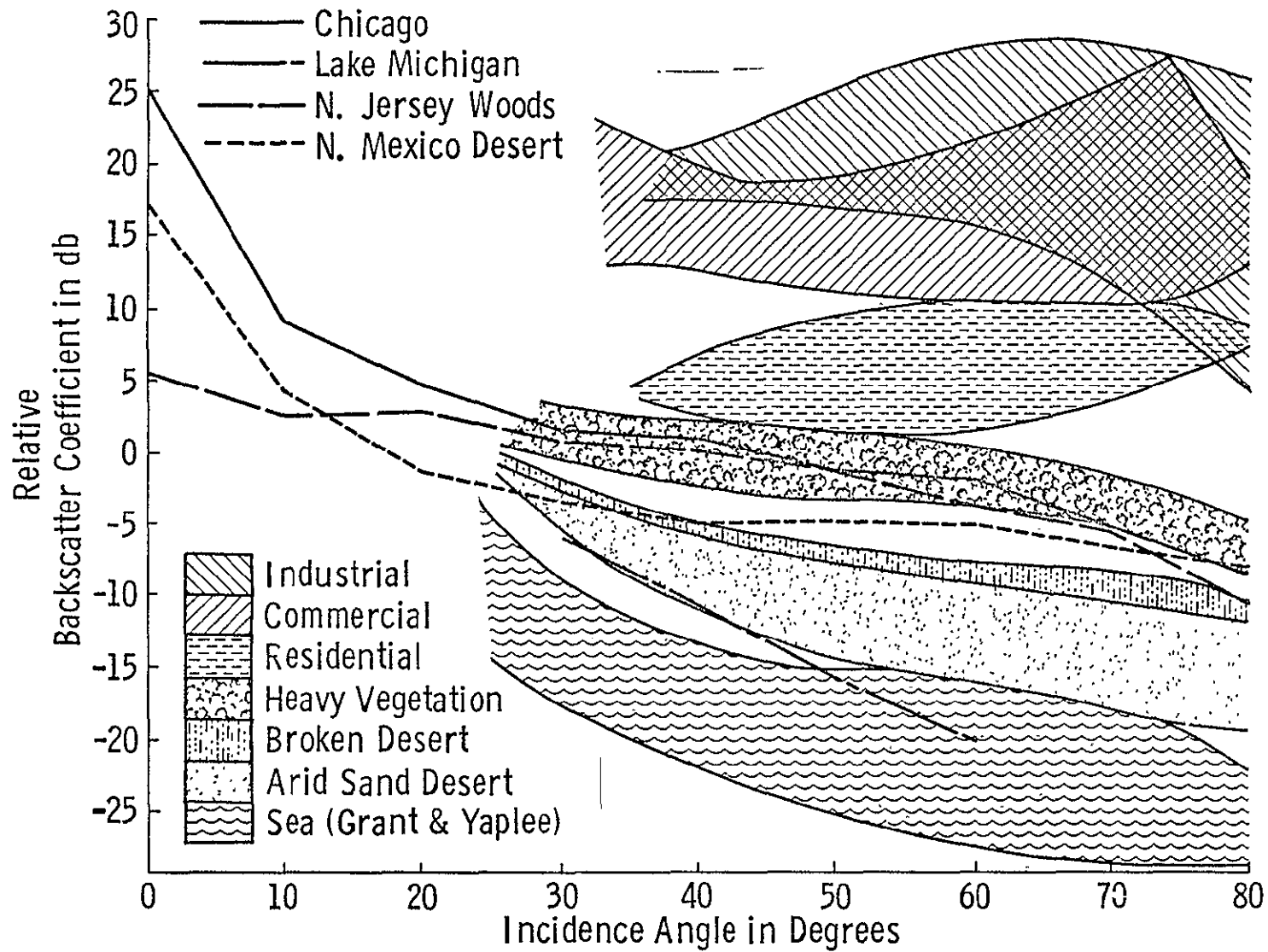


Figure 4.7. Goodyear adjusted data (+11.5 dB) HH polarization. Compared with NRL (Ament, et al.) data (+6.1 dB) reference of 0 dB for  $\sigma^0$  for heavy vegetation at 43°. From King and Moore, 1974.

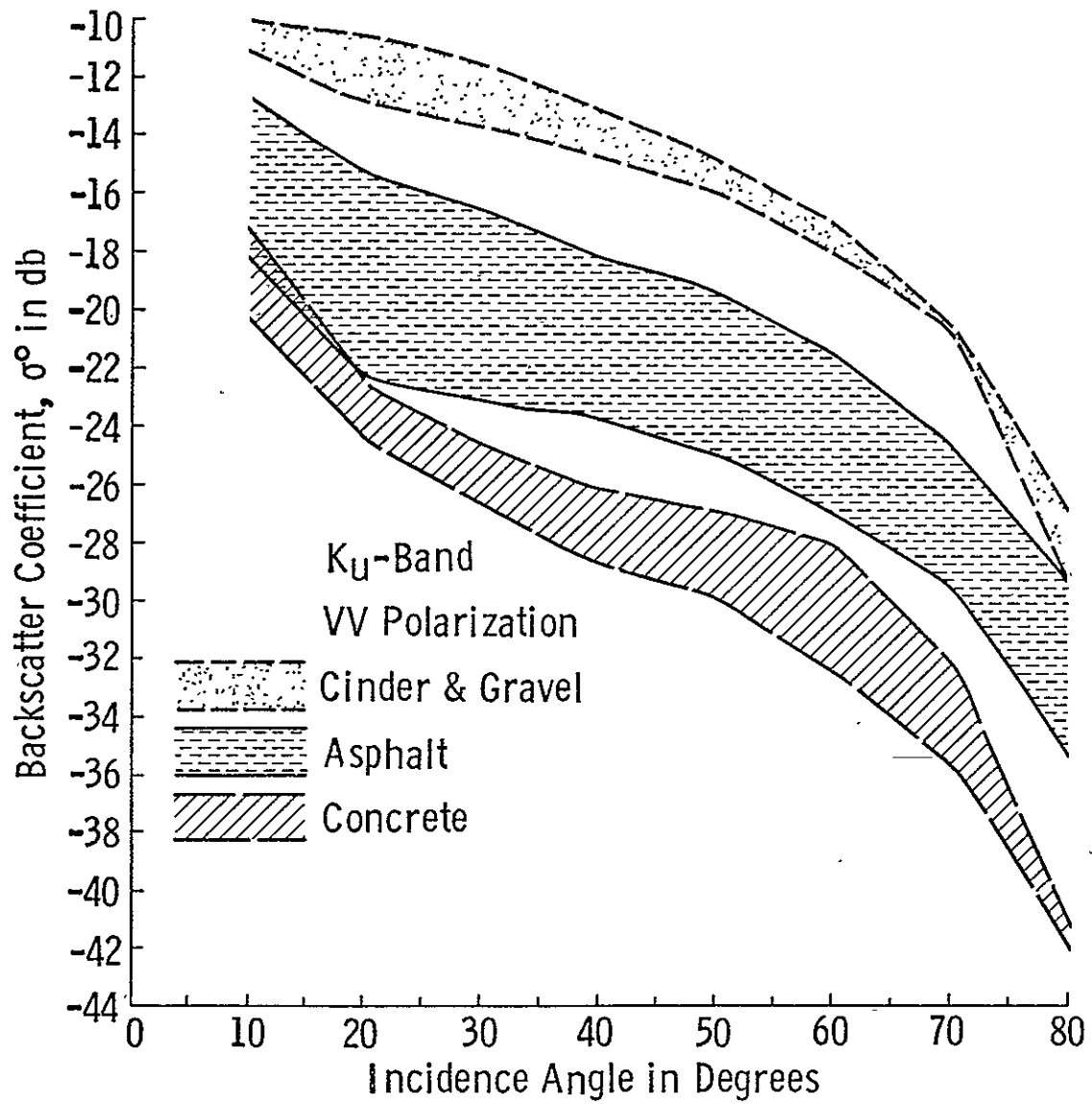


Figure 4.8. Backscatter coefficient of Road Surfaces Ku-band.  
After Cosgriff, et al., 1960.

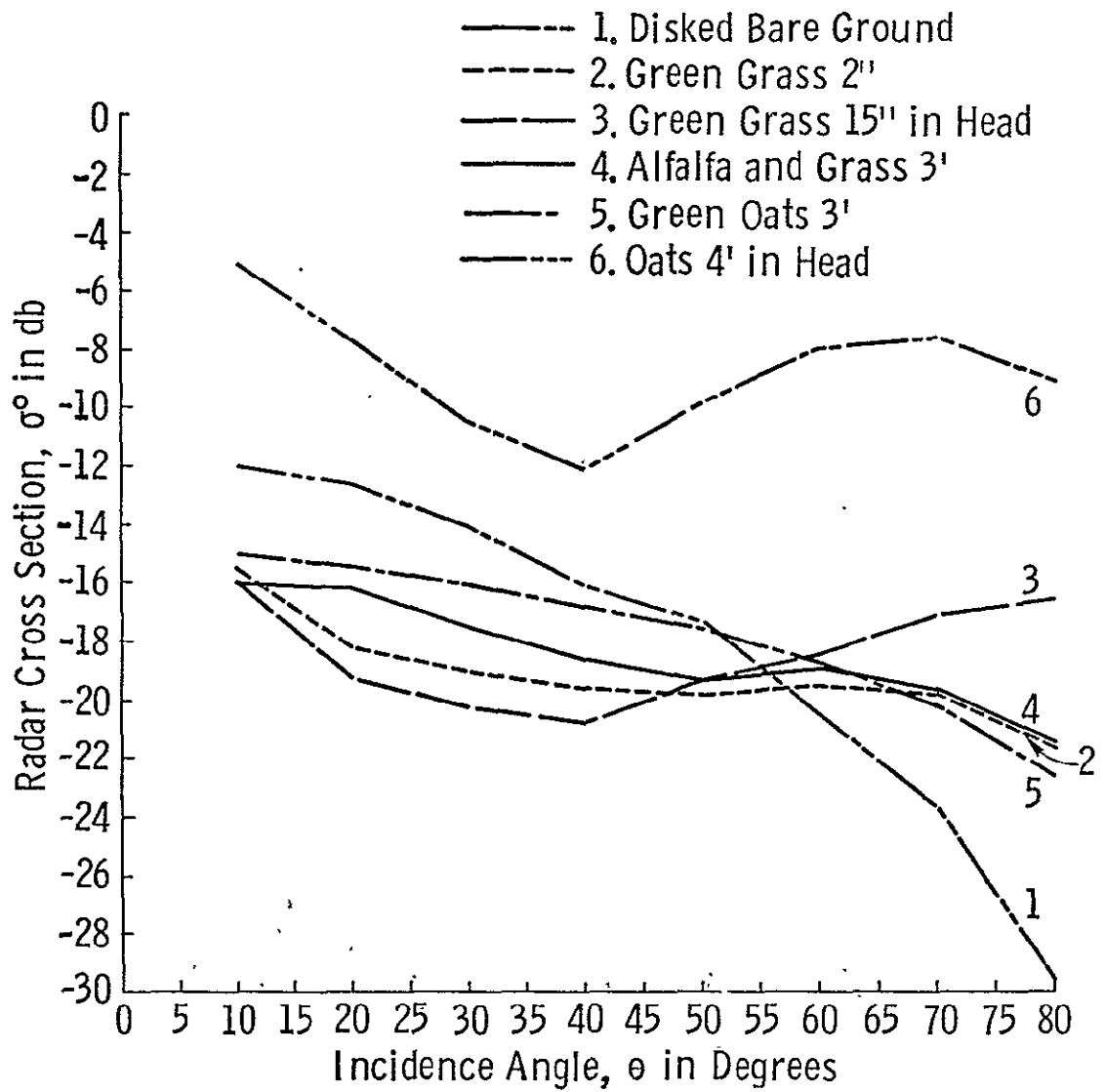


Figure 4.9a. Ohio State farmland data, Ku-band, 15.5 GHz, polarization VV. After Cosgriff, et al., 1960.

- 310. Wheat, in Head 48"
- 66. Bulk Wheat, in Head, 32"
- 103. Wheat Stubble
- 68. Oats, in Head, 26"
- 302. Oats, Green, 10"
- 306. Oats, Green, in Head, 36"
- 111. Soybeans, 36"
- 107. Corn, Not in Tassel, 7'
- 113. Corn, in Tassel, 6'
- 70. Alfalfa, 12 - 18"
- 156. Grass, 2"
- 158. Grass, 2 1/2"

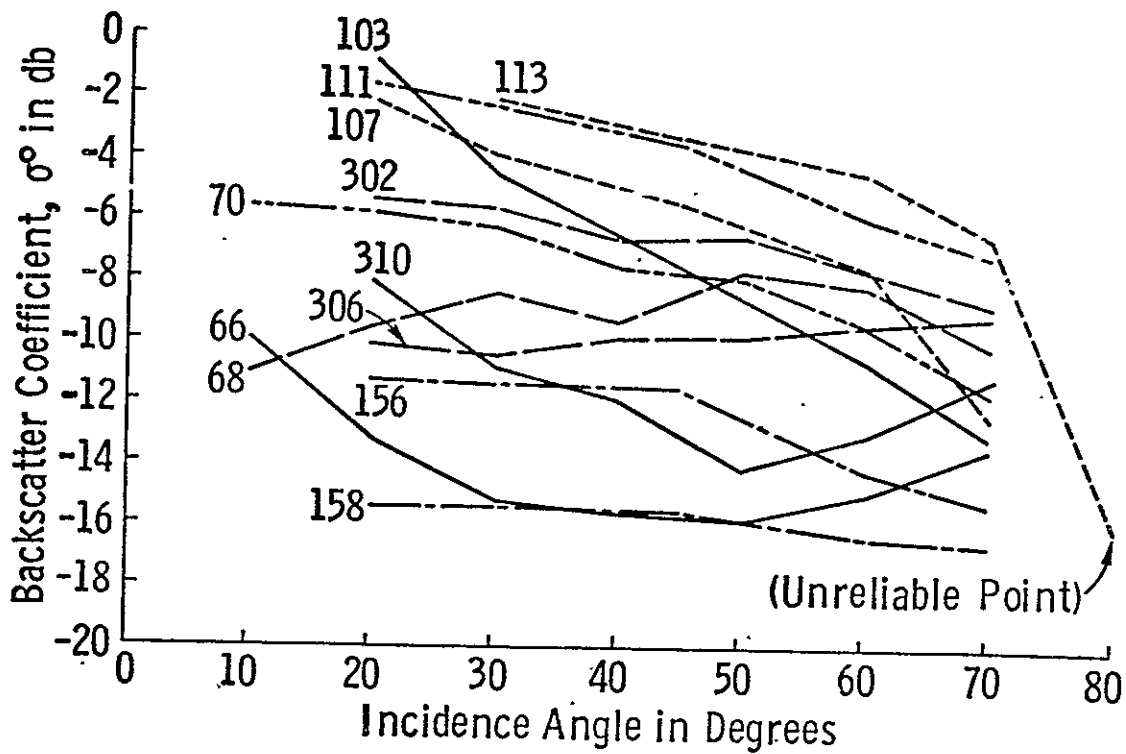
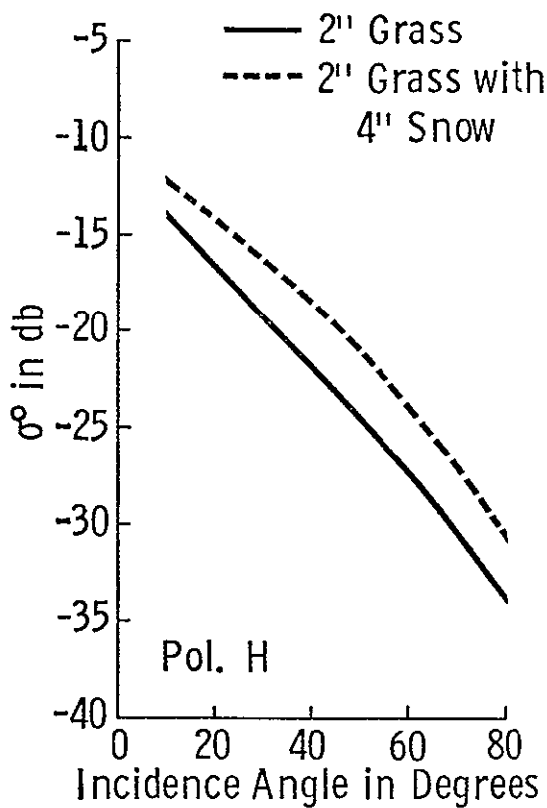
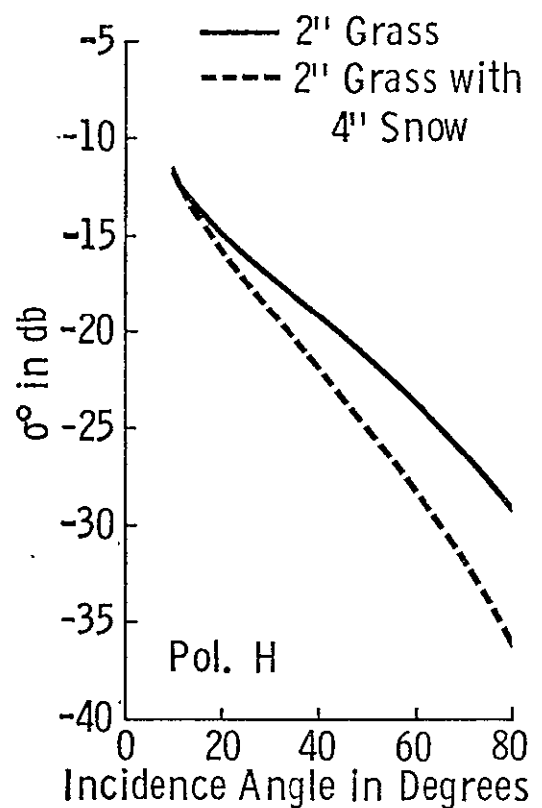


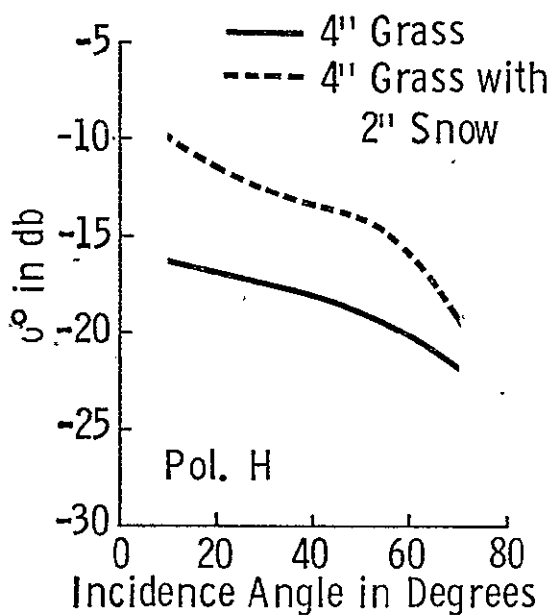
Figure 4.9b. Backscatter coefficient for farmland, Ohio State, Ku-band, polarization V. After Peake and Oliver, 1969.



(A) X-Band



(B) Ku-Band



(C) Ka-Band

Figure 4.10. Effects of snow cover on grass at X-, Ku-, and Ka-bands. After Cosgriff, et al., 1960.

Figures 4.11a through d. At Ka-band, (Figures 4.11a and 4.11 c) precipitation decreased the backscatter of a relatively smooth surface (asphalt) and increased the backscatter from a relative rough surface (vegetated field). The phenomenon was repeated at X-band (Figure 4.11b).

Shultz et al [1969] report on a series of measurements of terrain for geological interest. The terrain investigated included a volcanic area with lava flows and playa in California and limestone quarries in Ohio and Indiana. Figures 4.12 and 4.13 show the data from a volcanic area at Pisgah Crater and a limestone quarry in Columbus, Ohio, respectively.

The only bistatic radar terrain measurements that have been reported have been by Peake and Cost [1968]. The additional variable introduced in these measurements was the receiver azimuth angle. The targets were moved in a cart to generate the necessary Doppler signals. These experiments explored the effects of surface roughness, sensor polarization and verified the reciprocity theorem for scattering.

#### 4.2.4 NASA/MSC Scatterometer Measurements

Using a 13.3 GHz fan beam scatterometer, the NASA Manned Spacecraft Center conducted a series of radar terrain return programs. The radar, mounted on an aircraft, was flown over three major test sites: Pisgah Crater in California, Point Barrow, Alaska, and Western Kansas. The supporting evidence for these experiments included aerial photographs and radar imagery taken in flight; for the western Kansas site, ground crews were dispatched to collect information on the ground. Detailed information for the vegetation study in western Kansas included ground photographs, vegetation types and coverage, stages of crop development, crop vigor, planting direction and representative soil and plant moisture data. The scatterometer was vertically polarized and its fan beam spanned  $60^\circ$  fore and aft of nadir. The cross-track resolution at a nominal 1 km flight altitude corresponded to 40 meters.

The experiment at Pisgah Crater in California was to study the response of different geological formations. Fourteen different formations were flown, mostly of volcanic origin. Masenthin [1967] reported on the analysis of this data and attempted various schemes for the best possible representation of the  $\sigma^\circ$  vs  $\theta$  response so that a visual differentiation of the fourteen categories could be made from an examination of this data. The fourteen areas could be grouped into three more general categories to fit the categorization suggested by King and Moore [1974]: desert, lava flow and playa. Figure 4.14 shows the radar cross-sections observed at the Pisgah Crater area.

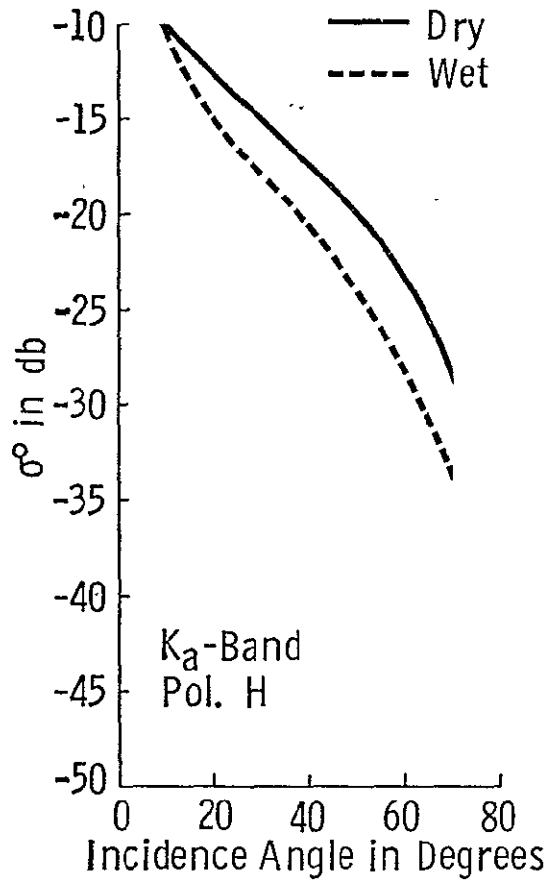


Figure 4.11a. Effect of rain on asphalt road. After Cosgriff, et al., 1960.

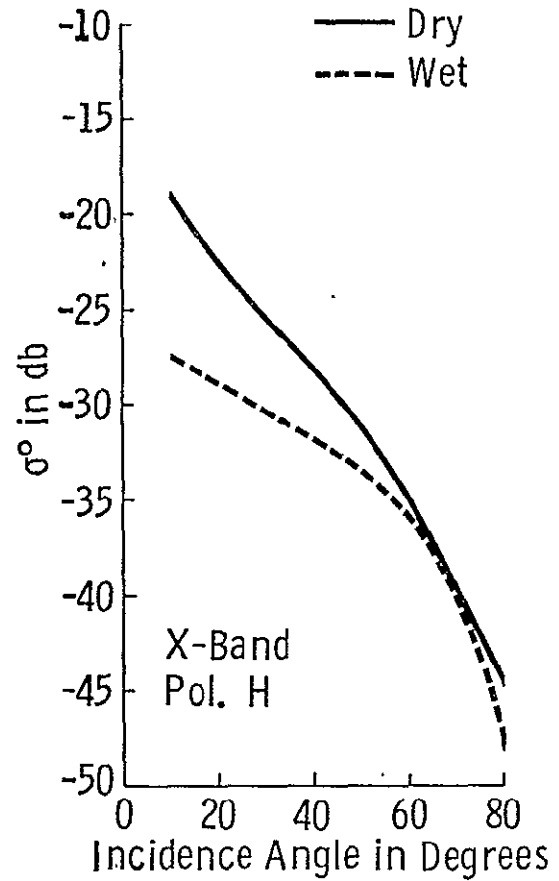


Figure 4.11b. Effect of spraying water on asphalt road. After Cosgriff, et al., 1960.

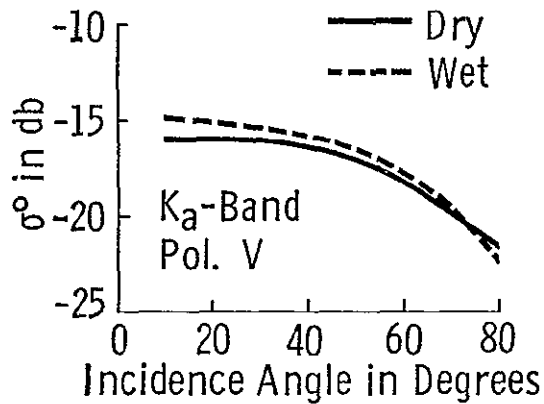


Figure 4.11c. Effects of light rain on 3' alfalfa and grass. After Cosgriff, et al., 1960.

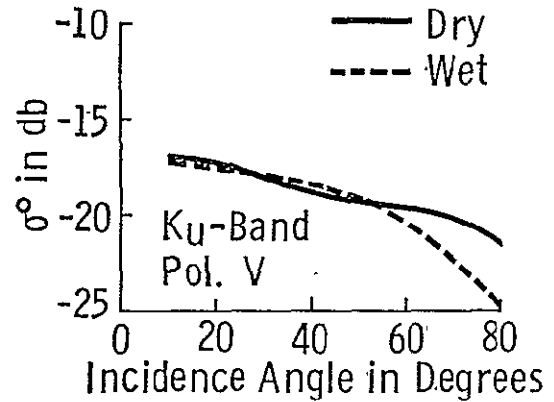


Figure 4.11d. Effect of light rain on 3' alfalfa and grass. After Cosgriff, et al., 1960.

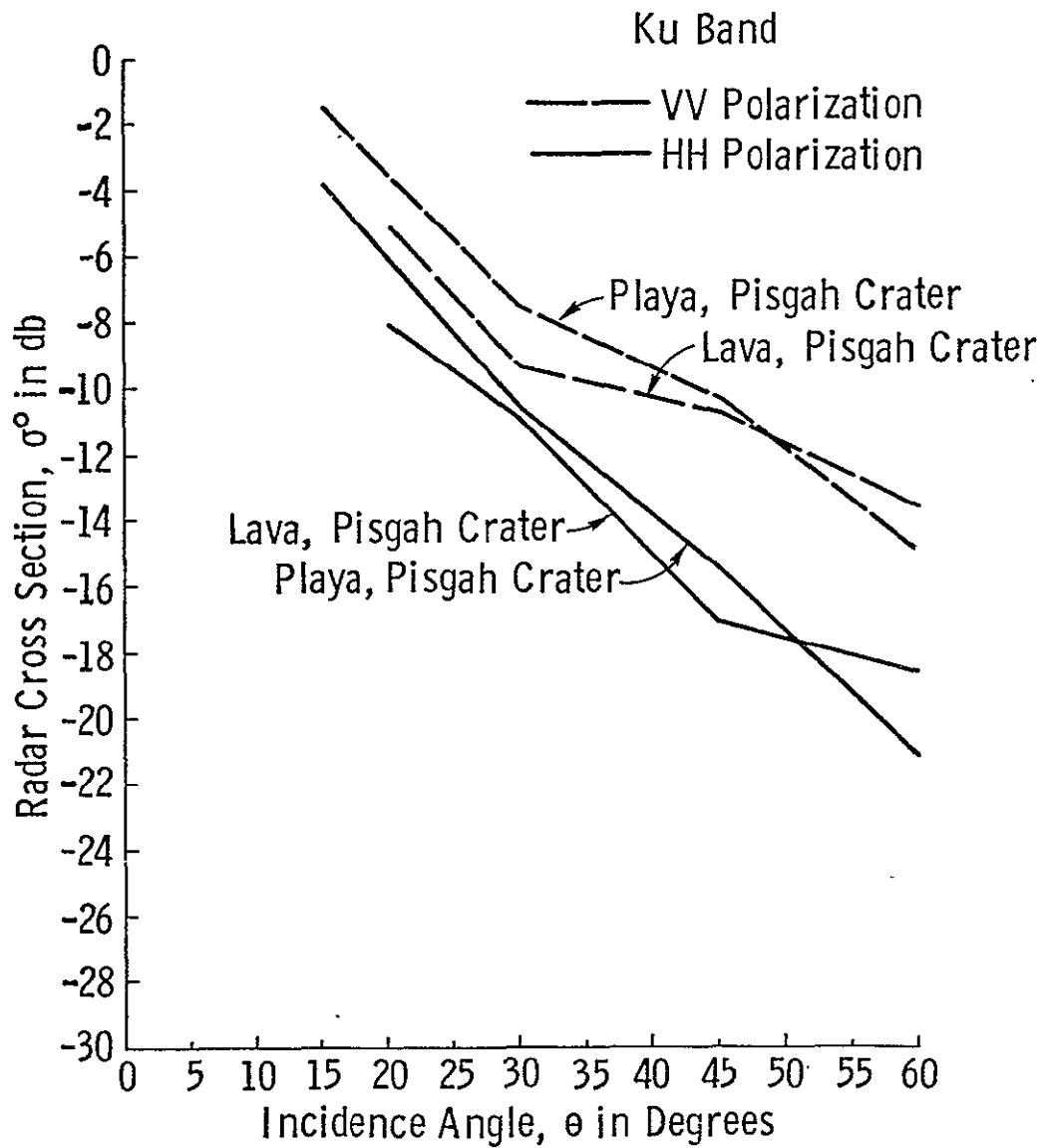


Figure 4.12. Backscatter coefficient of various volcanic soils. After Shultz, et al., 1969.

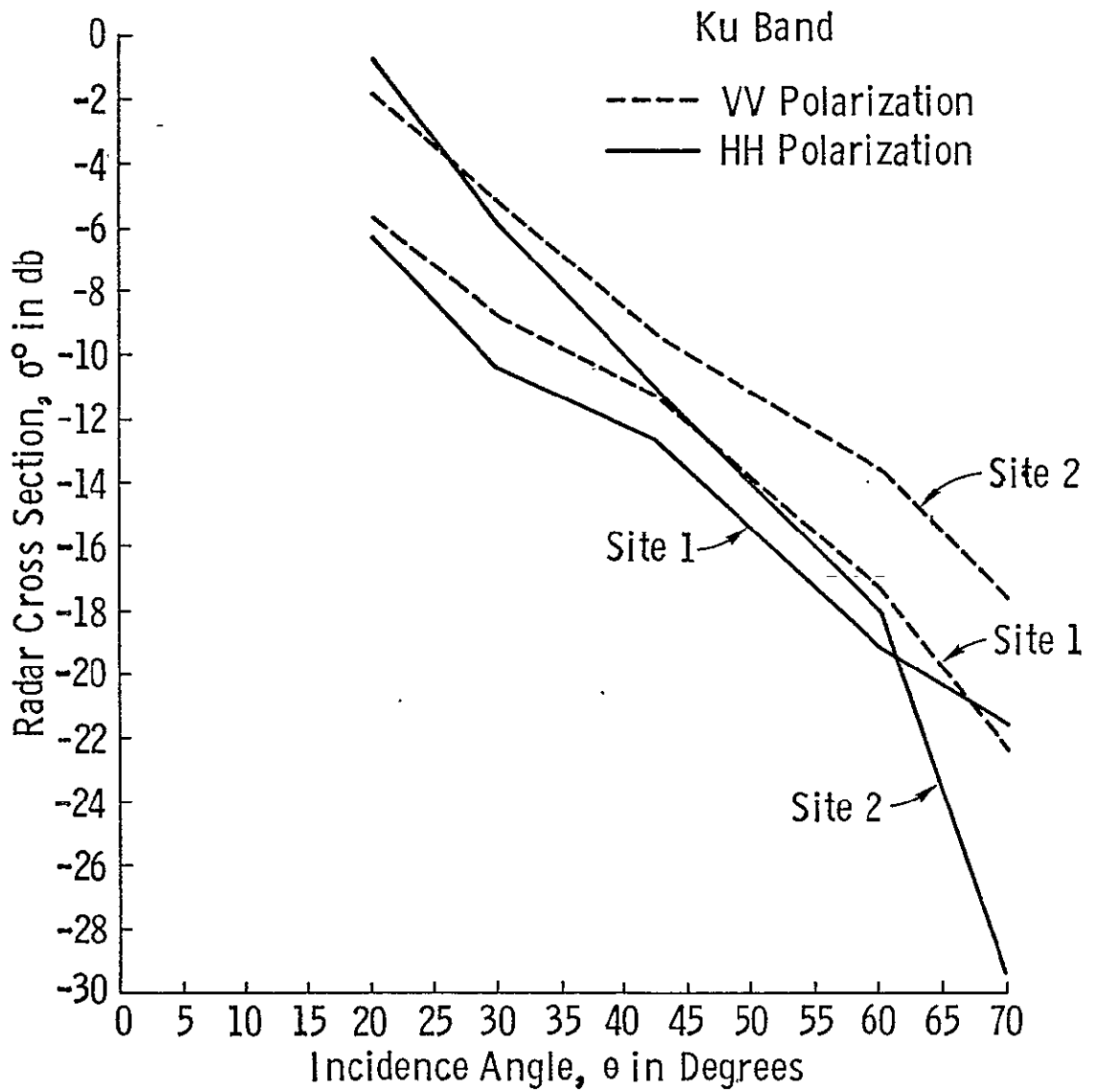


Figure 4.13. Backscatter of limestone quarry surfaces. After Shultz, et al., 1969.

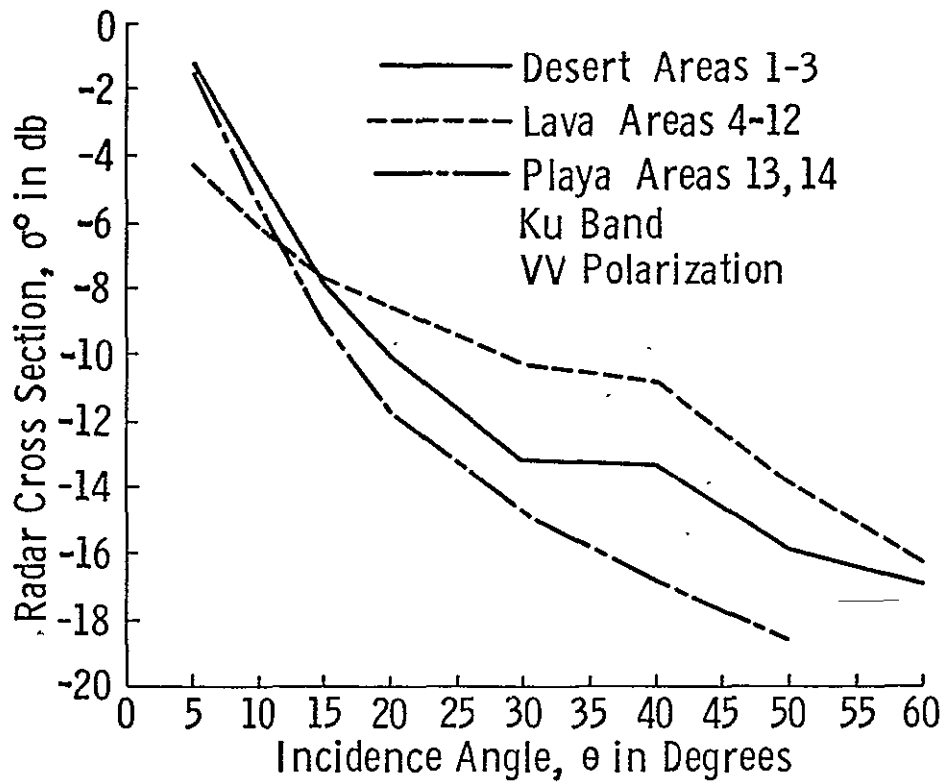


Figure 4.14. Radar cross-section of Pisgah Crater. After Masenthin, 1967.

The areas flown also included the regions flown observed by Ohio State, and except for a bias, the playa data showed the same result.

The experiment conducted off Point Barrow, Alaska, was to measure the radar response of different formations of sea-ice. Rouse [1969] first analyzed the data and found that the ice-types could be broken up into five categories. The identification of the ice-types was made by the help of aerial photographs taken simultaneously over the target site. Parashar [1974], in an exhaustive analysis of similar data collected in 1970, expanded the number of categories to seven. The backscatter from the different ice types is shown in Figure 4.15.

The third experiment with this same system was conducted over an agricultural site in Garden City, Kansas. The region is flat, sometimes farmed by irrigation and the crops grown include alfalfa, corn, grain sorghum, sugar beets, and wheat. The distinction among the various crop types was not marked. Figures 4.16 a-f illustrate the spread of backscatter data at the various angles. Each dot represents the mean value of a field and the bar is the mean value of all fields within a crop type. A recent study [Dickey et al, 1974] showed that the backscatter response was sensitive to the presence of irrigation water at angles within  $45^{\circ}$  of nadir. This study has been further substantiated by a more recent and thorough study reported by Ulaby et al [1974] on the effect of soil water content on the radar cross section. Another scatterometer operating at 400 MHz was also flown over the sea-ice and agricultural farmland experiment sites. The results over farmland are not yet conclusive; the result over sea-ice as reported by Parashar [1974] shows that at this wavelength first-year ice (1 to 3 feet thick) gave the strongest return and that open water could be differentiated.

No seasonal measurements were made, the seasonal behaviour of the response from various crop conditions therefore could not be established.

#### 4.2.5 University of Kansas Measurements

The only measurement program that has attempted to record the backscatter response of targets over one octave has been conducted at the University of Kansas. These experiments have evolved through many stages and the system used is currently called the Microwave Active Spectrometer (MAS). The basic concept of the system hardware has remained the same, but the sophistication and capability of the system has been greatly increased through metamorphic changes in system design. The measuring system is a 4-8 GHz (now extended to 1-18 GHz) radar spectrometer that operates as an FM-CW radar over regular frequency intervals. It is currently mounted on the boom of a truck with

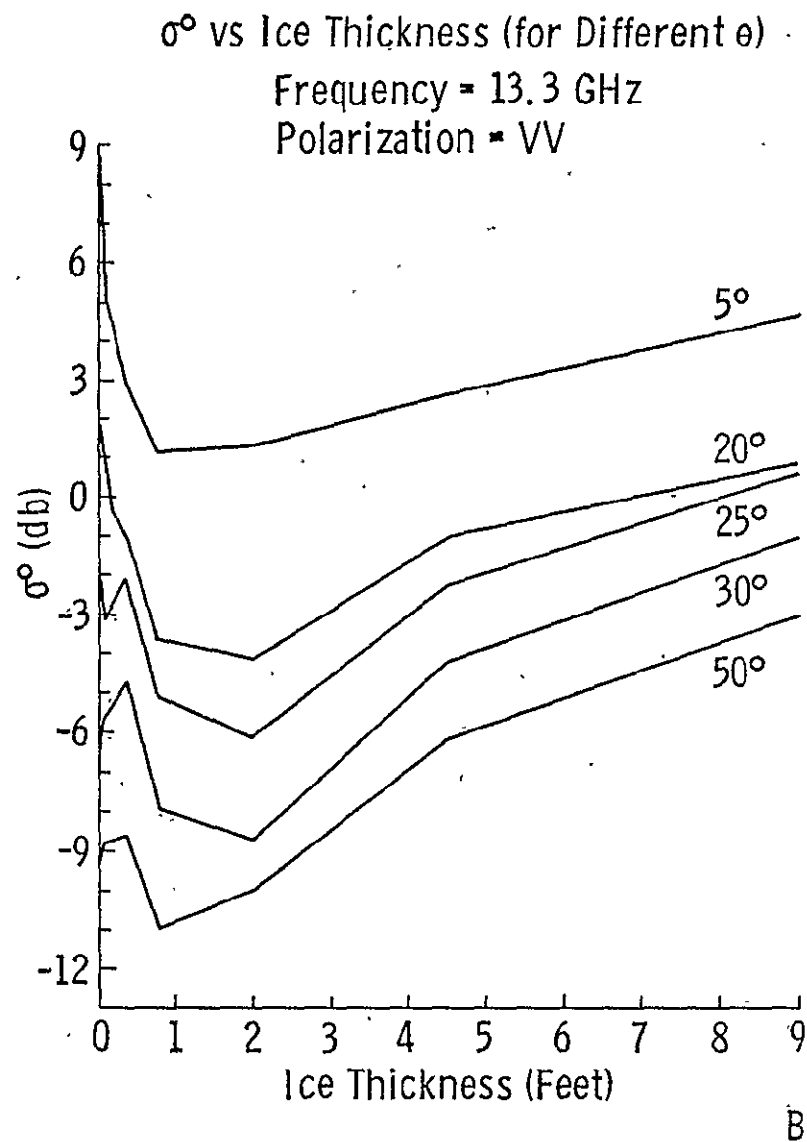
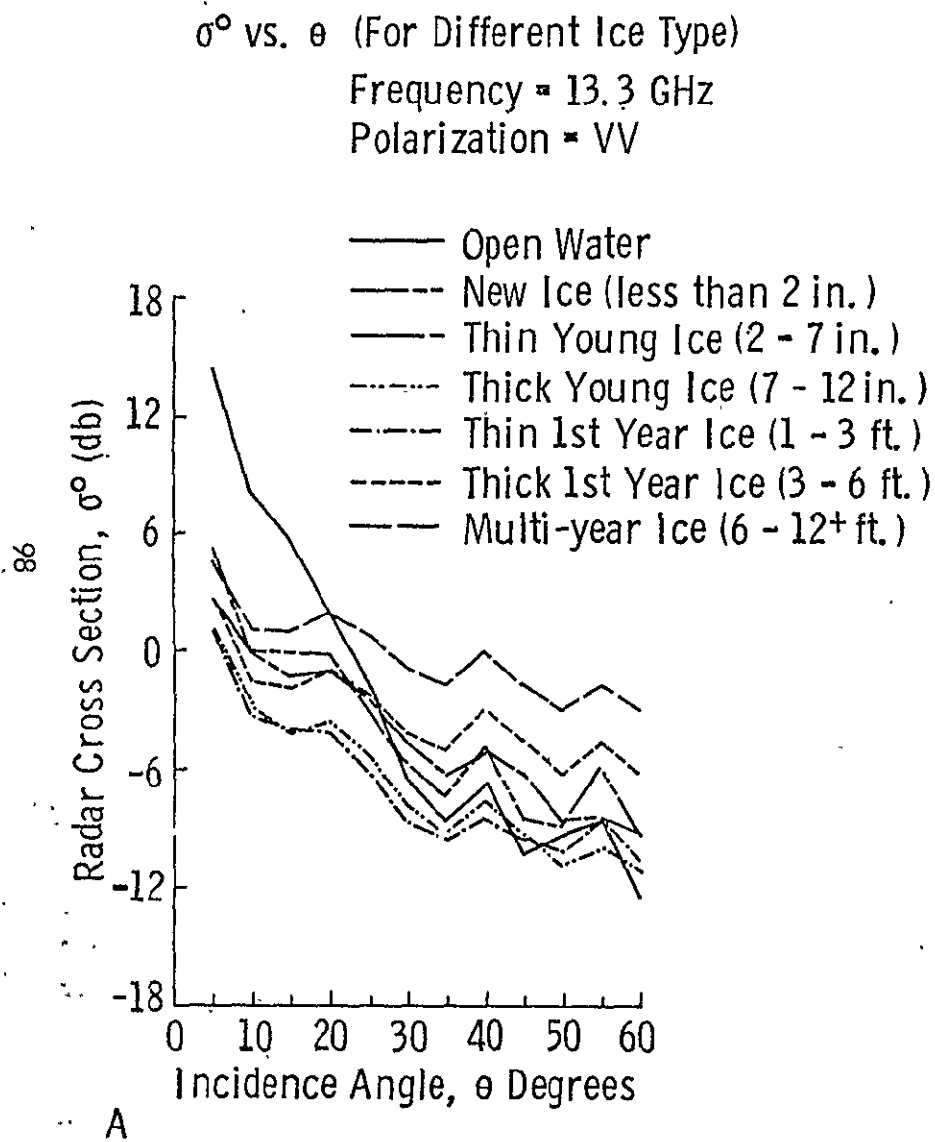


Figure 4.15. Scattering coefficient for sea ice off Point Barrow, Alaska. After Parashar, 1974.

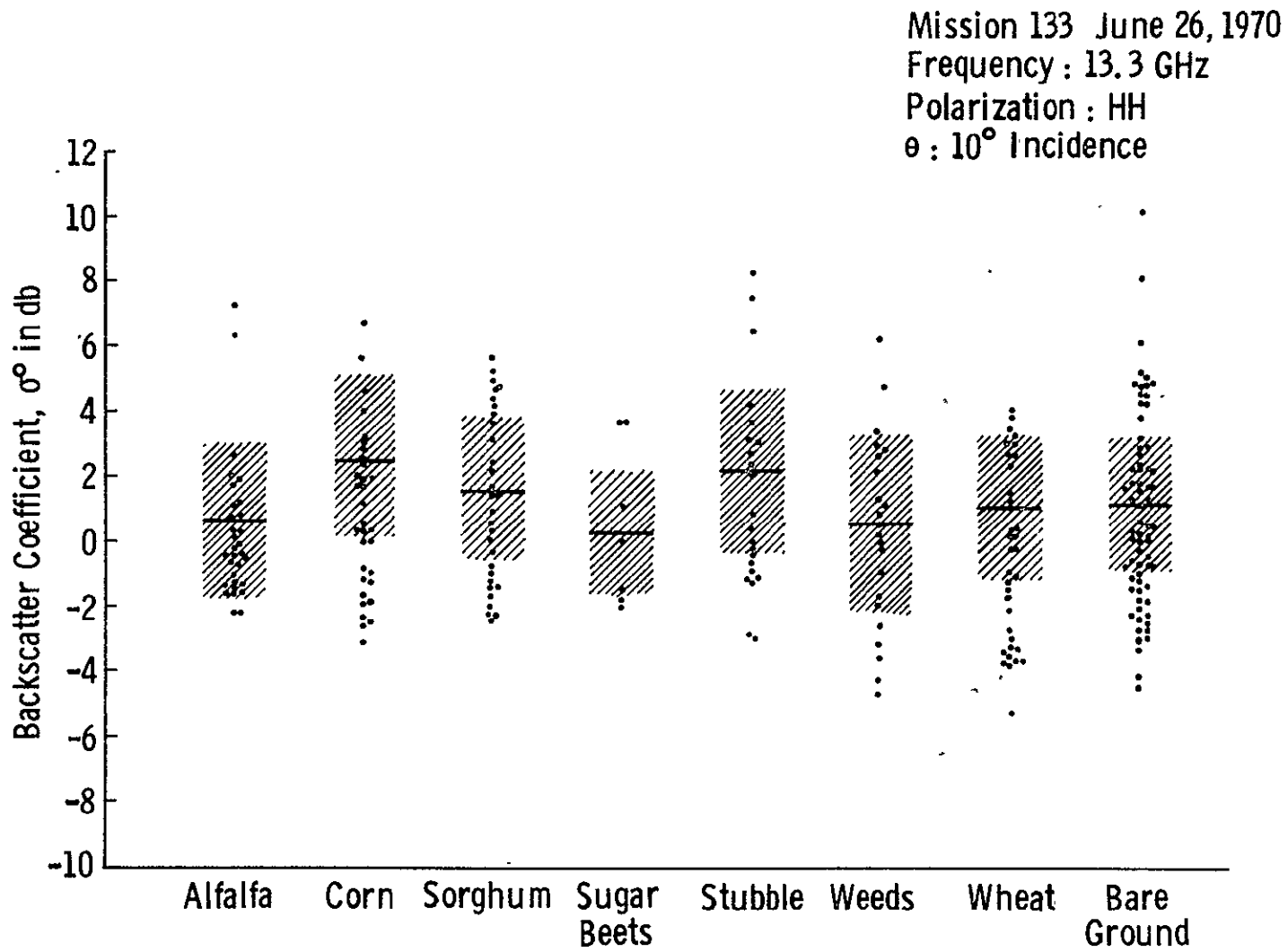


Figure 4.16a. Distribution of mean scattering coefficient of agricultural fields. From King and Moore, 1974.

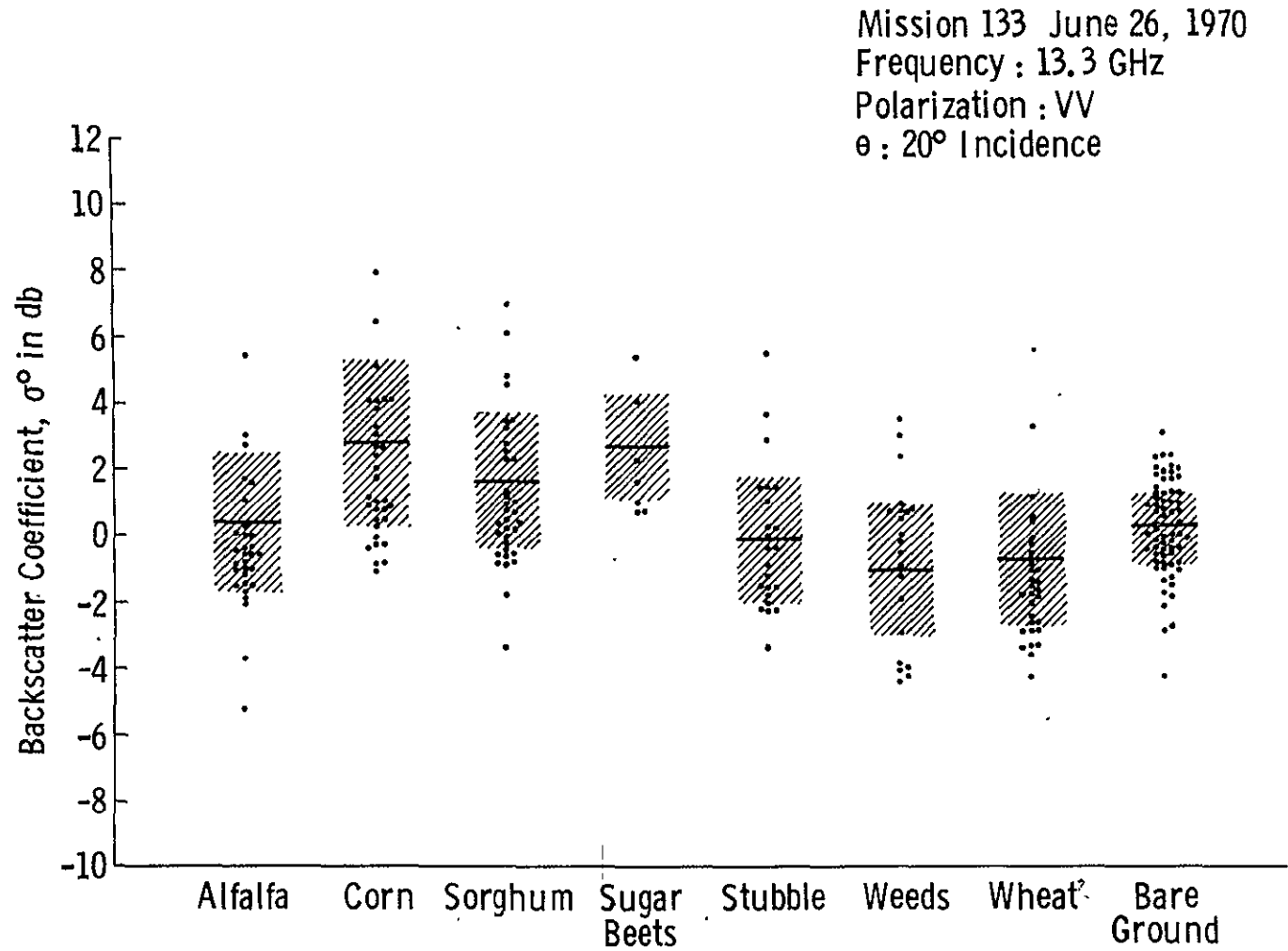


Figure 4.16b. Distribution of mean scattering coefficients of agricultural fields. From King and Moore, 1974.

REPRODUCIBILITY OF THE  
 ORIGINAL PAGE IS POOR

Mission 133 June 26, 1970  
Frequency : 13.3 GHz  
Polarization : VV  
 $\theta$  : 30° Incidence

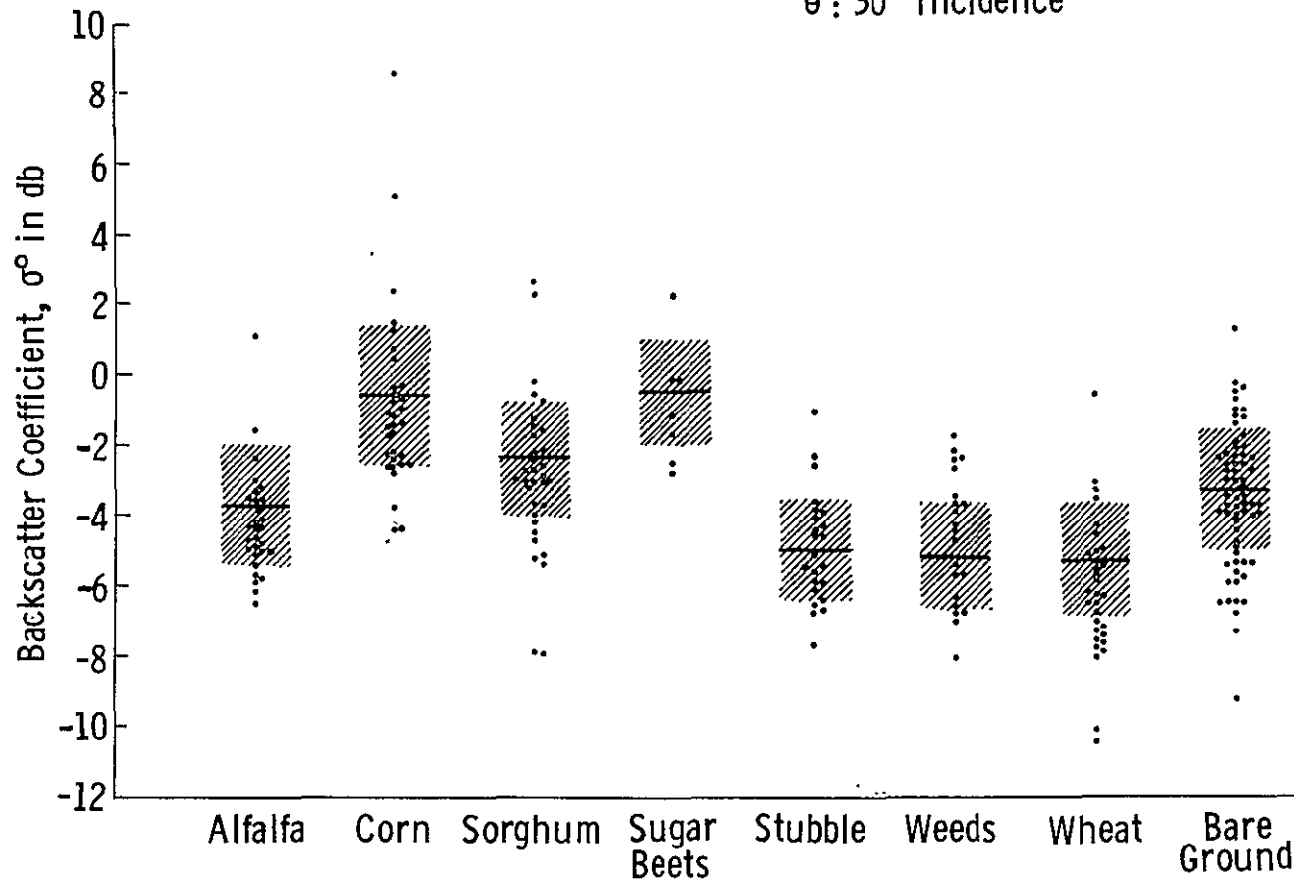


Figure 4.16c. Distribution of mean scattering coefficients of agricultural fields. From King and Moore, 1974.

Mission 133 June 26, 1970  
Frequency : 13.3 GHz  
Polarization : VV  
 $\theta$  : 40° Incidence

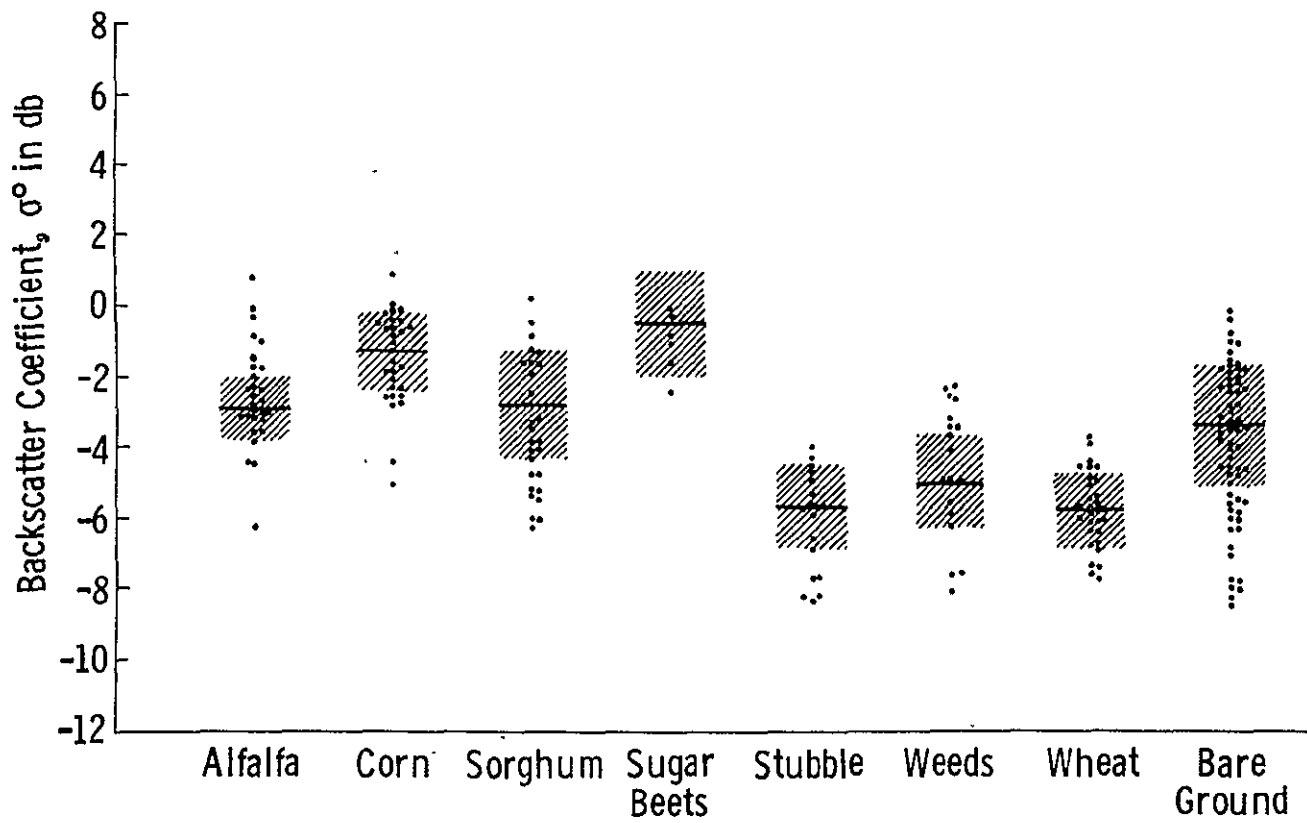


Figure 4.16d. Distribution of mean scattering coefficient of agricultural fields. From King and Moore, 1974.

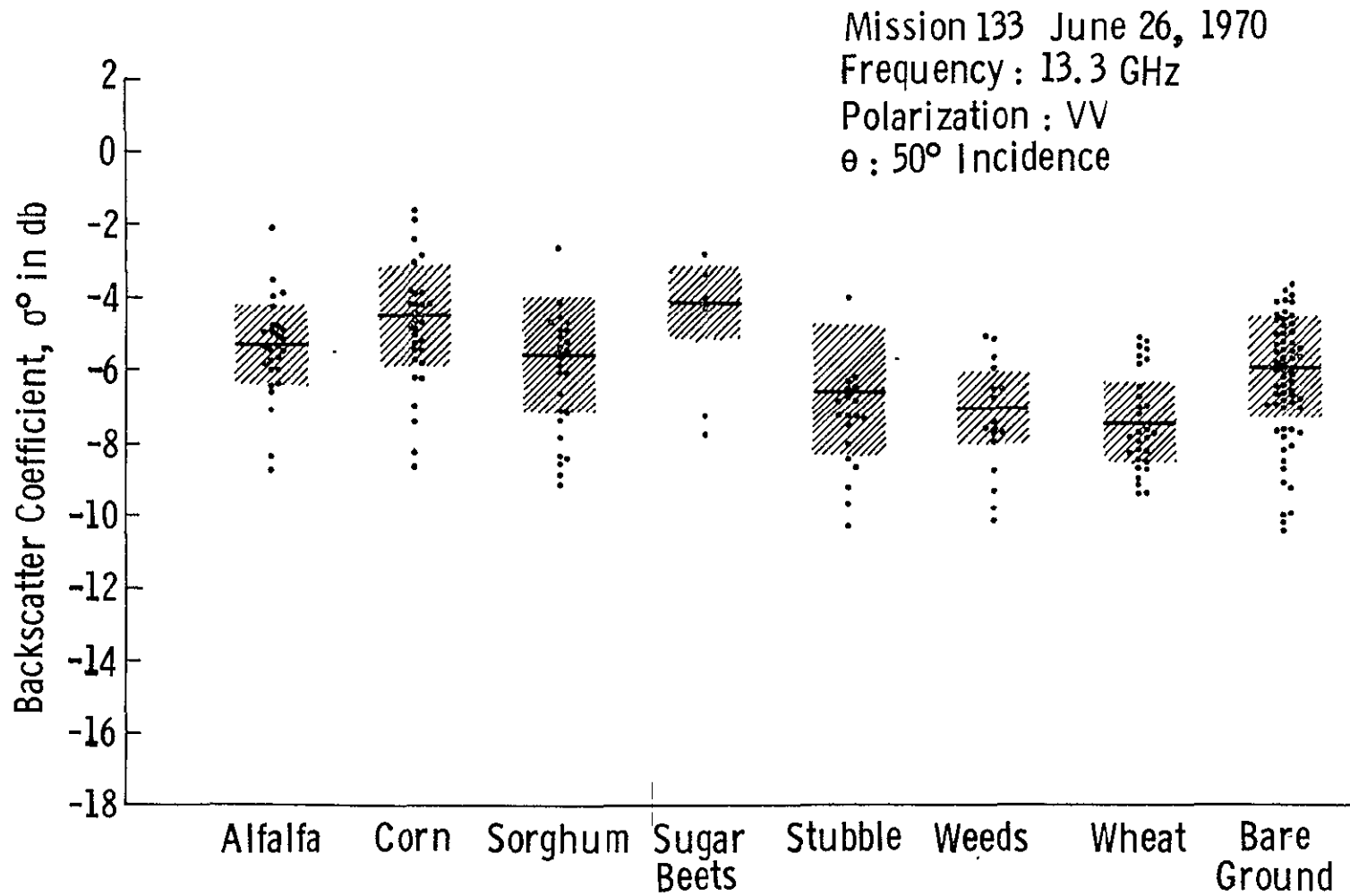


Figure 4.16e. Distribution of mean scattering coefficient of agricultural fields. From King and Moore, 1974.

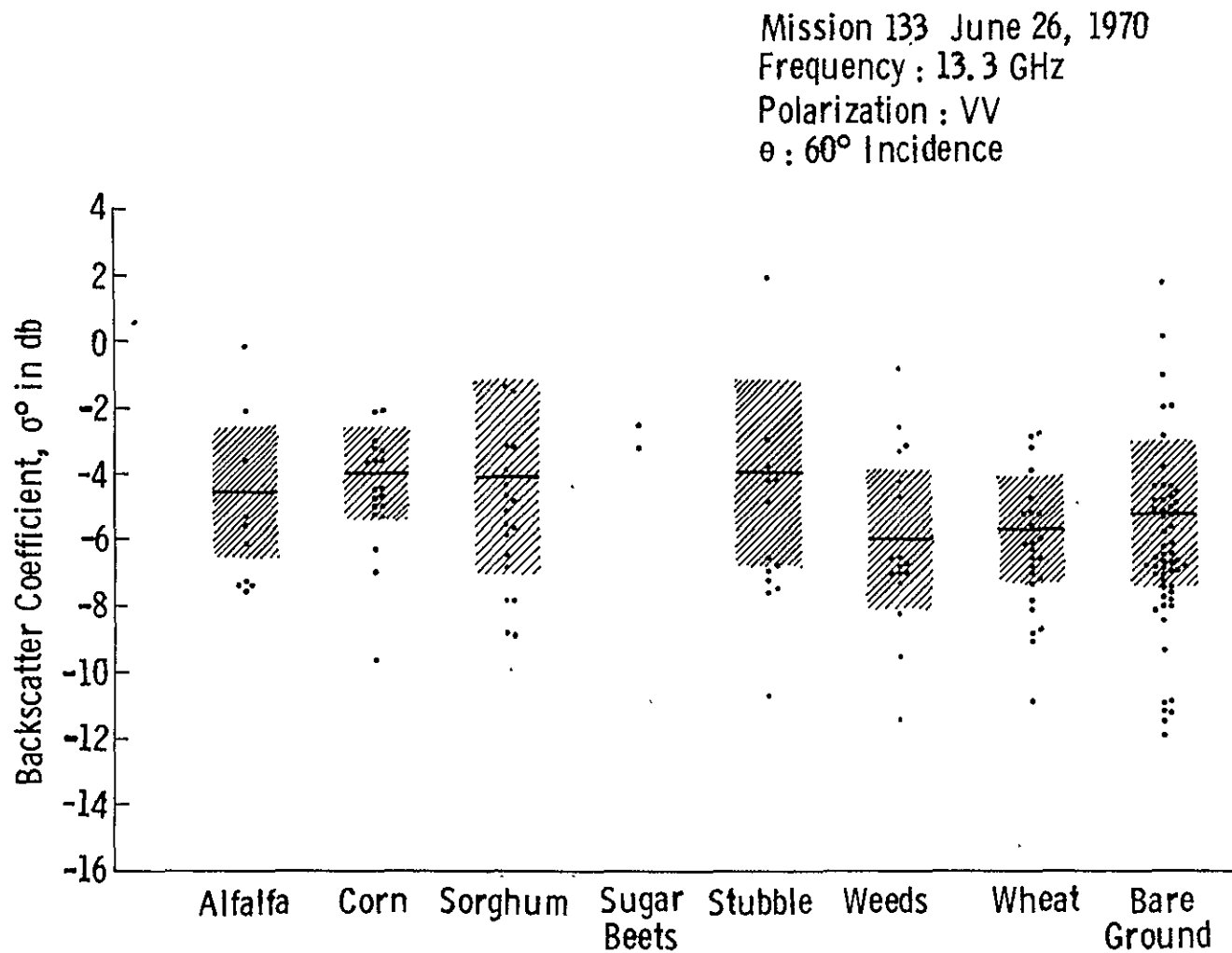


Figure 4.16f. Distribution of mean scattering coefficient of agricultural fields. From King and Moore, 1974.

the associated control hardware included in the van. It has, during an earlier stage of its development also been mounted on a roof-top. The first measurements conducted [Waite, 1970] with a short-pulse version of this system were to measure the spectral response of various targets at a fixed angle. The targets measured were grass, buildings, a car and trees. The normalized spectral response of some of these targets is shown in Figure 4-17. The system could also produce an image like a B-scan on a CRT and pseudo-images of targets were produced for a monochromatic and a frequency averaging mode.

During the next stage of evolution, which included some necessary calibration, the system was mounted exclusively on the boom of a truck and used to measure the backscatter from agricultural terrain in various stages of cultivation. These data are reported by Moe [1974], Ulaby et al [1972]. An example of the data collected from 83 fields with 4 crop types, measured at 10 frequency points at  $30^\circ$  incidence for vertical and horizontal polarization is shown in Figures 4.18 a, b. The data have been normalized so that corn is at 0 dB across the frequency spectrum. The system, however, suffered from calibration and hardware problems.

The radar was then mounted atop a 75-ft. truck-mounted boom. Two antennas (one transmit and one receive) were aligned so that they had maximum overlap on their main beams over 4-8 GHz. The FM-CW radar could be exercised in any of the four transmit-receive polarization pairs and could view a target from nadir to  $70^\circ$  off nadir. The radar return was averaged over 400 MHz, but to reduce signal variability due to fading, the 4-8 GHz spectrum data was reduced to three 1.2 GHz-wide bands with central frequencies: 4.7 GHz, 5.9 GHz and 7.1 GHz. The calibration was performed with a delay line as well as a Luneberg Lens. Since then, further modifications have been made. The system is now composed of two hardware assemblies, one capable of operating from 1-8 GHz, and the other from 8-18 GHz.

The targets measured have been exclusively natural terrain, with emphasis on soil and vegetation. Detailed analysis of this vast accumulation of data is still continuing. Figures 4.19a-d show some examples of the return [Ulaby, 1974]. Perhaps, the most significant accomplishment of this program, other than the collection of valuable radar-backscatter data, has been the establishment of the effect of soil water content to the radar backscatter. Since the effective depth of penetration of a radar signal into the subsurface is only about one skin-depth, the backscatter was correlated with the moisture in a skin depth as characterized by the attenuation coefficient (reciprocal of the skin depth). The measurements show an approximately

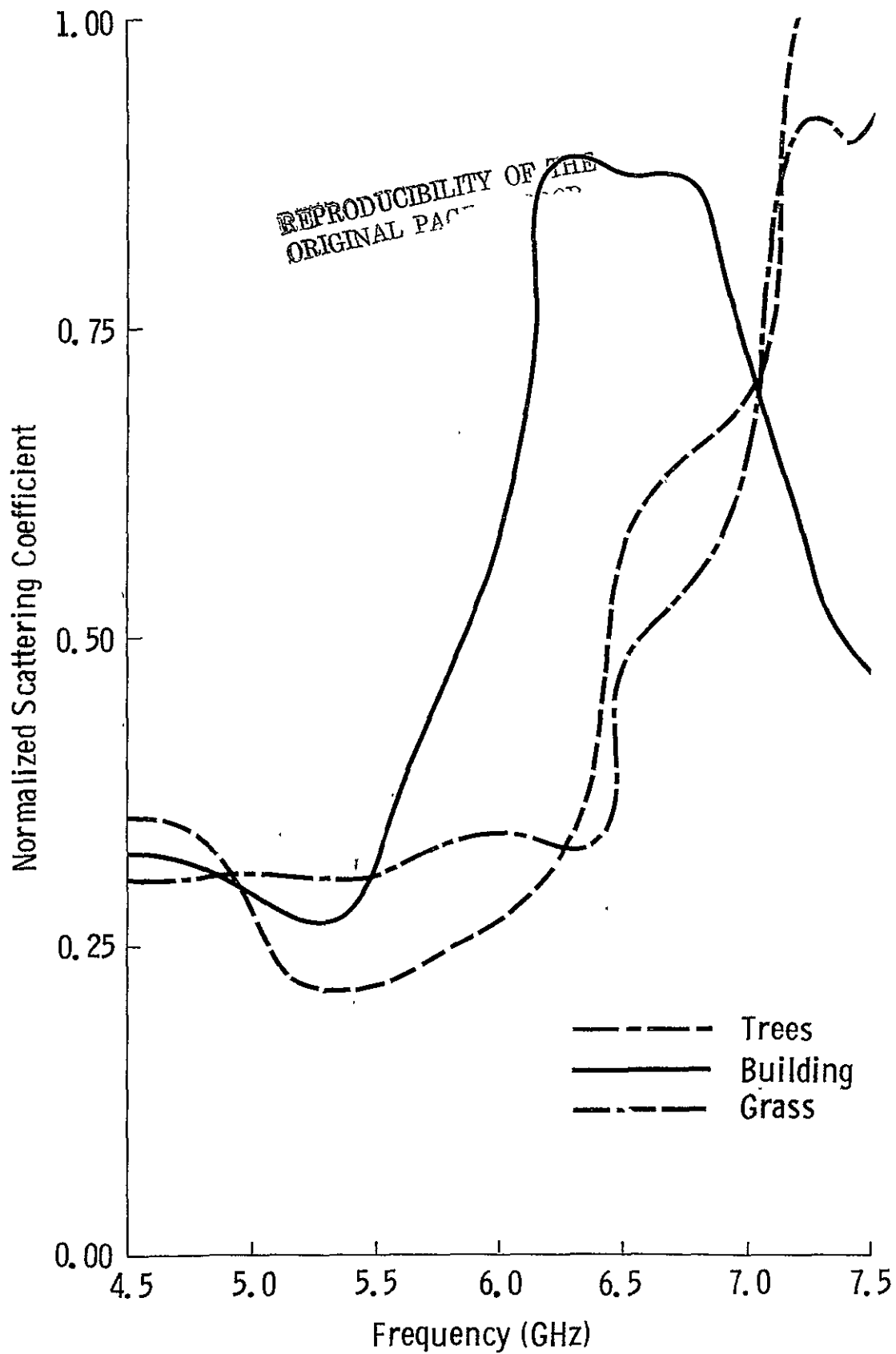
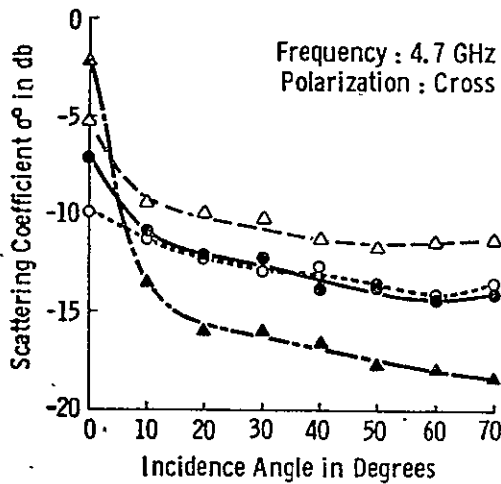
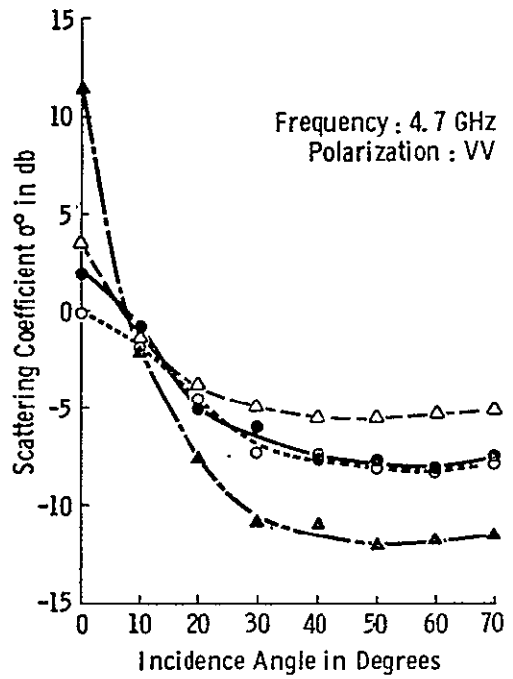
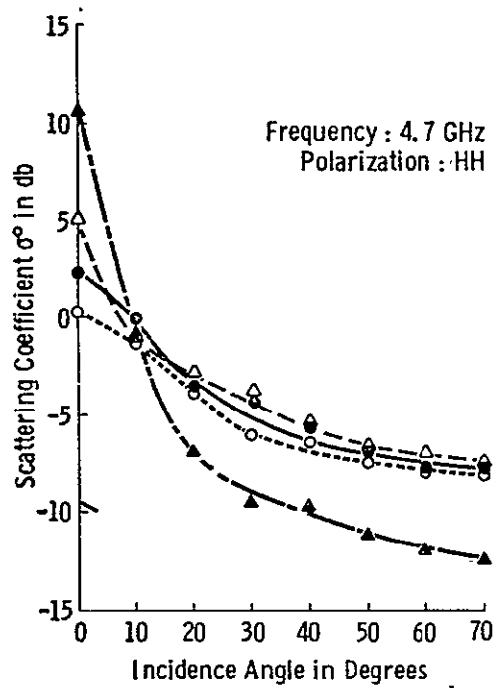
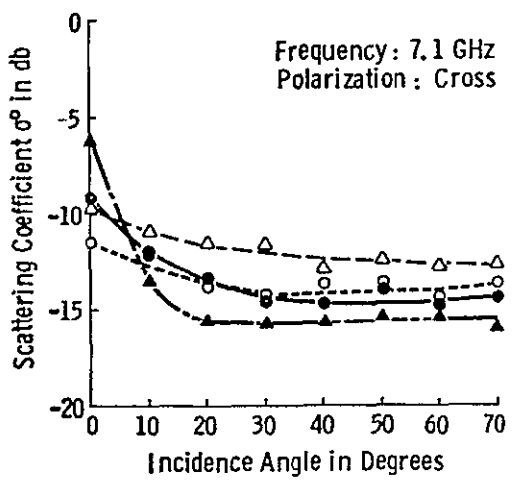
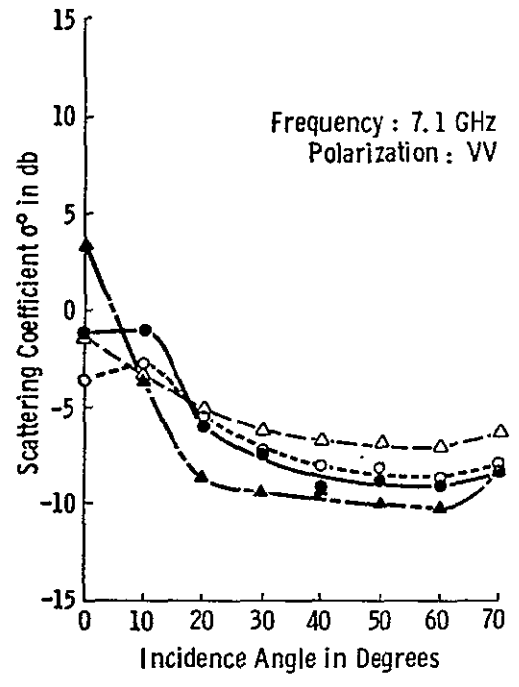
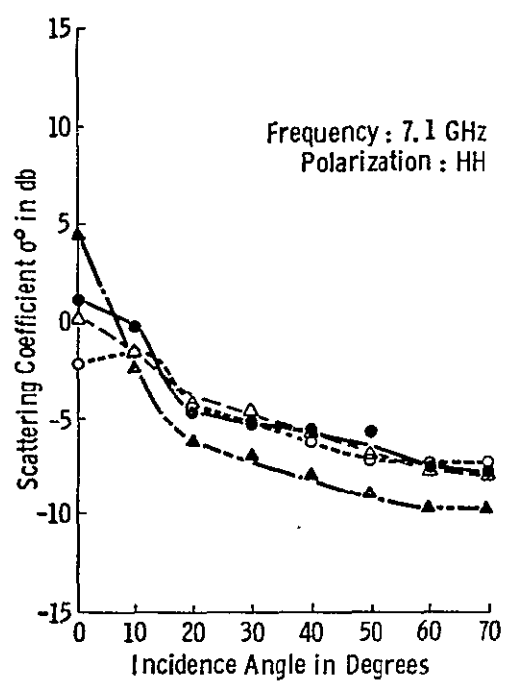


Figure 4.17. Normalized spectral response curves. From Waite, 1970.



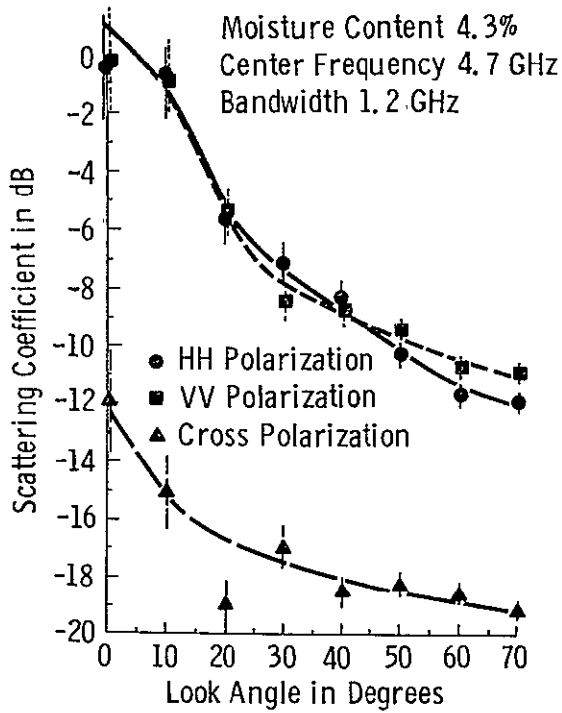
Crop Type	Corn	Milo	Soybeans	Alfalfa
Crop Height in Meters	2.4	1.0	1.0	0.5
Average Soil Moisture	10.6%	8.2%	8.1%	10.5%
Designation	---○---	—●—	---△---	—▲—

FIGURE 4.18A. SCATTERING COEFFICIENT RESPONSE AT 4.7 GHz FOR FOUR CROP TYPES. SOIL MOISTURE CONDITION IS LOW. FROM ULABY 1975.

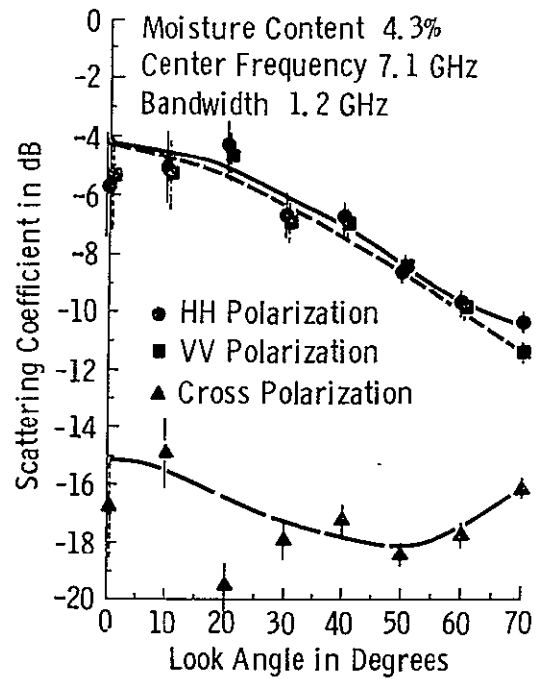


Crop Type	Corn	Milo	Soybeans	Alfalfa
Crop Height in Meters	2.4	1.0	1.0	0.5
Average Soil Moisture	10.6%	8.2%	8.1%	10.5%
Designation	---○---	—●—	---△---	—▲—

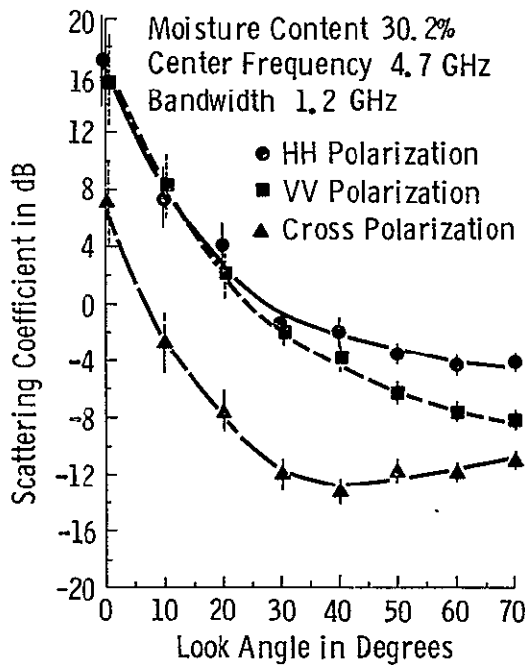
FIGURE 4.18B. SCATTERING COEFFICIENT RESPONSE AT 7.1 GHz FOR FOUR CROP TYPES. SOIL MOISTURE CONDITION IS LOW. FROM ULABY 1975.



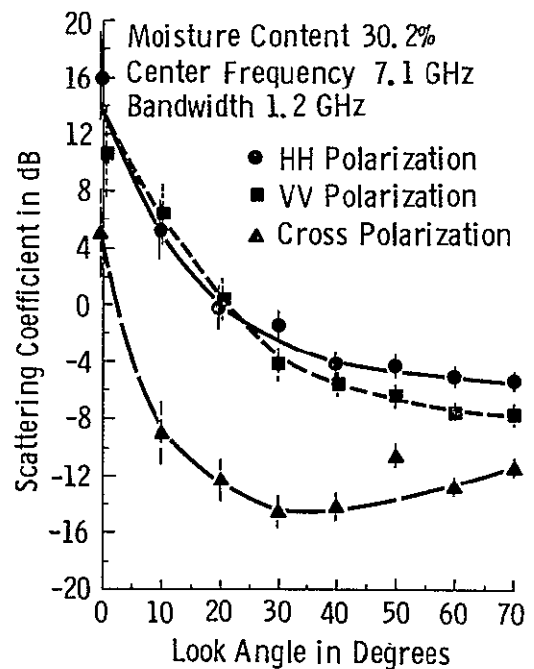
5a



5b



5c



5d

Figure 4.19. Scattering coefficient as a function of look angle. Soil type = Pawnee clay loam, rms surface height = 2.5 cm. (a) 4.7 GHz, 4.3 percent moisture. (b) 7.1 GHz, 4.3 percent moisture. (c) 4.7 GHz, 30.2 percent moisture. (d) 7.1 GHz, 30.2 percent moisture. From Ulaby, 1974.

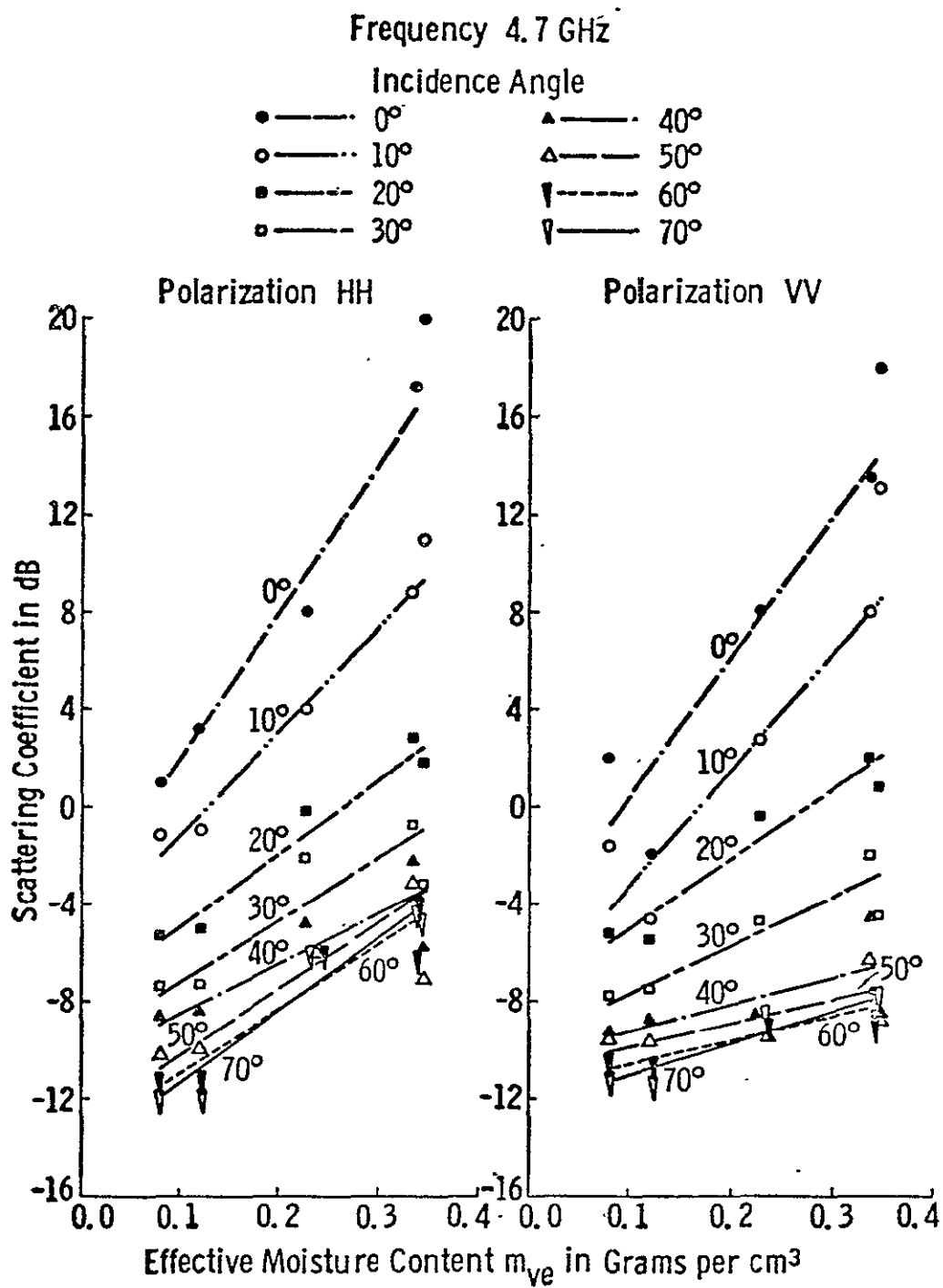


FIGURE 4.20A. SCATTERING COEFFICIENT AS A FUNCTION OF EFFECTIVE MOISTURE CONTENT. FREQUENCY IS 4.7 GHz. FROM ULABY ET AL., 1974.

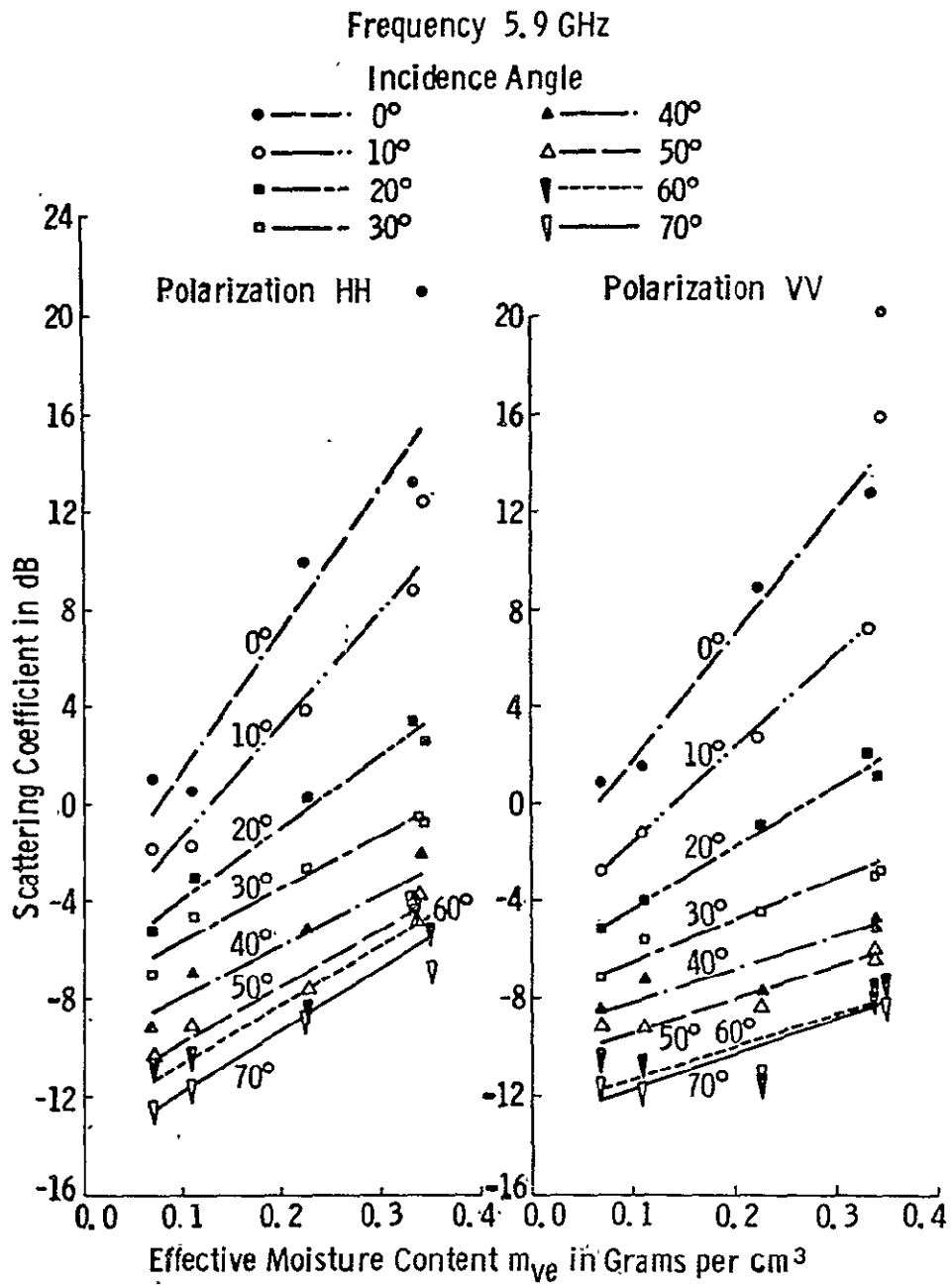


FIGURE 4.20B. SCATTERING COEFFICIENT AS A FUNCTION OF EFFECTIVE MOISTURE CONTENT. FREQUENCY IS 5.9 GHz. FROM ULABY ET AL., 1974.

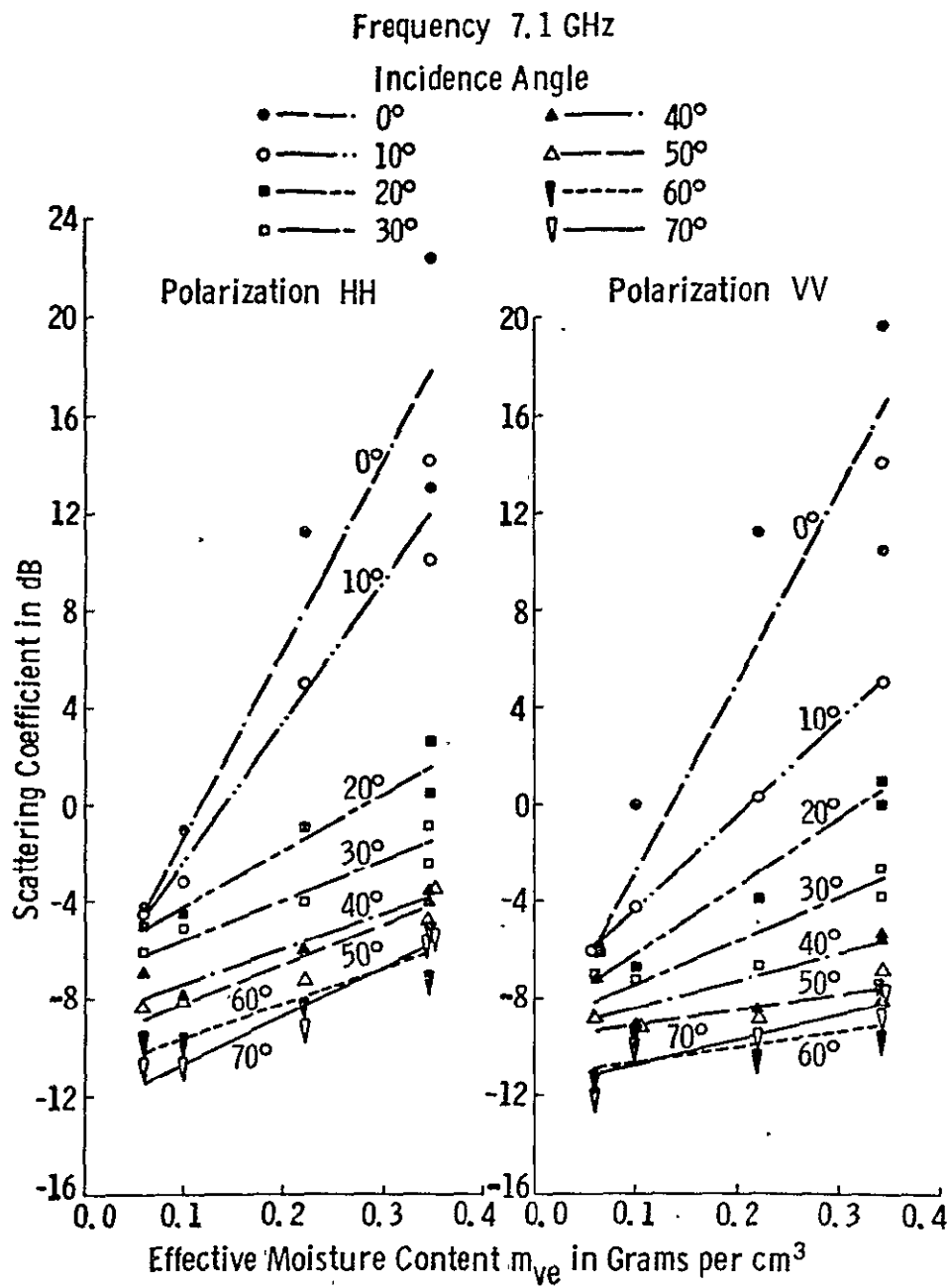


FIGURE 4.20C. SCATTERING COEFFICIENT AS A FUNCTION OF EFFECTIVE MOISTURE CONTENT. FREQUENCY IS 7.1 GHz. FROM ULABY ET AL., 1974.

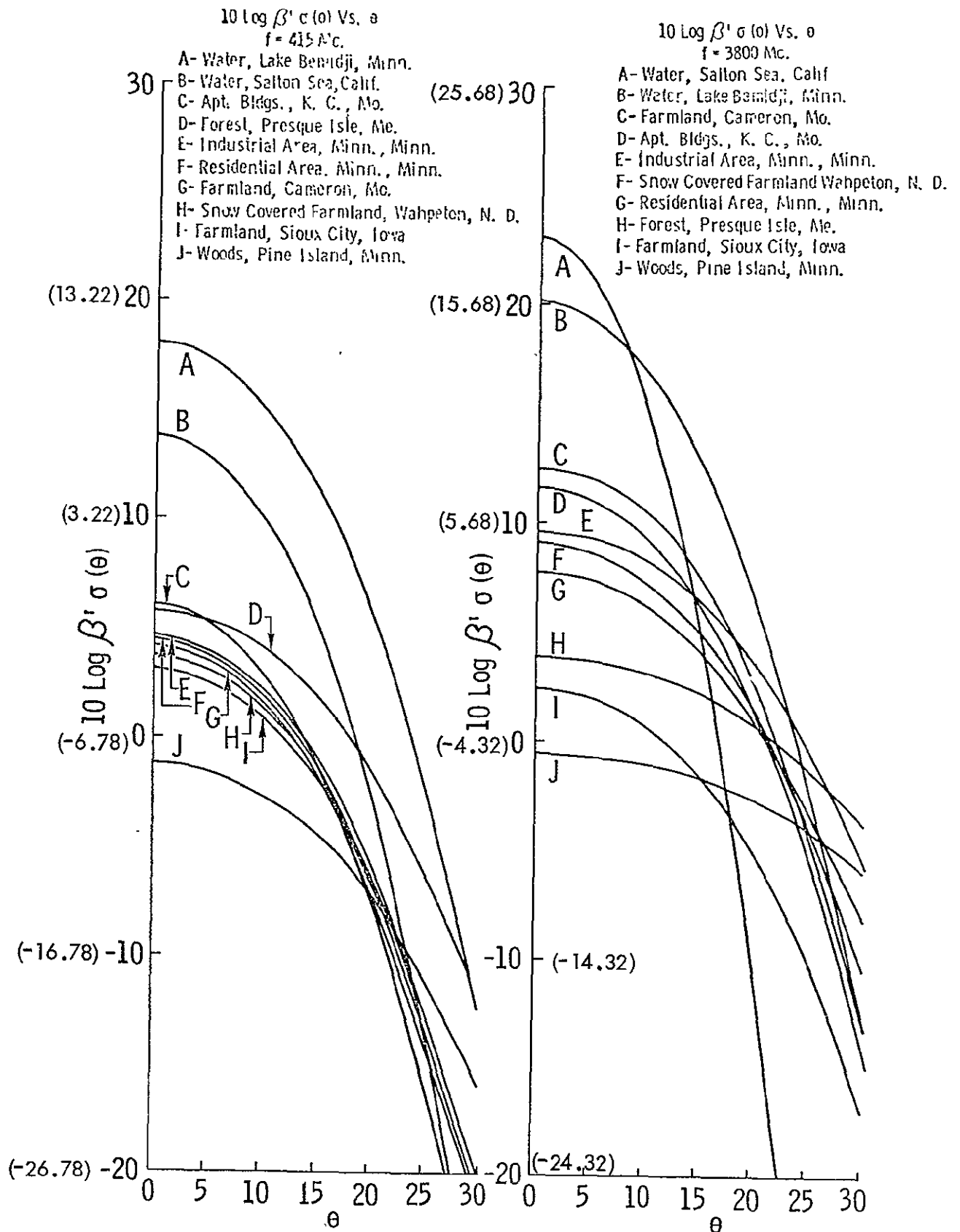


Figure 4.21. Relative plots of  $\sigma^\circ$  vs.  $\theta$  for various terrain types. After Janza, et al., 1959. Note values in parentheses correspond to  $10 \log \sigma^\circ$ .

linear increase in scattering with attenuation coefficient of the soil at angles within  $10^\circ$  of vertical and all frequencies. Figures 4.20 a-c (from Ulaby et al) show the scattering cross section as a function of the moisture profile of their target soils for the top 5 cms.

#### 4.2.6 Sandia Corporation Measurements

An experimental program to investigate the reradiation properties of terrain at near-vertical incidence was carried out by Sandia Corporation using two radars operating at 415 mcs and 3800 mcs [Edison et al, 1959], [Janza et al, 1959], and [Edison et al, 1960]. These radars were flown aboard a C-47 aircraft along with cameras and calibration gear [Janza and West, 1955] to measure the response over selected sites. The target sites selected included forested areas in Minnesota, farms near Cameron, Missouri, industrial areas in Minneapolis, desert areas near Salton Sea, California, residential areas in Kansas City, water bodies (lakes) with different roughness profiles and many more. They found that the reradiation pattern drops off rapidly with angle of incidence from the vertical for most targets. At 450 mcs, heavily wooded areas appeared as nearly isotropic scatterers. The measurements conducted over the various sites suggested that even at near vertical incidence most terrain reradiates toward the receiver a large scattered (incoherent) signal and a small specular (coherent) signal. The fading characteristics of the radar return were also analyzed. It was found that the fading range (defined as the range between the level below which only 5 percent of the power was found and the level below which 95 percent is found) varied from about 3 dB for smooth water exhibiting principally a specular return to about 19 dB for certain non-homogeneous targets. The range of incidence angles was from 0 to  $20^\circ$  off nadir. Figure 4.21 [Janza et al, 1959] shows a comparison of the backscattering response from various targets viewed. The scale along the ordinate is given in their work as  $(10 \log \beta' \sigma(\theta))$ . The value of  $\beta'$  for 415 MHz is given as 0.21 and for 3800 MHz as 0.37, therefore, conversion to the usual form of presentation of the backscatter response ( $\sigma^\circ$  vs  $\theta$ , with  $\sigma^\circ$  expressed in dB) requires that the ordinates of the two plots be rescaled. A constant subtraction of 6.777 dB from the ordinate values for 415 MHz and a subtraction of 4.318 dB from the ordinate values for 3800 MHz will reduce this plot to the more familiar form of a backscattering response curve.

A compilation of Sandia Corporation's measurement results at 415 MHz, containing graphs of the measured backscatter of each target type and in some cases a comparison with their theoretical expectation of the backscatter is presented by Edison et al [1960] in a University of New Mexico Technical Report. Descriptions of the targets are provided by geographic (spatial) location and a sentence describing the terrain. For example, a description for a response presented could read, "The target area was very flat and densely covered with pine, hemlock, birch, white ash and elm trees from 20 to 40 feet in height." The ground truth was by photographs and by manual observation (from the ground and from aircraft). Except for the fact that the range of incidence angles is limited to within  $20^\circ$  off nadir (although their extrapolation generally runs to  $30^\circ$ ), Sandia Corporation's measured program is one of the few carefully controlled experiments on radar backscatter.

#### 4.2.7 Other Measurement Programs

In keeping with the purpose of this brief treatise, which is to inform the reader of other measurement programs and not provide detailed accounts of all programs (which would make this effort prohibitively copious), the other measurement programs will only be enumerated. Where appropriate, a perfunctory account of their uniqueness will be made.

Under the auspices of NASA, a Westinghouse APQ-97 imaging radar system was flown over Garden City, Kansas. The data were analyzed at the University of Kansas [Simonett et al, 1967]. The imaging radar was a 35 GHz, real-aperture system which had a range of incidence angles from  $50^\circ$  to  $67^\circ$ . Data were collected at different times in the crop-growing season; the backscatter measurements conducted late in the season showed a much greater crop contrast.

The U. S. Army Engineer Waterways Experiment Station in Vicksburg, Mississippi, operated a four frequency system mounted on a 50-foot radius wooden arch. The antennas traveled along tracks mounted inside the arch and viewed a target at the center of the arch over an angular range of  $210^\circ$ . The system frequencies were 297 MHz (P-band), 5879 MHz (E-band), 9375 MHz (X-band) and 35,543 MHz (Ka-band). The purpose has been to determine the amount of penetration into soil and the effect of moisture content on backscattered return [Lundien, 1966]. The measurements were conducted on specially-prepared samples. Very few natural targets were measured.

The Swedish Research Institute of National Defense has an X-band search radar mounted on a tower [Linell, 1966] [Eklund, 1969]. This program is coordinated with an aircraft program [Erickson, 1966]. The emphasis is to study the level and amplitude distortion of backscattered signals at low grazing angles.

DeLoor [1972] has reported on some measurements conducted by the Physics Laboratory of National Defence in the Netherlands. An X-band and a Ka-band radar mounted on a television tower view agricultural sites near grazing angles, providing the backscatter from vegetation types through a complete growing season. Effects of local rainfall and varying wind speeds were also investigated.

King [1970] has reported on some experimental measurements conducted by the Aerospace Corporation in the 40-90 GHz range for terrain samples in a wet and dry condition. The samples included asphalt, concrete, gravel, wood, sod, tall weeds, and smooth and rough water. The antennas were mounted on a tower and the target placed at the foot of the tower.

Brown [1969], at the Jet Propulsion Laboratory of California Institute of Technology, reported on experiments conducted on aircraft and rockets over the Tularosa Basin in New Mexico in an effort to simulate the return from the moon.

#### 4.3 Comparison of Backscatter Cross-Section

As mentioned earlier, due to the variability in absolute values between measurements from different programs, some normalizing scheme must be applied to compare data from different programs. A truly normalizing scheme has not yet been established. Comparisons of land backscatter cross sections from the various programs have been made by King and Moore [1974]. They have chosen only data near the Skylab frequency. Rather than reproduce the numerous figures used to display the comparison, the reader is referred to their original work. A brief account of the contents of their comparison is provided here.

King and Moore [1974] chose nine general categories: grasslands, farmland, forest and woods, desert, snow-covered terrain, urban areas, swamp and marsh, road surfaces, and volcanic areas. The selections were made so that these data could be compared with the data obtained from Skylab. For the same reason, the angles of incidence for which they chose to display a histogram type comparison were  $0^\circ$ ,  $16.6^\circ$ ,  $30.4^\circ$ ,  $43.5^\circ$ , and  $52.5^\circ$ , the nominal design angles of incidence for the S-193 radiometer/scatterometer.

To facilitate comparison, a method of presentation similar to histograms is employed. The vertical axis represents the backscatter cross section,  $\sigma^\circ$ , in dB; and the various terrain categories are marked on the horizontal axis. If the original data was a curve, a bar represents the value of  $\sigma^\circ$  at that angle; if the data had a range of values then the range is represented by a shaded area.

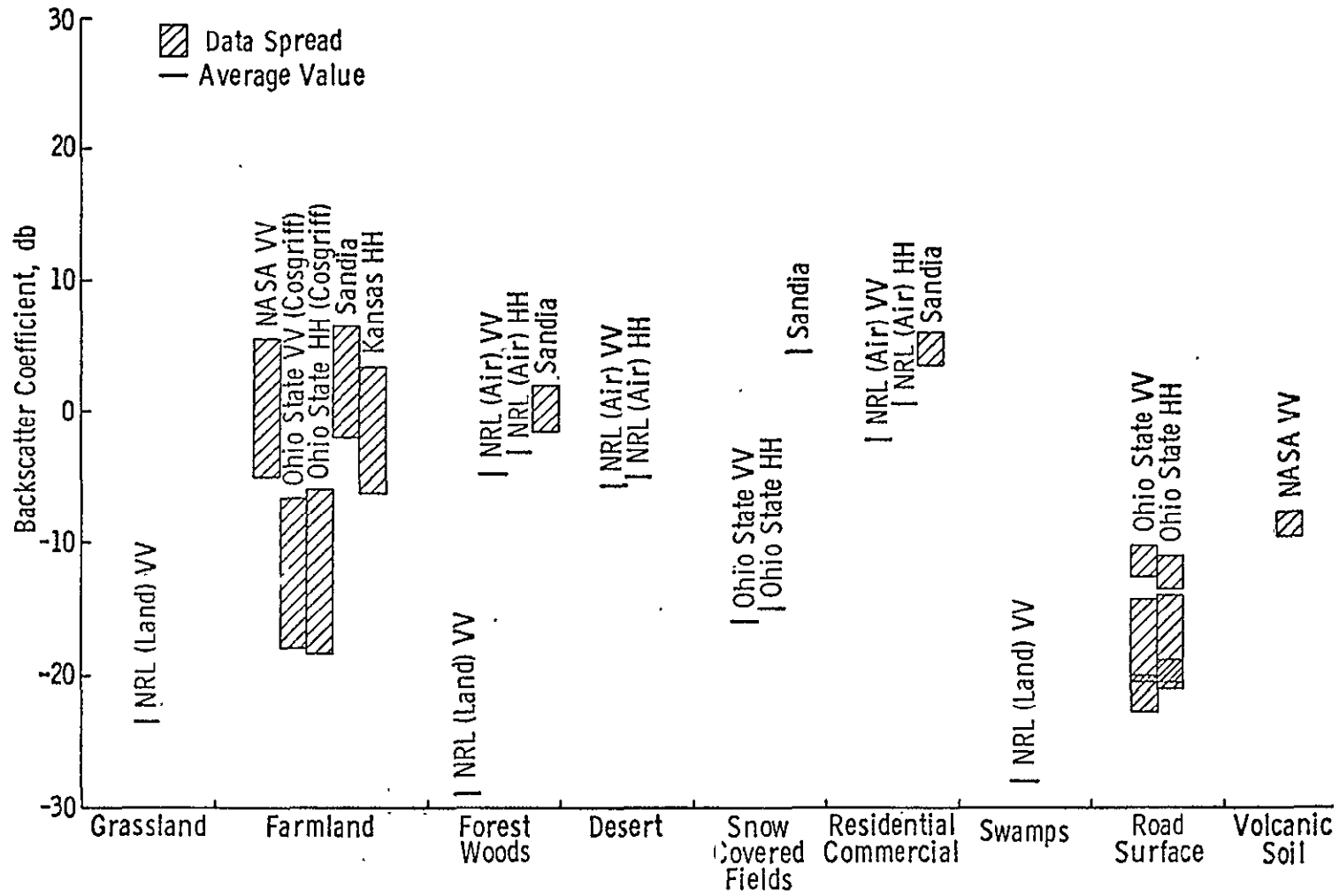


Figure 4.22. 16° incidence, original data. From King and Moore, 1974.

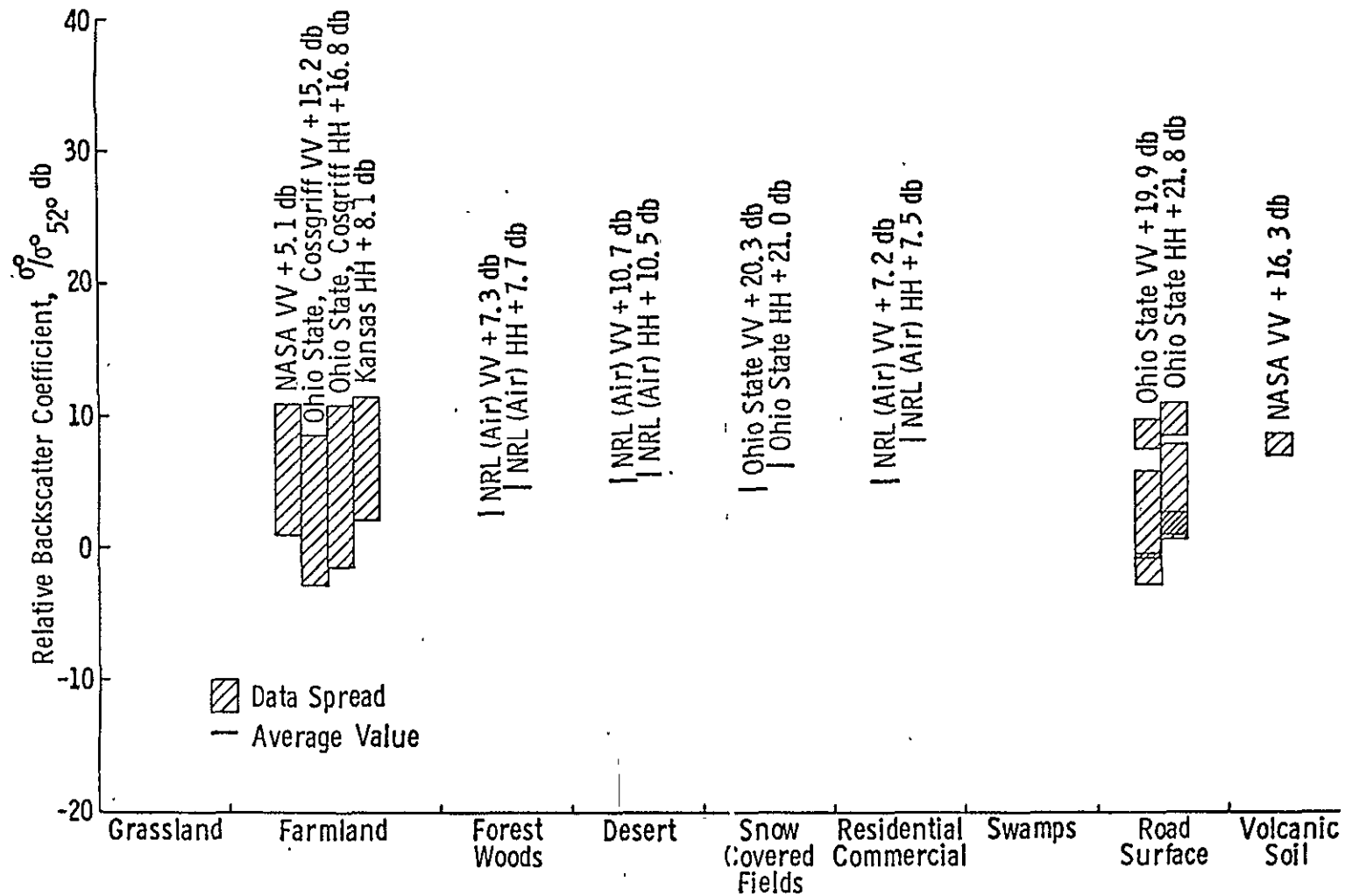


Figure 4.23.  $16^{\circ}$  incidence, relative  $\sigma^{\circ}$  (Normalized to one incidence angle). After King and Moore, 1974.

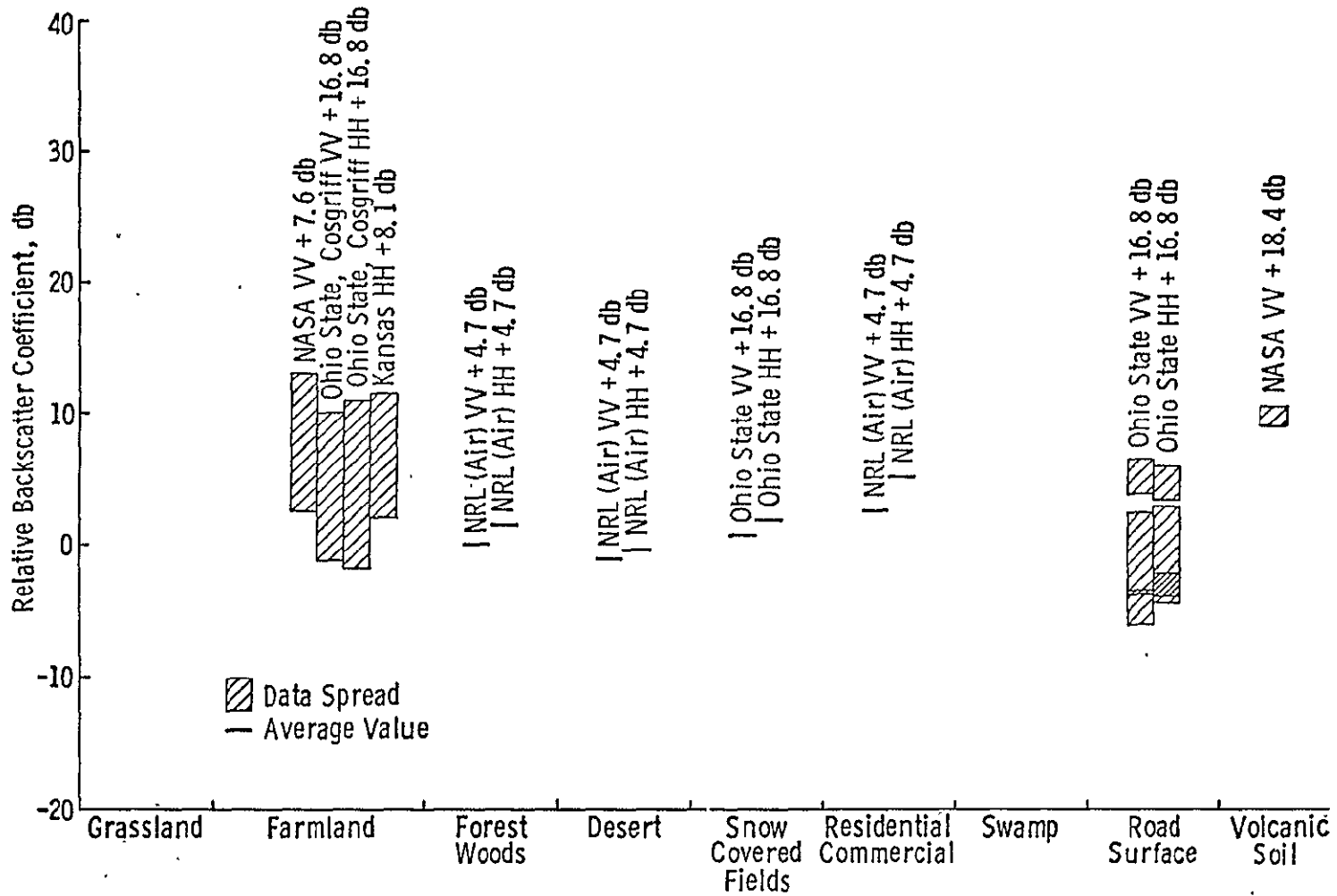


Figure 4.24.  $16^\circ$  incidence, relative  $\sigma^0$ . Normalized to farmland data at  $52^\circ$  HH polarization. From King and Moore, 1974.

The normalizing schemes used by King and Moore [1974] were 1) normalization to one angle of incidence (i.e.,  $\sigma^{\circ}$  at all angles was divided by  $\sigma^{\circ}$  at this angle), and 2) normalization to one terrain category (i.e.,  $\sigma^{\circ}$  at all angles for all terrain types was divided by the  $\sigma^{\circ}$  for a particular terrain at a particular angle). In the first normalizing scheme, the angle of incidence chosen to normalize by was  $52^{\circ}$ . In the second normalizing scheme, the terrain category chosen was farmland and the angle of incidence was again  $52^{\circ}$ .

An example of the comparison of raw (unnormalized) data is shown in Figure 4.22. An example of data normalized to one incidence angle is shown in Figure 4.23; and an example of data normalized to one terrain category is shown in Figure 4.24. The difficulties, pitfalls and other tribulations of such comparisons are enumerated in King and Moore's work and would be repetitious here.

A comparison of the oceanic backscatter cross sections for data near X- or Ku-band from different programs becomes difficult because not only are wind speed and wave height factors but wind direction is a major factor (which is most often not given). The data from individual measurement programs can, however, be normalized to either one incidence angle (as done by Bradley [1972]) or to one incidence angle and wind speed. An example of the original data and data normalized to one incidence angle,  $10^{\circ}$ , is shown in Figures 4.25 a, b.

#### 4.4 Radiometric Emission Measurement Programs

Radiometers, operating at microwave frequencies, have been used for well over 10 years to measure the brightness temperature of natural and man-made targets. Numerous programs have been initiated that measured the natural radiometric response of targets from towers, aircraft and even spacecraft. Each program selected a particular frequency (or a set of frequencies), polarization (one or both), and target-type(s) in its study. Comparison of the data documented by the various programs becomes very difficult, more so than in the case of the scattering cross-section because of the following reasons. The absolute values of the radiometric emission of a similar target as measured by different researchers are often quite distinct. The reasons for this are many, not the least of which is a lack of calibration of the measuring system. The radiometric emission is a function of the emissivity (described in Chapter Three) and the physical temperature of the target. Merely providing the apparent brightness temperature without providing the physical temperature of the target, as is done in so many

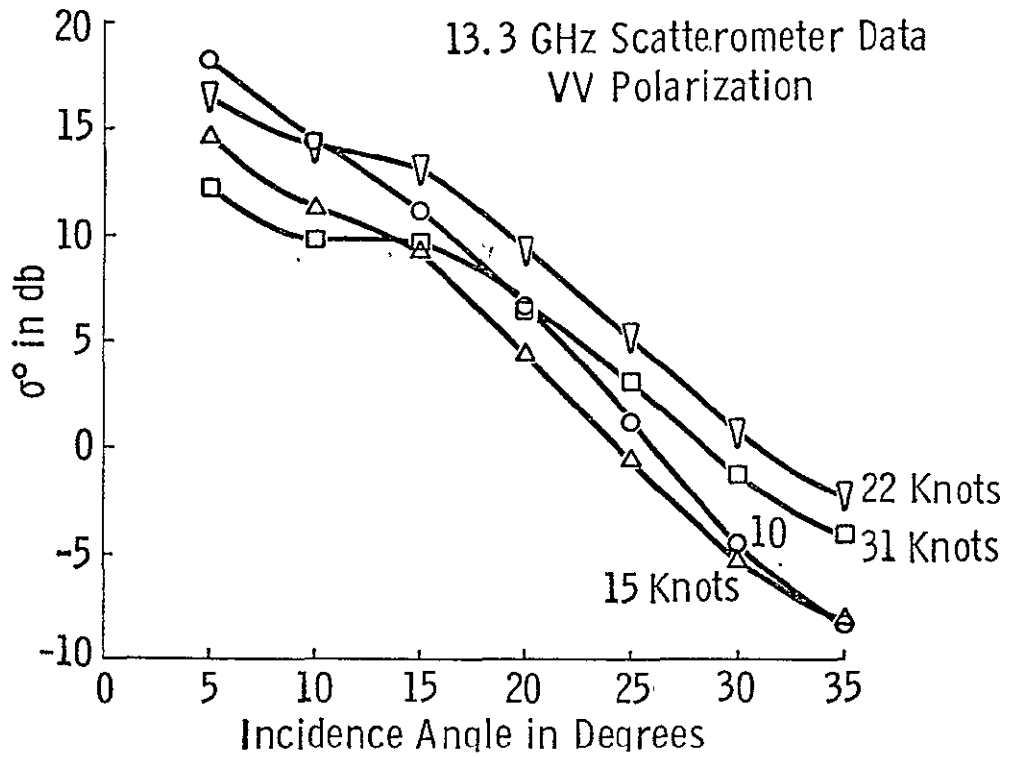


Figure 4.25a. Upwind radar scatterometer ocean data, mission 156. After Bradley, 1970.

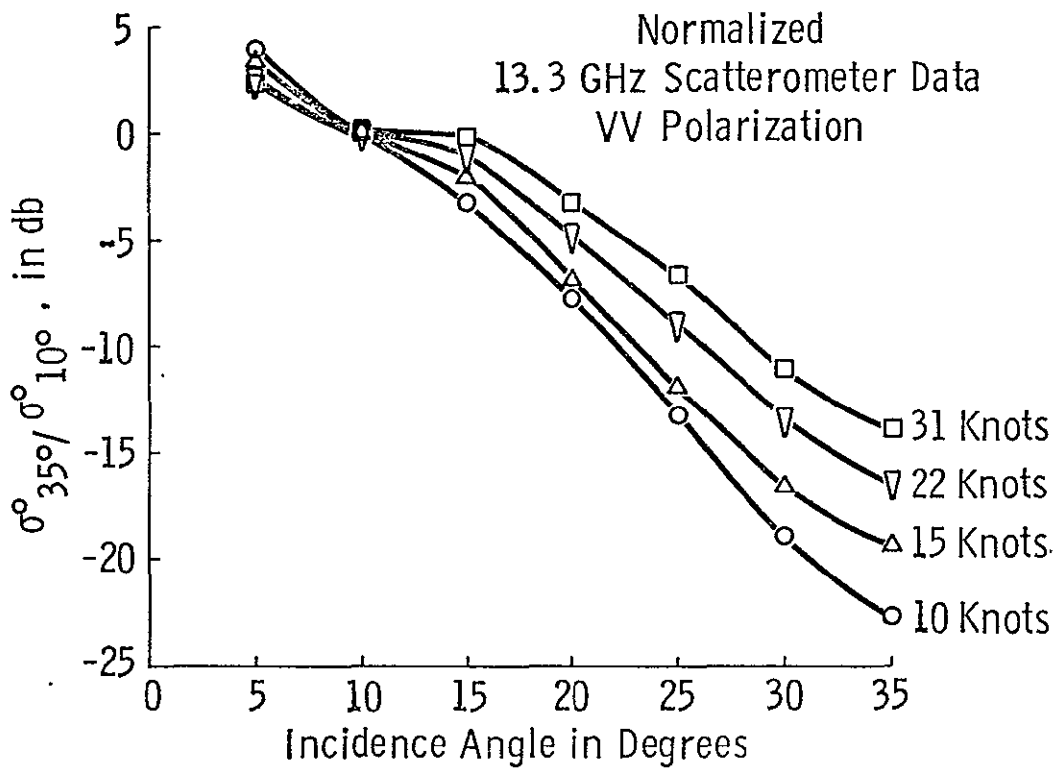


Figure 4.25b. Normalized upwind radar scatterometer ocean data, mission 156. After Bradley, 1970.

of the measurement programs, leaves the reader with no way of computing the emissivity of the target. As emphasized before it is the emissivity of a target that is the characteristic being sought. To compound the problem, the intervening atmosphere between the sensor and the target can, and very often does, modify the radiometric emission emanating from the target surface to the sensor. The measurement programs very seldom account for this modification. The meteorological state of the atmosphere is a variable which can cause a greater change than the entire dynamic range of the emission from a target scene over any angular range of incidence. The apparent temperature seen at the antenna (called antenna temperature) is a weighted average of radiation arriving from  $4\pi$  space; the weighting being the antenna power pattern. The weighting, and hence the contribution of a desired target to the overall contribution from all space, depends upon the antenna pattern. It is almost impossible for two measurement programs with two distinctly different sensors to have the same antenna pattern. Hence, it is almost impossible to account for the unwanted contribution (from other than the target of concern) for two different antenna temperature measurements. Some programs have provided the brightness temperature at the antenna terminals, others have adjusted for the radiation efficiency of the antenna, others have adjusted for the atmosphere and yet others have accounted for all sensor characteristics and unwanted signal sources.

The biggest shortcoming of the data, in general, is the lack of information regarding soil moisture. Only measurement programs which have concentrated on determining the effect of soil moisture on the radiometric emission, have taken care to measure or estimate the soil moisture. Other measurement programs have often chosen to ignore this important parameter. Since the radiometric response of any land terrain can change drastically with soil water content and since many programs do not provide soil moisture information, a comparison of the sort presented for backscatter cross-section measurements becomes wasted.

A brief description of some of the major radiometer measurement programs is provided below.

#### 4.5 Major Microwave Radiometric Emission Measurement Programs

There have been far more measurement programs with emphasis on monitoring the ocean than land targets. The reasons are obvious, the ocean surface can be considered homogeneous for larger stretches than land and the radiometer, as compared

to all other microwave or optical remote sensors, has a poorer resolution generally. There have been, however, many measurement programs conducted over land too. The significant measurement programs include tower mounted, ground based, aircraft mounted and spacecraft mounted measurements. The leading institutions for radiometer measurements are Aerojet General [Edgerton et al, 1970], [Poe and Edgerton, 1971] which conducted ground-based and aircraft mounted measurements; Raytheon Company [Porter, 1966] which had an aircraft mounted radiometer; Ohio State University [Peake, 1959], [Sinclair, 1960], [Oliver and Peake 1969] which had a truck mounted radiometer; Goddard Space Flight Center [Wilheit et al, 1972], [Schmugge et al, 1972] aircraft and spacecraft mounted radiometers; Naval Research Laboratory [Hollinger, 1969, 1970] a tower mounted radiometer; Institute of Radio and Electronics, Academy of Science of USSR [Basharinov et al, 1971] which also performed measurements from spacecraft; Texas A & M University [Jean et al, 1972], [Paris, 1971] aircraft and surface mounted radiometers.

#### 4.5.1 Aerojet General Measurements

The Space Division of Aerojet General Corporation, El Monte, California, has for many years been conducting a series of experimental measurements using a four-frequency dual polarized radiometer system that is mounted on a truck. The controls of the radiometer are in the van along with other scientific measuring equipment. This is called the mobile laboratory and is transported from place to place taking measurements. The radiometers operate at 1.42, 4.99, 13.4 and 37 GHz. One or more of these radiometers is used for each particular experiment. The results of one of their measurement programs [Edgerton et al, 1968] contains radiometric brightness temperature data for snow samples, various conditions of soils and a combination of snow-ice and water samples. Their emphasis has been to study the effect of water content in a soil on the radiometric temperature. To quantify this effect and to establish the feasibility of using multifrequency radiometers for monitoring the soil moisture profile, carefully prepared soil samples were used as targets. The radiometric response for various dry and wet conditions for all four frequencies are reported by Poe [1972]. Dielectric constants of the soil samples were measured by a free-space measuring system known as an ellipsometer operating at 13.4 GHz and 37 GHz [Poe, 1970]. These dielectric constants were then compared against several commonly used dielectric mixing formulas. Edgerton et al, [1971], report on an experiment where the emission from a field was measured for various soil moisture conditions. Figures 4.26 a-b show examples of the measured soil moisture and the measured emission for  $30^\circ$  and  $40^\circ$  incidence.

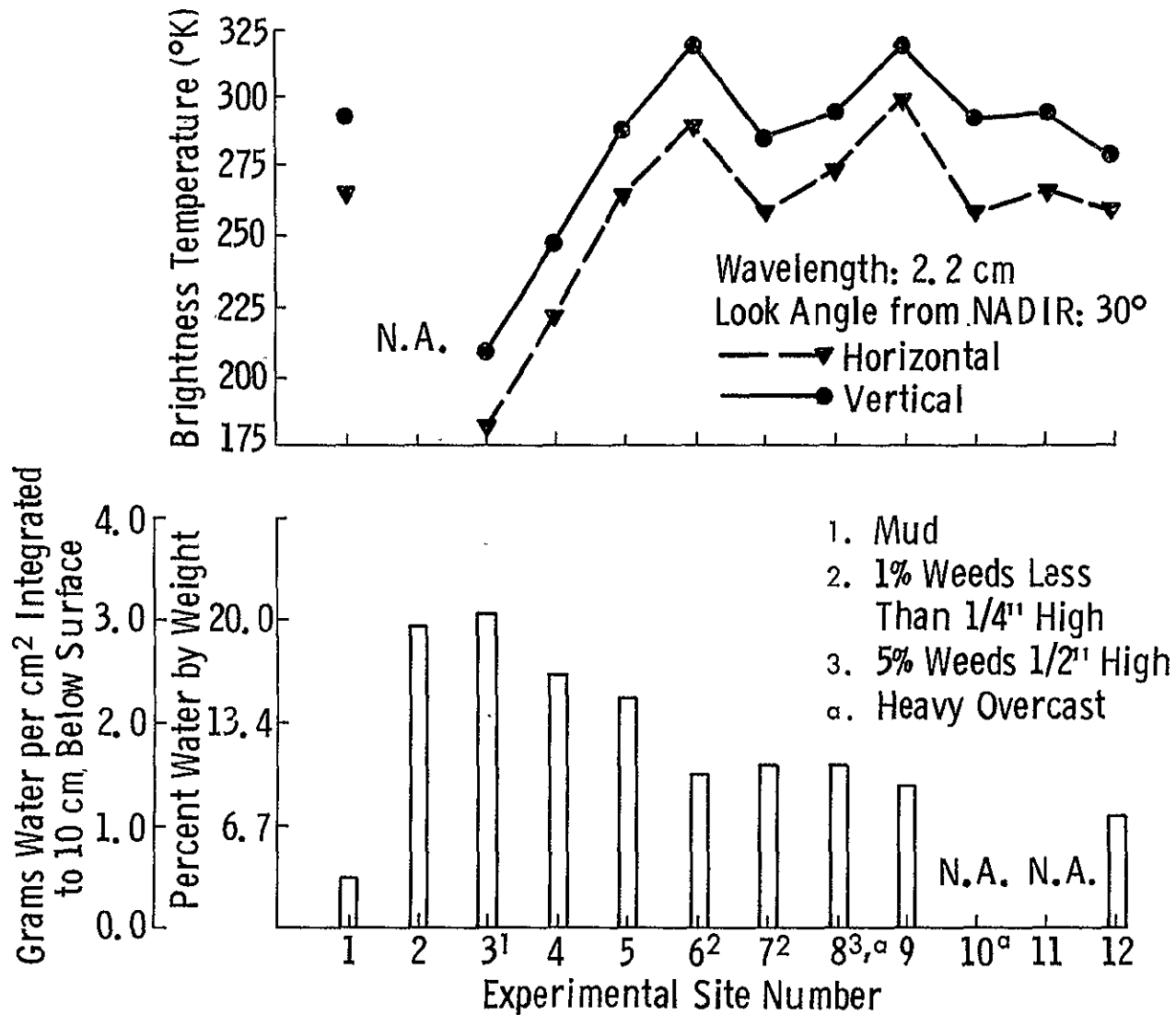


Figure 4.26a. Brightness temperature compared to volume soil moisture, bare\* ground, clear\* sky. After Edgerton, 1971. \*unless otherwise noted.

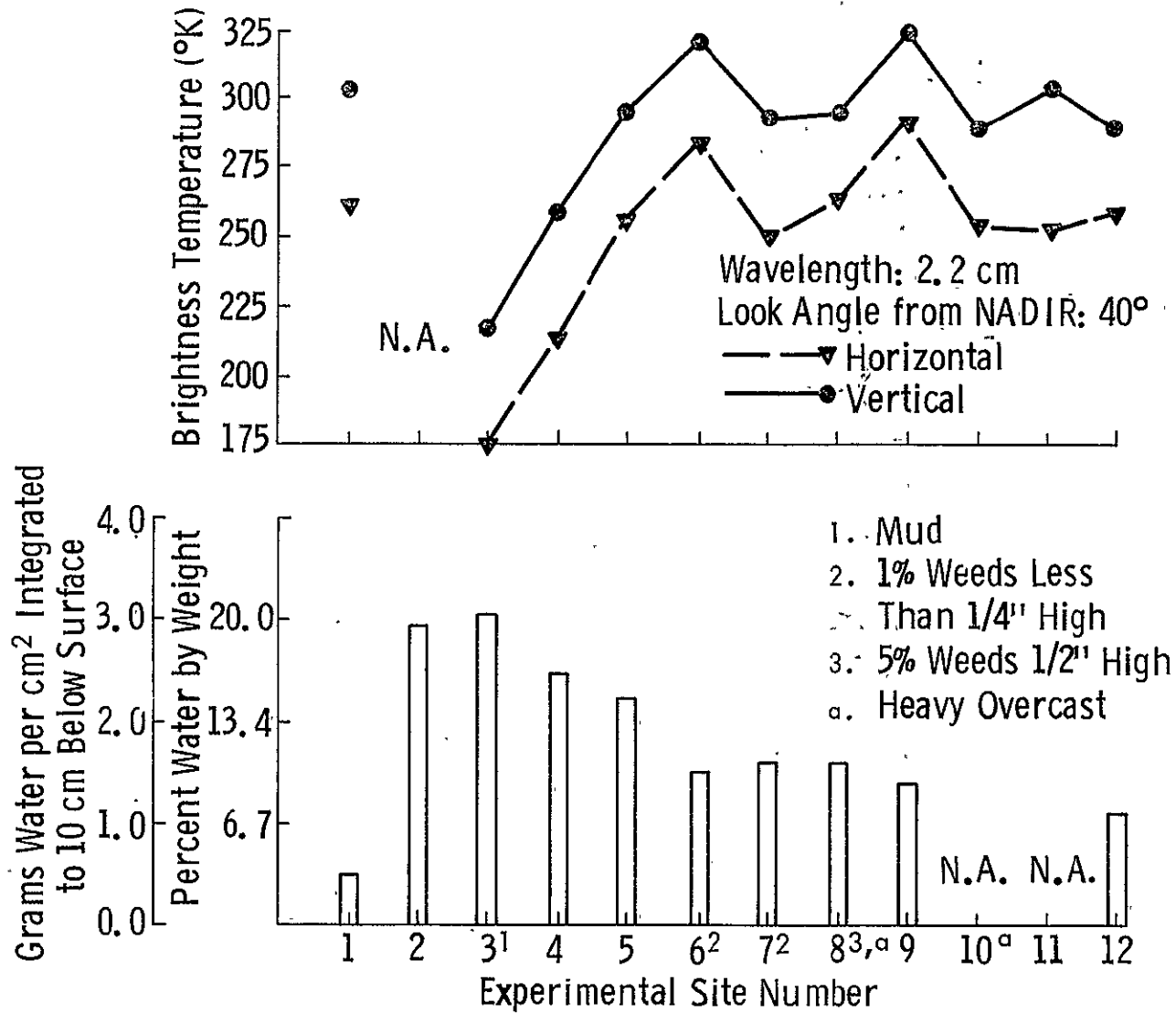


Figure 4.26b. Brightness temperature compared to volume soil moisture, bare\* ground, clear\* sky. After Edgerton, 1971. \*unless otherwise noted.

These same researchers also report on an aircraft program which observed fields either plowed or with crops [Edgerton et al, 1971b]. Their system was taken to Newport Beach in California to measure the emission from the littoral zone and near-shore environment [Edgerton and Trexler, 1972]. Data from a tidal marsh (San Francisco, California), playa sediments (Lavic Lake, California), beach sand (La Jolla, California), basalt (Pisgah Crater, California), and pumaceous soil (Crater Lake, Oregon) were measured and are reported by Edgerton [1970] to exhibit characteristics similar to dry natural materials. Figure 4.27 shows a comparison of these materials at 37 GHz. A significant feature of the radiometric response is that although the composition and grain size of saturated mud and playa deposits are very similar, at an incidence angle of  $10^\circ$ , the differential in radiometric temperature is  $94^\circ\text{K}$  or approximately  $0.8^\circ\text{K}$  for each one percent change in moisture content. The relation between soil moisture content and radiometric temperature was further verified by measurements on Harper Lake, a playa deposit in the Mojave Desert, California. Figure 4.28 illustrates this effect; the target is flat smooth and devoid of vegetation, the only variable is soil moisture content. A further correlation between the soil bearing strength and microwave brightness temperature was established by driving across the dry lake bed and taking repeated measurements. It was found that puffy surfaces and moist areas (which have low-bearing strength values) registered much colder radiometric temperatures. In another part of the experiment Meier and Edgerton [1971] report on results from carefully constructed snow samples (some with a metallic plate immersed at various depths) to find the variation of brightness temperature with snow depth, water equivalent, free water content and the character of the underlying material. These measurements were conducted with 4.99 GHz, 13.4 GHz and 37 GHz radiometers. Figure 4.29 shows an example of the measured dry snow brightness temperature taken from Meier [1971].

#### 4.5.2 Raytheon and Radiometric Technology

These two institutions have been combined because the same researcher, R. A. Porter, reported on data while he was at Raytheon [Porter, 1966] and again later while he was with Radiometric Technology [Porter et al, 1970]. Porter reports on carefully controlled measurements on asphalt and concrete obtained at the Santa Barbara airport with a set of radiometers operating at 9.5 GHz (X-band) and 16.5 GHz (Ku-band). These measurements made with Raytheon's Mobile Radiometric Station (MRS) were carefully contrasted to calculated values of emissivity obtained by determining the dielectric properties of the substances in a laboratory. Figures 4.30 a and b show the comparison of calculated (from laboratory dielectric measurements)

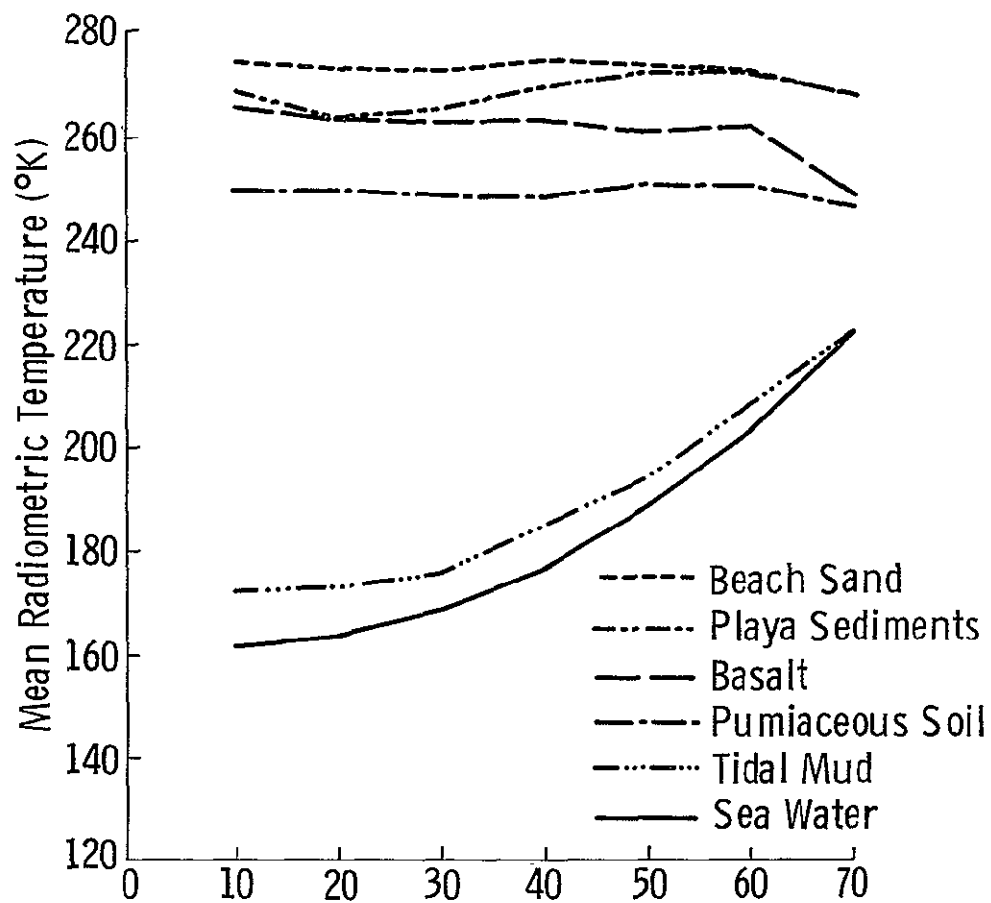


Figure 4.27. Comparison of radiometric temperatures, 37.0 GHz, vertical polarization. After Edgerton and Trexler, 1972.

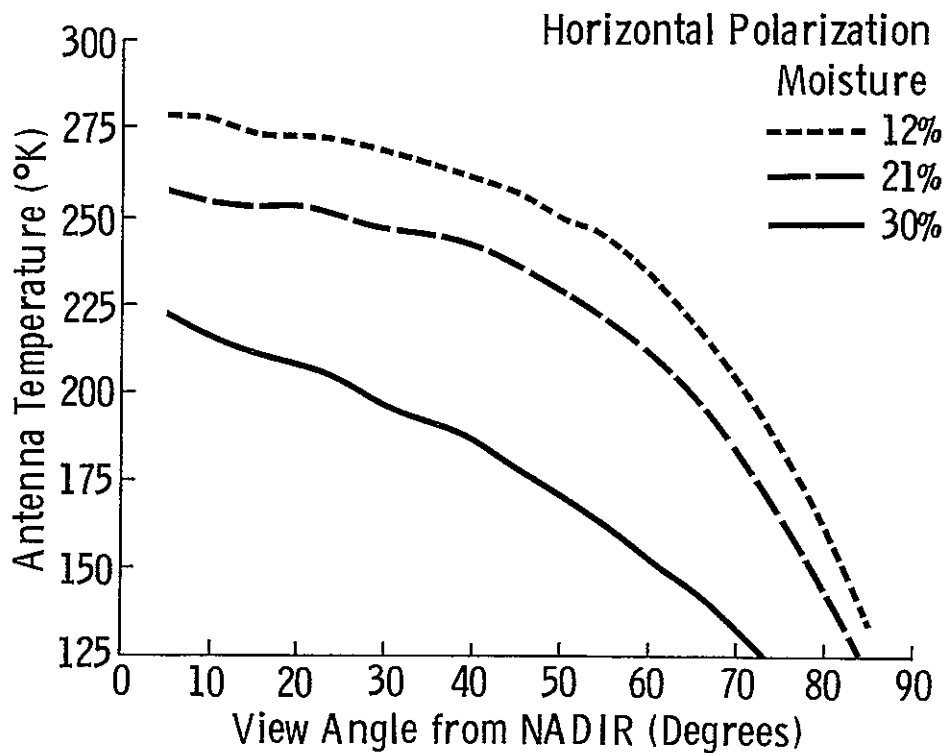
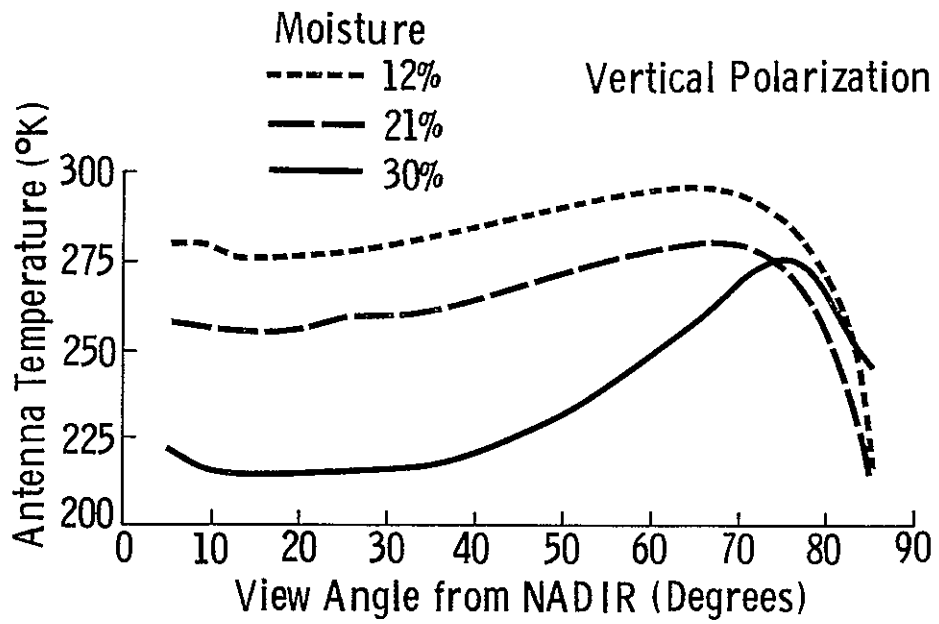


Figure 4.28. 13.4 GHz radiometric temperatures of Playa sediments with variable moisture. After Edgerton, 1971.

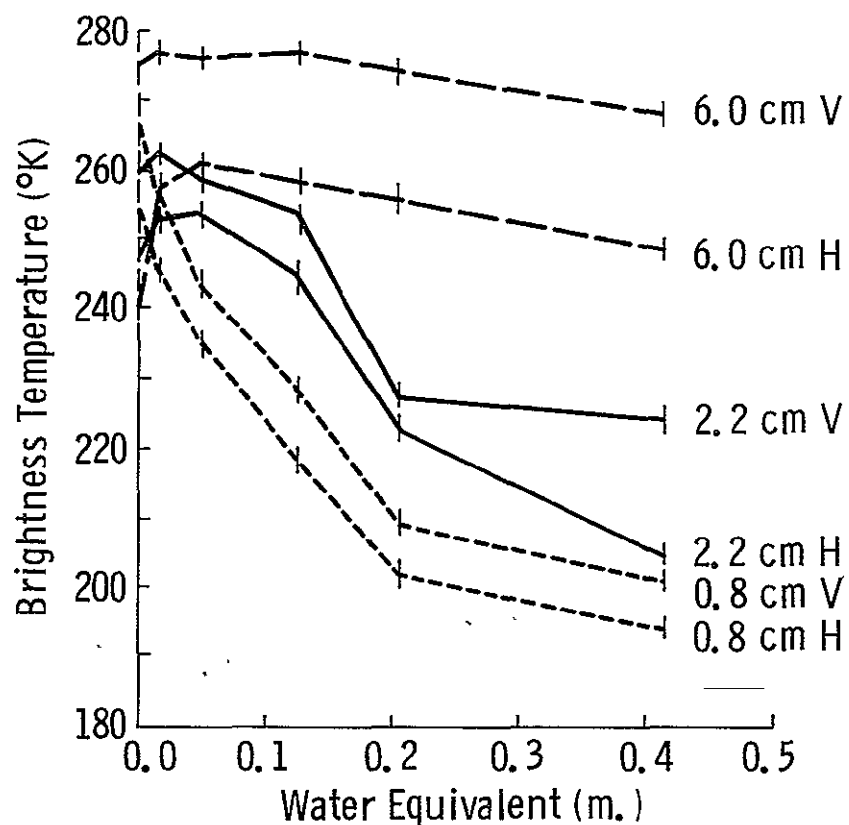


Figure 4.29. Measured dry snow brightness temperatures. These are given as a function of snow mass per unit area (water equivalent),  $45^\circ$  viewing angle, at 3 wavelengths and 2 polarizations (H=horizontal, V=vertical polarization). Absolute values of brightness temperature at 6 cm wavelength are not known, but relative variations in brightness are correct. Measurement errors indicated by short dashes. Crater Lake, Oregon, March 23, 1970. After Meier and Edgerton, 1971.

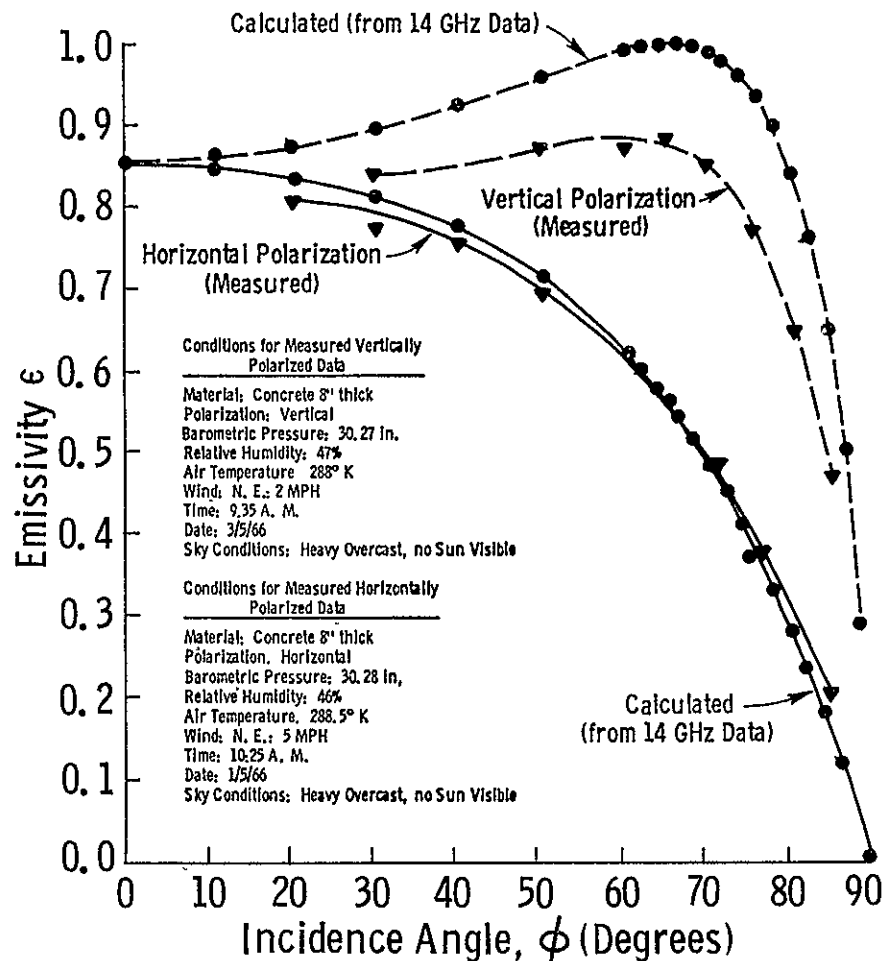
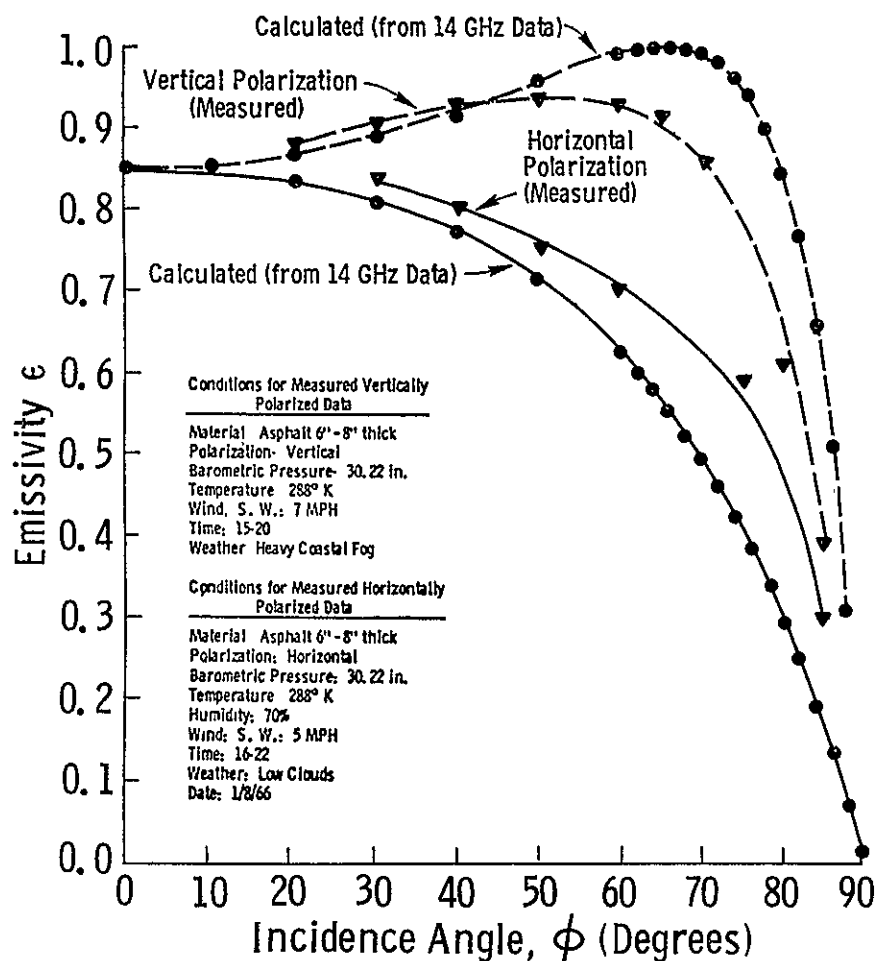


Figure 4.30. Calculated and measured emissivities for asphalt and concrete at 16.5 GHz. After Porter, 1966.

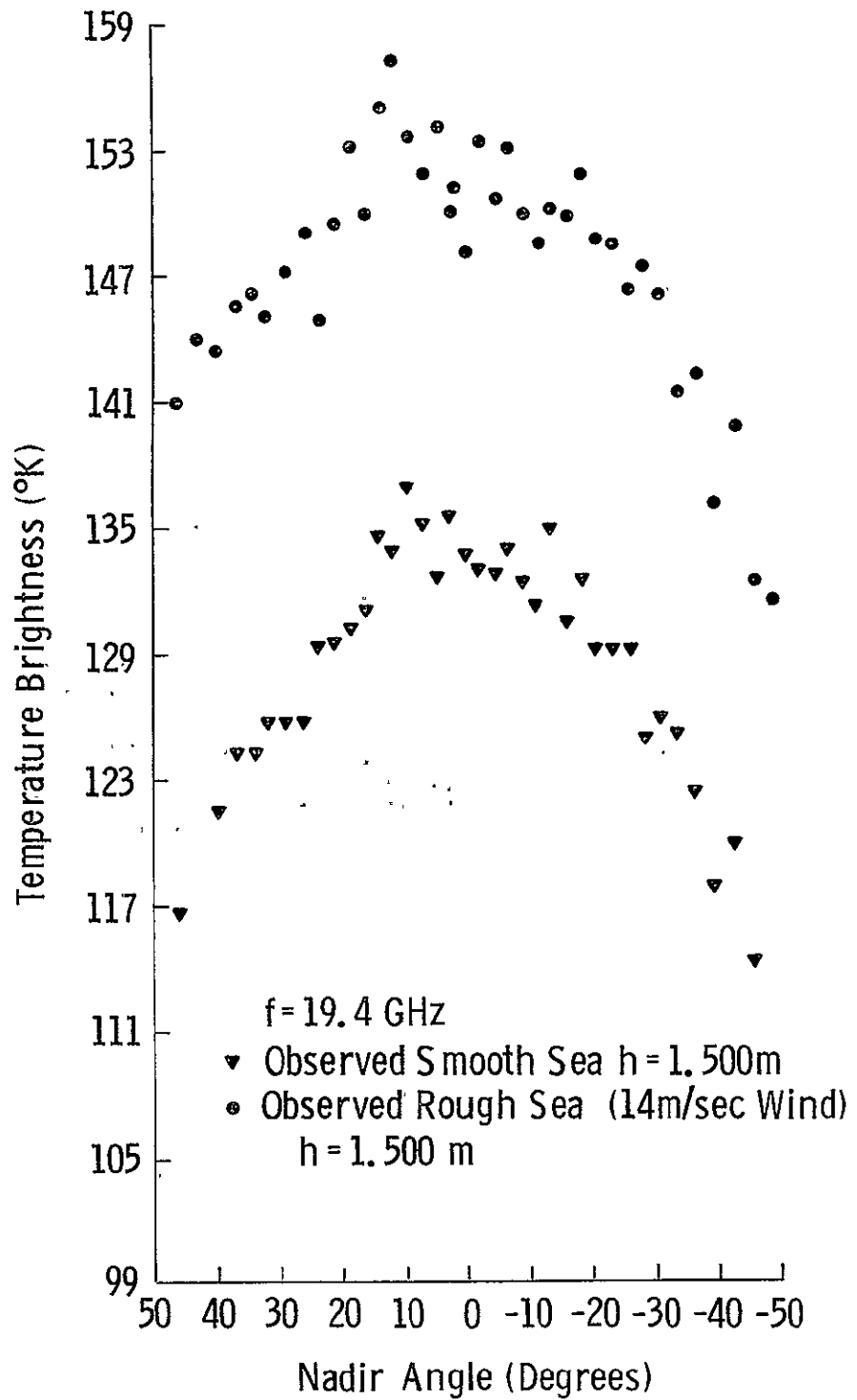


Figure 4.31. Observed brightness temperatures vs. nadir angle at 1.55 cms over smooth and rough portions of the Salton Sea. Each point is an average of 6 consecutive points at that angle. From Nordberg, et al., 1970.

and actually measured emissivity for concrete and asphalt at 16.5 GHz.

Porter et al [1970] also reported on measurements taken over ocean and land areas by a 19.35 GHz phased array scanner aboard a NASA Convair 990. Their emphasis was to estimate the effects of the atmosphere and in particular clouds. In keeping with this emphasis, the combined contribution of terrain and atmospheric emission was solved for the atmospheric portion. To do this, theoretical or modeled values based on previous measurements for terrain emission were assumed. For the ocean surface, dielectric constants as suggested by Paris [1966] were used, for land (mostly a desert site) Von Hippel's [1954] dielectric constant data for sand were used. To include effects of vegetation, Edgerton's [1968] data for weed covered soils at 13.4 GHz and 37 GHz were interpolated to 13.9 GHz.

#### 4.5.3 Goddard Space Flight Center Measurements

Goddard Space Flight Center has conducted a measurement program that even includes spacecraft borne radiometers. Nordberg et al [1968] reported on an experiment where a 1.55 cm radiometer on board an aircraft was flown over a variety of atmospheric and surface conditions (almost exclusively over water). Their data, constituting over a 100 hours of flying time, took a considerable time in processing and periodic reports [Nordberg et al, 1969, Nordberg et al, 1970] show that the data (over ocean) show a linear correlation between radiometric data and wind speed from  $7 \text{ msec}^{-1}$  to  $25 \text{ msec}^{-1}$ . This increase was directly proportional to the occurrence of white water on the sea surface. An example of the variation of brightness temperature to wind speed is shown in Figure 4.31 [Nordberg et al, 1970].

The Nimbus 5 satellite, launched in 1972, contained an Electrically-Scanning Microwave Radiometer (ESMR) operating at 19.35 GHz. The antenna beam scans  $\pm 50^\circ$  off nadir. Wilheit et al [1973] have used the data for meteorological interpretations as well as created a microwave brightness map of many regions of the world. Their main emphasis is, however, to study meteorological and sea-state conditions. It has been used successfully to map sea ice [Wilheit et al, 1972]. Wilheit et al [1972] also reported on an aircraft program which had 8 radiometers ranging in wavelength from 0.510 to 2.81 cms, which measured microwave emission from sea ice.

Schmugge et al [1972] reported on a program (aircraft) using four radiometers operating at 1.42, 4.99, 19.35, and 37 GHz to measure soil moisture. The test sites included agricultural sites in southwestern United States. Soil samples were subjected to gravimetric soil moisture measurements. They concluded that it was possible to moni-

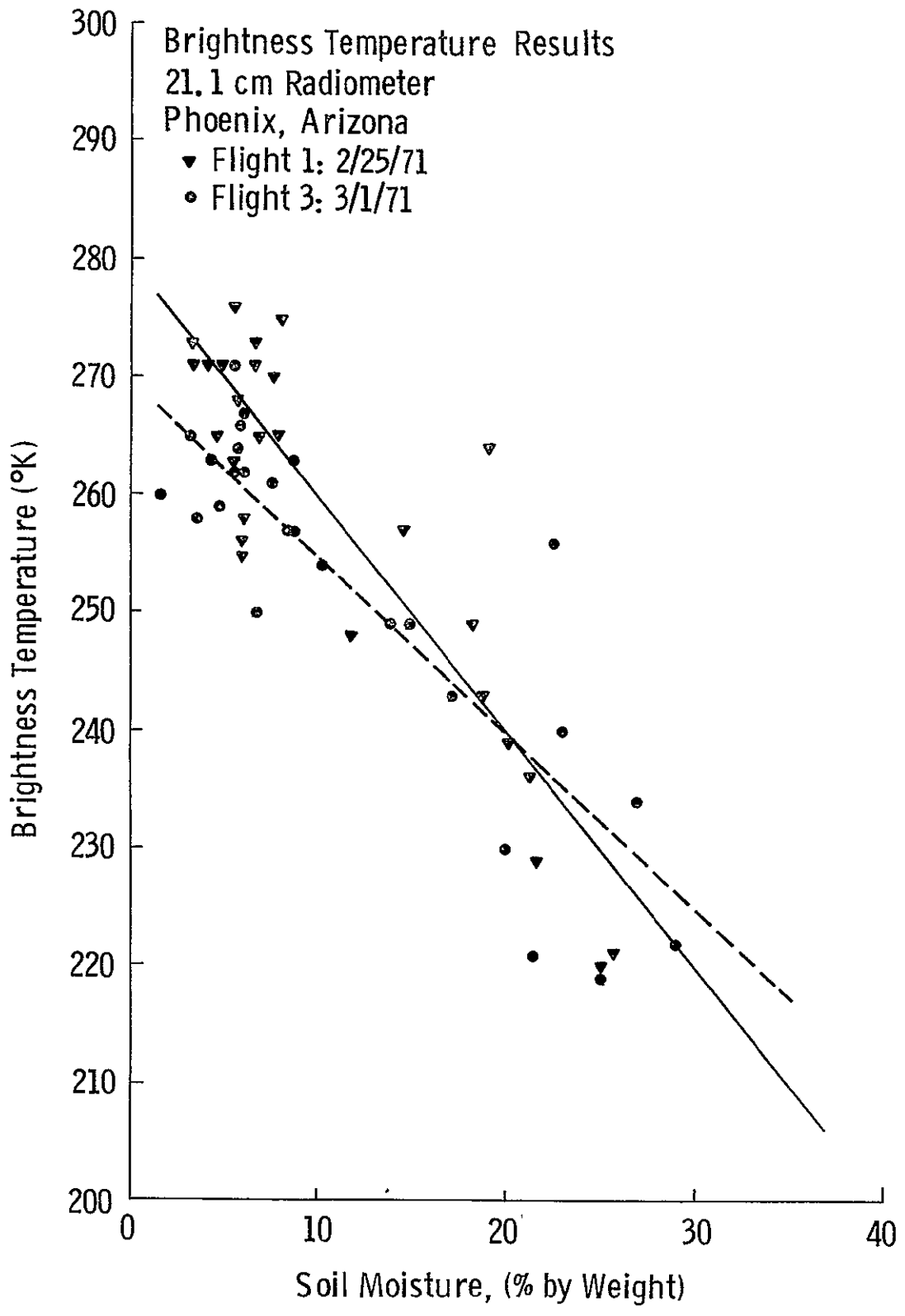


Figure 4.32. Plot of 21.1 cm brightness temperatures vs. soil moisture from Phoenix, Arizona. From Schmugge, et al., 1972.

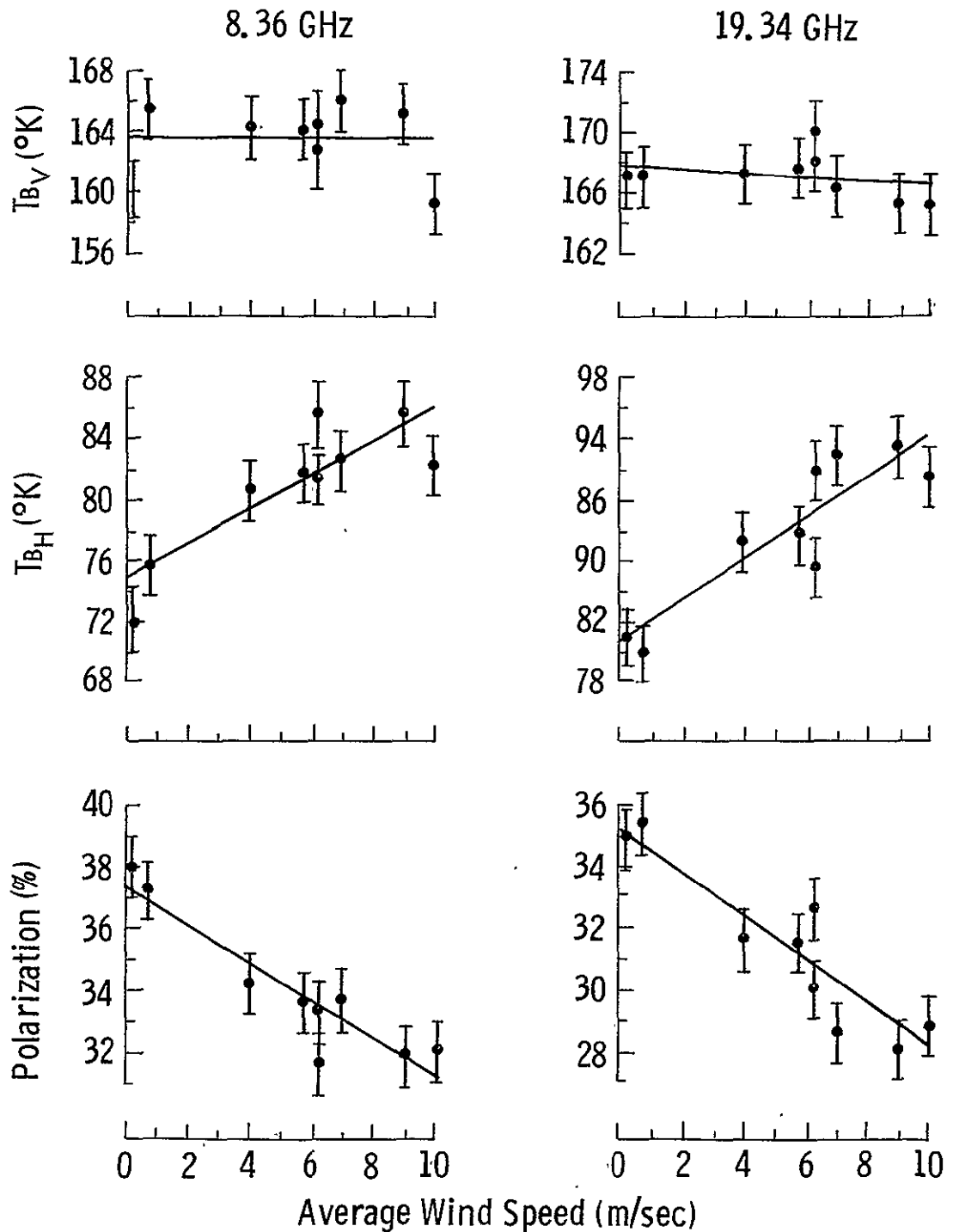


Figure 4.33. Individual measurements at 8.36 and 19.34 GHz of the vertical and horizontal components of brightness temperature and the percentage polarization of the sea at  $55^\circ$  incidence angle are plotted vs. wind speed. The solid lines are linear least-squares solutions to the data. From Hollinger, 1970.

C, 3

tor soil moisture with airborne radiometers. The emissions, in general, were not found to be linear functions of soil moisture and were affected by soil type and surface conditions such as roughness and vegetated cover. Figure 4.32 shows the variation of brightness temperature with soil moisture at 21.1 cms [Schmugge, 1972].

#### 4.5.4 Naval Research Laboratory

Hollinger [1970, 1971] has reported on measurements conducted by the Naval Research Laboratory on the ocean surface by radiometers mounted on Argus Island Tower. The radiometers operated at 8.36 and 19.34 GHz for both vertical and horizontal polarizations. The results show a definite dependence of microwave brightness temperature on wind speed over a range of wind speeds from calm sea to 10 m/sec (the range of wind speeds encountered in the course of the measurement program). Examples of Hollinger's data plotted against wind speed for an incidence angle of  $55^\circ$  are shown in Figures 4.33. The solid lines are linear least square solutions to the data. Hollinger also conducted some measurements over artificially generated foam in a laboratory and found the emissivity of foam to be close to unity. Naturally generated foam patches produced brightness temperature increases in excess of  $40^\circ\text{K}$  at  $50^\circ$  incidence.

#### 4.5.5 Texas A & M University Measurements

Jean [1971] reported on measurements conducted in an experiment to observe the effects of soil moisture on the radiometric emission. The experiment was conducted on a test site in the lower Rio Grande Valley near Weslaco, Texas. The measuring instruments included a Multifrequency Microwave Radiometer (MFMR) operating at frequencies of 1.42, 10.625, 22.235, and 31.4 GHz; the supporting instruments included two scatterometers (at 400 MHz and 13.3 GHz), a side-looking radar, some cameras and IR sensors. The radiometers flown aboard a NASA Convair 990 aircraft were provided by NASA/GFSC. The target sites consisted of fields under different conditions of irrigation. Soil condition information was collected by ground truth survey which collected soil samples along the flight path and found the amount of subsurface soil moisture in laboratory tests. Apart from this, a series of ground based microwave radiometer measurements were made of a simulated oil spill on a water surface. This experiment was conducted with a 37.4 GHz radiometer which viewed the target at  $0^\circ$ ,  $10^\circ$ ,  $20^\circ$ ,  $30^\circ$ ,  $40^\circ$ ,  $50^\circ$ , and  $60^\circ$  from nadir in both vertical and horizontal polarizations.

Siu Lin Lee [1974] reported on another experiment conducted using a dual frequency microwave radiometer operating at 1.4 GHz (L-band) and 10.69 GHz (X-band) to monitor soil moisture effects on bare and vegetated rough surfaces. The test site was a plot of the Texas A&M Farm in Burleson County, Texas.

#### 4.5.6 Institute of Radio and Electronics, Academy of Science (USSR) Measurements

The Institute of Radio and Electronics in USSR has conducted an on-going measurement program that included ground-based, aircraft-mounted, and spacecraft-mounted radiometers. Basharinov and Shutko [1971] reported on measurements made with a ground-based radiometer looking down on a sea surface at 0.8, 1.35, 1.6, 3.2 and 3.37 cm wavelengths. They also reported measurements at 3 cms from on board an aircraft and from radiometers operating at 0.8, 1.35, 3.4, and 8.5 cm wavelengths on board the Cosmos-243 satellite. These measurements were to correlate wind speed and foam generation to the radiometric brightness temperature. Results, in general, similar to those observed by Nordberg et al at Goddard were reported from their surface and aircraft measurements. The satellite-borne radiometers have resolution cells in "ten of kilometers" [Basharinov et al, 1971] and are comparable to the S-193 and S-194 radiometers on board Skylab. Large bands of precipitation were detected as were regions of rough seas. In the polar regions, boundaries of floating ice were detected. Homogeneous areas such as the Sahara Desert, the Continent of Australia, and a large traverse of South America were target candidates. For example, the change in the radiometric temperature across the Australian continent from north to south was 16<sup>o</sup>-18<sup>o</sup>K while the air temperature difference in these zones was 21<sup>o</sup>K. A general decrease in radiometric temperature for humid and swampy regions was observed.

#### 4.5.7 Voyeykov Main Geophysical Laboratory (USSR)

The Voyeykov Main Geophysical Laboratory in the USSR has created a catalog of microwave response from various terrain surfaces. Due to paucity of data reaching the western world, not all the details are known, but from their report Melentyev and Rabinovich [1972] have performed more measurements (i.e., on more terrain types) at the same frequencies that can be found anywhere in the western world. Table 4.2 taken from their work illustrates this point. These measurements are from ground-based and aircraft-mounted sensors. They have, in addition, studied the effects of salinity and foam on water surfaces in a laboratory. The foam was generated by egg and soap.

TABLE 4.2

Emissivity for some targets at 1.6 and 3.2 cms.  
From Melenteyev and Rabinovich, 1972

Surface	Brief Description	Wave-length	Emissivity
Sand	River, dry, middle grains smooth surface, layer thickness-- 25 cm	1.6	0.933
		0.8	0.393
Sand	River, damp, smooth surface layer thickness--25 cm River humidity--3.45 River humidity--105 River humidity--14.55	3.2	0.749
		1.6	0.769
		3.2	0.927
		3.2	0.703
		3.2	0.655
Sand	Dry, dusty	3.2	0.884
Detritus	Limestone, large, layer thickness--25 cm	3.2	0.877
Slate	Wavy, several layers, thickness--15 cm	3.2	0.742
Slag	Large, mean size 4-6 cm, layer thickness--25 cm	3.2	0.787
Grass	Dry, stalk height--15-20 cm	3.2	0.935
Cover	Soil layer thickness--20 cm	1.6	0.961
Grass	Damp, stalk height--15-20 cm		
Cover	Soil layer thickness--20 cm	3.2	0.890
Wood	Planks, pine, 10 cm thick	3.2	0.878
Foliage	Birchtree branches, layer thickness--25 cm	3.2	0.882
Concrete	Slab, 20 cm thick	3.2	0.836
Asphalt	Highway	3.2	0.874
Snow	Smooth surface, density 0.53 m/cm <sup>3</sup>	0.8	0.944

#### 4.5.8 Other Measurement Programs

Other measurement programs include one by NASA/MSC [Droppleman, 1970] which studied the effects of a wind blown sea on the radiometric response [also Strong, 1969]. The University of Miami [Williams, 1969] reports on brightness of foam, white-caps, and surfines at 9.4 GHz. Glushkov and Komarov [1972] from the Aerial Methods Laboratory, Ministry of Geology (USSR) reports some data for dry and wet soils and the effect of salinity.

Numerous atmospheric sensing measurement programs have been conducted. These will not be reported here.

## CHAPTER FIVE

### ATMOSPHERIC EFFECTS ON REMOTE MEASUREMENTS OF RADIOMETER/SCATTEROMETER SIGNALS

#### 5.0 Introduction

To estimate the emission or scatter from a target with a remote sensor, the effects of the intervening atmosphere must be compensated. This compensation becomes more important when the sensor is on an orbital platform and the target is an earth scene. The effects of the atmosphere upon active sensors (like the S-193 Scatterometer and altimeter) are quite different from those on passive sensors (like the S-193 Radiometer). For the radiometer, the opacity of the atmosphere has both an absorption and emission effect; for the scatterometer and altimeter the significant effect is one of attenuating the signal. The opacity of the atmosphere is dependent upon the frequency of the traversing signal and on the meteorological state of the atmosphere. Wu [1972] has computed the relationship between the attenuation of the microwave signal by the atmosphere and the correspondingly contribution to the apparent brightness temperature. Therefore, excess temperature contributed by the sky can be used to compute the opacity of the atmosphere, or, in reverse, a known or correctly modeled opacity of the atmosphere can be used to compute the contribution of brightness temperature by the atmosphere. Both the opacity (transmittance) and the excess temperature are required for relating the measured antenna temperature to the surface brightness temperature.

For the scatterometer, the parameters of interest are the atmospheric loss factors  $L_1, L_2$  that appear in the equation for the solution of  $\sigma^0$ , the differential backscattering coefficient.

$$\sigma^0 = \frac{(4\pi)^3 R^4}{\int_{\Omega} G_o^2 f(\psi) d\psi} \cdot \frac{P_r}{P_t} \cdot L_1 L_2 \quad (1)$$

$L_1, L_2$  are the transmit and receive path atmospheric loss factors. For monostatic measurements, they are considered equal. These loss factors can be considered similar to the loss factors encountered by a signal passing through a long lossy hardware component. The corresponding effects on a signal of much weaker strength (as in the passive detection case) are immediately seen to be two-fold; attenuation of the received signal and the self-generation of a noise signal due to thermal noise.

At a fixed frequency, the opacity of the atmosphere depends solely upon the state of the atmosphere, and is sensitive to clouds, rain, hail, fog or ice clouds. Even for a clear sky, the opacity varies due to the amount of absorbing gases in the signal

path. For a clear sky, the principal absorption at 13.9 GHz is due to oxygen and uncondensed water vapor; the absorption due to these gases depends upon the temperature, pressure and humidity at all points in the signal path. Condensed water has a stronger effect upon attenuation (and hence brightness temperature) than uncondensed water vapor.

Numerous experiments have been conducted to ascertain the absorption due to oxygen and water vapor. Based upon these experiments theoretical models have been propounded. The experiments consist of measuring atmospheric profiles for temperature, pressure and humidity along with radiometric measurements for a broad range of frequencies all the way from IR down to a few megahertz. The effects of clouds upon microwave signals have also been studied. The modelling of clouds has been more difficult, in that one can very seldom determine the height, thickness, water content and temperature of clouds over a wide region. Quantified values of cloud parameters which have been obtained from extensive measurements are usually invoked. The effects of rain have been studied mainly in terms of their effect on line-of-sight propagation. There are some reports which deal with the effects of hail, fog, and snow (for example Ryde and Ryde [1945], Langille and Thain [1951]).

In this study, as we attempt to find the effects that the atmosphere may have on the space borne S-193 radiometer/scatterometer, some past activity in the subject of atmospheric sensing and atmospheric profiling, as pertinent, will be mentioned.

## 5.1 Attenuation and Emission of Radio Waves by the Atmosphere

### 5.1.1 Background

The attenuation experienced by radio waves through the atmosphere is the result of two effects: absorption and scattering [Bean and Dutton, 1966]. At 13.9 GHz, the significant portion of this attenuation is due to atmospheric absorption. As the water particle size gets comparable to the wavelength the effects of scattering become more pronounced. Due to volume scattering, heavy clouds (large water content) or precipitating regions have more of a scattering effect than absorption. The relationship of the scattering and absorption of microwave signals has been extensively studied by Paris [1969]. For a clear sky, the major atmospheric gases that need to be considered as absorbers are oxygen and uncondensed water vapor. The variations of the absorption for these two gases with frequency, pressure, temperature and humidity are described by the Van Vleck theory of absorption [Van Vleck, 1947; Van Vleck and Weiskopf,

[1948]. Various modifications to the original terms appearing in Van Vleck's expressions have been incorporated [Meeks and Lilley, 1963; Barrett and Chung, 1962]. These modifications were based upon empirical results obtained through experimental measurements. Due to various reasons, most notable of which is the lack of total reproducibility of results, the empirical equations represent a best estimate. This fact, coupled with the difficulty of accurately profiling the pressure temperature and humidity causes results of any two researchers to often differ.

Ulaby et al [1974], in their report, cite numerous printing and calculation errors found in the abundance of literature that this subject has received. These can be misleading for an experimenter relying on an "established" model. Since the absorption of oxygen and water vapor is dependent upon the state of the atmosphere, high precision estimates of their effects would necessitate precise knowledge of the atmospheric temperature, pressure and humidity profiles. These are usually obtained by radiosonde soundings. Since radiosonde soundings are very often inconvenient and sometimes impossible to obtain for purposes of correcting for microwave signal distortions through the atmosphere, one must rely on the best estimate of the meteorological profiles. A key question to be asked at this stage is how much of an error will a person make if he only considers the ground temperature, pressure and humidity and models the profile according to some best fit? Clearly the error magnitudes for the case of the radiometer and the scatterometer signal are quite different. The range of attenuation for a clear sky (at 13.9 GHz) for nadir incidence can range from 0.1 to roughly 0.6 dB, for clouds from 0.1 to 1.6 dB, and for rain as much as 3-5 dB, or even more. The corresponding increase in antenna brightness temperature for an atmospheric temperature of 270° K can be 10° K for an attenuation of 0.1 dB.

The attenuation due to water vapor is directly proportional to the absolute humidity. The absolute humidity in gms/meter<sup>3</sup> can be as high as 25 gms/meter<sup>3</sup> (for a high temperature and a saturated atmosphere). In the following sections as we describe the formulae for computing the effects due to oxygen and water vapor, their dependence upon the meteorological parameters will be established.

The attenuation due to uncondensed water vapor is often minor in comparison to the attenuation due to clouds. The attenuation due to clouds is directly proportional to the liquid water content. The problem of computing the attenuation due to clouds is compounded by the fact that the clouds contain water in all three forms: uncondensed water vapor, condensed particles and ice. If one can clearly establish the cloud type,

amount (percentage of clouds above target cell), height and water content, one can apply established model equations to predict their effect. This estimation without radiosonde data or even simultaneous observations from the surface can be made with simultaneous imagery obtained from the sensor platform. If the only knowledge of clouds is through imagery, one can clearly see that any attempt to model the cloud type, etc., is reduced to an experienced judgment.

The most severe attenuation is due to condensed particles. This attenuation has another dimension to it, in that, as the drop sizes become significant with respect to a wavelength, the return signal will be dominated by volume scatter from the rain rather than the actual target. The attenuation due to rain is computed either by empirical methods (based on rainfall rate) or by estimating the terminal velocity, probability density function of drop-size diameter and the density function of rain drops. The latter method is more sophisticated and considers solutions as in Mie's volume scattering theory.

The emission contribution by the atmosphere is proportional to the attenuation constant and the physical temperature of the various layers of the atmosphere. The formulation of the problem is very much like that of estimating the contribution due to a lossy waveguide or circulator. The first step is to compute the attenuation coefficient (based upon the meteorological conditions and the empirical models); the next step is to modify the signal strength as it passes through each layer of the atmosphere. The equation used is the integral form of the equation of radiative transfer as described in chapter three.

### 5.1.2 Attenuation and Emission for the S-193 Radiometer/Scatterometer

Since the S-193 transmitter and receiver (for the scatterometer case) have the same orientation to the target (neglecting the slight displacement due to vehicle velocity and antenna slew), the atmospheric loss factors for the transmit and receive signal paths are the same. The one-way atmospheric loss factor,  $L$ , can be written as

$$L = \exp \left[ R/h \int_0^h \alpha(z) dz \right] \quad (2)$$

where  $R$  = slant range (due to oblique incidence)

$h$  = height of spacecraft

$\alpha(z)$  = attenuation coefficient/unit height at height

This formulation, especially the integral, considers a flat horizontal stratification of the atmosphere that is homogeneous in the horizontal plane. The attenuation coefficient  $\alpha(z)$ , is a function of height and decays rapidly with increasing height. The atmosphere does not contribute any significant amount beyond a height of 30 kms (even

for precise measurements). The limits on the integral can therefore be set at 30 kms. Sample calculations have shown that L for an integration carried out to 30 kms is very slightly different from that for an integration carried out to 20 kms. The factor R/h takes into account the fact that the signal passes through more of the atmosphere at any incidence angle greater than zenith.

At 13.9 GHz, and for the range of incidence angles encountered for the S-193 case, the refractive effects of the atmosphere can be ignored. The implications of homogeneity in a horizontal plane is used in translating the zenith case attenuation to that for a slant range. This implies a homogeneity over greater distances as the height above the earth increases. For example, at an incidence angle of  $52.5^\circ$  (the maximum angle expected for the S-193 case), the homogeneity conditions require the atmosphere to be constant for  $(h \tan 37.5^\circ)$  at height h. Fortunately, the atmosphere is most variable and significantly more absorptive (emissive) at low heights. The concentrations of absorbing constituents stabilizes as one reaches the troposphere.

The meteorological conditions of the atmosphere can be expressed as a change in the absorption coefficient. The total absorption of the atmosphere can be considered as the sum of the absorptions due to individual constituents of the atmosphere. Therefore,

$$\alpha(z) = \alpha_{O_2}(z) + \alpha_{H_2O}(z) + \alpha_{CLOUD}(z) + \alpha_{RAIN}(z) + \alpha_{HAIL}(z) \quad (3)$$

For a clear sky, only the first two terms of the right-hand side are required. Of the many atmospheric profile models researchers have used, one possible model, which follows the ARDC standard for temperature and pressure and modifications to it for the water vapor concentration has been compared in this study to actual radiosonde data obtained for four very differing atmospheric conditions. The details are provided later in the report. The aim of this exercise was to determine the errors introduced by considering a modeled profile rather than an actual measured profile in computing the effects of the atmosphere for a clear sky case. The minimum and maximum values of attenuation for various limiting conditions of the atmosphere (clear sky) were computed. The effects of pressure and temperature on the absorption due to oxygen and water vapor were explored.

The atmospheric model invoked and the empirical equations used to compute  $\alpha_{O_2}$  and  $\alpha_{H_2O}$  are described below. These formulae have been reproduced here from work done by Dr. F. T. Ulaby.

### 5.1.3 Clear Sky Model Atmosphere

The temperature, pressure and humidity profiles encountered in the signal path will greatly influence the total absorption or emission due to the atmosphere. One

possible atmospheric model that can be invoked is given below.

$$P(h) = P_0 \exp(-h/a) \quad (4)$$

$$T(h) = \begin{cases} T_0 - b_1 h & 0 \leq h \leq 11 \text{ kms} \\ T_{11} & 11 \leq h \leq 25 \text{ kms} \\ T_{11} + b_2(h-25) & 25 \leq h \leq 47 \text{ kms} \end{cases} \quad (5)$$

and the water vapor density proposed by Malkevich [1963]

$$f(h) = \begin{cases} f_0 \exp(-h/c_1) & 0 \leq h \leq 16 \text{ kms} \\ f_{16} \exp\left(\frac{h-16}{c_2}\right) & 16 \leq h \leq 31 \text{ kms} \end{cases} \quad (6)$$

where  $a = 7 \text{ km}$ ,  $b_1 = 6.5^\circ/\text{km}$ ,  $b_2 = 3.0^\circ/\text{km}$ ,  $C_1 = 2.1 \text{ km}$  and  $C_2 = 4.2 \text{ km}$ .  $P_0$ ,  $T_0$  and  $f_0$  are the pressure, temperature and humidity at the surface.

If either of the profiles, temperature or pressure, are known with a certain amount of confidence, the other can be computed from the equations of state and the equation for hydrostatic balance as follows.

$$dP = -\rho_A g dh \quad (7)$$

$$P = \rho_A R_A T \quad (8)$$

where  $\rho_A$  = air density

$g$  = gravitational constant

$R_A$  = gas constant for air

Dividing (7) by (8) we get

$$\frac{dP}{P} = -g/R_A T dh \quad (9)$$

Now  $P$ ,  $T$  are functions of  $h$ . Therefore integrating from surface to height  $h$  and pressure  $P_1$  to  $P_2$  we have

$$\int_{P_1}^{P_2} \frac{dP}{P} = -\frac{g}{R_A} \int_0^h \frac{1}{T(h')} dh' \quad (10)$$

If the temperature profile is known, say  $T(h) = T_0 - \gamma h$   
then equation (10) becomes

$$\ln(P_2/P_1) = -\frac{g}{R_A} \cdot \frac{1}{\gamma} \ln(T_0 - \gamma h)$$

$$P_2 = P_1 (T_0 - \gamma h)^{-\frac{g}{R_A \gamma}} \quad (11)$$

therefore the pressure profile can be estimated.

The standard atmospheric profile using surface parameters obtained from radiosonde soundings was compared to profiles measured by radiosonde soundings over four diverse atmospheric conditions. These profiles were provided by courtesy of Dr. V. Cardone at CUNY, New York. A cyclone was centered at 51 N, 50 W on May 12, 1972. A ship located in the warm front obtained sample A (warm front, Figure 5.1). Due to ascending warm air along the frontal surface, there were temperature and humidity inversions. At the same time there were soundings obtained from another ship in the warm sector (Figure 5.2), but with a cold front to the northwest. This sample, designated B (warm sector) had cool dry air. The third sample (C) was obtained from the Azores (Figure 5.3), located on the east side of the subtropical high. The fourth sample (D) is a typical air mass of the tropics and this sounding was obtained at Swan Island (Figure 5.4). The air is very hot and humid in the surface layers and very cold at the tropopause. The temperature gradient is very large. Two sample radiosonde measurements over the Topeka, Kansas, area one on June 21 at 12:00 hrs. GMT (6:30 a.m.) and the other at 00 hrs. GMT (6:30 p.m.) were also included. The sky was partly cloudy for the first radiosonde measurements and was heavily overcast for the second. These two profiles of pressure versus temperature are shown in Figures 5.5 and 5.6 compared to a standard (modelled) profile.

The following sections provide the formulae used to compute the absorption due to oxygen and water vapor, they are not dependent on any particular profile. The values of temperature, pressure and humidity at each point are inserted into the equations to compute the absorption coefficient.

#### 5.1.4 Water Vapor Absorption

The basic equation for the absorption due to a single line in the microwave region as given by Van Vleck and Weisskopf [1948] is:

$$\Gamma(\nu, \nu_{ij}) = (10^6 \log_{10} e) \frac{8\pi^3}{3hcG} \frac{N\nu}{G} |\mu_{ij}|^2 \frac{[\exp(-E_j/kT) - \exp(-E_i/kT)]}{f(\nu, \nu_{ij})} \quad (12)$$

where  $\Gamma(\nu, \nu_{ij})$  is the attenuation at frequency  $\nu$  (Hz) due to an absorption line centered at  $\nu_{ij}$  (Hz) in dB/km,  $E_i$  and  $E_j$  are the energies of states  $i$  and  $j$  in ergs,  $N$  is the number of absorbing molecules/c.c.,  $\mu_{ij}$  is the dipole matrix element connecting states  $i$  and  $j$ ,  $G$  is the rotational partition function,  $f(\nu, \nu_{ij})$  is the line-shape function,  $T$  is the temperature in  $^{\circ}K$ , and  $h$ ,  $k$ , and  $c$  are Planck's constant, Boltzman's constant, and the velocity of light, respectively, all in c.g.s. units.

$f(\nu, \nu_{ij})$ ,  $N$ , and  $|\mu_{ij}|^2$  may be expressed as follows:

$$f(\nu, \nu_{ij}) = \frac{1}{\pi} \frac{\nu}{\nu_{ij}} \left[ \frac{\Delta \nu_{ij}}{(\nu_{ij} - \nu)^2 + \Delta \nu_{ij}^2} + \frac{\Delta \nu_{ij}}{(\nu_{ij} + \nu)^2 + \Delta \nu_{ij}^2} \right] \quad (13)$$

$$N = 9.66 \times 10^{18} P/T = 3.35 \times 10^6 p \quad (14)$$

$$|\mu_{ij}|^2 = s_{ij} g_{ij} |\mu_0|^2 \quad (15)$$

where  $\Delta \nu_{ij}$  is the line width at half intensity in Hz,  $P$  is the atmospheric pressure in mm.Hg,  $p$  is the water vapor density in gm/m<sup>3</sup>,  $s_{ij}$  is the line strength (dimensionless)  $g_{ij}$  is a weighting factor accounting for nuclear spin [King et al, 1947] (has the value 1 or 3), and  $\mu_0$  is the dipole moment of the water molecule =  $1.94 \times 10^{-18}$  e.s.u. [Rogers, 1954]. The partition function  $G$  may be considered proportional to  $T^{3/2}$  and its value at 293°K was evaluated to be 170 [Van Vleck, 1947]. Hence, for any temperature  $T$ ,  $G$  may be expressed as:

$$G = 0.034 T^{3/2} \quad (16)$$

Since  $h\nu_{ij} = E_i - E_j$ , the expression inside the bracket in Equation (12) may be written as:

$$\left[ \exp(-E_j/kT) - \exp(-E_i/kT) \right] = \exp(-E_i/kT) \cdot \left[ \exp(h\nu_{ij}/kT) - 1 \right] \quad (17)$$

Furthermore, for transitions where  $h\nu_{ij}/kT \ll 1$  is satisfied, the above equation reduces to:

$$\left( h\nu_{ij}/kT \right) \cdot \exp(-E_i/kT) \quad (18)$$

The above low frequency approximation is valid for all lines below about 350 GHz and temperatures below about 350°K. Substituting Equation (16) into Equation (12)

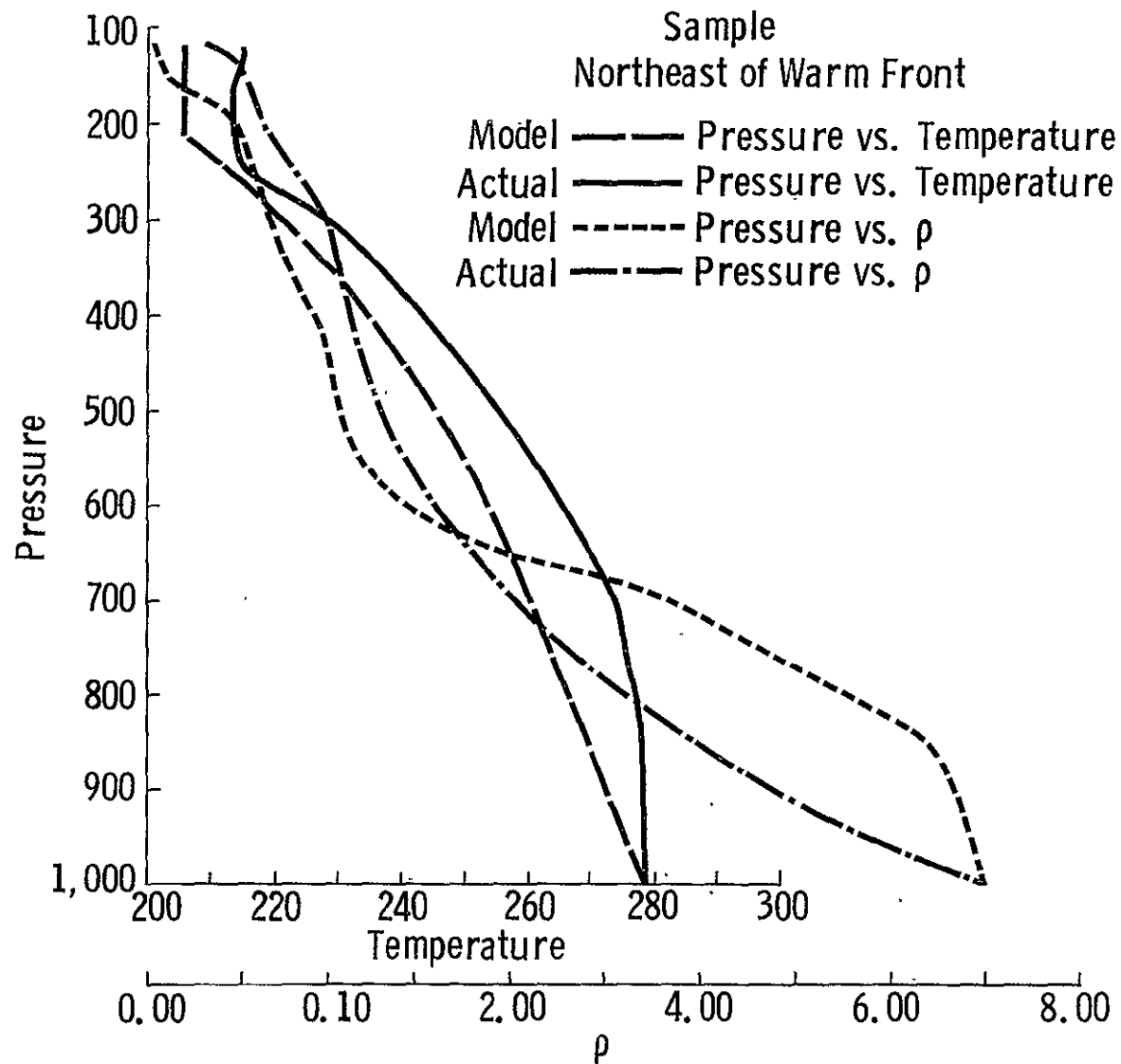


Figure 5.1. Radiosonde and model profiles of samples from northeast of warm front.

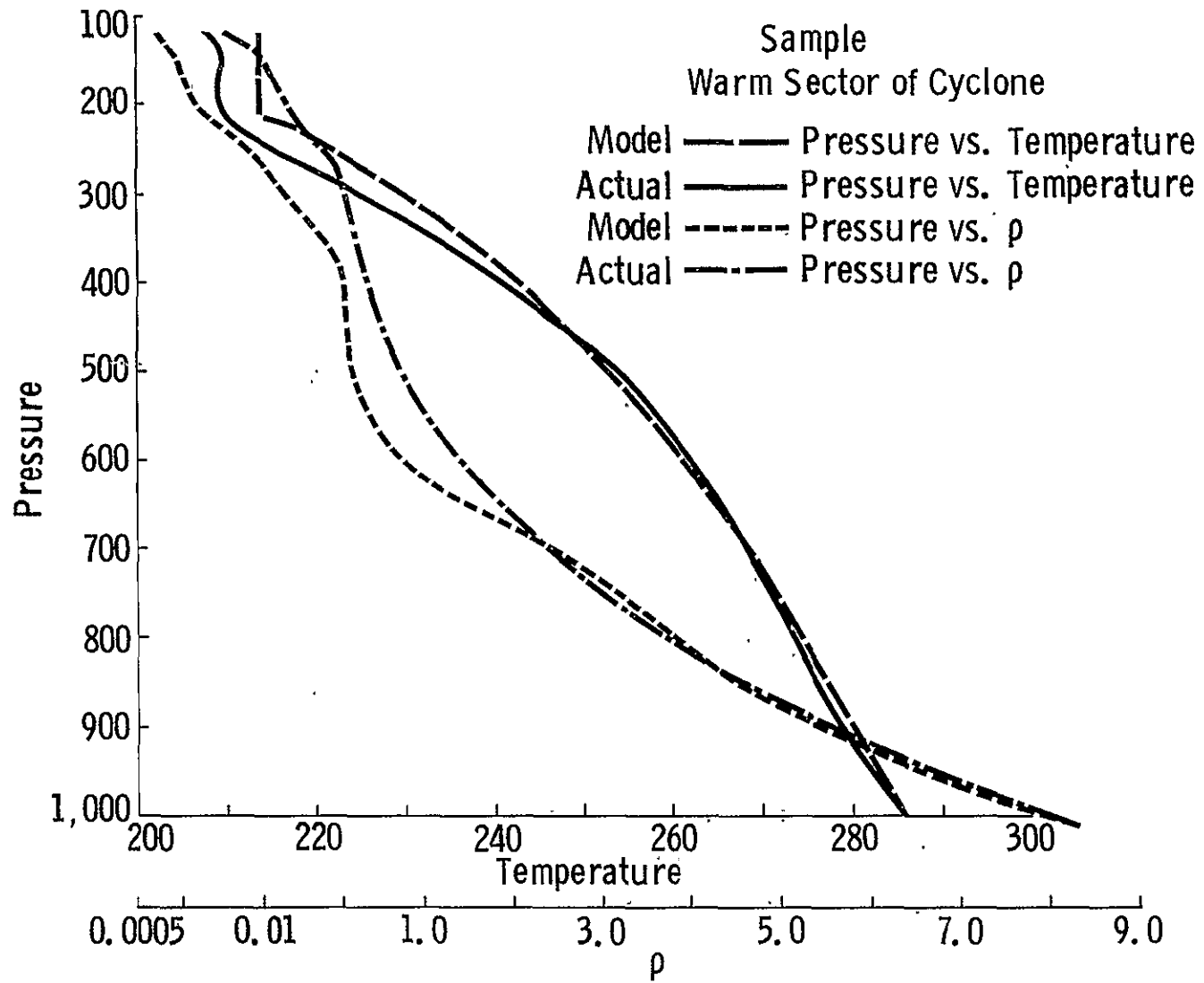


Figure 5.2. Radiosonde and model profiles of sample from warm sector of cyclone.

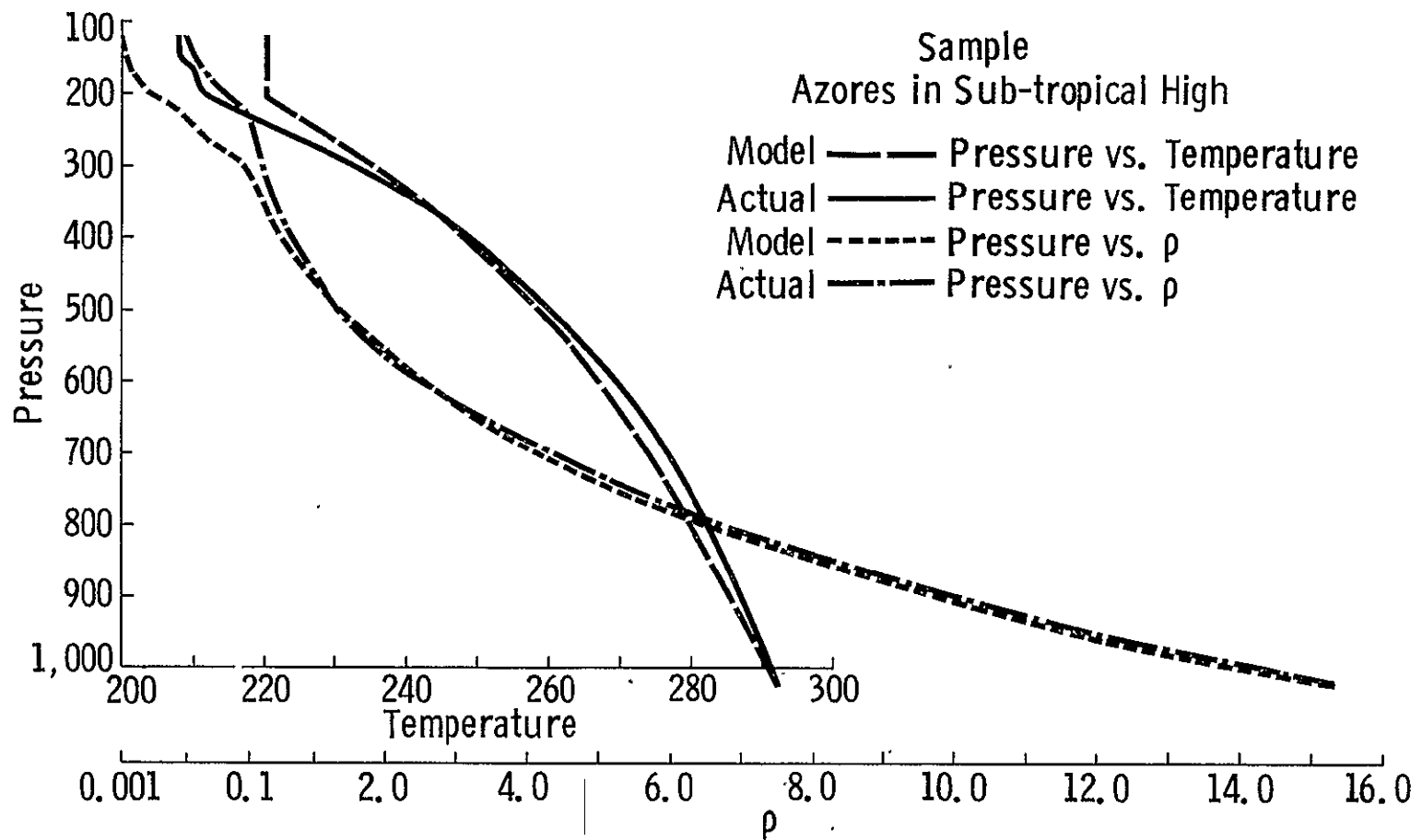


Figure 5.3. Radiosonde and model profiles of sample from Azores in sub-tropical high.

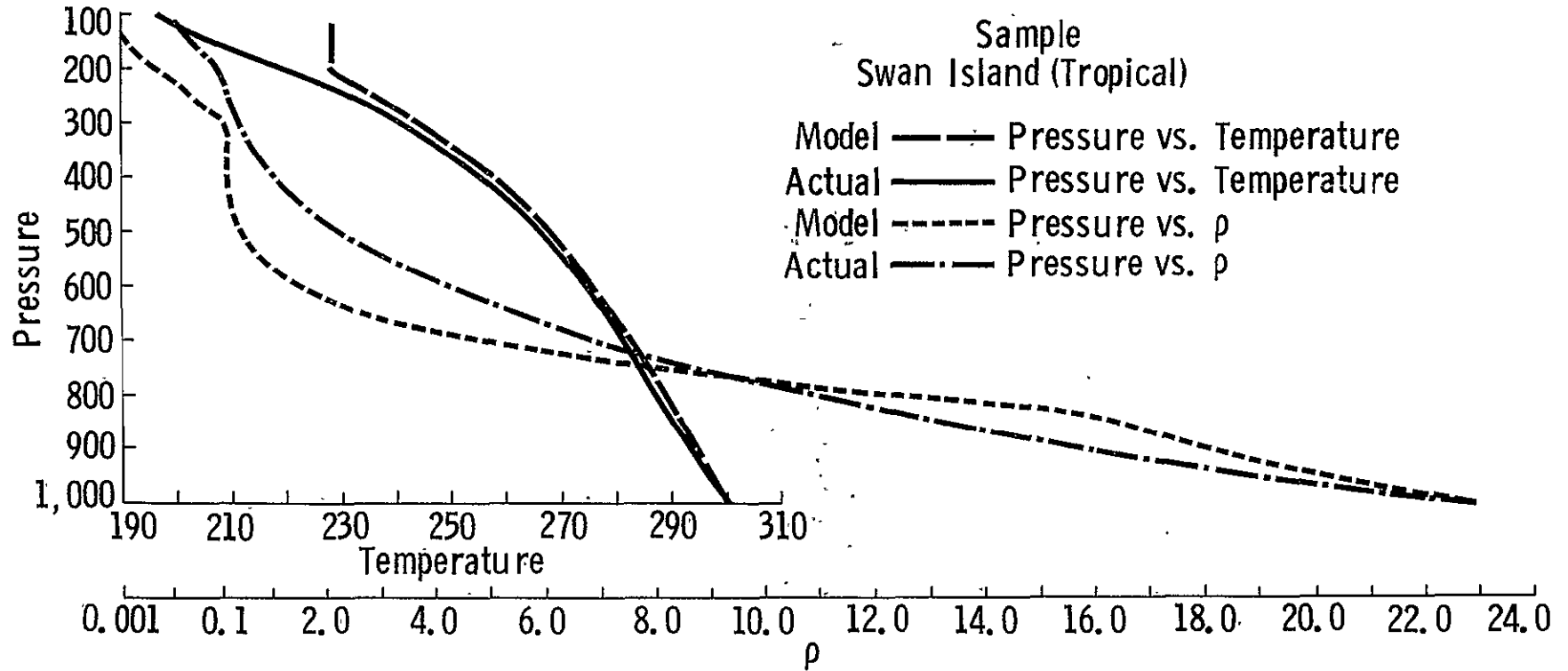


Figure 5.4. Radiosonde and model profiles of sample from Swan Island (tropical).

PRESSURE Vs. TEMPERATURE  
 TOPEKA RADIOSONDE PROFILE AND  
 CORRESPONDING MODEL PROFILE  
 JUNE 21, 1972 AT 12.00 HRS. (GMT)

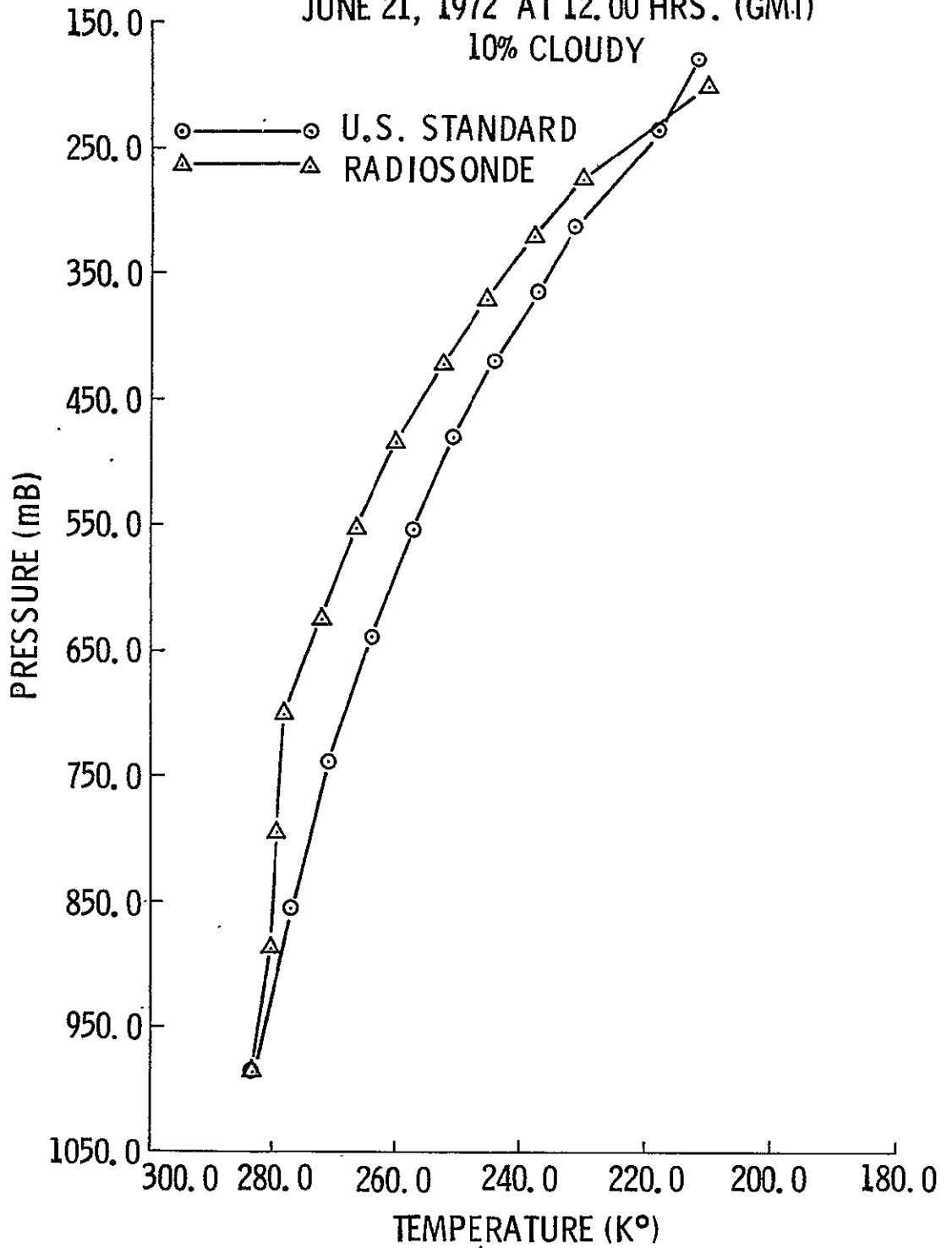


Figure 5.5.

PRESSURE Vs. TEMPERATURE  
 FOR TOPEKA RADIOSONDE  
 AND CORRESPONDING MODEL PROFILE  
 JUNE 22, 1972 AT 0.00 HRS (GMT)  
 OVERCAST SKY

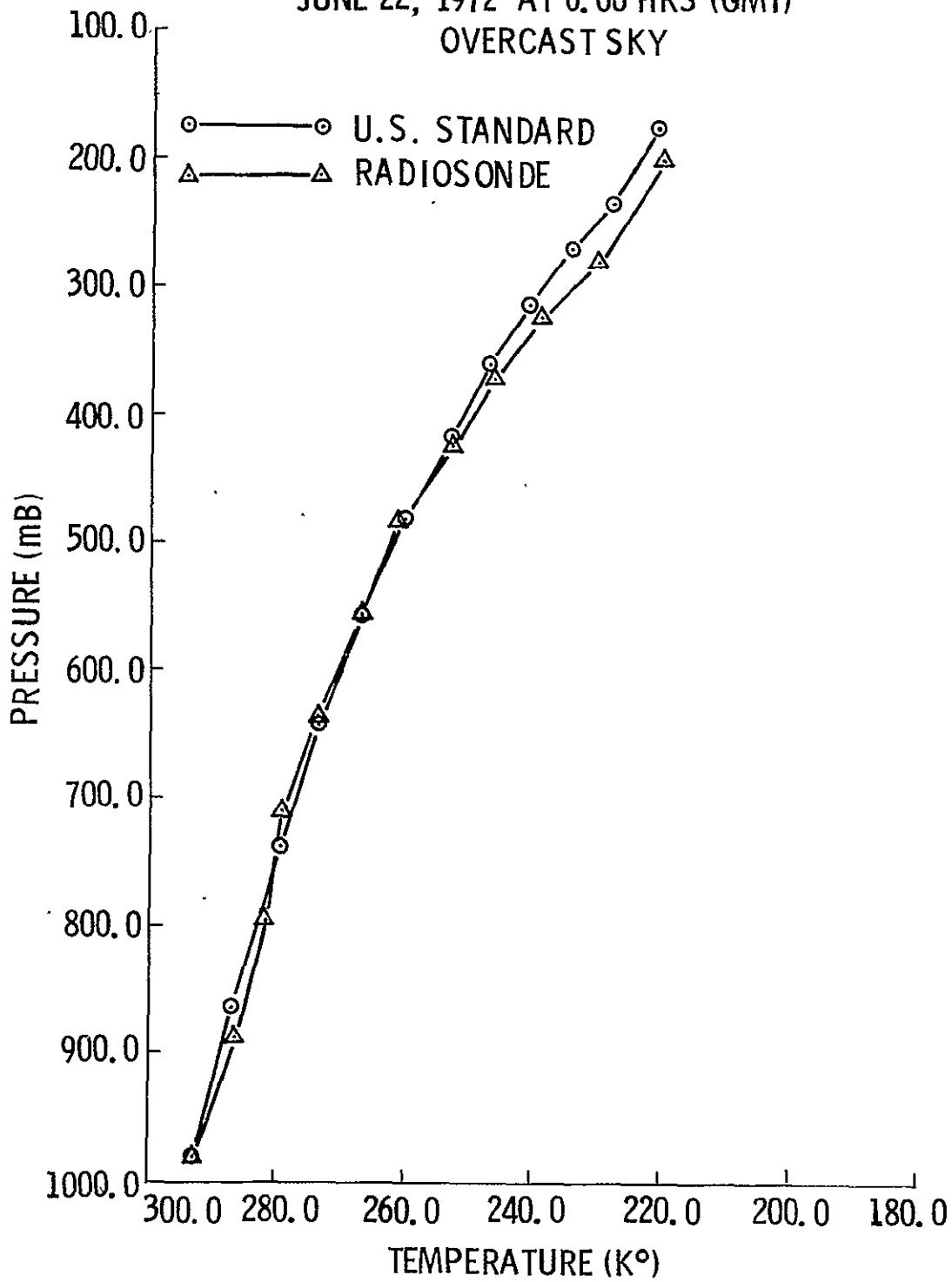


Figure 5.6.

and expressing  $\nu$ ,  $\nu_{ij}$  and  $\Delta\nu_{ij}$  in GHz yields:

$$\Gamma_w(\nu, \nu_{ij}) = 1.02 \times 10^4 \frac{\rho \nu^2}{T^{5/2}} s_{ij} g_{ij} \exp(-E_i/kT) \cdot \left[ \frac{\Delta \nu_{ij}}{(\nu - \nu_{ij})^2 + \Delta \nu_{ij}^2} + \frac{\Delta \nu_{ij}}{(\nu + \nu_{ij})^2 + \Delta \nu_{ij}^2} \right] \quad (19)$$

For the 22.235 GHz line the line parameters assume the following values:

$$\begin{aligned} \nu_{ij} &= 22.235 \text{ GHz} \\ s_{ij} &= .0549 \text{ [King et al. (1947)]} \\ g_{ij} &= 3 \text{ [King et al. (1947)]} \\ E_i/K &= 644 \text{ [Dennison (1940)]} \end{aligned}$$

Equation (19) thus reduces to:

$$\Gamma_w(\nu, 22.235) = 1.68 \times 10^3 \frac{\rho \nu^2}{T^{5/2}} \exp(-644/T) \left[ \frac{\Delta \nu}{(\nu - 22.235)^2 + \Delta \nu^2} + \frac{\Delta \nu}{(\nu + 22.235)^2 + \Delta \nu^2} \right] \quad (20)$$

Benedict and Kaplan [1959] have calculated the half-width and the temperature coefficient exponent of all significant transitions of the water molecule in the microwave and infrared regions of the spectrum. Becker and Autler [1946] studied the pressure dependence at 318°K. The combined effects have been formulated by Barrett and Chung [1962] as:

$$\Delta \nu = 2.62 \frac{P/760}{(T/318)^{0.625}} [1 + .0046 P] \quad (21)$$

### 5.1.5 Residual Absorption

The absorption due to a single water vapor line centered at frequency  $\nu_{ij}$  is given by Equation (12). In 1947, Van Vleck calculated the residual absorption due to water vapor lines whose resonances are at wavelengths shorter than 1.35 cm, the closest of which is the 183.3 GHz line. His treatment, which assumed a low-frequency approximation ( $\nu \ll \nu_{ij}$ ) in which the part inside the last bracket in Equation (19) reduces to:

$$\left[ \frac{\Delta \nu_{ij}}{(\nu - \nu_{ij})^2 + \Delta \nu_{ij}^2} + \frac{\Delta \nu_{ij}}{(\nu + \nu_{ij})^2 + \Delta \nu_{ij}^2} \right] \approx \frac{2 \Delta \nu_{ij}}{\nu_{ij}^2} \quad (22)$$

including contributions from all lines up to  $j = 6$ , inclusive, but excluding the 1.35 cm line ( $j$  is the rotational quantum number). His results may be expressed in the following form:

$$\Gamma_R(\nu) = 2.15 \times 10^{-3} \frac{\rho \nu^2 \Delta \nu}{T^{3/2}} \text{ dB/km} \quad (23)$$

Discrepancies between experimental and calculated attenuation values have led to further examination of the approximations used in deriving Equation (23). A refined form suggested by Zhavakin and Naumov [1963, 1964] yields a residual attenuation factor about four times larger than the Van Vleck [1947] expression, in closer agreement with experimental values. This form has been adopted by several investigators [Porter, 1969, 1972; Shifrin, 1968] and will be used in this report:

$$\Gamma_R'(\nu) = 1.11 \times 10^{-2} \frac{\rho \nu^2 \Delta \nu}{T^{3/2}} \text{ dB/km} \quad (24)$$

Except for the units, Staelin's [1965] expression for the residual water vapor absorption term is identical to Equation (24). The reference he gives for his expression is Barrett and Chung [1962] who used Equation (23).

#### 5.1.6 Total Water Vapor Absorption

The total water vapor absorption in dB/km is given by

$$\Gamma_w(\nu) = \Gamma(\nu, 22.235) + \Gamma_R(\nu) \quad (25)$$

where  $\Gamma(\nu, 22)$  and  $\Gamma_R(\nu)$  have been defined in Equations (20) and (24).

### 5.1.7 Oxygen Absorption

Following the same basic procedure outlined earlier for water vapor, the oxygen absorption coefficient can be expressed in dB/km as [Meeks and Lilley, 1963].

$$\Gamma_{\text{ox}}(\nu) = 2.6742 \frac{P\nu^2}{T^3} \sum_{N_{\text{odd}}} [F_{N_+} \mu_{N_+}^2 + F_{N_-} \mu_{N_-}^2 + F_0 \mu_{N_0}^2] \cdot A_N \quad (26)$$

where,

$$F_{N_{\pm}} = \left[ \frac{\Delta\nu}{(\nu_{N_{\pm}} - \nu)^2 + \Delta\nu^2} + \frac{\Delta\nu}{(\nu_{N_{\pm}} + \nu)^2 + \Delta\nu^2} \right] \quad (27)$$

$$F_0 = \frac{\Delta\nu}{\nu^2 + \Delta\nu^2} \quad (28)$$

$$\mu_{N_+}^2 = \frac{N(2N+3)}{N+1} \quad (29)$$

$$\mu_{N_-}^2 = \frac{(N+1)(2N-1)}{N} \quad (30)$$

$$\mu_{N_0}^2 = \frac{2(N^2+N+1)(2N+1)}{N(N+1)} \quad (31)$$

$$A_N = \exp(-2.068 N(N+1)/T) \quad (32)$$

and  $\mu_{\pm N}$  are listed in Table 5.1.

Although the empirical expression for  $\Delta\nu$  given by Meeks and Lilley [1963] has been used throughout the literature, more recent and extensive results by Carter et al [1968] suggest a more accurate form:

$$\Delta\nu = g(h) \left( \frac{P}{P_0} \right) \left( \frac{T_0}{T} \right) \quad (33)$$

where  $P_0$  and  $T_0$  are the atmospheric pressure and temperature at the surface and

N+	N+ (GHz)	N-	N- (GHz)
1	56.2648	1	18.7505
3	58.4466	3	62.4863
5	59.5910	5	60.3061
7	60.4348	7	59.1642
9	61.1506	9	58.3239
11	61.8002	11	57.6125
13	62.4112	13	56.9682
15	62.9980	15	56.3634
17	63.5685	17	55.7839
19	64.1272	19	55.2214
21	64.6779	21	54.6728
23	65.2240	23	54.1294
25	65.7626	25	53.5960
27	66.2978	27	53.0695
29	66.8313	29	52.5458
31	67.3627	31	52.0259
33	67.8923	33	51.5091
35	68.4205	35	50.9949
37	68.9478	37	50.4830
39	69.4741	39	49.9737
41	70.0000	41	49.4648
43	70.5249	43	48.9582
45	71.0497	45	48.4530

Table 5.1

Rotational states for oxygen absorption  
After Meeks and Lilley [1963]

REPRODUCIBILITY OF THE  
ORIGINAL PAGE IS POOR

$$g(h) = \begin{cases} g_1 & 0 \leq h \leq h_1 \\ g_1 + (g_2 - g_1) \frac{(h - h_1)}{h_2 - h_1} & h_1 \leq h \leq h_2 \\ g_2 & h_2 \leq h \end{cases} \quad (34)$$

The numerical values are :  $g_1 = 0.640$  GHz,  $g_2 = 1.357$  GHz,  $h_1 = 8$  km and  $h_2 = 25$  km.

## 5.2 Clear Sky Atmosphere--Results

The oxygen and water vapor attenuation models were used on radiosonde data and modeled profiles to study the effects of pressure, temperature and humidity on attenuation. A comparison of the attenuation and emission between actual radiosonde data and modeled profiles was sought. The results are presented first for the effects of pressure, temperature and humidity on the atmospheric transmittance and attenuation.

Recalling from chapter three, from the equation of radiative transfer (eq. (3.8))

$$T_A(\theta, z) = e^{-\sec\theta \int_0^z \alpha(z') dz'} \left[ \epsilon(\theta) T_g + (1 - \epsilon(\theta)) \int_z^0 \alpha(z') T_M(z') e^{-\sec\theta \int_z^0 \alpha(z'') dz''} dz' \right] + \int_0^z \alpha(z') T_M(z') e^{-\sec\theta \int_z^z \alpha(z'') dz''} dz' \quad (35)$$

Since the sensors are at 435 kms and the atmosphere extends (significant portion only) to 30 kms, the integration on  $z$  is carried out to only 30 kms. The left-hand side is thus independent of  $z$ . The first factor on the right-hand side is called the atmospheric transmittance. It is a direct measure of the "transparency of the atmosphere." This transmittance is one of the parameters studied. The last quantity on the right-hand side is the upwelling direct radiation of the atmosphere towards the receiver. This quantity called  $T_{atm}$  is a measure of the emission from the atmosphere. The terms in the square bracket correspond to the radiation emitted by the surface ( $\epsilon(\theta)T_g$ ) and the reflected portion of the atmospheric radiation incident upon the surface towards the receiver. For the model studies where estimates of  $T_A$  are predicted (reported later in this chapter), the downward radiation of the atmosphere was almost similar to the upward radiation.

The attenuation due to oxygen was found to change insignificantly due to changes in pressure. The attenuation due to oxygen caused by changes in surface temperature are shown in figure 5.7. These attenuation values are one-way values in dB for the incidence angles at the Skylab receiver. As can be seen, the attenuation decreases with increasing temperature. At 270°K, for 48° incidence, the attenuation is 0.074 dB and the lowest value is at 0.0° for 310°K where it is 0.035 dB. From this figure, one can see that totally ignoring the effects of oxygen attenuation at 13.9 GHz can cause a relative error of  $(0.073 - 0.035) \times 2 = 0.076$  dB, an insignificant amount as compared to the errors introduced by the measuring system and possibly other atmospheric constituents.

The attenuation due to water vapor is a function of the water vapor content. For a fixed value of  $\rho$ , the water vapor in  $\text{gms}/\text{m}^3$  at the surface, the values of attenuation are given in Figures 5.8 - 5.13. The figures are for fixed values of  $\theta$  at the surface of 5.0, 8.0, 11.0, 14.0, 17.0 and 20.0  $\text{gms}/\text{m}^3$ . Each connected line is an eyeball fit for the five incidence angles on Skylab data. The attenuation due to fixed values of surface water vapor, decreases with the increase in surface temperature. The maximum one-way attenuation for the cases considered was 48° incidence for 270°K surface temperature and 20  $\text{gms}/\text{m}^3$  absolute humidity. This value was 0.13 dB, the minimum value was for nadir incidence and a surface temperature and humidity of 310.0°K and 5.0  $\text{gms}/\text{m}^3$  respectively; this value was 0.0165 dB. The maximum error, if one totally ignored the effects of attenuation due to water vapor for the radar signal would be 0.227 dB.

The emission and transmittance of the atmosphere as a function of surface water vapor content is shown in Figures 5.14 through 5.17. These figures show the transmittance and emission (right vertical axis) for the five incidence angles for Skylab data for a range of  $\rho$  from 1  $\text{gms}/\text{meter}^3$  to 19  $\text{gms}/\text{meter}^3$  for a specific surface temperature. The four surface temperatures considered are 293°K, 300°K, 310°K and 320°K. The transmittance is found to be rather indifferent to surface temperature and changes rapidly for increases in  $\rho$ . The integration to compute the attenuation coefficient was till 30km from the surface. Figure 5.18 shows the emission and transmittance vs. surface temperature for a fixed value of  $\rho (= 8 \text{ gm}^3)$ .

To see the difference between modeling the atmospheric profile based upon surface parameters and using actual radiosonde data, six sets of radiosonde soundings were used. Four radiosonde values obtained from NYU and two obtained from Dr. J. Eagleman (University of Kansas, Department of Geography and Meteorology) were included in the comparison. Figures 5.1 through 5.6 show comparisons of the actual and modelled profiles; a description of the sites has been provided above. Figures 5.19 through 5.24

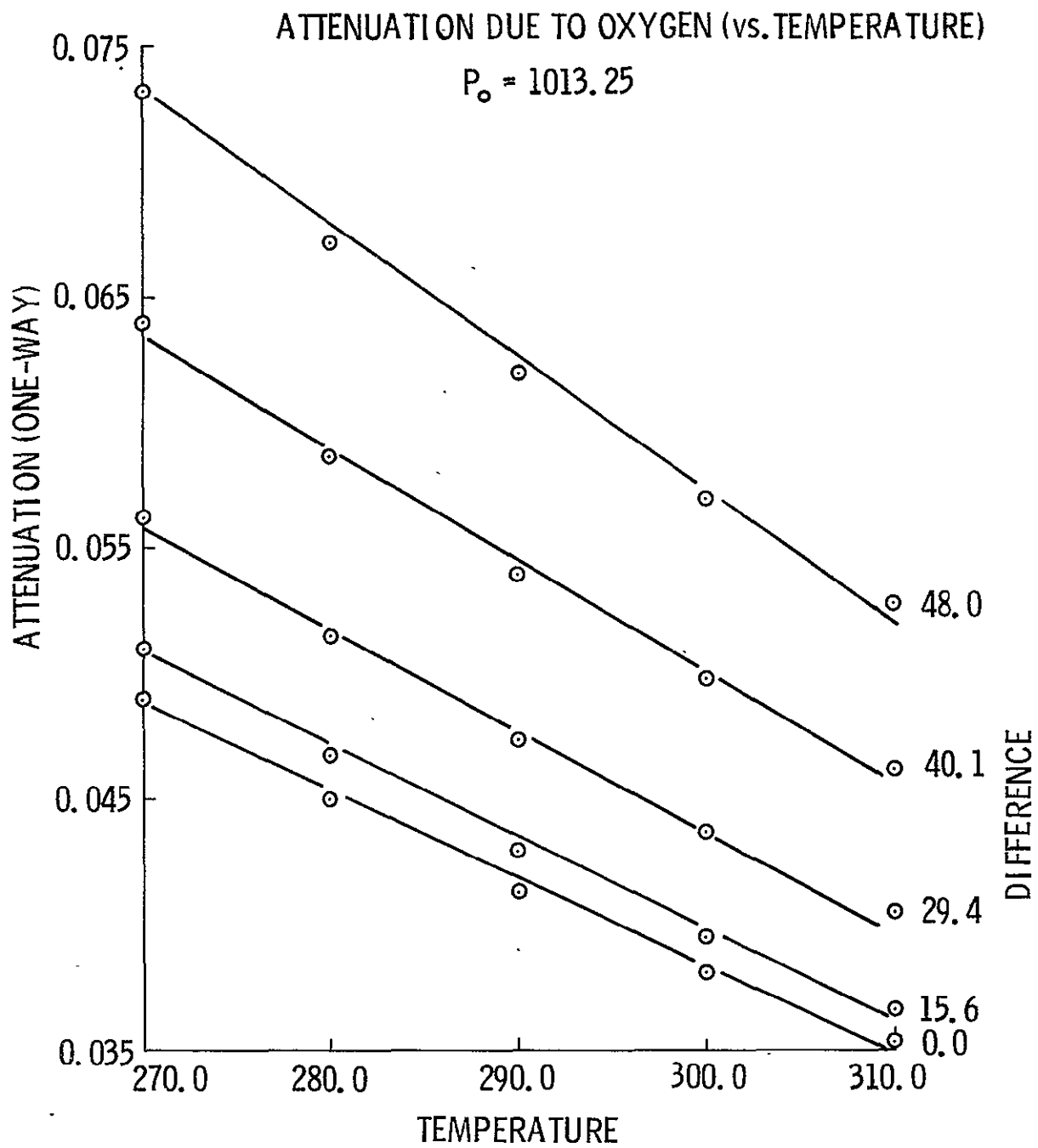


Figure 5.7.  
159

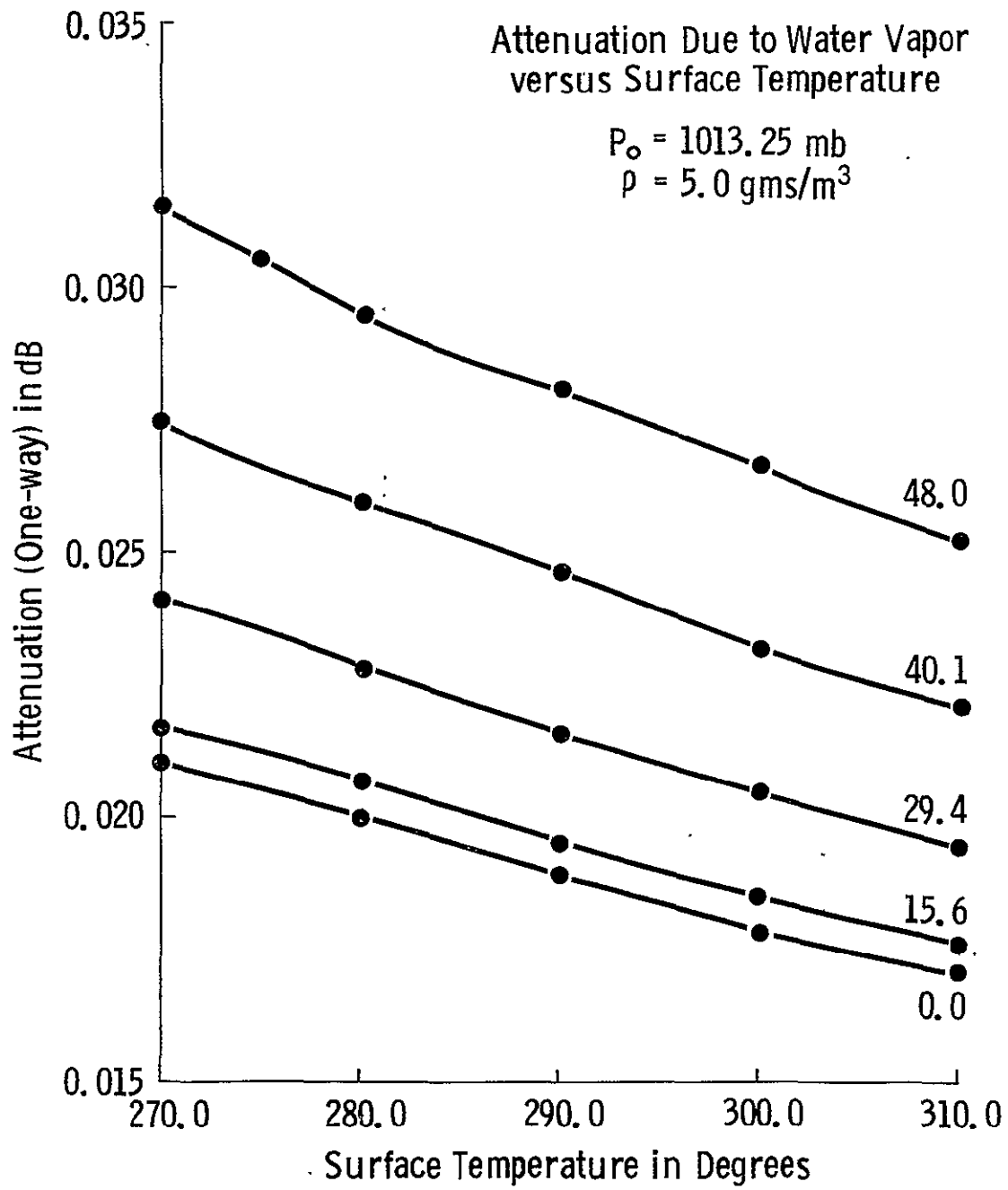


Figure 5.8.  
160

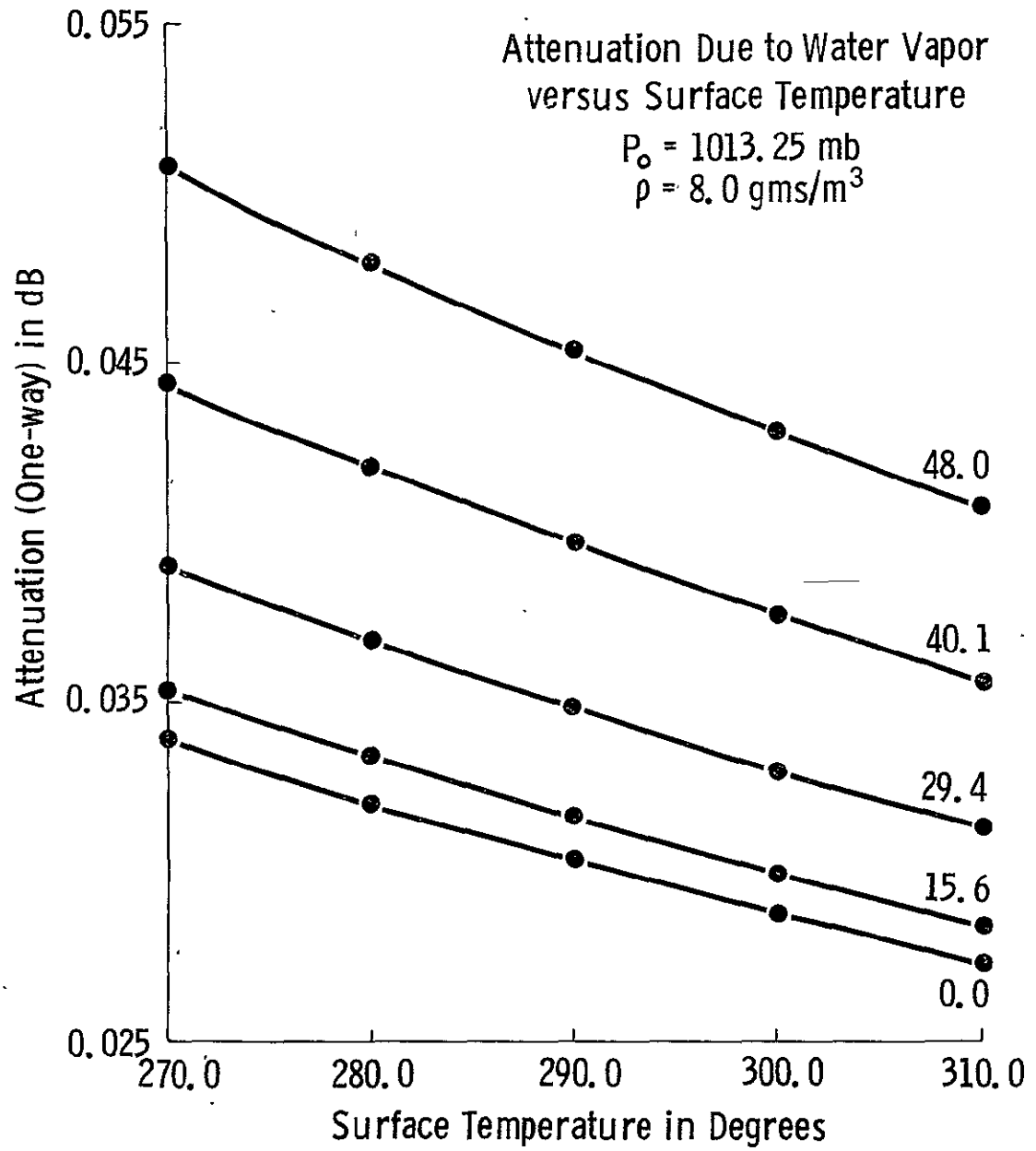


Figure 5.9.  
161

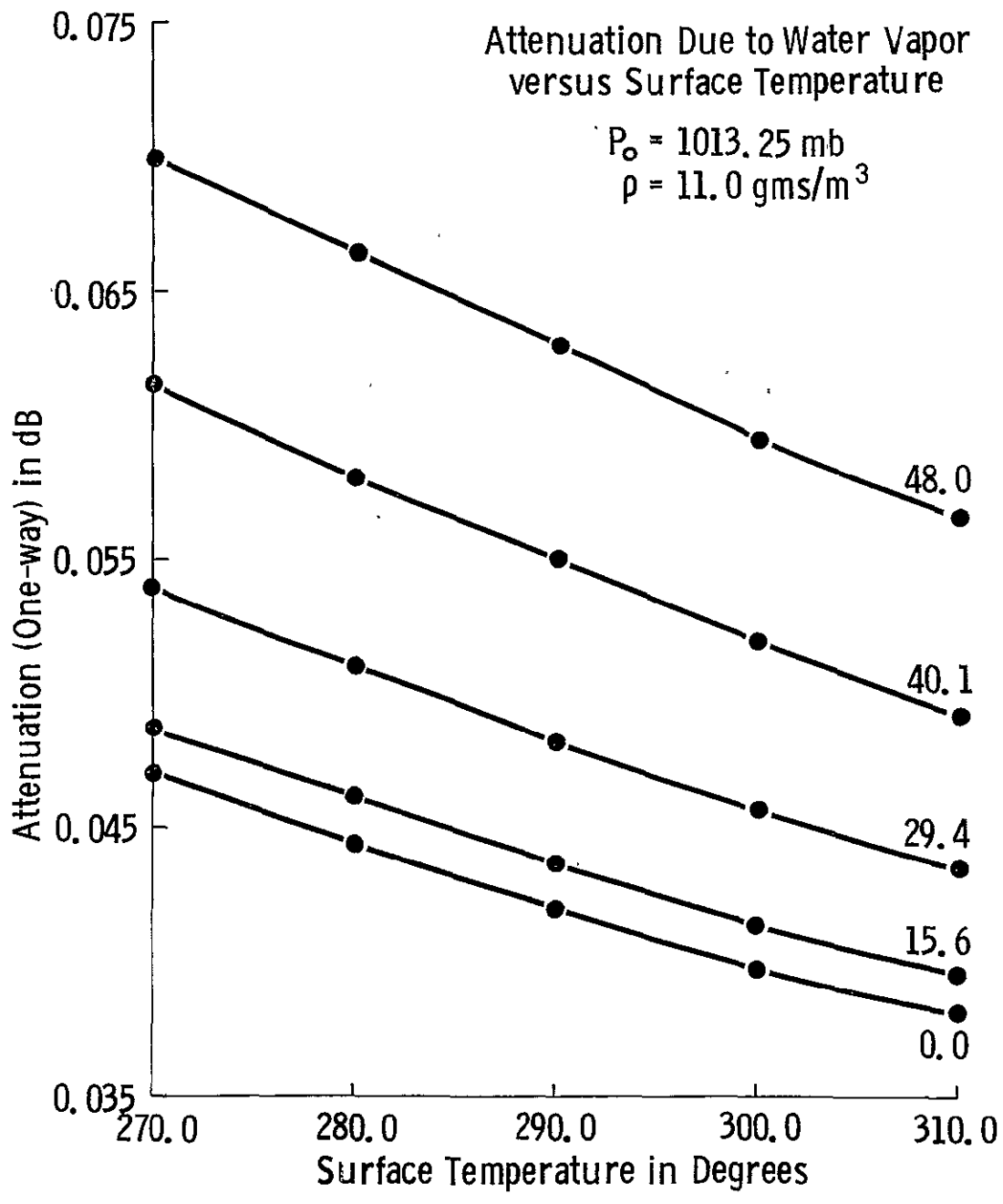


Figure 5.10.  
162

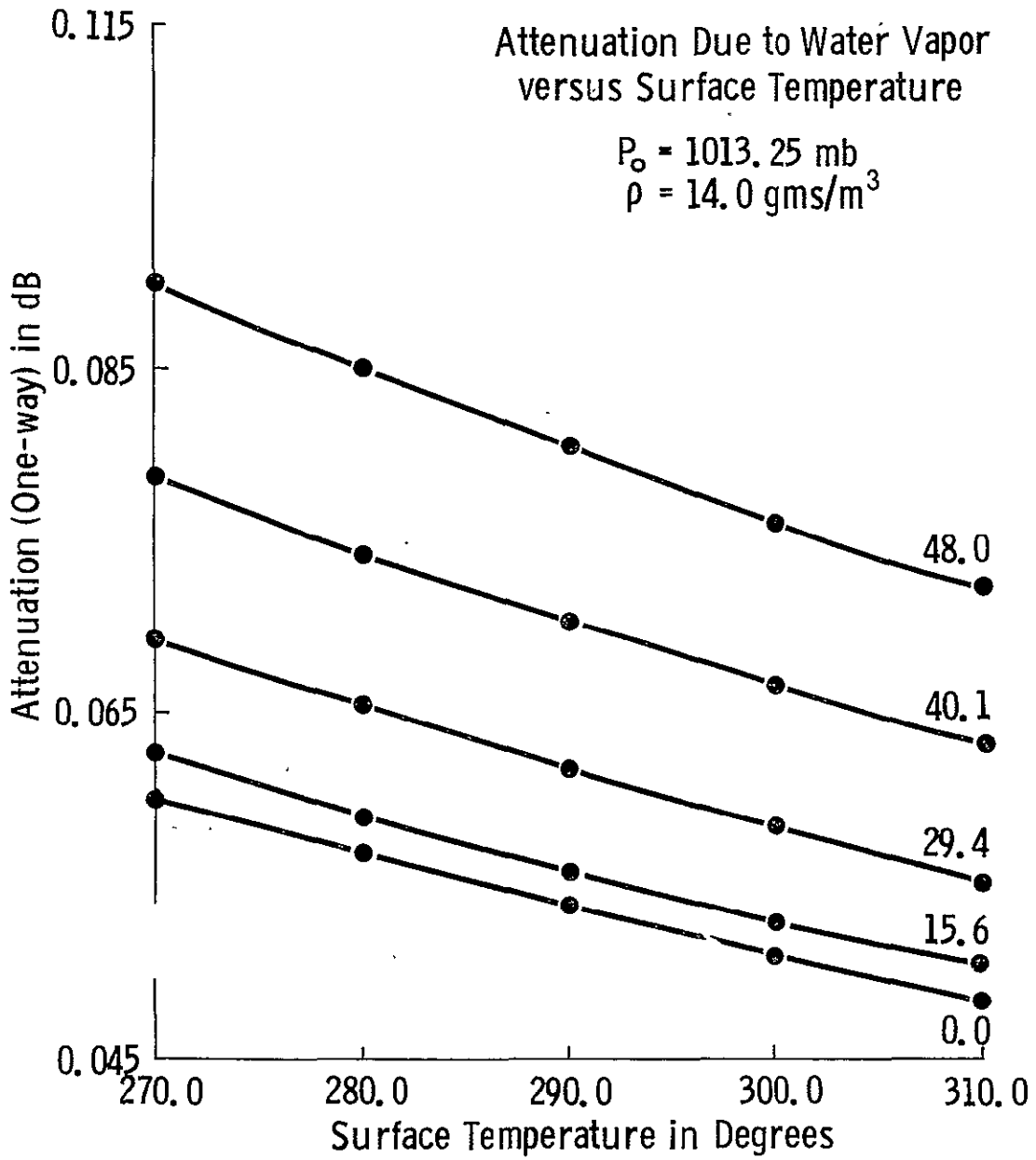


Figure 5.11.  
163

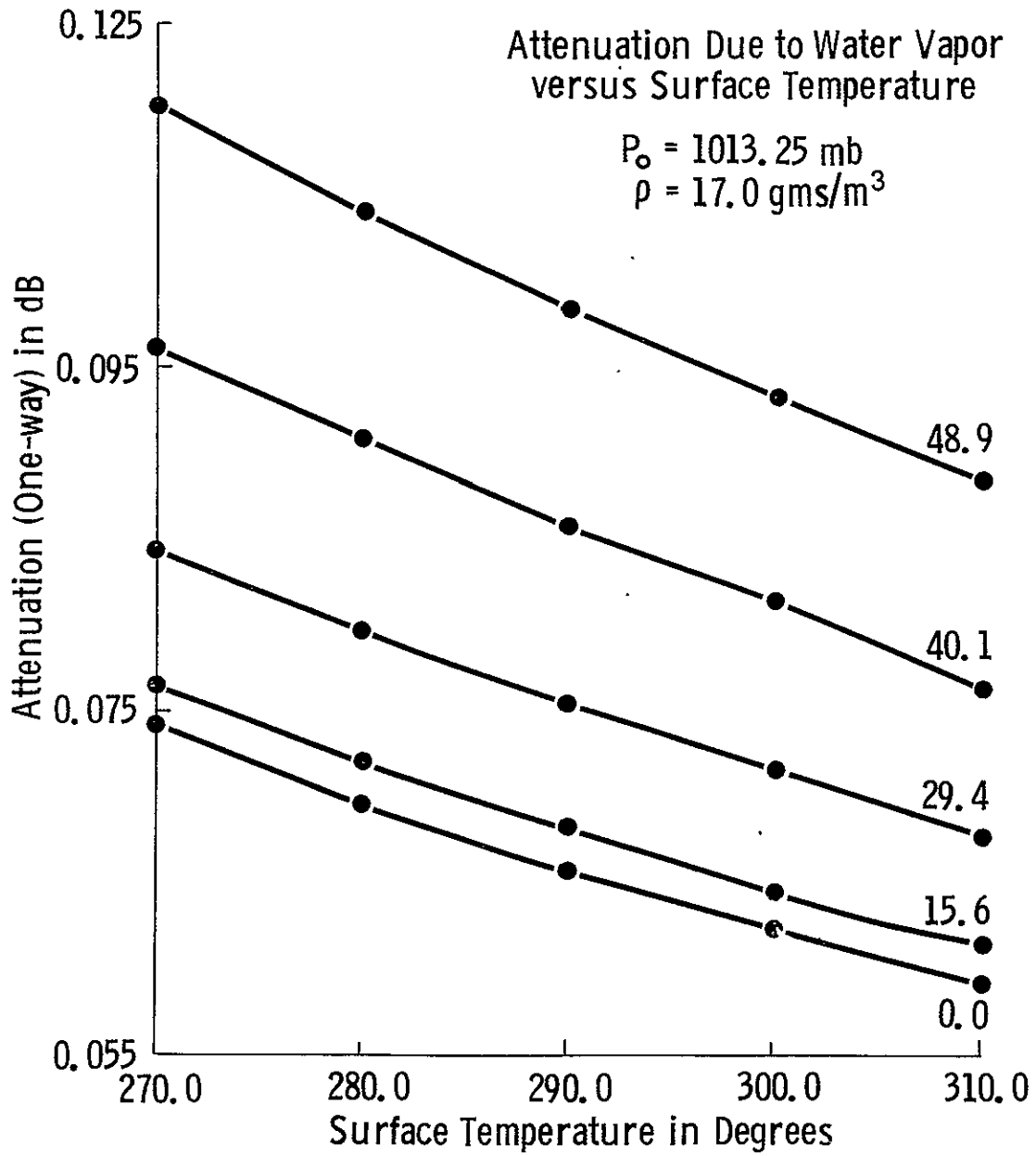


Figure 5.12.  
164

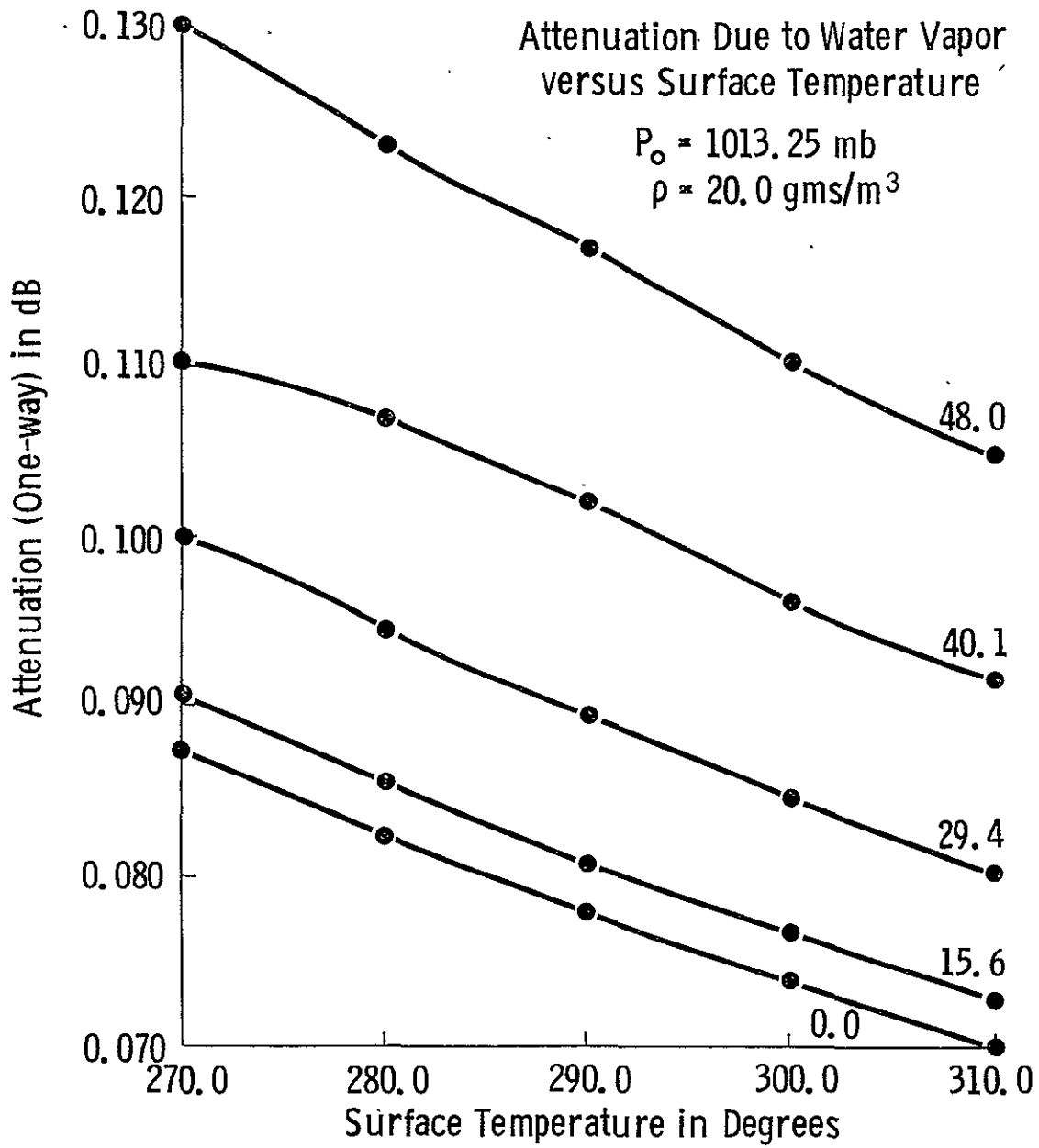


Figure 5.13.  
165

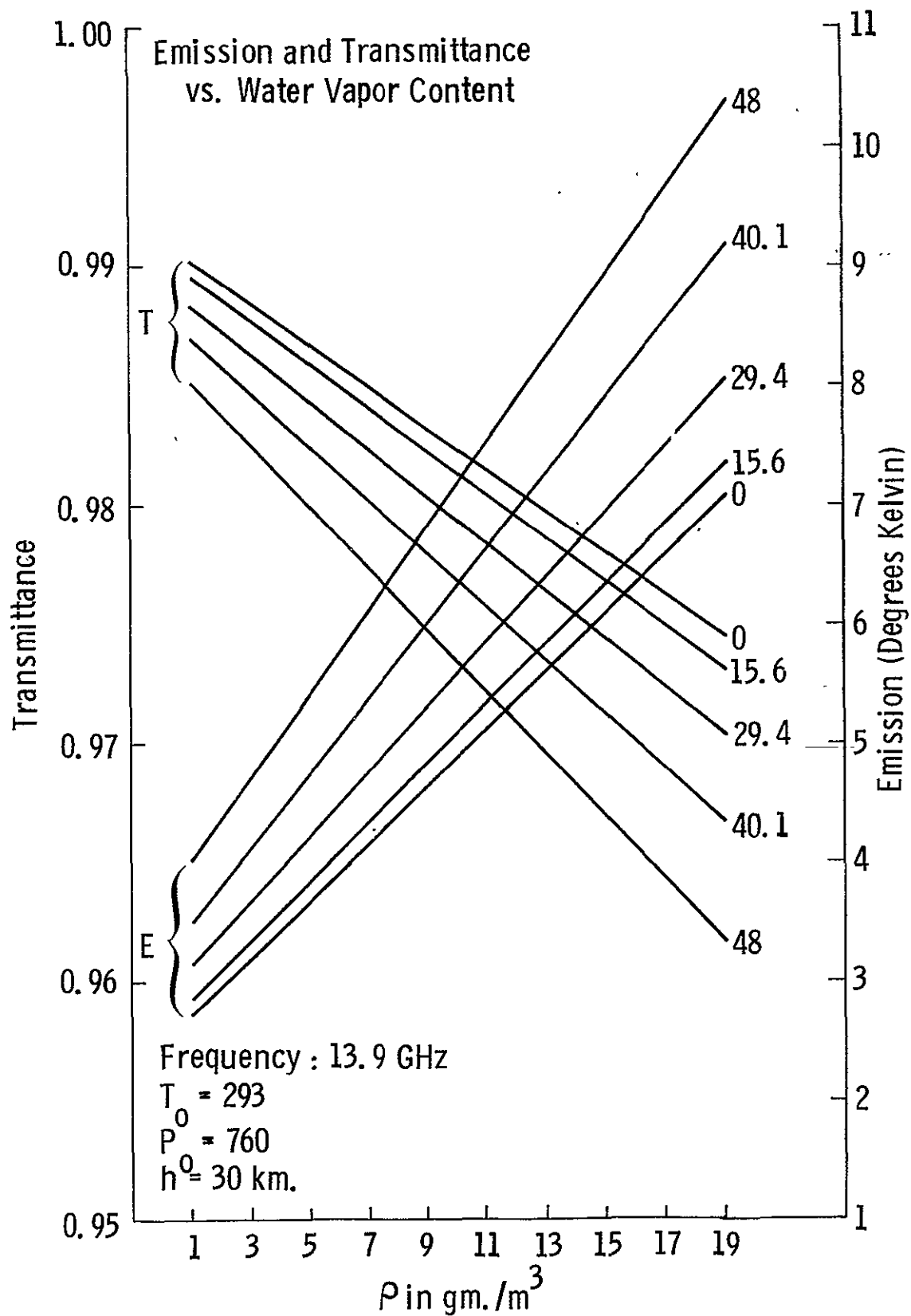


Figure 5.14.  
166

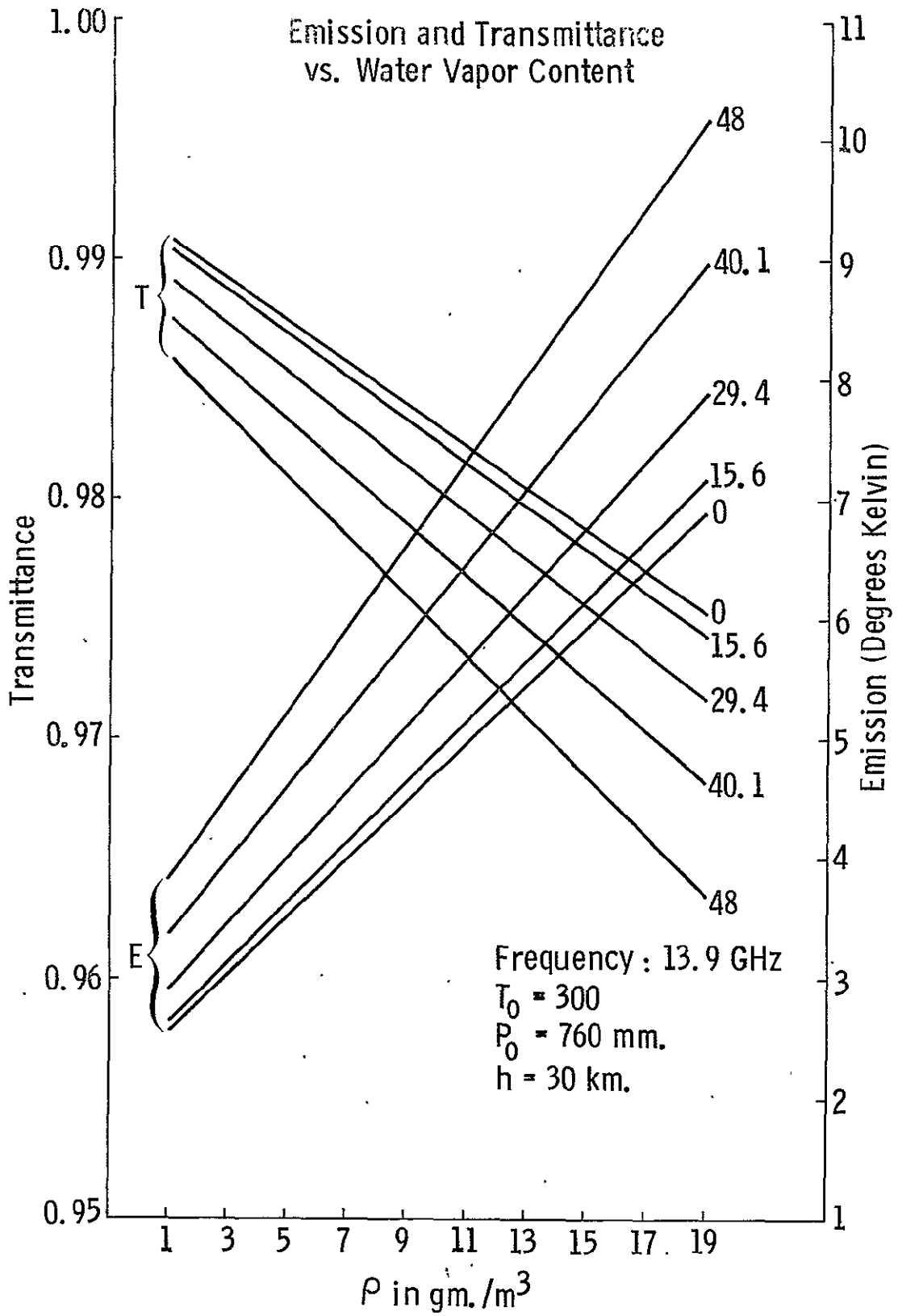


Figure 5.15.  
167

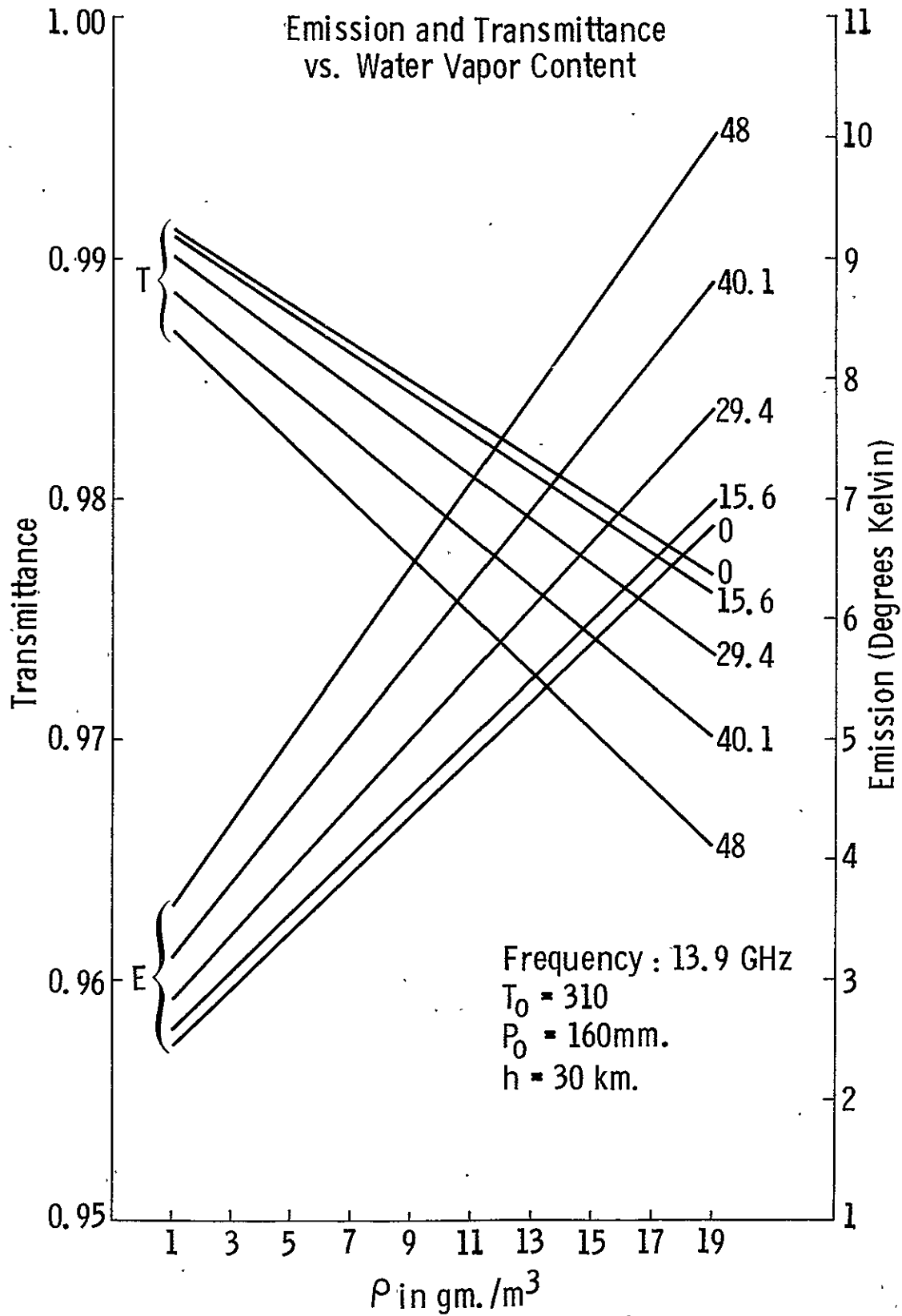


Figure 5.16.

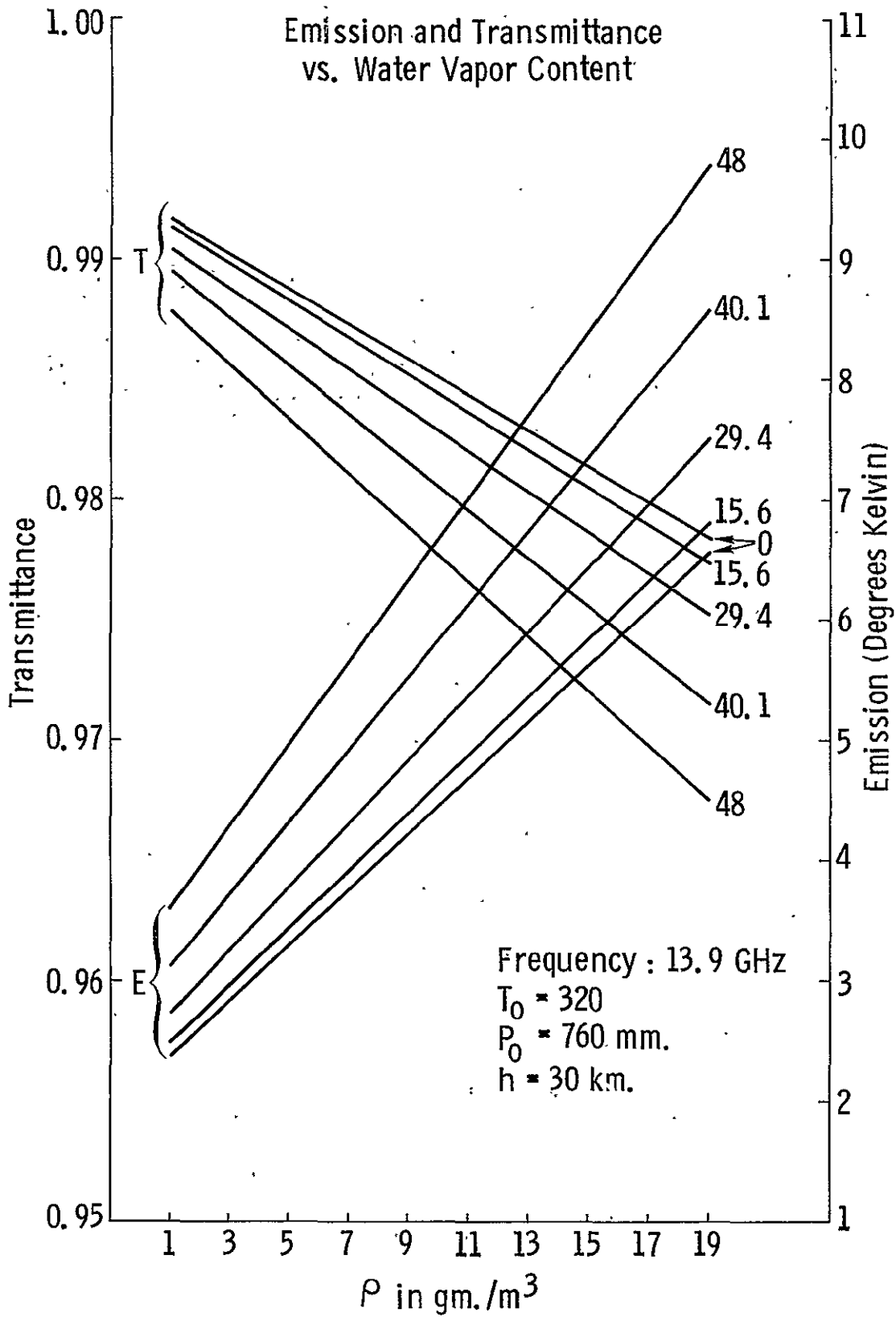


Figure 5.17.  
169

Emission and Transmittance vs. Surface Temperature

$\rho_{HO} = 8 \text{ gms./m}^3$

— Transmittance

● Emission

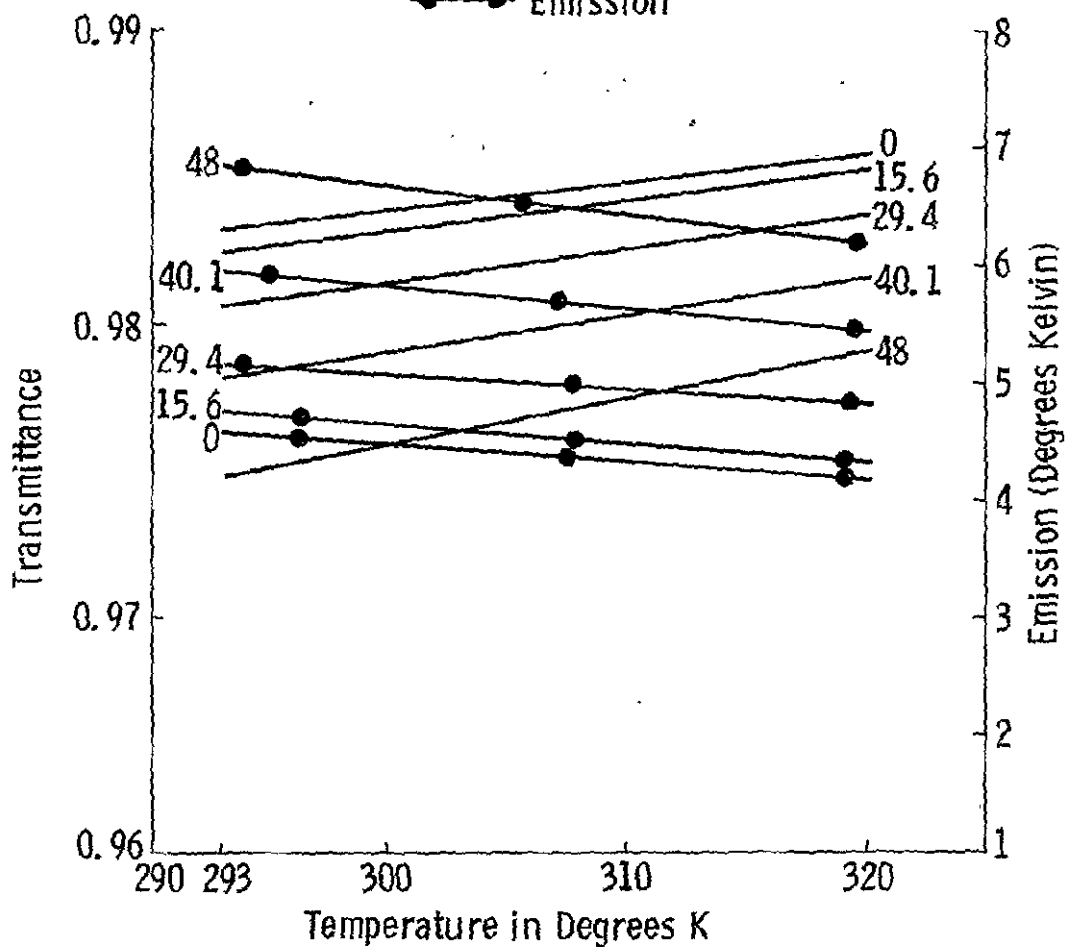


Figure 5.18.  
170

show the total transmittance computed from an integration over the actual profile and that computed from a model profile (called the U.S. Standard) for each of the six radiosonde soundings. The difference is given on the right-hand vertical axis. The maximum difference was only 0.0003. Boer [1962] has suggested some typical atmospheric models based upon geographic location and cloudy/clear sky conditions. The transmittance as computed according to his midlatitude profiles are compared to that computed for the actual profile for two samples shown in Figures 5.25 and 5.26. The errors in total transmittance are of opposite sign for the subtropical (Bermuda) high as compared to the U.S. Standard versus radiosonde.

The direct atmospheric contribution for these radiosonde data and the model profiles was examined. Figures 5.27 through 5.32 show the direct atmospheric emission using the radiosonde profile and the model profile and the difference in the two. The difference ranged from a minimum of  $0.21^\circ$  (at  $48^\circ$ ) for the Topeka June 21 sounding to a maximum of  $1.45^\circ$  (at  $48^\circ$ ) for the warm front soundings. The maximum could have been due to the fact that on this sounding there was evidence of a temperature and humidity inversion, which of course does not appear in the modelled profile. Figure 5.33 shows a comparison of the errors.

### 5.3. Attenuation and Emission Due to Clouds

The presence of clouds causes a change in the absorption coefficient. The amount of liquid water content is the most significant factor in computing the absorption due to clouds. It is not, however, the only factor; the temperature of the clouds can also be important for large variations in cloud temperatures. Once the amount of liquid water content, the temperature and extend of cloud thickness are known or estimated, models to compute the absorption coefficient can be applied. Since water content is not easily measured, the problem then becomes one of constructing meteorologically sound models for clouds based upon empirical data. This is the route most researchers have taken. Another factor that has hitherto not been a problem is the large resolution cell of a spacecraft based sensor. The assumption of homogeneity over a horizontal strata becomes rather hard to defend when the target cell measures over 20 kms across! One way to counteract this is to consider the percentage (fraction) of the target that is covered by clouds. One must realize that this fraction is only an observer's best estimate from examination of simultaneous imagery or meteorological reports if available. Once this fraction is estimated the effects due to clouds, i.e., the absorption coefficient due to clouds, is multiplied by this fraction to compute the actual effects to due to clouds.

TOTAL TRANSMITTANCE COMPUTED  
FOR ACTUAL RADIOSONDE PROFILE  
AND MODEL PROFILE (WARM FRONT)

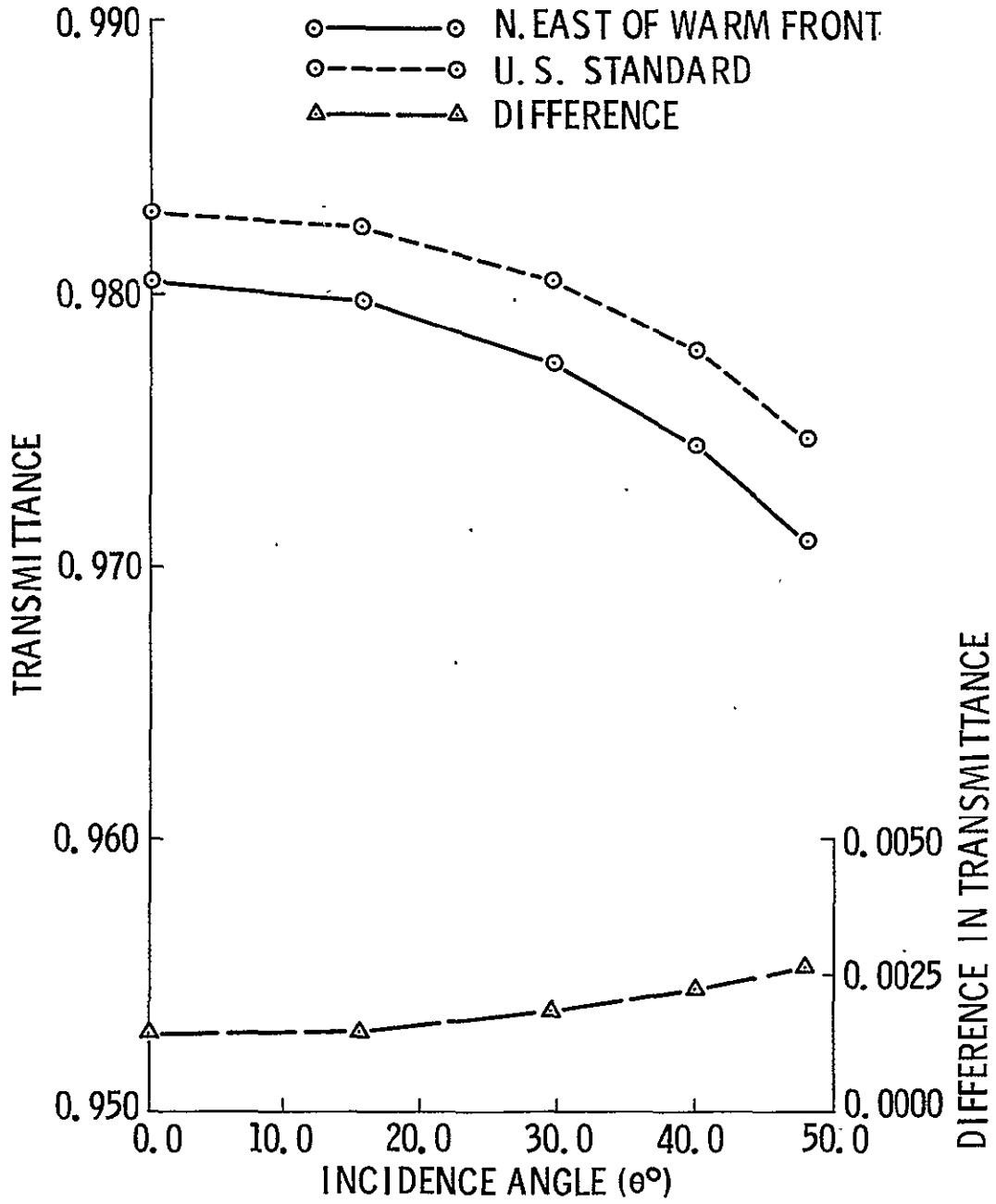


Figure 5.19.  
172

TOTAL TRANSMITTANCE COMPUTED  
FOR ACTUAL RADIOSONDE  
AND MODEL PROFILE (WARM SECTOR)

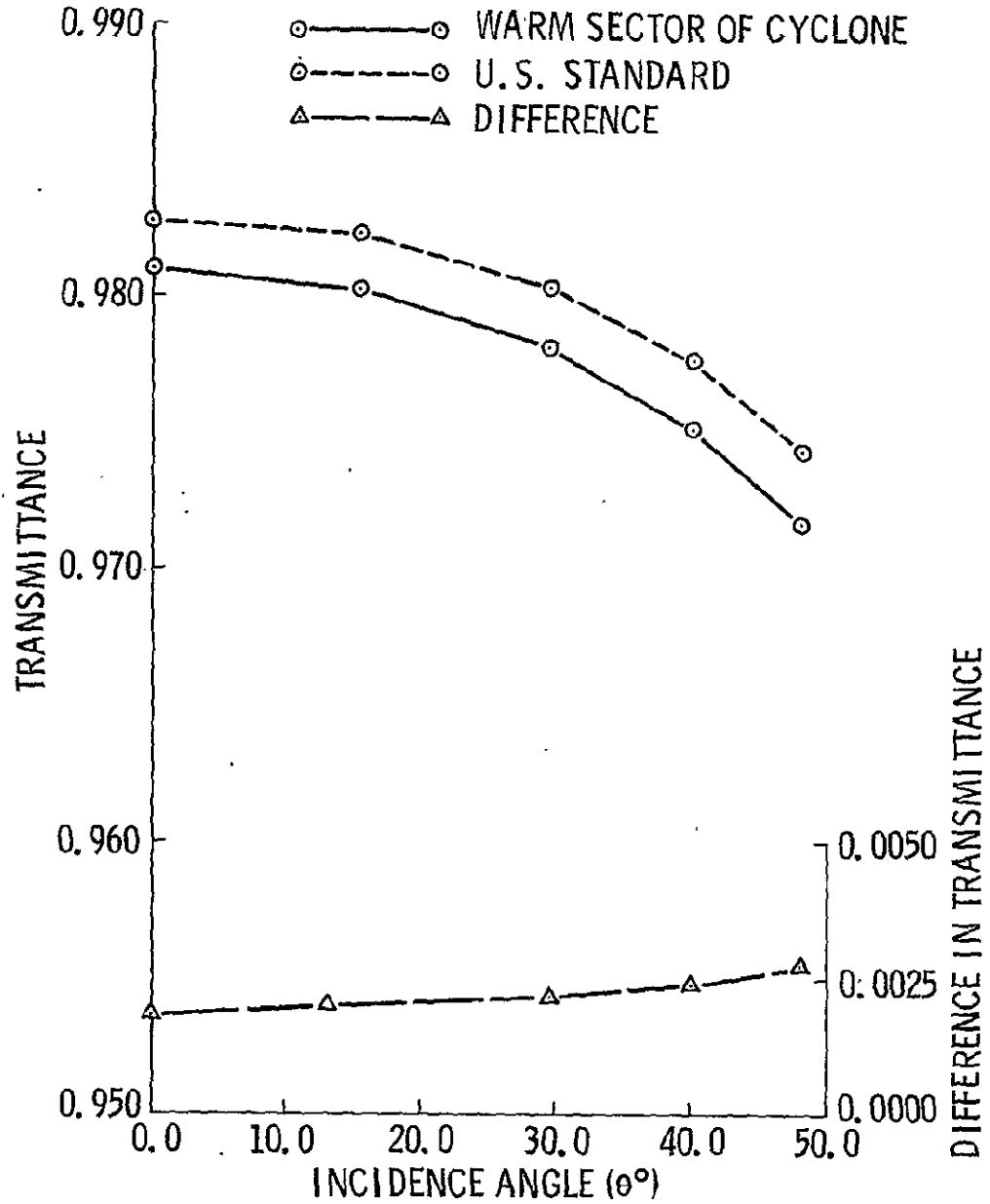


Figure 5.20.  
173

TOTAL TRANSMITTANCE COMPUTED  
FOR ACTUAL RADIOSONDE PROFILE  
AND MODELLED PROFILE (FOR BERMUDA HIGH)

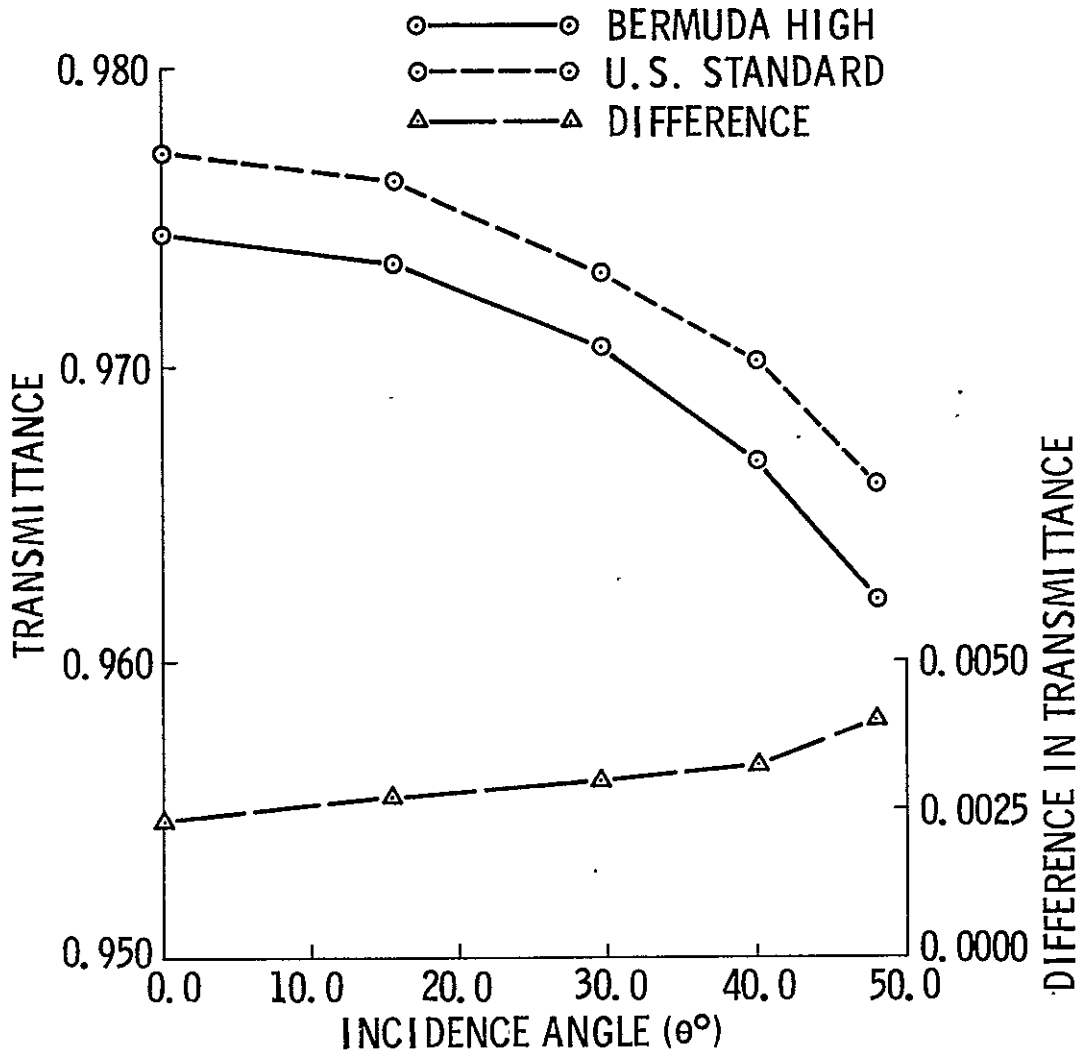


Figure 5.21.  
174

TOTAL TRANSMITTANCE COMPUTED  
FOR ACTUAL RADIOSONDE PROFILE  
AND MODEL PROFILE (SWAN ISLAND)

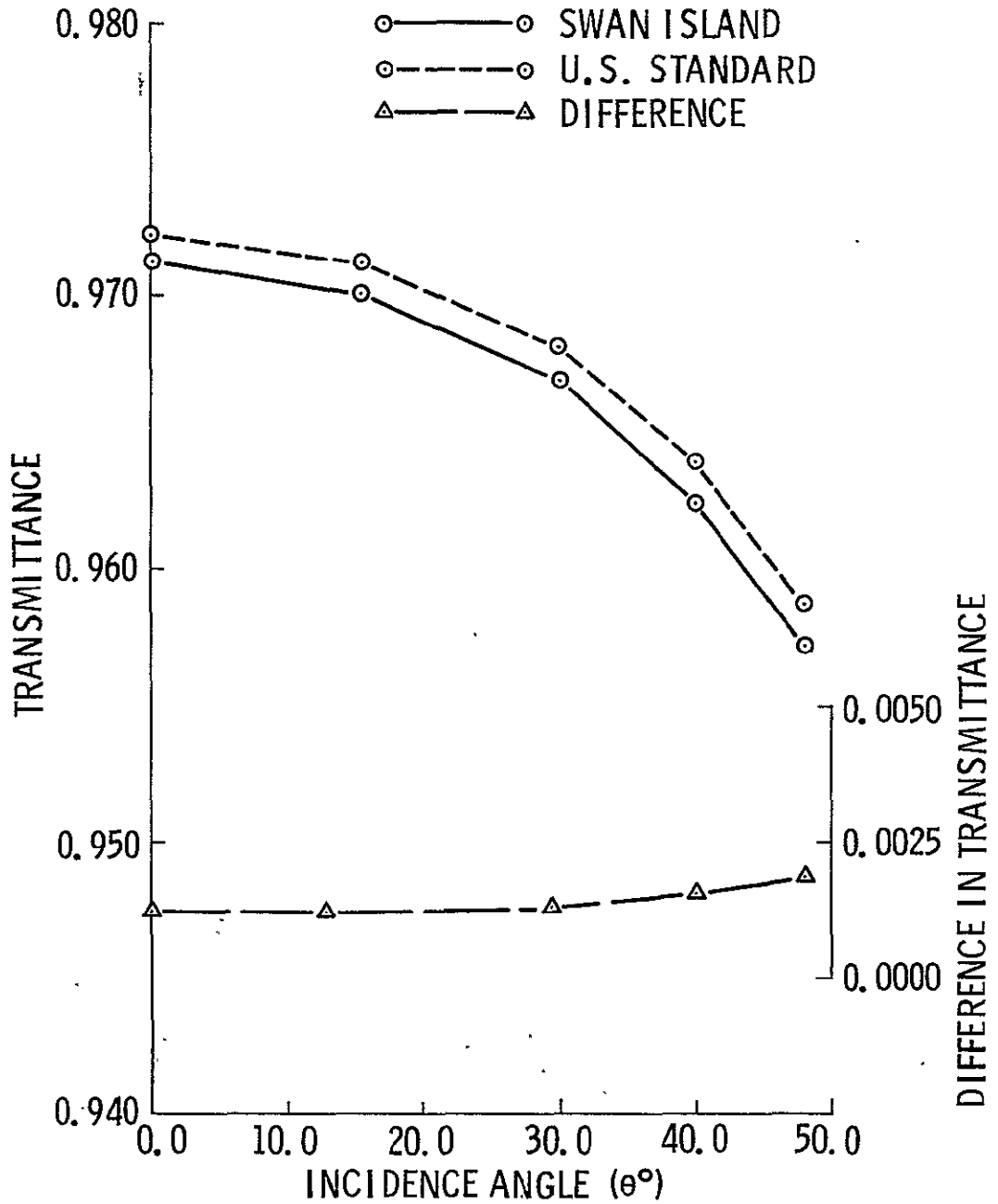


Figure 5.22.  
175

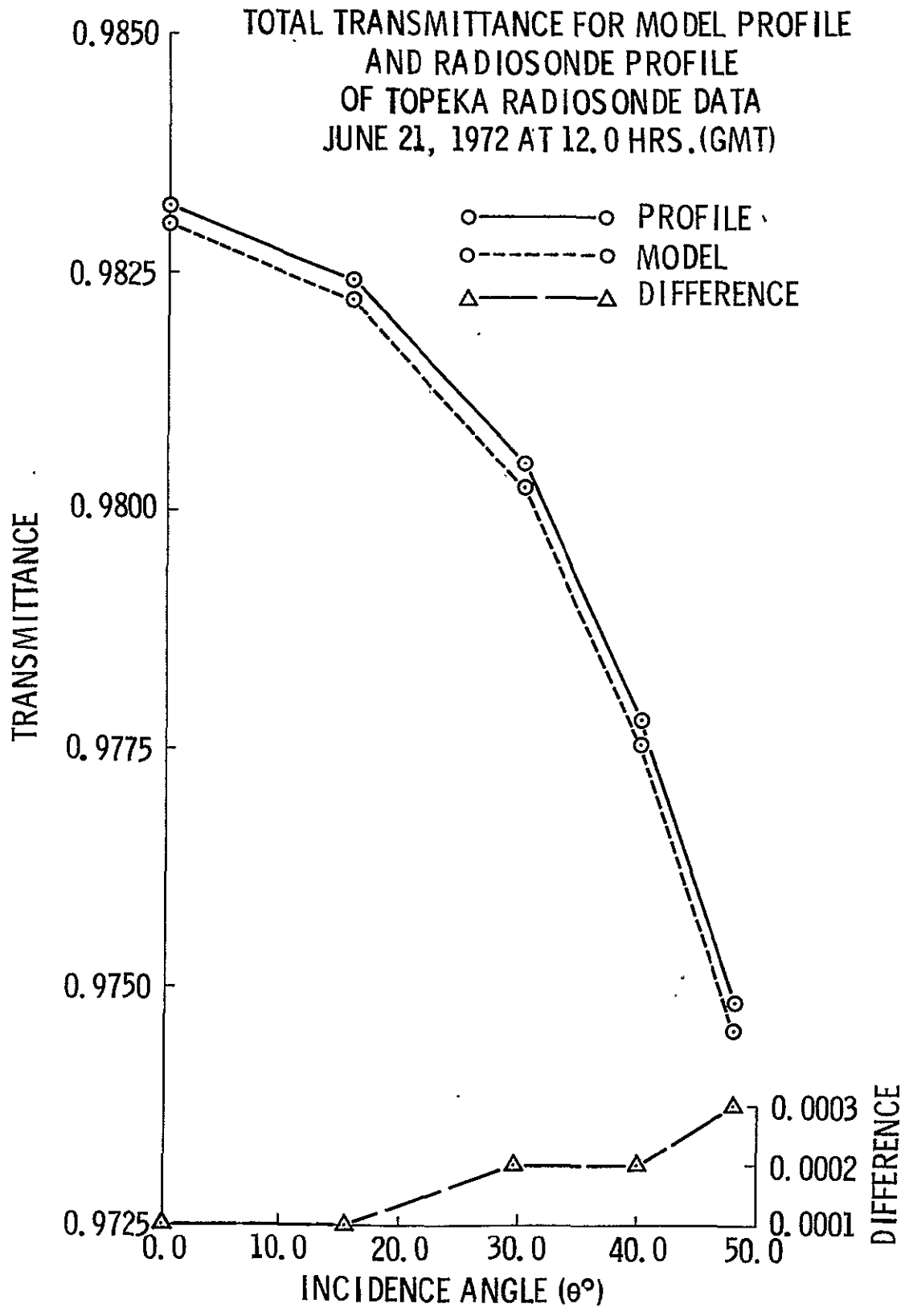


Figure 5.23.  
176

TOTAL TRANSMITTANCE FOR RADIOSONDE  
 AND MODELLED PROFILE OF ATMOSPHERE  
 JUNE 22, 1972 0.00 HRS.  
 TOPEKA RADIOSONDE

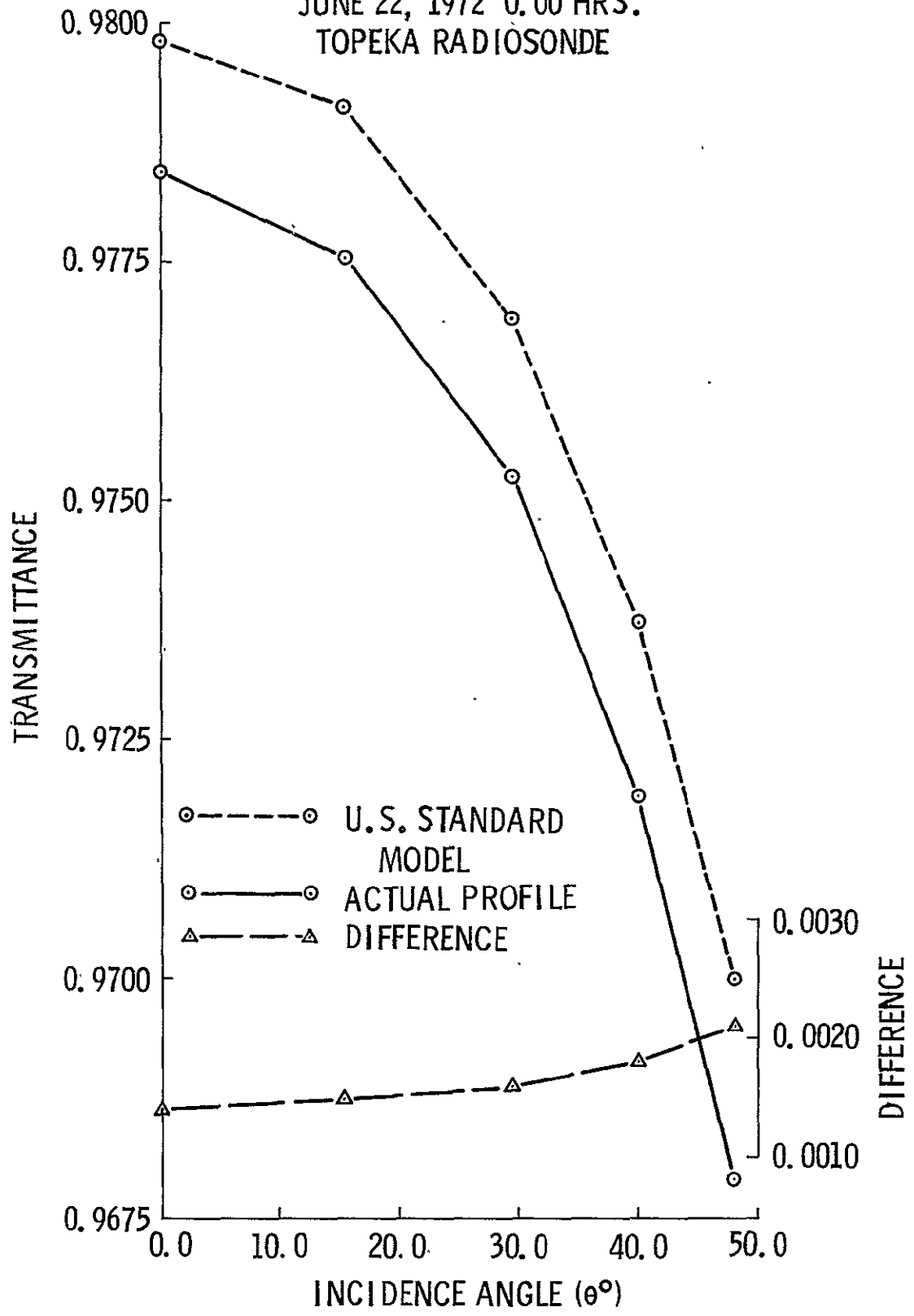


Figure 5.24.  
 177

DIFFERENCE IN TRANSMITTANCE BETWEEN  
WARM WAVE FRONT AND BOER MODEL  
(MIDLATITUDE MODELS)

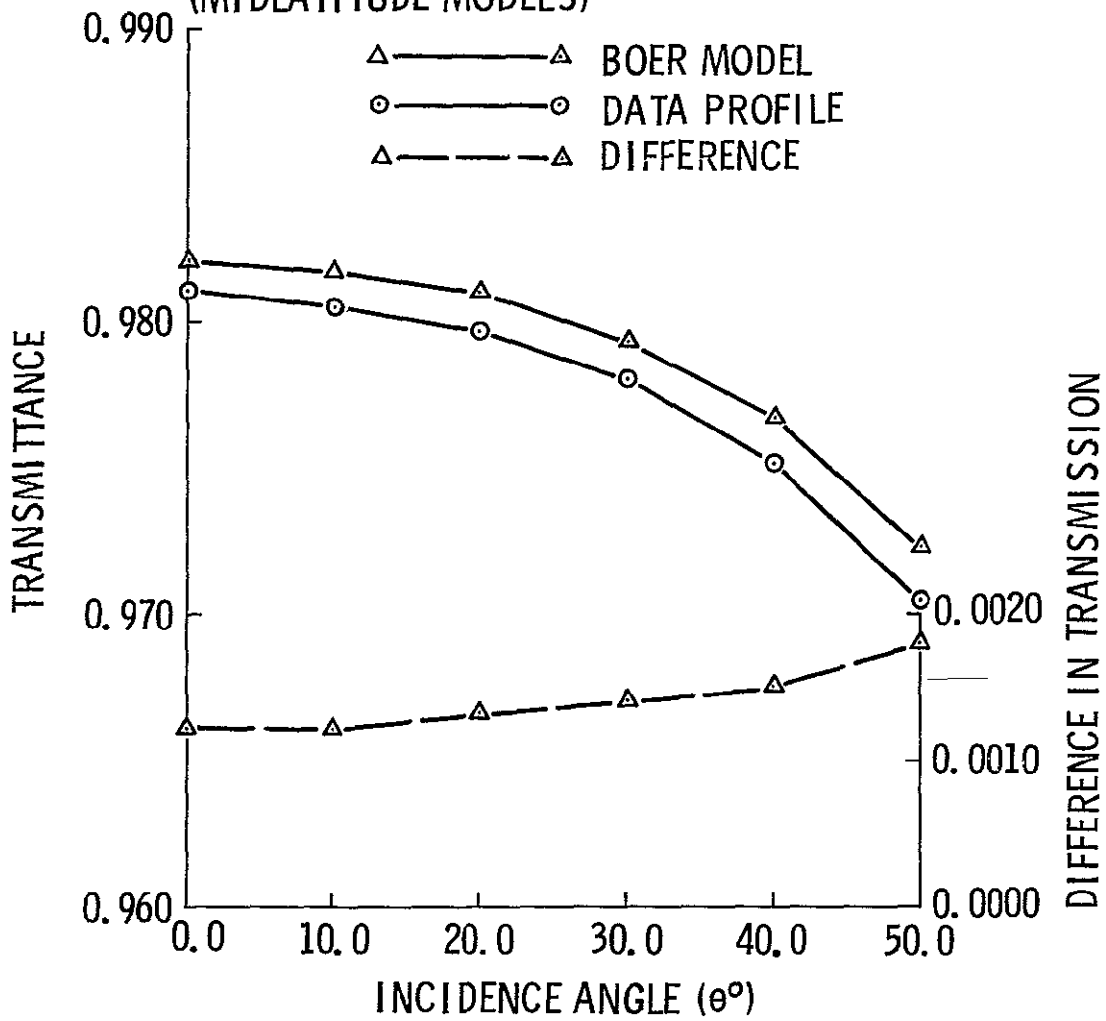


Figure 5.25.  
178

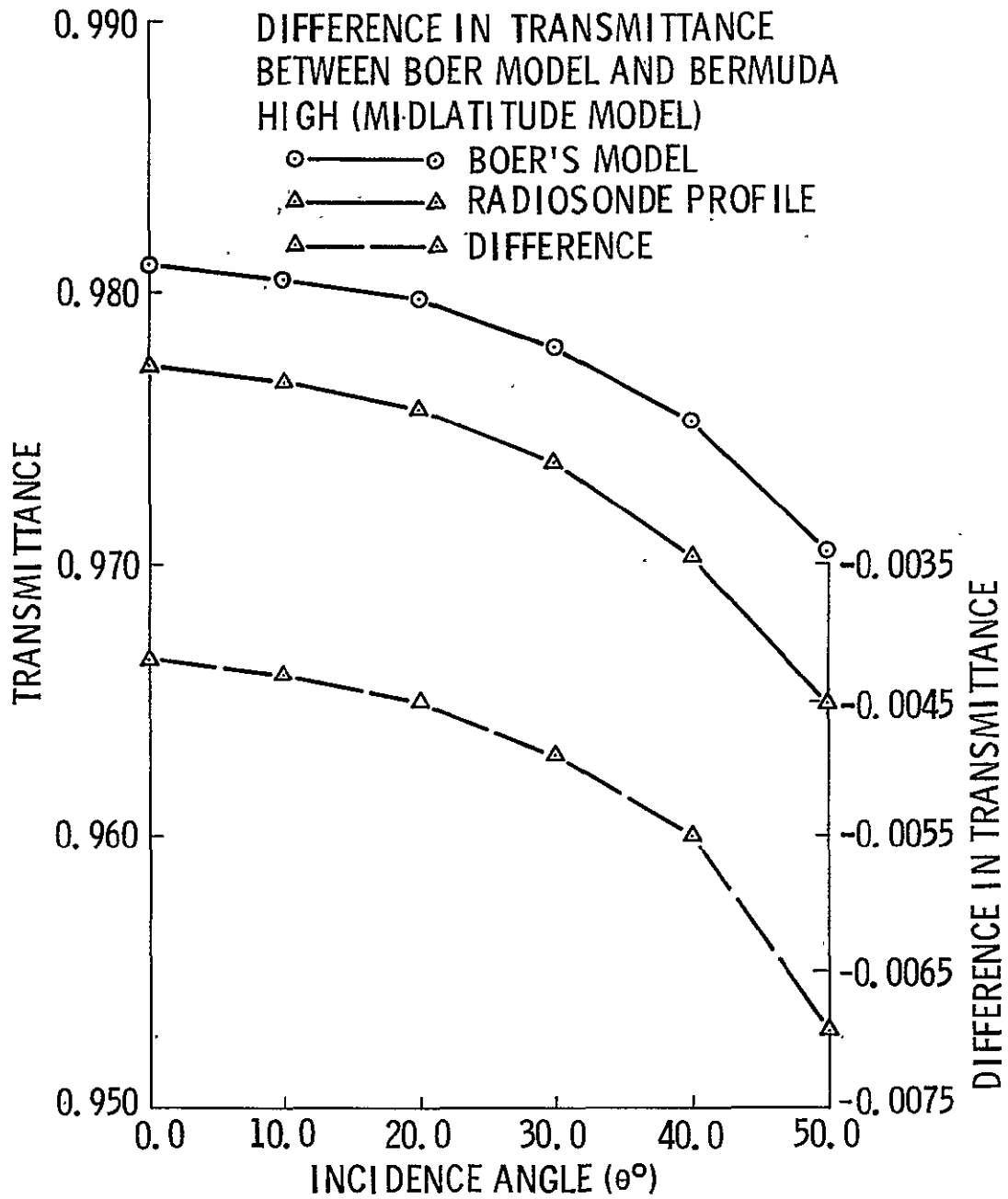


Figure 5.26.  
179

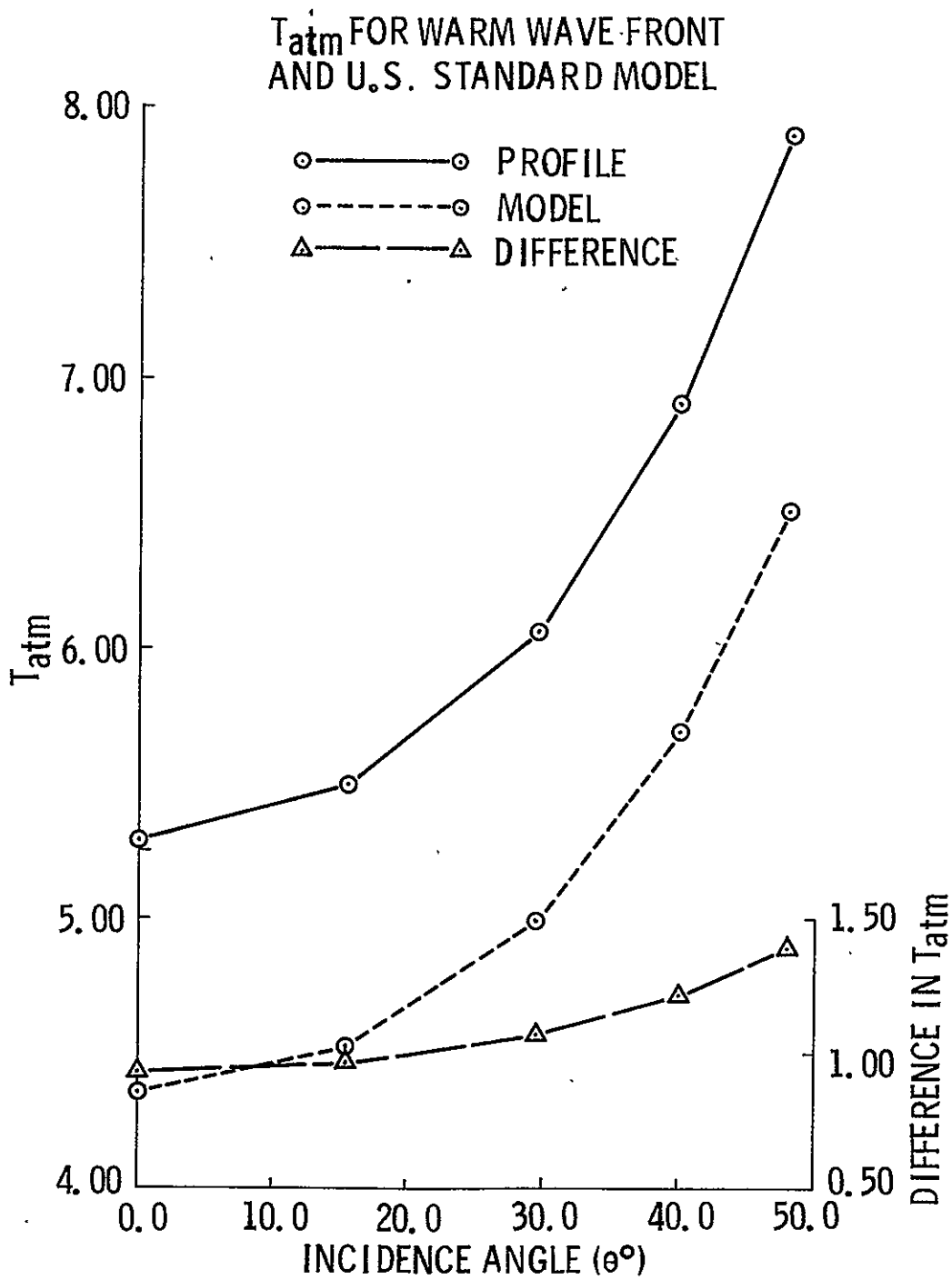


Figure 5.27.  
180

$T_{atm}$  FOR WARM SECTOR OF CYCLONE  
AND U. S. STANDARD MODEL

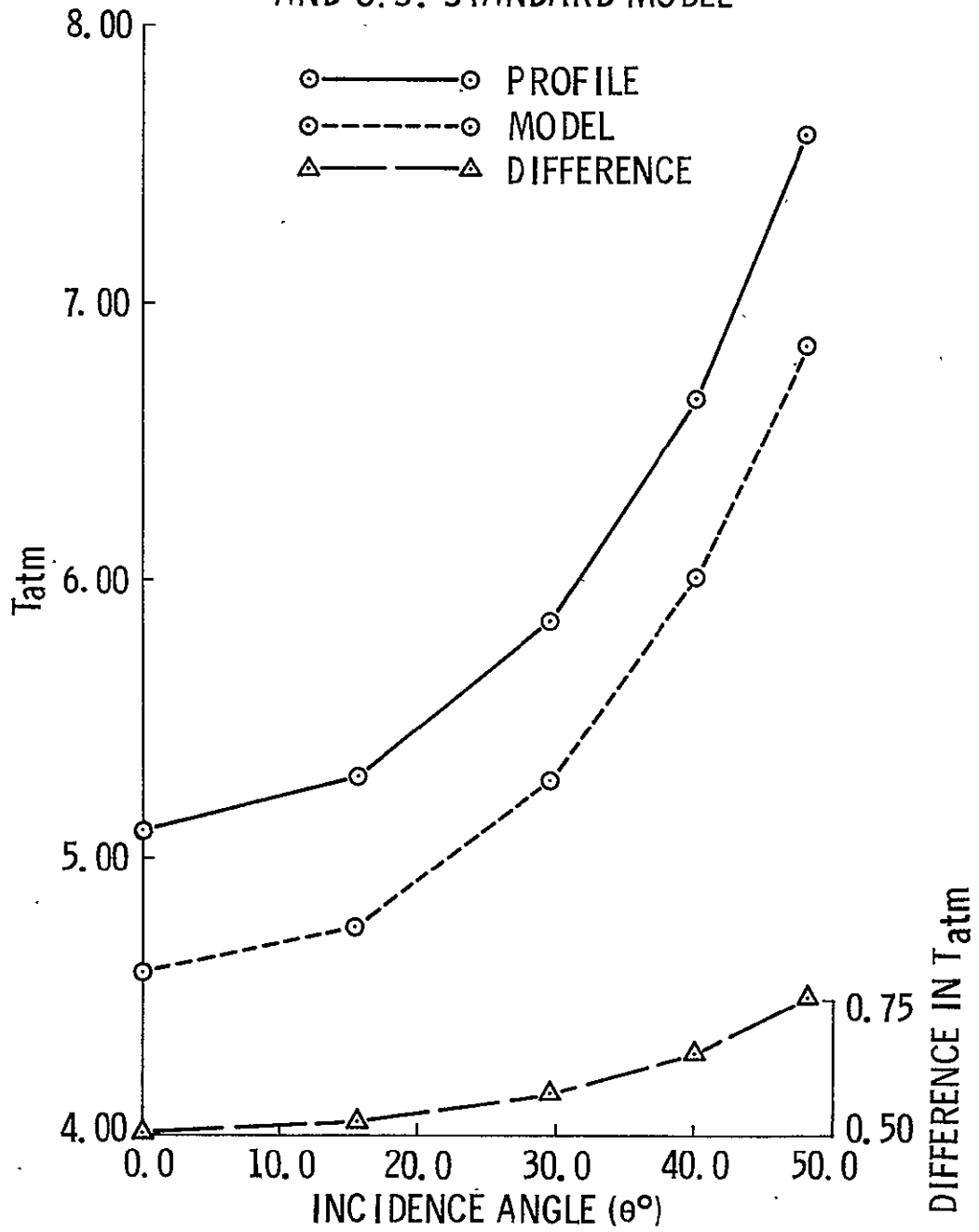


Figure 5.28.  
181

$T_{atm}$  FOR AZORES IN SUB-TROPICAL HEIGHTS  
AND U.S. STANDARD MODEL

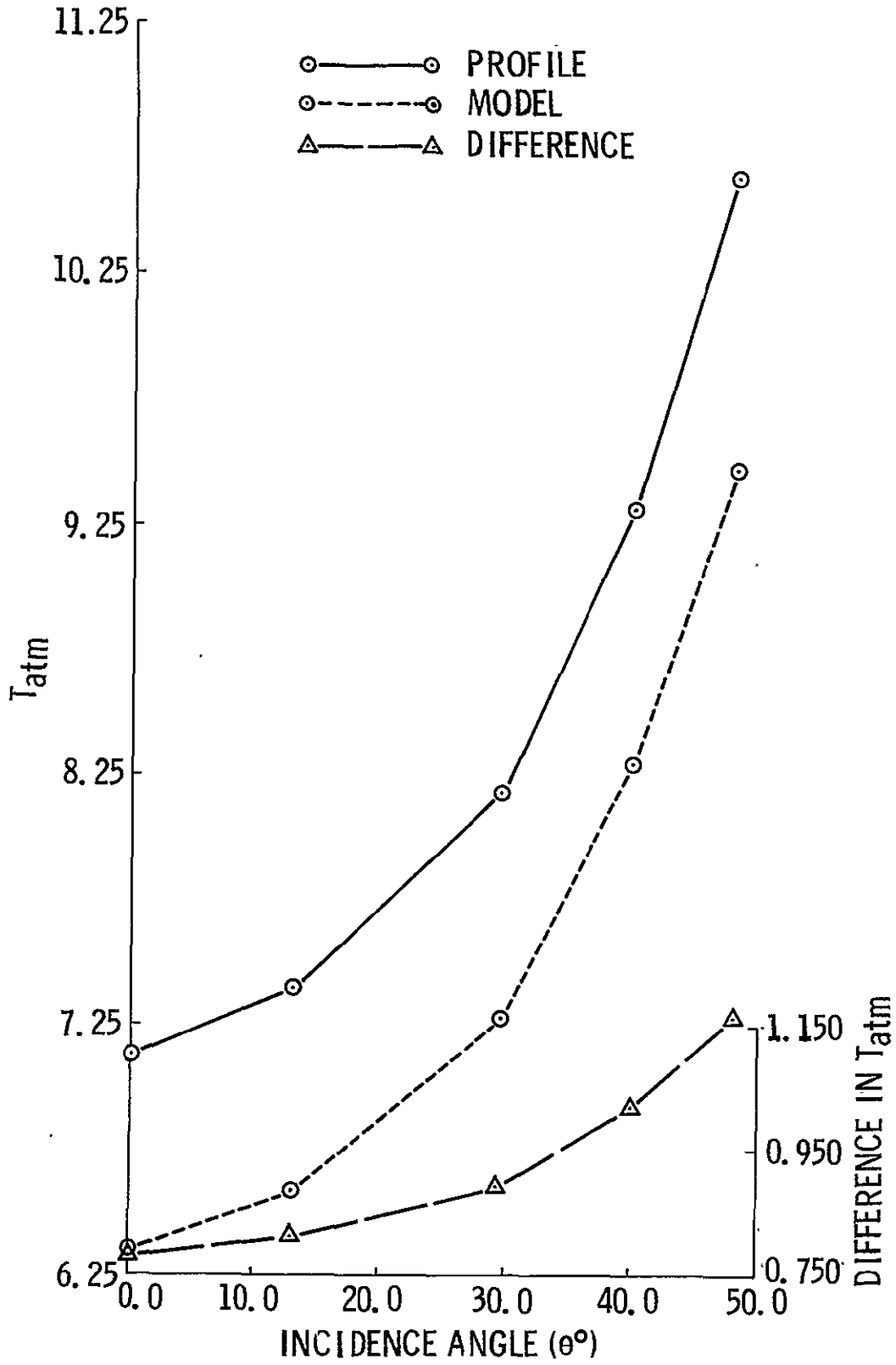


Figure 5.29.

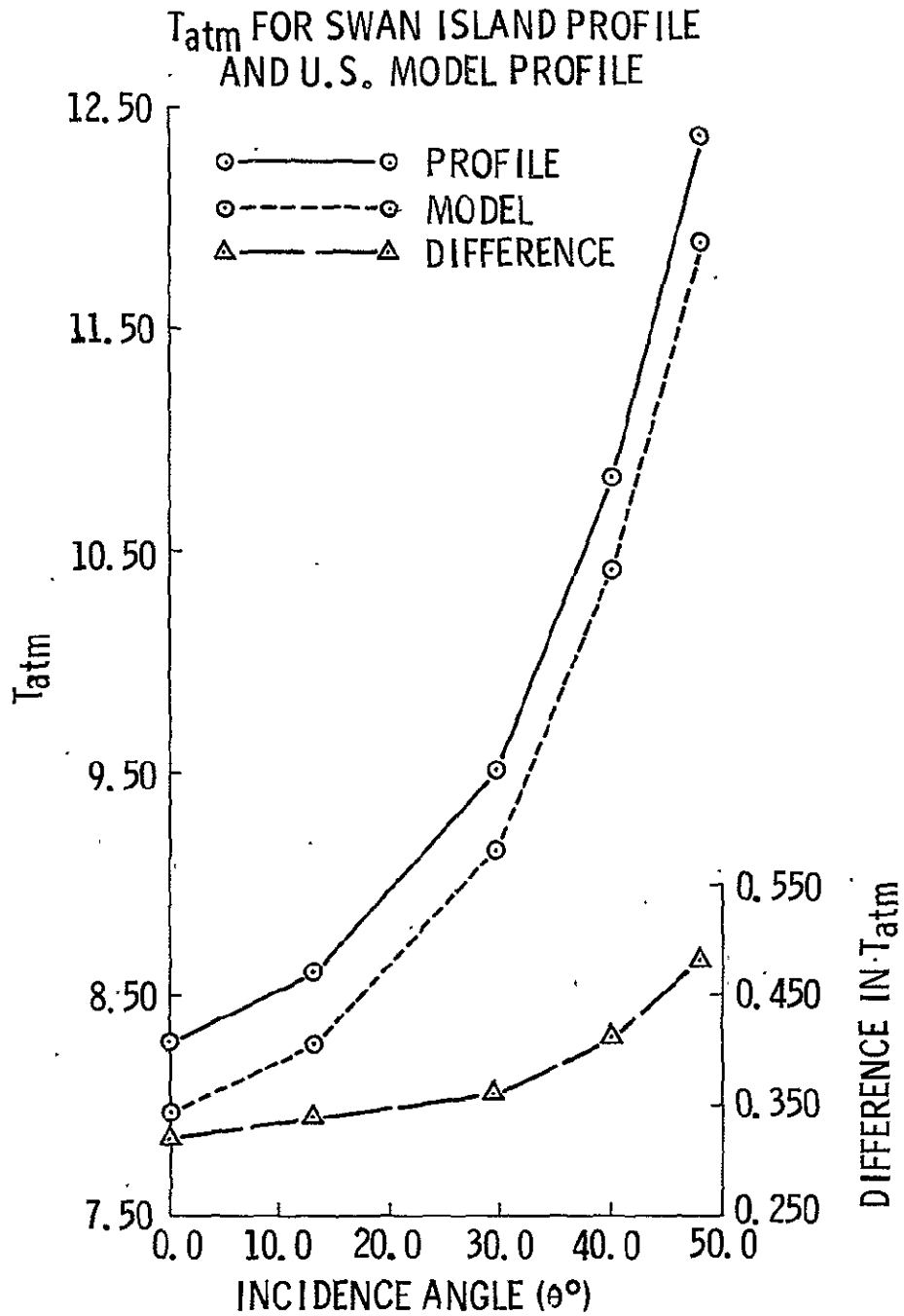


Figure 5.30.  
183

$T_{atm}$  FOR A RADIOSONDE PROFILE AND  
MODEL PROFILE

TOPEKA JUNE 21, 1972 AT 12.0 HRS (GMT)

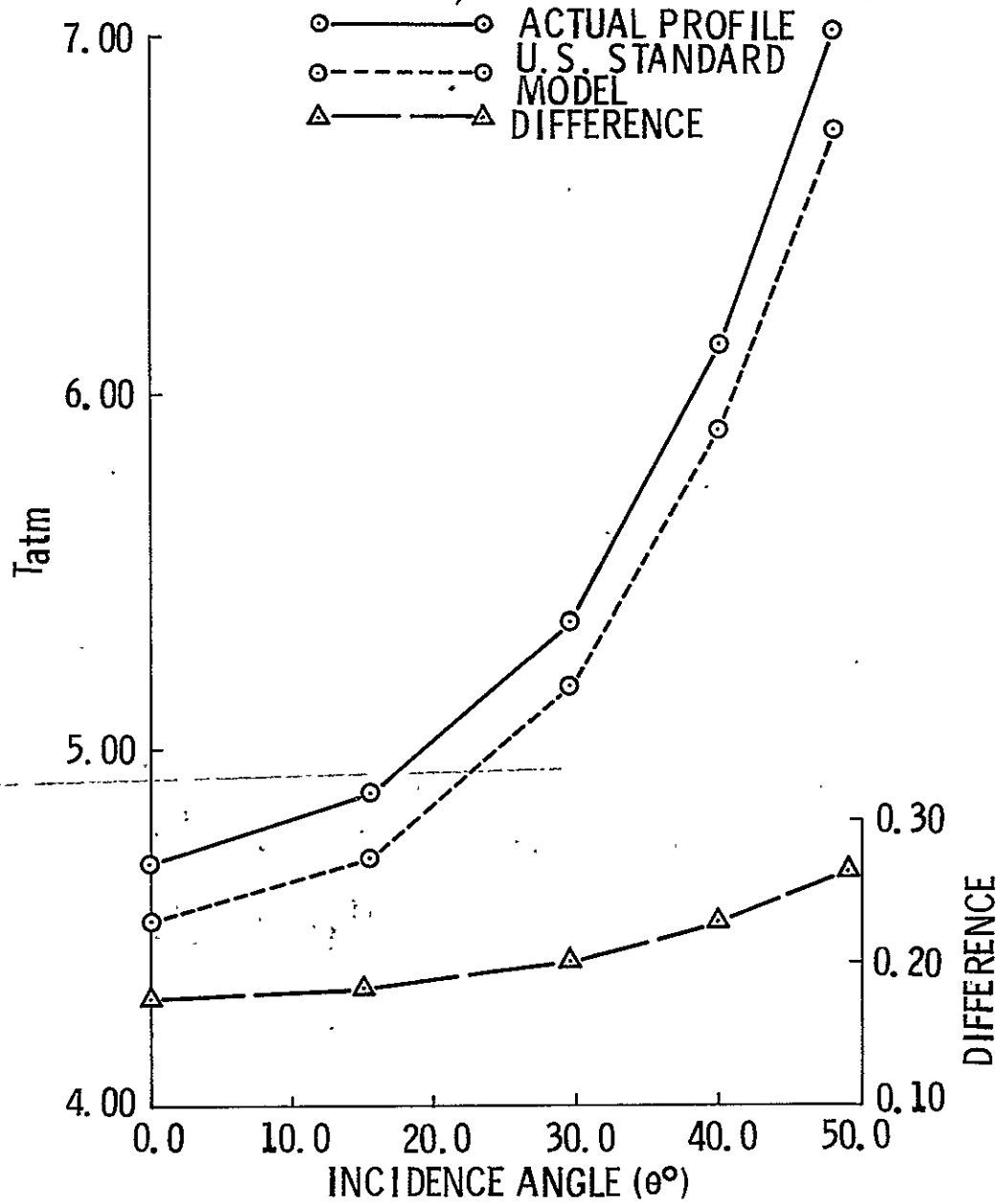


Figure 5.31.

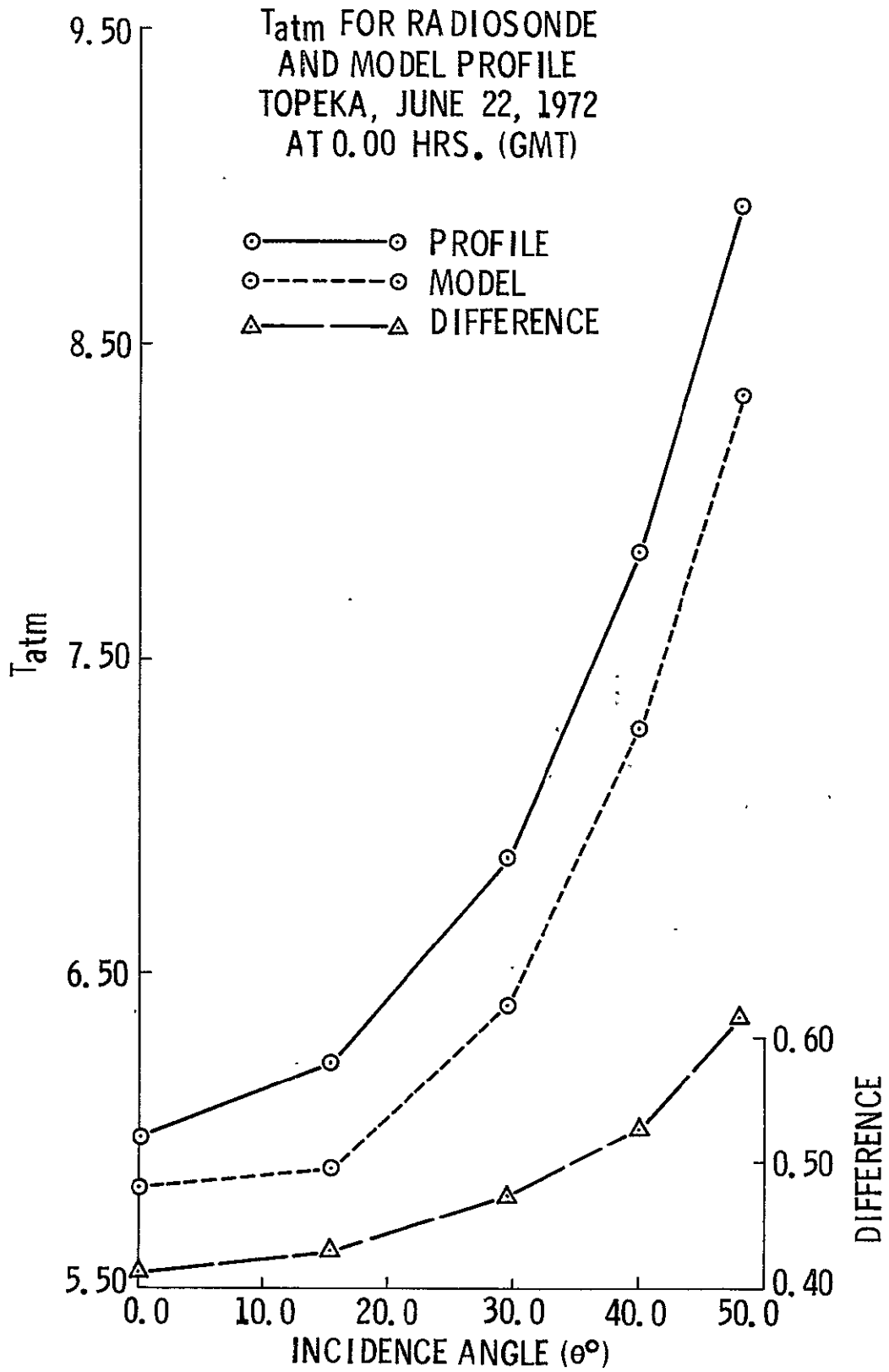


Figure 5.32.  
185

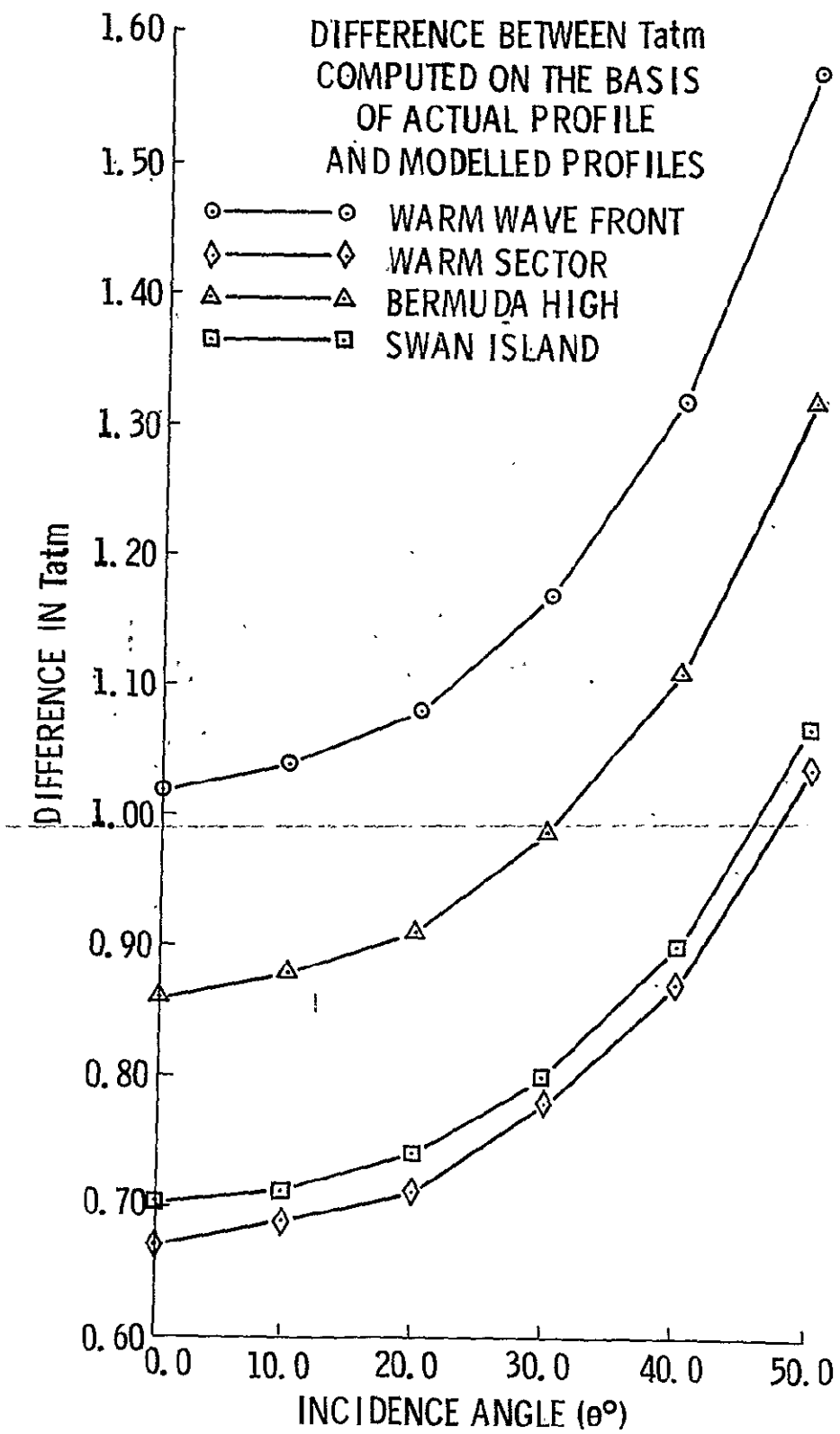


Figure 5.33.

### 5.3.1 Cloud Model

Meteorologists have defined ten types of clouds:

Cirrus	Nimbostratus
Cirrocumulus	Stratocumulus
Cirrostratus	Stratus
Alto cumulus	Cumulus
Altostratus	Cumulonimbus

Clouds may extend from sea level to the tropopause. This range is broken up into three levels: high, middle and low. Cirrus, cirrocumulus, and cirrostratus are in the high stage; altocumulus is in the middle level; and stratus and stratocumulus are in the lower level. Altostratus is usually found in the middle level, but it often extends higher; nimbostratus, cumulus, and cumulonimbus extend through several levels. The levels overlap and vary with latitude. The low level is from surface to 2 kms for polar, temperate and tropical regions; the middle from 2 - 4 kms at the polar regions to 2 - 8 kms for the tropical regions; the high level ranges from 3 - 8 kms at the polar regions to 6 - 18 kms at the tropical regions. Actually there are three basic cloud forms: cirrus, cumulus and stratus. All the other types of cloud forms are either these pure forms or modifications and combinations of them at different altitudes, where varying air and moisture conditions are responsible for their forms. Of the three cloud formations, it is only necessary to consider the effects of two of them because cirrus clouds normally stay above 6 kms and are then layers of ice. Their effect upon attenuation (hence emission) may be considered negligible.

Possible crude models for clouds have been used by various researchers.

Levine [1965] suggests the following classifications for cumulus clouds:

- Case 1  $457 \text{ m} \leq z \leq 1068 \text{ m}$ ,  $W = 0.5 \text{ gms/m}^3$
- Case 2  $457 \text{ m} \leq z \leq 2590 \text{ m}$ ,  $W = 1.0 \text{ gms/m}^3$
- Case 3  $457 \text{ m} \leq z \leq 3810 \text{ m}$ ,  $W = 1.25 \text{ gms/m}^3$

where  $z$  = height of clouds

$W$  = liquid water content.

The liquid water content as it appears here is the average liquid water content for the cloud. The distribution of water content in a cloud is not uniform; the water content usually reaches a maximum near the cloud top. For stratus clouds, Neiburger [1949] suggests the following classification:

- Case 1  $30 \text{ m} \leq z \leq 580 \text{ m}$ ,  $W = 0.35 \text{ gm/m}^3$

$$\text{Case 2 } 152 \text{ m} \leq z \leq 520 \text{ m}, W = 0.25 \text{ gm/m}^3$$

$$\text{Case 3 } 213 \text{ m} \leq z \leq 490 \text{ m}, W = 0.20 \text{ gm/m}^3$$

These classifications were studied for the purpose of comparisons. They were seldom considered in correcting for atmospheric corrections for Skylab data. Porter's [1970] classification is more general; he considers a combination of stratus and cumulus clouds, his classification is based upon an overcast sky:

Light overcast (sun image visible)

$$300 \text{ m} \leq z \leq 650 \text{ m}, W = 0.33 \text{ gm/m}^3$$

Medium overcast (no sun, light sky)

$$400 \text{ m} \leq z \leq 900 \text{ m}, W = 0.667 \text{ gm/m}^3$$

Heavy overcast

$$500 \text{ m} \leq z \leq 3200 \text{ m}, W = 1.0 \text{ gm/m}^3$$

Another classification is provided by Kreiss [1968]. He classified the clouds as stratus, thick stratus and tall cumulus with different water content. The liquid water content is not specified and a selection of a possible set of water contents is noted.

Stratus cloud

$$628 \text{ m} \leq z \leq 1457 \text{ m}, W = 0.0625, 0.25, 0.5, 1, 2, 4 \text{ gm/m}^3$$

$$628 \text{ m} \leq z \leq 1949 \text{ m}, W = 0.0625, 0.125, 0.25, 0.5, 1, 2, 4 \text{ gms/m}^3$$

Thick stratus cloud

$$628 \text{ m} \leq z \leq 3012 \text{ m}, W = 0.0625, 0.125, 0.25, 0.5, 1, 2, 4 \text{ gms/m}^3$$

Tall cumulus cloud

$$628 \text{ m} \leq z \leq 7185 \text{ m}, W = 0.0625, 0.125, 0.25, 0.5, 1, 4 \text{ gms/m}^3$$

It must be stressed that these cloud models are only models to use in systems studies, and that if actual data (from soundings or estimated from radar) is available, it should be used instead. Some of the other sources of estimating the cloud cover, and we emphasize "estimating," are weather stations that provide the percentage of sky cover and the lower ceiling of clouds, and simultaneous imagery which can be used to get lower and upper ceilings of cloud decks under certain circumstances. For example, in our study of a site in Texas, where the aim was to relate the soil moisture to the radiometer/scatterometer data, the corrections on the radiometric data were very important due to an uneven distribution of clouds over the target points in the site.

The lower and upper ceiling of the clouds were estimated by observing the shadow of the cloud edges and calculating the ceiling based upon sun elevation angle data. This would not have worked for a thick deck of totally contiguous clouds reaching far beyond the test site. The water content is, unfortunately, guessed at unless radiosonde data are available. Once again this guess is predicated upon statistics compiled by meteorologists on the average ceiling, thickness and water content of clouds for different regions in different months. The study of clouds is far too extensive to describe in this brief treatise. Suffice it to say that the maximum information available for the clouds is obtained first; if this information contains all necessary parameters required to compute the effect, the computation is performed. If the information is not sufficient, the appropriate models are invoked. Note that minimal information is required in invoking Porter's model which merely calls for a judgement of the overcast.

The inverse problem, that of detecting the amount of clouds from radiometer measurements can sometimes be solved. The conditions for its solution are that the terrain be homogeneous and that the target cells contain some cloud free samples. The decrease in radiometric temperature due to clouds (increase in the case of ocean targets) can then be estimated from the radiometric data and this estimate can be matched to that predicted by the cloud models. This exercise was also attempted for some Skylab data.

### 5.3.2 Attenuation and Emission by Clouds

The absorption coefficient of clouds has been computed by researchers using empirical models. The absorption coefficient equations used in this study were suggested by Benoit [1968]. His equations were a result of interpolation of Gunn and East's [1954] discrete data for fixed frequency and temperature. These equations are very convenient for computational purposes, especially because they allow for a variation in temperature. His simplified global formula for computing the absorption coefficient is

$$A_o = k \rho \tau \quad (36)$$

where

$A_o$  = Absorption coefficient

$\rho$  = Water content of clouds (gms/m<sup>3</sup>)

$r$  = Path length through the clouds in kms

$k$  = Coefficient of attenuation (dB km<sup>-1</sup> gm<sup>-1</sup> m<sup>3</sup>)

The coefficient of attenuation for frequencies in GHz are given by

$$k = \exp(a) f^b$$

where the coefficients  $a$  and  $b$  depend upon the cloud type, water or ice and on temperature. An approximation for the attenuation coefficient due to water and ice clouds is of the form

$$k_w = f^{b_w} \exp(a_{ow} (1 + mT))$$

and  $k_i = f^{b_i} \exp(a_{oi} (AT^2 + BT + 1))$  (37)

where the subscript  $w$  represents water and the subscript  $i$  represents ice. The temperature,  $T$ , is expressed in °C, the frequency in GHz and the attenuation coefficient is then in dB/km/gr/m<sup>3</sup>. Table 5.2 provides values for the constants as suggested by Benoit:

Table 5.2. Constants Used in Computation of Cloud Attenuation Coefficient (from Benoit [1968])

Water Clouds	Ice Clouds
$a_{ow} = -6.866$	$a_{oi} = -8.261$
$b_w = 1.095$	$b_i = 1.006$
$m = 0.0045$	$A = -4.37 \times 10^{-4}$
	$B = -1.767 \times 10^{-2}$

Note that in Benoit, Table 1 has the header labels for ice clouds and water clouds reversed. Benoit has considered certain cases for clouds and computed the absorption (attenuation coefficient). Since our equations have been those suggested by Benoit, his figures for the attenuation coefficients for clouds in Table 5.2 are shown in Figure 5.34. Benoit's vertical extent of clouds ranged from 5 to 10 km in the examples. This is greater than the extent expected in general.

REPRODUCIBILITY OF THE ORIGINAL PAGE IS POOR

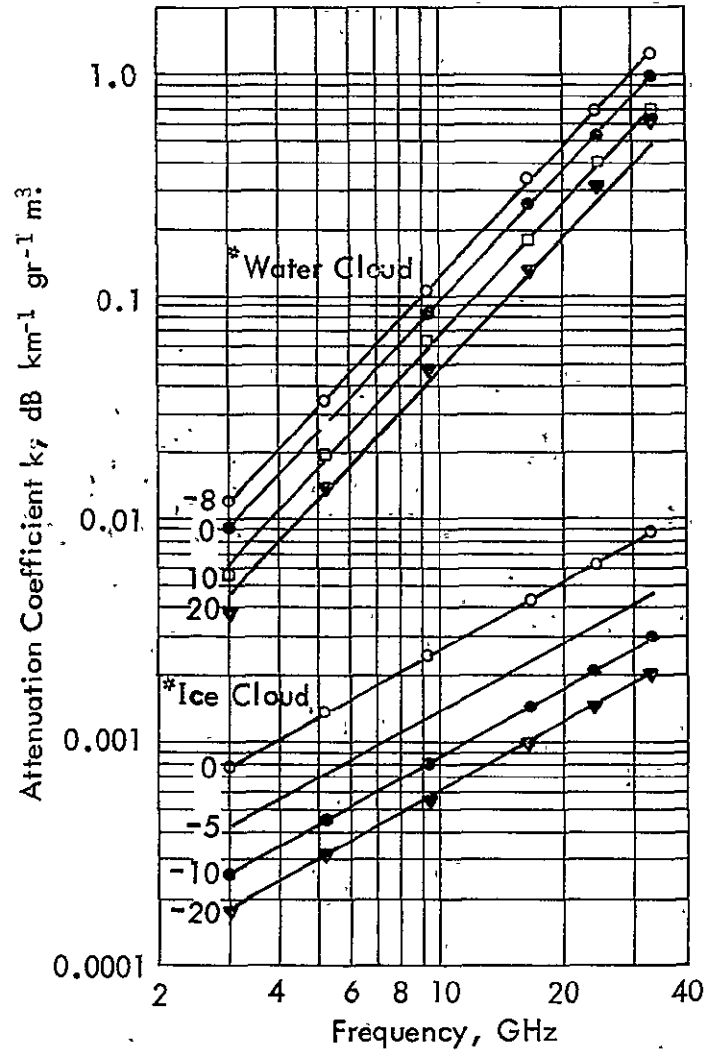


Figure 5.34. Attenuation Coefficient for Clouds. From Benoit, 1968.  
\* Note: From Reference in Gunn and East, 1954.

The cloud models described in the section above were used to determine the vertical extent and water content to be used in the equations suggested by Benoit. The temperature was profiled from the surface up to the cloud heights; gradations in surface temperatures were used to get different cloud temperatures. The attenuation due to clouds according to Kreiss's classification for clouds is shown in Fig. 5.35. Notice that a change in the mean temperature of the clouds causes a substantial change in the attenuation, with the lower temperature corresponding to a higher attenuation. Porter's classification of clouds was used to compute the cloud attenuation and is shown in Fig. 5.36. Porter's heavy overcast sky only has a thickness of 2.7 kms and has a cloud water content of  $1 \text{ gm/m}^3$ , consequently the attenuation is substantially lower than that predicted by many cases of Kreiss's classification. Kreiss's tall cumulus clouds are a rare occurrence in temperate regions and should very seldom be found without the associated precipitation. According to his worst case classification, the brightness temperature due to clouds (for a mean cloud temperature of  $0^\circ\text{C}$ ) could be as high as  $100^\circ\text{K}$ . Such a cloud deck would then preclude any possibility of sensing the radiometric temperature of targets.

A deck of clouds with a lower ceiling of 2 kms and a thickness of 2 kms was introduced in the atmospheric profiles being studied. The water content of the clouds was varied from  $0.1 \text{ gms/m}^3$  to  $2 \text{ gms/m}^3$ , and the atmosphere was profiled for temperature and pressure by the U. S. Standard with the surface temperature varying from  $280^\circ\text{K}$  to  $310^\circ\text{K}$ . The humidity was also profiled with the dew point temperature close to the surface temperature. The percentage of cloud cover was varied from 50% to 100%. An example of the attenuation and the transmittance of the atmosphere for some of these cases is provided in Fig. 5.37. This figure shows the attenuation and transmittance (zenith incidence one-way) for two cases; one, cloud water content  $0.5 \text{ gms/m}^3$  and the cloud cover over the target was 50% and two, cloud water content  $1 \text{ gm/m}^3$  and the cloud cover over the target was 100%. At  $300^\circ\text{K}$  surface temperature the attenuation for the two cases was 0.21 dB and 0.355 dB respectively, the corresponding transmittances were 0.952 and 0.9205. The overall effect of such clouds over an ocean and land surface is further provided in the section of simulation of radiometric response.

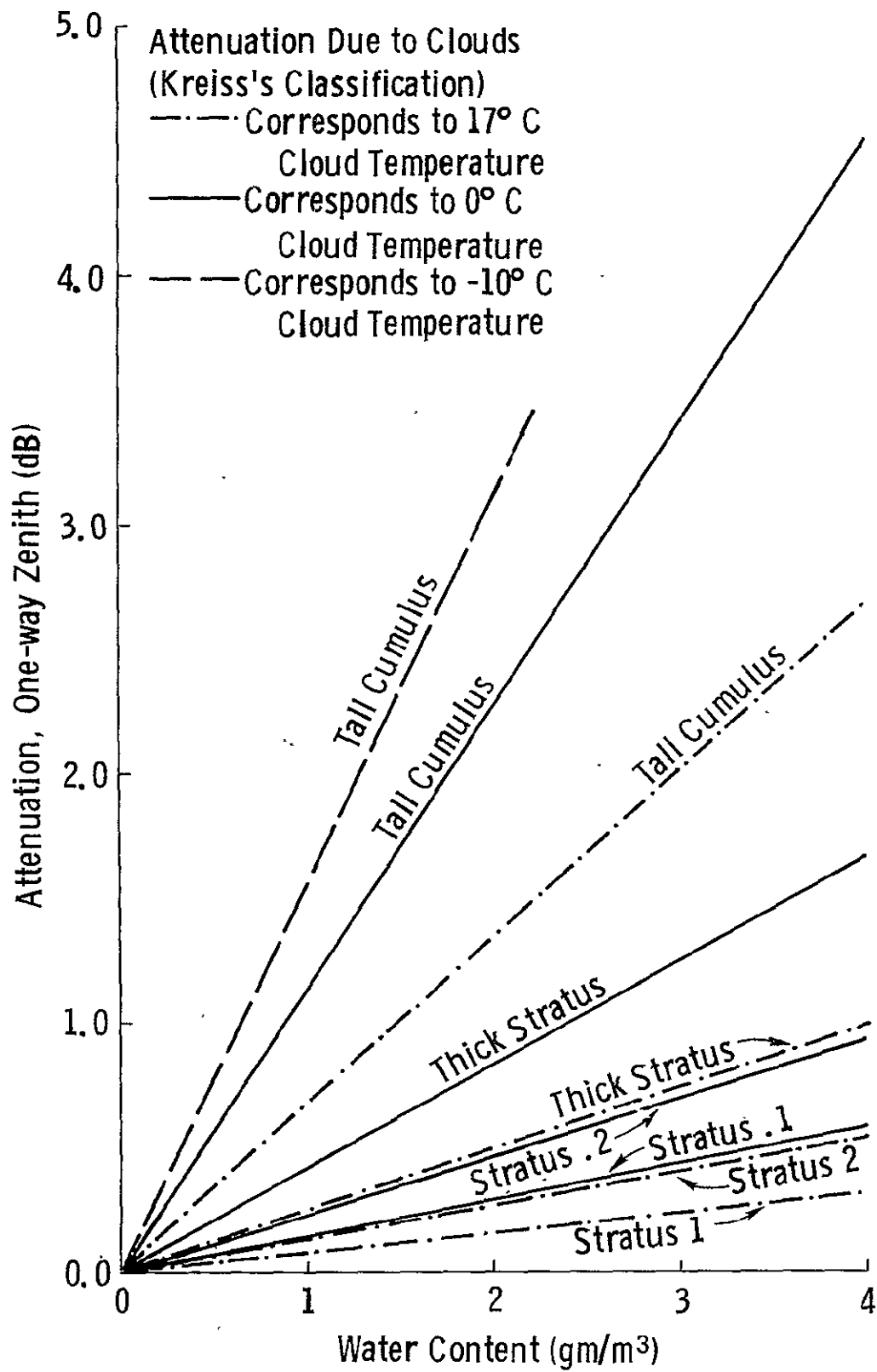


Figure 5.35.  
193

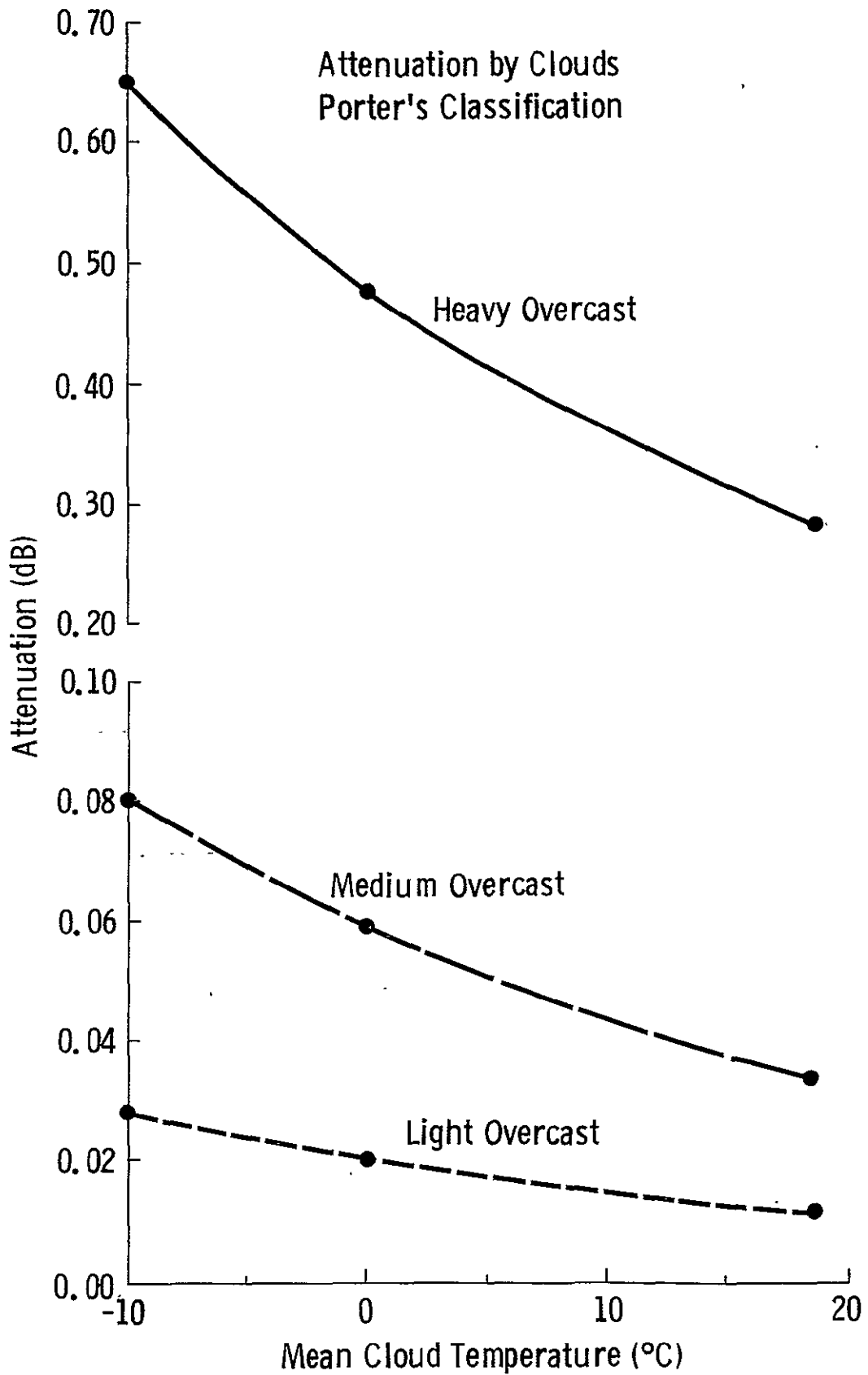


Figure 5.36.

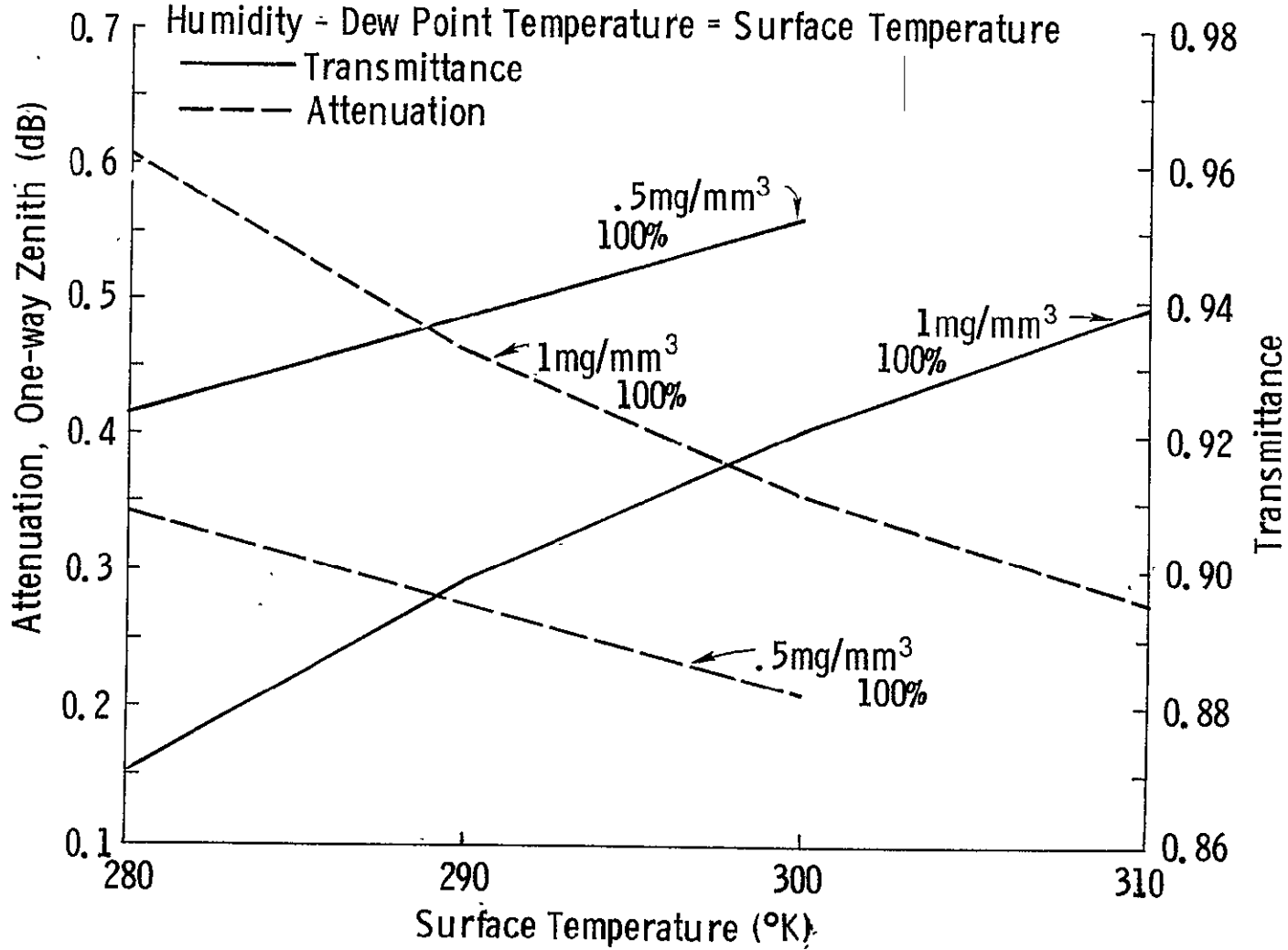
Atmospheric Attenuation and Transmittance with Clouds Present  
- A Sample Case

Surface Pressure - 1013.25 Millibars

Cloud Lower Ceiling - 2 Kms

Cloud Thickness - 2 Kms

Humidity - Dew Point Temperature = Surface Temperature



## 5.4 Attenuation and Emission Due to Rain

### 5.4.1 Rain Models

Meteorologists have compiled statistics on the average monthly (or yearly) rainfall for most parts of the world, but the factor germane to our study — precipitation rate can scarcely be found. Indeed this is a difficult parameter to compile statistics on, because the variations overshadow any differences documented. An alternative source of information regarding rain is through meteorological stations which sometimes specify the precipitation rate along with the total precipitation. These are only point samples and extrapolations to estimate the horizontal extent could be the only way to introduce the parameters required for the study of the effects of rain. To reinforce such an extrapolation, Bussey [1950] considered the comparison of time and space-averaged rainfall rates with instantaneous point rates and found reasonably good comparisons. Researchers have studied the effects of precipitation for point-to-point links along the surface (microwave towers). The variation of the precipitation rate with height has not yet been authoritatively documented. Formulas to be used as estimates have been suggested for regions having a steady sustained rain but no such estimates are known for the spontaneous, sporadic or brief thundershower. The models suggested cannot be applied to a storm. The precipitation rate and extent are very closely correlated with the water content of the clouds, so that one cannot be modelled without adequately compensating the other. Under steady conditions, the mass of cloud water per unit volume may be two or three times that of rain in the zone just below the melting level, especially in light precipitation.

For widespread uniform precipitation, and not for showery conditions Valley [1965] has suggested three models of vertical distributions of various precipitation parameters based upon empirical and theoretical data. They indicate approximate conditions in the different types of weather situations. His classification is quoted here.

Case I is representative of summer rain in temperate latitudes, and, with a slight increase of temperature, of widespread tropical rains as well.

Case II is associated with rain in the spring and fall months in temperate latitudes and also represents a likely thermal stratification during many orographic rains of temperate climes.

Case III, patterned after the atmospheric structure during severe snowstorms in New England, is representative of a winter snowstorm, and except for the low temperature, characterizes the winter rains as well.

Water content distributions with altitude for various updraft conditions and associated surface precipitation rates for case 1, 2, and 3 are shown in Figures 5.38, 5.39, 5.40, respectively. Vertical temperature distribution for situations of widespread precipitation with altitude for cases 1, 2, 3 are shown in Figure 5.41. The water content of the clouds associated with these rains is a function of the temperature. The distribution of water content increases upward till the melting level and then decreases gradually to zero. An example of the water content of clouds for rains in cases 1 and 2 are shown in Figure 5.42 and 5.43. As can be seen, the water content varies with altitude temperature and precipitation rate.

#### 5.4.2 Attenuation and Emission by Rain

The first attempt of significance to document the theoretical predictions of backscatter and attenuation from meteorological phenomenon was by Ryde [1946]. His predictions have been modified by Medhurst [1965] to some extent, but in general the results have agreed well with his predictions. There have been cases reported (Medhurst [1965]) where the actual attenuation measured exceeded the theoretical maximum. The theoretical predictions have relied upon one of two parameters to describe the attenuation — the drop-size distribution and the precipitation rate. These parameters have been correlated by Laws and Parsons [1943]. One can estimate (in a probability measure) the distribution of drop-sizes based upon the precipitation rate of the rain particles, as suggested by Burrows and Atwood [1949].

Ryde in his study found that the attenuation of microwaves by rain can be described by

$$K_R = K \int_0^H [R(z)]^\alpha dz \quad (38)$$

REPRODUCIBILITY OF THE ORIGINAL PAGE IS POOR

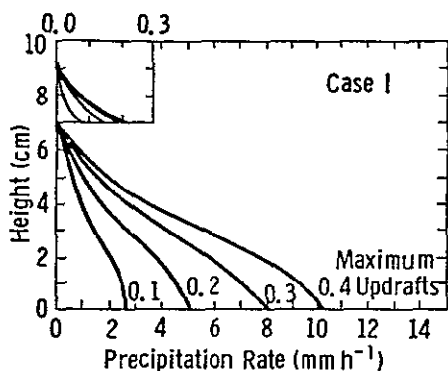


Figure 5.38a. Distribution of precipitation rate with altitude for case I. Values for maximum updraft in  $\text{m sec}^{-1}$  are given by each curve.

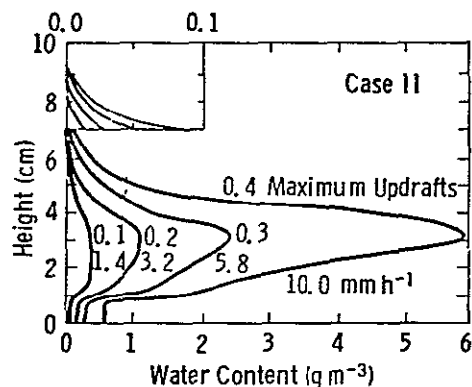


Figure 5.39. Concentration of pre-precipitation in  $\text{g m}^{-3}$ , with height, for case II. Values of maximum updraft in  $\text{m sec}^{-1}$  (above) and surface pre-precipitation rate in  $\text{mm h}^{-1}$  (below) are shown by each curve.

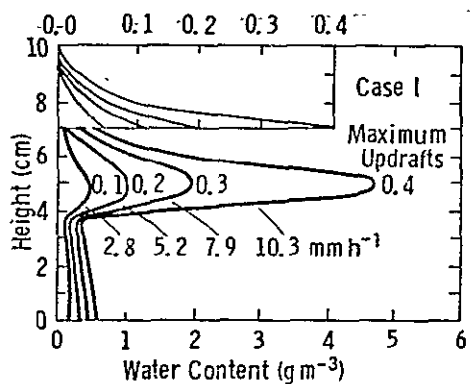


Figure 5.38b. Concentration of precipitation rate in  $\text{g m}^{-3}$ , with height, for case I. Values of maximum updraft in  $\text{m sec}^{-1}$  (above) and surface precipitation rate in  $\text{mm h}^{-1}$  (below) are given by each curve.

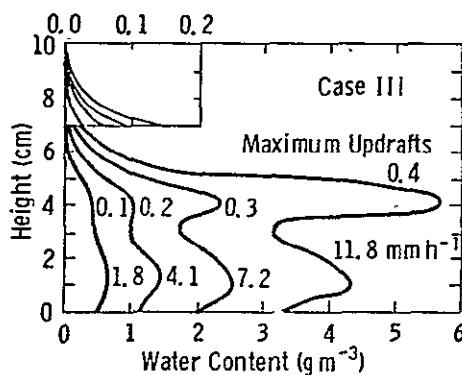


Figure 5.40. Concentration of pre-precipitation in  $\text{g m}^{-3}$ , with height, for case III. Values of maximum updraft in  $\text{m sec}^{-1}$  (above) and surface pre-precipitation rate in  $\text{mm h}^{-1}$  (below) are shown by each curve.

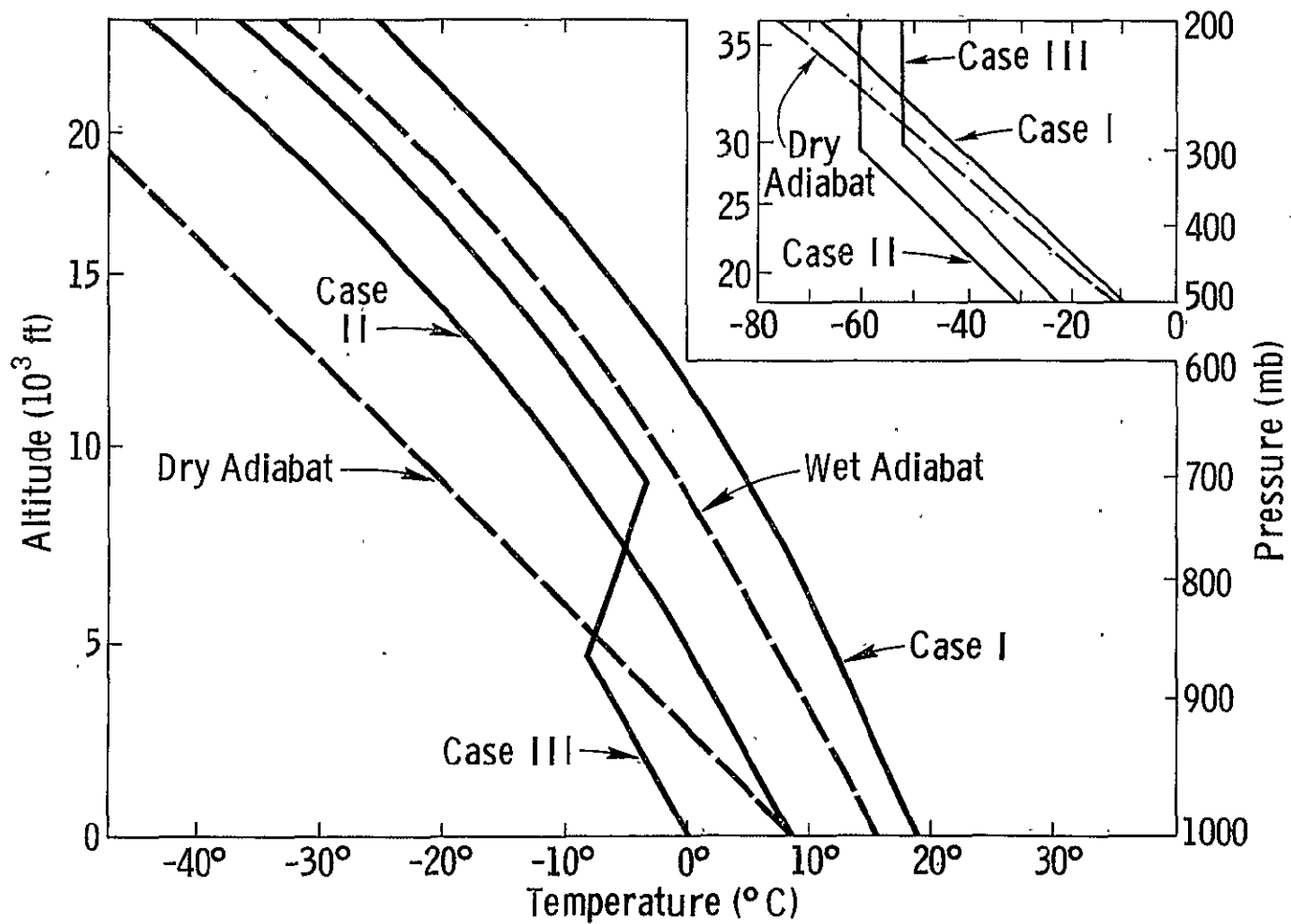


Figure 5.41. Vertical temperature distribution for situations of widespread precipitation.  
 Case I -- summer rain; case II -- spring or fall rain; case III -- winter snowstorm.

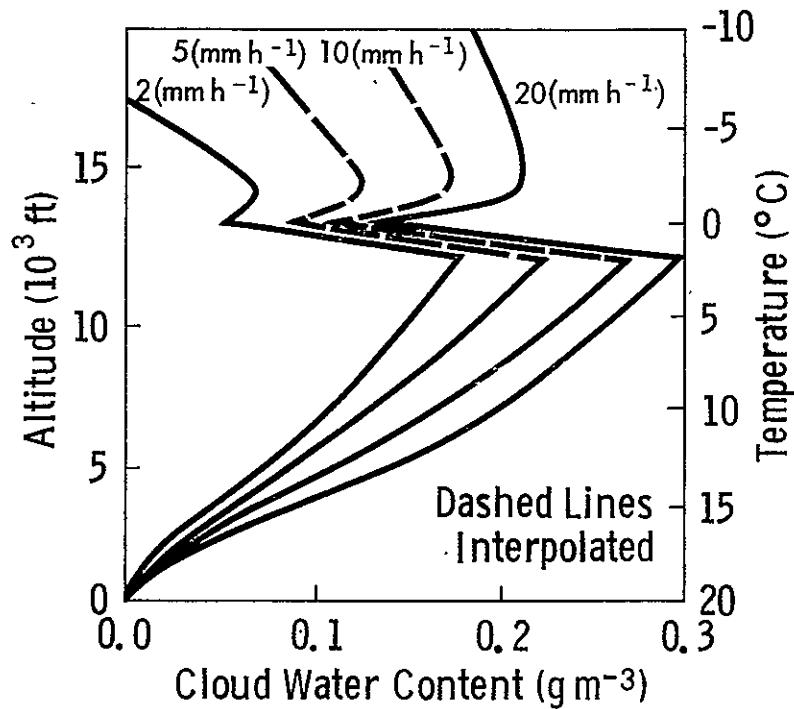


Figure 5.42. Steady-state water content of clouds for a situation similar to case I and for surface intensities of 2, 5, 10, and 20  $\text{mm h}^{-1}$  (derived from Wexler and Atlas, 1958).

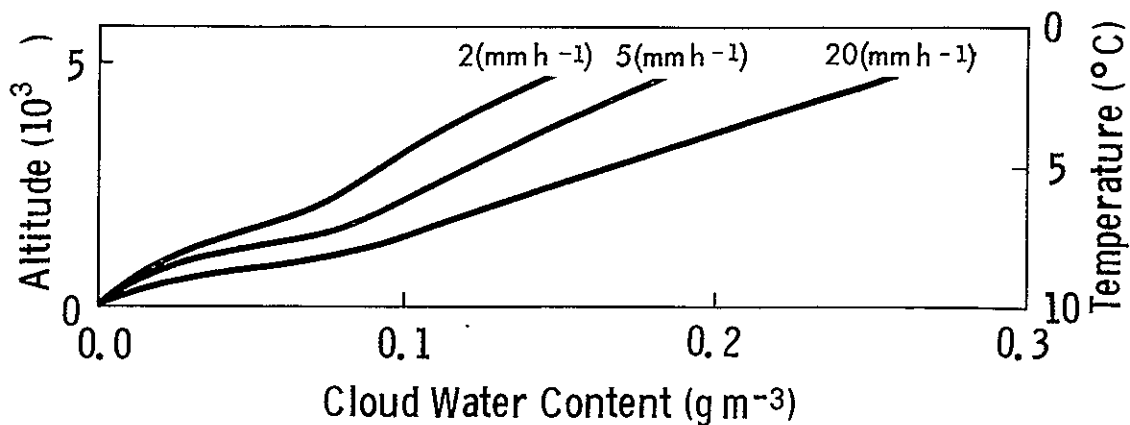


Figure 5.43. Steady-state water content of clouds for a situation similar to case II, for surface rain intensities of 2, 5, and 20  $\text{mm h}^{-1}$  (derived from Wexler and Atlas, 1958). Curves are cut off at the melting level. From there upward, the liquid water content varies in a manner similar to that for case I.

where  $K_R$  = total attenuation in dB  
 $K$  = constant (function of frequency)  
 $R(z)$  = rainfall rate along path  
 $H$  = length of propagation path  
 $\alpha$  = constant (function of frequency)

Medhurst [1965], showed that even though the Ryde theory predicts that the attenuation will not be strictly proportional to the precipitation rate (due to variation in drop size distribution with precipitation rate), a strictly linear relationship shows good agreement with measured data. This implies that a value of  $\alpha$  equal to 1 would be satisfactory.

The scattering due to individual rain drops is computed by the Mie [1905] theory of scattering where each droplet is considered as a sphere with a dielectric constant of water. The resulting expression for cases where the Rayleigh approximation holds (centimeter and millimeter wavelengths), the scattering is given by

$$q_{rs} = \frac{2\lambda^2}{3\pi} \beta^6 \left| \frac{m^2 - 1}{m^2 + 2} \right|^2 \quad (39)$$

where

$$\beta = \frac{2\pi r}{\lambda}$$

$r$  = radius of droplet

$m$  = complex index of refraction for water.

$\lambda$  = wavelength

For purposes of radar signals, the parameter of interest is the combined back-scattering effects in a unit volume; to quantify these effects, a parameter called the radar reflectivity, is introduced and this factor is computed as

$$\eta = \frac{\pi^5}{\lambda^4} |K|^2 z \quad (40)$$

where  $K = \frac{m^2 - 1}{m^2 + 2}$

$$z = \text{reflectivity factor} = \sum_{i=1}^N D_i^6$$

where  $D_i$  = diameter of a droplet  
 $N$  = total number of droplets/unit volume.

Gunn and East [1954], in an excellent review of the microwave properties of precipitation particles show the values of the constants suggested by researchers to relate  $z$  to the rainfall rate,  $R$ , by

$$z = aR^b \quad (41)$$

$$\text{where } R = \frac{\pi}{6} \rho \sum_{i=1}^N (v_D D^3)$$

$V_D$  = terminal velocity

$D$  = diameter

$\rho$  = density of water in  $\text{gms/cm}^3$

Considering the rainfall rate uniform through the propagation path, the integral (Eq. 38) reduces to a linear equation of the form

$$K_r = K(f, t) r^{\alpha(f)} \cdot H \quad (42)$$

The precipitation rate,  $r$ , is measured in millimeters/hour,  $H$  the path length in kilometers and the resulting attenuation in dB. Using Gunn and East's compilation for  $K$  and  $\alpha$ , Benoit [1968] has computed the attenuation coefficient in dB/km. His values are plotted in Figure 5.44 for  $18^\circ\text{C}$ . Attenuation by rain is a function of the temperature.

This study formulated the attenuation due to rain by the equation suggested by Gunn and East, as did Benoit. For more results on the effects of precipitation from orbital heights, the reader is referred to a report compiled by Ippolito [1972] on the results from the ATS-5 satellite.

### 5.5 A Simulation of Atmospheric Effects

A computer program was written to simulate the effects of the atmosphere upon a radiometer and scatterometer operating in space. The purpose of this was to establish the bounds and the magnitude of error introduced if the effects of the atmosphere had been ignored. The computer program was a very flexible, user-oriented program which accommodated a variety of atmospheric conditions as input and produced certain parameters as output. A listing of the program is provided in the appendix, it is documented within the listing so that all mnemonics are described.

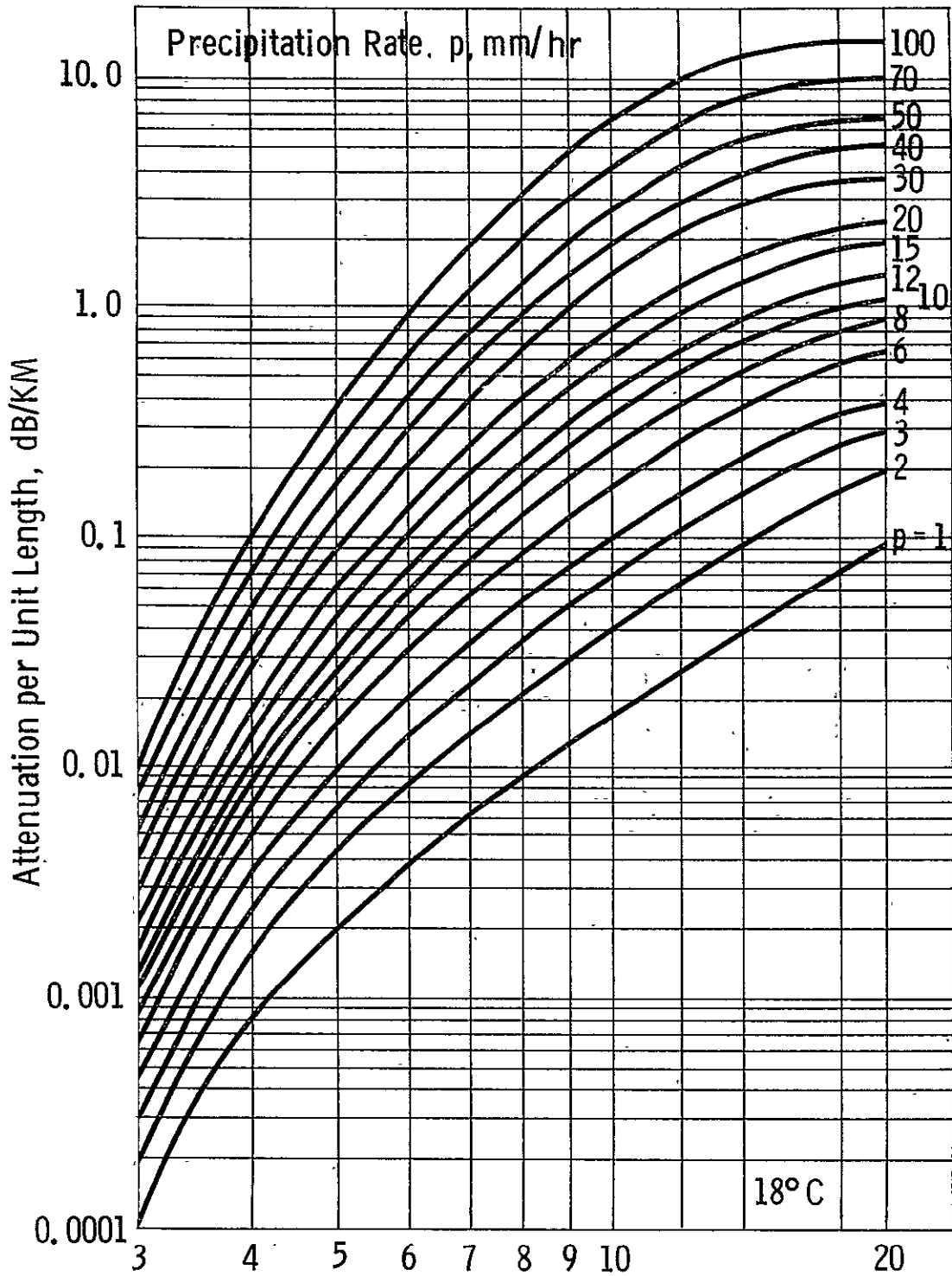


Figure 5.44. Attenuation (dB/km) due to rain. After Benoit, 1968.

The input parameters that can be supplied by the user can generally be in most acceptable units. For example, the temperature may be in Centigrade, Fahrenheit or Kelvin, the water vapor distribution in terms of specific humidity, relative humidity or dew point temperature. The program accepts either entire radiosonde profiles for temperature, pressure and humidity or only the surface values. In the latter case, the atmosphere is profiled according to a standard atmosphere. The lower ceiling of clouds, cloud thickness and water content, and the rate of precipitation if any can be specified, or, if the user chooses he may select a standard classification of light, medium or heavy clouds. The model for clouds is then taken according to Porter's classification. Another factor which may be specified for special cases (not Porter's model) is the percentage of sky cloud-cover. This may range from 0-100%.

Before providing some of the results from this program, certain simplifying assumptions inherent in the calculations should be explained. The program allows for an integration in the vertical extent of up to 20 kms in steps of 0.1 kms. The attenuation coefficient for each layer is computed for oxygen, water vapor, clouds if any and rain, if any. The clouds are assumed to have a uniform distribution of water content, the rain is assumed to originate at the lower ceiling of the clouds and the rate is assumed homogeneous across the vertical and horizontal transects. The cosmic background is assumed to contribute  $2.6^{\circ}\text{K}$ . The resultant output parameters are computed for the five S-193 Rad/Scat pitch or roll angles in the non-contiguous modes. A safety check is provided so that one does not integrate beyond the extent of the atmosphere (should a specific oblique angle output result be required). This safety check computes the ray path length when an oblique ray goes beyond the top of the atmosphere over a curved earth, and stops integration at that point. For S-193 Rad/Scat incidence angles, this condition is never exceeded.

The surface emissivity is computed from modelled responses. The surface must be specified as ocean or land. For an ocean surface, a constant temperature ( $293^{\circ}\text{K}$ ) of the water is assumed. The emissivity response is modelled to give the response from a calm sea. Figure 5.45 shows the emissivity considered for vertical and horizontal polarization for the ocean. For land, the specifications are more detailed. Two types of soil are allowed, sand and loam, the percentage of vegetation and the percent by weight of soil moisture must be specified. The responses are then modelled from data obtained from Dr. F. T. Ulaby (private communication) for sand and loam with the appropriate water content. The emissivity of vegetation is considered to be 0.90 for both polarizations and consequently when the composite emissivity of a vegetal covered ground is required, the emissivity is found by the weighted (by percent cover) average of vegetation

and soil. In other words, it has been tacitly assumed that vegetation does not permit any emission from the soil to reach the radiometer. Curves showing the emissivity of the two soil types without any vegetation for different soil moisture conditions for both vertical and horizontal polarization are shown in Figure 5.46 and 5.47.

While they do not cover all the possible land or ocean targets, these models for the surface description provide a basis by which the effects of the atmosphere can be studied. If a surface not considered in this simulation is to be studied, its expected emissivity response can be input and the effects of the atmosphere on it can be studied. There are two choices for assigning physical temperatures to the surface. In one case the surface air temperature is considered as the soil or surface temperature and in the other case the surface temperature is kept fixed at a preselected value and there can be a difference between the surface temperature and the air temperature adjacent to it.

One of the purposes served by this simulation and/or compensation for atmospheric effects was verification of some of the models invoked and the coding implemented to perform the necessary functions. The formulae used are described in the appropriate sections above. The parameters computed for each surface model and atmospheric condition were:

1. Total attenuation due to oxygen.
2. Total attenuation due to uncondensed water vapor.
3. Total attenuation for a clear sky (sum of the two above)
4. Total attenuation inclusive of clouds and rain.
5. Total transmittance with all attenuating factors accounted for.
6. Total upward (direct) emission from the atmosphere towards the receiver ( $T_{atm}(\theta)$ ) the radiation incident down to the surface  $T_{atmp}(\theta)$  was made equal to  $T_{atm}(\theta)$ .
7. The apparent brightness temperature as perceived by the receiver. The global formula is

$$T_A = L(\epsilon T_g) + \{T_{atm} + L(1-\epsilon)(T_{atmp} + 2.6)\} \quad (43)$$

where

$\epsilon$  = emissivity

$T_g$  = surface temperature

$L$  = total transmittance

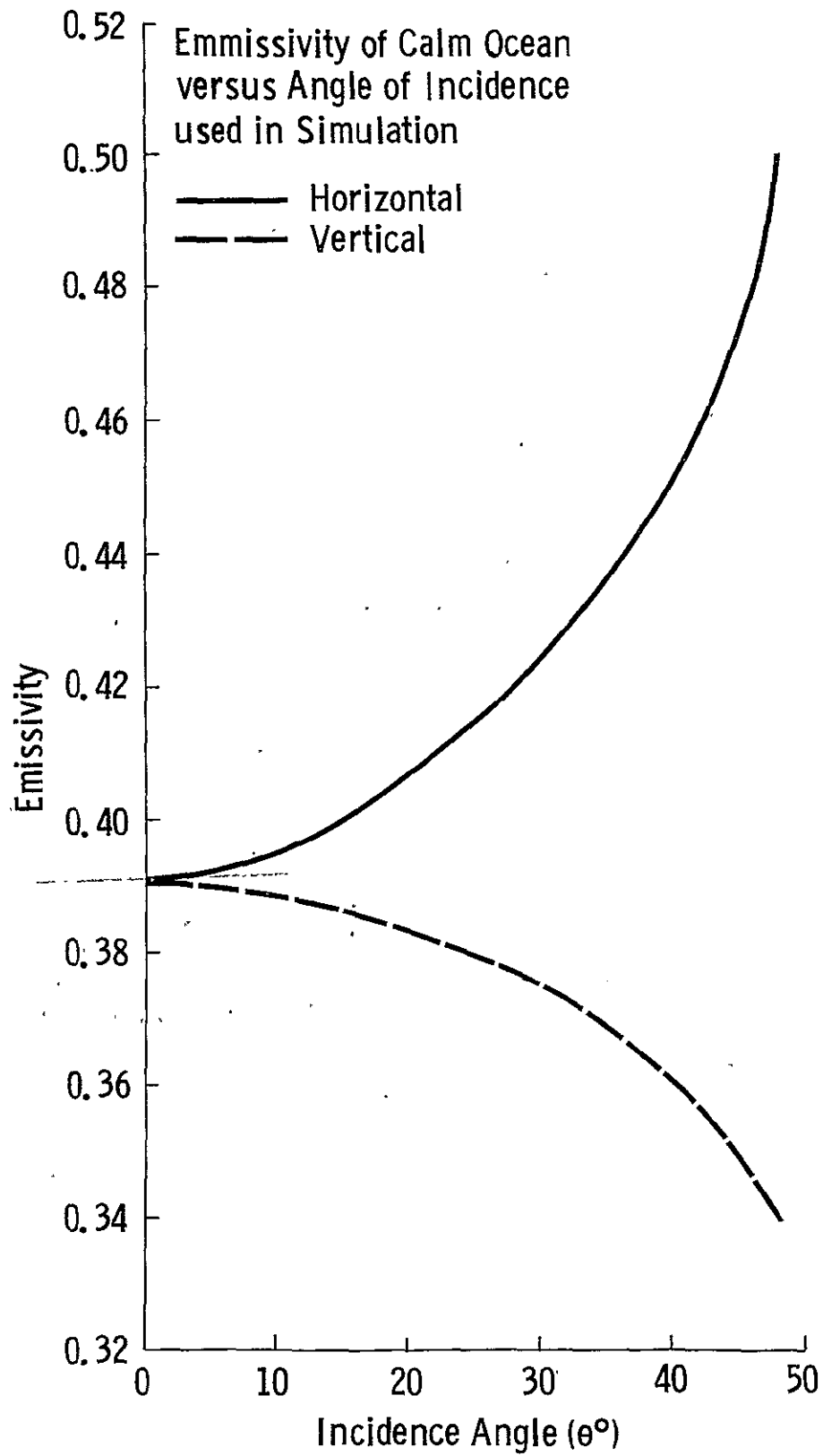


Figure 5.45.  
206

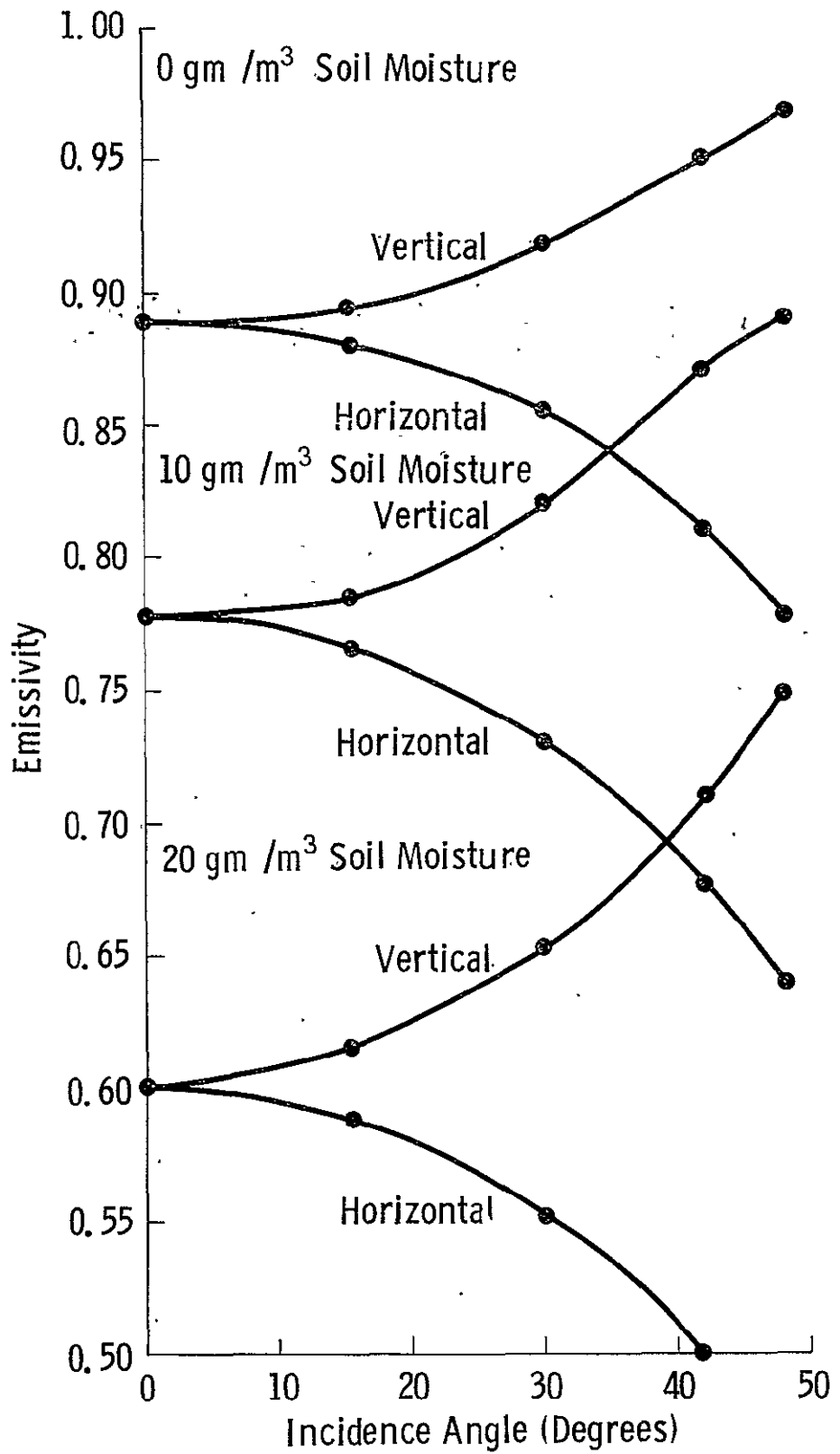


Figure 5.46. Emissivity of loam soil versus incidence angle for various soil moisture conditions. From F. T. Ulaby, 1975.

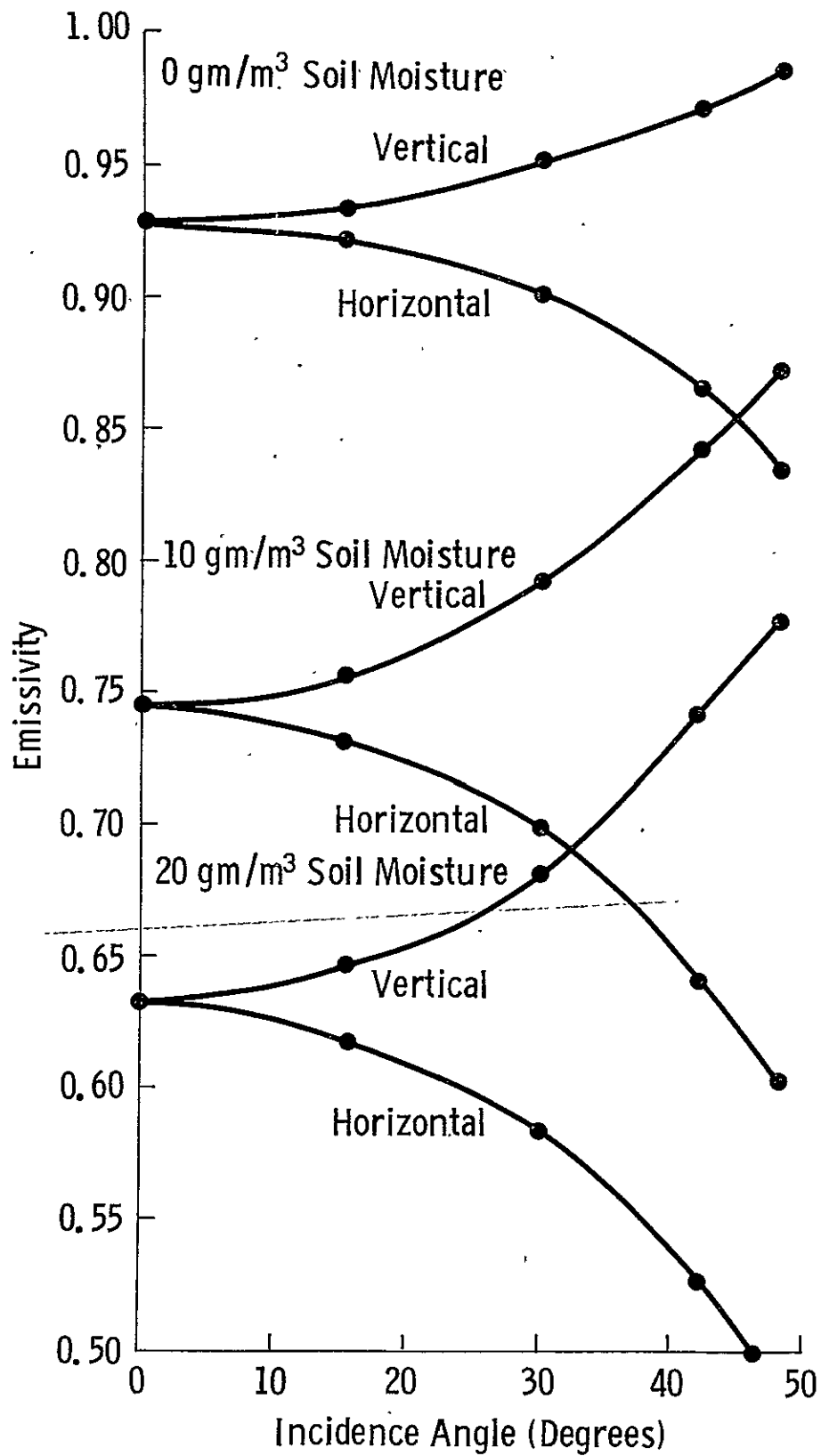


Figure 5.47. Emissivity versus incidence angle for sandy soil with 3 different soil moisture conditions. From F. T. Ulaby, 1975.

8. The total excess temperature defined as the difference between the true natural emission of the surface and that perceived by the receiver

$$T_{EX} = T_A - \epsilon T_g \quad (44)$$

This is a measure of the error introduced if one did not include the effects of the atmosphere.

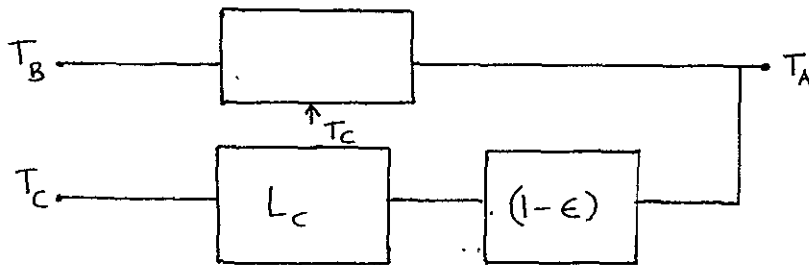
9. The total atmospheric contribution to the radiation received at the antenna. This is computed as

$$T_{tot} = T_{atm} + L(1-\epsilon) [T_{atmp} + 2.6] \quad (45)$$

It is a measure of how "lossy" the atmosphere was, when considered as an insertion loss.

With this brief explanation of the parameters, the reader can now understand the results presented from the simulation. It was established earlier (Section 5.2.) that the difference in the results obtained for an actual radiosonde profile and a modelled profile were minimal. The four radiosonde profiles obtained from NYU (Dr. Cardone) were modelled by the schemes presented in Section 5.1.3. These model profiles were then used with selected surface parameters to compute the results described above. The first surface chosen was a calm sea, the emissivity response for both horizontal and vertical polarization are provided in Figures 5.45. The temperature of the surface (ocean surface) was kept fixed at 293°K (18°C). With these surface parameters, two sets of profiles, one with no clouds and the other with Porter's classification of heavy clouds introduced at the appropriate heights, were used to model the atmosphere. The apparent temperature, excess temperature, and the total attenuation versus angle of incidence for both the profile with no clouds and the one with heavy clouds were computed. Figures 5.48 through 5.51 show these three parameters for horizontal polarization for the four ocean profiles. Notice how the presence of clouds causes the excess temperature to increase by a factor of almost 5. The excess temperature for a clear sky varies from approximately 12°K for the Swan Island profile (highest humidity) to a minimum of approximately 7°K for the profiles called Northeast of Warm Front (with the lowest surface temperature). The excess temperature for the warm sector of the Cyclone was also comparable to the minimum value. The profile at Azores in a

subtropical high contained more humidity and hence had a larger excess temperature. The excess temperature is seen to be only slightly a function of incidence angle. With the inclusion of heavy clouds, the maximum excess temperature is seen to be around 48°K for the same case that had the least excess without clouds (N.E. of warm front). This may seem erroneous, but a moment's reflection will show that these results are expected. It was determined in Section 5.4 (attenuation due to clouds) that the attenuation due to clouds is a function of the temperature. The lower the temperature of the clouds, the higher the attenuation coefficient. Notice that the total attenuation (for heavy clouds) is maximum for this case. The situation in lumped parameter representation is given by



where

- $L_c$  = attenuation coefficient for cloudy profile (lumped parameter)
- $T_c$  = temperature (equivalent lumped parameter) of cloudy profile
- $T$  = emission from the surface
- $\epsilon$  = emissivity of the surface

and

$$\text{where } T_A = \frac{T_B}{L_c} + \frac{T_c(L_c-1)}{L_c} + (1-\epsilon) \frac{T_c(L_c-1)}{L_c} \quad (46)$$

$$= \frac{\epsilon T_g}{L_c} + (2-\epsilon) \frac{T_c(L_c-1)}{L_c}$$

$$T_{EX} = \left(1 - \frac{1}{L_c}\right) [2T_c + \epsilon \Delta T] \quad (47)$$

$$\Delta T = T_g - T_c \quad (48)$$

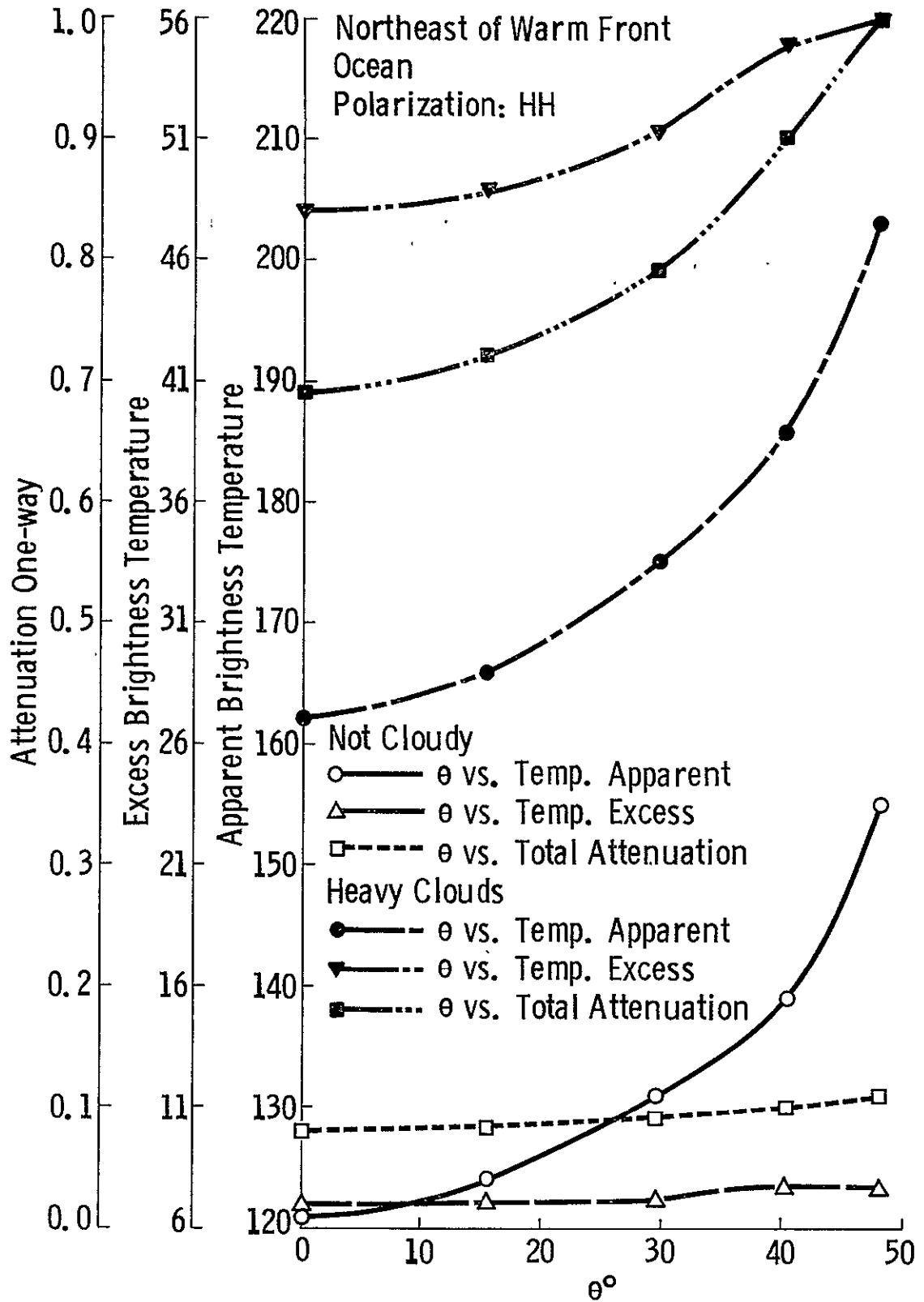


Figure 5.48. Simulated results for northeast of warm front sample; polarization HH, ocean surface.

Warm Sector of Cyclone  
 Ocean  
 Polarization: HH

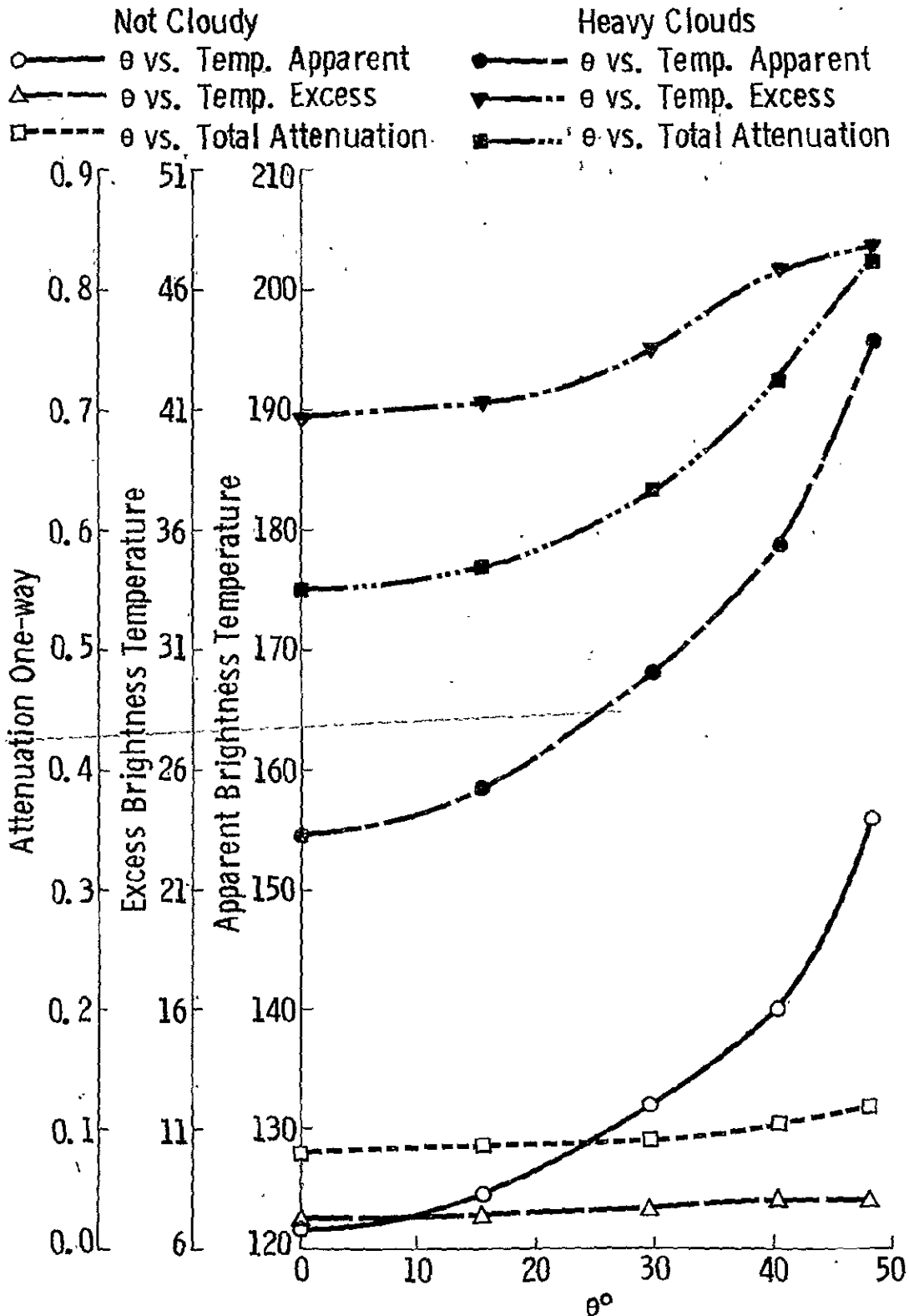


Figure 5.49. Simulated results for warm sector of cyclone sample; polarization HH, ocean surface.

Azores in Subtropical High  
Ocean  
Polarization: HH

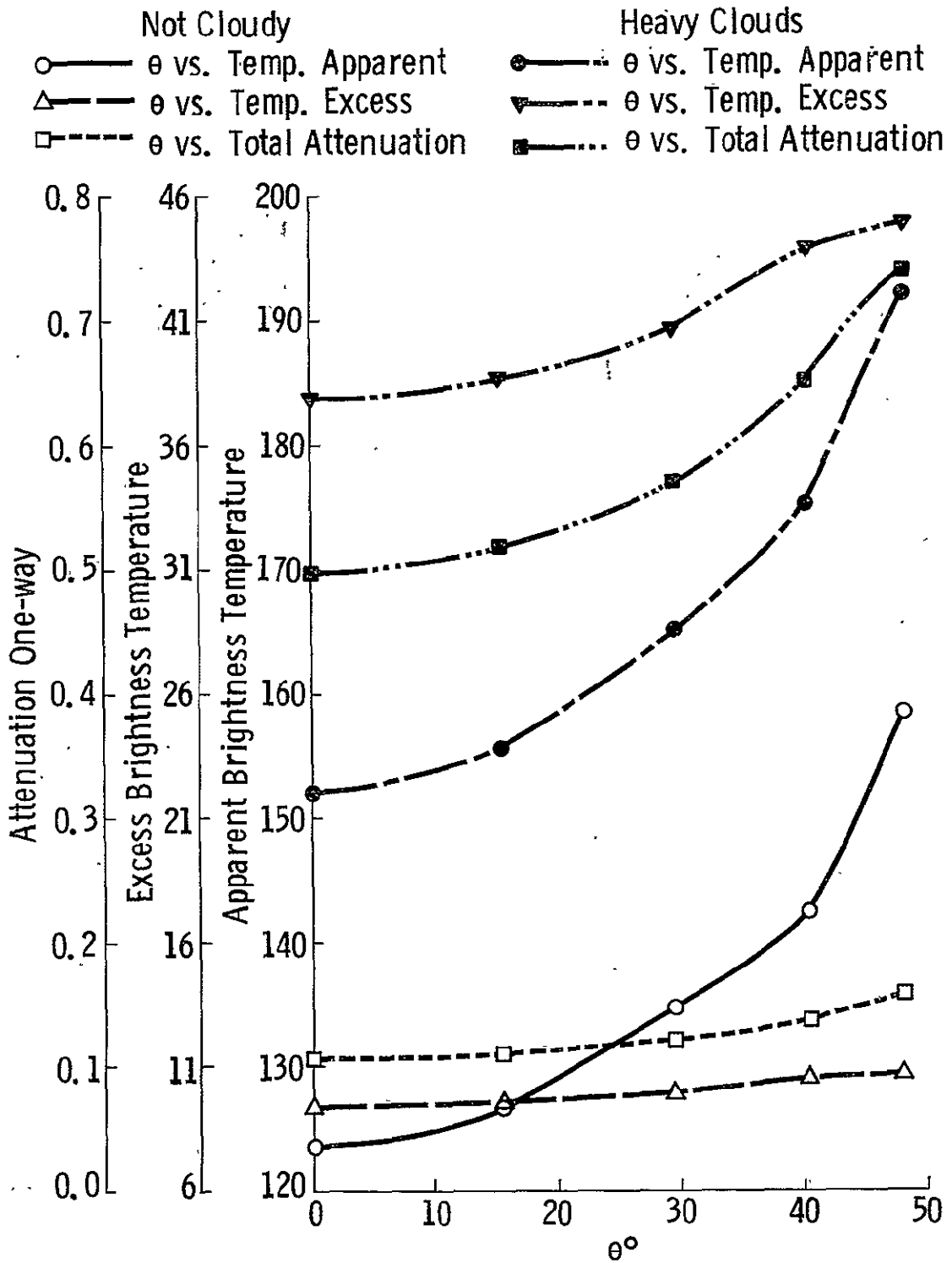


Figure 5.50. Simulated results for Azores in subtropical high sample; polarization HH, ocean surface.

Swan Island Tropical  
Ocean

Polarization: HH

Not Cloudy

- —  $\theta$  vs. Temp. Apparent
- △ —  $\theta$  vs. Temp. Excess
- - - -  $\theta$  vs. Total Attenuation

Heavy Clouds

- - - -  $\theta$  vs. Temp. Apparent
- ▼ - - -  $\theta$  vs. Temp. Excess
- - · - ·  $\theta$  vs. Total Attenuation

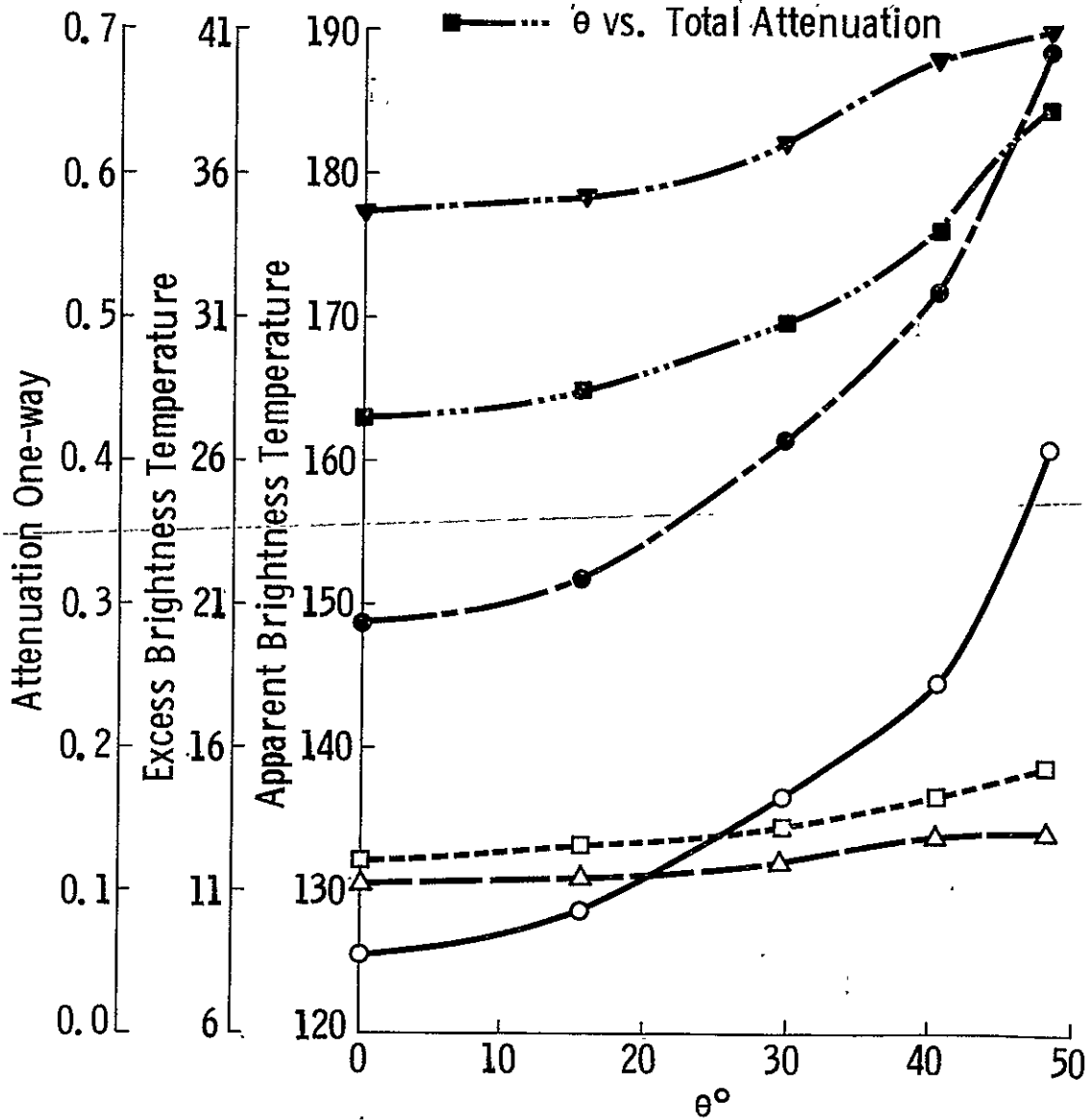


Figure 5.51. Simulated results for Swan Island tropical sample; polarization HH, ocean surface.

One can see that the excess temperature is a function of the insertion loss (attenuation coefficient), the temperature of the insertion loss (atmospheric temperature) and the difference between the lossy element (atmospheric) temperature and the signal (radiation from surface) temperature. Each of the four profiles can, therefore, be seen to contribute to the excess temperature in different ways. The dependence of the attenuation due to clouds on the cloud temperature is not straightforward because the temperature appears as part of an exponent in computing the attenuation coefficient. Observe, however, that the excess temperature increases monotonically with incidence angle for all four cases.

The response for vertical polarization over a calm sea at a physical temperature again of  $293^{\circ}\text{K}$  for both no clouds and heavy clouds for each of the four profiles discussed, is presented in Figures 5.52 through 5.55. Observe that for all four cases in the absence of clouds, the apparent temperature decreases with increasing angle and thus follows the expected response for vertical polarization for a calm sea (Figure 5.45). The excess temperature ranges from  $8^{\circ}\text{K}$  at nadir for the sample N.E. of Warm Front to approximately  $12^{\circ}\text{K}$  for the profile with high humidity (Swan Island), with the other two in between. The apparent temperature computed when heavy clouds are introduced increases with angle of incidence in all four cases, with the sharpest rise being for the N.E. of Warm Front sample. Once again the effects of clouds predominates on this one. The excess temperature is again highest for this case. The maximum attenuations for these cases are the same as for the cases discussed above for horizontal polarization because the attenuation is not considered to be polarization selective.

The Warm Front and Swan Island profiles were next considered with land targets. The land targets considered were either a loam soil or a sand soil. The soil moisture was considered zero, the corresponding emissivity for the two soils for vertical and horizontal polarizations are given in Figure 5.46 and 5.47. The surface temperature was considered equal to the atmospheric temperature at the surface. The apparent temperature, excess temperature, and total attenuation versus incidence angle for both cloud-free and heavy conditions were computed. Figures 5.56 and 5.57 show the apparent temperature, excess temperature and the total attenuation versus angle of incidence for no clouds and heavy clouds using the sample profile from N.E. of Warm Front and Swan Island respectively over a dry sandy soil. There is a dramatic difference between the apparent temperature for the cloud-free cases in the two profiles. The emissivity of the surface in these cases is much higher than for the ocean cases so that a difference in the surface temperature causes a great difference in the apparent temperature. The excess temperature, however, shows a decrease with incidence angle and is of a much smaller magnitude than for the ocean surface.

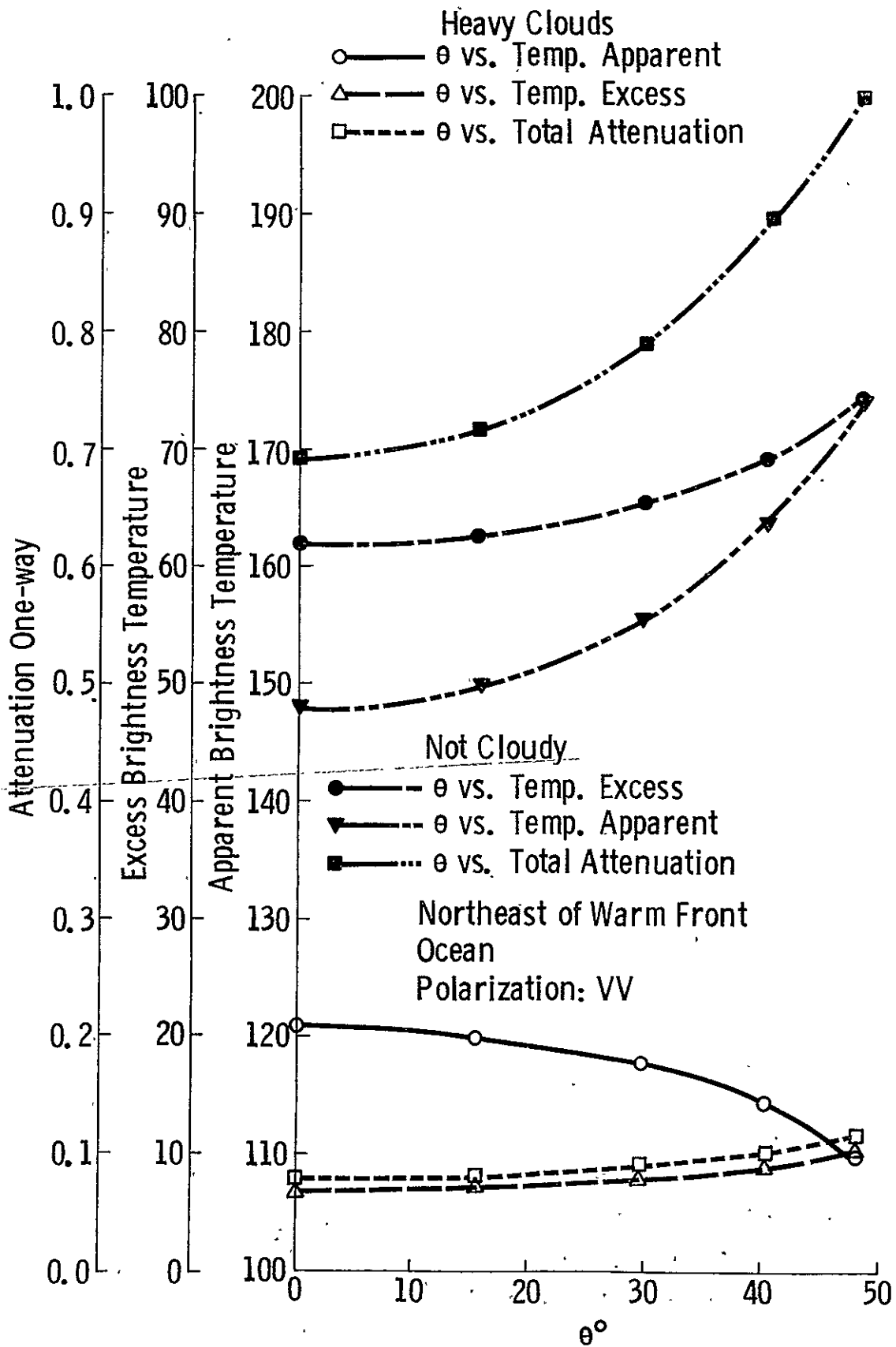


Figure 5.52. Simulated results for northeast of warm front sample; polarization VV, ocean surface.

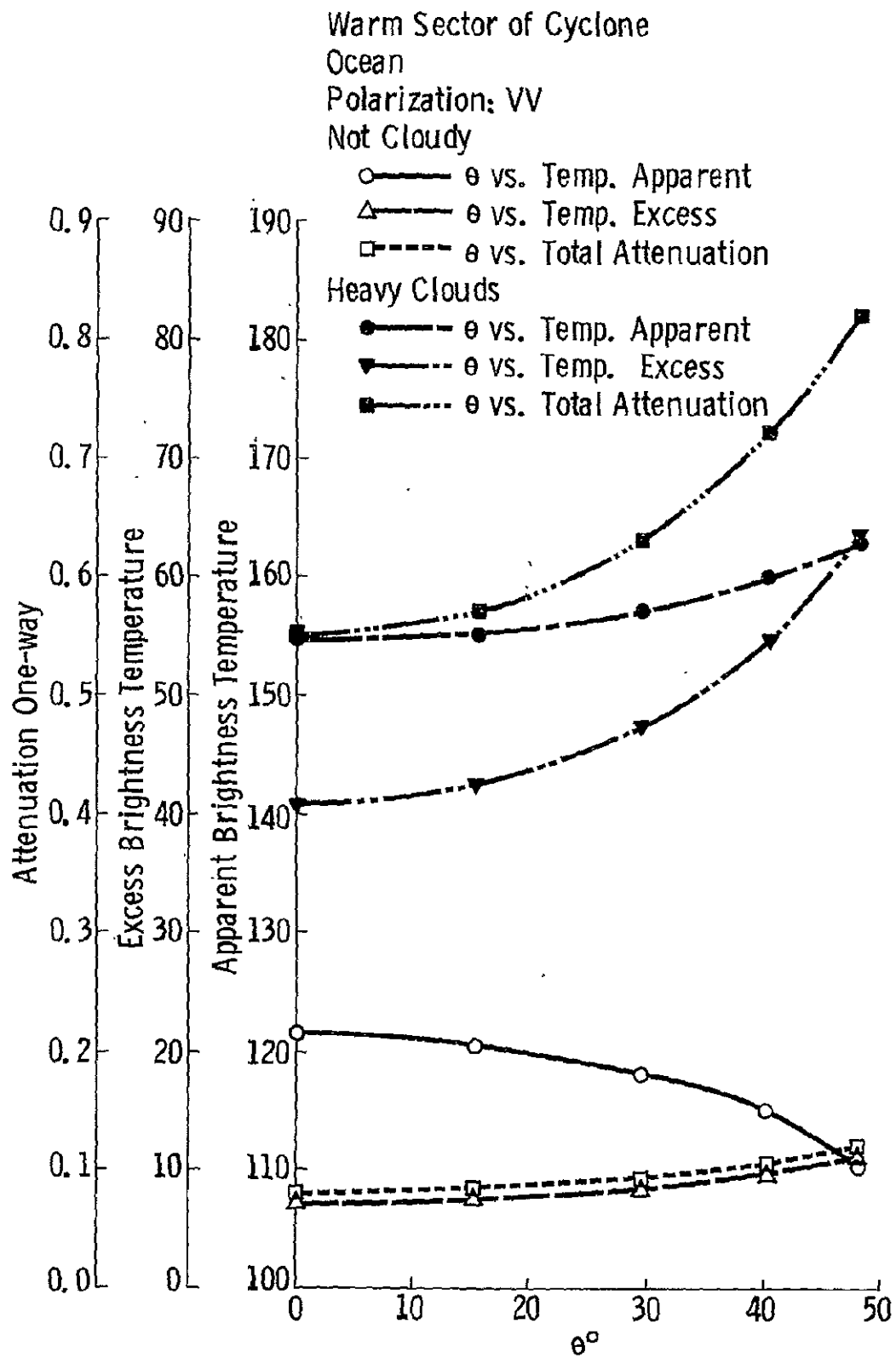


Figure 5.53. Simulated results for warm sector of cyclone sample; polarization VV, ocean surface.

Azores in Subtropical High  
 Ocean  
 Polarization: VV  
 Not Cloudy

○ —  $\theta$  vs. Temp. Apparent  
 △ —  $\theta$  vs. Temp. Excess  
 □ - -  $\theta$  vs. Total Attenuation

Heavy Clouds  
 ● —  $\theta$  vs. Temp. Apparent  
 ▼ —  $\theta$  vs. Temp. Excess  
 ■ —  $\theta$  vs. Total Attenuation

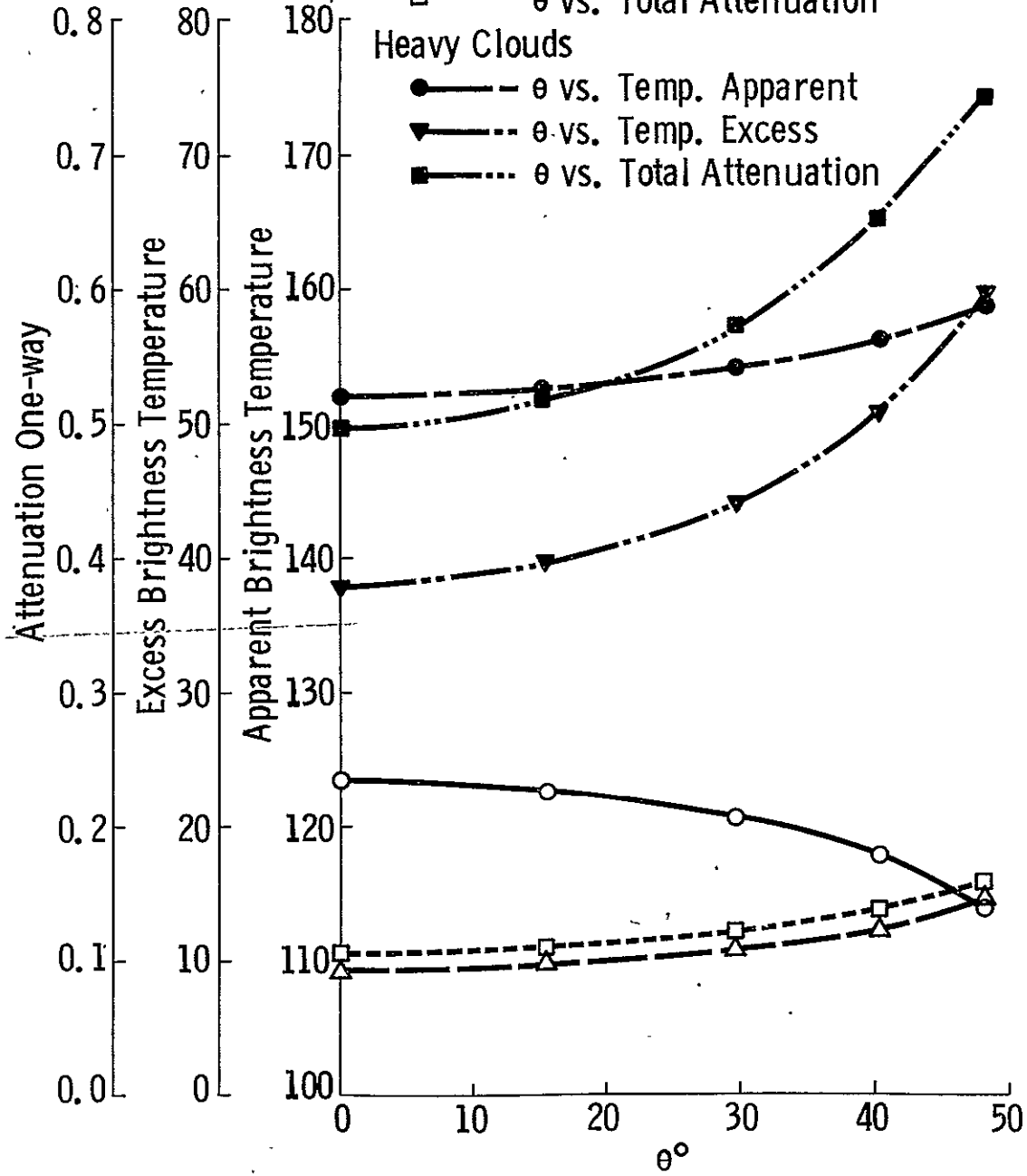


Figure 5.54. Simulated results for Azores in sub-tropical high sample; polarization VV, ocean surface.

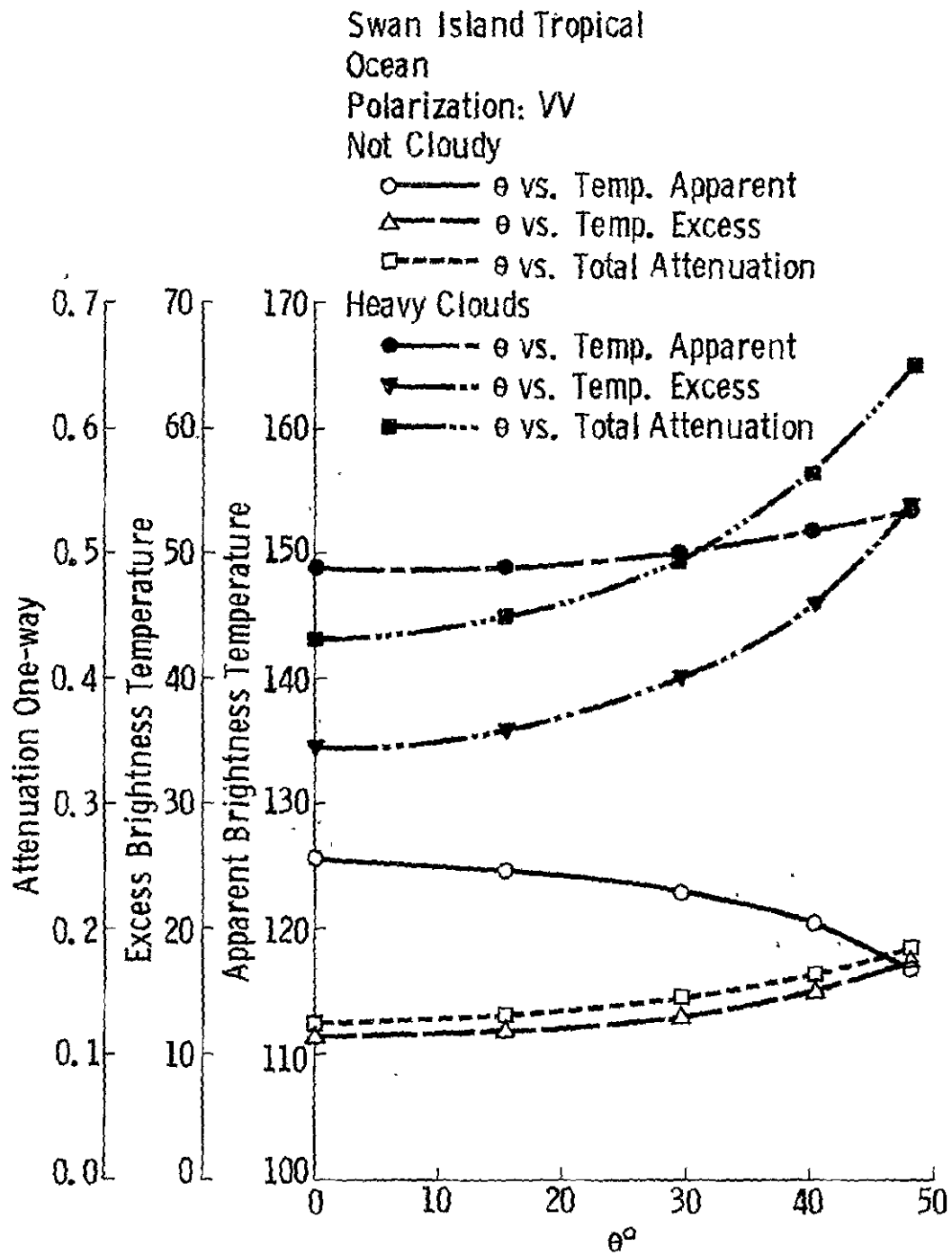


Figure 5.55. Simulated results for Swan Island tropical sample; polarization VV, ocean surface.

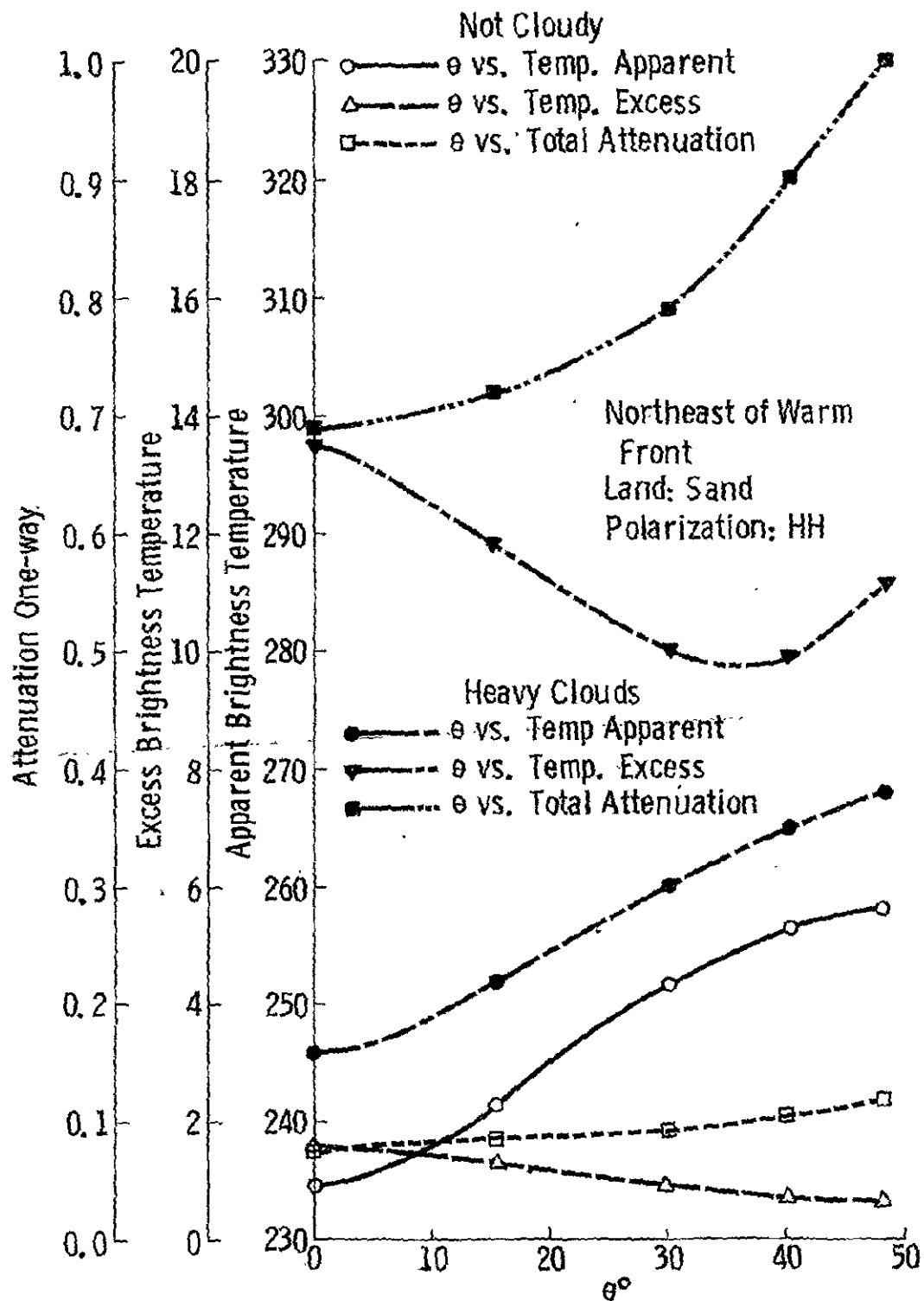


Figure 5.56. Simulated results for northeast of warm front sample; polarization HH, sand surface.

Swan Island Tropical  
 Land: Sand  
 Polarization: HH

Not Cloudy		Heavy Clouds	
○—	$\theta$ vs. Temp. Apparent	●—	$\theta$ vs. Temp. Apparent
△—	$\theta$ vs. Temp. Excess	▼—	$\theta$ vs. Temp. Excess
□- - -	$\theta$ vs. Total Attenuation	■- - -	$\theta$ vs. Total Attenuation

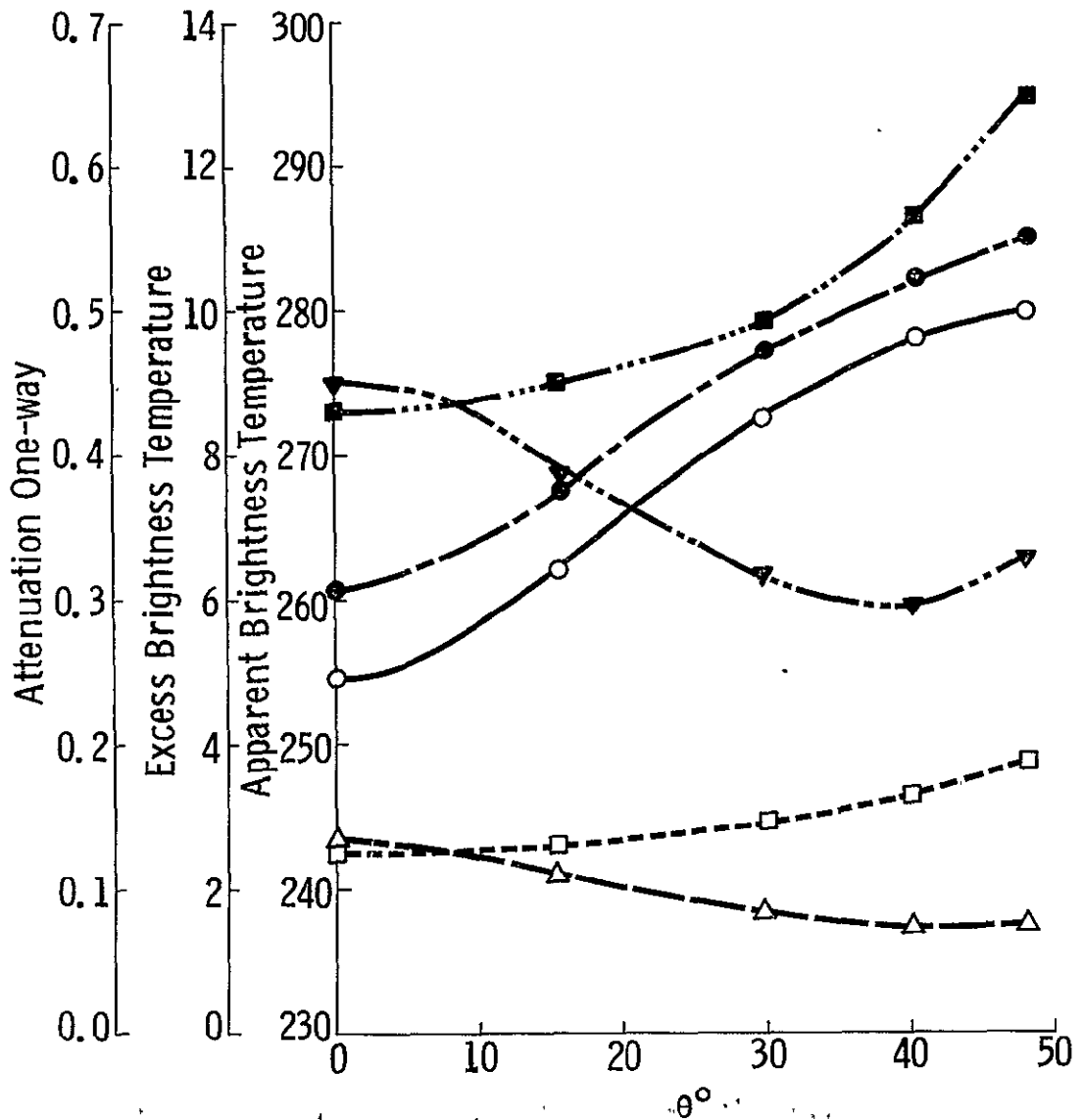


Figure 5.57. Simulated results for Swan Island tropical sample; polarization HH, sand surface.

This is because the  $\epsilon\Delta T$  contributes a much larger negative component to cancel out the  $2T_c$  in equation 5.48, because of the greater emissivity. The apparent temperature computed for the profiles with heavy clouds maintains the same general shape as that for the cloud-free case but is a few degrees higher in both cases. This is seen in the curves for the excess temperature. The excess temperature decreases till a certain angle (about  $35^\circ$ ) and then starts to increase again. This excess temperature for heavy clouds for the N.E. Warm Front sample profile (cold surface temperature) is much higher ( $13.6^\circ\text{K}$  at nadir) than that for the Swan Island sample profile (higher temperature, higher humidity) which is only  $9^\circ\text{K}$  at nadir incidence. From these figures, it can be seen that over land even with such diverse profiles, the excess temperature without the presence of heavy clouds is less than  $3^\circ\text{K}$  (at nadir incidence) and increases slowly to  $50^\circ$  incidence. The effect of the presence of clouds cannot be compensated for by a bias shift in apparent temperature which may be possible for the cases without clouds.

The effects for vertical polarization can be seen in Figures 5.58 and 5.59. The target is a loam soil, the two profiles are again the N.E. Warm Front and Swan Island and the curves again show apparent temperature, excess temperature and total attenuation. The apparent temperature in the absence of clouds follows the general decay with incidence angle and again the physical difference in temperatures of the surfaces is seen in the apparent temperatures. The excess temperature for these cases is almost zero for nadir incidence and increases slightly with angle of incidence. The extremely small excess temperature for nadir incidence seen in this case is because of the value of emissivity for loam (being different from sand, it made the  $T$  terms almost cancel the  $2T_c$  value in equation 5. ). The presence of heavy clouds causes the apparent temperature versus incidence angle curve to flatten out at higher angles of incidence. This is reflected in the excess temperature which rises sharply with angle of incidence. The excess temperature at nadir incidence is less than  $2^\circ\text{K}$  even with heavy clouds for the warmer Swan Island Profile surface. The excess temperature for the cold surface (N.E. Warm Front) rises to  $14.5^\circ\text{K}$  from  $3.2^\circ\text{K}$  as the angle of incidence goes from nadir to  $48^\circ$ .

Having observed the effects with a warm moist profile and a cold profile with average moisture, the simulation was carried out with a profile modelled after a radiosonde sounding over Topeka, Kansas. The profile has been discussed above. The surface temperature was again kept equal to the air temperature ( $283^\circ\text{K}$ ). The same parameters as for the cases discussed above were computed and plotted. This profile was chosen because it represents a case that will cause more error (excess temperature) than most of the cases one expects to encounter over the U.S. with the Skylab S-193 Radiometer. It may, therefore, be considered

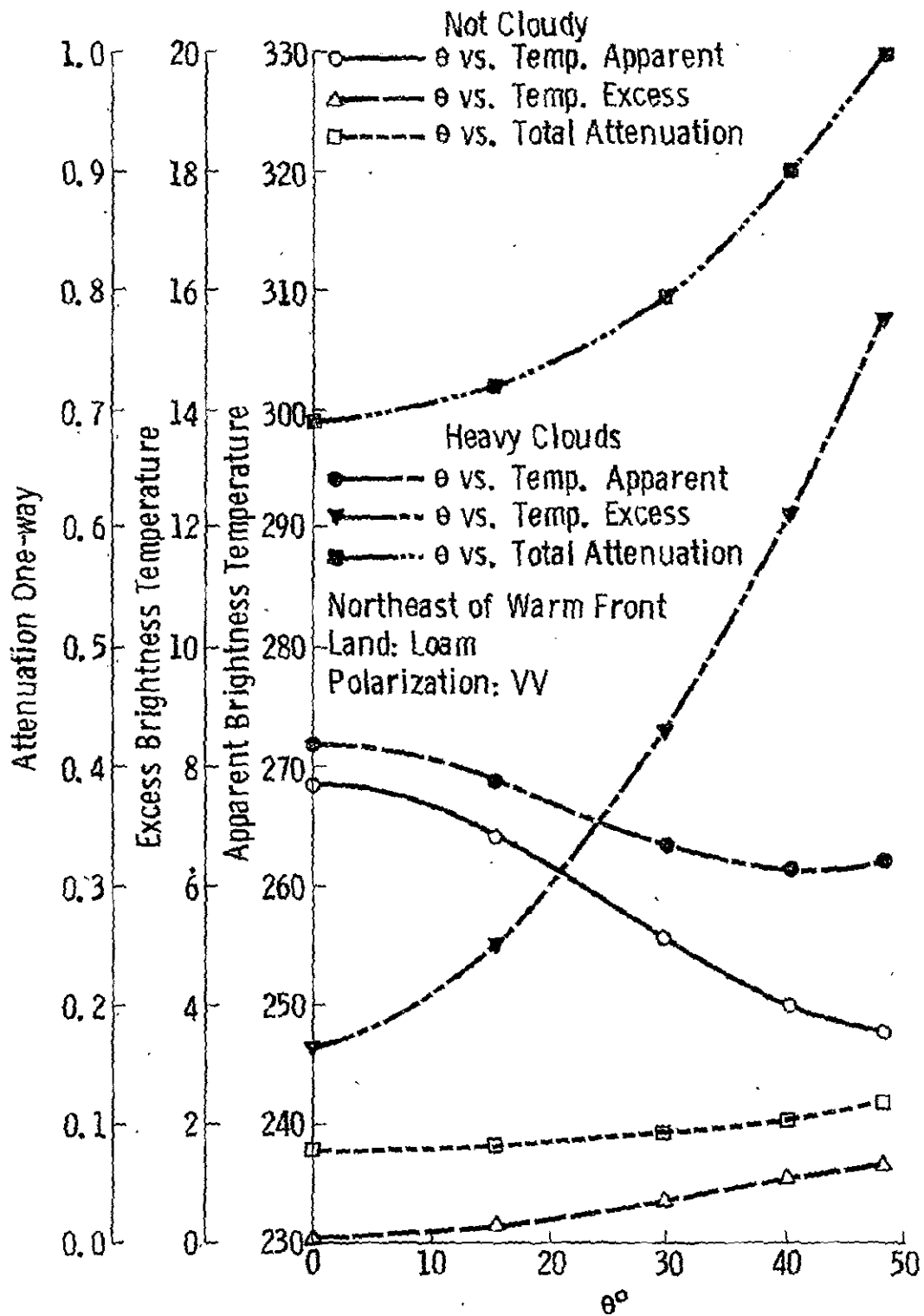


Figure 5.58. Simulated results for northeast of warm front sample; polarization VV, loam surface.

Swan Island Tropical  
 Land: Loam  
 Polarization: VV

Not Cloudy  
 $\theta$  vs. Temp. Apparent  
 $\theta$  vs. Temp. Excess  
 $\theta$  vs. Total Attenuation

Heavy Clouds  
 $\theta$  vs. Temp. Apparent  
 $\theta$  vs. Temp. Excess  
 $\theta$  vs. Total Attenuation

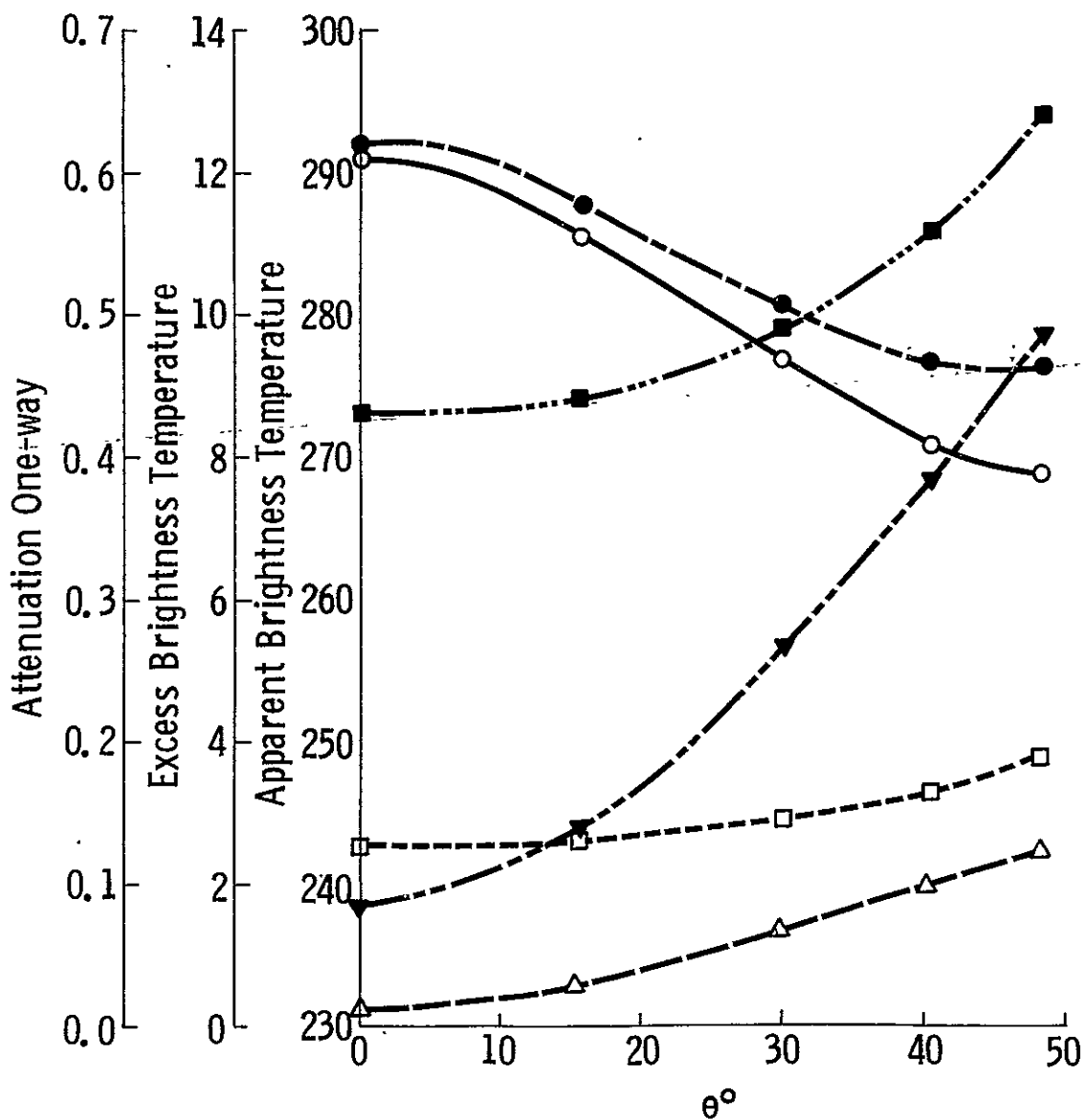


Figure 5.59. Simulated results for Swan Island tropical sample; polarization VV, loam surface.

an  $\alpha\%$  upper confidence limit on the error. The value of  $\alpha$  is left to the reader to decide. Figures 5.60 and 5.61 show the apparent temperature, etc. for a sand surface for vertical and horizontal polarizations respectively. The excess temperature is seen to be in the neighborhood of  $1^{\circ}\text{K}$  for a range of incidence angles from nadir to  $48^{\circ}$ , for the cloud-free cases. The excess temperature for horizontal polarization (Figure 5.60) again shows the reversal in slope. The maximum excess temperature in the presence of heavy clouds for horizontal polarization is  $11.7^{\circ}\text{K}$  (nadir incidence) and  $9.3^{\circ}\text{K}$  ( $48^{\circ}$  incidence) for vertical polarization. For the sake of comparison, the corresponding results for a loam soil are provided in Figure 5.62. The excess temperature in the presence of clouds is much more for the loam soil than for the sand soil and reaches a maximum of  $13^{\circ}\text{K}$  at  $48^{\circ}$  incidence.

We have seen that at higher surface temperatures and high emissivities the effects of the atmosphere are much smaller. In all of the land cases considered so far, we have assumed that the surface temperature was the same as the air temperature at the surface. The simulation was next exercised by considering a pressure of 1011.4 millibars, specific humidity of  $7.5 \text{ gms/m}^3$  and the air temperature at the surface was considered at  $290^{\circ}\text{K}$  and  $310^{\circ}\text{K}$ . The atmosphere was again profiled as in section 5.1.3. Two cases were considered, one in which the surface temperature was the same as the air temperature at the surface and the other where the surface temperature was  $290^{\circ}\text{K}$  while the air temperature was  $310^{\circ}\text{K}$ . Figures 5.63, 5.64, and 5.65 show the results for sand with horizontal polarization, sand with vertical polarization and loam with vertical polarization. The curves denoted as temperature alike are the ones where the surface temperature was kept equal to the air temperature at the surface. The ones denoted Temperatures not alike are ones where the surface temperature was  $290^{\circ}\text{K}$  and the air temperature  $310^{\circ}\text{K}$ . The smallest excess temperature recorded in all three conditions was for the cases where the surface temperature was maximum and equal to the air temperature. The maximum excess temperature with heavy clouds at angles away from vertical was always for the case with the lowest air temperature. For cloud-free profile cases, the maximum excess temperature was always for the case where the surface and air temperature differed.

## 5.6 Summary

The effects of the intervening atmosphere upon active (S-193 scatterometer and altimeter) sensors and passive (S-193 radiometer) sensors operating at 13.9 GHz on an orbital platform were found. The equations to compute the attenuation due to oxygen and water vapor are described. The atmospheric profile was modelled according to the formulae suggested in Section 5.1.3. With this model profile, the effects of pressure and

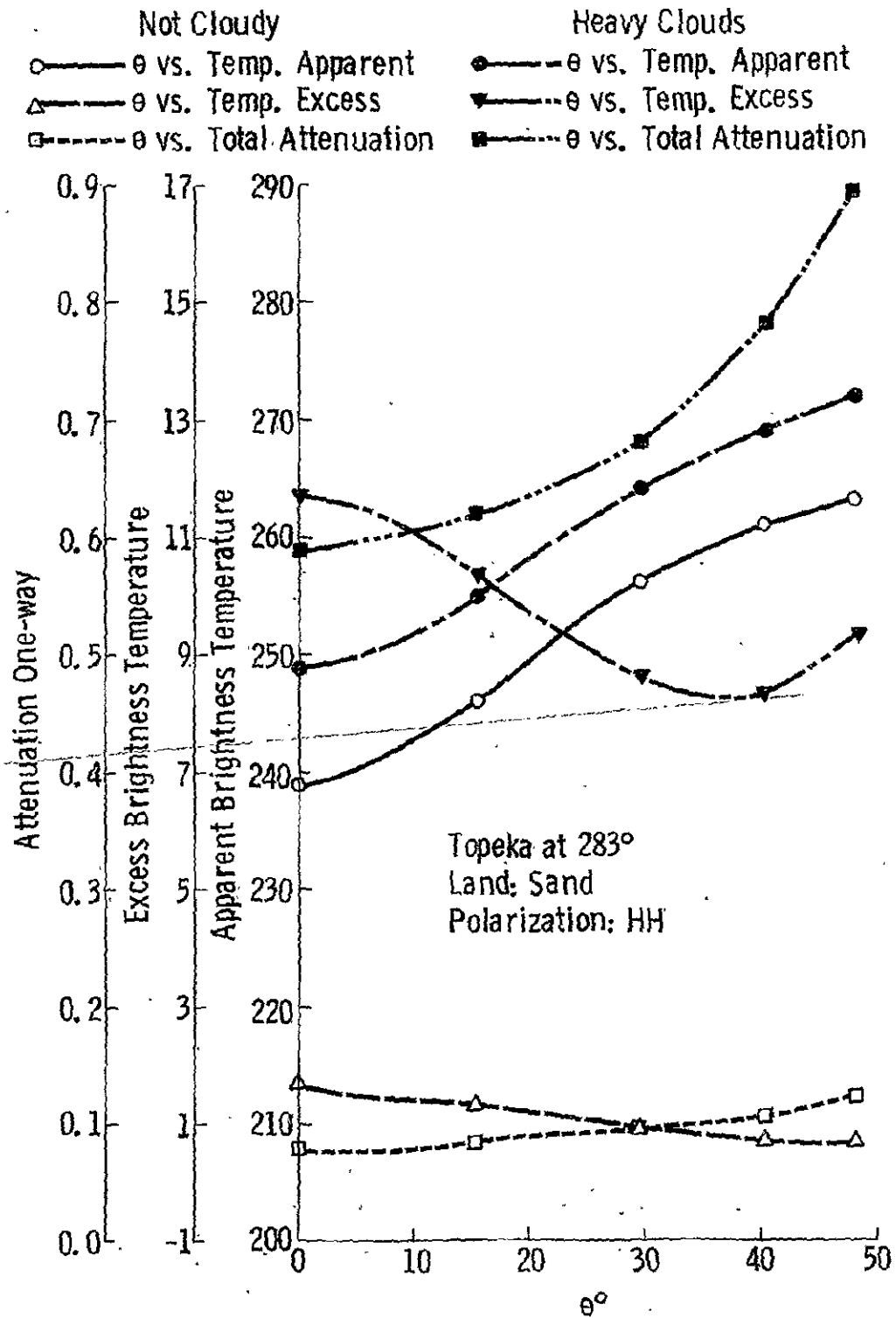


Figure 5.60. Simulated results for Topeka sample with surface temperature at 283° K; polarization HH, sand surface.

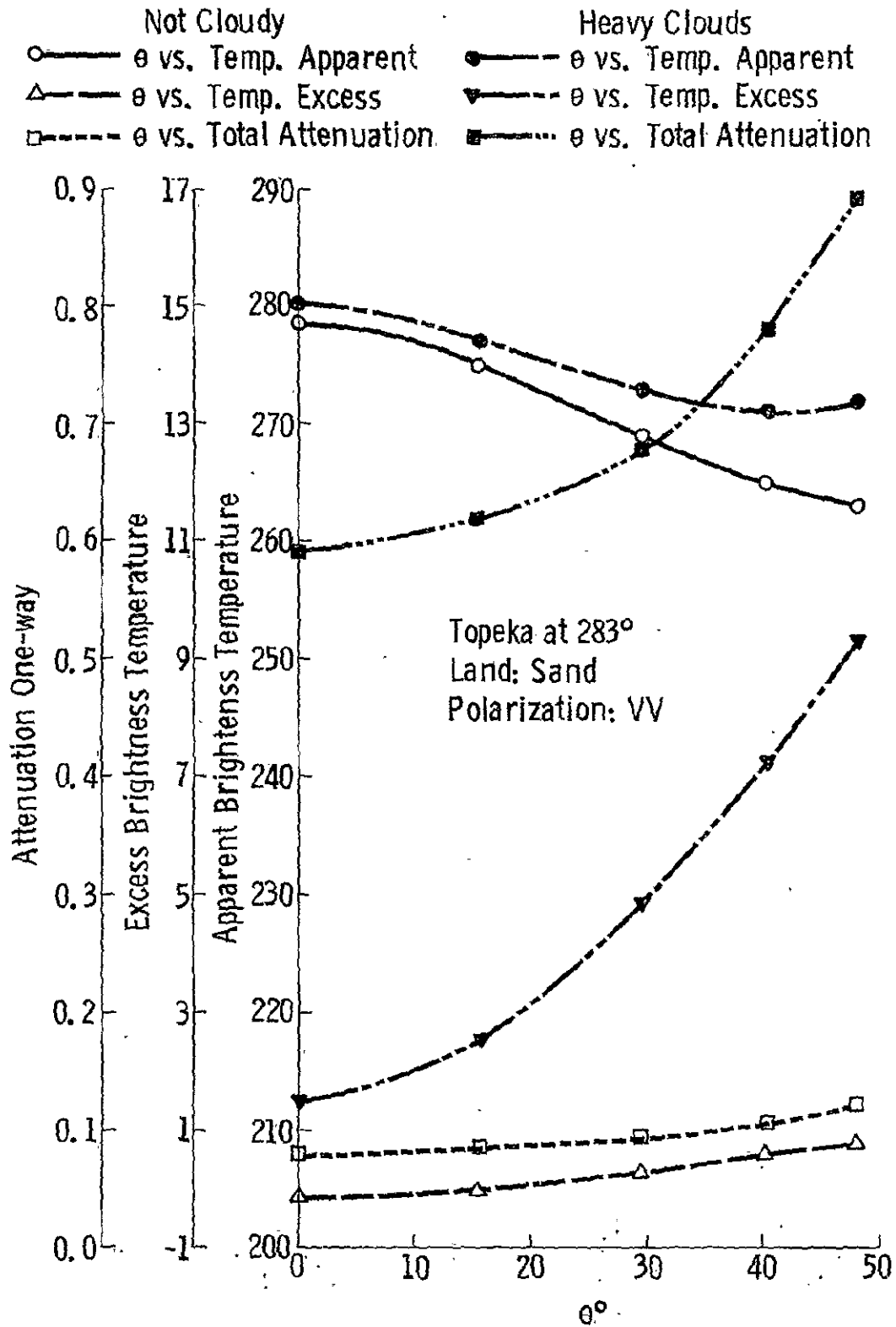


Figure 5.61. Simulated results for Topeka sample with surface temperature at 283° K; polarization VV, sand surface.

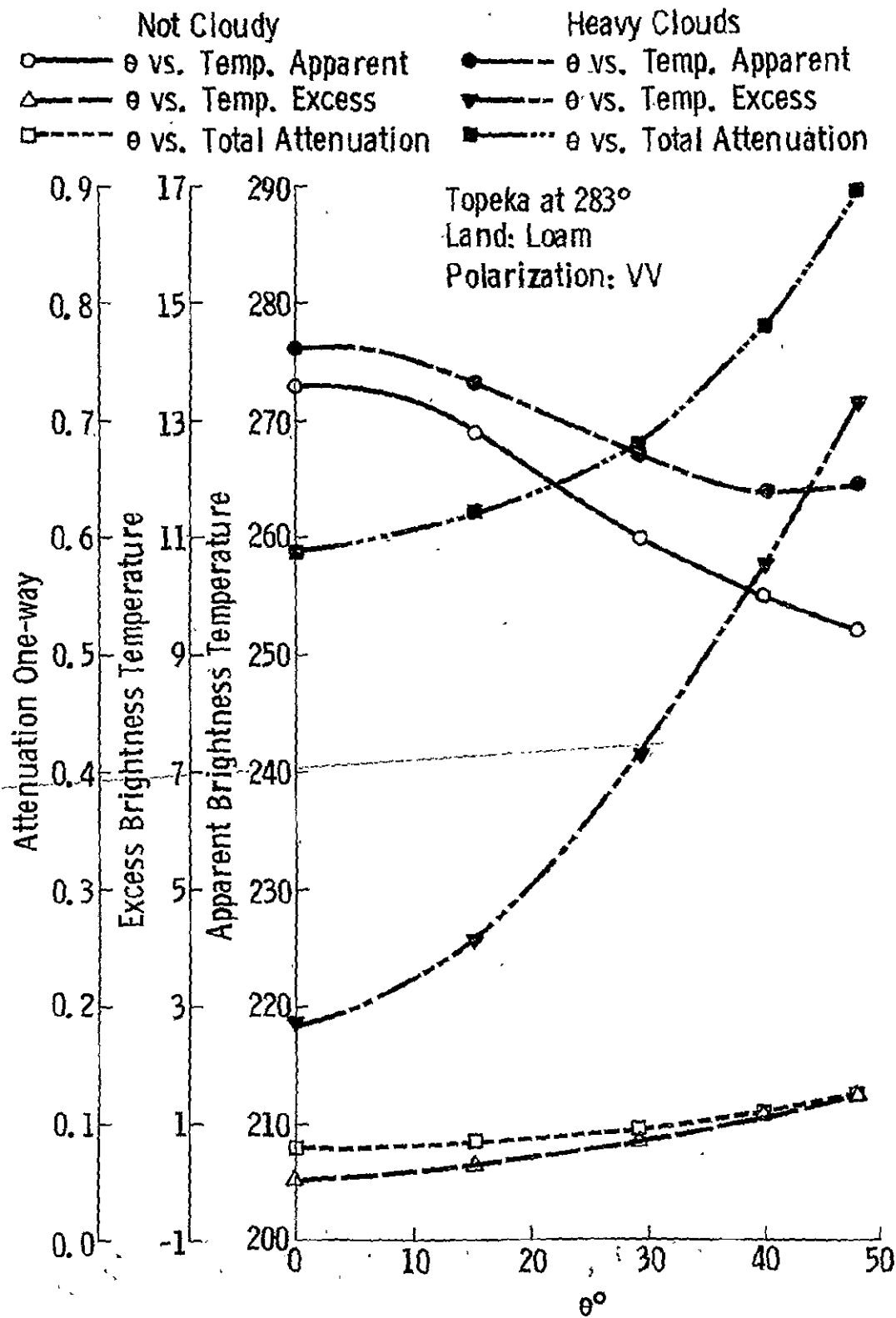


Figure 5.62. Simulated results for Topeka sample with surface temperature at 283° K; polarization VV, loam surface.

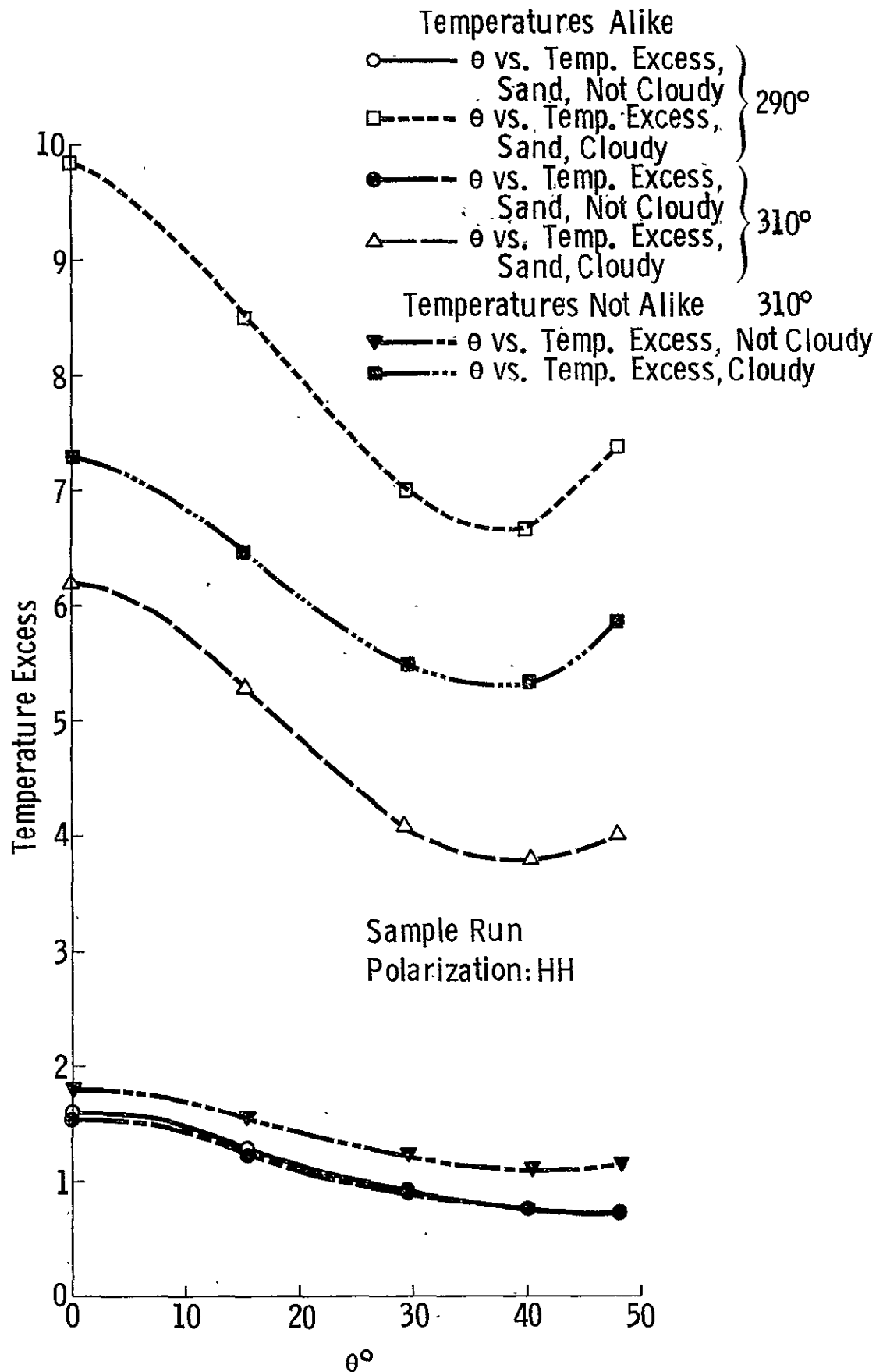


Figure 5.63. Simulated results for cloudy and not cloudy conditions over a sand surface with two temperature conditions.

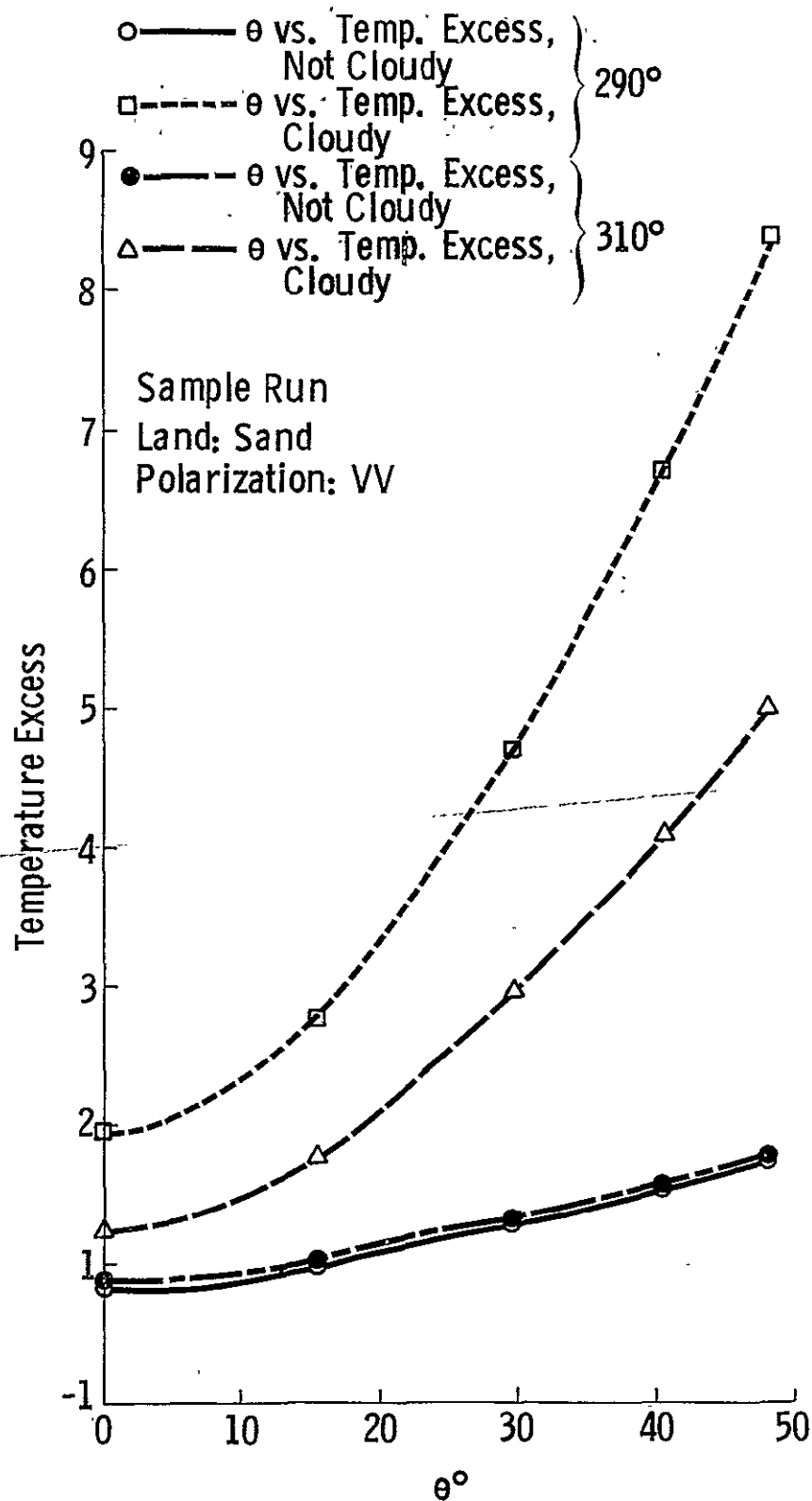


Figure 5.64. Simulated results for cloudy and not cloudy conditions over a sand surface for two surface temperatures, polarization VV.

temperature upon the attenuation due to oxygen were computed. It was found that the variations in attenuation due to these parameters was small and that the total error in attenuation by ignoring the effects due to oxygen attenuation were 0.076 dB. The attenuation due to uncondensed water vapor was computed for various surface temperature and humidity conditions. The attenuation was found to vary linearly with specific humidity and the variations due to temperature were very small (less than 0.3 dB at nadir incidence for a 40°C change in temperature and a specific humidity of 20 gm/m<sup>3</sup>).

A comparison of the transmittance computed by using actual radiosonde soundings over four diverse atmospheric conditions and that computed from a model profile using the surface parameters from the soundings showed that the difference was negligible, the maximum difference occurring for a case which had a temperature and humidity inversion. A comparison of the direct emission of temperature from the atmosphere as computed from actual radiosonde data and the corresponding model profile also showed small differences.

The effects of clouds upon the microwave signals were explored. Some quantized models of clouds were invoked, an empirical equation to compute the attenuation was used and the results are provided. It was found that the total water content of the clouds was the most important factor, but that the temperature of the clouds also had a significant effect upon the attenuation. Examples of results obtained by invoking various cloud models are provided.

The effects of rain upon the microwave signals were explored. The rain models suggested were described. None of these models, however, was used. Empirical expressions to compute the attenuation due to rain based upon rainfall rate, extent of rain (range) and temperature are described along with an example of the results.

A simulation program to estimate the effects of the atmosphere upon ocean and land targets was described. For each selection of target, polarization and atmospheric conditions, the following parameters were estimated: the apparent brightness temperature at the antenna, the excess brightness temperature (defined as the difference between the apparent brightness temperature at the antenna and the surface brightness temperature), the direction emission due to the atmosphere, the total contribution due to the atmosphere (direct and reflected by the surface), the attenuation and the transmittance. The sample targets were a calm ocean and two land targets--loam and sand soil with varying soil moisture and vegetation. The examples of the results are provided for

a calm ocean. The effects of clouds for the various atmosphere profile conditions are provided. It was found that the excess brightness temperature has two principal components. One, the difference between the surface temperature and the mean atmospheric temperature (at any layer considered) multiplied by the emissivity of the surface, and, two, the temperature of the attenuating atmosphere. The excess temperature was maximum for an ocean target having a cold atmospheric surface temperature. The excess temperature for land targets was much smaller and in some cases was less than  $1^{\circ}\text{K}$ . The effects of clouds were, however, angle dependent and no bias adjustment could be made to compensate for the effects due to clouds. A simple bias adjustment for cases without clouds could yield results that were accurate to within  $1^{\circ}\text{K}$  for some cases.

In estimating the excess temperature, it was found that the higher the surface temperature (or emissivity) the smaller the excess temperature. This variation of excess temperature with soil and air temperature at the surface is provided for sample cases.

In the absence of clouds and rain, and for temperate regions characterized by low water vapor concentrations, the effects of the atmosphere upon the scatterometer signal can be compensated by a fixed transmission loss to a first approximation. For the radiometer case, no such simple approximation is valid.

## CHAPTER SIX

### DESCRIPTION AND ANALYSIS OF S-193 RADIOMETER/SCATTEROMETER

#### 6.1 General Description

Since the S-193 Radiometer/Scatterometer is the prime sensor for designing the terrain microwave data catalog for this study, the details of the sensor must be presented. Several analytical studies on its capabilities and expected performance have been documented [Hanley, 1972; Fisher, 1972; Sobti, 1973; Krishen and Pounds, 1974]. Some of these studies have been critiques [Hanley, 1972]; others have tried to derive, mathematically, the expected limits of precision/accuracy [Fisher, 1972]; while others have tried to mathematically model the subsystems in an effort to simulate the functioning of the S-193 Radiometer/Scatterometer [Krishen and Pounds, 1974]. A simulation study of the sensors on their orbital platform has been documented [Sobti, 1973] to verify certain design objectives. A detailed description of the sensors can be found in the vendors (General Electric) Hardware Specification Document [G.E., 1972].

The S-193 Radiometer/Scatterometer is a complex instrument and a detailed description of its design or the various analytical studies that are required to estimate its capabilities will be too voluminous to report. Some of the highlights in the design and some analyses of a general nature will be presented here; the reader is referred to an exhaustive volume on such a subject [Hanley, 1972] for a critical review of the sensor.

#### 6.2 Experiment Design

The S-193 was a composite radiometer/scatterometer and altimeter operating at 13.9 GHz; it was part of the Earth Resources Experiment Package on board Skylab. The three instruments shared a parabolic dish antenna and the r.f. section; the instruments were, however, operated in time multiplex. The design, objectives and functioning of the altimeter were sufficiently different from the radiometer/scatterometer so that nearly simultaneous operation was not possible. The altimeter experiment consisted of five sub experiments, of which only two provided data that is of immediate use in this study.

A block diagram of the S-193 system is given in Figure 6.1. Seven major subassemblies constitute the S-193 sensor. They are:

1. Synthesizer and Transmitter Pulse Generator
2. RF Section
3. Radiometer Processor
4. Scatterometer Processor
5. Altimeter Processor
6. Integrated Electronics Package
7. Gimbal Assembly

There are other minor subassemblies, but they can be classified into one of the seven mentioned above. A detailed description of each can be found in the General Electric documents [GE, 1971, 1972, a,b]. Since an attempt has been made here to establish some of the performance characteristics of the radiometer/scatterometer system, a brief account of the second, third and fourth subassemblies listed above is provided in the appendix.

The scatterometer is an Interrupted Continuous Wave (ICW), beam-limited  $(1.454^\circ$  two-way effective beamwidth) device. It has a Twenty-Watt Traveling-Wave-Tube Amplifier (TWTA) that feeds into a parabolic dish reflector antenna with a gain of over 40 dB. As will be seen later, the transmit power level and the noise figure of the receiver can result in an instantaneous signal to noise ratio far below unity for terrain targets at oblique incidence angles. To improve the precision of the estimated backscatter, post-detection integration is performed on board and an integrated value of the signal plus noise power level recorded. No amount of post detection integration, alone, can help in estimating the signal power level precisely if the signal to noise ratio is close to unity. To remedy such a situation, an integration of the receiver noise is performed following each signal-plus-noise measurement and its value also recorded. The integration times were designed to provide a reasonable estimate over the expected dynamic range of terrain backscatter values.

The parabolic dish antenna is capable of scanning in the along-track and cross-track directions and its scan excursions are programmed through a selection of one of four possible modes.

The radiometer is a modified Dicke type with two reference temperature sources. It is very similar to a design documented by Hach [1972] but deviates from it only in that this radiometer records the voltage bias offset due to zero signal input and a voltage that corresponds to the difference in the reference temperatures. The slope [or gain] is thereby readily computed from these measurements. The radiometer actually integrates the difference between the incoming radiation and the mean of the two reference temperatures. The radiometer bandwidth is approximately 210 MHz and the integration time is mode and incidence angle dependent. The radiometer processor includes an automatic gain control network that renders the measurements insensitive to system gain, noise level or bandwidth changes.

During altimeter operations, the antenna remains fixed at nadir, or scans to a maximum of  $15.6^\circ$  off nadir (defined as the z-local-vertical axis). During radiometer, scatterometer, or joint radiometer/scatterometer operation, the gimballed antenna is mechanically driven to scan the earth's surface with its pencil beam. This provides measurements at various angles relative to nadir. Several scan modes and various transmit/receive polarizations are provided in order to study the sensitivity of the terrain to type of polarization pairs used. No fixed-angle mode is provided.

The S-193 RADSCAT has four basic modes of operation:

- In-Track Non-Contiguous (ITNC)
- Cross-Track Non-Contiguous (CTNC)
- In-Track Contiguous (ITC)
- Cross-Track Contiguous (CTC)

The designed values for the 4 modes of operation are described below, the scan performance during spaceborne operation is reported later.

### 6.3 Modes of Operation of S-193 Radiometer/Scatterometer

#### 6.3.1 In-Track Non-Contiguous

In the ITNC mode, the scatterometer and the radiometer are used jointly. In this mode, the antenna excursions are only in pitch (along track) and the scan dwells at five angles ( $48^\circ$ ,  $40.1^\circ$ ,  $29.4^\circ$ ,  $15.6^\circ$ ,  $0.0^\circ$ ) during which time the target is viewed by both the scatterometer and the radiometer. Note that these angles are at the spacecraft; the incident angles differ because of the earth's curvature.

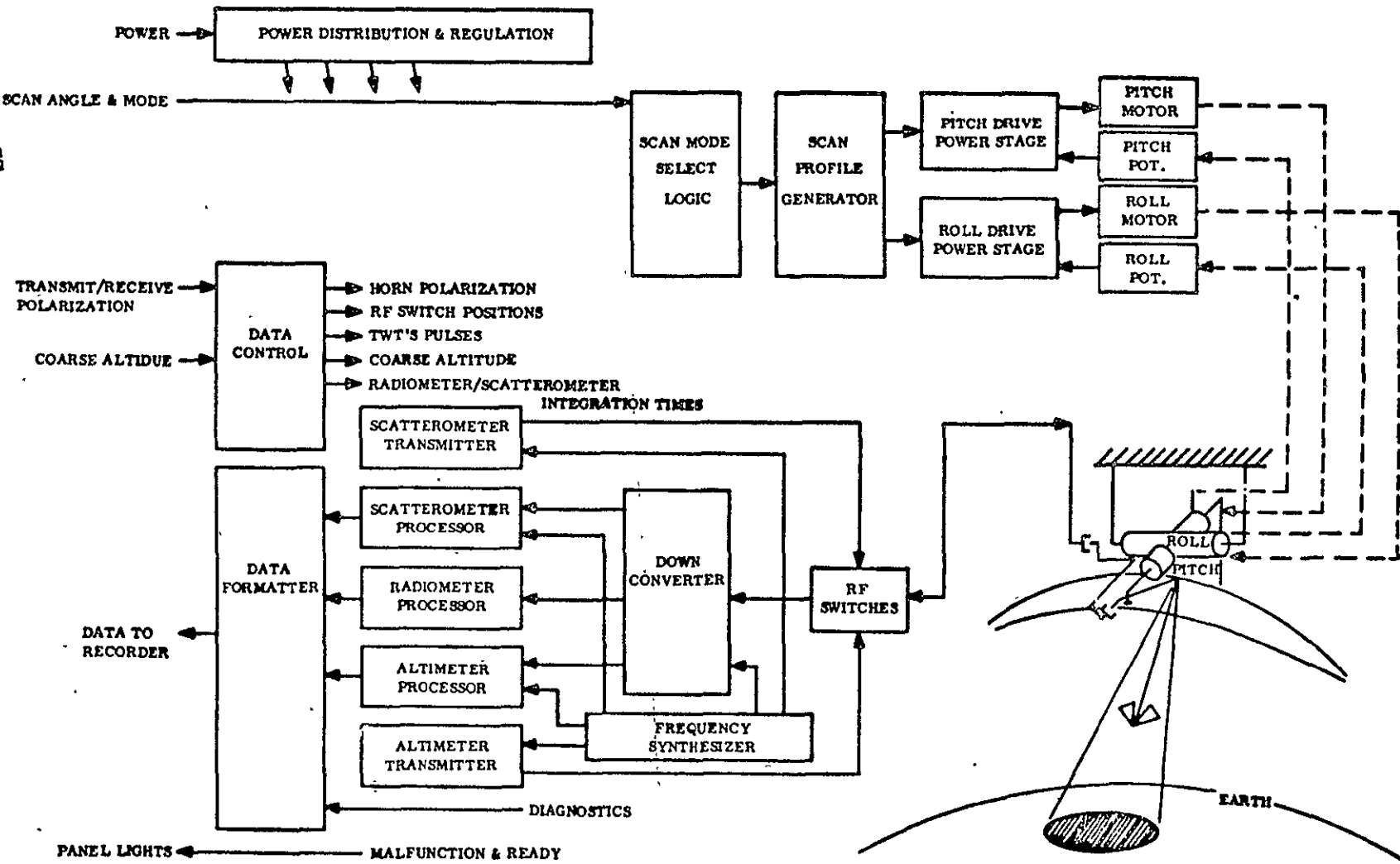
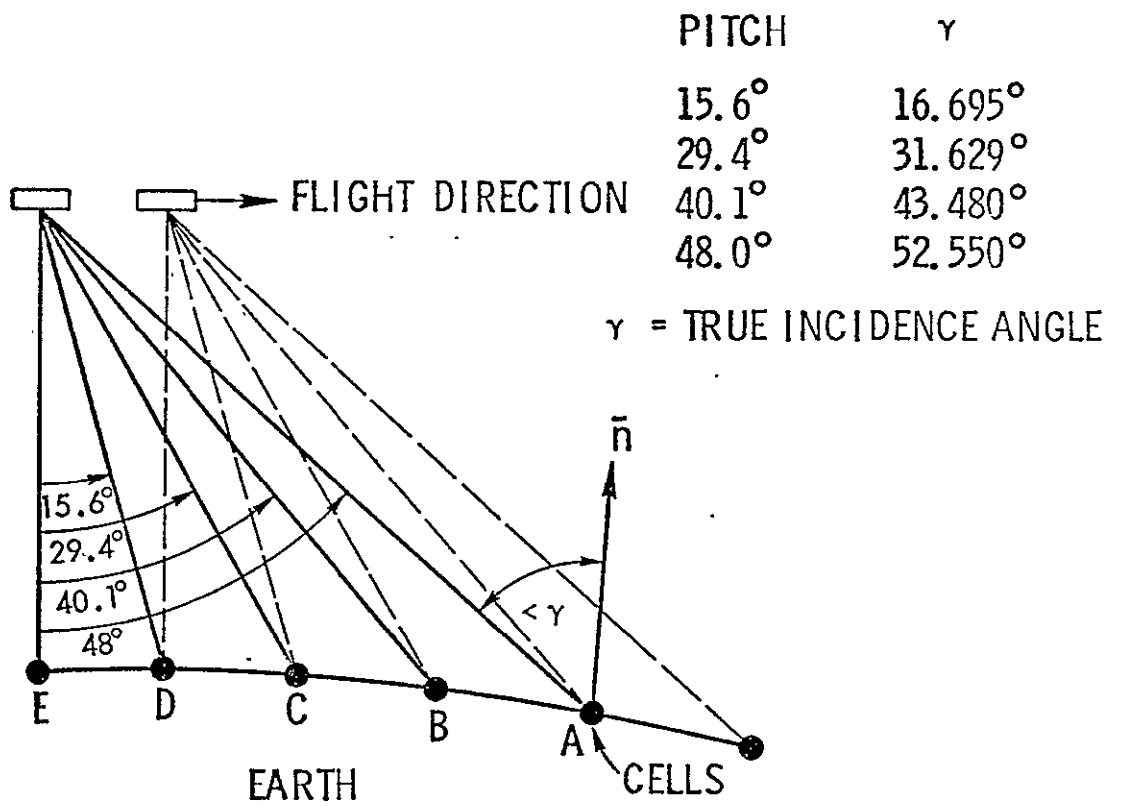
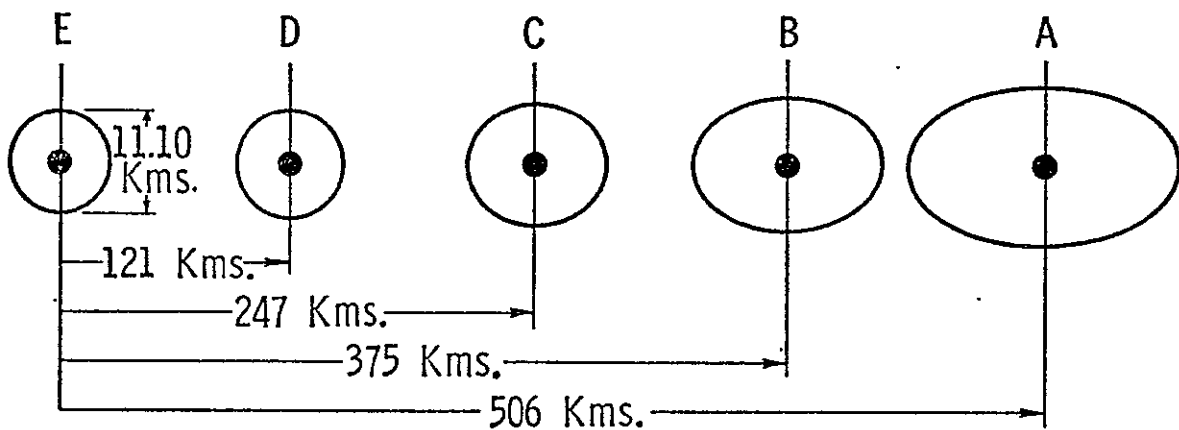


Figure 6.1. Block diagram of S-193 system.



IN-TRACK NON-CONTIGUOUS MODE



FOOTPRINTS FOR ITNC MODE

(Drawn to scale)

Figure 6.2.

The mode is shown pictorially in Figure 6.2. At each angle, data for four transmit/receive polarization pairs (HH, HV, VH and VV) are recorded in the scatterometer and for both vertical and horizontal polarizations in the radiometer. This gives a total of six data words recorded at each dwell position of the antenna. The dwell time at each angle is fixed, with greater integration time per measurement allowed for larger incidence angles. The measurement time for each angle and polarization during one scan in this mode is given in Table 6.1(a). The scan cycle takes 15.25 seconds during which time the vehicle moves a distance approximately 107 kilometers; the incident angles and the scan cycle timing were chosen so that a target viewed at a certain incident angle in one scan cycle would be viewed again at a smaller incidence angle in the successive scan. The object was to view the same target (for a sufficiently long period to improve measurement accuracy) at five discrete angles and study the differential backscattering coefficient and radiometer brightness temperature variations with the incidence angle. Obviously, such targets are displaced along track by approximately 107 kms. The section on footprint analysis shows that indeed, the targets viewed in successive scans by smaller incidence angle do not overlap perfectly and that this overlap is very sensitive to vehicle orbit height and orbital position. This lack of total overlap (at nominal orbit height) is attributed to the effect of the earth's rotation and an oblique inclination angle of the Skylab orbit.

During a scan cycle, internal calibration measurements are made for the radiometer and the scatterometer receiver noise measurements (which follow every signal measurement). The scatterometer transmitter power is recorded in the first scan cycle upon turn-on of this mode and this measurement is recorded every 240 seconds thereafter, this means that any fluctuations in transmit power occurring within 240 seconds are not recorded. Further, a slow drift in transmitted power (a greater likelihood) may also go undetected unless the instrument has been operating in the same mode for over 240 seconds. One way to get more recordings of the transmit power is to switch from one mode selection to another (after switching the S-193 for a very short period to standby).

Due to the relatively larger integration times for each measurement, the precision of signal recorded in this mode is better than in the contiguous modes. It was intended primarily for use over a homogeneous terrain (such as the ocean)

where data taken at discrete targets (some sixty miles apart) could be meaningful. Note that it takes roughly 75 seconds of flight to get a five-angle look at a single target.

### 6.3.2 Cross-Track Non-Contiguous

In the CTNC mode, the radiometer and scatterometer are again used jointly. In this mode the antenna excursions are in roll (cross-track) rather than in pitch. The antenna slew and dwell positions are at the same relative angles to nadir as in the ITNC mode. There are three submodes for this mode, differing only in the direction of antenna slewing. They are:

CTNC - Right Only (CTNC-R)

CTNC - Left Only (CTNC-L)

CTNC - Left/Right (CTNC-L/R)

The mode sequence (angles, polarizations and integration times) is exactly the same as in the ITNC and Table 6.1(a) once again gives the measurement time for each angle and polarization during one scan cycle.

There can be no overlap of targets in this mode, i.e. no target is ever viewed in one pass at more than one incidence angle. This mode was intended for observing the variability of the ocean over a 506-1012 kms swath, and can be used to good advantage for viewing targets of opportunity lying off the satellite track. An example would be to study a storm front lying off the satellite track. The mode is shown pictorially in Figure 6.3.

### 6.3.3 In-Track Contiguous

In the ITC mode, the radiometer and scatterometer are again used jointly. The scan is initialized by a step command to move the antenna to  $48^\circ$  pitch. The antenna then slews down to nadir at a constant rate ( $23.099^\circ/\text{sec.}$ ) and scatterometer data is taken for short periods as the antenna moves by  $48.0^\circ$ ,  $40.1^\circ$ ,  $29.4^\circ$ ,  $15.6^\circ$  and  $0.0^\circ$ . During the rest of the scan, radiometer measurements are made. The total scan cycle lasts 4.0 seconds; due to the short period of the cycle, data is taken for only one transmit/receive polarization pair for the scatterometer and one polarization (the same polarization as the receive polarization for the scatterometer) for the radiometer. The polarizations can, however, be selected through the Control and

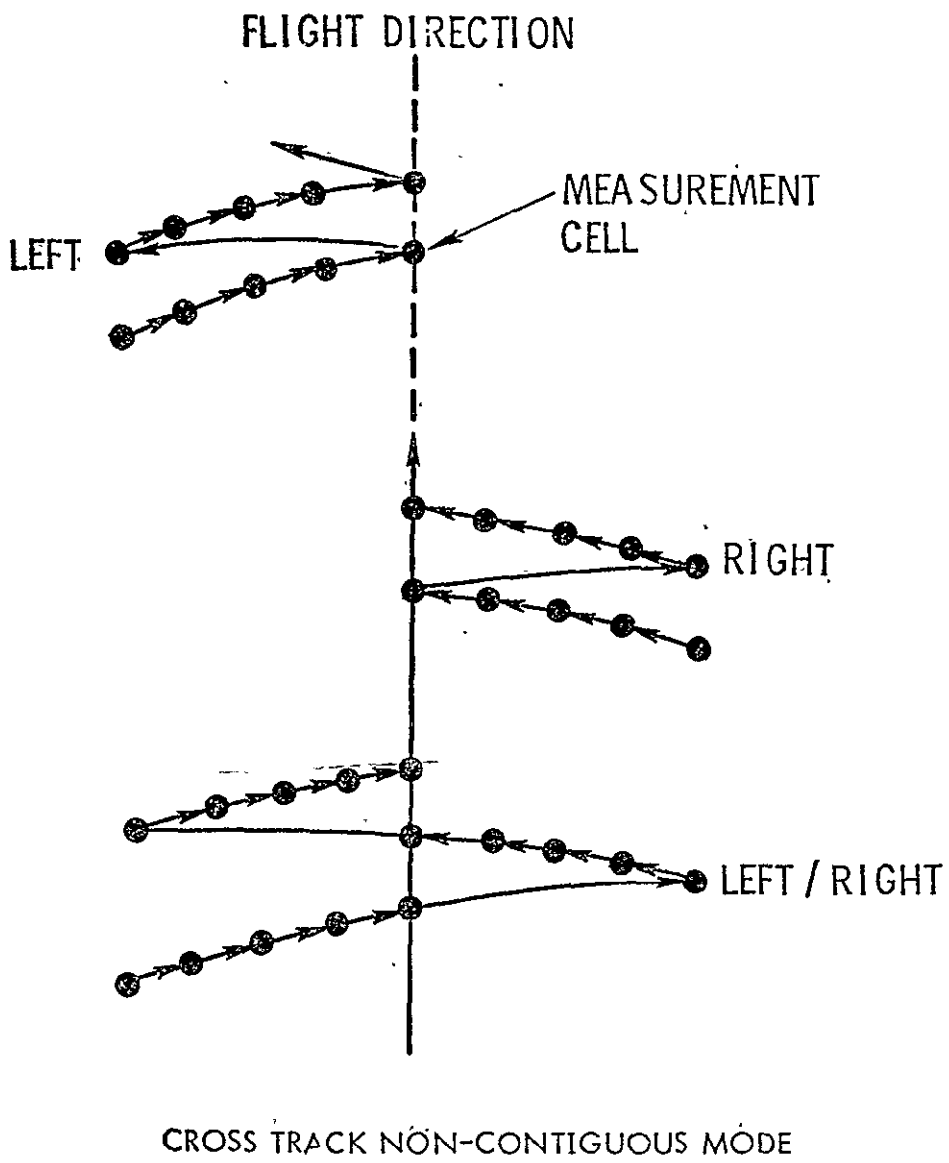


Figure 6.3.

Display panel in the Multiple Docking Adapter in the Skylab vehicle. Table 6.1(b) shows the mode sequence and timings.

Due to the rapid scan of the mode, a target cell viewed in a scan at  $48.0^\circ$  overlaps a cell viewed at  $48^\circ$  in the previous scan. The amount of overlap between successive scans is a function of incidence angle, being greater at higher angles, decreasing as the incidence angle approaches nadir, where a gapping rather than an overlap occurs. On successive scans as the vehicle progresses, virtually the entire path is viewed from  $48^\circ$  down to the lower angles (near about  $15.6^\circ$ ). The antenna beam illuminates targets every 27 kilometers for nadir incidence. The beamwidth of the antenna corresponds to a target cell at nadir of diameter 11.1 kilometers. It takes 19 scans (roughly 75 seconds) to get a 5 angle look at any single target cell.

Since the integration times in this mode are not as large as in the non-contiguous modes, some measurement precision is sacrificed, but the target cell spacing is greatly reduced. This mode was intended to be used primarily over land, but it can also be used over the ocean effectively if steeper gradients of oceanic parameters are to be measured. The mode is shown pictorially in Figure 6.4. The section on footprint analysis details the overlap structure of a cell viewed at five angles. Due to the slewing of the antenna during data taking intervals, the target cell per pulse shifts in the direction of the slew causing a "smearing" effect of the target on the ground. The antenna slew per scatterometer measurement is  $1.664^\circ$  (greater than the effective scatterometer beamwidth); the effective target area per angle is therefore larger than in the non-contiguous modes.

#### 6.3.4 Cross-Track Contiguous

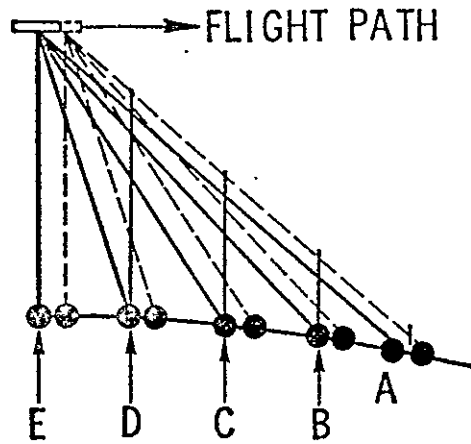
This is the only mode in which the radiometer and scatterometer can each be operated individually and jointly. There are three submodes:

Radiometer Only (RAD only)

Scatterometer Only (SCAT only)

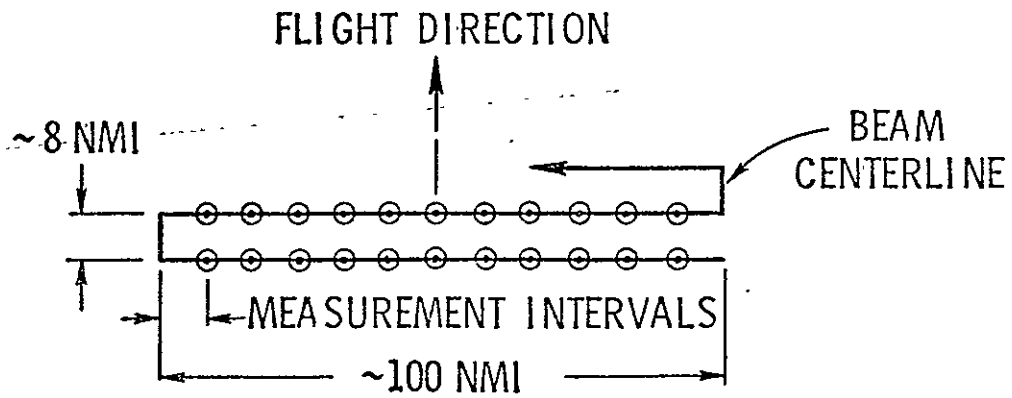
Radiometer/Scatterometer (RAD/SCAT)

In the CTC mode, the antenna sweeps in the roll plane, both to the left and right of an initialized point. The sweep of the antenna can be initialized at one of four pitch angles ( $0.0^\circ$ ,  $15.6^\circ$ ,  $29.4^\circ$ ,  $40.1^\circ$ ) or three roll angles ( $0.0^\circ$ ,  $15.6^\circ$ ,



IN-TRACK CONTIGUOUS MODE

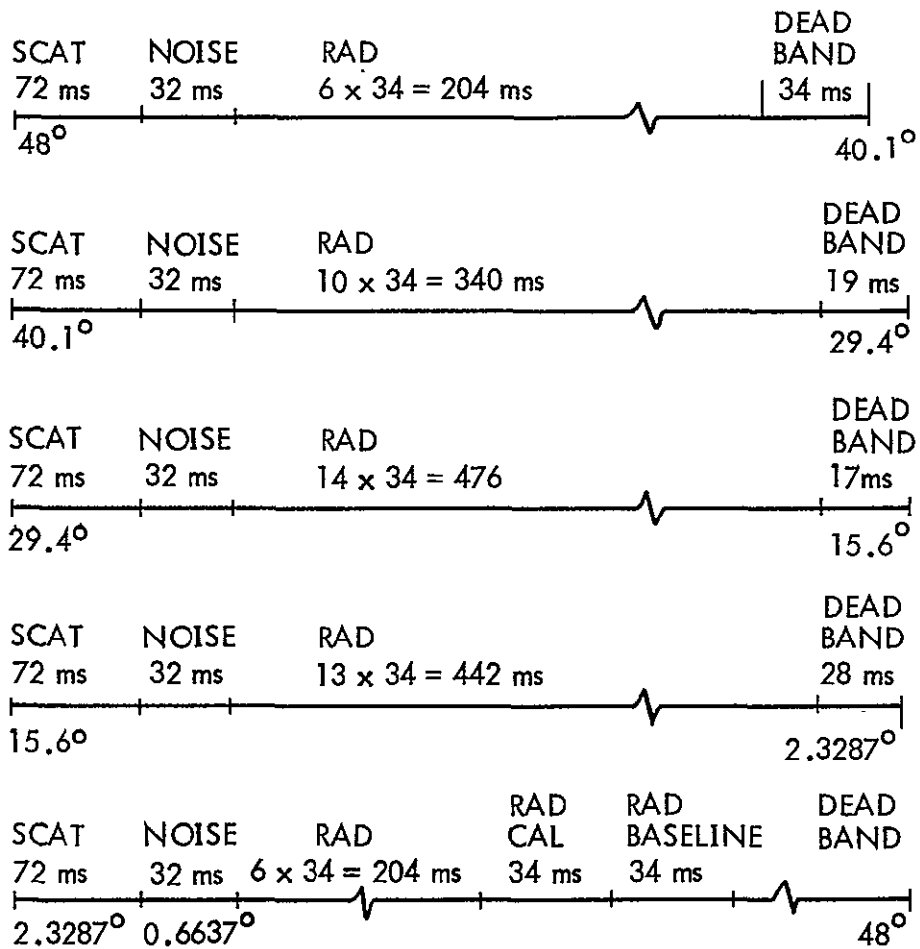
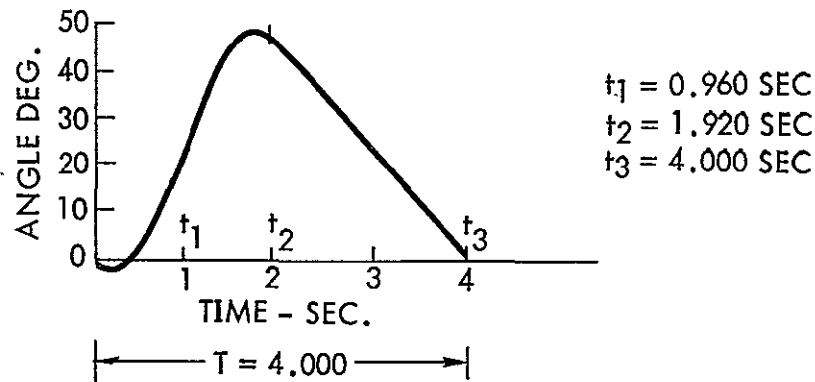
Figure 6.4.



CROSS-TRACK CONTIGUOUS MODE

Figure 6.5.

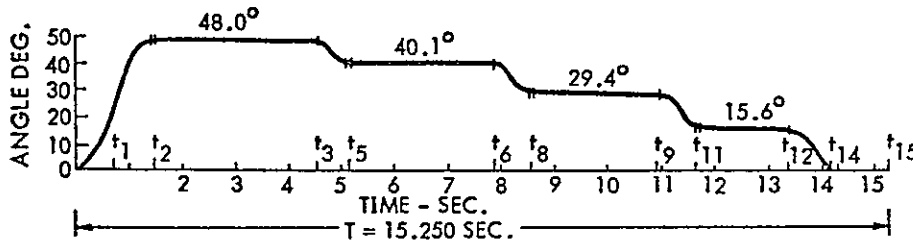
Table 6.1 (b)  
IN-TRACK CONTIGUOUS\*  
TIMINGS



9 SCAT periods,  $9 \times 8 = 72 \text{ ms}$   
 Each RAD integration period is 32 ms plus a 2 ms readout.

\*G. E. Calibration Data Report, Flight Hardware, Vol. 1, RevA, May, 1972.

PITCH ANGLE FOR INTRACK AND ROLL ANGLE FOR CROSS-TRACK\*



t <sub>1</sub>	0.692 SEC
t <sub>2</sub>	1.386
t <sub>3</sub>	4.541
t <sub>5</sub>	5.103
t <sub>6</sub>	7.913
t <sub>8</sub>	8.567
t <sub>9</sub>	10.908
t <sub>11</sub>	11.651
t <sub>12</sub>	13.387
t <sub>14</sub>	14.177
t <sub>15</sub>	15.250

At each angle the following order of measurements takes place

SCAT (VV)	SCAT (HV)	RAD & SCAT NOISE (V)	SCAT (HH)	SCAT (VH)	RAD & SCAT NOISE (H)	RAD CALIBRATE	RAD BASELINE
m <sub>1</sub>	m <sub>2</sub>	m <sub>3</sub>	m <sub>4</sub>	m <sub>5</sub>	m <sub>6</sub>	m <sub>7</sub>	m <sub>8</sub>

The values of m<sub>1</sub> for different pitch/roll angles in milliseconds as given below:

Table 6.1(a)

NON CONTIGUOUS MODE DWELL SEQUENCE

	ANGLE				
m <sub>1</sub>	48.0	40.1	29.4	15.6	0.0°
m <sub>1</sub>	592	512	456	312	184
m <sub>2</sub>	592	512	456	312	184
m <sub>3</sub>	258	258	130	130	60
m <sub>4</sub>	592	512	456	312	184
m <sub>5</sub>	592	512	456	312	184
m <sub>6</sub>	258	258	130	130	60
m <sub>7</sub>	258	258	130	130	60
m <sub>8</sub>	258	258	130	130	60
Max. number of SCAT pulses per polarization	74	64	57	39	23

\* G. E. S-193 Microwave Radiometer/Scatterometer Altimeter Critical Design Review, Vol. I, Flight Hardware Configuration Specification, January 6, 1971.

TABLE 6.1(c)

RAD/SCAT CONTIGUOUS MODE (CROSS TRACK)  
MEASUREMENT PERIOD 151.5 ms \*\*

(A) RAD/SCAT	POLARIZATION	TIME	DEADTIME	
SCAT	EITHER	112 ms	5.5 ms	—
	VV or HH		5.5 ms	—
RAD & SCAT NOISE	SAME AS SCAT RECEIVE	34 ms	—	—
(B) RAD(only)	DUAL POLARIZATION	TIME	DEADTIME	
	VERTICAL	60 ms	15.75 ms	—
	HORIZONTAL	60 ms	15.75 ms	—
(C) SCAT(only)	DUAL POLARIZATION	TIME	DEADTIME	
	VERTICAL VERTICAL	64 ms	—	
	SCAT NOISE	11.75 ms	—	
	HORIZ. HORIZ.	64 ms	—	
	SCAT NOISE	11.75 ms	—	

\* The beam center roll motion is  $1.896^\circ$

\* Scan-measurement consists of 12 periods of 151.5 ms each followed by RAD.CAL. & RAD. BASELINE

\* All submode timings occur in order listed.

\*\* G. E. Calibration Data Report, Flight Hardware, Vol. 1, kevA, May, 1972.

29.4°) but simultaneous roll and pitch offsets are not possible. In all cases the antenna excursions extend about the initialized point 11.375° to the left and right of this point. The antenna slews at a rate of 12.5 degrees/sec. and it takes 1.82 seconds to complete one side-to-side scan and 0.3 seconds to position itself for the next scan.

During one scan cycle, a total of twenty-four data measurements are recorded; the sub-mode chosen dictates whether they are all radiometer (RAD only), all scatterometer (SCAT only) or half (twelve) of each (RAD/SCAT). Since the scan is quite rapid, not all possible polarization pairs are allowed. In the RAD only mode, twelve vertically polarized and twelve horizontally polarized measurements are recorded, each polarization occurs alternately. In the SCAT only mode, twelve measurements for vertical transmit/receive (VV) and twelve measurements of horizontal transmit/receive (HH) are recorded. The data for each polarization pair occurs alternately. The cross-polarized combinations (HV or VH) are not allowed in the CTC mode. In the RAD/SCAT mode data are taken for only one polarization pair in the scatterometer and for one polarization (the same polarization as the receive of the scatterometer) in the radiometer. The polarization pairs (VV or HH) can, however, be chosen by the astronaut.

The scan is broken up into twelve data taking intervals; during each interval two measurements (according to sub-mode) are recorded. The antenna slews 1.896° during each data taking interval. To insure that the target cells viewed do indeed lie in the cross-track plane, a pitch offset (w.r.t. initialized point) of +1° is introduced at the start of the scan. The pitch is also varied as the scan proceeds so that at the end of the scan, there is a resultant pitch of -1° from the initialized point. This was done to insure that the line traverses of two successive scans (starting from either side of nadir) would be parallel. The section on footprint analysis elaborates on the target traces for different offsets. Table 6.1a shows the scan sequence timings (integration times and angles). Figure 6.5 shows the mode pictorially.

This mode, also called the mapping mode, was primarily intended for viewing land targets. It comes closest to a terrain mapping radar or radiometer. The integration times for the scatterometer are longer than in the ITC mode, but the only

overlap of target cells occurs because the time (in the SCAT only) between two measurements is small and the target cells are large so that a portion of the target cell is viewed twice.

#### 6.4 Characteristics of Operation of S-193 Scatterometer

A general description of the S-193 has been provided above, this section will elaborate on details regarding its operation. The purpose here is to describe the operation so that a systems analysis may be performed. As pointed out in chapter two, the back-scattering coefficient,  $\sigma^0$ , is given by

$$\sigma^0 = \frac{(4\pi)^3}{\lambda^2} \left( \frac{1}{\int_{\Omega} \frac{G^2}{R^4} dA} \right) \left( \frac{R_r}{R_t} \right) (L_1 L_2) \quad (1)$$

The individual parameters have already been described. The equation has been broken up as shown above to facilitate interpretation. The term in the first braces is a constant for a particular frequency. The second term is a function of the target-sensor geometry and the antenna pattern; for a constant altitude and fixed incidence angle it is a constant. The third braces include the scatterometer measurements. These are the quantities that were recorded on tape and brought down to earth with the astronauts. The fourth term is an atmospheric correction and has been discussed in some detail in chapter five.

The parameters of interest for the present discussion are in the second and third terms. The scatterometer transmits a long pulse (5.0 milliseconds) and has a pulse repetition frequency of 125 pulses per second. The receiver is gated on about 0.3 milliseconds after the end of transmission of a pulse, and receives for 2.2 milliseconds. The signal received then corresponds to a return from all sources that have a round-trip delay time of roughly 7.2 milliseconds. This translates to a range of 1125.9 kms, which for nadir incidence and a nominal altitude of 435 kms translates to a cone with a solid angle of  $67.27^\circ$ . The timing of the receiver gating is designed to ensure that the transmitter has achieved its peak power. The round-trip delay for nadir incidence at the nominal altitude of 435 kms is 2.9 milliseconds. The received signal is amplified by a low-noise amplifier, down converted, band-pass filtered and then fed to the scatterometer processor. The signal is then further down converted, attenuated (see appendix for description of scatterometer processor), passed through a bank of "doppler" filters (see appendix) and

square law detected. The output of the square law detector is fed to a gated integrator; this is the gating referred to above. The integrated signal is then dumped onto the EREP recorder.

Due to motion of the vehicle with respect to a target, the return signal suffers variations in phase which translate to a Doppler frequency. This Doppler frequency is a function of the relative velocity of the spacecraft with respect to the target. The antenna excursions allow pitch dwells at only five angles (for the cross-track contiguous modes, the excursions can be  $\pm 11.375^\circ$  to the left and right of four of these pitch dwells), and, consequently, the "Doppler" filters are so designed that the expected range of Doppler frequencies falls within the "Doppler" filter banks. The bandwidths of the Doppler filters are given in Table 6.1, they correspond roughly to a Doppler frequency spread of  $\pm 6.1^\circ$  off antenna boresight. Thus, the Doppler filters allow a sampling of an area much smaller than the receiver gate width.

### 6.5 Scatterometer Sensor Analysis

The scatterometer sensor analysis is broken up into two sections, one deals with an examination of the  $(P_r/P_t)$  ratio encountered in Eq. 6.1 and the other deals with effects of the target-sensor geometry and the antenna pattern. For purposes of identification, the first is called Sensor Measurement Analysis and the second is called Sensor-Terrain Geometry Analysis.

#### 6.5.1 Sensor Measurement Analysis

Consider the block diagram shown in Figure 6.6. This block diagram represents an overall view of the signal path. Amplifiers, a second down converter, attenuation

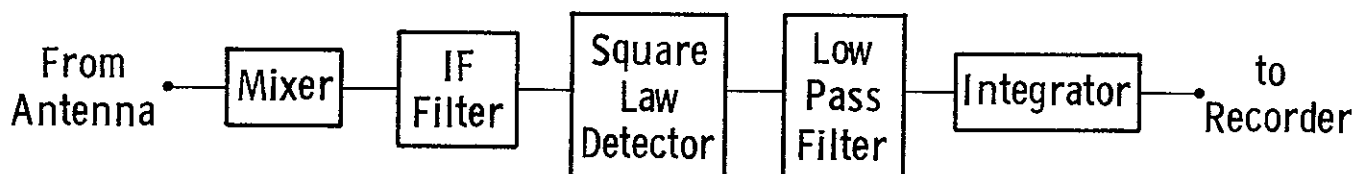


Figure 6.6. Block diagram of signal path through S-193 scatterometer.

paths and Doppler band filters have all been included in the two blocks called the mixer and the IF filter. The IF filter bandwidth is set by the Doppler band filters. The measurement  $\hat{P}_r$  is computed from a measurement of the incoming microwave signal along with the noise from the system, and a separate measurement of the system noise itself; i.e., it is proportional to  $\hat{V}_s$  (an  $\hat{\wedge}$  sign over a variable is used to denote a normalized measurement--normalized for gains, bandwidths, etc.) where

$$\hat{V}_s = \hat{V}_{S+N} - \hat{V}_N \quad (2)$$

where the subscript  $S + N$  refers to signal-plus-noise and the subscript  $N$  refers to noise by itself. Then

$$P_r = C_r \hat{V}_s \quad (3)$$

Similarly, the transmitted power  $P_t$  is proportional to the voltage measured during scatterometer calibration (see appendix for details)

$$P_t = C_t \hat{V}_c \quad (4)$$

The estimate for  $(P_r/P_t)$  is thus obtained from

$$P_r/P_t = (C_r/C_t) (\hat{V}_{S+N} - \hat{V}_N) / \hat{V}_c \quad (5)$$

The terms  $V_{S+N}$ ,  $V_N$  and  $V_C$  are outcomes of a random process; consequently, the "adjusted" values  $\hat{V}_{S+N}$ ,  $\hat{V}_s$  and  $\hat{V}_c$  (which involve linear transformations from  $V_{S+N}$ ,  $V_N$  and  $V_C$ ) are also outcomes of a random process. Since each of them is the mean (along time) of sample functions from the random processes from which they were obtained, they are random variables. To obtain statistical estimates of the expected value and the other moments of the random variable  $(P_r/P_t)$  one must make some assumptions regarding the random processes from which  $V_{S+N}$ ,  $V_N$  and  $V_C$  are sample functions.

Before we make any assumptions regarding the random processes, let us reconstruct the motivation for making these measurements in the first place. The return power (scattered back towards the receiver) is a function of the target characteristics. The instantaneous power scattered is a function of the geometry. An assumption made in most scattering theories is that the instantaneous energy scattered is a summation of the energy scattered by many small elements which scatter with uniform phase distribution so that the amplitude of the envelope of scattered field has a Rayleigh distribution.

A sample function of the process is obtained when a time record of duration  $\tau$  seconds is gated into the receiver. A mean (or integrated value) is obtained when this sample function is integrated for  $\tau$  seconds. We claim that the return from the same class of targets viewed under the same conditions would have a sample function mean whose

expected value again would be the same. We are therefore implying a wide-sense stationarity of the random process. This means that the return signal as well as the noise are both wide-sense stationary processes. Further, we claim that, under the conditions of the particular measurement, if we take time samples the moments of these sample functions are the same as the ensemble moments of the process; i.e., we are claiming that the signal is produced by an ergodic process. These are reasonable assumptions made to justify the experiment, and conform with theoretical predictions. There are other assumptions made during the course of the analysis; they too will appear reasonable, but they will be made for facilitation of analysis only.

With the assumption of Rayleigh fading, the return signal can be described by

$$s(t) = A_0(t) \cos [\omega_c t + \theta(t)] \quad (6)$$

where  $s(t)$  = return signal

$A_0(t)$  = magnitude of signal, Rayleigh distributed

$\omega_c$  = carrier frequency

$\theta(t)$  = random phase, uniform distribution  $[0 - 2\pi]$

The transmitted power has an amplitude spectrum given by Figure 6.7.

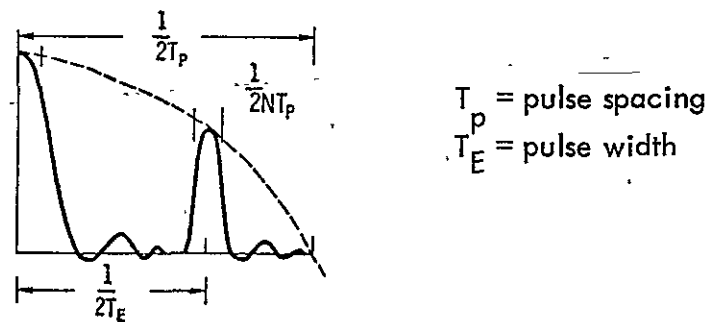


Figure 6.7. Transmitted power spectrum.

The number,  $N$ , of pulses transmitted varies from a minimum of 9 for the In-track Contiguous (ITC) mode to a maximum of 74 for the In-track Non-Contiguous (ITNC) mode (at  $48^\circ$  incidence). The receiver has a gating which occurs  $T$  after the leading edge of the transmitted pulse, the gate-width being roughly 2.3 milliseconds. The width of the receiver modulation spectral distribution at each harmonic of the pulse repetition frequency will be the same as the transmitter waveform but the envelope will be wider by a factor of  $\frac{5}{2 \cdot 3} \approx 2$ . The overall spectrum then is given by the convolution of the carrier, the transmitter, the ground function (which causes the Doppler spreading) and the receiver spectrum. Since the receiver and transmitter

spectra have an envelope which cuts off at  $\frac{2\pi}{5}$  kHz and  $\frac{2\pi}{2 \cdot 3}$  kHz respectively, and the Doppler spectrum is in the order of hundreds of kHz, the net effect of the receiver and transmitter spectra can be ignored.

The Doppler shift of a return is caused by the relative velocity of the vehicle with respect to the ground. For a narrow beam antenna, the Doppler spectrum generated (for uniform illumination) can be considered to be uniform across the Doppler bandwidth set by antenna beam geometry and velocity. That is, for the cases under study (either pitch or roll offset, but not both) the iso-Doppler lines are assumed to be parallel to each other and perpendicular to the suborbital track across the beamwidth. The width of the target cell in the across-track direction is considered to be equal across the beamwidth; i.e., the beam is assumed square instead of round. Under such conditions, the return Doppler spectrum can be considered flat across the beam. This is a considerable simplification of the real situation.

The antenna pattern can be described in one of two ways, one way is to define an equivalent beamwidth, which says that the pattern energy in the main beam can be considered to be contained in a cone (with gain at all points in the cone equal to that at boresight), and the other way is to actually describe (or approximate functionally) the distribution of energy in the pattern.

Another factor which can affect the Doppler spectrum is the scattering of the ground. At angles close to nadir the backscatter response of terrain is a rapidly decaying function of angle, and, the scattering by the edge (to nadir) of a target can be substantially higher than that by the far edge, thus making the Doppler spectrum even more complex. At angles away from nadir, however, this effect can be ignored and the important weighting is due to the antenna pattern.

Cook\*, in his studies of the S-193 antenna pattern, discovered that a Gaussian curve of the form

$$f(\theta) = \beta e^{-\alpha\theta^2} \quad (7)$$

$\theta$  = angle from boresight in radians

fit the actual main beam of the pattern down to -15 dB. The transformation of this angular distribution of energy to a distribution across the Doppler band is a function of the target-sensor geometry. In general, it is very complex to go from this angular distribution (with the parameters  $\alpha, \beta$  defined) to a distribution across frequency, i.e.

$$f(\omega) = \beta_{\omega} e^{-(\omega - \omega_c)^2 / \alpha_{\omega}} \quad (8)$$

There are, however, other schemes by which the parameters describing the Gaussian shape can be approximated. In this study we shall start with the assumption (used also by

\*A. C. Cook, Private communications.

Hanley [1972], Fisher [1973] and Waite [1970]) of a flat Doppler spectrum. Then, we shall find a Gaussian pattern function, make the assumptions of a rectangular target cell, and claim that the return doppler spectrum is given by this Gaussian shape. This reduces the complex two-dimensional problem to one dimension.

The questions we would like to answer are: How does the mean and variance of the voltage measurements translate to a mean and variance of the backscatter measurement? What is the expected value of the signal? What is the confidence interval (90%) of the mean of the incoming signal? What is the expected normalized standard deviation? What is the confidence interval for this parameter? To answer these questions we establish general results and then proceed to include specifics of our system.

Consider the block diagram of Figure 6.6. Let the signal voltage after mixing and IF zonal filtering be given by  $x(t)$ , where

$$x(t) = s(t) + n(t) \quad (9)$$

i.e., we have assumed that noise is additive. The signal  $s(t)$  is assumed to have narrow band Gaussian statistics and to be stationary. The noise is also assumed to have narrow band Gaussian statistics. The bandlimiting is by the IF filter bandwidth for noise and by the Doppler bandwidth for the signal. Both terms are assumed to have zero-mean and variances equal to the individual average powers.

$$\bar{s}(t) = 0 \quad (10)$$

$$\bar{n}(t) = 0 \quad (11)$$

$$\text{var} \{s(t)\} = \sigma_s^2 = P_s \quad (12)$$

$$\text{var} \{n(t)\} = \sigma_n^2 = P_n \quad (13)$$

The output of the square law detector is given by

$$y(t) = a x^2(t) = a [s^2(t) + 2s(t)n(t) + n^2(t)] \quad (14)$$

where  $a$  is the proportionality constant of the detector. It is assumed to be an unbiased square-law detector. This signal is passed through a low pass filter, the resulting signal  $z(t)$  is given by

$$z(t) = \int_{-\infty}^{\infty} h(t-\tau) y(\tau) d\tau \quad (15)$$

where  $h(t)$  is the impulse response of the filter. This signal is then fed to an integrator and after integration for  $T$  seconds the value dumped onto the tape recorder. Therefore, the measurement corresponding to the signal plus noise is given by

$$V_{S+N} = \int_0^T I(t) z(t-\tau) d\tau \quad (16)$$

where  $I(t)$  is the impulse response of the integrator. Now we must establish a relationship between the mean and dispersion of  $V_{S+N}$  and statistics of  $s(t)$  and  $n(t)$ .

The mean and variance of  $V_{S+N}$  are readily seen to be

$$\bar{V}_{S+N} = E \left[ \int_0^T I(t) \overline{z(t-\tau)} d\tau \right] = \bar{z} \int_0^T I(t) dt \quad (17)$$

$$E [V_{S+N}^2] = \int_0^T \int_0^T I(t) \overline{z(T-t) z(T-\tau)} I(\tau) dt d\tau \quad (18)$$

and

$$\text{var} \{V_{S+N}\} = \overline{V_{S+N}^2} - \bar{V}_{S+N}^2 \quad (19)$$

If  $I(t)$  is a constant given by

$$I(t) = \begin{cases} g/T & 0 < t \leq T \\ 0 & \text{elsewhere} \end{cases} \quad (20)$$

where  $g$  is the integration gain.

Then

$$\bar{V}_{S+N} = \frac{g}{T} \bar{z} \quad (21)$$

$$\text{var} \{V_{S+N}\}^* = \frac{2g^2}{T} \int_0^T (1 - \frac{\tau}{T}) C_z(\tau) d\tau \quad (22)$$

where  $C_z(\tau)$  is the autocovariance function of  $z$  and related to the autocorrelation function  $R_z(\tau)$  as

$$C_z(\tau) = R_z(\tau) - \bar{z}^2 \quad (23)$$

which says that for large  $T$ , as  $\tau$  increases  $C_z(\tau)$  tends to zero, the variance of  $V_{S+N}$  is given by

$$\text{var} \{V_{S+N}\} = \frac{2g^2}{T} \int_0^\infty C_z(\tau) d\tau \quad (24)$$

\*See for example Bendat and Piersol, "Random Data," pp. 172-176.

From equation (15),  $z(t)$  was related to  $y(t)$ , so to find the covariance of  $z(t)$ , we must find it for  $y(t)$ . From equation (14), which relates  $y(t)$  to  $s(t)$  and  $n(t)$ , we have the autocorrelation of  $y(t)$  as

$$R_Y(t_1, t_2) = a^2 E \left[ s^2(t_1) + 2s(t_1)n(t_1) + n^2(t_1) + s^2(t_2) + 2s(t_2)n(t_2) + n^2(t_2) \right] \quad (25)$$

Noting that  $s(t)$  and  $n(t)$  have both been assumed to be stationary zero mean random processes and that the two are independent, we have

$$R_Y(\tau) = a^2 \left( \overline{s_1^2 s_2^2} + 2 \overline{s_1 n_1 s_2^2} + 4 \overline{s_1 n_1 s_2 n_2} + 2 \overline{s_1 n_1 n_2^2} + 2 \overline{s_1^2 s_2 n_2} + \overline{s_1^2 n_2^2} + \overline{n_1^2 s_2^2} + 2 \overline{n_1^2 s_2 n_2} + \overline{n_1^2 n_2^2} \right) \quad (26)$$

where

$$\begin{aligned} S_1 &= s(t) \\ S_2 &= s(t + \tau) \\ N_1 &= n(t) \\ N_2 &= n(t + \tau) \end{aligned}$$

and the overbar indicates an expectation. Since it is assumed that  $s(t)$  and  $n(t)$  are independent

$$\overline{2 S_1^2 S_2 N_2} = \overline{2 S_1 S_2^2 N_1} = 0$$

because  $\overline{N_1} = \overline{N_2} = 0$

similarly  $\overline{2 S_1 N_1 N_2^2} = \overline{2 S_2 N_2^2 N_1} = 0$

because  $\overline{S_1} = \overline{S_2} = 0$

This leaves

$$R_Y(\tau) = a^2 \left( \overline{s_1^2 s_2^2} + \overline{n_1^2 n_2^2} + 2 \overline{n_1^2 s_1^2} + 4 \overline{s_1 s_2 n_1 n_2} \right) \quad (27)$$

To evaluate this expression, we must assume some more about the signal and noise. We shall, for the sake of comparison, use two different power spectral density representations for the signal; one, a narrow-band noise-like spectrum which is flat across the Doppler bandwidth and the other a narrow band noise spectrum shaped by passing through a

filter with the response characteristics of the S-193 antenna pattern.

Consider the signal again to be

$$s(t) = A_o(t) \cos(\omega_c t + \theta) \quad (28)$$

where  $\theta$  is uniformly distributed over the interval  $0 \leq \theta \leq 2\pi$  and where  $A_o(t)$  is a sample function of a stationary real random process which is independent of  $\theta$  and of the noise input to the detector. The autocorrelation function of the input signal is

$$\begin{aligned} R_i(\tau) &= E[A_o(t) A_o(t+\tau)] E[\cos\{\omega_c t + \theta\} \cos\{\omega_c(t+\tau) + \theta\}] \\ &= \frac{1}{2} R_A(\tau) \cos \omega_c \tau \end{aligned} \quad (29)$$

where  $R_A(\tau)$  is the autocorrelation function of the input signal modulating process. The spectral density of the input signal is

$$S_s(f) = \frac{1}{4} [S_A(f-f_c) + S_A(f+f_c)] \quad (30)$$

where  $S_A(f)$  is the spectral density of the input signal modulating process. Now, due to Doppler spreading the spectral density can be assumed to be (considering uniform antenna weighting across the Doppler frequency band) a rectangle of width  $B_D$  (the Doppler band width), i.e.,

$$\text{Define } S_A = \begin{cases} \frac{A_o^2}{2} & f-f_c - B_D/2 \leq |f| \leq f-f_c + B_D/2 \\ 0 & \text{elsewhere.} \end{cases} \quad (31)$$

Then the total signal power is given by  $P_s = A_o^2 \cdot B_D$ . Since we are considering zero mean narrow band Gaussian statistics, this will also be the variance of the  $s(t)$ . Similarly we define a noise spectral density

$$S_B = \begin{cases} \frac{A_N^2}{2} & f-f_c - B_{IF}/2 \leq |f| \leq f-f_c + B_{IF}/2 \\ 0 & \text{elsewhere.} \end{cases} \quad (32)$$

i.e., the noise is contained in the IF bandwidth and is flat across it. The noise power is  $P_n = A_N^2 \cdot B_{IF}$  and since it is zero mean, the variance of  $n(t) = P_n = A_N^2 \cdot B_{IF}$ . The autocorrelation function is the inverse Fourier Transform of the spectral density function; so,

$$R_s(\tau) = \overline{S_1 S_2} = \frac{A_o^2}{2} B_D \frac{\sin \pi B_D \tau}{\pi B_D \tau} [\cos \omega_c \tau + \cos(-\omega_c \tau)] \quad (33)$$

Now define  $\text{sinc } u = \frac{\sin \pi u}{\pi u}$  (34)

$$R_s(\tau) = \overline{S_1 S_2} = A_0^2 B_d \text{sinc}(B_d \tau) \cos \omega_c \tau \quad (35)$$

Therefore

$$\begin{aligned} R_{SS}(\tau) &= \overline{S_1^2 S_2^2} = \overline{S_1 S_2 S_1 S_2} = 2 \overline{S_1 S_2} \overline{S_1 S_2} + \overline{S_1^2} \overline{S_2^2} \\ &= 2 A_0^4 B_d^2 \text{sinc}^2(B_d \tau) \cos^2 \omega_c \tau + A_0^4 B_d^2 \end{aligned} \quad (36)$$

$$R_N(\tau) = \overline{N_1 N_2} = \frac{2 A_N^2}{2} B_{IF} \text{sinc}(B_{IF} \tau) \cos \omega_c \tau \quad (37)$$

and  $R_{NN}(\tau) = \overline{N_1^2 N_2^2} = 2 A_N^4 B_{IF}^2 \text{sinc}^2(B_{IF} \tau) \cos^2 \omega_c \tau + A_N^4 B_{IF}^2 \quad (38)$

$$\begin{aligned} 4 R_{SN}(\tau) &= 4 \overline{S_1 S_2 N_1 N_2} = 4 \overline{S_1 S_2} \overline{N_1 N_2} \\ &= 4 A_0^2 B_d \text{sinc}(B_d \tau) A_N^2 \text{sinc}(B_{IF} \tau) B_{IF} \cos^2 \omega_c \tau \cos \Delta \omega_c \tau \end{aligned} \quad (39)$$

where  $\Delta \omega_c = \omega_f - \omega_c$

i.e., when the doppler spectrum is not centered with the noise bandwidth.

The remaining term in equation 6.26  $2 \overline{N_1^2 S_2^2}$  is found by

$$2 \overline{N_1^2 S_2^2} = 2 \overline{N_1^2} \overline{S_2^2} = 2 A_N^2 B_{IF} A_0^2 B_d = 2 \sigma_S^2 \sigma_N^2 \quad (40)$$

Therefore,

$$R_Y(\tau) = \alpha^2 \left[ 2 \sigma_S^2 \sigma_N^2 + R_{SS}(\tau) + R_{NN}(\tau) + 4 R_{SN}(\tau) \right] \quad (41)$$

These terms can be recognized as a modulation of signal with itself, noise with itself and noise with the signal. In the absence of noise, the only term occurring would be the  $R_{SS}$  term. Rewriting the expression for  $R_Y(\tau)$ , with  $\sigma_S^2$  and  $\sigma_N^2$  substituted and making use of the trigonometric identity

$$\cos^2 \alpha = \frac{1}{2} + \frac{1}{2} \cos 2\alpha \quad (42)$$

$$R_y(\tau) = a^2 \left[ 2\sigma_s^2 \sigma_n^2 + (1 + \cos 2\omega_c \tau) \left[ \sigma_s^4 \text{sinc}^2(B_d \tau) + \frac{\sigma_s^4}{2} + \frac{\sigma_n^4}{2} + \sigma_n^4 \text{sinc}^2(B_{IF} \tau) + 2\sigma_s^2 \sigma_n^2 \cdot \text{sinc}(B_d \tau) \text{sinc}(B_{IF} \tau) \cos \Delta\omega_c \tau \right] \right] \quad (43)$$

$$E[Y^2] = R_y(0) = a^2 [\sigma_s^4 + 6\sigma_s^2 \sigma_n^2 + \sigma_n^4] \quad (44)$$

The next stage is a low-pass zonal filter. If this filter cuts off all components around  $2\omega_c$ , then only the d.c. term and components centered at zero frequency are left.

$$z(t) = h(t) * y(t) \quad (45)$$

$$\therefore S_z(f) = |H(f)|^2 S_y(f)$$

Since  $y(t) = a(s(t) + n(t))^2 = a(s^2(t) + 2s(t)n(t) + \underline{n^2(t)})$  (46)

$$E[Y] = a(\sigma_s^2 + \sigma_n^2)$$

Therefore the mean of z will be given by

$$E[z] = |H(0)| a(\sigma_s^2 + \sigma_n^2) \quad (47)$$

$$(E[z])^2 = |H(0)|^2 a^2 (\sigma_s^2 + \sigma_n^2)^2 \quad (48)$$

Substituting these results in equation (21) and (22), we have

$$\bar{V}_{S+N} = \frac{g}{T} a |H(0)| (\sigma_s^2 + \sigma_n^2) \quad (49)$$

and var  $\{V_{S+N}\} = \frac{2g^2}{T} \int_0^T \left(1 - \frac{\tau}{T}\right) \left\{ \frac{g}{T} \left( |H(f)|^2 S_y(f) \right) \right\} d\tau$  (50)

Assuming that  $H(\omega)$  is an ideal low pass filter, i.e.  $\frac{2g^2}{T} \frac{\bar{z}^2}{2}$

REPRODUCIBILITY OF THE ORIGINAL PAGE IS POOR.

$$H(\omega) = \begin{cases} 1 & |\omega| < B_{IF} \\ 0 & \text{elsewhere} \end{cases} \quad (51)$$

the variance in the measurement is given by

$$\text{var} \{V_{s+N}\} = \frac{2g^2 a^2}{T} \int_0^T \left(1 - \frac{\tau}{T}\right) \left\{ \sigma_s^4 \text{sinc}^2(B_d \tau) + \sigma_N^4 \text{sinc}^2(B_{IF} \tau) + \sigma_s^4 + \sigma_N^4 + 2\sigma_s^2 \sigma_N^2 \left(1 + \text{sinc}(B_{IF} \tau) \cdot \text{sinc}(B_d \tau) \cos \Delta \omega_c \tau\right) \right\} d\tau \quad (52)$$

this integral can be broken up into three integrals

$$\text{var} \{sxs\} = \frac{2g^2 a^2}{T} \int_0^T \left(1 - \frac{\tau}{T}\right) [\sigma_s^4 \text{sinc}^2(B_d \tau)] d\tau \quad (53)$$

$$\text{var} \{nxn\} = \frac{2g^2 a^2}{T} \int_0^T \left(1 - \frac{\tau}{T}\right) [\sigma_N^4 \text{sinc}^2(B_{IF} \tau)] d\tau \quad (54)$$

$$\text{var} \{sxn\} = \frac{2g^2 a^2}{T} \int_0^T \left(1 - \frac{\tau}{T}\right) \left[ 2\sigma_s^2 \sigma_N^2 \left( \frac{\text{sinc}(B_d \tau) \text{sinc}(B_{IF} \tau)}{\cos \Delta \omega_c \tau} \right) \right] d\tau \quad (55)$$

where  $\{sxs\}$ ,  $\{nxn\}$ ,  $\{sxn\}$  represent signal modulating signal, noise modulating noise, and signal modulating noise respectively. When the time bandwidth product (TB) is large, the following approximation may be applied

$$\int_0^T \left(1 - \frac{\tau}{T}\right) \text{sinc}^2(B \tau) d\tau \approx \int_0^{1/2B} \left(1 - \frac{\tau}{T}\right) d\tau \quad (56)$$

Applying this approximation to the equations for the individual variance contribution, we get

$$\text{var} \{V_{s+N}\} = \frac{2g^2 a^2}{T} \sigma_s^4 \left( \frac{1}{2B_d} - \frac{1}{16B_d^2 T} \right) + \frac{2g^2 a^2}{T} \sigma_N^4 \left( \frac{1}{2B_{IF}} - \frac{1}{16B_{IF}^2 T} \right) + \frac{4g^2 a^2}{T} \sigma_s^2 \sigma_N^2 \left( \frac{1}{2B_{IF}} - \frac{1}{8B_{IF}^2 T} \right) \frac{\text{sinc} \Delta f}{B_{IF}^2} + \text{sinc} \left( \frac{\Delta f}{B_{IF}} \right) \cdot \frac{1}{8B_{IF}^2} \quad (57)$$

$$\begin{aligned} \text{Var} \{V_{S+N}\} = & \frac{K P_S^2}{T B_d} \left(1 - \frac{1}{8 T B_d}\right) + \frac{K P_N^2}{T B_{IF}} \left(1 - \frac{1}{8 T B_{IF}}\right) \\ & + \frac{2 P_S P_N K}{T B_{IF}} \left[ \left(1 - \frac{1}{2 T B_{IF}}\right) \text{sinc}\left(\frac{\Delta f}{B_{IF}}\right) + \text{sinc}^2\left(\frac{\Delta f}{2 B_{IF}}\right) \cdot \frac{1}{4 T B_{IF}} \right] \end{aligned} \quad (58)$$

where  $K = 2g^2 a^2$

This says that the variance due to the signal alone (the first term) is modified by the variance due to the noise and the cross products between signal and noise. The sinc terms appearing in the expression are due to a possible shift between the center of the Doppler spectrum and the IF filter. The IF filter has been designed to be at least 3 times as large as the Doppler bandwidths. Since the Doppler signal is always assumed to fall within this IF bandwidth, the maximum that  $\Delta f$  can be is  $1/3 B_{IF}$ , with this value, the sinc term equals 0.9816 and the sinc<sup>2</sup> term is less than 0.25. Therefore, for our purposes, we shall assume that  $\Delta f$  is zero. The variance of the measurement then reduces to

$$\begin{aligned} \text{Var} \{V_{S+N}\} = & \frac{K P_S^2}{T B_d} \left(1 - \frac{1}{8 T B_d}\right) + \frac{K P_N^2}{T B_{IF}} \left(1 - \frac{1}{8 T B_{IF}}\right) \\ & + \frac{2 P_S P_N K}{T B_{IF}} \left[ \left(1 - \frac{1}{2 T B_{IF}}\right) \right] \end{aligned} \quad (59)$$

For large time bandwidth products, this reduces to the familiar expression

$$\text{Var} \{V_{S+N}\} = K \left[ \frac{P_S^2}{T B_d} + \frac{P_N^2}{T B_{IF}} + \frac{2 P_S P_N}{T B_{IF}} \right] \quad (60)$$

### 6.5.2 Sensor Measurement Analysis Considering a Gaussian Signal Spectrum

In the above section we assumed for simplicity a rectangular input spectrum for the signal. This facilitated the analysis. The actual signal spectrum will, however, be influenced by the antenna weighting. The antenna power pattern (two-way) can be estimated very closely by a Gaussian\* over the main beam. The return doppler spectrum will therefore have a Gaussian shape. We have used the term "main beam" loosely here. By definition it could mean either the crest of the pattern up to the half power points or the crest of the pattern up to the first null in the pattern. The uniform weighting

---

\*A. C. Cook, private communication.

(rectangular Doppler spectrum) considered above was due to an equivalent antenna beamwidth. The computation of this term will be discussed in a following section; it is a hypothetical conical antenna pattern that contains as much of the pattern energy as the main beam (to the first null). Clearly the Doppler spectrum for the effective pattern will extend only to the edge of this pattern. For the Gaussian pattern, the Doppler spectrum should now be spread further. We will, therefore, make the assumption that our pattern with the Gaussian fit produces a spectrum whose width will be such that the signal power is the same as that of the uniform or effective pattern. Let us then define this bandwidth as  $B_d'$ . We will now define our Doppler bandwidth as the spectral width within the half power points on the spectral density distribution. The parameters introduced in our analysis of this Gaussian spectrum will be related back to those for the rectangular spectrum so that the results from these two cases may be readily compared. Let us assume that the return power spectral density  $S_{s_g(f)}$  is given by

$$S_{s_g(f)} = \beta_\omega e^{-(\omega - \omega_c)^2 / \alpha_\omega^2} \quad (61)$$

where the subscript  $s_g$  implies that this is the signal power spectral density for Gaussian spectrum, and the subscript  $\omega$  refers to the fact that these parameters are with respect to frequency rather than to incidence angle as in Cook's\* development. The signal and noise are again considered independent and of zero mean. The assumption of stationarity for both still holds. From equation (27) we find that

$$R_y(\tau) = \overline{S_1^2 S_2^2} + \overline{N_1^2 N_2^2} + 4 \overline{S_1 S_2 N_1 N_2} + 2 \overline{N_1^2 S_2^2}$$

The terms on the right hand side involving the signal term will now be computed.

$$\overline{S_1^2 S_2^2} = 2 E[S_1 S_2] E[S_1 S_2] + E[S_1^2] E[S_2^2]$$

$$\text{and } \overline{S_1 S_2} = \mathcal{F}^{-1} [S_{s_g(f)}]$$

$$\text{Therefore, } \overline{S_1 S_2} = \frac{1}{\sqrt{\pi}} \alpha_\omega \beta_\omega e^{-\tau^2 \alpha_\omega^2 / 4} \cos \omega_c \tau \quad (62)$$

$$\text{and } E[S_1^2] = E[S_2^2] = \frac{1}{\sqrt{\pi}} \alpha_\omega \beta_\omega \quad (63)$$

---

\*Ibid.

Therefore 
$$\overline{S_1^2 S_2^2} = 2 \left( \frac{1}{\sqrt{\pi}} \alpha_\omega \beta_\omega e^{-\tau^2 \alpha_\omega^2 / 4} \cos \omega_c t \right)^2 + \frac{1}{\pi} \alpha_\omega^2 \beta_\omega^2 \quad (64)$$

and 
$$4 \overline{S_1 S_2 N_1 N_2} = 4 \left( \frac{1}{\sqrt{\pi}} \alpha_\omega \beta_\omega e^{-\tau^2 \alpha_\omega^2 / 4} \right) \cdot \frac{A_N^2 B_{IF} \text{sinc}(B_{IF} \tau)}{\cos^2 \omega_c \tau} \quad (65)$$

$$2 \overline{S_2^2 N_1^2} = \frac{2}{\sqrt{\pi}} A_N^2 B_{IF} \alpha_\omega \beta_\omega \quad (66)$$

We have assumed in this case that the Doppler spectrum is centered at the center of the IF bandwidth. It was found in the above analysis for a rectangular spectrum that a shift in the center frequency produced a negligible effect on the result.

The mean of  $y$  and hence the mean of  $z$  can be found from equations 46 and 47.

$$E[Y] = a \left( \frac{1}{\sqrt{\pi}} \alpha_\omega \beta_\omega + \sigma_N^2 \right) \quad (67)$$

$$E[z] = |H(0)| a \left( \frac{1}{\sqrt{\pi}} \alpha_\omega \beta_\omega + \sigma_N^2 \right) \quad (68)$$

$$(E[z])^2 = |H(0)|^2 a^2 \left( \frac{1}{\sqrt{\pi}} \alpha_\omega \beta_\omega + \sigma_N^2 \right)^2 \quad (69)$$

The mean and variance of the measurement  $V_{S+N}$  can again be found from equations 21 and 22. Before we actually compute the result, let us express the new parameters introduced  $\alpha_\omega$ ,  $\beta_\omega$  in terms of parameters for the rectangular spectrum. By our assumption, the mean power from the Gaussian spectrum should be the same as the mean power for the rectangular spectrum; further, the power spectral density at boresight for the two cases must be the same. Equating the power at boresight we have

$$\beta_\omega = \frac{A_0^2}{2} \quad (70)$$

Now equating the expected signal power from the Gaussian spectrum to that of the rectangular spectrum, we have upon substitution for  $\beta$

$$\frac{1}{\sqrt{\pi}} \alpha_\omega \beta_\omega = A_0^2 B_d$$

or 
$$\alpha_\omega = 2\sqrt{\pi} B_d = 3.549 B_d \quad (71)$$

The bandwidth  $B_d'$  associated with these parameters can be found by considering the frequency spread at which the spectral energy is one half that at boresight, i.e.

$$e^{-(2\pi (B_d'/2)^2) / \alpha_\omega^2} = 0.5$$

from which upon substitution of  $\alpha_\omega$  in terms of  $B_d$ , we have

$$B_d' = 0.939 B_d \quad (72)$$

The autocorrelation function for  $y$ , in terms of parameters for the rectangular spectrum becomes

$$\begin{aligned} R_Y(\tau) &= 2 (A_0^2 B_d e^{-\tau^2 \pi B_d^2} \cos \omega_c \tau)^2 + \sigma_S^4 + \sigma_N^4 \\ &+ 4 (A_0^2 B_d e^{-\tau^2 \pi B_d^2} \cos \omega_c \tau) \cdot A_N^2 B_{IF} \text{sinc}(B_{IF} \tau) \quad (73) \\ &+ 2 \sigma_S^2 \sigma_N^2 + 2 (A_N^2 B_{IF} \text{sinc}(B_{IF} \tau))^2 \end{aligned}$$

Once again we assume that the low pass filter does not allow frequencies at  $2\omega_c$  to pass through. By the trigonometric identity

$$\cos^2 \alpha = \frac{1}{2} + \frac{1}{2} \cos 2\alpha$$

we have

$$\begin{aligned} R_Y(\tau) &= \sigma_S^4 e^{-2\tau^2 \pi B_d^2} + \sigma_S^4 + \sigma_N^4 + 2\sigma_S^2 \sigma_N^2 \cdot \quad (74) \\ &\left( e^{-\tau^2 \pi B_d^2} \text{sinc}(B_{IF} \tau) \right) + \sigma_N^4 \text{sinc}^2(B_{IF} \tau) \end{aligned}$$

The mean and variance of  $V_{S+N}$  is again

$$\begin{aligned} \bar{V}_{S+N} &= |H(0)| \frac{ag}{T} (\sigma_S^2 + \sigma_N^2) \\ \text{var} \{V_{S+N}\} &= \frac{2g^2}{T} \int_0^T (1 - \frac{\tau}{T}) C_z(\tau) d\tau \\ C_z(\tau) &= R_z(\tau) - \bar{z}^2 \end{aligned}$$

Once again assuming an ideal low pass filter we have

$$\bar{z}^2 = a^2 (\sigma_S^2 + \sigma_N^2)$$

The variance of  $V_{S+N}$  can then be written as

$$\begin{aligned} \text{var}\{V_{s+N}\} &= \frac{2g^2 a^2}{T} \int_0^T \left(1 - \frac{\tau}{T}\right) \left[ \sigma_s^4 e^{-2\tau^2 \pi B_d^2} \right. \\ &\quad + \sigma_N^4 \text{sinc}^2(B_{IF} \tau) + \\ &\quad \left. 2\sigma_s^2 \sigma_N^2 \left( e^{-\tau^2 \pi B_d^2} \text{sinc}(B_{IF} \tau) \right) \right] d\tau \end{aligned} \quad (75)$$

This can again be split up as before

$$\text{var}\{sxs\} = \frac{2g^2 a^2 \sigma_s^4}{T} \int_0^T \left(1 - \frac{\tau}{T}\right) \left( e^{-2\tau^2 \pi B_d^2} \right) d\tau \quad (76)$$

$$\text{var}\{n \times n\} = \frac{2g^2 a^2 \sigma_N^4}{T} \int_0^T \left(1 - \frac{\tau}{T}\right) \left( \text{sinc}^2(B_{IF} \tau) \right) d\tau \quad (77)$$

$$\text{var}\{nxs\} = \frac{4g^2 a^2 \sigma_s^2 \sigma_N^2}{T} \int_0^T \left(1 - \frac{\tau}{T}\right) \text{sinc}(B_{IF} \tau) e^{-\tau^2 \pi B_d^2} d\tau \quad (78)$$

where, as before  $\{sxs\}$ ,  $\{n \times n\}$ ,  $\{nxs\}$  represent signal modulating signal, noise modulating noise, and noise modulating signal respectively. When the time bandwidth product (TB) is large, the following approximation may be applied

$$\int_0^T \left(1 - \frac{\tau}{T}\right) \text{sinc}^2(B_{IF} \tau) d\tau \approx \int_0^{\frac{1}{2} B_{IF}} \left(1 - \frac{\tau}{T}\right) d\tau$$

with this the  $\{n \times n\}$  is seen to be the same as for the rectangular case

$$\begin{aligned} \text{var}\{sxs\} &= \frac{2g^2 a^2 \sigma_s^4}{T} \int_0^T \left(1 - \frac{\tau}{T}\right) e^{-2\tau^2 \pi B_d^2} d\tau \\ &= \frac{2g^2 a^2 \sigma_s^4}{T} \left[ \int_0^T e^{-2\tau^2 \pi B_d^2} d\tau - \frac{1}{T} \int_0^T \tau e^{-2\tau^2 \pi B_d^2} d\tau \right] \\ &= \frac{2g^2 a^2 \sigma_s^4}{T} \left[ \frac{1}{\sqrt{2\pi}} \Phi(\sqrt{2\pi} B_d T) - \frac{1}{\sqrt{2\pi} B_d^2} \left[ \frac{1}{2} - e^{-2\pi B_d^2 T^2} \right] \right] \end{aligned} \quad (79)$$

where

$$\Phi(u) = \frac{2}{\sqrt{\pi}} \int_0^u e^{-t^2/2} dt$$

For large time bandwidth products, the argument of  $\Phi$  is large and hence the value can be considered to be unity. The second term in the second square braces has  $2(B_d T)^2$  as a negative exponent, with large time bandwidth products, this term can be assumed to be zero. Hence,

$$\begin{aligned} \text{var} \{s_x s\} &= \frac{2g^2 a^2 \sigma_s^4}{T} \left[ \frac{1}{2\sqrt{2}} B_d - \frac{1}{2\sqrt{2}\pi T B_d^2} \right] \quad (80) \\ &= \frac{K P_s^2}{T B_d} \left[ \frac{1}{\sqrt{2}} - \frac{1}{\sqrt{2}\pi T B_d^2} \right] \end{aligned}$$

Note that the terms in the braces are different from those for a rectangular spectrum. The resultant variance in this case (for large time bandwidth products where the second fraction in the braces is insignificant) becomes smaller by a factor of  $\frac{1}{\sqrt{2}} = 0.707$  from that of a rectangular spectrum.

$$\text{var} \{s_x n\} = \frac{2g^2 a^2 \sigma_s^2 \sigma_N^2}{T} \int_0^T \left(1 - \frac{\tau}{T}\right) e^{-\pi \tau^2 B_d^2} \text{sinc}(B_{IF} \tau) d\tau$$

Applying the approximation

$$\int_0^T \left(1 - \frac{\tau}{T}\right) f(\tau) \text{sinc}(B_{IF} \tau) d\tau \approx \int_0^{\frac{1}{2B_{IF}}} f(\tau) d\tau$$

for a rapidly decaying function  $f(\tau)$ .

We have

$$\text{var} \{s_x n\} = \frac{4g^2 a^2 \sigma_s^2 \sigma_N^2}{T} \int_0^{\frac{1}{2B_{IF}}} e^{-\pi \tau^2 B_d^2} d\tau$$

$$\text{var} \{s_{xN}\} = \frac{4g^2 a^2 \sigma_s^2 \sigma_N^2}{T} \frac{1}{2B_d} \left( \frac{\Phi \left( \frac{\sqrt{\pi} B_d}{2B_{IF}} \right)}{2B_{IF}} \right) \quad (81)$$

Expanding  $\Phi$  in a series and retaining only the first two terms we have

$$\begin{aligned} \text{var} \{s_{xN}\} &= 4g^2 a^2 \sigma_s^2 \sigma_N^2 \left( \frac{1}{2B_d} \frac{2}{\sqrt{\pi}} \left\{ \frac{\sqrt{\pi} B_d}{2B_{IF}} - \frac{\pi^{3/2} B_d^3}{48B_{IF}^3} \right\} \right) \quad (82) \\ &= \frac{4g^2 a^2 \sigma_s^2 \sigma_N^2}{T} \left[ \frac{1}{2B_{IF}} - \frac{\pi B_d^2}{48B_{IF}^3} \right] \end{aligned}$$

The second factor in the braces may be safely ignored because the IF bandwidth is at least 3 times larger than the Doppler bandwidth. The variance of  $V_{S+N}$  for the Gaussian spectrum is therefore given by

$$\text{var} \{V_{S+N}\} = \frac{K P_S^2}{T B_d} \left[ \frac{1}{\sqrt{2}} - \frac{1}{\sqrt{2\pi T B_d}} \right] + \frac{K P_N^2}{T B_{IF}} \quad (83)$$

$$\left[ 1 - \frac{1}{8 T B_{IF}} \right] + \frac{2 K P_S P_N}{T B_{IF}} \left[ 1 - \frac{\pi B_d^2}{16 B_{IF}^2} \right]$$

where

$$K = g^2 a^2$$

The variance of the noise-only measurement can be similarly found. The noise in the absence of the signal has narrow band Gaussian statistics (after the IF filter). The mean and variance of the noise-only measurement are given by

$$\bar{V}_N = g a P_N \quad (84)$$

and

$$\text{var}\{V_N\} = \frac{K' P_N^2}{T_N B_{IF}} \left( 1 - \frac{1}{8 T_N B_{IF}} \right) \quad (85)$$

where  $T_N$  is the integration time for the noise-only measurement, different from that of the signal-plus-noise measurement. From equations (2) and (3),

$$P_r = C_r (\hat{V}_{S+N} - \hat{V}_N)$$

If the two measurements are considered independent, then

$$\bar{P}_r = C_r (\bar{\hat{V}}_{S+N} - \bar{\hat{V}}_N) \quad (86)$$

and

$$\text{var}\{P_r\} = C_r^2 \left\{ \text{var}(\hat{V}_{S+N}) + \text{var}(\hat{V}_N) \right\} \quad (87)$$

Substituting values for the variance of  $V_{S+N}$  and  $V_N$ , the variance of  $P_r$ , the received power can be found. Note that the variance due to the Gaussian spectrum will not be the same as that for the rectangular spectrum. For large time bandwidth products, the variance for the power received for the two cases of input spectrum are

$$\text{var}\{P_r\}_{\text{rect}} = C_r^2 \left[ \frac{K P_S^2}{T B_d} + \frac{K P_N^2}{T B_{IF}} + 2 \frac{K P_S P_N}{T B_{IF}} + \dots \right] \quad (88)$$

$$\dots \left[ \frac{K' P_N^2}{T B_{IF}} \right] \quad (89)$$

$$\text{var}\{P_r\}_{\text{gauss}} = C_r^2 \left[ \frac{K P_S^2}{T B_d \sqrt{2}} + \frac{K P_N^2}{T B_{IF}} + 2 \frac{K P_S P_N}{T B_{IF}} + \frac{K' P_N^2}{T B_{IF}} \right]$$

### 6.5.3 Number of Independent Samples

When one has used post-detection integration of partially correlated signals, the equivalent number of independent samples may be estimated by taking the ratio of the input and output variances.

$$N = \frac{\text{var \{input\}}}{\text{var \{output\}}}$$

The equivalent number of independent samples using this definition will be found for the two input signal spectra considered above. The variance of a noise-like signal with Rayleigh fading characteristics after square law detection is equal to the square of the mean power. The output variance after square law detection and integration is given by equations (88) and (89) for the uniform and Gaussian signal spectrums respectively. Considering a noiseless receiver, the variance after integration for T seconds is given by

$$\text{var} \{V_S\} = \frac{P_S^2}{TB_d} \quad \text{for uniform signal spectrum} \quad (90)$$

$$\text{var} \{V_S\} = \frac{P_S^2}{\sqrt{2}TB_d} \quad \text{for Gaussian signal spectrum} \quad (91)$$

The number of independent samples are therefore given by

$$N = \frac{\text{var \{input\}}}{\text{var \{output\}}} = \begin{cases} TB_d \\ \sqrt{2}TB_d \end{cases} \quad \text{for uniform signal spectrum} \quad (92)$$

for Gaussian signal spectrum

The number of independent samples for receiver noise above are similarly obtained

$$N_{\text{NOISE}} = TB_{\text{IF}} \quad \text{for both cases of input signal spectrum} \quad (93)$$

When the input consists of narrow band Gaussian signals and additive narrow band Gaussian noise, the variance of the output of a low pass zonal filter is given by (see for example Davenport and Root, p. 255, eq. 12-23)

$$\text{var} \{ z(t) \} = E [ z(t)^2 ] - E^2 [ z(t) ] = (P_S + P_N)^2$$

The output variance after integration for T seconds is given by equations (88) and (89) for the uniform and Gaussian spectrum cases. The effective number of independent samples for signal plus noise for the rectangular spectrum are then given by

$$N_{(S+N)_{\text{rect}}} = \frac{(P_S + P_N)^2}{\frac{P_S^2}{TB_d} + \frac{P_N^2}{TB_{IF}} + \frac{2P_S P_N}{TB_{IF}}} \quad (94)$$

$$= \frac{((P_S/P_N) + 1)^2 TB_{IF}}{\left(\frac{P_S}{P_N}\right)^2 \frac{B_{IF}}{B_d} + 1 + 2\frac{P_S}{P_N}}$$

Noting that  $P_S/P_N$  is the signal to noise ratio (S/N), this reduces to

$$N_{(S+N)_{\text{rect}}} = \frac{((S/N) + 1)^2 TB_{IF}}{(S/N)^2 \frac{B_{IF}}{B_d} + 2(S/N) + 1} \quad (95)$$

The corresponding number of independent samples for the Gaussian input spectrum is given by

$$N_{(S+N)_{\text{gauss}}} = \frac{(P_S + P_N)^2}{\frac{P_S^2}{\sqrt{2}TB_d} + \frac{P_N^2}{TB_{IF}} + \frac{2P_S P_N}{TB_{IF}}} \quad (96)$$

$$= \frac{((S/N) + 1)^2 TB_{IF}}{\frac{1}{\sqrt{2}}(S/N)^2 B_{IF}/B_d + 1 + \sqrt{2}(S/N)}$$

The limits of these equations as a function of signal-to-noise ratio are

$$\begin{array}{ll} \text{Rectangular Spectrum} & \text{Gaussian Spectrum} \\ \text{Limit } (S/N) \rightarrow \infty & \text{Limit } (S/N) \rightarrow \infty \\ N_{S+N} = TB_d & N_{S+N} = \sqrt{2} TB_d \quad (97) \end{array}$$

$$\begin{array}{ll} \text{Limit } (S/N) \rightarrow 0 & \text{Limit } (S/N) \rightarrow 0 \\ N_{S+N} = TB_{IF} & N_{S+N} = TB_{IF} \quad (98) \end{array}$$

This states that with high signal to noise ratios, the rectangular (uniform) spectrum contains fewer independent samples. For a single pulse and rectangular spectrum, the minimum value of N will be for a pitch of  $48^\circ$ , and, therefore,

$$N_{(S+N)_{\text{rect}}} \geq TB_{d_{\text{min}}} = 27.18$$

For a Gaussian input spectrum

$$N_{(S+N)_{\text{Gauss}}} \geq \sqrt{2} TB_{d_{\text{min}}} = 38.44$$

The S-193 scatterometer measurement is actually an integrated value for more than one pulse. The incoming signal plus noise for the first pulse is detected, integrated and this value is compared to a threshold value for gain selection (see appendix B for details). If the test criterion is met, the integrator value is retained and the detected outputs from the other pulses for that measurement period are added (integrated) along with this one. The mean and variance on a per-pulse basis has been found in the above sections. If the return from each pulse can be considered an independent sample then, the mean and variance of the entire measurement is related to the mean and variance of the voltage on a per-pulse basis as.

$$\begin{aligned} \bar{V}_M &= \sum_{n=1}^K \bar{V}_{S+N} = K \bar{V}_{S+N} \\ \sigma_M^2 &= \sum_{n=1}^K \text{var} \{ V_{S+N} \} = K \text{var} \{ V_{S+N} \} \end{aligned}$$

The normalized variance is therefore given by

$$\frac{\sigma_M^2}{\bar{V}_M^2} = \frac{1}{K} \frac{\text{var} \{ V_{S+M} \}}{\bar{V}_{S+M}^2} \quad (99)$$

Therefore, the number of independent samples obtained is seen to increase by a factor of K. This implies that the interrupted mode of integration is the same as if integration had been performed for KT seconds.

#### 6.5.4 Precision of Power Received Measurement

As mentioned before, the power received is computed by measuring first the signal and noise followed by noise alone and after adjusting for the gains, subtracting the noise voltage from the signal plus noise voltage. The mean and variance of the power estimate is given by

$$\begin{aligned}\hat{P}_S &= K_1 \bar{V}_{S+N} - K_2 \bar{V}_N = \hat{P}_{S+N} - \hat{P}_N \\ \text{var} \{ \hat{P}_S \} &= E \left[ (K_1 \bar{V}_{S+N} - K_2 \bar{V}_N)^2 \right] - \overline{(K_1 V_{S+N} - K_2 V_N)^2} \\ &= \text{var} \{ K_1 V_{S+N} \} + \text{var} \{ K_2 V_N \} \\ &= \text{var} \{ \hat{P}_{S+N} \} + \text{var} \{ \hat{P}_N \}\end{aligned} \quad (100)$$

If the integration time for the signal plus noise measurement is  $T_{S+N}$  and the integration time for the noise alone is  $T_N$ , then from the estimates of variance for  $P_{S+N}$  and  $P_N$ , we have for the rectangular spectrum

$$\text{var} \{ \hat{P}_S \} = \frac{1}{T_{S+N}} \left[ \frac{P_S^2}{B_D} + \frac{P_N^2}{B_{IF}} + \frac{2P_S P_N}{B_{IF}} \right] + \frac{P_N^2}{T_N B_{IF}}$$

and the corresponding normalized variance is given by

$$\frac{\text{var} \{ \hat{P}_S \}}{\bar{P}_S^2} = \frac{1}{T_{S+N}} \left[ \frac{1}{B_D} + \frac{1}{B_{IF}} \left( \frac{S}{N} \right)^2 \left( 1 + \frac{T_{S+N}}{T_N} \right) + \frac{2}{B_{IF}} \left( \frac{S}{N} \right) \right] \quad (101)$$

and in terms of signal to noise density ratios, this becomes

$$\frac{\text{var} \{ \hat{P}_S \}}{\bar{P}_S^2} = \frac{1}{T_{S+N} B_D} \left\{ 1 + 2 \frac{A_N^2}{A_S^2} + \frac{A_N^2}{A_S^2} \frac{B_{IF}}{B_D} \left( 1 + \frac{T_{S+N}}{T_N} \right) \right\} \quad (102)$$

This form of the equation shows the degradation in normalized variance (the square root of which is often talked about as precision in many engineering discussions) due to the presence of noise. The multiplier on the right hand side shows the reduction in normalized variance for a noise-free case. For a Gaussian input spectrum, the corresponding variance and normalized variance are given by

$$\text{var} \left\{ \hat{P}_S \right\}_{\text{Gauss}} = \frac{1}{T_{S+N}} \left[ \frac{P_S^2}{\sqrt{2} B_D} + \frac{P_N^2}{B_{IF}} + \frac{2 P_S P_N}{B_{IF}} \right] + \frac{P_N^2}{T_N B_{IF}}$$

$$\frac{\text{var} \left\{ \hat{P}_S \right\}_{\text{Gauss}}}{\bar{P}_S^2} = \frac{1}{T_{S+N}} \left[ \frac{1}{B_D \sqrt{2}} + \frac{1}{B_{IF} (S/N)^2} \left( 1 + \frac{T_{S+N}}{T_N} \right) + \frac{\sqrt{2}}{B_{IF} (S/N)} \right] \quad (103)$$

$$= \frac{1}{\sqrt{2} T_{S+N} B_D} \left[ 1 + \frac{2 A_N^2}{A_0^2} + \sqrt{2} \frac{A_N^2}{A_0^2} \left( \frac{B_{IF}}{B_D} \right) \left( 1 + \frac{T_{S+N}}{T_N} \right) \right]$$

Again the effects of the system are seen by examination of the terms inside the braces. The second term in equations (102) and (103) is a function of the signal and noise densities, the third term takes into account the bandwidths and integration times. An ideal receiver would have the second and third terms as zero. To reduce the second term, which is a function of the receiver noise figure, antenna gain, transmitter power and the geometry, any of these variables can be manipulated to maximize the signal to noise density ratios.

The signal to noise density ratios for the S-193 scatterometer will vary due to geometry and the backscattering coefficient of the ground. Table 6.2 provides a sample of the signal to noise density ratios expected for the incidence angles of the non-contiguous modes. The backscatter coefficient has been taken as an expected minimum and maximum at that angle. The inverse of the normalized standard deviation is sometimes expressed as an output signal to noise ratio.

Table 6.2  
Minimum and Maximum Expected Signal to Noise Density Ratios

<u>Pitch/Roll Angle</u>	<u>Backscattering Coefficient <math>\sigma^0</math> (dB)</u>	<u>Signal Density to Noise Density Ratio (dB)</u>
0.0	+15	52.6
0.0	-10	27.6
15.6	- 5	32.4
15.6	-20	17.4
29.4	- 5	32.2
29.4	-25	12.2
40.1	-10	26.8
40.1	-30	6.8
48.0	-15	21.8
48.0	-30	6.4

It can be seen that the expected contributions to the normalized variance will not be appreciable at the low incidence angles, and for worst case signal levels at 40.1 and 48.0 will still be small.

The integration times for the scatterometer measurements for all modes including the largest and smallest integration times due to gain selection are shown in Table 6.3. The Doppler bandwidths and the IF bandwidths are given in Table 6. 4. Using these figures, the expected normalized standard deviation for a rectangular input spectrum versus noise-to-signal density for three angles of the Intrack Non-Contiguous modes is shown in Figure 6.8a. Figure 6.8b shows the effect of integration time of the signal and noise measurement on the normalized standard deviation for a fixed noise to signal density, noise integration time and the Doppler and IF bandwidths.

#### 6.5.5 Specification, Verification and Expectation of Normalized Standard Deviation for Power Received Measurements

There is no accuracy specification on the power received measurement. There is only a precision specification. The specification is derived from a goal of having the estimated value of  $P_r$  with  $\pm 0.5$  dB of the true value of  $P_r$  90% of the time. To achieve this, a 90% confidence interval was symmetrically placed about the estimated power received  $\hat{P}_r$  and the corresponding specification of normalized standard deviation achieved. For Gaussian statistics, which we assume  $\hat{P}_r$  to possess, the 90% confidence interval (5-95%) is related to the variance as

TIMINGS

MODE	ANGLE	PULSES		$T_{S+N}$		$T_N$
		High	Low			
In track non-contiguous and cross track non-contiguous	0.0	23	20	50.76	44.14	26.532
	15.6	39	36	86.07	79.45	61.532
	29.4	57	54	125.80	119.178	61.532
	40.1	64	61	141.248	134.63	125.532
	48.0	74	71	171.99	164.92	125.532
In track contiguous	0.0	9	6	19.86	13.24	27.063
	15.6	9	6	19.86	13.24	27.063
	29.4	9	6	19.86	13.24	27.063
	40.1	9	6	19.86	13.24	27.063
	48.0	9	6	21.159	14.106	27.063
CTC. SCAT/RAD	0.0	14	11	30.899	24.277	16.00
	15.6	14	11	30.892	24.277	16.00
	29.4	14	11	30.892	24.277	16.00
	40.1	14	11	30.892	24.277	16.00
CTC SCAT only	0.0	8	5	17.656	11.035	6.813
	15.6	8	5	17.656	11.035	6.813
	29.4	8	5	17.656	11.035	6.813
	40.1	8	5	17.656	11.035	6.813

INT. TIME CONSTANTS

Non Contiguous	0°	10.22 ms
Non Contiguous	15.6, 29.4, 40.1, 48.0	33.0 ms
CTC RAD/ SCAT	ALL	10.22 ms
CTC SCAT only	ALL	4.0 ms
In track contiguous	ALL	4.0 ms

Table 6.3 Integration times for scatterometer measurements.

Pitch Angle Degrees	Doppler* Bandwidth KHz	IF Filter Bandwidth KHz
0.0	17.055	76.5
15.6	16.627	74.8
29.4	15.040	69.1
40.1	13.200	62.7
48.0	11.562	55.6

\*For ITNC mode, two-way equivalent beamwidth.

Table 6.4

Doppler and IF Filter Bandwidths for S-193 Scatterometer Operation

$$C = 3.29 \cdot [\text{var} \{ \hat{P}_r \}]^{1/2} \quad (104)$$

The estimates of  $P_r$  at the limits of this interval are given by

$$\hat{P}_{r \text{ LOW}} = \hat{P}_r - C/2 = \hat{P}_r \left[ 1 - 1.645 \left( \frac{\text{var} \{ \hat{P}_r \}}{\bar{P}_r^2} \right)^{1/2} \right]$$

$$\hat{P}_{r \text{ HIGH}} = \hat{P}_r + C/2 = \hat{P}_r \left[ 1 + 1.645 \left( \frac{\text{var} \{ \hat{P}_r \}}{\bar{P}_r^2} \right)^{1/2} \right]$$

Since the goal was to make  $\hat{P}_{r \text{ LOW}}$  and  $\hat{P}_{r \text{ HIGH}}$  within  $\pm 0.5$  dB of  $\hat{P}_r$ , taking logarithms and equating the terms in braces to  $\pm 0.5$  dB we get

$$\frac{\text{var} \{ \hat{P}_r \}}{\bar{P}_r^2} = 0.0743 \quad \text{for } \Delta \epsilon = +0.5 \text{ dB} \quad (105)$$

$$\frac{\text{var} \{ \hat{P}_r \}}{\bar{P}_r^2} = 0.0662 \quad \text{for } \Delta \epsilon = -0.5 \text{ dB} \quad (106)$$

These are not equal because  $\pm 0.5$  dB on the decibel scale does not translate to equal intervals from unity on the numeric scale. A compromise was struck as the specification on the bound for the normalized standard deviation. The end-item-specification finally read that the normalized standard deviation for the allowable worst-case in the non-contiguous mode would be less than 0.0707. This, according to the definition would imply that for a backscatter coefficient of -30 dB and an incidence angle of  $52^\circ$  the specification of 0.0707 should be met. Now, the mean and variance when estimated by sampling from a random process provide estimates which are random variables. That is, the sample mean and sample variance are random variables. To see that the specification is met then implies setting a confidence interval around the estimation. For the purpose of testing, a confidence region from 0 to 95% was chosen, i.e., the critical region for rejection of the hypothesis that the estimate was greater than or equal to 0.0707, with a power level of  $\alpha = 0.05$  was sought. During testing, a limited number of samples are taken and a decision made regarding the actual normalized

standard deviation. Obviously, the larger the number of independent samples, the better the estimates for the true mean and variance, but again the larger the sample size, the greater the time and money spent. For the scatterometer testing this problem of ascertaining the sample size and the region of rejection was found by considering certain simplifying assumptions regarding the distribution of the mean and variance of the signal power measurement. If the underlying distribution for the signal power measurement is Gaussian or if the number of samples taken is sufficient for the application of the central limit theorem, the sample mean,  $P_s$ , will have a  $N(P_s, \sigma^2/n)$  distribution where  $P_s$  is the true mean,  $\sigma^2$  the variance and  $n$  the number of independent samples. Therefore, the variable  $((P_s/\sigma)\sqrt{n})$  will have a  $N(P_s\sqrt{n}/\sigma, 1)$  distribution and therefore  $nP_s^2/\sigma^2$  will have a non-central chi-square distribution with one degree of freedom and a centrality parameter  $(P_s^2 n/\sigma^2)$ . If we define  $s^2$ , as

$$s^2 = \frac{1}{n} \sum_{i=1}^n (P_{si} - \hat{P}_s)^2 \quad (107)$$

where  $P_{si}$  = individual samples of signal power  
 $\hat{P}_s$  = sample mean,

then the statistic  $\frac{n}{n-1} s^2$  is an unbiased estimator for the true or population variance. The random variable  $(ns^2/\sigma^2)$  has a chi-square distribution with  $(n-1)$  degrees of freedom. Therefore,

$$\frac{n P_s^2 \sigma^2}{n s^2 / (n-1) \sigma^2} \sim F' \left( 1, n-1, \frac{P_s^2 n}{\sigma^2} \right) \quad (108)$$

where  $F'$  = Non central F distribution with non-centrality parameter  $\frac{P_s^2 n}{\sigma^2}$ .

Using the approximation (Abramowitz and Stegun) (1954)

$$P(F' | \nu_1, \nu_2, \lambda) \approx P(F | \nu_1^*, \nu_2) \quad (109)$$

where  $F = \frac{\nu_1}{\nu_1 + \lambda} F'$ ,  $\nu_1^* = \frac{(\nu_1 + \lambda)^2}{\nu_1 + 2\lambda}$

which translates a non-central F distribution into a central F distribution, we now have a distribution that is tabulated and that is a function of  $P_s^2/\sigma^2$  and of  $n$ . What we really

want is to compute an expected value of  $nP_s^2/\sigma^2$  whose 95% upper bound translates to a value of  $\sigma/P_s$  of 0.0707. The first degree of freedom on the F distribution, for allowable or reasonable values of  $P_s^2/\sigma^2$  will be large so that the variation in the F distribution due to this parameter will be minimal. The second parameter on the F distribution is merely  $(n-1)$  where  $n$  is the sample size. The tables for the F distribution with the first parameter at infinity and the second one less than the sample size can be consulted to give  $F$  for a value of  $\alpha = 0.05$ . This will translate to the non-central F through equation (109) which can be approximated by

$$F = \frac{F'}{\lambda} = \frac{F'}{nP_s^2/\sigma^2} = \frac{F'}{A} \quad (110)$$

$$\therefore F' = n(P_s^2/\sigma^2) F(\infty, n-1)$$

That is, the 95% upper confidence bound of the variable  $A$  will be given by equation (110). But  $A$  is  $n$  times the sample estimate for the inverse of the normalized variance. Therefore, the estimate of normalized variance will have an upper bound given by  $(P_s^2/\sigma^2)F$ . The criterion we would like is that this upper bound not exceed 0.0707. This implies that the ratio of the true mean square to variance should be  $0.0707/F(\infty, n-1)$ . To maintain a 95% confidence that the unbiased estimate of the variable  $(P_s^2/\sigma^2)$  be less than specification, the variable  $(P_s^2/\sigma^2)$  will have to be lower than the estimate by a factor of  $1/F(\infty, n-1)$ . As  $n$  tends to infinity, the F distribution 95% values will tend to 1. Figure 6.9 shows the critical region of  $(\sigma/P_s)$  to test the hypothesis that the  $(\sigma/P_s)$  is greater than or equal to 0.0707, as a function of the number of samples. During system testing, a noise source was input to the polarization circulator and the scatterometer operation for various operating modes was simulated. The measured samples were then used to compute the sample mean and the sample variance. The resultant ratio in equation (108) was then tested for conformance for the non-contiguous modes; it was found satisfactory.

The equation for estimating the normalized variance (eq. 102) was solved by substituting the bandwidths and integration times for all modes and incidence angles. The results as shown in Tables 6.5 through 6.9 are for the signal densities corresponding to the worst case (lowest) backscatter coefficients at that angle. The noise density is found by considering a receiver noise temperature of 1200°K. This estimate of the

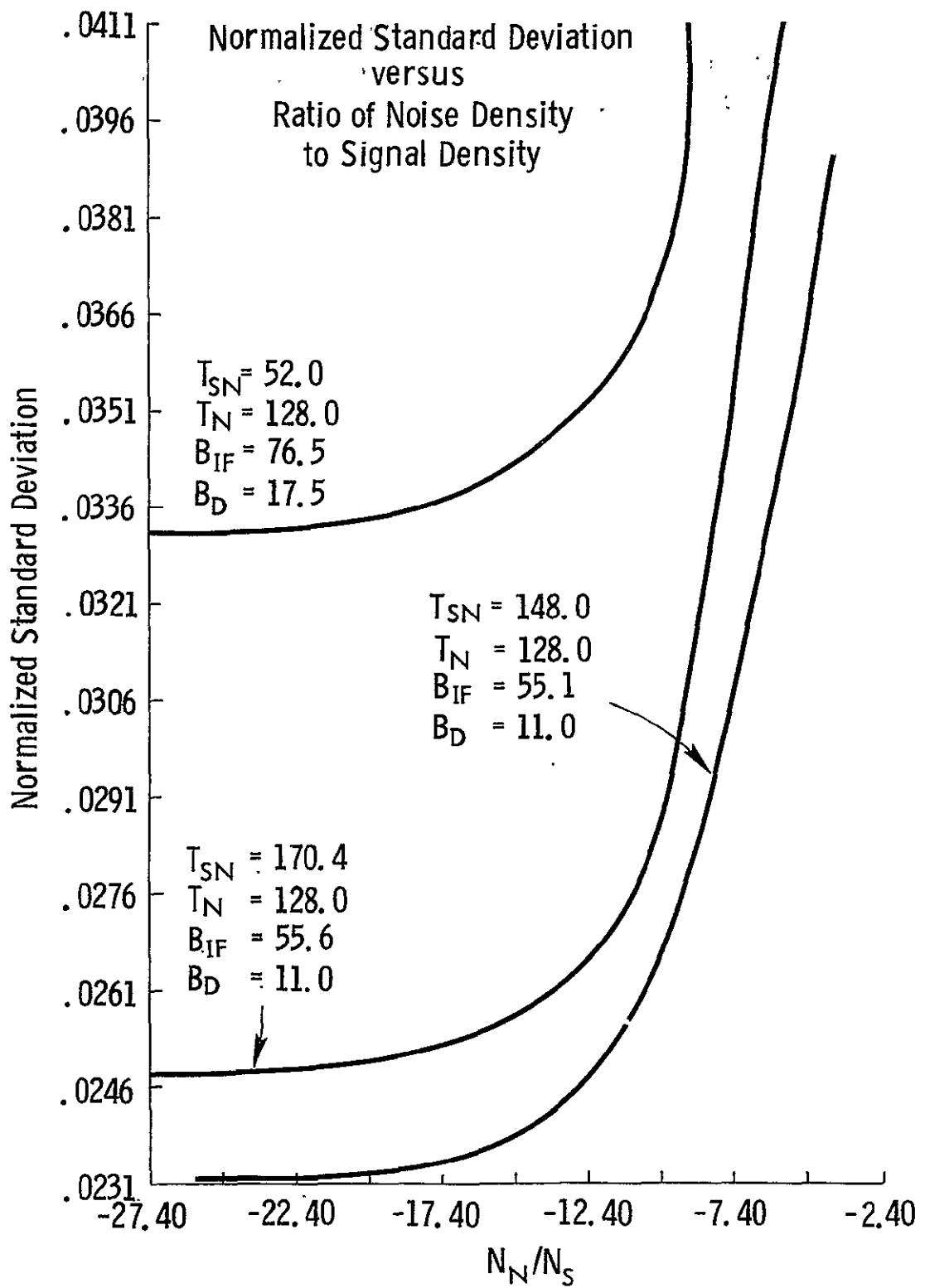


Figure 6.8a.

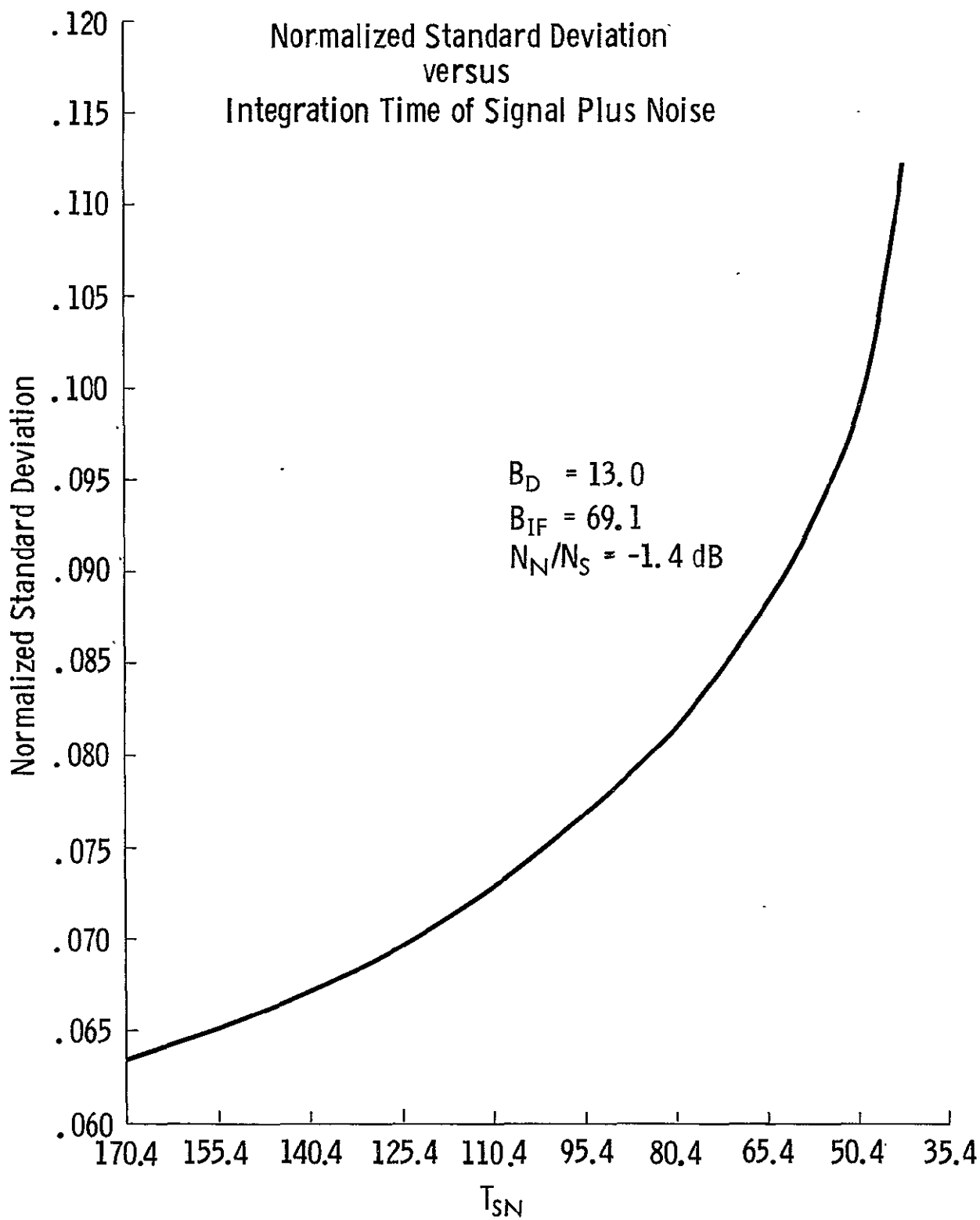


Figure 6.8b.

### Region of Acceptance for Testing Normalized Standard Deviation Specifications

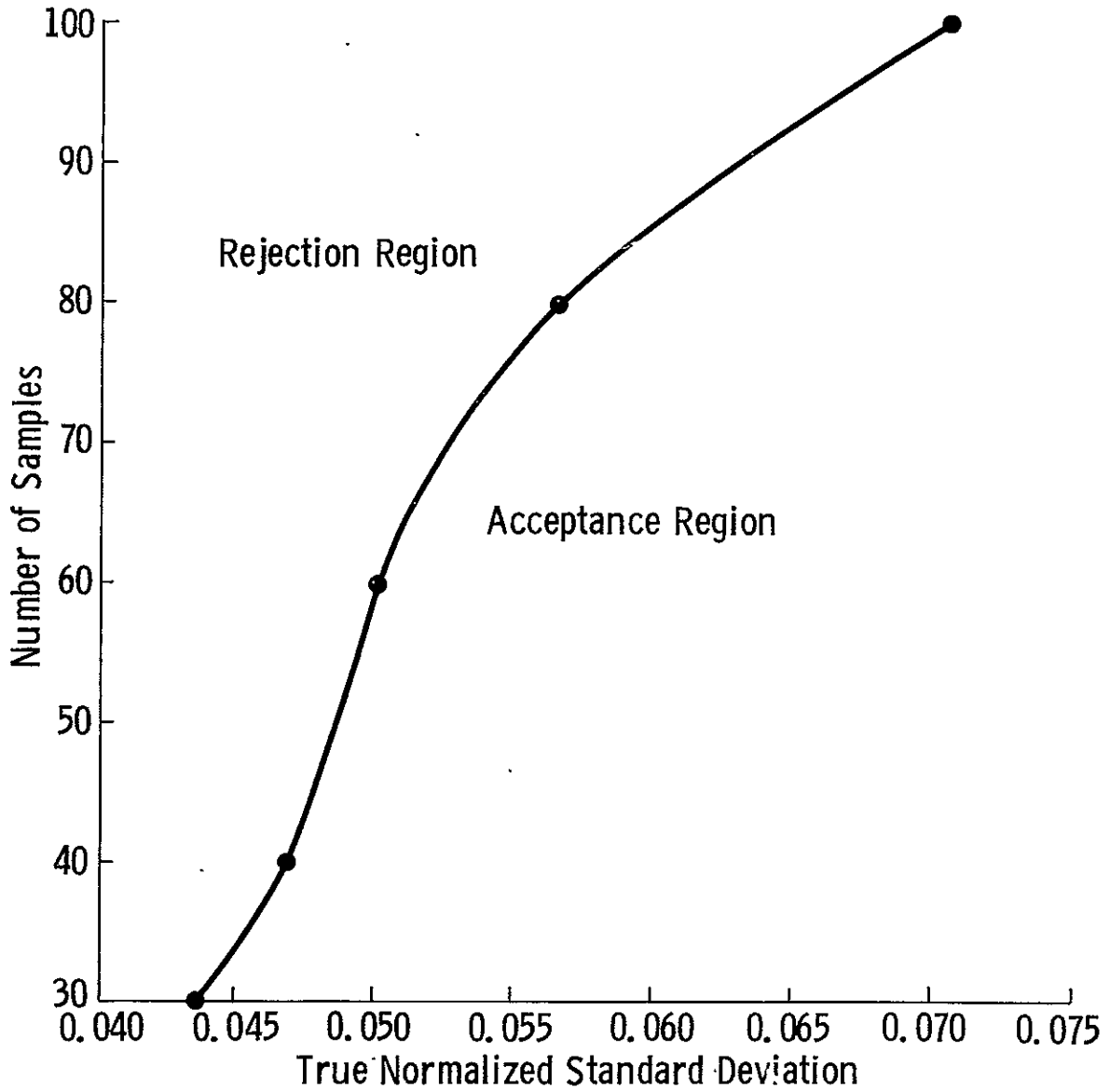


Figure 6.9.

MODE -- IN-TRACK CONTIGUOUS

In-track Angle	0.0	15.6	29.4	40.1	48.0
Cross-track Angle	0.0	0.0	0.0	0.0	0.0
$T_{S+N}$ (ms)	16.1	16.1	16.1	16.1	20.7
$T_N$ (ms)	27.0	27.0	27.0	27.0	27.0
$B_D$ (KHz)	17.263	16.69	15.112	13.349	11.717
$B_{IF}$ (KHz)	76.5	74.8	69.1	62.7	55.6
$N_N$ dB/Hz	-196.8	-196.8	-196.8	-196.8	-196.8
$(S/N)_{in}$ (dB)	+18.0	+7.78	+2.56	-2.84	-3.20
Normalized Std. Dev.	.06645	.06969	.08007	.120185	.10791
$(S/N)_{out}$ (dB)	11.78	11.57	10.97	9.20	9.67

$$(S/N)_{out} \text{ (dB)} = \frac{1}{(\text{normalized standard deviation}) \text{ in dB.}}$$

$$(S/N)_{out} \text{ (dB)} = 10 \log_{10} \left( \frac{\hat{P}_s}{\sigma} \right)$$

Table 6.5. Expected precision - In-track contiguous (system noise temperature - 1200°K).

MODE -- CROSS-TRACK CONTIGUOUS (SCAT ONLY)

In-track Angle	0.0	15.6	29.4	40.1
Cross-track Angle	-11.375 to +11.375	-11.375 to +11.375	-11.375 to +11.375	-11.375 to +11.375
$T_{S+N}$ (ms)	13.8	13.8	13.8	18.4
$T_N$ (ms)	6.75	6.75	6.75	6.75
$B_D$ (KHz)	17.262	16.579	15.001	13.118
$B_{IF}$ (KHz)	76.5	74.8	69.1	62.7
$N_N$ dB/Hz	-196.8	-196.8	-196.8	-196.8
$(S/N)_{in}$ (dB)	+17.60	+7.70	+2.49	-3.03
Normalized Std. Dev.	.07282	.07689	.0901	.1299
$(S/N)_{out}$ (dB)	11.38	11.14	10.45	8.86

Table 6.6. Expected precision - Cross-track contiguous (system noise temperature = 1200° K).

MODE -- CROSS-TRACK CONTIGUOUS  
(SCAT & RAD)

In-track Angle	0.0	15.6	29.4	40.1
Cross-track Angle	-11.375 to +11.375	-11.375 to +11.375	-11.375 to +11.375	-11.375 to +11.375
$T_{S+N}$ (ms)	27.6	27.6	27.6	32.2
$T_N$ (ms)	11.0	11.0	11.0	11.0
$B_D$ (KHz)	17.262	16.579	15.001	13.118
$B_{IF}$ (KHz)	76.5	74.8	69.4	62.7
$N_N$ dB/Hz	-196.8	-196.8	-196.8	-196.8
$(S/N)_{in}$ (dB)	+17.60	+7.70	+2.49	-3.03
Normalized Std. Dev.	.04899	.05167	.0605	.0930
$(S/N)_{out}$ (dB)	13.10	12.87	12.18	10.31

Table 6.7. Expected precision - Cross-track contiguous (system noise temperature = 1200°K).

MODE -- IN-TRACK NON-CONTIGUOUS

In-track Angle	0.0	15.6	29.4	40.1	48.0
Cross-track Angle	0.0	0.0	0.0	0.0	0.0
$T_{S+N}$ (ms)	48.3	85.1	126.5	147.2	170.2
$T_N$ (ms)	25.0	60.0	60.0	124.0	124.0
$B_D$ (KHz)	17.055	16.627	15.040	13.200	11.562
$B_{IF}$ (KHz)	76.5	74.8	69.1	62.7	55.6
$N_N$ dB/Hz	-196.8	-196.8	-196.8	-196.8	-196.8
$(S/N)_{in}$ (dB)	+17.90	+8.70	+2.35	-3.00	-3.40
Normalized Std. Dev.	.036577	.02858	.02767	.04091	.04185
$(S/N)_{out}$ (dB)	14.37	15.44	15.58	13.88	13.78

Table 6.8. Expected precision - In-track contiguous (system noise temperature - 1200°K).

MODE -- CROSS-TRACK NON-CONTIGUOUS

In-track Angle	0.0	0.0	0.0	0.0	0.0
Cross-track Angle	0.0	15.6	29.4	40.1	48.0
$T_{S+N}$ (ms)	48.3	85.1	126.5	147.2	170.2
$T_N$ (ms)	25.0	60.0	60.0	124.0	124.0
$B_D$ (KHz)	17.20	17.254	17.26	17.36	17.365
$B_{IF}$ (KHz)	76.5	74.8	69.1	62.7	55.6
$N_N$ dB/Hz	-196.8	-196.8	-196.8	-196.8	-196.8
$(S/N)_{in}$ (dB)	+17.9	+8.70	+2.35	-3.00	-3.40
Normalized Std. Dev.	.0364	.02779	.02634	.039226	.039876
$(S/N)_{out}$ (dB)	14.39	15.56	15.79	14.06	13.99

Table 6.9. Expected precision - Cross-track contiguous (system noise temperature = 1200°K).

receiver noise temperature may be considered conservative because the noise temperature computed from certain ground based tests (during the developmental stage) was around 1150°K. The signal-to-noise ratio as shown in the last row, is the effective signal to noise ratio defined as the inverse of the normalized standard deviation when expressed in decibels. This definition provides a basis for assessing the confidence in a measurement. The signal to noise ratio, taken as a ratio of the signal power and the effective noise power at the input to the receiver is found from the link calculations involving the familiar radar range equation.

$$(S/N) = \frac{P_t A \sigma^0 \lambda^2 L_{tr} L_{atm} G^2}{(4\pi)^3 K T_s B_{IF} R^4}$$

where  $L_{tr}$  = the two-way losses in the transmitted signal (hardware)  
 $L_{atm}$  = the two-way attenuation of the signal due to the intervening atmosphere  
 $K$  = Boltzman's constant  
 $T_s$  = Effective noise temperature  
 = 290 +  $T_{sys}$ , where  $T_{sys}$  = system noise temperature

The other terms have been defined earlier. This expression can be rearranged to see how the various factors influence the signal to noise ratio

$$(S/N) = \left( \frac{\sigma^0 L_{atm}}{(4\pi)^3 K} \right) \frac{P_t L_{tr} G^2 \lambda^2}{(T_s B_{IF})} \left( \frac{A}{R^4} \right)$$

The terms in the first braces are either constants or depend upon the target and the state of the intervening atmosphere. The terms in the second set of braces depend upon the hardware design of the instrument. The third set of braces are more a function of the target sensor geometry. For fixed, chosen values of  $\sigma^0$  and  $L_{atm}$ , the link calculations for the various modes were performed. Tables 6.10 through 6.12 show the results. The worst case signal to noise power ratio is seen to be 2.7, this upon post detection integration and measurement of noise produces an effective output signal to noise ratio as defined above of 13.78 dB.

NON-CONTIGUOUS IN-TRACK AND CROSS-TRACK MODES

In-track Angle °	48.0	40.1	29.4	15.6	0.0
Cross-track Angle °	0.0	0.0	0.0	0.0	0.0
$P_f$ (dBW) $P_f = 20$ Watts	+13.0	+13.0	+13.0	+13.0	+13.0
$G^2$ (dB) $G = 41.5$ dB	+83.0	+83.0	+83.0	+83.0	+83.0
A (km <sup>2</sup> -dB)	+25.8	+23.7	+21.85	+20.35	+19.8
$\sigma^0$ (dB)	-30.0	-30.0	-25.0	-20.0	-10.0
(dB) $(4\pi)^3 = 1.98 \times 10^3$	-33.0	-33.0	-33.0	-33.0	-33.0
R <sup>4</sup> (km <sup>4</sup> -dB)	-113.4	-110.7	-108.4	-106.25	-105.5
B <sub>IF</sub> (Hz - dB)	-47.6	-48.1	-48.5	-48.9	-49.0
$\lambda^2$ (km <sup>2</sup> - dB)	-93.3	-93.3	-93.3	-93.3	-93.3
K <sub>T<sub>S</sub></sub> (dB) $T_S = 1490^\circ$ K	+196.8	+196.8	+196.8	+196.8	+196.8
L <sub>tr</sub> (dB)	-2.2	-2.2	-2.2	-2.2	-2.2
L <sub>atm</sub> (dB)	-1.8	-1.5	-1.2	-1.1	-1.0
(S/N) <sub>in</sub> (dB)	-2.7	-2.3	+3.05	+8.4	+18.6

Table 6.10. Link calculations ITNC and CTNC modes.

IN-TRACK CONTIGUOUS MODE

In-track Angle °	48.0	40.1	29.4	15.6	0.0
Cross-track Angle °	0.0	0.0	0.0	0.0	0.0
$P_t$ (dBW) $P_t = 20$ Watts	+13.0	+13.0	+13.0	+13.0	+13.0
$G^2$ (dB) $G = 41.5$ dB	+83.0	+83.0	+83.0	+83.0	+83.0
$A$ (km <sup>2</sup> - dB)	+25.6	+23.56	+21.66	+20.30	+19.8
$\sigma^0$ (dB)	-30.0	-30.0	-25.0	-20.0	-10.0
(dB) $(4\pi)^3 = 1.98 \times 10^3$	-33.0	-33.0	-33.0	-33.0	-33.0
$R^4$ (km <sup>4</sup> - dB)	-113.0	-110.4	-108.0	-106.12	-105.4
$B_{IF}$ (Hz - dB)	-47.6	-48.1	-48.5	-48.9	-49.0
$\chi^2$ (km <sup>2</sup> - dB)	-93.3	-93.3	-93.3	-93.3	-93.3
$KT_S$ (dB) $T_S = 1490^\circ K$	+196.8	+196.8	+196.8	+196.8	+196.8
$L_{tr}$ (dB)	-2.2	-2.2	-2.2	-2.2	-2.2
$L_{atm}$ (dB)	-1.8	-1.5	-1.2	-1.1	-1.0
$(S/N)_{in}$ (dB)	-2.5	-2.14	+3.26	+8.48	+18.7

Table 6.11. Link calculations - ITC mode.

CROSS-TRACK CONTIGUOUS (SCAT ONLY)

In-track Angle °	0.0	15.6	29.4	40.1
Cross-track Angle °	-11.375 to +11.375	-11.375 to +11.375	-11.375 to +11.375	-11.375 to +11.375
$P_t$ (dBW) $P_t = 20$ Watts	+13.0	+13.0	+13.0	+13.0
$G^2$ (dB) $G = 41.5$ dB	+83.0	+83.0	+83.0	+83.0
A (km <sup>2</sup> - dB)	+20.00	+20.50	+22.15	+24.17
$\sigma^0$ (dB)	-10.0	-20.0	-25.0	-30.0
(dB) $(4\pi)^3 = 1.98 \times 10^3$	-33.0	-33.0	-33.0	-33.0
$R^4$ (km <sup>4</sup> - dB)	-106.0	-106.4	-108.56	-111.2
$B_{IF}$ (Hz - dB)	-49.0	-48.9	-48.5	-48.1
$\lambda^2$ (km <sup>2</sup> - dB)	-93.3	-93.3	-93.3	-93.3
$KT_s$ (dB) $T_s = 1490^\circ$ K	+196.8	+196.8	+196.8	+196.8
$L_{tr}$ (dB)	-2.2	-2.2	-2.2	-2.2
$L_{atm}$ (dB)	-1.0	-1.1	-1.2	-1.5
$(S/N)_{in}$ (dB)	+18.3	+8.40	+3.19	-2.33

Table 6.12. Link calculations - CTC (scat only) mode.

## 6.6. Radiometer Operating Characteristics

An internally calibrated modified Dicke-type radiometer is used. It differs from other internally calibrated radiometers in that it has two reference temperature sources and the gain slope is established by a measurement of the difference in temperature of the reference sources and a bias obtained by alternately switching between the temperature sources and summing or subtracting so that the net effective temperature is  $0^{\circ}\text{K}$ . The reference temperatures consist of two noise sources in precisely maintained ovens, yielding an effective noise temperature of  $393.2^{\circ}\text{K}$  and  $318.6^{\circ}\text{K}$ . The switching for reference and antenna temperature inputs is performed by circulators in the WaveGuide Switching Assembly (WGSA). A detailed description of the operation of the WGSA as well as the radiometer processor may be found in the vendors description of the hardware (G.E. 1972). A brief account of the elements in the WGSA, along with a block diagram are provided in the appendix. A comprehensive review of the transfer function is provided by Sobti and Collins [1975]. The purpose of the study here is to establish the precision of the radiometer measurement and compute an estimate of the bias errors if any.

The radiometer during one data-taking sequence (one integration and dump) has three basic sub-modes of operation. Two of these submodes are for the purpose of calibration and selecting a gain slope, the third sub-mode is where the antenna temperature is compared to the reference temperatures. The switching is done by circulators in the WGSA. An Automatic Gain Control (AGC) amplifier is incorporated in the feedback loop of the amplification stage after down conversion and IF filtering and before the video amplifier (see Figure 6.10). The AGC is operational (in the feedback loop) at all times when the input to the radiometer processor is either of the two reference loads, but is not operational (in a hold mode) when the input to the radiometer processor is the antenna temperature. The time constant of this AGC is in the order of 1 second, so that it tracks slow drifts in the overall gain (due to gain changes, bandwidth changes, or unbalance in switching) but is sluggish enough so that it does not cause a variation in gain due to the instantaneous random errors associated with measuring noise signals.

The signals fed to the radiometer processor are all noise signals, be they reference noise temperatures or antenna noise temperatures or the system noise temperature. The noise signals can all be considered Gaussian and stationary; therefore, each signal source will be considered to exhibit narrowband Gaussian statistics. Further, we assume

ORIGINAL PAGE IS  
OF POOR QUALITY

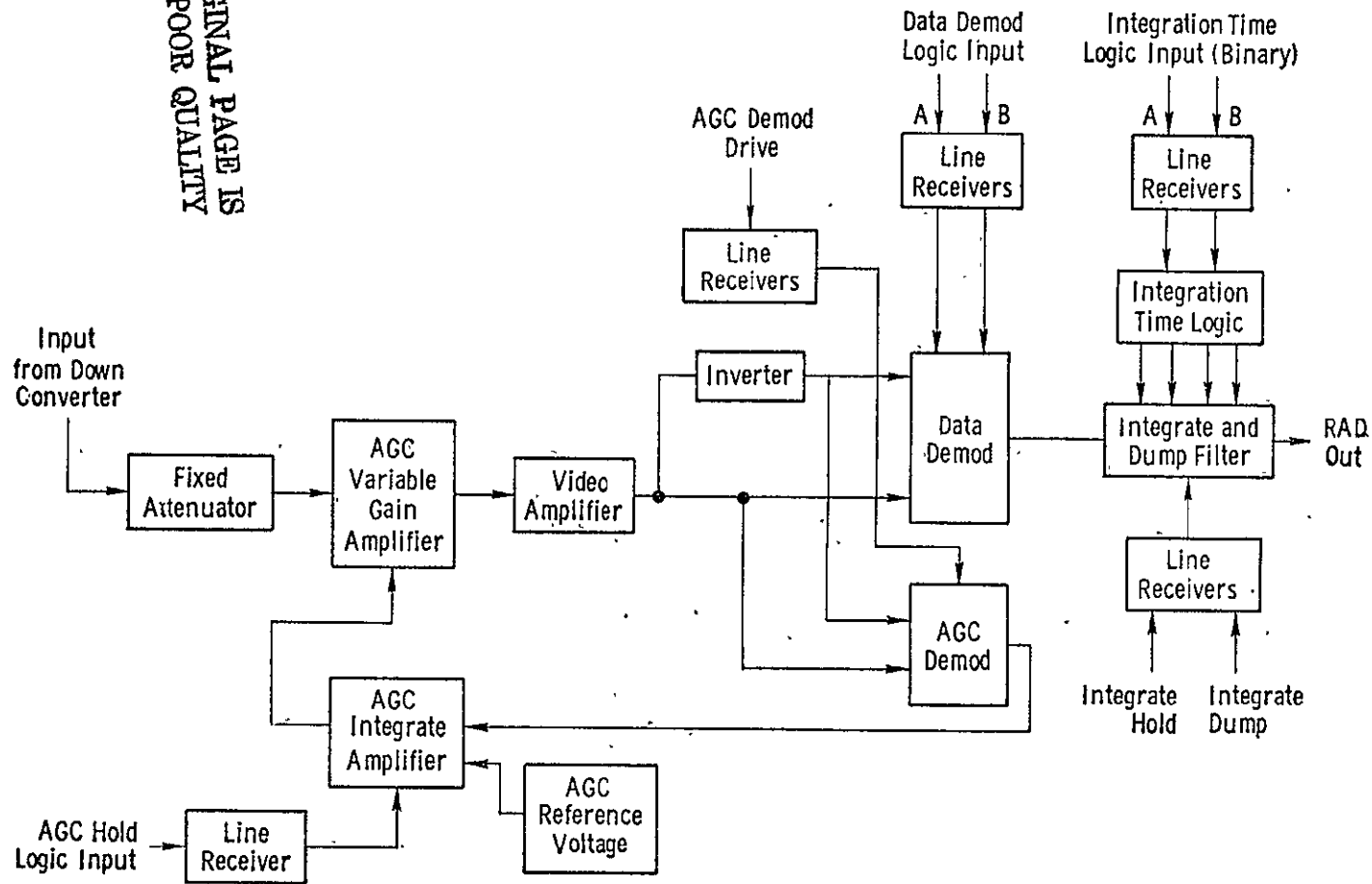


Figure 6.10. "Radiometer Processor Block Diagram" from GE Calibration Data Report.

that the random processes which are producing these noise signals are all independent and of zero mean. The situation is thus as follows: a sample function from a normal random process is subtracted from a sample function of another normal random process and the integrated value (mean multiplied by a constant) obtained (Antenna Mode). This value is stored on tape and represents the radiometer reading in volts. To convert this voltage to temperature (in degrees Kelvin) a sample function of one normal random process is subtracted from a sample function of another normal random process and the output integrated to provide a mean multiplied by a constant (Calibrate Mode). The temperatures (mean) of the input random processes are known and the output voltage (mean obtained by integrating for time T) are known. These provide one point on a gain curve to go from volts to degrees Kelvin. The other point on the gain curve is similarly obtained, but the switching functions are such that the net mean temperature input to the radiometer processor is  $0^{\circ}$  Kelvin, the voltage recorded for this mean input temperature of zero degrees Kelvin provides the second point of the gain curve (Baseline Mode). The gain is assumed to be linear so that the voltage recorded during the Antenna Mode can be directly converted to a value in temperature. The signals, from the reference temperature sources and from the antenna, upon passage through the hardware elements undergo attenuation; the hardware elements are maintained at some ambient operating temperature and due to the insertion losses they possess, generate thermal noise of their own. The net effect is that an attenuated value of the signal sources and a great deal of self-generated noise is input to the radiometer processor. The thermal noise generated by these lossy hardware elements is considered to also have zero mean narrow band Gaussian statistics and is considered independent of the signals considered above.

With all these means of random processes being used to estimate the mean of the incoming temperature, we would like to know two things: 1) what is the precision of our estimate of the mean temperature input to the antenna? and 2) Does it have a bias error, if so, what is the bias error?

### 6.7 Radiometer Precision and Bias Errors

We will assume for the purpose of this analysis that the rise and fall times of the circulators are negligible. Then, the measurement during the antenna mode is given by

$$V_A = GKB_{IF} \left[ \int_0^{\tau/4} T_1'(t) dt - \int_{\tau/4}^{\tau/2} T_A'(t) dt + \int_{\tau/2}^{3\tau/4} T_2'(t) dt - \int_{3\tau/4}^{\tau} T_A'(t) dt \right] + V_{BIAS} \quad (111)$$

where  $B_{IF}$  = IF bandwidth  
 $G$  = system gain  
 $K$  = Boltzman is constant  
 $T_1'$  =  $T_1 + T_{sysR}$   
 $T_2'$  =  $T_2 + T_{sysR}$   
 $T_A'$  =  $T_A + T_{sysA}$   
 $V_{bias}$  = bias voltage

and

$T_1, T_2$  are the reference temperatures  
 $T_{sysR}$  is the associated system noise temperature  
 and  $T_A, T_{sysA}$  are the antenna temperature (signal)  
 and system noise temperature for this circulator setting.

The system noise temperatures when the circulators are switched to receive  $T_1, T_2$  or  $T_A$  are not equal. When receiving signals from  $T_1$  and  $T_2$ , however, the two system noise temperatures can be considered equal (they may vary by at most  $0.2^\circ K$ ). Fisher [1972] and Hanley [1972] assume the system temperature to be equal for the reference and antenna temperature connection.

Each of the temperature sources,  $T_1, T_2$ , and  $T_A$ , is assumed to have a flat spectrum across the IF bandwidth, with spectral densities proportional to  $T_1 + T_{sysR}$ ,  $T_2 + T_{sysR}$  and  $T_A + T_{sysA}$  respectively. If the integration can be considered ideal (linear), i.e.

$$\int_0^{\tau} f(t) dt = G_{\tau} f(\tau) = G_{\tau} \tau f(\tau)$$

where  $G_{\tau}$  can be lumped with system gain  $G$ .

then, the expected value of  $V_A$  is given by

$$\bar{V}_A = GKB_{IF} \tau \left[ \frac{1}{4} T_1' + \frac{1}{4} T_2' - \frac{1}{2} T_A' \right] + V_{BIAS} \quad (112)$$

The parameter of interest is actually  $T_A = T_A' - T_{sysA}$ ; therefore, the optimum estimate of  $T_A$  is given by

$$\hat{T}_A = -\frac{V_A - V_{BIAS}}{G_o B_{IF} \tau} + \frac{(T_1 + T_2)}{2} - (T_{SYS A} - T_{SYS R}) \quad (113)$$

where  $G_o = GK/2$

This, of course, assumes that all terms on the right hand side are known. If they are, then  $T_A$  is an optimum unbiased estimate of  $T_A$ . We have considered the system gain to be fixed, the bias voltage to be fixed and known, and  $(T_{sysA} - T_{sysR})$  to be known and fixed. The system gain is actually computed from the calibrate and baseline mode measurements. The  $V_{Bias}$  term is due to leakage current flowing into the integrator. A measure of this (although not the actual value) can be estimated from the baseline measurement. The bias error of  $T_A$  can be expressed as

$$\hat{T}_A - T_A = \frac{V_{BIAS}}{G_o B_{IF} \tau} + \Delta \frac{(T_1 + T_2)}{2} + \Delta (T_{SYS A} - T_{SYS R}) \quad (114)$$

where

$\Delta T$  = error in temperature  $T$ .

This would be true if we claim that  $G_A$  can be exactly known. But, actually,  $G_A$  is estimated from the calibrate and baseline voltages. The calibrate measurement is given by

$$V_c = KGB_{IF} \int_0^{\tau/2} (T_1'(t) - T_2'(t)) dt + V_{cBIAS} \quad (115)$$

where  $V_{cBIAS}$  = bias (leakage) voltage during calibrate mode measurement.

Again assuming ideal integration, the expected value of  $V_c$  is

$$\bar{V}_c = G_o B_{IF} \tau (T_1 - T_2) + V_{cBIAS} \quad (116)$$

The baseline measurement is given by

$$V_B = \int_0^{\tau/4} (T_1'(t) - T_2'(t)) dt - \int_{\tau/4}^{\tau/2} (T_2'(t) - T_1'(t)) dt + V_{B_{BIAS}} \quad (117)$$

Once again assuming ideal integration and using the assumption of stationarity,

$$V_B = V_{B_{BIAS}} \quad (118)$$

If we assume that the bias error during the baseline and calibrate voltages is the same (it should be, if one considers the source assumed for this error), then the gain  $G$  is estimated by  $\hat{G}$

$$\hat{G} = \frac{V_C}{KB_{IF} \tau \frac{(T_1 - T_2)}{2}} = \frac{2 V_C}{KB_{IF} \tau (T_1 - T_2)} \quad (119)$$

Let the error in this estimate be  $\Delta G$ ,

$$\Delta G = \hat{G} - G$$

This error will now modify our equation for bias error in  $\hat{T}_A$ . The bias error will now have a component due to this error in estimating the gain.

$$\hat{T}_A - T_A = \frac{V_{BIAS}}{G_0 B_{IF} \tau} + \frac{\Delta(T_1 + T_2)}{2} + \Delta(T_{SYS A} - T_{SYS R}) + \frac{\Delta G V_A}{G_0 B_{IF} \tau} \quad (120)$$

It remains to find  $G$ , the error in estimating gain. The sources of error in estimating the gain are

$$\begin{aligned} \Delta V_C &= \text{error in calibrate voltage measurement} \\ \Delta V_B &= \text{error in baseline voltage measurement} \\ \Delta(T_1 - T_2) &= \text{error in reference temperatures} \end{aligned}$$

For small errors  $\Delta V_C$ ,  $\Delta V_B$  and  $\Delta\left(\frac{T_1 - T_2}{2}\right)$ , the error in gain can be approximated by

$$\Delta G \approx \frac{2\Delta V_C - \Delta V_B}{\tau B_{IF} K (T_1 - T_2)} + \frac{2V_C \Delta(T_1 - T_2)}{B_{IF} \tau K (T_1 - T_2)^2} \quad (121)$$

Therefore, the bias error of  $\hat{T}_A$  is given by

$$\begin{aligned} \hat{T}_A - T_A = & \frac{V_{BIAS}}{G_0 B_{IF} \tau} + \frac{\Delta(T_1 + T_2)}{2} + \Delta(T_{SYS A} - T_{SYS R}) \\ & + \frac{V_A}{\tau G_0 B_{IF}} \left[ \frac{2(\Delta V_C - \Delta V_B)}{\tau B_{IF} K (T_1 - T_2)} + \frac{2V_C \Delta(T_1 - T_2)}{B_{IF} \tau K (T_1 - T_2)^2} \right] \end{aligned} \quad (122)$$

The form of this equation shows how the error in each type of measurement or estimation (as in the case of system noise temperature) error contributes to the bias error of the estimate for antenna temperature.

The precision of a radiometer can be interpreted in many ways. Some investigators choose to describe the rms-error in estimating  $T_A$ , others define precision as the minimum difference in input temperature that can be detected by the radiometer. These investigators imply a certain probability measure in their statement regarding detectibility. Because of the usual assumptions of normality of distributions, confidence intervals of 1 $\sigma$ , 90% and 95%, are often used as indicators of detectibility. The range from the expected value to the upper or lower value of the confidence interval is then the resolving capability of the radiometer under investigation. The fact that the estimate of the antenna temperature is biased does not therefore enter into the criterion for precision.

The second interpretation of precision, i.e., one that does not contain the effects of the bias but instead only considers the mean and the standard deviation of the estimator will be used in this study to compute the precision. One possible parameter for describing the precision is the standard deviation of the estimate, i.e.

$\Delta T = \sigma_R$   
 where  $\sigma_R$  = standard deviation of estimate for  $T_A$ .

If we assume that the gain, bandwidth and bias voltage do not change during a measurement, then the variance in the voltage measurement is

$$\text{var} \{V_A\} = C^2 \left[ 2 \text{var} \left\{ \int_0^{\tau/4} T_A'(t) dt \right\} + \text{var} \left\{ \int_0^{\tau/4} T_1'(t) dt \right\} + \text{var} \left\{ \int_0^{\tau/4} T_2'(t) dt \right\} \right] \quad (123)$$

$$C^2 = G^2 B_{IF}^2 K^2$$

$T_1'$ ,  $T_2'$ ,  $T_A'$  are as defined earlier where we have assumed that  $T_1'$ ,  $T_2'$ , and  $T_A'$  are independent, and are stationary. Since each of the temperature sources has been considered to be zero mean, the variances will be equal to their second moments.

$$\text{var} \{V_A\} = C^2 \left\{ 2 E \left[ \int_0^{\tau/4} T_A'(t) dt \right]^2 + E \left[ \int_0^{\tau/4} T_1'(t) dt \right]^2 + E \left[ \int_0^{\tau/4} T_2'(t) dt \right]^2 \right\} \quad (124)$$

To get the second moments, let us recall that the temperatures (multiplied by gain, bandwidth, and Boltzmann's constant) have a flat spectrum across the IF bandwidth. For such noise sources we found earlier that the variance is given by

$$\text{var} \{N_s\} = \frac{2P_N^2}{T} \int_0^T \left(1 - \frac{\tau}{T}\right) R_{N_s}(\tau) d\tau \quad (125)$$

$$= \frac{2P_N^2}{T} \int_0^T \left(1 - \frac{\tau}{T}\right) \text{sinc}^2(B_{IF}\tau) d\tau$$

Which for large time band-width products can be approximated by

$$\text{var} \{N_s\} \approx \frac{P_N^2}{B_{IF}T}$$

Applying this result to the values in equation (124), we have

$$\begin{aligned} \text{Var} \{V_A\} &= \frac{c^2 \tau^2}{16} \left[ \frac{2T_A'^2}{B_{IF} \tau/4} + \frac{T_1'^2}{B_{IF} \tau/4} + \frac{T_2'^2}{B_{IF} \tau/4} \right] \quad (125) \\ &= \frac{G^2 K^2 B_{IF}^2 \tau^2}{4} \left[ \frac{2T_A'^2 + T_1'^2 + T_2'^2}{B_{IF} \tau} \right] \end{aligned}$$

From the equation relating  $\hat{T}_A$  to  $V_A$ , we have

$$\hat{T}_A = \frac{2V_A}{GKB_{IF}\tau} - \frac{2V_{BIAS}}{GKB_{IF}\tau} - \frac{(T_1 + T_2)}{2} - (T_{SYS A} - T_{SYS R}) \quad (126)$$

Therefore, variance of  $\hat{T}_A$  is related to the variance of  $V_A$  by

$$\text{Var} \{ \hat{T}_A \} = \frac{4}{G^2 K^2 B_{IF}^2 \tau^2} \text{Var} \{ V_A \} \quad (127)$$

where we have assumed everything else in the equation is known and not random. Applying this result into equation (113), we have

$$\begin{aligned} \text{Var} \{ \hat{T}_A \} &= \frac{4}{(G^2 K^2 B_{IF}^2 \tau^2)} \cdot \frac{(G^2 K^2 B_{IF}^2 \tau^2)}{4} \cdot \left[ \frac{2T_A'^2 + T_1'^2 + T_2'^2}{B_{IF} \tau} \right] \quad (128) \\ \therefore \text{Var} \{ \hat{T}_A \} &= \frac{2T_A'^2 + T_1'^2 + T_2'^2}{B_{IF} \tau} \end{aligned}$$

Therefore,  $\Delta T_A = \sigma_R$  is given by

$$\Delta T_A = \sigma_R = \frac{(2T_A'^2 + T_1'^2 + T_2'^2)^{1/2}}{\sqrt{B_{IF} \tau}} \quad (129)$$

This is the same result obtained with a modified Dicke-type radiometer. The contributions are seen to arrive from the input signal temperature, the reference temperatures, and the receiver noise temperature. The reduction in standard deviation (hence improved resolution) is obtained by increasing the bandwidth and/or the integration time. Using this basic expression and using the values of the system noise temperature, reference temperatures, bandwidth and integration times for the various modes, the expected precision is given in Table 6.13 for the two input signal temperature-- 100°K and 300°K.

The expressions derived above are valid for a radiometer which has a constant gain (one of the underlying assumptions in the derivation above) through a measurement period. The resolution is seen to decrease with increasing input temperature. Although the time constant in the AGC loop is many times larger than the integration time during a radiometer measurement, the assumption of constant gain cannot still be made. This is made evident by the system test results of the S-193 radiometer where the standard deviation of the estimate of the antenna temperature was found to decrease with increases in input signal temperature.

The following analysis closely parallels one suggested by Hach [1972] where the gain fluctuations caused by the AGC in the loop are included in computing the standard deviation.

Signal Temp. °K	Signal Int. Time (msec)	T <sub>A</sub>
100	32	1.03
300	32	1.10
100	58	0.765
300	58	0.82
100	128	0.36
300	128	0.41
100	256	0.26
300	256	0.29

Table 6.13

Resolution of S-193 Radiometer, assuming no gain changes during measurement (Dicke radiometer operation). Bandwidth = 210 MHz, T<sub>1</sub> = 393°K, T<sub>2</sub> = 318°K, T<sub>sysA</sub> = T<sub>sysR</sub> = 1100°K.

Ignoring the rise and fall time effects of the circulators (the rise and fall times are of the order of microseconds) upon the composite detected video signals we have, as above.

$$V_A = -G_{sig} C G_o \left[ \int_0^{\tau/4} T_A'(t) dt - \int_{\tau/4}^{\tau/2} T_1'(t) dt + \int_{\tau/2}^{3\tau/4} T_A'(t) dt - \int_{3\tau/4}^{\tau} T_2'(t) dt \right] \quad (130)$$

where  $G_{sig}$  = gain of the signal synchronous detector  
 $G_o$  = variable gain (controlled by AGC)

Again applying our assumptions of stationarity, we have

$$V_A = \frac{1}{4} C G_{sig} G_o [T_1 + T_2 - 2T_A] \quad (131)$$

The signal output of the AGC synchronous detector is given by

$$V_{AGC} = \frac{G_{AGC} G_o C}{\tau} \left[ \int_0^{\tau/4} T_1'(t) dt - \int_{\tau/2}^{3\tau/4} T_2'(t) dt \right] \quad (132)$$

and again, applying the same assumptions, we have

$$V_{AGC} = \frac{1}{4} G_{AGC} C G_o [T_1 - T_2] \quad (133)$$

The output of the AGC synchronous detector is compared to a fixed voltage and the gain altered to force this voltage to a fixed voltage, let the fixed voltage be denoted by  $V_o$ , then

$$V_{AGC} = V_o$$

Therefore, the controllable gain  $G_o$  is given by

$$G_o = \frac{4V_o}{C G_{AGC} (T_1 - T_2)} \quad (134)$$

using this result for  $G_o$  in the output of the signal synchronous detector we have

$$V_A = \frac{1}{4} C G_o \left[ T_1 + T_2 - 2T_A \right] \cdot \frac{4V_o}{C G_{AGC} (T_1 - T_2)} \quad (135)$$

$$= V_o \frac{G_{SIG}}{G_{AGC}} \frac{(T_1 + T_2 - 2T_A)}{(T_1 - T_2)}$$

The factor  $V_o G_{SIG} / G_{AGC}$  is held constant and is pre-designed value. It can therefore, be lumped with the constant C. The AGC integrates with a time constant  $\tau_{AGC}$ , its output voltage is seen to be proportional to  $(T_1 - T_2)$ ; therefore, the rms value of  $\Delta V_{AGC} / V_{AGC}$  of the relative fluctuation is given by

$$\frac{\Delta V_{AGC}}{V_{AGC}} = \frac{\Delta(T_1 - T_2)}{(T_1 - T_2)} \quad (136)$$

$$= \frac{\sqrt{(T_1 + T_{SYSR})^2 + (T_2 + T_{SYSR})^2}}{(T_1 - T_2) \cdot \sqrt{B_{IF} \tau_{AGC} / 4}}$$

Similarly, the rms fluctuations for the signal voltage are given by

$$\frac{\Delta V_A}{V_A} = \frac{\Delta(T_1 + T_2 - 2T_A)}{(T_1 + T_2 - 2T_A)} \quad (137)$$

$$= \frac{\sqrt{(T_1 + T_{SYSR})^2 + (T_2 + T_{SYSR})^2 + 2(T_A + T_{SYSR})^2}}{(T_1 + T_2 - 2T_A) \cdot \sqrt{B_{IF} \tau / 4}}$$

The fluctuations of the AGC detector output that are proportional to  $\Delta(T_1 - T_2)$  are transferred to a corresponding fluctuation  $\Delta G_o$  in the post amplifier gain by the AGC. Therefore,

$$\frac{\Delta G_o}{G_o} = \frac{\Delta(T_1 - T_2)}{(T_1 - T_2)} \quad (138)$$

This gain fluctuation results in an additional signal detector output fluctuation. The total rms value of which is given by

$$\frac{\Delta V_A}{V_A} = \sqrt{\left(\frac{\Delta G_o}{G_o}\right)^2 + \left(\frac{\Delta(T_1 + T_2 - 2T_A)}{T_1 + T_2 - 2T_A}\right)^2} \quad (139)$$

Now, to compute  $\Delta G_o/G_o$ , we must recall that the temperature fluctuations causing them are the result of integration time of the AGC loop. These changes in post amplifier gain then appear after smoothing of the signal detector output for  $\tau$  seconds. Therefore, for the time constant, we must use  $\tau_{AGC} + \tau$ . Then

$$\frac{\Delta G_o}{G_o} = \frac{\sqrt{(T_1 + T_{SYSR})^2 + (T_2 + T_{SYSR})^2}}{(T_1 - T_2) \sqrt{B_{IF} (\tau_{AGC} + \tau)}} \quad (140)$$

Inserting equation (140) and (137) into equation (139), we get

$$\frac{\Delta V_A}{V_A} = \frac{2}{\sqrt{B_{IF} \tau}} (T_1 + T_2 - 2T_A) \left\{ \frac{1}{(T_1 - T_2)} \left[ (T_1'^2 + T_2'^2) \left( \frac{T_1 + T_2 - 2T_A}{T_1 - T_2} \right)^2 \right. \right. \\ \left. \left. \cdot \frac{1}{(1 + \tau_{AGC}/\tau)} \cdot (T_1'^2 + T_2'^2 + 2T_A'^2) \right] \right\}^{1/2} \quad (141)$$

From equation (131), we substitute for  $V_A$  to get

$$\Delta V_A = \frac{2}{\sqrt{B_{IF} \tau}} \frac{1}{C} \left\{ \frac{(T_1'^2 + T_2'^2)}{(1 + \tau_{AGC}/\tau)} \frac{(T_1 + T_2 - 2T_A)^2}{(T_1 - T_2)^2} + \right. \\ \left. (T_1'^2 + T_2'^2 + 2T_A'^2) \right\}^{1/2} \quad (142)$$

where  $C = -\frac{1}{4} KB G G_0 G_{sig}$

$$\frac{\partial V_A}{\partial T_A} = 2C$$

∴  $\Delta T_A$  is given by

$$\Delta T_A = \left\{ \frac{(T_1 + T_{sysR})^2 + (T_2 + T_{sysR})^2}{1 + \tau_{AGC}/\tau} \cdot \frac{(T_1 + T_2 - 2T_A)^2}{(T_1 - T_2)^2} + (T_1 + T_{sysR})^2 + (T_2 + T_{sysR})^2 + 2(T_A + T_{sysA})^2 \right\}^{1/2} \quad (143)$$

$$\sqrt{B\tau}$$

This expression differs from the one given in Hach [1972], because the AGC synchronous detector in the case of the S-193 radiometer is not in the loop when the radiometer is viewing the antenna temperature, whereas in Hach's radiometer, the antenna temperature is also gated in to the AGC synchronous detector. The Appendix shows the switching wave forms for the various modes for both the signal detector and the AGC detector.

Assuming a noise temperature of 1100°K, an AGC time constant of 1.125 seconds (determined by Sobti and Collins [1975] from spaceflight data) and the nominal IF bandwidth and reference temperatures, the resolution of the radiometer is given in Table 6.14 for the various integration times used in the S-193 radiometer. It can be shown that as the ratio of AGC time constant to the signal time constant approaches infinity, the AGC compensated radiometer approaches the Dicke radiometer resolution. The resolution for a small ratio in these time constants makes the AGC type radiometer less precise than the Dicke. Figure 6.11 from Ulaby [1974] shows the precision ( $\Delta T_A$ ) of the gain compensated radiometer (a la Hach) versus input temperature for various ratios of AGC to signal time constants. Observe that as this ratio approaches infinity the resolution approaches that for a Dicke radiometer. Although the ratios of AGC time constant to signal time constant in various operating modes of the S-193 radi-

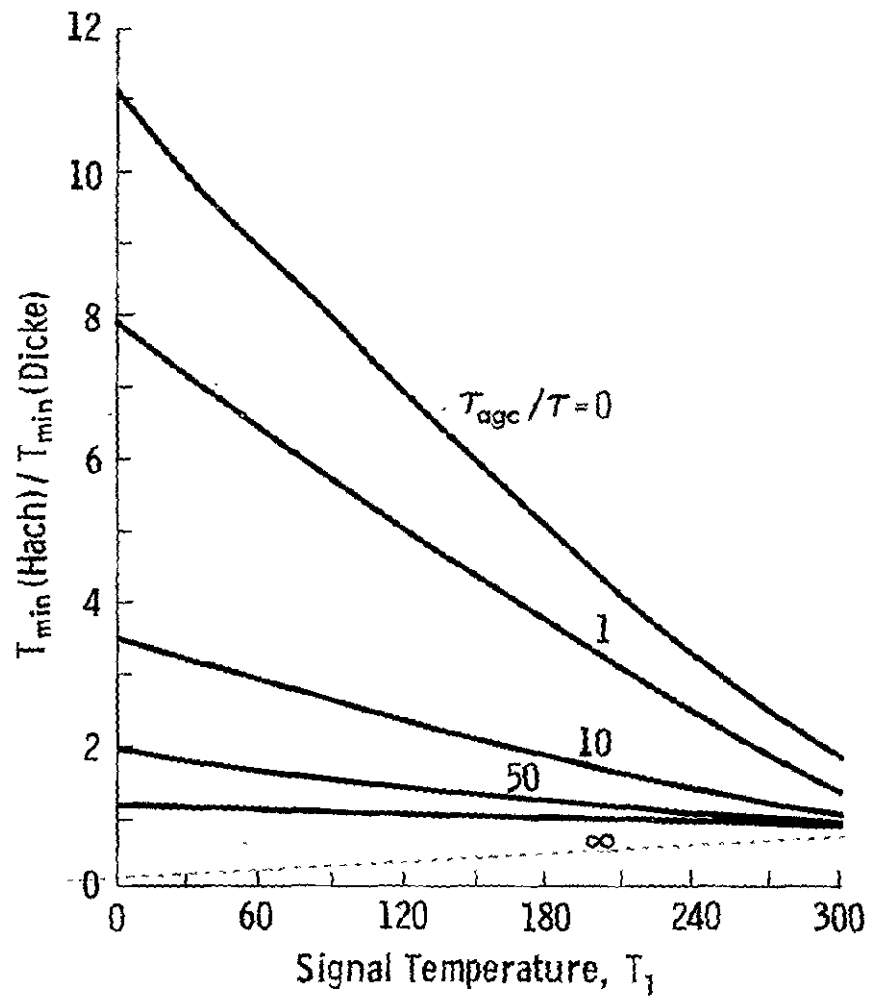


Figure 6.11. Ratio of the temperature resolution of a two-reference temperature radiometer (with AGC) to the resolution of a conventional balanced-Dicke radiometer, as a function of signal temperature  $T_1$  for several values of the ratio  $T_{\text{agc}}/T$ , where  $T_{\text{agc}}$  and  $T$  are the AGC feedback amplifier and, AGC and signal integration times, respectively. Both radiometers are assumed to have the same bandwidth and integration time. Receiver noise temperature  $T_m = 1200^\circ\text{K}$ , and reference temperature  $T_1 = 318^\circ\text{K}$  and  $T_2 = 393^\circ\text{K}$ . [Ulaby, 1974]

ometer are very large (approximately 30), the resolution is seen to decrease with increasing input temperature. This is in agreement with the expression derived.

Signal Temp. °K	Signal Integration Time (msec)	$\Delta T_A$
100	32	1.16
300	32	1.12
100	58	0.93
300	58	0.84
100	128	0.73
300	128	0.58
100	256	0.62
300	256	0.43

Table 6.14

Resolution of S-193 Radiometer with AGC effects included. Bandwidth  $B_{IF} = 210$  MHz,  $T_1 = 393^\circ\text{K}$ ,  $T_2 = 318^\circ\text{K}$ ,  $T_{\text{sysA}} = T_{\text{sysR}} = 1100^\circ\text{K}$ ,  
 AGC = 1.15 secs.

### 6.8. Antenna Pattern Analysis

It has already been mentioned that a significant term in the radar equation is the antenna gain function. This pattern function also plays a very significant role in the interpretation of radiometric data. The radar equation defined earlier can be broken up as

$$\sigma^0 = \left( \frac{(4\pi)^3 R^4}{\lambda^2} \right) (L_1 L_2) \left( \frac{P_r}{P_t} \right) \left[ \int_A G_o^2(\psi) f(\psi) dA \right]^{-1}$$

where the individual terms have been defined earlier. The factor of concern for this study is the term in the square brackets. The effects of this term will be explored in this study.

The S-193 antenna is a parabolic reflector with a dual-polarization feed system. The reflector is a 44.5 inch diameter spun aluminum parabolic structure and the effective f/D ratio is approximately 0.3. The tunnel diode amplifier and the r.f. oven are mounted immediately behind the antenna to minimize the insertion loss. The measurements performed on the antenna include azimuth over elevation antenna pattern cuts (in the far range  $(\frac{24D^2}{\lambda})$  for both the dominant and cross polarization patterns. The antenna orientation on the Skylab vehicle was such that elevation on the pattern range (for a particular setting of the antenna on the range) corresponded to the pitch direction of gimbals scan during spaceborne operation. The azimuth then provided the roll excursion. The antenna was rotated about its electrical axis by 90° increments and azimuth-over-elevation cuts obtained again. It was assumed (through a cursory examination of the principal axes) that the antenna pattern was symmetrical about the electrical axis, so only two of the four possible quadrants were measured in detail (elevation cuts other than the principal axes). The antenna patterns so obtained showed some asymmetry about the boresight, but this could have been due to the range, the test equipment (particularly the mount and rotation pedestal) or actual variations due to slight mechanical intolerances. Gain measurements obtained by the standard comparison technique were also obtained.

The antenna power patterns for the vertical and horizontal polarizations showing the dominant and cross-polarized energy along one set of principal axes are shown in Figures 6.12 and 6.13. The side lobe levels as reported by G.E.\* for the S-193 along with the beamwidth and gain are shown in Table 6.15 for frequencies 13.8, 13.9 and 14.0 GHz.

PORT FREQ	3 dB Beamwidth Avg. Degrees	Max. Sidelobe First & Second	Other Sidelobes	Cross Pol.	Gain
Horizontal 13.8	1.650	21.2	33.2		41.1
Horizontal 13.9	1.588	22.8	33.5	16.3	41.3
Horizontal 14.0	1.639	21.8	32.1		41.2
Vertical 13.8	1.643	20.5	35.7		41.0
Vertical 13.9	1.60	20.5	34.5	16.3	41.1
Vertical 14.0	1.645	20.2	33.7		41.2

Table 6.15

Results of Antenna Pattern Measurements (After G.E.\* (1972))

\*G.E. Quality Control Performance Data Sheet-Rpt. # TP S19305, Rev. No. 4, 3/2/72, Prepared by A. Marble.

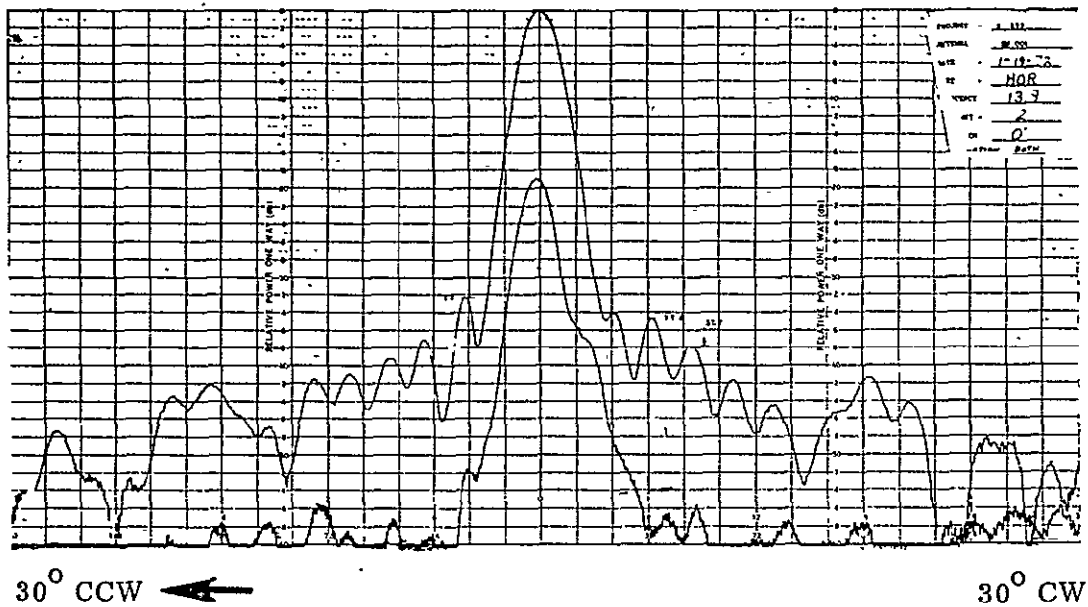


Figure 6.12. S-193 Radiometer/Scatterometer antenna pattern, horizontal polarization. From GE Calibration Report, Vol. II, 1972.

REPRODUCIBILITY OF THE ORIGINAL PAGE IS POOR

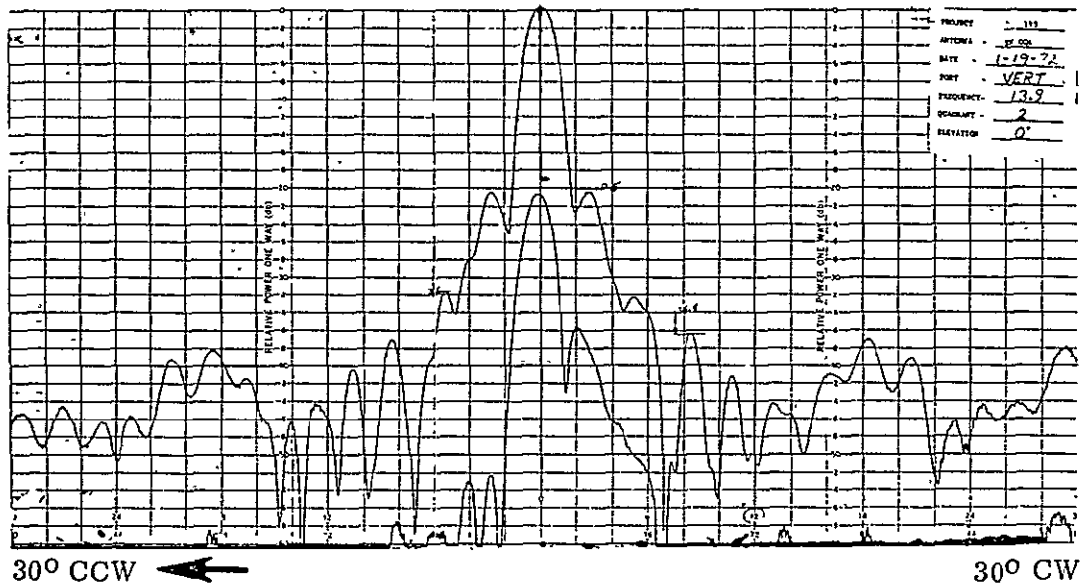


Figure 6.13. S-193 Radiometer/Scatterometer antenna pattern, vertical polarization. From GE Calibration Report, Vol. II, 1972.

Measured values of the antenna pattern on a chart recorder, tables of the form shown above and antenna pattern measurements on a magnetic tape were received at the University of Kansas; the subsequent analysis showed some startling inconsistencies. To document the analyses conducted and the subsequent efforts to correct for these inconsistencies would be too voluminous. A thumbnail sketch of the analyses is provided below.

The antenna pattern was recorded on a rectangular chart recorder as well as on a magnetic tape by digitizing values at  $1/12^\circ$  azimuth increments. The patterns recorded on tape were then the data base for the analysis. The pattern obtained for quadrant 1 and quadrant 2 (for definitions, see G.E. Calibration Data Report, Vol. II, Rev. D, May 1972) were used to compute the directivity. The directivity defined as

$$D = \frac{4\pi}{\int_0^{2\pi} \int_0^\pi f(\theta, \phi) d\theta d\phi} \quad (144)$$

where  $f(\theta, \phi)$  = normalized power pattern

$\theta$  = azimuth

$\phi$  = elevation

was computed for the two polarizations and for both polarizations. The integral in the denominator contains terms  $f(\theta, \phi)$  which are expressed in cylindrical coordinates. The integration out to  $5^\circ$  from boresight was performed by a Gaussian quadrature technique and verified by a trapezoidal rule integration. The integration beyond  $5^\circ$  out to  $180^\circ$  was performing by a trapezoidal rule. This integration was verified independently by a one-dimensional trapezoidal rule integration where symmetry in the other (elevation) dimension was assumed. The results showed that this measure of the directivity was lower than the gain measured on the pattern range by the standard comparison technique. It is well-known that the directivity should be greater than the measured gain by at least the ohmic losses in the antenna and feed assemblies. This, then, suggested that the patterns were in error. Upon close examination, it was found that the measurements of the pattern had been such that there had been a compression in the gain towards the top end of the recording dynamic range. This resulted in a compression of the main beam, and, since normalized patterns are used in computing the directivity, these patterns tended to show the relative power levels off boresight greater than they should actually have been. Verifications of the main beam compression using a Gaussian fit to the slopes of the main beam showed that the region

immediately around boresight deviated significantly from the Gaussian fit. Reconstruction efforts were attempted by Dr. A. C. Cook, using a Gaussian type fit to the main beam pattern. These efforts are documented in a report written by the University of Kansas on the evaluation of performance of the S-193 during space operation [Cook, 1975]. The significant result of Dr. Cook's study was that a set of possible Gaussian shaped peaks could be constructed, but that no justifiable arguments for selecting any one of them could be found.

The values of the antenna pattern parameters quoted here are from patterns which, according to the vendor are more reliable, i.e., there is less suspicion of a compression of the beam peak. The results in the form of beam efficiencies for a conical beam of central half angle,  $\alpha$ , with the axis of the cone along boresight were computed. Table 6.16 provides the beam efficiencies for both the dominant and cross-polarization patterns for vertical and horizontal polarizations. These figures are to be used for the case of the radiometer. Table 6.17 provides the beam efficiencies for the two-way pattern (transmit and receive) for the dominant and cross polarizations for vertical and horizontal polarization modes of operation. In both tables, the main beam efficiency is defined as the amount of radiated energy between beam center and the point at which the pattern is -20 dB. It was found that a choice of -20 dB on the pattern eliminated the energy from all side lobes and contained at least 98% of the energy in the main beam to the first null. The main beam efficiency computation did not include energy arriving in the cross polarization. The design goal had been to have a beam-efficiency of 90% or more. The engineering unit of the S-193 antenna, designed according to the same specifications as the flight unit, had a beam efficiency of approximately 89%. It should be stated that integrations performed by staff at General Electric (the vendor of the hardware) to compute the beam efficiency (defined in the same way as described here) showed slightly different results. Their estimates of beam efficiency were also computed by a Gaussian quadrature technique, so it is apparent that the data base from which the two sets of integrations were performed were different. The data base received from General Electric on magnetic tape was found to have numerous errors in the A/D conversion. These were carefully removed with consultation from G.E.\* The results as presented in the Calibration Data Report [G.E., 1972] are shown in Figures 6.14 and 6.15; for comparison the numbers quoted in Table 6.16 are included.

---

\*Art Marble, G.E., Valley Forge, Private Communications.

$\alpha$	Vertical Polarization		Horizontal Polarization	
	Dominant	Crossed	Dominant	Crossed
1°	54.20	0.43	53.30	0.30
2°	82.10	2.25	81.14	1.90
3°	84.82	3.66	83.20	3.58
4°	85.90	4.08	83.56	4.14
5°	86.30	4.28	83.73	4.32
180°	93.10	6.90	90.38	9.62
Main Beam	83.08	—	82.55	—

Table 6.16

One-way Beam Efficiencies (Values shown are percent of total energy radiated in a cone with generating angle  $\alpha$ )

$\alpha$	Vertical Polarization		Horizontal Polarization	
	Dominant	Crossed	Dominant	Crossed
1°	84.00	0.01	84.75	0.00
2°	95.70	0.06	97.00	0.04
3°	95.78	0.07	97.06	0.06
4°	95.79	0.07	97.06	0.06
5°	95.79	0.07	97.06	0.06
180°	99.92	0.08	99.93	0.07
Main Beam	95.76	—	97.06	—

Table 6.17

Two-way Beam Efficiencies (Values shown are percent of total energy radiated and received back in a cone with generating angle  $\alpha$ )

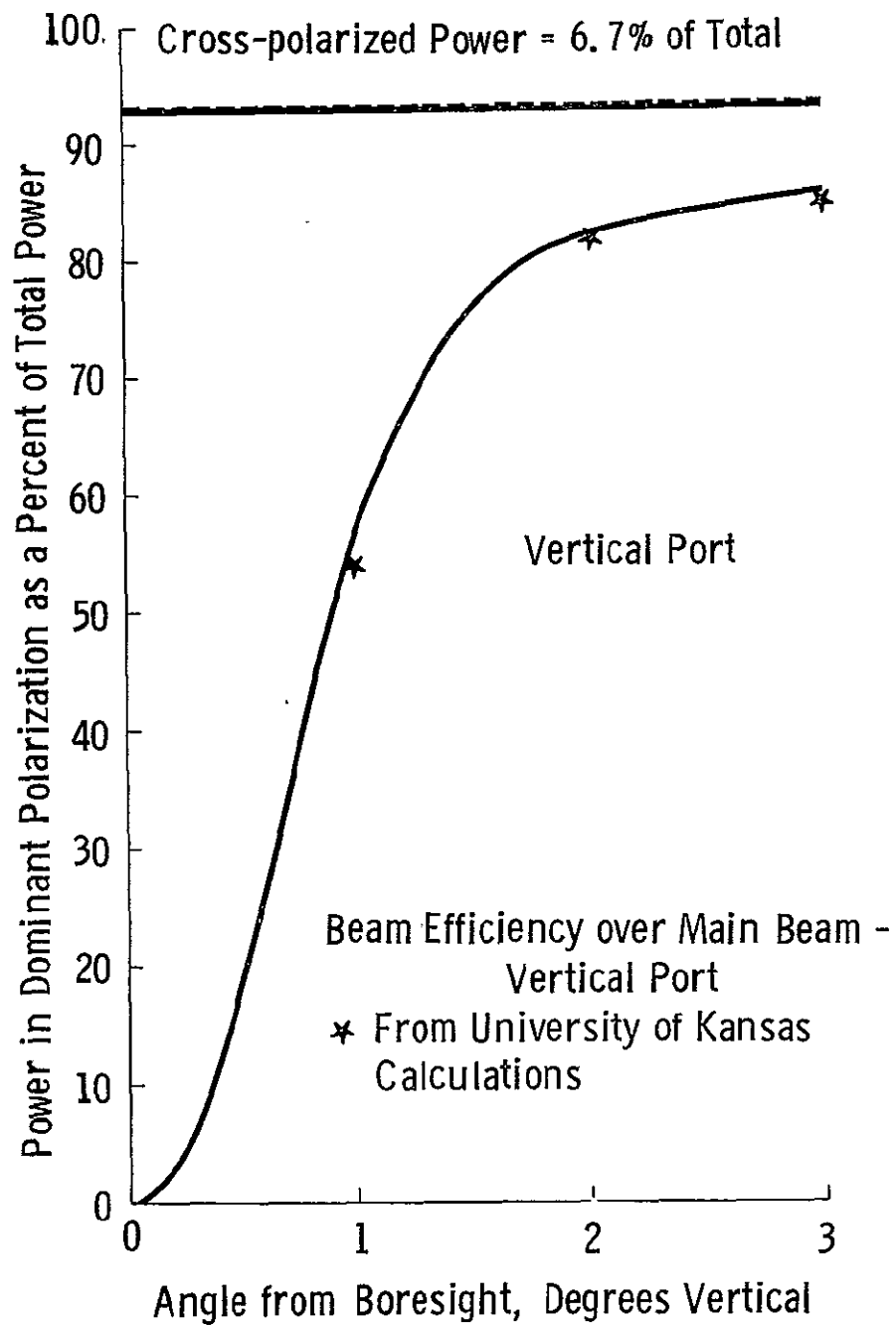


Figure 6.14. Beam Efficiency for S-193 Antenna. After GE Calibration Data, 1973.

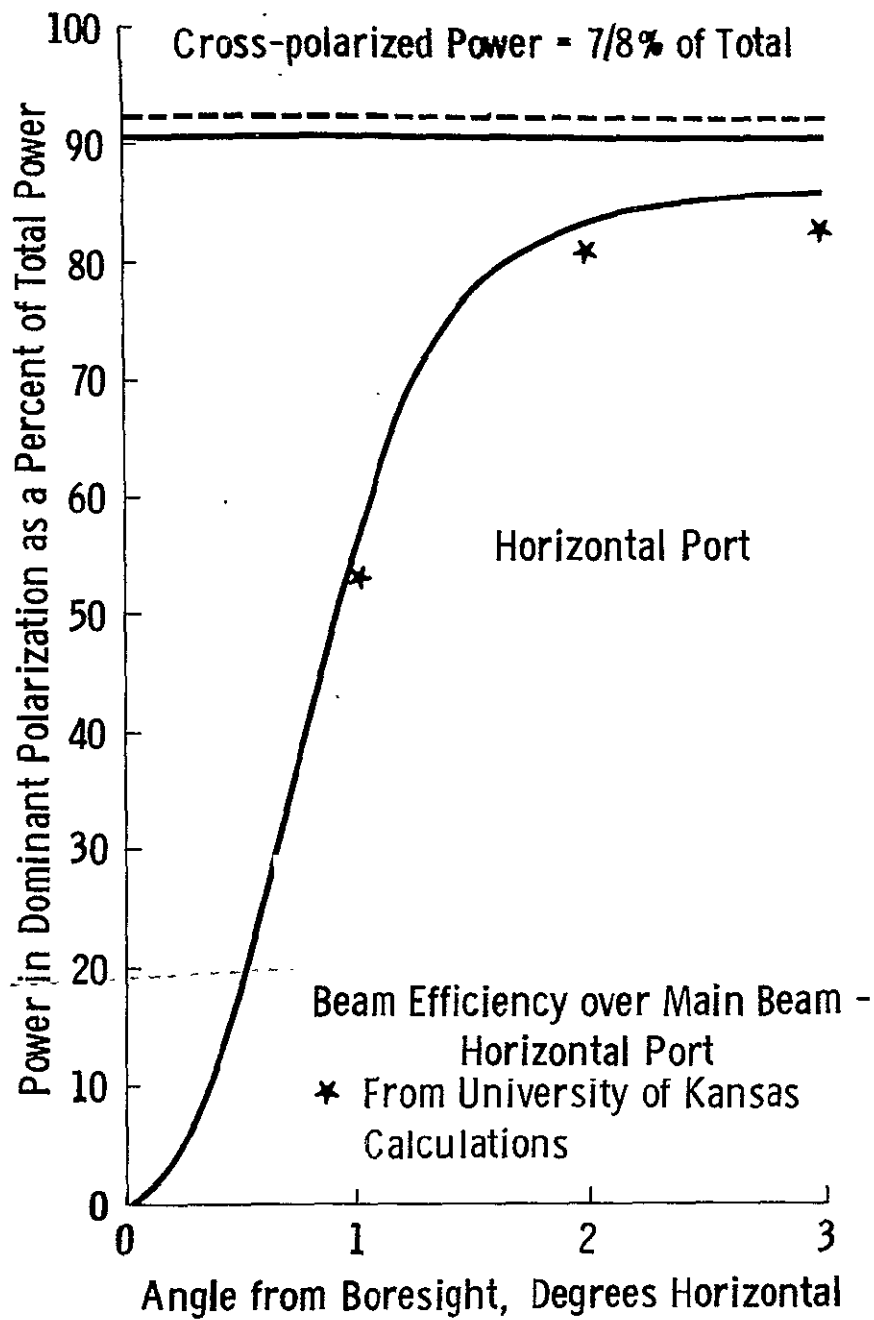


Figure 6.15. Beam Efficiency for S-193 Antenna. After GE Calibration Data, 1973.

An equivalent beam width is defined as the beam-width of a hypothetical conical antenna which has unit normalized gain at all points in the beam, and which contains the same energy as the main-beam of the actual antenna pattern. From the integration values reported in Tables 6.16 and 6.17, the effective beamwidths for the one-way (radiometer) and the two-way (scatterometer, altimeter) patterns for both vertical and horizontal polarization are given in Table 6.18.

	Vertical Polarization	Horizontal Polarization
One-Way	2.00	2.06
Two-Way	1.46	1.56

Table 6.18  
Effective beamwidths for the S-193 Antenna (in degrees).

There is a slight ellipticity noted in the pattern.

The directive gain computed from the antenna pattern integrations, as defined in eq.(144), for the two polarizations is found to be 40.39 dB for the vertical and 40.08 dB for the horizontal. These directive gains are computed by integrating both the dominant and cross polarization components in the antenna pattern.

The form of equation(1) suggests that the integration of the antenna pattern be performed for every incidence angle. To actually perform such an integration for each angle would be extremely time consuming even if the integration were carried out to a small angle off boresight. To arrive at a simplification of this integration, the following analysis was carried out. It was verified by actually integrating the pattern function over the area illuminated by the antenna pattern as described in the appendix.

### 6.9 Illumination Integral Analysis

Before we start simplifying the integral, let us first define it in its most exact form. Actually, the integral defined in equation (1) is a simplification of the

equation to solve for  $\sigma^0$ , which is

$$\sigma^0(\psi) = \frac{(4\pi)^3}{\lambda^2} \left(\frac{P_r}{P_t}\right) (L_1 L_2) \left[ \frac{\iint_{\Omega} G_o^2 f(\theta, \phi, \psi) d\theta d\phi}{R^4(\theta, \phi, \psi)} \right]^{-1} \quad (145)$$

where

$\psi$  = incidence angle.

This equation has already assumed that the differential backscattering coefficient within the solid angle is constant. It has further assumed that all the energy is included in the solid angle from boresight. The analysis here is aimed to find a simplification for the terms in the square brackets for the purpose of computation.

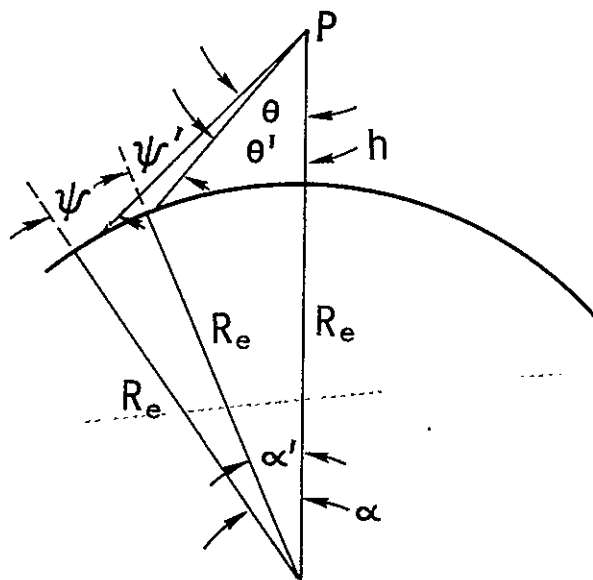


Figure 6.16. Geometry of illumination for S-193 measurements (sensor at point P).

Figure 6.16 provides the geometry of illumination for an oblique angle from an orbital height  $h$  over a curved earth. If the pitch and roll angles of antenna boresight with respect to the Z-Local Vertical (ZLV axis) are given by  $\theta_p$  and  $\theta_r$  respectively; the incidence angle at the antenna is given by

$$\cos \theta = \cos \theta_p \cos \theta_r \quad (146)$$

Let the coordinates of any point in the illuminated region relative to antenna boresight be given by  $\phi_p$  and  $\phi_r$  in the orthogonal direction of pitch and roll respectively. The illuminated region for all practical purposes can be assumed to be within  $3^\circ$  off boresight (see table 6.16). The illumination integral,  $I$ , can then be written as

$$I = \iint_{\Omega} f_t(\phi_p, \phi_r) f_r(\phi_p, \phi_r) \left[ \frac{R^2(\theta_p + \phi_p, \theta_r + \phi_r) \cos \phi_p \cos \phi_r}{\cos(\psi')} \right] d\phi_p d\phi_r \quad (147)$$

where the quantity in the square braces is the Jacobian of the transformation of the area integral to an integral over solid angle. The angles  $\Psi$  and  $\Psi'$  are as shown in Figure 6.16. The incidence angle (at the antenna terminals) with respect to ZLV,  $\theta'$ , will be given by

$$\cos \theta' = \cos(\theta_p + \phi_p) \cdot \cos(\theta_r + \phi_r) \quad (148)$$

Due to the curvature of the earth, the incidence angle will be given by  $\Psi'$ . If we define  $\delta$  as the angular displacement of the nadir angle for the ray to the target point and that at antenna boresight,  $\delta = \theta - \theta'$ , then  $\delta$  will be a maximum of  $3^\circ$ . The variation in the earth's included angle  $\alpha$  will be very small so that  $(\Psi - \Psi') \approx \delta$

Due to the fact that the angular excursions  $\delta$  will be extremely small,

$$R(\theta_p + \phi_p, \theta_r + \phi_r) - R(\theta_p, \theta_r) \ll R(\theta_p, \theta_r) \quad (149)$$

i.e., the range terms will not vary significantly within the illuminated region. Then, the illumination integral can be written as

$$I = \frac{1}{R^2(\theta)} \iint_{\Omega} \left[ \frac{f_t(\phi_p, \phi_r) f_r(\phi_p, \phi_r) \cos \phi_p \cos \phi_r}{\cos(\Psi + \Delta)} \right] d\phi_p d\phi_r \quad (150)$$

Expanding  $\cos(\Psi + \Delta)$ , we have

$$\cos(\Psi + \Delta) = \cos \Psi \cos \Delta - \sin \Psi \sin \Delta \quad (151)$$

Since  $\Delta$  is a small angle

$$\begin{aligned}\sin \Delta &\approx \Delta \\ \cos \Delta &\approx 1\end{aligned}$$

Hence

$$\cos (\Psi+\Delta) = \cos \Psi (1-\Delta \tan \Psi) \quad (152)$$

Therefore, the integral reduces to

$$I = \frac{1}{R^2(\theta) \cos \Psi} \iint_{\Omega} \frac{f_t(\phi_p, \phi_r) f_r(\phi_p, \phi_r) \cos \phi_p \cos \phi_r}{(1-\Delta \tan \Psi)} d\phi_p d\phi_r \quad (153)$$

We have thus removed the effect of the incidence angle,  $\Psi$ , from the integral except through the factor  $\tan \Psi$ . The value of  $\tan \Psi$  for the incidence angles of Skylab S-193 operation reaches a maximum of  $\approx 1.3$  (at  $53^\circ$  incidence), the multiplier  $\Delta$ , however, is of the order of 0.05; therefore, the total range of the denominator is from approximately 0.93 to 1.00. The numerator now contains only the antenna power pattern. The angle  $\Delta$  is a function of  $\phi_p, \phi_r$  and increases to its maximum value (0.05) when  $\phi_p, \phi_r$  reach their maximum value. But fortunately when  $\phi_p, \phi_r$  increase, the transmit and receive pattern decrease. The decay in these pattern functions is very rapid. We have considered a point where  $\Psi > \Psi'$ , so that  $\Delta$  is positive, but in considering the entire illuminated area, there will be as many points with  $\Delta$  less than zero as there are with  $\Delta$  greater than zero. The total range of the denominator can, therefore, be from 0.93 to 1.07. The inverse of the denominator is then a weighting on the power pattern in the numerator. It can, therefore, be seen that this integral will be almost exact for nadir incidence and the error will be proportional to the angle of incidence. The worst case would then be for an antenna angle of  $48^\circ$ . The error was found to be negligible even for this angle.

So, let us define the integral as  $I_p$ . Now  $I$  is given by

$$I = \frac{I_p \sec \Psi}{R^2(\theta)} \quad (154)$$

For a case where the antenna boresight is along the ZLV axis, the range will be the orbital height, the illumination integral will then be

$$I_o = \frac{I_p}{h^2}$$

where  $h =$  orbital height,

Now, taking the ratio of  $I$  to  $I_o$ , we have

$$\frac{I}{I_o} = \frac{I_p \sec \psi}{R^2(\theta)} \left( \frac{I_p}{h^2} \right)^{-1}$$

$$\therefore I = \frac{h^2}{R^2(\theta)} I_o \sec \psi \quad (155)$$

The form of this equation is very similar to one suggested by Hanley [1972] where he used the effective beamwidth concept to compute the illumination integral. He treated the illuminated area as a projection of the circular disk obtained from the conical beam onto the tangent plane on the earth's surface at antenna boresight. His expression [pp. 3-48] is

$$I = \frac{\pi}{4} \frac{\theta_e^2}{R^2} \sec \psi \quad (156)$$

where  $\theta_e =$  effective beamwidth of the antenna.

In the formulation suggested here, the projection is of the area on to a tangent plane at an oblique incidence, with the appropriate weighting due to the range terms.

This formulation was tested against values of the illumination integral computed for each angle of the various modes and submodes by a simulation program [Sobti, 1974] that actually performed the integration. The approximation was tested for various orbital heights and incidence angles. Details of these results are documented by Cook and Sobti [1974]. The approximation was extremely good for an orbital height of 435 kms and any lower values (till 415 kms). The error in the approximation grew with the orbital height. The approximation was valuable because  $I_o$  was a predetermined

number which was modified by the range, incidence angle, and orbital height to get the illumination integral, thus making computation relatively easy.

The relative contributions as a percentage of the total illumination integral for angles off boresight is shown in Figure 6.17. The antenna pattern considered in this figure is that of the development model of the S-193 antenna. The width of the main beam (extent of integration) was considered to be  $3^\circ$ . This figure shows that even though the pattern function falls off in value from boresight its decay is not as large as the increase in the illuminated area for some angles for boresight. The shape of the antenna pattern of the development antenna does not deviate considerably from that of the flight unit at angles  $0.5^\circ$  off boresight. The cumulative contribution to the illumination integral is shown in Figure 6.18 versus angle off boresight.

#### 6.10 Polarization Performance of S-193 Antenna

The S-193 antenna has a dual polarization feed assembly, the feed structure is fed by a circular waveguide, in view of these hardware elements, it is not surprising that the S-193 antenna does not have great polarization isolation. From Table 6.16, it can be seen that the percentage of cross-polarized energy is not a negligible part of the total energy. Due to the relatively poor isolation for the cross-polarized component, a simple analysis will show that the energy in the cross-polarization plays a significant role in the total power returned. For angles of incidence close to nadir, the response from terrain (land and ocean) is not particularly polarization selective. As the angle of incidence increases, the polarization selectivity of targets for radiometric observations becomes pronounced. This selectivity is very pronounced in ocean targets and to a much lesser extent in land targets.

Apart from the cross-coupling of the two orthogonal polarizations, the antenna, because of its excursions in pitch and roll can cause the power received (and hence scattered) for the case of the scatterometer) by the surface to appear with different orientations. An example will help illustrate this effect.

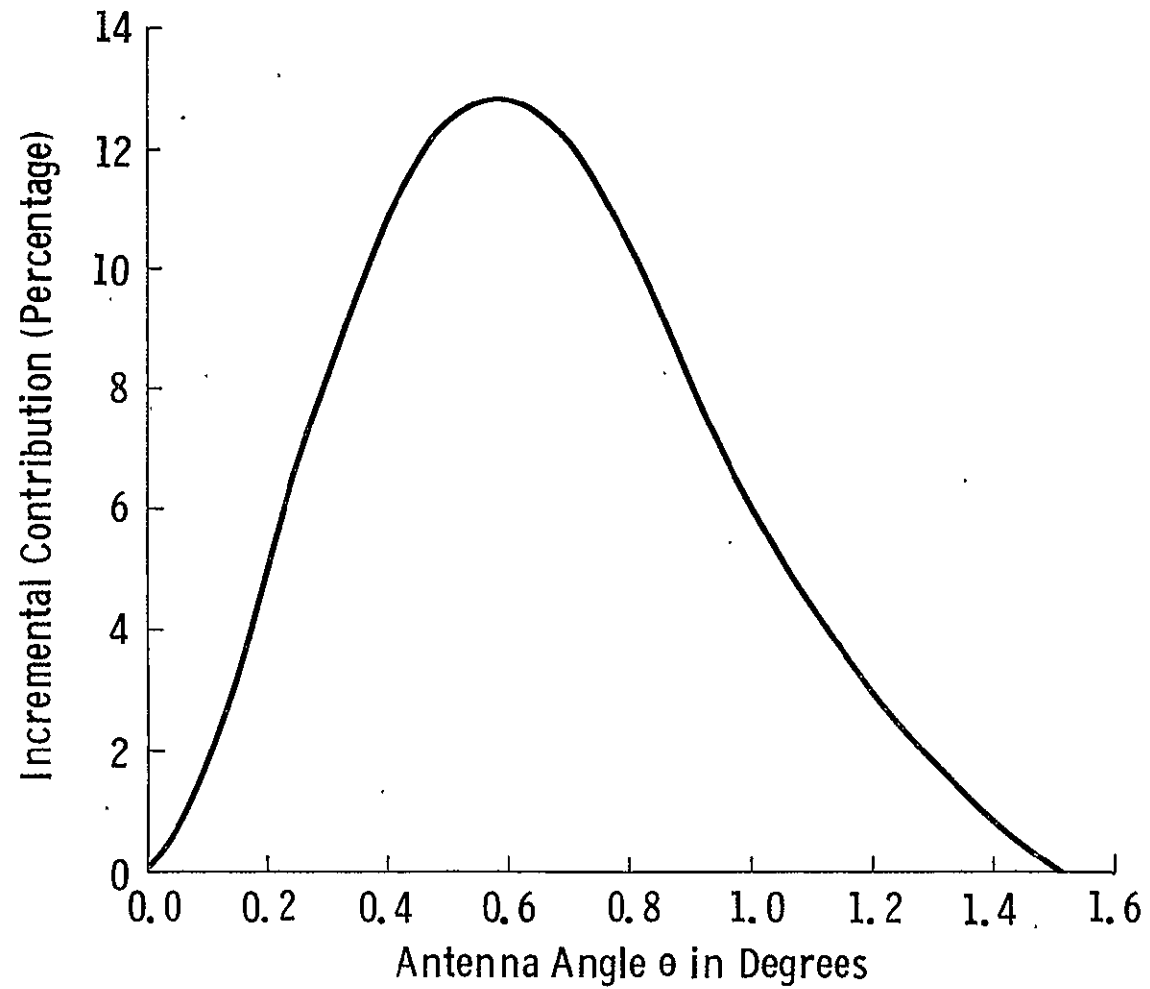


Figure 6.17. Incremental (relative) energy contribution to illumination integral in beam angle from antenna boresight.

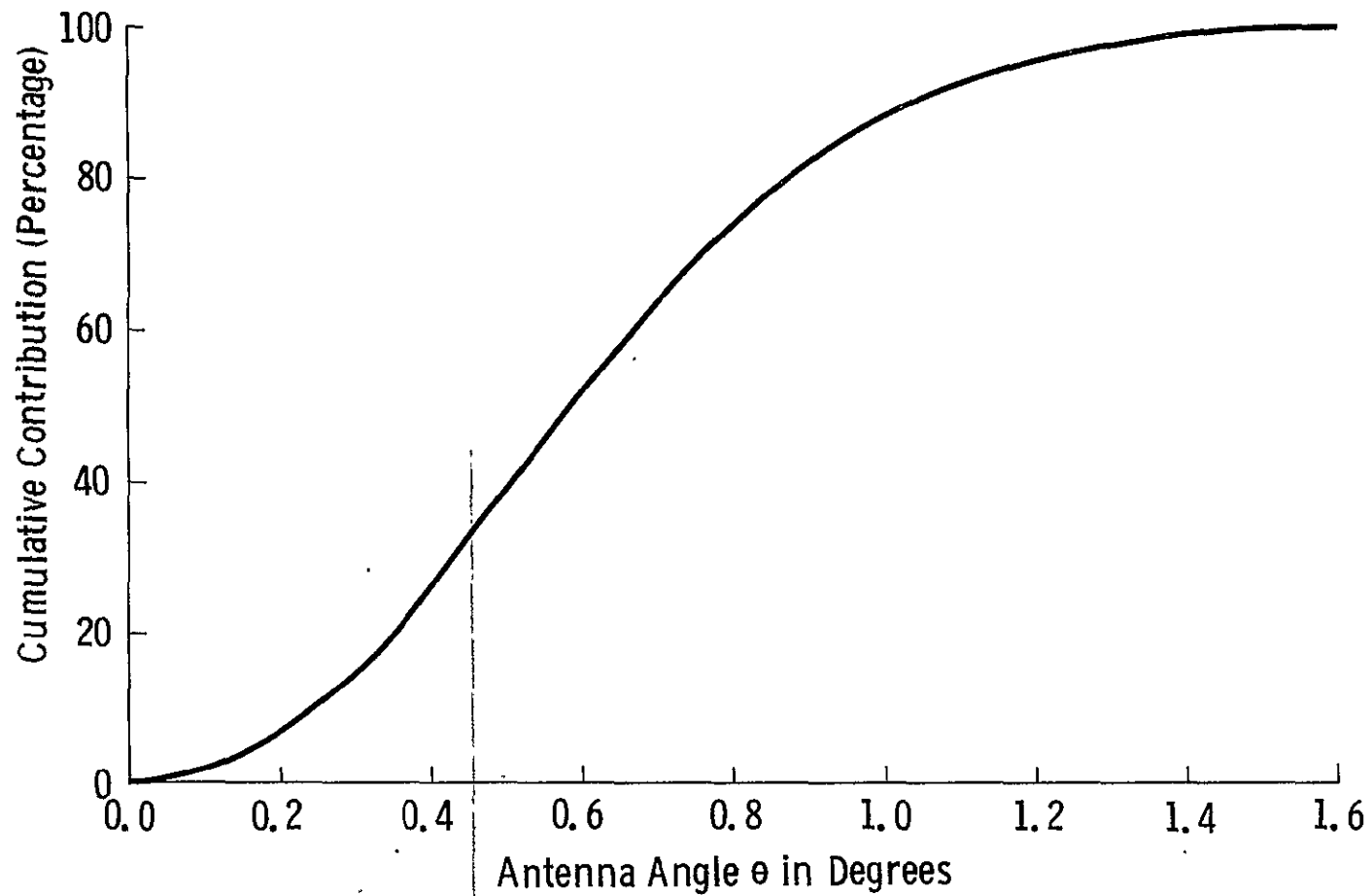


Figure 6.18. Cumulative energy contribution to illumination integral in beam angle from antenna boresight.

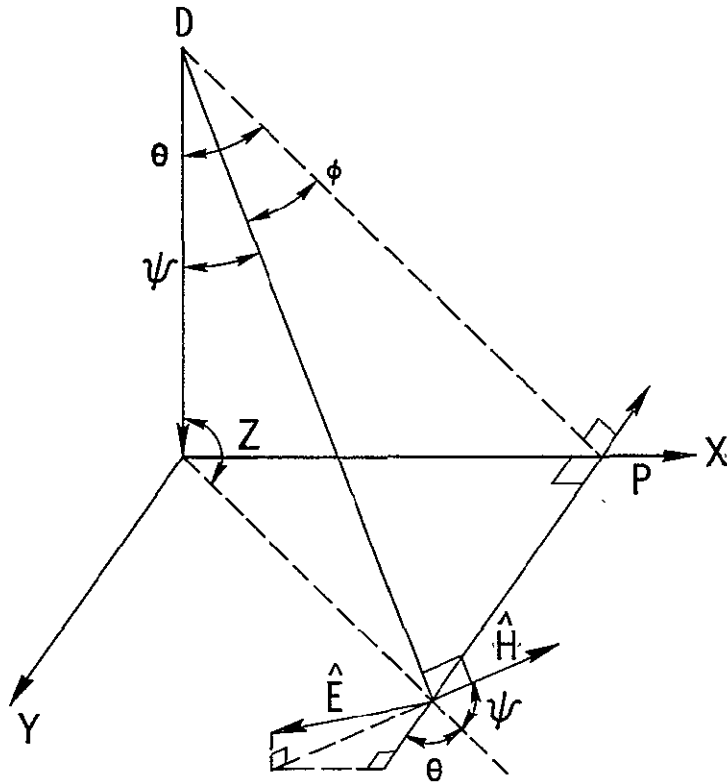


Figure 6.19. Geometry for a pitch and roll excursion measurement.

Consider the vehicle to be moving along the  $x$ -axis of a coordinate system with the  $z$ -axis pointing to the  $Z$  local vertical. Let the antenna be pitched ahead an angle  $\theta$  and then rolled to the right an angle  $\phi$ . Let the polarization selected on the antenna be horizontal so that the  $\vec{E}$  vector lies along the surface along the  $Y$  direction during nadir incidence. It is clear that as the antenna is pitched ahead, the  $\vec{E}$  vector will continue to lie in the  $XY$  plane and be parallel to the  $y$ -axis. There is, therefore, no change to the target (if it is a flat surface). Now consider a roll of an angle  $\phi$ . This will now lift the  $E$  vector out of the  $XY$  plane. The new  $\vec{E}$  vector can be resolved into two orthogonal components, one along the surface and the other in the direction of the  $\vec{H}$  vector during pitch only excursions. Thus, already we observe that the field vectors appear different to the surface. If the target has no polarization selectivity, then, of course, the entire exercise is for naught. But if the target has a polarization selectivity, then this polarization selectivity is defined with respect to a particular set of orthogonal  $\vec{E}$  and  $\vec{H}$  vectors (receiving or transmitting). We will now try to resolve the new  $\vec{E}$  vector  $\vec{H}$  (after a pitch and a roll excursion) into the  $\vec{E}$  vector for the pitch only case (along the  $XY$  axis). Figure 6.19 shows the resultant  $\vec{E}$  and  $\vec{H}$

vectors after a pitch excursion  $\theta$  and a roll excursion  $\phi$ . The projection vector of the new  $\vec{H}$  vector onto the XY plane is given by  $\vec{H} \cos \psi$ . This projected along the old  $\vec{E}$  vector (along PQ in Figure 6.19)

$$\vec{E}_{o_H} = \vec{H} \sin \psi \cos \psi \quad (157)$$

where 
$$\cos \psi = \cos \theta \cos \phi \quad (158)$$

and  $\vec{E}_{o_H}$  is the component along the same orientation as in the pitch only excursion from the  $\vec{H}$  vector.

Similarly from the  $\vec{E}$  vector we have

$$\vec{E}_{o_V} = \vec{E} \cos \phi \quad (159)$$

Therefore, along the same orientation as the pitch only case the resultant vector is now

$$\begin{aligned} \vec{E}_{o_H} + \vec{E}_{o_V} &= \vec{H} \sin \psi \cos \psi + \vec{E} \cos \phi \\ &= \vec{H} \cos \theta \cos \phi \sqrt{1 - \cos^2 \theta \cos^2 \phi} + \vec{E} \cos \phi \end{aligned} \quad (160)$$

To resolve the  $\vec{E}$  vector into an orthogonal set  $\vec{E}_\theta$  and  $\vec{E}_\phi$ , where  $\vec{E}_\theta$  lies along the surface and the orientation is as if on a sphere we get

$$\vec{E}_\theta = \vec{E} \frac{\sin \theta \cos \phi}{\sin \psi} = \frac{\vec{E} \sin \theta \sin \phi}{\sqrt{1 - \cos^2 \theta \cos^2 \phi}} \quad (161)$$

$$\vec{E}_\phi = \frac{\vec{E} \sin \theta}{\sqrt{1 - \cos^2 \theta \cos^2 \phi}} \quad (162)$$

It can be seen for verification that

$$\vec{E}_\theta^2 + \vec{E}_\phi^2 = 1 \quad (163)$$

This clearly demonstrates that for polarization selective targets, the orientation of the antenna boresight plays a very important part. For pitch only excursions, there is no polarization "mixing," for roll only excursions, the orientation of the electric and magnetic fields at the surface for a particular polarization are quite different from pitch only excursions. An increase in roll makes the H vector stay parallel to the ground (for a horizontal polarization selection) and the E vector moves away from the X-Y plane. For pitch only excursions, the

$\vec{E}$  vector stays in the XY plane with the  $\vec{H}$  vector moving away from the XY plane with increase in incidence angle. So, to a surface which has a polarization selectivity defined with respect to a particular geometry, the pitch and roll excursions will appear to be opposite polarization selections even though the same polarization was selected.

Since our analysis of the data does not take into account this orientation effect due to the geometry, let us try to interpret the measurements we record in an alternate way. In this approach, the effects of the rotation of the  $\vec{E}$  and  $\vec{H}$  fields will be incorporated into the scattering properties of the surface. For the case of the radiometer, one must consider these orientations. For the case of the scatterometer, consider the following interpretation.

Let the transmitted polarization be  $i$  ( $i = v$  or  $h$ ), then because of the poor isolation of the antenna, the transmitted power is given by

$$P_{t_i} = P_i \hat{i} + a_i P_i \hat{j} \quad (164)$$

where

$$\begin{aligned} P_i &= \text{total power transmitted with polarization } i \\ \hat{i} &= \text{unit vector for polarization } i \\ a_i &= \text{depolarization factor } (a_i < 1) \text{ for polarization } i \\ \hat{j} &= \text{unit vector for polarization } j \\ P_i \hat{i} &= \text{amplitude factor such that } P_i \hat{i} \text{ gives total power transmitted} \\ &\quad \text{with orientation } \hat{i} \end{aligned}$$

In this case the factor  $a_i$  is the ratio of the cross-polarized energy to the dominant polarized energy. The scattering cross-section of the surface can be decomposed into four coefficients as follows

$$\sigma = \sigma_{ii} + \sigma_{ij} + \sigma_{ji} + \sigma_{jj} \quad (165)$$

where  $\sigma_{ij}$  is the scattering coefficient that returns incident energy with polarization  $i$  with polarization  $j$ , i.e.,

$$\begin{aligned} P_i \hat{i} (\sigma_{ii}) &= P_i \sigma_{ii} \hat{i} & P_i \hat{i} (\sigma_{jj}) &= 0 \\ P_i \hat{i} (\sigma_{ij}) &= P_i \sigma_{ij} \hat{j} & P_i \hat{i} (\sigma_{ji}) &= 0 \end{aligned} \quad (166)$$

and similarly for  $P_j \hat{j}$ .

Since we are dealing with power rather than the complex notation of fields with amplitude and phase, the underlying assumptions of random scattering should be understood. The power returned thus represents the expected values due to an ensemble of individual scattering elements. When the scattering mechanism cannot be considered random, the transformation of returned electric fields into power will have to include the coherent phasor relationships between the various fields.

The energy reflected from the surface is given by

$$\begin{aligned}
 P_{ref} &= P_t \cdot \sigma \\
 &= P_i \sigma_{ii} \hat{i} + P_i \sigma_{ij} \hat{j} + a_i [P_i \sigma_{ji} \hat{i} + P_i \sigma_{jj} \hat{j}] \quad (167) \\
 &= [P_i \sigma_{ii} + a_i P_i \sigma_{ji}] \hat{i} + [P_i \sigma_{ij} + a_i P_i \sigma_{jj}] \hat{j} \\
 &= P_1 \hat{i} + P_2 \hat{j}
 \end{aligned}$$

If the reception of the signal is also with an i polarization, then the power at the antenna terminals is given by

$$\begin{aligned}
 P_{ii} &= [P_1 \hat{i} + P_2 \hat{j}] \cdot [P_i \hat{i} + a_i P_i \hat{j}] \quad (168) \\
 &= P_1 P_i \hat{i} \cdot \hat{i} + a_i P_2 P_i \hat{j} \cdot \hat{i}
 \end{aligned}$$

substituting for  $P_1$  and  $P_2$ , we have

$$P_{ii} = P_i^2 \sigma_{ii} + a_i P_i^2 \sigma_{ji} + a_i P_i^2 \sigma_{ij} + a_i^2 P_i^2 \sigma_{jj} \quad (169)$$

If the isolation had been perfect ( $a_i = 0$ ), then the return power would have been

$$P_{ii_{Ideal}} = P_i^2 \sigma_{ii} \quad (170)$$

Thus, it is seen that scattering coefficients other than the one selected for measurement also contribute. Fortunately, the cross polarization scattering coefficients are much smaller than those for like polarizations. The  $\sigma_{jj}$  term is of comparable magnitude to the  $\sigma_{ii}$ ; its contribution is, however, reduced by the  $a_i^2$  term.

If the reception is of polarization j, then the power received at the antenna is

$$P_{ij} = [P_1 \hat{i} + P_2 \hat{j}] \cdot [P_j \hat{j} + a_j P_j \hat{i}] \quad (171)$$

$$P_{ij} = a_j P_i P_j + P_i P_j$$

$$\text{i.e. } P_{ij} = a_j P_i P_j \sigma_{ii} + a_i a_j P_i P_j \sigma_{ji} + P_i P_j \sigma_{ij} + a_i P_i P_j \sigma_{jj} \quad (172)$$

The ratios of  $\sigma_{ij}$  to  $\sigma_{ii}$  or  $\sigma_{jj}$  is of the order of 0.05. Therefore, it can be readily seen that a cross polarization measurement with an antenna having an isolation factor ( $a_i$  or  $a_j$ ) around 0.05 cannot provide good results. The value of the constants  $a_i$  and  $a_j$  for the case of the S-193 scatterometer can be seen from Table 6.16 to be approximately 0.07 and 0.09. This implies that the cross polarization measurements using the S-193 scatterometer must be processed first to get the scattering coefficient associated with the power received  $P_{ij}$ , then, they must be reprocessed using values of  $\sigma_{ii}$  and  $\sigma_{jj}$  (the  $\sigma_{ji}$  term will be negligible) to get  $\sigma_{ij}$  from equation (172).

### 6.17 System Transfer Functions

To reduce the voltage measurements recorded on the EREP recorder to values of differential backscattering coefficient or antenna brightness temperature, the system transfer functions must be applied. The inputs to these transfer functions are not only the signal voltages for the radiometer/scatterometer but also status bits describing the configuration of the hardware for that measurement, housekeeping voltages describing analog values of hardware elements and some predetermined constants. The system transfer function for the scatterometer is much more complex than that for the radiometer. The derivation of the system transfer function for the scatterometer has been documented by Hanley [1972]. The derivation of the system transfer function for the radiometer has been documented in various stages of complexity by Pounas [1975], Sobti [1973], and by the vendor [G.E., 1972].

Although the form of the system transfer function actually used to reduce scatterometer measurements from spaceborne operation has been that suggested by Hanley, the constants that are required for the computations have been updated repeatedly. The constants actually used during the data processing at NASA/JSC may be found in the most recent version of a document prepared by Philco Ford called PHO-TR524 [1974].

The system transfer function for the radiometer was not as well established prior to flight of Skylab as that for the scatterometer. The insertion loss of the antenna

assembly had never really been measured; only an estimate was obtained from the dimensions, materials used, and some VSWR measurements on individual components. Another factor which was nebulous was a certain gain adjustment factor that the vendor had introduced into the system transfer function to correctly predict results during system testing. The basis for introducing this gain adjustment factor was none other than the inability of the existing transfer function to model the operation of the radiometer.

The transfer functions to reduce the data will not be repeated here, but in the following chapter, a brief description of the study to modify the transfer function of the radiometer based upon results during spaceborne operation is provided.

## CHAPTER SEVEN

### DATA PROCESSING

#### 7.0 INTRODUCTION

The S-193 Microwave Radiometer/Scatterometer was flown as part of EREP (Earth Resources Experiment Package) on board Skylab. Data from the first and second occupancies of Skylab along with other supporting data form the data base for this study. Extensive data was collected during the third occupancy of Skylab but due to some malfunctions in the operation of the S-193 hardware, the processing of these data at NASA/JSC was not complete at the time of this study. These data are, however, being reprocessed with algorithms to circumvent the malfunctions and should be the subject of a report in the near future.

The first occupancy of Skylab lasted from 30 May, 1973, to 14 June, 1973. During this occupancy, 12 EREP missions were flown apart from a calibration experiment over Deep Space and the Lunar background and one special mission over Hurricane Ava in the Pacific. The number of EREP missions was limited because each mission required the Skylab vehicle to be in a Z-Local-Vertical disposition rather than in the Solar Pointing disposition. Failure of one of the power panels caused a drain on the electrical power production of the Skylab vehicle so that a displacement from the Solar Pointing disposition (which is optimal for solar power production) was minimized.

The second occupancy of Skylab lasted from 3 August, 1973, to 21 September, 1973. During this occupancy a total of 28 EREP missions and 2 Lunar Calibration passes were conducted. The targets viewed included ocean surfaces and land surfaces over many parts of the world. Special emphasis during the data takes was, however, given to targets within the continental United States. The inclination of the Skylab orbit was  $50^\circ$ , so that only regions lying within  $\pm 50^\circ$  Latitude could be viewed. The orbital radius ranged from 6802 to 6810 kilometers with a very slight eccentricity.

Data from all the passes (EREP missions) were received at the University of Kansas in the form of magnetic tapes. The format of the tapes was the universal non-imaging format adopted by NASA/JSC for dissemination of data. Apart from the magnetic tapes, tabulations and plots of selected parameters were also received. These tabulations and plots were of voltage recordings of S-193 measurements and associated housekeeping information and also of the finished products, namely the backscattering coefficient and the radiometric temperature. In all cases, the data were tagged by time in GMT. The finished product ( $\sigma^0$  and  $T_B$  values) also included the necessary ephemeris information

describing the target location (center) on a latitude, longitude scale. The tabulations were of many formats grouping various collections of output parameters. For example, one might contain the  $\sigma^0$  and  $T_B$  values, the pitch, roll, incidence angle, target coordinates, all indexed by time, while another might contain the voltage recordings during radiometer and scatterometer measurements, the ephemeris information of the Skylab, the pitch and roll, all indexed by time. The plots were similarly of  $\sigma^0$  or  $T_B$  versus time or voltage recordings versus time, or the spatial location of target centers.

Apart from the data obtained from the S-193 instrument, imagery and associated ephemeris tabulations from the S-190A and S-190B cameras was also received. This was mostly colored imagery 4" by 6" per frame although some black and white imagery was also received. The tabulations described the spatial location of the four corners of each frame along with the center point. Ephemeris information about the orbit and the Skylab vehicle were also provided.

As further ancillary data to aid the investigation of the S-193 data, topographic maps with a scale of 1:250,000 were obtained for all regions in the United States. Land-use maps and potential natural vegetation maps (Kuchler) were also collected for the U.S. Weather reporting station summaries were used to get temperature and rainfall values for 5 days prior to and for the day of each pass for many stations lying close to the pass. These data along with some ERTS mosaics provided further ancillary data used for interpretation of S-193 data.

Of all the S-193 data received at the University of Kansas, the data base selected ~~for the purpose of designing the data catalogue was limited to the segments given in~~ Table 7.1 (CTC passes), Table 7.2 (ITC passes), and Table 7.3 (ITNC passes). The segments over the continental United States for each of the modes are shown in Fig. 7.1-7.3. These passes were selected after careful screening of all the data and the emphasis was on selection of segments over the continental U.S. Data over the ocean were maintained in a separate group and were processed by other members of the investigation team at the University of Kansas. Some ocean data, however, were included in the data base for this study. The data selected to form the data base were further screened and some segments were totally discarded while others were flagged as probably erroneous and treated with caution. The total number of observations including all polarization angles, and modes was a staggering sum of over 40,000. This total (when divided by mode, polarization and incidence angle) often provided very few if any samples in some of the groups.

The greatest amount of data included in the data base was for the contiguous modes (ITC and CTC). The data over South America was included to contrast the

ORIGINAL PAGE IS  
OF POOR QUALITY

CTC

Day	SL	Sub Mode	Pass	Inst.	Pol.	Time		Start		Stop		# of Points	Map Code	Area
						Start	Stop	Lat.	Long.	Lat.	Long.			
154	2	P29	3	R	V	19:22:06	19:24:26	40.90	-123.29	35.55	-114.51	748	A	California, Nevada, Arizona
155	2	P29	4	R	H	17:08:10	17:09:01	36.94	-88.00	35.14	-84.84	280	B	E. Missouri, W. Kentucky, Tennessee
156	2	PO	5	R/S	V	17:57:15	17:58:15	41.16	-114.43	39.60	-111.74	255	C	Utah
156	2	P29	5	R	V	18:00:15	18:01:16	33.51	-102.24	31.06	-99.04	347	D	Texas
160	2	P29	6	R		15:02:53	15:03:11	47.65	-114.39	47.42	-112.82	97	E	Montana
161	2	P29	7	S		14:38:59	14:44:21	2.24	-48.75	-14.35	-37.76	1818		Brazil
162	2	P29	8	R/S	V	15:12:35	15:13:20	45.50	-120.59	44.43	-117.09	253	F	Oregon
162	2	P29	8	S		15:28:49	15:36:28	4.31	-70.02	-18.15	-52.47	2562		Venezuela, Brazil
164	2	P40	10	S		13:50:25	13:51:15	39.56	-97.29	37.92	-94.05	283	G	Kansas, Missouri
164	2	PO	10	R/S	V	13:51:37	13:51:43	38.89	-96.28	38.92	-96.05	20	H	Kansas City Area
165	2	P29	11	S		14:42:08	14:43:45	37.89	-113.39	34.29	-107.64	516	J	Utah, Arizona
165	2	P29	11	S		14:57:33	15:01:06	15.36	-64.51	-4.99	-72.49	1188		Brazil
215	3	PO	12	R/S	H	17:58:37	17:59:09	46.12	-126.99	45.44	-124.56	176	K	Washington Coast
215	3	PO	12	R	V	17:59:11	18:00:39	45.31	-124.22	42.87	-117.59	477	L	Oregon, Utah
215	3	P29	12	R/S	V	18:01:10	18:01:29	40.56	-112.90	40.03	-111.73	111	M	Utah
215	3	P29	12	R	H	18:01:31	18:01:59	39.88	-111.44	38.95	-109.61	161	N	Utah
216	3	P15	13	R/S	V	17:19:52	17:20:44	38.21	-103.91	36.14	-100.96	267	O	Colorado, Texas
216	3	PO	13	R/S	H	17:25:20	17:26:59	25.21	-87.30	20.72	-82.90	563		Gulf of Mexico
216	3	PO	13	R/S	V	17:27:00	17:32:00	20.52	-82.72	6.15	-70.86	1658		Gulf of Mexico, Venezuela

Table 7.1. Data segments of CTC mode used in design of data catalogue.

## CTC Cont.

Day	SL	Sub		Inst.	Pol.	Time		Start		Stop		# of Points	Map Code	Area
		Mode	Pass			Start	Stop	Lat.	Long.	Lat.	Long.			
217	3	P0	15	R/S	V	16:44:05	16:45:05	20.28	-77.55	18.35	-76.07	226		Yucatan Chanel Cuba Gulf
220	3	P15	16	R/S	V	15:58:58	16:03:41	44.58	-121.95	34.91	-103.09	1558	P	Oregon to New Mexico
220	3	P29	16	R/S	V	16:03:58	16:04:39	33.51	-100.96	31.74	-98.89	209	Q	Texas
221	3	P0	17	R/S	V	13:40:53	13:42:15	47.73	-104.40	46.52	-98.94	363	R	North Dakota
221	3	P0	17	R	H	13:42:15	13:43:26	46.44	-98.78	44.67	-93.38	395	S	Minnesota, Wisconsin
224	3	R15	20	R/S	V	14:46:29	14:47:20	34.93	-106.02	33.07	-103.16	265	T	New Mexico
249	3	P0	27	R/S	V	21:27:30	21:28:59	39.47	-102.36	42.50	-96.26	500	U	Colorado, Nebraska
249	3	P0	27	R	H	21:29:01	21:30:29	42.67	-96.20	45.17	-89.59	487	V	Nebraska, East Iowa
250	3	P29	28	R/S	V	20:38:50	20:41:04	26.54	-114.87	32.48	-108.21	709	X	S. W. Mexico to New Mexico
253	3	P0	31	R/S	V	20:08:53	20:11:47	38.98	-107.80	44.59	-95.50	933	Y	Colorado, Nebraska S. W. Minnesota
253	3	P0	31	R	V	20:12:15	20:14:59	45.39	-93.29	49.03	-79.42	926	Z	Minnesota, Wisconsin, Michigan
253	3	P0	31	R	V	20:15:02	20:17:53	49.09	-79.04	50.39	-62.94			Canada
254	3	RR15	32	R/S	V	21:05:41	21:06:09	48.20	-95.39	48.66	-92.91	165	AA	Minnesota
256	3	P0	38	R	V	18:00:31	18:00:37	39.80	-92.20	39.85	-91.84	36	BB	E. Missouri
256	3	P0	38	R	H	18:00:39	18:00:46	39.81	-91.41	40.29	-91.19	39	CC	Illinois
256	3	P0	38	R	V	18:00:48	18:01:19	40.20	-90.92	41.34	-89.00	175	DD	Illinois

Table 7.1. (cont.)

ITC

Day	SL	Sub Mode	Pass	Inst.	Pol.	Time		Start		Stop		# of Points	Map Code	Area
						Start	Stop	Lat.	Long.	Lat.	Long.			
153	2		2	R/S	H	20:12:49	20:13:43	21.66	-103.43	16.43	-98.55	696		Mexico near Mexico City
153	2		2	R/S	V	20:11:57	20:12:46	24.08	-105.75	19.11	-100.87	652		S.W. Mexico near Guadalajara
154	2		3	R/S	V	19:24:47	19:25:36	36.13	-115.43	31.81	-109.26	667	A	Nevada, Arizona
155	2		4	R/S	H	17:07:01	17:07:46	40.62	-94.67	37.02	-88.14	579	B	Missouri, Illinois
156	2		5	R/S	V	17:58:35	17:59:56	38.74	-110.12	33.34	-101.77	1113	C	Utah, Colorado, New Mexico, Texas
160	2		6	R/S	V	15:08:59	15:09:59	37.85	-89.80	33.32	-82.87	819	D	Missouri, Tennessee, Alabama, Georgia
160	2		6	R/S	H	15:10:02	15:11:02	35.37	-85.96	30.63	-79.49	770	E	Tennessee, Georgia
161	2		7	R/S	V	14:19:18	14:23:21	49.37	-118.59	42.60	-96.63	3271	F	Montana, South Dakota Nebraska, Iowa
161	2		7	R/S	H	14:23:26	14:25:04	44.11	-97.57	39.03	-86.58	1351	G	South Dakota, Iowa, Illinois, Indiana
162	2		8	R/S	V	15:14:00	15:15:06	44.26	-116.94	40.34	-108.02	907	H	Idaho, Wyoming, Colorado
162	2		8	R/S	V	15:15:08	15:16:34	42.16	-111.96	37.09	-102.41	1186	J	Idaho, Wyoming, Colorado
162	2		8	R/S	H	15:16:40	15:17:50	38.98	-105.75	34.07	-97.99	903	K	Colorado, Oklahoma, Texas
162	2		8	R/S	H	15:18:00	15:19:20	35.94	-100.87	30.19	-93.07	1085	L	Texas, Oklahoma, Louisiana
165	2		11	R/S	V	14:47:40	14:48:30	25.45	-97.64	20.53	-92.65	668		Gulf of Mexico
165	2		11	R/S	H	14:48:32	14:49:30	23.06	-95.26	17.67	-90.10	752		Gulf of Mexico
223	3		18	R/S	H	15:26:14	15:27:45	40.86	-122.41	35.58	-113.23	1169	M	California, Nevada, Arizona
224	3		20	R/S	V	14:47:36	14:47:58	31.31	-102.99	28.14	-99.07	238	N	Texas
224	3		20	R/S	V	14:49:15	14:53:00	27.75	-98.84	16.74	-88.34	2823		San Antonio, Texas, to Honduras
250	3		28	R/S	V	20:41:29	20:43:15	38.46	-99.30	32.04	-108.83	1210	O	New Mexico, Kansas

Table 7.2. Data segments of ITC mode of operation used in design of data catalogue.





CROSS-TRACK CONTIGUOUS

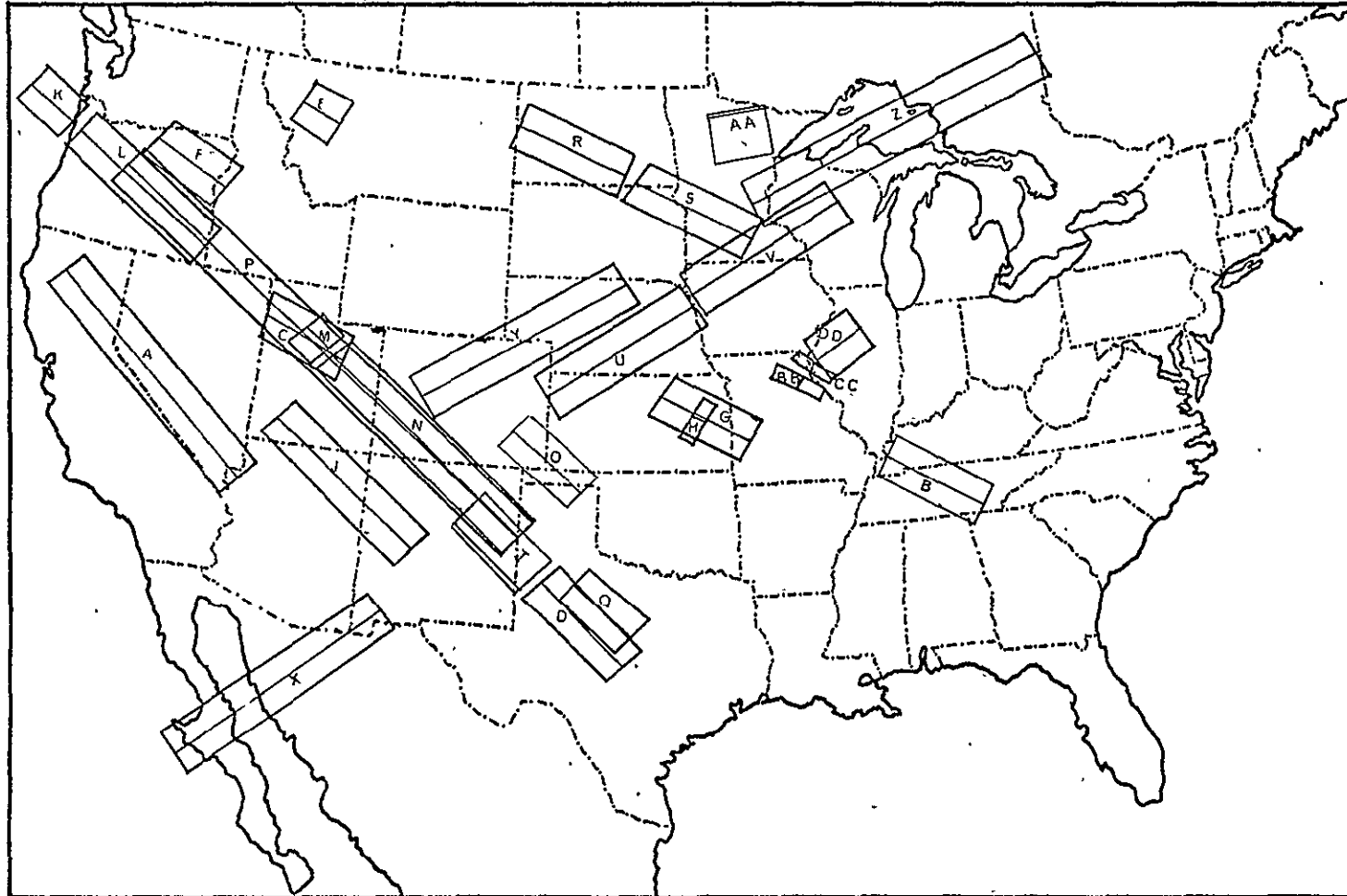


Figure 7.1. Cross-track contiguous data takes over U.S.A. during SL2 and SL3 missions considered in designing data catalogue.

IN-TRACK CONTIGUOUS

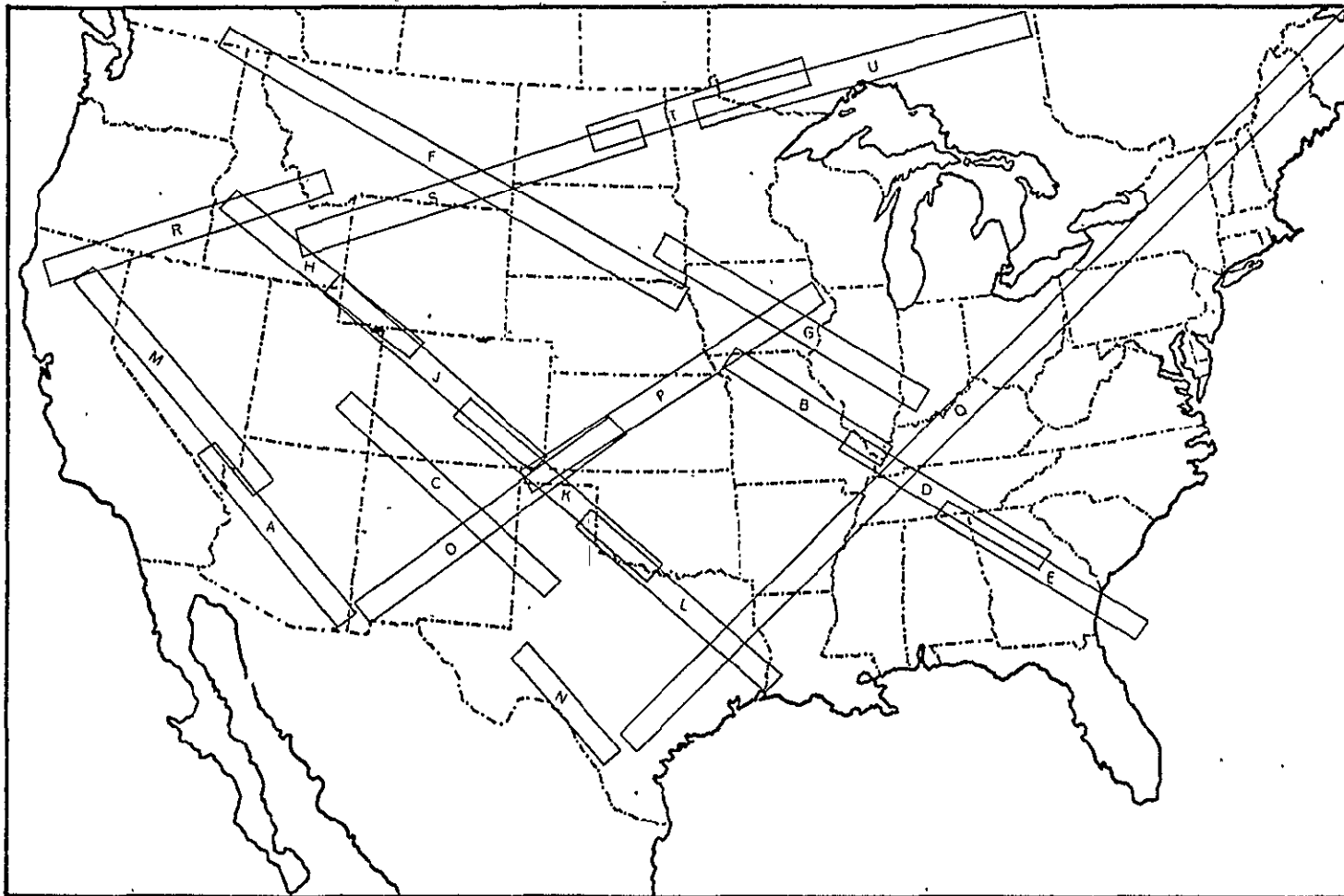


Figure 7.2. In-track contiguous data segments over U.S.A. during SL2 and SL3 missions considered in design of data catalogue.

IN-TRACK NON-CONTIGUOUS

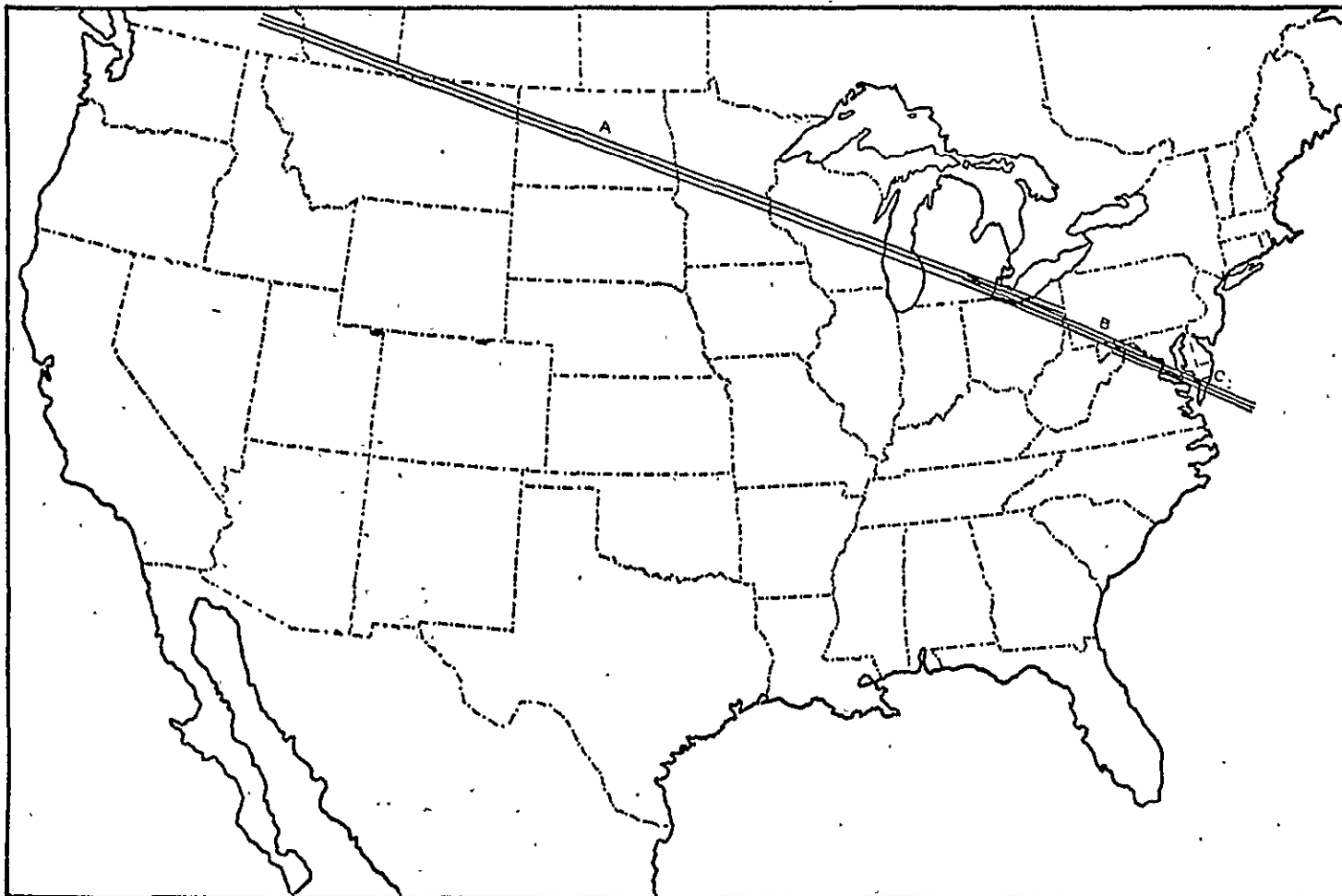


Figure 7.3. In-track non-contiguous data segments over U.S.A. during SL2 and SL3 missions considered in design of data catalogue.

results obtained from that region with the results obtained over North America, because of the great differences in vegetation. The data from South America, however, were for only one mode--CTC Pitch 29°. This mode is perhaps the best mode for mapping regions, and the large areas of homogeneity in South America provided an excellent opportunity of mapping the region even with a resolution as coarse as that of the S-193.

To appreciate the complexity of the data reduction and management problem, the following section describes in capsule form the various stages of data processing required to form a data base from which the data catalog was prepared.

### 7.1 Evolution of S-193 Radiometer/Scatterometer Data for Design of Data Catalogue

There were essentially two stages of data processing involved in the preparation of the data base. The first stage involved the transformation of data by NASA/JSC from the EREP recorder to the data products disseminated by NASA/JSC. The second stage involved the processing of these data products to form the data base for this study.

STAGE I.

The processing of data, recorded in PCM counts on an FM 28 track tape recorder to the computer-compatible magnetic tapes, tabulations and plots disseminated by NASA/JSC to users of these data are described in a document called PHO TR 524 (1973). This document describes the processing for all non-imagery output from EREP sensors. Figure 7.4, taken from this document, describes the data-flow chart of the processing conducted at NASA/JSC.

Data for the S-193 radiometer/scatterometer were recorded on one track of a 28 track tape recorded on board Skylab. On another track of this tape recorder, the time was recorded. This "Astronauts Mean Time" (AMT) was supposed to be synchronized with GMT, but there were some differences between the two. The first step was to strip the individual channels containing data from the five EREP sensors. This process also included some skew removal and reformatting. This processing was performed on a dedicated hardware device designed for this purpose. The output of each channel was on 14 track tapes. An auxiliary output to scan the quality of data was incorporated in the form of a stripchart event recorder and a video display on an oscilloscope.

The next step included the editing and proper time tagging to convert AMT to GMT. The data were recorded with framing and subframing markers so that GMT time tagging was possible onto the tapes for each sensor. The 14 track tapes containing S-193R/S data, still in PCM format, were then converted to voltages, temperatures and other sensing parameters through constants obtained prior to space operation. The data

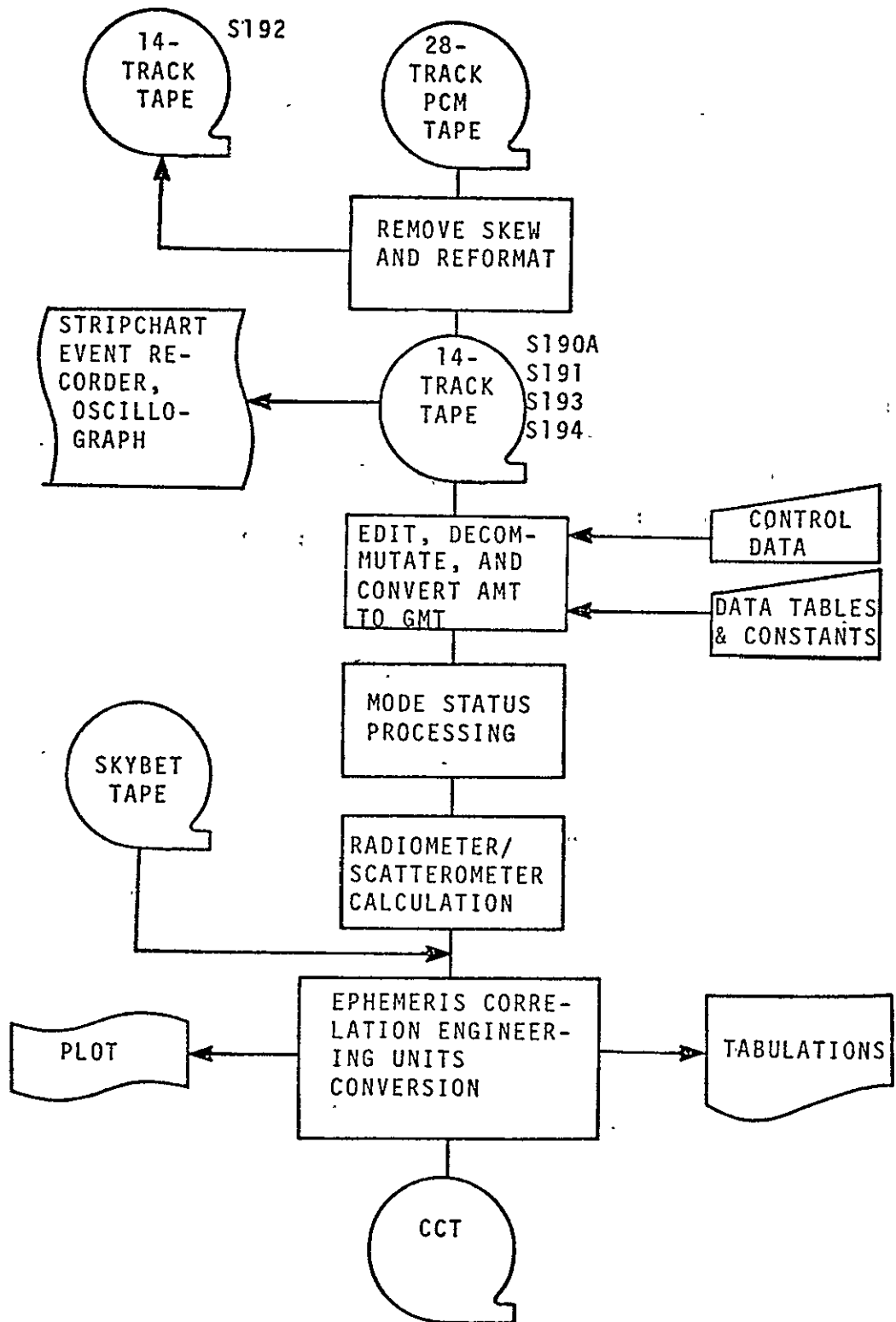


Figure 7.4. S-193 RS processing flow (stage I). From PHO-TR524.

were then ready for processing. The S-193 radiometer/scatterometer is a complex instrument capable of operating in various configurations. The particular configuration for each measurement is recorded in bi-level status bits preceding each radiometer or scatterometer measurement. The coding of these status bits may be found in the vendor's documentation (G.E., 1972). From the status bits, the necessary information regarding sensor and mode operation are obtained. The calculation of  $\sigma^{\circ}$  or  $T_B$  requires a system transfer function to be applied to many parameters recorded on the Skylab tape and includes many constants obtained prior to flight. These constants, however, are mode and in some cases angle dependent. The necessary transfer function is applied after decommutation of the status bits.

To relate the measurement with the target location, the ephemeris information of the Skylab vehicle is used. This information is stored on a magnetic tape and is obtained from a process called Skylab Best Estimate of Trajectory (Skybet). This processing scheme is very complicated and involves many Euler angle transformations, and many ephemerides and is updated by telemetry sensing results obtained when Skylab is in a telemetry link with a ground station. The ephemeris information from the Skybet tape along with the pitch, roll and other necessary parameters recorded on the EREP tape, is used to compute the subsatellite point and the Instantaneous Field of View (IFOV) coordinates in Latitude-Longitude. These coordinates should describe the middle point of the extended target site for each measurement on Latitude-Longitude scale.

The output from this stage of processing is in the form of selected time-tagged parameters required for further processing. The computer-compatible magnetic tapes are formatted according to a scheme described in a document called PHO TR 523 [1972] and the format is referred to in NASA's terminology as Universal Non-Imagery Format. The tabulations are merely various combinations of the parameters (written onto tape) printed out on paper. The combinations of the parameters are all indexed by time and the  $\sigma^{\circ}$  and  $T_B$  values if present are also indexed by target location. The plots are two-dimensional plots showing the variation of any one parameter with time or a spatial location of the target in a Latitude-Longitude scale.

For purposes of sensor performance evaluation, computer compatible tapes providing time indexed parameters as read from the EREP tapes are also provided. The transformation of data on these tapes has only included skew removal, reformatting and time tagging but no further processing. Tabulations providing the Housekeeping parameters (e.g. scatterometer processor temperature, gimbal torque current, etc.) also time indexed are provided. These data were used by the University of Kansas in

evaluation of the sensor. In particular, data from the Lunar Calibrate missions were analyzed to update the transfer function for the radiometer.

## STAGE II.

This stage of the processing was performed at the University of Kansas and sequentially follows stage I. S-193 data received from NASA/JSC along with imagery (S190A, S190B and aircraft-borne cameras) and some other ancillary information described above form the inputs to this stage. A data flow chart for this stage of processing is provided in Figure 7.5 .

Data received from NASA is first checked for errors. Numerous tapes were received that contained data that could at "best" be called suspicious. This checking procedure involves the verification of the operation of a mode correctly and sets a screen which traps outliers of one of many variables on the tape. If the tape, or segments in it, passes this check, it is logged into the tape library and conversion from the Non-Imagery Format to a format compatible with the computational facility at the University of Kansas is made. This is the first level of decommutation. This level of decommutation, apart from conversion to an acceptable format for the existing computing facility also removes some extraneous information contained on each tape. The decommutated version of these tapes is then disseminated to the investigators at the University of Kansas working on various aspects of analysing data from Skylab.

The data received in the decommutated form is, however, in a format that makes any analysis with it very cumbersome. Therefore, another level of decommutation is performed. This step could not have been tied into the earlier step because the optimal formats of data storage for the various investigations are different. The Catalog Standard Format (CSF) is one designed for the purpose of this study. The data are stored in records which contain either a radiometer measurement or scatterometer measurement or both along with the time, scan number and measurement number within the scan, the IFOV coordinates (latitude, longitude), pitch, roll, true incidence angle, measurement value ( $\sigma^0$  or  $T_p$ ), and polarization. The data are arranged so that one universal read program can be used to read data for any mode on any tape.

The next stage is a housekeeping type chore where the data on the tape is examined and any obviously erroneous data are tagged or removed (if they exceed a certain threshold). Apart from this, data for every segment which is on a separate file on magnetic tape are labeled. Header labels describing the time, mode, pass number extent (spatial), target area, etc., are inserted so that the reading of a particular file does not require any special prior information and associated reprogramming.

ORIGINAL PAGE IS  
OF POOR QUALITY  
341

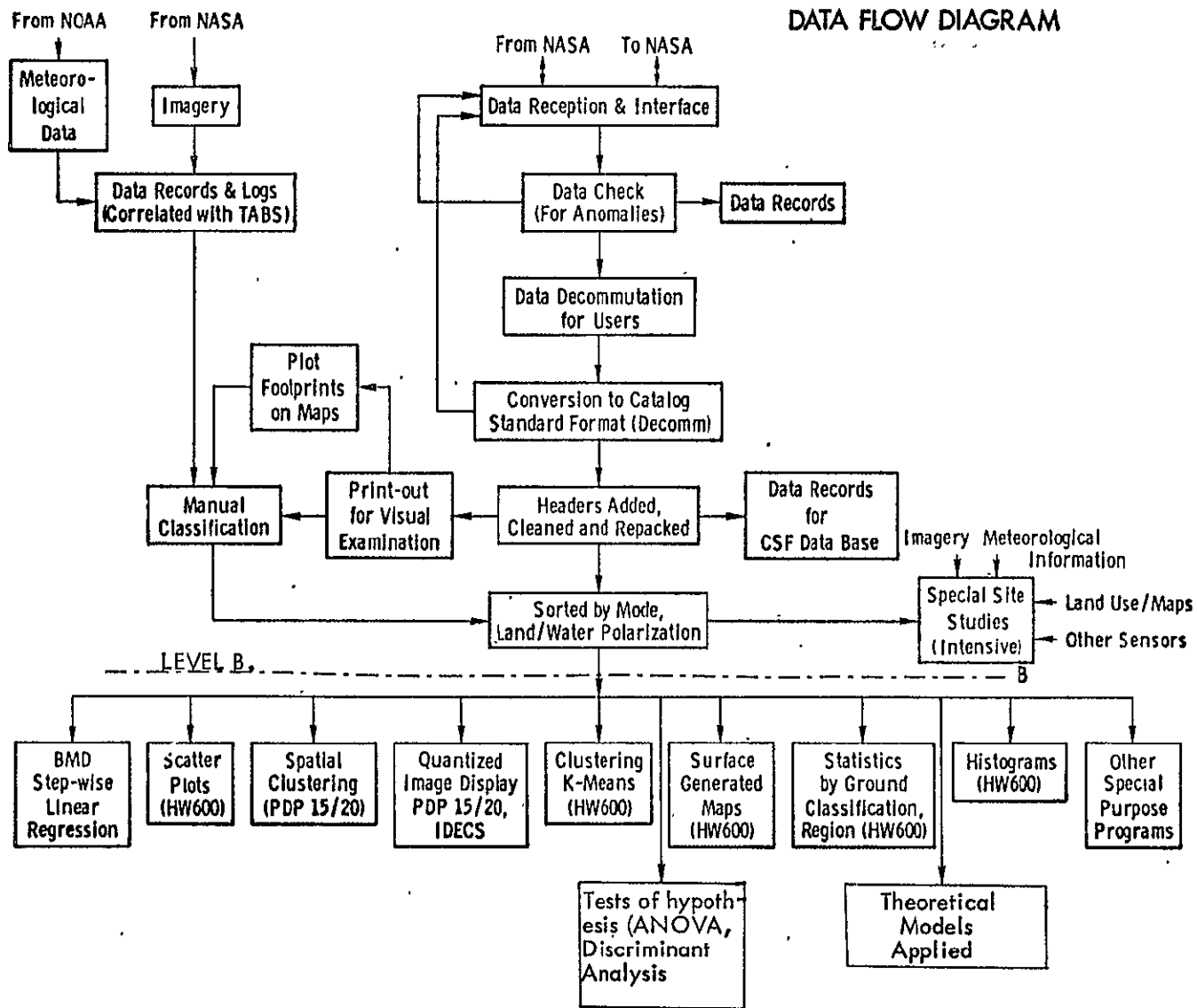


FIGURE 7.5. DATA FLOW DIAGRAM FOR STAGE II OF PROCESSING

The data are then sorted according to mode of operation, land/water target regions, and polarization; separate files of these are maintained. It is understood that merging and sorting of the tape files is easily accomplished and that files containing merged data (merged so that a particular common set of parameters are either present or absent) are retained for particular processing requirements. For example data from all possible modes were merged into four files by incidence angle only so that single-angle histograms could be generated without excessive computer time.

These tape files then constitute the S-193 data base for the present study. Imagery obtained from NASA (from space borne cameras S190A and S190B and from aircraft based sensors) along with associated tabulations describing the spatial location of the target for each frame were received and maintained in a library, appropriately indexed. Meteorological data were obtained from summaries printed by NOAA of the weather reports from various stations across the United States. These summaries are monthly or weekly and contain the daily maximum temperature, rainfall and in some cases even contain soil and other atmospheric conditions. These, too, were logged into the data library.

Data from the magnetic tape files in CSF format were printed for visual examination. This examination was qualitative in nature. If during this qualitative examination a segment of data showed potential for an expected correlation with known ground truth, or, if the data were of a nature quite distinct from the norm, the segment was tagged for intensive studies. These intensive studies were a more exhaustive analysis of the microwave response and usually had a particular ground parameter, such as soil moisture, for which a correlation was sought with the S-193 response. An example of a segment included in the special site studies was a pass in the CTC Pitch  $29^{\circ}$  mode over Texas on the 7th of June 1973 which suggested a strong correlation between the microwave response and soil moisture.

The print outs for visual examination were also used to determine the type of manual analysis that was required. Some segments were classified manually by examination of topographic maps and imagery to determine the proportion of various land use categories in a footprint. Others were classified manually to search for footprints that had a predominance of only one category so that the target could be considered as comprised of only that category. The soil moisture for many segments was obtained from NOAA climatic summaries. The soil moisture was estimated by computing a statistic called the composite rainfall. This statistic, for a particular soil type is a fairly good estimator of the soil moisture. The soil type, in general,

was not considered, so that the composite rainfall computed for two soil types could actually lead to two different soil moisture conditions. For the special site studies, however, whenever possible the soil permeability was also included in the formulae to compute the composite rainfall. The composite rainfall statistic was computed from precipitation reports for five days prior to and including the day of the pass. The formula used was

$$CR = \sum_{i=0}^5 R_i (0.85)^i \quad (1)$$

where  $i$  = number of days prior to pass,  $i = 0$  being the day of the pass  
 $R_i$  = rainfall on day  $i$

The factor 0.85 is a factor to account for the retention capability of a soil. It is valid for a sandy or loam soil and should be different (higher) for a clay type soil.

To account for differences in the physical temperatures in various areas, which directly influence the passive microwave response, the actual temperatures were obtained from weather report summaries. The physical temperatures were then gridded so that an extrapolation and interpolation provided the temperature of the target cell for each radiometric measurement. This physical temperature was used as a divisor of the radiometric temperature to get an estimate of the emissivity. As pointed out in chapter 3, the emissivity of a target is the parameter actually sought. This reduction to emissivity could not be performed for every radiometer measurement, because of the excessive manual time involved in performing the necessary reduction (searching for reporting stations closest to the target site). The reduction was, however, accomplished for CTC Pitch 29° offset passes over the continental U.S.A. The scatterometer measurements ( $\sigma^0$ ) and the radiometric measurements ( $\epsilon$ , emissivity) were then the S-193 response descriptor variables.

To classify a target manually, the center of the target as available on the magnetic tape was plotted on a topographic sheet. Stencils of the size of various angle footprints were overlaid on the map according to the azimuth settings computed from the subsatellite point and the IFOV coordinates. Either the centers of the target points were plotted on topographic sheets on 1:250,000 scale by hand, or a mask was prepared under computer control showing the footprint centers on a scale (and of dimension) equal to the topographic sheets. This mask, when placed over the appropriate topographic sheet, provided the interpreter with the centers of targets, the placing of the elliptical stencils then allowed him to classify the data.

As further aids to the manual classification, plots of the S-193 response for each segment versus distance, versus angle, and between S-193 measurements (radiometer and scatterometer, or scatterometer with VV polarization and scatterometer with HH polarization) were produced. A cursory examination of such plots allowed the interpreter to assess the probability of finding homogeneous regions; suggested regions which differed widely in microwave response, and, in some instances, showed that data had been processed incorrectly by NASA/JSC.

The next level of processing was done both by computer applications and manual classification. Computer programs were generated as needed and an interaction of the results from computer analysis and manual classification was maintained to satisfy the objectives of the study. The computer-aided analyses are represented by boxes below level B (see Figure 7.5). An account of each of these is provided in a section below. The results from the study are provided in the next chapter. Before we actually describe the various individual analyses conducted, let us first establish the purpose for even considering them.

## 7.2 Purpose of Analysis

The global objective of the study is to design a data catalogue of the microwave response of terrain to an orbiting radiometer/scatterometer. The design of such a catalogue has many aspects to it. Each aspect requires a different sort of investigation. For example, the response of a particular type of terrain requires that one classify the targets according to some measure of similarity. Another purpose could be to describe the expected bounds of the microwave response with a scatterometer or radiometer looking down on the earth. Unlike many investigations which are conducted only to prove or disprove a particular set of hypotheses, this investigation was much more exploratory, in that the nature of the response of terrain to microwave sensors at orbital heights was sought. The hypotheses could then be generated after examination of these results. For the exploration of the nature of the response, the following analyses were conducted.

### 7.2.1 Ensemble Statistics of Microwave Response

This investigation was aimed at determining the distribution of the response for each set of sensor configurations exercised by the S-193. These sets of sensor configurations are composed of unique polarization, incidence angle, and major target types. The polarization, incidence angle decomposition is, of course, self-explanatory. The major target types considered were: the land mass of the continental United States, ocean surfaces, and the land areas in South America (mainly the Amazon forest region). The

targets in South America were excluded from those in North America because of a readily apparent difference in response.

The analysis conducted was through computer programs which provided the histograms (frequency counts) of the distribution of the backscattering response or brightness temperature for intervals of incidence angle and for each polarization. Separate histograms for the three major regions were prepared. Although these histograms showed the distribution graphically, the bounds of the distribution in terms of quartiles and deciles could not easily be discerned from these bar graphs. Therefore, separate calculations to compute the decile values were performed. The decile values were computed according to

$$D_n = R_i \mid \left\{ N(R_j < R_i) = \frac{n}{10} M \right\} \quad (2)$$

where

- $D_n$  = nth lower decile
- $R_i$  = Response of S-193 ( $\sigma^0$  or  $T_B$ ) for particular measurement number  $i$ .
- $M$  = total number of measurements.
- $N(R_j < R_i)$  = Total number of measurements where  $R_j < R_i$ .

This formula says that the nth lower decile of the microwave response is equal to the microwave response value such that the number of responses lower than this value is  $n$  tenths of the total number.

### 7.2.2 Microwave Response Statistics of Manually Classified Categories

The ensemble statistics considered all possible target types encountered in each major region without any further breakdown by physiographic or land-use features. They could be useful for assessing the total dynamic range and expected values of microwave response over a large region. Another set of statistics similar to those described above were computed for regions which had been selected as homogeneous, based upon physiographic and land-use considerations. The regions so chosen were farmland, woodland, rangeland, various conditions of an ocean surface and some special types of surfaces such as playas and salt flats. Histograms for each angle and polarization group (where sufficient samples were available) and decile values were computed.

The classification based upon physiographic and land-use features was performed by a manual classification based upon examination of topographic maps, land-use maps, potential natural vegetation maps and imagery.

### 7.2.3 Terrain Features from Microwave Response

This investigation was in a sense the inverse of the one just described above. In this analysis, the entire microwave response obtained with a particular sensor configuration (in this case also broken up by mode) was used to provide the classification. Various groups of sensor response, for example the response in the ITC mode for three angles of incidence, were used to perform the classification. The data were pooled into one large set of data vectors and a clustering algorithm applied to partition the data into natural clusters. The clustering schemes employed were K-Means clustering and a technique called Spatial Clustering [Haralick et al, 1974]. The grouped data (clusters) were then examined to find the terrain features (physiographic and land-use) of the targets included in each cluster. An ideal situation would have been that each cluster based upon microwave response contained only one of the terrain categories. Unfortunately, such was not the case. Therefore, the percentage of each terrain category included in each cluster was found.

The two methods of clustering are thoroughly described by MacQueen [1972] for K-Means Clustering and by Haralick et al. [1974] for Spatial Clustering. The philosophies of the two clustering procedures are distinct and consequently the results in some instances are also distinct. Provided below are thumbnail sketches of the procedures involved in the clustering. The program used for K-Means clustering was obtained from the library of programs maintained at the University of Kansas Center for Research. The program used for spatial clustering was obtained through courtesy of Dr. R. Haralick and Mr. Amrendra Singh.

#### 7.2.3.1 Non-Supervised Spatial Clustering Procedure

The spatial clustering algorithm differs from the usual clustering algorithms in that contextual information is used in the form of the spatial location of target cells. This algorithm was developed for analysis image-like data where the partitioning of data into like regions must take into account the spatial distribution of each cell. The algorithm is carried out in two phases.

In the first phase, the spatial information of the image-like data base is used to determine regions of homogeneity. To create an image-like data base from data collected by the in-track modes of the S-193 sensors, the target cell was repeated in one direction (orthogonal to the track) so that there was a grid produced which had each column equal. The clustering then only affected the rows. The regions of homogeneity are found by a boundary enhancement technique. This is shown in Figure 7.6 as the

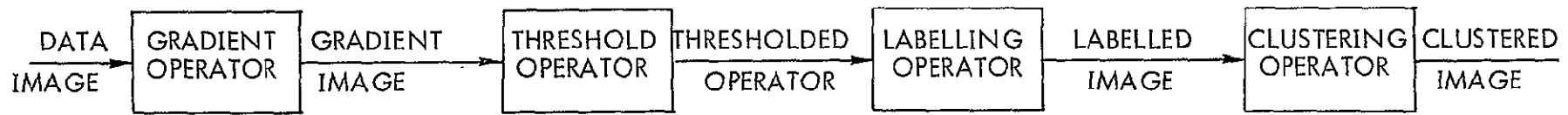


Figure 7.6 The Non-Supervised Spatial Processing Approach

gradient operator. The gradient image so produced is then processed through a threshold detector and the output image should then contain regions of homogeneity separated by boundaries where the gradient exceeded the threshold. The next step is labelling each homogeneous region.

The second phase of the algorithm consists of an iterative clustering procedure where each homogeneous region finds another homogeneous that is closest (in measurement space) to it; and if the two regions are close enough, they are merged to one cluster. This process of grouping homogeneous regions continues iteratively till there are only a few major clusters.

### 7.2.3.2 K-Means Clustering Procedure

This procedure attempts to break up the data space into similarity groups. The procedure is not intended to find some unique, definitive grouping, but rather to simply aid the investigator in obtaining a qualitative and quantitative understanding of large amounts of N-dimensional data. The data base included for this study consisted of all CTC pitch  $29^{\circ}$  data where the clustering was performed on the radiometer (reduced to emissivity) and scatterometer data for vertical polarization; ITC data using all five angles for scatterometer measurements and ITC data using the middle three angles for scatterometer measurements, and CTC pitch  $29^{\circ}$  data where the clustering was performed only on the scatterometer measurements.

The procedure involves two parameters: C for "coarsening" and R for refinement. The data base is first converted so that all the data lie within a unit n dimensional sphere. This is a scaling procedure and the data can then be weighted by assigning weights to individual variables. The program starts with a user-specified value of K, and takes the first K points in the sample as the initial means. This selection can, however, be forced to select any particular points as the initial means (or seeds, as they are sometimes called). The clustering procedure then is an iterative one where the nearest sample (in measurement space) based upon a distance criterion (usually square of the difference in magnitudes) is compared to the threshold values (C) selected; if the proximity is close enough, the sample is included in the group and a new mean computed. If the sample is greater than a distance R from each cluster, it is allowed to be another seed. In doing this, the group means are updated and each point iteratively assigned to groups or allowed to form its own cluster which can attract other samples. The final classification is performed with the means of the clusters obtained by the above iteration process. This classification is again based upon a least distance criterion.

#### 7.2.4 Regression Analysis

The microwave response as observed from the S-193 sensors was displayed through histograms and quantitatively illustrated through deciles. To be able to predict the backscatter or brightness temperature response based upon polarization and angle of incidence, a regression analysis is most appropriate. A step-wise linear regression procedure was used to relate the backscattering coefficient and radiometric temperature to functionals of incidence angle. The various functionals used were quite arbitrary, the choice was guided by the shape of the  $\sigma^0$  vs  $\theta$  or  $T_B$  vs  $\theta$  curves.

The Step-wise Linear Regression program used was obtained from the Biomed Program Library [Dixon, 1973]. The input to the program was a set of S-193 measurement and incidence angle pairs, the program computed the regression equation relating the dependent variable (S-193 microwave response) to the independent variables (functional of the incidence angle). The linear regression was performed on a least square error criterion.

#### 7.2.5 Correlation Analysis

Two basic questions to be answered lead to the use of correlation analysis: (1) What, if any, was the correlation between a parameter describing the target (for example soil moisture) and the corresponding microwave response of the target? (2) What, if any, was the correlation between the response of a particular target under different configurations of the sensor? For example, what was the correlation between the response of a target when viewed with vertical and horizontal polarization with a scatterometer? These questions can be answered by a correlation study.

The correlation analysis procedure for both types of questions is similar, but the input parameters are different. Correlation analysis applied to answer the two questions provides results which can be interpreted to gauge the performance of the sensor for geoscientific uses. The correlation of a ground descriptor, like soil moisture, and the microwave response like brightness temperature, may suggest that a radiometer operating in space, with a resolution as poor as the S-193 can still be used to estimate the soil moisture. A lack of correlation in some cases is just as meaningful. The correlation between the microwave response of a particular target, with two sensor configurations, like scatterometer at vertical-vertical polarization and at horizontal-horizontal polarization, may suggest that the use of two polarizations is redundant.

Since our purpose is also to provide design information for future fine resolution imaging type sensors, the results of this correlation analysis are useful. The correlation

coefficient computed is the familiar Pearson correlation coefficient defined by

$$\rho_{ij} = \frac{E \left[ (x_i - \bar{x}_i) (x_j - \bar{x}_j) \right]}{\sqrt{E (x_i - \bar{x}_i)^2 E (x_j - \bar{x}_j)^2}} \quad (3)$$

$X_i, X_j$  are the two parameters

$\rho_{ij}$  = correlation coefficient between  $X_i, X_j$ .

$$\rho_{ij} = \frac{\sum_{i=1}^n \sum_{j=1}^n (x_i - \bar{x}_i) (x_j - \bar{x}_j)}{\sqrt{\sum_{i=1}^n (x_i - \bar{x}_i)^2} \sqrt{\sum_{j=1}^n (x_j - \bar{x}_j)^2}} \quad (4)$$

$x_i, x_j$  are samples from  $X_i$  and  $X_j$ .

### 7.2.6 General Linear Hypothesis

A pertinent question that needs to be answered upon examination of microwave data from the S-193 sensors is whether the microwave response from various known target types is similar or not. In other words, we set up the null hypothesis that the mean microwave response for various target types is the same. We consider the rejection of this null hypothesis through an analysis-of-variance procedure. Since we are only talking at this stage of the mean response (either rad or scat) from each target type, the procedure appropriate for considering the hypothesis is the one-way layout of the analysis of variance procedure. The rejection of the hypothesis is then considered through the familiar F-statistic which then determines the rejection criterion. The procedure employed is quite standard and would be repetitious if described here.

The underlying assumptions of the use of analysis of variance are hard to defend in some instances. For those sets of data where the population variances are very different, the results are not meaningful. For small differences in variance, testing the F-statistic is at best a conservative measure and more stringent rejection confidences must be sought. The analysis of variance used took these factors into account. An assumption of normality of errors has, however, been tacitly assumed.

Quite often more than one variable can lead to an inequality of the sample means. For example, samples from one population (ground type) could have another variable involved that was varying over this population as well as the population to which these means of the microwave response are being tested. The analysis procedure in this case becomes the two-way layout. This procedure is again very widely used and documented in numerous statistics texts. The two variables considered in the two-way layout were the microwave response (either rad or scat) and soil moisture.

### 7.2.7 Discriminant Analysis

#### 7.2.7.1 General

Another question that must be answered upon examination of microwave data is, can the microwave response be partitioned in any way so that a sample taken from the population can be classified according to some decision rule into one of several known categories? The procedure often invoked to answer such a question is discriminant analysis. The procedure involved the computation of a set of discriminant functions such that the error of misclassifying is minimized according to some least square criterion. This, too, is a widely used procedure and details can be found in many texts. The discriminant functions produced by the procedure involved in our study did not include any a priori probabilities of the presence or absence of categories; so, in a sense, they were a set of Bayes procedures with a priori probabilities of the occurrence of a category all equal and the risk or gain function also equal.

The analysis was performed by the use of a program obtained from the Biomed Program Library [Dixon, 1973]. The mathematical procedures are documented in the manual describing the programs. Provided below is a thumbnail sketch of the procedure.

#### 7.2.7.2 Step-Wise Discriminant Analysis Procedure

This procedure performs a multiple group discriminant analysis. A set of linear classification functions is computed by choosing the independent variables in a step-wise manner. The independent variables in our case are the microwave response with various sensor configurations. The groups are defined by a manual classification and include the broad categories included in the manual classification process.

A set of linear functions of the variables is found which partition the measurement space. The partition is based upon the likelihood ratio criterion of the hypothesis that a sample was drawn from a certain population. The procedure works in a step-

wise fashion, the variable entered at each step is the one which has the largest F ratio; i.e., it can describe the most variance in the measurement space. At each step, a variable is entered or removed according to its F-ratio. The resultant discriminant functions are then used along with the apriori probabilities of occurrence of each group to assign the samples into the various groups. In our case, we considered the apriori probabilities equal. The risk or gain function was also equal.

The populations of the groups were found by computing the mean and standard deviation within each group for each variable. One of the assumptions of the discriminant analysis procedure is that the covariance matrices for each group is equal. This assumption was not exactly met when the sample covariance matrices were computed, but the differences were small and it is felt that these could not substantially alter the results obtained.

A computational review of the procedure can be found in the Biomed Manuals describing this procedure. The mathematical derivations can be found in Anderson [1858].

#### 7.2.8 Comparison of Microwave Backscatter Response with Theoretical Scattering Models

S-193 microwave data should be used to check the validity of some existing theoretical models. If these models do apply the parameters that appear in these models should be computed to predict the backscatter response. Scientists have, for many years, suggested models for explaining the backscattering response from extraterrestrial targets. Among these are Pettengill et al [1973], Hagfors [1968], and Fung and Moore [1964].

A simple physical optics approach using an exponential autocorrelation function yields a result for the backscattering coefficient as [Pettengill, 1973]

$$\sigma^{\circ}(\theta) = \frac{P_0 C}{2} (\cos^4 \theta + C \sin^2 \theta)^{-3/2} \quad (5)$$

where  $\theta$  = angle of incidence

$P_0$  = Fresnel reflection coefficient

$1/\sqrt{C}$  = rms slope of the surface (for  $C > 20$ )

Small perturbation theory is only valid at angles greater than  $20^\circ$  off nadir. The first order approximation of the small perturbation theory yields a result for the differential backscattering coefficient as

$$\sigma_{hh}^0 = 8k^4 \sigma_s^2 \cos^4 \theta |R_h(\theta)|^2 W(2k \sin \theta) \quad (6)$$

$$\sigma_{vv}^0 = 8k^4 \sigma_s^2 |\alpha_{vv}(\theta)|^2 W(2k \sin \theta) \quad (7)$$

where

$$\begin{aligned} \alpha_{vv}(\theta) &= F(R_v, \theta) \\ &= R_v(\theta) \cos^2 \theta + T_v^2 (k'^2 - k^2) \sin^2 \theta / 2k'^2 \end{aligned}$$

$$R_h(\theta) = \frac{k \cos \theta - k' \cos \phi}{k \cos \theta + k' \cos \phi}$$

$$R_v(\theta) = \frac{k' \cos \theta - k \cos \phi}{k' \cos \theta + k \cos \phi}$$

$$T_v = 1 + R_v$$

and

$$\begin{aligned} k' \sin \phi &= k \sin \theta \\ \cos \phi &= \sqrt{1 - \sin^2 \phi} = \sqrt{1 - \frac{k'^2}{k^2} \sin^2 \theta} \\ k &= \frac{2\pi}{\lambda} \end{aligned}$$

and  $k'$  is related to  $k$  by

$$\epsilon_R = \frac{k'^2}{k^2}$$

Equations (6) and (7) were solved to get values of  $W(2k \sin \theta)$ . These values are then point sample estimates of the power spectrum of the surface. Recall from Chapter 2 that  $W(2k \sin \theta)$  was related by a Fourier Transform to the spatial autocorrelation function of the surface. The point samples of the power spectrum may be used, by making many assumptions, to estimate the power spectrum and hence the autocorrelation of the surface. This may be the subject of subsequent research and is not reported in this study.

Selected regions were candidates for this study.

The application of this model is valid from nadir to  $20^\circ$  off nadir. Backscatter data obtained from Skylab were used along with the associated incidence angle to solve for  $P_0$  (the reflection coefficient) and  $C$  which is inversely proportional to the square of the rms slope. The solutions were obtained in two ways. In one case, the data for angles of incidence closest to nadir were taken as one set of values and data at  $(10^\circ \pm 2^\circ)$  off vertical were taken as the second set and equation 7.4 was solved simultaneously for  $P_0$  and  $C$ . Then, backscatter values (and incidence angles) were chosen for incidence angles closest to nadir,  $(10 \pm 2)^\circ$ , and  $(20 \pm 3)^\circ$  off nadir and the corresponding solutions for  $P_0$  and  $C$  found by a least square error criterion. This, of course, involved a non-linear regression and the solutions were obtained on a computer by Newton's method of successive approximation.

The values of  $P_0$  and  $C$  were found for the clustered means, ensemble means and for selected regions. The second approach was to consider data in the contiguous mode and compute the  $P_0$  and  $C$  based upon a set of either 2, 4, 6, 8, or 10 values of  $\sigma^\circ$  and  $\theta$  from each curve. The solutions were again obtained for a least square error criterion. The dielectric constant of the surface was found from the Fresnel reflection coefficient. It was assumed that the real part of the dielectric constant was 10 times as large as the imaginary part. With this assumption then, the solution for the dielectric constant was

$$\epsilon_R = \left( \frac{1 + P_0^{1/2}}{1 - P_0^{1/2}} \right)^2 \quad (8)$$

where  $\epsilon_R = \epsilon_1 + j \frac{\epsilon_2}{10}$

where  $\epsilon_1$  = the real part of the dielectric constant

The physical optics approach using a Gaussian autocorrelation function yields a result for the backscattering coefficient as

$$\sigma^\circ(\theta) = \frac{k}{2 s^2 \cos^3 \theta} \exp(-\tan^2 \theta / 2 s^2) \quad (9)$$

where  $s^2$  = variance of the surface slopes

This result is also achieved when one uses the Geometric Optics approach. This model is constrained to regions around nadir (to  $15^\circ$  off nadir). It has been suggested as a possible descriptor of the return from an ocean surface.

### 7.3 Display of Microwave and Supportive Data

A problem with data obtained from non-imaging sensors, especially ones where two or more variables are to be simultaneously displayed or where the spatial distribution of the response is to be examined, is that some suitable display scheme is required. Numbers are all that is provided in terms of radiometer and scatterometer data. A correlation of various numbers or the spatial distribution of the numbers can be performed only by a skilled interpreter. In general, a display scheme of some sort is required to aid in the interpretation process. The display schemes, to pictorially "show" the interpreter the data, range from the simple to the complex, where many levels of coding are used in the display.

To display the S-193 data, some simple display schemes were developed. These did not consider the display of many dimensional data, rather they were merely to show the spatial distribution of the response. They could be considered as an attempt to produce "images" using the data from the coarse resolution sensors of S-193. The displays were produced on computer print-outs, as well as on a color video monitor.

To display the spatial distribution of the S-193 response, by computer print-out, a program generated and maintained by the Kansas Geological Survey called "Surface" (part of the Surface Graphics Package) was used. The program is documented by Sampson [1974]. The main features of this routine are the interpolation and extrapolation on a two-dimensional grid from samples obtained within the gridded area. The resulting display is printed out by a high speed line printer. These outputs can then be used to produce regions of similar (or homogeneous) response and contours of similar microwave response can be generated. "Surface" generated maps were used for the qualitative examination of each data segment and in some cases even for detailed analysis.

Needless to say, only the cross-track contiguous modes were candidates for such a display scheme. Pitch-offset cross-track mode operation with offsets at  $29^{\circ}$  and  $40^{\circ}$  were the most suitable for producing backscatter response maps because the angle of incidence stayed almost constant across a sweep. The resulting maps were then like a pseudo-image, produced by smoothing over the large resolution area.

The second scheme was again to display the spatial distribution of the response. This scheme utilized an incremental plotter operated under computer control. It was mainly used to post the location of regions found homogeneous by the S-193 (as per the cluster analysis) on a map of North or South America. The number of points included in

the clustering procedure was sometimes in excess of 7000; to manually determine which target point fell into which cluster and where the target point lay, was almost impossible in the limited time for this study. The clustered data were posted on maps of North America and South America, one cluster group per map. An overlaying of the maps showed the relative contribution of each area to each cluster.

The third scheme of display was by the use of a color video monitor. This scheme was definitely more aesthetically appealing and allowed for a simultaneous display of more than one variable. The display was created by the use of a near real-time analog-digital image processing and display unit which was created at the University of Kansas\*. The data are stored on secondary storage of a PDP 15/20 computer which processes the data and through computer control transfers the data by way of the image processing device onto a color video display. The documentation of the hardware and the software instructions for the processing device are provided by Anderson [1973]. The software for processing the data to transfer an image-like file to this device was obtained through the courtesy of Mr. Gary Minden (with authorization from Dr. R. Haralick).

Many unique and helpful features are incorporated in the computer driven video display unit, not all of them were exercised. An attractive feature of this display device was the capability of selectively thresholding the data on the screen and assigning various colors to the thresholded regions. Simultaneous display of the S-193 response and, say, a topographic map were possible by scanning the topographic map on a and routing the signal to the video monitor. Ground parameters as established through manual classification of each S-193 target cell could also be displayed.

#### 7.4 Processing Philosophy and Data Management

When one has data from many sources, of different kinds, and, in some cases, in abundance, an important decision that should be made prior to the actual data processing is the management scheme of data. Once this has been made, the next step is to construct the processing algorithms so that an optimal (or even just economical) processing-to-result ratio is obtained. This criterion is stated in many ways by data processing specialists but the meaning in all instances is the same.

When one is dealing with data that is received on different media (for example, the S-193 data were on magnetic tape, S-190A and S-190B products were imagery, and

---

\*This system called IDECS (Image Discrimination Enhancement and Combination System) has been used for many years for image-type processing at the University of Kansas.

weather information was on booklets containing weather summaries, the problem of data management is made even more complex. To convert all the data into quantized values and store on computer memory (be it tapes, discs, or even punched cards) is not feasible. It is also not particularly desirable.

One way to handle data of this nature is to use the outputs from one medium of data storage, which incidentally contains information of intrinsic value to itself only, to aid in the analysis of data on another medium. For example, an examination of imagery can be used to determine the regions of homogeneity of a particular ground category. These regions can be coded so that the corresponding S-193 microwave response can be processed. In reverse, the S-193 data can be sorted on some measure of similarity and the target cells so sorted can be examined through imagery to determine their ground-truth classification. This was the process chosen to relate ground truth with the S-193 microwave response.

When analyzing the S-193 data by itself, i.e., computing descriptive statistics of the data, the storage of the data has to be in some convenient format. The programs to determine the descriptive statistics should also be optimized so that the same set of programs can be used repeatedly for data from various configurations of the S-193 operation.

The S-193 data were stored on magnetic tapes in a format called the Catalog Standard Format as mentioned previously. The appendix contains a listing of the program used to read data recorded on this format. Each data segment contained a header label which described the contents of the file. To access a particular segment of data, it was necessary to know either the day and pass number or the physical location of the file on a tape. The latter method was preferred for all accesses to a file.

The computer programs performing individual functions like preparing histograms of the distribution of any parameter, or preparing a spatial display through computer print-out, were mostly in modular form. The use, therefore, called in the necessary programs to perform any analysis on the data base. Quite often this concept of modular programs was violated because of the paucity in time to process the data. In some instances, special "doctoring" of the programs, because of unexpected or erroneous data on the files, was required.

The data base was stored redundantly on separate magnetic tapes sorted by mode, major region (North America, South America, and Ocean), and in some cases by incidence angle. It was possible through the universal read program to sort and merge segments of

various files based upon preselected criterion. This was often done in the interest of saving execution time of a program.

The computer programs written fall into three major categories:

- 1) Decommutation, Reading/Writing and Reformatting
- 2) Display schemes
- 3) Statistical Analysis.

Decommutation, Reading/Writing and Reformatting required special programs written specifically for this particular study. The philosophy for the other two categories was to use as many existing, generally available, programs as possible. Sometimes these programs were modified to suit the particular processing need. This cut down on the programming effort and also ensured a result that had been obtained through a program package which had undergone sufficient testing.

Listings and descriptions of the various computer programs used for this study will be documented in a forthcoming report.

## 7.5 Special Analyses of S-193 Microwave Data

### 7.5.1 General

Unlike aircraft-based or ground-based measurement programs where the hardware is available after the measurements for post measurement calibrations or testing, space-borne measurement programs have to rely upon any data recorded during the operation of the sensor. Fortunately, there were many housekeeping-type parameters recorded which allowed one to evaluate the performance of the S-193 sensor. These parameters and the voltage recordings of the measurements form the only source of evaluating the sensor's performance. As aids to evaluate the performance of the radiometer, some special data takes over the galactic background were conducted. The transfer functions to reduce the data from space-borne operation had been suggested prior to flight. Verifications and modifications to these transfer functions were, however, a part of the special analyses. In particular a major study to evaluate the transfer function of the radiometer was conducted. The details of this study have been documented elsewhere [Sobti, 1975]. Provided below is a synopsis of the study.

### 7.5.2 Review of Radiometer Transfer Function

An examination of data obtained from the space-borne operation of the S-193 Radiometer showed that the transfer function as suggested by the vendor of the hardware (General Electric) required modifications. This fact was borne out when the radiometer data from space when viewing a homogeneous target was being used to compute a better

estimate of the antenna assembly insertion loss values. A computation of the estimate for the antenna assembly insertion values, when coupled with a lack of confidence in the transfer function suggested by the vendor, became a problem of greater complexity than had originally been anticipated. Selected data from the first and second occupancies of Skylab, along with laboratory-based results obtained during the development and testing stage of the hardware formed the data base for this study.

Specifically, the problem with the transfer function suggested by the vendor, was that it considered an arbitrary empirical value as a "gain adjustment" factor for all modes of operation. This factor was introduced because the estimates from system testing (using the estimates for insertion loss, gain, etc. of the hardware) of the applied input temperature varied considerably from the actual temperature applied. An empirical gain adjustment factor was then introduced so that certain operating modes, with certain input temperatures produced an estimate of the input temperature (when applying the system transfer function to the voltage measurements) which agreed with the actual temperature input for the tests. This empirical gain adjustment factor was considered mode-independent. An examination of the results of system testing show that this single gain adjustment factor for all modes was not sufficient. That is, the gain was found to be mode-dependent.

It was felt that from the space-flight data obtained during the Lunar Calibrate/Deep Space passes, an optimum set of gain adjustment factors could be found. The assumption was that these gain adjustment factors computed for the low end of the radiometer dynamic range (in fact, lower than the value recommended as the low end of the dynamic range by the vendor) would be acceptable for the entire dynamic range of input temperatures expected during operation over land and ocean targets. This assumption was hard to defend. Computations performed using the PCM bit count obtained from the raw data tape showed that the algorithm suggested by the vendor was not adequate. The only target which could be considered homogeneous and for which all operational modes of the S-193 Radscat had been exercised was deep space. The radiometric response as suggested by reducing the PCM counts on the raw data showed great variation in the temperature of deep space from mode to mode. To make the overall mean of the estimate of the temperature for deep space conform to our expectations, the antenna assembly insertion loss values were varied so that the effective temperature of incoming radiation was 4°K. This value of the antenna assembly insertion loss which satisfied this criterion was much too large, so that data for an ocean pass over known weather and wind conditions, when reduced using this value of antenna assembly insertion loss was too low. The problem could now be seen to be complex. In essence, an

optimum set of gain adjustment factors and an antenna assembly insertion loss were to be found so that when inserted into our best estimate of the radiometer system transfer functions, the estimates of antenna (or apparent) temperature would be acceptably close to our prior or theoretical expectations. This is not stated to confuse the reader, merely to point out the complexity of the problem.

Various schemes were applied to treat the radiometer calibrate\* and radiometer baseline\* signals and to reduce the variance of the computed antenna temperature for deep space (a known homogeneous target at 13.9 GHz). The schemes included and the results from this study are reported by Sobti and Collins [1975]. To reduce the variance, the scheme which was recommended was a linear fit to the calibrate and baseline voltages obtained during the contiguous operation of the S-193 radiometer in an operational mode.

A solution of gain adjustment (K) factors and the associated antenna assembly insertion loss values using the scheme to reduce antenna temperature variance was sought using deep space data. The optimal set of gain adjustment factors were considered those which brought the means of the antenna temperature estimates from the various modes closer together. The radiometer transfer function was split into two parts, one that considered the hardware beyond the polarization circulator (towards the receiver) and the other which considered the hardware before the polarization circulator. From the voltage recording, working back through the system transfer function, the estimates of the temperature signal at the input of the polarization circulator were forced to converge to a single temperature by variation of the gain adjustment factors for each mode. The temperatures chosen as the converging limit were varied. The grand mean of the temperature for all data takes included in the study (all Lunar Calibration passes with no sizeable variation in antenna temperature), and some arbitrary selected values were included as convergence limit values. The antenna insertion loss values were then altered so that, by the transfer function from the polarization circulator towards the antenna, the estimate of the input temperature was held to a fixed value. This was usually kept at 4°K (2.7°K is the expected brightness temperature of the galactic background with 4°K on the galactic plane), although some results were also obtained for 8°K.

It was thus possible to find many combinations of K's and the antenna assembly insertion loss values to satisfy the data for deep space temperatures. But deep space

---

\*Described in Chapter Six and in the Appendix.

was not a primary target for any geoscientific investigation using the radiometer, in fact, it was even lower than the suggested dynamic range (defined as region where the precision specification is met) by the vendor. To check the parameters computed from examination of Lunar Calibration/Deep Space data, an ocean pass with known wind and weather conditions was selected as a candidate for verification. Using a smooth-sea approximation, and applying scattering theory, and adjusting for contributions from the atmosphere, the theoretical or expected brightness temperature at the antenna was computed. This expectation or prediction had been used in the past to predict radiometric data over smooth seas accurately. This then was the set of temperatures (for various angles) for verification, and the transfer function was supposed to reduce the voltages recorded for the ITNC mode to these temperatures. The K-factors for the ITNC mode had been computed relative to the K-factors of the other modes in trying to fix the estimates from all modes to a single temperature.

Of the set of K-factors and antenna assembly insertion loss values which satisfied the Lunar Cal/Deep Space mission, none produced temperatures close to the expected temperatures for the ocean pass. This again demonstrated that either the transfer function was not linear from  $4^{\circ}\text{K}$  to  $170^{\circ}\text{K}$  or that our estimates of actual input temperature for either deep space or the ocean pass or both were in error. At this point, a decision had to be made as to which of the possibilities to entertain. It was felt that the dynamic range of input temperatures for which the radiometer should provide results more commensurate with past knowledge (theory and measurements from other radiometers operating with characteristics not too dissimilar) was from  $80^{\circ}\text{K}$  to around  $300^{\circ}\text{K}$ . Therefore, the decision was made to weigh more heavily the response from the ocean pass.

Once again there was a set of gain adjustment factors and antenna assembly insertion loss values that could be found which would make the computed antenna temperatures appear reasonably close to the expected or predicted values of the radiometric temperature for the ocean. These sets of parameters could not be checked by deep space data because we had already relinquished the notion that the system transfer function was linear down to  $4^{\circ}\text{K}$ . The grouping of data had been established by the selection of K-factor ratios, the absolute magnitude of the radiometric response for the mean of the various modes was, therefore, arbitrary. The only guiding criterion was that the lower the computed input temperature for deep space, the more linear we could consider the transfer function.

At this point, it was felt that a body of data obtained from more controlled conditions was required. The only such measurements to be found were from system testing

with single point temperature reference (SPTR) sources and variable point temperature reference sources (VPTR). The results of these system tests were found in the Calibration Data Report [G.E., 1973] for the hardware by the vendor (G.E.). Since the voltages were not provided in the document and efforts to obtain them proved fruitless, an inversion of the equations used by G.E. to compute the estimates of input temperatures provided ratios of the form  $(EOB-EOA)/(EOC-EOB)$ . These ratios were then inserted into the transfer function recommended by Pounds [1974]; (which was the transfer function recommended for Production Data Processing) to compute the input temperatures. A difference in the temperature computed by the G.E. algorithm and the Pounds algorithm for a similar set of voltages and temperatures was found to be small, with a maximum of 1°K at the higher temperatures.

With the ratios of  $(EOB-EOA)/(EOC-EOB)$  obtained, the gain adjustment parameters were varied so that the computed input temperature matched the actual temperature applied, at each input temperature where results were available. This then constituted the optimal set of gain adjustment parameters for each temperature for each operating mode. There was a spread in the gain adjustment factors for each input temperature within each operating mode. Rather than make the gain adjustment factors a function of temperature (and hence admit that the radiometer transfer function was non-linear even in the regular operating range of the radiometer), the average (weighted) of the gain adjustment factor for each mode was selected. Using these gain adjustment factors for each mode, the estimate of the input temperature when computed using voltage recordings and the transfer function was quite close to the actual input temperature applied. These gain adjustment factors were thus another possible set which satisfied some test results. These gain adjustment factors were used with the voltage and temperature recordings from the ocean pass, and, by a choice of values for the antenna assembly insertion loss which were very close to the loss values estimated by the vendor, the estimates of input temperature matched those predicted; these gain adjustment factors thus qualified. Based upon these K-values and the antenna assembly insertion loss that the vendor estimated, results were within the tolerances of the prediction estimate and measurement error. Thus, there were grounds to uphold the estimate (based upon the measurements and dielectric and conductive properties of materials) of the antenna assembly insertion loss as suggested by the vendor.

The antenna assembly insertion loss values are certainly not mode dependent; therefore, any expectation of grouping together the deep space results from various modes had to be done with the gain adjustment factors. Unfortunately, the grouping of temperatures

Average K-Factors

<u>Mode</u>	<u>K</u>
ITC	.83965
CTC R/S	.8595
CTC RAD ONLY	.8377
ITNC 48-40	.8325
ITNC 29-15	.8381
ITNC 0	.8386

TABLE 7.4

Mode-dependent gain adjustment factors.

measured from deep space, as computed from the K-values obtained from system test results and the vendors antenna assembly insertion loss, was not as close or as near to 4°K as hoped. The grouping, however, was a great deal closer than when using a single K-value for all modes. The computed input temperatures using these K-factors and antenna assembly insertion values were compared to those computed by using combinations of other K-factor and antenna assembly insertion loss values suggested by Martin-Marietta Co. and G.E. The closest grouping of the means from deep space data for various modes was obtained by using the K-factors recommended by this study and the antenna assembly insertion loss suggested by Martin-Marietta (assumed polarization independent and equal to  $1.06959 = 0.2927733$  dB). This combination, however, did not provide as good a match for the ocean data as the set of values recommended by this study. It was felt that a match at ocean temperatures was more important than a grouping at deep space temperatures.

With this brief description of the study, the reader is referred to a comprehensive documentation (Sobti and Collins, 1975]. The mode-dependent gain adjustment factors are given in Table 7.4, the antenna assembly insertion loss values (polarization dependent) recommended were

$$L^*_{av} = 1.0629 \quad (0.264 \text{ dB})$$

$$L^*_{ah} = 1.07325 \quad (0.3070 \text{ dB})$$

## CHAPTER EIGHT

### RESULTS FROM S-193 RADIOMETER/SCATTEROMETER OPERATION IN ORBIT

#### 8.0 General

A description and interpretation of the results obtained from the orbital operation of the S-193 radiometer/scatterometer are provided in this chapter. A description of the analyses procedures is provided in chapter seven. Being the first time that a radar scatterometer has ever operated in space and also the first time that both a radiometer and scatterometer have in near-simultaneity viewed the same target scenes, it was not possible to predict the responses beforehand. To gauge the characteristics of the response was more of an exploratory process where many diverse analyses were conducted. Most of the analyses conducted are statistical in nature. Cautionary comments have been made with each analysis where the assumptions regarding the data base have not been statistically verified prior to the analysis. Care has, however, been taken to adhere to the assumptions and in cases where a significant inference is implied, the underlying assumptions have been deemed valid.

Some attempts to compare the S-193 responses with theoretical models have been made. The gross resolution of the S-193 scatterometer provided an interesting opportunity to apply some of the analyses conducted by radar astronomers for gross scattering data from planets.

Attempts to discriminate/identify terrain features based upon the microwave response have been made and the results are provided. Some examples of image-like displays are provided. Since each type of analysis is quite distinct they are reported separately. Provided below are some of the results

## 8.1 Ensemble Statistics

### 8.1.1 General

A coarse resolution sensor like the S-193 radiometer/scatterometer has somewhat limited capability for remote sensing over land targets where the spatial resolution required is better than 200 meters. The capabilities of sensing variations on the ocean surfaces and thereby determining wind fields above the surface do, however, appear feasible even with this gross resolution. Over land, certain gross shifts in the response caused by parameters such as soil moisture can be detected; the cause for the gross shift can be expressed qualitatively but quantitative results with such resolution, if possible at all, require excessive processing and acquisition of ground data.

A major purpose of designing the data catalogue of backscattering coefficients and brightness temperatures at this resolution is to provide design information for future fine-resolution sensors operating in the 2 cms. regime, on an orbital platform. The sensors of the future will no doubt include imaging radars which have preprocessing resolutions of kilometers, even though the post-processing resolutions are fine. The response of terrain to a gross-resolution sensor is greatly affected by the large spatial extent of the target; the target can be considered as composed of many little targets whose response is added to give the response measured. The response measured by the sensor is thus the mean response of all little targets lying in the sensor's instantaneous field of view. Clearly this mean will have bounds which are much smaller than the bounds of the response of the little targets. The corresponding preprocessing dynamic range requirements for an imaging sensor will be relatively small.

For years, theoreticians have been suggesting models to describe the backscatter from extra-terrestrial targets. The scatter from large targets can hopefully be verified by applying these models to the earth response where collateral information is available; or, conversely, the applicability of the models can be tested.

For the purpose of preparing descriptive statistics of the data, all data in CSF\* format obtained from the first and second occupancies of Skylab were broken up into 3 groups: land surfaces over the continental United States of America, ocean surfaces,

---

\*Catalog Standard Format, described in Chapter Seven.

and land surfaces in South America. The North and South American regions were separated because of an obvious difference in the physiographic composition of the two regions; the North American land region contains a sampling of desert, range, agricultural terrain, and some forests, whereas the South American region contains mainly forested and savannah regions.

The data base for preparing the descriptive statistics is listed in Tables 7.1, 7.2, and 7.3 for the CTC, ITC and ITNC modes of operation. Apart from these segments, data for the ocean surfaces were obtained from Mr. James Young. These data constitute 11 files of S-193 operation using the non-contiguous mode. Data for all four groups were maintained on separate files. Each file was then sorted according to incidence angle. Histograms of the distribution of backscattering coefficient and radiometric brightness temperature were produced by considering data for each polarization state between angles separated by  $1^\circ$  increments from  $0^\circ$  to  $4^\circ$  and then in  $2^\circ$  increments from  $4^\circ$  to  $42^\circ$ . The data between incidence angles  $42^\circ$  to  $48^\circ$  were merged into one group. Means, standard deviations and decile values were also computed.

The microwave data considered in the preparation of the histograms has not been corrected for atmospheric effects. These atmospheric effects are much more severe on the radiometer than on the scatterometer signals. For example, the presence of clouds can alter the received brightness temperature by as much as  $20^\circ\text{K}$ . Precipitation can totally mask the radiation from the surface. The attenuation due to the atmosphere upon the scatterometer signals can vary by as much as 0.2 to 0.6 dB for a clear sky (depending upon incidence angle and the humidity). Due to heavy clouds, the attenuation can exceed 1 dB and, for precipitating regions, the scatter from rain particles can mask the scatter from the ground.

The physical temperature of the surface has not been accounted for in reporting on the radiometric temperature statistics. It has been shown in Chapter Three that a product of the emissivity and the physical temperature constitute the brightness temperature. Emissivity is the variable which is descriptive of the surface. For land targets in the North American region, the physical temperature of the surface can change from region to region and from day to day more than for ocean surfaces. During SL2 and SL3, data was obtained from the northern-tier states to the southwestern desert region; the difference in temperature could easily have exceeded  $15\text{-}20^\circ\text{K}$ . The period of data coverage extends from June

to August, 1973. During this period the variations in temperature over the same region can be substantial. The means of the radiometric temperature show the effect of the variations in physical temperature. To actually compute the emissivity of each target (to a first approximation divide the radiometric temperature by the physical temperature) would have been extremely time-consuming. The radiometric data, with the time, spatial coordinates and viewing angle have been archived on tape and are available for a detailed investigation at a later date.

The number of samples obtained for each polarization state and incidence angle bracket varied from nil to over 3000. The problem of determining how many "independent" samples are included in each group is very difficult. It would require classifying each sample. By "independent" samples, we mean samples from diverse physiographic and geographic regions. This is not a statistical definition, but is one which helps us appreciate how representative the statistics are of the overall North American region. Clearly, if all our samples for an angle group were obtained from a rather "pathological" case like the Utah Salt Flat, then the overall  $\sigma^0$  value would be skewed at that angle group.

To appreciate how many samples are obtained per second for the various modes, it would be instructive to review the first part of Chapter Six where the modes and their timings are described. In a nutshell, one may consider that for a particular angle group with the proper pitch dwell offset of a cross-track contiguous mode, one obtains 12 samples per scan which lasts roughly 2.12 seconds. In the non-contiguous modes of operation, the number of samples per angle group per polarization are 1 per scan which lasts 15.25 seconds. This number may be increased to four if a single polarization state was selected. The number of samples in the in-track-contiguous mode is different for the radiometer and the scatterometer (unlike the other modes): there are 50 radiometer measurements per scan to only 5 scatterometer measurements. The number of samples in an angle group for the scatterometer case is 1 per scan, which lasts 4 seconds.

With this brief explanation and cautionary note, we shall describe the statistics of each region separately.

### 8.1.2 Statistics of Response from North American Targets

The data base considered in the compilation of these statistics is shown in Figures 7.1, 7.2, and 7.3 for the CTC, ITC and ITNC modes of operation. It can be seen that the CTC modes which provide more scatterometer samples per second than any other mode, were exercised more over the western part of the country. There will perhaps be a bias

towards that part of the country. The ITC modes criss-crossed most of the country with no particular emphasis on any. The ITNC modes were only exercised over the Northern part of the country in two long sweeps. Other short segments of ITNC mode operation were discarded due to detected errors in processing or due to the extremely short length of the passes. The cross-track contiguous mode has several submodes, the areas of coverage shown in Figure 7.1 are indexed by letters, the details of the modes are provided in Table 7.1 indexed by the same letters.

Histograms have been prepared for all angles from 0 to 48° in 2° increments, with finer 1° increments for the 0° to 4° case and a grouped histogram of all data between 42° and 50°. Examples for only 6 angle groups are shown here. The angle groups shown here are those which had large sample size and provided samples along the incidence angle axis adequate to fully describe the angular nature of the backscattering coefficient. The histograms for the radiometric brightness temperature showed no angular response, whereas the backscattering coefficient showed a decisive angular response.

#### Backscattering Coefficient

The histograms for the backscattering coefficient shown here are for the angle groups 1-2°, 10°-12°, 16°-18°, 32°-33°, 33°-34°, 42°-50°. The same angle groups are chosen for the radiometric brightness temperature histograms. There were very few samples between 0° and 1°. The number of samples for horizontal polarization (scatterometer) was much less than that for vertical polarization.

Examining the histogram of the backscattering coefficient between 1° and 2°, for vertical (VV) incidence, one finds that there are two peaks (fig. 8.1). One of these is a little one from approximately +14 dB to 18 dB. This return is probably from regions like the Utah Salt Flats and some water surface which might have accidentally been included in the land regions (if it were a coastal region and the corresponding radiometer value was higher than 200°K, but the scatterometer measurement was over water). The response between 13 dB and 18 dB may actually have been much higher, but because of saturation of the scatterometer receiver at these levels, it was registered at these levels. The dispersion for this incidence angle group is quite large. The mean is at 1.59 dB and the total spread between the 10% level and the 90% level is 10.2 dB. It is interesting to observe that the lower decile is at -3.0 dB. This is much higher than the lower range reported by many aircraft programs. The spatial averaging has, no doubt, a large effect in raising the minimum. This lower decile further suggests

that altimeters need be designed to allow only for a signal slightly lower than -3.0 dB. The number of samples in the  $2^{\circ}$ - $3^{\circ}$  incidence angle group for the horizontal polarization was much more than for the  $1^{\circ}$ - $2^{\circ}$  case, and, therefore, the  $2^{\circ}$ - $3^{\circ}$  histogram was chosen as an example of near-vertical incidence with horizontal polarization. This is shown in Figure 8.2. Notice that there are three modes in the histogram. The highest one is probably due to saturation from specular or quasi-specular type targets. The mode centered at around +8 dB is from some targets which were relatively smooth. It is interesting to observe that between  $2^{\circ}$  and  $3^{\circ}$  off vertical there is still some specular-type reflection. This can be caused by one of two possibilities; either the pointing of the antenna was erroneously computed and the incidence angle was much closer to vertical than computed, or the mean slope of the surface subtended an angle of  $2^{\circ}$  to  $3^{\circ}$  so that Snell's law was satisfied for specular reflection. The latter seems like a much more remote possibility when one considers the nature of specular targets (sea surface or the Salt Flats). The fact that the mean for this set is higher than that of the  $1^{\circ}$ - $2^{\circ}$  set for vertical polarization should not be misinterpreted. The regions of coverage with the two polarizations were not the same. The horizontal polarization values were obtained more from the ITC modes than from the CTC modes. The reverse is true for the vertical polarization. The number of specular type targets that could have been subtended by the two sets probably gave rise to the difference between the two. The lower decile, however, still stays at -3 dB. The histogram for the incidence angle group  $2^{\circ}$ - $3^{\circ}$  for vertical polarization is shown in Figure 8.3. Notice again that this is a bimodal distribution with the specular portion being present just as in the case of group  $1^{\circ}$ - $2^{\circ}$ . The range of values between the upper and lower deciles is greater. The large standard deviation is again characteristic of the near nadir incidence backscatter and commensurate with past aircraft measurement programs.

The next angle group considered is between  $8^{\circ}$ - $10^{\circ}$ . The histogram of the distribution of "vertical polarization" backscatter is shown in Figure 8.4. Observe that the histogram is now unimodal and that the dispersion is comparatively less, although the number of samples is much greater. This histogram is produced solely from CTC data because no other mode of operation can provide scatterometer measurement at these angles. The mean is substantially lower and the standard deviation is less than the near nadir cases. The range from the lower decile to the upper decile is barely 4.8 dB. The two points



HISTOGRAM OF THE SCATTEROMETER BACKSCATTER COEFFICIENT

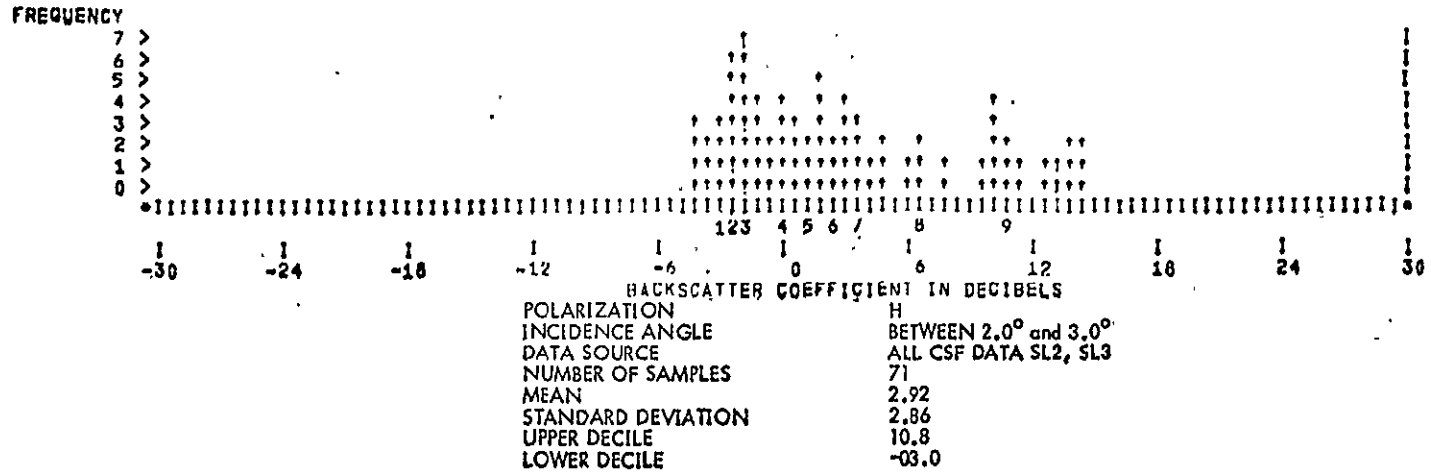


Figure 8.2.

HISTOGRAM OF THE SCATTEROMETER BACKSCATTER COEFFICIENT

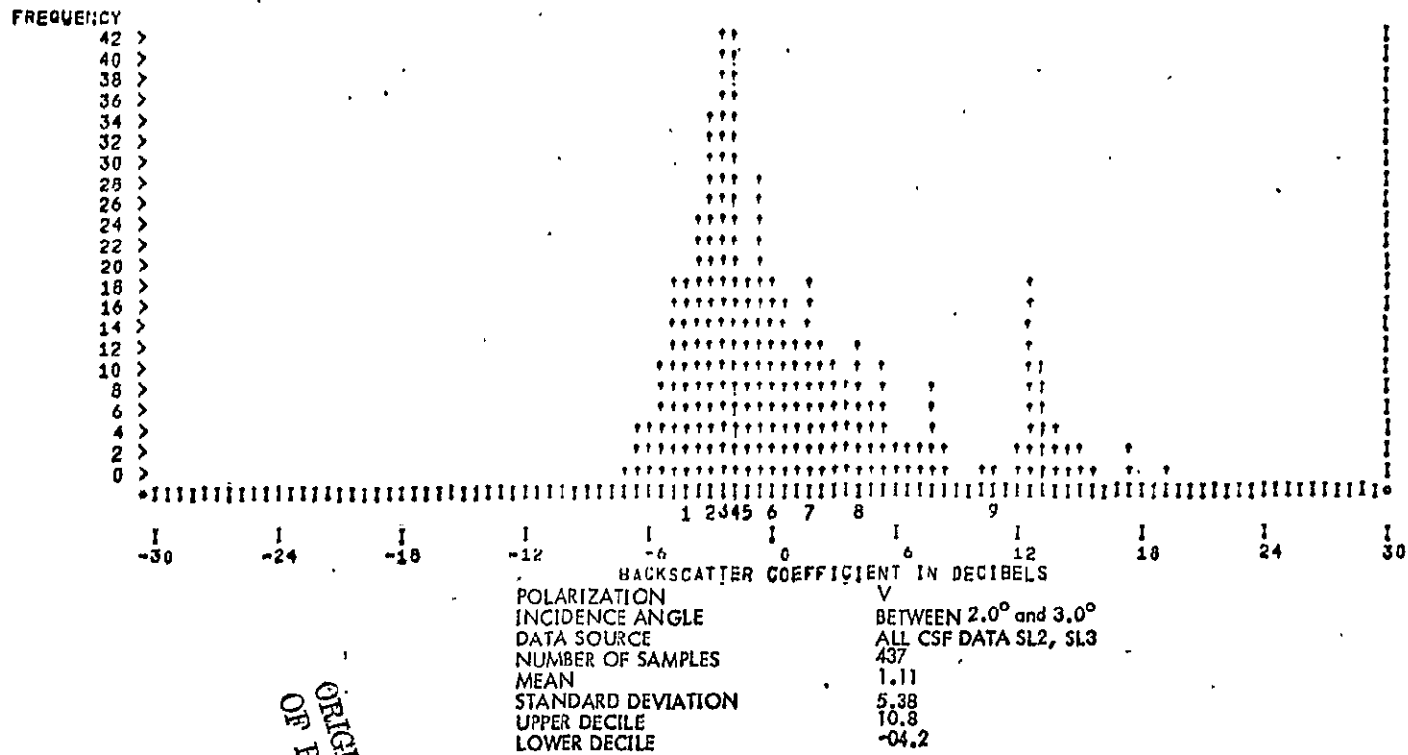


Figure 8.3.

ORIGINAL PAGE IS  
OF POOR QUALITY



below -12 are probably due to ocean surfaces or the Utah Salt Flat. The number of horizontally polarized samples was not sufficient to warrant a histogram for this angle group.

The next angle group considered here is from  $16^{\circ}$ - $18^{\circ}$ . The histogram for vertical polarization is shown in Figure 8.5. Observe now that the distribution has one major sharp mode and little one above 0 dB. The reason for the little mode above 0 dB is not known. A probable cause is erroneous processing of data from the voltages of the EREP tape to a backscatter value or an erroneous processing of the incidence angle. The number of samples is much higher than any of the angle groups considered so far. The mean is, as expected, lower and the spacing between the upper and lower deciles is 4.6 dB. This is again commensurate with prior measurement programs and with theoretical estimates. The theory suggests that this may be a cross-over region between smooth and rough surfaces. The data here seem to bear this out. The histogram for the same angle group ( $16^{\circ}$ - $18^{\circ}$ ) for horizontal polarization shows the same characteristics although the number of samples is much much smaller.

The largest number of samples was for the angle group  $32^{\circ}$ - $34^{\circ}$ . The contributions to this angle group come from all three modes, but the largest contribution is from the CTC pitch-offset  $29^{\circ}$ , mode. This mode was concentrated over the southern to southwestern region. The histogram for vertical polarization is shown in Figure 8.6. The range between deciles is below 5 dB. The histogram for horizontal polarization for this angle group is shown in Figure 8.7.

Angles between  $42^{\circ}$  and  $50^{\circ}$  were lumped into one group to get enough samples. The only CTC which could contribute would be pitch offset  $40^{\circ}$  and this configuration was exercised only once over North America. Therefore, a majority of samples for this angle group are from the ITC and ITNC modes. The histogram for vertical polarization is shown in Figure 8.8. Notice that the range is from -5 dB to -25 dB. The -25 dB values are probably a patch of the ocean surface that sneaked in this histogram for land. The backscatter response seems to be leveling off with angle because the difference between the means for the  $32^{\circ}$ - $34^{\circ}$  incidence angle group and the  $42^{\circ}$ - $50^{\circ}$  angle group is of the order of 1.5 dB. The histogram for the horizontal polarization is shown in Figure 8.9; the mean for this is higher than for vertical polarization but the difference should not be construed as significant. The histograms suggest that the range of targets from very smooth to very rough will provide a backscatter between -5 dB and -26 dB. The range of the decile values is only about 7dB, implying that the values beyond these deciles are either not provided proper representation in these statistics or are truly isolated cases. Observing that the ITC modes are fairly even in their coverage of the U.S., one would tend to prefer the latter possibility.

HISTOGRAM OF THE SCATTEROMETER BACKSCATTER COEFFICIENT

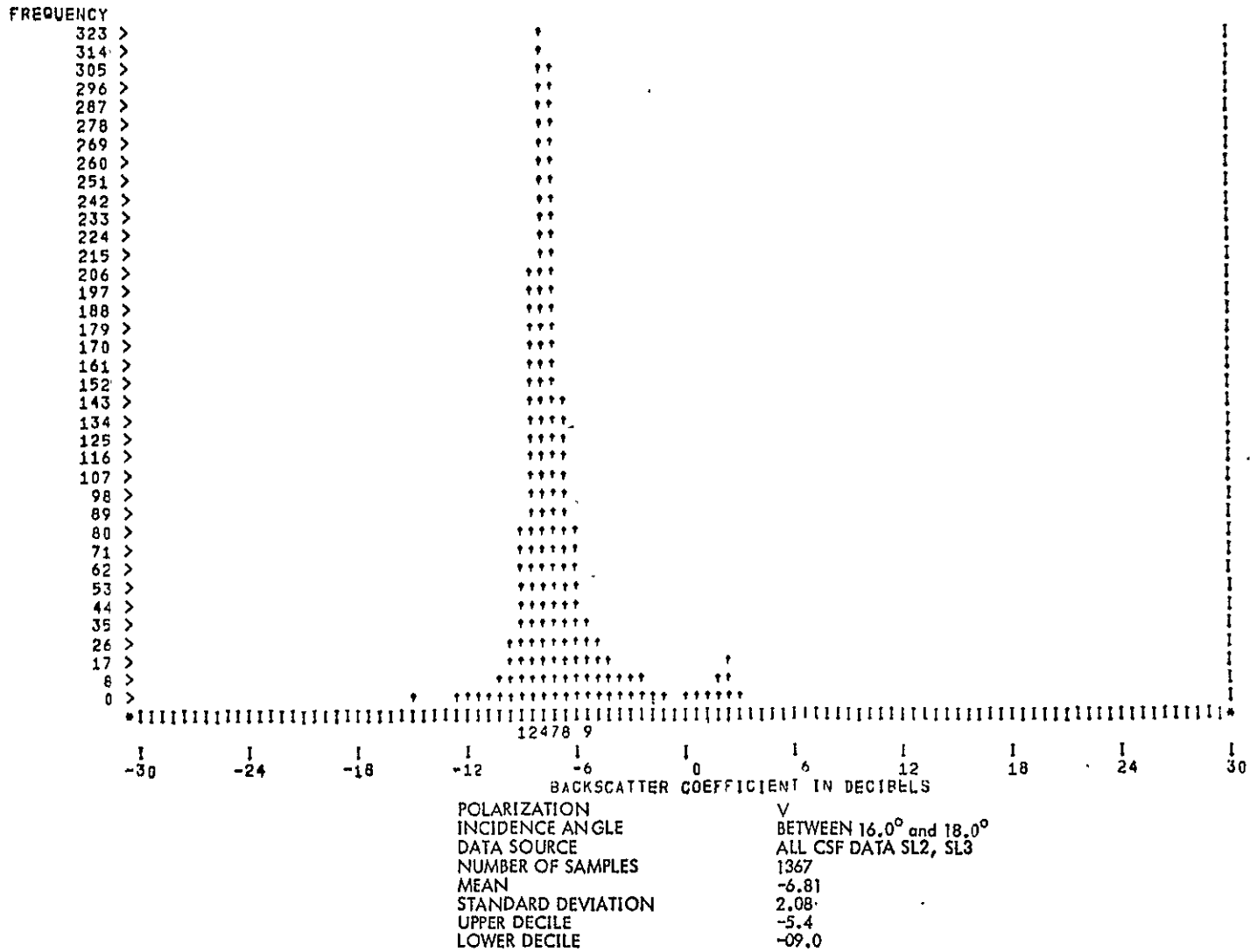
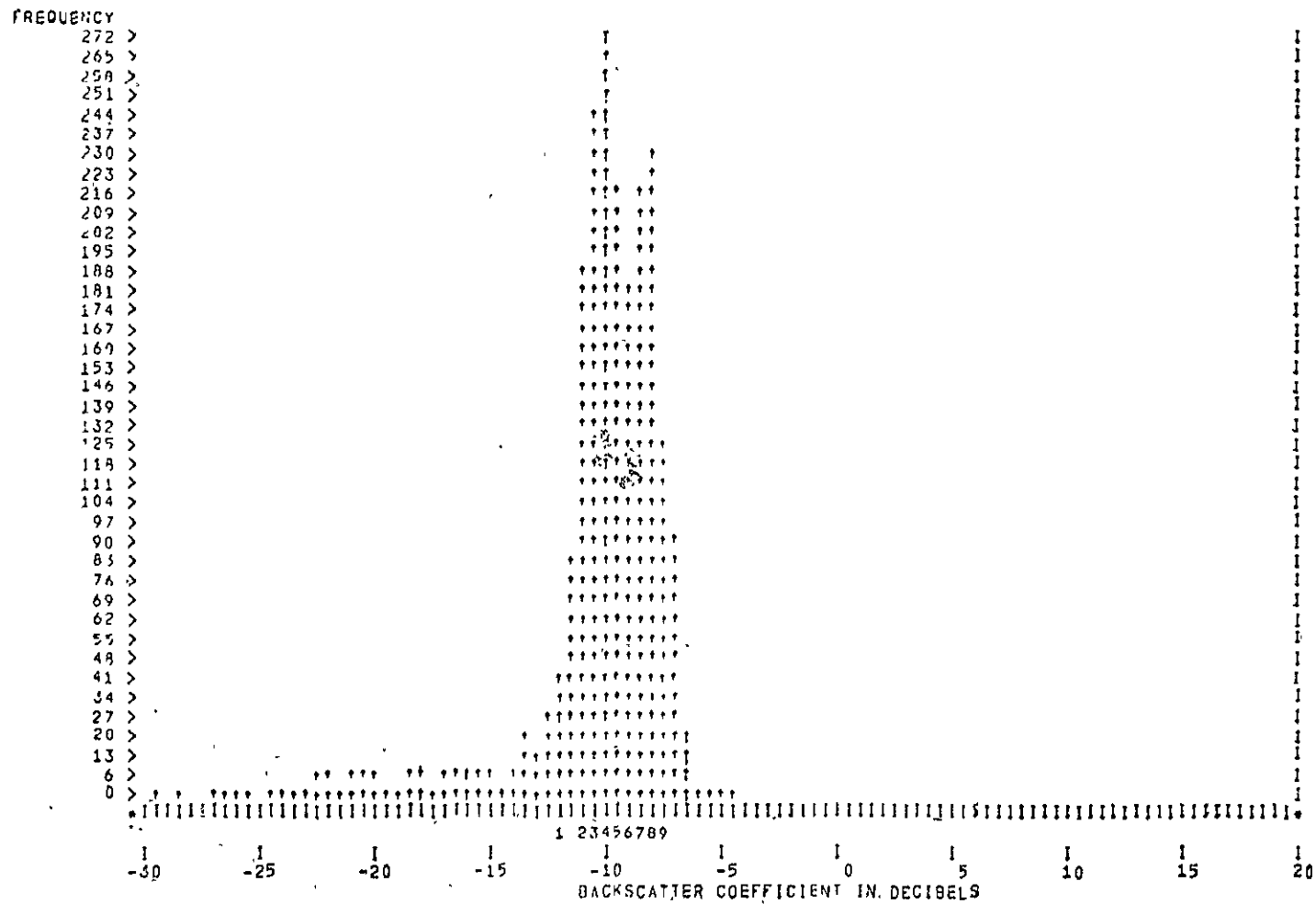


Figure 8.5.

ORIGINAL PAGE IS  
 OF POOR QUALITY

HISTOGRAM OF THE SCATTEROMETER BACKSCATTER COEFFICIENT



POLARIZATION V  
 INCIDENCE ANGLE BETWEEN 32 AND 34°  
 DATA SOURCE ALL CSF DATA SL2, SL3  
 NUMBER OF SAMPLES 2161  
 MEAN -9.86  
 STANDARD DEVIATION 2.97  
 UPPER DECILE -7.5  
 LOWER DECILE -12.0

Figure 8.6.

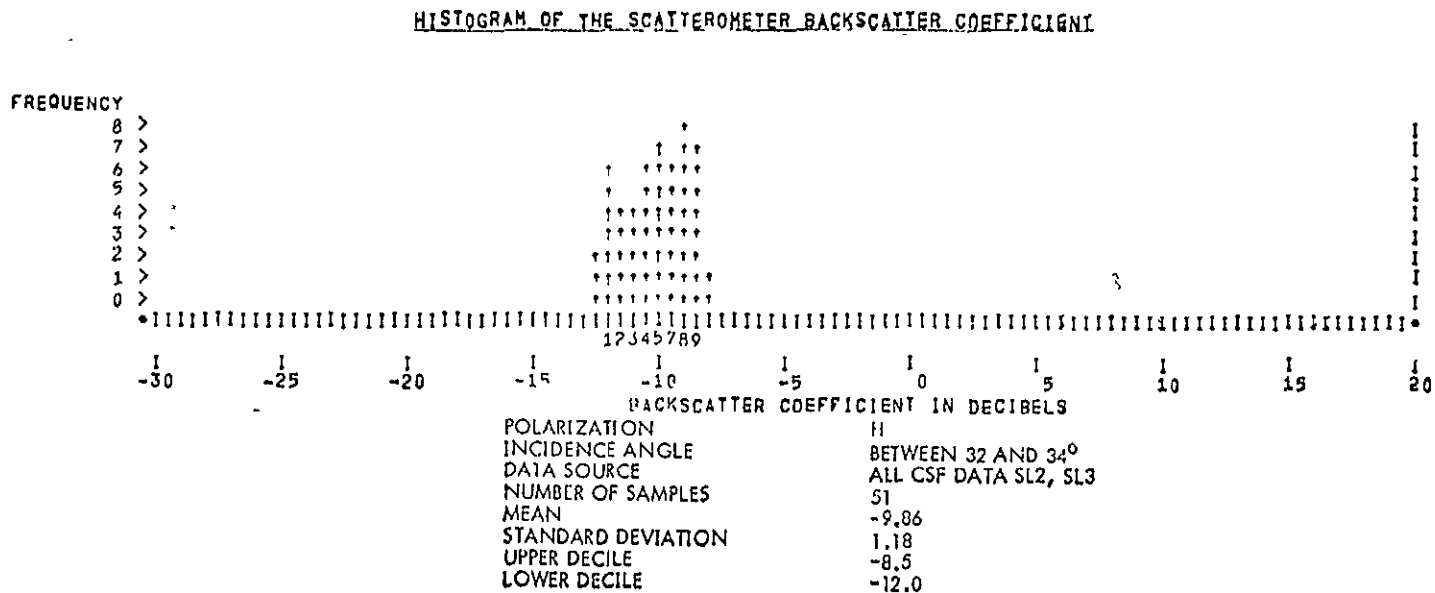
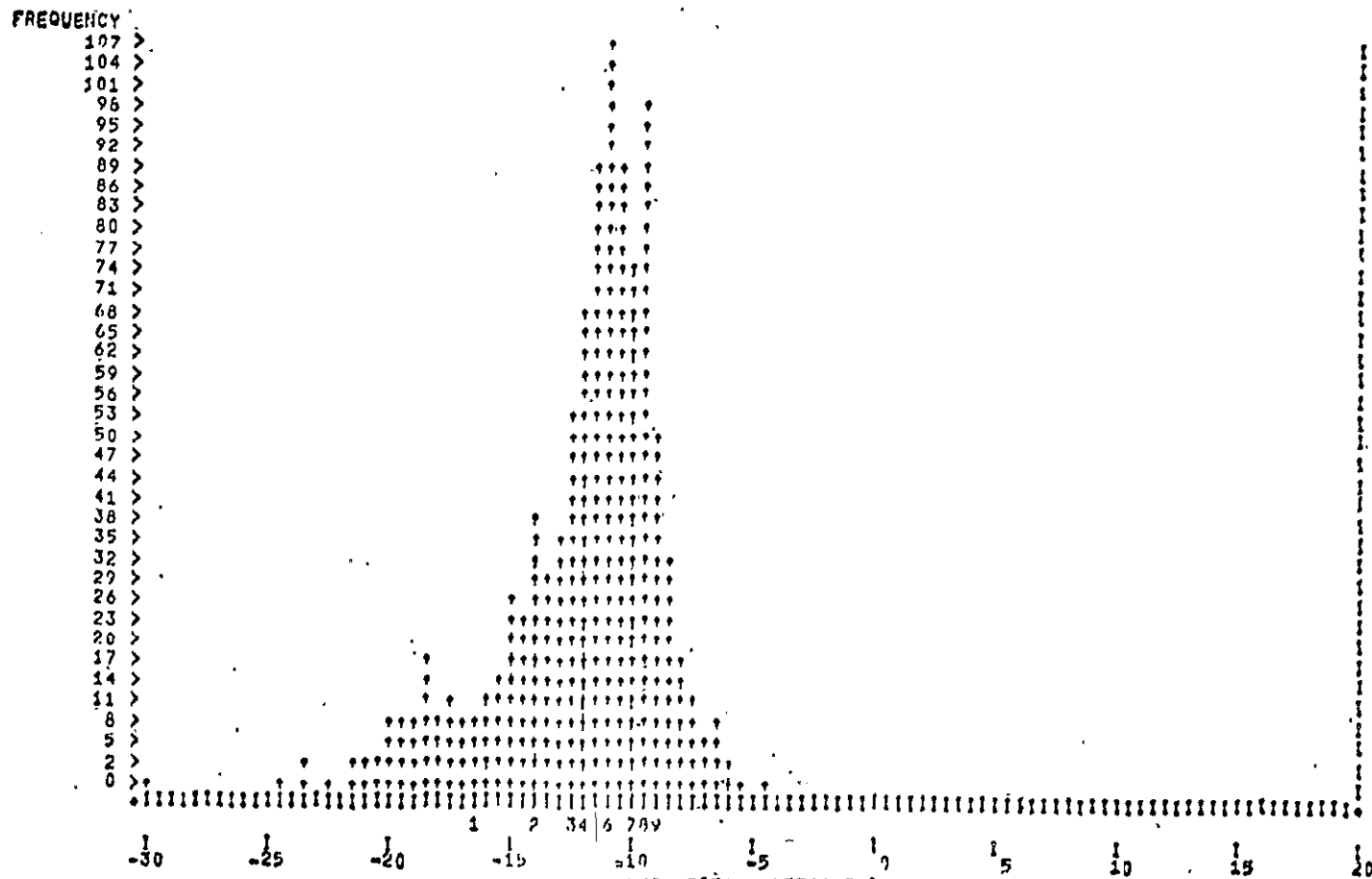


Figure 8.7.

HISTOGRAM OF THE SCATTEROMETER BACKSCATTER COEFFICIENT



379

POLARIZATION VV  
 INCIDENCE ANGLE BETWEEN 42.0° and 50.0°  
 DATA SOURCE ALL CSF DATA SL2, SL3  
 NUMBER OF SAMPLES 1004  
 MEAN -11.66  
 STANDARD DEVIATION 3.05  
 UPPER DECILE -9.0  
 LOWER DECILE -16.5

Figure 8.8.

HISTOGRAM OF THE SCATTEROMETER BACKSCATTER COEFFICIENT

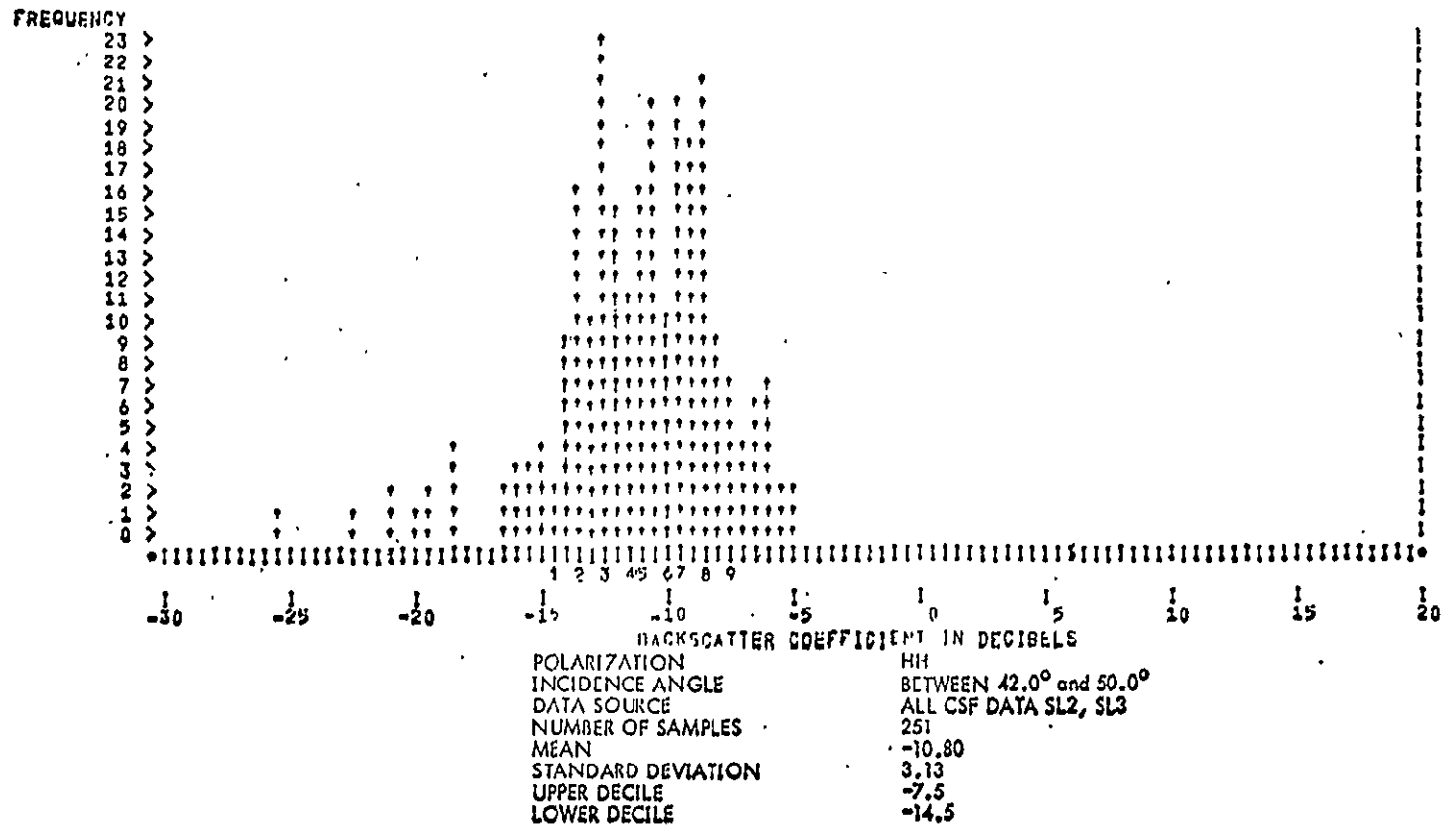


Figure 8.9.

ORIGINAL PAGE IS  
OF POOR QUALITY

381

### HISTOGRAM OF THE RADIOMETER BRIGHTNESS TEMPERATURE

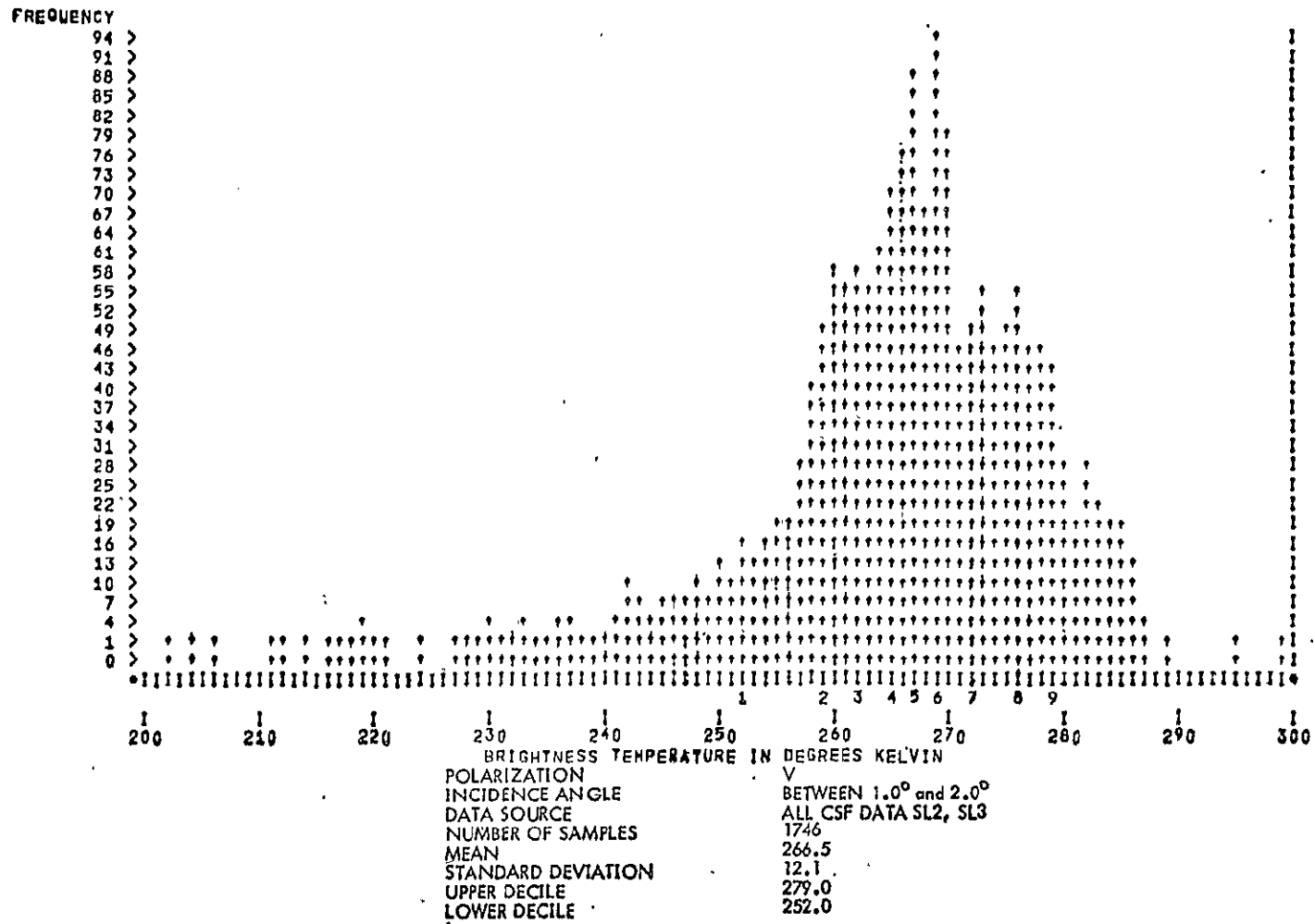


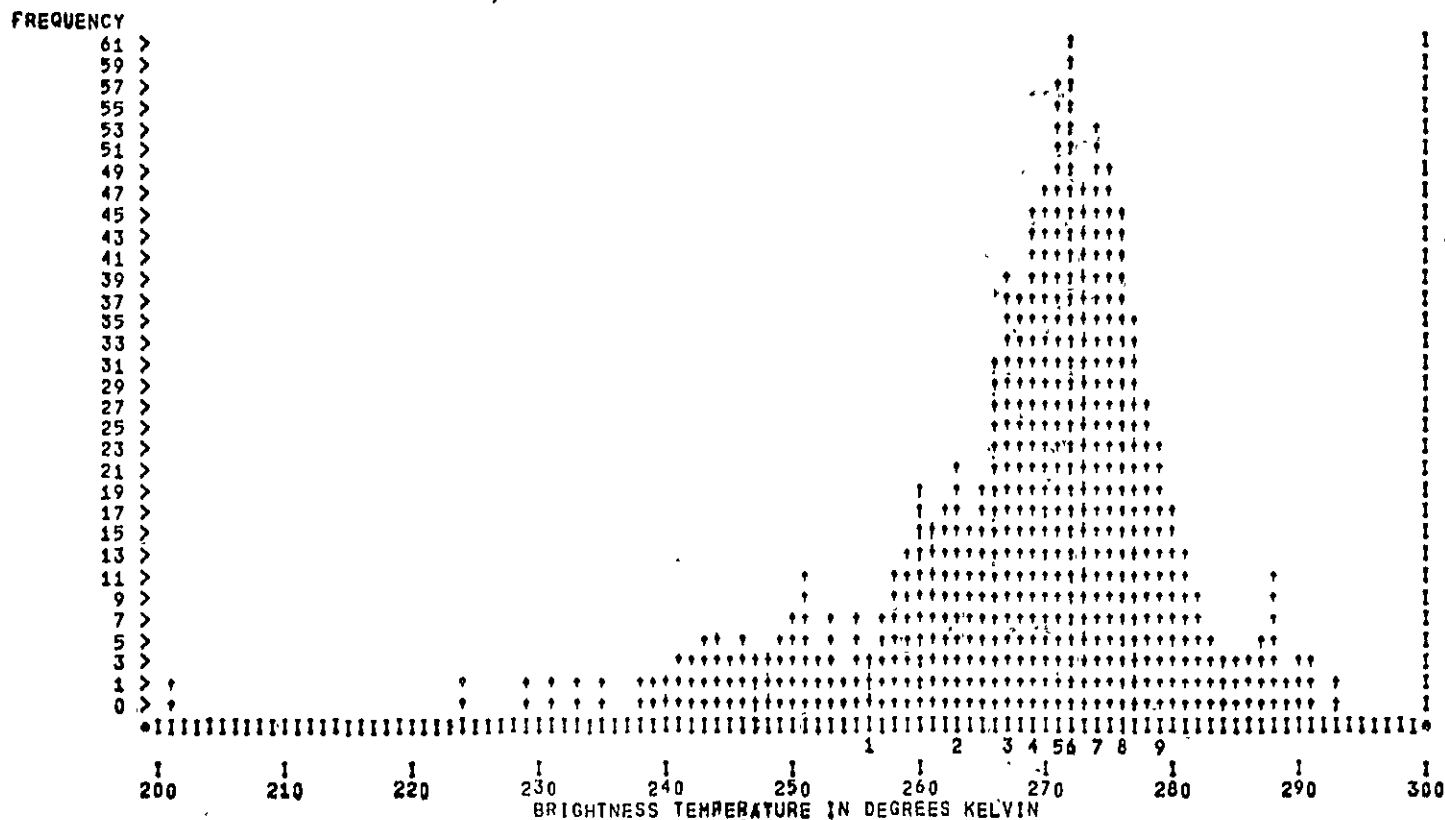
Figure 8.10.

## Radiometric Temperature

Histograms of the radiometric brightness temperature were prepared for the same angle groups as for the scatterometer measurements. There was no particular angular trend noted in the means for the radiometric temperature for the various angle groups. The radiometric temperatures ranged from around 200°K to about 295°K. Some measurements registered below 200°K, but all of them could be attributed to the presence of large water bodies lying in the target area. These measurements were ignored in compiling both the histograms and the statistics for the radiometric response.

The radiometric response for the angle group 1°-2° for vertical polarization is shown in Figure 8.10. The distribution is unimodal, but has a wide dispersion and trails off all the way down to 202°K. The lower tail is probably from the specular-type targets like the Salt Flat where it was determined that the subsurface was saturated with moisture and the covering dry surface layer was much thinner than the skin depth at 2 cms. [Ulaby et al., 1975]. No corrections were made for the physical temperature; if such corrections were made the scatter would be less. The mean for this angle group was 266.5°K with standard deviation of 12.1°K. The number of samples of radiometer measurements is much more than that for the scatterometer because of the CTC rad-only modes that were exercised. Also many data segments had the scatterometer data incorrectly processed (at NASA/JSC), but the radiometer temperature appeared to be correct. The corresponding histogram for horizontal polarization for the same angle group is shown in Figure 8.11. The number of samples in this group is much smaller than for vertical polarization. At or near nadir incidence, the response for vertical and horizontal polarizations should be the same. Since the data for vertical and horizontal polarizations were obtained from different regions, there is a slight difference in the statistics. The radiometer temperature is extremely sensitive to soil moisture, and the values in the neighborhood of 230°K could perhaps be caused by a greater soil moisture content. Figure 8.12 shows the histogram of the distribution for the angle group 2°-3° for vertical polarization. The shape of the distribution curve merely reflects the various geographic areas (with perhaps differing physical temperatures) that were included in compiling the histogram. The lower temperatures (below 215°K) are attributable to the Salt Flat region where the moisture phenomenon is the cause. The number of samples for horizontal polarization for this angle group (2°-3°) is much less; the histogram is shown in Figure 8.13. The radiometer measurements in this group have a large proportion obtained from ITC (HH) passes. These passes can be seen from Figure 7.2 to be over very diverse regions of the country.

HISTOGRAM OF THE RADIOMETER BRIGHTNESS TEMPERATURE



POLARIZATION H  
 INCIDENCE ANGLE BETWEEN 1.0° and 2.0°  
 DATA SOURCE ALL CSF DATA SL2, SL3  
 NUMBER OF SAMPLES 918  
 MEAN 269.6  
 STANDARD DEVIATION 10.1  
 UPPER DECILE 279.0  
 LOWER DECILE 256.0

ORIGINAL PAGE IS  
OF POOR QUALITY

Figure 8.11.

HISTOGRAM OF THE RADIOMETER BRIGHTNESS TEMPERATURE

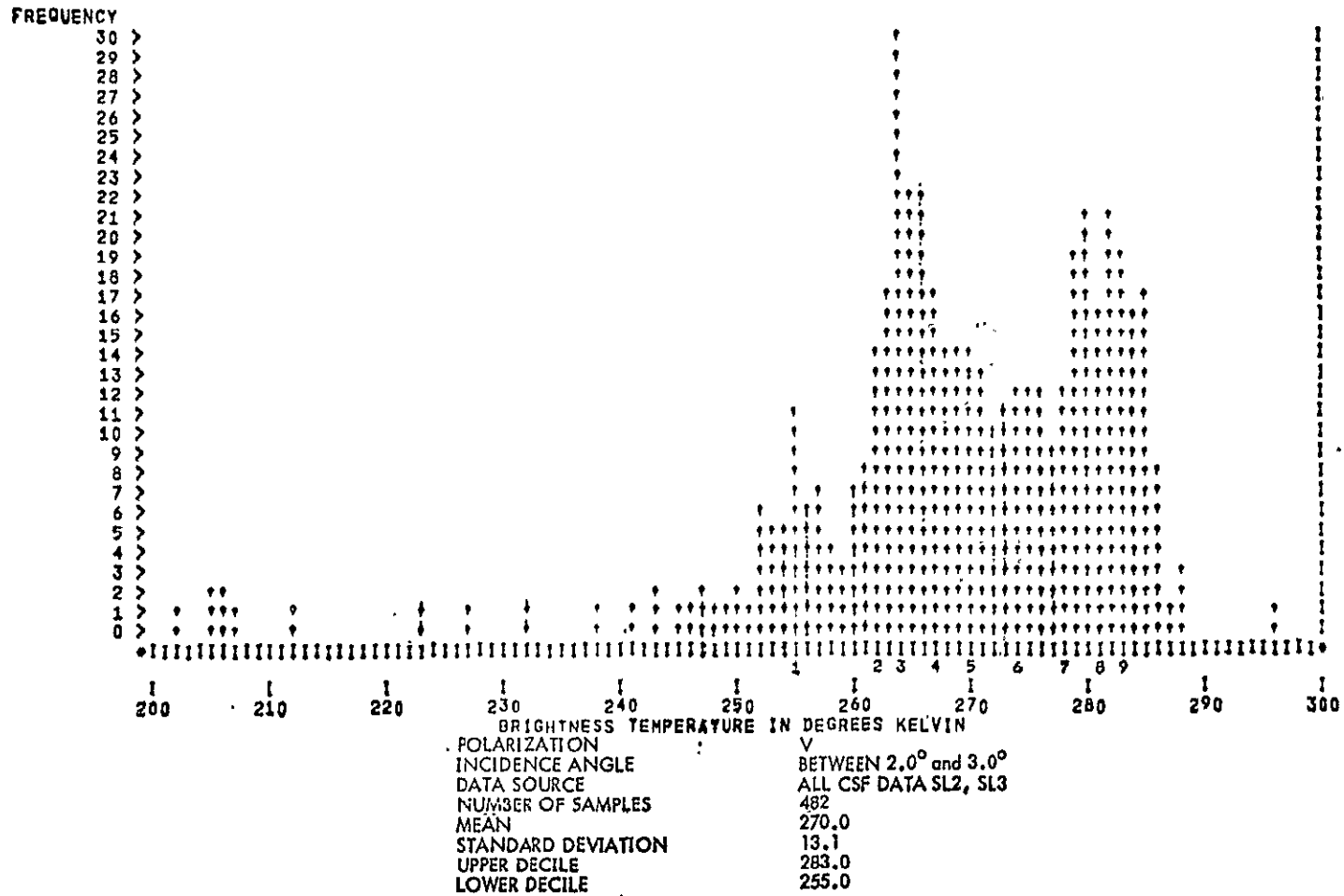


Figure 8.12.

HISTOGRAM OF THE RADIOMETER BRIGHTNESS TEMPERATURE

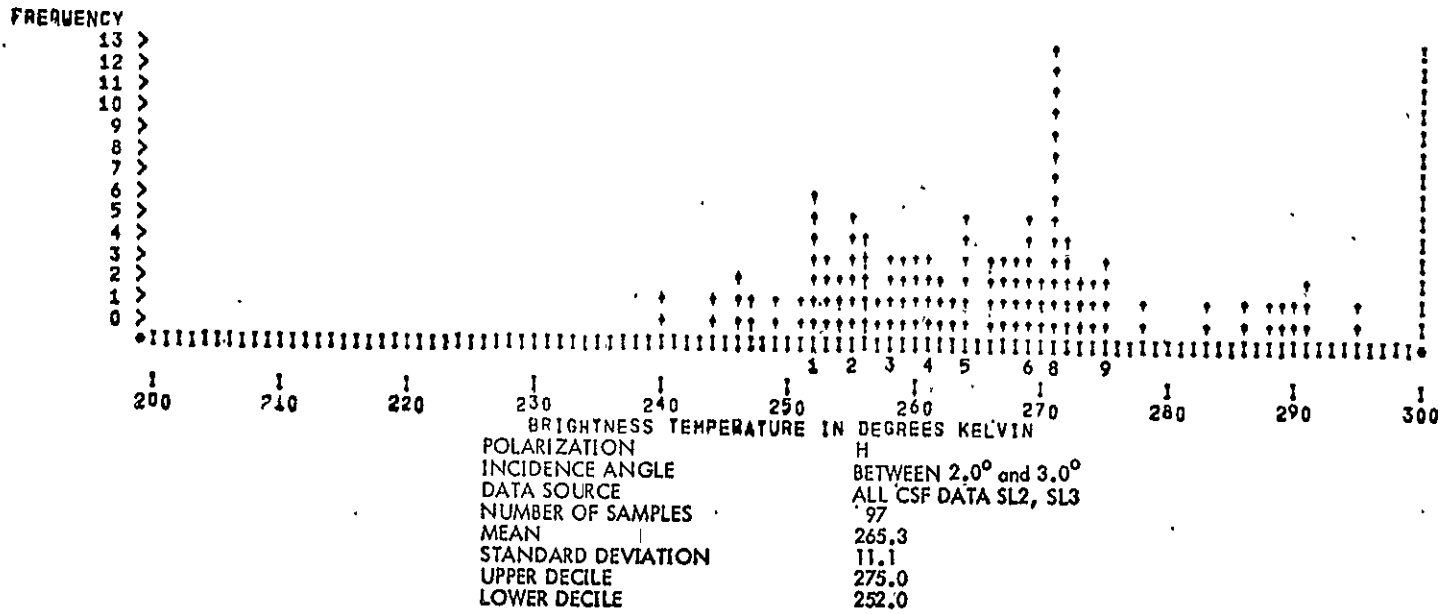


Figure 8.13.

Figure 8.14 shows the histogram for vertical polarization between  $8^{\circ}$  and  $10^{\circ}$ . The number of samples is 1453. The contribution to this histogram came from CTC (R/S) and ITC (HH) passes. Figure 8.15 shows the corresponding histogram for horizontal polarization. There is a little mode centered at  $290^{\circ}\text{K}$ . This came predominantly from the southwest desert region where the physical temperature was high and the soil moisture was probably low. The mean for this angle group has not deviated substantially from the near nadir cases. Figure 8.16 shows the histogram for the angle group  $16^{\circ}$ - $18^{\circ}$  for vertical polarization. There is a mode at around  $273^{\circ}\text{K}$  and then an almost uniform distribution all the way till  $201^{\circ}\text{K}$ . One possible cause of this trail of values from  $262$  to  $201^{\circ}\text{K}$  is that the CTC R/S roll right  $15^{\circ}$  mode was operated over Minnesota. There are many water bodies in that region and, consequently, the radiometric temperature ranged from about  $220$  to about  $260^{\circ}\text{K}$ . The temperatures registered below  $220^{\circ}\text{K}$  are probably due to the saturated conditions in the Salt Flat region and any land/water boundaries where the total footprint was not all land or all water. The histogram for the corresponding horizontal polarization case is shown in Figure 8.17. Histograms for the incidence angle groups  $18^{\circ}$ - $20^{\circ}$  for vertical and horizontal polarization are shown in Figures 8.18 and 8.19. The response is very similar to the  $16^{\circ}$ - $18^{\circ}$  angle group. Observe, however, the point made repeatedly about not having corrected for physical temperature; the  $18^{\circ}$ - $20^{\circ}$  response with vertical polarization shows a mean which is lower than that of the  $16^{\circ}$ - $18^{\circ}$  group. Theory and all prior measurements suggest that with the exclusion of a Lambert law type surface, the response with vertical polarization should rise with incidence angle till the Brewster angle. There is no obvious difference in the data base for the two angle groups between  $16^{\circ}$ - $18^{\circ}$  and  $18^{\circ}$ - $20^{\circ}$ , except that more of the ITC data should fall in the  $18^{\circ}$ - $20^{\circ}$  group than in the  $16^{\circ}$ - $18^{\circ}$  group (which includes a scatterometer measurement at those angles). The histogram for horizontal polarization also shows a slight decrease from the preceding  $16^{\circ}$ - $18^{\circ}$  angle group. This is in accordance with theory and prior measurements. The angle group  $32^{\circ}$ - $34^{\circ}$  contains the most samples and data are contributed by both

HISTOGRAM OF THE RADIONETER BRIGHTNESS TEMPERATURE

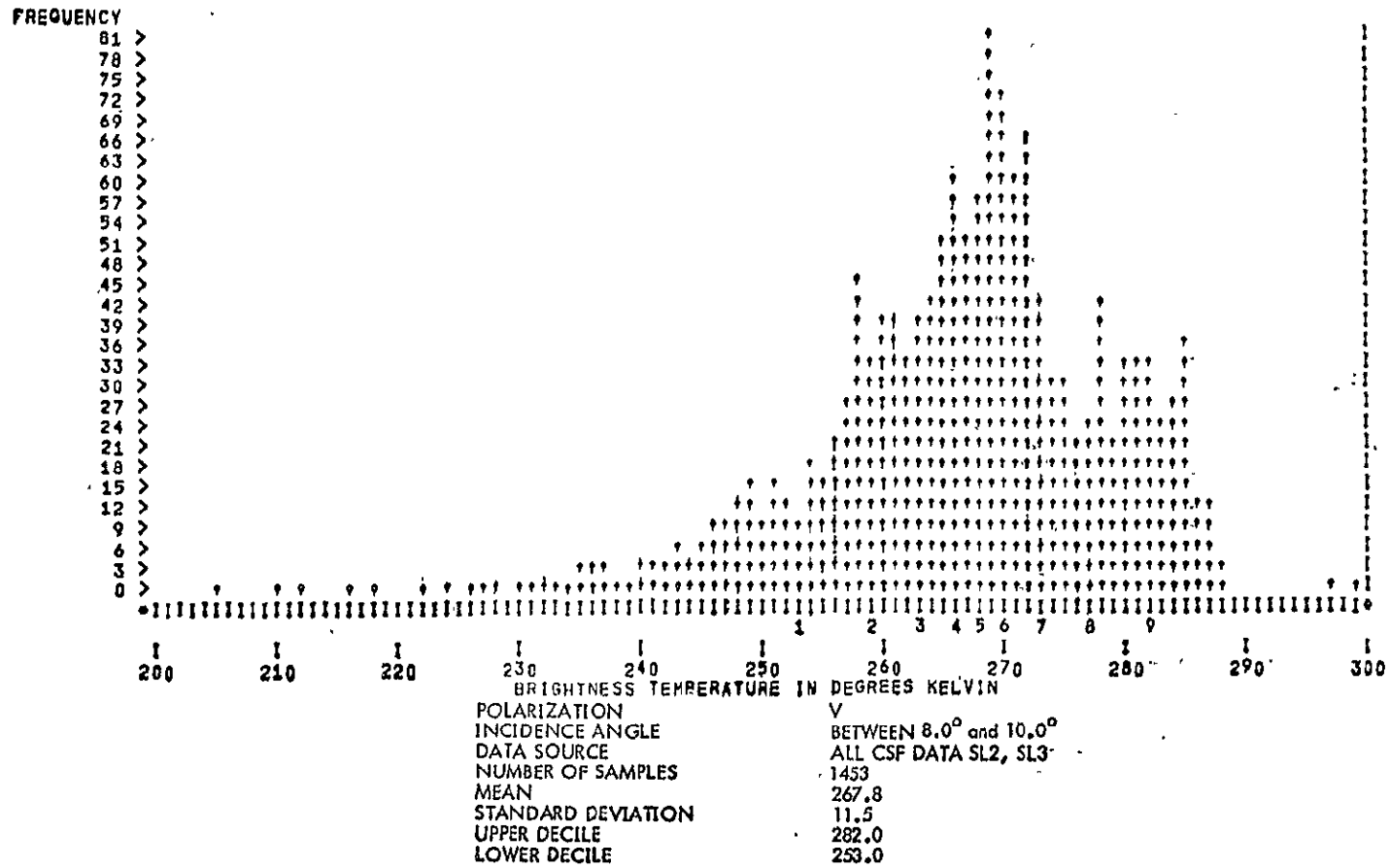


Figure 8.14.

HISTOGRAM OF THE RADIOMETER BRIGHTNESS TEMPERATURE

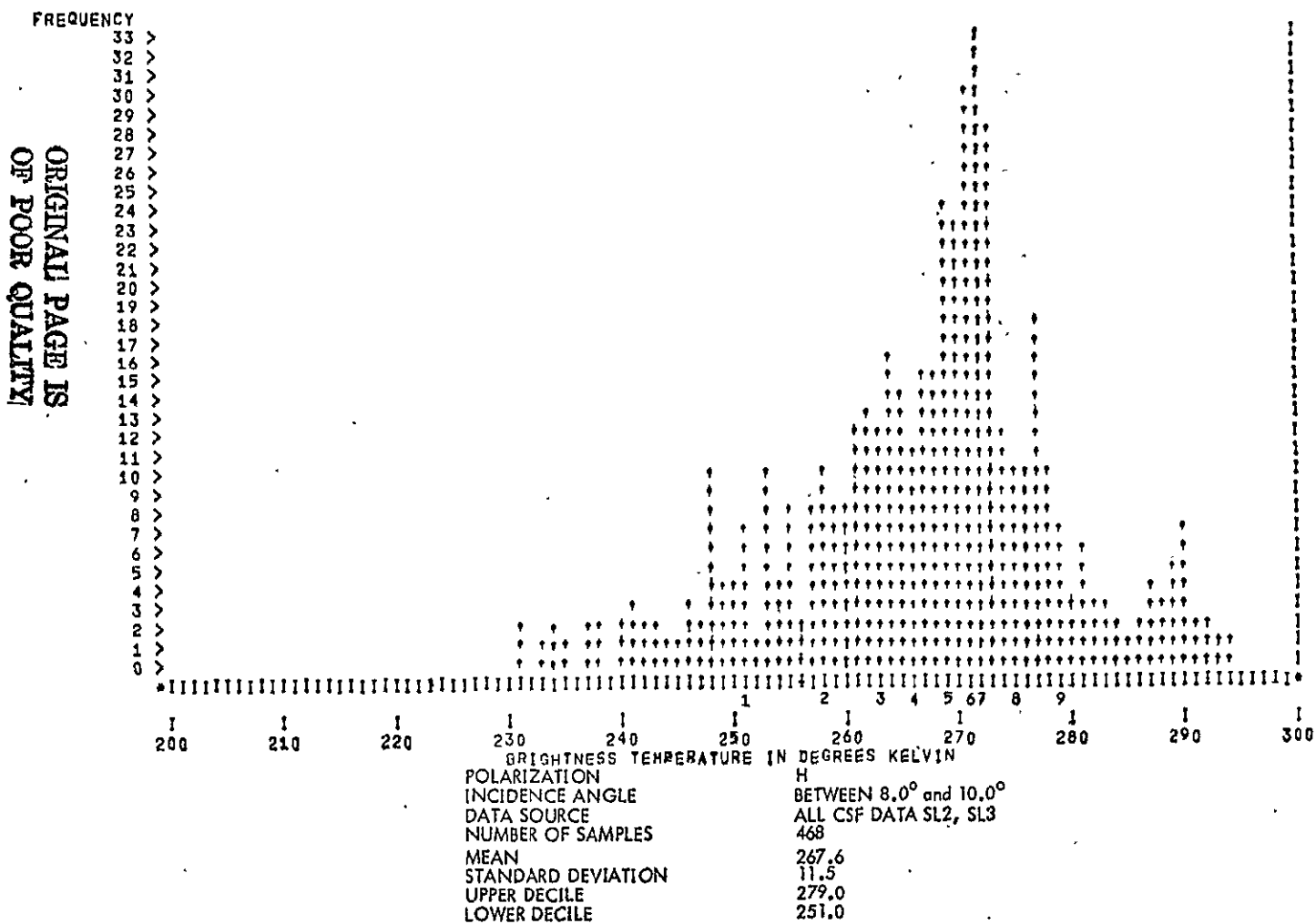


Figure 8.15.

HISTOGRAM OF THE RADIMETER BRIGHTNESS TEMPERATURE

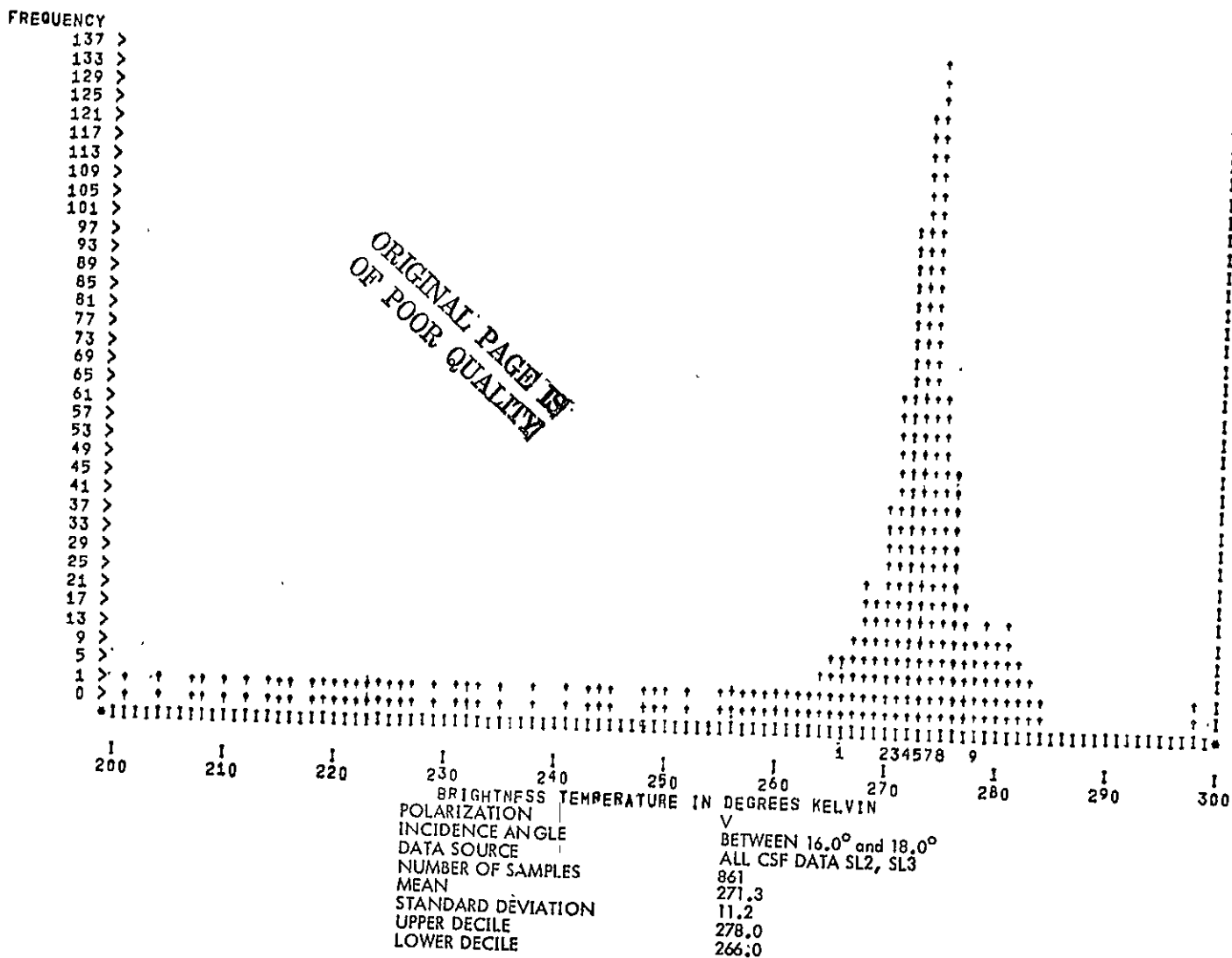


Figure 8.16.

HISTOGRAM OF THE RADIOMETER BRIGHTNESS TEMPERATURE

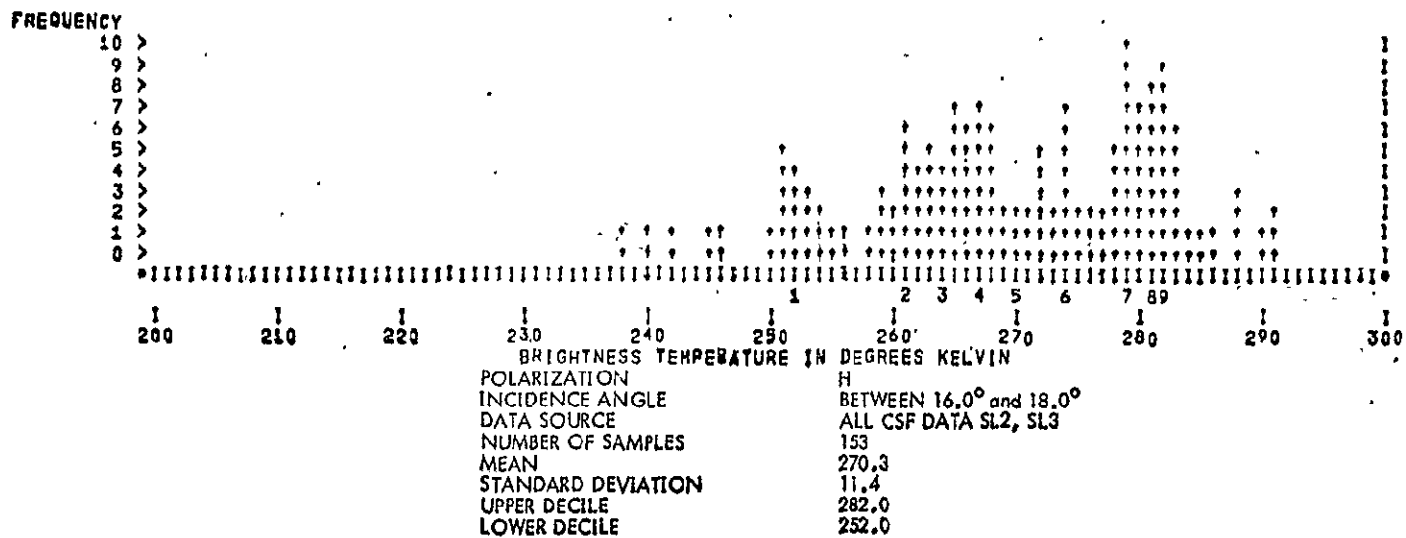


Figure 8.17.



HISTOGRAM OF THE RADIOMETER BRIGHTNESS TEMPERATURE

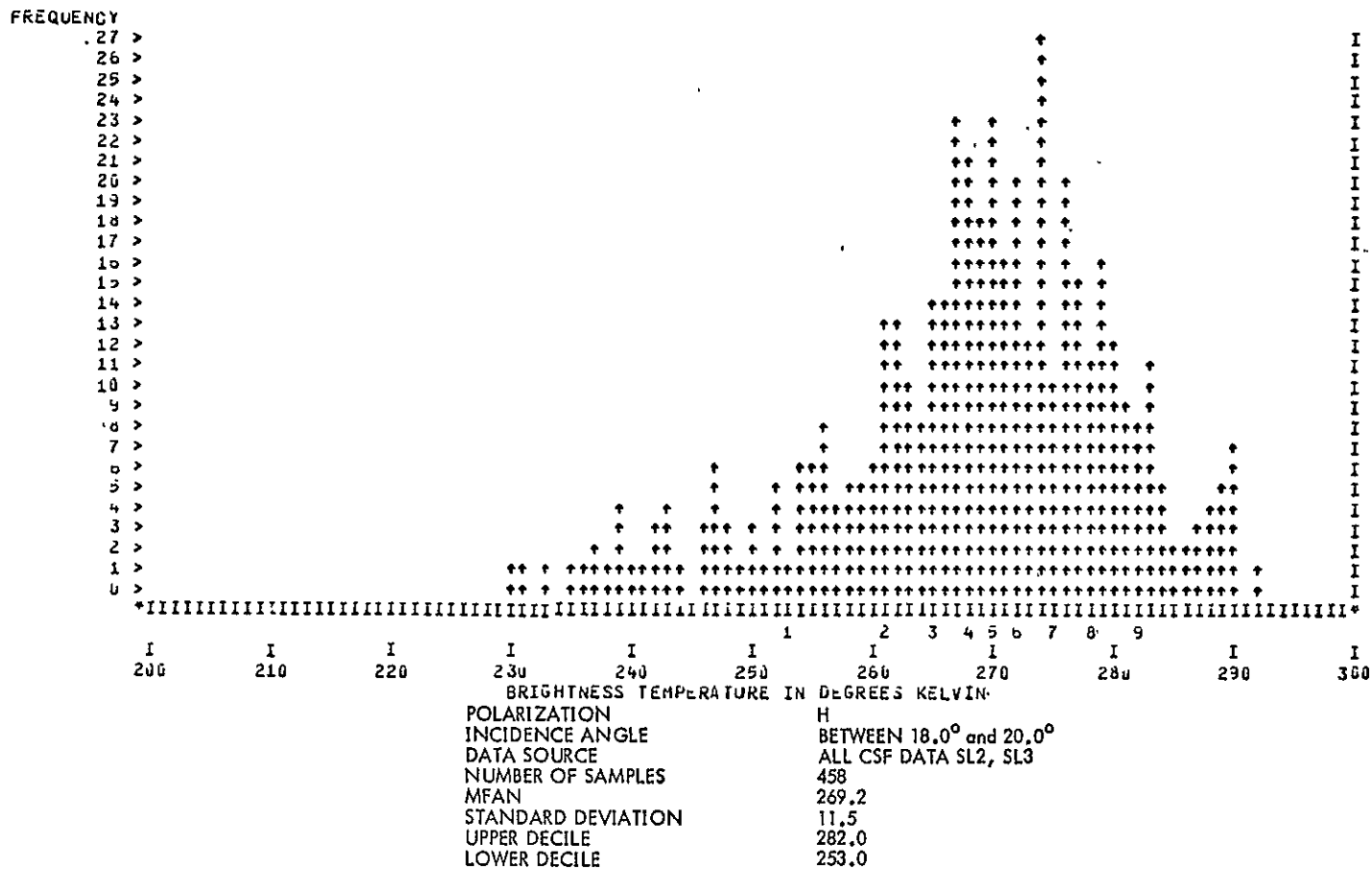


Figure 8.19.

in-track modes and the CTC pitch offset  $29^\circ$  radiometer/scatterometer mode. The histogram for this group is shown in Figure 8.20. Observe that the mean is higher and the deciles are also tending higher. The trail of points below  $255^\circ\text{K}$  could be present due to some large water bodies, or, more likely, due to land/water interfaces. The main lobe of the distribution peaks up at about  $284^\circ\text{K}$ , even though the mean is computed as  $277.7^\circ\text{K}$ . This is due to the points lying below  $260^\circ\text{K}$  which tend to bring down the mean. The histogram for the corresponding horizontal polarization response is shown in Figure 8.21. The number of samples is much less than for vertical polarization; the mean is higher than for the  $18^\circ$ - $20^\circ$  angle group, although the difference is not great. This is not characteristic of any measurements conducted with aircraft sensors.

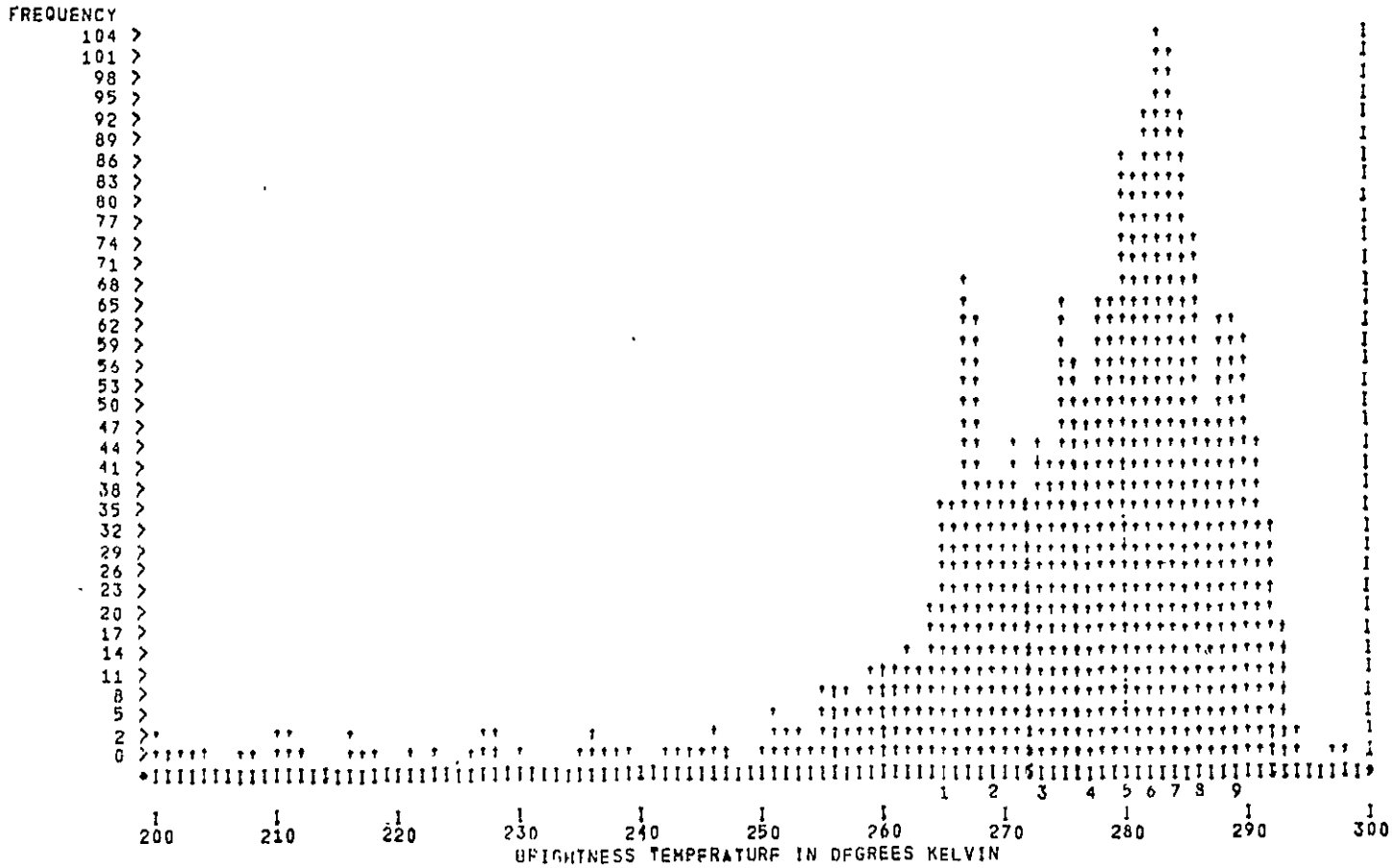
At this point, it might be conjectured that the terrain surface with contributions arriving from such a large area appears to the radiometer like a mild Lambert law surface, the word "mild" being suggestive of roughness with a truly Lambert law surface being one which shows a flat angular response to both polarizations. Blinn [1975] in his experiments found that it does not require much roughness before the surface starts appearing in its response like a Lambert-law surface. His experiments were conducted by raking fields and measuring responses for various surface roughnesses. It is not entirely clear if the response of the terrain would lack an angular dip or upheaval if the radiometric response had been appropriately corrected for physical temperature differences. This study, due to lack of time could not include such corrections, but such a correction should be made in future studies.

The angular response between  $42^\circ$ - $50^\circ$  for vertical and horizontal polarization is shown in Figures 8.22 and 8.23. The contributions to this angle group arrive from the in-track modes and from a CTC pitch offset  $40^\circ$  mode operated over the mid-American region. The mean for vertical polarization registers a sharp drop from the corresponding  $32^\circ$ - $34^\circ\text{K}$  angle group. The number of samples is the largest of all angle groups because of the large angular spread included in this group. There is no apparent reason for the drop in the mean radiometric temperature except that the targets viewed are not the same as for the  $32^\circ$ - $34^\circ$  case which included a large proportion of CTC pitch  $29^\circ$  passes which emphasized the Southern and Southwestern part of the country. The peak of the main lobe is centered at  $272^\circ\text{K}$ , and, as usual, values trail down all the way to  $200^\circ\text{K}$ . The histogram for horizontal polarization for this angle group is shown in Figure 8.23. The mean is lower than the corresponding  $32^\circ$ - $34^\circ$  angle group.

ORIGINAL PAGE IS  
OF POOR QUALITY

394

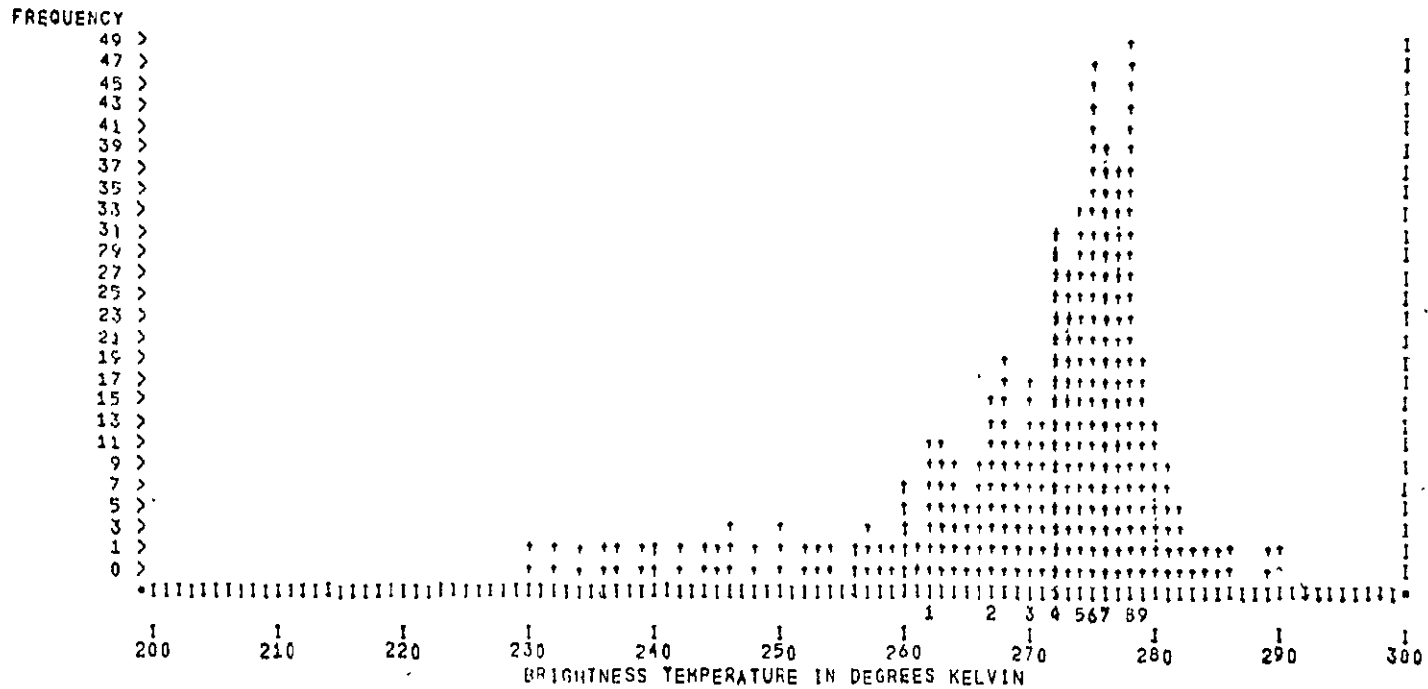
HISTOGRAM OF THE RADIOMETER BRIGHTNESS TEMPERATURE



POLARIZATION V  
 INCIDENCE ANGLE BETWEEN 32 AND 34°  
 DATA SOURCE ALL CSF DATA SL2, SL3  
 NUMBER OF SAMPLES 1094  
 MEAN 277.72  
 STANDARD DEVIATION 11.91  
 UPPER DECILE 289.0  
 LOWER DECILE 265.0

Figure 8.20.

HISTOGRAM OF THE RADIOMETER BRIGHTNESS TEMPERATURE

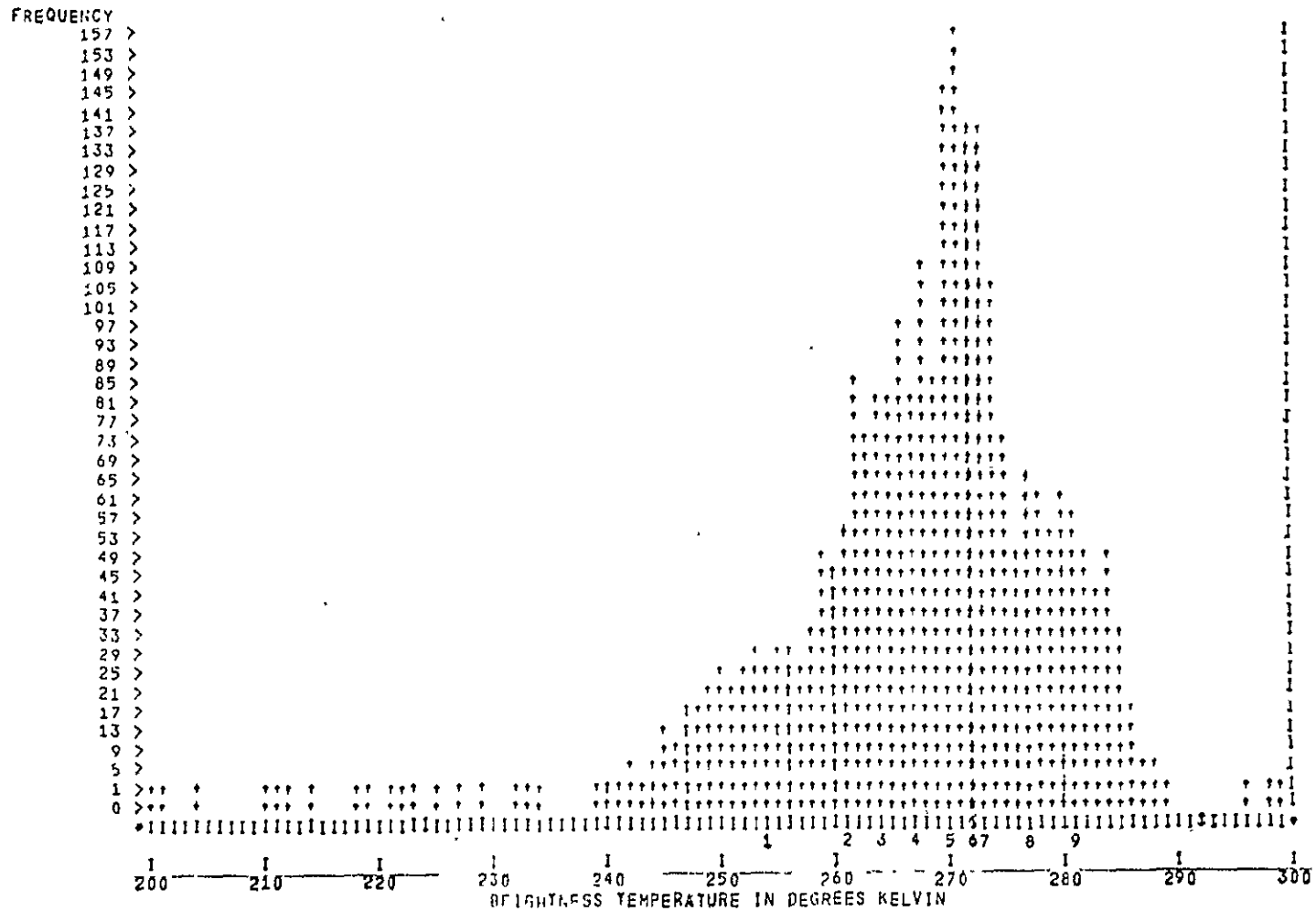


POLARIZATION H  
 INCIDENCE ANGLE BETWEEN 32 AND 34°  
 DATA SOURCE ALL CSF DATA SL2, SL3  
 NUMBER OF SAMPLES 486  
 MEAN 272.12  
 STANDARD DEVIATION 8.52  
 UPPER DECILE 279.0  
 LOWER DECILE 262.0

ORIGINAL PAGE IS  
OF POOR QUALITY

Figure 8.21.

HISTOGRAM OF THE RADIOMETER BRIGHTNESS TEMPERATURE



POLARIZATION V  
 INCIDENCE ANGLE BETWEEN 42 AND 50  
 DATA SOURCE ALL CSF DATA SL2, SL3  
 NUMBER OF SAMPLES 2570  
 MEAN 268.72  
 STANDARD DEVIATION 10.51  
 UPPER DECILE 281.0  
 LOWER DECILE 254.0

Figure 8.22.

HISTOGRAM OF THE RADIOMETER BRIGHTNESS TEMPERATURE

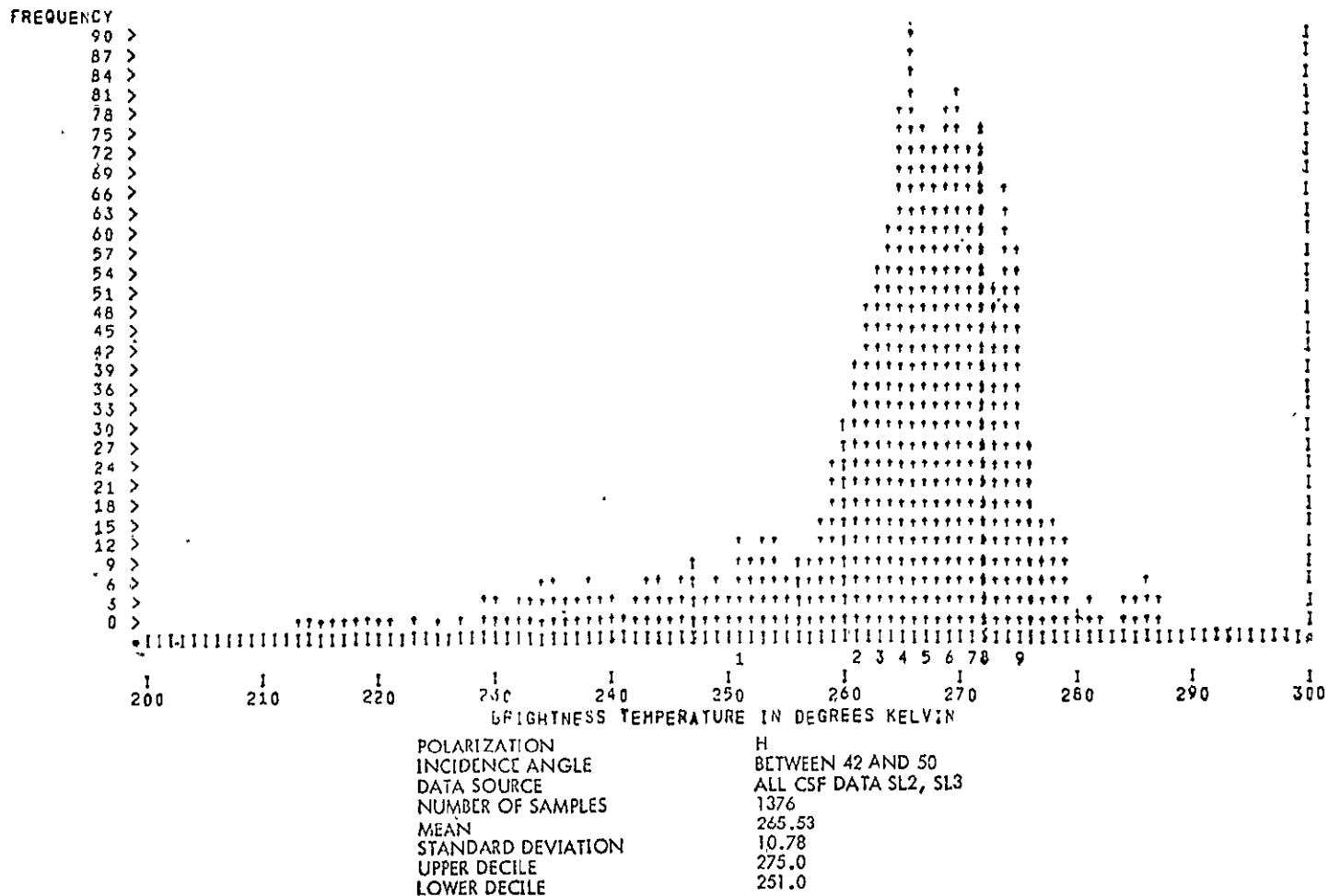


Figure 8.23.

It is interesting to note the trend of the radiometer response for both polarizations. A characteristic of a Lambert-law surface is that it is polarization insensitive, i.e., the response for both polarization appears independent of viewing angle. The response over terrain surfaces does not show any strong polarization selectivity. The difference between the mean vertical and horizontal polarization response or between  $42^\circ$ - $50^\circ$  is only  $3.2^\circ\text{K}$ . Where the mean vertical polarization is the highest ( $32^\circ$ - $34^\circ$ ) the horizontal polarization response is also high. The target areas are not even the same for the two cases. The indications are that the radiometric response over terrain is as though from a rough surface and that variations of soil moisture and physical temperature obscure any particular angular characteristics.

### 8.1.3 Backscatter Response from South America

There were three passes considered in the compilation of statistics over South America. If the data from South America (which were only present for one angle group) were merged with the corresponding data for North America, the distinct nature of the South American backscatter response and the large quantity of data would bias the composite statistics over North America. The three passes over Brazil in South America are shown in Figure 8.24 which also shows the general vegetation patterns of this region. All three passes chosen over South America were with a CTC pitch offset  $29.4^\circ$ , scatterometer-only, configuration. No radiometer data are included in compiling the descriptive statistics over South America. The radiometer data over Brazil will no doubt be interesting to study and a future study should consider compiling statistics of the radiometric emission over Brazil.

More than 4000 points were obtained in the angle group  $32^\circ$ - $34^\circ$  for both polarizations. Figure 8.25 shows the histogram of the distribution of backscatter with VV polarization. The mean is  $-7.33$  dB. This is approximately  $3.4$  dB higher than the corresponding angle group over North America. The trail of points all the way down to  $-28$  dB is probably due to water surfaces which could have been included on either side of the trans-continental sweep by the scatterometer. They are so few that they will not affect the mean substantially. Quite a few points which registered below  $-13$  dB were in the interior of the continent. The histogram for horizontal polarization is shown in Figure 8.26. It has an even sharper lobe than the vertical polarization case. There are fewer points which lie below  $-10$  dB than for the corresponding vertical polarization case. The range between deciles is only  $3.5$  dB for the vertical and



HISTOGRAM OF THE SCATTEROMETER BACKSCATTER COEFFICIENT

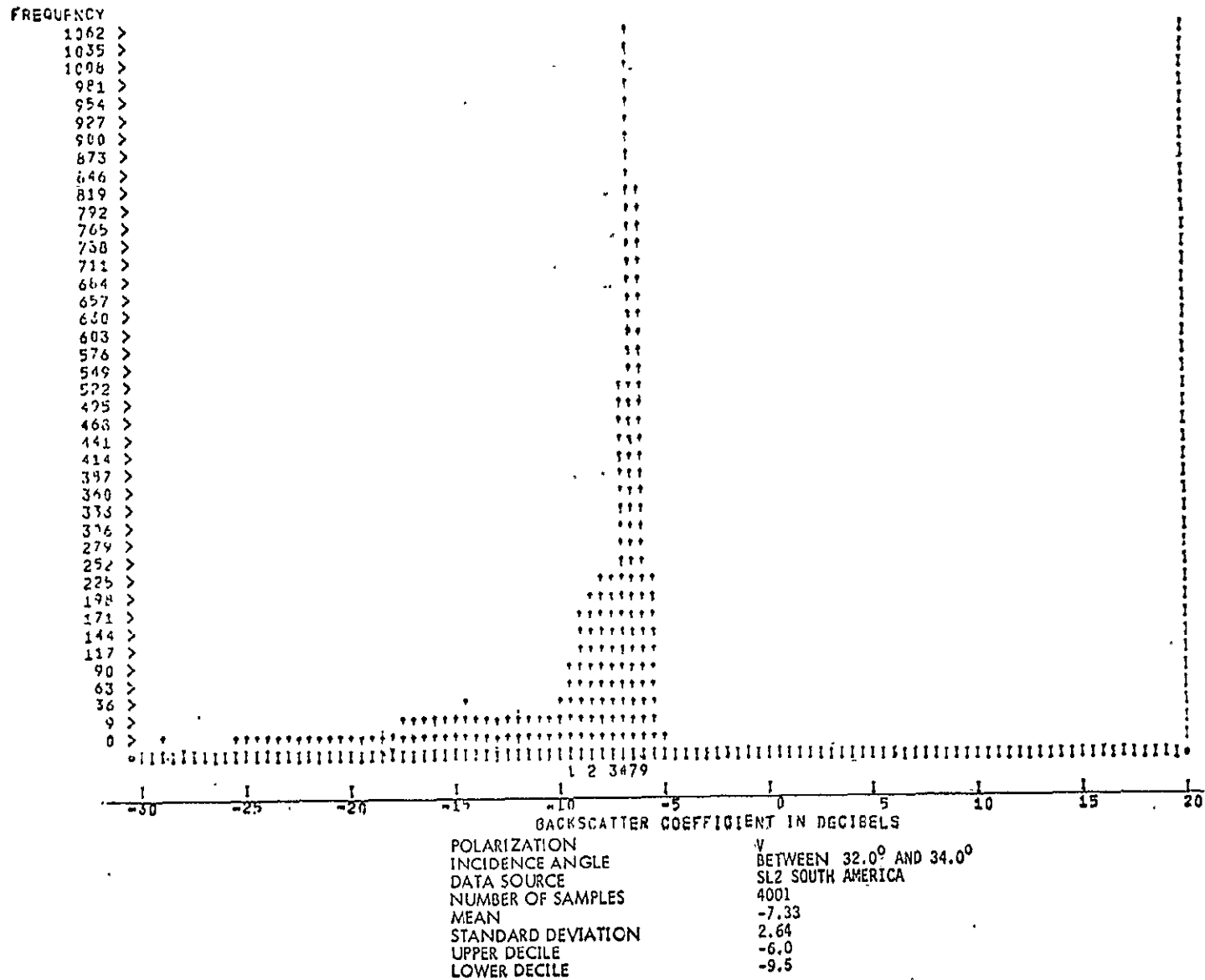


Figure 8.25.

3.0 dB for the horizontal. In fact, the lower decile value is higher than the mean backscatter response over North America. A separate analysis was conducted to compute the correlation between the responses with vertical and horizontal polarization at around  $33^\circ$ . The correlation coefficient was approximately 0.96. There should be no particular partiality to polarization for a truly rough surface. The Amazon forest is a rough surface as is evidenced by its high backscatter at around  $33^\circ$ . The major lobes in the histograms are from areas which are predominantly dense forests. The lower shoulder region of the lobe in figure 8.25 is from savannah type vegetation. Because of the vast regions of homogeneity in vegetation (as also evidenced by the backscatter response), the South American region was selected as a candidate for preparing psuedo-images with the CTC pitch  $29^\circ$  mode.

#### 8.1.4 Statistics of Response from Ocean Surfaces

The data base for compiling descriptive statistics of the response from ocean surfaces consisted of only non-contiguous modes of operation. Unlike the data for North America, these data were not "cleaned" for erroneous or suspect processing. A copy of the data maintained by a group involved in the oceanographic applications of S-193 data was converted to Catalog Standard Format and processed similarly to the North American data segments. The resolution required for useful feature selection of land targets is of the order of 200 meters, but for remote sensing applications over the ocean surfaces, the resolution required can be considerably poorer. Variations in the response to the scatterometer and radiometer from an ocean surface are due to the surface roughness. The dielectric constant changes very slightly due to salinity changes and its effects can be safely ignored. The roughness of a sea surface is a function of the long term and short term meteorological conditions over the surface. The relationship between the wind speed and direction over an ocean surface and its corresponding microwave response has been established earlier [Bradley, 1971; Young et al., 1974]. The resolution of the S-193 is acceptable for monitoring global wind patterns. Data are presented here, however, in a form especially suitable for system design; the study of wind response is not considered.

#### Backscatter Response of Ocean

The angular backscatter response over ocean surfaces shows a sharper drop with

HISTOGRAM OF THE SCATTEROMETER BACKSCATTER COEFFICIENT

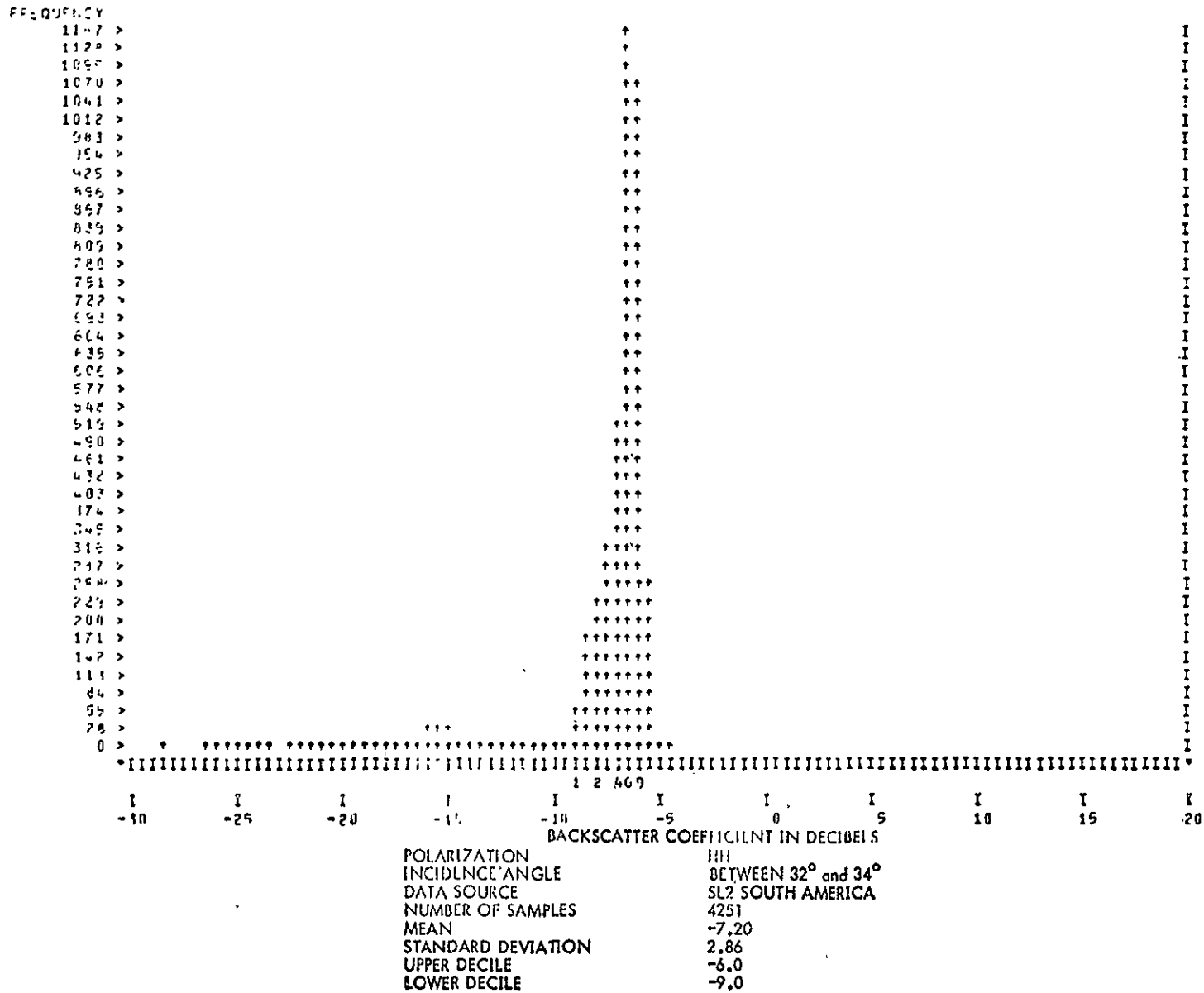
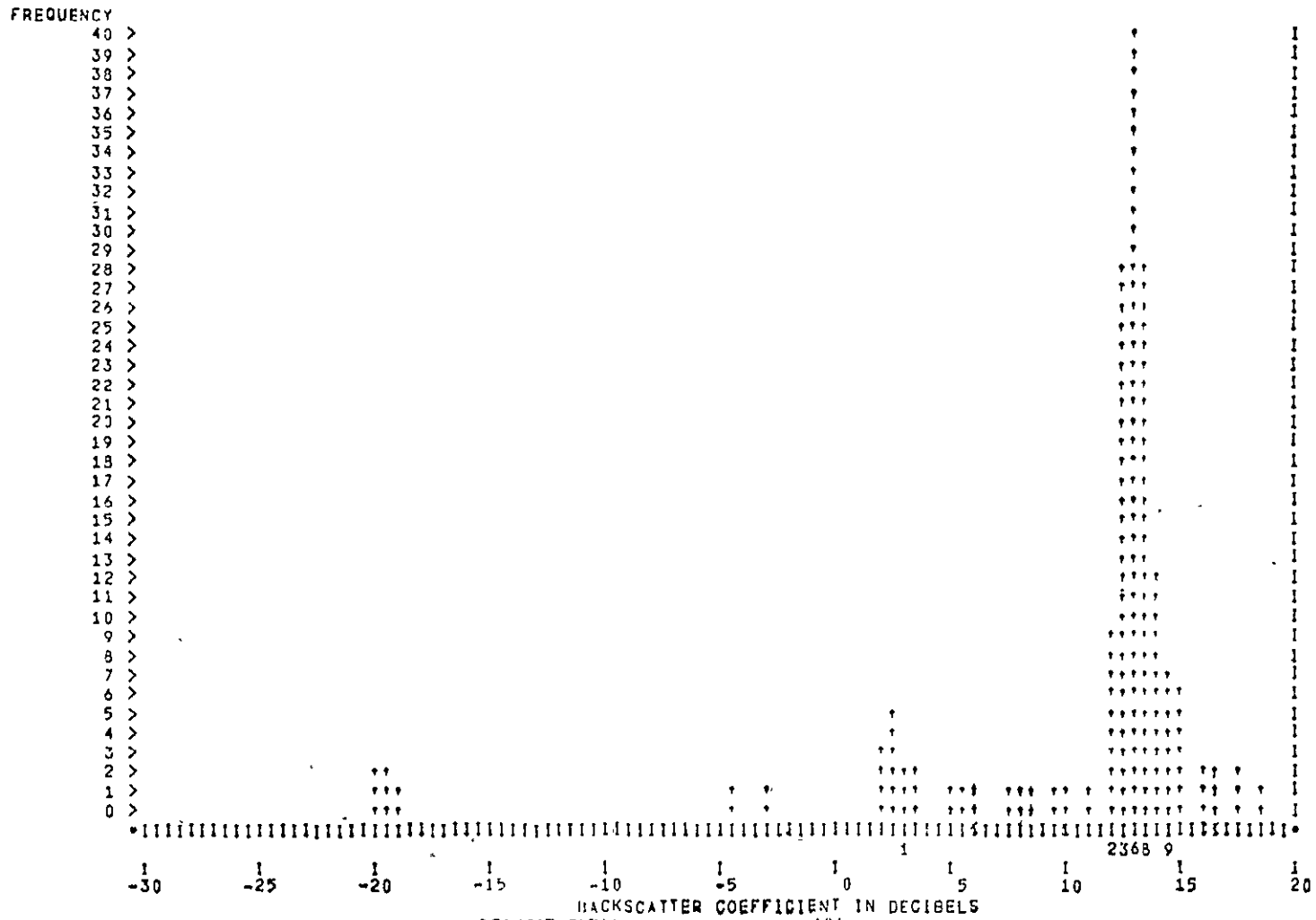


Figure 8.26.

HISTOGRAM OF THE SCATTEROMETER BACKSCATTER COEFFICIENT



POLARIZATION VV  
 INCIDENCE ANGLE BETWEEN 0° and 2°  
 DATA SOURCE ALL CSF DATA SL2, SL3 OCEAN  
 NUMBER OF SAMPLES 165  
 MEAN 12.3  
 STANDARD DEVIATION 6.52  
 UPPER DECILE 14.5  
 LOWER DECILE 5.5

Figure 8.27.

incidence angle away from nadir than does the corresponding response over land surfaces. This is expected and has been observed by prior aircraft measurements. The response close to nadir incidence from an ocean surface for vertical polarization is shown in Figure 8.27 (for incidence angle group  $0^{\circ}$ - $2^{\circ}$ ). The saturation level of the scatterometer corresponds to a backscatter response around 14 dB to 15 dB. One can see that the nadir response from an ocean surface often reaches this level. This implies that the responses registering above 14 dB may in fact be much higher than those computed. The peak of the main lobe is centered at around +13 dB which is close to the upper end of the dynamic range of the instrument. Although the response near vertical incidence contains some specular component, most of the return power is due to diffuse scattering. The Rayleigh distribution response has a 90% confidence that extends from +5 dB to -13 dB relative to the mean. The few points lying near -20 dB can be attributed to incorrect processing (at NASA/JSC). For example, if the incidence angle is not computed correctly, the data for an incidence angle other than that included in this angle group could be included. These very-low-return points were not included in computing the statistics for this group. There is a sizable number of responses between -5 dB and +10 dB. Lower backscatter for near-nadir incidence for rougher seas has been observed in prior aircraft measurements. The scatter near nadir incidence is the largest of any angle group considered and this is expected. The non-contiguous modes offer a chance to make backscatter measurements with four polarization pairs. The response for HH polarization for the angle group  $0^{\circ}$ - $2^{\circ}$  is shown in Figure 8.28. It is quite similar to the response with VV polarization except for the points around -20 dB, the mean is higher, and there is a much smaller number of points between -5 dB and +10 dB. Examination of some select passes showed that the VV response was similar to the HH response. The response with cross-polarized configurations HV and VH for the  $0^{\circ}$ - $2^{\circ}$  angle groups are shown in Figures 8.29 and 8.30. These two are very similar in distribution of the response. The means for both are much below the corresponding dominant polarization cases; the differences are of the order of 16 dB. It is interesting to observe that even the cross-polarized measurements can register over 0 dB. The scatter for cross-polarized measurements is much less than for dominant polarization measurements with the range between the upper and lower deciles being only 2.5 dB (from 2.5 dB to -5.0 dB). The angular backscatter response close to nadir is a very sharply decreasing function, consequently small pointing errors can contribute to large errors in backscatter. The errors should be larger for the like polarization cases than for

HISTOGRAM OF THE SCATTEROMETER BACKSCATTER COEFFICIENT

ORIGINAL PAGE IS  
OF POOR QUALITY

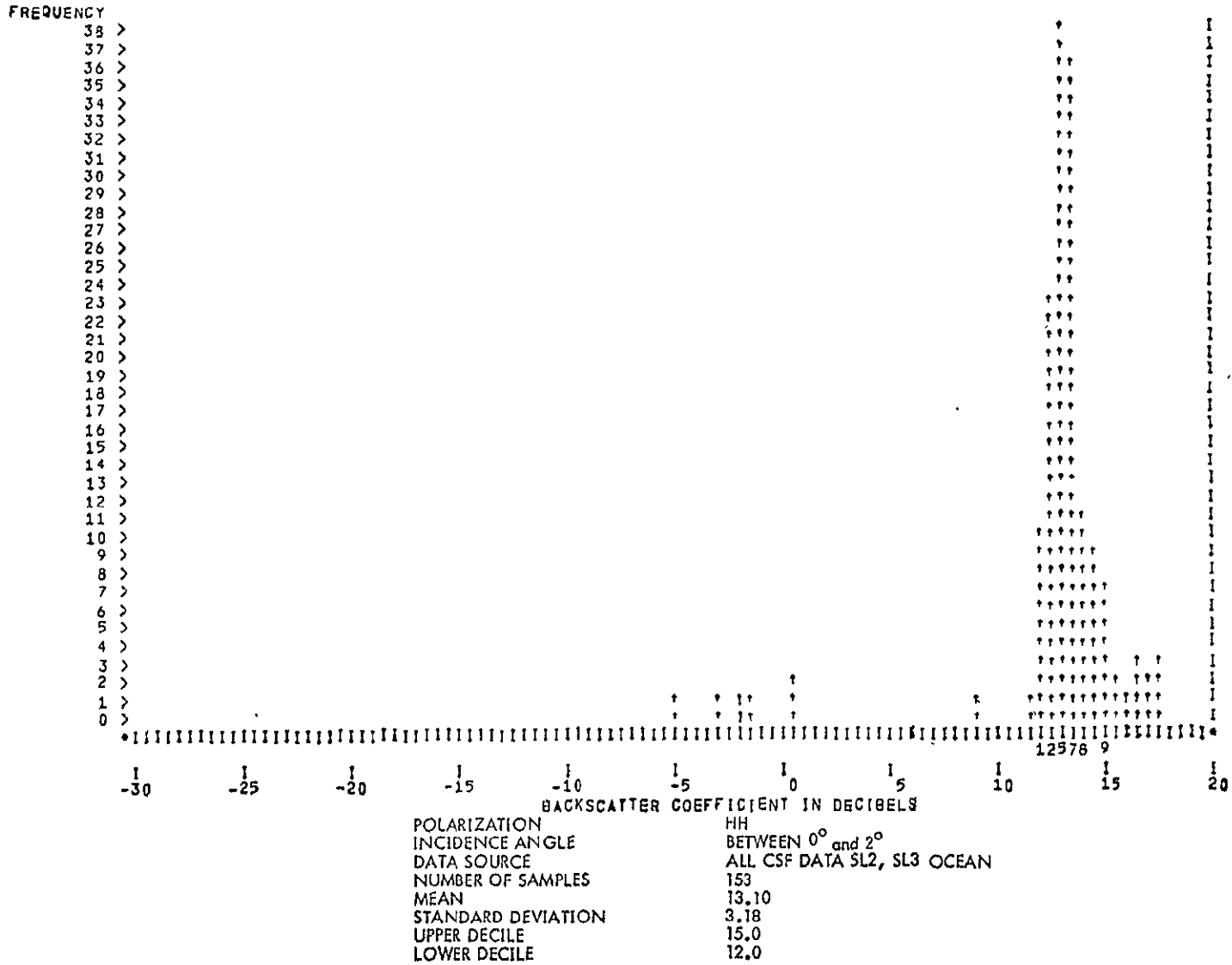


Figure 8.28.

HISTOGRAM OF THE SCATTEROMETER BACKSCATTER COEFFICIENT

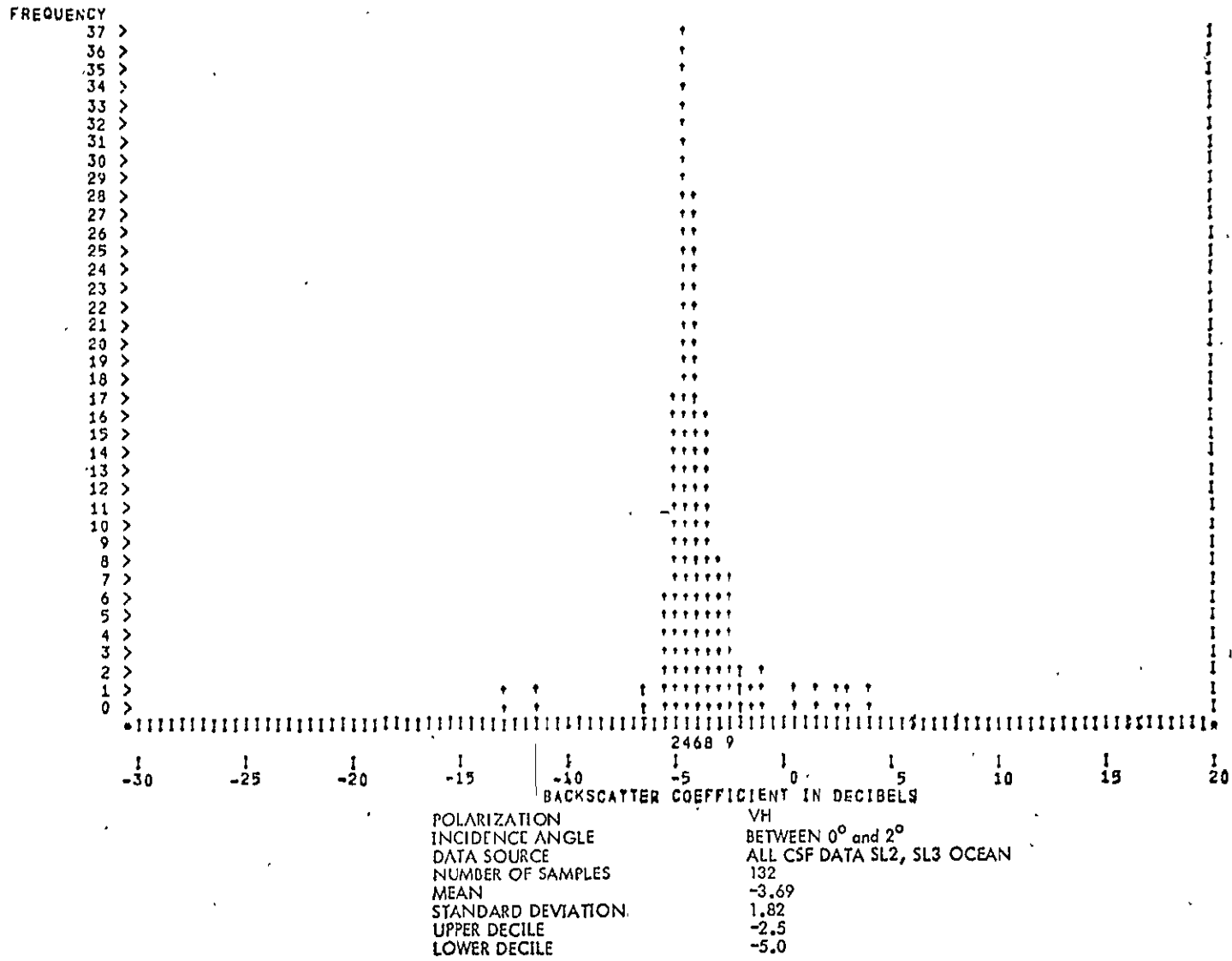
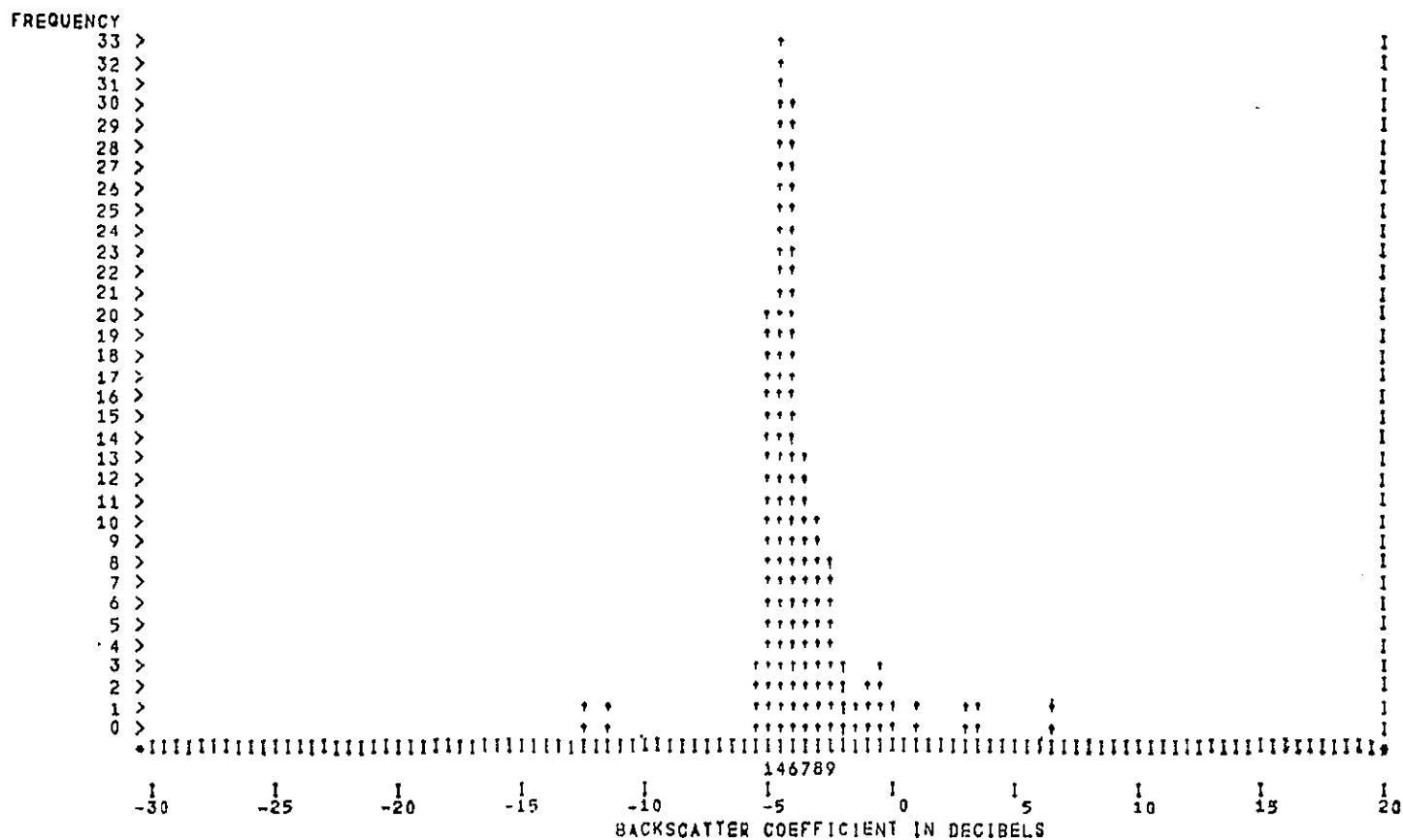


Figure 8.29.

HISTOGRAM OF THE SCATTEROMETER BACKSCATTER COEFFICIENT



POLARIZATION HV  
 INCIDENCE ANGLE BETWEEN 0° and 2°  
 DATA SOURCE ALL CSF DATA SL2, SL3 OCEAN  
 NUMBER OF SAMPLES 133  
 MEAN -3.52  
 STANDARD DEVIATION 1.96  
 UPPER DECILE -2.5  
 LOWER DECILE -5.0

ORIGINAL PAGE IS  
OF POOR QUALITY

Figure 8.30.

HISTOGRAM OF THE SCATTEROMETER BACKSCATTER COEFFICIENT

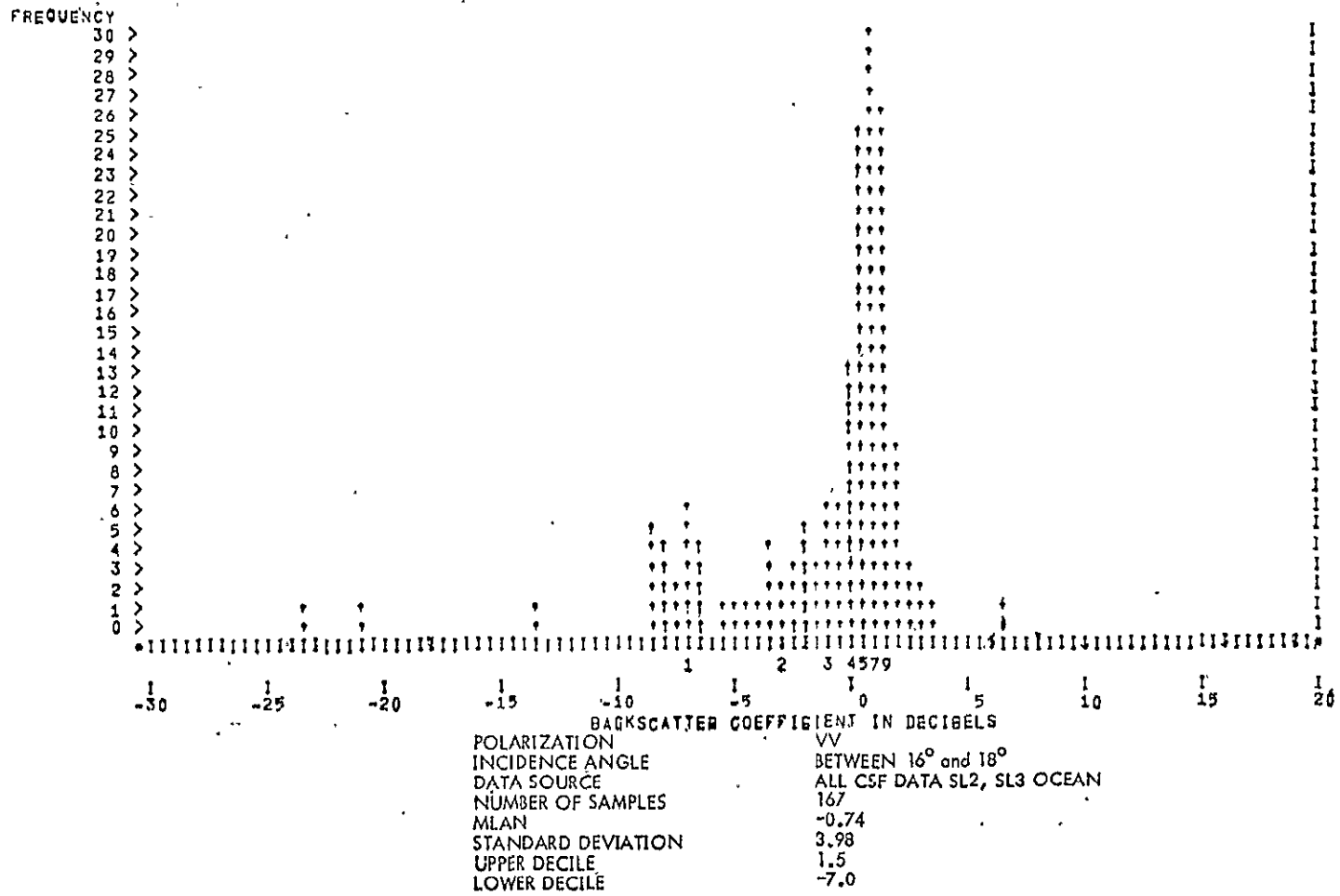


Figure 8.31.

HISTOGRAM OF THE SCATTEROMETER BACKSCATTER COEFFICIENT

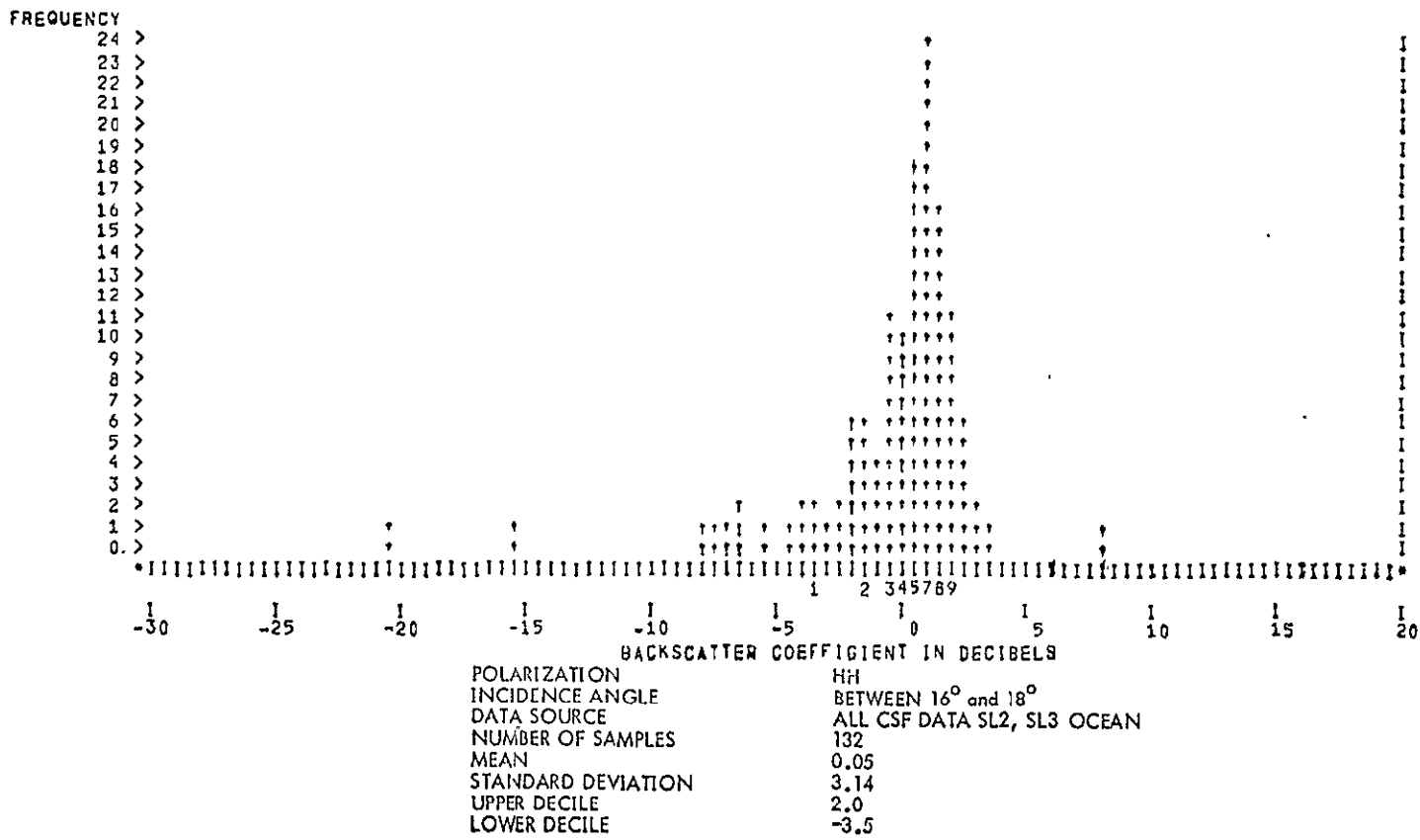


Figure 8.32.

the cross-polarization cases because the slope of the response curve is much greater for the dominant polarization cases. This may have contributed to the wider scatter in these cases.

The next angle group for which backscatter measurements are recorded with the ITNC mode is  $16^{\circ}$ - $18^{\circ}$ . The histogram of the response with vertical polarization is shown in Figure 8.31. There is one major lobe with a peak at 1 dB and minor lobe between -8.5 dB and -6.5 dB. The scatter is still large and the range between the upper and lower deciles is 8.5 dB (-7.0 to 1.5 dB). The corresponding range for North American targets was only 4.6 dB (-9.0 dB to -5.4 dB). This again tends to point to the fact that the ocean surface can be more diverse in its response than land at this angle. This is further substantiated by observing the response with horizontal polarization in the same angle group (shown in Figure 8.32). The mean is now over 0.0 dB and the range between the upper and lower deciles is only 5.5 dB. Selected passes were examined to see if there were differences between the response for vertical and horizontal polarization in this angle group and no discernible differences were detected. The response for cross-polarization cases for this angle group are shown in Figures 8.33 and 8.34. The few points registered above 4 dB in Figure 8.33 are erroneous and were included in this polarization and angle group because the backscatter data for some other angle and polarization group were inadvertently put in this slot (by the data reduction program at NASA/JSC). Ignoring these few points, the responses for the two cases are similar. The range between the upper and lower decile is around 4.0 dB.

The histogram for the angle group  $32^{\circ}$ - $34^{\circ}$  for VV polarization is given in Figure 8.35. The mean is -13.40 dB and the range between deciles is 10 dB. This range overlaps some of the corresponding range for North America, but extends much lower. This histogram for HH polarization for the same angle group is shown in Figure 8.36. It is quite similar to that for VV polarization. The range between deciles is 9.5 dB (-20 dB to -10.5 dB). There is a slight difference in the means (0.8 dB). Histograms for the cross-polarized cases for this angle group are shown in Figures 8.37 and 8.38. The lower cut-off of values included for purposes of compiling these statistics was -30 dB. Some points are, therefore, not included. The mean, and other statistics are, therefore, biased a little upwards.

Although the precision of the scatterometer is specified to be  $\pm 0.5$  dB for a backscatter coefficient of -30 dB at  $48^{\circ}$  incidence, we decreased the limits on the

HISTOGRAM OF THE SCATTEROMETER BACKSCATTER COEFFICIENT

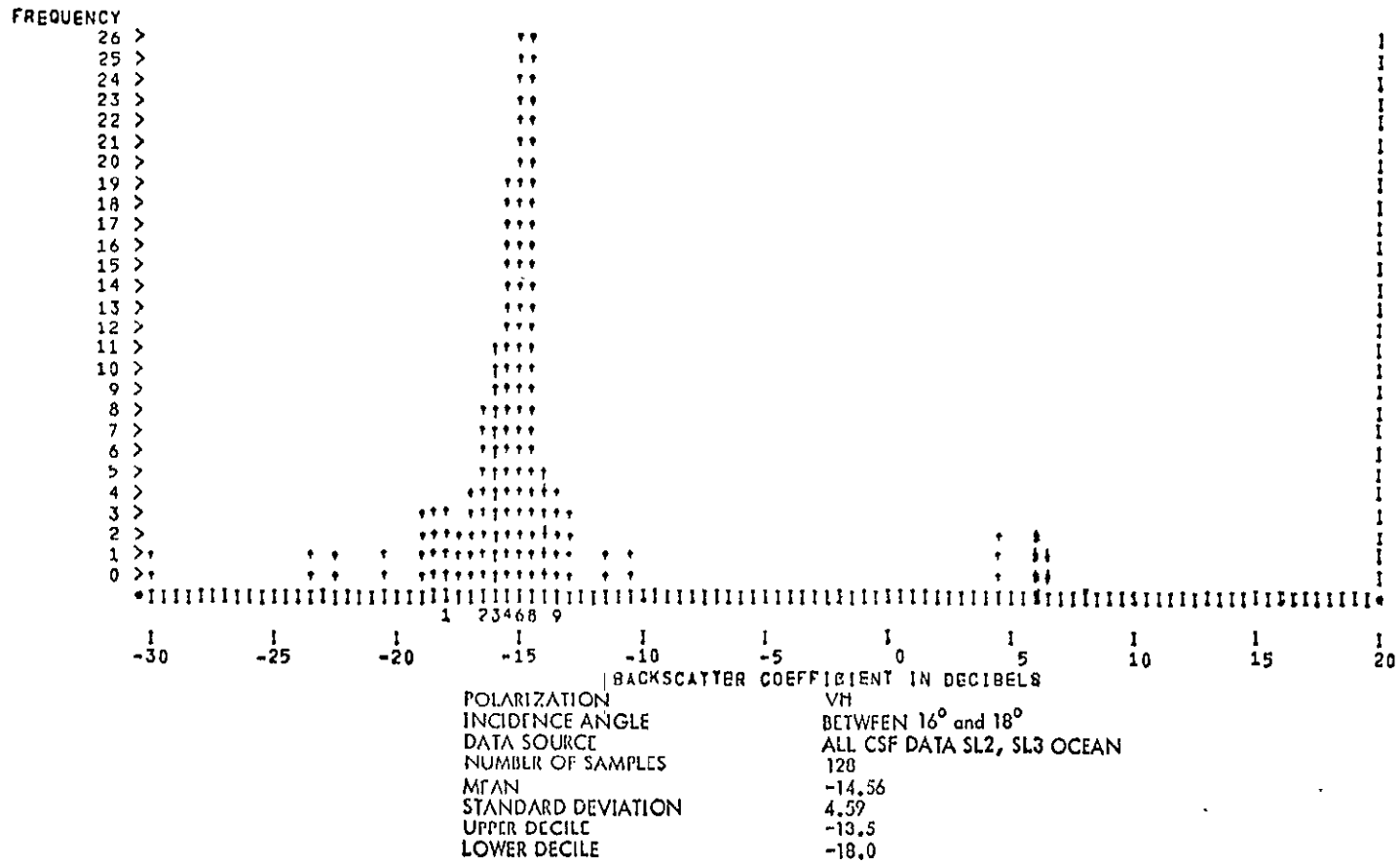


Figure 8.33.

HISTOGRAM OF THE SCATTEROMETER BACKSCATTER COEFFICIENT

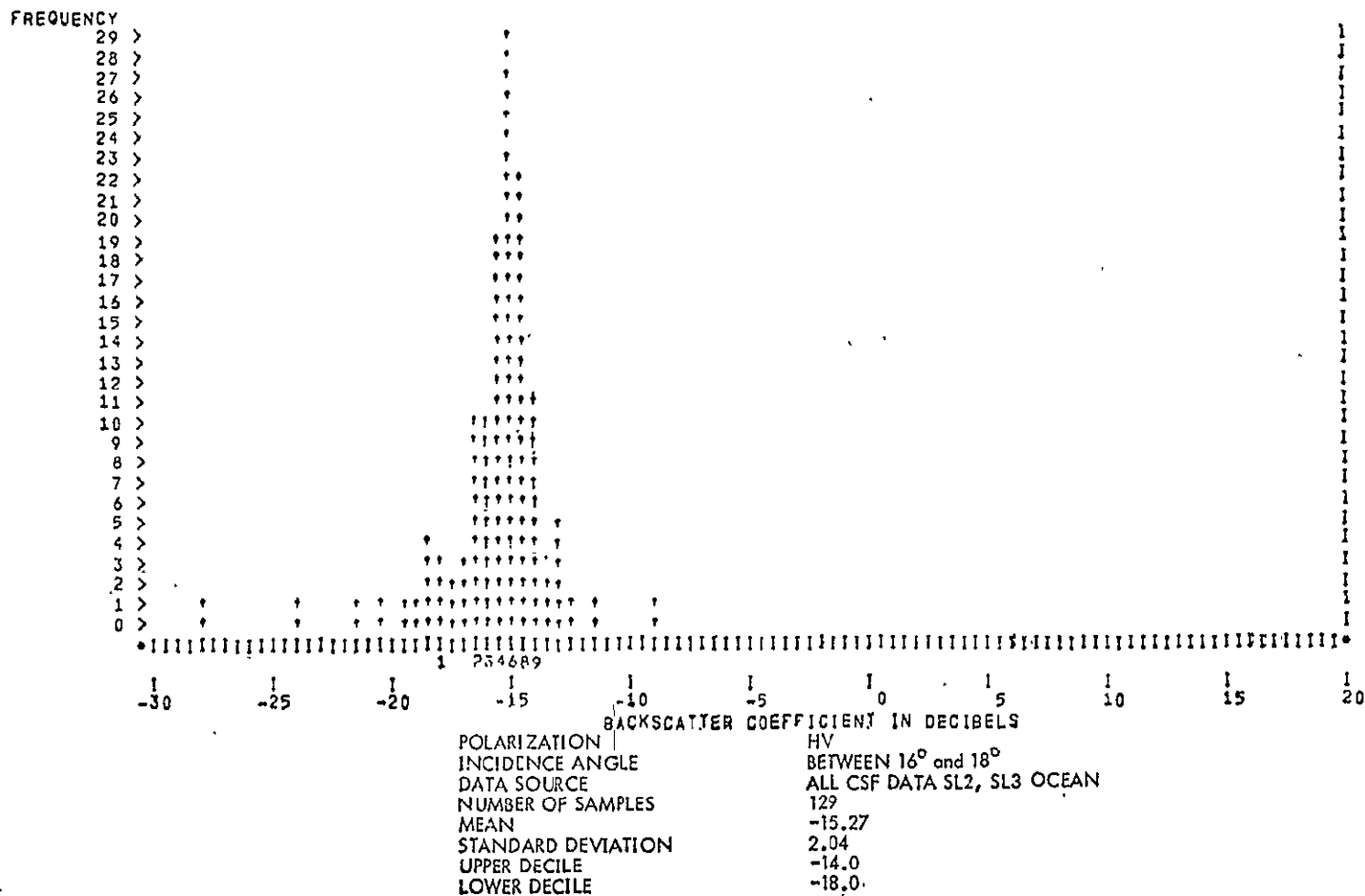


Figure 8.34.

ORIGINAL PAGE IS  
OF POOR QUALITY

413

HISTOGRAM OF THE SCATTEROMETER BACKSCATTER COEFFICIENT

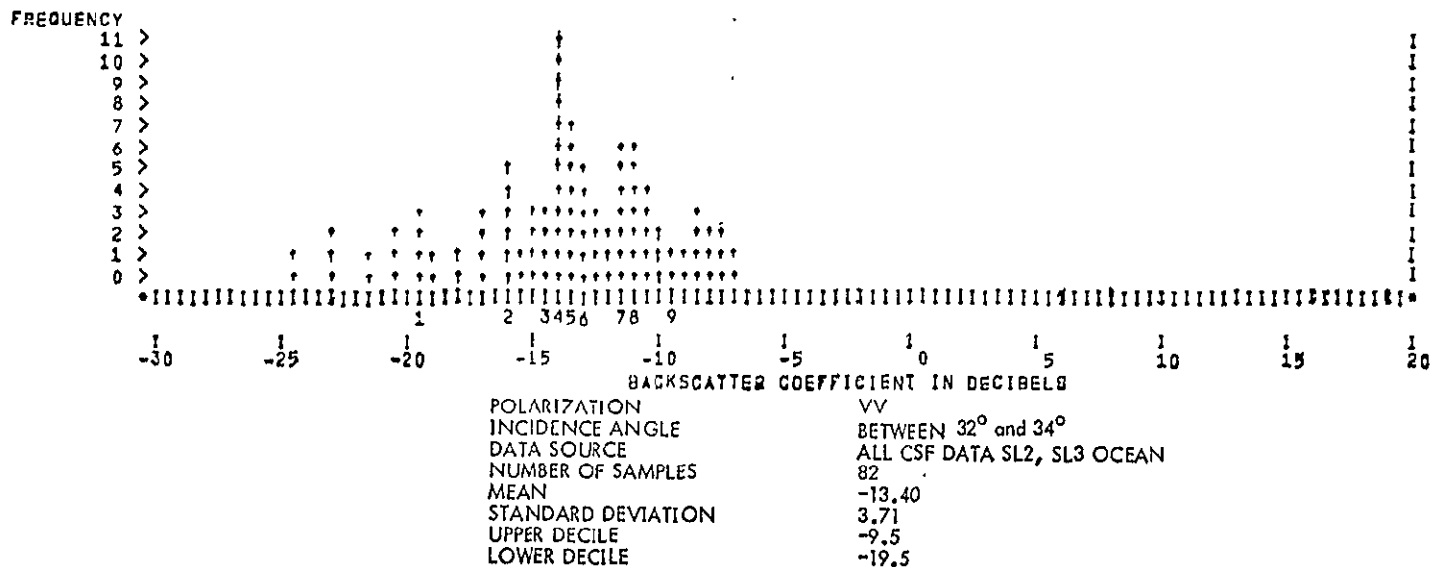


Figure 8.35.

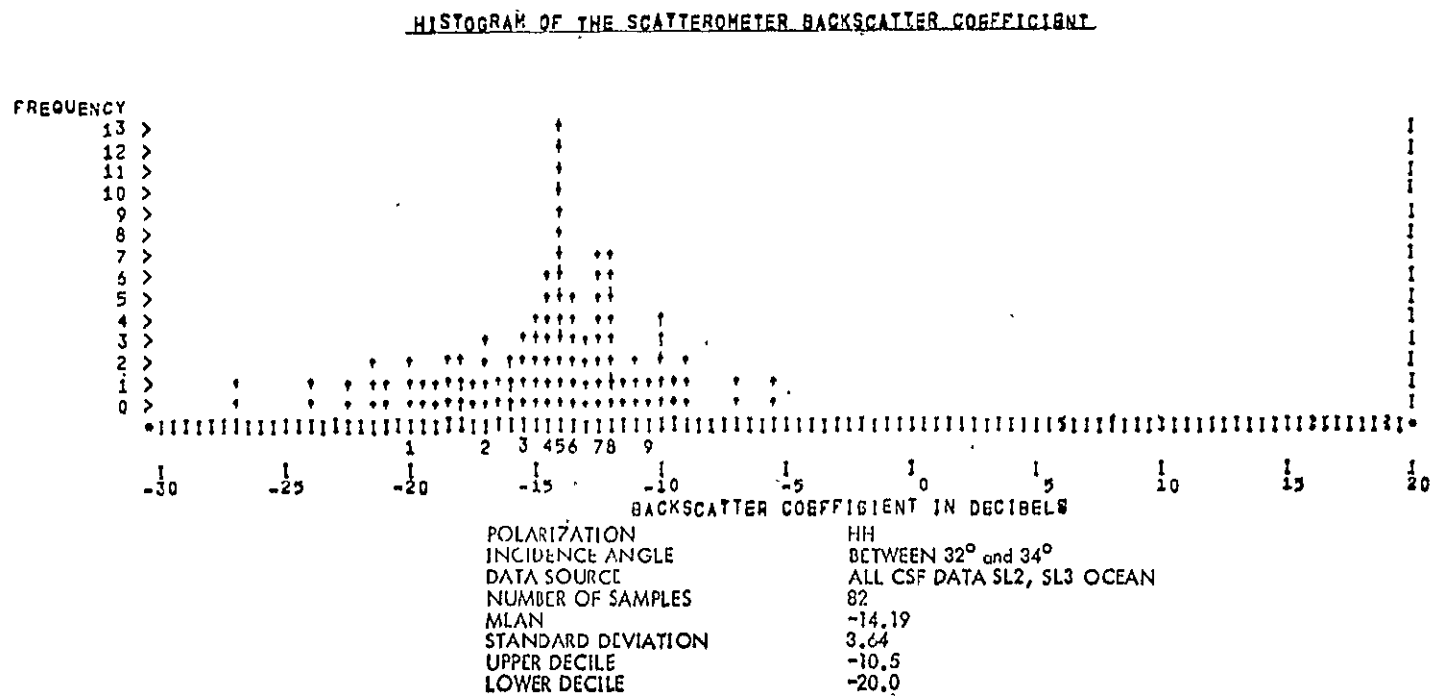
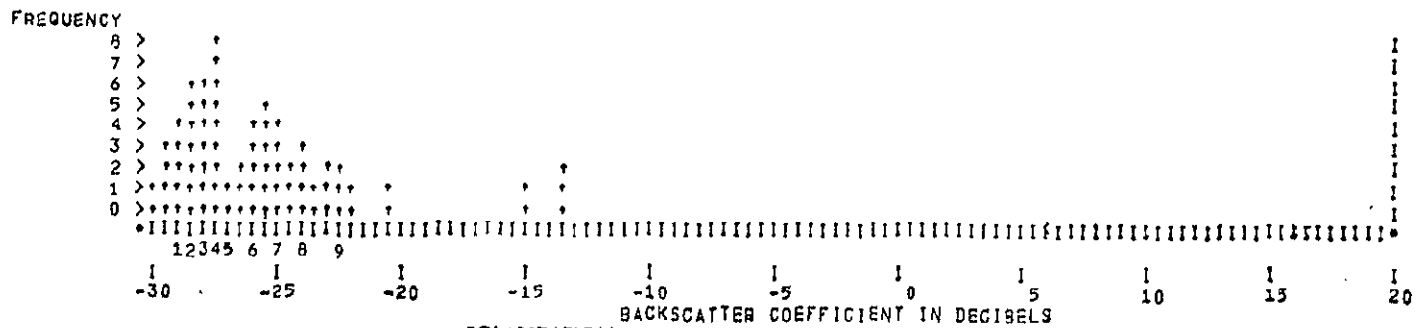


Figure 8.36.

HISTOGRAM OF THE SCATTEROMETER BACKSCATTER COEFFICIENT



POLARIZATION VV  
 INCIDENCE ANGLE BETWEEN 32° and 34°  
 DATA SOURCE ALL CSF DATA SL2, SL3 OCEAN  
 NUMBER OF SAMPLES 59  
 MEAN -25.61  
 STANDARD DEVIATION 3.48  
 UPPER DECILE -22.5  
 LOWER DECILE -29.0

ORIGINAL PAGE IS  
OF POOR QUALITY

Figure 8.37.

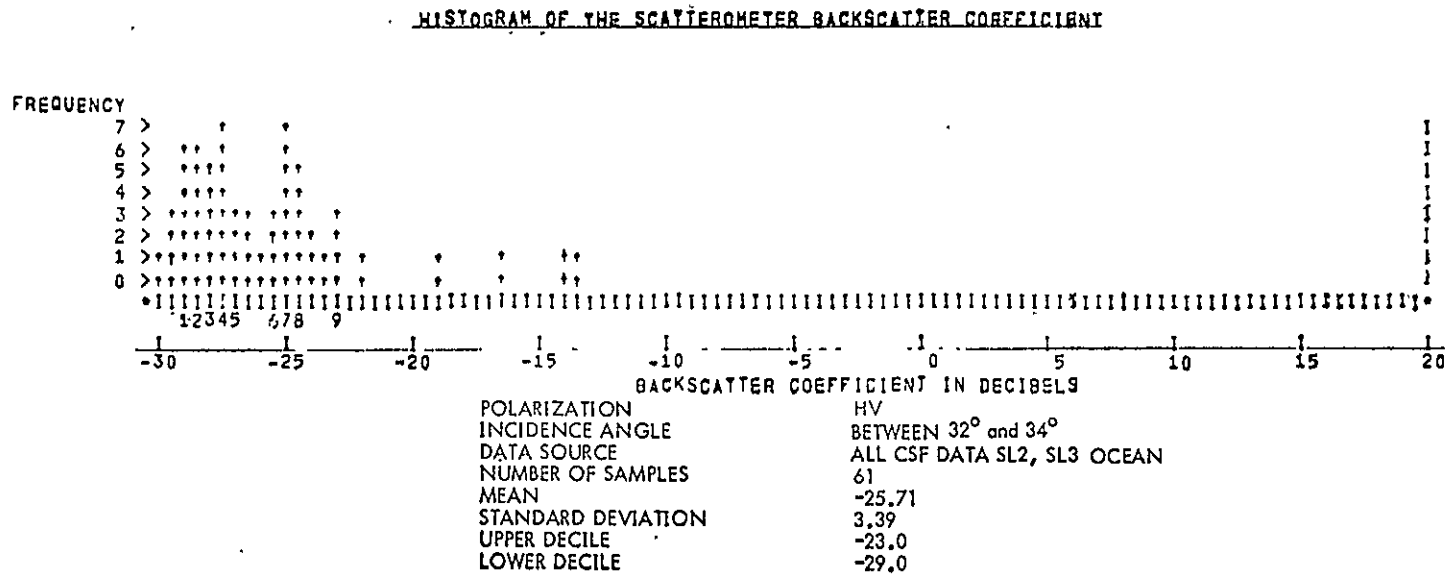


Figure 8.38.

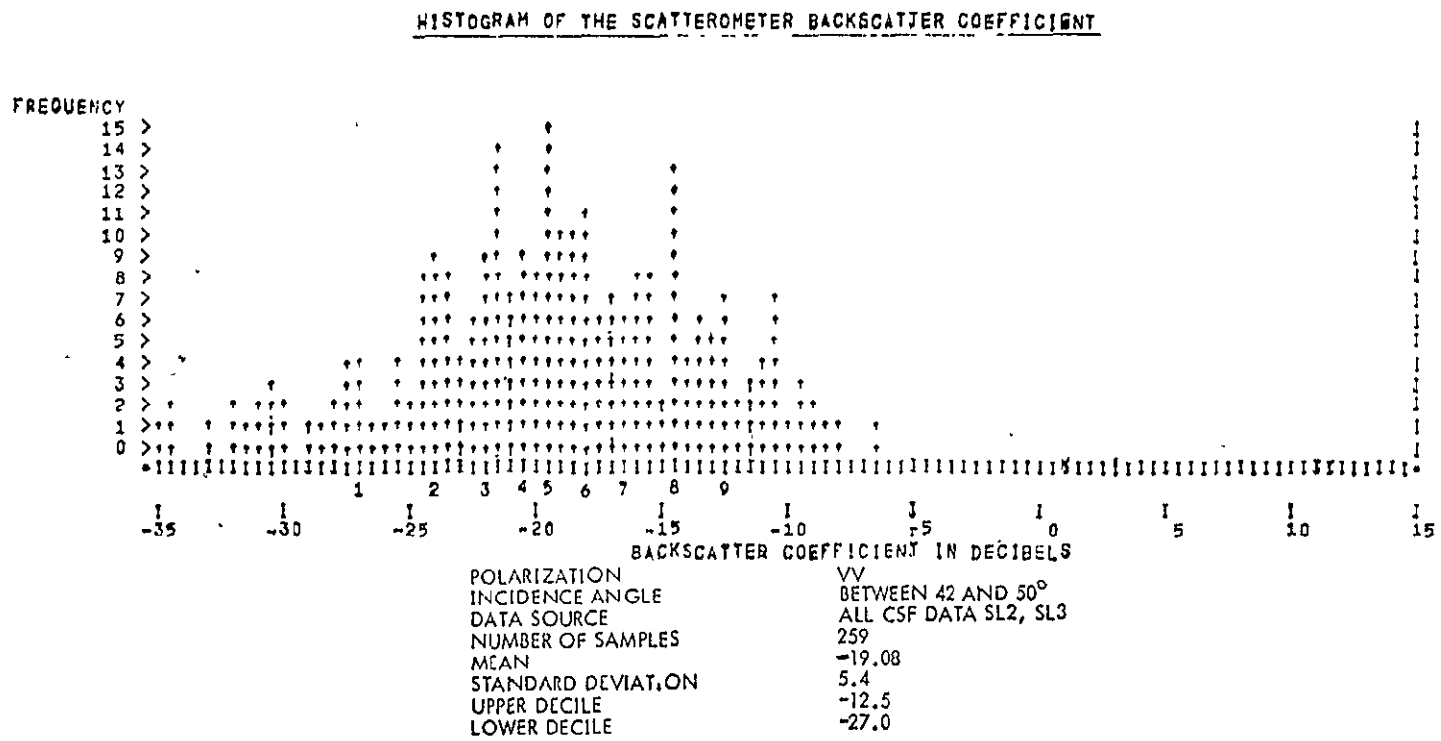
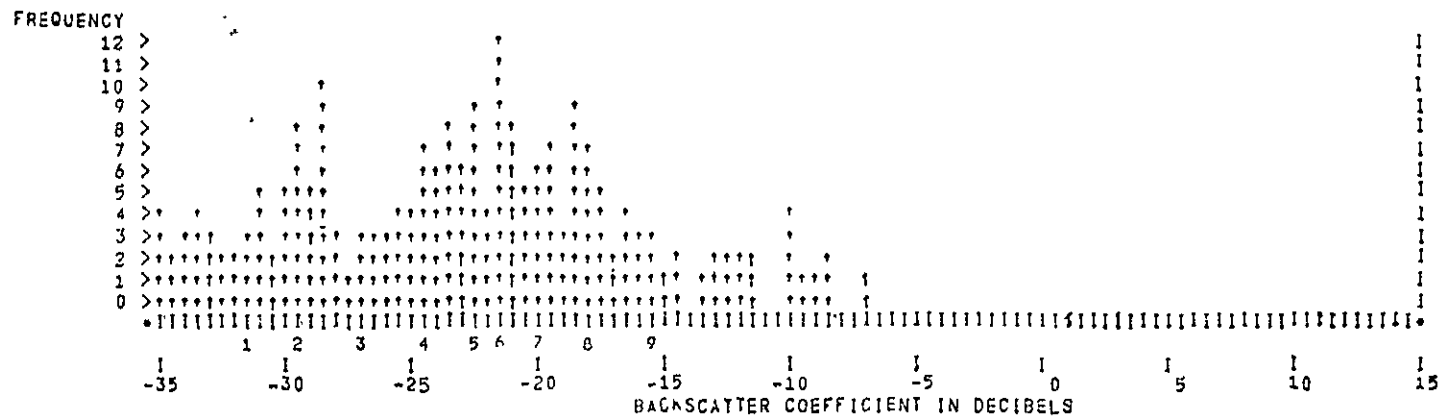


Figure 8.39.

HISTOGRAM OF THE SCATTEROMETER BACKSCATTER COEFFICIENT



POLARIZATION HH  
 INCIDENCE ANGLE BETWEEN 42 AND 50°  
 DATA SOURCE ALL CSF DATA SL2, SL3  
 NUMBER OF SAMPLES 214  
 MEAN -22.8  
 STANDARD DEVIATION 6.3  
 UPPER DECILE -15.5  
 LOWER DECILE -31.5

Figure 8.40.

ORIGINAL PAGE IS  
OF POOR QUALITY

HISTOGRAM OF THE SCATTEROMETER BACKSCATTER COEFFICIENT

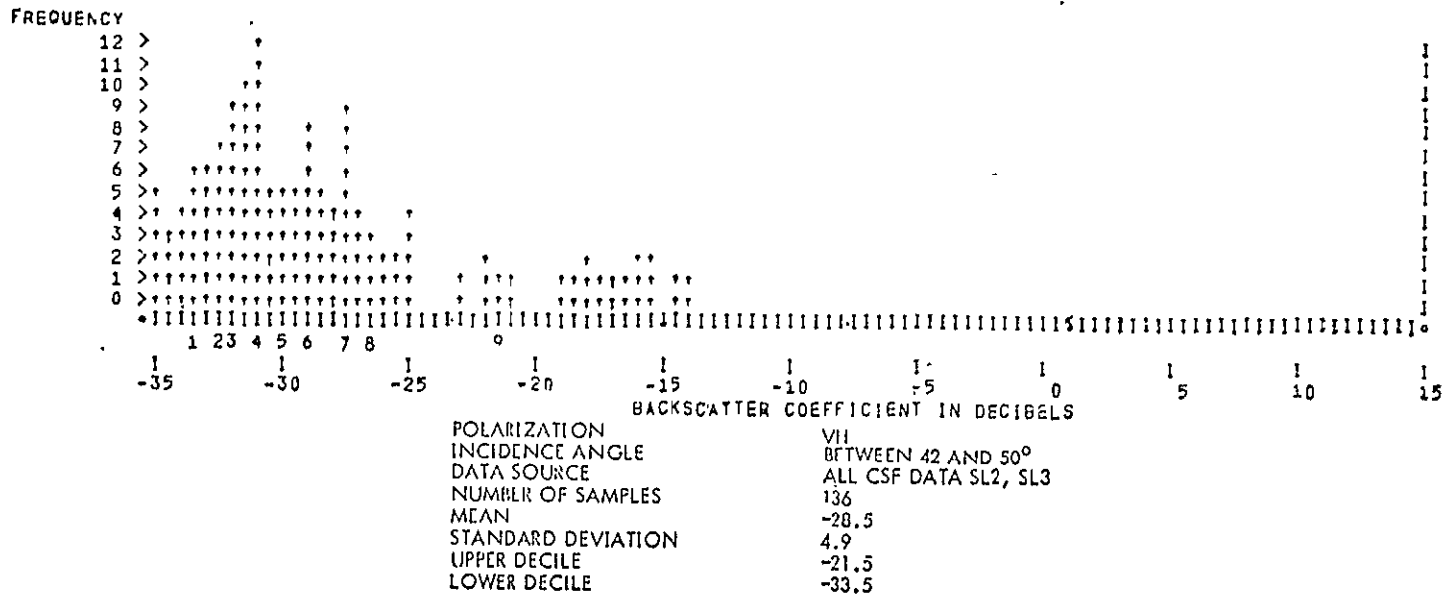


Figure 8.41.

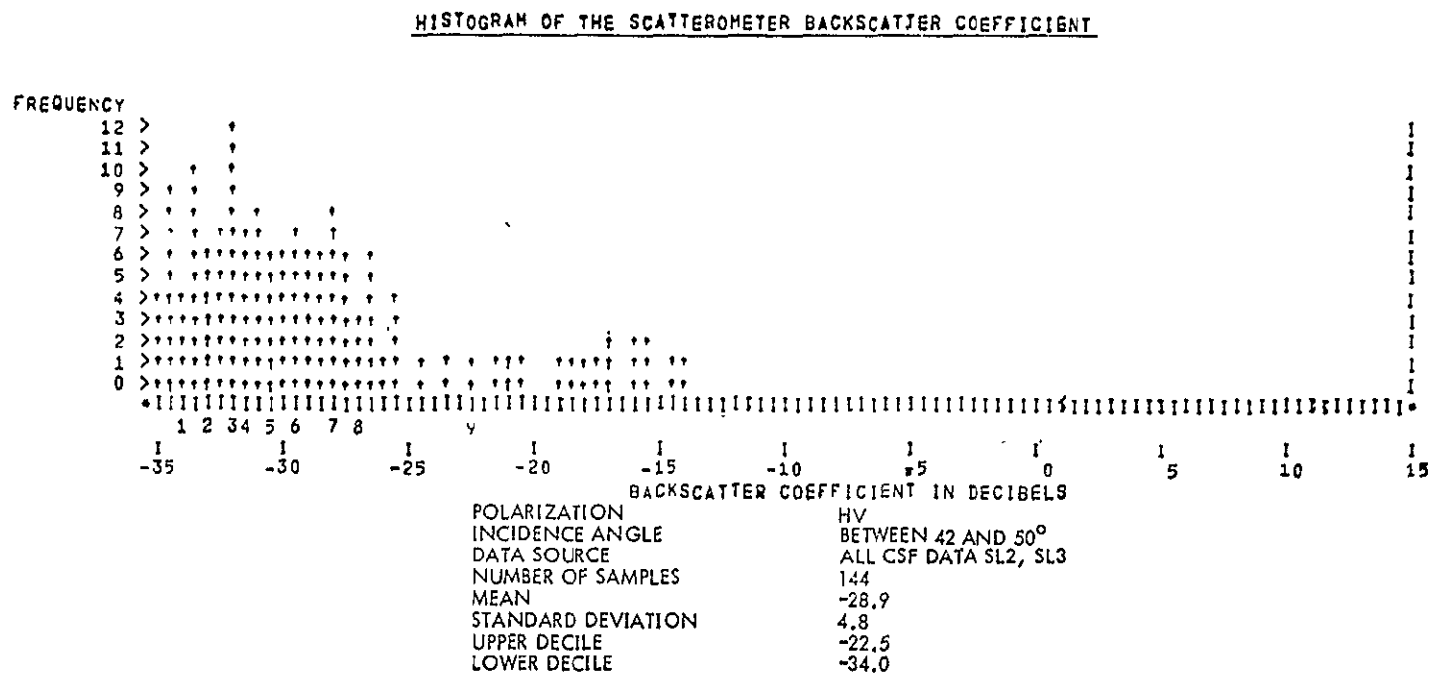


Figure 8.42.

lower end of the histograms for the angle group  $42^{\circ}$ - $50^{\circ}$  to  $-35$  dB. The histograms for the angle groups  $42^{\circ}$ - $50^{\circ}$  have a range from  $-35$  dB to  $15$  dB. In spite of this decrease, there were some points which still fell out of the range, especially for the cross-polarized measurement cases. The histogram for the angle group  $42^{\circ}$ - $50^{\circ}$  for VV polarization is shown in Figure 8.39. The statistics for this polarization case are not biased much because only a very few points registered below  $-35$  dB. The mean is  $-19$  dB and the range between deciles is  $14.5$  dB. This wide range is partially due to the wide angle range considered, but also comes about because of the great wind-speed sensitivity at these angles. The distribution is unimodal with sharp peaks at some values. This histogram for the corresponding HH polarization case is shown in Figure 8.40. The mean is about  $3.8$  dB lower (at  $-22.8$  dB). This is a significant difference from the VV case. The range between deciles is  $15$  dB and stretches all the way down to  $-31.5$  dB. There were a few points (more than for the corresponding vertical polarization case) which registered below our lower cut-off limits. The histograms for the cross-polarized cases are shown in Figure 8.41 and 8.42. The statistics listed below the histograms should be taken with caution. The values are biased upwards because a non-negligible portion of the data registered below  $-35$  dB. With the precision of the scatterometer being poor at the low signal (low backscatter) levels, the statistics computed even with  $-40$  dB as the lower cut-off may not be too meaningful. The mean of the returns is  $-28.5$  (VH) and  $-28.9$  (HV) and the two cross-polarized cases appear to be similar, as they should. The difference in mean backscatter between the dominant and cross-polarized cases is around  $7$  to  $10$  dB.

A cautionary note in interpreting the cross-polarized returns is in order. It was shown in Chapter Six that a sizable amount of energy arriving at the antenna during the cross-polarized configuration measurements is from dominant polarization backscatter. We have seen that the dominant polarization backscatter is anywhere from  $7$  dB to  $14$  dB higher than the "measured" cross-polarized backscatter. Therefore, the cross-polarized backscatter values reported here are again an upper bound. The true values will be a little lower. With the isolation characteristics of the S-193 antenna, this error could be as much as  $3$  dB.

## Radiometer Response

The radiometer brightness temperature histograms for ocean surfaces were computed from data obtained from non-contiguous modes of operation. Data for both polarizations for the angle groups  $0^{\circ}$ - $2^{\circ}$ ,  $16^{\circ}$ - $18^{\circ}$ ,  $32^{\circ}$ - $34^{\circ}$ , and  $42^{\circ}$ - $50^{\circ}$  were used to prepare histograms of the distribution. The response observed over the ocean is very much like that reported from prior aircraft- and tower-based measurement programs and quite in line with theoretical predictions. The radiometric emission is a function of the roughness of the ocean surface, which in turn is a function of the wind speed. Since all the data over the ocean were pooled to obtain these histograms, no differentiation by wind speed was attempted. A pass over Hurricane Ava in the Pacific and a pass over tropical storm Christine in the Atlantic are included in the data base. These passes were included to show the bounds of radiometric emission under unstable and rare meteorological conditions. No corrections have been made for atmospheric effects on the radiometer signals.

Figure 8.43 shows the histogram of the distribution of the radiometer response for vertical polarization for the incidence angle group  $0^{\circ}$ - $2^{\circ}$ . The few points beyond approximately  $150^{\circ}$  K are from the storms. The mean temperature is approximately  $128^{\circ}$  K and the bounds between the lower and upper deciles are  $15^{\circ}$  K. The points lying off the major lobe are either due to the presence of clouds or due to rare wind conditions or both. Figure 8.44 shows the histogram for the same angle group for horizontal polarization. As expected, the histograms for the two polarizations in this angle groups show a similar response and this is reflected in the statistics.

Figure 8.45 shows the histogram for the incidence angle group  $16^{\circ}$ - $18^{\circ}$  for the vertical polarization. The mean has shown an increase over the small incidence angle case (as expected) and the few points above  $150^{\circ}$  K are again from the storm passes. Figure 8.46 shows the histogram for horizontal polarization for the same angle group. The mean is now lower than for the corresponding near nadir case (as expected). The few points towards the upper end of the distribution are from the storm passes. Figure 8.47 and 8.41 show the histogram for the angle group  $32^{\circ}$ - $34^{\circ}$  for the vertical and horizontal polarizations; the response is quite like that expected. The points lying below  $130^{\circ}$  K in the vertical polarization case are rare and the reason for such low response may be a very calm sea. Figure 8.49 shows the histogram for the  $42^{\circ}$ - $50^{\circ}$  angle case for vertical polarization; the scatter is larger because of the large angle group considered, but the mean shows expected increase from the smaller incidence angles. Figure 8.50 shows the histogram for the horizontal polarization; the mean has decreased and the bounds considered are  $50^{\circ}$  K to  $150^{\circ}$  K, the lower decile is at  $98^{\circ}$  and the upper decile is at  $120.5^{\circ}$ .

HISTOGRAM OF THE RADIOMETER BRIGHTNESS TEMPERATURE

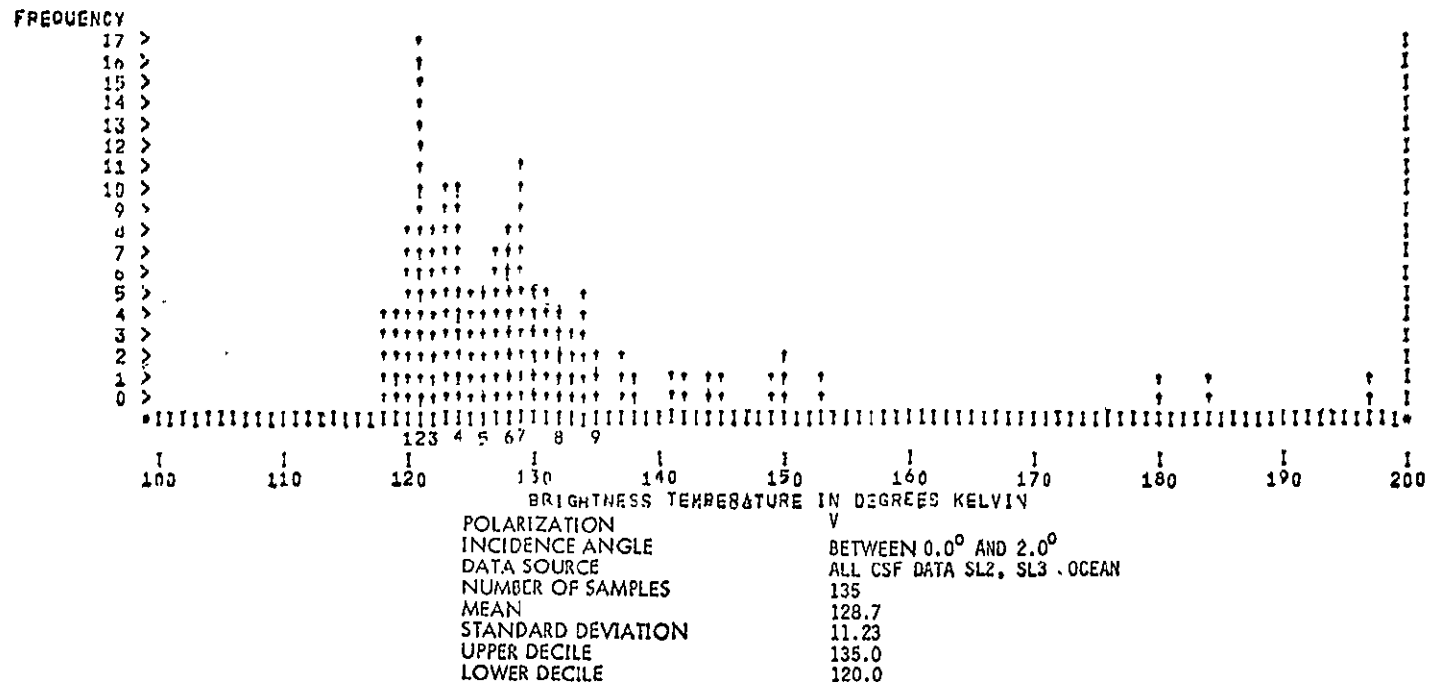


Figure 8.43.

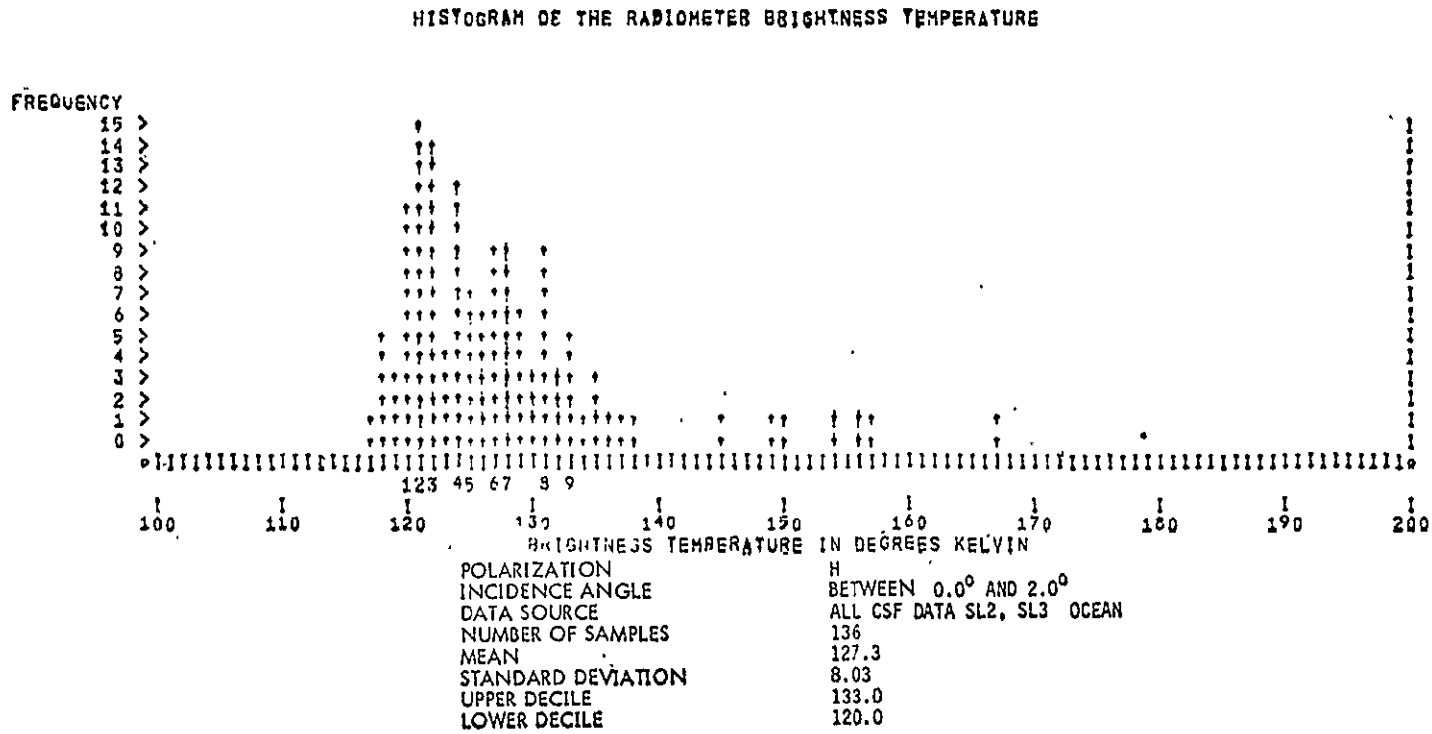
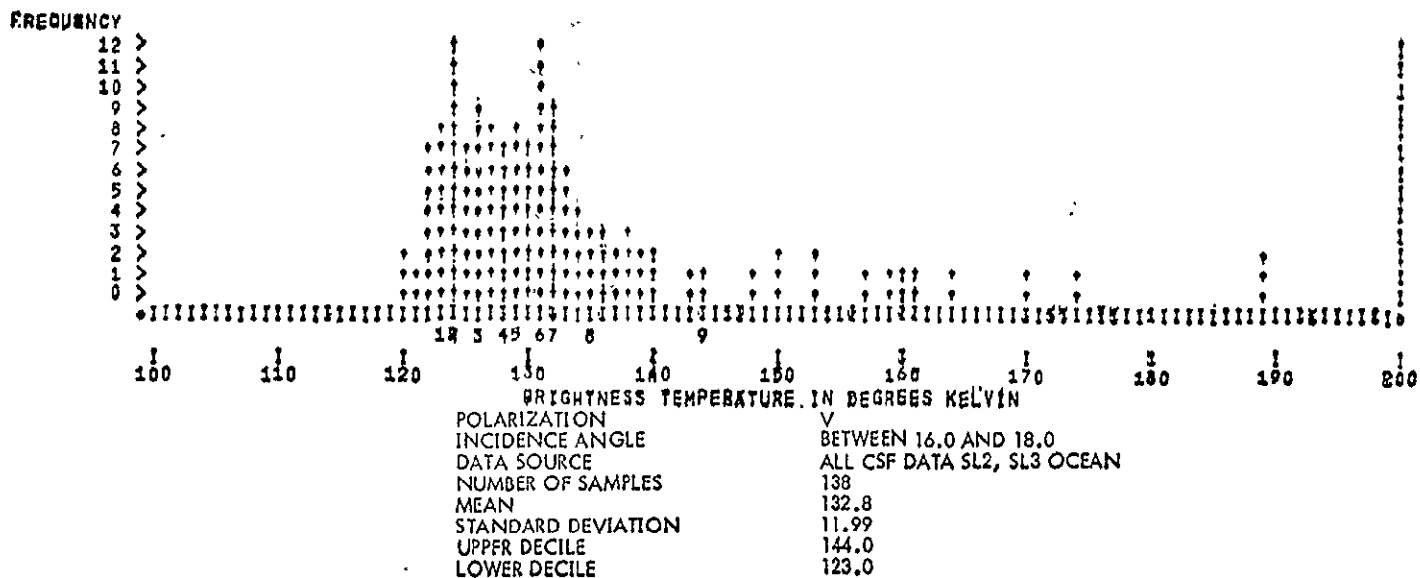


Figure 8.44.

C. 4

ORIGINAL PAGE IS  
OF POOR QUALITY

### HISTOGRAM OF THE RADIOMETER BRIGHTNESS TEMPERATURE



425

Figure 8.45.

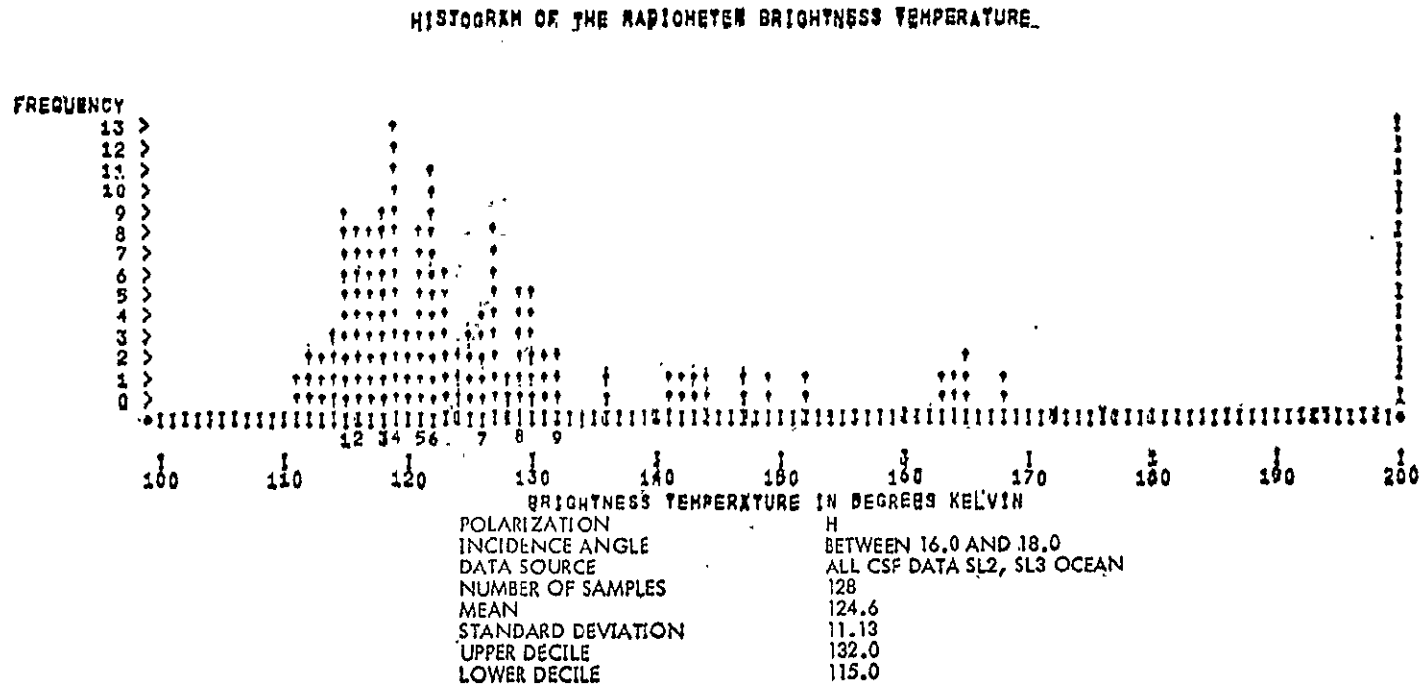


Figure 8.46.

ORIGINAL PAGE IS  
OF POOR QUALITY

427

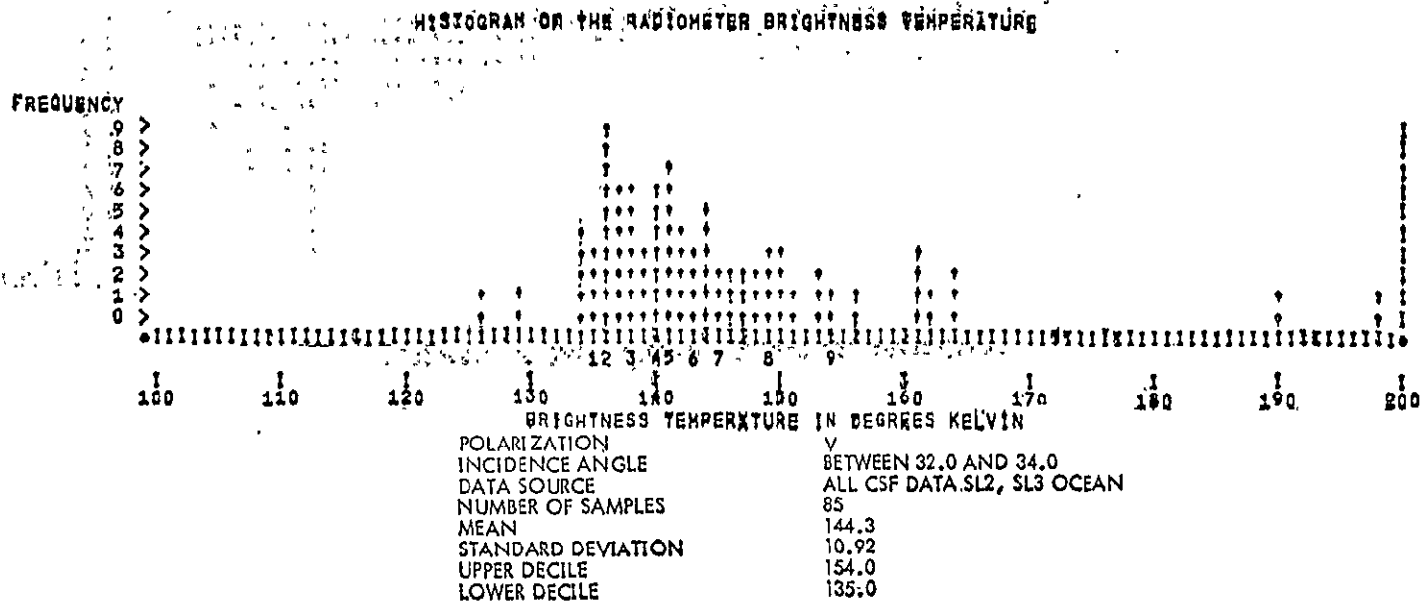


Figure 8.47.

HISTOGRAM OF THE RADIOMETER BRIGHTNESS TEMPERATURE

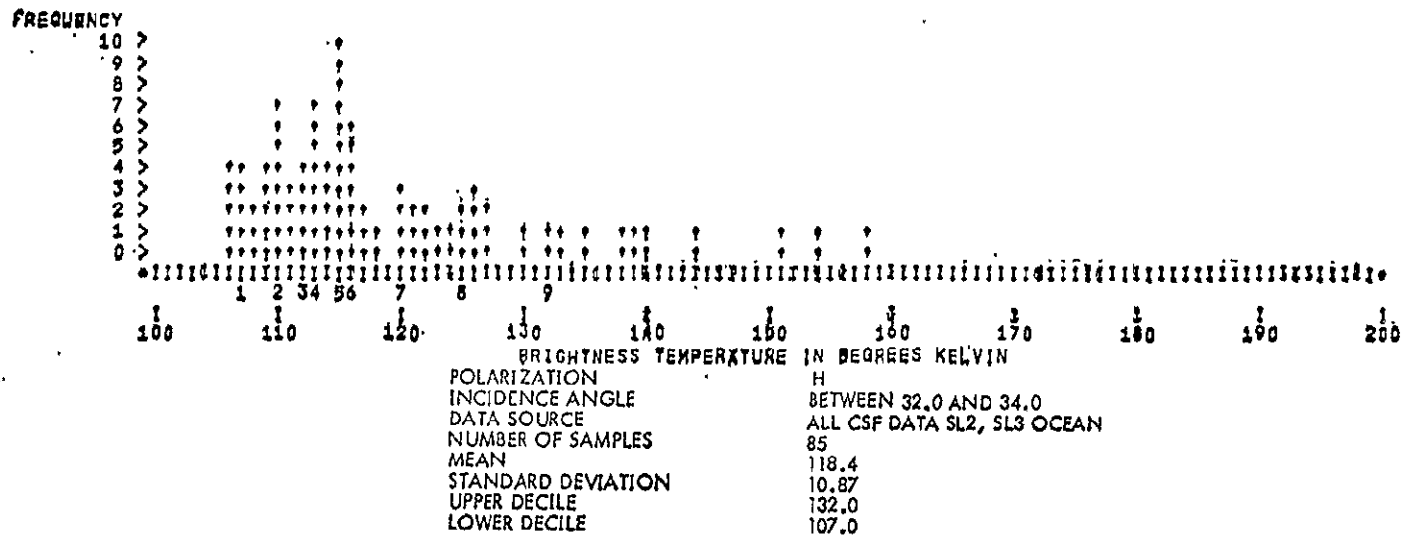


Figure 8.48.

ORIGINAL PAGE IS  
OF POOR QUALITY

429

### HISTOGRAM OF THE RADIOMETER BRIGHTNESS TEMPERATURE

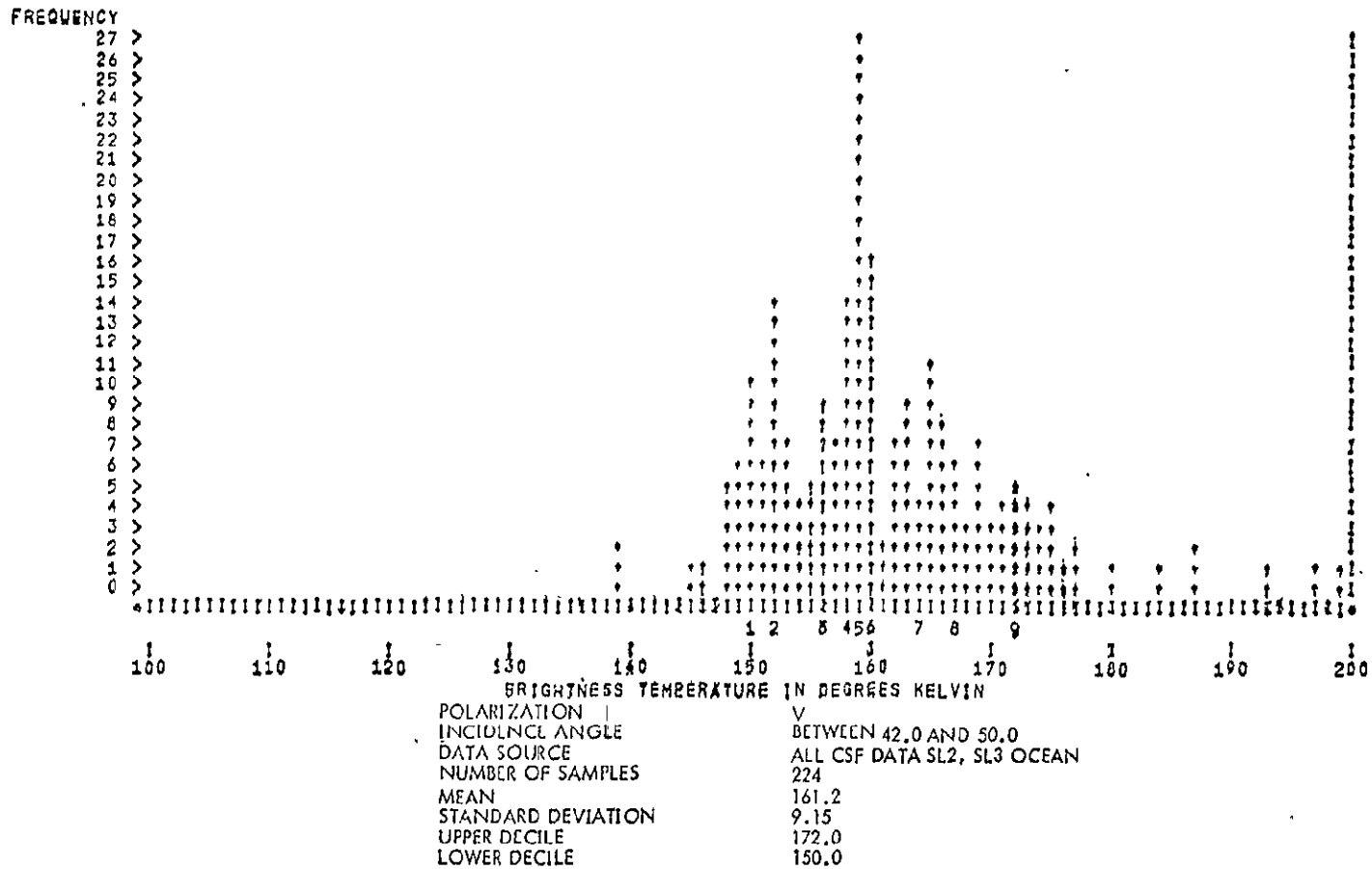


Figure 8.49.

HISTOGRAM OF THE RADIOMETER BRIGHTNESS TEMPERATURE

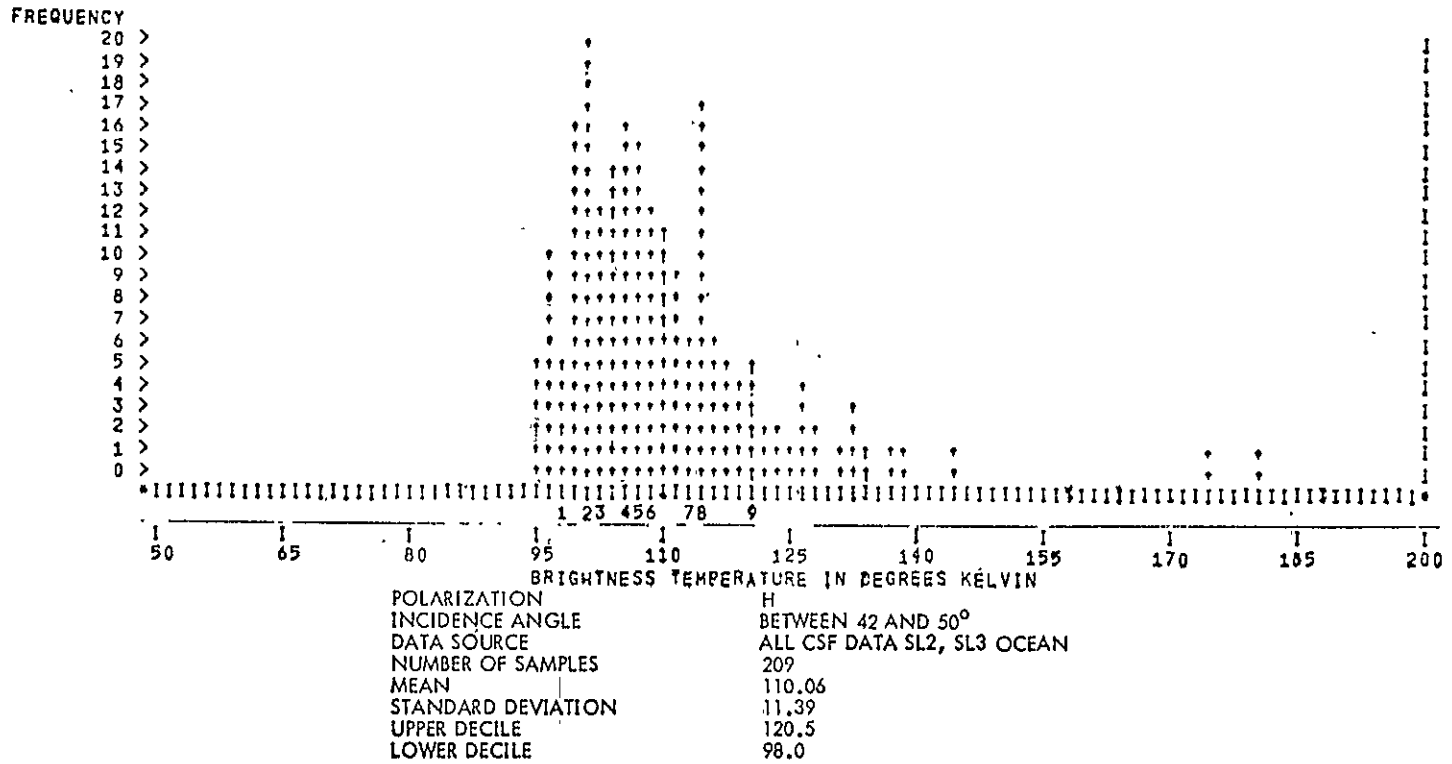


Figure 8.50.

### 8.1.5 Summary of Ensemble Statistics

No consistent trend of angular variation was observed for the brightness temperature over North America. A distinct angular trend was observed for ocean surfaces. The backscatter measurements over both land and ocean show extremely consistent trends.

Figure 8.51 shows a summary curve of the backscatter coefficient over North America. The numbers of samples included are indicated in the bar charts at the top of the figure. The mean and upper and lower deciles are plotted versus angle of incidence. The narrow bounds between deciles at angles around  $15^{\circ}$  is obvious from this figure. The lines are an eyeball fit and do not represent any mathematical curve-fitting. Polynomials and exponentials have been used to fit these data and the results are reported in a later section. The spread in the measured values is greatest at angles close to nadir. Figure 8.52 shows a similar summary for HH polarization. The number of samples is much smaller and the angular coverage is spotty. The trends, however, are consistent with those of VV polarization. Figure 8.53 shows the standard deviation computed for each angle group. This is a measure of the scatter at each angle and illustrates the point about the narrowest bounds at around  $15^{\circ}$ . The lines drawn are again eye-ball fits.

Figure 8.54 shows a summary of the radiometric response for vertical polarization over North America, and illustrates the lack of the angular trend suggested earlier. Figure 8.55 shows the summary for horizontal polarization and once again the lack of an angular trend is illustrated. The bounds differ by between  $22^{\circ}$  and  $30^{\circ}$ K for all angles. Figure 8.56 shows the standard deviations for each angle versus angle of incidence. The points showing low standard deviation (less than  $9^{\circ}$ K) are due to a small sample size which probably originated from one pass. This means that the regions considered are probably alike for that short extent of one data-take.

The angular backscatter response over the ocean surface is more steep than that over land. It saturated the receiver for near nadir incidence and was often well below the dynamic range of the instrument where precision specifications hold. The response for VV polarization is shown in Figure 8.57. The spread at  $47^{\circ}$  appears largest, but this point should be interpreted with the knowledge that the angle group considered for this case was a factor of 4 larger than the others. The spread between deciles at  $33^{\circ}$  and  $47^{\circ}$  is considerably greater than over land surfaces. Figure 8.58 shows the corresponding summary over ocean but with HH polarization. The response is similar to that for VV polarization; it is slightly higher near nadir and lower at  $47^{\circ}$  than the VV case. Figure 8.59 shows the summary of the backscatter response over an ocean surface with HV polarization. The range between deciles at angles close to nadir is extremely small. The range at

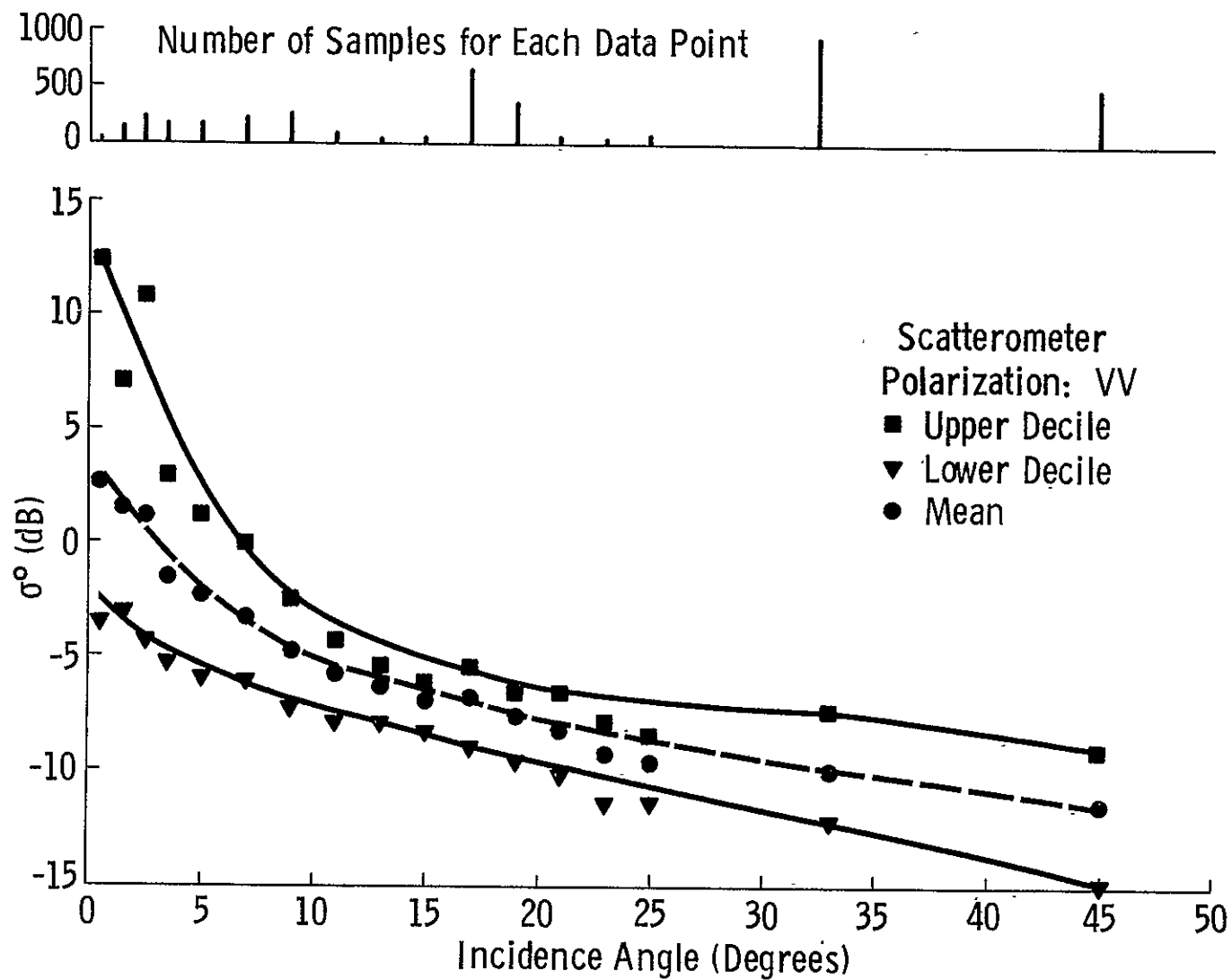


Figure 8.51. Summary of angular scatterometric response for VV polarization from S-193 scatterometer operations during SL2-SL3.

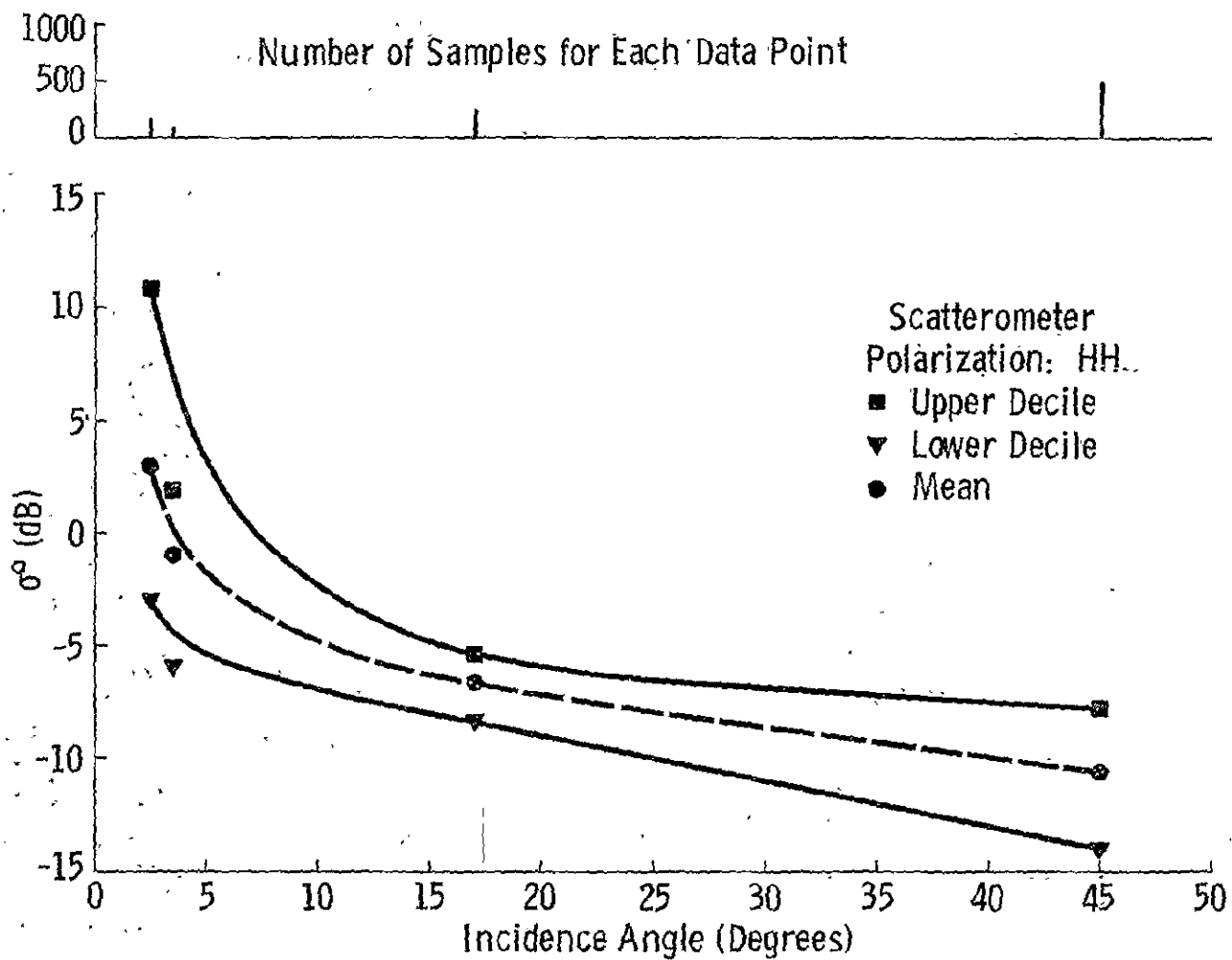


Figure 8.52. Summary of angular scatterometric response for HH polarization from S-193 scatterometer operation during SL2-SL3.

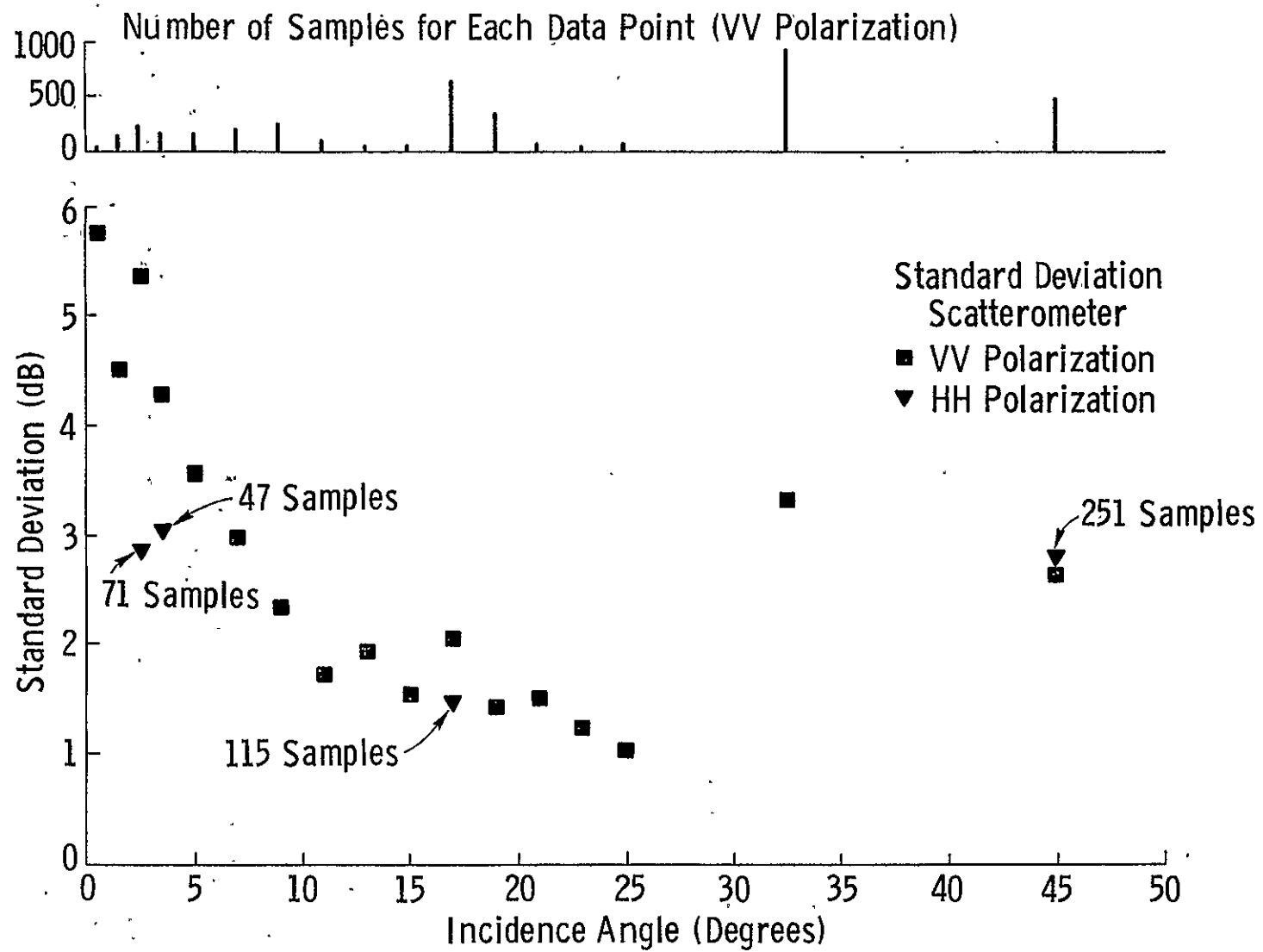


Figure 8.53. Standard deviations of backscatter measurement versus angle of incidence for VV and HH polarization over North America.

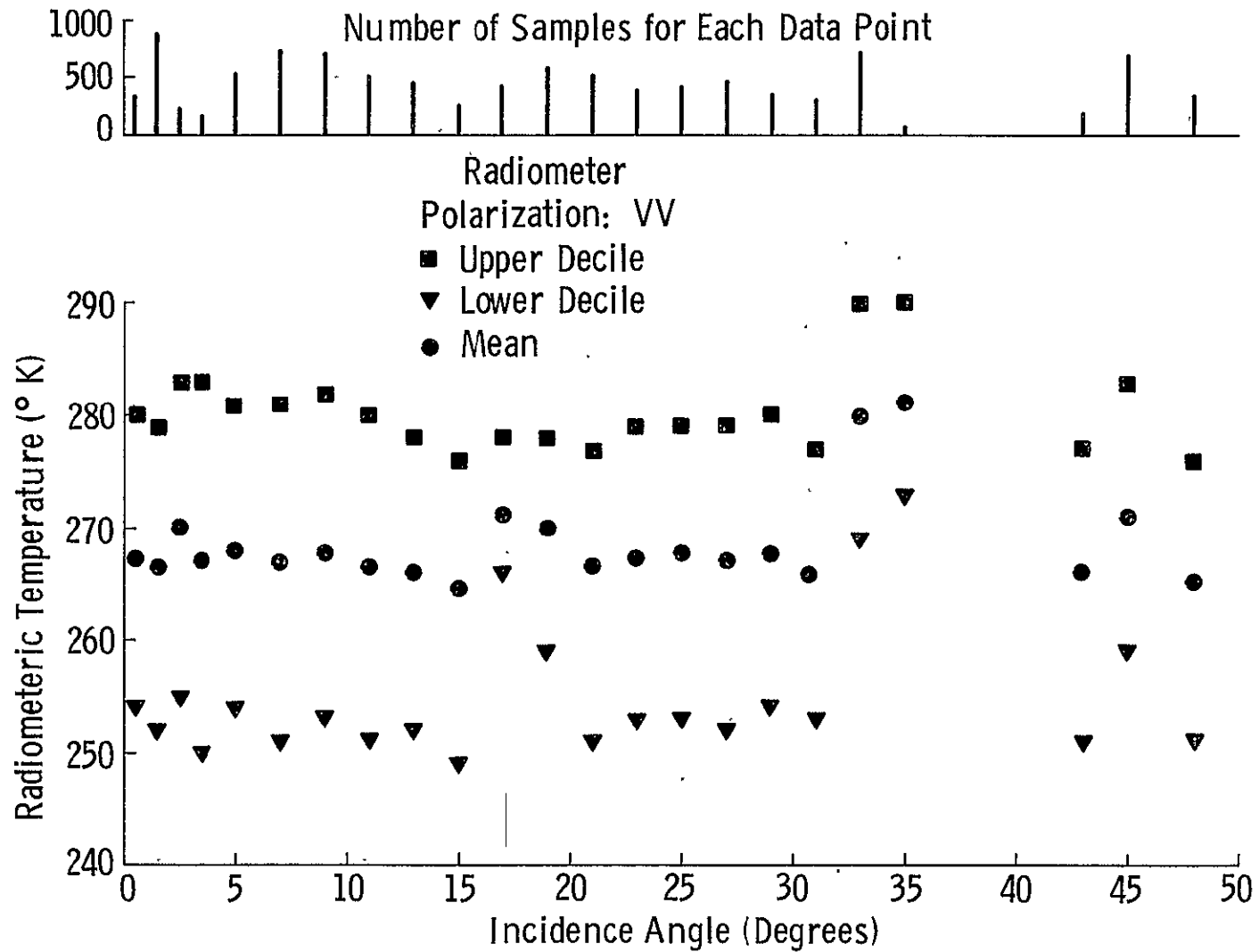


Figure 8.54. Summary of angular radiometric response for VV polarization from S-193 radiometer operations during SL2-SL3.

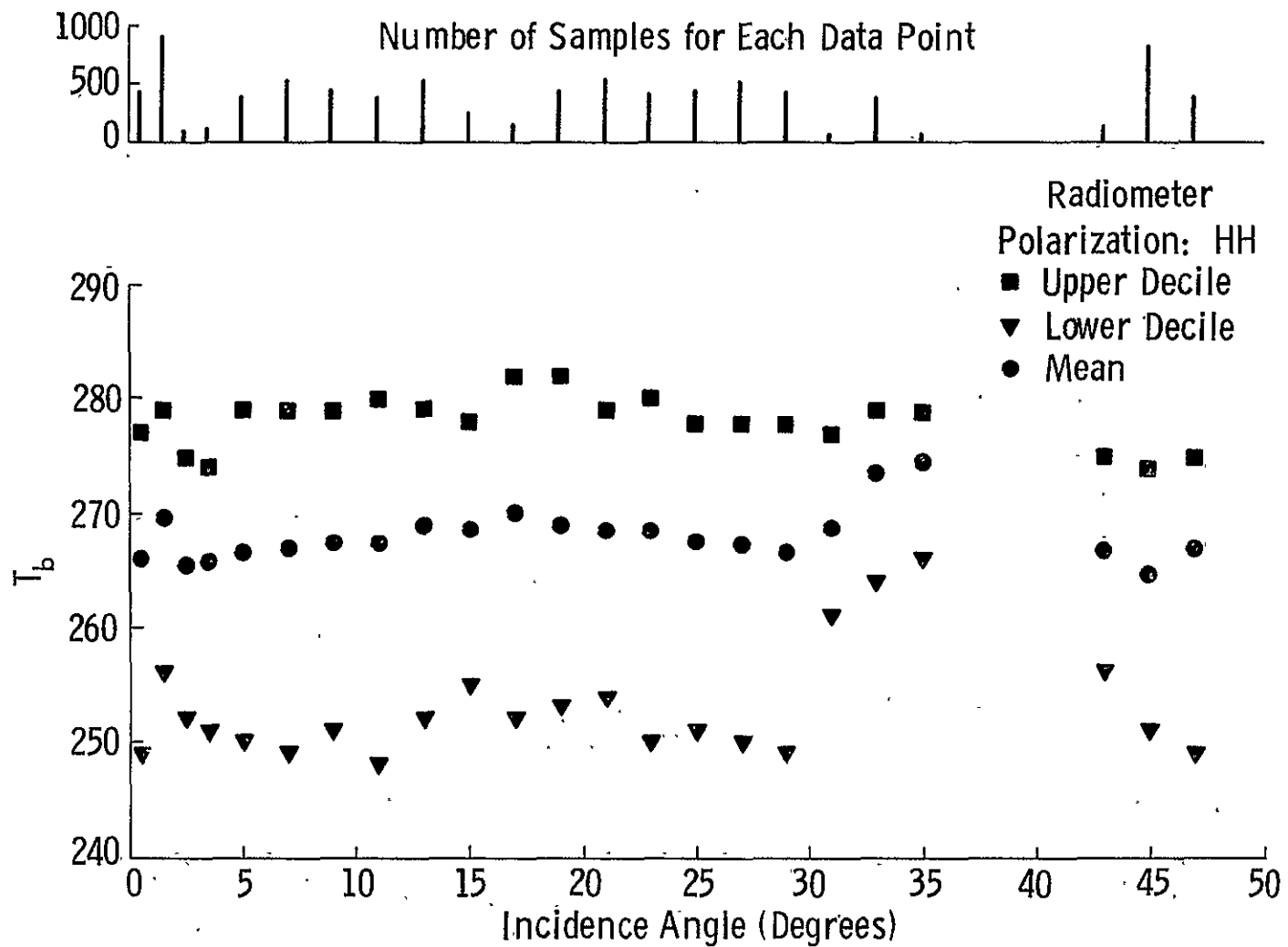


Figure 8.55. Summary of angular radiometric response for HH polarization from S-193 radiometer operations during SL2-SL3.

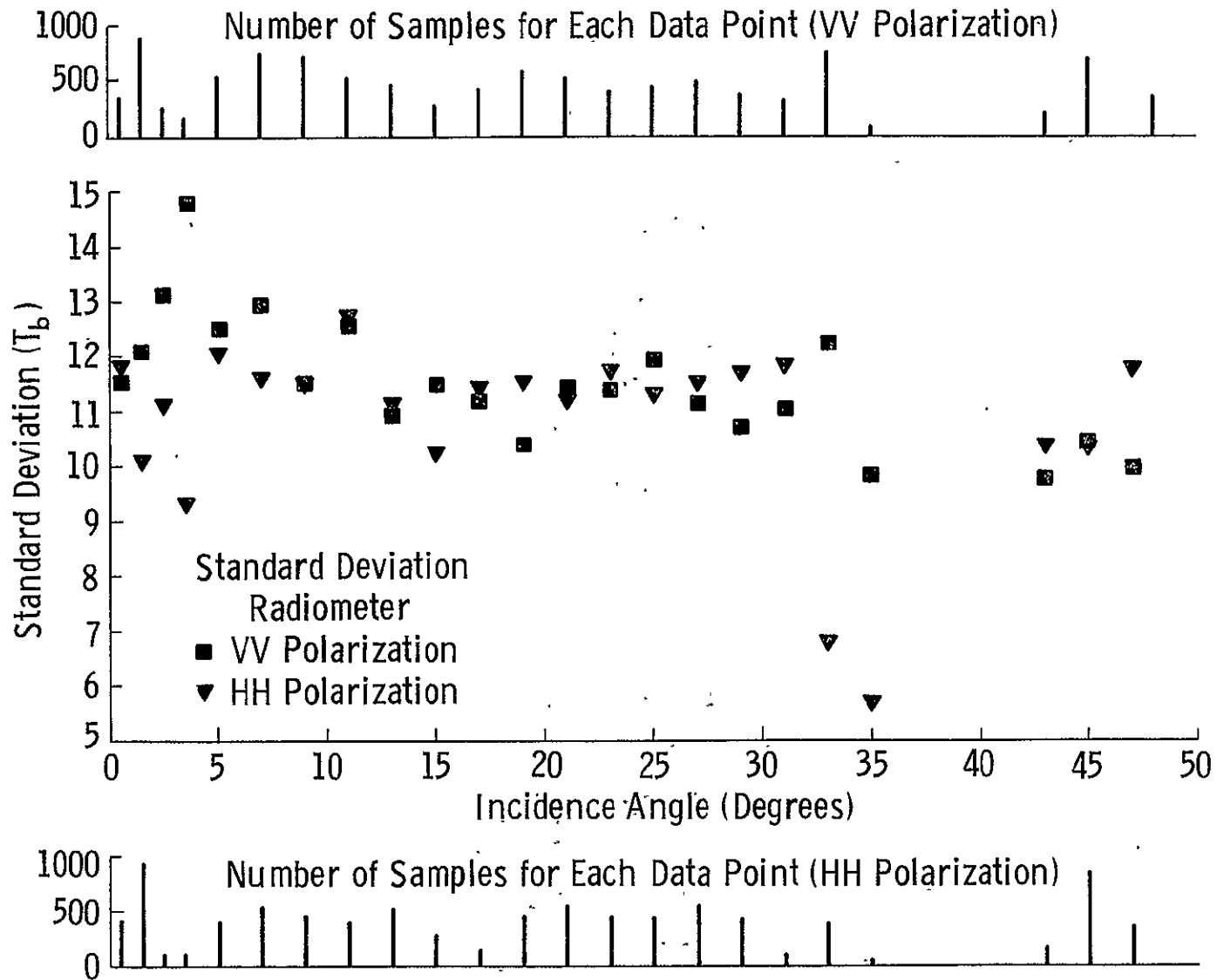


Figure 8.56 Standard deviations of S-193 Radiometer measurement (VV and HH polarizations) versus angle of incidence for North American targets from SL2-SL3 operations.

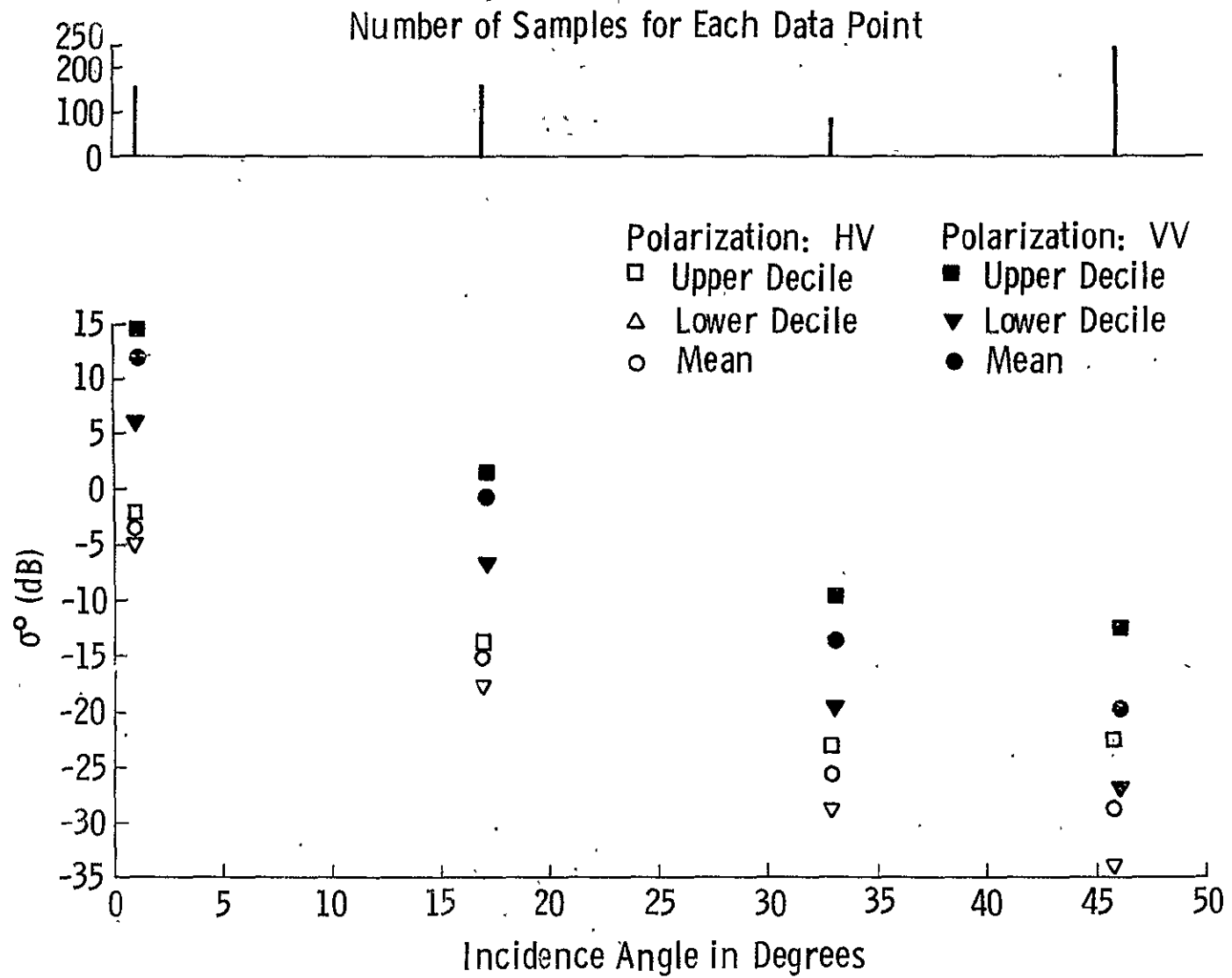


Figure 8.57. Summary of angular scatterometric response over ocean surfaces for VV and HV polarizations from S-193 scatterometer operations during SL2-SL3.

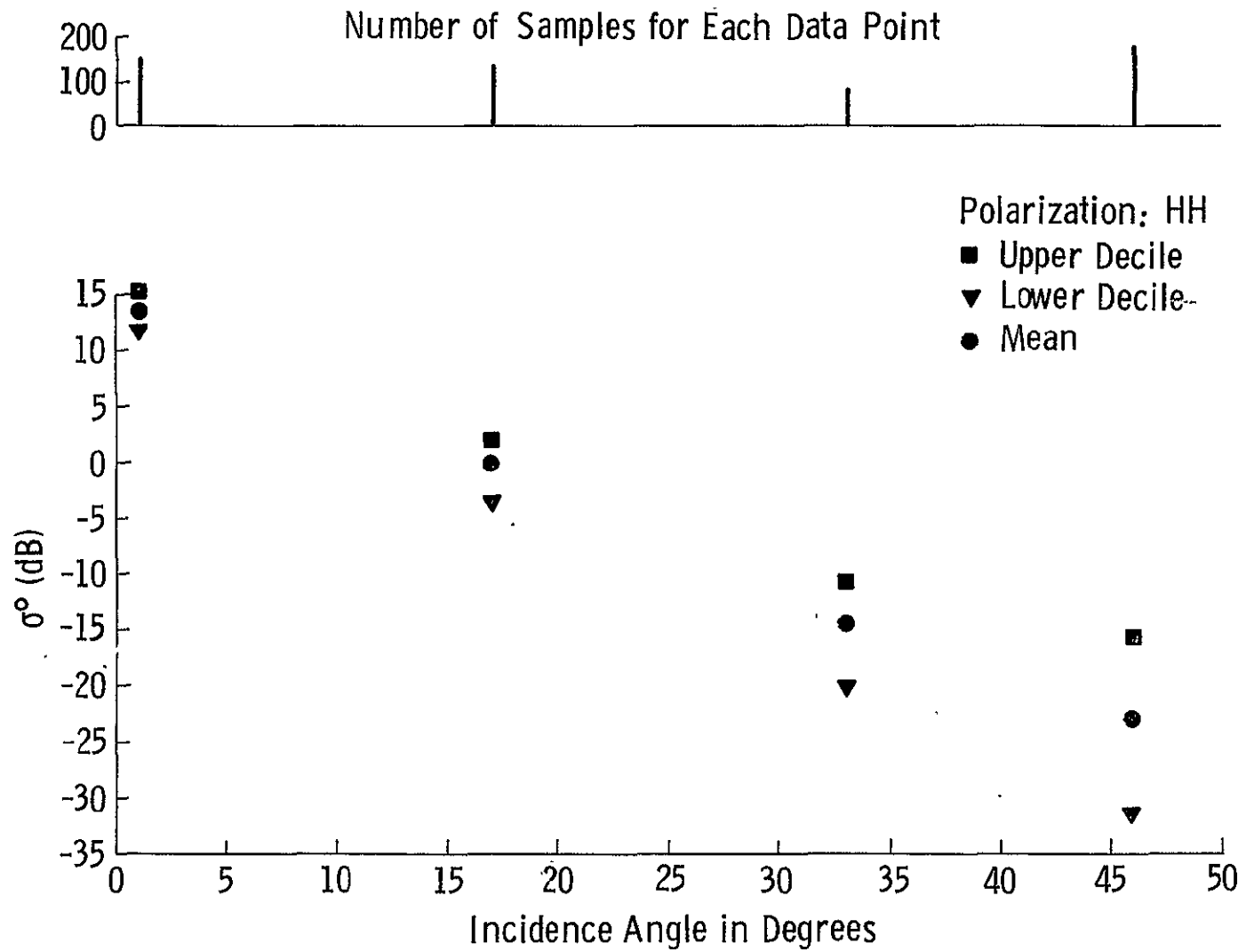


Figure 8.58. Summary of angular scatterometric response over ocean surfaces for HH polarization from SL2- SL3 data.

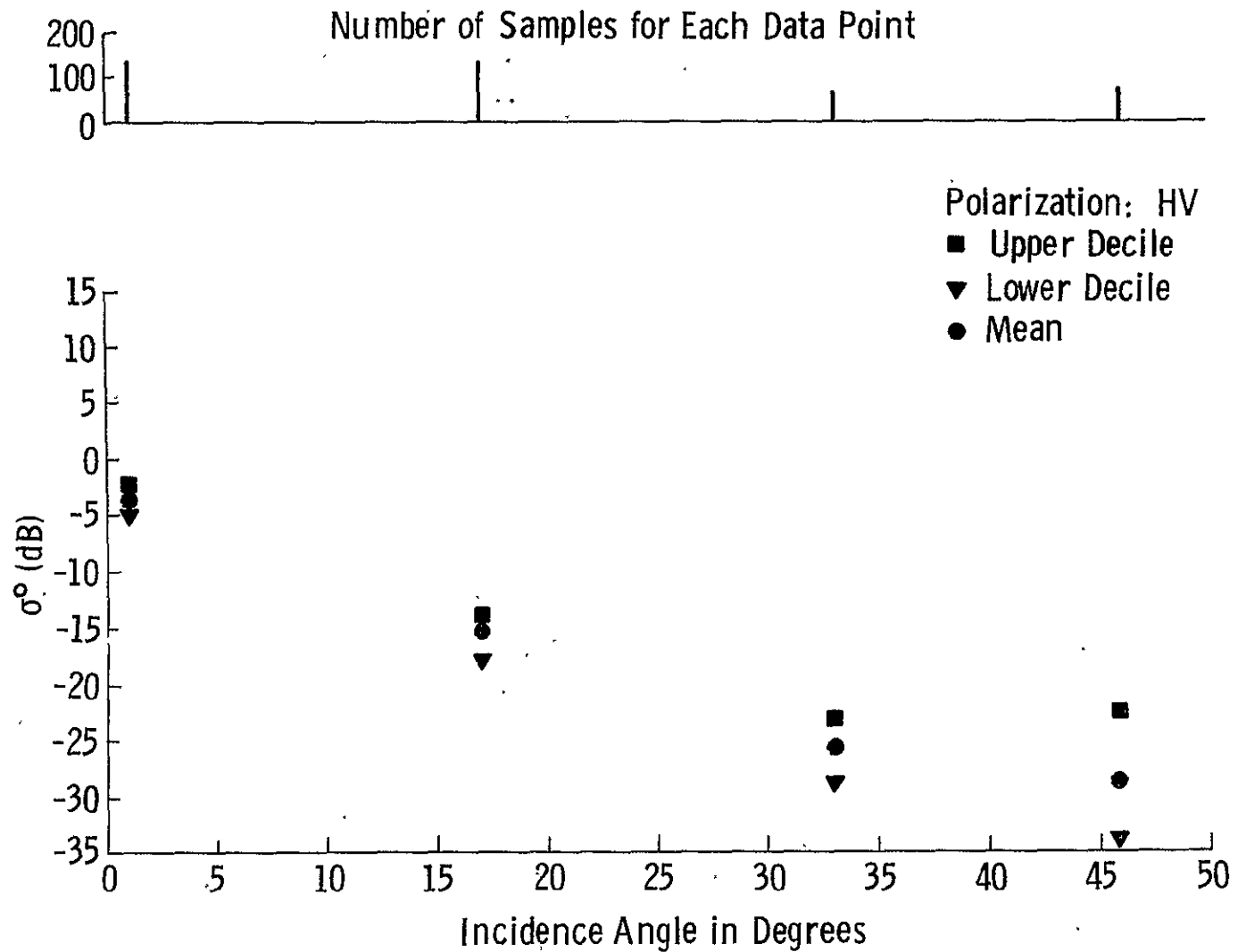


Figure 8.59. Summary of angular scatterometric response over ocean surfaces for HV polarization from SL2-SL3 data.

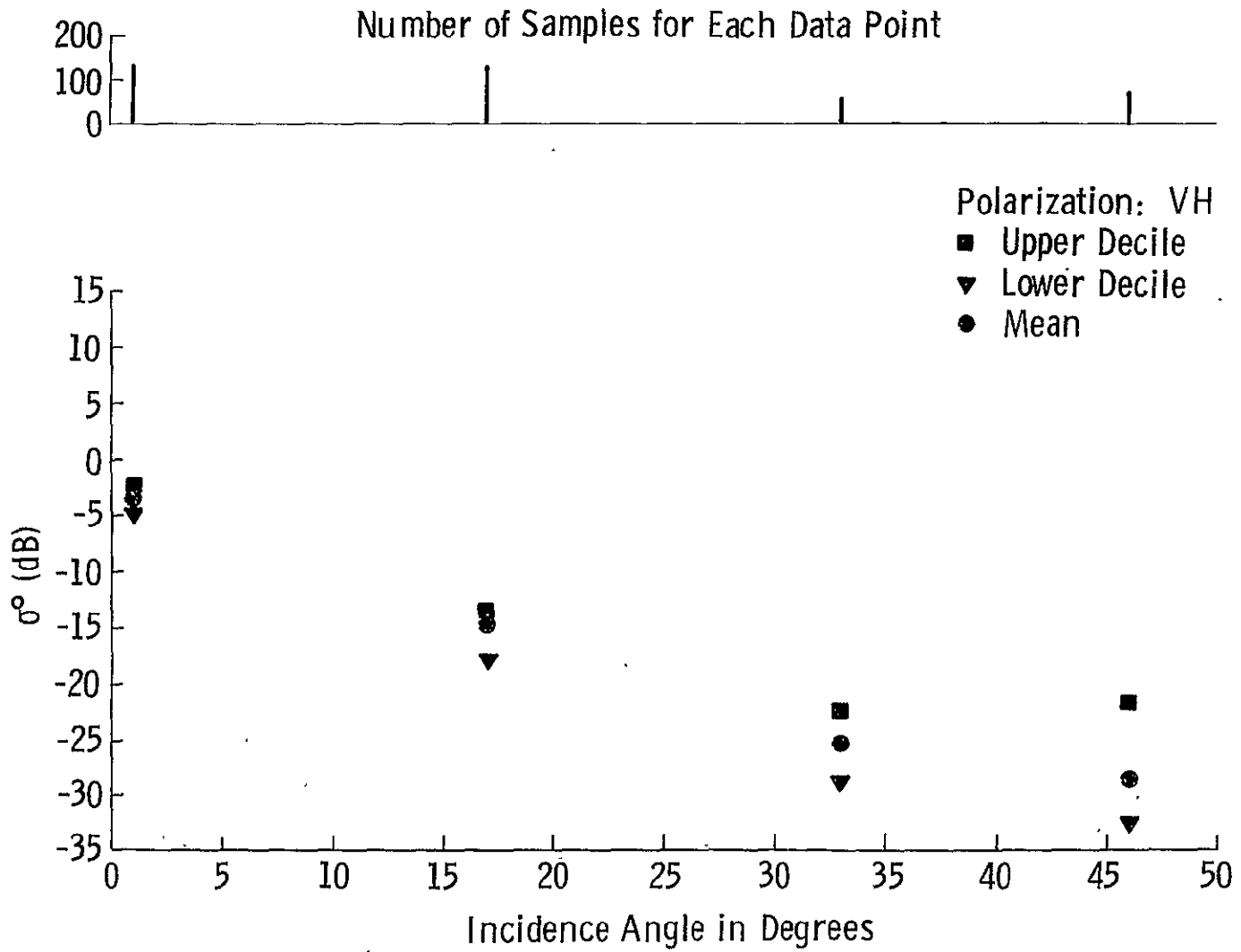


Figure 8.60. Summary of angular scatterometric response over ocean surfaces for VH polarization from SL2 - SL3 data.

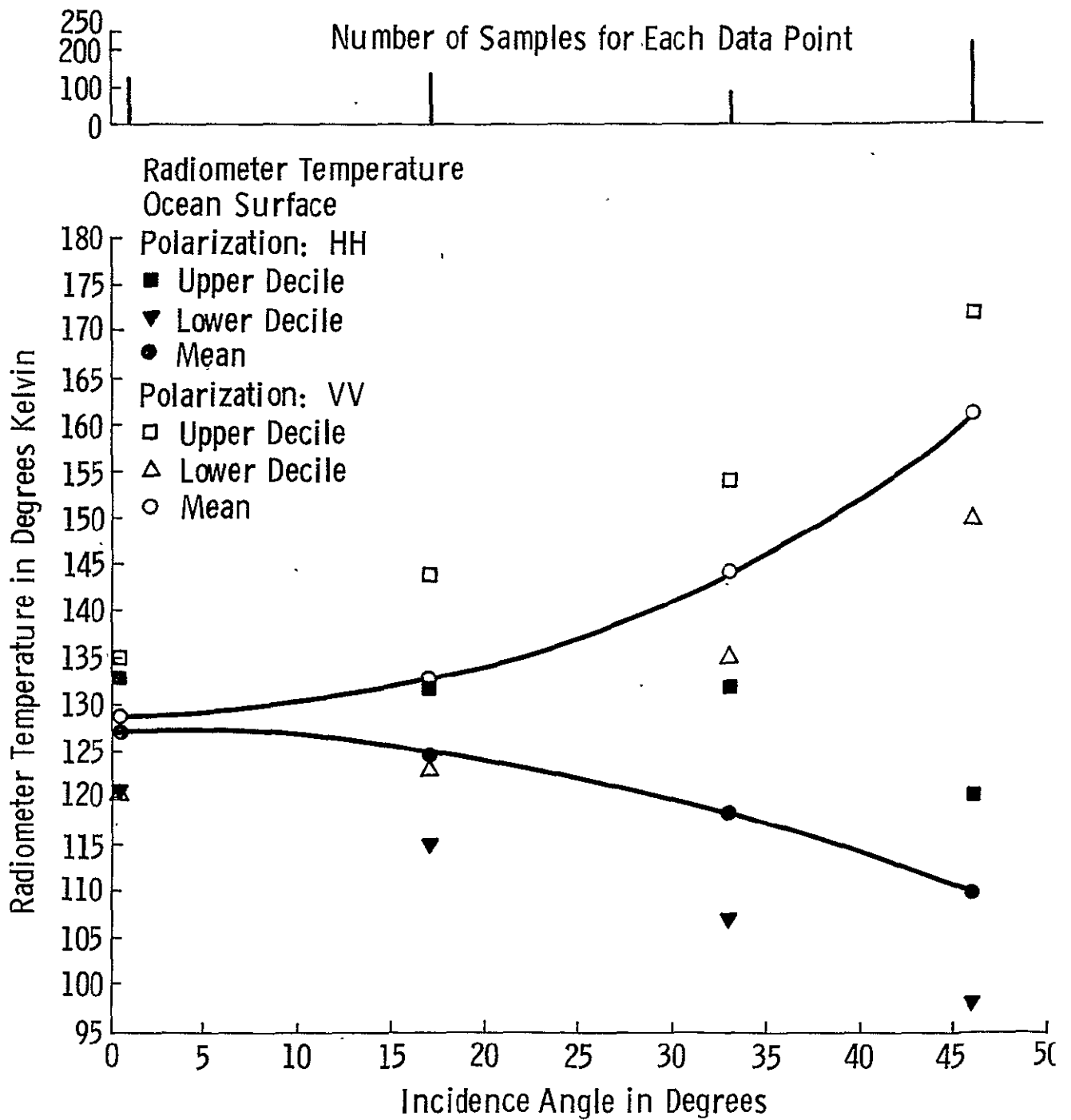


Figure 8.61. Summary of angular radiometric response over ocean surfaces from S-193 radiometer, non-contiguous mode operations during SL2-SL3.

$47^\circ$  was computed by considering a lower threshold of inclusion at  $-35$  dB. Many points fell below this threshold and so the values are probably biased upwards. The distinct angular trend is, however, consistent. Figure 8.60 shows the corresponding summary, but for VH polarization. It is almost exactly the same as that for HV polarization and is consistent with prior measurements and theoretical expectations.

Figure 8.61 shows the summary for the radiometric response for vertical and horizontal polarization. Unlike the land surface, the oceanic radiometric emission shows a definite angular trend that is consistent with prior measurements.

The response from South American targets is about  $2$  dB higher at around  $33^\circ$  than the corresponding North American targets and the lower decile of points from South America is comparable to the mean for the corresponding North American targets. The bounds between deciles at  $30^\circ$  over South America are about one half as large as over North America.

## 8.2 Design Data for Radar Systems

From the ensemble statistics prepared for the North American targets and for the ocean surface, some equations have been computed which describe the mean angular behaviour of the backscattering coefficient. These equations may be helpful along with the summary curves showing means and upper and lower deciles of backscatter vs angle, in the design of future radar systems.

The north American targets seemed to be best described by either a fourth order polynomial in incidence angle  $\theta$  up to  $50^\circ$ , or by an exponential of the form

$$\sigma^\circ = k_1 e^{-\theta/k_2}$$

(1)

for the range of incidence angles  $0^\circ$ - $11^\circ$  and another such exponential from  $11^\circ$ - $49^\circ$ . A summary table of the best fits as obtained from a stepwise linear regression analysis for the North American region and for ocean surfaces is provided in Table 8.1. The polynomials do not describe the  $\sigma^\circ$  vs  $\theta$  decay beyond  $50^\circ$ . A fourth order polynomial was obtained as a best fit for some cases where the variables to be entered for regression were chosen by the procedure considered. The variables were chosen in the order of the uncertainty they removed in the behaviour of the dependent variable, namely  $\sigma^\circ$ . The exponentials and polynomials were also computed for two separate sections of the

TABLE 8.1  
SUMMARY OF OPTIMAL REGRESSION EQUATIONS DESCRIBING  
THE ANGULAR BACKSCATTER FROM NORTH AMERICA AND FROM THE OCEAN

444

Target	Polarization	Type Of Fit	Region of Fit	Function of Theta	Correlation Coefficient
N. America	VV	Polynomial	0° - 45°	$1.656 + 0.0196\theta^2 - .84266\theta^3 - .000004\theta^4$	0.9988
N. America	VV	Polynomial	0° - 11°	$3.09145 - 1.1939\theta + 0.03506\theta^2$	0.9971
N. America	VV	Polynomial	11° - 45°	$-6.81362 - 0.002\theta^2$	0.9989
N. America	VV	Exponential	0° - 11°	$1.667 \exp(-\theta/5.595)$	0.9713
N. America	VV	Exponential	11° - 45°	$.3635 \exp(-\theta/29.551)$	0.9296
Ocean	VV	Polynomial	0° - 49°	$13.11133 - 0.57\theta - 0.01874\theta^2 + .00033\theta^3$	0.9992
Ocean	HH	Polynomial	0° - 49°	$14.004 - .59865\theta - 0.05642\theta^2 + 0.00032\theta^3$	0.9998
Ocean	HV	Polynomial	0° - 49°	$-3.1064 - .61619\theta - 0.01487\theta^2 + 0.00031\theta^3$	0.9981
Ocean	VV	Exponential	0° - 49°	$15.60763 \exp(-\theta/6.13)$	0.9882
Ocean	HH	Exponential	0° - 49°	$21.91891 \exp(-\theta/5.348)$	0.9946
Ocean	HV	Exponential	0° - 49°	$0.317157 \exp(-\theta/6.99)$	0.9777

NOTE: Polynomials are for  $\sigma^\circ$  in dB; Exponentials are for  $\sigma^\circ$  in numeric.

$\sigma^{\circ}$  vs  $\theta$  response because a qualitative curve to be composed of two quite distinct regions. The correlation coefficient for each of the fits is also shown in the summary table. The fits seem to be excellent for some instances and all show a correlation better than 0.93. All except one are better than 0.97. In interpreting the relationships, please note that the polynomials are fit to  $\sigma^{\circ}$  expressed in dB and the exponentials are fits to  $\sigma^{\circ}$  expressed in numerics.

It is interesting to note that backscatter from land follows two types of decay curves: one from near nadir to approximately  $11^{\circ}$ , and another from  $11^{\circ}$  out to  $47^{\circ}$ . Actually, the data at incidence angles between  $11^{\circ}$  and  $17^{\circ}$  is very scarce so that the incidence angle where the cross-over occurs may not be  $11^{\circ}$ , but instead higher. The ocean seems to follow an exponential decay and is fit very well with a third order polynomial. There is no noticeable distinction between the decay in backscatter for the  $0^{\circ}$ - $11^{\circ}$  and  $11^{\circ}$ - $47^{\circ}$  angle groups for the ocean as there is in the case for land.

In summary, it appears as though the land backscatter may be a two-process phenomenon; one predominating in near nadir region ( $0^{\circ}$ - $11^{\circ}$ ) and the other in the region from  $11^{\circ}$ - $47^{\circ}$ . The ocean backscatter, on the other hand, appears to be a single process phenomenon.

### 8.3 Correlation Study Results

The correlation between the response by terrain for various S-193 radiometer/scatterometer configurations of operation was computed. The correlation was estimated by computing the Neyman-Pearson correlation coefficient for various sensor configurations. In particular the following cases are reported.

1. Correlation coefficients between the response of an ocean surface to all possible configurations using the ITNC mode. There are 30 possible sensor configurations.
2. Correlation coefficients between the radiometric and scatterometric responses at incidence angles close to  $32^\circ$ , for vertical polarization. The data base consists of some CTC pitch offset  $29^\circ$  data and includes land and ocean data. The radiometer data has been reduced to emissivity by approximating the physical temperature from climatological records.
3. Correlation coefficient between the radiometer and scatterometer response for vertical polarization for incidence angles close to  $32^\circ$  from an ocean surface. The data base is obtained from CTC pitch  $29^\circ$  R/S mode of operation.
4. Correlation coefficient between the radiometer and scatterometer response under the same conditions as (3) but over land surfaces. The data base is from the CTC pitch  $29^\circ$  R/S mode.
5. Correlation coefficient between the backscatter response for vertical and horizontal polarization at around  $32^\circ$  incidence over land targets. The data base is obtained from the CTC pitch  $29^\circ$  (scat only) mode of operation.
6. Correlation coefficient between the response at five angles of incidence of scatterometer operation (vertical polarization) from ITC passes over land and ocean.
7. Correlation coefficient between the response at five angles of incidence of scatterometer operation (vertical polarization) from the long pass from Texas to Maine on day 253.

The intrack modes of operation provide five angle looks at the same target point, if run long enough. The time it takes to get even one five-angle look at a target is in the neighborhood of 75 seconds. The correlation coefficients are computed for responses, under various sensor configurations, of the same target. This means that the in-track data were grouped to find five angle sets before the responses were included in the data base for this study. With the in-track contiguous mode of operation, only the scatterometer data at the polarization selected was included. For the In-Track Non-Contiguous

(ITNC) mode of operation, there are again five angles, but for each angle there are four scatterometer observations (at polarizations VV, VH, HV, and HH) and two radiometer observations (polarizations V and H). This provides 30 sensor configuration responses over the same target cell. The data were merged accordingly and data over the ocean were used to compute correlation coefficients.

### Results of Correlation Study

It has been suggested by Moore and Ulaby [1969] that a combination of a scatterometer and a radiometer can provide more information than is available by operating each instrument singly. If, however, the correlation coefficient between the response of the radiometer and the scatterometer over diverse target and atmospheric conditions is very high, then the use of the two sensors operated jointly is redundant. On the other hand, if the correlation between the response of the two is not high, then it can be assumed that the sensitivity of each sensor to target and atmospheric differences is not similar, and, indeed, information obtained from one sensor could augment that from the other. A similar argument exists for operation of the scatterometer and radiometer with various polarization configurations and for operation at various angles of incidence.

The In-Track Non-Contiguous Mode was exercised mainly over the ocean. The data obtained provides enough samples (over 130) of responses with all thirty sensor configurations over the same target cell. The thirty sensor configuration responses were treated as separate variables and correlations among all of them computed. The result was a 30 x 30 matrix of correlation coefficients. This matrix was too large to report as it was; therefore, selected elements of it were grouped and are reported in Tables 8.2 through 8.5. The selection of the variables grouped together in the tables shown should allow one to estimate all the important elements in the 30 x 30 matrix. Below each table is a legend which describes the variable. For quick reference, one can convert from variable number to the sensor configuration by considering that the first six variables are for a 48° pitch, second six for 40.1°, third six for 29.4°, fourth six for 15.6°, and the fifth six for 0.0° pitch. Each group of six is arranged according to  $\sigma^{\circ}$  (VV),  $\sigma^{\circ}$  (VH),  $\sigma^{\circ}$  (HV),  $\sigma^{\circ}$  (HH),  $T_B(V)$ ,  $T_B(H)$ .

Table 8.2 shows the correlation matrix for the backscatter response for VV polarization, radiometric temperature for vertical and for horizontal polarization at all five pitch angles of ITNC mode operation. As expected, the correlation between vertical and horizontal polarization radiometer temperatures is high for near nadir incidence

ORIGINAL PAGE IS  
OF POOR QUALITY

Table 8.2.

Correlation Matrix for 15 of the 30 sensor configurations of ITNC mode operation. Responses considered are  $\sigma_{VV}^{\circ}$ ,  $T_{BV}$ ,  $T_{BH}$  at five angles of incidence.

448

	1	5	6	7	11	12	13	17	18	19	23	24	25	29	30
1	<u>1.0000</u>														
5	0.2374	<u>1.0000</u>													
6	0.3476	<u>0.8810</u>	<u>1.0000</u>												
7	<u>0.7498</u>	0.1127	0.1362	<u>1.0000</u>											
11	0.2935	<u>0.8808</u>	<u>0.7262</u>	0.2387	<u>1.0000</u>										
12	0.3690	<u>0.7635</u>	<u>0.7523</u>	0.3253	<u>0.8692</u>	<u>1.0000</u>									
13	0.3779	-0.1241	-0.1030	<u>0.6770</u>	-0.0732	-0.0178	<u>1.0000</u>								
17	0.2224	<u>0.5576</u>	0.4133	0.1727	<u>0.6675</u>	<u>0.5497</u>	0.0149	<u>1.0000</u>							
18	0.2359	0.4762	0.4057	0.1957	<u>0.6120</u>	<u>0.5791</u>	0.1100	<u>0.8673</u>	<u>1.0000</u>						
19	0.0105	-0.2704	-0.2050	0.2085	-0.2824	-0.1746	<u>0.5377</u>	-0.1619	-0.0601	<u>1.0000</u>					
23	0.2404	0.4220	0.2982	0.1960	<u>0.5510</u>	0.4624	0.0840	0.4822	<u>0.5130</u>	-0.1290	<u>1.0000</u>				
24	0.2277	0.4644	0.3819	0.1873	<u>0.6099</u>	<u>0.5767</u>	0.0954	<u>0.5580</u>	<u>0.6284</u>	-0.1059	<u>0.9207</u>	<u>1.0000</u>			
25	-0.0094	-0.1476	-0.1248	0.0388	-0.0876	-0.1424	0.0293	-0.0566	-0.0973	0.0658	-0.0434	-0.1067	<u>1.0000</u>		
29	0.1217	0.3773	0.2182	0.1237	0.4765	0.3462	0.0782	0.4216	0.3946	-0.0199	0.4088	0.4584	-0.0307	<u>1.0000</u>	
30	0.1626	0.4626	0.3234	0.1231	<u>0.5832</u>	0.4781	0.0456	<u>0.5078</u>	<u>0.5110</u>	-0.0997	0.4874	<u>0.5859</u>	-0.0965	<u>0.9411</u>	<u>1.0000</u>

LEGEND

- |                                   |                                  |                                 |
|-----------------------------------|----------------------------------|---------------------------------|
| 1. $\sigma_{VV}^{\circ}$ at 48.0° | 12. $T_{BH}$ at 40°              | 23. $T_{BV}$ at 15°             |
| 5. $T_{BV}$ at 48.0°              | 13. $\sigma_{VV}^{\circ}$ at 29° | 24. $T_{BH}$ at 15°             |
| 6. $T_{BH}$ at 48.0°              | 17. $T_{BV}$ at 29°              | 25. $\sigma_{VV}^{\circ}$ at 0° |
| 7. $\sigma_{VV}^{\circ}$ at 40°   | 18. $T_{BH}$ at 29°              | 29. $T_{BV}$ at 0°              |
| 11. $T_{BV}$ at 40°               | 19. $\sigma_{VV}^{\circ}$ at 15° | 30. $T_{BH}$ at 0°              |

Correlations exceeding 0.5 have been underlined to facilitate locating them in the table.

(variables 29 and 30). The reason that this correlation is not much closer to unity is not readily apparent. No doubt the precision of the instrument is a reason for some decorrelation. The bounds of the radiometer data are small if one discards the CTNC pass over Hurricane Ava and the tropical storm Christine pass. The variations due to imprecision of the instrument can be seen to be a non-negligible portion of the total variations and cause the correlation coefficient to be only 0.94. The correlation between the vertically and horizontally polarized response at any angle remains relatively high, reaching a low of 0.867 at 30° (variables 17 and 18). The correlation between the vertically polarized radiometer response at 48° and the vertically polarized response at 40° is as high as that between the two polarizations at 48°, while the corresponding correlation between  $T_{BH}$  at 48° and 40° is only 0.75. In fact, the vertically polarized brightness at 48° is more correlated with the horizontal at 40° than the horizontal at 48° is with the horizontal 40°. The same phenomenon occurs between 40° and 29° for the two brightness temperatures. It is reversed between 29° and 15° cases and between the 15° and 0° cases. Since  $T_{BH}$  is more sensitive to ocean variations at larger angles than  $T_{BV}$ , the results are not totally unexpected.

The correlation of the backscatter coefficient (vertical polarization) at 48° is highest with the backscatter at 40°. The correlation between the response for all other angles is small. There is almost total decorrelation between the  $\sigma^0$  at 48° and  $\sigma^0$  near nadir. The correlations between adjacent incidence angles (for example 15° and 30°, rather than 15° and 40°) is much higher than others. This correlation decreases to only 0.066 between the backscatter at 15° and that near nadir. The correlation of backscatter near nadir with radiometric temperature at all angles and backscatter measurements at all angles away from nadir is low. Probably this is caused by saturation of many near-nadir  $\sigma^0$  measurements. The maximum negative correlation is between backscatter (VV) at 15° and brightness temperature (V) at 40°. It is only -.28. It would be too voluminous to describe each of the correlations in the matrix. The reader is requested to scan the matrix for any other correlations of interest.

Table 8.3 shows the correlation matrix considering backscatter at VV and HH polarizations for all five angles (10 x 10 matrix). The backscatter for both polarizations at any angle is correlated with the exception of the near nadir incidence case. The correlation is highest at 15° where it is 0.987. The problem with the near nadir incidence case is that often due to saturation, the responses recorded are not correct. The responses for adjacent angles for both polarizations show a mild correlation. As before, the near nadir cases do not correlate with any other incidence angle case.

Table 8.3.

Correlation Matrix for 10 sensor configurations of ITNC mode. Responses considered are  $\sigma_{VV}^{\circ}$  and  $\sigma_{HH}^{\circ}$  at five angles of incidence.

	1	4	7	10	13	16	19	22	25	28
1	<u>1.0000</u>									
4	<u>0.8650</u>	<u>1.0000</u>								
7	<u>0.7498</u>	<u>0.6594</u>	<u>1.0000</u>							
10	<u>0.6320</u>	<u>0.6326</u>	<u>0.9315</u>	<u>1.0000</u>						
13	0.3779	0.3631	<u>0.6770</u>	<u>0.6344</u>	<u>1.0000</u>					
16	0.3570	0.3268	<u>0.6659</u>	<u>0.6336</u>	<u>0.9595</u>	<u>1.0000</u>				
19	0.0105	0.0688	0.2085	0.2233	<u>0.5377</u>	<u>0.5508</u>	<u>1.0000</u>			
22	0.0159	0.0816	0.2153	0.2321	<u>0.5282</u>	<u>0.5456</u>	<u>0.9874</u>	<u>1.0000</u>		
25	-0.0094	-0.0667	0.0388	0.0682	0.0293	0.0790	0.0658	0.0943	<u>1.0000</u>	
28	-0.1049	-0.1372	-0.0509	-0.0021	0.0633	0.1598	0.3115	0.3330	0.3421	<u>1.0000</u>

LEGEND

- |   |   |
|---|---|
| 1. $\sigma_{VV}^{\circ}$ at $48^{\circ}$  | 16. $\sigma_{HH}^{\circ}$ at $29^{\circ}$ |
| 4. $\sigma_{HH}^{\circ}$ at $48^{\circ}$  | 19. $\sigma_{VV}^{\circ}$ at $15^{\circ}$ |
| 7. $\sigma_{VV}^{\circ}$ at $40^{\circ}$  | 22. $\sigma_{HH}^{\circ}$ at $15^{\circ}$ |
| 10. $\sigma_{HH}^{\circ}$ at $40^{\circ}$ | 25. $\sigma_{VV}^{\circ}$ at $0^{\circ}$  |
| 13. $\sigma_{VV}^{\circ}$ at $29^{\circ}$ | 28. $\sigma_{HH}^{\circ}$ at $0^{\circ}$  |

Correlations exceeding 0.5 have been underlined to facilitate locating them in the table.

Table 8.4 shows the correlation matrix for backscatter with VH polarization and radiometric temperature with vertical polarization. There appears to be very little correlation between the cross-polarized backscatter and the brightness temperature with V polarization. Unlike the dominant polarization backscatter near nadir incidence, the cross-polarized backscatter near nadir has a correlation of 0.567 with the backscatter at  $15^{\circ}$ . Also, where there was total decorrelation between backscatter near nadir and all other angles, for dominant polarization cases, the cross-polarized backscatter (because of its lower value and, hence, no saturation) shows a negative correlation of  $-0.237$  with the corresponding backscatter at  $48^{\circ}$ . The adjacent angle cross-polarized backscatter seems more correlated than for any other angle pair.

Table 8.5 shows the correlation matrix between cross-polarized (VH) backscatter and dominant polarized (HH) backscatter for all five angles. The cross-polarized backscatter shows remarkable correlation with the dominant polarization backscatter at the same incidence angle. This correlation increases as the incidence angle gets smaller. Near nadir the correlation is 0.973. This is a very high correlation and the saturation of the dominant polarization case has no doubt helped this correlation.

In summary, it can be stated that the correlation between radiometer measurements and backscatter measurements is not high. The correlation between adjacent angles for backscatter and for radiometric temperature is higher than for angles of incidence which are further apart. The cross-polarized measurements do not correlate with the radiometric temperature, but they do correlate with the backscatter at the same angle with dominant polarization. The correlation between the two cross-polarized cases of backscatter (VH and HV polarization) is very high (not shown in tables). There appears to be no correlation between the near nadir incidence backscatter and that with the same or different polarizations for angles away from nadir. This could be, in part, due to the saturation of the receiver for backscatter measurements above 14 dB.

The cross-track contiguous pitch  $29^{\circ}$  radiometer/scatterometer data with VV polarization was used to find the correlations between the radiometric temperature and the backscatter. To reduce effects of the physical temperature on the radiometric temperature, the radiometric temperature was divided by the physical temperature of the target to get a measure of the emissivity. No atmospheric effects were corrected for. The physical temperature was estimated by extrapolation and interpolation of daily maximum temperatures obtained from NOAA summaries for the region and day of the pass. The fact that the actual temperature during the time of the pass was not the daily maximum temperature could cause some errors. The passes were mostly conducted within a couple hours of the

Table 8.4.

Correlation Matrix for 10 sensor configurations of ITNC mode. Responses considered are  $\sigma_{VH}^{\circ}$  and  $\sigma_{HH}^{\circ}$  at five angles of incidence.

	3	4	9	10	15	16	21	22	27	28
3	<u>1.0000</u>									
4	<u>0.8360</u>	<u>1.0000</u>								
9	<u>0.6562</u>	<u>0.6542</u>	<u>1.0000</u>							
10	<u>0.5565</u>	<u>0.6326</u>	<u>0.8817</u>	<u>1.0000</u>						
15	0.3457	0.3765	<u>0.5381</u>	<u>0.5852</u>	<u>1.0000</u>					
16	0.2708	0.3268	<u>0.5592</u>	<u>0.6336</u>	<u>0.9081</u>	<u>1.0000</u>				
21	0.0177	0.0643	0.1428	0.2397	0.3985	<u>0.5433</u>	<u>1.0000</u>			
22	0.0190	0.0816	0.1584	0.2321	0.4351	<u>0.5456</u>	<u>0.9205</u>	<u>1.0000</u>		
27	-0.2370	-0.1182	-0.1262	0.0075	0.0131	0.1664	<u>0.5671</u>	0.3379	<u>1.0000</u>	
28	-0.2506	-0.1372	-0.1311	-0.0021	0.0040	0.1598	<u>0.5794</u>	0.3330	<u>0.9727</u>	1.0000

452

LEGEND

- |   |   |
|---|---|
| 3. $\sigma_{VH}^{\circ}$ at $48^{\circ}$  | 16. $\sigma_{HH}^{\circ}$ at $29^{\circ}$ |
| 4. $\sigma_{HH}^{\circ}$ at $48^{\circ}$  | 21. $\sigma_{VH}^{\circ}$ at $15^{\circ}$ |
| 9. $\sigma_{VH}^{\circ}$ at $40^{\circ}$  | 22. $\sigma_{HH}^{\circ}$ at $15^{\circ}$ |
| 10. $\sigma_{HH}^{\circ}$ at $40^{\circ}$ | 27. $\sigma_{VH}^{\circ}$ at $0^{\circ}$  |
| 15. $\sigma_{VH}^{\circ}$ at $29^{\circ}$ | 28. $\sigma_{HH}^{\circ}$ at $0^{\circ}$  |

Correlations exceeding 0.5 have been underlined to facilitate locating them in the table.

Table 8.5.

Correlation Matrix for 10 sensor configurations of ITNC mode. Responses considered are  $\sigma_{VH}^{\circ}$  and  $T_{BV}$  for five angles of incidence.

	3	5	9	11	15	17	21	23	27	29
3	<u>1.0000</u>									
5	0.2602	<u>1.0000</u>								
9	<u>0.6562</u>	0.1801	<u>1.0000</u>							
11	0.2410	<u>0.8808</u>	0.3207	<u>1.0000</u>						
15	0.3457	-0.1146	<u>0.5381</u>	-0.0616	<u>1.0000</u>					
17	0.1287	<u>0.5576</u>	0.2129	<u>0.6675</u>	0.1560	<u>1.0000</u>				
21	0.0177	-0.2295	0.1428	-0.2198	0.3985	-0.0969	<u>1.0000</u>			
23	0.1479	0.4220	0.2250	<u>0.5510</u>	0.0697	0.4822	-0.0467	<u>1.0000</u>		
27	-0.2370	-0.1723	-0.1262	-0.1192	0.0131	-0.0511	<u>0.5671</u>	-0.0473	<u>1.0000</u>	
29	-0.0065	0.3773	0.1466	0.4765	0.0545	0.4216	0.0170	0.4088	-0.0172	<u>1.0000</u>

LEGEND

- |   |   |
|---|---|
| 3. $\sigma_{VH}^{\circ}$ at $48^{\circ}$  | 17. $T_{BV}$ at $29^{\circ}$              |
| 5. $T_{BV}$ at $48^{\circ}$               | 21. $\sigma_{VH}^{\circ}$ at $15^{\circ}$ |
| 9. $\sigma_{VH}^{\circ}$ at $40^{\circ}$  | 23. $T_{BV}$ at $15^{\circ}$              |
| 11. $T_{BV}$ at $40^{\circ}$              | 27. $\sigma_{VH}^{\circ}$ at $0^{\circ}$  |
| 15. $\sigma_{VH}^{\circ}$ at $29^{\circ}$ | 29. $T_{BV}$ at $0^{\circ}$               |

Correlations exceeding 0.5 have been underlined to facilitate locating them in the table.

local noon (due to sun elevation angle constraints) so that the deviations due to the diurnal variations of temperature should be small. The radiometric data for ocean surfaces was reduced to emissivity by considering an ocean temperature of 293°K. The total number of points included in the computation of the correlation coefficient was over 2000. There were no corrections made for the incidence angle which can vary from 32° to 36° for the CTC pitch 29° mode of operation. The correlation coefficient between the radiometric response and the backscatter was computed at 0.647.

Next, the targets over land and over water were separated and correlations between the radiometer and scatterometer responses at around 33° (VV) for both were computed. The correlation coefficient for ocean surfaces was 0.333. This is much higher than the one computed by using ITNC data (Table 8.2 variables 13 and 17). The cause for this is not known; one possible explanation is that the ITNC modes considered a more diverse set of oceanic conditions, whereas the CTC pitch 29° data over the ocean surface is very little. The correlation coefficient between the radiometric response and the backscatter over land surfaces was only 0.0831. There was considerably more land data than ocean data with CTC pitch 29° mode of operation; albeit mostly from the South and Southwestern region. Thus, the radiometer and scatterometer seem to provide quite different measures of the land. It can be seen that there is a big difference in the correlation coefficients computed by pooling land and ocean together and treating them separately. This is because part of the correlation is the fact that both respond differently to water and land.

The CTC pitch 29° scatterometer-only mode of operation was exercised extensively over South America. This mode provides backscatter measurements for VV and HH polarizations in an alternating sequence. The correlation coefficient between the backscatter with the two polarizations at around 33° incidence was computed. The number of points used in computing the correlation coefficient was around 4000. The correlation was 0.962. It could have been higher if one considers that the precision of the instruments is around  $\pm 0.25$  and the average spread for vast tracks of data were of the order of 1 or 2 dB. The means were also very close, with the vertical being slightly higher. No reliable data over North America, particularly the Southwest region, with the CTC pitch 29° scatterometer-only mode of operation could be found.

The In-Track contiguous mode provides a five-angle look at the same target point. The data were sorted so that the backscatter response at all five angles over a target were grouped. This was done for all ITC data in CSF format. There were only 226 data points which had been viewed by all five angles of incidence. The correlation matrix for the response at all five angles for ITC (VV) mode of operation is shown in Table 8.6 .

	$\sigma^{\circ}_{44^{\circ}}$	$\sigma^{\circ}_{40^{\circ}}$	$\sigma^{\circ}_{32^{\circ}}$	$\sigma^{\circ}_{17^{\circ}}$	$\sigma^{\circ}_{0^{\circ}}$
$\sigma^{\circ}_{44^{\circ}}$	<u>1.0</u>				
$\sigma^{\circ}_{40^{\circ}}$	0.3158	<u>1.0</u>			
$\sigma^{\circ}_{32^{\circ}}$	0.0261	<u>0.7464</u>	<u>1.0</u>		
$\sigma^{\circ}_{17^{\circ}}$	<u>-0.6396</u>	-0.3598	0.1158	<u>1.0</u>	
$\sigma^{\circ}_{0^{\circ}}$	<u>-0.6083</u>	-0.4551	-0.0780	<u>0.8077</u>	<u>1.0</u>

TABLE 8.6.

Correlation Matrix of  $\sigma^{\circ}_{VV}$  at five angles of incidence from ITC data.

The highest correlation is between  $\sigma^{\circ}$  near nadir and  $\sigma^{\circ}$  at around  $17^{\circ}$ . This is probably influenced by the fact that land and water are very distinct in their backscatter response near nadir. The correlation between the response at  $40^{\circ}$  and that at around  $33^{\circ}$  is also fairly high. There seems to be a problem with the response at  $44^{\circ}$ . The designed value for the pitch angle was actually  $48^{\circ}$ . The Doppler filters have a bandwidth which allows the spectrum to be contained within  $\pm 6^{\circ}$  of this nominal value. During operation of the ITC mode, the pitch excursion rarely exceeded  $42^{\circ}$ . Consequently the return power fell on the skirts of the Doppler filters. Measures to account for this malfunction were taken by NASA/JSC and an algorithm established to account for the attenuation. Unfortunately, the estimated attitude errors of the spacecraft have some uncertainties and the true incidence angle can be in error. The shape of the filter response is very steep at the skirts and a small error in incidence angle translates to an error in the Doppler spectrum and the corrections (gain adjustments) applied can be in error. In view of this, the reader is asked to consider correlations relating backscatter at  $44^{\circ}$  with that at any other angle with caution. There seems to be a negative correlation between the response near nadir incidence and that at  $40^{\circ}$ , while there is almost total decorrelation with the response at  $33^{\circ}$ .

An ITC (VV) pass that was exercised over the eastern part of the U.S. (Day 253, shown in Figure 7.2) was used to find correlations between the backscatter response at various incidence angles for land targets. The correlation matrix is shown in Figure 8.7.

	$\sigma^{\circ}_{44^{\circ}}$	$\sigma^{\circ}_{40^{\circ}}$	$\sigma^{\circ}_{33^{\circ}}$	$\sigma^{\circ}_{17^{\circ}}$	$\sigma^{\circ}_{0^{\circ}}$
$\sigma^{\circ}_{44^{\circ}}$	<u>1.0</u>				
$\sigma^{\circ}_{40^{\circ}}$	0.1197	<u>1.0</u>			
$\sigma^{\circ}_{33^{\circ}}$	0.0178	<u>0.7969</u>	<u>1.0</u>		
$\sigma^{\circ}_{17^{\circ}}$	0.0691	<u>0.7374</u>	<u>0.7520</u>	<u>1.0</u>	
$\sigma^{\circ}_{0^{\circ}}$	0.0774	0.1092	-0.0385	0.2098	<u>1.0</u>

TABLE 8.7.

Correlation matrix for  $\sigma^{\circ}_{VV}$  at five angles of incidence considering data from ITC pass on Day 253.

In contrast to the correlation coefficient computed between backscatter at  $2^{\circ}$  and  $17^{\circ}$  by considering both ocean and land data, the correlation computed for the same angles for only land targets is 0.2098. This is because of the wide variation in the near-nadir case. There is, however, a similar correlation, as in the all ITC-data-cases, between the  $\sigma^{\circ}$  at  $40^{\circ}$  and  $33^{\circ}$ . The correlation between  $33^{\circ}$  and  $17^{\circ}$  was very weak when considering both ocean and land data but increases to 0.752 when considering only land data. The negative correlations between the near-nadir response and those at other angles are now positive, although extremely small. The shape of the  $\sigma^{\circ}$  vs.  $\theta$  curves for ocean is much steeper than that for land. The correlation between the backscatter at  $40^{\circ}$  and that at  $17^{\circ}$  is 0.7374 suggesting that  $17^{\circ}$  is beyond the "pivotal" point of the  $\sigma^{\circ}$  vs.  $\theta$  curves. The "pivotal" point is a region which is relatively insensitive to roughness.

In summary, it can be stated that the intermediate angles of ITC operation offer backscatter measurements which appear to be correlated for land targets. The correlation between the near nadir and  $17^{\circ}$  case is high if one considers data from both land and ocean, and is not high when considering land alone. This implies that the correlation is introduced in the first case because of a marked diversity in sensitivity to land and ocean targets at these angles.

#### 8.4 Analysis of Variance Results

An analysis of variance exercise was performed on manually classified data for certain CTC pitch  $29^{\circ}$  passes. The purposes of performing the analyses were,

1. To establish if the major physiographic and land/use categories considered were distinct in their microwave response.
2. To show that the land/use categories did not by themselves provide a good classification tool, and that variations in the category from region to region would be important.
3. To show that temporal variations in the response from a category could cause problems in classification.
4. To show that variables such as soil moisture which were not considered in the classification process could influence the response.

The object was to show by way of examples some of the problems associated with the classification of terrain by simply considering the land/use categories. The nature of problems is not explored in detail, but examples to show that certain categories appear separate and distinct while others do not are shown. The separation into groups was done by manual classification where each target cell in a candidate pass (CTC pitch  $29^{\circ}$  vertical polarization only) was examined to determine if it contained a predominance of any one category. The categories are defined as in King and Moore [1974], and as described earlier in this report. There was a further level of classification where a major category such as forest was broken down into types of forests. There was no attempt to do anything with target cells that contained a sizable contribution from more than one category.

Samples drawn of each group from each region, for each day (or pass) of concern were then used for the analysis of variance. A one-way simple lay-out was chosen with the backscattering coefficient being the measured variable. The null hypothesis was that the samples from the two groups were from the same population.

The results from this analysis should not be considered too rigorously. Certain underlying assumptions in the analysis of variance procedure regarding the equality of variances of the two groups were not verified in all cases. It must therefore be recognized that the rejection of the null hypothesis based upon the F-static is not as strong as the confidence indicated. However, to compensate for this lack of homoscedasticity, the

confidence level entertained for rejection of the null hypothesis was considered to be at least 95%. The sample sizes are not very large and may not in some cases be descriptive enough of the category in the region. But an attempt was made to find as many "homogeneous" targets of a category in a region as time permitted. The analysis procedure employed here is also to demonstrate the feasibility of performing such an exercise for purposes of creating categories which are distinct as gauged by their backscattering coefficient.

Table 8.8 provides all the results from this study. The case number refers to the one-way lay out considered; groups 1 and 2 are the two categories from the two regions on the two passes of concern. The target areas are described by major geographic regions. Figure 7.1 shows the passes for the CTC (pitch  $29^{\circ}$ , see table 7.1 for a listing) modes. The degrees of freedom in the one-way layout are shown as is the F-ratio and the confidence level of the rejection of the null hypothesis. The degrees of freedom correspond to the number of groups minus one and to the total number of samples minus two. The classification of target type is in some cases more detailed than the major classifications, for example the South American forest region has been broken up into the various forest formations found in that region.

Case 1 considers samples from the Washington, Oregon area for forest target cells and compares them to forest target cells from the southwestern region (Nevada, Arizona, New Mexico). The null hypothesis can be rejected at the 99.9% that the two samples are from the same population. This is an example of how one category-forest can have subclasses which are quite distinct. For example the forests in the Washington, Oregon region are typically dense coniferous forests whereas the forest in the southwest region is typically the juniper woodland type. Further illustration of this effect is seen in case 2 where the forest in the Nevada, Arizona region is compared to the thornbush type high savannah found in South America. These two samples do not appear to be from "one" category. A large F-ratio occurs when this juniper forest is compared to the South-Bahia evergreen forests in South America.

The South-Bahia is probably one of the most dense forest canopies in the world and a mere classification of "forest" would leave a lot of ambiguity between the juniper woodland or the thornbush and the evergreen complexes found in the Brazilian region. Cases 4 and 5 are comparisons of the juniper forest to other South American forest formations and the rejection is always greater than 99.9%.

Table 8.8  
 Analysis of Variance, One-Way Lay-Out  
 For Backscatter Response of Terrain Categories at 33°

Case No.	GROUP 1			GROUP 2			Deg. of Freedom	F. Ratio	Confidence of Rejection (%)
	Day	Target Type	Target Area	Day	Target Type	Target Area			
1	162	Forest	Washington Oregon	165	Forest	Nevada, Arizona New Mexico	1-69	245	99.9
2	165	Forest	Nevada Arizona New Mexico	161	Thornbush Forest	Brazil	1-68	11.5	99.5
3	165	Forest	"	161	S.B. Evergreen Forest	"	1-52	59.4	99.9
4	165	"	"	162	Am. Evergreen	Brazil Venezuela	1-50	13.8	99.9
5	165	"	"	162	Am. Semi-deciduous	"	1-61	110	99.9
6	162	"	Washington Oregon	162	Range	Washington Oregon	1-62	5.48	97.5
7	162	"	"	"	Farm	"	1-47	0.037	Not Rejected
8	165	Forest	Nevada Arizona New Mexico	165	Desert	Nevada, Arizona New Mexico	1-71	8.62	99.5
9	165	"	"	"	Range	"	1-56	0.968	95
10	165	Range	"	162	Range	Washington Oregon	1-49	77.9	99.9
11	165	"	"	215	"	Utah	1-23	20.9	99.9
12	220	Range	New Mexico Texas	165	Range	Nevada, Arizona New Mexico	1-24	111	99.9
13	220	"	"	215	"	Utah	1-15	111	99.9
14	220	"	"	162	"	Washington Oregon	1-41	0.784	95

459

Case No.	GROUP 1			GROUP 2			Deg. of Freedom	F. Ratio	Confidence of Rejection (%)
	Day	Target Type	Target Area	Day	Target Type	Target Area			
15	215	Range	Utah	162	Range	Washington Oregon	1-40	4.94	95
16	165	Range	Nevada Arizona New Mexico	165	Desert	Nevada, Arizona New Mexico	1-47	0.395	Not Rejected
17	162	"	Washington Oregon	162	Farm	Washington Oregon	1-51	2.41	Not Rejected
18	220	"	New Mexico Texas	220	Farm	New Mexico Texas	1-39	0.456	Not Rejected
19	220	"	"	"	Woodland	"	1-47	0.998	Not Rejected
20	220	Farm	"	162	Farm	Washington Oregon	1-49	5.73	97.5
21	220	Farm	"	220	Woodland	New Mexico Texas	1-70	6.09	97.5
22	250	Desert	Texas New Mexico	165	Desert	"	1-92	9.02	99.5

Next, the difference, if any, between the category classified as forest and the other categories in the same region is sought. Case 8 compares "forest" in the Washington, Oregon area to "range" in the same area. The classification to a category called rangeland implies that the target was not wooded, was not mainly agricultural terrain and did not have a sizable amount of water bodies or urban regions. The two groups were considered dissimilar, although more mildly so than any of the rejections considered so far. The same forest category was compared in case 7 to agricultural terrain in the same region and one could not reject the hypothesis that they were from the same population. Case 8 considers forest in the southwestern region versus desert in the same region and the two can be considered as separate categories. The corresponding comparison with rangeland (Case 9) for the same region with the forest, however, shows that the two are dissimilar but only a marginally confident statement can be made to that effect. A comparison between rangeland in Washington, Oregon to that in Nevada, Arizona shows that the two appear as though from different populations. In fact, the difference is greater between these two groups than the difference between two categories such as forest and desert in Nevada, Arizona. This tells us one of two things: either the two physiographic and land/use features of the two regions are totally different or some other variable that we have ignored in our classification process is influencing the return in a major way. One possible (and most likely) candidate for such a parameter would be the soil moisture. Since we have found samples from a large region, the soil moisture would be an overall mean soil moisture, not an isolated patch that received an abundance of rainfall immediately prior to the pass. Case 11 compares the rangeland in the Nevada, Arizona region to rangeland in the Utah region but for day 215; the null hypothesis can again be rejected. One would think that the rangeland in New Mexico and Texas would be similar to that in Nevada, Arizona, New Mexico (at least in their microwave response), but we can reject the null hypotheses here too. The variation in soil moisture might again be the cause of the difference, or it may be that the difference in time (Day 220 as opposed to day 165) causes different amounts of vegetation coverage. The New Mexico, Texas rangeland appeared different from the Utah rangeland (Case 11) separated by only five days between data takes for the two regions. Rangeland in Texas, New Mexico was only marginally different from the Washington, Oregon rangeland (Case 14). Rangeland in Utah was also different from the rangeland in Washington, Oregon (Case 15).

To no surprise rangeland in the Nevada, Arizona region could not be differentiated from the desert in the same region (Case 16). This is expected because the task of assigning a target to either category and not the other was very difficult. Agricultural terrain in Washington, Oregon could not be differentiated between rangeland in Washington, Oregon (Case 17); and neither could agricultural terrain in New Mexico, Texas from rangeland in that region (Case 18). Agricultural terrain is a classification that is not easily described and in regions like New Mexico, Texas could very well be similar in biomass of cover to rangeland. When some form of irrigation is applied, the category called agricultural terrain can be separable from others, but for dry farming there seems to be no difference between it and open grazing land (rangeland). Woodland in Texas, New Mexico consists of sparse stands of juniper and mexquite which cannot be separated from rangeland in the same area (Case 19). Farmland in the Washington, Oregon area can be differentiated from the farmland in the Texas, New Mexico area (Case 20). The basic vegetation patterns are probably the cause; with the Texas region being more sparsely vegetated and the Washington, Oregon area being more heavily wooded. Surprisingly farmland in New Mexico, Texas can be differentiated from woodland in the same area (Case 21). Farmland was not differentiable from rangeland and woodland was not differentiable from rangeland, but the two categories when compared together are separable. This implies that rangeland probably falls somewhere in between farmland and woodland. Finally the desert category in the New Mexico, Texas area on Day 250 can be separated from the same category on Day 165 (Case 22). This could be due to soil moisture differences.

In conclusion, it might be stated that a classification based upon only scatterometer measurements at  $30^\circ$  incidence must include many more factors than a mere classification by major land/use or physiographic categories. The variations within a major category are often more than between major categories. These variations can be due to geographic locations where relief, density of vegetation or soil moisture differences can account for the variations, or they can be solely due to soil moisture differences (for example, in the case of the desert response for two different times). The objectives of this study were sufficiently borne out by examples, and, indeed could be used as constructive evidence in preparing a classification scheme.

## 8.5 Linear Discriminant Analysis Results

To ascertain whether one could assign a sample microwave response into distributions of responses from different categories, a step-wise linear discriminant analysis exercise was conducted. The distributions to which the sample was to be assigned were found by manually classifying targets into homogeneous and distinguishable (by examination of land use and topographic maps and imagery) categories and then computing the mean and variance. Although the usual tests of significance for discriminant functions and generalized distances require the assumption of homogeneity of covariance matrices to be validly applicable, this assumption was not specifically tested. Indeed in some instances there is no homogeneity, for example, cases where the backscatter response near nadir incidence is considered as one variable and backscatter at say  $17^\circ$  is considered as another. Such cases were ignored. In general, discriminant functions were sought as linear combinations of variables which did conform to the homogeneity of covariance matrices assumption. For example, the middle three angles of in-track-modes of operation had comparable variances and covariances and these were used as variables to perform the linear discriminant analysis. The backscatter response at  $33^\circ$  for vertical and horizontal polarization had very similar distributions and they were used as variables for discriminant analysis of South America. In many cases, for example in the case just cited of the backscatter response for vertical and horizontal polarization over South America, one could do as well with just one variable (either polarization) as with both.

The results from this discriminant analysis exercise showed once again that categories based on land use features are not necessarily separable in their microwave response.

The most promising results obtained from the linear discriminant analyses were from the South American region. This is because the "homogeneous" areas are vast in extent and no adulteration of other categories can compound the problem. A second cause is probably the dense vegetation which totally masks the effects of the soil moisture variations on the surface. Another factor which made the results from South America so promising is that the categories picked as underlying groups did indeed have a smaller scatter and appeared on a qualitative examination to show a substantial difference in the means. The analysis of variance exercise over this same region also showed the categories chosen could be considered to arrive from different populations.

The categories were chosen by examination of a vegetation map of Brazil. The scale of the vegetation map was very gross and only showed boundaries of various vegetation patterns. The authenticity of details of the vegetation map is doubtful. Targets lying in the vegetation types suggested by the map were assigned by manual classification to that category. There were three major categories so found: Amazon evergreen forest complex, Amazon semi-deciduous forest formations and savannah. The backscatter response at  $33^\circ$  for vertical and horizontal polarization were chosen as the discriminating variables. Table 8.9 shows a summary of the classifications based upon the linear discriminant functions computed. The linear discriminant functions are also shown in the table. One can see that there is a confusion between the evergreen and the semi-deciduous forests. Indeed there should be; the semi-deciduous forests are, during some parts of the year, quite similar to the evergreen forests. It is reassuring to note that the savannah was assigned properly. The errors in classifying should not be totally attributed to the sensor response. There could be as much error in our manual classifications as in the sensor response.

The In-track contiguous mode of operation was exercised mostly over North America. The backscatter response at the middle three angles of ITC operation ( $41^\circ$ ,  $33^\circ$ ,  $17^\circ$ ) were used as the discriminating variables. The regions were first classified manually and targets assigned to various categories; the underlying distributions were created from these groups. The categories so found were: agricultural land, forest and rangeland. The manual classification was performed as described in chapter seven. Only the targets which were "homogeneous" in any one category were chosen for this exercise. No further breakdown by forest types, or types of agriculture land was attempted to establish the feasibility of selecting land/use features by combinations of various sensor configuration responses. Table 8.10 shows a summary of the success in classification. The agricultural terrain was overwhelmingly classified as either forest or rangeland. The reason for this is that the response of agricultural land has a wide scatter. This scatter is understandable because agricultural land can be anything from furrowed ground to tall corn. The soil moisture can also vary due to irrigation and rainfall history. The agricultural terrain which has a dense vegetation canopy can no doubt have the same backscatter response as a forest and an agricultural terrain which has very sparse vegetation is just like rangeland. The manual classification considered the target to be rangeland if it was not forest, agricultural terrain, urban, desert or water bodies. Obvious exceptions like the Salt Flats were, of course, not included as rangeland. Forests were sometimes

C  
L  
A  
S  
S  
I  
F  
I  
C  
A  
T  
I  
O  
N  
S

	Groups (Underlying Distributions)		
	Evergreen	Savannah	Semi-Deciduous
Evergreen	25	5	16
Savannah	5	45	0
Semi-Deciduous	10	0	27

Classifications summary for CTC Pitch 29° (VV and HH) data over South America.

	Classification Functions		
	Evergreen	Savannah	Semi-Deciduous
$\sigma_{29^\circ}^{VV}$	-21.24870	-27.39255	-19.49598
$\sigma_{29^\circ}^{HH}$	5.88211	7.79349	5.34048

Table 8.9.

Classification summary and Classification Functions

Classification Results  
(Groups Underlying Distributions)

	Agric.	Forest	Range
Agric.	2	41	31
Forest	0	31	14
Range	0	6	29

Table 8.10.

Classification summary using ITC (VV) backscatter data at  $42^\circ$ ,  $33^\circ$ ,  $17^\circ$  from North American targets.

Groups (Underlying Distributions)

	Farm	Forest
Farm	11	2
Forest	2	9

Table 8.11.

Classification summary using ITC (VV) backscatter response at  $42^\circ$ ,  $33^\circ$ , and  $17^\circ$  for pass from Texas to Maine. The underlying distributions were created by considering only homogeneous areas.

mistaken for rangeland, and once again the errors should not be totally attributed to the microwave response. Rangeland was mostly classified as rangeland, although a few cases were mistaken for forest. This exercise suggests that agricultural land is not a proper definition of a category when trying to differentiate it from both range on the one hand and forest on the other.

Agricultural terrain can be separated from forest if those two are the only two populations in the underlying universe. This is shown by considering targets from the long Texas to Maine ITC pass on day 253. The targets were again classified manually and all targets which appeared to be over 80% of either farmland or forest were assigned to these two groups respectively. The middle three angles of ITC operation were again chosen as the discriminating variables. The separation for this case is shown in Table 8.11. Notice that with the exception of a few mistaken classifications, a separation is possible. When the underlying groups or distributions are created by considering targets which are over 90% (this is qualitative, but representative of homogeneity) of either farmland or forest, the errors of misclassification are reduced. This suggests that the underlying distribution may not be properly created for the case shown in Table 8.11.

Discriminant analysis considering all the variables of ITNC operation and selected groups of these variables were attempted for the limited overland data obtained with this mode of operation. The results were not encouraging. An added factor was introduced in the manual classification; the relief (large scale) was considered for each target being used to create the underlying groups. Each major land/use type was assigned two subcategories, one with low relief and one with high relief. The classifications of the relief were keyed by U. S. Geological Survey indexes. The discriminant analysis conducted by considering ITC backscatter data for the middle three angles showed that major relief does not appear to be a major factor in the response at these angles of incidence.

It may be that when more ground descriptors are incorporated in assigning the underlying distributions, the discriminant analysis results will be more encouraging. Certainly specification of soil moisture in creating the underlying distributions will help. Most target cells seem to be composed of a combination of land/use categories and consequently a discrimination based upon microwave response is not only difficult but also serves very little purpose. Discriminant analysis of groups broken up by some other descriptor like soil moisture may hold promise.

## 8.6 Results of Clustering Analysis

Using the microwave response with various combinations of sensor configurations as the data base, natural partitions of the data were found by means of clustering. Two clustering procedures were attempted: K-means clustering and spatial clustering. Both of these clustering procedures are described in Chapter 7. The proportions of the land-use and physiographically distinct categories in each cluster were then found by manual classification. For some sensor configurations the total number of measurements included was small enough that almost all the observations were manually classified; for others the number of measurements was exorbitant (over 7000 in some cases) and only a selected sample of random observations from each cluster was manually classified.

When considering only the land use and physiographic classifications as descriptors, the results of the clustering analysis were not encouraging. It would appear that factors other than those suggested by major biomes alone should be considered. The combinations of sensor responses that were considered in this study may not have been optimal for partitioning the terrain according to the physiographic features. Due to paucity in time only a few clustering exercises were conducted. Future studies should consider clustering procedures with variables not considered here and should try to determine the causal relationship between some key parameters of the terrain and the microwave response. For example, one could introduce soil moisture variations as a terrain characteristic and assess if the clustered microwave measurements are keyed by the soil moisture variations of the surface. Such an analysis is more complicated than it would appear on the surface, because soil moisture variations can often be masked by vegetation canopies. Clustering on some set of terrain descriptors and on some set of microwave response should provide similar clustered groups. This choice of terrain descriptors and set of microwave responses will be a culmination of many clustering attempts with various terrain descriptors and various sensor configuration responses.

The results reported here represent a first step in the exploratory process and suggest that more sophistication in the definition of the terrain categories is required. The clustering analyses reported here were conducted by considering the following combination of sensor configuration responses.

1. The ITC (VV) backscattering coefficient for the middle three angles ( $17^\circ$ ,  $33^\circ$ ,  $41^\circ$ ) for all targets which were viewed by all three angles. This included some ocean targets and some targets that were not in the U.S.A.
2. The CTC pitch-offset- $29^\circ$  rad/scat-mode data including both the backscatter and radiometric temperature for vertical polarization. Only North American targets are included.
3. The CTC pitch-offset- $29^\circ$  backscatter-only data for vertical polarization. North America, South America and Ocean data are all included.
4. The ITC (VV) backscattering data for the middle three angles ( $17^\circ$ ,  $33^\circ$ ,  $41^\circ$ ) for the long Texas to Maine pass on day 253. This pass was also clustered by a spatial clustering procedure for comparison.

Other clustering exercises were also conducted, using ITNC data over land and using ITC data for other combinations of sensor configurations than those listed above. These showed similar or worse results, although the number of samples to be clustered was in some cases not sufficient for any proper inference. These cases are not reported.

The ITC (VV) data were sorted so that the backscatter responses of a target to the three angles considered were grouped. This was the three-dimensional measurement vector used for clustering. A K-means clustering procedure produced 10 significant clusters. Three others were discarded because of obvious errors in the computation of backscatter or the ephemerides of the target or both. These ten clustered sets of observations were manually classified to assess the proportion of various land-use and physiographically distinct categories in each clustered region. The physiographic categories are shown on top of Table 8.12. The proportions of these terrain categories in each cluster are shown in Table 8.12. One can see that water is always separable from land (clusters 3, 9 and 10). The three clusters of water correspond to distinctly different backscattering coefficients for each. The probable cause of the three separate water clusters is wind speed. Below a wind speed of 4-6 knots the backscattering coefficient at these oblique incidence angles falls very rapidly. There seems to be some confusion between rangeland, agricultural land and forested regions. Obviously, very few targets would be completely composed of only one category; our manual classification considered a target to be contained in a certain physiographic (land-use) category if it was predominantly (a qualitative subjective decision) composed of that category.

Table 8.12.

D = Desert	M1 = Range / Agriculture	F = Forest
R1 = Range - Grassland	A = Agriculture	T = Tropical Rain Forest
R2 = Range - Thornbush	M2 = Agriculture / Forest	W = Water
R3 = Range - Savanna	M3 = Range / Forest	U = Urban
		N = Non Vegetated Terrain

CLUSTER	NUMBER OF FOOTPRINTS													TOTAL
	D	R1	R2	R3	M1	A	M2	M3	F	T	W	U	N	
1	-	4	-	-	-	1	-	-	-	-	-	-	-	5
2	-	7	-	-	-	4	25	-	15	-	-	-	-	51
3	-	-	-	-	-	-	-	-	-	-	3	-	-	3
4	-	12	-	-	-	-	-	-	-	-	-	-	-	12
5	-	3	-	-	-	3	9	-	-	-	-	-	-	15
6	-	13	-	-	-	8	-	-	-	-	-	-	-	21
7	-	10	-	-	-	4	-	-	-	-	-	-	-	14
8	-	6	-	-	-	1	19	-	16	-	-	-	-	42
9	-	-	-	-	-	-	-	-	-	-	9	-	-	9
10	-	-	-	-	-	-	-	-	-	-	15	-	-	15
TOTAL	-	55	-	-	-	21	53	-	31	-	27	-	-	187

Proportions Of Land/Use And Physiographic Categories In Clusters Produced By Considering Backscatter Coefficients At  $42^{\circ}$ ,  $33^{\circ}$  And  $17^{\circ}$  From ITC (VV) Data. Only U.S. And Some Ocean Targets Are Considered.

The mixture categories were then those where a decision about a particular pure category (e.g. forest) could not be made. The manual classification of a target into a terrain category was based upon examination of potential natural vegetation maps, topographic maps and supplemented by spacecraft imagery where available. The manual assignment of targets to terrain categories can often be in error because of two reasons: the maps were produced a few years ago and the land-use could have been somewhat altered, and, examination of a gross-resolution map like the potential natural vegetation map calls for a subjective judgement on the part of the manual interpreter. The results from this analysis suggest that the backscatter response with the middle three angles cannot be used to differentiate between major physiographic or land-use features as created from maps and imagery.

The CTC (VV) rad/scat pitch offset  $29^{\circ}$  mode was exercised extensively over North America. There were many target points obtained from oceanic surfaces as well, but these were excluded from the data base. K-means clustering using the radiometer response and backscatter response as the two-dimensional clustering variable produced 5 significant clusters. The total number of footprints was greater than 3000 so only a few random samples were manually classified for clusters that contained over a 100 points. The results are shown in Table 8.13. Once again there seems to be no selection of terrain physiography by clustering of these microwave responses.

The backscatter data from CTC (VV) pitch offset  $29^{\circ}$  rad/scat and scat only modes was used as a one-dimensional clustering variable. The number of points was over 7000 and the targets were in North America, South America and in the oceans. The number of significant clusters was 10 and are shown in Table 8.14. For the larger clusters, manual classification was only performed on a few random samples. This time, of the four clusters in which there were water bodies, one contained a sizable number of land targets. Cluster 5, shown in Table 8.14, contained some desert and rangeland along with water bodies. The water targets are in the Gulf of Mexico and the land targets are spread over Texas, New Mexico and Arizona. A verification of the clustering showed that the backscatter from the regions included in this cluster was indeed similar and approximately  $-15$  dB. There was one significant result; tropical rain forests in South America were distinct from the other categories (cluster 9 and 10); although some rangeland (probably with a high soil moisture content) also appeared in one of the two tropical forest clusters. In general, no other terrain category was differentiated by this clustering procedure although some clusters tended to contain much more of regions with less vegetation (clusters 1 and 2) than others.



An ITC (VV) pass on day 253<sup>1</sup> was considered as a sample case where two clustering approaches were compared. Backscattering coefficient at the middle three angles of ITC operation was quantized separately by an equal probability quantizing algorithm. This three angle backscatter was considered as the three dimensional variable. A spatial clustering algorithm (described in chapter seven) was exercised for this region. The gradient threshold for creating homogeneous areas prior to clustering was set at unity (see Haralick et al [1974] for details). The resulting homogeneous regions were clustered iteratively till the number of clusters were equal to those obtained from the K-means clustering approach. Results from the two clustering approaches are shown in Tables 8.15 a and b. Although the classifications are not the same, there seems to be no difference in the ability of either procedure in selecting physiographic differences. There is a confusion between agricultural land, forest and a mixture of the two.

In summary it may be stated that a clustering of the variables entertained as measurement vectors in this study did not provide adequate selection of physiographic features. Stated another way, many land-use features produced the same microwave responses. The manual assignment (verification) of targets to physiographic features was made by examination of potential natural vegetation maps, topographic maps and supplemented by spacecraft imagery. These assignments are subjective and could be in error, causing the poor results in these clustering analyses.



## 8.7 Special Site Studies

Due to paucity in time, only a few sites could be exhaustively studied. These sites were picked because of a readily apparent correlation or influence of some ground parameter on the microwave response, or, because a pass was sufficiently long that the targets covered under the same sensor configuration were hopefully distinct in their microwave response. This analysis must of necessity be an ongoing effort and further refinements of the estimated ground conditions in terms of the attributes which influence the microwave response are required. The purpose of this study is to demonstrate that certain terrain conditions can be identified and that other conditions may be overshadowed by some stronger influence of another aspect of the terrain conditions. We know that the backscatter response of terrain is a function of the roughness, the dielectric constant and the orientation of the target. But the roughness and dielectric constant can be functions of topography, soil structure, vegetal cover and soil moisture. It is difficult, therefore, to find a unique combination of these variables which had the measured response. In such cases, we try to find how much one of the variables can be affecting the backscatter. After having seen how much this variable can explain about the backscatter, the next variable is introduced and so on. This could go on till one finds an almost causal relationship which allows one to predict the backscatter from the ground conditions. The reverse is a much more difficult problem and can only be tackled if one has some knowledge of the terrain conditions which only required some refinement.

The radiometric response is also a function of the roughness and the dielectric constant. The dielectric constant, however, is more important for radiometer measurements. The same problems, essentially, are encountered in ascertaining the nature of a terrain surface from its passive microwave response. The procedure must again be sequential and iterative with one variable of ground conditions being entertained at a time.

The influence of one of the ground parameters, soil moisture, was studied in somewhat more detail for one area of coverage. A more detailed account of this study can be found in Ulaby and Barr [1975]. A parallel and much more exhaustive study was conducted by Eagleman and Wen Lin [1975]; his efforts have suggested a very strong correlation between the soil moisture and the radiometric response.

### Texas Soil Moisture Study

Upon qualitative examination of the backscatter and the radiometric temperature over a site in Texas (shown in Figure 8.62) which was flown on June 5, 1973, with the instrument in the CTC R/S pitch  $29^{\circ}$  offset, VV polarization, we discovered that the radiometric temperatures ranged from  $236.3^{\circ}\text{K}$  to  $288.7^{\circ}\text{K}$  and the corresponding backscatter ranged from  $-7.83$  dB to  $-11.4$  dB. The vegetation or topography of the region could not possibly suggest such a dynamic range in radiometric temperature. It was felt that the variations in soil moisture were responsible.

Soil moisture in the upper layers is a very difficult parameter to estimate. Therefore, the usage of the term soil moisture should not be construed to mean that we have in any way mastered the technique of estimating soil moisture. The soil moisture is a function of the initial abstraction, precipitation history, the soil type, the runoff routing on the surface, and evapo-transpiration. The soil type can be classified according to its field capacity and permeability. To account for all the parameters included in the maintenance of hydrological balance would be prohibitively time-consuming.

The amount of infiltration (moisture from precipitation which enters the soil) is a function of the precipitation and of the actual runoff. Runoff is the amount of moisture that travels over the surface without entering the soil. The actual runoff is given by [Green and Pogge, 1973].

$$RO = \frac{(P - IA)^2}{(P - IA) + S}$$

where RO = runoff (in inches)

(P - IA) = potential runoff rate, in/hour

S = potential (2)

Soil potential was shown by Harmon [1963] to be a linear function of the antecedent soil moisture. This shows that the runoff will be different for equal amounts of precipitation if the rate of precipitation is different. In the upper soil zone, moisture is added by infiltration from the surface and is lost by evapo-transpiration and percolation to the lower soil zone. The evapo-transpiration rate is a function of the free surface evaporation rate and the mean daily temperature. The percolation rate is a function of the mean soil moisture content in the upper soil zone, the permeability and a parametric constant indicative of a particular soil type. Percolation takes place only when the moisture exceeds the field capacity.



The skin depth at 13.9 GHz for moist soils is of the order of 1 - 2 cms. We can, therefore, not concern ourselves with the lower soil zone. The estimation of soil moisture for the upper soil zone is a problem of great magnitude and we regret that time did not permit us to model all factors required to estimate the soil moisture in the upper soil zone.

An alternate approach to "estimate" (and we use the word "estimate" very loosely here) the soil moisture is to compute a statistic used for flood forecast purposes called the Antecedent Precipitation Index (API). This index attempts, through one universal factor, to account for all the functions of the hydrologic balance. The API is computed according to

$$API = \sum_{i=0}^N (0.85)^i R_i \quad (3)$$

where

$R_i$  = precipitation in inches on day  $i$

$N$  = total number of days prior to day  $i$  being considered

The factor (0.85) hopefully accounts for the infiltration rate, evapo-transpiration and percolation. The purpose is to weight in decreasing order the precipitation for days prior to the day for which the API is being computed. The precipitation can be found from NOAA weather reporting summaries for the region.

The Texas test site covered an area roughly 224 miles long and 108 miles wide. The number of weather reporting stations in this region was 41. The API was computed by considering the precipitation for up to 5 days prior to the pass. The terrain consists of rangeland with some areas under cultivation (mainly cotton), brushland, and scattered areas of woodland. Since the API computed was only an estimate and the (0.85) factor was quite arbitrary (i.e., did not consider the physiography and vegetation) another index was computed. This one assumed that the evapotranspiration rate was much higher and, therefore, weighted the precipitation for prior days with a more sharply decreasing function.

$$API_B = \sum_{i=1}^N R_i \left(\frac{1}{i}\right) + R_0 \quad (4)$$

where  $R_0$  = precipitation of day of concern

The radiometric temperature is a function of the emissivity and the physical temperature of a surface. The emissivity is the descriptor sought. To reduce the radiometric temperature to emissivity, one must divide the radiometric temperature by the physical temperature. The physical temperature at the time of the pass (13:00 hrs) was not available; the daily maximum air temperature was, however, available from NOAA summaries. These daily maximum temperatures were used for the reduction.

The effects of the atmosphere upon radiometer/scatterometer signals have already been established in Chapter Five. The region was covered with intermittent cloud formations. To correct for these atmospheric conditions, the cloud cover was classified into one of four types: no clouds, light clouds ( $0.33 \text{ gms/m}^3$ ), medium clouds ( $0.66 \text{ gms/m}^3$ ) and heavy clouds ( $1 \text{ gm/m}^3$ ). The thickness of the clouds and height was estimated by shadows on imagery. The sun elevation angle was found from printouts describing the ephemerides of the sensor at the time of concern. The lower ceiling was augmented by those weather reporting stations which provided such information. These estimates suggested a height of from 1.6 kms to 2.4 kms and a thickness from 1 km to 2.5 kms. The simulation program (described in Chapter Five) was run to compute the excess temperature and the term  $T_g$  (surface emission). The two-way attenuation was found for the scatterometer signals by the same program.

Having obtained point samples in the region which did not overlap, the next step was to extrapolate and interpolate to fill a standard grid with values at each node so that comparisons could be made. This effort was conducted by J. Barr [1975] using the "surface" routine as described in Chapter Seven. The extrapolation and interpolation was performed by finding the four nearest neighbors and weighting the values inversely to the distance from these points. Standard grids 46 by 59 with a value at every node were prepared. These were then used to plot contours of iso-intensity of any variable. The regions of iso-precipitation for the five days prior to and on the day of the pass are shown in Figures 8.63 through 8.67. The API shown in Figure 8.68 is called composite rainfall. The radiometric temperature is shown in Figure 8.69. The maximum daily temperature is shown in Figure 8.70. The backscatter response is shown in Figure 8.71.

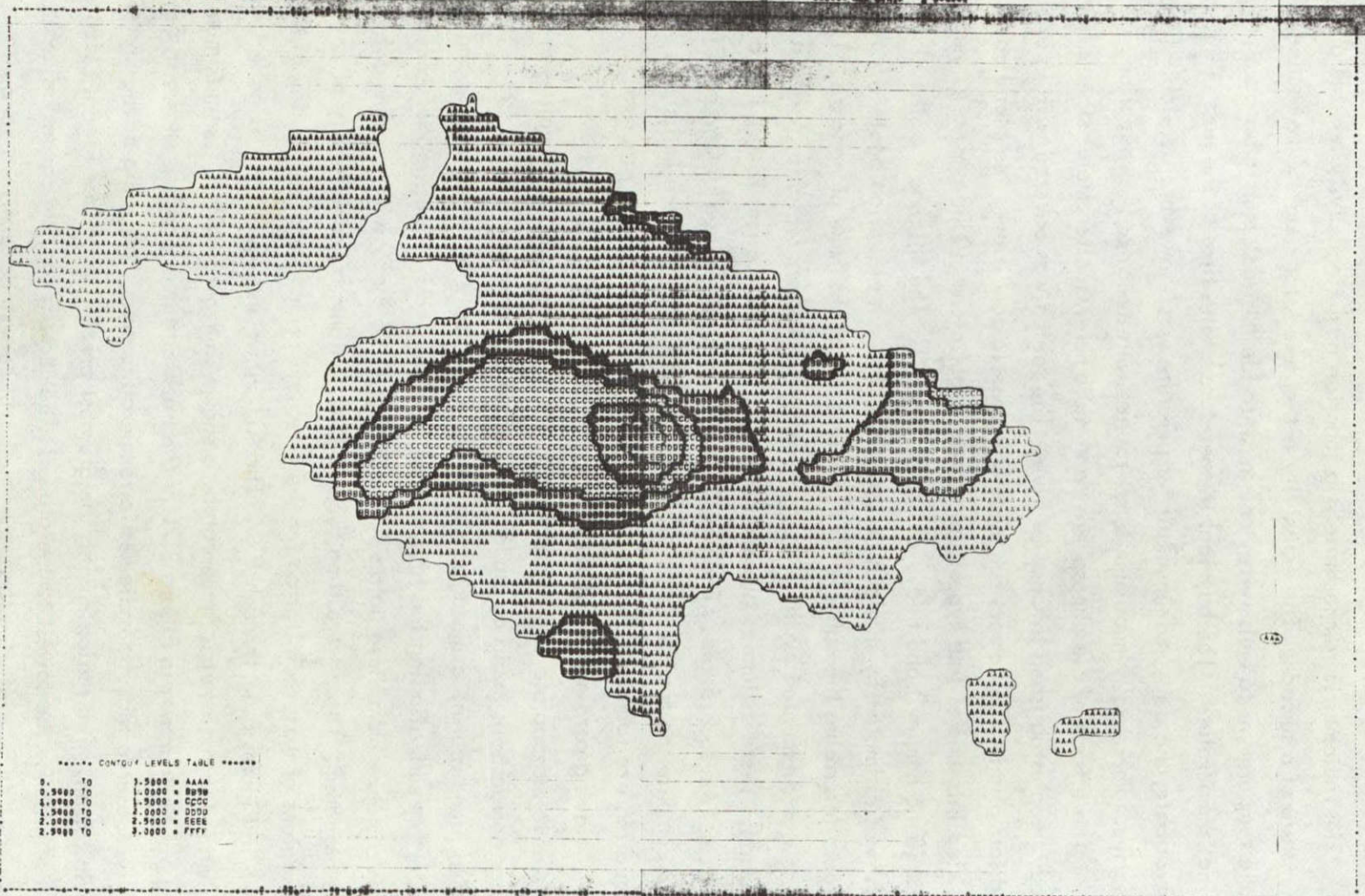
Observe that the radiometric temperature does show a dip at regions of greater precipitation. The region having the greatest precipitation (see Figure 8.68), however, did not produce the lowest temperatures. The reasons for this cannot be ascertained; because of the overall simplicity our modelling does not take into account

\*\*\*\*\* MAP STRIP \*\*\*\*\*

\*\*\*\*\* MAP STRIP \*\*\*\*\*

ORIGINAL PAGE IS  
OF POOR QUALITY

480



\*\*\*\*\* CONTOUR LEVELS TABLE \*\*\*\*\*

0.0000 TO	3.5000 = AAAA
0.5000 TO	1.0000 = BBBB
1.0000 TO	1.5000 = CCCC
1.5000 TO	2.0000 = DDDD
2.0000 TO	2.5000 = EEEE
2.5000 TO	3.0000 = FFFF

Figure 8.63

June 1 Rainfall Extrapolated To a 46X59 Grid Over Texas Site

\*\*\*\*\* MAP STYLE \*\*\*\*\*

\*\*\*\*\* MAP STYLE \*\*\*\*\*



\*\*\*\*\* CONT. H.R. LEVELS TABLE \*\*\*\*\*

0.0000 TO	0.9999 =	A
1.0000 TO	1.9999 =	B
2.0000 TO	2.9999 =	C
3.0000 TO	3.9999 =	D

481

Figure 8.64

June 2 Rainfall Extrapolated To a 46X59 Grid Over Texas Site

\*\*\*\*\* MAP STRIP 1 \*\*\*\*\*

\*\*\*\*\* MAP STRIP 2 \*\*\*\*\*

482

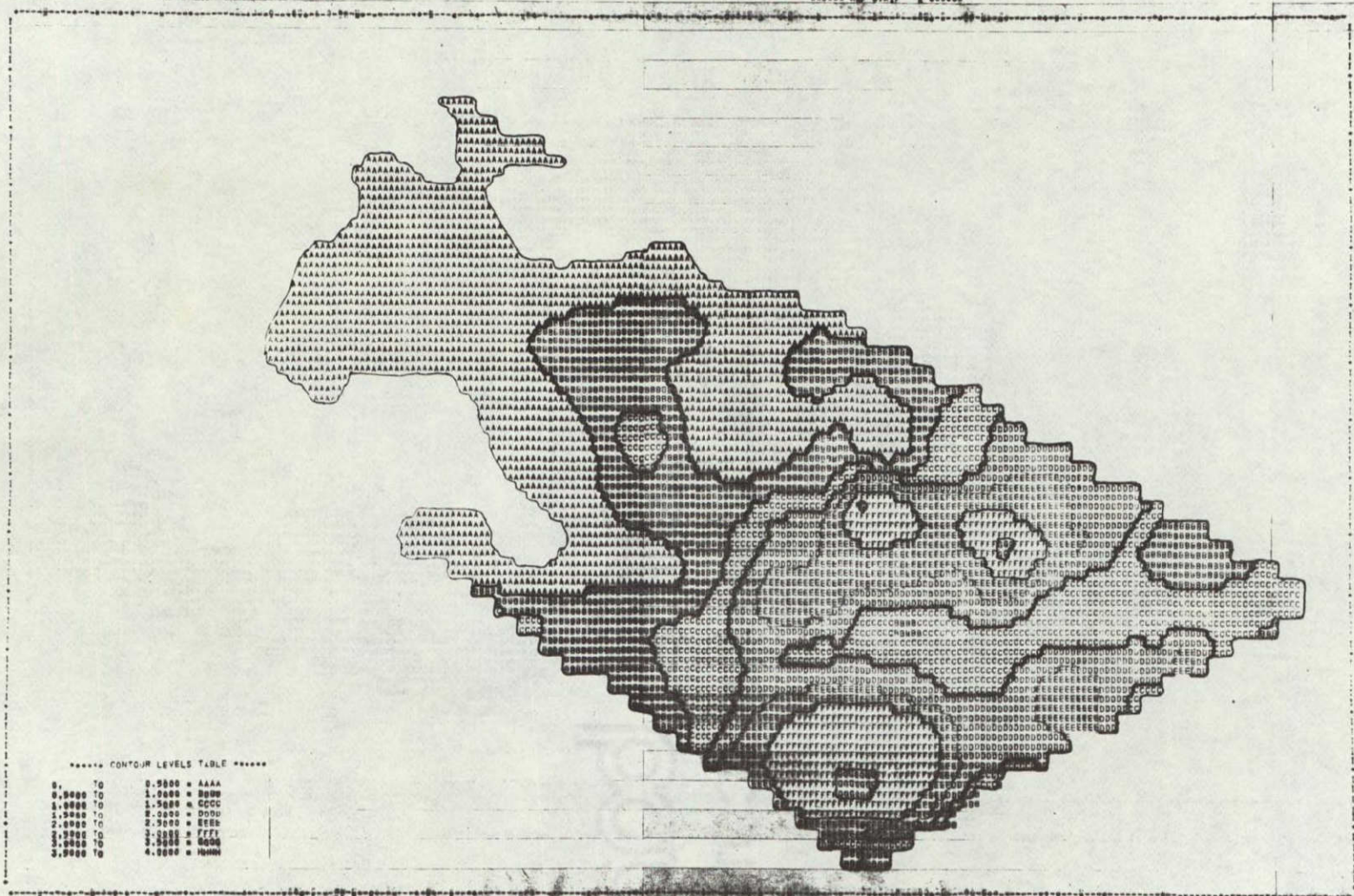


Figure 8.65

June 3 Rainfall Extrapolated To a 46X59 Grid Over Texas Site

\*\*\*\*\* MAP STRIP 1 \*\*\*\*\*

\*\*\*\*\* MAP STRIP 2 \*\*\*\*\*

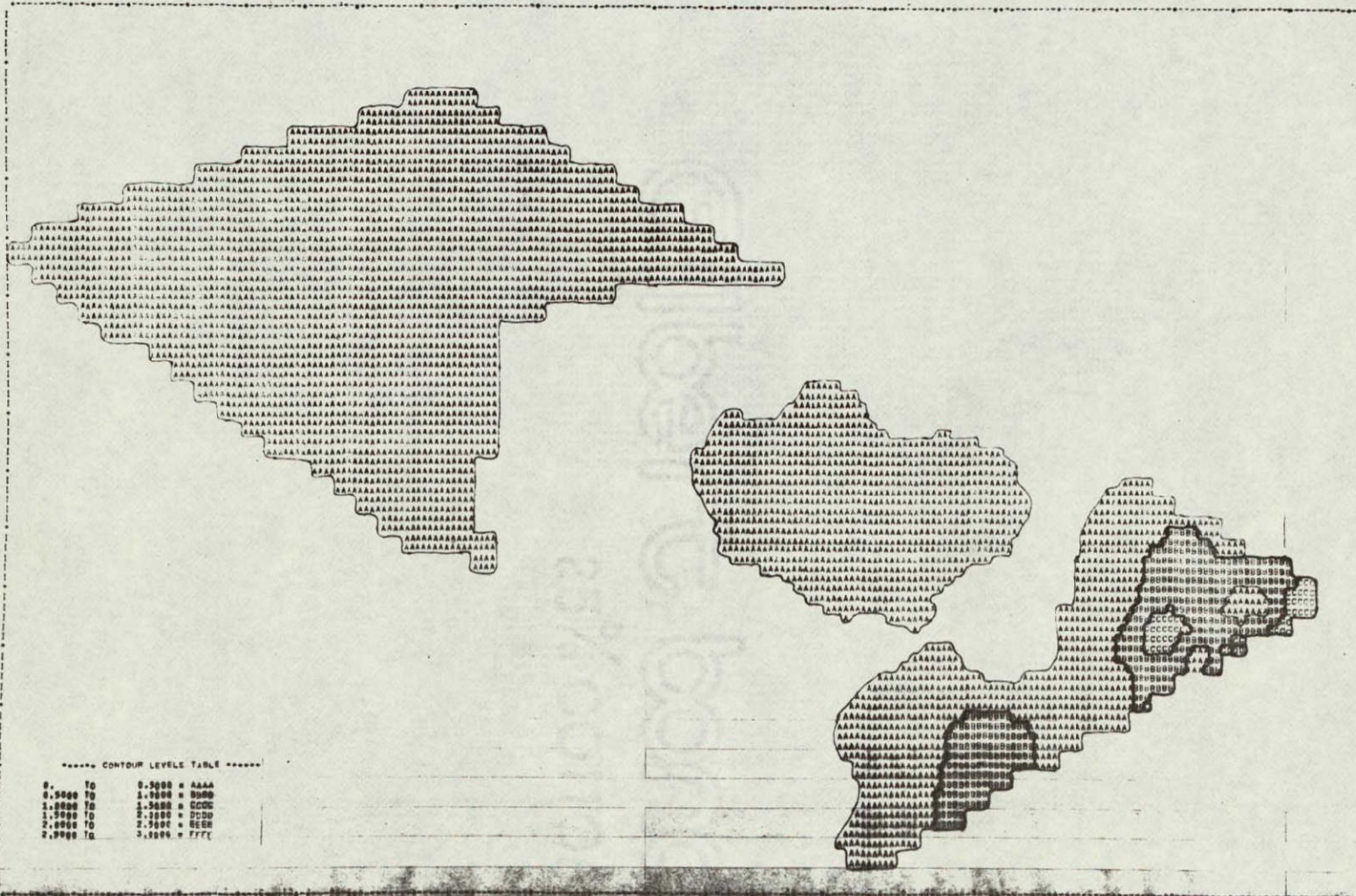


Figure 8.66

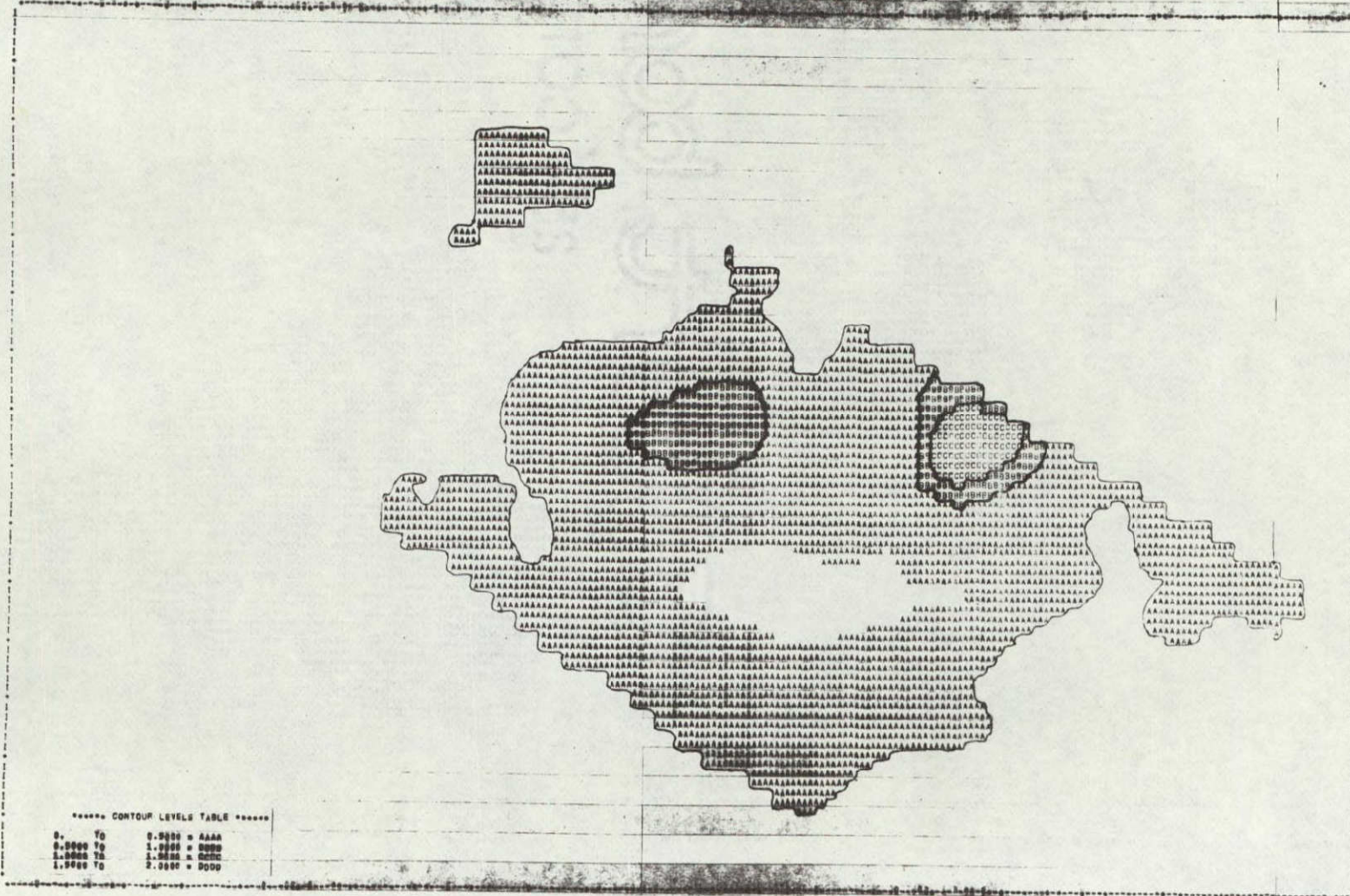
June 4 Rainfall Extrapolated To a 46X59 Grid Over Texas Site

\*\*\*\*\* MAP STRIP 1 \*\*\*\*\*

\*\*\*\*\* MAP STRIP 2 \*\*\*\*\*

ORIGINAL PAGE IS  
OF POOR QUALITY

484



\*\*\*\*\* CONTOUR LEVELS TABLE \*\*\*\*\*

0.	To	0.9999	=	AAAA
0.9999	To	1.9999	=	BBBB
1.9999	To	2.9999	=	CCCC
2.9999	To	3.9999	=	DDDD

Figure 8.67

June 5 Rainfall Extrapolated To a 46X59 Grid Over Texas Site

485

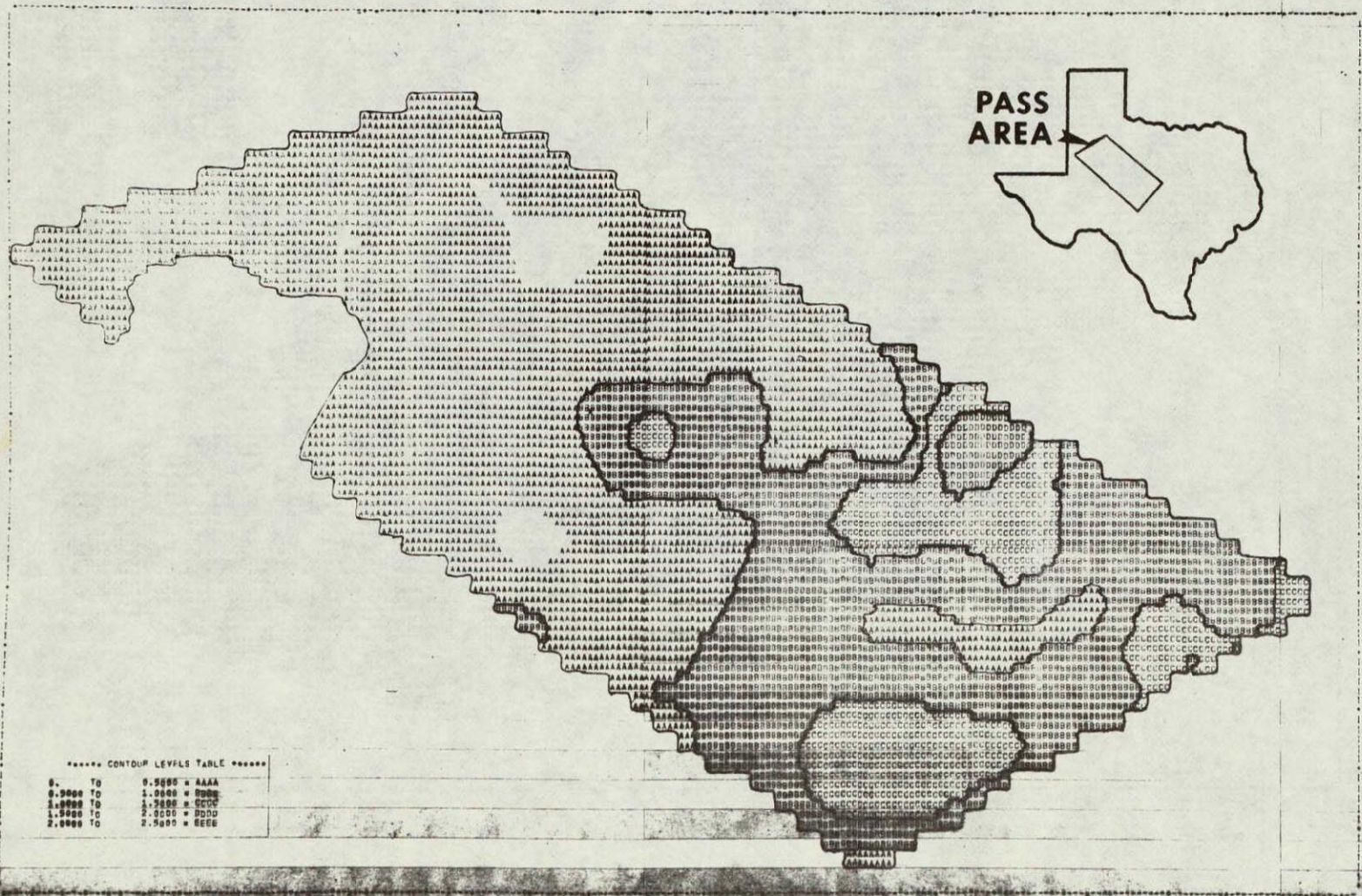


Figure 8.68

Composite Rainfall History (API) For June 1-5 Extrapolated To a 46X59 Grid Over Texas Site

ORIGINAL PAGE IS  
OF POOR QUALITY

486

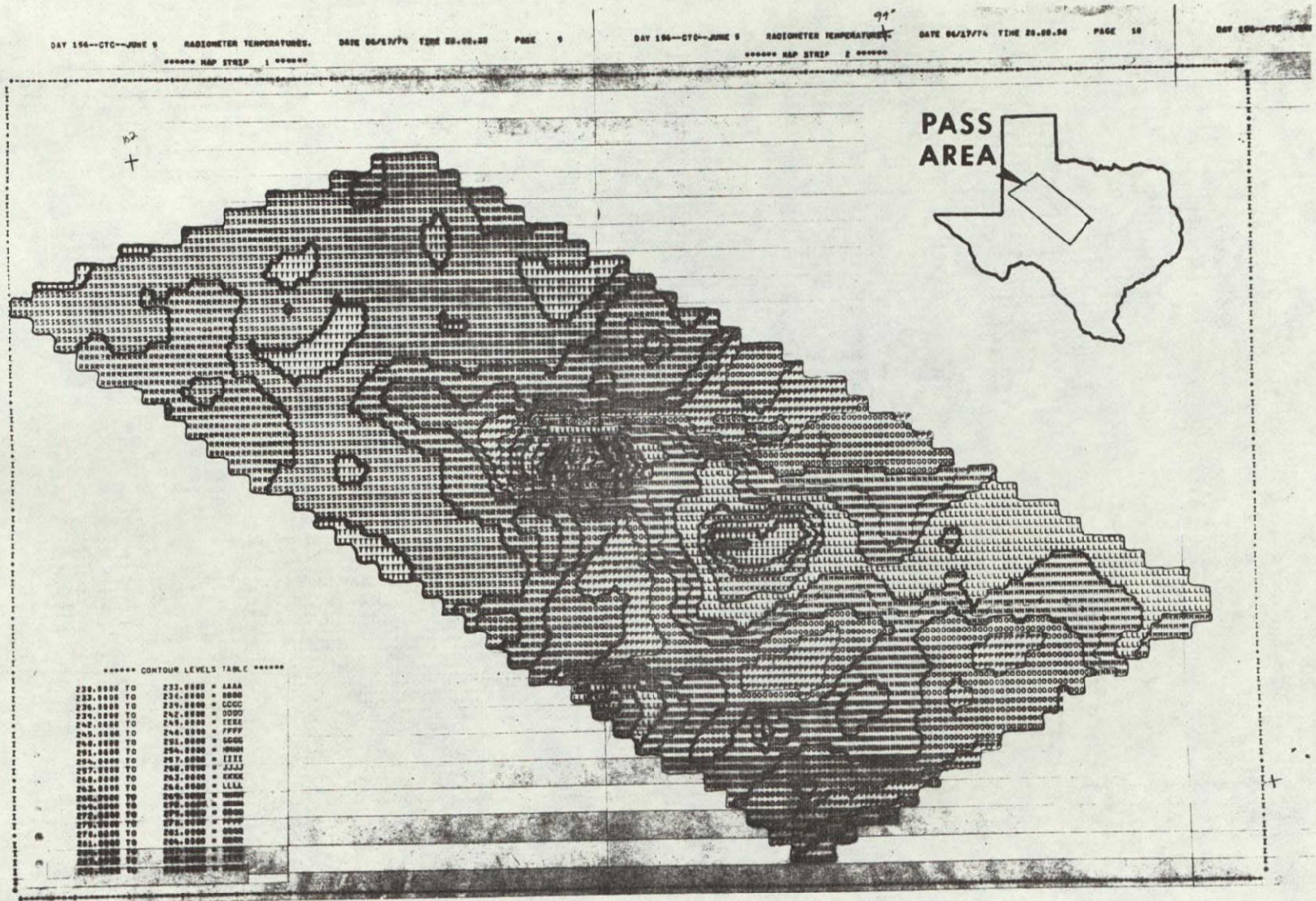


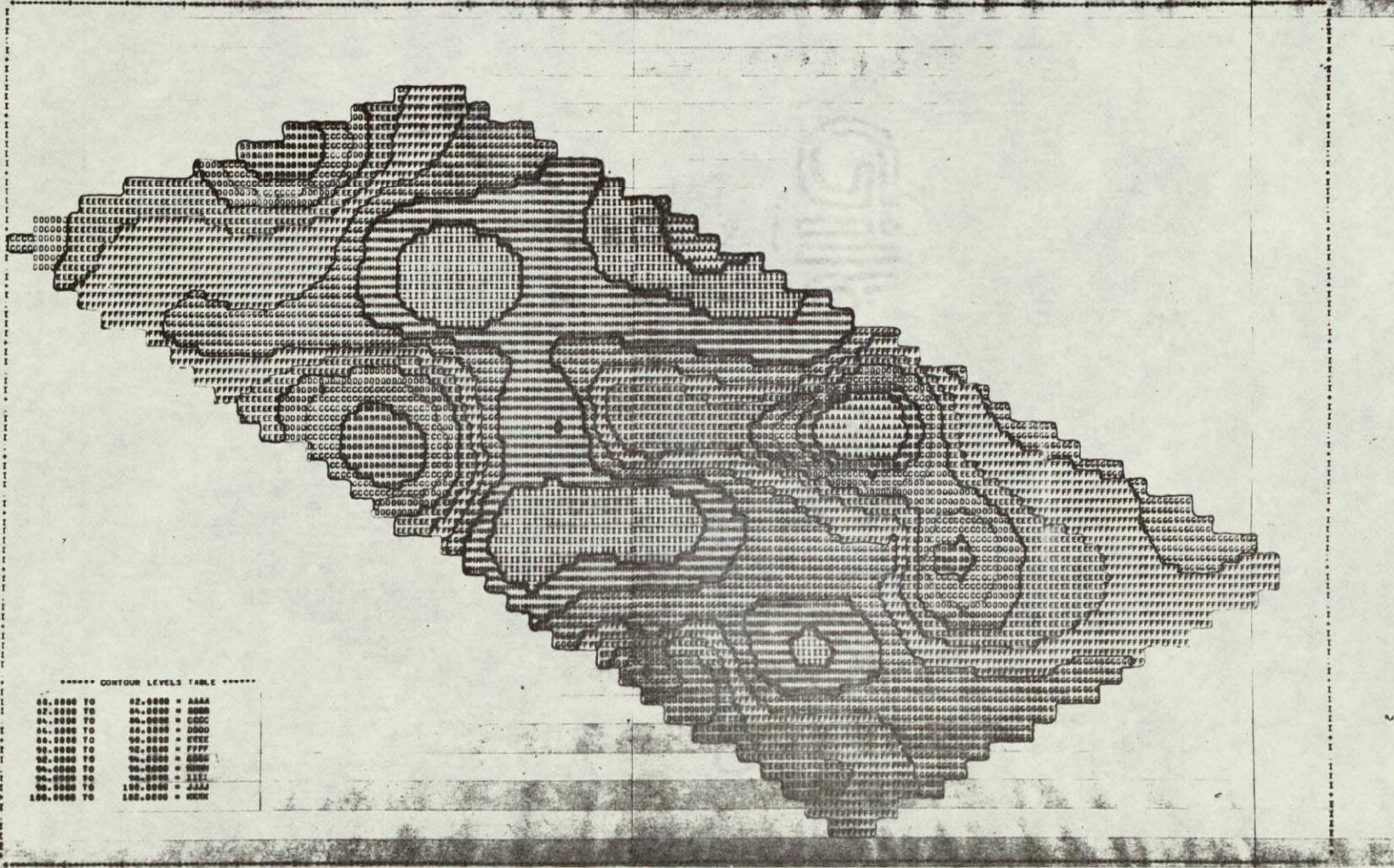
Figure 8.69

Radiometer Temperatures Extrapolated To a 46X59 Grid Over Texas Site

ORIGINAL PAGE IS  
OF POOR  
QUALITY

\*\*\*\*\* MAP STRIP 1 \*\*\*\*\*

\*\*\*\*\* MAP STRIP 2 \*\*\*\*\*



\*\*\*\*\* CONTOUR LEVELS TABLE \*\*\*\*\*

80.0000 TO 82.0000	AAAA
82.0000 TO 84.0000	BBBB
84.0000 TO 86.0000	CCCC
86.0000 TO 88.0000	DDDD
88.0000 TO 90.0000	EEEE
90.0000 TO 92.0000	FFFF
92.0000 TO 94.0000	GGGG
94.0000 TO 96.0000	HHHH
96.0000 TO 98.0000	IIII
98.0000 TO 100.0000	JJJJ
100.0000 TO 102.0000	KKKK

487

Figure 8.70

June 5 Daily Maximum Temperatures Extrapolated To a 46X59 Grid Over Texas Site



Figure 8.71

Backscattering Coefficient Extrapolated To a 46X59 Grid Over Texas Site

many factors, any of which may provide the reason. A region between Roscoe and Lorrain (towards the middle of the site) showed the minimum radiometric temperature ( $236.3^{\circ}\text{K}$ ). The precipitation summaries show that there was precipitation at Lorraine between 1 a.m. and 6 a.m. of 0.33 inches. The region of the radiometer footprint was witnessed by a member of the ground truth collection team for another project related to soil moisture studies at the University of Kansas. Mr. Norman Hardy indicates that the region was composed of a heavy clay surface almost devoid of vegetation and was extremely wet. The API for the region was well below the largest for the total region. Clearly our estimation of soil moisture was not as good as the microwave response as seen by the radiometer. The scatterometer measured a backscatter of  $-8.15$  dB which was not the highest value recorded in the region. This could be due to the fact that we considered the radiometer and scatterometer footprints to overlap completely, whereas in actual operation they are separated by a slight distance.

A scatter diagram of the radiometer temperature and the API is shown in Figure 8.72. A linear regression between the API and the radiometric temperature and the correlation coefficient are shown in the plot. The correlation using  $\text{API}_b$  was never as good as when using API to estimate soil moisture, a scatter plot of backscatter and emissivity versus  $\text{API}_b$  are shown in Figures 8.75 and 8.74 respectively. The scatter plot of emissivity and API is shown in Figure 8.75. This combination had the best correlation. The backscatter (in dB) and API is shown in Figure 8.76. The backscatter in numeric value and API is shown in Figure 8.77. The numeric value of backscatter correlation is better with the API than the  $\sigma^{\circ}$  expressed in dB.

The next phase of the study then tried to account for soil types, the motivation being that if runoff is inversely proportional to the soil potential then the infiltration rate must be directly related to the soil potential. The classification of soils was also performed by J. Barr [1975] and for details of his classification procedures, the reader is referred to his original work. The region was divided into eight soil types according to a classification by Aandahl [1967]. An estimate of the soil potential for each soil type was found. This soil potential for each type of soil was normalized to that of clay which was arbitrarily picked as 3. The corresponding values then were used as multiplicative constants which altered the API. This procedure accounted for the fact that some soils retain more moisture than others. The classification of soils and the procedure employed to compute the normalized API, however, are not optimal and represent only one

ORIGINAL PAGE IS  
OF POOR QUALITY.

490

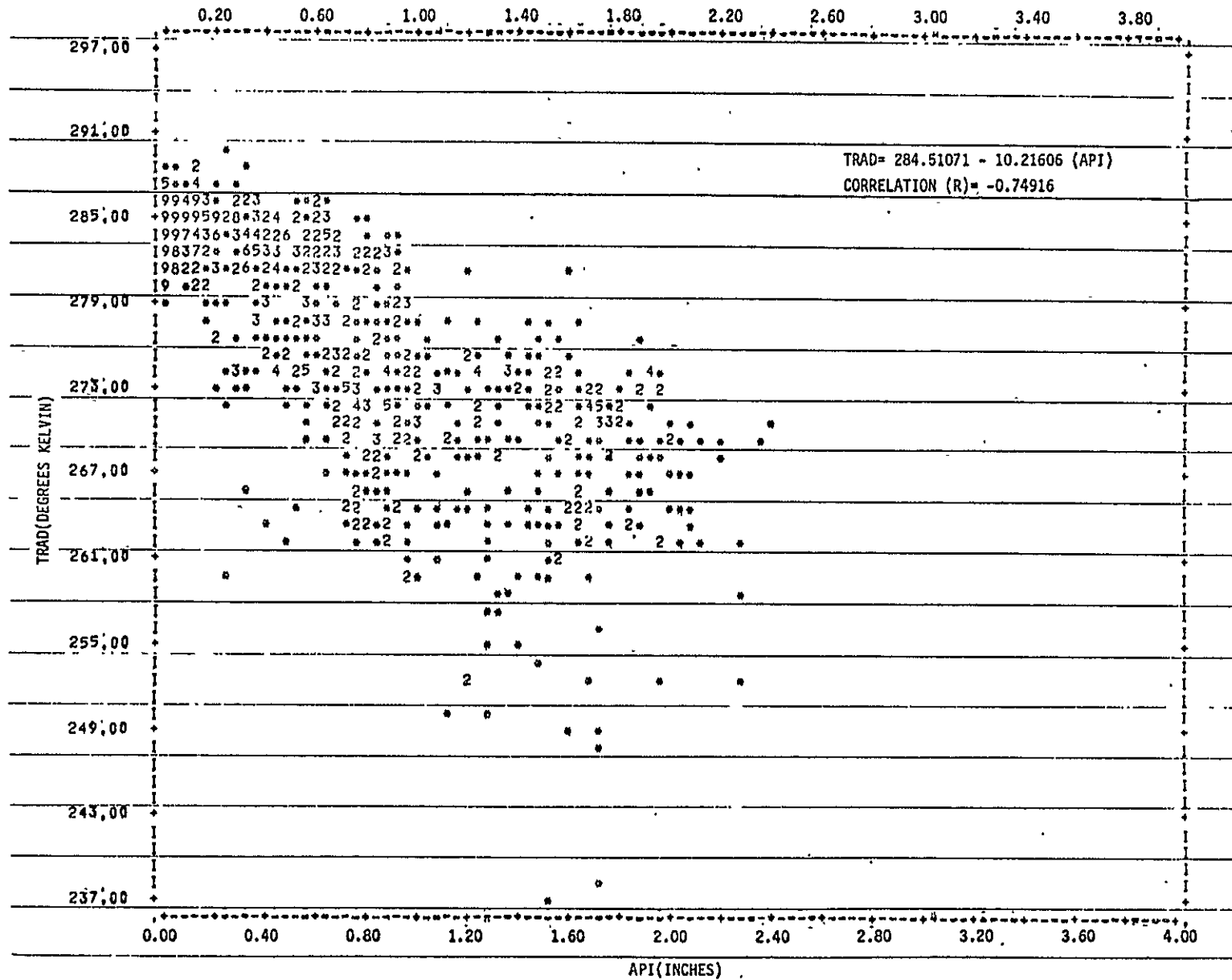


Figure 8.72  
Scatter Plot of Radiometric Temperature and API Over Texas Site

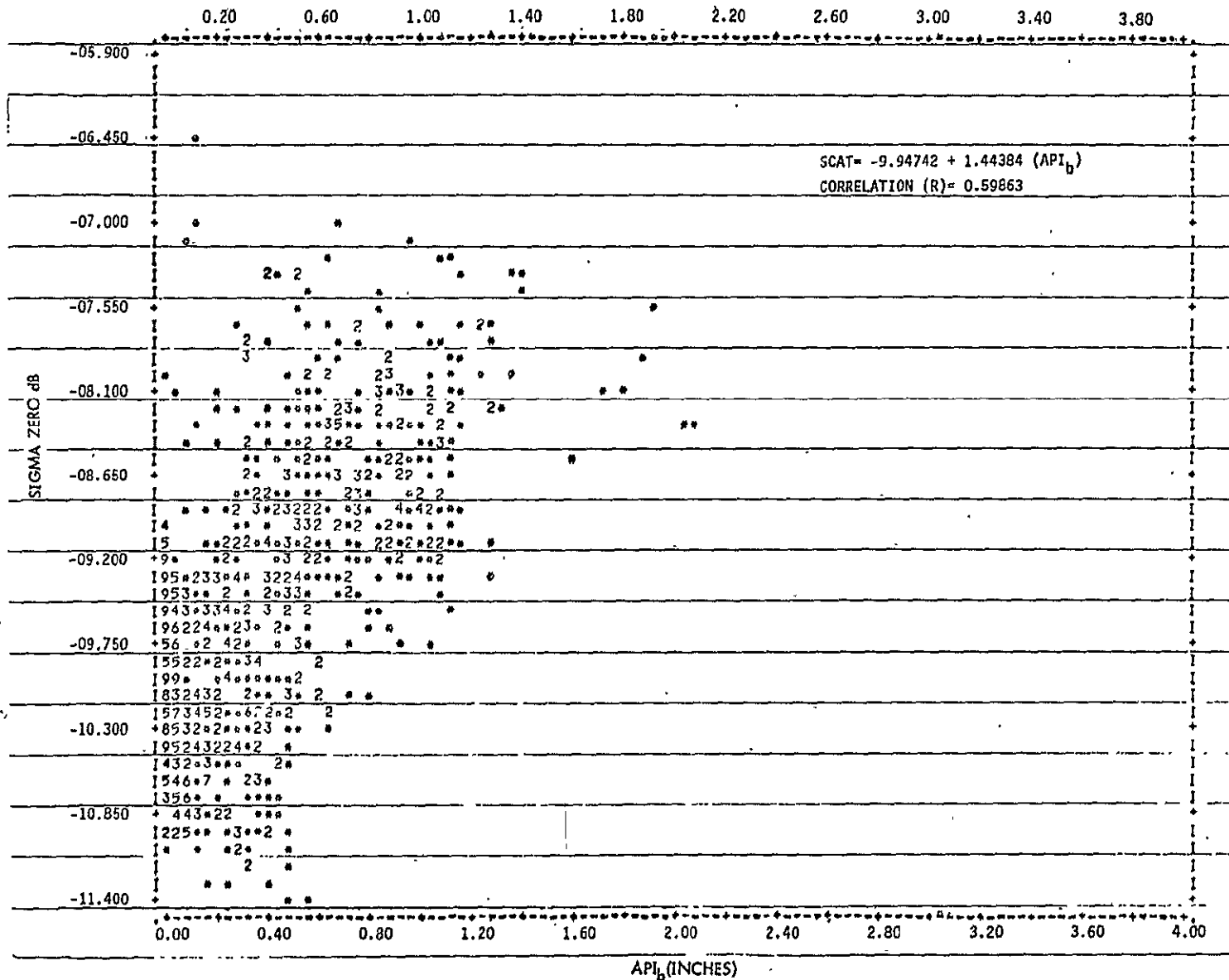


Figure 8.73

Scatter Plot of Backscatter in dB and  $API_b$  Over Texas Site



ORIGINAL PAGE IS  
OF POOR QUALITY

493

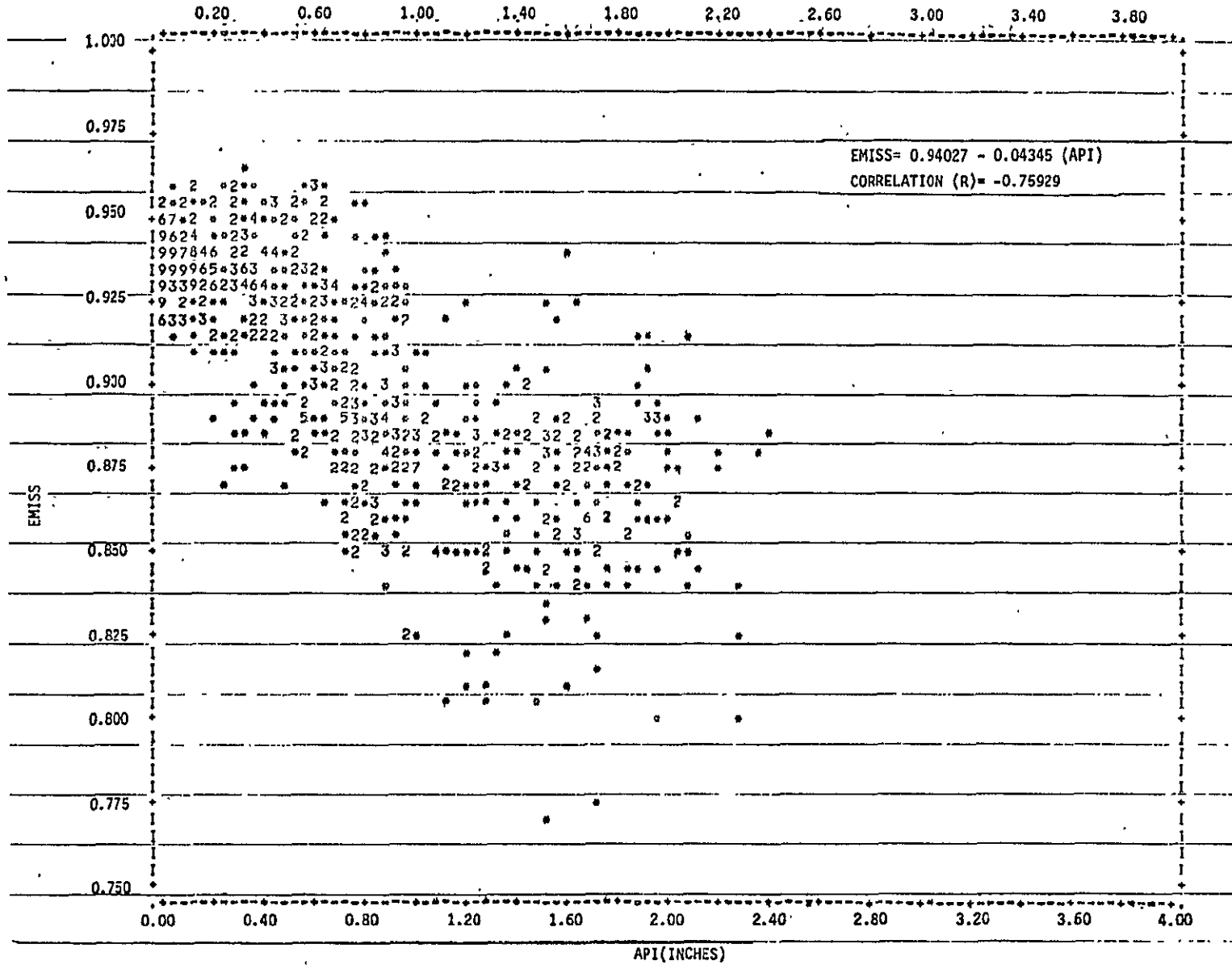


Figure 8.75

Scatter Plot of Emissivity and API Over Texas Site

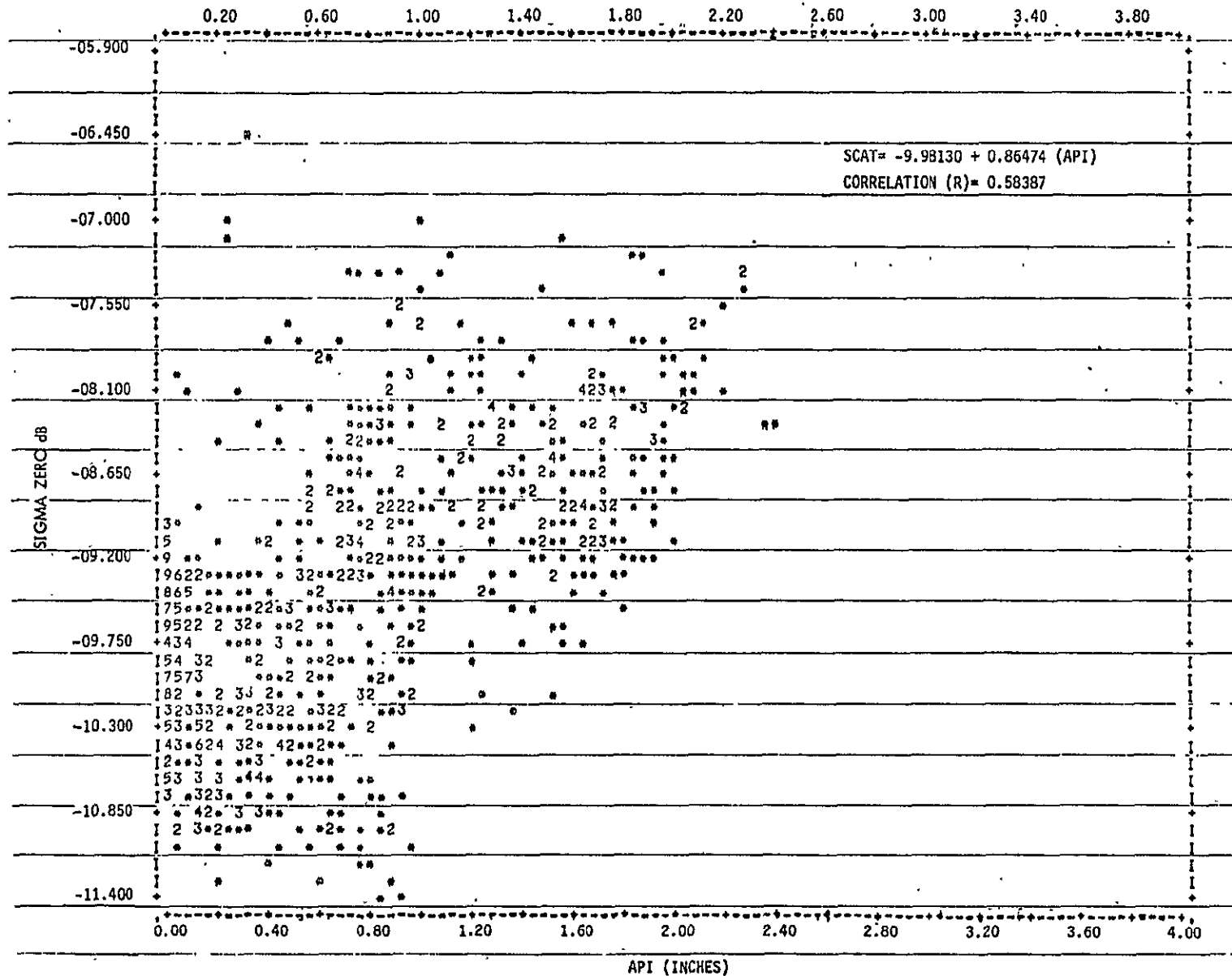


Figure 8.76

Scatter Plot of Backscatter in dB and API Over Texas Site



possible approach. The correlation of the emissivity (using a linear regression with the normalized API) was -0.78. The corresponding correlation of the backscatter in numerics was 62. These two microwave responses are shown in scatter plots with the normalized API in Figures 8.78 and 8.79. A summary of the regression analysis and the correlation coefficients is provided in Table 8.16. A stepwise linear regression routine was then used to see if a second order polynomial would provide a better correlation. The only second order relationship which had a better correlation coefficient was between the emissivity and the normalized API. The equation was

$$\text{Emiss} = 0.94436 - 0.7923 * \text{CRN} + 0.0266 * \text{CRN}^2 \quad (5)$$

The correlation coefficient with this relationship was 0.8095.

The study revealed that it is difficult to predict the soil moisture using the gross resolution sensors, but that it is feasible in some cases to refine estimates where crude ones exist. It showed further that the soil moisture has a substantial influence on the active and passive microwave response and that this influence may overshadow differences caused by variation in physiographic features. No doubt this helps explain the fact that the results from cluster analysis and discriminant analysis are so poor when we have considered only physiographic land-use features as our classification parameters.

## 8.8 Utah Site Study

This study was initiated because the radiometer temperature over the Utah Salt Flat registered 206°K. The reasons for such low radiometric emission, and high backscatter at near vertical incidence were studied exhaustively by Ulaby et al. [1975]. This study is mentioned here for the sake of completeness; details may be found in Ulaby et al. [1975]. The inference drawn by the investigators suggests the Salt Flat subsurface consists of a thin dry crust at the surface which may be from 2 to 4 cms thick below which is a saturated suspension of brine and soil in water. It is encouraging to note that the S-193 radiometer responses over the Salt Flat were similar to those of the Electrically Scanning Microwave Radiometer (ESMR) on board Nimbus E.

The backscatter response at near vertical incidence saturated the receiver. The sharp roll off of the backscatter with incidence angle implied a very smooth surface (as expected).

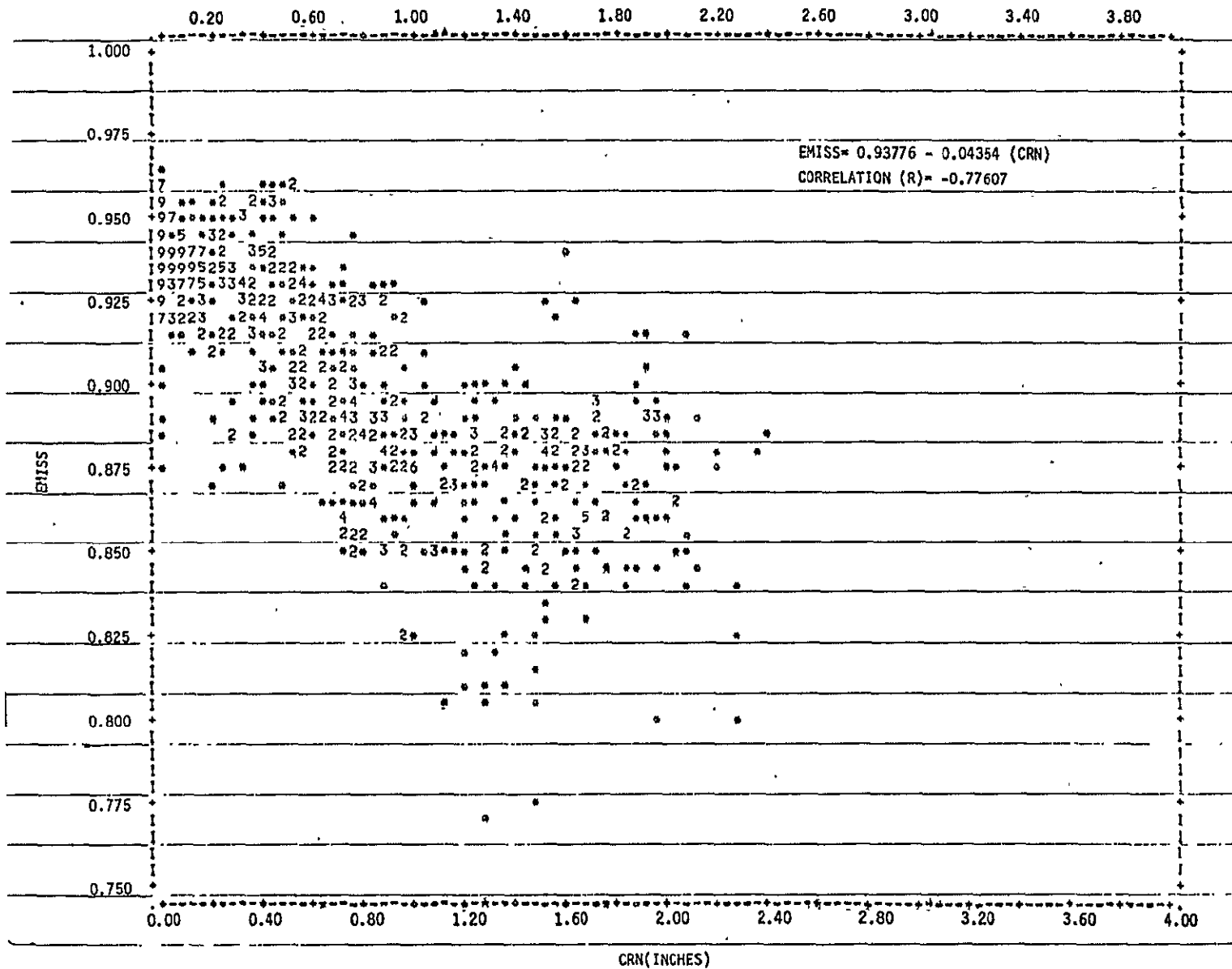


Figure 8.78

Scatter Plot of Emissivity and Normalized API Over Texas Site

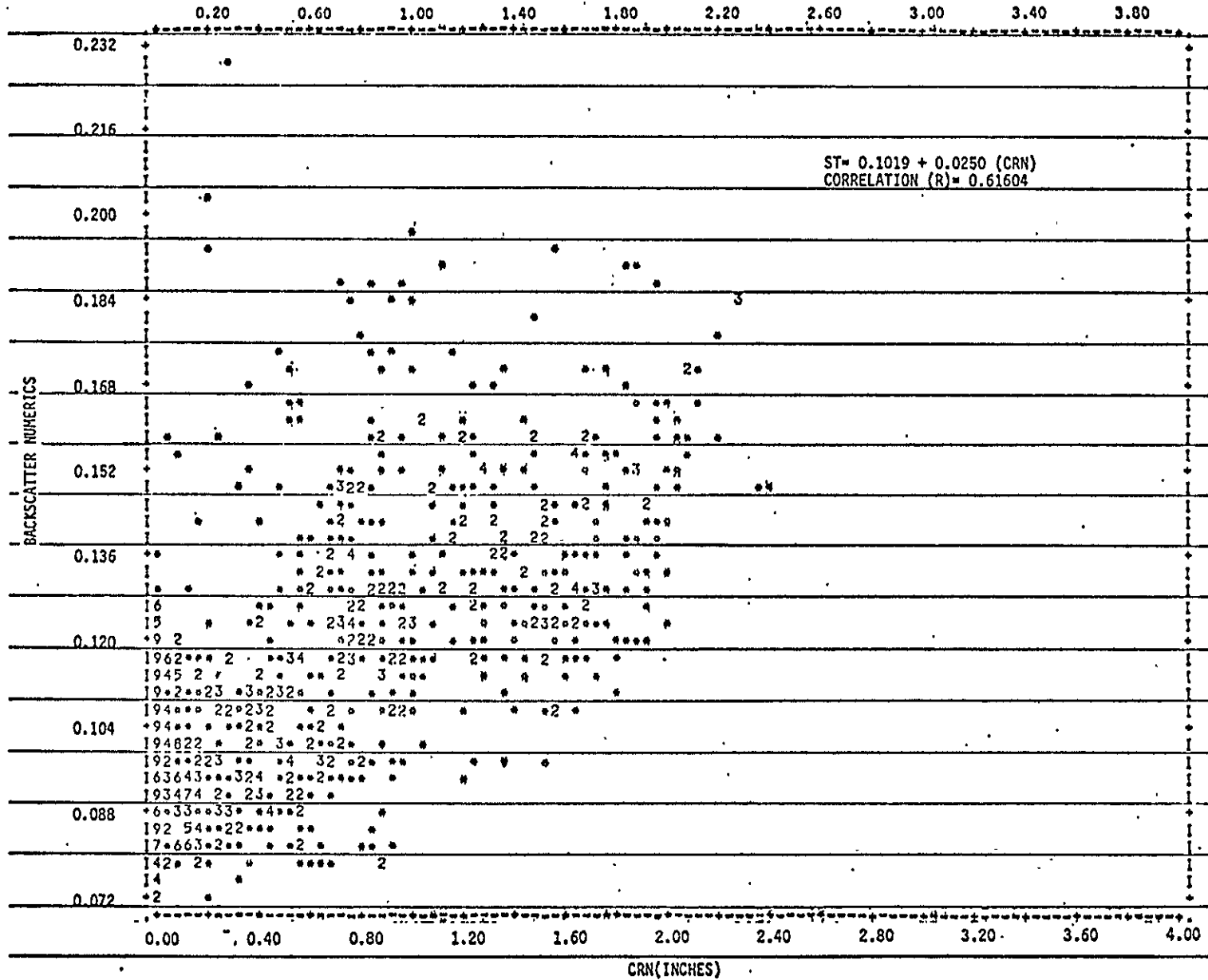


Figure 8.79

Scatter Plot of Backscatter and Normalized API Over Texas Site

Table 8.16.

Dependent Variable	Independent Variable	Linear Least Squares Fit		Correlation Coefficient
		$A_1$	$A_0$	
Rad Temp	API <sub>b</sub>	-16.33823	283.82604	-0.73574
Rad Temp	API	-10.21606	284.51071	-0.74916
Rad Temp	CRM	-16.10351	283.25773	-0.73520
Rad Temp	CRN	-10.04725	283.7998	-0.75157
Emiss	API <sub>b</sub>	-0.06879	0.93708	-0.73813
Emiss	API	-0.04345	0.94027	-0.75929
Emiss	CRM	-0.06894	0.93510	-0.74999
Emiss	CRN	-0.04354	0.93776	-0.77607
Backscat Coefficient (dB)	API <sub>b</sub>	1.44384	-9.94742	0.59863
Backscat Coefficient (dB)	API	0.86474	-9.98130	0.58387
Backscat Coefficient (dB)	CRM	1.48500	-9.91983	0.62424
Backscat Coefficient (dB)	CRN	0.89803	-9.95160	0.61851
Scattering Coefficient (numeric)	API <sub>b</sub>	0.0407	0.1019	0.60217
Scattering Coefficient (numeric)	API	0.0243	0.1009	0.58631
Scattering Coefficient (numeric)	CRM	0.0416	0.1027	0.62380
Scattering Coefficient (numeric)	CRN	0.0250	0.1019	0.61604

Summary Table showing linear fits and correlations between various soil moisture estimates and the S-193 microwave response for the Texas site (Day 156).

## 8.8 Scan Performance

It was pointed out in Chapter 6 that the intrack modes of operation provided a five angle look at the same target point. This was a design goal; the choice of dwell angles and timings had been adjusted to achieve just such a goal. During the space operation of the S-193 sensor, however, the actual pitch dwell angles were sometimes not the designed values. The reasons for this may be one of many; the static friction in a zero g environment may not have been the same as that expected during the design, the amplification in the feedback loop of the servomechanism may not have been up to par, or, the flex harness containing the telemetry and other signal cables may have gotten warped, knotted or become more rigid. In any event, the scan during the intrack non-contiguous mode did not provide a five angle look at the same target point. The problem was at the highest pitch angle which rarely exceeded  $46.0^\circ$ . The five angle footprint actually achieved looks very close to the one shown in Figure 8.80. This is a sample case and quite representative of the performance during SL2 and SL3.

The scan during the intrack contiguous mode is continuous and more rapid. There is also a considerable slew of the antenna during the data taking interval, causing the target to be "smeared." The five-angle footprints for this mode are shown in Figure 8.81. The grouping of the data for this five-angle look was found by taking the  $42^\circ$  pitch angle (this was supposed to be the  $48^\circ$  pitch angle, but the scan never reached beyond  $42 - 43^\circ$ ) for scan 1, the  $40^\circ$  footprint for scan 5, the  $29^\circ$  footprint for scan 8, the  $15^\circ$  footprint for scan 11, and the  $0^\circ$  footprint (the actual angle was around  $2 - 3^\circ$ ) for scan 14.

The performance of the cross-track modes of operation is not critical since each target is viewed only once. The performance during these modes was nominal except for the fact that the scan in CTC did not always extend to  $\pm 10.5^\circ$  of either side of the initialized point. It reached over  $9^\circ$  for most scans and reached over  $10^\circ$  for some. The spatial distribution of the target points is given in Appendix 3, (Figures C13 through C17) for the various pitch offset modes of CTC operation. The figures in the appendix show the target footprint corresponding to the first and last pulse at each measurement. The CTNC mode was operated only over the ocean. Except for the fact that the pitch did not reach  $48^\circ$ , the scan performance was nominal.

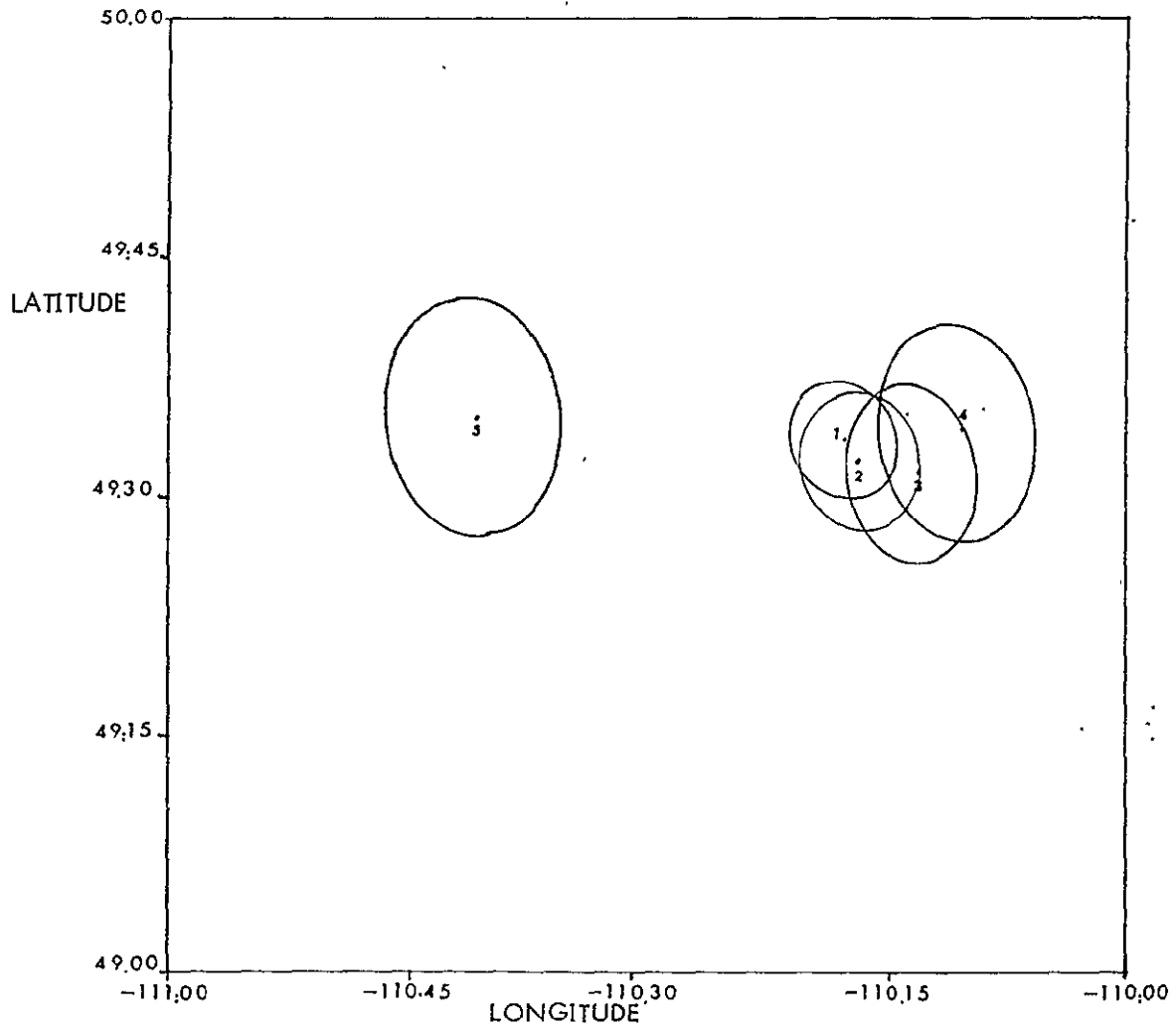


FIGURE 8.80  
INSTANTANEOUS FIELD OF VIEW FOR FIVE  
ANGLE FOOTPRINT [SCATTEROMETER] FOR IN-TRACK NON-CONTIGUOUS MODE

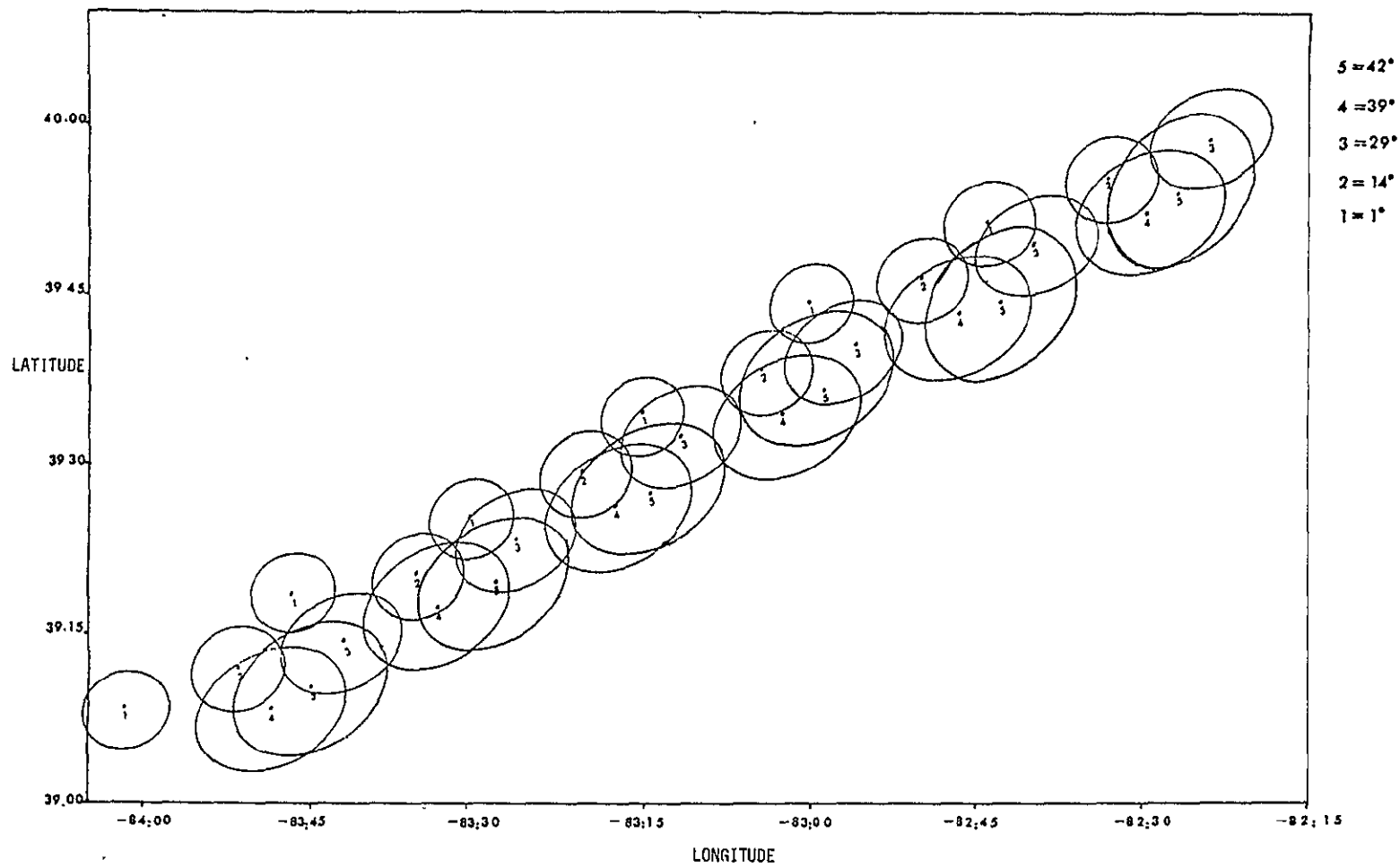


FIGURE 8.8] INSTANEIOUS FIELD OF VIEW FOR FIVE ANGLE FOOTPRINT ( SCATTEROMETER ) FOR IN-TRACK CONTIGUOUS MODE

### 8.9.1 Comparison of S-193 Scatterometer Measurements with Theoretical Models

This is the first experiment to view the earth from afar with coarse resolution radar analogous to the conditions of radar observations of the planets. Consequently, analyses similar to those used in radar astronomy provide a chance for interesting comparisons. Unlike radar astronomers, we do know the physical composition and general geometric characteristics of the surface. A computation of the surface descriptors used by radar astronomers to interpret signals from other planets and their satellites was performed for signals received at Skylab from the planet earth.

The few target types considered in these computations certainly are not descriptive of the entire surface of the earth. Also, unlike radar astronomy which sometimes draws conclusions based on radar signals from a large portion (if not all) of the planetary disc, our observations are from only small patches of the earth. A comparison of the radar signals from the earth to those of other planets might be more meaningful if one averaged the radar return from all points on the earth. One way would be to find the proportion of all land targets; subdivide these land targets into proportions of major biomes and roughness regimes, find the proportions of all water bodies, subdivide these into proportions of roughness categories, find the average cloud cover over land and over ocean surfaces, and then with this data base, concoct the average radar return to an observer on a distant planet. This, of course, would be comparable to the gross radar returns being interpreted by the radar astronomers, but from these returns, one could know very little of the true diversity of the earth's surface.

Of course, most planetary scattering vs. angle curves are for moderately small areas about the sub-earth point, so our analysis for major earth regions may not differ so much. Furthermore, our resolution is comparable with that obtained by Doppler mapping of Mars and Venus. To compare the results from gross resolution radar returns from other planets, we also considered the ensemble angular scattering coefficient means from the North American region and for the ocean.

By applying the theoretical models to radar returns from selected regions and computing the surface descriptors used by radar astronomers, one can better appreciate the values quoted in the literature for some of the extraterrestrial targets. For example, if one finds that the mean or rms slope computed from an ocean surface is much smaller than that from the surface of the moon, then we can imagine how rough the moon is at 2 cms wavelength.

As the understanding of the nature of the radar return from extraterrestrial targets grew, the models to infer results changed. Some of the pioneers in this evolutionary refinement of the models for lunar (and other planets) scattering have been Hagfors (1964, 1966),

Evans (1969), Pettengill et al. (1967), Fung and Moore (1966), Hayre (1961), and Beckmann and Klemperer (1965).

The physical optics model has usually been invoked to explain the gross scattering from other planets and the moon. The geometric optics model has been shown to provide the same results as the physical optics model if one considers a Gaussian autocorrelation function for the surface (Hagfors, 1966). The treatment of scattering from planetary surfaces in the 2 cms. regime usually considers the physical optics model with assumed statistical distributions of the surface height density function (always normal) and autocorrelation function. Two cases have been extensively cited in the literature, the "Gaussian case", i.e., the surface-height autocorrelation function is given by

$$p(d) \propto \exp\left[-\frac{1}{2}\left(\frac{d}{d_0}\right)^2\right] \quad (6)$$

and the exponential case, where

$$p(d) \propto \exp(-d/d_0) \quad (7)$$

According to Hayre and Moore (1961), this function describes many terrestrial surfaces, but at scales relevant to topographic maps rather than cm scales.

When allowance is made for the mean curvature of the surface and it is not assumed that the surface is perfectly conducting, adopting a Gaussian autocorrelation function yields a solution for the backscatter as

$$\sigma^0 = \frac{|p|^2}{2s^2 \cos^4 \theta} \exp(-\tan^2 \theta / 2s^2) \quad (8)$$

where  $s = h_0/d_0$ ;  $h_0$  is the rms height deviation, and  $d_0$  is the correlation length. The mean slope or mean value of the tangent between the normal to an arbitrary surface element and the normal to the mean surface becomes

$$\overline{\tan \theta} = \left(\frac{\pi}{2}\right)^{1/2} \frac{h_0}{d_0} = 1.25s \quad (9)$$

The rms of the tangent is

$$\left\{ \overline{(\tan^2 \theta)} \right\}^{1/2} = \sqrt{2} \frac{h_0}{d_0} = 1.41s \quad (10)$$

A number of attempts to derive an "average slope" for planetary surfaces have appeared in the literature, but as Evans (1969) rightfully points out, it is not entirely clear if this should be taken to mean the angle  $s$ , the mean tangent ( $\overline{\tan \theta}$ ) or the rms tangent ( $\{(\tan^2 \theta)\}^{1/2}$ ). Since we are working with one  $\sigma^0$  vs  $\theta$  curve (the mean curve) per category of target and since our method of solution involves computing one value of  $s$ , we chose to express the slope as  $s$ . Since we computed the value of  $s$  based upon a least square error criterion, we sometimes call the  $s$  computed rms slope.

If we consider an exponential autocorrelation function for the surface, one obtains

$$\sigma^{\circ}(\theta) = \frac{C P}{2} (\cos^4 \theta + C \sin^2 \theta)^{-3/2}$$

where

$$C = \left[ \frac{2k h_0^2}{d_0} \right]^2 \quad (11)$$

A mean surface slope is really dictated by the second derivative of the autocorrelation function at the origin. The exponential autocorrelation function is not differentiable at the origin and, therefore, to ascribe a mean surface slope for a truly exponential autocorrelation quite meaningless. In a real case, the exponential is an approximation of the correlation function valid outside an arbitrarily small region about zero lag. Inside this region the autocorrelation function becomes quadratic and the second derivative, therefore, exists. Since this second derivative is not specified, however, it cannot be used here. Another interpretation of rms slope is provided if one considers Fung and Moore's (1964) approach of treating the exploring wavelengths as a filter which only allows roughness scales down to the size of a wavelength to affect the rms slope. This is to say that a wide spectrum of slopes exists and the rms slope as measured at a particular wavelength is sensitive to that wavelength because it relates to the size of that wavelength. A similar argument has been promoted by Hagfors (1966). The angular spectrum is also a function of the incidence angle. For small angles  $\theta$ , Evans (1969) suggests a definition of an effective rms slope  $s'$  by analogy with the Gaussian case. He quotes Hagfors (private communications) as the source of the formula presented

$$s' = \frac{h_0'}{d_0'} \approx \frac{1}{\sqrt{2C}} \quad (12)$$

where  $h_0'$  and  $d_0'$  are the effective height and effective correlation length at that wavelength. Evans (1969) goes on to explain that this effective slope will be wavelength dependent, unlike the Gaussian case which is not (it is a zero wavelength approximation). To get an equivalent rms slope (described above as rms tangent) from the exponential autocorrelation function case comparable to the rms tangent for the Gaussian case, one must then consider  $(1/\sqrt{C})$ . Since we have chosen to describe  $s$  as the rms slope for the Gaussian case, we shall describe  $s'$  as the rms slope for the exponential case.

It is interesting to note that Pettengill et al. (1967) suggest that the rms slope is given by  $1/\sqrt{C}$  and quote Hagfors (1966). Hagfors (1966), in the publication cited does not mention anything to that effect. In fact in 1968, Evans and Hagfors suggest the proper interpretation of mean slope which they attribute to Hagfors (1966) as

$$\bar{\theta} = \frac{\int_{\theta} \theta \bar{P}(\theta) \cos \theta \sin \theta d\theta}{\int_{\theta} \bar{P}(\theta) \cos \theta \sin \theta d\theta} \quad (13)$$

where  $\bar{P}(\theta)$  is the mean echo power at angle  $\theta$ .

They suggest an approximation for the case of the exponential autocorrelation function which again they attribute to Hagfors (1966) as valid for  $C > 100$  as

$$\overline{\tan \theta} = \frac{1}{2\sqrt{C}} \frac{C-4}{C-\sqrt{C}-2} \ln 4C \quad (14)$$

Yet, the paper they cite as a reference does not contain any such reference.

One can see that the expression for  $\overline{\tan \theta}$  from equation (14) can never approach  $1/\sqrt{2C}$  as  $C$  gets larger, and it is considerably off at 100. Now both Evans and Hagfors (1968) and Pettengill et al. (1967) quote the same Hagfors publications and interpret the results in different ways.

The purpose of the present study is not to provide new interpretations of the slope or better approximations of its computation. It is merely to show the response of the earth in terms used to describe the response from other planets. One can see that the radar astronomy community have not resolved one commonly acceptable interpretation of the descriptors they use in analyses of planetary data. For our purposes, we would simply inundate the reader if we provided him with three sets of mean slopes (with the three interpretations of mean slope) and then provide 2 other sets of such sets of mean slope as we used the various interpretations relating  $C$  to the mean slope. So, we have compromised; we will only provide a partially complete listing and apologize to the reader whose interpretation was not included.

#### Application of Lunar Models to S-193 Scatterometer Data

The lunar models described above, viz. physical optics formulation with the Gaussian and exponential autocorrelation functions were applied on only a selected sample of targets. The ensemble statistics over the North American region and the oceans were also used to compute the mean surface descriptors for these regions. In particular, three samples were selected from the midwest U.S.A. Due to a suspected saturation in the S-193 receiver when viewing ocean target near nadir incidence, no selected samples of ocean passes were considered. The saturation can cause the  $\sigma^0$  vs  $\theta$  curve to appear compressed and may give false values for rms slope which depends upon the shape of the curve. The only  $\sigma^0$  vs  $\theta$  curve considered for the ocean was from the ensemble statistics where data at angles away from nadir ( $17^\circ$  and  $33^\circ$ ) were used along with those near nadir.

The angular backscatter response was used to compute the reflection coefficient and the rms slope for both the Gaussian autocorrelation function and the exponential autocorrelation function. The solutions of the rms slope and reflection coefficient were found by a variety of ways. Non-linear regression using various combinations of incidence angles and backscatter values were used as well as pairs of these values for solution of two simultaneous equations. Details of the non-linear regression are provided

□ MEAN FOR NORTH AMERICAN TARGETS (LAND)  
 △ MEAN FOR OCEAN  
 ● Forest Day 253 Pass 31 Colo., Neb., Minn.  
 ■ Farmland Day 253 Pass 31 Colo., Neb., Minn.  
 ▼ Sandhill Day 253 Pass 31 Colo., Neb., Minn.  
 Polarization: VV

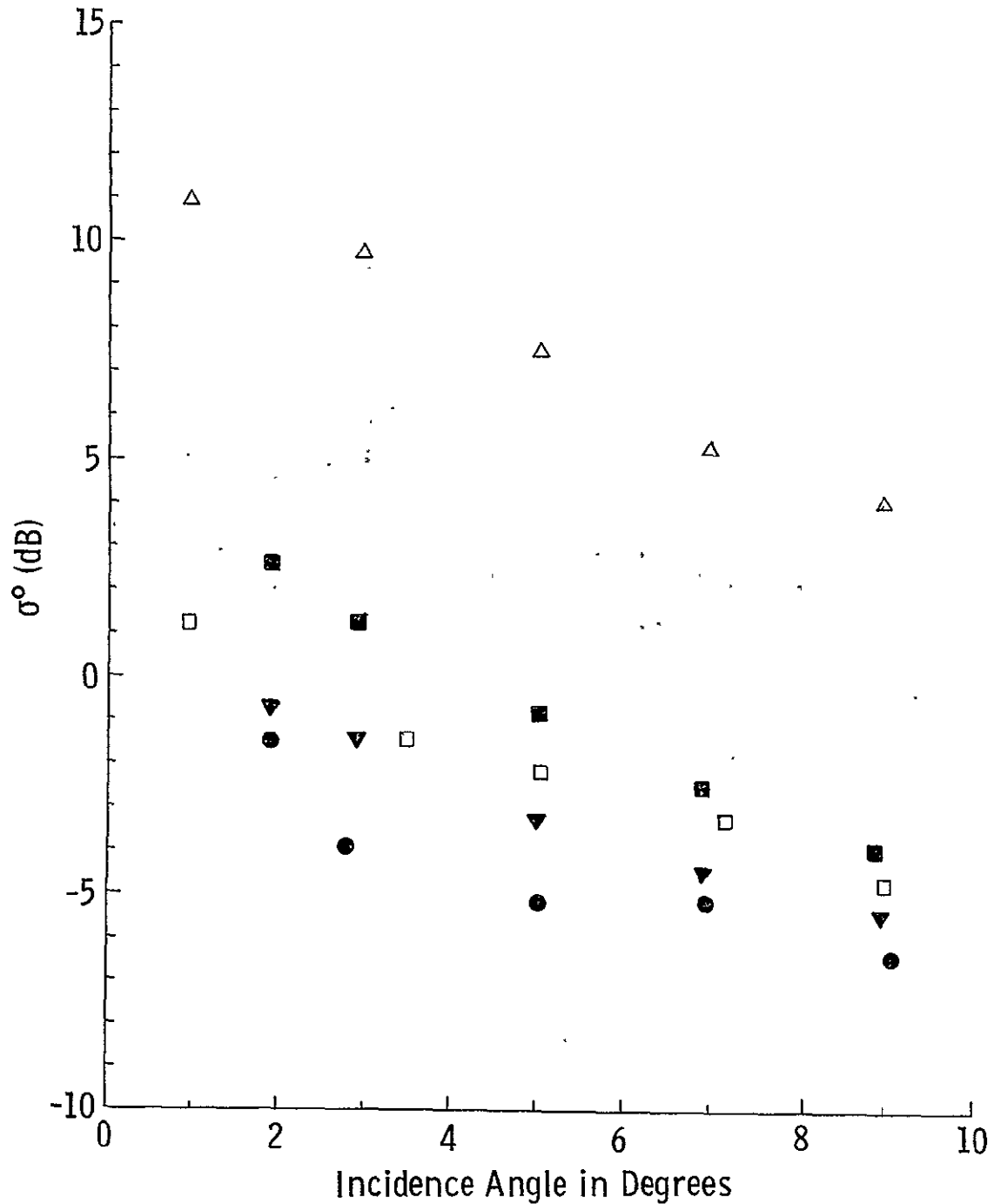


Figure 8.82. Six sample backscatter responses for computation of mean slope and reflection coefficient by lunar theories.

Table 8.17 Summary of results showing computed values of slope and reflection coefficient by using the Gaussian and exponential autocorrelation functions

Curve No.	Gaussian Autocorrelation Function		Exponential Autocorrelation Function		Target*
	Mean Slope (deg)	Reflection Coefficient	Mean Slope (deg)	Reflection ** Coefficient	
1	5.614	.154	5.10	.144	Forest, Midwest U.S.A.
2	4.40	.21	3.97	.20	Farmland, Midwest U.S.A.
3	5.28	.168	5.08	.17	Sandhills, Midwest U.S.A.
4	4.33	.532	4.20	.531	Ensemble Ocean
5	4.76	.178	4.25	.171	Ensemble N. America

\*Angular response of targets shown in Fig. 8.82

\*\*Voltage reflection coefficient

in Appendix 2. The results reported are from the non-linear regression using five angles close to nadir (1.8°- 9.8°). The results using the Gaussian autocorrelation function and the exponential autocorrelation function are shown in table 8.17. The first three cases are selected targets where the number of samples used to compute the mean angular backscatter was under a 100. For the ensemble statistics over land and ocean, the number of samples are well over 200. The value of slope is expressed in degrees and computed from  $1 / \sqrt{2C}$  for the exponential case. It has often been suggested that a Gaussian autocorrelation function is more descriptive of ocean surface near vertical and that an exponential autocorrelation function is more descriptive of land surfaces. It is interesting to observe that both these cases seem to provide similar results over land and ocean. The Fresnel reflection coefficient of the ocean surface is lower than that measured by prior programs. It is, however, much higher than that for land (as expected). The roughest surface, as expected was the forest and the smoothest was farmland. From the ensemble statistics the mean slope for both ocean and land was very comparable.

In comparing these results with those obtained from the moon and Venus we find that all the surfaces considered here are smoother than the moon which as an rms slope of approximately 10.4° (Ingalls and Evans, 1969). The slope for Venus (7.3°) is slightly more than the roughest category considered here (Ingalls and Evans, 1969).

The interpretations of mean slope  $s'$  suggested by Hagfors eq (13), attributed to Hagfors by Pettengill et al (1967) eq (12), are all consistent. The interpretation of slope  $s'$  attributed to Hagfors by Hagfors and Evans which is valid for  $C > 100$  does not seem to agree with the other three. The three interpretations of mean slope  $s'$  are shown in table 8.18 for three selected targets along with the mean slope for the Gaussian case. There is good conformance between all three cases.

Table 8.18 Comparisons of Mean Slope As Computed by Various Suggestions in the Literature (Expressed in Degrees)

	$1 / \sqrt{2C}$ eq (12)	Hagfors eq (13)	Gaussian	Surface
1	5.10	5.851	5.614	Forest
2	3.97	3.741	4.40	Farmland
3	5.08	5.7538	5.282	Sandhills

The radar astronomers often describe the planetary surfaces by their roughness and the dielectric constant. The dielectric constant is computed from the reflection coefficient as

$$\epsilon_R = \left( \frac{1 + \rho^{1/2}}{1 - \rho^{1/2}} \right)^2 \quad (15)$$

where we have considered  $\epsilon_R = \epsilon_1 - 0.1j\epsilon_1$  i.e. the real part is 10 times the imaginary part. Since the reflection coefficients computed for the Gaussian and exponential functions are very close, we computed the dielectric constant from the reflection coefficient obtained from the exponential case. These are shown in Table 8.19. Although there seems to be a rank order correlation between the computed dielectric constants and those measured by prior programs, the magnitudes are considerable off. The dielectric constant for water at 296° K and for 35 parts per 100 salinity has been estimated to be (47.4 - j37.4), Wu (1973). This is much higher than what we observe. The dielectric constant for the land cases are also suspect. Campbell and Ulrich (1969) report on the dielectric constants of rocks, and even at 35 GHz, none of their values is as low as that for the ensemble land mass. The reflection coefficient is very sensitive to absolute levels of  $\sigma^0$  which govern the reflection coefficient.

In summary, it was found that both the Gaussian autocorrelation function and the exponential autocorrelation function provide similar results over land and ocean. The ocean and land seem to be comparably rough at 2 cms wavelength. For all the targets considered and for ensemble cases of land and ocean, the mean slopes are smaller than for the moon and Venus, implying that the earth is smoother than both. The Fresnel reflection coefficient over the ocean is much higher than over land but not as high as that measured by prior programs.

Table 8.19

Dielectric Constants Computed From Reflection Coefficients for the Exponential Autocorrelation Function

Case No.	Target	Exponential $\epsilon_1$	Function $\epsilon_2$
1	Forest, Midwest	1.77	0.18
2	Farmland, Midwest	2.23	0.22
3	Sandhills, Midwest	1.97	0.20
4	Ensemble, North America	1.97	0.20
5	Ensemble, Ocean	10.58	1.06

### 8.9.2 Comparison of S-193 Radiometer Measurements with Theoretical Models

Theoretical models employed to describe the radiometric emission are by and large models that describe the bistatic scattering coefficients. The models often invoked stem from either the geometric optics model, the physical optics model or the composite model. The solutions to estimate the emissivities from these models are not trivial and, apart from the ocean surfaces, the predictions of the models are only rarely in agreement with measurements.

Some surfaces are rough and treated like Lambertian surfaces. The radiometric response from a Lambertian surface is independent of viewing angle and of polarization. Data obtained over land by the S-193 show no particular angular trend and show a remarkable similarity between the response for both polarizations. It appears as though land is a rough surface to the radiometer at these wavelengths. The ocean surface has sometimes been modelled as a smooth planar surface. This formulation is very straightforward and offers an easy comparison with measured results.

According to the planar surface model, the emissivity is related to the reflection coefficient as

$$e_i(\theta) = 1 - |p_i(\theta)|^2 \quad (16)$$

where  $i = v$  or  $h$  polarization

$e$  = emissivity

$p$  = Fresnel reflection coefficient

The Fresnel reflection coefficients can be computed from the dielectric constant by

$$p_v = \frac{\epsilon_R \cos \theta - \sqrt{\epsilon_R - \sin^2 \theta}}{\epsilon_R \cos \theta + \sqrt{\epsilon_R - \sin^2 \theta}} \quad (17)$$

$$p_h = \frac{\cos \theta - \sqrt{\epsilon_R - \sin^2 \theta}}{\cos \theta + \sqrt{\epsilon_R - \sin^2 \theta}} \quad (18)$$

where  $\epsilon_R$  = complex dielectric constant.

The dielectric constant of an ocean surface is sensitive to physical temperature but, at 13.9 GHz it is not particularly sensitive to salinity (Wu, 1973). If the estimates of the dielectric constant for an ocean surface can be found, the theoretical or predicted emissivity can be computed. This of course assumes that the ocean is a flat specular type surface.

Wu (1973) has computed the dielectric constant for sea water for various salinities and physical temperatures. From his work, the dielectric constant at 13.9 GHz for an ocean surface having 35 parts per thousand salinity and at 296°K is 47.4 - j37.4. This value reduces to 39.84 - j39.33 at 284°K. For comparison with the S-193 data we must therefore make a judicious choice of the temperature of the ocean. There are two choices open to us: we can either furnish our best guess of the temperature of the ocean surface or we can assume a number of ocean surface temperatures and compute the nadir response for each and see which one gives us the best match with data obtained. The temperatures of the ocean surface vary with latitude and time of year. Since our data were obtained during the summer months, we find that during August the isotherms range from 28°C to 29°C for the Gulf of Mexico and can get as low as 15°C for 50° North latitude in the Pacific (Neumann and Pierson, 1969). Our data set is biased towards the Gulf of Mexico, so, a good guess would be either 23°C or 27°C. We have computed the emissivities for a plane surface model considering dielectric constant values at 11°C and 23°C because of readily available dielectric constant data at these temperatures Wu (1973). The emissivity of an ocean surface decreases with increasing temperature, although the variation, according to Wu's predictions are extremely small beyond 296°K.

The antenna temperature measured by the S-193 radiometer has been subjected to atmospheric effects. If we assume a simplified model for the atmosphere to go along with our plane surface model, then the antenna temperature is given by

$$T_{ant}(\theta) = L(\theta) [ T_{sky}(\theta) |P(\theta)|^2 + (1 - |P(\theta)|^2) T_s ] + T_{atm}(\theta) \quad (19)$$

where  $\theta$  = angle of incidence

$T_{sky}$  = downward radiation due to the sky

$T_{atm}$  = direct upwelling radiation by the atmosphere to the receiver

$L$  = transmittance (opacity) of the atmosphere.

The transmittance and atmospheric contribution are dependent upon the state of the atmosphere. For our calculation we assumed an atmosphere with a specific humidity of 7.75 gms/m<sup>3</sup>, pressure at 1013.25 millibars, temperature at 293°K. The temperature of the Galactic background was taken at 2.7°K. The models described in chapter five were used to compute the atmosphere dependant terms in eq (19). By considering the ensemble statistics over the ocean and selecting the mean value at each angle and by assigning physical temperatures to the ocean surface we can compute the reflection coefficient. By assuming the plane surface model, we can then compute an emissivity from the reflection coefficient so computed. These emissivities can be compared to those predicted by considering dielectric constant values at the same temperature.

Figure 8.83 shows the emissivities computed from S-193 data for a physical temperature of 284°K (11°C) and 296°K (23°C). Also shown in the figure are emissivities computed from the dielectric constant data at these two temperatures. One can observe that there is a slight discrepancy between the emissivity at nadir for vertical and horizontal polarization. This difference is probably due to erroneous processing (the antenna pattern and the loss terms in the S-193 transfer function are known to be polarization dependent). From the figure one can see that the emissivities computed from the S-193 data are higher than those computed for a plane surface from dielectric constant data. This is expected because the ocean is indeed not a plane surface and must have some roughness.

It is, however, interesting to note that the difference between the emissivity computed from S-193 data (hereinafter called data) and that from dielectric data (hereinafter called predicted value) increases with incidence angle for horizontal polarizations. This is in accordance with the predictions of the geometric optics model. The vertical polarization appears to be much more insensitive to roughness as is witnessed by the difference between the data and predicted values in Figure 8.83. It has often been suggested, based upon empirical evidence that the radiometric temperature is rather insensitive to roughness at nadir (Ross et al 1970). We find that there is a difference in emissivity of .0235 (6.95°K) between the data and the predicted value. This increase corresponds to a great deal of roughness, suggesting either that maybe a bias error exists in our data, or more likely, our conversion for S-193 antenna temperature did not properly account for the atmosphere. If we may assume that the differences at nadir are due to our calculations, then, we must lower the data by .0235 at each angle.

Ross et al (1970) and Hollinger (1971) have found that at around 50°-55°, the sensitivity of radiometric emission (horizontal polarization) to windspeed follows a slope of approximately 1°K/m/sec at 19.4 GHz. Hollinger estimates that this slope is only 0.6°K/m/sec for 8.36 GHz. If we interpolate to 13.9 GHz from 8.36 GHz and 19.34 GHz, we get roughly 0.75°K/m/sec at 46° incidence. The temperature difference between the adjusted data and the predicted value at 46° incidence is .0255 (7.5°K). This corresponds to a wind speed of 10 m/sec or 19.7 knots.

On the fifth of June, 1973, with the S-193 radiometer/scatterometer operating in the ITNC mode, data was obtained over the Gulf of Mexico. Aircraft underflight provided wind, wave and atmospheric descriptions for the targets viewed by the S-193 radiometer. The atmospheric conditions were quite similar to those described above. The wind speed was estimated as 14 knots and the ocean temperature was found to be approximately 300°K (Hayes et al, 1973). Data for a footprints were averaged and reduced to emissivities. These values are shown in Table 8.20 along with all those described above.

Table 8.20 Summary of Results Showing Emissivities Computed from a Plane Surface Model Using Dielectric Constant Data and Using S-193 Data

Angle (deg)	P o L	From Dielectric Constant at 284°K	From Dielectric Constant at 296°K	From S-193 (Ensemble) Sea Temperature 284°K	From S-193 (Ensemble) Sea Temperature 296°K	From S-193 Day 156 Sea Temperature 300 ° K	From S-193 (Ensemble) Sea Temper. 300°K
0	V	.391	.387	.430	.412	.396	.407
0	H	.391	.387	.425	.409	.389	.403
17	V	.405	.400	.444	.426	.405	.420
17	H	.378	.373	.414	.397	.377	.392
33	V	.440	.441	.485	.464	.440	.459
33	H	.340	.336	.389	.373	.357	.368
46	V	.504	.499	.542	.519	.508	.512
46	H	.296	.292	.356	.341	.320	.336

515

\*Wind speed 14 knots, clear sky

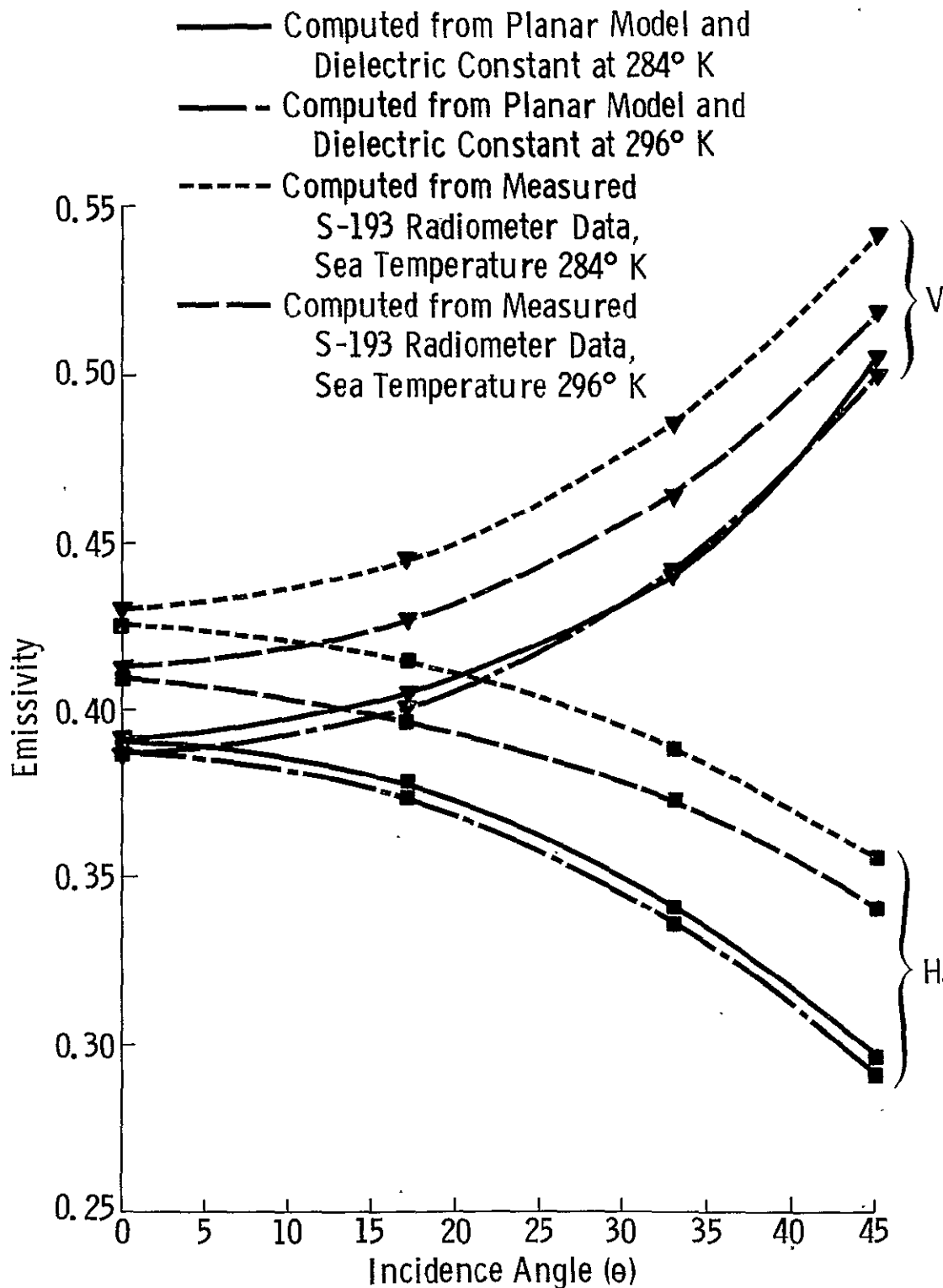


Figure 8.83 Comparison of emissivities computed from S-193 radiometer measurements over ocean and some predicted values based upon a plane surface model.

If we again claim that there exists a difference in the nadir response between the data and the predicted value only due to our errors in processing, then adjusting for this bias error we find that there is an increase of  $6.75^{\circ}\text{K}$  at  $46^{\circ}$  incidence. This corresponds to  $9\text{ m/sec}$  or  $17.6\text{ knots}$ .

This result is encouraging because with minimal computations we have achieved a result that is within 3 knots. The slope of  $0.75^{\circ}\text{K/m/sec}$  was read from a small figure in a journal and is subject to error. From our result we estimate this slope to be  $0.94^{\circ}\text{K m/sec}$ . From the result obtained above, if we were to find the mean wind speed over the ocean, we could reduce the data to emissivity, perform our calibration near nadir and compute the wind speed according to our empirically obtained slope. For a physical temperature of  $296^{\circ}\text{K}$  we obtain a wind speed of  $8\text{ m/sec}$  or  $15.7\text{ knots}$ . For a physical temperature of  $300^{\circ}\text{K}$  we obtain  $8.3\text{ m/sec}$  or  $16.3\text{ knots}$ .

It is interesting to observe that in spite of the overly simplistic model for the surface and specially for the atmosphere, these results are fairly close to those predicted by the radar. The radar scatterometer is comparatively impervious to atmospheric effects and it viewed the same targets over the ocean as did the radiometer. From the scatterometer data, using J.D.Young's (private communication) latest estimate of the regression between wind speed and backscatter at  $30^{\circ}$  and  $40^{\circ}$  incidence for horizontal polarization, we find that the mean wind speed was approximately  $13\text{ knots}$ .

In summary, the radiometer data over the ocean appear to have consistent trends. A very simple model for the atmosphere and for the surface show that the wind speed dependence is evident and that horizontal polarization is more sensitive to it than vertical. The data over land have no angular trends and the response for both polarizations appear similar. This suggest that land is almost a Lambertian surface at this wavelength.

## 8.10 Display of S-193 Microwave Data

The cross-track contiguous mode provides data that can be treated as though from a gross-resolution imaging sensor. The resolution is much too poor for any of the applications currently being used for imaging radars, but, if one considers that this is the first time a radar has been used to look down on the earth, the gross resolution can be tolerated if only to show the capabilities of finer resolution sensors. Nimbus E has a scanning microwave radiometer with a smaller beam width, but because of its much higher orbit, the spatial resolution of the S-193 radiometer is much better. The display of backscattering coefficient data has been attempted earlier by Masenthin [1967], and numerous other schemes have been proposed by R. K. Moore [1966]. A problem with the display of microwave data is that there are many variables involved and a display of one or two at a time does not convey the whole picture. Only where image-like presentations are produced can an interpreter get an instant spatial orientation of the various microwave responses. The current effort has totally circumvented the more difficult task of displaying multidimensional data and concentrated on producing image-like displays for facility in interpretation. The display of the angular backscatter or radiometric response characteristics of a target should be attempted by first finding a way of reducing the dimensionality of the multiple dimension (multi-angle) data into perhaps one dimension (or at most two dimensions) and displaying these data in an image-like format, the latter part of the effort being similar to that attempted here. A reduction in dimensionality of data has traditionally been accomplished in one of two ways: a principal components analysis is first used to get either the first few principal components and these are then displayed as intensities on an image-like format, or only a few of the significant variables are displayed, once again as intensities on an image-like format. The first method has the advantage of having considered all of the variables, but the disadvantage is that one does not really know what the variables mean. The second approach has the disadvantage of having used only a (small) portion of the information, but the advantage is that one knows from intensity variations across an image what the value of the variable should be.

We have essentially taken the second approach. Also, we have not considered a dimensionality of data greater than one; i.e., the intensity variations across an image-like display are either backscatter variations at a certain angle or radiometric variations at a certain angle, but not any combinations of the two. The combination of images can, however, be easily accomplished by the hardware and software developed at the

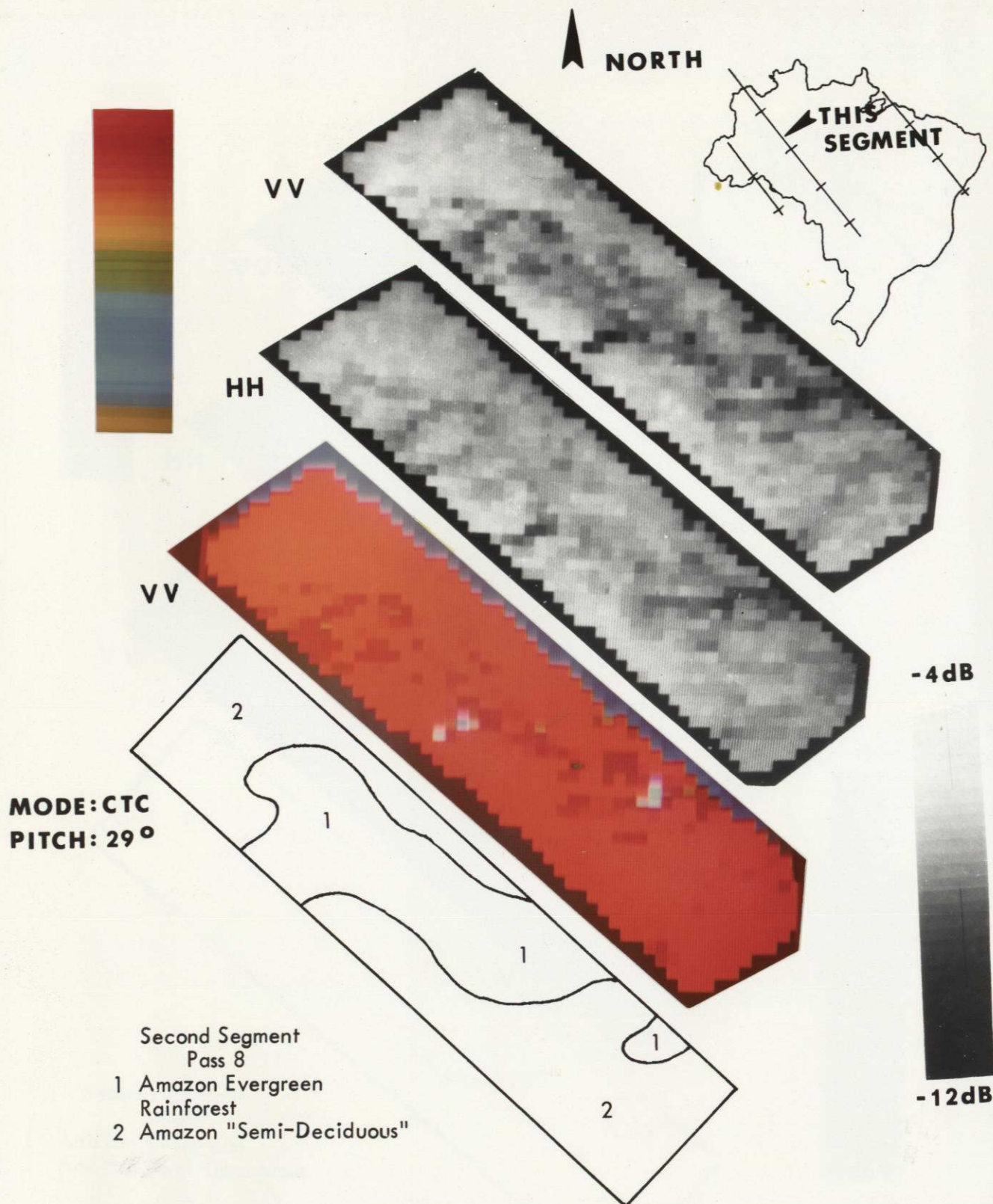
University of Kansas. The IDECS system with the attached PDP 15/20 computer has the capability of registering, combining in any logical operation and displaying a number of images.

The IDECS system was used along with the PDP 15/20 computer to transfer the extrapolated and cleaned image-like files on to a video monitor. The image-like files were produced on a HIS 635 computer by use of the Surface Graphics II package [Sampson, 1975]. The details of the image producing scheme shall be the subject of a future report, contained herein are examples of image-like displays produced by the current scheme.

Figure 8.83 shows a pair of black and white images (one of VV polarization and one for HH polarization), a false color image, a vegetation demarkation, and a color and gray tone bar. These are pseudo-images prepared from backscatter data obtained over Brazil. The geographic region is shown on a map of Brazil in the corner of the figure. The range of backscatter coefficients included were from -12 dB to -4 dB. The backscatter was quantized to 32 levels providing 0.25 dB per bit. Notice how the Amazon semideciduous forest formations appear to be differentiated by the scatterometer response. The vegetation map boundaries should not be considered absolute.

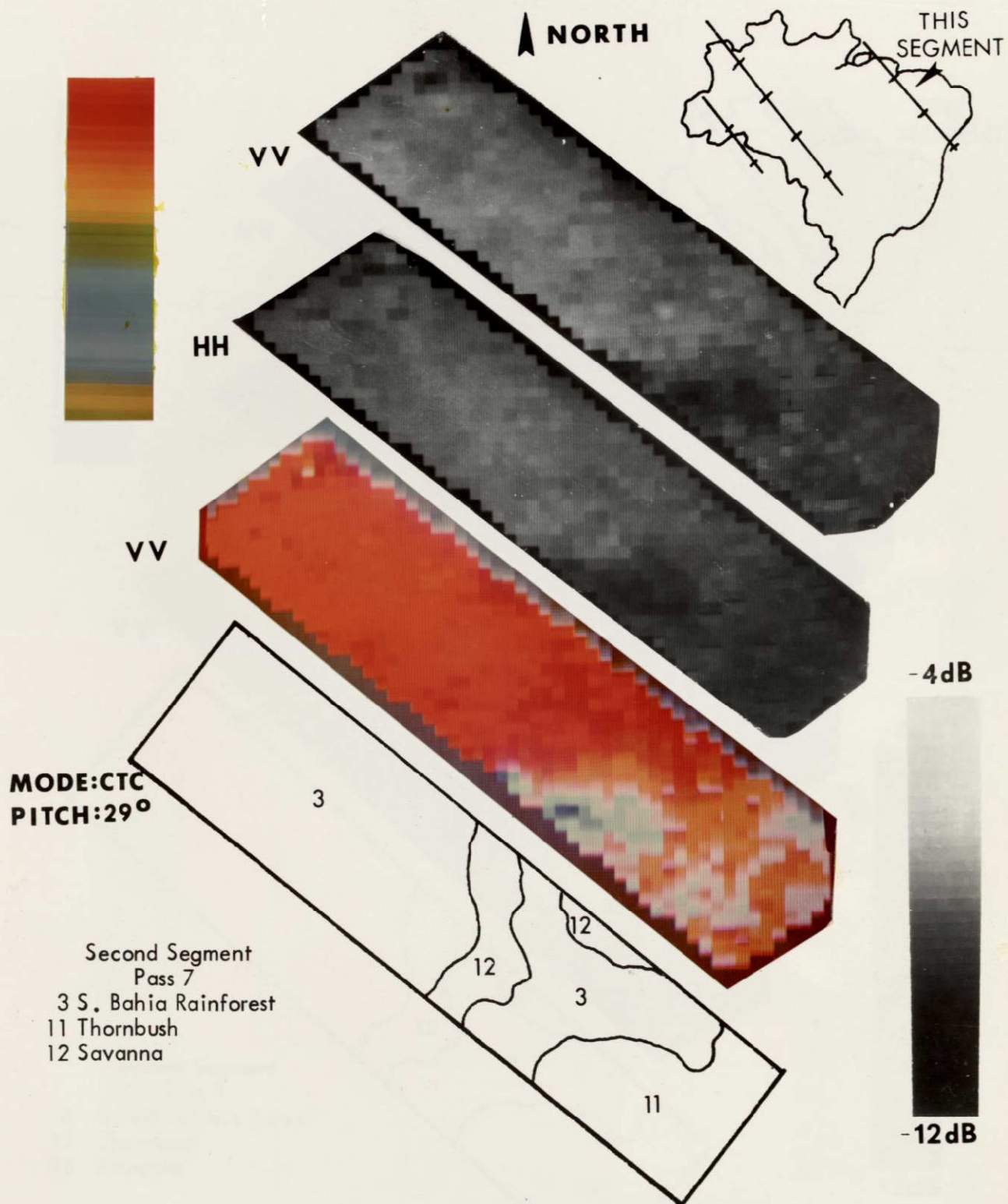
Figure 8.84 shows another region of Brazil produced from a different pass, but with the same sensor configuration. Observe how the evergreen forests appear as one large homogeneous region showing a higher backscatter than the rest of the region. The variations in backscatter do not correspond in a one-to-one fashion with the vegetation map, but there is evidence of lower backscatter in regions which are shown in the vegetation maps to be thronbush or savannah.

Figure 8.85 shows a pseudo-image over Texas on Day 156 using the CTC pitch offset  $29^\circ$  rad/scat mode. The image was prepared from the backscattering coefficient. The range of values entertained was from -12 dB to -6 dB in roughly 0.2 dB per bit quantization. The variations in the response have been ascertained to be due to soil moisture variations. Indeed, this is the same region for which the soil moisture study results were reported. The radiometric response is represented in a pseudo-image in Figure 8.86. Observe that the general variations are similar to those of the scatterometer. The range of radiometric temperatures was only  $260^\circ\text{K}$  to  $291^\circ\text{K}$  with 32 level quantization. There were some points which registered below  $260^\circ\text{K}$  and appear in the color image as the background tone. The graytone image shows them to be perfectly black.



PSEUDO-IMAGES PRODUCED FROM BACKSCATTER RESPONSE  
WITH CROSS-TRACK CONTIGUOUS, PITCH 29° MODE OF  
S-193 OPERATION ON DAY 162, PASS 8, SL-2 OVER BRAZIL

FIGURE 8.84

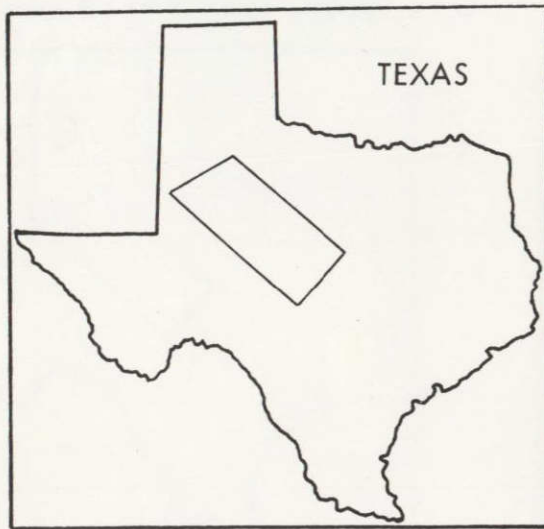


PSEUDO-IMAGES PRODUCED FROM BACKSCATTER RESPONSE  
WITH CROSS-TRACK CONTIGUOUS, PITCH 29° MODE OF  
S-193 OPERATION ON DAY 161, PASS 7, SL-2 OVER BRAZIL

FIGURE 8.85



PSEUDO-IMAGES PRODUCED FROM  
BACKSCATTER RESPONSE



CROSS-TRACK CONTIGUOUS, PITCH  $29^{\circ}$   
MODE OF S-193 OPERATION  
PASS 5, DAY 156

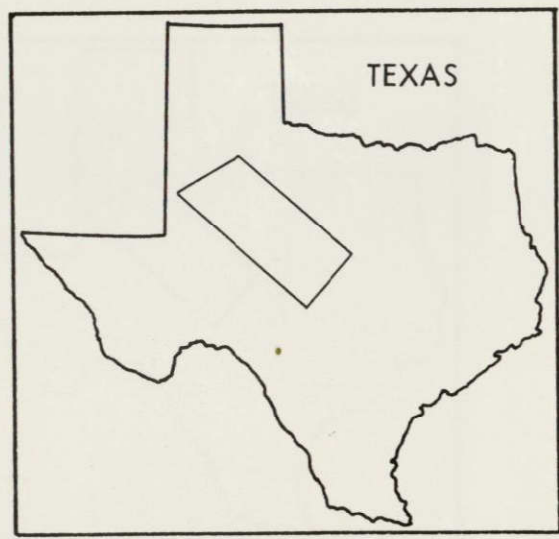
FIGURE 8.86

C-7

REPRODUCIBILITY OF THE ORIGINAL PAGE IS POOR



PSEUDO-IMAGES PRODUCED FROM RADIOMETRIC TEMPERATURES



CROSS-TRACK CONTIGUOUS, PITCH 29°  
MODE OF S-193 OPERATION  
PASS 5, DAY 156

FIGURE 8.87

These images were produced to show that the response of the S-193 radiometer/scatterometer can be treated like that from a gross resolution imager. The detection of major vegetation categories and variations in soil moisture can be appreciated even with such gross resolution.



## CHAPTER NINE

### SUMMARY AND CONCLUSIONS

The objectives of the study were two-fold: to obtain information for the design of future fine resolution sensors, and, to explore the capabilities and limitations of geoscientific investigation with gross resolution microwave sensors operating on an orbital platform. For the purpose of satisfying the first objective, a catalogue of the microwave response over various terrain was to be prepared.

Valuable design information was obtained from the space operation of the S-193. The S-193 radiometer/scatterometer experiment provided the first opportunity of examining the microwave backscatter response from orbital heights. The design of a data catalogue from the scatterometer and radiometer as reported here is the very first such design. Perhaps the most significant results were obtained in compiling the ensemble statistics over land and ocean. It was found that due to the large spatial averaging involved, the dynamic range of the backscatter over land at any angle is much smaller than that measured by fine resolution sensors. This is reflected in the range between the upper and lower deciles of the backscatter computed for the angles of operation of the S-193. This spread between the upper and lower deciles was a maximum near nadir (approximately 14dB) and a minimum near  $17^\circ$  (3.6dB). It decreased from near nadir till  $17^\circ$  and then again increased till at  $46^\circ$  it was approximately 7.5dB. The angular decay of the backscattering coefficient was as expected.

An interesting effect of this vast spatial averaging is that the lower decile of the backscattering coefficient near vertical incidence (within  $3^\circ$ ) is above -4dB. This provides a good design value for the lowest signal levels to be expected for altimeters operating on space platforms, although some margin should be included to account for the lower 10%.

The dispersion of the backscattering coefficient at almost all angles considered was larger for ocean surfaces than for land. The decay of the backscattering coefficient was steeper for the ocean than for land (as expected); it was approximately 10dB higher in the mean near nadir and approximately 10dB lower at  $46^\circ$ . The backscattering coefficient near nadir incidence had an upper decile at approximately 13dB. This is much lower than the mean value for water surfaces as reported by Williams et al (1975), who report that at nadir the backscatter for a smooth water body is approximately 20dB and for the ocean is 17.7dB. A probable cause for the low values obtained by the S-193 scatterometer is that the receiver operating dynamic range only extended to +15dB.

There could have been some non-linearity in the receiver response for backscatter as low as 13dB to 14dB.

Over ocean surfaces, the cross polarized backscatter is approximately 16dB lower than the dominant polarization backscatter near nadir and only 8dB lower at  $46^\circ$ . The values recorded for the higher incidence angles appear to be at the lower end of the dynamic range of the receiver and therefore the values observed at these high angles may be even lower than those reported. The range between upper and lower deciles for the cross polarization backscatter is extremely small near nadir (2.5dB) and increases with incidence angle till at  $46^\circ$  this range is 12dB.

The backscatter response obtained over vast transects of South America (mainly the Brazilian region) at  $33^\circ$  incidence showed a range between upper and lower deciles of only 3.5dB. The lower decile of this response was higher than the mean backscatter response over North America. The region viewed in South America is composed of much more forests albeit of ranging vegetation density. The response for both vertical and horizontal polarization was similar.

Over land there appeared to be no consistent angular trend for the radiometric response. In fact, both polarizations exercised showed remarkably similar angular characteristics from nadir till  $46^\circ$ . This is indicative of a rough surface; as expected the land responds like a rough surface at 2 cms. wavelength. The dispersion in the radiometric data was quite large; the range between upper and lower deciles being of the order of  $30^\circ\text{K}$  at some angles (even so, this is less than 0.5dB). This could be partially due to the fact that no corrections were made for the physical temperature or for atmospheric effects. The data were collected from regions ranging from the northern tier states down to the southwestern desert region. The change in physical temperature could be significant.

Over ocean the expected angular characteristics of emission for both vertical and horizontal polarization are observed. There is an increase in the range between upper and lower deciles with incidence angle. This ranges from approximately  $16^\circ\text{K}$  near nadir to approximately  $22^\circ\text{K}$  at  $46^\circ\text{K}$ . It has been suggested that the horizontal polarization emission is more sensitive to roughness (Hollinger, 1971), Ross et al, 1970), (Stogryn, 1967); however, no noticeable increase in dispersion was noted for the horizontal polarization response over the vertical response even at the largest angle of observation ( $46^\circ$ ).

It was found that the angular decay of the backscattering coefficient over land appears to be a two-process phenomenon, whereas the backscattering coefficient over ocean does not. For the design of radar systems, some empirical equations describing

the mean angular decay are provided. The equations are exponentials (two of them for land, one governing the nadir to  $11^\circ$  region and the other governing the  $11^\circ - 47^\circ$  region, and one for ocean and polynomials; a fourth order polynomial for land and a third order polynomial for the ocean. In comparing the exponentials computed ( $k_1 \exp(-\theta/k_2)$ ) from S-193 data to those computed by Sandia Corporation personnel (Williams et al, 1975) from their investigations from an aircraft based scatterometer operating at 3.8 GHz, we find that although the constant multiplier  $k_1$  is considerably different the factor  $k_2$  which describes the decay is not. They report a value of  $k_2$  for the ocean surface as  $5.0^\circ$  and we obtain approximately  $5.7^\circ$  (mean for VV and HH polarization). This decay is quite similar to that for land targets between  $0 - 11^\circ$ .

The small dynamic range of the backscattering coefficient at each angle implies that a design for a radar for identification of various features will have to provide greater precision to obtain more distinguishable levels. On the other hand, a design for a radar for detection will not have to consider great variations in ground clutter.

It had been suggested by Moore and Ulaby (1969) that the joint operation of a radar and a radiometer would provide more information than could be obtained by the operation of each instrument singly. It was determined that the correlation between the radar scatterometer response and the radiometer response was less than 0.1 over land at  $33^\circ$  incidence. It was only 0.3 over ocean and increased to 0.6 when considering both land and ocean. This suggests that the operation of the two sensors jointly could provide more information because their sensitivity to various terrain and atmospheric conditions are indeed distinct. Various other combinations of sensor configurations were found to provide results that appeared to be highly correlated with each other. The joint operation of these combinations of sensor configurations appears redundant. For example, over land, the backscatter response at  $17^\circ$ ,  $33^\circ$ , and  $42^\circ$  appear to be correlated. There is another implication to this, side-looking radars viewing swaths from  $17^\circ$  to  $42^\circ$  will not have to worry about the variations in sensitivity of the backscatter to the terrain conditions. The operation of dual polarizations appears from examination of S-193 data to be redundant for both scatterometer and radiometer operation, at least for these gross resolutions.

It was found that categories based upon land-use or physiographic features as discerned from topographic maps, potential natural vegetation maps and spacecraft imagery are not necessarily separable in their microwave response. This was established by an exercise in clustering and linear discriminant analysis. The variable considered were an n-dimensional set of responses with the radiometer and scatterometer in various configurations. Various combinations of sensor responses over a target were included as

the clustering or discriminating variable. By clustering on the backscatter response at  $33^\circ$  alone, it was found that the evergreen forest formations in Brazil was the only category that appeared to belong to an almost unique cluster. With discriminant analysis by considering the backscatter at  $33^\circ$  (VV and HH polarization) it was possible to separate evergreen and semideciduous forests from the savannah and thornbush, but the two forest formations appeared inseparable. By considering the backscatter at  $17^\circ$ ,  $33^\circ$  and  $42^\circ$ , it was possible to separate (with a marginal misclassification ratio) forest from rangeland, but agricultural terrain was often mistaken for either forest or rangeland.

There are many reasons why a clustering or discriminating exercise as conducted and reported, failed. Not the least of these is the fact that the creation of categories based upon maps and imagery could be considerably in error. The variations in soil moisture and vegetation biomass within a category and between categories must, no doubt, have been a cause for the failure. The variations within a category are illustrated by an analysis of variance one-way lay-out design based upon the backscatter response at  $33^\circ$ . It was found that the samples drawn from one category (eg. forest) but from two geographic regions or from the same geographic region but at different observation times (separated by days) often appear statistically to belong to two populations. In other words there is a wide dispersion in the response (as there is in the vegetation density) within a terrain category. One noteworthy inference was that major relief was not a major factor in the backscatter response.

The design of a data catalogue for the microwave response for each category would then mean that no distinguishable responses could be found. A distribution of the response for each category and for each sensor configuration would be the only way to present such a data catalogue. In fact this result concurs with the results obtained by prior measurement programs. Examples of the results from many of the significant programs are provided as are comparisons of the result from various investigations. More carefully controlled ground-based or fine resolution experiments are needed to establish the important variables that cause this overlap. Since microwave "sees" different things, which may be important, this is urgent.

As suggested by prior measurements, the radiometer and scatterometer are sensitive to soil moisture variations. This was illustrated by an examination of a pass over Texas in June, 1973. The radiometer appears to be more sensitive at  $33^\circ$  incidence

than the scatterometer for regions with sparse vegetation. A correlation of  $-0.81$  was obtained between the soil moisture and the measured emissivity and of  $0.61$  between the soil moisture and the backscattering coefficient. This correlation could have been much higher if a better estimate of the soil moisture variations had been obtained. For regions with dense vegetation canopies, it appears as though the correlation may not be as high.

This is the first time that a radar with such coarse resolution has viewed the earth from afar. This provided an opportunity for us to compare the results obtained from earth with those obtained from other planets. The analyses and interpretations, conducted similar to the radar astronomers, showed that the ocean and land in North America are comparably rough with the ocean having a slightly smaller mean slope. Both the oceans and land appear smoother than either the moon or Venus. Selected targets in the midwest region of the U.S.A. showed that, as expected, the forest was roughest and that farmland was the smoothest. The Fresnel reflection coefficient for the ocean was much larger than that for land (as expected) but considerably less than that measured by prior programs.

It has often been suggested that a Gaussian autocorrelation function of the surface height was more descriptive of an ocean surface near nadir and that an exponential autocorrelation function was more descriptive for land. Our results show that the mean slope and the reflection coefficient computed by assuming either of these two autocorrelation functions over land and ocean are remarkably similar. The reflection coefficient computations are sensitive to the absolute level of the backscattering coefficient. The dielectric constants for various target computed from the Fresnel reflection coefficient were considerably lower than any measured heretofore and appear suspect.

A plane surface model was used to describe the ocean surface and based upon dielectric constant data, an emissivity was computed for various physical temperatures. Assuming a simple model for the atmospheric effects and a standard atmosphere as described in chapter five, the S-193 radiometer data were reduced to surface brightness temperatures. As expected it was found that the emissivities computed from S-193 data were higher than those predicted for a plane surface. There was a sizable difference at nadir between the emissivity from S-193 measurements and for the planar surface prediction. Prior measurements have indicated that the sensitivity of emissivity to roughness is small at nadir. It has also been reported by measurements that this sensitivity

is greater for horizontal polarization, and further, that it increases with incidence angle till about  $55^\circ$ . This is also predicted by the geometric optics model. It was observed that the deviation of the mean S-193 response from the planar surface was considerably larger for horizontal polarization than for vertical polarization at  $46^\circ$  incidence.

Based upon the above mentioned and other simplistic assumptions, it was determined that the sensitivity of the radiometric response with horizontal polarization at  $46^\circ$  incidence was approximately  $0.94^\circ\text{K}/\text{m}/\text{sec}$ . Based upon this figure, the mean wind speed of the oceans in the summer months was computed as 16.3 knots.

It is interesting to observe that even though the radiometer is sensitive to atmospheric effects and that no account was taken in the atmospheric corrections for variations in atmospheric effects from the mean profile considered, the mean wind speed computed is reasonably close to the value predicted by the radar which is comparatively impervious to atmospheric effects. The mean wind speed as computed by the radar was found to be approximately 13 knots.

Even though the S-193 scatterometer was not an imaging system, image-like presentations can be prepared from some data obtained from some of its modes (particularly the cross-track contiguous mode). These images show clearly the variation of the microwave response over an area and are very helpful in interpreting the response. It was shown that microwave response variations due to soil moisture variations can be easily discerned as can boundaries of major biomes.

A study of the type reported here would not be complete without ascertaining the effects of the intervening atmosphere. It is shown that the effects of a clear atmosphere (devoid of clouds and rain) in a temperate climate on the scatterometer signals can easily be compensated by considering a standard atmospheric profile. The variations due to oxygen absorption can be ignored and that the attenuation is almost a linear function of the specific humidity. The effects of the atmosphere on the radiometer are more severe, but a standard atmospheric profile can still be used instead of actual radiosonde providing the surface temperature pressure and humidity are known. The effects of the atmosphere are less severe for a higher radiometric temperature source (land) than for a lower radiometric temperature source (ocean). If an inversion in either humidity or temperature occur, the compensation by the standard profiling technique will have more error. Clouds can have a significant effect upon

radiometer signals; the effects upon scatterometer signals are less, but can be significant. The effects of clouds depends not only on the water content but also on the temperature of the clouds.

Before describing the results obtained from a sensor, it is important to describe the sensor and to establish its operating capabilities and limitations. Some analyses to establish the S-193 precision and other operating characteristics were conducted. The precision of the scatterometer and the radiometer were computed. These showed that these values were within the design goals set for these sensors. Some potential problems are identified, for example, due to the imperfect isolation of the antenna the cross polarized measurements can be in error by as much as 3 dB. A pitch and roll excursion of the antenna causes the polarization states received on the ground to vary. An efficient scheme to compute the illumination integral (required in the computation of backscattering coefficient from the voltage recordings) is provided. Modifications to the radiometer transfer function based upon a calibration looking at deep space are provided.

## CONCLUDING REMARKS

The results from our examination of S-193 radiometer/scatterometer data obtained from space operation show that there is significant overlap between the backscatter and radiometric response of various physiographic and land-use categories. Stated another way, physiographic features as determined by maps and imagery do not necessarily have distinct and differentiable microwave responses. There are other parameters such as soil moisture and vegetation biomass which can significantly affect the recognition of terrain by the gross-resolution microwave response of the S-193. These results concur with measurements conducted in the past from aircraft and ground based sensors. A gross-scale averaging causes more overlap in the microwave response; only phenomenon on a large spatial scale can be effectively monitored. A prime candidate of such a phenomenon is the variation of soil moisture over a large region.

The space operation of the S-193 provided valuable design information for future radar systems. The principal discoveries were: due to the large spatial averaging involved, the dynamic range of the backscatter response at each angle from nadir till  $47^{\circ}$  was much smaller than had been reported by prior programs. There was a greater spread in the backscatter response from ocean targets at each angle

than for land targets. The land surfaces appeared like rough surfaces to the radiometer. The ocean surface showed expected angular trends, the horizontal polarization showed no particularly greater dispersion than vertical polarization. There was a distinct correlation between the microwave response and soil moisture. The earth, as interpreted in radar astronomers' parlance appears smoother than the moon and Venus at 2 cms wavelength. The ocean and land are comparably rough, but the ocean is slightly smoother. The reflection coefficient computed from S-193 scatterometer data using both the Gaussian autocorrelation function and the exponential autocorrelation function appear to be less than measured earlier, this could, perhaps, be due to a saturation problem associated with the receiver. The radiometric temperature, by considering a plane surface and a simple model for the atmosphere showed that the horizontal polarization showed more sensitivity to roughness. The reflection coefficient computed from the radiometer data was in accordance with earlier estimates. It was possible, even with the crude resolution of the S-193 sensor, to prepare images showing the spatial variations of backscatter and radiometric temperature. These showed that the sensor is capable of recognizing variations in soil moisture or vegetation density. These images can be prepared through clouds. The clear sky atmosphere has no effects upon the scatterometer signals and only marginal effects upon radiometer signals (in temperature climes). The effects of clouds are more on the radiometer where they depend upon the water content and the temperature of the clouds. Rain can cause problems in the remote measurements of backscatter and radiometric temperature.

This almost all-weather capability and the fact that they are not dependent upon sun angle constraints should make microwave remote sensing sensors more attractive for orbital operation. The resolution of the microwave sensors considered useful for remote sensing applications over land should be considerably finer than that of the S-193. For remote sensing over the ocean, the resolution need not be as fine.

This study could not determine an optimum selection of sensor configurations i.e. polarizations and viewing angles. Some suggestions are, however, implied by the results of the correlation analysis. It is entirely obvious that the various modes and submodes of operation of the S-193 are not required in future systems. Adequate information could have been obtained with far fewer modes. The inclusion of the many modes made the hardware complex and significantly increased the complexity of the subsequent data processing; so, although they may have been justified in this pioneer experiment, the complexity of further systems may be less.

This study was not meant to be an exhaustive assessment of the capabilities of the S-193 radiometer/scatterometer for geoscientific investigation. Only some simple exercises, where the ground truth was very crude, were conducted. It should not be inferred that the S-193 cannot be of more geoscientific value with more detailed investigations where the terrain scene is properly described by other sources.

The data from the S-193 are available and should be examined to assess their value for particular geoscientific investigations. The information provided here should help in this assessment. If only as much effort was spent in the design of the S-193 hardware had been spent in the processing of data from these sensors and collecting "ground truth", the space operation of the S-193 radiometer/scatterometer would have provided more useful results.

## BIBLIOGRAPHY

- Aandahl, A. R., "Soils of the Great Plains," Lincoln, Nebraska, 1972.
- Abramowitz, M., and I. A. Stegun, Handbook of Mathematical Functions, National Bureau of Standards Applied Mathematics Series 55, 1964.
- Ament, W. S., F. C. MacDonald, and R. D. Schewbridge, "Radar Terrain Reflections for Several Polarizations and Frequencies," Naval Research Laboratory, Unpublished Report, 1959.
- Anderson, P. N., "Image Processing with a Hybrid System: The IDECS," D.Sc. Project, The University of Kansas; also appears as "Image Processing with a Hybrid System: The IDECS," by P.N. Anderson et al., edited by P. L. Currier, The Bulletin of Engineering No. 64, University of Kansas 1972.
- Anderson, T. W., An Introduction to Multivariate Statistical Analysis, John Wiley & Sons, Inc., 1958.
- Barrett, A. H., and V. K. Chung, "A Method for the Determination of High-Altitude Water-Vapor Abundance from Ground-Based Microwave Observations," Journal of Geophysical Research, vol. 67, no. 11, October 1962.
- Barrick, D. E., and W. H. Peake, "Scattering from Surfaces with Different Roughness Scales: Analysis and Interpretation," Res. Rep. Bat. 197A-10-3, Battelle Memorial Institute, Columbus, November 1, 1967.
- Barrick, D. E., and W. H. Peake, "A Review of Scattering from Surfaces with Different Roughness Scales," Radio Science, vol. 3, 1968.
- Basharinov, A. E., and A. Shutko, "The Microwave Radiometric Measurements of Soil Moisture," Institute of Radio Engineering and Electronics of the Academy of Science of the USSR, 1970.
- Basharinov, A. E., S. T. Yegorov, A. S. Gurvich, and A. M. Oboukhov, "The Results of Microwave Sounding of the Earth's Surface According to Experimental Data from the Satellite Cosmos 243," in Space Research XI, Proc. Open Meetings of Working Groups of the Plenary Meeting of COSPAR (Leningrad, USSR, May 1970); Berlin, Germany, Akademie-Verlag, vol. 1, pp. 713-716, 1971.
- Bass, F. G., and V. G. Bocharov, "On the Theory of Scattering of Electromagnetic Waves from a Statistically Uneven Surface," Radio Telehnika i Elektronika, 1958.
- Bean, B. R., and E. J. Dutton, Radio Meteorology, U. S. Department of Commerce, National Bureau of Standards, Monograph 92, March 1966.
- Becker, Gordon E., and Stanley H. Autler, "Water Vapor Absorption of Electromagnetic Radiation in the Centimeter Wave-length Range," Physical Review, vol. 70, no. 5 and 6, September 1 and 15, 1946.

- Beckmann, P., and W. K. Klemperer, "Interpretation of the Angular Dependence of Backscattering from the Moon and Venus," *J. Res. NBS*, 69D, 12, 1965.
- Beckmann, P., "Shadowing of Random Rough Surfaces," IEEE Transactions on Antennas and Propagation AP-13, 1965.
- Beckmann, P., and A. Spizzichino, The Scattering of Electromagnetic Waves from Rough Surfaces, MacMillan Company, 1963.
- Benedict, W. S., and L. D. Kaplan, "Calculation of Line Widths in  $H_2O-N_2$  Collisions," J. Chem. Phys., vol. 30, February 1959.
- Benoit, Andre, "Signal Attenuation Due to Neutral Oxygen and Water Vapor, Rain and Clouds," Microwave Journal, vol. 11, no. 11, November 1968.
- Blinn, J. C., and J. G. Quade, "Dependence of Microwave Emissions on Moisture Content for Three Soils," *URSI, Colorado* 1973.
- Boer, , "Research to Develop a Microwave Radiometric Ocean Temperature Sensing Technique," Chapter 4, Final Report authored by Porter and Wentz, Contract 2-352309, Radiometric Technology, Wakefield, Mass., December 1972.
- Bradley, G. A., "Remote Sensing of Ocean Winds Using a Radar Scatterometer," Ph.D. Thesis, University of Kansas, Lawrence, Kansas, September 1971.
- Brown, W. E., "Radar Studies of the Earth," Proc. IEEE, vol. 57, no. 4, pp. 612-620, April 1969.
- Burrows, C. R., and S. S. Atwood, "Radio Wave Propagation," Consolidated Summary Technical Report of the Committee on Propagation, NDRC, Academic Press, Inc., New York, N. Y., 1949.
- Bussey, H. E., "Microwave Attenuation Estimated from Rainfall and Water Vapor Statistics," Proc. Inst. Radio Eng., vol. 38, 1950.
- Campbell, J. P., "Backscattering Characteristics of Land and Sea at X-Band," Proc. Natl. Conf. Aeron. Electronics, Dayton, Ohio, May 1958.
- Campbell, M. J., and J. Ulrichs, "Electrical Properties of Rocks and Their Significance for Lunar Radar Observations," *Journal of Geophysical Research*, vol. 74, no. 25, November 1969.
- Carlson, N. L., "Dielectric Constant of Vegetation at 8.5 GHz," Ohio State University, Electro Science Laboratory, Tech. Report 1903-5, 1967.
- Carter, C. J., R. L. Mitchell, and E. E. Reber, "Oxygen Absorption Measurements in the Lower Atmosphere," Journal of Geophysical Research, vol. 73, no. 10, May 15, 1968.
- Chan, H. L., and A. K. Fung, "Two-Scale Rough Surface Scattering Models,"

- Chan, H. L., and A. K. Fung, "Backscattering of Waves by Composite Rough Surfaces," IEEE Trans. on Antennas and Prop., vol. AP-17, no. 5, 1969.
- Chan, H. L., and A. K. Fung, "Backscattering from a Two-Scale Rough Surface with Application to Radar Sea Return," NASA Contractor's Report, NASA CR-2327, November 1973.
- Cihlar, J., and F. T. Ulaby, "Dielectric Properties of Soils as a Function of Moisture Content," RSL Technical Report 177-47, University of Kansas Center for Research, Inc., Lawrence, Kansas, November 1971.
- Claassen, J. P., and A. K. Fung, "An Efficient Technique for Determining Apparent Temperature Distributions from Antenna Temperature Measurements," The University of Kansas Center for Research, Inc., CRES Technical Report 186-8, 1973.
- Clapp, R. E., "A Theoretical and Experimental Study of Radar Ground Return," MIT Rad. Lab. Report no. 1024, 1946.
- Cook, C., and A. Sobti, "Development of an Algorithm for Evaluating the Scatterometer Illumination Integral," Technical Memorandum 236-1, The University of Kansas Center for Research, Inc., Remote Sensing Laboratory, Lawrence, Kansas, February 1973.
- Cook, A. C., Private Communications, 1975.
- Cosgriff, R. L., W. H. Peake, and R. C. Taylor, "Terrain Scattering Properties of Sensor System Design," Terrain Handbook II, Engr. Expt. Sta., Ohio State University, Bull. 181, May 1960.
- Cox, C., and W. H. Munk, "Measurements of the Roughness of the Sea Surface from Photographs of the Sun's Glitter," J. Opt. Soc. of Am., vol. 44, November 1954.
- Cullen, J. M., and G. A. Bradley, "The Correlation of Radar Scatterometer Data with Aerial Terrain Photography," University of Kansas Center for Research, Inc., CRES Technical Report 118-13, April 1969.
- Daley, J. C., J. T. Ransone, Jr., J. A. Burkett, and J. R. Duncan, "Sea-Clutter Measurements on Four Frequencies," U.S. Naval Res. Lab Rep. 6806, November 19, 1968.
- Daley, J. C., W. T. Davis, and N. R. Mills, "Radar Sea Return in High Sea States," U.S. Naval Res. Lab. Rep. 7142, September 25, 1970.
- Daley, J. C., J. T. Ransone, Jr., and J. A. Burkett, "Radar Sea Return --- JOSS I," U.S. Naval Res. Lab Rep. 7268, May 11, 1971.
- Daley, J. C., J. T. Ransone, Jr., and W. T. Davis, "Radar Sea Return --- JOSS II," U.S. Naval Res. Lab Rep. 7534, February 21, 1973.
- Davis, H., "The Reflection of Electromagnetic Waves from a Rough Surface," Proc. IEEE, Pt. III 102, p. 148, 1955.

- Dedye, P., "Polar Molecules," The Chemical Catalogue, New York, 289 pp., 1929.
- deLoor, G. P., and A. A. Jurriens, "Radar Ground Returns, Part I: The Radar Backscatter of Vegetation," Physics Lab of the Natl. Def. Res. Org. TNO (Dutch), Report Ph.L. 1972-73, January 1972.
- Dennison, D. M., "The Infrared Spectra of Polyatomic Molecules, Pt. II," Rev. Mod. Phys., vol. 21, July 1940.
- Dicke, R. H., "The Measurement of Thermal Radiation at Microwave Frequencies," Rev. Sci. Instru., vol. 17, pp. 268-275, July 1946.
- Dickey, F. M., C. King, J. C. Holtzman, and R. K. Moore, "Moisture Dependency of Radar Backscatter from Irrigated and Non-irrigated Fields at 400 MHz and 13.3 GHz," IEEE Trans. on Geoscience Electronics, vol. GE-12, no. 1, pp. 19-22, 1974.
- Dixon, W. J., "BMD Biomedical Computer Programs," School of Medicine, University of California at Los Angeles, 1973.
- Droppleman, J. D., "Apparent Microwave Emissivity of Sea Foam," J. Geophys. Res., vol. 75, pp. 696-698, January 1970.
- Eagleman, J. R., and W. C. Lin, "Detection of Moisture and Moisture Related Phenomena from Skylab -- Soil Moisture Distribution in the Test Sites," CRES Technical Report 239-16, Atmospheric Science Laboratories, University of Kansas, Lawrence, Kansas.
- Edgerton, A. T., "Microwave Radiometry Data Study," Report No. 1344R-2, Aerojet Publication, Contract No. NAS 9-9363, June 1970.
- Edgerton, A. T., R. Ruskey, D. Williams, A. Stogryn, G. Poe, D. Meeks, and O. Russell, "Microwave Emission Characteristics of Natural Materials and the Environment," Final Technical Report 9016R-8, Aerojet-General Corporation, El Monte, California, 1971.
- Edgerton, A. T., and D. T. Trexler, "Oceanographic Applications of Remote Sensing with Passive Microwave Techniques," Aerojet-General Corporation, El Monte, California, 1972.
- Edgerton, A. T., "Engineering Applications of Microwave Radiometry," Aerojet-General Corporation, Space Division, El Monte, California, 1968.
- Edgerton, A. R., D. T. Trexler, G. A. Poe, A. Stogryn, S. Sakamoto, J. E. Jenkins, D. Meeks, and F. Soltis, "Passive Microwave Measurements of Snow, Soils, and Oceanographic Phenomenon," Technical Report No. 6, Aerojet-General Corporation, El Monte, 1970.
- Edgerton, A. T., R. M. Mandl, G. A. Poe, J. E. Jenkins, F. Soltis, and S. Sakamoto, "Passive Microwave Measurement of Snow, Soils, and Snow-Ice-Water Systems," Aerojet-General Corporation, Space Division, 1968.

- Edison, A. R., R. K. Moore, and B. D. Warner, "Radar Return at Near-Vertical Incidence," University of New Mexico Engr. Expt. Station Technical Report EE-24, September 1959.
- Edison, A. R., R. K. Moore, and B. D. Warner, "Radar Terrain Return Measured at Near Vertical Incidence," Trans. IRE AP-8, pp. 246-254, 1960.
- Eklund, F., "Experimental Investigation of Scattering from Irregular Surfaces," Swedish Def. Res. Inst. Report, 1969.
- Ericson, L. O., "Terrain Return Measurement with an Airborne X-Band Radar Station," Swedish Res. Inst. of Natl. Def. Report, October 1966.
- Evans, J., and T. Hagfors, "Study of Radio Echoes from the Moon at 23 cms. Wavelength," Journal of Geophysical Research, vol. 71, No. 20, 1966.
- Evans, J., and T. Hagfors, Radar Astronomy, McGraw Hill Publications 1968. Chapter 4 by T. Hagfors, Chapter 5 by Hagfors and Evans.
- Evans, J., "Radar Studies of Planetary Surfaces," Astronomical Journal, 1969.
- Fischer, R. E., "Standard Deviation of Scatterometer Measurements from Space," IEEE Trans. Geoscience Electronics, Vol. GE-10, pp. 106-113, April 1972.
- Fung, A. K., and R. K. Moore, "Effects of Structure Size on Moon and Earth Radar Returns of Various Angles," Journal of Geophysical Research, 69: 1075-1081, 1964.
- Fung, A. K., "Scattering Theories and Radar Return," Ph.D. Thesis, CRES Technical Report No. 48-3, University of Kansas, 1966.
- Fung, A. K., "Exact Solution to the Scattering of Waves From a Rough Surface," CRES Technical Report 48-1, June 1964.
- Fung, A. K., "Frequency Dependence of Waves Scattered From Rough Surfaces," CRES Technical Report 48-6, December 1965.
- Fung, A. K., "Scattering and Depolarization of EM Waves From a Rough Surface," Proceedings of IEEE, Letters.
- Fung, A. K., "Theory of Radar Scatter from Rough Surfaces, Bistatic and Monostatic, with Applications to Lunar Radar Return," JGR, 69, 1964.
- Fung, A. K., and R. K. Moore, "Effects of Structure Size on Moon and Earth Radar Returns of Various Angles," Journal of Geophysical Research, 69, 1964.
- Fung, A. K., and A. Leovaris, "Experimental Verification of the Proper Kirchhoff Theory of Wave Scattering from Known Randomly Rough Surfaces," Journal of the Acoustical Society of America, Vol. 46, No. 5, Part 1, 1057-1061, November 1969.
- Fung, A. K., and H. L. Chan, "Backscattering from a Two-Scale Rough Surface with Applications to Radar Sea Return," NASA Contractor's Report, NASA CR-2327, November 1973.

- Fung, A. K., and R. K. Moore, "The Correlation Function in Kirchoff's Method of Solution of Scattering of Waves from Statistically Rough Surfaces," JGR, vol. 71, June 1966.
- GE Calibration Data Report, vol. IA, Rev D, S-193 Document, May 1973.
- Glushkov, V. M., and V. B. Komarov, "Side-Looking Imaging Radar System Toros and Its Application to the Study of Ice Conditions and Geological Explorations," Aerial Methods Laboratory, Ministry of Geology, Leningrad, U.S.S. R., 1972.
- Goldstein, H., "Frequency Dependence of the Properties of Sea Echo," Phy. Rev. 70, pp. 938-946, 1946.
- Grant, C. R. and B. S. Yaplee, "Backscattering from Water and Land at Centimeter and Millimeter Wavelengths," Proc. IRE 45, pp. 976-982, July 1957.
- Gunn, K. L. S., and T. W. R. East, "The Microwave Properties of Precipitation Particles," Quart. J. Met. Soc., vol. 80, pp. 522-545, 1954.
- Hack, Johan-Peter, "A Very Sensitive Airborne Microwave Radiometer Using Two Reference Temperatures," Transactions on Microwave Theory and Techniques, vol. MTT-16, 1968.
- Hagfors, T., Radar Astronomy, Chapter 4, McGraw-Hill, Inc., 1968.
- Hagfors, T., "Backscattering from an Undulating Surface with Applications to Radar Returns from the Moon," JGR, 69, 1964.
- Hagfors, T., "Relationship of Geometric Optics and Autocorrelation Approaches to the Analysis of Lunar and Planetary Radar," JGR, vol. 71, 1966.
- Hamon, W. R., "Computation of Direct Runoff Amounts from Storm Rainfall," International Association of Scientific Hydrology, Publication 63, pp. 52-62.
- Hanley, W. R., "Analysis of S193 Microwave Radiometer/Scatterometer for Skylab," Ph.D. Dissertation, The University of Kansas, 1972.
- Haralick, R. M., and I. Dinstein, "A Spatial Clustering Procedure for Multi-Image Data," IEEE Transactions on Circuits and Systems, Vol. CAS-22, May 1975.
- Hayes, J., W. Spring, V. Cardone, and W. Pierson, "A Preliminary Analysis of the Surface Truth Data to be Correlated with the Skylab II Data Obtained for the S-193 Microwave Investigators," University Institute of Oceanography, City University of New York, August 1973.
- Hayre, H. S., and R. K. Moore, "Theoretical Scattering Coefficient for Near Vertical Incidence from Contour Maps," J. Res. NBS. 65-D, 1961.
- Hayre, H.S., "Radar Scattering Cross Section Applied to Moon Return," Proceedures of IRE 49, p. 1433, 1966.
- Hollinger, J. P., "Passive Microwave Measurements of the Sea Surface," Journal of Geophysical Research, vol. 75, no. 27, pp. 5209-5213, September 1970.

- Hollinger, J. P., "Passive Microwave Measurements of Sea Surface Roughness," IEEE Trans. Geosci. Electron. vol. GE-9, pp. 165-169, July 1971.
- Hollinger, J. P., "Passive Microwave Measurements of the Sea Surface," Journal of Geophysical Research, April 1970.
- Hollinger, J. P., "Passive Microwave Measurements of Sea Surface Roughness," IEEE Transactions, Vol. GE-9, No. 2, pp. 165-169, July 1971.
- Hughes, V., "Diffraction Theory Applied to Radio Wave Scattering from the Lunar Surface," Proceedings of the Physical Society, 68, vol. 80, 1962.
- Ingalls, R. P., and J. V. Evans, "Scattering Properties of Venus at 3.8 cms," Astronomical Journal, vol. 74, no. 2.
- Ippolito, Louis J., "Millimeter Wave Propagation Measurements from the Applications Technology Satellite (ATS-V)," IEEE Transactions on Antennas and Propagation, vol. AP-18, no. 4, July 1970.
- Janza, F. J., et al., "Pulse Response of Terrain Return Program Receivers," Technical Memorandum Sandia Corporation 208-54-54, 1954.
- Janza, F. J., R. K. Moore, and B. D. Warner, "Radar Cross-Sections of Terrain Near Vertical Incidence at 415 Mc, 3800 Mc and Extension of Analysis to X-band," University of New Mexico Engineer Experiment Station Technical Report EE-21, March 1959.
- Jean, B. R., C. L. Kroll, J. A. Richerson, J. W. Rouse, Jr., T. G. Sibley, and M. I. Wiebe, "Microwave Radiometer Measurements of Soil Moisture," Technical Report TSC-32, Remote Sensing Center, Texas A & M University, College Station, Texas, 41p., 1972.
- Jean, B. R., "Selected Applications of Microwave Radiometric Techniques," Technical Report RSC-30, Remote Sensing Center, Texas A & M University, College Station, Texas, August 1971.
- Katzin, M., "On the Mechanisms of Radar Sea Clutter," Proceedings of the IRE, January 1957.
- Kerr, D. E., editor, Propagation of Short Radio Waves, Dover Publications, 1951.
- Khamisi, H. R., "Rough Surface Scattering Based on Facet Model," Ph.D. Dissertation, The University of Kansas, 1974, Also with A. K. Fung and F. T. Ulaby, CRES Technical Report 177-52, 1974.
- King, C., "Agricultural Terrain Scatterometer Observations with Emphasis on Soil Moisture Variation," University of Kansas Center for Research, Inc., CRES Technical Report 177-44, 1973.

- King, C., and R. K. Moore, "A Survey of Terrain Radar Backscatter Coefficient Measurement Programs," University of Kansas Center for Research, Inc., CRES Technical Report 243-2, December 1973.
- King, D. D., "Passive Detection," Chapter 39 in Radar Handbook by M. I. Skolnick (Ed.), McGraw-Hill Book Company, New York, 1970.
- King, G. W., R. M. Hainer, and P. C. Cross, "Expected Microwave Absorption Coefficients of Water and Related Molecules," *Phys. Rev.*, vol. 71, April 1974.
- Kodis, R., "A Note on the Theory of Scattering from an Irregular Surface," IEEE Trans. on Antennas and Prop., AP-14, No. 1, 1966.
- Kreiss, W. T., "The Influence of Clouds on Microwave Brightness Temperatures Viewing Downward Over Open Seas," *Proc. IEEE*, vol. 57, pp. 440-446, April 1969.
- Krishen, K., and D. Pounds, "S-193 Radiometer and Scatterometer Sensor Mathematical Models," Lockheed Electronics Co., Houston, Job Order 73-213, 1974.
- Kuchler, A. W., "Potential Natural Vegetation of the Conterminous U. S.," American Geographical Society Special Publication No. 36, 1964.
- Langville, R. C., and R. S. Thain, "Some Quantitative Measurements of Three-Centimeter Radar Echoes of Falling Snow," *Canadian Journal of Physics*, No. 29, 1951.
- Laws, J. O. and D. A. Parsons, "The Relation of Drop Size to Intensity," Trans. Am. Geographers Union, 1943.
- Leovaris, A., "Literature Survey on Scattering From Layered Media," CRES Technical Report 48-7, July 1966.
- Levin, J., "The Dynamics of Cumulus Convection in the Trades; a Combined Observational and Theoretical Study," Woods Hole Oceanographic Institution, Ref. no. 65-43, 1965.
- Linell, T., "An Experimental Investigation of the Amplitude Distribution of Radar Terrain Return," Swedish Res. Inst. of Natl. Def. Report, October 1966.
- Lundien, J. R., "Terrain Analysis by Electromagnetic Means," Technical Report No. 3-693, Report 2, U.S. Army Engineer Waterways Experiment Station, Vicksburg, Mississippi, 55p., 1966.
- MacDonald, F. C., "Recent Sea Clutter Measurements by NRL," Proc. of Second Radar Symposium, University of Michigan, 1956.
- MacQueen, J., "Some Methods for Classification and Analysis of Multivariate Observations," Fifth Berkeley Symposium on Probability and Statistics, 1972.
- Malkevich, M. S., Yu. V. Samsonov, and L. I. Kprovs, "Water Vapor in the Stratosphere," U Kr. Fiz. Ah., vol. 80, no. 1, 1963.

- Masenthin, H. W., "Scatterometer Data Analysis Technique," University of Kansas Center for Research, Inc., CRES Technical Report 118-3, July 1967.
- Medhurst, R. G., "Rainfall Attenuation of Centimeter Waves: Comparison of the Theory and Measurement," IEEE Trans. on Antenna and Propagation, vol. AP-13, July 1965.
- Meeks, M. L., and A. E. Lilley, "The Microwave Spectrum of Oxygen in the Earth's Atmosphere," Journal of Geophysical Research, vol. 68, no. 6, March 1963.
- Meier, M. F., and A. T. Edgerton, "Microwave Emission from Snow--A Progress Report," Proceedings Seventh International Symposium on Remote Sensing of Environment, University of Michigan, Ann Arbor, 1971.
- Melentyev, VV. and Yu. I. Rabinovich, "Emission Properties of Natural Surfaces at Microwave Frequencies," Council of Ministers of the USSR, Leningrad, USSR, 1972.
- Mie, G., "Beitrage Zur Optik truber Medien, Speziell Kolloidale Metallosungen," Ann. Phys., vol. 25, 1908.
- Mitzner, K. M., "Theory of the Scattering of Electromagnetic Waves by Irregular Surfaces," Antenna Lab., Cal., Inst. Tech. Report No. 30, January 1974.
- Moe, R., "Spectral Characteristics of Agricultural Lands at Microwave Frequencies," Ph.D. Dissertation, University of Kansas, 1973; also CRES Tech. Report 133-27, 1973.
- Moore, R. K., "Radar Scatterometry - An Active Remote Sensing Tool," CRES Technical Report 61-11, April 1966. Also published in the Proceedings of the Fourth International Symposium on Remote Sensing, University of Michigan, April 1966.
- Moore, R. K., W. P. Waite, J. R. Lundien, H. W. Masenthin, "Radar Scatterometer Data Analysis Techniques," Center for Research, Inc., Engineering Science Division, University of Kansas, Lawrence, Kansas, April 1968.
- Moore, R. K., and F. T. Ulaby, "The Radar Radiometer," Proceedings of the IEEE, vol. 57, No. 4, pp. 587-590, April 1969.
- Moore, R. K., "Ground Echo," Radar Handbook, M. I. Skolnik, ed., McGraw-Hill, 1970.
- Muhleman, D., "Radar Scattering From Venus and the Moon," The Astronomical Journal, 69, No. 1, 1964.
- Neiburger, M., "Reflection, Absorption and Transmission of Insolation by Stratus Clouds," Journal of Meteorology, vol. 6, no. 2, April 1949.
- Neumann, G. and W. J. Pierson, Jr., Principles of Physical Oceanography, Prentice Hall Inc., Englewood Cliffs, N. J., 1969.
- Newbry, L. E., "Terrain Radar Reflectance Study," Photogrammetric Engineering, pp. 630-637, 1961.

- Nordberg, W., J. Conoway, and P. Thaddens, "Microwave Observation of Sea State From Aircraft," Quarterly Journal of the Royal Meteorological Society, vol. 95, pp. 408-413, 1969.
- Nordberg, W., J. Conoway, D. B. Ross, and T. Wilhert, "Measurement of Microwave Emission from a Foam-Covered Wind-Driven Sea," Goddard Space Flight Center, X-650-70-384, October 1970.
- Nordberg, W., J. Conoway, and P. Thaddeus, "Microwave Observation of Sea State from Aircraft," NASA Reprint X-620-68-414, 1968.
- Oliver, T. L., and W. H. Peake, "Microwave Brightness Temperature of Terrain," Air Force Avionics Laboratory, Air Force Systems Command, Technical Report 2440-4, 1969.
- Oliver, T. L., and W. H. Peake, "Radar Backscattering Data for Agricultural Surfaces," Ohio State University ElectroScience Lab, Technical Report 1903-9, February 1969.
- Parashar, S. K., "Investigation of Radar Discrimination of Sea Ice," The University of Kansas Center for Research, Inc., CRES Technical Report 185-13, December 1973.
- Paris, Jack F., "Transfer of Thermal Microwaves in the Atmosphere," Texas A & M University, Department of Meteorology, College Station, Texas, May 1971.
- Paris, Jack F., "Microwave Radiometry and Its Application to Marine Meteorology and Oceanography," Texas A & M University, Department of Oceanography, College Station, Texas, January 1969.
- Peake, W. H., "Interaction of Electromagnetic Waves with Some Natural Surfaces," Trans. IRE AP-7 (Special Supplement), pp. 5324-5329, 1959.
- Peake, W. H., "Interaction of Electromagnetic Waves with some Natural Surfaces," IEEE Trans. on Antennas and Propagation, AP-7, December 1959.
- Peake, W. H., "The Microwave Radiometer as a Remote Sensing Instrument," Technical Report 1903-8, Ohio State University, January 1969.
- Peake, W. H., R. L. Reigler, and C. H. Shultz, "The Mutual Interpretation of Active and Passive Microwave Sensor Outputs," Proc. of the Fourth Symposium on Remote Sensing of Environment, Univ. of Michigan, Ann Arbor, April 1966.
- Peake, W. H., and S. N. C. Chen, "Apparent Temperature of Smooth and Rough Terrain," IRE Transactions on Antennas and Propagation, vol. AP-9, November 1961.
- Peake, W. H., and S. T. Cost, "The Bistatic Echo Area of Terrain at 10 GHz," 1968 WESCON Technical Papers, August 20-23, 1968.
- Pettingil, G. H., "A Review of Radar Studies of Planetary Surfaces," J. of Res., NBS G9D: 1617-1623, 1965.

- Pettingil, G. H., Counselman, Rainville, L.P., and Shapiro, A., "Radar Measurements of Martian Topography," *Astronomical Journal*, Vol. 74, April 1969.
- Pettingil, G. H., Shapiro, A., "Topography and Radar Scattering Properties of Mars," *ICARUS* 18, 22-28, 1973.
- PHO-TR524, "Earth Resources Production Processing Requirements for EREP Electronics Sensors," MSC Form 2026A, Rev A, 1973.
- Planck, M., The Theory of Heat Radiation, New York, Dover Publications, 224 pp., 1959.
- Poe, G., A Stogryn, and A. T. Edgerton, "Determination of Soil Moisture Content Using Microwave Radiometry," Final Technical Report 168 4R-1, Aerojet-General Corp., Microwave Division, El Monte, California, June 1971.
- Poe, G. A. and A. T. Edgerton, "Determination of Soil Moisture Content with Airborne Microwave Radiometry," Aerojet-General Corp., Summary Rep. 4006 R-2, April-September 1971.
- Porter, R. A., "Microwave Radiometric Measurements of Sea Water, Concrete, and Asphalt," Report No. FR-399. Raytheon Company, Subbury, Mass., 1966.
- Porter, R. A., "Measured Radiometric Data at X-band and Ku-Band," Raytheon Company, Space and Information Systems Div., Massachusetts, 1966.
- Porter, R. A., "An Analytical Study of Measured Radiometric Data," Vol. I, II, III. Prepared by Radiometric Technology, Inc., Cambridge, Mass for Jet Propulsion Laboratory, Pasadena, California, Contract No. 952397, December 1969.
- Porter, R. A., "An Analytical Study of Measured Radiometric Data," Radiometric Technology, Inc., Wakefield, Mass., December 1969.
- Porter, R. A., J. C. Comstock, A. Conaway, "An Analysis of Airborne Microwave Radiometric Data," Final Report, Contract NAS 5-11685, Radiometric Data Technology Inc., Cambridge, Mass., February 1970.
- Porter, R. A., and F. J. Wentz, "Research to Develop a Microwave Radiometric Ocean Temperature Sensing Technique," Final Report: Contract 2-352309, Radiometric Technology Inc. Mass., December 1972.
- Pounds, D., "Revised Data Reduction Equations for the S193 Radiometer," Technical Memo Ref. no. 642-1215, Lockheed Electronics Co. Houston, 1975.
- Porter, R. A., and F. J. Wentz III, "Research to Develop a Microwave Radiometric Ocean Temperature Survey Technique," Radiometric Technology, Inc., Wakefield, Mass., December 1972.
- Ramo, S., J. R. Whinnery, and T. Van Duzer, Fields and Waves in Communication Electronics, pp. 245, 1967.

- Riegler, R. L., "Microwave Radiometric Temperatures of Terrain," Report 1903-2, The Antenna Laboratory, Ohio State University Research Foundation, Columbus, June 1966.
- Reitz, E. A., "Radar Terrain Return Study Final Report: Measurements of Terrain Backscattering Coefficients with an Airborne X-Band Radar," Goodyear Aerospace Corp. Rept. GERA-463, 1959.
- Rice, S. O., "Reflection of Electromagnetic Waves from Slightly Rough Surfaces," Comm. and Appl. Math., 4, pp. 351-378, 1951.
- Rogers, T. F., "Absolute Intensity of Water Vapor Absorption of Microwave Frequencies," Phys. Dev., vol. 93, 1954.
- Ross, D. B., V. J. Cardone, and J. W. Conaway, Jr., "Laser and Microwave Observations of Sea-Surface Conditions for Fetch-Limited 17- to 25- m/s Winds," IEEE Transactions, Geoscience Electronics vol. GE-8, pp. 326-336. October, 1970.
- Rouse, J. W. Jr., "Arctic Ice Type Identification by Radar," Proc. IEEE, vol. 57, pp. 605-611, April 1969.
- Ryde, J. W. and D. Ryde, "Attenuation of Centimeter and Millimeter Waves by Rain, Hail, Fogs and Clouds," G. E. C. Research Laboratory Report, London No. 8670, 1945.
- Ryde, J. W., "The Attenuation and Radar Echoes Produced at Centimeter Wavelengths by Various Meteorological Phenomena," Meteorological Factors in Radio Wave Propagation, Phys. Soc., London, 1946.
- Sampson, R. J., "Users Manual for the Surface-II Graphics System", Tech. Report, Kansas Geological Survey, Lawrence, Kansas, 1973, 144p.
- Saxton, J. A., and J. A. Lane, "Electrical Properties of Sea Water," Wireless Engineer, October 1972.
- Schmugge, T., P. Gloersen and T. Wilhelm, "Remote Sensing of Soil Moisture with Microwave Radiometers," Goddard Space Flight Center, NASA, Greenbelt, Maryland, 32p., Preprint X-652-72-305, August 1972.
- Schultz, C. H., and R. L. Oliver and W. H. Peake, "Radar Backscattering Data for Surfaces of Geological Interest," Ohio State University Electroscience Lab, Technical Report 1903-7, December 1969.
- Semyonov, B. J., "Approximate Computation of Scattering of Electromagnetic Waves by Rough Surface Contours," Radio Engineering and Electronic Physics, 1966 (English Translation).
- Shifrin, K. S., "Transfer of Microwave Radiation in the Atmosphere," N69-31851-868, Translation of "Perenos Mikrovolnovogo Izlucheni ya v Atmosfere," Trudy Glavnaya Geofizicheskaya Observator i ya, Im. A. I. Voyeykova, Vypuskzzz, Hydrometeorologic Press, Leningrad, 1968 (Transactions of the Main Geophysical Observatory).

- Simonett, D. S., J. E. Eagleman, A. B. Erhart, D. C. Rhodes and D. E. Schwartz, "The Potential of Radar as a Remote Sensor in Agriculture: A Study with K-Band Imagery in Western Kansas," University of Kansas Center for Research, Inc., CRES Technical Report 61-21, March 1967.
- Sinclair, C. C., "Apparent Temperatures of Smooth and Rough Terrain," Report No. 41131, The Antenna Laboratory, Ohio State University Research Foundation, Columbus, 1960.
- Sobti, A., "A Simulation Study of the S193 RADSCAT in Orbit," Technical Report 190-2 The University of Kansas Center for Research, Inc., Remote Sensing Laboratory, Lawrence, May 1973.
- Sobti, A. and C. Collins, "Review of S193 Radiometer Transfer Function," Technical Report 236-2, Remote Sensing Laboratory, The University of Kansas Center for Research, Inc., Lawrence, 1975.
- Spetner, L. M. and I. Katz, "Two Statistical Models for Radar Terrain Return," Trans. IRE, AP-8, pp. 242-246, May 1960.
- Staelin, David H., "Measurements and Interpretation of the Microwave Spectrum of the Terrestrial Atmosphere near 1-cm. Wavelength," Symposium on Electromagnetic Sensing of the Earth from Satellites, Polytechnic Press, November 1965.
- Stogryn, A., "The Apparent Temperature of the Sea at Microwave Frequencies," IEEE Transactions on Antenna and Propagations, vol. AP-15, no. 2, pp. 278-286, March 1967.
- Straiton, A. W., C. W. Tolbert, and C. O. Britt, "Apparent Temperatures of Some Terrestrial Materials and the Sun at 4.3 millimeter Wavelength," The University of Texas, Austin, Texas, January 1968.
- Stratton, J. A., "Electromagnetic Theory," McGraw-Hill, New York, 1941.
- Strong, A. E., "Mapping Sea-Surface Roughness Using Microwave Radiometry," Journal of Geophysical Research, vol. 76, December 20, 1971.
- Sui, Lin Lee, "Dual Frequency Microwave Radiometer Measurements of Soil Moisture for Bare and Vegetated Rough Surfaces," Technical Report RSC-56, Remote Sensing Center, Texas A & M University, College Station, Texas, August 1974.
- Twersky, V., "Scattering Theories for Bounded Periodic Structures," Journal of Applied Physics, 2, 7, 1956.
- Twersky, V., "On Scattering and Reflection of Electromagnetic Waves by Rough Surfaces," IRE Trans. P. G. A. D. AP-5, 81, 1957.
- Ulaby, F. T., J. Cihlar, and R. K. Moore, "Active Microwave Measurements of Soil Water Content," Remote Sensing of Environment, vol. 3, pp. 185-203, January 1975.
- Ulaby, F. T., "Radar Measurement of Soil Moisture Content," IEEE Trans. on Antennas and Propagation, vol. AP-22, no. 2, pp. 257-265, March 1974.

- Ulaby, F. T., "Radar Response to Vegetation," University of Kansas Center for Research, Inc., CRES Technical Report 177-42, September 1973.
- Ulaby, F. T., "Manual of Remote Sensing," Section 8.4: Microwave Radiometry, 1974.
- Ulaby, F. T., A. Sobti, and P. P. Batlivala, "Atmospheric Effects of S193 Radiometer/ Scatterometer Signals," CRES Technical Report 243-1, The University of Kansas Center for Research, Inc., Remote Sensing Laboratory, Lawrence, Kansas, July 1974.
- Ulaby, F. T., R. K. Moore, R. Moe and J. Holtzman, "Microwave Spectral Measurements of Agricultural Targets," presented at the Spring URSI Meeting, Washington, D. C., April 1972.
- Ulaby, F. T., "Radar Response to Vegetation," CRES Technical Report 177-42. Also published by IEEE Transactions on Antennas and Propagation, vol. AP-23, No. 1, January 1975.
- Ulaby, F. T., L. F. Dellwig and T. Schmutge, "Satellite Microwave Observations of the Utah Great Salt Lake Desert," Radio Science.
- Ulaby, F. T., J. Barr, A. Sobti and R. K. Moore, "Soil Moisture Detection by Skylab's Microwave Sensors," Proceedings of the URSI Commission II, 1974. BERNE
- Valley, S. L., Handbook of Geophysics and Space Environment, McGraw-Hill Book Company, New York 1965.
- Valenzuela, G. R., "Depolarization of EM Waves by Slightly Rough Surfaces," IEEE Trans. Antennas and Propagation, vol. AP-15, July 1967.
- Van Vleck, J. H. and V. F. Weisskopf, "On the Shape of Collision-Broadened Lines," Reviews of Modern Physics, vol. 17, no. 2 and 3., April-July, 1948.
- Van Vleck, J. H., "The Absorption of Microwaves by Oxygen," vol. 71, no. 7, Physical Review, April 1, 1947.
- Von Hippel, A., Dielectric Materials and Applications, MIT Press, Cambridge, Mass. 1954.
- Waite, W. P., "Broad-Spectrum Electromagnetic Backscatter," CRES Technical Report 133-17, University of Kansas Center for Research, Inc., Lawrence, Kansas, August 1970.
- Wilheit, T. W., Nordberg, J. Blinn, W. Campbell, and A. Edgerton, "Aircraft Measurements of Microwave Emission from Arctic Sea Ice," Remote Sensing of Environment 2, 129-139, 1972.
- Wilheit, T., J. Theon, W. Shenk, and L. Allison, "Meteorological Interpretations of the Images from Nimbus 5 Electrically Scanned Microwave Radiometer," Goddard Space Flight Center, Greenbelt, Maryland, X-651-73-189, June 1973.

- Williams, G. F. Jr., "Microwave Emissivity Measurements of Bubbles and Foam," IEEE Trans. Geosci. Electron., vol. GE-9, pp. 221-224, October 1971.
- Wright, J. W., "A New Model for Sea Clutter," IEEE Trans. Antennas and Propagation, vol. AP-16, pp. 217-223, March 1968.
- Wu, Steve, "The Meteorological Effects on Microwave Apparent Temperatures Looking Downward Over a Smooth Sea," CRES Technical Report 186-1, University of Kansas Center for Research, Inc., Lawrence, Kansas, October 1970.
- Wu, Steve T., "A Theory of Microwave Apparent Temperature Over the Ocean," CRES Technical Report 186-7, Ph.D. Dissertation, University of Kansas, University of Kansas Center for Research, Inc., Lawrence, Kansas, 1973.
- Wu, Steve, "The Meteorological Effects on Microwave Apparent Temperatures, Looking Downward Over a Smooth Sea," The University of Kansas Center for Research, Inc., CRES Technical Report 186-1, October 1970.
- Young, J. D., and J. P. Claassen, "Operational Success Criteria S193 Oceanography Experiments," CRES Technical Memorandum 254-1, January 1974.
- Young, J. D., Private Communications .
- Zhevakin, S. A., and A. P. Naumov, "The Absorption Coefficient of Electromagnetic Waves by Water Vapors in the Range of 10-20 cm," Izv. VUS, ser. Radiotizika, vol. 6, 1963.
- Zhevakin, S. A. and A. P. Naumov, "Absorption of Centimeter and Millimeter Radio Waves by Atmospheric Water Vapors," Radiotekhnika i elektronika, vol. 9, 1964.

APPENDIX ONE  
Description of Selected Hardware  
Subassemblies of the S193 Sensor

To appreciate some of the analyses and results of the study, a brief description of the following hardware subassemblies are provided.

1. RF section and Down Converter
2. Radiometer Processor
3. Scatterometer Processor

For detailed descriptions of these and the other subassemblies of the S193 system, the reader is referred to the vendor's documentation on the sensor (GE, 1971, 1972, a, b).

RF Section and Down Converter

The RF section of the S193 is shared by all three sensors: radiometer, scatterometer and altimeter. The major components in this subassembly are the antenna assembly, the RF oven (which houses the Wave Guide Switching Assembly (WGSA) and the reference temperature sources) and the Low Noise Tunnel-Diode Amplifier (TDA).

Antenna Assembly

The antenna assembly consists of a parabolic reflector 44.5" in diameter made out of spun aluminum, fed by a dual polarization through feed splash cup feed system. The through feed is conveyed to the feed section by a circular waveguide which couples to an OrthoMode Transducer (OMT) on the other side. The f/D ratio is approximately 0.30. The RF oven is mounted on the back of the antenna so as to minimize insertion losses in the wave guide section. Figure A.1 shows a schematic of the antenna and the WGSA.

The OMT split the polarization and has two ports towards the receiver, one of these allows the propagation of the TE mode (vertical polarization) and the other allows the propagation of the TM mode (horizontal polarization). These outputs are fed through a series of waveguides to the two input ports of the polarization circulator inside the RF oven.

### RF Oven

The RF oven is a temperature controlled chamber (maintained at  $18^{\circ} - 20^{\circ}\text{C}$ ). It houses the WGSAs and the reference temperature sources and the TDA.

The polarization circulator is a three port ferrite circulator which is energized for either clockwise or counterclockwise transmission. All the circulators are essentially the same. The polarization circulator is fed by the transmit/receive circulator (D in Fig. A.1) which switches in the transmitted signal towards the antenna and routes the incoming signal to the receiver. The transmit/receive circulator is fed by the transmitter output from one side and by the Dicke Switch (E in Fig. A.1) on the other. The Dicke Switch is again a 3 port circulator which switches between the reference temperature and the antenna. The arm towards the reference temperature is coupled to one port of a three port circulator (F in Fig. A.1). The other two ports of the F circulator are connected to the two reference temperatures  $T_1$  and  $T_2$ . The E circulator (Dicke Switch) switches at a rate of 1000 cycles per second, the F circulator switches at a rate of 500 cycles per second.

The antenna or reference temperatures are routed through the Dicke switch to a low pass filter which rejects EMI interference (primarily from the S-band telemetry link). The Dicke switch is not operational during scatterometer measurements and is energized to receive signals from the antenna side. For calibration purposes, the transmit/receive circulator is set to receive and an attenuated value of the transmitted signal is fed through a series of couplers to the waveguide section between the D and G circulators. This signal is detected as if it were a received signal and the value recorded on tape.

There are two filters following the Dicke Switch, one is a low pass filter and the other is a bandpass filter. The output of this filter is fed to a 3 stage Tunnel Diode Amplifier with a gain of approximately 30 dB and a noise figure of approximately 5.7 dB.

### Down Converter

The amplified signal is mixed with a signal at 14.4 GHz to get a signal with a carrier of 500 MHz. This signal is amplified band pass filtered and then split into three outputs for distribution to the altimeter, radiometer and scatterometer.

### Radiometer Processor

The signal to the radiometer processor is fed to two synchronous detectors— the signal detector and the AGC detector. The detection is square law and the input to the detectors is controlled by switching waveforms generated by the demodulation networks.

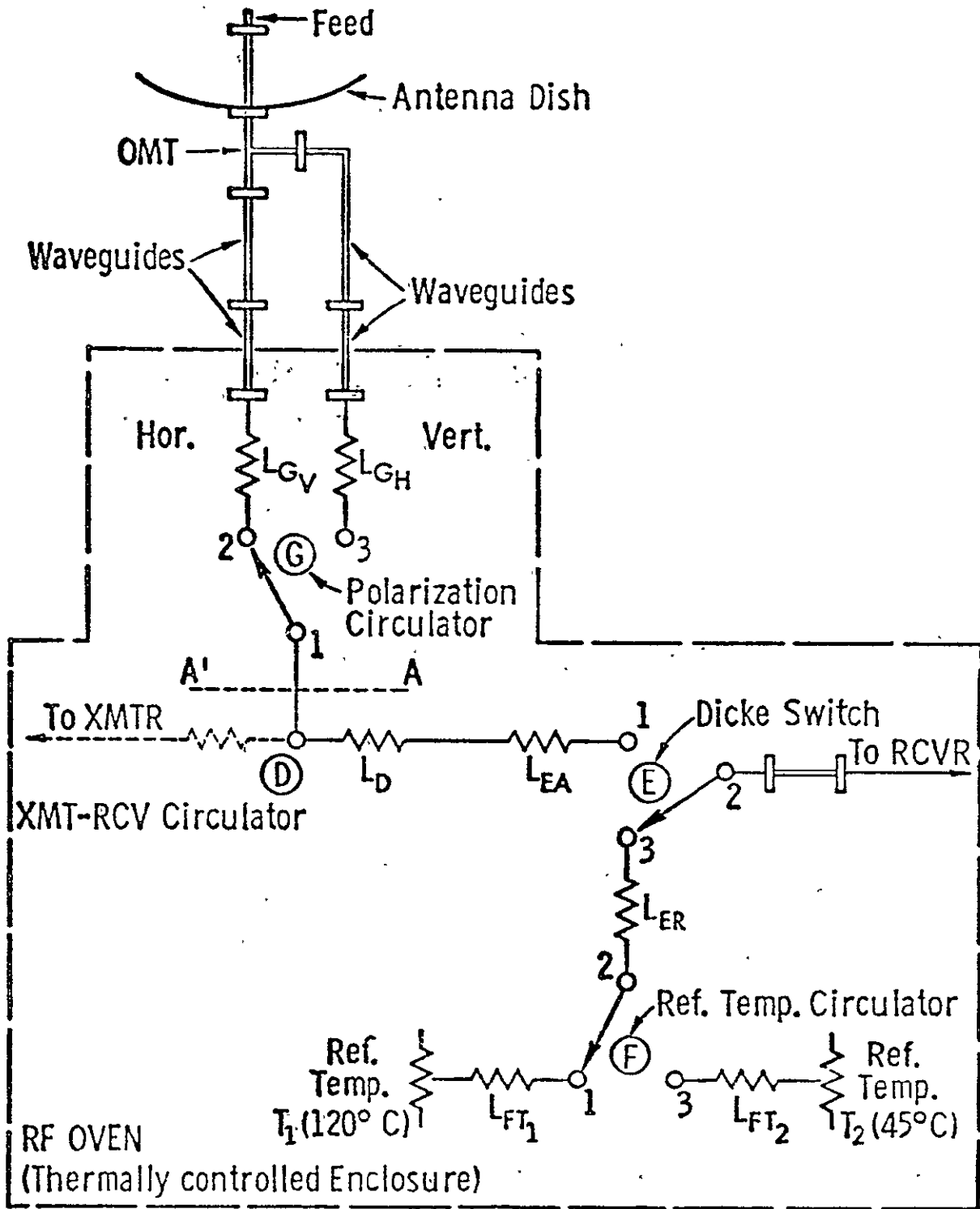


Figure A1 Antenna and Waveguide Switching Assembly

The AGC is in a feedback loop and has a threshold value to which the output of the AGC detected signal is compared. The comparison dictates the changes in AGC gain which are then translated to gain changes in the signal path prior to the video amplifier. The time constant of the AGC is approximately 1.1 seconds.

The AGC detector is fed only when the incoming signal is from the reference temperatures. There are three modes of operation for the radiometer. Two of these are for the calibration purposes (Calibrate Mode and Baseline Mode) and the other is the antenna temperature measurement (antenna mode).

The switching is maintained so that each radiometer operation in the three submodes has a waveform shown in Figures A2, A3, and A4 for the antenna mode, Calibrate Mode and Baseline modes respectively. The AGC waveforms during the three submodes are also shown in Figures A2, A3, and A4.

The output of the video amplifier is fed to an integrator. The integrator is an RC network with an operational amplifier of high gain so that the integration is linear. The integrated output is then fed to an Analog/Digital converter and the digital output is recorded on one track of the EREP tape recorder.

### Scatterometer Processor

The signal to the scatterometer processor from the three way power divider is amplified and then further mixed with a signal at 550 MHz to get a carrier at 50 MHz. The output of this mixer is amplified and fed to four switches. These are the gain selection switches, which allow only one of the four paths for the signal to travel. Three of the four paths have attenuation pads of 10 dB, 20 dB, and 30 dB respectively. The selection of which path to allow the signal to travel is controlled by the Data Handling and Control Unit (DHCU) which checks the detected integrated output for the first pulse against a threshold and determines whether an attenuation is necessary to remain in the dynamic range of the square law detector. If it is, then the remaining pulses are also gated through the same path. If the threshold is exceeded, an alternate switch with a 10 dB increase in attenuation in the path is chosen. The output of the integrator is dumped and integration starts again. This can happen three times, till the highest attenuation (lowest gain) path is chosen. The gain setting (the path chosen) is recorded as part of the status word prior to each measurement of the scatterometer.

The signal is then channeled, according to the pitch setting of the antenna (commanded, not actual) into one of five filter banks. The filter banks each contain

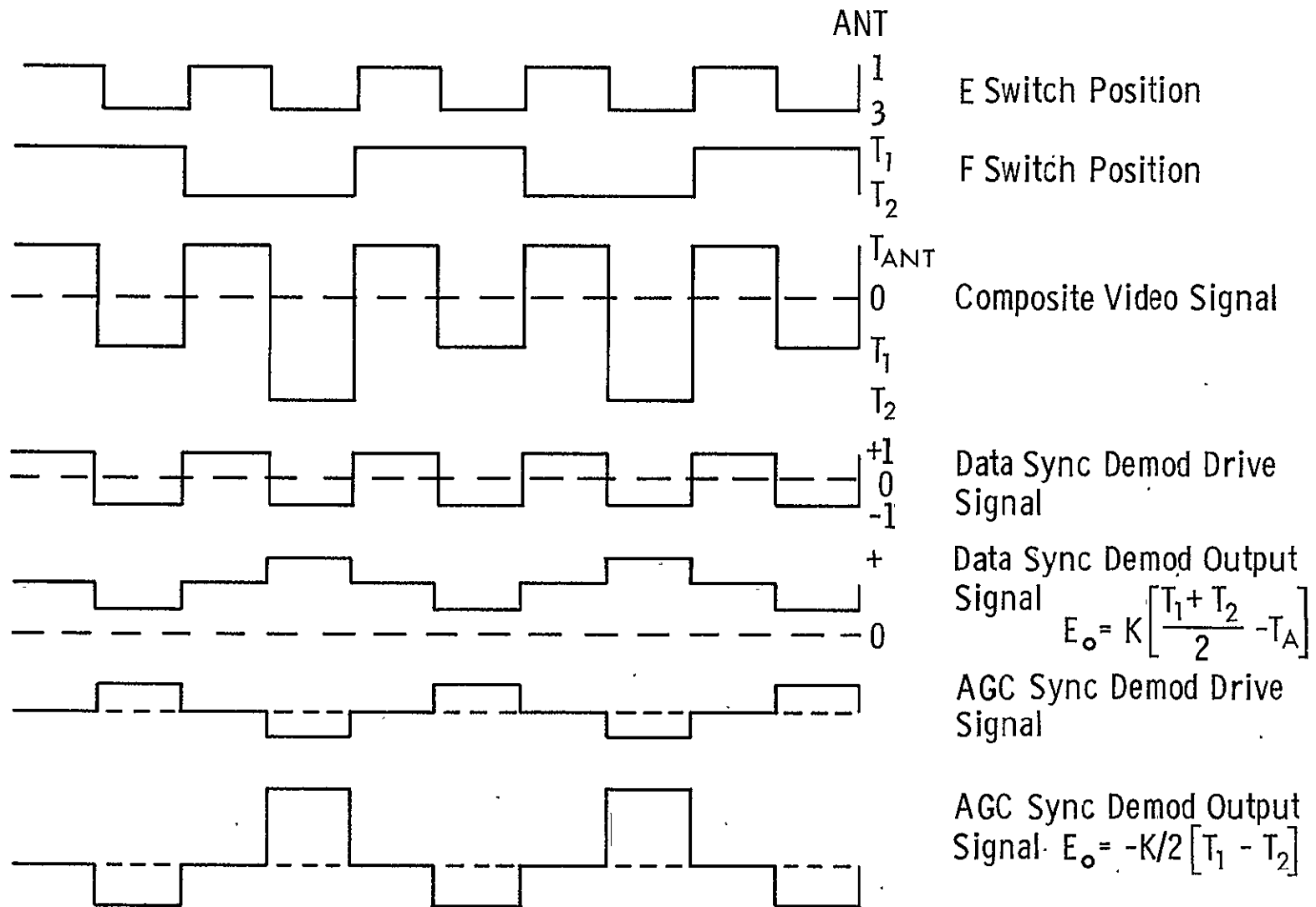


Figure A.2. Radiometer antenna mode: Switching waveforms for video signal and AGC input. (From G.E., 1971.)

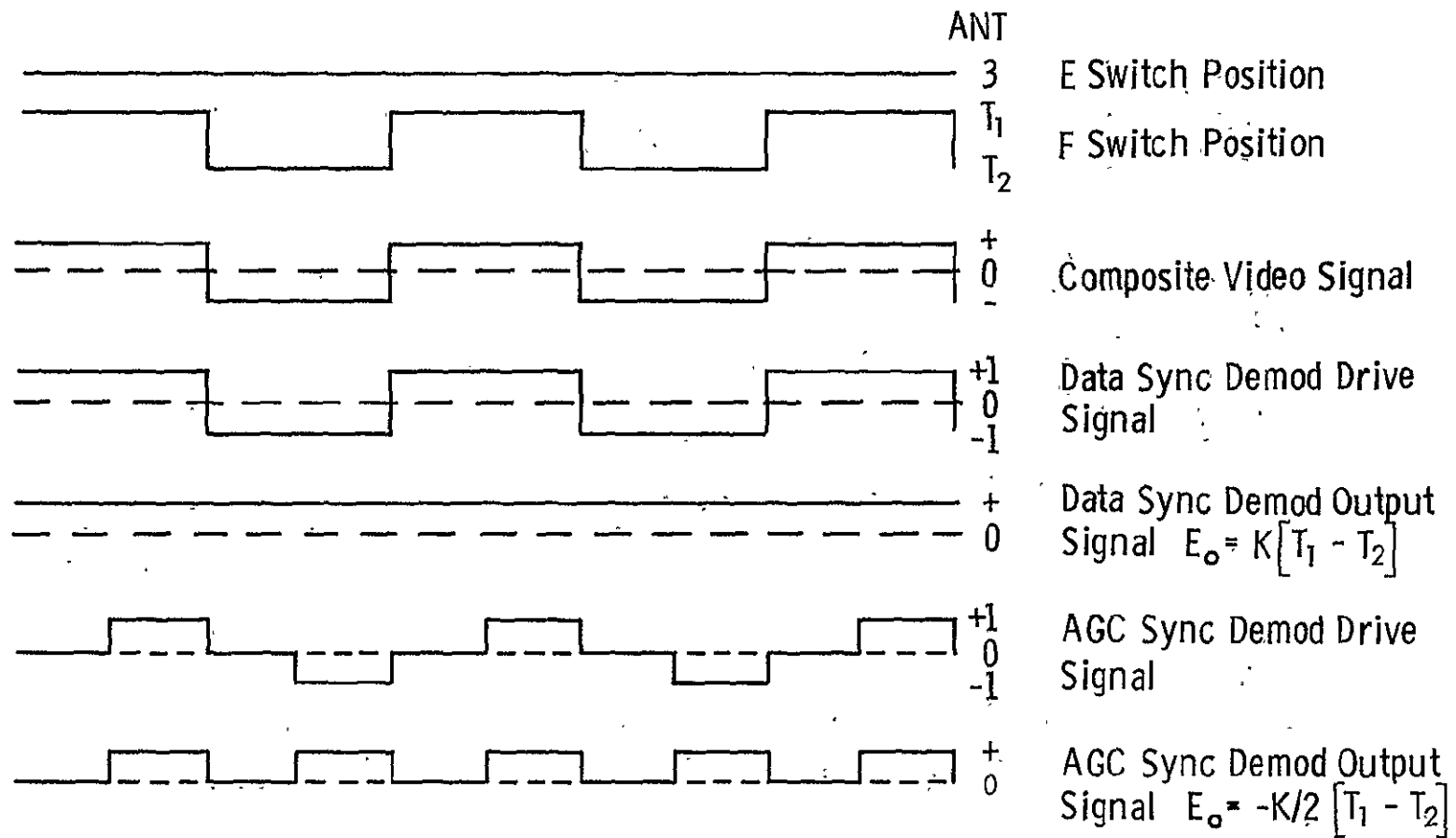


Figure A.3. Radiometer calibrate mode: switching waveforms for video signal and AGC input. (From G.E., 1973.)

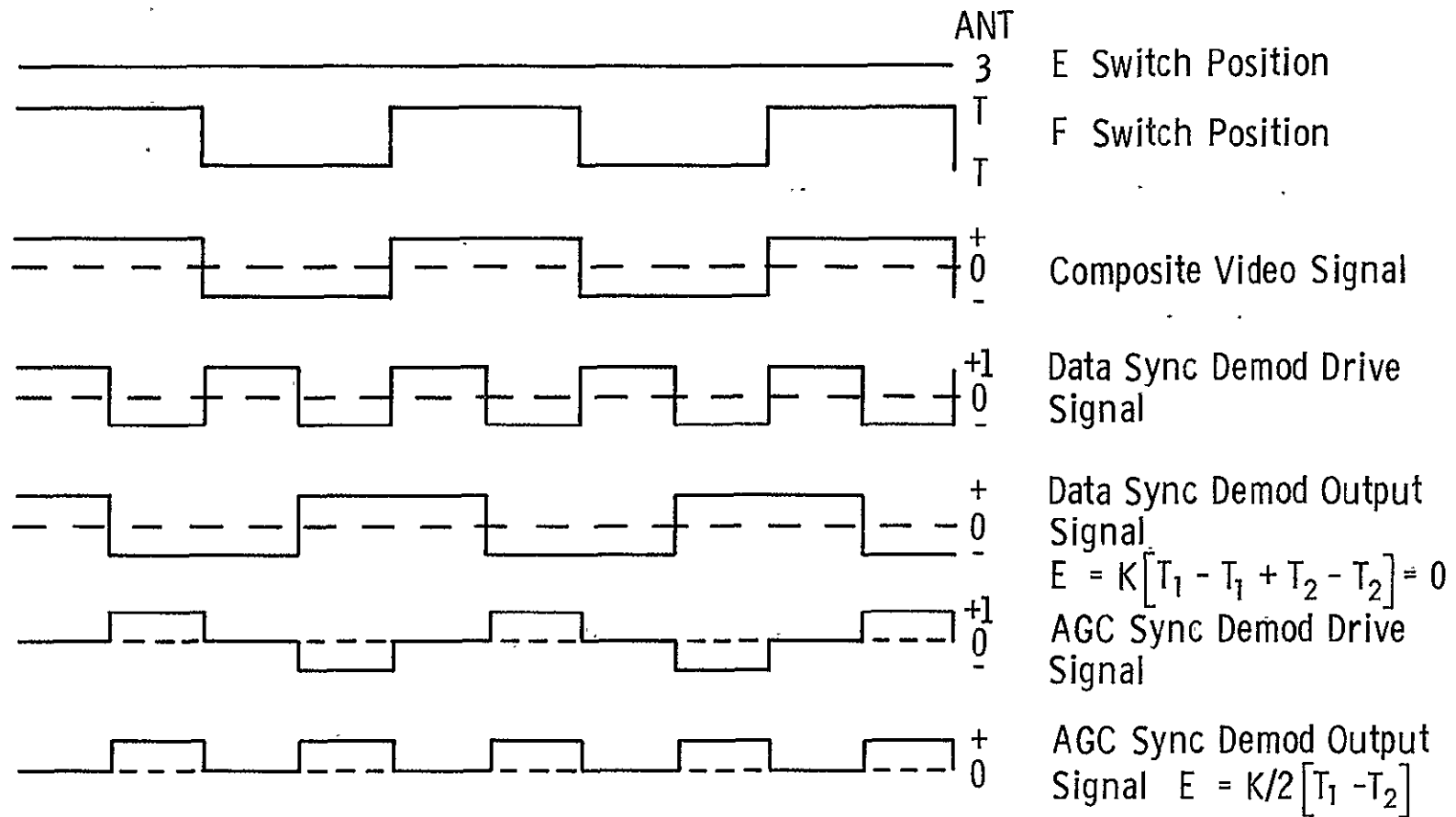


Figure A.4. Radiometer base mode: switching waveforms for video signal and AGC input. (From G.E., 1971.)

three filters. The filters are arranged as shown in Figure A5.

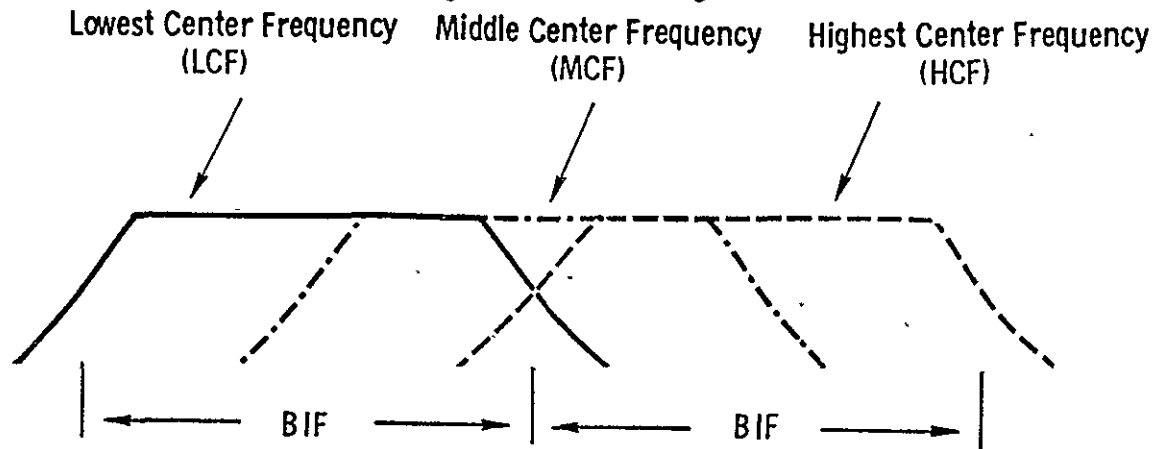


Figure A5

Arrangement of filters per angle command in Scatterometer processor.

The center frequency of the middle filter is the expected center of the Doppler frequency plus 50 MHz (carrier) at that pitch angle setting. The width of each filter is at least three or four times the expected Doppler bandwidth.

The output of the lowest center frequency (LCF) filter for each of the five filter banks is fed to one square law detector. Similarly, the outputs from the middle center frequency (MCF) filter is fed to a second square law detector and the HCF to the third. The square law detectors are all fed signals, and each detected output is integrated by an RC filter (with an operational amplifier to maintain linearity). The detected integrated output of the three parallel paths is compared to find the one with the maximum value. This value is chosen as the scatterometer measurement; it is converted to digital form by an A/D converter and stored on tape (on the same track as the radiometer signal).

The purpose of having the three filters and selecting only one is to minimize the noise bandwidth and yet leave enough flexibility so that any deviation from the commanded pitch will still result in a signal within the filter bandwidths.

Following each scatterometer measurement, a noise measurement is made. The noise measurement is made with the transmitter and the receiver operating as if a signal were appearing at the antenna ports. This signal is again amplified, detected, integrated, and dumped on the recorder. The noise is always allowed to travel the path of least attenuation (highest gain) and always go through the middle filter.

The system transfer function for scatterometer operations must take into account the gain selection, the filter responses, the integrator response and the transmitted power (recorded on tape).

APPENDIX TWO  
Some Notes on Regression Analysis

2.0 Weighted Least Squares

In performing the regression analysis we did not have an equal number of samples at each of the observation angles. The corresponding sample variances were also unequal. This implies that the usual regression equation

$$[Y] = [A][X] + [E] \quad (1)$$

where  $[Y]$  = column of observed values ( $n \times 1$ )

$[A]$  = matrix of regression coefficients ( $n \times p$ )

$[X]$  = column of independent variables ( $p \times 1$ )

$[E]$  = the error matrix ( $n \times n$ )

cannot really be applied because our error vector is not of the form  $\sigma^2[I]$ , where  $[I]$  is the identity matrix and  $\sigma^2$  is the error.

We do, however, assume that the error matrix does not contain values of the diagonal (i.e. the observations are uncorrelated).

We can transform the observations  $Y$  to other variables  $Z$  which do appear to satisfy the necessary requirements for the regression model (Draper and Smith, 1966)

$$[Z] = [A][W] + [F] \quad (2)$$

where  $E(f) = 0$

$$V(f) = I\sigma^2$$

Suppose the model under consideration is

$$[Y] = [A][X] + [\epsilon] \quad (3)$$

where  $E(\epsilon) = 0$  and  $\text{Var}(\epsilon) = V\sigma^2$  and  $\epsilon \sim N(0, V\sigma^2)$

It can be shown that it is possible to find a unique non-singular symmetric matrix  $P$  such that

$$P'P = PP' = P^2 = V \quad (4)$$

Let  $f = P^{-1}\epsilon$ ,

Then it can be shown that

$$f \sim N(0, I\sigma^2)$$

The new model which can therefore be solved is

$$P^{-1}Y = P^{-1}AW + P^{-1}\epsilon \quad (5)$$

or  $Z = AW + F$ .

In our case, each observation is the sample mean computed from a number of samples. The number of samples used to compute the means for various values of  $x$  are not the same. Since we can also compute the sample variance at each set of observation points, we know that the variance of the sample mean will be

$$\text{var}\{y_i\} = \frac{\sigma_i^2}{n_i} \quad (6)$$

where  $\sigma_i^2$  = sample variance of observation  $i$ .

$n_i$  = sample size of observation  $i$ .

i.e. the observation  $y_i$  will have a variance which is  $n_i$  times smaller than the sample variance.

Since we are trying to fit the model

$$E\{y\} = Ax \quad (7)$$

We find that

$$V\sigma^2 = V_y = \begin{bmatrix} \frac{\sigma_1^2}{n_1} & & & \\ & \ddots & & \\ & & \frac{\sigma_i^2}{n_i} & \\ & & & \ddots \\ & & & & \frac{\sigma_k^2}{n_k} \end{bmatrix} \quad (8)$$

Therefore the matrix  $P$  is now found to be

$$P = \begin{bmatrix} \frac{\sqrt{n_1}}{\sigma_1} & & & \\ & \ddots & & \\ & & \frac{\sqrt{n_i}}{\sigma_i} & \\ & & & \ddots \\ & & & & \frac{\sqrt{n_k}}{\sigma_k} \end{bmatrix} \quad (9)$$

The resulting model will now have an error matrix which is an identity and the regression coefficients ( $a$ ) will still apply to the model we wish to fit.

## 2.1 Non Linear Regression

### 2.1.1 General

When variables are related through a non-linear equation, a solution using the usual linear regression models is often misleading. Also, if the solution of two unknown variables is sought from two equations, the substitution method again implies a linear type relationship. In the case of solving for the surface descriptor parameters (Fresnel reflection coefficient, r.m.s. slope etc.), the equations relating the backscattering coefficient to these parameters is a non-linear one. The solutions for the surface descriptors associated with the measured values of backscatter must therefore take this non-linearity into account. The least-square error criterion has been used in the solution of the parameters. The two models considered in the test are the physical optics model with the Gaussian autocorrelation function and the physical optics model with an exponential autocorrelation function. In both cases, the error criterion (least squares) is set up and a solution sought which minimizes it.

### 2.1.2 Physical Optics with Exponential Autocorrelation Function

The equation relating the backscatter to the surface descriptors is

$$\sigma^{\circ} = \frac{pC}{2} \left[ \cos^4 \theta + C \sin^2 \theta \right]^{-3/2} \quad (10)$$

where

$\sigma^{\circ}$  = backscattering coefficient

$p$  = Fresnel Reflection coefficient

$C$  = inverse of the rms slope squared (for  $C = 20$ )

$\theta$  = the angle of incidence.

The error criteria is set up as

$$E[p, C] = \sum_{i=1}^n \left( \sigma_i^{\circ} - \frac{pC}{2} \left[ \cos^4 \theta_i + C \sin^2 \theta_i \right]^{-3/2} \right)^2 \quad (11)$$

This criteria is now a function of  $p$  and  $C$ . To minimize it we differentiate with respect to  $p$  and  $C$  and set the results equal to zero.

$$\begin{aligned} \frac{\partial E}{\partial p} &= \sum_{i=1}^n -2 \left( \frac{C}{2} \left[ \cos^4 \theta_i + C \sin^2 \theta_i \right]^{-3/2} \right) \cdot \\ &\quad \left( \sigma_i^{\circ} - \frac{pC}{2} \left[ \cos^4 \theta_i + C \sin^2 \theta_i \right]^{-3/2} \right) \\ &= 0 \end{aligned} \quad (12)$$

and

$$\frac{\partial E}{\partial C} = \sum_{i=1}^N 2 \left( -\frac{P}{2} [\cos^4 \theta_i + C \sin^2 \theta_i]^{-3/2} + \left[ \frac{3PC}{4} \sin^2 \theta_i (\cos^4 \theta_i + C \sin^2 \theta_i)^{-5/2} \right] \right) \cdot \left[ \sigma_i^0 - \frac{PC}{2} [\cos^4 \theta_i + C \sin^2 \theta_i]^{-3/2} \right] = 0 \quad (13)$$

Equating the two equations to a common quantity  $\{C/2\}$ , from equation (12)

$$\frac{PC}{2} = \frac{\sum_{i=1}^N \sigma_i^0 F^3(\theta_i, C)}{\sum_{i=1}^N F^6(\theta_i, C)} \quad (14)$$

and from equation (13)

$$\frac{PC}{2} = \frac{\sum_{i=1}^N \sigma_i^0 \sin^2 \theta_i F^5(\theta_i, C)}{\sum_{i=1}^N \sin^2 \theta_i F^8(\theta_i, C)} \quad (15)$$

where

$$F(\theta_i, C) = [\cos^4 \theta_i + C \sin^2 \theta_i]^{-1/2} \quad (16)$$

Equating the two reduced equations we get,

$$\frac{\sum_{i=1}^N \sigma_i^0 F^3(\theta_i, C)}{\sum_{i=1}^N F^6(\theta_i, C)} = \frac{\sum_{i=1}^N \sigma_i^0 \sin^2 \theta_i F^5(\theta_i, C)}{\sum_{i=1}^N \sin^2 \theta_i F^8(\theta_i, C)} \quad (17)$$

Rearranging, we get

$$G(C) = \frac{\sum_{i=1}^N \sigma_i^0 \sin^2 \theta_i F^5(\theta_i, C) \sum_{i=1}^N F^6(\theta_i, C)}{\sum_{i=1}^N \sigma_i^0 F^3(\theta_i, C) \sum_{i=1}^N \sin^2 \theta_i F^8(\theta_i, C)} - 1 = 0 \quad (18)$$

This is now an equation in  $C$ . To solve for the roots of  $G(C)$ , we must use some iterative technique. The one used was Newton's method of successive approximation (see for example Hovanessian and Pipes (1969), pp. 125, 126, which gives a solution according to

$$\hat{C}_{i+1} = \hat{C}_i - \frac{G(\hat{C}_i)}{G'(\hat{C}_i)} \quad (19)$$

where

$\hat{C}_i$  = estimated solution at  $i$ th iteration

$G'(\hat{C}_i)$  = derivative of  $G(\ )$  evaluated at the estimated solution  $C_i$ .

The convergence of a solution is not guaranteed. It helps a great deal if an approximate solution is used as a starting point.

After computing  $C$ , we can then compute  $\rho$  from equation (14) as

$$\hat{\rho} = \frac{2 \sum_{i=1}^N \sigma_i^0 F^3(\theta_i, \hat{C})}{\hat{C} \sum_{i=1}^N F^6(\theta_i, \hat{C})} \quad (20)$$

### 2.1.3 Physical Optics with a Gaussian Autocorrelation Function

The solution for the backscatter using a Gaussian autocorrelation function is

$$\sigma^0 = \frac{K}{s^2 \cos^3 \theta} e^{-\tan^2 \theta / 2s^2} \quad (21)$$

where

$$K = \rho_0^2 / 2 \cos \theta$$

$s^2$  = the square of the rms slope

The other variables are same as defined above.

The error criterion is set up as

$$E \left[ K, \frac{1}{s^2} \right] = \sum_{i=1}^N \left( \sigma_i^0 - \frac{K}{s^2 \cos^3 \theta_i} e^{-\tan^2 \theta_i / 2s^2} \right) \quad (22)$$

To get the minimum we differentiate with respect to  $K$  and  $1/s^2$  and set the result equal to zero.

$$\frac{\partial E}{\partial K} = \sum_{i=1}^N -2 \left( \frac{1}{s^2 \cos^3 \theta_i} \exp(-\tan^2 \theta_i / 2s^2) \right) \cdot \left( \sigma_i^0 - \frac{K}{s^2 \cos^3 \theta_i} \exp(-\tan^2 \theta_i / 2s^2) \right)^2 = 0 \quad (23)$$

$$\frac{\partial E}{\partial 1/s^2} = \sum_{i=1}^N 2 \left( -\frac{K}{\cos^3 \theta_i} \exp\left(-\frac{\tan^2 \theta_i}{2s^2}\right) + \frac{K \tan^2 \theta_i}{2s^2 \cos^3 \theta_i} \exp\left(-\frac{\tan^2 \theta_i}{2s^2}\right) \cdot \left( \sigma_i^0 - \frac{K}{s^2 \cos^3 \theta_i} \exp\left(-\frac{\tan^2 \theta_i}{2s^2}\right) \right) \right) = 0 \quad (24)$$

After considerable manipulation, we equate both the derivatives to a common parameter. From equation (23), we get

$$\frac{K}{s^2} = \frac{\sum_{i=1}^N \sigma_i^0 \left( \frac{1}{\cos^3 \theta_i} \right) \exp(-\tan^2 \theta_i / 2s^2)}{\sum_{i=1}^N \left( \frac{1}{\cos^3 \theta_i} \right) \exp\left(-\frac{\tan^2 \theta_i}{s^2}\right)} \quad (25)$$

and from equation (24), we get

$$\frac{K}{s^2} = \frac{\sum_{i=1}^N \sigma_i^0 \left( \frac{\tan^2 \theta_i}{\cos^3 \theta_i} \right) \exp\left(-\frac{\tan^2 \theta_i}{2s^2}\right)}{\sum_{i=1}^N \left( \frac{\tan^2 \theta_i}{\cos^6 \theta_i} \right) \exp\left(-\frac{\tan^2 \theta_i}{2s^2}\right)} \quad (26)$$

Equating the two equations so obtained, and rearranging we get

$$G\left(\frac{1}{s^2}\right) = \frac{\left\{ \sum_{i=1}^N \sigma_i^0 \left( \frac{1}{\cos^3 \theta_i} \right) \cdot \exp\left(-\frac{\tan^2 \theta_i}{2s^2}\right) \cdot \sum_{i=1}^N \left( \frac{\tan^2 \theta_i}{\cos^6 \theta_i} \right) \right\}}{\exp(-\tan^2 \theta_i / 2s^2)}$$

$$= 0 \quad \left\{ \sum_{i=1}^N \frac{1}{\cos^6 \theta_i} \exp(-\tan^2 \theta_i / s^2) \sum_{i=1}^N \sigma_i^0 \left( \frac{\tan^2 \theta_i}{\cos^3 \theta_i} \right) \cdot \exp(-\tan^2 \theta_i / 2s^2) \right\} - 1 \quad (27)$$

This is an equation in  $1/s^2$ . The roots of  $G(1/s^2)$  can be found by Newton's method of successive approximation, which yields

$$\frac{1}{\hat{s}_{i+1}^2} = \frac{1}{\hat{s}_i^2} - \frac{G\left(\frac{1}{\hat{s}_i^2}\right)}{G'\left(\frac{1}{\hat{s}_i^2}\right)} \quad (28)$$

The resulting solution of  $1/s^2$  is then used to compute K as

$$K = \frac{\hat{s}^2 \sum_{i=1}^N \sigma_i^0 \frac{1}{\cos^3 \theta_i} \exp(-\tan^2 \theta_i / 2\hat{s}^2)}{\sum_{i=1}^N \frac{1}{\cos^6 \theta_i} \exp(-\tan^2 \theta_i / \hat{s}^2)} \quad (29)$$

## APPENDIX THREE

### Selected Results from Simulation Study

Some results pertinent for the present study were obtained from the simulation package described in Appendix 4 and are provided here. The results presented here are

1. The spatial location of target cells for the various operating modes of the S-193 radiometer/scatterometer.
2. The variation of target cell area with incidence angle for a nominal orbit height of 435 kms.
3. The variation of range with incidence angle for a nominal orbit height of 435 kms.

These results are presented as figures C1 through C 13. For a discussion of these results, the reader is referred to the report from which they were obtained [Sobti, 1974].

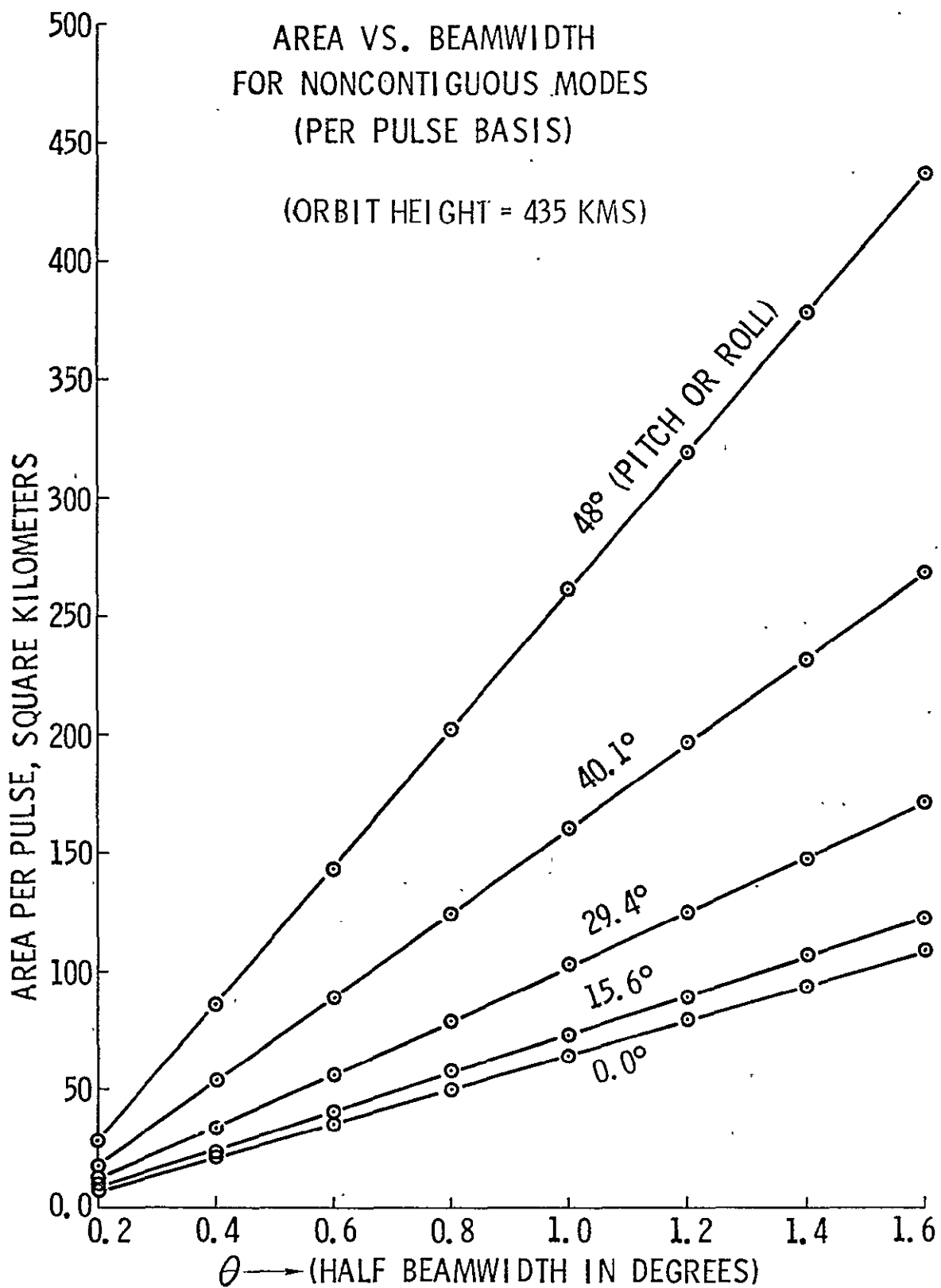
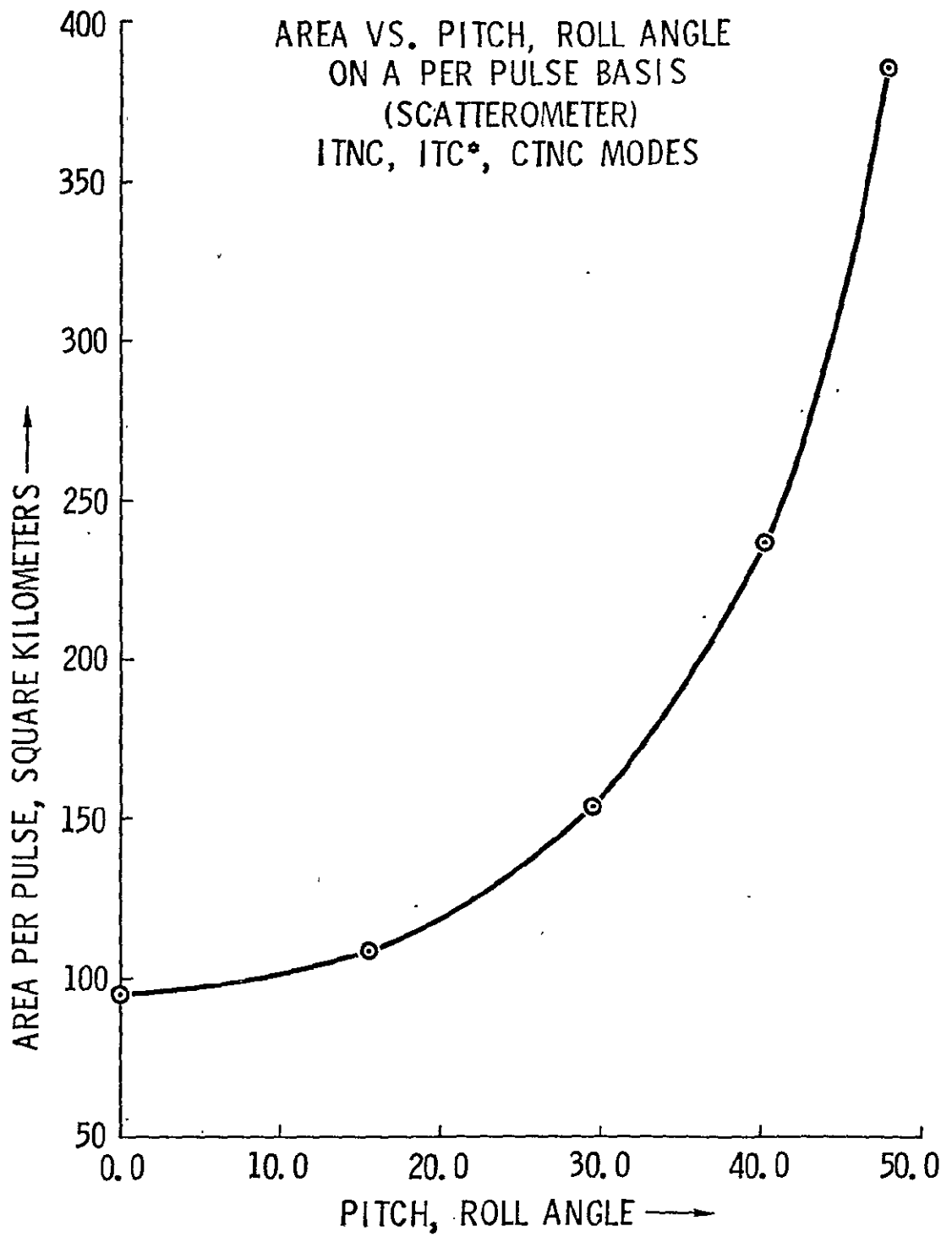


FIGURE C1



\*FIRST PULSE IN MEASUREMENT PERIOD

FIGURE C2

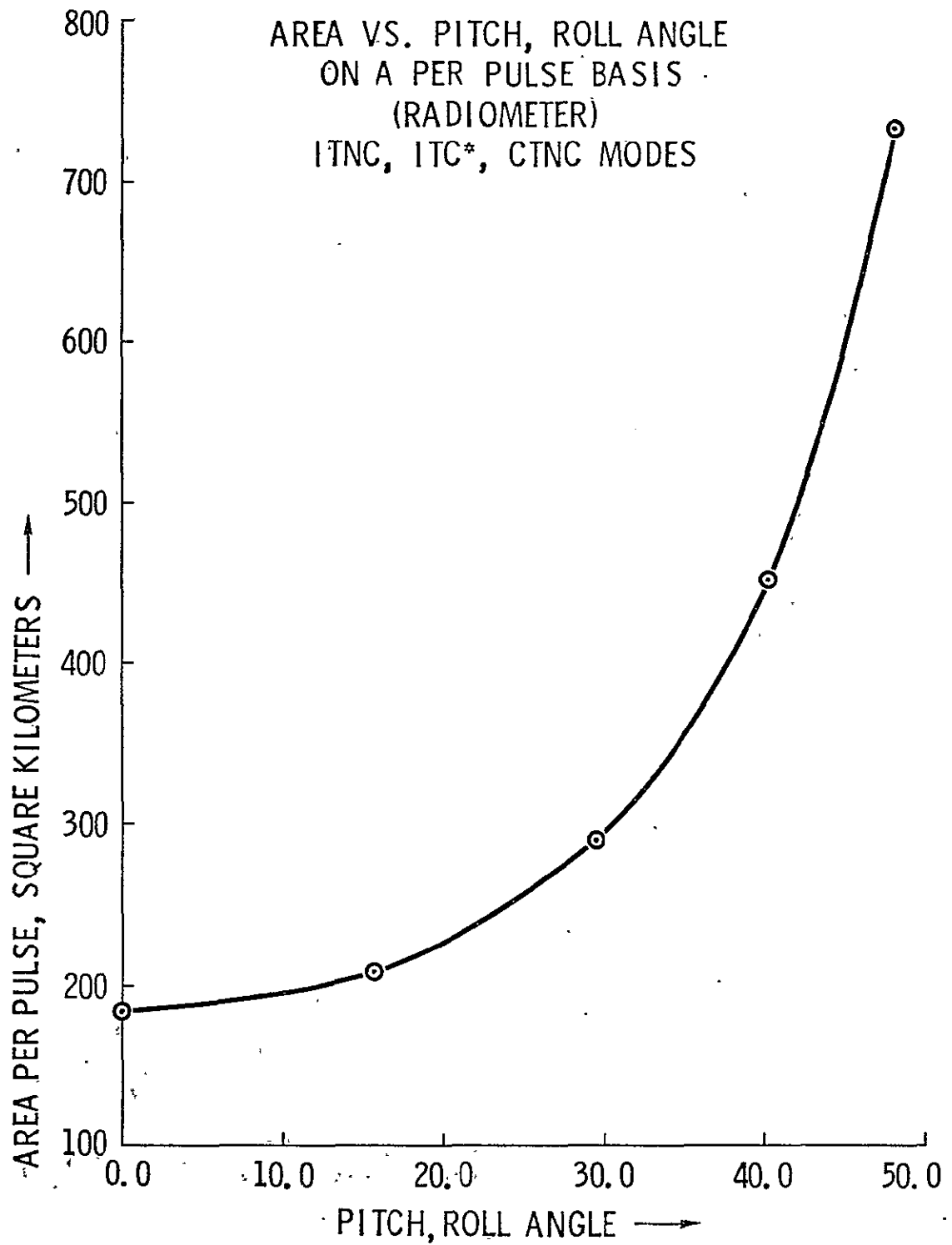
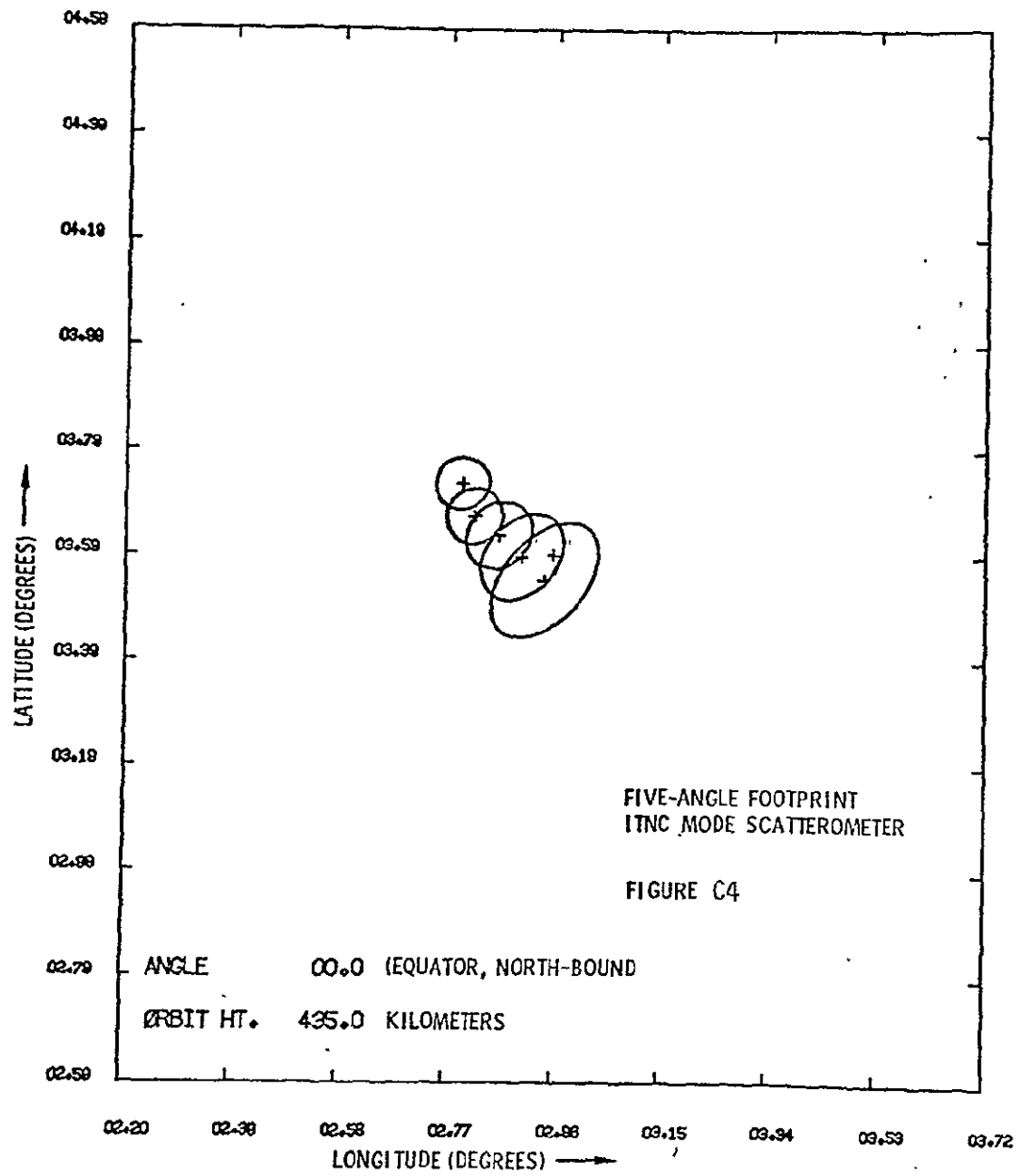
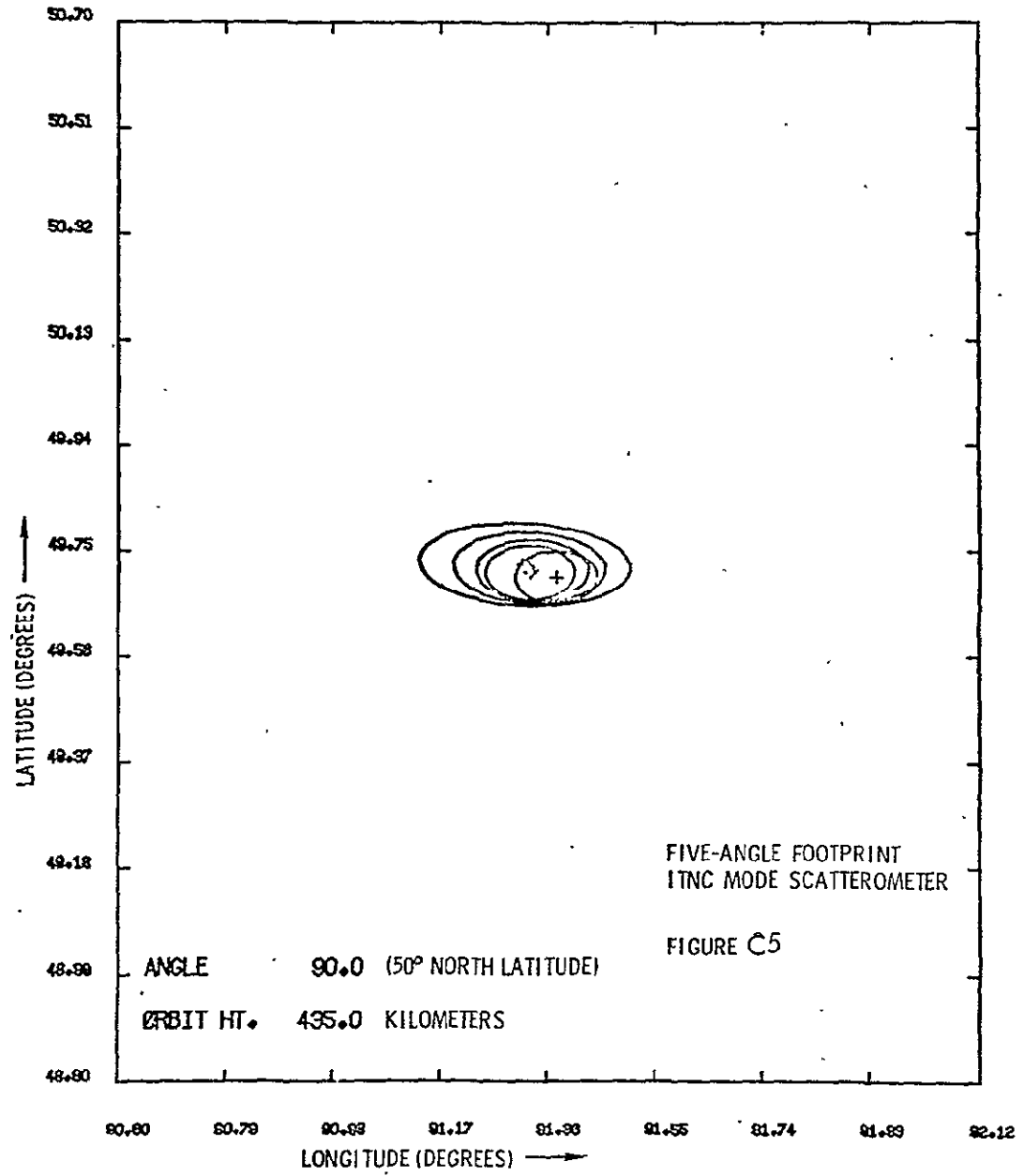
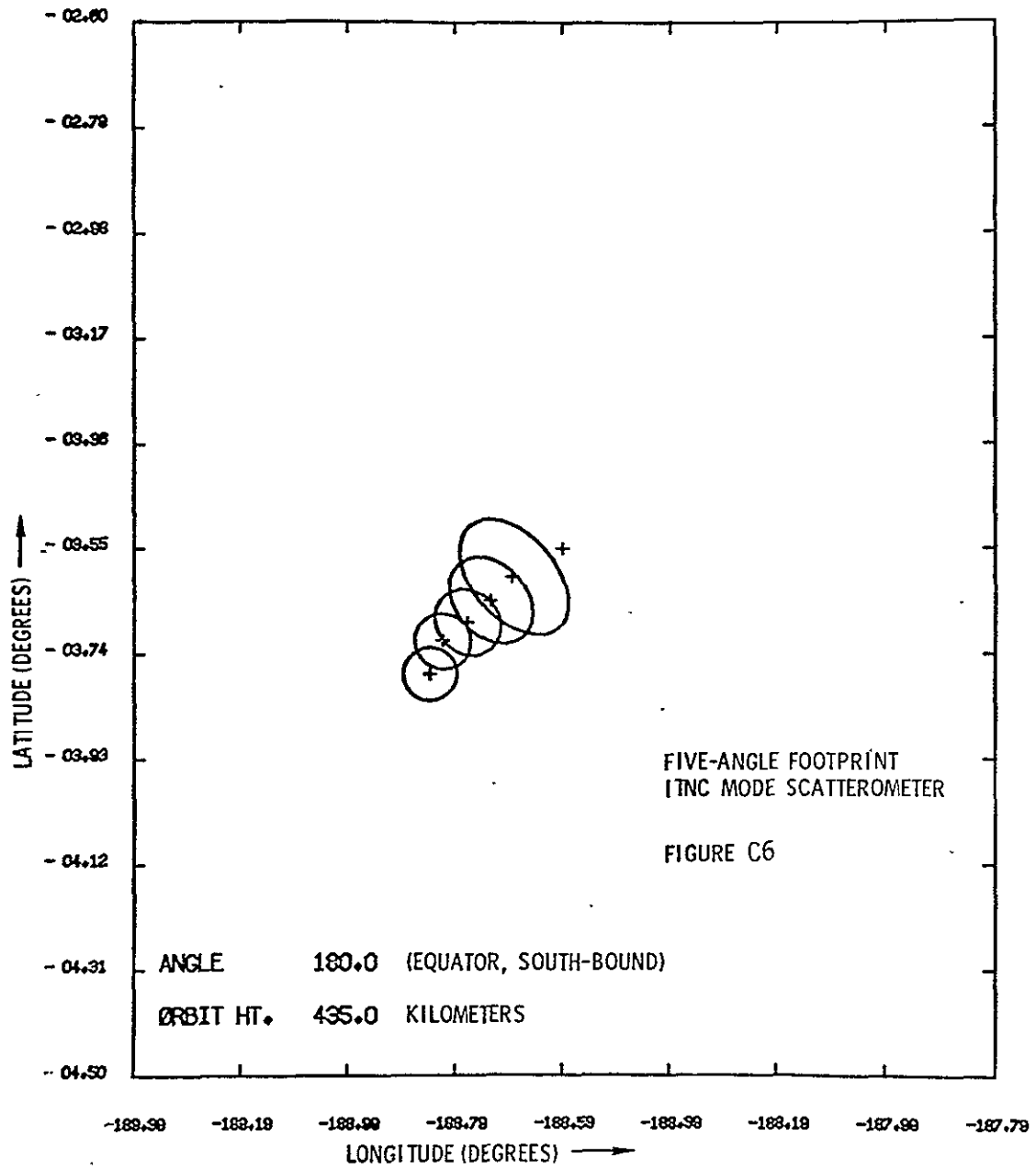


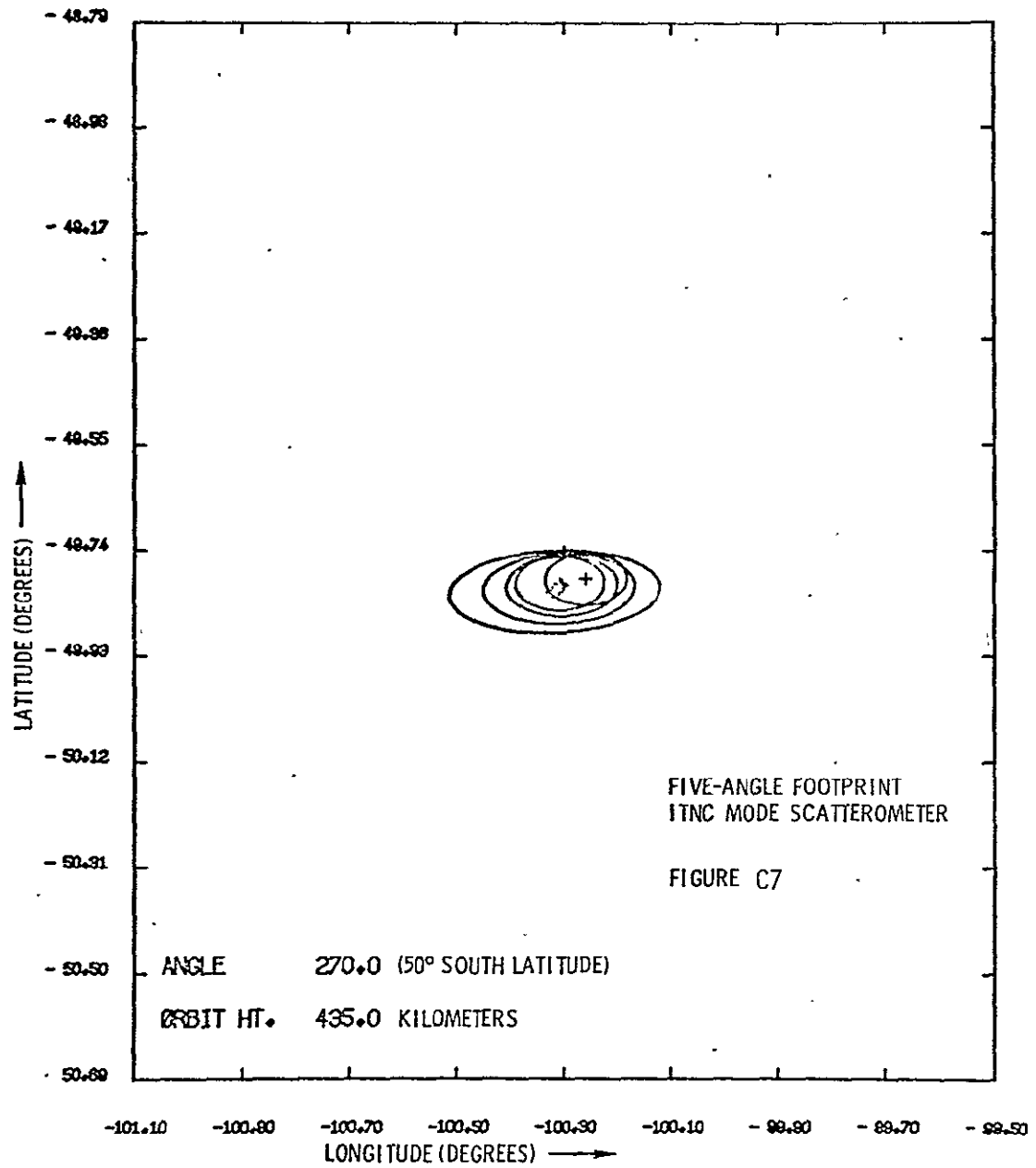
FIGURE C3

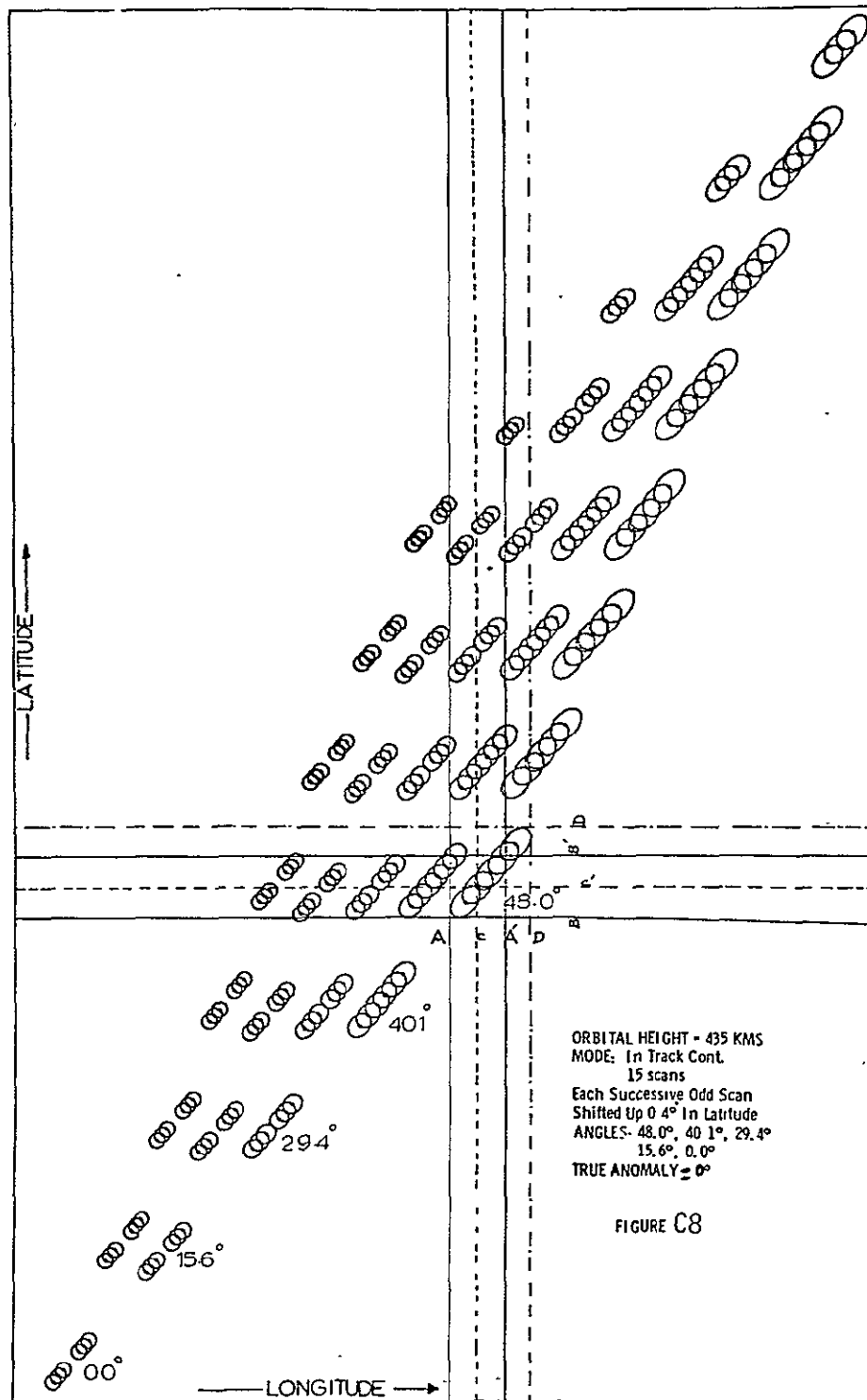
\*FIRST PULSE IN MEASUREMENT PERIOD











LATITUDE (degrees)

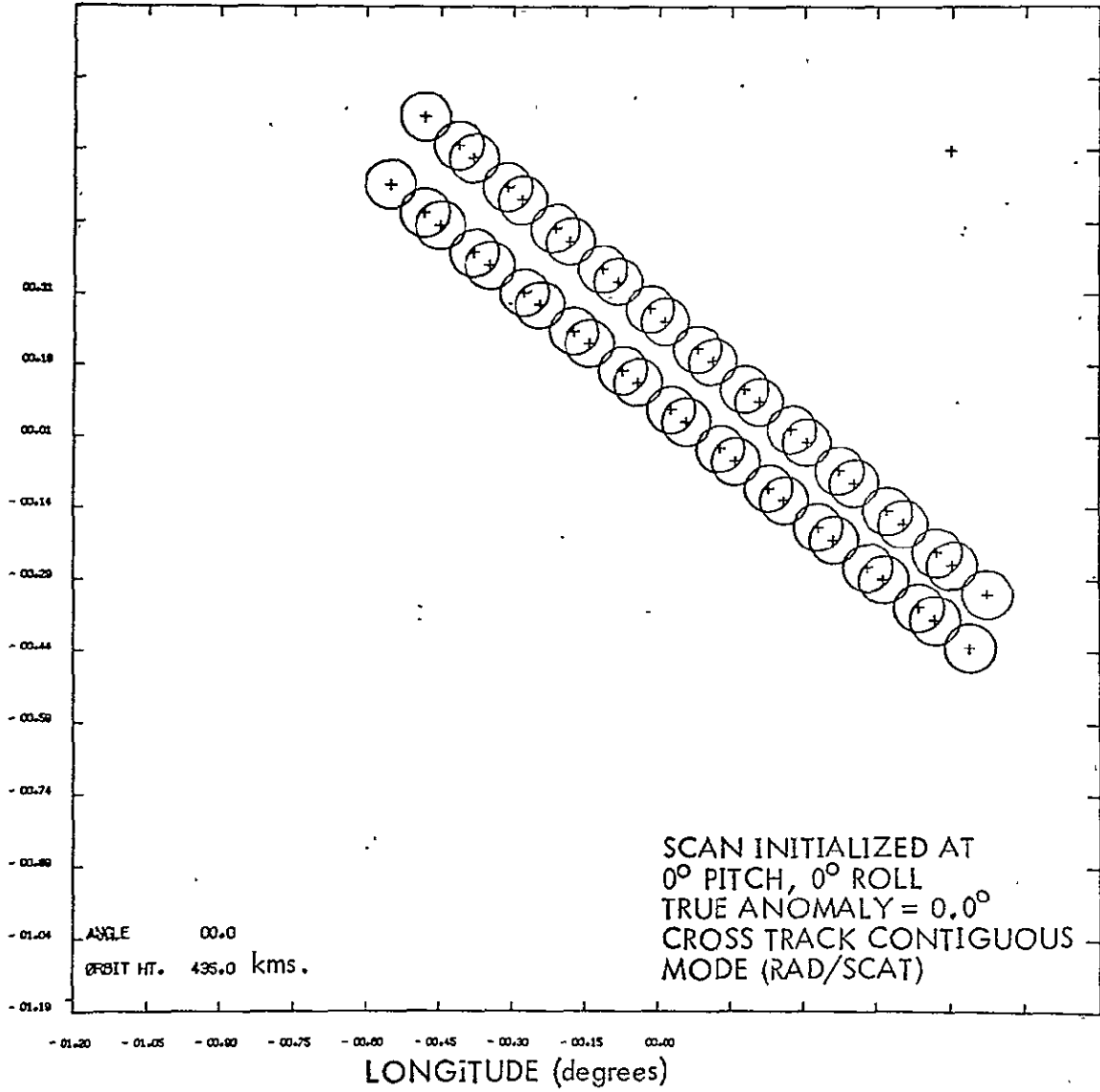


FIGURE C9

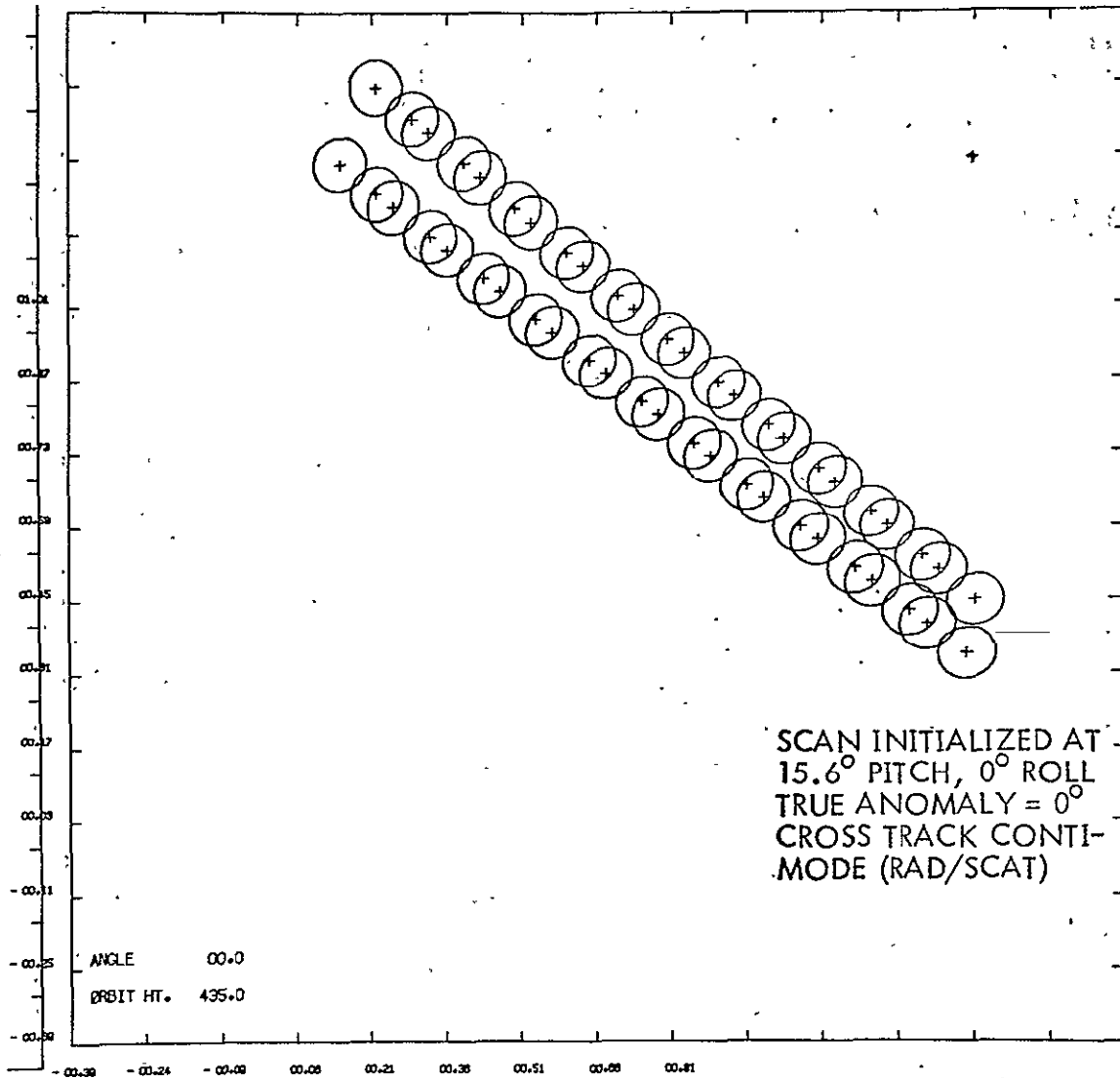


FIGURE C10

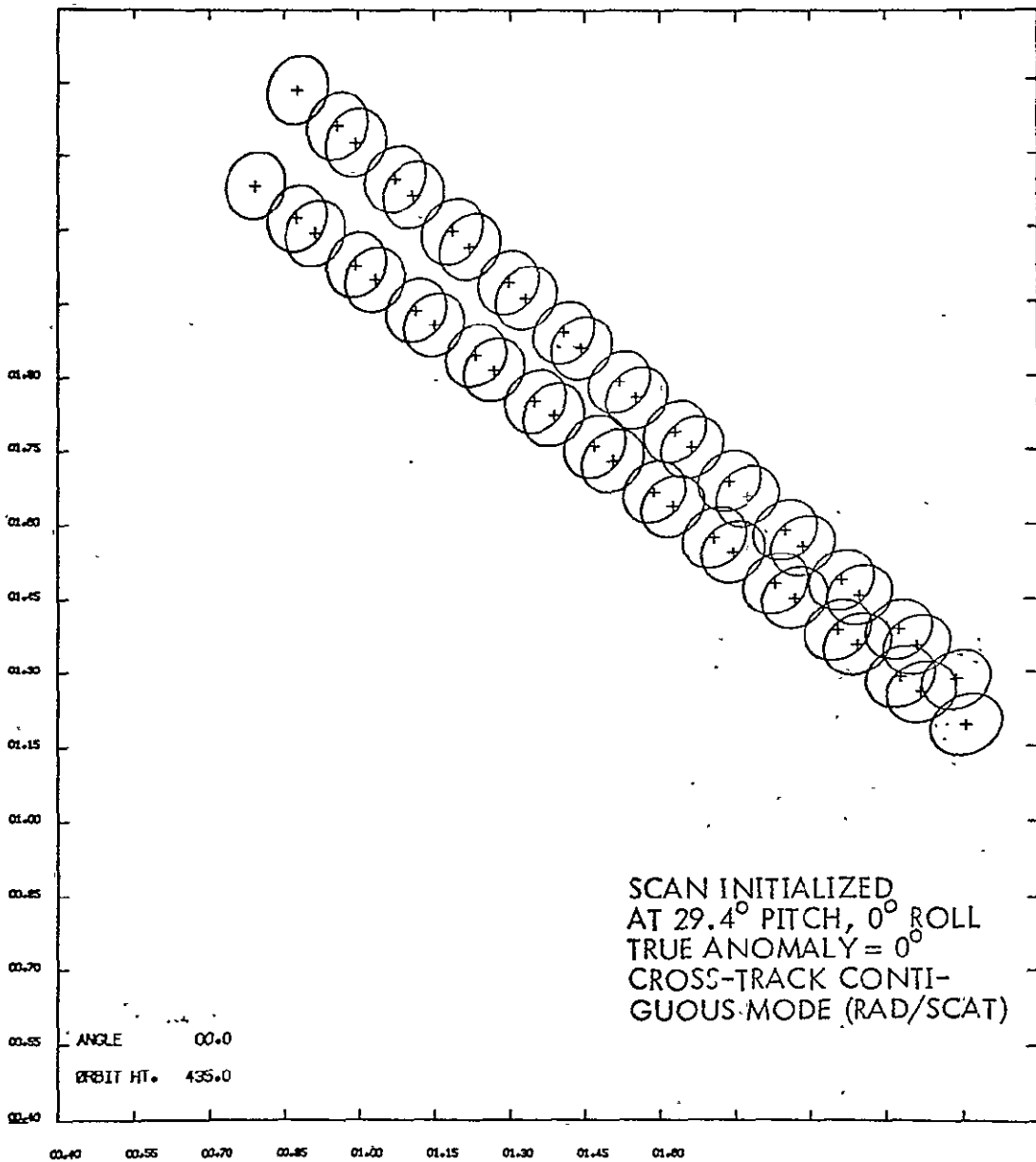


FIGURE C11

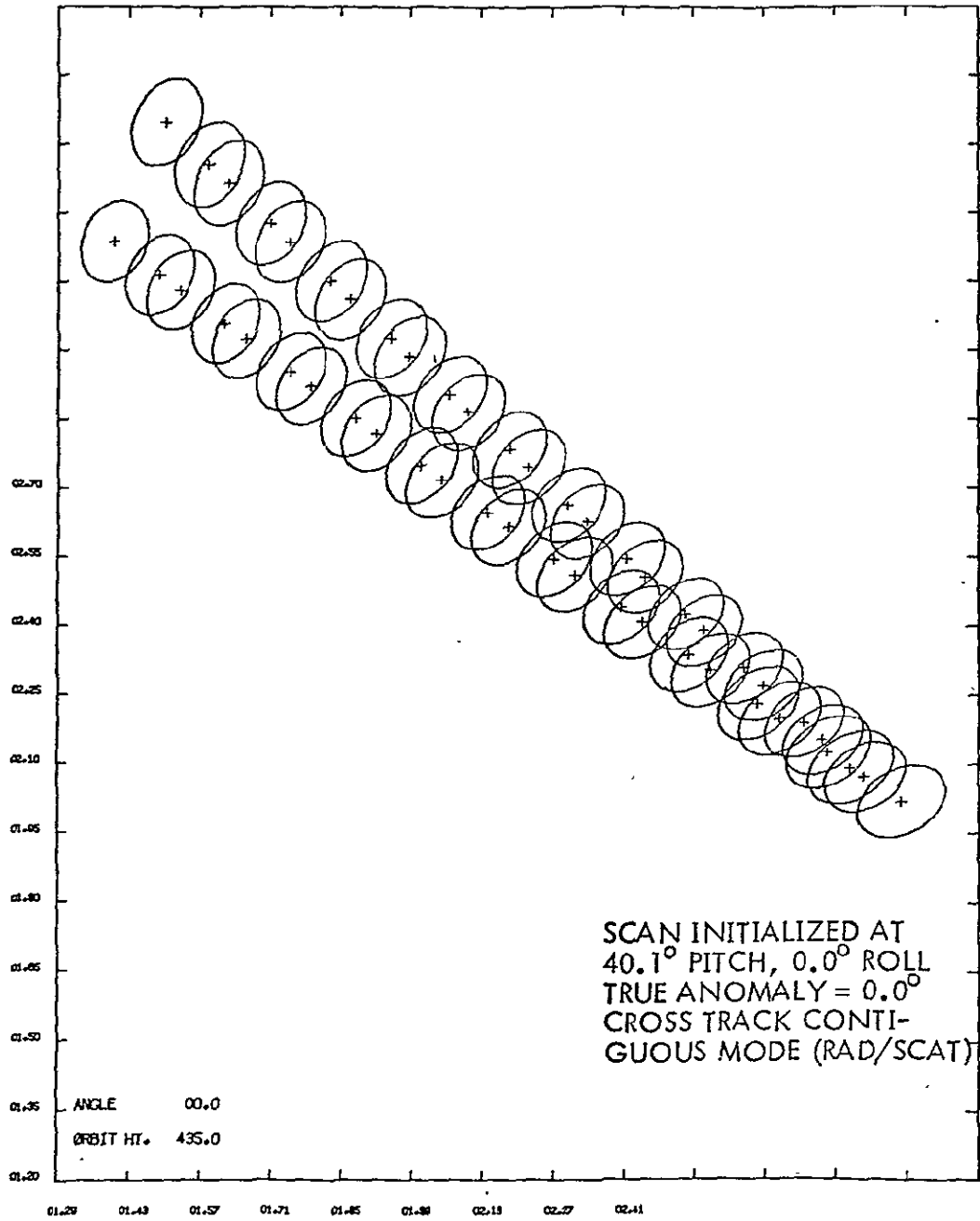


FIGURE C12

REPRODUCIBILITY OF THE ORIGINAL PAGE IS POOR

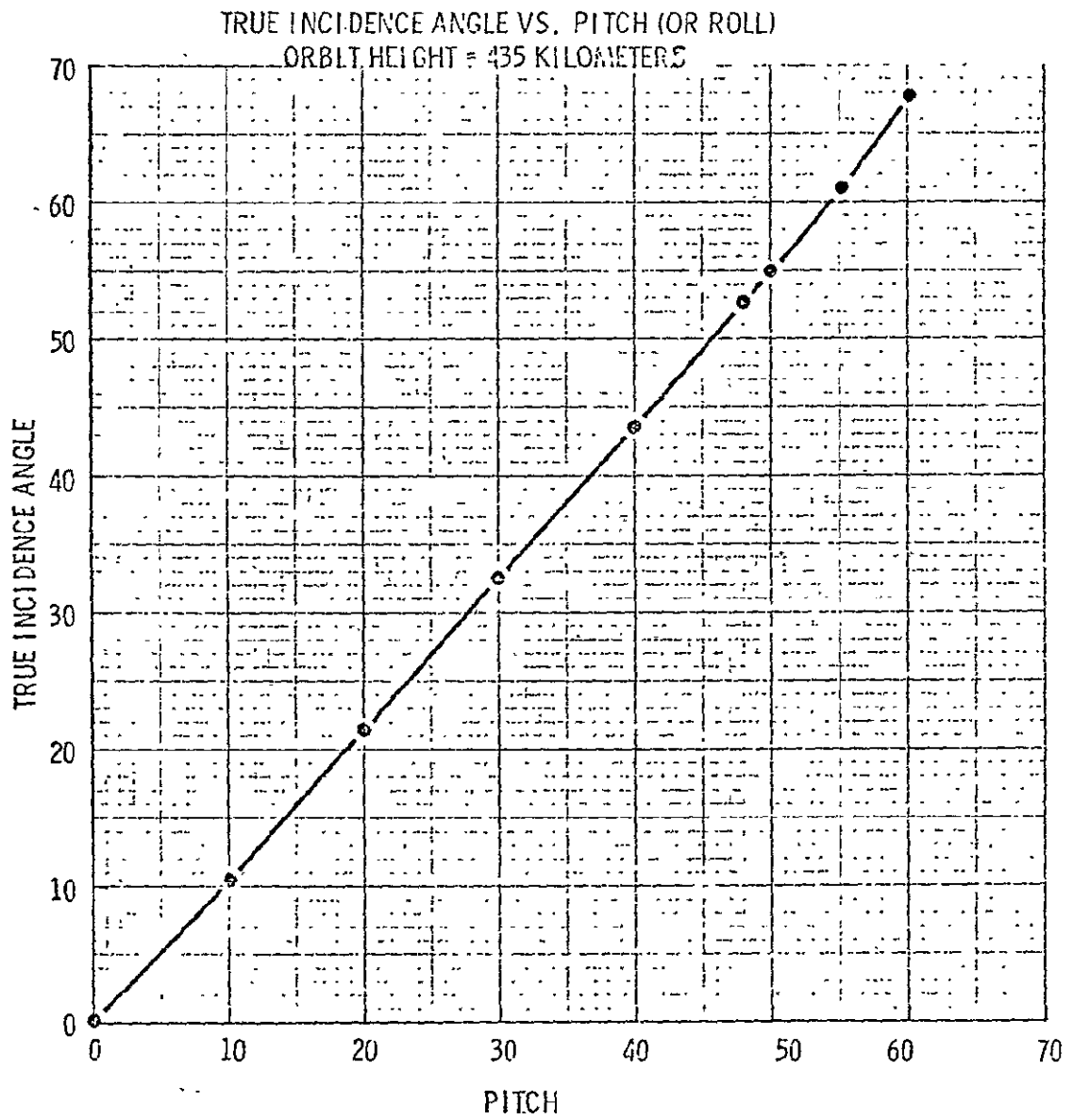


FIGURE C13

## APPENDIX FOUR

### Description of Simulation Program Package

#### 4.1 General

The following is a description of the computer program package called SKYLAB ORBITAL DATA. It is a compilation of most major simulation routines into one program driven by the mainline of the program. The program was initially written to be run on a PDP 15/20 Digital Computer which has only a 12 K memory size. The program then grew in complexity as the amount of simulation performed increased, and now runs on a Honeywell 635 computer. The coding which can be accommodated by the PDP 15/20 has been stored on tape and consists of selected portions of the current program. The general purpose program can perform many functions. The user has a choice of controlling the sequence of operation and obtaining only the result desired and no more by a set of switch functions. These switch functions can be viewed as a combination of status bits in the data stream of the S193 tape and control functions for the program. There is, however, no one-to-one correspondence so far between the status bits and the switch options. The output of the program is controllable and can be either an immediate print out or a tape written for later plotting. The program requires 37 K of storage and the processing and core time are entirely governed by the amount of computation required. Both COMPRESSED and OBJECT decks of the program are available upon request.

A brief description of the individual subroutines, a listing of the program, the data format and some examples of the printout are given below.

#### 4.2 ROUTINES

##### 4.2.1 Mainline — General

The mainline of program drives all the subroutines and controls the flow of processing. It handles all the input/output communications and processes data returned from subroutines. Since this is a very flexible, general purpose program it has many capabilities, not all of which are to be exercised each time the program is run. To provide the user with a set of controls to exercise only that coding required for the immediate result, switch options are provided. At present there are thirteen quaternary level switches: only a few of these utilize the four levels, most of them utilize

only two. Because of the growing nature of the simulation more combinations of switch levels may become required. The functions of these switch options are elaborated in D.2.2, a directory of switch options is provided in Table D.1. Incidentally, a listing of the source or compressed deck of the program prints a directory for reference.

The program models the SKYLAB path through its orbit. The S193 RADSCAT operation is simulated by commanding the mode, sub-mode and position of SKYLAB at time of turn-on. The index to keep track of events is not a master time reference as on the EREP tape. It was found to be easier to work with orbital angular position of the vehicle and the scan and pulse numbers of the S193 RADSCAT operation; these terms are directly relatable to an adjusted Greenwich Mean Time. The program computes the vehicle velocity and position vectors in Earth - Centered - Inertial coordinates and further in latitude and longitude. It computes the position and velocity of the subsatellite point at all pertinent times in the same set of coordinate spaces. The program then computes, through a set of orthogonal transformations (which account for misalignment and vehicle attitude errors) the unit vector in ECI coordinates corresponding to a line-of-sight vector in the antenna beam. The range to the target point for each LOS vector in the antenna beam is found and used to compute the position of the target point in ECI coordinates and in latitude and longitude. The area within the loci of target points generated by rotating the LOS vector about the antenna boresight is computed. The gain (two-way for the scatterometer and one-way for the radiometer) to each target point in the antenna beam is computed. The ratio of power received to power transmitted is computed for the scatterometer as

$$\frac{P_r}{P_t} = \iint_{\Omega_s} \frac{G^2(\theta, \phi) A(\theta, \phi, \gamma) \sigma^\circ(\theta, \phi, \gamma)}{(4\pi)^3 R(\theta, \phi, \gamma)^4} d\theta d\phi \cdot \frac{\lambda^2}{L_r L_{atm}} \quad (11)$$

The symbols have the same meaning as in eq. (1) (Chapter 6).  $\sigma^\circ(\theta, \phi, \gamma)$  is accessed from a ground model file which simulates an area with a preassigned distribution of two chosen categories. For the radiometer, the antenna temperature is computed as

**TABLED.1**  
 DIRECTORY OF SWITCH OPTIONS

	0	1	2	3
SWITCH 1	Increments in $\theta$ of $0.20^\circ$ .	Only effective beamwidth used.	N/A	N/A
SWITCH 2	Unit vector in gimbal mount coordinates printed.	Unit vector in gimbal mount coordinates not printed.	N/A	N/A
SWITCH 3	Unit vector in vehicle coordinate <u>axis</u> printed.	Unit vector in vehicle coordinates not printed.	N/A	N/A
SWITCH 4	Unit vector in ZLV coordinates printed.	Unit vector in ZLV coordinates not printed.	N/A	N/A
SWITCH 5	Unit vector in ECI coordinates printed.	Point vector in ECI coordinates not printed.	N/A	N/A
SWITCH 6	Position and velocity vectors of satellite printed.	Position and velocity vectors of satellite not printed.	N/A	N/A
SWITCH 7	Position of target point, range, doppler, lat., long, printed.	Position of target point, range, doppler, lat., long, not printed.	N/A	N/A
SWITCH 8	Used for plot initialization only active when Switch 11 is 1. Implies plot initialization only at first scan, first look, first pulse in any mode.	Incidence angle calculations are required.	Used for plot initialization only active when switch 11 is 1. Implies plot initialization for first pulse at any angle.	Used for plot initialization only active when switch 11 is 1. Initialize plot for every pulse.
SWITCH 9	Antenna calculations not required.	Antenna calculations are required.	Printout plots of area and illumination versus incidence angles are required.	Illumination integral calculations are not required.
SWITCH 10	In track contiguous.	In track non-contiguous.	Cross track non-contiguous.	Cross track contiguous.
SWITCH 11	Footprint plots are not required.	Footprint plots are required.	N/A	N/A
SWITCH 12	Scatterometer operation.	Radiometer operation.	N/A	N/A

**ORIGINAL PAGE IS  
 OF POOR QUALITY**

$$T_a(\gamma) = \frac{1}{G_0} \iint_{\Omega_1} G(\theta, \phi) T_B(\theta, \phi, r) d\theta d\phi \quad (12)$$

The symbols have the same meaning as in eq. (2). The value of  $T_B(\tau, \phi, \gamma)$  is accessed from the same ground model files as  $\sigma^0$ .

The incremental area due to vehicle motion and antenna slewing is computed on a per measurement basis. The relative contribution to the  $P_r/P_t$  ratio from iso gain areas is computed. The normalized power versus incidence angle and area vs. incidence angle are computed and plotted.

The loci of points in the antenna beam that have the same gain (assuming a symmetric pattern in the azimuthal dimension) are plotted for any incidence angle, pulse number and vehicle position.

The program computes the doppler frequency for any target point and the extremities of the target area illuminated per measurement. A macro flow of instructions is shown in Figure D.1.

#### 4.2.2 Mainline — Controls

Described here are the controls that the program itself exercises once it is running and not the controls to the computer for precessing the program. All controls are commanded through input data and must follow a fixed sequence, this sequence is shown in the READ and FORMAT statements provided in Table 5.2. The table of symbols should be consulted to check the variable represented by the symbol.

To begin with, an option for printing out certain results is exercised. This is done by a variable called PNT OUT. If the word PRINT is read in for this variable, the satellite coordinates, range, doppler frequency, and coordinates for target points lying on an isogain contour are printed; otherwise they are not.

From Table D.2 we see that the first control card requires values for MSIM, MHITE and MGRAF which are defined below

ORIGINAL PAGE IS  
OF POOR QUALITY

582 :

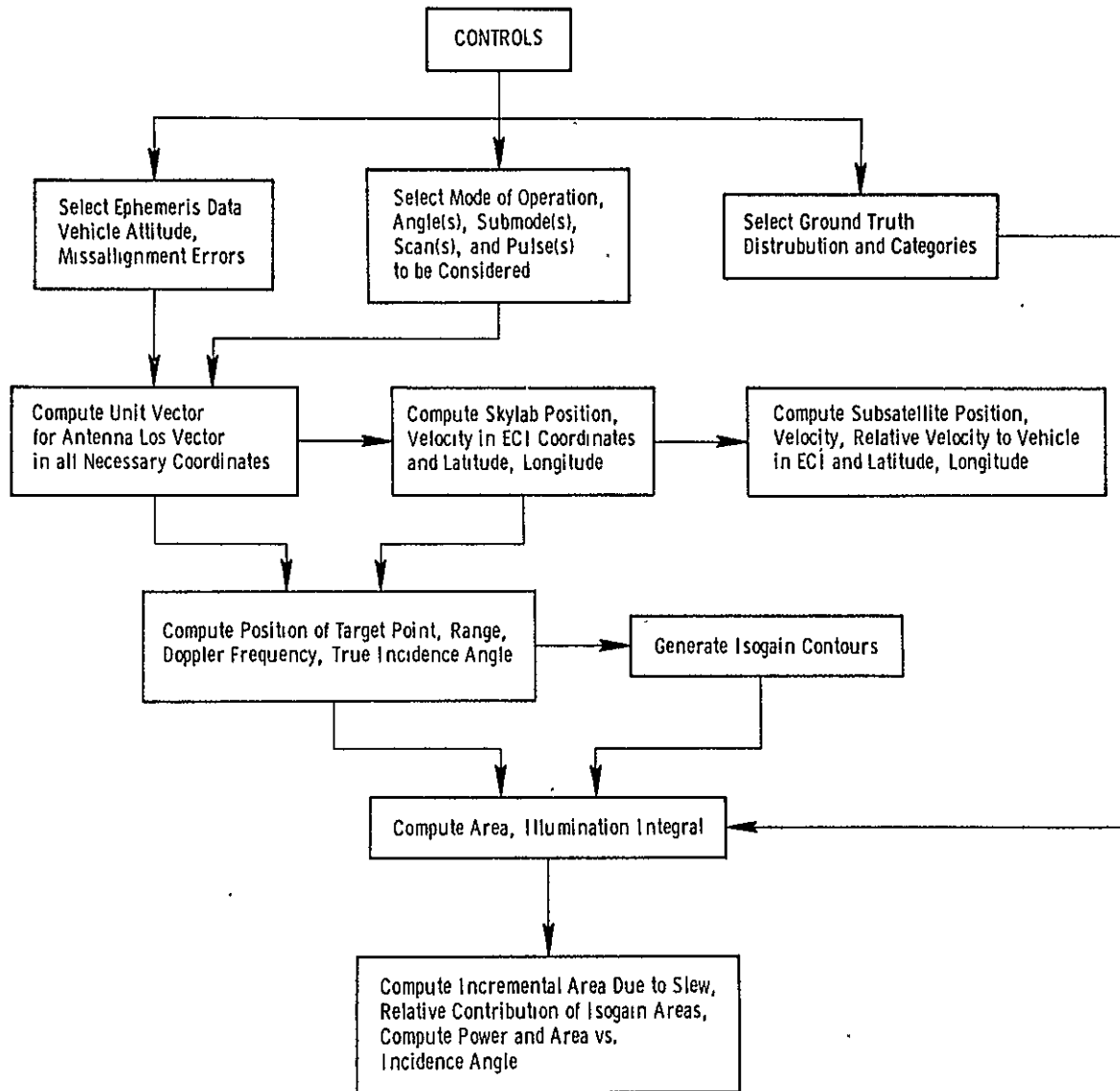


FIGURE D.1  
MACRO FLOW CHART FOR SIMULATION PROGRAM

- MSIM a three-way switch which chooses the type of ground simulation. If a negative integer the ground truth file read into core is a pre-assigned distribution of bare-ground and tree-cover. If MSIM is zero, no further changes are made to the ground truth file. If MSIM is a positive integer, a normal distribution of the two categories, generated earlier, is stored in the ground truth files. The numbers range from 0 to 1.
- MHITE a variable which adjusts for the height of the orbit. It modifies the nominal height of 435 kilometers by its value in kilometers.
- MGRAF a two-way switch which if positive plots the  $\sigma^0$  vs.  $\theta$  values assumed for tree-cover and bare-ground. This variable is only used to plot  $\sigma^0$  vs.  $\theta$ .

The next control card requires values for NUMB, and ITERN

- NUMB an integer which establishes the number of iterations to be performed with the above ground truth and orbit height according to its value.
- ITERN an integer which establishes the number of iterations to be performed with the same switch conditions according to its value.

The next control card reads in the 13 switch values through ISWICH.

- ISWICH(13) a dimensioned integer array which allows a maximum of five values for a particular switch but generally uses only two values - 0 and non-zero. The directory of switch options provided in Table 4.1 explains the individual switches.

The next control card requires a value for IFILE.

- IFILE a number denoting the ground truth files to be considered. At present two files, FILE 1 and FILE 2 are stored. If IFILE is 1 it chooses FILE 1, if 2 chooses FILE 2.

The next card read in is more of a data card than a control card, but it is reported here. It requires values for SIGMA, OMEGA, PHIM, THETAM, PSIM, PHIVEH, THETAH, PSIVEH, OINC, and F.

- SIGMA the pitch angle of the antenna in degrees. It is the initialized value at start of scan for the contiguous modes (e.g.,  $48^{\circ}$  for ITC) and the required antenna angle for the non-contiguous measurement.
- OMEGA the roll angle of the antenna in degrees. It has the same conditions as SIGMA.
- PHIM the yaw misalignment between the gimbal axes and vehicle axes (in degrees).
- THETAM the pitch misalignment between the gimbal axes and vehicle axes (in degrees).
- PSIM the roll misalignment between the gimbal axes and vehicle axes (in degrees).
- PHIVEH  
THETAH  
PSIVEH yaw, pitch and roll attitude errors of the vehicle (in degrees).
- OINC the orbital inclination angle (in degrees).
- F the true anomaly of the orbit or the angular position in the orbital plane (in degrees).

The next control card requires the observation period desired in a particular mode and angle combination. It requires numbers for ISCNST, ISCUP, ISCNND.

- ISCNST starting scan number. The program adjusts for the vehicle position if the starting scan number is different from one.
- ISCNND final scan number. This indicates the final scan to be considered for the above vehicle starting position, in this mode, and antenna angle.
- ISCUP it specifies the spacing of scans to be considered. If 1, it considers consecutive scans from ISCNST to ISNND. If 2, it considers alternate scans.

The next control card requires input for ISTART, ISMEAR, LAPSE, NUMLUP, NFIN, JBIAS.

- ISTART the starting pulse number to be observed in the measurement period.
- ISMEAR the final pulse number to be observed in the measurement period.
- LAPSE the increment in pulse numbers per iteration. If 1 it considers all pulses from ISTART to ISMEAR.
- NUMLUP an internal variable, used in coding. It helps in adjusting the loop when considering the first, middle and final pulse in any measurement period. It should be equal to the number of pulses to be observed per measurement.
- NFIN a number which defines the number of angles to be viewed in the scan. It is very useful in the contiguous modes. For example in the ITC mode there are five angles per scan so NFIN should be five. It should be 1 for non-contiguous modes.
- JBIAS this variable indexes a set of time biases stored in the program. The bias referred to here is the time from initiation of mode to actual data-taking time for that angle (in seconds).

The next control card is an optional one and should only be exercised if a plot (on the Benson-Lehner Plotter) is required. It requires dimensions of the plot.

- XD dimension in inches of the plots in the x and direction.
- YD dimension in inches of the plots in the y direction.
- SPREDX the magnitude of the maximum excursion (either positive or negative) possible in the x values to be plotted from the x value of the first point plotted.
- SPREDY Same as SPREDX but in Y direction instead of X.

#### 4.2.3 Mainline - Computing Algorithm

This section discusses the salient points of the processing algorithm, and points out the links with the subroutines. Figure D.1 shows the algorithm flow chart. The controls shown at the top of Figure D.2 are those described above. At the start of the program certain ephemeris parameters are assumed and are updated by input control cards; orbit height is a significant one of these parameters. With the adjusted orbit height the circumferential velocity of the vehicle is computed. This velocity is used later in computing the vehicle velocity and position in ECI coordinates. The antenna pointing angles, orbital inclination, gimbal misalignment errors, attitude errors and the vehicle angular position in the orbit are stored. With these inputs the following transformation matrices are set up by subroutines

1. Transformation from Antenna L.O.S. coordinate space to gimbal-mount coordinate space by subroutine FILSIG
2. Transformation from gimbal mount coordinate space to vehicle-centered coordinate space by subroutine FILPSM
3. Transformation from vehicle centered space to Z - local-vertical coordinate space by subroutine FILPSV
4. Transformation from ZLV coordinate space to ECI coordinate space by subroutine FILSPZ.

The individual subroutines are explained later.

With the transformation matrices returned to the mainline by the individual subroutines the matrix product of a unit vector with the transformation matrix provides a unit vector in any desired coordinate space. The matrix products were found by subroutine MPRD. The matrix inverses were found by subroutine MINV.

The position and velocity of the vehicle are computed in ECI coordinates by subroutine FILECI. With this position and velocity, the subsatellite position and velocity are computed. The projected linear velocity of the spacecraft onto the earth's surface is next computed. Considering the rotation of the earth the relative velocity of the subsatellite point to the spacecraft is computed. The computed velocities are resolved into latitudinal and longitudinal components. In these computations the slow precession of the orbit has been ignored, further, to simplify computation at no great loss of generality, the eccentricity of the orbit has been ignored. These factors can be introduced at a later date, their influence

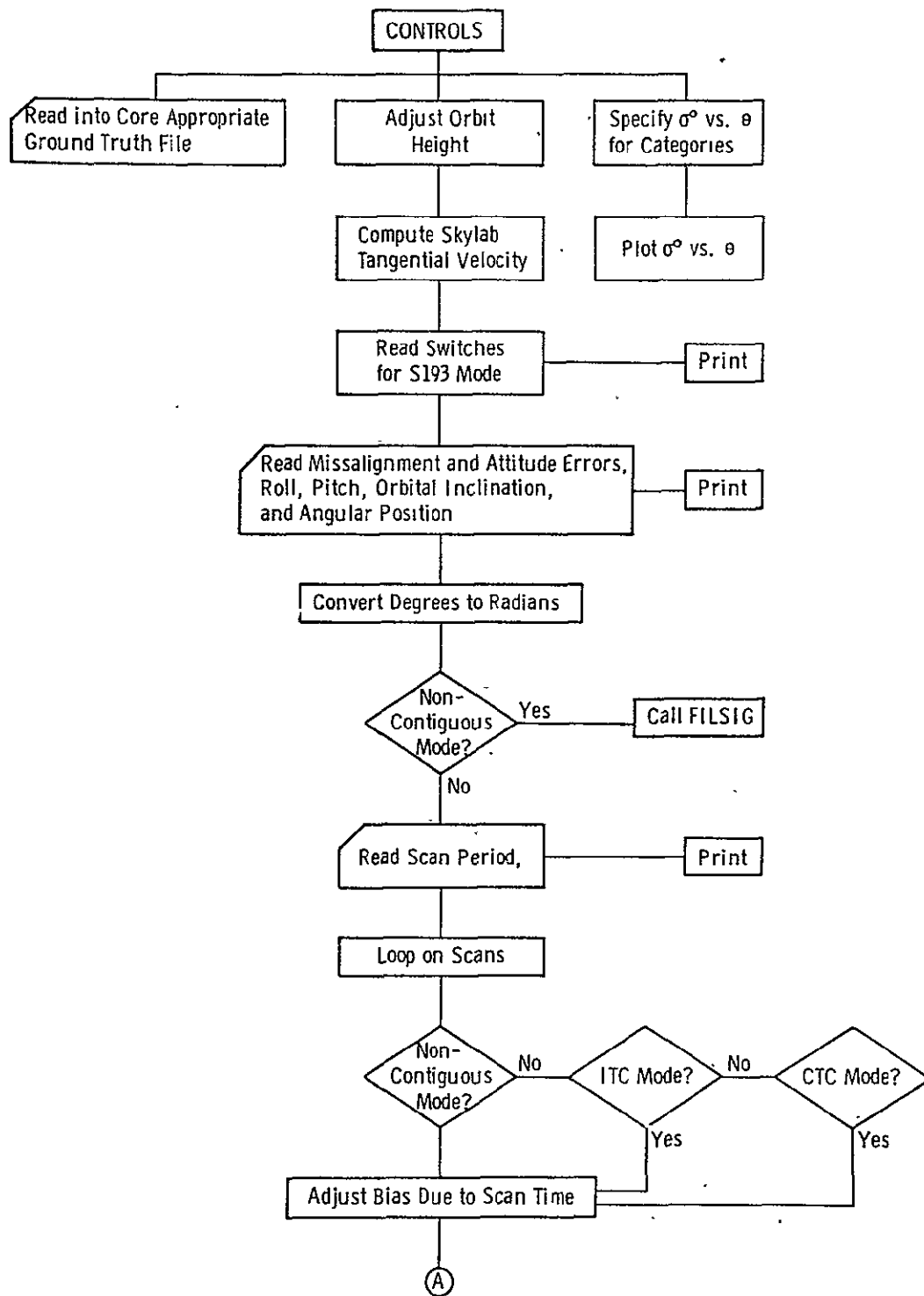
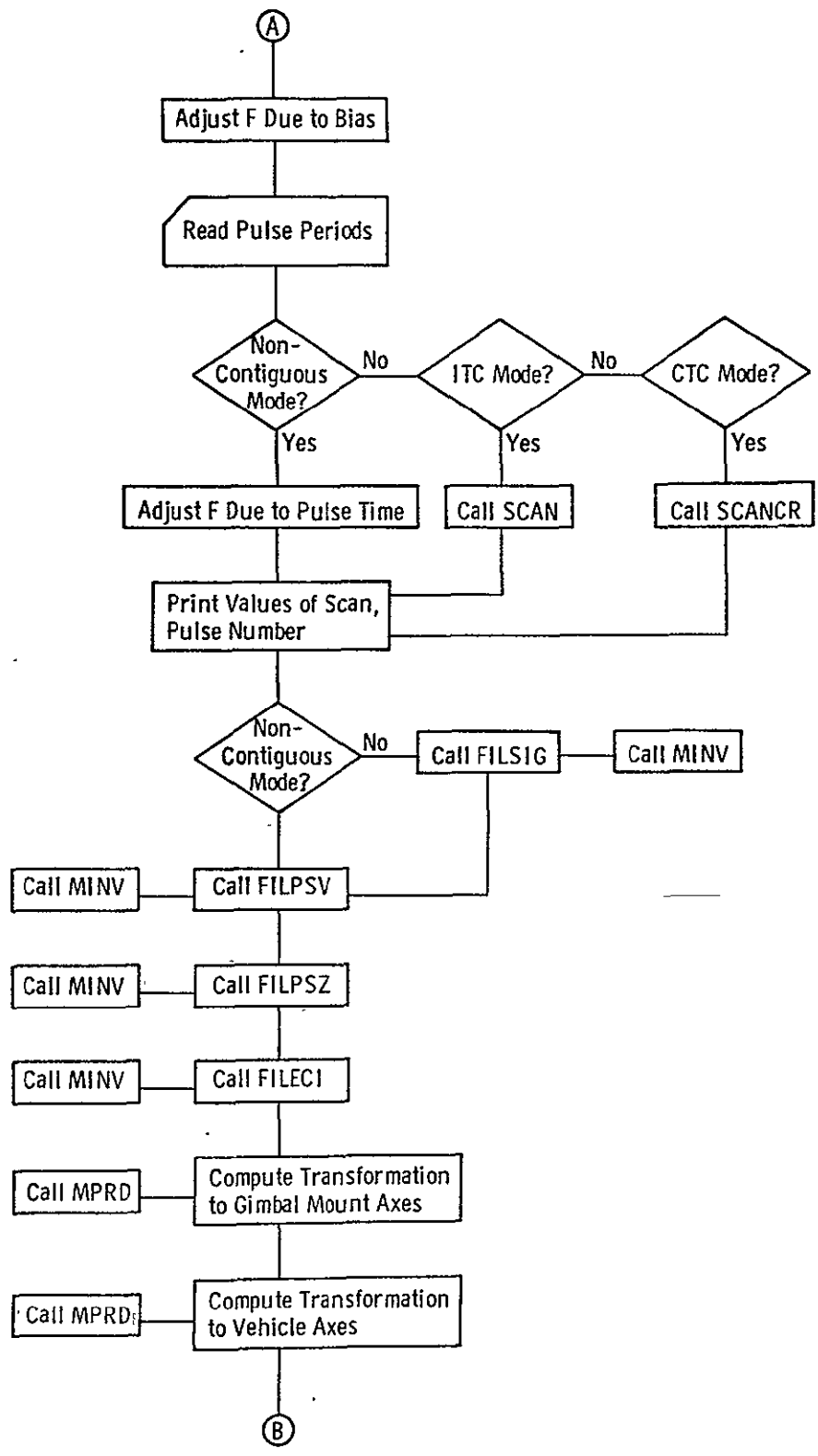
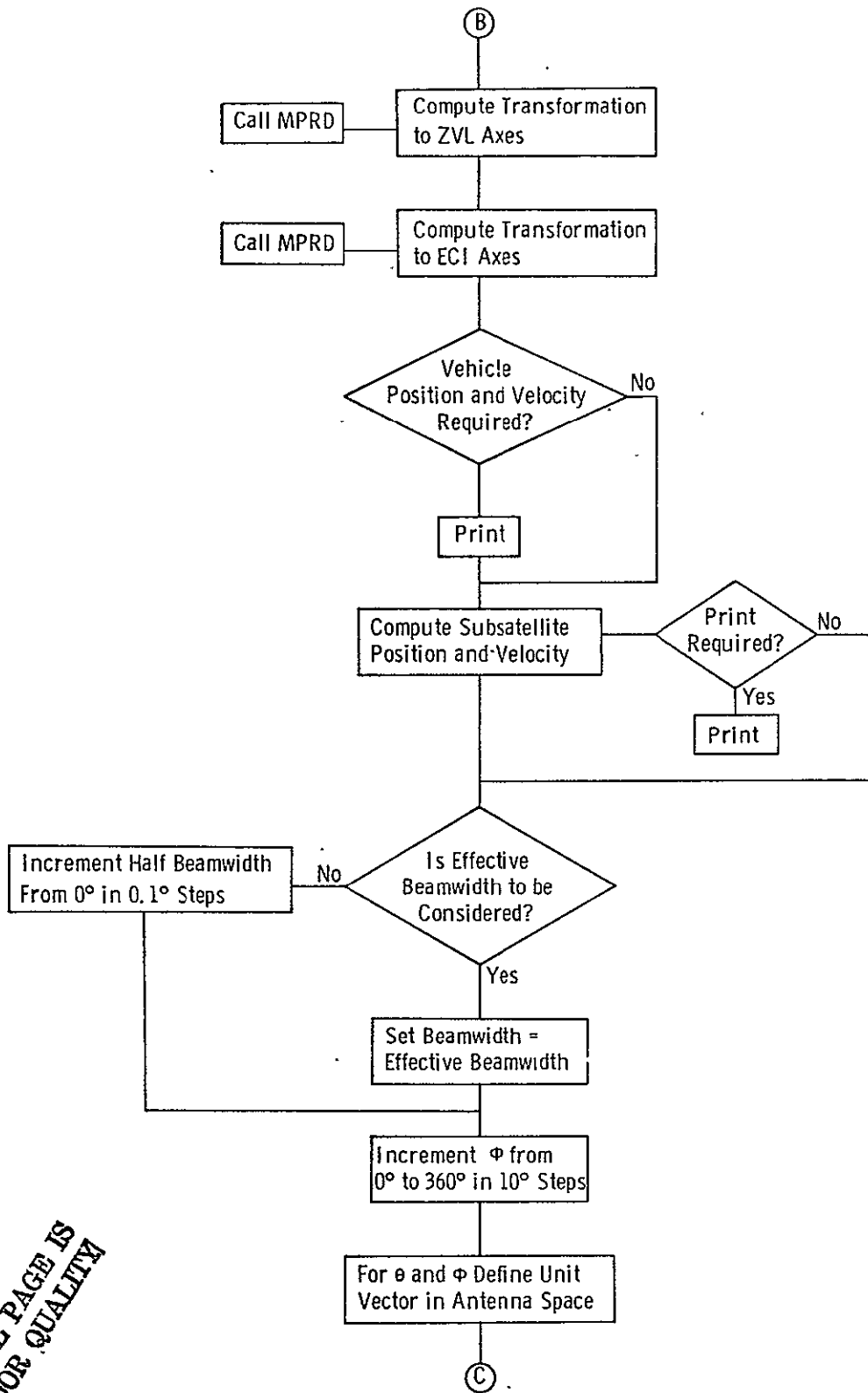


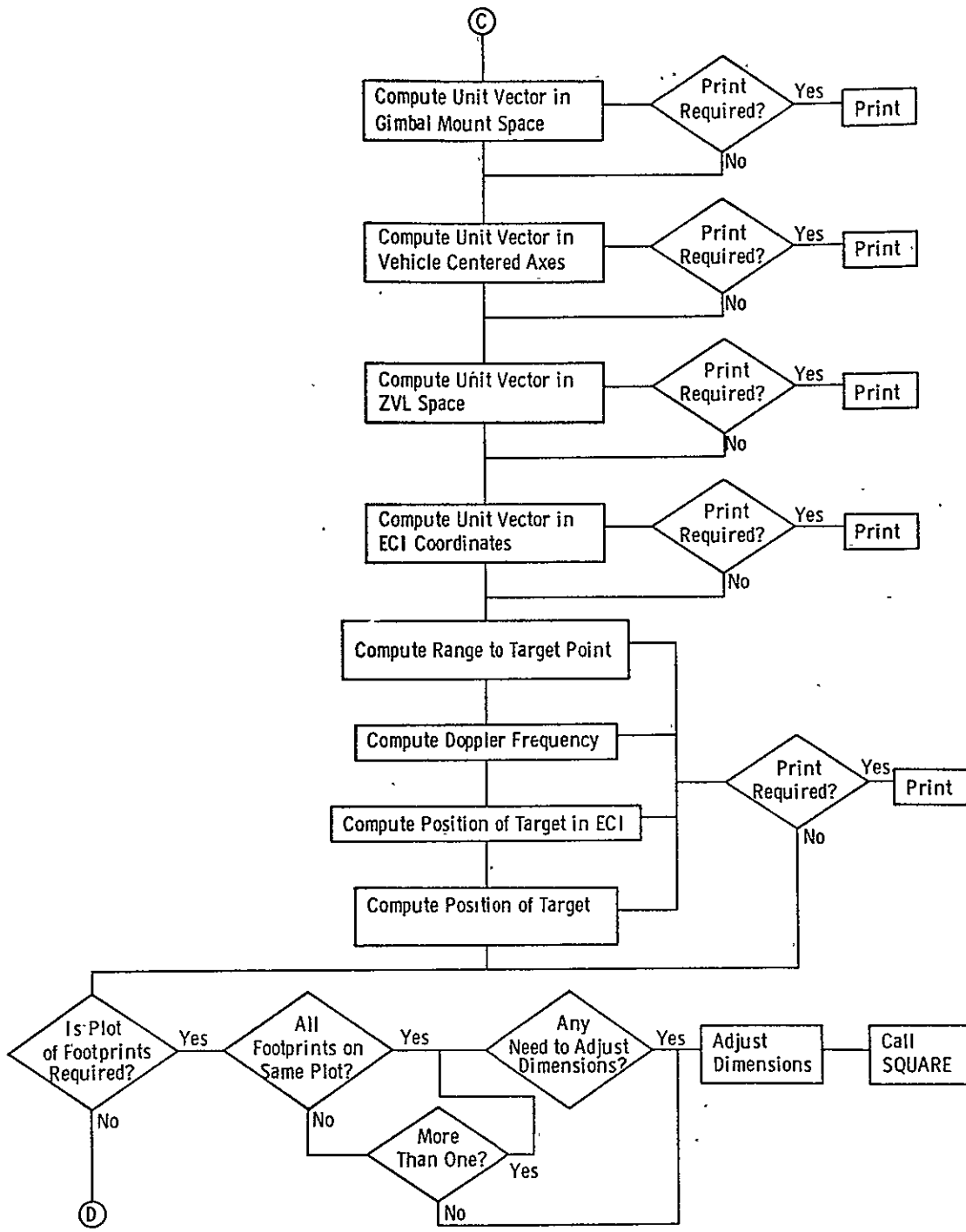
FIGURE D.2

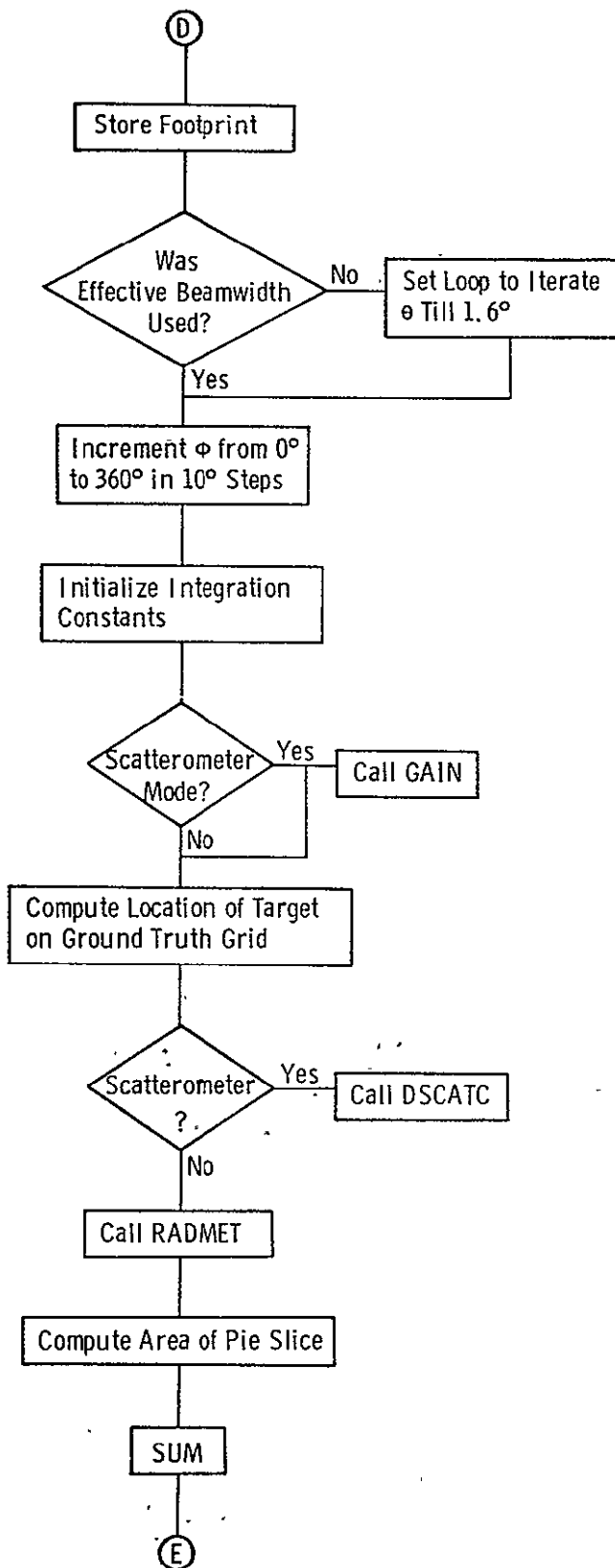
ORIGINAL PAGE IS OF POOR QUALITY

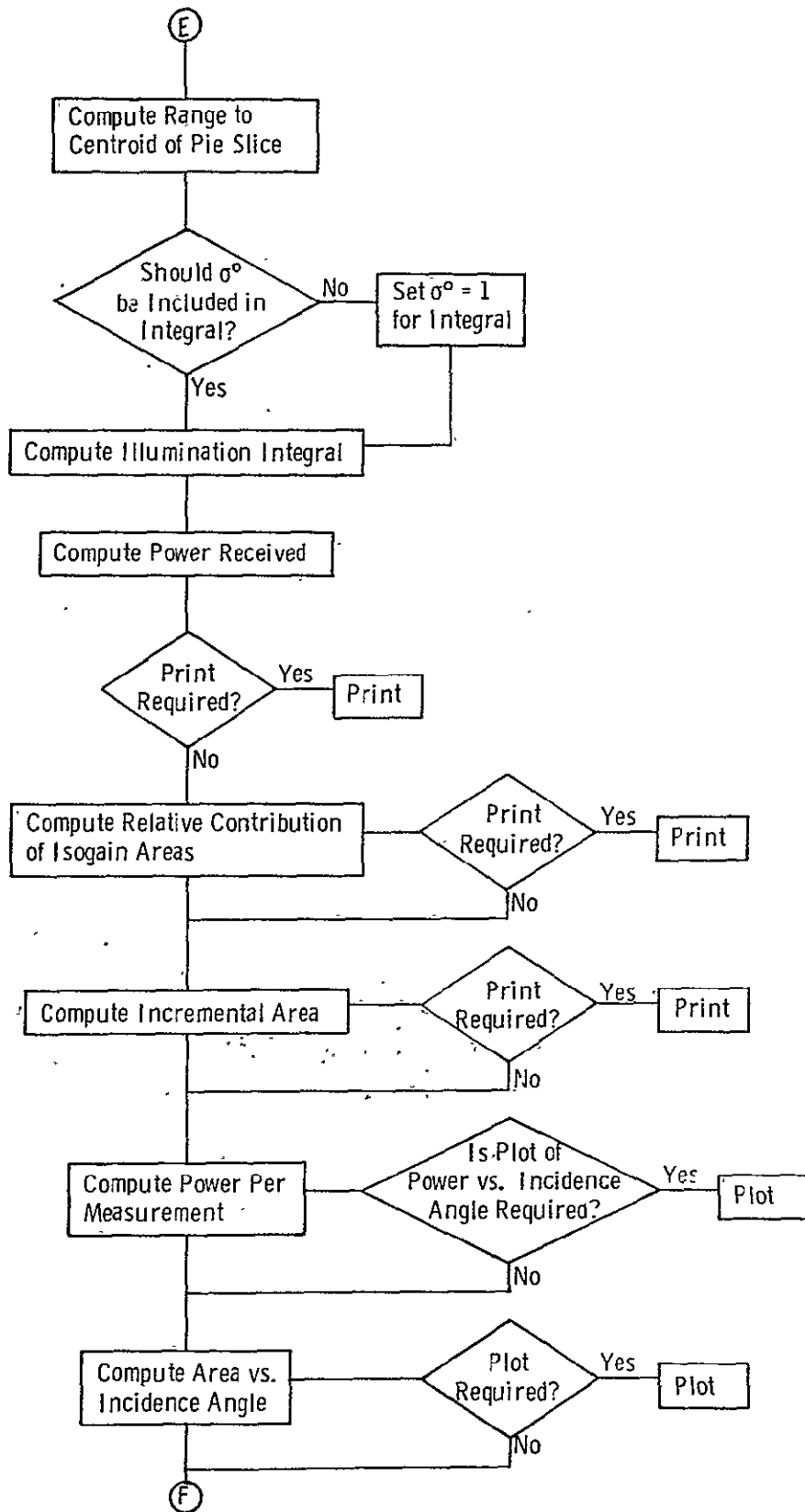


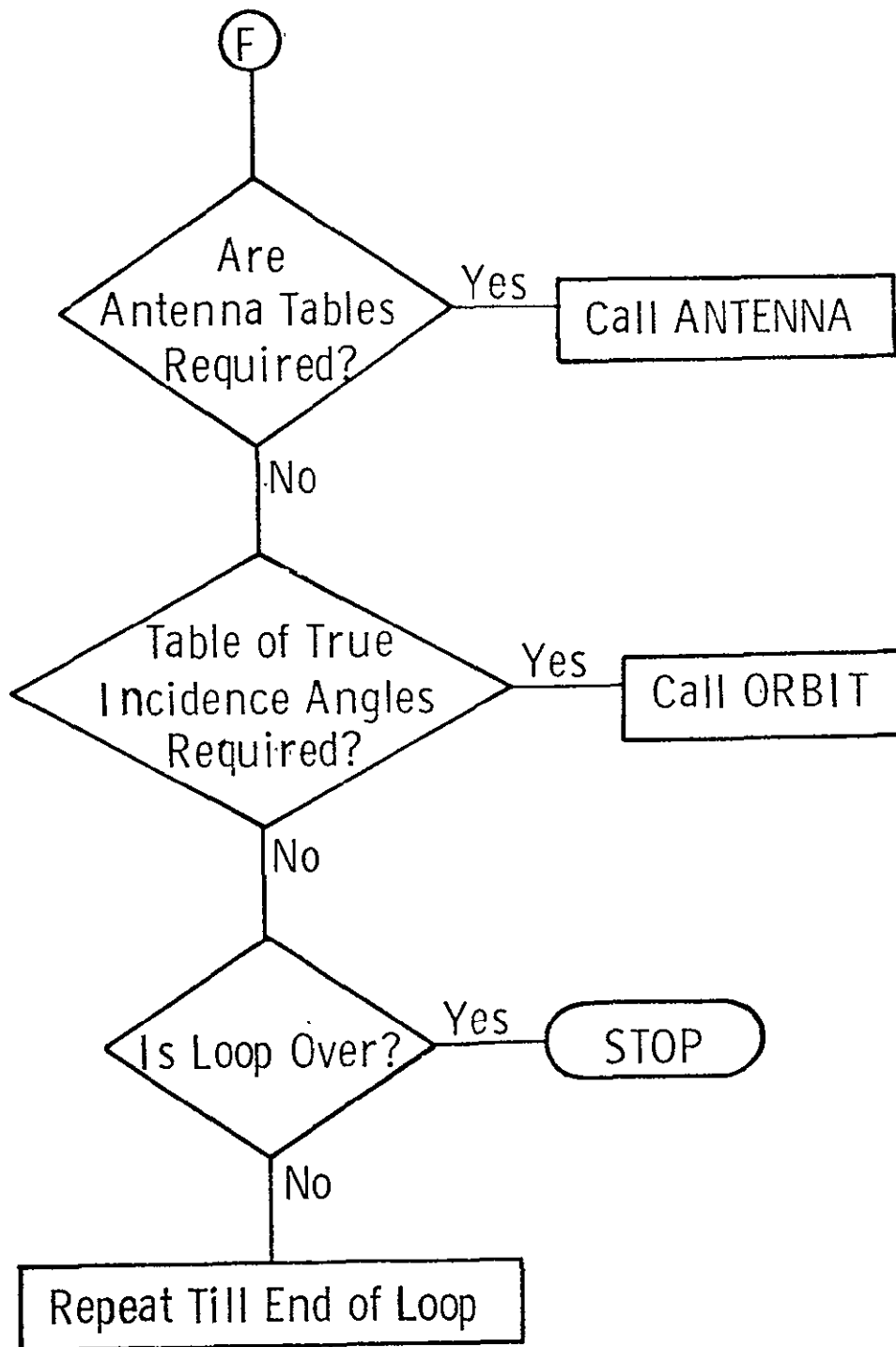


ORIGINAL PAGE IS  
OF POOR QUALITY









---

will not be substantial. In considering the orbit, the right ascension was considered to coincide with that of the Greenwich Meridian, this fact merely states that we are describing one particular orbit out of many possible ones. The transfer of the results obtained for this orbit to any other orbit are, however, trivial.

To compute the target area illuminated by the antenna beam, the loci was found of points on the earth's surface (in ECI coordinates and in latitude longitude) corresponding to a rotation in the azimuthal direction of the line of sight vector for angles off antenna boresight. The area enclosed by this loci of points for an off-boresight angle equal to the antenna half-beamwidth was the target area illuminated. The antenna beamwidth was computed in subroutine ANTENA. This antenna beamwidth was the one-way effective beamwidth for the radiometer operation and the two way effective beam width for the scatterometer operation. To further study the shape of the footprints (iso-gain contours), the contours produced by extending the off-boresight angle to  $1.5^\circ$  in steps of  $0.1^\circ$  were computed. These contours (in latitude, longitude) can be plotted by storing data on tape for later plotting on a Benson-Lehner Incremental Plotter. Subroutine SQUARE takes care of the dimensions of the plots. The range to each point and the doppler frequency were computed.

To get the illumination integral, in eq. (1), the area within two isogain contours was weighted by the average two-way gain of the two gain contours. The two-way gain for any off boresight angle was computed by the function GAIN. Dividing by the fourth power of average range to each isogain area gives the illumination integral. The  $\sigma^\circ$  value was accessed from the ground truth files and returned by the function DSCATC. This function accesses the appropriate point in the grid and multiplies the number (ranging from 0 to 1) by the  $\sigma^\circ(\gamma)$  for one of the two chosen categories and, one minus the number by the  $\sigma^\circ(\gamma)$  of the second category. The combined average then is the differential backscattering coefficient for that cell. The  $\sigma^\circ(\gamma)$  for both categories is stored in function DSCATC and can be modified. The summation of the integrations for all isogain areas up to the effective antenna beamwidth (or the first null in the antenna beam pattern) multiplied by fixed values of  $\lambda^2$ ,  $L_{tr}$  and  $L_{atm}$  provided the  $P_r/P_t$  ratio.

The received power per pulse is computed by multiplying the illumination ratio by  $P_t$ . The total power received per measurement is next computed by multiplying by the number of pulses in the measurement period. The total area illuminated is computed on a per pulse basis.

The incremental area due to antenna and vehicle motion is next found by numerically computing the area lying outside the intersection of the footprints corres-

ponding to the first and last pulses in the measurement. The relative contribution of each isogain area (indexed by the off-boresight nadir angle) integral to the illumination is computed. The area per measurement vs. incidence angle or vs. angular displacement from boresight can both be plotted by subroutine PLTHRZ.

The radiometric temperature seen at the antenna is computed by accessing a value of brightness temperature from a file, much the same way as  $\theta$  is accessed. The total integrated radiometer temperature (weighted by antenna beam) is printed out. The weather effects and cross polarized return have not been simulated at present, but a routine is being written to include these effects.

The true incidence angle corresponding to an antenna pointing angle is found by routine ORBIT.

To follow the formulae of the program, a table of symbols is provided in Table D.2. The program listing is fairly well documented with COMMENT cards and should be easy to follow. A brief statement of purpose, the inputs and outputs of the sub-routines is provided below.

#### 4.2.4 Antenna

This subroutine fits a polynomial to the antenna pattern provided in G. E.'s Critical Design Review Document, and then computes the beam efficiency and effective beamwidth for different levels of side lobes. The beam efficiency and effective beamwidth for a two-way pattern is also computed.

The E plane pattern was used because it was the wider of the two. The curve to fit the antenna pattern is a piece-wise fit over the entire  $180^\circ$  angle.

$$P = 1/3 (-5.3y + 9.7582y^2 - 10.605y^3 + 3.3708y^4 - 0.5752y^5 + 0.0333y^6)$$

$y = 2x,$	$0 \leq x < 3^\circ$	P in number
$P = -28.0 - 9.0/3(x - 3.0)$	$3^\circ \leq x < 6^\circ$	P in dB
$P = -37.0 - 25.0/30(x - 6)$	$6^\circ \leq x < 36^\circ$	P in dB
$P = -62.0$	$36^\circ \leq x < 72^\circ$	P in dB
$P = -62.0 + 11.0(\cos 3(x - 102.0)^5)$	$72^\circ \leq x < 132^\circ$	P in dB
$P = -56.0$	$132^\circ \leq x < 138^\circ$	P in dB
$P = -61.0$	$138^\circ \leq x < 180^\circ$	P in dB

## TABLE D.2

## TABLE OF SYMBOLS

<u>Symbol</u>	<u>Dimension</u>	
A	15, 37	Area of each isogain pie with $\phi = 10^\circ$ spacings
AA	8	Incremental area per isogain contour
AMINI		Subroutine (system) for finding minimum
AMAXI		Subroutine (system) for finding maximum
AREA	15	Area of each isogain contour
AREAB	50	Array for plotting area vs. beamwidth
AREAC	50	Array for plotting area vs. incidence angle
ASCAT		Average scattering coefficient of footprint
ATAN2*		Subroutine (system) to compute arc tangent
AXGRID		Average deviation of contour from centroid (long.)
AYGRID		Average deviation of contour from (lat.)
ANTENA*		Subroutine to compute antenna parameters
BANGLE		Dummy variable
BIAS	7	Index for accessing bias time per scan
CARDS		Logical variable to punch output
CNTRLA		Latitude of point corresponding to boresight
CNTRLO		Longitude of point corresponding to boresight
COMAND		Variable to option to write if PRINT
CROXH		Upper location of cross hair on plot (long.)
CROXL		Lower location of cross hair on plot (long.)
CROSYH		Upper location of cross hair on plot (lat.)
CROSYL		Lower location of cross hair on plot (lat.)
DANGLE		Dummy variable
DELTAT		Angle of travel in long., lat.
DELTAV		Angle of travel excluding earth's rotation
DMIN		Maximum negative deviation between assigned categories and actual categories in cell
DMAX		Max. + ve. deviation between assigned and actual categories.
DMAXTO		Average + ve. deviation between assigned and actual categories.

DMINTO		Average - ve. deviation between assigned and actual categories
DOMEGA		Dummy variable
DOPP		Doppler frequency spread
DSIGMA		Dummy variable
ERROR		Random error
F		True anomaly
FCNTLA		Dummy variable
FCNTLO		Dummy variable
FD		Doppler frequency
FDMAX		Maximum Doppler frequency
FDMIN		Minimum Doppler frequency
FILE1	50,50	Ground truth file
FILE2	50,50	Ground truth file
FILECI*		Subroutine to compute vehicle velocity and position
FILPSM*		Subroutine to transform coordinates
FILPSV*		Subroutine to transform coordinates
FILPSZ*		Subroutine to transform coordinates
FILSIG*		Subroutine to transform coordinates
FLIVEL		Flight velocity
FORCED		Variable to pick type of ground truth
G		Time bias to measurement time
GA		Gain
GAMMA		Incidence angle
GMU		Gravitational force
I5		Index on loop
ICN		Counter
IEND		Counter
IF		Index on loop
IFILL		Counter
IFOOT		Counter
ILINE		Counter
INDEX		Counter

IPAPER	Counter
ISCNND	Limit of loop (counter)
ISCNST	Start of loop
ISCUP	Increment in loop
ISMEAR	Limit of loop
IST	Variable for computing random numbers
ISTART	Start index on loop
ISWICH	Switches
IXMING	Minimum of longitude (for plotting)
IYMING	Minimum of latitude (for plotting)
JBIAS	Time bias index
KK	Dummy variable
KKK	Dummy variable
L1	Counter
L2	Counter
LAPSE	End counter of loop
LAT	Latitude of target joint (g.t.**coordinates)
LALO	Minimum latitude of footprint (g.t. coordinates)
LAHI	Maximum latitude of footprint (g.t. coordinates)
LNUM	Dummy
LL	End of loop
LOOP	End of loop
LONG	Longitude of target point
LOHI	Maximum long. of footprint
LOLO	Minimum long. of footprint
LTR*	Subroutine for plotting
MFG	Dummy variable for plotting
MGRAF	Variable - option to plot $\sigma^{\circ}$ vs. $\Theta$
MSIM	Variable to pick out ground truth
MPRD*	Subroutine to compute product of 2 matrices

13

NFILE		Variable to pick g.t. file
NFIN		End of loop
NN		Counter
NOPSHN		End of loop
NSCAN		Index of loop
NSTART	5	Index to determine antenna pointing angle
NUMB		End of loop
NUMF		Index to loop
NUMI		Index to loop
NUMLUP		Number of loops
OINC		Orbital inclination angle
OMEGA		Roll
ORVRA		Orbital radius
ORVEL		Orbital velocity
P	3	Unit vector
PERCEN		Percentage of a category
PERILL		Percentage illumination (isogain area)
PERTOL		Total percentage of category in cell
PHI		Azimuth angle w.r.t. antenna boresight
PHIGM	3,3	Matrix for coord. transformation
PHIVEC	3,3	Matrix for coord. transformation
PHIM		Missalignment error-yaw
PHIVEH		Transformation error-yaw
PHIZLV	3,3	Transformation to ZLV coordinates
PILUM	15	Illumination integral
PILUM2	15	Illumination integral (no $\sigma^0$ )
PILUMB	50	Array for plotting PILUM
PITCH		Pitch
PLAT		Latitude of target point
PLATHI		Max. lat. of target point
PLATLO		Min. lat. of target point
PLONG		Longitude of target point
PLONLO		Min. longitude of target point

PLONHI		Max. longitude of target point
PLTHRZ*		Subroutine to plot
PLTMFY*		Subroutine (system) for plotting
PRECOD		Power recorded
PROVEL	3	Projected velocity on earth
POSI	3	Position of spacecraft in ECI
POWER		Power returned
POWERC	80	Array for plotting power
POWR2		Power excluding $\sigma^0$
PSIM		Missalignment error -roll
PSIGM	3,3	Transformation to g.m. axes
PSIVEC	3,3	Transformation to vehicle axes
PSIVEH		Transformation error (g.m. to veh.) -roll
PSTATS		Variable used to repeat input
PVECTR	3	Unit vector
PSIZLV		Transformation error ZLV to ECI
Q		Dummy variable
R	15,37	Range
RADIUS		Radius of earth
RATRAD		Ratio of earth to orbital radius
RATEMP		Radiometric temperature
RANDOM		Variable to pick a random field
RANGE		Range
RCENTR		Range to center
RO	3,3	Dummy array used for storage
ROLL		Roll
ROMEGA	3,3	Dummy array used for storage
RP	3	Unit pointing vector
RSCR	3,3	Dummy array
RSIGMA	3,3	Dummy array

SAVE1		Variable to compute percentage categories
SAVE2		Variable to compute percentage categories
SCAN*		Subroutine to compute In-track Contiguous Scan
SCANCR*		Subroutine to compare Cross-Track Contiguous Scan
SCRACH		Scratch location
SCATDB		Scattering coefficient in dB
SDMAX		Dummy variable to compute FDMAX
SDMIN		Dummy variable to compute FDMIN
SERROR		Error in assigning $\sigma^0$
SIGDB		Return signal in dB
SIGMA		Pitch
SIGMAZ	49	Array for plotting $\sigma^0$ vs. $\Theta$ for trees
SIGPWR		Signal power returned
SIGPW2		Signal power (excluding $\sigma^0$ )
SS		Dummy variable
SUBLAT		Subsatellite point latitude
SUBLON		Subsatellite point longitude
SUBSAT	3	Subsatellite coordinates in ECI
SUBVEL	3	Velocity of subsatellite point in ECI
SZ		Dummy variable
SZERO		$\sigma^0$ deduced from illumination integral
THETAH		Transformation error-pitch
THETAM		Missalignment (antenna to g.m.) pitch
THETAG	3,3	Transformation to vehicle coordinates (pitch)
THETA V	3,3	Transformation to ZLV (pitch)
THETA Z	3,3	Transformation to ECI coordinates (pitch)
TIME		Time from mode turn-on
TIMEO		Time from orbital position
TIMSCN		Time at start of pulse
TISCAN	5	Time at start of scan
TOTILL		Total illumination
TOTDB		Total illumination in dB
TRUINC		True incidence angle

VEHPLO		Vehicle position in latitude at start
VEHPLT		Vehicle position at time t
VELI	3	Velocity of spacecraft in ECI
VPLAT		Vehicle position in lat.
VPLONG		Vehicle position in long.
W	15,37,2	Displacement of points on contour from center (lat. lon.
WE		Earth's rotational velocity
WW	15,37,2	Dummy array to compute incremental area
WWW	15,37,2	Dummy array to compute incremental area
WWWW		Dummy variable
X		Orbital radius
XD		Dimension of plot
XDN		Dimension of lettering used for plotting
XMG		Used for plotting
XMAX		Used for plotting
XMIN		Used for plotting
XXMG		Used for plotting
XGRID		Location of target w.r.t. g.t. file (long. )
Y		
YDN		Used in plotting
YMG		Used in plotting
YGRID		Location of target w.r.t. g. t. file (lat.)
YMAX		Used in plotting
YMXG		Used in plotting
YMIN		Used in plotting
Z		Dummy variable

---

\* Subprograms

\*\* g. t. stands for ground truth and g. t. coordinates are memory location pointers in the ground truth files.

where

P = relative power level

X = angle off boresight

The effect of side lobe levels upon beam efficiency was found by tabulating the beam efficiency versus a constant (0.5 to 2.5) which multiplied the entire side lobe level.

#### 4.2.5 Subroutines for Transforming from one Coordinate Space to Another

The following subroutines are called by the Mainline of the program and they transform a unit vector from one coordinate space to another.

##### 4.2.5.1 FILSIG

This subroutine transforms a unit vector from the antenna-coordinate space to the gimbal-mount-coordinate space. It takes into account the antenna pitch and roll, and provides two three-by-three matrices which perform the transformation.

INPUTS — Pitch and roll angles of antenna

OUTPUT — Two 3 x 3 matrices for transformation

##### 4.2.5.2 FILPSM

This subroutine transforms a unit vector in the vehicle centered coordinate space. It takes into account the misalignment between the gimbal-mount and the vehicle center and provides three 3 x 3 matrices.

INPUTS — Yaw, pitch and roll misalignment errors

OUTPUT — Three 3 x 3 matrices for transformation

##### 4.2.5.3 FILRSV

This subroutine transforms a unit vector in vehicle-centered coordinate space to a unit vector in Z-local-vertical coordinate space. It takes into account the attitude errors of yaw, pitch, and roll, and provides three 3 x 3 matrices for transformation.

INPUTS — Vehicle attitude errors in yaw, pitch, and roll

OUTPUT — Three 3 x 3 matrices for transformation

#### 4.2.5.4 FILPSZ

This subroutine transforms a unit vector in Z-local-vertical coordinate space into Earth centered-inertial coordinate space. It takes into account the angular position in orbit and height of orbit, and orbital inclination and it provides three  $3 \times 3$  matrices for transformation.

INPUTS — Angular position in orbit, height of orbit, angular inclination of orbit  
OUTPUT — Three  $3 \times 3$  matrices for transformation

#### 4.2.6 FILECI

This subroutine computes the position and velocity vectors of the spacecraft in ECI coordinates.

INPUTS — Orbital height, inclination of orbit, angular position in orbit, velocity of spacecraft.

OUTPUT — Velocity and position vectors in ECI coordinates.

#### 4.2.7 MINV

This subroutine computes the inverse of a  $3 \times 3$  matrix. It must be symmetric.

INPUTS — A  $3 \times 3$  matrix.

OUTPUT — The inverse of the INPUT matrix.

#### 4.2.8 MPRD

This subroutine computes the product of two matrices.

INPUTS — The two matrices, number of rows and columns of first, columns of second.

OUTPUTS — The product of the two INPUT matrices.

#### 4.2.9 SQUARE

This subroutine is called upon to set up the boundaries of an individual plot output. It fills up a tape to be used for plotting on the Benson-Lehner Plotter. It provides a rectangular boundary of programmable size and sets a cross hair in the middle for congruencing the plot with a calibration grid.

INPUTS — Dimensions of rectangular plot, in x and y coordinates (inches) maximum value for plot in x and y coordinates.

OUTPUT — A plot of a rectangle of required dimensions and a congruency cross hair.

#### 4.2.10 PLTHRZ\*

This routine plots the value of an element in an array, against its location in the array.

INPUTS — Dimensioned array, dimension of array, maximum and minimum value of any element in array, maximum and minimum locations of interest in array, output file, granularity or number of lines for values of array.

OUTPUT — Plot of values of elements of the array versus their location in area.

#### 4.2.11 SCAN

This subroutine simulates the antenna movement according to the in-track contiguous scan. It updates the orbital position and provides the pitch angle corresponding to the time from turn on of mode.

INPUTS — Angular position in orbit, time from start, pulse number

OUTPUT — angular position, pitch angle

#### 4.2.12 SCANCR

This subroutine simulates the antenna movement in the cross track contiguous mode. It takes into account the time from start, whether moving left or right (called scan 1 or scan 2 respectively) pulse number and angular position in orbit. It updates the angular position in orbit.

INPUTS — Angular position in orbit, pulse number, scan number, time from start,

OUTPUT — Pitch and roll angles of antenna, updated orbital angular position of spacecraft.

#### 4.2.13 RADMET

This routine was written to simulate the radiometric temperature of a target. A 50 x 50 grid was made up and terrain features assigned. The subroutine accesses the right point in the grid and converts the terrain value to a radiometric temperature for the particular angle of incidence.

INPUTS — Latitude, longitude of target point, angle of incidence

OUTPUT — Radiometric temperature of target point for corresponding angle of incidence

---

\*Written by Tom James, Kansas University (now with Sandia Corp., Albuquerque).

#### 4.2.14 DSCATC

This routine was written to simulate the backscattering coefficient of a target. A 50 x 50 grid was made up and terrain features assigned. The routine accesses the required point on the grid and computes the backscattering coefficient for that angle.

INPUTS — Latitude, longitude of target point, angle of incidence

OUTPUT —  $\sigma^0$  value of target point for that angle of incidence

#### 4.2.15 GAIN

This function computes the one-way or two-way gain of the antenna to the target point. It takes into account the nadir angle only. The antenna pattern (in the CDR document) has been fitted by a polynomial.

INPUTS - Angle  $\theta$  (nadir angle) and whether Radiometer operation or Scatterometer

OUTPUT - Gain to that point (one way or two way).

#### 4.2.16 ORBIT

This subroutine computes the true incidence angle for given antenna pointing angle. The output is a table of true incidence angle versus antenna pointing angle (from  $0^\circ$  to  $70^\circ$ ).

#### 4.2.17 LTR

This subroutine prints the ordinates and titles for the plots made by the Benson-Lehner Plotter.

INPUTS - Dimensions of plot, size of letters, number of characters to be printed.

OUTPUT - Labeling of the plot.

#### 4.2.18 CHAR

This is a subroutine called by LTR which prepares the printout file format.

INPUT - Ordinate

OUTPUT - Transliterated ordinate.

## APPENDIX 5

This Appendix contains computer listings of two computer programs:

1. A simulation study of S-193 Radiometer/Scatterometer in orbit.  
Called Skylab Orbital Data.
2. A simulation program to predict the atmospheric effects on the  
S-193 radiometer/scatterometer.

Appendix Five  
Listing of Computer Programs

```
C           S K Y L A B O R B I T A L   D A T A
C
C           WRITTEN BY   ARUN SOBTI
C
C           $      OPTION  FORTRAN
C           $      FORTRAN NDECK
C           $      LIMITS  ,35K
C           $      INCODE  IBMF
C           SKYLAB,6-6-71   S-K-Y-L-A-B O-R-B-I-T-A-L D-A-T-A
C
C*****
C           THIS PROGRAM PACKAGE COMPUTES THE TRANSFORMATION OF A UNIT VECTOR
C           IN THE ANTENA COORDINATE SPACE TO A UNIT VECTOR IN ANY OTHER
C           COORDINATE SPACE CONSIDERED ON THE SATELITE OR TO THE EARTH
C           CENTERED INERTIAL COORDINATE SPACE.
C           IT WILL ALSO COMPUTE THE POSITION AND VELOCITY VECTOR OF THE
C           SATELITE IN ECI COORDINATES. THIS CAN BE DONE BY PROVIDING THE
C           ORBITAL INCLINATION ANGLE, THE TRUE ANOMALY AND THE VELOCITY OF
C           THE SPACECRAFT IN THE A CIRCULAR ORBIT.
C           THE PROGRAM ALSO COMPUTES THE RANGE OF THE TARGET FROM THE
C           SATELITE FOR EACH ANGLE OF ANTENA ORIENTATION. IT THEN FINDS THE
C           POSITION VECTOR OF THE TARGET POINT IN ECI COORDINATES. IT CAN
C           THUS GENERATE THE FOOTPRINT ILLUMINATED FOR ANY BEAMWIDTH AND
C           FIND THE CENTROID OF THE FOOTPRINT.
C           IT CAN ALSO PROVIDE THE TRUE INCIDENCE ANGLE FOR EACH VALUE
C           OF THE ANGLE GAMMA CONSIDERED-GAMMA IS THE ANGLE BETWEEN THE
C           UNIT LOS VECTOR AND THE LOCAL VERTICAL Z-AXIS.
C           THE SPACECRAFT PARAMETERS ARE AVAILABLE IN EITHER ECI OR
C           GEOGRAPHIC COORDINATES. THE POSITION AND VELOCITY PROJECTED ON THE
C           EARTH'S SURFACE ARE ALSO COMPUTED. THE PARAMETERS OF THE SLB-
```

**ORIGINAL PAGE IS  
OF POOR QUALITY**

C SATELITE POINT CAN ALSO BE PRINTED OUT.  
 C THE ABOVE VALUES CAN BE PRINTED OUT IN PIECE OR IN TOTAL UPON  
 C OPTIONS REQUESTED IN THE DATA CARDS. THE SCANNING MODE IS ALSO  
 C SPECIFIED IN THE DATA CARDS AND IS HANDLED ACCORDINGLY.  
 C THE NON-CONTIGUOUS MODES BOTH INTRACK AND CROSS TRACK CAN BE  
 C HANDLED, THE CONTIGUOUS MODES AS SPECIFIED IN THE C.C.R CAN ALSO  
 C BE HANDLED.  
 C  
 C THE FOOTPRINT IN ECI COORDINATES IS THEN CONVERTED TO LATITUDE  
 C AND LONGITUDE AND THE ILLUMINATION INTEGRAL COMPUTED.  
 C THE INCREMENTAL AREA PER SCAN MEASUREMENT IS COMPUTED, A PLOT OF AREA  
 C VERSUS INCIDENCE ANGLE OF POWER VERSUS INCIDENCE ANGLE ARE AVAILABLE  
 C UPON REQUEST. A SIMULATION OF GROUND TRUTH IN TERMS OF ESTIMATING  
 C PROPORTIONS OF A CATEGORY IN A CELL CAN BE FED TO MULTIPLY THE  
 C THE ILLUMINATION INTEGRAL TO GET THE POWER RETURN  
 C THE ARGUMENTS ARE EXPLAINED IN A WRITE-UP AVAILABLE, OTHERWISE CO  
 C NSULT A REPORT WRITTEN ON THE PROGRAMS.

C\*\*\*\*\*

C  
 DIMENSION PVECTP(3), P(3), PSIGMA(3,3), ROMEGA(3,3), ROTAT(3,3),  
 1 PSIGM(3,3), PHIGM(3,3), THETAG(3,3), PSIVC(3,3), PHIVC(3,3),  
 2 THETA(3,3), PSIZLV(3,3), PHIZLV(3,3), THETAZ(3,3), PO(3,3), RSCR(3,3)  
 3 ,VELI(3), POSI(3), PP(3), ISWICH(13), SUBSAT(3), PRCVL(3), SLBVEL(3),  
 4 FLIVL(3), R(15,37), W(15,37,2), A(15,37), PILUM(15), APEA(15)  
 5, NSTART(5), POWERC(83), PILUM2(15), PICH(25), ROLE(25), PULSE(5),  
 6 AREAC(50), SIGMAZ(49), PILUMB(50), AREAB(50),  
 7 WW(15,37,2), AA(8), HWW(15,37,2), RATEMP(15), BIAS(7), TISCAN(5)  
 INTEGER COMAND, PNTOUT, REPEAT, PSTATS, CARDS, PANDGM, FORCED, PUNCH  
 1, FOTO, DRAW, CONST, ANG, XTC  
 COMMON FILE1(50,50), FILE2(53,53)

ORIGINAL PAGE IS  
OF POOR QUALITY

LOGICAL EOF

COMMON IST

C

C\*\*\*\*\*

C GMU--GRAVITATIONAL CONSTANT, X--ORBITAL RADIUS, WE--ANGULAR

C ROTATION OF THE EARTH IN RADIANS.

C NSTART IS A STARTING BIAS NUMBER IN MILLISECONDS USED FOR THE

C SCAN ROUTINE WHICH COMPUTES THE BIAS AND PITCH AND TRUE ANAMOLY.

C\*\*\*\*\*

C

DATA GMU,X,WE/3.986E5,6.811E3,7.292E-5/

DATA RADIUS/6373.3715/

DATA NSTART/0.342,805,1402,2076/

DATA BIAS/1.922,0.592,4.149,7.566,10.289,12.585,0.15/

DATA TISCAN /0.0,.342,1.007,1.604, 2.079/

DATA COMAND ,REPEAT,CARDS,FORCED,RANDOM/5HPRINT,6HREPEAT,5HFUNCH,

1 6HFORCED,6HRANDOM/

DATA XTC,ITNC/3HXTC,4HITNC/

DATA FOTO/4HORAW /

DATA NONLIN/6HNONLIN/

DATA CONST/5HCONST/

DATA PULSE/37.0,32.0,29.0,18.0,12.0/

C

C\*\*\*\*\*

C THE DIRECTORY OF SWITCH FUNCTIONS IS AS FOLLOWS--

C ISWICH(1)=1 IMPLIES THETA WILL ONLY BE EQUAL TO THE ANTENA BEAM

C WIDTH I.E. 0.727 DEGREES

C IF IN RADICMETER MODE THE BEAMWIDTH IS 1.01 DEGREES.

C ISWICH(2)=1 IMPLIES PCINT VECTOR AND GIMBAL MOUNT COORDINATES

C WILL NOT BE PRINTED

C ISWICH(3)=1 IMPLIES THE VECTOR IN VEHICLE COORDINATES WILL NOT  
 C BE PRINTED  
 C ISWICH(4)=1 IMPLIES THE VECTOR IN Z-LOCAL VERTICAL COORDINATES  
 C WILL NOT BE PRINTED  
 C ISWICH(5)=1 IMPLIES THE VECTOR IN ECI COOD WILL NOT BE PRINTED  
 C ISWICH(6)=1 IMPLIES THE POSITION AND VELOCITY VECTORS OF THE  
 C SPACECRAFT WILL NOT BE PRINTED  
 C ISWICH(7)=1 IMPLIES THAT POSITION OF POINT, RANGE, GAMMA, DOPPLER  
 C AND THE LATITUDE AND LONGITUDE OF THE POINT WILL NOT BE PRINTED  
 C ISWICH(8)=1 IMPLIES ANTENA CALCULATIONS ARE REQUIRED  
 C ISWICH(8)=2 IMPLIES THAT THE FOOTPRINT WILL BE SLEWED BY VEHICLE  
 C MOTION, THE NUMBER OF PULSES INTEGRATED IS READ IN.  
 C ISWICH(8)=3 IMPLIES CONTOURS OF CONSTANT GAIN ARE REQUIRED ON  
 C THE SAME PLOT.  
 C ISWICH(8)=4 IMPLIES CONTOURS OF 0-DB. GAIN FOR DIFFERENT  
 C PITCH ANGLES ARE REQUIRED ON THE SAME PLOT. (ROLL ANGLE X TOO).  
 C IF ISWICH(8) IS EITHER 0 OR 2 INDIVIDUAL PLOTS OF AREA OF ILLUM  
 C -INATION ARE NOT PLOTTED  
 C ISWICH(9)=1 IMPLIES THAT ANTENA CALCULATIONS ARE REQUIRED.  
 C ISWICH(9)=2 IMPLIES PLOTS OF AREA PER INCIDENCE ANGLE AND POWER  
 C PER PULSE PER INCIDENCE ANGLE ARE REQUIRED.  
 C ISWICH(10)=0 IMPLIES IN TRACK CONTIGUOUS  
 C ISWICH(10)=1 IMPLIES IN TRACK NON-CONTIGUOUS.  
 C ISWICH(10)=2 IMPLIES CROSS TRACK NON CONTIGUOUS  
 C ISWICH(10)=3 IMPLIES CROSS TRACK CONTIGUOUS  
 C ISWICH(11)=1 IMPLIES THAT THE PLOT ROUTINE IS REQUIRED.  
 C ISWICH(11)=0 IMPLIES THAT PLOTTING IS NOT REQUIRED.  
 C ISWICH(12)=1 IMPLIES THE MODE IS RADIOMETER  
 C  
 C CHECK FOR OPTIONS REQUIRED IN THE PROGRAM

```

C*****
C
      IST=1574326533
      CALL PLTMFY(2,0)
      IPAPER=0
C
      AB = 1.0/[0.9966466077]**2
C*****
C      FILE1 FILE2 ARE GROUND TRUTH FILES READ FROM FILES CREATED BY
C      ASSUMING A GROUND MODEL - THEY CONTAIN PERCENTAGES OF EACH CATEGORY
C      IN EACH CELL CONSIDERED
C      MSIM IS AN INDICATOR WHICH IF 1 MEANS RANDOM NUMBERS ARE TO BE
C      INPUT IN THE FIELD.
C      WRITE INPLT TO CHANGE THE ORBITAL HEIGHT, MGRAF-INDICATOR TO
C      PLOT GRAPH OF SIGMA VERSUS THETA OF ASSUMED CATEGORIES.
C*****
C
      READ(5,5111)MODE,N9N
5111  FORMAT( A6,I4)
      READ(5,5014) PNTOUT,PUNCH,ORAW
5014  FORMAT(3A5)
      READ(5,5015) ANG,IH,IM,SEC,NANT,ICAY
5015  FORMAT(A5,2I2,F5.2,A6,I3)
      WRITE(6,5110) IDAY,IH,IM,SEC,ANG,NANT
5110  FORMAT(1H0,' DAY ',I3,' START TIME ',2I2,F5.2,/' OPTION ',2A6)
      START=FLOAT(IH)+FLOAT(IM)/60.0+SEC/3600.0
      PRINT 5113,IDAY,IH,IM,SEC
5113  FORMAT(1X,25X,' DAY ',I3,' START TIME ',2I3,F8.4)
      READ(5,5005) (PICH(I),ROLE(I),I=1,N9N)
5005  FORMAT(10F7.3 )

```

```

5004 READ(5,5000)MSIM,MHITE,MGRAF,MADJX,MACJY
5000 FORMAT(1I2,1I3,1I1,2I2)
      IF(MSIM.EQ.(-1)) STOP
      IF(MSIM) 6010,6011,6012
6010 NFILE=FORCED
      GO TO 6011
6012 NFILE=RANDOM
6011 IF(MGRAF)6002,6003,6001
6001 SIGMAZ(1)=-5.0
      SIGMAZ(16)=-18.0+ALOG10(COS(15.6/57.2958)) *10.0
      SIGMAZ(33)=-19.0+ALOG10(COS(29.4/57.2958)) *10.0
      SIGMAZ(41)=-19.0+ALOG10(COS(40.1/57.2958)) *10.0
      SIGMAZ(48)=-19.0+ALOG10(COS(48.0/57.2958)) *10.0
      CALL PLTPRZ(SIGMAZ,50,55.6,-0.1,-30.0)
      WRITE(6,406)
406  FORMAT(25X,'SIGMA ZERO FOR TREES')
6000 X=6836.0+FLOAT(MHITE)
      IF(MSIM)5001,1121 ,1131
5001 DO 1 III=1,50
      DO 1 JJJ=1,50
      FILE1(III,JJJ)=0.0
1    IF((III/2*2).EQ.III.02.(JJJ-1)/2*2).EQ.(JJJ-1)) FILE1(III,JJJ)=1.
      GO TO 1121
1131 REAC(5,5008) FILE1
5008 FORMAT(20F4.2)
      DO 1118 I=1,50
      DO 1118 J=1,50
      IF(FILE1(I,J).LE.1.0) GO TO 1118
      IF(COMANS.NE.PNTCUT) GO TO 1117
      WRITE(6,1116) I,J,FILE1(I,J)

```

ORIGINAL PAGE IS  
OF POOR QUALITY

```

1116 FORMAT(1X,'FLAG AT ',2I6,' VALUE ',F8.3)
1117 FILE1(I,J)=1.0
1118 CONTINUE
C
C*****
C   NUMB--NUMBER OF SWITCH OPTIONS REQUIRED
C   ITERN--NUMBER OF ITERATIONS PER SWITCH OPTION
C*****
C
1121 READ(5,45) NUMB,ITERN
45  FORMAT(I2,I3)
      NCOUNT=0
      DO 300 NOPSHN=1,NUMB
      SF=0
      JF=0
C
C*****
C   NCOUNT IS A TALLY WHICH WHEN ONE CAUSES A NEW SQUARE TO BE
C   GENERATED WITH APPROPRIATE LIMITS, OTHERWISE THE SAME LIMITS ARE
C   USED.THIS OPTION IS ONLY WITH ISWICH(8)=4
C*****
C
      READ(5,50) ISWICH
50  FORMAT(13I1)
      DO 100 N=1,ITERN
      IFOOT=1
      WRITE(6,226)
226  FORMAT(1H0,33X,'1 2 3 4 5 6 7 8 9 0 1 2 3')
      WRITE(6,225) ISWICH
225  FORMAT(1H0, ' THE SWITCH OPTIONS CHOSEN ARE - ',13I2)

```

```

        IF (MODE.EQ.XTC) GO TO 2255
5109  IF((N-1)/05*15.EQ.(N-1))JP=0
        GO TO 2266
2255  IF((N-1)/12*12.EQ.(N-1))JP=0
2266  JP =JP+1
        IF(JP.EQ.1) SP=SP+1.0
        VEHPLT=C
        IF(ISWICH(12).EQ.1) NN=1
C*****
C      OMEGA--ROLL ABOUT X-AXIS IN GIMBAL-MOUNT SPACE.
C      SIGMA--PITCH ABOUT TRANSFORMED Y-AXIS IN G.M SPACE.
C      SIGMA--PITCH ABOUT TRANSFORMED Y-AXIS IN G.M SPACE.
C      PHIM,THETA,PSIM--MECHANICAL MISSALIGNMENT ERRORS ABOUT X,Y,Z
C      AXES RESPECTIVELY.
C      PHIVEH,THETAH,PSIVEH--YAW,PITCH AND ROLL ERRORS RESPECTIVELY.
C      OINC--ORBITAL INCLINATION, F--TRUE ANOMALY.
C*****
C
        READ(5,777) ID,X,PHIM,THETA,PSIM,PHIVEH,THETAH,PSIVEH,
        1 OINC,F,RA
777  FORMAT(I2,F6.2,9F8.4)
        IF(ANG.EQ.CONST) GO TO 522
707  READ(5,2) SIGMA,OMEGA
2    FORMAT(F6.2,F6.2)
        GO TO 5112
522  SIGMA=PICH(JP)
        OMEGA=ROLE(JP)
        IF(NONLIN .EQ.NANT) SIGMA = PICH(1)
        IF(NONLIN .EQ.NANT) OMEGA = ROLE(1)
5112  GMT=START+(SP-1.0)*15.25/3600.0

```

ORIGINAL PAGE IS  
OF POOR QUALITY.

```

GMT1=GMT+BIAS(JP+1)/3600.0
NH=GMT1
NM=(GMT1-FLOAT(NH))*60.0
SEC=(GMT1-FLOAT(NH)-FLOAT(NM)/60.0)*3600.0
WRITE(6,5222) NH,NM, SEC
5222 FORMAT(25X,/'START TIME OF MEASUREMENT IN GMT IS ',2I3,F5.2)
WRITE(6,52) SIGMA,OMEGA,PHIM,THETAM,PSIM,PHIVEH,THETAH,PSIVEH,
1 OINC,F,RA
52 FCFMAT(1H),8HSIGMA = ,F8.3,5X,8HOMEGA = ,F8.3,5X,7HPHIM = ,F7.3,5X
1 ,9HTHETAM = ,F7.3,5X,7HPSIM = ,F7.3,5X,9HPHIVEH = ,F7.3,5X,
2 /1X,9HTHETAH = ,F7.3,5X,9HPSIVEH = ,F8.4,5X,7HGOINC = ,F8.4,3X,
33HF = ,F10.6/,4HRA = ,F10.6)
PSTATS=1.0
IF(X.LT.6000.0) X=X+RADIUS
ORVEL=SQRT(GMU/X)
CRVRA=ORVEL*10.**3/X
RATRAD=RADIUS/X
XCRBIT=X-RADIUS
WRITE(6,5154)XORBIT
5154 FORMAT(1X,' THE ORBIT HEIGHT WAS ',F10.5)
IF(ISWICH(11).EQ.1) GO TO 9444
IF(ISWICH(13).NE.1) WRITE(6,996) NFILE,MSIM
IF(ISWICH(13).NE.1) WRITE(6,996) NFILE,MSIM
996 FORMAT(1H0,10X,'THE GROUND SIMULATION WAS FROM FILE ',A6,
1 '--DISTRIBUTION ',1I2)
IF(ISWICH(11).EQ.1) GO TO 9933
3444 IF(ISWICH(10).LT.2) WRITE(6,994)
994 FCFMAT(1H0,' IN TRACK IN TRACK ')
IF(ISWICH(10).GE.2) WRITE(6,993)
993 FORMAT(1H0,20X,'CROSS-TRACK CROSS-TRACK CROSS-TRACK ')

```

```

      IF(ISWICH(12).EQ.?) WRITE(6,991)
      IF(ISWICH(12).EQ.1) WRITE(6,992)
      IF(ISWICH(12).EQ.2) WRITE(6,993)
991  FORMAT(1H0,30X,'SCAT ONLY MODE ')
992  FORMAT(1H0,30X,'RAD ONLY MODE ')
993  FORMAT(1H0,30X,' SCAT AND RAD MODE ')
C
C*****
C   THE FOLLOWING IS DONE TO CONVERT DEGREE VALUES TO RADIANS
C*****
C
9933  SIGMA= SIGMA/57.2958
      OMEGA= OMEGA/57.2958
      F=F/57.2958
      OINC=OINC/57.2958
      THETAH= THETAH/57.2958
C   PSIM = PSIH/57.2958
C   PHIM = PHIH/57.2958
C   THETAM = THETAH/57.2958
      PSIVEH= PSIVEH/57.2958
      THETAM =-0.180/57.2958
      PHIM = -0.08/57.2958
      PSIM = 0.210/57.2958
      PSIM=0
      PHIM=0
      THETAM=0
      PHIVEH=PHIVEH/57.2958
      RAN = RA/57.2958
      ROTAT(1,1) = -SIN(F)*COS(RAN)-COS(F)*COS(OINC)*SIN(RAN)
      ROTAT(1,2) = SIN(OINC)*SIN(RAN)

```

```

      ROTAT(1,3) = COS(RAN)*COS(F)-SIN(F)*COS(OINC)*SIN(RAN)
      ROTAT(2,1) = -SIN(F)*SIN(RAN)+COS(F)*COS(OINC)*COS(RAN)
      ROTAT(2,2) = -SIN(OINC)*COS(PAN)
      ROTAT(2,3) = COS(F)*SIN(RAN)+SIN(F)*COS(RAN)*COS(OINC)
      ROTAT(3,1) = COS(F)*SIN(OINC)
      ROTAT(3,2) = COS(OINC)
      ROTAT(3,3) = SIN(F)*SIN(OINC)
      CALL MINV(ROTAT)
C
C*****
C   THE FOLLOWING CODING CALLS THE INDIVIDUAL SUBROUTINES WHICH
C   FILL THE MATRICES TO BE USED IN THE TRANSFORMATION.
C*****
C
7077 IF(ISWICH(10),EQ.1) CALL FILSIG(RSIGMA,SIGMA,ROMEGA,CMEGA)
      IF(ISWICH(10),EQ.2) CALL FILSIG(RSIGMA,SIGMA,RCMEGA,CMEGA)
      CALL FILPSM(PSIGM,PSIM,PHIGM,PHIM,THETAG,THETAM)
      CALL FILPSV(PSIVEC,PSIVEH,PHIVEC,PHIVEH,THETAV,THETAH)
C
C*****
C   LOOP FOR GETTING FOOTPRINT FOR EACH PULSE AND INITIALIZE LOOP
C   ISCNST--START OF SCAN (NUMBER). ISCNLC--END OF SCAN (NUMBER).
C   ISCLP--INCREMENT IN SCAN NUMBER TO BE COMPUTED.
C   ISCAN --LOOP INDEX FOR ADJUSTING FOR DIFFERENT SCANS.
C   TO BE SCANNED IN ONE COMPUTATION OF TOTAL SCAN NUMBER ISCAN.
C   ISMEAR--THE FINAL PULSE NUMBER FOR THAT LOOK ANGLE.
C   BIAS--THE TIME DELAY FROM START OF SCAN TO THE START OF THAT
C   PARTICULAR MEASUREMENT. IT ALWAYS ADDS TO INITIAL VALUE.
C   LAPSE--THE REQUIRED NUMBER OF PULSES BETWEEN TWO SUCCESSIVE
C   COMPUTATIONS.

```

```

C   NUMLUP--THE NUMBER OF PULSES PER LOOK ANGLE REQUIRED IN COMPUTATIO
C   N.IT ENSURES THAT FINAL CCMPUTATION OF LOOP WILL BE OF FINAL PULSE.
C   KK,KKK--COUNTERS TO KEEP TRACK.
C   JBIAS=1---INTPACK CONTIGUOUS,JBIAS=2---INTRACK NON CONT. 48.0DEG
C   JBIAS=3--INTC 40.1,JBIAS=4--INTC 29.4,JBIAS=5--INTC 15.6 JBIAS=6
C   --INTC 0.J DEG.,JBAS=7--CIC
C *****
C
      IF (ANG.EQ.CONST) G=F
      FS=F
      DCMEGA=OMEGA
      DSIGMA=SIGMA
      IF (ANG.EQ.CONST) GO TO 774
      READ (5,748) ISCNST,ISCNND,ISCUP
748  FORMAT(3I2)
      GC TO 775
774  ISCNST=1
      ISCNND=1
      ISCUP=1
775  IF (NCOUNT.GT.3) GO TO 7489
      IF (ISWICH(8).EQ.4) NCCOUNT=1
      GO TO 7498
7489  NCOUNT=3
7498  ICN=0.0
      FCMAX=-10000000
      SCMAX=-10000000
      FDMIN=1000000
      SCMIN=10000000
      GO 751 ISCAN=ISCNST,ISCNND,ISCUP
      IF (ISWICH(10).GE.1) WRITE (6,762) ISCAN

```

C. 8

ORIGINAL PAGE IS  
OF POOR QUALITY

```

762  FORMAT(1X,/31X,' SCAN NUMBER ',I2)
      IF((ISCAN-1).GE.1) IFCOT=IFCOT+1
      IF(PSTATS.EQ.REPEAT) GO TO 7515
      IF(ANG.NE.CONST) GO TO 7504
      NUMLUP=1
      NFIN=1
      IF(NONLIN.EQ.NANT) NFIN=5
      LAPSE=1
      ISTART=PULSE(JP)
      IF(NONLIN.EQ.NANT) ISTART=5
      ISMEAR=ISTART
      JBIAS=JP+1
      IF(NONLIN.EQ.NANT) JBIAS=1
      GO TO 7505
7504 READ(5,750) ISTART,ISMEAR,LAPSE,NUMLUP,NFIN,JBIAS,PSTATS,LNUM
750  FORMAT(6I2,A6,I2)
7505 IF(ISWICH(10).EQ.0) GO TO 7499
      GO TO 765
7499 NFIN=5
      JBIAS=1
      ISMEAR=9
      IF(ISCNND.GT.1) SIGMA=48.0/57.2958
765  IF(ISWICH(11).EQ.0) GO TO 7550
      IF(ISWICH(8).EQ.0.AND.SIGMA.LT.0.78.AND.OMEGA.LT.0.78) GO TO 7550
      IF(ISWICH(8).EQ.4.AND.NCOUNT.EQ.0) GO TO 7550
      READ(5,7500) XD,YD,SPREOX,SPREYD
7500 FORMAT(4F4.1)
7550 IF(ISWICH(10).EQ.3) GO TO 731
      IF(ANG.EQ.CONST) GO TO 729
      IF(ISWICH(10).EQ.1.OR.ISWICH(10).EQ.2) GO TO 730

```

```

G=FS+ORVRA*10.0**(-3)*(BIAS(JBIAS)+FLOAT(ISCAN-1)*4.0)
TIMSCN=BIAS(JBIAS)+FLCAT(ISCAN-1)*4.0
GO TO 729
730 G=FS+ORVRA*10.0**(-3)*(BIAS(JBIAS)+FLOAT(ISCAN-1)*15.25 -8.0)      C*
TIMSCN=BIAS(JBIAS)+FLOAT(ISCAN-1)*15.25 -8.0                          T**T
GO TO 729
731 G=FS+ORVRA*10.0**(-3)*(BIAS(JBIAS)+FLOAT(ISCAN-1)*2.12)
TIMSCN=BIAS(JBIAS)+FLOAT(ISCAN-1)*2.12
729 DC 749 NSCAN=1,NFIN
IF(NONLIN.EQ.NANT) SIGMA=FICH(NSCAN)/57.2958
IF(NONLIN.EQ.NANT) CALL FLSIG(RSIGMA,SIGMA,ROMEGA,CMEGA)
PLATLO=1000
PLONLO=1000
PLATHI=-1000
PLONHI=-1000
AFEAC(16*NSCAN)=0.0
KKK=1
POWER=0.0
SAVE2=0.0
POWR2=0.0
DC 150 NUMF=ISTART,ISHEAR,LAPSE
IF(ISWICH(8).EQ.4.AND.NUMF.NE.1) NCCUNT=NCCUNT+1
IF(ISWICH(10).EQ.3.AND.ISCAN.NE.1) NCCUNT=NCCUNT+1
IF(NSCAN.GT.1) NCCUNT=1
KK=NUMF
IF(KKK.EQ.NUMLUP) KK=ISHEAR
NMP=KK
IF(ISWICH(10).EQ.1.OR.ISWICH(10).EQ.2) GO TO 44
IF(ISWICH(10).EQ.3) GO TO 732
CALL SCAN(ISCAN,NSCAN,NSTART,KK,G,F,SIGMA)

```

```

TIME=TIMSCN+TISCAN(NSCAN)+FLOAT(KK-1)/125.0
GO TO 148
732 CALL SCANCR(ISCAN,NSCAN,KK,G,F,PITCH,ROLL,OSIGMA,COMEGA)
TIME=TIMSCN+FLOAT(NSCAN-1)*.1515+FLOAT(KK-1)/125.0
WRITE(6,149) PITCH,ROLL,NUMP,ISCAN
PITCH=PITCH/57.2958
ROLL=ROLL/57.2958
CALL FILSIG(RSIGMA,PITCH,ROMEGA,ROLL)
GO TO 46

C
C*****
C   SUBROUTINE GENERATES THE CONTIGUOUS SCAN AND RETURNS VALUES FOR
C   THE BIAS AND PITCH ANGLE FOR THE VARIOUS POINTS WITHIN THE SCAN
C   WHOSE VALUES ARE FED IN AS PARAMETERS TO SCAN.
C*****
C
148 WRITE(6,149) SIGMA,OMEGA,NUMP,ISCAN
149 FORMAT(1H0,10X,8H SIGMA = ,F6.3,5X,8H OMEGA = ,F7.3,5X,
1 24HCONT. MODE PULSE NUMBER ,3X,I2,3X,11HSCAN NUMBER ,3X,I2)
SIGMA=SIGMA/57.2958
CALL FILSIG(RSIGMA,SIGMA,ROMEGA,OMEGA)
GO TO 46
44 WRITE(6,128) NUMP
128 FORMAT(1H0,30X,9HON CONT. ,5X,14HPULSE NUMBER ,I2)
IF(KKK.EQ.NUMLUP) KK=ISMEAR
IF(ANG.EQ.CONST) GO TO 46
F=G+ORVRA*10.0**(-3)*FLOAT(KK-1)/125.0
TIME=TIMSCN+FLOAT(KK-1)/125.0
46 KKK=KKK+1
TIMEO=F/(ORVRA*10.0**(-3))

```

```

C*****
C   FILL UP MATRICES WHOSE VALUES DEPEND ON F
C*****
C
C   CALL FILEGI(POSI,VELI,X,F,GMU,OINC,WE,RA,TRAD)
43  CALL FILPSZ(PSIZLV,X,F,OINC,PHIZLV,THETAZ)
C
C*****
C   THE FOLLOWING CODING IS FOR MULTIPLYING THE INDIVIDUAL MATRICES
C   SO THAT THE RESULTING MATRIX WILL UPON PRE-MULTIPLYING PROVIDE
C   THE TRANSFORMED UNIT VECTOR.
C*****
C
C   CALL MPRD(RSIGMA,ROMEGA,RC,3,3,3)
C   CALL MPRD(THETAG,PSIGM,RSCR,3,3,3)
C   CALL MPRD(FSCR,PHIGM,FSIGM,3,3,3)
C   CALL MPRD(THETA V,PSIVEC,RSCR,3,3,3)
C   CALL MPRD(RSCR,PHIVEC,PSIVEC,3,3,3)
C   CALL MPRD(RSCP,PSIVEC,PHIVEC,3,3,3)
C   CALL MPRD(THETA V,PHIVEC,RSCP,3,3,3)
C   CALL MPRD(PSIZLV,THETA Z,RSCR,3,3,3)
C   CALL MPRD(RSCR,PHIZLV,PSIZLV,3,3,3)
C
C*****
C   WRITE HEADING
C*****
C
C   IF(ISWICH(6).NE.0) GO TO 131
C   WRITE(6,89)
80  FC9MAT(1HJ,/4CX,'VEHICLE POSITION AND VELOCITY')

```

ORIGINAL PAGE IS  
OF POOR QUALITY

```

      WRITE(6,8)
      8  FORMAT(1HC,10X,'POSITION VECTOR(VEH)',10X,'VELOCITY VECTOR(VEH)',
1  9X,'VPLAT',6X,'VPLONG',5X,'VLAT',7X,'VLONG'/3X,'X',10X,'Y',10X,
2  'Z',12X,'X',10X,'Y',10X,'Z')
C
C*****
C  THE POSITION AND VELOCITY VECTORS OF THE VEHICLE BOTH IN ECI
C  VPLONG--THE LONGITUDE OF THE VEHICLE AT A PARTICULAR F
C  AND GEOGRAPHIC COORDINATES ARE COMPUTED AND PRINTED OUT.C
C  VPLAT--POSITION(LATITUDE) OF VEHICLE
C  VLONG--LONGITUDINAL VELOCITY OF VEHICLE,VLAT--LATITUDAL VELOCITY
C  OF THE VEHICLE
C*****
C  THE FOLLOWING PARAMETERS WERE NOT CONSIDERED IN THE PROGRAM AND
C  THEIR VALUES WERE CONSIDERED ZERO.
C  PERIFOCAL ANGLE,RIGHT OF GREENWICH MERIDIAN,ECCENTRICITY.
C  SCRACH--JUST A SCRATCH LOCATION.
C*****
C
131  SCRACH=SQRT(POSI(1)**2+PGSI(2)**2)*AB
      VPLAT=ATAN2(POSI(3),SCRACH)
      VPLONG=ATAN2(POSI(2),FOSI(1))
      VLONG=ORVEL*(COS(VPLONG)*COS(OINC)*COS(F)+SIN(VPLONG)*SIN(F))
      DANGLE=COS(VPLONG)*COS(OINC)*COS(F)+SIN(VPLONG)*SIN(F)
      BANGLE=SQRT(1.0-DANGLE**2)
      IF(VPLONG.GT.1.57079) BANGLE=-BANGLE
      IF(VPLONG.GT.(-3.14159).AND.VPLONG.LT.(-1.57079)) BANGLE=-BANGLE
      DELTAV=ATAN2(BANGLE,DANGLE)
      VLAT=ORVEL*SIN(DELTAV)
      VPLONG=VPLONG*57.2958+RA

```

```

VCASH=360.C-VPLONG
VPLAT=VPLAT*57.2958
IF (ISCAN.EQ.1.AND.NSCAN.EQ.1.AND.NUMF.EQ.1) GPLAT=VPLAT
IF (ISCAN.EQ.1.AND.NSCAN.EQ.1.AND.NUMF.EQ.1) GPLONG=VPLONG
C
C*****
C THE SUBSATELITE POINT PARAMETERS ARE COMPUTED NEXT AND PRINTED
C OUT
C SUBSAT--POSITION VECTOR OF SUBSATELITE POINT IN ECI COORDINATES
C SUBVEL--THE VELOCITY OF THE POINT ON THE TRACK
C PROVEL--THE PROJECTED VELOCITY OF THE VEHICLE ON THE EARTH
C FLIVEL--THE RELATIVE VELOCITY IN ECI COORDINATES OF THE VEHICLE
C WITH RESPECT TO A POINT ON THE EARTH.
C*****
C
SUBSAT(1)=RATRAD *POSI(1)
SUBSAT(2)=RATRAD *POSI(2)
SUBSAT(3)=RATRAD *POSI(3)
PROVEL(1)=RATRAD *VELI(1)
PROVEL(2)=RATRAD *VELI(2)
PROVEL(3)=RATRAD *VELI(3)
SUBVEL(1)=-WE*SUBSAT(2)
SUBVEL(2)=WE*SUBSAT(1)
SUBVEL(3)=0.0
FLIVEL(1)=PROVEL(1)-SUBVEL(1)
FLIVEL(2)=PROVEL(2)-SUBVEL(2)
FLIVEL(3)=PROVEL(3)-SUBVEL(3)
VTLONG=VLONG-WE*X*CGS(VPLAT/57.2958)
DELTA=ATAN2(VLAT,VTLONG)*57.2958
F=F*57.2958

```

```

OINC=OINC*57.2958
IF(COMAND.EQ.PNTOLT) WRITE(6,7603) F,OINC,VLAT,VPLONG
7603 FORMAT(1H0,' F',F8.3,' INCLINATION ',F8.3,' LAT. VEL. ',F7.4,'
1LCNG. VEL ',F7.4)
DELTA V=DELTA V*57.2958
IF(COMAND.EQ.PNTOUT) WRITE(6,7605) DELTA V,DELTA T
7605 FORMAT(1H0,' DELTA V = ',F9.3,' DELTA T = ',F9.3)
F=F/57.2958
OINC=OINC/57.2958
IF(ISWICH(6).NE.0) GO TO 106
WRITE(6,81)
81 FORMAT(1H0,'/40X,'SUBSATELITE POINT PARAMETERS')
WRITE(6,7) POSI,VELI,VPLAT,VPLONG,VLAT,VLONG
7 FORMAT(1H),3(F7.2,4X),3(F7.4,4X),F9.4,4X,F9.4,4X,F8.4,4X F8.4)
F=F*57.2958
WRITE(6,82)
82 FORMAT(1H0,3X,'F',8X,'SUBSAT POINT POSITION',7X,'SUBSAT POINT VELO
1CITY',10X,'VEH PROJECTED VELOCITY',7X,'VEH RELATIVE VELOCITY'/
2 13X,3('X',9X,'Y',9X,'Z',9X),'X',9X,'Y',9X,'Z')
WRITE(6,83) F,SUBSAT,SUBVEL,PROVEL,FLIVEL
83 FORMAT(1H0,F9.5,2X,3(F7.1,3X),3(F7.4,3X),3(F7.4,3X),3(F7.4,3X))
F = F/57.2958
C
C*****
C WRITE HEADING
106 IF(ISWICH(2).EQ.1.AND.ISWICH(5).EQ.1) GO TO 115
C
C*****
WRITE(6,9)
9 FORMAT(1H0,'/16HCOORDINATE SPACE,6X,5HTHETA,4X,3HPhi,7X,

```

```

1 24HPCINT VECTOR, (X), (Y), (Z) /)
GO TO 117

C*****
C   LCOF ON THETA AND PHI, PHI IS THE ANGULAR ROTATION OF THE UNIT
C   LOS VECTOR ABOUT THE X-AXIS OF THE G.M SPACE AND THETA IS THE
C   ANGULAR ROTATION OF THE UNIT VECTOR ABOUT THE TRANSFORMED Y-AXIS
C   THERE IS AN OPTION IN THE PROGRAM BY WHICH EITHER THE 3DB BEAM
C   WIDTH VALUE OF THETA IS USED OR THE VALUE OF THETA IS INCREMENTED
C
C   THE FOLLOWING IS AN ATTEMPT TO FIND THE RIGHT OUTPUT -JUST A LOT
C   OF CHECKS TO PRINT HEADINGS AND COMPUTED RESULTS.
C   IT SHOULD BE NOTED THAT ALL RESULTS ARE AVAILABLE BECAUSE THE
C   COMPUTATION HAS TO BE SEQUENTIAL, THE OPTIONS ARE FOR MERELY
C   PRINTING THEM OUT
C*****
C
115 IF (ISWICH(7).EQ.0.OR.ISWICH(2).EQ.0) WRITE(6,116)
116 FORMAT(1H3,/40X,'DATA OF FOOTPRINT ON THE GROUND')
    L2=0.0
    L1=1.0
    IF (ISWICH(7).EQ.0) WRITE(6,119)
119 FORMAT(1H9,'THETA',6X,'PHI',7X,'GAMMA',8X,'RP(1)',8X,'RP(2)',
1 8X,'RP(3)',6X,'DOPPLER',10X,'PLAT',7X,'FLCNG',4X,'RANGE')
    MP=20
    IF (ISWICH(1).EQ.0) GO TO 117
    INDEX=0
    GO TO 101
117 LL=310
    GO TO 151
101 LL=30

```

**ORIGINAL PAGE IS  
OF POOR QUALITY**

```

151  DO 10 I=1,LL,MM
      THETA=0.01*FLOAT(I)-0.01
C
C*****
C      L2,L1,--TALLY COUNTERS FOR KEEPING TRACK OF FILLING LAT AND
C      LONG VALUES OF GAIN CONTOURS
C*****
C
      L2=1
      IF(LL.EQ.30) THETA=0.7
      IF(LL.EQ.30.AND.INDEX.EQ.1) THETA=0.7278
      IF(LL.EQ.30.AND.INDEX.EQ.1.AND.ISWICH(12).EQ.1) THETA=1.31
      INDEX=INDEX+1
200  THETA=THETA/57.2958
      IF(THETA.EQ.0.0) GO TO 205
      LOOP=370
      GO TO 201
205  LOOP=10
201  DO 20 J=1,LOOP,10
      IF(LOOP.EQ.10.AND.ISWICH(7).EQ.0) WRITE(6,202)
202  FORMAT(1H0,/40X,'THE CENTROID OF THE FOOTPRINT')
      PHI=FLOAT(J)-1.0
      PHI=PHI/57.2958
C
C*****
C      THE UNIT VECTOR IS DEFINED IN THE FOLLOWING 3 STATEMENTS.
C*****
C
      FVECTR(1)=SIN(THETA)*COS(PHI)
      PVECTR(2)=SIN(THETA)*SIN(PHI)

```

```

      PVECTR(3)=COS(THETA)
C
C*****
C      CONVERT TO DEGREES FOR PRINTOUT.
C*****
C
      THETA=THETA*57.2958
      PHI=PHI*57.2958
C
C*****
C      START TRANSFORMING AND WRITING OUT COORDINATES
C*****
C
      CALL MPRD(R0,PVECTR,P,3,3,1)
      P(2)=-P(2)
      P(3)=-P(3)
      IF(ISWICH(2).NE.0) GO TO 102
      WRITE(6,23) THETA,PHI,PVECTR
23  FORMAT(1HG,12HPPOINT VECTOR,10X,F5.2,5X,F5.2,3(5X,F7.2))
      WRITE(6,3) THETA,PHI,(P(K),K=1,3)
3   FORMAT(1H0,17HGINEAL MOUNT AXIS,5X,F4.2,5X,F6.2,3(5X,F7.2))
102 CALL MPRD(P SIGM,P,PVECTR,3,3,1)
      IF(ISWICH(3).NE.0) GO TO 103
      WRITE(6,4) THETA,PHI,(PVECTR(K),K=1,3)
4   FORMAT(1HC,12HVEHICAL AXIS,10X,F4.2,5X,F6.2,3(5X,F7.2))
103 CALL MPRD(P SIVEC,PVECTR,P,3,3,1)
C103 CALL MPRD(PHIVEC,PVECTR,P,3,3,1)
      P(2)=-P(2)
      P(3)=-P(3)
      IF(ISWICH(4).NE.0) GO TO 104

```

ORIGINAL PAGE IS  
OF POOR QUALITY

```

        WRITE(6,5)THETA,PHI,(F(K),K=1,3)
5      FORMAT(1H0,16HZ LOCAL VERTICAL,6X,F4.2,5X,F6.2,3(5X,F7.2))
104   CALL MPRD(Psizlv,P,PVECTR,3,3,1)
C104  CALL MPRD ( ROTAT,P,PVECTR,3,3,1)
        IF(ISWICH(5).NE.0) GO TO 105
        WRITE(6,6)THETA,PHI,(FVECTR(K),K=1,3)
6      FORMAT(1H0,15HECI COORDINATES7X,F4.2,5X,F6.2,3(5X,F7.2))
C*****
C      COMPUTE ANGLE GAMMA TO GET RANGE AND POSITION VECTOR OF THE TARGET
C      RCENTR--RANGE TO THE CENTROID USED TO FIND RANGE (AVERAGE).
C      FOR EACH DIFFERENTIAL AREA.
C*****
C
105   Q=P(3)
        Z=SQRT(1.-Q**2)
        GAMMA=ATANZ(Z,Q)
        YDUMY=X/RADIUS*SIN(GAMMA)
        GAMMAT=ATAN(YDUMY/SQRT(1.-YDUMY**2))
        IF(THETA.EQ.0.0.AND.PHI.EQ.0.0) TRUINC=GAMMAT
        RANGE=X*COS(GAMMA)*(1.-SQRT(1.-(1.-RATRAD**2)/COS(GAMMA)**2))
        IF(THETA.NE.0.0) GO TO 450
        RCENTR=RANGE
C
C*****
C      RP --DEFINES THE POSITION VECTOR OF THE TARGET IN ECI COORDINATES
C      POSI IS THE POSITION VECTOR OF THE SPACE CRAFT IN ECI COORDINATES
C*****
C
450   RP(1)=RANGE*PVECTR(1)+POSI(1)
        RP(2)=RANGE*PVECTR(2)+POSI(2)

```

```

RP(3)=RANGE*PVECTR(3)+PCSI(3)
C
C*****
C  FD--DOPPLER FFEQUENCY IN CPS
C  PLAT--LATITUDE OF POINT,PLONG--LONGITUDE OF THE POINT
C*****
C
  FD=2.C*((VELI(1)+HE*RF(2))*PVECTR(1)+(VELI(2)-HE*RF(1))*
1 PVECTR(2)+VELI(3)*PVECTR(3))/(2.1583*1E.0**(-5))
  FDMAX=AMAX1(FD,FDMAX)
  FDMIN=AMIN1(FD,FDMIN)
  DOPP=FDMAX-FDMIN
  IF(COMAND.NE.PNTOUT) GO TO 1339
  IF(FDMIN.LT.SDMIN.CR.FDMAX.GT.SDMAX) WRITE(6,693)
1  FITCH,ROLL,FDMIN,FDMAX ,DOPP
693  FORMAT(1HC,' PITCH ',F7.3,' ROLL ',F7.3,' FDMIN ',F10.3,' FDMAX '
1 ,F10.3,' DOPPLER ',F10.3)
1339  SDMAX=FDMAX
      SDMIN=FDMIN
      GAMMA=GAMMA*57.2958
      Y=SQRT(RP(1)**2+RP(2)**2)*AB
      PLAT=ATAN2(RP(3),Y)*57.2958
C  PLONG=ATAN2(RP(2),RP(1))*57.2958-HE*TIME *57.2958  +RA
      PLONG=ATAN2(RP(2),RP(1))*57.2958 +RA
      IF(ISWICH(1) .EQ. 0) GO TO 461
      ILINE=(ISCAN-1)/2
C
C*****
C  THE FOLLOING CODING IS FOR THE PLOT ROUTINE.IT FILLS LP THE TAPE
      IF(THETA.EQ.0.0) GO TO 589

```

ORIGINAL PAGE IS  
OF POOR QUALITY

```

GO TO 590

589 LAT=PLAT*10.0
LONG=PLONG*10.0

C
C*****
C PLOT. . NCTE--THIS CODING IS ONLY DONE IF ISWICH(11)=1.
C PLACE TO THE CENTROID OF THE FIRST FOOTPRINT TO BE DRAWN ON THAT
C PLOT IS SO CHOSEN THAT IT IS THE CLOSEST NUMBER TO ONE DECIMAL
C THE PLOT AND THE CENTROID OF EACH FOOTPRINT, THE CENTER OF THE
C THE INDIVIDUAL PLOTS AND PUTS CROSS-HAIRS TO MARK THE CENTER OF
C ACCORDING TO THE OPTICNS REQUESTED, IT PROVIDES THE LIMITS OF
IF((PLAT*10.0-FLOAT(LAT)).GE.0.5) LAT=LAT+1
IF((PLONG*10.0-FLOAT(LONG)).GE.0.5) LONG=LONG+1
XMIN=FLOAT(LONG)/10.0-SPREDX-FLOAT(MADJX)
XMAX=FLOAT(LONG)/10.0+SPREDX-FLOAT(MADJX)
YMIN=FLOAT(LAT)/10.0-SPRECY-FLOAT(MADJY)
YMAX=FLOAT(LAT)/10.0+SPRECY-FLOAT(MADJY)
IF(ISWICH(10).EQ.0) YMAX=YMAX-2.5
IF(ISWICH(10).EQ.0) YMIN=YMIN-2.5
IF(ISWICH(10).EQ.0) XMAX=XMAX-2.0
IF(ISWICH(10).EQ.0) XMIN=XMIN-2.0
IF(ISWICH(10).EQ.3) YMIN=YMIN+1.0
IF(ISWICH(10).EQ.3) YMAX=YMAX+1.0
IF(ISWICH(8).EQ.2.AND.NUMF.EQ.1) GO TO 2149
IF(ISWICH(8).EQ.3) GO TO 2149
IF(ISWICH(8).EQ.0.AND.ISCAN.EQ.1.AND.NSCAN.EQ.1.AND.NUMF.EQ.1)
1 GO TO 2149
IF(ISWICH(8).EQ.4.AND.NCOUNT.GT.1) GO TO 2149
GO TO 2148
2149 CALL SQUARE(XMIN,XMAX,YMIN,YMAX,XD,YC)

```

```

XDN=XD+1.5
YDN=YD+1.5
XMG=XMIN-(XMAX-XMIN)/XD*0.75
YMG=YMIN-(YMAX-YMIN)/YD*0.75
XMXG=XMAX+(XMAX-XMIN)/XD*0.75
YMXG=YMAX+(YMAX-YMIN)/YD*0.75
CALL PLOT(XMIN,YMIN,3)
CALL PLOT(XMG,YMG,-2)
CALL INPLOT(XMG,XMXG,YMG,YMXG,XDN,YDN)
IXMING=XMIN*100.0
IYMING=YMIN*100.0
IFG=F*100.0*57.2958
MFG=XORBIT*100.0
IDAYO=IDAY*100
CALL LTR (IXMING,IYMING,XMIN,YMIN,XMAX,YMAX,IFG,MFG,XC,YD,IDAYO)
2148 CROSSL=PLAT-0.01
CROSSH=PLAT+0.01
CROSYL=PLONG-0.01
CROSYH=PLONG+0.01
CALL PLOT(PLONG,CROSSL,3)
CALL PLOT(PLONG,CROSSH,2)
CALL PLOT(CROSYL,PLAT,3)
CALL PLOT(CROSYH,PLAT,2)
IFAPER=IPAPER+1
IF(ANG.NE.CONST.AND.ISWICH(10).NE.2) GO TO 126
SUBTL=VPLAT-0.05
SUBLTH=VPLAT+0.05
SUBLOL=VPLONG-0.05
SUBLOH=VPLONG+0.05
CALL PLOT(SUBLOL,VPLAT,3)

```

```

      CALL PLOT(SUBLON,VPLAT,2)
      CALL PLOT(VPLONG,SUBLTL,3)
      CALL PLOT(VPLONG,SUBLTH,2)
126  WRITE(6,127) PLONG,PLAT
127  FCRMAT(1H0, //25X,9HCENTROID ,F11.6,3X,F13.6)
      VEHPLT=VPLAT
      VEHPL0=VPLONG
      GO TO 461
590  IF(PHI.EQ.0.0) CALL PLOT(PLONG,PLAT,3)
      CALL PLOT(PLONG,PLAT,2)
461  IF(THETA.NE.0.0) GO TO 451
C
C*****
C   CNTRL0,CNTRLA--LONGITUDE AND LATITUDE OF CENTRICAL POINT.
C*****
C
453  CNTRLA=PLAT
      CNTRL0=PLONG
      IF(NUMP.NE.1) GO TO 451
      FCNTLA=CNTRLA
      FCNTL0=CNTRL0
C*****
C   THE RIGHT ASCENSION OF THE GREENWICH MERIDIAN HAS BEEN TAKEN AS 0
C*****
451  IF(ISWICH(7).NE.0) GO TO 107
      WRITE(6,21) THETA,PHI,GAMMA,RP,FC,PLAT,FLONG,RANGE
21   FCRMAT(1H0,F5.2,5X,F6.2,5X,F6.2,5X,3(F8.2,5X),F9.2,5X,F9.5,3X,
1    F9.5,4X,F6.1)
107  THETA=THETA/57.2958
C

```

```

C*****
C   A(I,J)--AREA OF ISOGAIN AREA OF FOOTPRINT
C   W(I,J,1)--THE LATITUDE OF POINT AT ANGLE THETA GIVEN BY VALUE OF I
C   AND ANGLE PHI IS GIVEN BY J. W(I,J,2)--THE LONGITUDE OF SAME
C   FCINT .R(I,J)- -THE RANGE TO THE POINT..PILUM(I)--THE ILLUM
C   INATION OF ISOGAIN ELLIPSE-INTEGRAL OF GAIN SQUARE*AREA/RANGE**4
C   AREA(I)--AREA OF ISOGAIN ELLIPSE.RCENTR--RANGE TO CENTROID.
C*****
C
      IF(I.EQ.1) GO TO 20
      WW(L1,L2,1)=PLAT
      WW(L1,L2,2)=PLONG
      W(L1,L2,1)=PLAT-CNTRLA
      W(L1,L2,2)=PLONG-CNTRL0
      PLATLO=AMIN1(PLATLO,PLAT)
      PLONLO=AMIN1(PLONLO,PLONG )
      PLATHI=AMAX1(PLATHI,PLAT)
      PLONHI=AMAX1(PLONG,PLONHI)
      P(L1,L2)=RANGE
452  L2=L2+1
20   CONTINUE
      L1=L1+1
C
C*****
C   THE FOLLOWING COJING IS DONE TO MOVE THE PEN TO THE NEXT POSITION
C   TO PLOT THE NEXT FIGURE.
C*****
C
      IF(ISWICH(11).EQ.0) GO TO 10
      IF(INDEX.NE.2.OR.ISWICH(8).NE.3) GO TO 10

```

ORIGINAL PAGE IS  
OF POOR QUALITY

```

        IF(IPAPER.NE.IPAPER/2*2) GO TO 595
594  CALL PLOT(C.0,0.0,-4)
        GO TO 10
595  CALL PLOT(0.0,0.0,-5)
10   CONTINUE
        IF(COMAND.EQ.PNTOUT) WRITE(6,7600) TIME
7600 FORMAT(1H0,20X,'TIME OF MEASUREMENT ',F7.3)
        IF(ISWICH(9).EQ.3) GO TO 150
        IF(COMMAND.EQ.PNTOUT) WRITE(6,475)
475  FORMAT(1HC,5HTHETA,8X,4HGAIN,15X,4HAREA,9X,
1 12HILLUMINATION,4X,9HTOTAL ILL,2X,1CHSIGMA-ZERO,4X,8HSIGMA-DB
2 2X,'GRID POINT')
        SIGPWR=0.0
        SAVE1=0.0
        TCTILL=C.0
        SIGPW2=C.0
        IF(ISWICH(1).EQ.1) GO TO 575
        NUMI=LL/MM
        GO TO 576
575  NUMI=1
576  GO 503 I=1,NUMI
        AXGRID=C.0
        AYGRID=C.0
        ASCAT=0.0
        PILUM(I)=0.0
        PILUM2(I)=0.0
        PERTOL=C.0
        RATEMP(I)=0.0
        AREA(I)=0.0
        IF(ISWICH(1).EQ.1) GO TO 586

```

```

      XX=FLOAT(2*I)/10.0-0.10
C
C*****
C   IF NN=1 ,THE RADICMETER MODE IS BEING CONSIDERED SO THE ONE WAY
C   ANTENA PATTERN IS RETURNED BY GAIN,IF NN=J THE TWO WAY PATTERN IS
C   RETURNED. THE EFFECTIVE BEAMWIDTH 1.01 DEGREEAS.
C*****
C
      GA=GAIN(XX,NN)
      GO TO 587
586  GA=1.
      XX=6.7278
      IF(ISHICH(12).EQ.1) XX=1.01
587  DO 504 J=1,36
      YGRID=(W(I,J,1)+W(I,J+1,1)+3.0*CNTRLA)/3.0
      XGRID=(W(I,J,2)+W(I,J+1,2)+3.0*CNTRL0)/3.0
      AXGRID=AXGRID+XGRID
      AYGRID=AYGRID+YGRID
C*
C*****
C   THE SCATTERING COEFFICIENT USED IN THE ILLUMINATION INTEGRAL IS
C   COMPUTED BY A FUNCTION CALLED DSCATCZ IT RETURNS VALUES CORRESPONDING
C   TO THE GROUND TRUTH VALUES INJECTED IN FILES FOR GROUND TRUTH
C*****
C*
      IF(ISHICH(12).EQ.1) TEMP=RADMET(XGRID,YGRID,SIGMA,CPEGA)
      IF(ISHICH(12).EQ.1) GO TO 515
      SCAT=DSCATC(XGRID,YGRID,TRUINC,0.0,PERCEN)
      PERTOL=PERTCL+PERCEN
      SZ=SCAT

```

```

515 A(I,J)=ABS(W(I,J,1)*W(I,J+1,2) -W(I,J,2)*W(I,J+1,1))*3600.0*
1 1.852**2/2.0 *COS(CNTRLA/57.2950)
IF(I.EQ.1) GO TO 505
A(I,J)=A(I,J)- ABS(W(I-1,J,1)*W(I-1,J+1,2)-W(I-1,J,2)*
1 W(I-1,J+1,1))*3600.0*1.852**2/2.0 *COS(CNTRLA/57.2950)
R(I,J)=(R(I,J)+R(I-1,J)+R(I-1,J+1)+R(I,J+1))/4.0
GO TO 510
505 R(I,J)=(R(I,J)+R(I,J+1)+RCENTR)/3.0
510 PILUM(I)=PILUM(I)+GA*10.0**8.3*A(I,J)*SZ /R(I,J)**4/(4.*3.14159)
1 **3
PILUM2(I)=PILUM2(I)+GA*10.**8.23*A(I,J)/R(I,J)**4/(4.*3.14159)**3
SIGPW2=20.0*10.**3*0.78**2*2.16**2*10.**(-10)*PILUM2(I)+SIGPW2
SIGPWR=20.0*10.**3*0.78**2*2.16**2*10.**(-10)*PILUM(I)+SIGPWR
RATEMP(I)=RATEMP(I)+GA*A(I,J)*TEMP
AREA(I)=AREA(I)+A(I,J)
ASCAT=ASCAT+SCAT
504 CCNTINUE
PERTOL=PERTOL/36.0
SAVE1=SAVE1+PERTOL
AXGRID=AXGRID/36.0
AYGRID=AYGRID/36.0
ASCAT=ASCAT/36.0
AREAB(5*I)=AREA(I)+AREAB(5*I-5)
PILUMB(5*I)=PILUM(I)+PILUMB(5*I-5)
IF(ISWICH(1).NE.1) XX=XX+0.10
IF(ISWICH(12).EQ.1) GO TO 517
TCTILL=TCTILL+PILUM2(I)
IF(COMAND.NE.PNTOLT) GO TO 503
GO TO 5171
517 TOTILL=TOTILL+RATEMP(I)

```

```

      IF (ISWICH(12).EQ.1) GO TO 514
5171 SCATDB=10.C*ALOG10(ASCAT)
      IF (I.NE.NUMI) GO TO 533
      WRITE(6,511) XX,GA,AREA(I),PILUM2(I),TOTILL,ASCAT,SCATCB,AXGRID ,
1 AYGRID
511  FORMAT(1H0,F4.2,5X,F14.12,5X,F13.5,6X,E11.4,3X,E11.4,2X,F10.8,4X,
1F8.4,3X,F5.2,3X,F5.2)
      GO TO 503
514  WRITE(6,527) XX,GA,AREA(I),RATEMP(I),AXGRID,AYGRID
527  FORMAT(1H0,F4.2,5X,F14.12,5X,F10.5,5X,F12.6, 3CX,F5.2,3X,F5.2)
      AREAC(5*NSCAN)=AREA(I)+AREAC(5*NSCAN-5)
503  CONTINUE
      SAVE1=SAVE1/FLOAT(NUMI)
      SIGDB=10.*ALOG10(SIGPWR)
      SIG2DB=10.0*ALOG10(SIGPW2)
      TOTDB=10.0*ALOG10(TOTILL)
      TRUINC=TRUINC*57.2958
      FOR=SIGMA*57.2958
      SIDE=OMEGA*57.2958
      CNTRLO=36).0-CNTRLO
      PRINT 530,NH,NM,SEC,FOR,SIDE,TRUINC,CNTRLA,CNTRLO,TOTILL,RCENTR
1,VPLAT,VDASH
      PUNCH 532,NH,NM,SEC,FOR,SIDE,TRUINC,CNTRLA,CNTRLO,VPLAT,VDASH
532  FORMAT(1X,2I3,F6.2,3F9.3,2X,2F8.2,2X,2F8.2)
530  FORMAT(1X,2I2,F5.2,3(1X,F7.3),2(1X,F8.4),2X,F10.8,1X,F10.4,2(F16.6
1))
      IF (ISWICH(11).EQ.1) GO TO 1108
      WRITE(6,4666) SIGPW2,SIG2DB,TOTDB,RCENTR,TRUINC
4666  FORMAT(1HC,' POWER RECEIVED FOR THIS PULSE IS. ',E11.4,' OR ',
1 F8.3,' DB ',INT ',F12.5,' RANGE ',F10.5,' INC ',F10.6)

```

ORIGINAL PAGE IS  
OF POOR QUALITY

```

      IF (ISWICH(13).NE.0) GO TO 1103
      IF (ISWICH(1).EQ.1) GO TO 1108
      WRITE (6,1111)
1111  FORMAT(1H0,30X,'PERCENTAGE ILLUMINATION OF ISO GAIN AREAS'/'ANGLE',
      1 7X,'PERCENTAGE')
      DO 1109 I4=1,NUMI
      FERILL=PILUM(I4)/TOTILL*100.0
1109  WRITE (6,1110) I4,FERILL
1110  FCRMAT(1H ,I2,10X,F8.5)
1138  IF (ISWICH(7).EQ.2) GO TO 4644
      IF (KKK.LT.3) GO TO 463

```

C

C\*\*\*\*\*

C THE FOLLOWING CODING COMPUTES THE INCREMENTAL AREA DUE TO MOTION  
C OF THE VEHICLE AND ANTENNA SCAN. WW IS AN ARRAY WHICH IS USED TO  
C STORE THE FOOTPRINT OF THE PREVIOUS PULSE, THE NEW AREA ONLY IS  
C COMPUTED.

C\*\*\*\*\*

C

```

      WRITE (6,465)
465  FCRMAT(1H0,'ANGLE',12X,'INCREMENTAL AREA' )
      IEND=1
      IF (ISWICH(1).EQ.0) IEND=8
      DO 454 I=1,IEND
      AA(I)=C.0
      DO 462 J=1,35
456  WW=SQRT((WWW(I,J,1)-WW(I,J,1))**2+(WWW(I,J,2)-WW(I,J,2))**2)
      SS=SQRT((WW(I,J,1)-WW(I,J+1,1))**2+(WW(I,J,2)-WW(I,J+1,2))**2)+
1  SQRT((WWW(I,J,1)-WWW(I,J+1,1))**2+(WWW(I,J,2)-WWW(I,J+1,2))**2)
      SS=SS/2.0

```

```

      AA(I)=AA(I)+WWW*SS
462  CONTINUE
      AA(I)=AA(I)*3600.0*1.85**2/2.0*ABS(CNTRLA/57.2958)
      ANGUL=C.2*FLOAT(I)
      IF(IENO.EQ.1) ANGUL=2.727
      WRITE(6,467) ANGUL,AA(I)
467  FORMAT(1HC,F6.2,15X,F6.4)
454  CONTINUE
      IF(COMAND.NE.PNTOLT) GO TO 463
      WRITE(6,1013) FCNTLA,FCNTLO
1013  FORMAT(1HC,'INITIAL FOOTPRINT CENTROID',5X,F11.6,5X,F11.6)
      WRITE(6,1011) CNTRLA,CNTRLO
1011  FORMAT(1HC,'FINAL CENTROID',5X,F11.6,5X,F11.6)
C*****
C   STORE PRESENT FOOTPRINT FOR NEXT LOOPS CALCULATION.
C*****
463  IFILL=1
      IF(LL.EQ.170) IFILL=8
      DO 464 I=1,IFILL
      DO 464 J=1,37
          WWW(I,J,1)=WW(I,J,1)
464  WWW(I,J,2)=WW(I,J,2)
4644  POWER=POWER+SIGPWR
          POWR2=POWR2+SIGPW2
          SAVE2=SAVE2+SAVE1
          IF(ISWICH(9).NE.2) GO TO 150
          IF(NUMF.NE.1) GO TO 497
C
C*****
C   THE FOLLOWING PLOTS THE AREA PER GAIN CONTOUR AND THE CONTRIBUTION

```

```

C      TO THE ILLUMINATION INTEGRAL
C      POWERB=POWER PER PULSE FOR EACH INCIDENCE ANGLE
C      POWERC=POWER (AVERAGE) PER INCIDENCE ANGLE.  AREA8 AND AREA9
C      ARE THE CORRESPONDING AREAS.
C*****
C
      CALL FLTHRZ(AREA8,50,55,6,500.0,10.0)
      WRITE(6,408)
408  FOPMAT(40X,'AREA VERSUS ANGLE THETA')
      CALL PLTHRZ(PILLME,50,55,6,0.10,0.0)
      WRITE(6,409)
409  FOPMAT(40X,'ILLUMINATION VERSUS ANGLE THETA')
407  IF (ISWICH(10).EQ.0.ANC.ISWICH(8).EQ.4) NCOUNT=NCCOUNT+1
150  CCNTINUE
      SAVEZ=SAVEZ/FLOAT(NUMLUP)*100.0
      POWER=POWER*FLOAT(ISMEAR)/FLOAT(NUMLUP)
      POWR2=POWR2*FLOAT(ISPEAR)/FLOAT(NUMLUP)
      ERROR=2.0*RMS(IST)-1.0
      IF(ERROR) 4077,4078,4079
4077 PRECOG=POWER*(1.0-ERROR*.1088)
      GO TO 4381
4079 PRECOI=POWER*(1.0+ERROR*.122)
      GO TO 4381
4078 PRECOD=POWER
4381 PRECOC=10.0*ALOG10(PRECOD)
      POWP2=10.0*ALOG10(POWR2)
      POWR=10.0*ALOG10(POWER)
      SZERO=POWER-POWR2
      SERPOR=PRECOD-POWR2
      IF (ISWICH(11).EQ.1) GO TO 9353

```

```

WRITE(6,1001) POWER,PRECOC,SZERO,SERROR,SAVE2,POWP2
1001 FORMAT(1H0, 'ACTUAL POWER RECEIVED ',F10.4,' RECORDED POWER ',
1 F10.4,/' ACTUAL SIGMA ZERO ',F10.4,' RECORDED SIGMA ZERO ',
2 F10.4,' AVERAGE PERCENTAGE ',F8.3,F12.5)
9353 LALO=PLATLO*10.0+25.0
LAHI=PLATHI*10.0+25.0
LOLO=PLONLO*10.0+25.0
LOHI=PLONHI*10.0+25.0
IF(LOLO.LT.C.OR.LALO.LT.0) GO TO 9123
IF(LAHI.GT.50.OR.LOHI.GT.50) GO TO 9123
DC 911 IFF=LALO,LAHI
DC 911 JFF=LOLO,LCHI
IF(FILE2(IFF,JFF).GT.C.0) GO TO 912
FILE2(IFF,JFF)=SAVE2/100.0
GO TO 911
912 FILE2(IFF,JFF)=(FILE2(IFF,JFF)+SAVE2/100.0)/2.0
911 CONTINUE
GO TO 9125
9123 IF(ISWICH(10).EQ.2) GO TO 9125
WRITE(6,9124) LALO,LOLO,LAHI,LOHI
9124 FORMAT(1H0,'FLAG NUMBER 10 G.T. FIELD EXCEEDED , THE NUMBERS ARE '
1 ,4(I3,2X))
9125 IF(ISWICH(13).EQ.1) GO TO 4555
WRITE(6,455) ISTART,ISHEAR,PLATLO,PLONLO,PLATHI,PLCNHI
455 FORMAT(1X,'THE TCTAL CELL FOR THIS ANGLE FROM PULSE ',I2,' TO PUL
1SE ',I2,' IS FROM',/'LAT ',F8.5,' LONG',F8.5,' TC LAT',F8.5,' LONG
2 ',F8.5)
4555 IF(NFIN.LT.5) GO TO 733
POWERC(10*NSCAN)=POWER/FL0AT(ISHEAR)
733 IF(ICN.GT.80) GO TO 749

```

ORIGINAL PAGE IS  
OF POOR QUALITY

```

      ICN=ICN+1
      POWERC(ICN)=POWER
      POWER=0.3
749  CCNTINUE
      IF(ISWICH(9).NE.2) GO TO 751
      CALL PLTPRZ(AREAC,50,55,6,500.0,100.0)
      WRITE(6,404)
404  FORMAT(25X,'AREA VERSUS ANGLE OF INCIDENCE')
      CALL PLTPRZ(POWERC,50,55,6,0.5,0.0)
      WRITE(6,403)
403  FORMAT(1H0,25X,'POWER VERSUS ANGLE OF INCIDENCE')
751  CCNTINUE
100  CCNTINUE
      IF(FOTO.NE.DRAW) GO TO 4019
      CALL PITCHR(FILE1,50,50,0,0,0.0,1.0,,,,,2.00,,)
      CALL PITCHR(FILE2,50,50,0,0,0.0,1.0,,,,,2.00,,)
      IS=I.0
      DMAXTO=0
      DMINTO=0
      DMIN=1.0
      DMAX=-1.0
      DO 4033 J4=1,50
      CC 4033 I4=1,50
      IF(FILE2(I4,J4).EQ.0.0) GO TO 4033
      FILE2(I4,J4)=FILE1(I4,J4)-FILE2(I4,J4)
      DMAX=AMAX1(DMAX,FILE2(I4,J4))
      DMIN=AMIN1(DMIN,FILE2(I4,J4))
      DMAXTO=AMAX1(0.0,FILE2(I4,J4))+DMAXTO
      DMINTO=AMIN1(0.0,FILE2(I4,J4))+DMINTO
      IS=IS+1

```

```

      IF(DMAX.GT.1.0.OR.DMIN.LT.(-1.0)) WRITE(6,4035) I4,J4,CMAX,
1 DMIN
4035 FORMAT(1X,'FLAG AT ',2I6,'---',2F6.2)
4033 CONTINUE
      CALL PITCHR(FILE2,57,50,C,0,-1.0,1.0,,,,,2.0,,)
      DMAXTO=DMAXTC/FLCAT(I5)
      DMINTC=CMINTO/FLCAT(I5)
      WRITE(6,4034) DMAX,DMIN,I5,DMAXTO,DMINTO
4034 FORMAT(1H0,'THE MAX +VE DEV. IS ',F7.3,' THE MAX -VE DEV. IS ',
1 'F8.3,' NUMBER ',I5,' AVE ',2F8.3)
4019 IF(PUNCH.EQ.CARDS) WRITE(43,699) (POWERC(I),I=1,ICN)
699  FORMAT(8F10.5)
      IF(ISWICH(9).EQ.1) GO TO 300
300  CONTINUE
C*****
C   IF MORE THAN ONE GROUND TYPE SIMULATION IS REQUIRED MAKE MSIM'GE 3
C*****
C
      IF(MSIM.GE.3) GO TO 5004
      WRITE(6,400)
400  FORMAT(1H0,/'NOTE-THE PARAMETERS ARE DEFINED IN THE PROGRAM CR IN
1 WALT HANLEYS PH.D. DISSERTATION')
      WRITE(6,401)
401  FORMAT(1H0,'FOR INFORMATION REGARDING SWITCH OPTIONS CONSULT WRITE
1 (P,NOT ALL COMBINATIONS ARE ALLOWED')
      IF(ISWICH(11).EQ.1) CALL PLOT(0.0,0.0,-1)
      STOP
      END
$   FORTRAN NCECK
$   INCODE  IBMF

```

```

CGAIN                GAIN
C                    GAIN OF ANTENA
C*****
C    P IS THE POLYNOMIAL FIT TO THE ANTENA PATTERN
C*****
C
    FUNCTION GAIN(Y,N)
    X=Y*2.0
    P=(-5.3*X+9.7582*X**2-10.665*X**3+3.708*X**4-.5752*X**5+
1 .(333*X**6)/3.0
    IF(N.EQ.1) GO TO 3
    GAIN=(10.0**(P/10.0))**2
    RETURN
3    GAIN=10.0**(P/10.0)
    RETURN
END
$    FORTRAN NDECK
$    INCODE  IBMF
CFILSIG              SUBROUTINE FILSIG
C                    FILL MATRIX FOR CONVERSION TO G.M.
C
C*****
C    FILSIG IS A SUBROUTINE TO FILL UP THE MATRIX WHICH UPON PRE-
C    MULTIPLYING WITH THE UNIT VECTOR IN ANTENA SPACE WILL GIVE THE
C    UNIT VECTOR IN GIMBAL MOUNT AXES.THE ROTATIONAL ANGLES INVOLVED
C    ARE THE PITCH--SIGMA AND THE ROLL--OMEGA.THE VALUES OF BOTH THESE
C    ANGLES ARE FED FROM THE CALLING PROGRAM
C*****
C
    SUBROUTINE FILSIG(RSIGMA,SIGMA,ROMEGA,OMEGA)

```

```

DIMENSION RSIGMA(3,3),ROMEGA(3,3)
RSIGMA(1,2)=0.0
RSIGMA(2,1)=0.0
RSIGMA(2,2)=1.0
RSIGMA(2,3)=0.0
RSIGMA(3,2)=0.0
RSIGMA(1,1)=COS(SIGMA)
RSIGMA(1,3)=-SIN(SIGMA)
RSIGMA(3,1)=SIN(SIGMA)
RSIGMA(3,3)=COS(SIGMA)
CALL MINV(RSIGMA)
ROMEGA(1,1)=1.0
POMEGA(1,2)=0.0
ROMEGA(1,3)=0.0
ROMEGA(2,1)=0.0
ROMEGA(3,1)=0.0
ROMEGA(2,2)=COS(OMEGA)
ROMEGA(2,3)=SIN(OMEGA)
ROMEGA(3,2)=-SIN(OMEGA)
ROMEGA(3,3)=COS(OMEGA)
CALL MINV(POMEGA)
RETURN
END
$   FORTPAN NDECK
$   INCOE  IBMF
CFILPSM          SUBROUTINE FILPSM
C           FILL MATRIX FOR CONVERSION TO VEH.AXES.
C
C*****
C   FILPSM FILLS UP THE MATRIX WHICH CONVERTS THE UNIT VECTOR IN

```

ORIGINAL PAGE IS  
OF POOR QUALITY

```

C   GIMBAL MOUNT SPACE TO A UNIT VECTOR IN VERTICAL CENTRED AXES.
C   THE DISTANCE BETWEEN THE CENTRES OF THE TWO COORDINATES SPACES
C   HAS BEEN IGNORED. THE ROTATIONAL ANGLES ARE THE MISSALIGNMENT
C   ERRORS IN YAW, PITCH AND ROLL. THEY ARE DENOTED BY PSIM, THETAM,
C   AND PHIM, THEIR VALUES ARE FED BY THE CALLING PROGRAM.
C*****
C
SUBROUTINE FILPSM(PSIGM,PSIM,PHIGM,PHIM,THETAG,THETAM)
DIMENSION PSIGM(3,3),PHIGM(3,3),THETAG(3,3)
PSIGM(1,3)=0.0
PSIGM(2,3)=0.0
PSIGM(3,1)=0.0
PSIGM(3,2)=0.0
PSIGM(3,3)=1.0
PSIGM(1,1)=COS(PSIM)
PSIGM(1,2)=SIN(PSIM)
PSIGM(2,1)=-SIN(PSIM)
PSIGM(2,2)=COS(PSIM)
CALL MINV(PSIGM)
PHIGM(1,1)=1.0
PHIGM(1,2)=0.0
PHIGM(1,3)=0.0
PHIGM(2,1)=0.0
PHIGM(3,1)=0.0
PHIGM(2,2)=COS(PHIM)
PHIGM(2,3)=SIN(PHIM)
PHIGM(3,2)=-SIN(PHIM)
PHIGM(3,3)=COS(PHIM)
CALL MINV(PHIGM)
THETAG(1,2)=0.0

```

```

    THETAG(2,1)=0.0
    THETAG(2,2)=1.0
    THETAG(2,3)=0.0
    THETAG(3,2)=0.0
    THETAG(1,1)=COS(THETAM)
    THETAG(1,3)=-SIN(THETAM)
    THETAG(3,1)=SIN(THETAM)
    THETAG(3,3)=COS(THETAM)
    CALL MINV(THETAG)
    RETURN
    END

```

```

$   FORTRAN NDECK
$   INCODE -IBMF

```

```

CFILPSV          SUBROUTINE FILPSV

```

```

C              FILL MATRIX FOR CONVERSION TO Z.L.V

```

```

C

```

```

C*****

```

```

C   FILPSV FILLS UP THE MATRIX USED TO CONVERT A UNIT VECTOR IN VEH-
C   ICAL CENTRED AXES TO A UNIT VECTOR IN THE Z-LOCAL VERTICAL COOD.
C   THE ROTATIONAL ANGLES ARE THE ATTITUDE ERRORS OF YAW, PITCH AND ROLL
C   THEY ARE DENOTED BY PSIVVEC, THETA V, AND PHIVEC RESPECTIVELY.

```

```

C*****

```

```

C

```

```

    SUBROUTINE FILPSV(PSIVVEC, PSIVEH, PHIVEC, PHIVEH, THETA V, THETA H)
    DIMENSION PSIVVEC(3,3), PHIVEC(3,3), THETA V(3,3)
    PSIVVEC(1,3)=0.0
    PSIVVEC(2,3)=0.0
    PSIVVEC(3,1)=0.0
    PSIVVEC(3,2)=0.0
    PSIVVEC(3,3)=1.0

```

ORIGINAL PAGE IS  
OF POOR QUALITY

```

      PSIVVEC(1,1)=COS(PSIVFH)
      PSIVVEC(1,2)=SIN(PSIVFH)
      PSIVVEC(2,1)=-SIN(PSIVFH)
      PSIVVEC(2,2)=COS(PSIVFH)
      CALL MINV(PSIVVEC)
      PHIVEC(1,1)=1.0
      PHIVEC(1,2)=0.0
      PHIVEC(1,3)=0.0
      PHIVEC(2,1)=0.0
      PHIVEC(3,1)=0.0
      PHIVEC(2,2)=COS(PHIVFH)
      PHIVEC(2,3)=SIN(PHIVFH)
      PHIVEC(3,2)=-SIN(PHIVFH)
      PHIVEC(3,3)=COS(PHIVFH)
      CALL MINV(PHIVEC)
      THETAV(1,2)=0.0
      THETAV(2,1)=0.0
      THETAV(2,2)=1.0
      THETAV(2,3)=0.0
      THETAV(3,2)=0.0
      THETAV(1,1)=COS(THETAH)
      THETAV(1,3)=-SIN(THETAH)
      THETAV(3,1)=SIN(THETAH)
      THETAV(3,3)=COS(THETAH)
      CALL MINV(THETAV)
      RETURN
      END
$   FORTRAN NDECK
$   INCODE  IBMF
CFILPSZ          SUBROUTINE FILPSZ

```

```

C          FILL MATRIX FOR CONVERSION TO ECI
C
C*****
C  FILPSZ FILLS UP THE MATRIX WHICH CONVERTS A UNIT VECTOR IN ZLV
C  COOD. TO A UNIT VECTOR IN EARTH CENTERED INERTIAL COORDINATES.
C  THE ROTATIONAL ANGLES CONSIDERED ARE THE VEHICAL YAW,PITCH AND
C  ROLL.THEY ARE DENOTED BY PSIZLV,THETAZ,PHIZLV RESPECTIVELY.
C  L AND M ARE SCRATCH VECTORS,F IS THE TRUE ANOMALY,OINC IS THE
C  ORBITAL INCLINATION ANGLE,AIS THE ORBITAL RADIUS.
C*****
C
C          SUBROUTINE FILPSZ(PSIZLV,A,F,OINC,PHIZLV,THETAZ)
C          DIMENSION PSIZLV(3,3),PHIZLV(3,3),THETAZ(3,3)
C          PSIZLV(1,3)=0.0
C          PSIZLV(2,3)=0.0
C          PSIZLV(3,1)=0.0
C          PSIZLV(3,2)=0.0
C          APSI=((SIN(F)**2)+((COS(F)**2)*((COS(OINC))**2) )
C          PSIZLV(3,3)=1.0
C          SINPSI=COS(F)*COS(OINC)/SQRT(APSI)
C          COSPSI=-SIN(F)/SQRT(APSI)
C          PSIZLV(1,1)=COSPSI
C          PSIZLV(1,2)=SINPSI
C          PSIZLV(2,1)=-SINPSI
C          PSIZLV(2,2)=COSPSI
C          CALL MINV(PSIZLV)
C          THETAZ(1,2)=0.0
C          THETAZ(2,1)=0.0
C          THETAZ(2,2)=1.0
C          THETAZ(2,3)=0.0

```

```

      THETAZ(3,2)=0.0
      COSTHE=SQRT(AFS1)
      SINTHE=-COS(F)*SIN(CINC)
      THETAZ(1,1)=COSTHE
      THETAZ(1,3)=-SINTHE
      THETAZ(3,1)=SINTHE
      THETAZ(3,3)=COSTHE
      CALL MINV(THETAZ)
      PHIZLV(1,1)=1.0
      PHIZLV(1,2)=0.0
      PHIZLV(1,3)=0.0
      PHIZLV(2,1)=0.0
      PHIZLV(3,1)=0.0
      SINPHI=-SINPSI*COS(F)+COSPSI*SIN(F)*COS(OINC)
      COSPHI=-(SINTHE*COSPSI*COS(F)+SINTHE*SINPSI*SIN(F)*COS(OINC)
1 +COSTHE*SIN(F)*SIN(OINC) )
      PHIZLV(2,2)=COSPHI
      PHIZLV(2,3)=SINPHI
      PHIZLV(3,2)=-SINPHI
      PHIZLV(3,3)=COSPHI
      CALL MINV(PHIZLV)
      RETURN
      END
$   FORTRAN NDECK
$   INCODE  IBMF
C4PRD          SUBROUTINE MPRD
C              MATRIX PRODUCT
C
C*****
C   MPRD COMPUTES THE PRODUCT OF TWO MATRICES, THE TWO MATRICES ARE

```

C IN A(L,M), AND B(M,N) THE RESULT IS STORED IN R(L,N).THE VALUES OF  
 C ALL ARGUMENTS ARE SUPPLIED BY THE CALLING PROGRAM.

SUBROUTINE MPRD(A,B,R,L,M,N)

C\*\*\*\*\*

C

DIMENSION A(L,M),B(M,N),R(L,N)

DO 1 I=1,L

DO 2 K=1,N

R(I,K) = 0.0

DO 3 J=1,M

R(I,K)=R(I,K)+A(I,J)\*B(J,K)

3 CONTINUE

2 CONTINUE

1 CONTINUE

RETURN

END

\$ FORTRAN NDECK

\$ INCODE IEMF

CMINV SUBROUTINE MINV

C MATRIX INVERSE

C

C\*\*\*\*\*

C MINV COMPUTES THE INVERSE OF A SYMMETRIC ORTHONORMAL 3X3 MATRIX

C THE COORDINATE TRANSFORMATIONS REQUIRE SUCH A INVERSION ONLY

C\*\*\*\*\*

C

SUBROUTINE MINV(A)

DIMENSION A(3,3)

DO 10 I=1,2

II=I+1

```

      DC 10 J=11,3
      HOLD=A(I,J)
      A(I,J)=A(J,I)
      A(J,I)=HOLD
10   CONTINUE
      RETURN
      ENC

$     FORTRAN NDECK
$     INCODE  IBMF

C SQUARE          SUBROUTINE SQUARE
C                TO GENERATE SQUARE
      SUBROUTINE SQUARE (XMIN,XMAX,YMIN,YMAX,XD,YD)
C*****
C     SUBROUTINE GENERATES A SQUARE FOR CALIBRATION AND SETS LIMITS.
C     IT PUTS A SMALL CROSS HAIR IN THE CENTER FOR ALIGNMENT PURPOSES.
C*****
C
      CALL INPLOT(XMIN,XMAX,YMIN,YMAX,XD,YD)
      IXFILL=XD
      XINCH=XMIN
      YDASH=YMIN+.02
      DO 1 I=1,IXFILL
      CALL PLOT(XINCH,YMIN,2)
      CALL PLOT(XINCH,YDASH,2)
      CALL PLOT(XINCH,YMIN,2)
      XINCH=XINCH+(XMAX-XMIN)/XC
1     CONTINUE
      CALL PLOT(XMAX,YMIN,2)
      IYFILL=YD
      XDASH=XMAX-0.02

```

```

YINCH=YMIN
DO 2 J=1,IYFILL
CALL PLOT(XMAX,YINCH,2)
CALL PLOT(XDASH,YINCH,2)
CALL PLOT(XMAX,YINCH,2)
YINCH=YINCH+(YMAX-YMIN)/YC
2 CONTINUE
CALL PLOT(XMAX,YMAX,2)
XBACK=XMAX
YDASH=YMAX-0.02
DO 3 K=1,IXFILL
CALL PLOT(XBACK,YMAX,2)
CALL PLOT(XBACK,YDASH,2)
CALL PLOT(XBACK,YMAX,2)
XBACK=XBACK-(XMAX-XMIN)/XC
3 CCNTINUE
CALL PLOT(XMIN,YMAX,2)
YBACK=YMAX
XDASH=XMIN+0.02
DO 4 L=1,IYFILL
CALL PLOT(XMIN,YBACK,2)
CALL PLOT(XDASH,YBACK,2)
CALL PLOT(XMIN,YBACK,2)
YBACK=YBACK-(YMAX-YMIN)/YC
4 CCNTINUE
CALL PLOT(XMIN,YMIN,2)
XHIGH=(XMIN+XMAX)/2.0+0.01
XLOW=(XMIN+XMAX)/2.0-0.01
YHIGH=(YMIN+YMAX)/2.0+0.01
YLOW=(YMIN+YMAX)/2.0-0.01

```

ORIGINAL PAGE IS  
OF POOR QUALITY

```

      XMID=(XMIN+XMAX)/2.0
      YMID=(YMIN+YMAX)/2.0
      CALL PLOT(XMID,YLOW,3)
      CALL PLOT(XMID,YHIGH,2)
      CALL PLOT(XLOW,YMID,3)
      CALL PLOT(XHIGH,YMID,2)
      RETURN
      END

$      FORTRAN NDECK
$      INCODE  IBMF

CSCAN          SUBROUTINE SCAN
C              COMPUTATION OF SCAN FOR CONTIGUOUS MODE
C*****
C      SUBROUTINE IS CALLED UPON TO COMPUTE THE PITCH ANGLE AND
C      THE TRUE ANAMOLY FOR THE CONTIGUOUS (INTRACK) MODE OF OPERATION.
C      IT IS FED THE POINT IN SCAN,THE SCAN NUMBER,THE STARTING BIAS
C      AND IT GENERATES THE SCAN IN ACCORDANCE WITH THE C.C.R VOLUME
C      BY G.E.
C*****
C
      SUBROUTINE SCAN(ISCAN,NSCAN,NSTART,KK,G,F,SIGMA)
      DIMENSION NSTART(5)
      SIGMA=48.0-FLOAT(KK-1)*23.099*.009-FLOAT(NSTART(NSCAN))*23.099*
1 10.0**(-3) -23.099*5.17*10.0**(-3)
      F=G+(1.125*10.0**(-3)*FLOAT(KK-1)/125.0)+FLOAT(NSTART(NSCAN))*
1 1.125*10.0**(-6) +.009*1.125*10.0**(-3)
      RETURN
      END

$      FORTRAN NDECK
$      INCODE  IBMF

```

CSCANCR

CROSS TRACK CONTIGUOUS SCAN

C

C\*\*\*\*\*

C SCANCR CONTAINS THE CROSS TRACK CONTIGUOUS SCAN .

C\*\*\*\*\*

C

SUBROUTINE SCANCR(ISCAN,NSCAN, KK,G,F,PITCH,ROLL,SIGMA,OMEGA)

F=G+(1.125\*10.\*\*(-3)\*(FLOAT(KK-1)/125.0+FLOAT(NSCAN-1)\*0.1515+

1.(5) )

IF(ISCAN/2\*2.EQ.ISCAN) GO TO 10

ROLL=OMEGA\*57.2958-11.375+(12.5\*(FLOAT(NSCAN-1)\*.1515+FLCAT(KK-1)

1/125.(+.JCS) )

GO TO 11

10 ROLL=OMEGA\*57.2958+11.375-(12.5\*(FLOAT(NSCAN-1)\*.1515+FLCAT(KK-1)

1 /125.0+.JCS ) )

11 PITCH=SIGMA+1.0/57.2958-2.0/1.82\*(FLOAT(NSCAN-1)\*.1515+FLOAT(KK-1)

1/125.+0.005)/57.2958

PITCH=PITCH\*57.2958

RETURN

END

\$ FORTPAN NDECK

\$ INCODE, IBMF

CFILECI SUBROUTINE FILECI

C SPACECRAFT POSITION AND VELOCITY

C

C\*\*\*\*\*

C FILECI COMPUTES THE POSITION AND VELOCITY VECTORS OF THE SPACE-

C CRAFT IN ECI COORDINATES.

C POSI--POSITION VECTOR(X,Y,Z) IN ECI COOD. VELI--VELOCITY VECTOR

C (X,Y,Z) IN ECI COOD.A--ORBITAL RADIUS, F--TRUE ANOMALY,GMU--GRAVI

```

C      TATIONAL CONSTANT,OINC----ORBITAL INCLINATION.
C*****
C
      SUBROUTINE FILECI (PCSI,VELI,A,F,GMU,OINC,WE,RATRAD)
      DIMENSION POSI(3),VELI(3)
      CIRVEL=SQRT(GMU/A)
5     POSI(1)=A*COS(F)
      POSI(2)=A*SIN(F)*COS(OINC)
      POSI(3)=A*SIN(F)*SIN(OINC)
      DUMMY1=SQRT(POSI(1)**2+POSI(2)**2)
      FLAT=ATAN2((ABS(PCSI(3))),DUMMY1)
      FLONG=ATAN2(POSI(2),POSI(1))
C     WEBAR=WE/RATRAD*6371.0
      WEBAR=WE/RATRAD*6378.0
      VELI(1)=-CIRVEL*SIN(F)+WEBAR*COS(FLONG)*COS(FLAT)
      VELI(2)=CIRVEL*COS(F)*COS(OINC)-WEBAR*SIN(FLONG)*COS(FLAT)
      VELI(3)=CIRVEL*COS(F)*SIN(OINC)
      RETURN
      END
$     FORTRAN NOECK
$     INCODE IBMF
CLTR      SUBROUTINE LTR
      SUBROUTINE LTR(IX,IY,X,Y,XMAX,YMAX,IF,IHT,XD,YD,IDAYD)
      DIMENSION IDAY(2)
      INTEGER XCHAP(2),YCHAR(2),FCHAR(4),MCHAR(4)
      INTEGER SCBTI(2)
      DATA FCHAR(1),FCHAR(2),MCHAR(1),MCHAR(2)/'ANGLE ',' = ','
1 'ORBIT ','HT. = '/
      DATA IDAY(1)/*DAY */
      DATA SOBTI(1),SOBTI(2)/*ARUN ','SOBTI */

```

```

X3=X
Y3=Y
XINC=(XMAX-X)/XD
YINC=(YMAX-Y)/YD
X1=X-XINC*0.8
Y1=Y-0.5*YINC
NXD=XD
NYD=YD
DO 10 I=1,NYD
  CALL CHAR(IY,YCHAR)
  CALL LETTER(X1,Y,0.09,0,7,YCHAR,6)
  Y=Y+YINC
10  IY=IFIX(Y*100.)
  DC 20 I=1,NXD
  CALL CHAR(IX,XCHAR)
  CALL LETTER(X-XINC/4.0,Y1,0.09,0,7,XCHAR,6)
  X=X+XINC
20  IX=IFIX(X*100.)
  CALL CHAR(IDAYO,I(AY(2) )
  X2=X3+XINC/4.0
  Y2=Y3+YINC*1.5
  CALL LETTER(X2,Y2,0.12,0,12,IDAY,6)
  CALL CHAR(IF,FCHAR(3))
  Y2=Y3+YINC
  CALL LETTER(X2,Y2,0.12,0,18,FCHAR,6)
  CALL CHAR(IHT,MCHAR(3))
  Y2=Y3+YINC*0.5
  CALL LETTER(X2,Y2,0.12,0,18,MCHAR,6)
  X=X-4.0*XINC
  CALL LETTER(X,Y2,0.12,0,12,SOSTI,6)

```

ORIGINAL PAGE IS  
OF POOR QUALITY

```

        RETURN
        END
$      FORTRAN NDECK
$      INCODE  IBMF
DSCATC          FUNCTION D-S-C-A-T-C
C
C*****
C      FUNCTION DSCATC IS A FUNCTION THAT RETREIVES THE DATA FROM THE TABLE
C      OF SCATTERING COEFFICIENT DATA THAT HAS FREVIOUSLY BEEN PUT ON FILE
C      THE DATA WAS PUT ON THE FILE BY EXAMING A PIECE OF GROUND 300 BY 300'
C      NAUTICAL MILES AND ASSIGNING GEOGRAPHIC PARAMETERS TO PARTS OF THE
C      GROUND, THEN UPON CONSULTATION OF THE TERRAIN HANDBOOK THE CORRESPONDING
C      VALUE OF THE SCATTERING COEFFICIENT FOUND AND PUT IN TABLE.
C*****
C
      FUNCTION DSCATC(X,Y,PITCH,ROLL,PERCEN)
      COMMON FILE1(50,50)
      IX=AMIN1((X*10.+25.0),50.0)
      IY=AMIN1((Y*10.+25.0),50.0)
$      PERCEN=FILE1(IX,IY)
      T=AMAX1(ABS(PITCH),ABS(ROLL))/29.4
      T=T*57.2958
      A=-5.0-49.47*T+63.54*T**2-36.38*T**3+7.41*T**4
      B=-2.0-50.93*T+53.86*T**2-23.64*T**3+2.92*T**4
      A=10.0**(A/10.0)
      B=10.0**(B/10.0)
      DSCATC=A*PERCEN+(1.0-PERCEN)*B
      RETURN
      END
$      FORTRAN NDECK

```

```

$      INCODE  IBMF
CRAOMET          FUNCTION RADMET
C              SIMULATION OF RADIOMETRIC TEMP.
C*****
C      RADMET IS A VERY STRAIGHTFORWARD ROUTINE IT ACCESSES THE
C      APPROPRIATE POINT IN THE GRID AND COMPUTES THE RADIOMETRIC TEMP.
C*****
C
      FUNCTION RADMET(X,Y,PITCH,ROLL)
      COMMON FILE1(50,50)
      IX=AMIN1(20.0*X+1.0,100.0)
      IY=AMIN1(20.0*Y+1.0,100.0)
      EMISS=0.5+FILE1(IX,IY)/3.0
      RADMET=EMISS*290.0/CCS(AMAX1(PITCH,ROLL)/57.2958)

11  RETURN
      END

$      GMAP    NDECK
$      INCODE  IBMF
      SYMDEF   CHAR
SAVE  0BSS    9
CHAR  SREG    SAVE
      STI     SAVE+8
      STX1    .CHAR
      EAX2    2,1*
      EAX3    3,1*
      LDA     0,2
      BCD     =80000,0L
      BCD     =64000,0L
      BCD     =51200,0L
      BCD     =40960,0L

```

ORIGINAL PAGE IS  
OF POOR QUALITY

```

    ECD      =32768,CL
    QLS      6
    LDA      =3H00 ,DL
    LOX5     0,2
    TPL      ++2
    LDA      =3H00-,DL
    LLS      18
    ALS      6
    CRA      =3H00.,DL
    LLS      6
    STQ      1,3
    STA      0,3
    ANA      =0607700,DU
    TNZ      ++5
    LDA      0,3
    ANA      =0775077777777
    ORA      =0002000,DU
    STA      0,3
    LREG     SAVE
    LOI      SAVE+8
.CHAR TRA   **
    END

```



```

C
C   COMPUTE CONSTANTS THAT DO NOT CHANGE WITH TEMP.,PRESS.,OR WATER
C
      DO 2 N = 1,45,2
      ROT(N) =FLOAT(N*(2*N+3) )/FLOAT(N+1)
      ROTMIN(N) =FLOAT((N+1)*(2*N-1))/FLOAT(N)
2     POTO(N) =FLOAT(2*(N**2+N+1)*(2*N+1) )/FLOAT(N*(N+1))
C
C           COMPUTE SOME NEEDED CONSTANTS
C
      FWPLUS = (FREQ+FZZ)**2
      FWMIN = (FREQ-FZZ)**2
      FREQSQ = FREQ*FREQ
      ANAP = 1J.J*ALOG10(EXP(1.0))
C
C           THE ATMOSPHERE CAN BE SPECIFIED IN ONE OF
C           MANY WAYS, THE TWO CHOICES AVAILABLE ARE
C           RADIOSONDE DATA OR A MODEL PROFILE CALLED
C           THE U.S.STANDARD
C           THE CHOICE IS MADE BY THE VALUE OF NN
C           IF NN IS LESS THAN 2 THE PROFILE IS
C           MODELLED BY THE U.S.STANDARD, ELSE
C           THE RADIOSONDE DATA (NN TERMS) ARE READ
C           IN. THE OTHER PARAMETERS ARE
C           N1--SAMPLE NUMBER (ONLY FOR HEADER INFO)
C           NN--NUMBER OF SAMPLES OF ATMOS. MEASUREMENTS
C               IN THE PROFILE
C           NCC--A SWITCH (VALUES=1,REL. HUMIDITY DATA,
C               =2,DEW POINT (C),=3,SPEC.HUMIDITY)
C           LBL--ANY TEN WORD HEADER LABEL
C           NS--INPUT DATA FILE NUMBER
C
C           NTRGET--TYPE OF TARGET,=0 LAND,=1 OCEAN
C           NUMA--NUMBER OF ANGLES TO CONSIDER,
C               IF NUMA IS ZERO,ONLY ZENITH ANGLE CONSIDERED
C
C           THE SURFACE TEMPERATURE FOR AN OCEAN
C           SURFACE IS KEPT FIXED AT 293 K (18C)
C           IT IS THE SURFACE AIR TEMPERATURE FOR
C           LAND TARGETS. THIS VALUE IS USED TO
C           COMPUTE THE APPARENT TEMP. AND THE
C           EXCESS TEMPERATURE DUE TO THE ATMOS.
C
C           NLCLOUD IS A SWITCH TO INDICATE THE CLOUD
C           STRUCTURE. IT CAN BE EXERCISED TO INVCKE
C           A CLOUD MODEL RATHER THAN ACTUAL CLOUD
C           SPECIFICATIONS. IF NLCLOUD IS SET EQUAL
C           TO 4HPORT (*PORT*),THEN PORTER'S MODEL
C           FOR CLOUDS IS INVOKED. THE SPECIFICATION
C           OF MEDIUM,LIGHT OR HEAVY IS BY NSPEC
C           NSPEC=1,LIGHT; =2,MEDIUM; =3,HEAVY
C

```

```

TGS=293.0
C      LAND TARGETS HAVE A TEMPERATURE ASSIGNED
C      TO THEM ONLY WHEN ONE IS KNOWN.
C      IF NOT KNOWN, A VALUE OF 300.0 IS USED
C
C
C      READ(5,425) NUMA,NCLOUD,NSPEC
425  FORMAT(I2,A4,I2)
      IF(NUMA.EQ.0) NUMA=1
199  READ(5,325) N1,NTRGET,NN,NCC,NS,LBL
325  FORMAT(I4,2I2,I1,I2,10A6)
      IF(NTRGET.NE.1) TGS=300
      IF(NN.EQ.3) GO TO 99
      CALL KADIO(Z(I),P(I),T(I),RO(I))
      GO TO 130
C      THIS SECTION OF CODING IS IF ONE IS
C      GIVEN ONLY THE SURFACE VALUES -NO PROFILE
C      THE TEMPERATURE CAN BE IN DEG CENT,FAHRENHEIT
C      OR IN KELVIN,IT MUST BE SPECIFIED BY KIND
C      THE PARAMETER CARDS ARE READ BY THE
C      FOLLOWING STATEMENT
C      TEMP--TEMPERATURE SPECIFICATION (K-KELVIN,C-CENT
C              F-FAHRENHEIT)
C      TG--GROUND(SURFACE) TEMPERATURE
C      PG--SURFACE PRESSURE IN MILLIBARS
C      RG--SURFACE HUMIDITY IN GMS/M**3, OR ABS
C              HUMIDITY OR DEW POINT
C      PRCN--PERCENTAGE OF CLOUDS IN FRACTION OF 1
C      PPT--PRECIPITATION RATE IN MM/HR
C      HMX--MAXIMUM HEIGHT FOR INTEGRATION (KMS)
C      HITE--LOWER CEILING OF CLOUDS
C      THICK--THICKNESS OF CLOUD STACK (KMS)
C      WCONT--WATER CONTENT OF CLOUDS (GMS/M**3)
C      NG--A SWITCH TO INDICATE THE TYPE OF HUMIDITY
C              DATA,IF=1,RELATIVE HUMIDITY,=2
C              SPECIFIC HUMIDITY,IF ANYTHING ELSE=GMS/M**3
C
99  READ(5,25) KIND,NG,HMX,PG,TG,PG,RCG,PRCN,PPT,HITE,THICK,WCONT
      WRITE(11,25) KIND,NG,HMX,PG,TG,RCG,PRCN,PPT,HITE,THICK,WCONT
25  FORMAT(A2,I1,F6.2,3F7.2,5F6.2)
C
C      A ZERO TEMPERATURE ENDS THE PROGRAM ACTIVITY .
C
C      IF(TG.EQ.0) STOP
C
C      A BRACKETING OF TEMPERATURES IS ALLOWED
C      BY SETTING MENJ AND MUP TO TOTAL INCREMENT
C      AND INCREMENT SIZE RESPECTIVELY
C      IF A PRINT OUT OF THE PROFILE IS REQUIRED
C      SET JPRINT TO ANY NON ZERO VALUE. THE
C      PROFILE IS WRITTEN TO FILE CODE 08(EIGHT)
C

```

ORIGINAL PAGE IS  
OF POOR QUALITY

```

225 READ(5,225) MEND,MUP,JFLAG,JPRINT
   FORMAT(4I4)
C
C       JFLAG IS THE ARGUMENT THAT NOTIFIES
C       SUBROUTINE EMISUN WHEN TO READ
C       A NEW SET OF DATA IN
C
C       IF EMISSIVITY IS NOT TO BE READ IN THE
C       VALUE IS SET TO J.90
C
   TGB=TG
   IF(NTRGET.NE.1) TGS=TGJ
   EMISS=J.90
   IF(NTRGET.EQ.1) EMISS=J.40
   PAT = (PRCN+1.0)*2.0-1.0
   IP = PAT
   IF(NCLOLD.NE.PORT) GO TO 889
   HITE=CEILING(NSPEC)
   WCONT=GMSM3(NSPEC)
   THICK=UCLNG(NSPEC)-CEILING(NSPEC)
   PRCN=1.0
   IP=NSPEC
889  HMX = HMX+0.1
   LOOP = 0
C
C       DETERMINE WHAT TYPE TEMPERATURE IS SPECIFIED
C       AND CONVERT TO DEGREES KELVIN
C
   DO 5 I = 1,3
   IF(DEG(I).EQ.KIND) ITYPE=I
5  CONTINUE
   IF(ITYPE.EQ.2) GO TO 6
   IF(ITYPE.EQ.3) GO TO 7
   GO TO 177
6  TG=(TG-32.0)*5.0/9.0+273.0
   GO TO 177
7  TG=TG+273.0
C
C       THIS LOOP INCREMENTS SURFACE TEMPERATURE
C
177 IF(NN.NE.0) MEND=1
   IF(NN.NE.0) MUP=1
100 DO 125 KKKK=1,MEND,MUP
   TG=TGE+FLOAT(KKKK-1)
   OXYGEN = 0.0
C
C       IF HUMIDITY IS GIVEN IN ABS HUM. COMPUTE RO
C
   IF(NG.EQ.2) RG=RG*.34038*PG/TG
C
   IF(NG.EQ.1) RG=216.5*VAPOR(RG-273.16)/TG
C

```

```

C           INITIALIZE SOME VALUES
C
C           AZ(1) = J.C
C           WATER = J.0
C           OXYGEN=0
C
C           START COMPUTING THE ABSORPTION VALUES FOR WATER AND OXYGEN
C           WRITE HEADING FOR OUTPUT
C
C           IF(NN.EQ.0) WRITE(6,70) LBL
102        WRITE(6,3) PG,TG,RG,TGS
C
C           MAIN LOOP FOR COMPUTING ALPHA, ZJKMS
C
C           DO 10 I=1,200
C           XI = I
C           Z(I) = (100.*XI-50.0)/1000.0
C
C           IF HIEGHT EXCEEDS MAXIMUM QUIT
C           IF((Z(I)-0.05).GT.HMX) GO TO 10
C
C           BRANCH FOR MODEL OR ACTUAL(RADIOSCNCE) PROFILE
C
C           IF(NN.EQ.0) GO TO 55
C           CALL EXTRAP
C           GO TO 54
C
C           MODEL PROFILE FOR PRESSURE
C
55        P(I) = PG*(EXP(Z(I)/(-7.0)))
C           HP = Z(I)
C
C           MODEL PROFILE FOR HUMIDITY
C
C           IF(HP-16.0) 57,57,56
56        IF(HP.NE.16.0) HP=16.0
57        RHOZ = RG *EXP(HP/(-2.1))
C           IF(Z(I).LT.16.01)GO TO 58
C           RHOZ = RHOZ*EXP((Z(I)-16.0)/(-4.2))
58        RO(I) = RHOZ
C
C           MODEL PROFILE FOR TEMPERATURE
C
C           IF(HP-11.0) 23,23,21
21        IF(HP.GT.11.0) HP =11.0
23        TEMPZ = TG-(6.5*HP)
C           IF(Z(I).LT.25.91)GO TO 24
C           TEMPZ = TEMPZ + 3.9*(Z(I)-25.0)
24        T(I)=TEMPZ
C           IF(JPRINT.EQ.0) GO TO 54

```

ORIGINAL PAGE IS  
OF POOR QUALITY

```

C
C           THE PROFILES MAY BE PRINTED OUT ON
C           FILE CODE 08 BY SETTING JPRINT TO NON
C           ZERO IN STATEMENT REGARDING LCOPS
C
      IF(I.EQ.1) WRITE(8,70) L3L
      IF(((I+5)/5*5).EQ.(I+5)) WRITE(8,86)
1     Z(I),F(I),T(I),RO(I)
86    FORMAT(1X,4F12.4)
C
      CCMPUTE WATER VAPOR ABSORPTION
C
54    DELH2O = 2.62*P(I)/1013.25*(1.0+0.0046*RO(I))/(T(I)/318.)**0.625
      WZZ = 1682.6*PO(I)*FREQSQ*EXP(-64+.)/T(I))/T(I)**2.5
      WZZ = WZZ*DELH2O*(1./(FWMIN+DELH2O**2)+1./(FWPLUS+DELH2O**2) )
      WRES = 1.11*J.01*RO(I)*FREQSQ*DELH2O/T(I)**1.5
      ALPHZO(I) = ((WZZ+WRES)*J.1)/ANAP
C
      CCMPUTE OXYGEN ABSORPTION
C
      IF(I.LE.80 ) G = 9.640
      IF(I.GT.80 .AND.I .LE. 250 ) G = 0.640+J.717*(XI-80.0)/(170.0)
      IF(I.GT.250) G = 1.357
      DELOZ = (G*P(I)/PG)*(TG/T(I))
      DELSQ = DELOZ*DELOZ
      FO = DELOZ/(FREQSQ+DELSQ )
      SUM = 0.0
      M=1
      DO 4 N = 1,45,2
      YN = N
      AN = EXP(-2.0684*XN*(XN+1.0)/T(I) )
      FNPLUS = DELOZ*(1./((ANPLUS(M)-FREQ)**2+DELSQ))+
1     1./((ANPLUS(M)+FREQ)**2+DELSQ )
      FNMIN = DELOZ*(1./((ANMIN(M) -FREQ)**2+DELSQ )+
1     1./((ANMIN(M)+ FREQ)**2+DELSQ )
      M=M+1
4     SUM = SUM +(FNPLUS*ROT(M)+FNMIN*ROTMIN(N)+FC*ROTO(N))*AN
      PAMM=F(I)*76(.)/1013.25
      ALPHOZ(I) = ((2.6742*PAMM*FREQSQ*SUM/T(I)**3)*J.1)/ANAP
      IF(I.NE.1) GO TO 11
      AZ(I) = ALPHZO(I)+ALPHOZ(I)
      GO TO 12
11    AZ(I) = ALPHZO(I)+ALPHOZ(I)+AZ(I-1)
C
      SEE IF CLOUDS ARE PRESENT THIS LAYER, IF SO
      CALL CLOUD WITH THE APP. PARAMETERS
C
      IF(PRCN.EQ.0) GO TO 12
      IF(Z(I).LT.HITE.JR.Z(I).GT.(HITE+THICK)) GO TO 13
      CALL CLCUD(CLATN,PRCN,WCONT,T(I))
C
      THE FOLLOWING WRITE TO FILE CODE

```

```

C          58, IS WRITTEN TO SEE THE GRADIENT OF
C          THE ATMOSPHERIC CONDITIONS AND THE
C          CORRESPONDING CONTRIBUTIONS GUE
C          TO LAYERS OF THICKNESS (Z(I)-Z(I-1)).
C
111 WRITE(11,111) Z(I),T(I),P(I),RO(I),CLATN
    FORMAT(1X,5F15.5)
    AZ(I)=AZ(I)+CLATN
C
C          SEE IF IT IS PRECIPITATING, IF SO
C          CALL RAIN WITH THE APP. PARAMETERS
C
13  IF(PPT.EG.G) GO TO 12
    IF(Z(I).GT.HITE) GO TO 12
    CALL RAIN( ATRAIN,PPT)
    AZ(I)=AZ(I)+ATRAIN
12  WATER = ALPHZO(I)+WATER
    IJ=I
    TOTAL=AZ(I)
    OXYGEN = ALPHOZ(I)+ OXYGEN
    WT(I)=WATER
    OX(I)=OXYGEN
10  CONTINUE
C
C          DESCRIBE THE STATE OF THE ATMCS.
C
90  WRITE(6,34) CLOUDS(IP), PRCN,WCNT,HITE,THICK,PPT
C
C          COMPUTE TRANSMITTANCE , EXCESS TEMP. ETC.
C
    IJ=IJ+1
    DO 20 J = 1,NUMA
    SECANT = 1.0/ COS(THETA(J)/RAD )
    TATM(P = 0.0
    JUP=J
C
C          THE CURVATURE OF THE EARTH IMPLIES
C          THAT A RAY AT AN OBLIQUE ANGLE DOES
C          GO THROUGH H*SEC(THETA) OF THE
C          ATMOSPHERE. TO CHECK HOW MUCH THE
C          MAXIMUM SLANT DISTANCE TO THE TCP OF
C          THE ATMOSPHERE IS, FUNCTION SLRANG
C          COMPUTES THE MAXIMUM. THIS IS CHECKED
C          AND IF EXCEEDED, THE INTEGRATION STOPS.
C
UPPER=SLFANG(HMX,JUP)
TATMTO = 0.0
TRANTO = 5.0
C
C          TRANSFER EXECUTION TO SUBROUTINE EMISON
C
SUBROUTINE EMISON CALLS ANOTHER

```

```

      ATOTL=AZ(IJ-I)-AZ(IJ-2)
      GO TO 127
129  RTOTL=AZ(I)-AZ(I-1)
      IJK=IJ-I-1
      IF(IJK.EQ.3) GO TO 131
      ATOTL=AZ(IJ-J)-AZ(IJK)
      GO TO 127
131  ATCTL=AZ(1)
127  TATM(I) = SECANT*T(I)*(RTOTL)*ATTEN
      TATMZ(I) =SECANT*(T(IJ-I))*(ATOTL)*ATTENZ
      TATMUP = TATMUP+TATMZ(I)
      TRANS(I) = EXP(-SECANT*AZ(I))
66  FOFMAT(5X,I5,5E15.4)
15  TATMTO = TATMTO+TATM(I)
16  TRANTO = TRANS(I-1)
      IF(TRANS(I).GE.3.995) TRANTO=TRANS(I-2)
      TTOTAL = TATMTO+(1.0-EMISS)*(TATMUP+2.6)*TRANTO
      TAPP = TRANTO*EMISS*TGS+TTOTAL
      TEX = TAPP - EMISS*TGS
159  ATWAT=WATER*SECANT*ANAP
      ATOZ = OXYGEN*SECANT*ANAP
      ATOTAL=TOTAL*SECANT*ANAP
      IF(SLHMX.LT.LPPER) GO TO 879
      SLHMX=SLHMX/SECANT
      WRITE(11,149) THETA(J),UPPER,SLHMX
149  FORMAT(1X,/,1X,'ANGLE ',F6.2,' SLANT RANGE ',F8.4
1    ,' EFFECTIVE HEIGHT ',F8.4)
879  IF(J.EQ.1) WRITE(6,33)
20  WRITE(6,30) THETA(J),ATWAT,ATOZ,ATOTAL,EMISS,TRANTO,TATMTO,
1    TATMUP,TEX,TAPP,TTOTAL
14  CONTINUE
3    FORMAT(1H0,5X,9X,' PRESS.',F10.4,5X,' TEMP ',
1    F10.2,5X,' RO ',F10.4,/,15X,' SURFACE TEMPERATURE ',F10.4)
22  FORMAT(/,/,14X,'ATTEN. COEFF.',4X,'ATTEN.(P20) ',4X,'ATTEN.(O2)')
30  FORMAT(1F3,F6.2,10F12.5)
33  FORMAT(1F3,'THETA',3X,'ATTEN(P20)',2X,'ATTEN(O2)'
1    ,7X,'TOTAL',6X,'EMISS',5X,'TRANSMIT',5X,'T(ATM)',6X,
2    'T(UPWARD)',4X,'T(EXCESS)',3X,'T(AFFAR)',3X,
3    'ATMOS.CCNT')
34  FORMAT(1H0,/,25X,' THE ATMOSPHERIC CONDITIONS ARE ',
1    /*THE SKY IS ',A6,' CLOUDY, PERCENTAGE COVER ',F6.2,
2    /*THE WATER CONTENT OF THE CLOUDS IS ',F6.2,' GMS/MM**3'
3    /*THE CIELING IS ',F6.2,' KMS AND THE THICKNESS'
4    ,' IS ',F6.2,' KMS',/*THE PRECIPITATION IS ',F6.2,
5    ' MM/HP')
44  FORMAT(19X,'HIGHT ',12X,' PRESS.',12X,' TEMP.',12X,' DENSITY' )
77  FORMAT(1X,I4,3F15.7)
70  FORMAT(1FL,3JX,1;A6,/,3JX,'U.S.STANDARD ATMOSPHERIC PRO.',/)
88  FCRMAT( 18,4F15.4)
125  CONTINUE
      IF(NN.LI. 2 ) GO TO 199
65  LOOP = J

```

```

C          PROGRAM (EMISV) TO COMPUTE THE
C          EMISSIVITY. EMISON RETURNS
C          THE TOTAL TRANSMITTANCE IN
C          EMISS. J, THE COMMAND ANGLE
C          NUMBER, MUST BE TRANSFERRED.
C          JFLAG IS THE SWITCH TO
C          NOTIFY THE ROUTINE TO READ
C          OR NOT READ IN NEW DATA.
C          NEW DATA MUST BE READ IN
C          EVERY TIME THIS MAINLINE
C          READS IN A NEW CARD.
C          EMISCN READS IN FIVE CARDS,
C          ONE FOR EVERY ANGLE.
C
C          FOR ARGUMENT LISTING AND FORMAT
C          INFORMATION, CHECK WITH
C          A.S. OR C.C.
C
C          JJ=J
C          SEE IF THE TARGET IS LAND OR OCEAN AND
C          CALL APPROPRIATE EMISSIVITY ROUTINE
C
C          IF (NTRGET.EQ.0) GO TO 91
C          CALL EMICCN (EMISS, JJ, JFLAG)
C          GO TO 92
91        CALL EMISCN (EMISS, JJ, JFLAG)
92        JFLAG = 0
C
C          COMPUTE TEMPERATURE CONTRIBUTIONS ETC
C
C          THE PARAMETERS USED IN THE FOLLOWING
C          CODING ARE:
C          SLHM--MAXIMUM SLANT RANGE
C          ATTN--ATTENUATION UPWARDS
C          ATTNZ--ATTENUATION DOWNWARDS
C          TATM--UPWELLING CONTRIBUTION OF ATMOS.
C          TATMUP--TOTAL RADIATION FROM ABOVE
C          TRANO--TRANSMISSION COEFFICIENT
C          TEX--EXCESS TEMPERATURE DUE TO ATMOS
C          TAPP--APPARENT TEMPERATURE AT ANTENNA
C          ATWAT--ATTENUATION DUE TO WATER
C          ATOZ--ATTENUATION DUE TO OXYGEN
C          ATOTAL--TOTAL ATTENUATION
C          2.6 DEGREES IS ADDED FOR COSMIC RADIATION
C
C          DO 15 I = 1, 20
C          SLHM=Z(I)*SECANT
C          IF (SLHM.GT.LPPER) GO TO 16
C          ATTN = EXP(-SECANT*(TOTAL-AZ(I))*0.1)
C          ATTNZ = EXP(-SECANT*(TOTAL-AZ(IJ-I))*0.1)
C          IF (I.NE.1) GO TO 129
C          RTOTL=AZ(I)
C
C          GO TO 199
C          END

```

ORIGINAL PAGE IS  
OF POOR QUALITY

```

CRAOIO          RADIOSONDF INPUT
C              THIS SUBROUTINE COMPUTES THE PRESSURE
C              TEMPERATURE,HUMIDITY FOR RADIOSONDF DATA
C              THE VALUE AT ANY HEIGHT IS FOUND BY
C              LINEAR INTERPOLATION BETWEEN BRACKETING
C              VALUES
C
C              SUBROUTINE RADIO(HT,PT,TT,P=0)
C              DIMENSION Q(15),ROD(15),ROV(15),ST(15), SAMPLE(10),
1  EA(20 ),T(15),P(15),H(15),C(15),TEMP(15),E(15)
C              COMMON NI,N,NC,SAMPLE,h,P,T,Q,NS
C              DATA EXD,CSP/34.146,0.34838/
C
C              *NC* IS THE OPTION SWITCH FOR GIVEN VALUES LIKE *HUMIDITY*,
C              *DEW POINT TEMP.* AND *DENSITY* *NC* CAN TAKE CONSECUTIVE VALU
C              FOR EACH OF THEM STARTING FROM 1 TO 3
C
C              READ THE PROFILE FROM FILE CODE NS
C              THERE SHOULD BE N VALUES FOR TEMP,
C              PRESSURE,AND HUMIDITY
C
C              READ(NS,77)((H(I),P(I),T(I),Q(I)),I=1,N)
77  FORMAT(4F8.4)
C              DO 12 I = 1,N
C
C              CHECK FOR TYPE OF INFORMATION FOR
C              WATER VAPOR, NC=1,RELATIVE HUMIDITY
C              NC=2,DEW POINT TEMP.,NC=3,SPECIFIC
C              HUMIDITY,NC=4 OR 0,GMS/M**3
C
C              IF(NC.EQ.0) NC=4
C              GO TO ( 9,10,11,12) , NC
C
C              CONVERT FROM RELATIVE HUMIDITY
C
C              9  T(I) = T(I) + 273.0
C              Q(I) = 216.5*VAPOR(T(I)-273.0)*Q(I)/T(I)
C              GO TO 12
C
C              CONVERT FROM DEW POINT TEMPERATURE
C
C              10 T(I) = T(I) + 273.0
C              IF (Q(I).NE.0.0) GO TO 19
C              Q(I) = Q(I-1)
C              GO TO 12
C              19 Q(I) = 216.5*VAPOR(Q(I) )/T(I)
C              GO TO 12
C
C              CONVERT FROM SPECIFIC HUMIDITY
C
C              11 Q(I) = Q(I)*0.001

```

```

      Q(I) = Q(I)*CSP*P(I)/T(I)*1000.0
12  CONTINUE
C
C          PRINT SAMPLE LABEL
C
      WRITE(6,41) NI ,( SAMPLE(M), M= 1,10)
C
C          HAVING READ THE DATA AND CONVERTED
C          TO THE PROGRAM REQUIREMENTS RETURN
C          AND AWAIT A CALL TO EXTRAP
C
      RETURN
C
CEXTRAP
C          THIS ENTRY POINT ALLOWS ONE TO GET
C          A LINEAR INTERPOLATION OF THE TRUE
C          (RADIOSONDE) VALUES AS READ IN BY
C          SUBROUTINE RADIO
C
      ENTRY EXTRAP
45  KK = NS
C
C          FIND THE TWO BRACKETING HEIGHTS OF
C          INPUT HEIGHT.
C
      DO 15 I = 1,N
      HI = H(I+1)
      HO = H(I)
      IF( HT.EQ.HO ) GO TO 65
      IF ((HT.GT.HO).AND.(HT.LT.HI)) GO TO 20
15  CONTINUE
      IF(I.EQ.N) GO TO 99
C
C          IF NO UPPER BOUND FOUND THEN
C          PRINT AN ERROR MESSAGE AND
C          RETURN LAST VALUE OF RADIOSONDE
C
C          OTHERWISE COMPUTE BY LINEAR INTER
C          POLATING AS DONE IN THE FOLLOWING
C          SECTION OF CODING
C
65  TT = T(I)
      PT = P(I)
      RHO = Q(I)
      GO TO 88
20  DT = (T(I)-T(I+1) )
      DH = (H(I) -H(I+1) )
      ST(I) = (DT/DH )
C
C          HAVING COMPUTED THE SLOPE COMPUTE
C          THE TEMPERATURE

```

C

```
C(I) = T(I)-(ST(I)*H(I))
TEMPZ = C(I)+(ST(I)*HT)
TT = TEMPZ
DT = (T(I)-TT)
DH = H(I) - HT
ST(I) = (DT/DH)
STH = ST(I)*H(I)
C(I) = T(I)-STH
TEMP(I) = C(I)+(ST(I)*HT)
TEMPZ = C(I)+(ST(I)*H(I))
TEMP(I) = (TEMP(I)/TEMPZ)
E(I)=(EXP/ST(I))*(-1.0)
IF (ABS(E(I)).GT. 38.0) GO TO 35
TEMP(I) = TEMP(I)**E(I)
PT = TEMP(I)*P(I)
GO TO 55
35 TEMP(I) =(ALOG(TEMP(I)))*E(I)
TEMP(I) = EXP( TEMP(I) )
PT = TEMP(I)*P(I)
55 DT = ALOG10(Q(I))-ALOG10(Q(I+1))
DH = (H(I) -H(I+1) )
ST(I)=(DT/DH)
C(I)= ST(I)*(HT-H0)+ALOG10(Q(I))
RHO = (10.0**C(I) )
GO TO 88
99 WRITE(6,42)
HT=H(I)
PT=P(I)
TT=T(I)
RHO=Q(I)
WRITE(6,22) H(I),P(I),T(I),C(I)
3 FORMAT(1F0,F5.0,5X,'HIGHT ',2X,F15.4,'PRESS.',2X,F10.3,' TEMP.',
1 5X,F10.2,5X,'RO ',F10.3)
22 FORMAT( 4F15.5,9X,' HIGHT, PRESSURE, TEMP. , HUMIDITY ' )
41 FORMAT(1F1,/,/,20X,'SAMPLE = ',I3, / / , 15X,8A6 // / )
42 FORMAT( 2X,'VALUES DO NOT LIE BETWEEN THE VAUES GIVEN' )
88 RETURN
END
```

C CLOUD

COUD ATTENUATION

C

SUBROUTINE CLOUD COMPUTES THE ATTENUATION

C

COEFFICIENT DUE TO CLOUDS, ACCORDING

C

TO BENOIT'S MODEL

C

```
SUBROUTINE CLOUD( ATTN,PRCN,GMS,T)
DATA B,FREQ/1.95,13.9/
ANAP=10.*ALOG10(EXP(1.0))
TT=T-273.3
AW=-6.866*(1.0+.0045*TT)
GNU=FREQ**B
ATTN=GMS*GNU*EXP(AW)
ATTN=ATTN/ANAP*0.10*PRCN
50 RETURN
END
```

```

CVAPOR                                V A P O R
C                                     RETURNS THE VAPOR PRESSURE FROM THE DEW POINT
C
C      FUNCTION VAPOR(T)
C
C                                     THE VAPOR PRESSURE OF WATER (OVER THE
C                                     ENTIRE LIQUID RANGE, 0 DEG C TO THE
C                                     CRITICAL TEMPERATURE 374.15 DEG C) CAN
C                                     BE REPRESENTED BY A POLYNOMIAL
C                                     APPROXIMATION DEVELOPED BY O. G.
C                                     BRIDGEMAN AND E. W. ALDRICH (TRAN. ASME,
C                                     J. HEAT TRANSFER SERIES C-D, 86, 279-286
C                                     (1964))
C
C      REAL K,L,M
C      DATA A,B,C,D,E,F,G,H,K,L,M/1.06423320,1.0137921,0.000583531,
*4.16385282,237.098157,0.30231574,0.003377565,1.152894,0.745794,
*654.2906,266.778/
C      X1=L/(T+M)
C      COSH=ALOG(X1+SQRT(X1*X1-1.))
C      Z=-1.87+3.74*(H-K*COSH)
C      ALPHA=Z*Z*(1.87*1.87-Z*Z)/F*(1.+G*T)
C      X=0.01*(T-187.)
C      Y2=((3.*SQRT(3.))/(2.*1.87*1.87*1.87))*(X-0.01*ALPHA)*(1.87*1.87-(
* X-0.01*ALPHA)**2)/100.
C      Y1=0*(T-187.)/(T+E)
C      VAPOR=(10.**((A+Y1-B*(1.+C*T)*Y2))*1013.3
C      RETURN
C      END

```

```

CRAIN                                  RAIN ATTENUATION
C                                     SUBROUTINE RAIN COMPUTES THE ATTENUATION
C                                     COEFFICIENT DUE TO RAIN ACCORDING TO
C                                     BENOIT'S RAIN MODEL
C
C      SUBROUTINE RAIN( ATRAIN,PPT)
C
C                                     TO EVALUATE THE ATTENUATION COEFF. DUE TO RAIN
C                                     CCIR RECOMMENDS THE USE OF FORMULA
C      A(P) = K(F,T) * PI ** ALFA(F)*R
C      PI = PRECIPITATION RATE IN MM./HR.
C      R = PATH LENGTH IN KM.
C
C      DATA A,B/0.026,1.18/
C      ANAP=10.*ALOG10(EXP(1.0))
C      ATRAIN=A*PPT**B
C      ATRAIN=ATRAIN/ANAP*0.1
C      RETURN
C      END

```

```

CEMIOGN                                OCEAN EMISSIVITY
C
C                                     A SIMPLE ROUTINE TO ESTIMATE EMISSIVITY OF
C                                     THE OCEAN SURFACE. IT ONLY PROVIDES BALL
C                                     PARK FIGURES, ACTUAL VALUES DEPEND UPON THE
C                                     WIND SPEED, TEMPERATURE, SALINITY ETC.
C
C      SUBROUTINE FMIOCN(EMISS,J,N)
C      DIMENSION HOR(5),VERT(5),JPOL(2)
C      DATA VERT,HOR/0.39,0.385,0.375,0.360,0.340,0.39,0.40,
1 0.425,0.45,0.504/
C      DATA JPOL/2H V,2H H/
C      IF(J.EQ.1) READ(5,1) IPOL
C      IF(J.EQ.1) WRITE(6,2) IPOL
C      FORMAT(1H0,20X,' POLARIZATION SELECTED ',A2,
2
1  FOPMAT(A2)
C      IF(IPOL.EQ.JPOL(1)) GO TO 10
C      EMISS=HOR(J)
C      RETURN
C      EMISS=VERT(J)
10
C      RETURN
C      END

```

ORIGINAL PAGE IS  
OF POOR QUALITY

```

CEMISON          BARE SOIL EMISSIVITY
SUBROUTINE FMISON (FMISS,J,N)
DIMENSION EPSILS(9),SOIL(9),IT(?),IP(2)
DIMENSION THETA(5),ITYP(5),IPOL(5),VEG(5),SOILMO(5)
DATA IT/4HSAND,4HLOAM/
DATA IP /2HHH,2HVV/
DATA THETA /48.,42.1,29.4,15.6,0./

C
C          THIS ROUTINE READS IN FROM DATA CARDS
C          THE INCIDENCE ANGLE,SOIL TYPE,PCLARIZATION,
C          PER CENT VEGETATION,AND SCIL MOISTURE.
C
C          THETA    INCIDENCE ANGLE OF ANTENNA (DEGREES)
C          SOIL TYPE      1 = SAND , 2 = LOAM
C          POLARIZATION   1 = H  , 2 = V
C          PER CENT VEGETATION BETWEEN ZERO AND ONE
C          SOIL MOISTURE  MUST BE ONE OF THE FOLLOWING
C
DATA SOIL/0.,2.5,5.,7.5,10.,12.5,15.,17.5,20./

C
C          THIS ROUTINE CALL PERCYOS EMISV
C          PROGRAM THAT RETURNS NINE ANSWERS. THIS
C          PROGRAM SELECTS THE RIGHT ONE ACCORDING
C          TO SOIL MOISTURE.
C
I=0
IF (N.LT.1) GO TO 7
DO 8 K=1,5
8  READ (5,1) ITYPE(K),IPOL(K),VEG(K),SOILMO(K)
1  FOPMAT(2I2,F4.2,F5.2)
7  CALL EMISV (THETA(J),ITYPE(J),IPOL(J),EPSILS)
2  I=I+1
   IF(I.GT.9) CALL ABOFT(2HCC)
   IF(ABS (SOIL(I)-SOILMO(J)).GT.0.5) GO TO 2
   EMISS=EPSILS(I)*(1,-VEG(J)) + 0.9*VEG(J)

C
C          EMISV REURNS THE EMISSIVITY OF BARE
C          SOIL. THE EMISSIVITY OF VEGETATION IS
C          ASSUMED TO BE 0.9
C
IF(J.NE.1) GO TO 10
WRITE(6,4)
4  FORMAT(//20X,'THE GROUND CONDITIONS ARE ',//)
WRITE (6,5) IT(ITYPE(J)),100.*VEG(J),SOILMO(J)
5  FORMAT(5X,A4,5X,F6.2,' PER CENT VEGETATION',10X,
*      F6.2,' SOIL MOISTURE'//)
WRITE (6,6) THETA(J),IP(IPOL(J))
6  FORMAT(' INCIDENCE ANGLE IS',F6.2,5X,' POLARIZATION ',A6)
10  RETURN
END

```

```

CEMISV          EMISSIVITY DRIVER
SUBROUTINE EMISV COMPUTES THE EMISSIVITY
OF A SOIL (SAND OR LOAM) FOR POL. H AND V
C
SUBROUTINE EMISV(THETA,ITYPE,IPOL,EPSILS)
DIMENSION EPSILS(9),XK1(9,2),XK2(9,2)
DATA ((XK1(I,J),I=1,9),J=1,2)/3.0,3.5,4.6,6.3,8.7,10.6,12.5,13.6
$,14.8,4.0,4.2,4.8,5.3,6.9,9.5,12.0,14.2,17.5/
DATA ((XK2(I,J),I=1,9),J=1,2)/0.0,0.3,0.8,1.7,2.4,3.2,4.3,5.2,
$,6.0,0.0,0.5,1.0,1.7,2.7,3.6,4.9,5.7,6.8/
THETA1=3.1416*THETA/180.
NMOIST=9
IF(IPOL.EQ.1) CALL IPOLHH(THETA1,XK1,XK2,ITYPE,NMOIST,EPSILS)
IF(IPOL.EQ.2) CALL IPOLVV(THETA1,XK1,XK2,ITYPE,NMOIST,EPSILS)
RETURN
END

```

```

CIPOLHH                EMISSIVITY FOR POL HCR.
C                      SUBROUTINE IPOLHH COMPUTES THE EMISSIVITY
C                      FOR POLARIZATION H
C
SUBROUTINE IPOLHH(THETA1, XK1,XK2,ITYPE,NMOIST,EPSILS)
DIMENSION XK1(9,2),XK2(9,2),EPSILS(1)
XMU=COS(THETA1)
DO 1 I=1,NMOIST
P1=XK1(I,ITYPE)+XMU*XMU-1.
P2=SQRT((XK1(I,ITYPE)+XMU*XMU-1.)**2+XK2(I,ITYPE)**2)
P=SQRT((P1+P2)/2.)
Q=SQRT((P2-P1)/2.)
A=(P-XMU)**2+Q*Q
B=(P+XMU)**2+Q*Q
EPSILS(I)=1.-A/B
1 CONTINUE
RETURN
END

```

```

CIPOLVV                EMISSIVITY FOR POL VERT.
C                      SUBROUTINE IPOLVV COMPUTES THE EMISSIVITY
C                      OF THE SOIL FOR POLARIZATION H
C
SUBROUTINE IPOLVV(THETA1, XK1,XK2,ITYPE,NMOIST,EPSILS)
DIMENSION XK1(9,2),XK2(9,2),EPSILS(1)
XMU=COS(THETA1)
DO 1 I=1,NMOIST
P1=XK1(I,ITYPE)+XMU*XMU-1.
P2=SQRT((XK1(I,ITYPE)+XMU*XMU-1.)**2+XK2(I,ITYPE)**2)
P=SQRT((P1+P2)/2.)
Q=SQRT((P2-P1)/2.)
A=(XMU*XK1(I,ITYPE)-P)**2+(XMU*XK2(I,ITYPE)-Q)**2
B=(XMU*XK1(I,ITYPE)+P)**2+(XMU*XK2(I,ITYPE)+Q)**2
EPSILS(I)=1.-A/B
1 CONTINUE
RETURN
END

```

```

CSLRANG                FUNCTION SLRANG
C                      THIS FUNCTION COMPUTES THE SLANT RANGE
C                      INCLUSIVE OF EARTH'S CURVATURE
C
FUNCTION SLRANG(H,J)
DIMENSION AI(5)
DATA AI/0.1,15.6,29.4,40.1,48.0/
E = 6373.0
Q = AI(J)/57.2958
C = COS(Q)
S = SIN(Q)
R = (E+H)*C-SQRT(((E*C)*(E*C))-2*E*H*S*S-(H*S*H*S) )

```

## **CRINC LABORATORIES**

**Chemical Engineering Low Temperature Laboratory**

**Remote Sensing Laboratory**

**Flight Research Laboratory**

**Chemical Engineering Heat Transfer Laboratory**

**Nuclear Engineering Laboratory**

**Environmental Health Engineering Laboratory**

**Information Processing Laboratory**

**Water Resources Institute**

**Technical Transfer Laboratory**

**Air Pollution Laboratory**

**Satellite Applications Laboratory**

---

**CRINC**

